On Using Multiple Modes to Reconstruct Conductor Locations in a Power Transformer Winding

M. Dalarsson, A. Motevasselian, and M. Norgren
Division of Electromagnetic Engineering, School of Electrical Engineering
Royal Institute of Technology, Stockholm SE-100 44, Sweden

Abstract— An initial study of a novel method to diagnose the effects of the various degradation mechanisms on the power transformers, while in operation, is presented. We model a transformer winding surrounded by the transformer-tank wall and the magnetic core as a two-dimensional parallel plate waveguide, where one plate represents the wall of the transformer tank and the other plate represents the iron core that conducts the magnetic flux. In between there is a set of parallel conductors representing the winding segments. The new principle is to insert antennas inside the transformer tank to radiate and measure microwave fields that interact with the metallic structure and the insulation. The responses from the radiated waves are assumed to be sensitive to material properties that reflect any harmful deterioration processes. In particular, we study the mechanical deformations of the transformer winding by determining the locations of the individual conductors, from measurements of the scattered fields at both ends. The propagation problem is solved accurately and efficiently by conventional waveguide theory, including mode-matching and cascading techniques. We employ optimization as a suitable method to solve the inverse problem and obtain a good agreement between the calculated and measured positions of winding segments.

1. INTRODUCTION

The power transformer is one of the most critical components in the electric power grid and a failure may result in major consequences for the power supply ability of the grid. While in operation, power transformers are subject to several degradation mechanisms, e.g., thermal degradation at hot spots, partial discharges due to local electric field surges, winding deformations caused by mechanical forces from short circuit currents, and increased levels of moisture in the cellulose insulation due to decomposition [1–3].

In this paper we investigate a proposed new principle to diagnose power transformers while in operation. The existing diagnostics consists of either the coarse methods or off-line methods that require disconnection from the grid, and they imply a non-service stress of a transformer [3–7]. The idea of the present approach is to insert antennas inside the transformer tank to radiate and measure microwave fields that interact with the metallic structure and the insulation. The responses from the radiated waves are expected to be sensitive to material properties that reflect the effects of the above mentioned degradation mechanisms. The analysis of the measured signals and their complex relations to the material and structure parameters, being the critical signatures of deterioration, is an inverse electromagnetic problem [8] that requires development of advanced algorithms.

We model a transformer as a two-dimensional parallel plate waveguide where one plate represents the wall of the transformer tank and the other plate represents the iron core that conducts the magnetic flux. In between there is a set of parallel conductors representing the winding segments. The propagation problem is solved accurately and efficiently by conventional waveguide theory, including mode-matching and cascading techniques [9].

We use optimization as a suitable method for solving the inverse problem. From a parametric study of the optimization function, we have found that wide band data may stabilize the reconstructions and that the information from multiple modes is likely to decrease the occurrence of local minima. Hence, it is important that several waveguide modes can be transmitted and received with high accuracy, which implies that many antennas (i.e., ports) are needed in the measurement system.

2. PROBLEM FORMULATION

The geometry of our model of a transformer as a two-dimensional parallel plate waveguide, where one plate represents the wall of the transformer tank and the other plate represents the iron core that conducts the magnetic flux, is shown in Fig. 1. We denote the four regions (1–4) between the plates and the conductive obstacle as indicated in Fig. 1.
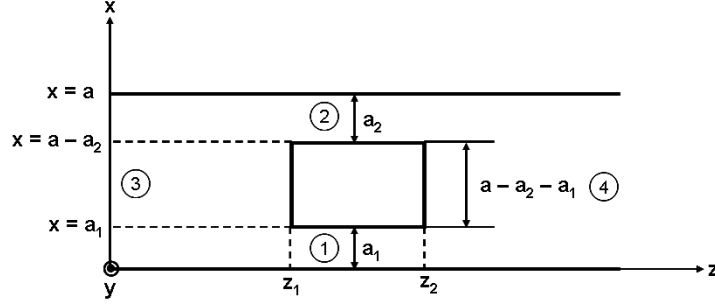
Figure 1: Two-dimensional parallel-plate waveguide as a model of a transformer winding.

For the propagation problem we only consider TM-modes ($\mathbf{H} = H_y \mathbf{e}_y$), motivated by that their dominant mode is the TEM-mode, which propagates at all frequencies. The basis functions in the regions 1 (below the conductive obstacle) and 2 (above the conductive obstacle), are then given by

$$\psi_n^{(1)}(x) = \sqrt{\frac{2 - \delta_{n,0}}{a_1}} \cos\left(\frac{n\pi x}{a_1}\right), \quad \psi_n^{(2)}(x) = \sqrt{\frac{2 - \delta_{n,0}}{a_2}} \cos\left[\frac{n\pi}{a_2}(a - x)\right], \tag{1}$$

while in the regions 3 and 4, with no obstacle present, the basis functions are equal to each other and given by

$$\psi_n^{(3)}(x) = \psi_n^{(4)}(x) = \sqrt{\frac{2 - \delta_{n,0}}{a}} \cos\left(\frac{n\pi x}{a}\right). \tag{2}$$

Let us now use the definition of the wave vector γ_n, i.e., $\gamma_n^2 = \omega^2 \mu \epsilon - k_{zn}^2$, where we denote the longitudinal wave vector for the n-th mode by k_{zn}, and we use the usual notation $k^2 = \omega^2 \mu \epsilon$. Thus the longitudinal wave vector k_{zn} and the TM$_n$-mode [10] impedances for the four regions ($i = 1, 2, 3, 4$) are given by

$$k_{zn}^2 = \omega^2 \mu \epsilon - \gamma_n^2 = k^2 - \left(\frac{n\pi x}{a}\right)^2, \quad Z_n^{(i)} = \frac{k_{zn}^{(i)}}{k} \eta, \quad \eta = \sqrt{\frac{\mu}{\epsilon}}. \tag{3}$$

The transverse electric fields $E_{xn}^{(i)}$ and magnetic fields $H_{yn}^{(i)}$ are linear combinations of the basis functions $\psi_n^{(i)}(x)$ for the respective region. For waves propagating in positive z-direction $\left(e^{-ik_z z}\right)$, we have the relationship between the fields $E_{xn}^{(i)} = Z_n^{(i)} H_{yn}^{(i)}$, for each mode and each region. The transverse fields can then be expanded, in terms of the basis functions, as follows:

$$E_x^{(i)}(x, z) = \sum_{n=0}^{\infty} \left[c_n^{(i)+}(z) + c_n^{(i)-}(z)\right] Z_n^{(i)} \psi_n^{(i)}(x), \tag{4}$$

$$H_y^{(i)}(x, z) = \sum_{n=0}^{\infty} \left[c_n^{(i)+}(z) - c_n^{(i)-}(z)\right] \psi_n^{(i)}(x). \tag{5}$$

Now we need to consider the boundary conditions at the planes $z = z_1$ and $z = z_2$. First, we have the continuity of the transverse electric field component E_x over the entire surface, where $\mathbf{E} = \mathbf{0}$ inside the conductive material yields that E_x vanishes at the metallic part of the boundary. The second condition is that H_y must be continuous over the aperture parts of the surface. In Equations (4) and (5), the sum is performed over all modes ($0 \le n \le \infty$), but in the numerical implementation each summation is reduced from ∞ to a maximum mode number N_i ($i = 1, 2, 3, 4$). Thus, with a finite number of modes ($0 \le n_i \le N_i$), the boundary conditions result in six matrix equations:

$$\mathbf{D}_{(3)}\left[\mathbf{c}_{(3)}^+(z_1) + \mathbf{c}_{(3)}^-(z_1)\right] = \mathbf{K}_{(1,3)}^T \left[\mathbf{c}_{(1)}^+(z_1) + \mathbf{c}_{(1)}^-(z_1)\right] + \mathbf{K}_{(2,3)}^T \left[\mathbf{c}_{(2)}^+(z_1) + \mathbf{c}_{(2)}^-(z_1)\right] \tag{6}$$

$$\mathbf{D}_{(1)}\left[\mathbf{c}_{(1)}^+(z_1) - \mathbf{c}_{(1)}^-(z_1)\right] = \mathbf{K}_{(1,3)} \left[\mathbf{c}_{(3)}^+(z_1) - \mathbf{c}_{(3)}^-(z_1)\right] \tag{7}$$

$$\mathbf{D}_{(2)}\left[\mathbf{c}_{(2)}^+(z_1) - \mathbf{c}_{(2)}^-(z_1)\right] = \mathbf{K}_{(2,3)} \left[\mathbf{c}_{(3)}^+(z_1) - \mathbf{c}_{(3)}^-(z_1)\right] \tag{8}$$

$$\mathbf{D}_{(4)}\left[\mathbf{c}_{(4)}^{+}(z_2) + \mathbf{c}_{(4)}^{-}(z_2)\right] = \mathbf{K}_{(1,4)}^{T}\left[\mathbf{c}_{(1)}^{+}(z_2) + \mathbf{c}_{(1)}^{-}(z_2)\right] + \mathbf{K}_{(2,4)}^{T}\left[\mathbf{c}_{(2)}^{+}(z_2) + \mathbf{c}_{(2)}^{-}(z_2)\right] \tag{9}$$

$$\mathbf{D}_{(1)}\left[\mathbf{c}_{(1)}^{+}(z_2) - \mathbf{c}_{(1)}^{-}(z_2)\right] = \mathbf{K}_{(1,4)}\left[\mathbf{c}_{(4)}^{+}(z_2) - \mathbf{c}_{(4)}^{-}(z_2)\right] \tag{10}$$

$$\mathbf{D}_{(2)}\left[\mathbf{c}_{(2)}^{+}(z_2) - \mathbf{c}_{(2)}^{-}(z_2)\right] = \mathbf{K}_{(2,4)}\left[\mathbf{c}_{(4)}^{+}(z_2) - \mathbf{c}_{(4)}^{-}(z_2)\right] \tag{11}$$

where the vectors $\mathbf{c}_{(i)}^{\pm}(z)$ are defined by

$$\mathbf{c}_{(i)}^{\pm}(z) = \begin{bmatrix} c_1^{(i)\pm}(z) & c_2^{(i)\pm}(z) & \dots & c_{N_i}^{(i)\pm}(z) \end{bmatrix}^{T}, \quad i = 1,2,3,4. \tag{12}$$

The mode impedances in the four regions are collected into four diagonal impedance matrices as follows:

$$\mathbf{D}_{(i)} = \operatorname{diag}\left\{ Z_n^{(i)} \right\}_{n=0}^{N_i}. \tag{13}$$

The mode coupling matrix elements and their respective transposed counterparts are given by

$$K_{(i,j)n_i,n_j} = Z_{n_i}^{(i)}\langle \psi_{n_i}^{(i)}(x)|\psi_{n_j}^{(j)}(x)\rangle_i, \quad K_{(i,j)n_i,n_j}^{T} = Z_{n_i}^{(i)}\langle \psi_{n_j}^{(j)}(x)|\psi_{n_i}^{(i)}(x)\rangle_i. \tag{14}$$

They are collected into the mode coupling $\mathbf{K}_{(i,j)}$-matrices, where

$$n_i = 0,1,2,\dots,N_i, \quad n_j = 0,1,2,\dots,N_j, \quad i = 1,2, \quad j = 3,4. \tag{15}$$

The definitions (15) indicate that any of the regions $i = 1,2$ couples to any of the regions $j = 3,4$. On the other hand there is no coupling between regions 1 and 2 or between regions 3 and 4 respectively. The matrix elements $\langle \psi_{n_i}^{(i)}(x)|\psi_{n_j}^{(j)}(x)\rangle_i$ are calculated using the definition formula

$$\langle \psi_{n_i}^{(i)}(x)|\psi_{n_j}^{(j)}(x)\rangle_i = \int_{I_i} \psi_{n_i}^{(i)}(x)\,\psi_{n_j}^{(j)}(x)\,dx, \tag{16}$$

where I_i denotes the interval of integration for each of the regions. For example for the region 1, we have $I_1 = [0, a_1]$. The propagation equations for different nodes and regions are summarized into the following matrix equation:

$$\mathbf{c}_{(i)}^{\pm}(z_2) = \mathbf{P}_{(i)}^{\pm}(\Delta z)\mathbf{c}_{(i)}^{\pm}(z_1) = \mathbf{P}_{(i)}^{\pm}(z_2 - z_1)\mathbf{c}_{(i)}^{\pm}(z_1), \quad i = 1,2,3,4, \tag{17}$$

where we introduce the following diagonal matrix:

$$\mathbf{P}_{(i)}^{\pm}(z_2 - z_1) = \operatorname{diag}\left\{ \exp\left[\mp j k_{zn}^{i}(z_2 - z_1)\right] \right\}_{n=0}^{N_i}, \quad i = 1,2,3,4. \tag{18}$$

3. SCATTERING ANALYSIS

Let us now consider the scattering of TM_n waves from the conductive obstacle depicted in Fig. 1 above. From the geometry of the problem we see that it is convenient to use the same number of modes at each side of the conductive obstacle, i.e., in the regions 3 and 4. Thus we assume that $N_3 = N_4 = N_0$. Hence, we can write

$$\mathbf{D}_{(3)} = \mathbf{D}_{(4)} = \mathbf{D}_{(0)}, \quad \mathbf{K}_{(1,3)} = \mathbf{K}_{(1,4)} = \mathbf{K}_{(1)}, \quad \mathbf{K}_{(2,3)} = \mathbf{K}_{(2,4)} = \mathbf{K}_{(2)} \tag{19}$$

Furthermore, in the regions 1 and 2, we can define the shorthand notation

$$\mathbf{P}_{(1)} = \mathbf{P}_{(1)}^{+}(z_2 - z_1) = \mathbf{P}_{(1)}^{-}(z_1 - z_2), \quad \mathbf{P}_{(2)} = \mathbf{P}_{(2)}^{+}(z_2 - z_1) = \mathbf{P}_{(2)}^{-}(z_1 - z_2). \tag{20}$$

With the above notations, we obtain after some straightforward matrix algebra

$$\begin{bmatrix} \mathbf{c}_{(3)}^{-}(z_1) \\ \mathbf{c}_{(4)}^{+}(z_2) \end{bmatrix} = \mathbf{S}' \begin{bmatrix} \mathbf{c}_{(3)}^{+}(z_1) \\ \mathbf{c}_{(4)}^{-}(z_2) \end{bmatrix} = \begin{bmatrix} \mathbf{S}'_{11} & \mathbf{S}'_{12} \\ \mathbf{S}'_{21} & \mathbf{S}'_{22} \end{bmatrix} \begin{bmatrix} \mathbf{c}_{(3)}^{+}(z_1) \\ \mathbf{c}_{(4)}^{-}(z_2) \end{bmatrix}, \tag{21}$$

with

$$\mathbf{S}' = \begin{bmatrix} \mathbf{D}_{(0)} + \mathbf{M} & \mathbf{N} \\ \mathbf{N} & \mathbf{D}_{(0)} + \mathbf{M} \end{bmatrix}^{-1} \times \begin{bmatrix} \mathbf{D}_{(0)} - \mathbf{M} & -\mathbf{N} \\ -\mathbf{N} & \mathbf{D}_{(0)} - \mathbf{M} \end{bmatrix}, \tag{22}$$

where

$$\mathbf{M} = \mathbf{K}_{(1)}^T \mathbf{A}_{(1)} + \mathbf{K}_{(1)}^T \mathbf{P}_{(1)} \mathbf{B}_{(1)} + \mathbf{K}_{(2)}^T \mathbf{A}_{(2)} + \mathbf{K}_{(2)}^T \mathbf{P}_{(2)} \mathbf{B}_{(2)}, \tag{23}$$

$$\mathbf{N} = \mathbf{K}_{(1)}^T \mathbf{B}_{(1)} + \mathbf{K}_{(1)}^T \mathbf{P}_{(1)} \mathbf{A}_{(1)} + \mathbf{K}_{(2)}^T \mathbf{B}_{(2)} + \mathbf{K}_{(2)}^T \mathbf{P}_{(2)} \mathbf{A}_{(2)}, \tag{24}$$

with

$$\mathbf{A}_{(1)} = \left(\mathbf{I} - \mathbf{P}_{(1)}^2\right)^{-1} \mathbf{D}_{(1)}^{-1} \mathbf{K}_{(1)}, \quad \mathbf{B}_{(1)} = \left(\mathbf{I} - \mathbf{P}_{(1)}^2\right)^{-1} \mathbf{P}_{(1)} \mathbf{D}_{(1)}^{-1} \mathbf{K}_{(1)}. \tag{25}$$

This scattering Equation (21) describes the propagation over the metal obstacle (from z_1 to z_2). Since the conductor is immersed in a "cell" extending from z_L ($< z_1$) to z_R ($> z_2$), we need to find the scattering matrix for the propagation over the entire "cell", that is from z_L to z_R. In order to do that, we introduce the matrices

$$\mathbf{P}_\mathrm{L} = \mathbf{P}_{(0)}^+(z_1 - z_\mathrm{L}), \quad \mathbf{P}_\mathrm{R} = \mathbf{P}_{(0)}^+(z_\mathrm{R} - z_2). \tag{26}$$

Using these matrices, we readily obtain

$$\begin{bmatrix} \mathbf{c}^-(z_\mathrm{L}) \\ \mathbf{c}^+(z_\mathrm{R}) \end{bmatrix} = \mathbf{S} \begin{bmatrix} \mathbf{c}^+(z_\mathrm{L}) \\ \mathbf{c}^-(z_\mathrm{R}) \end{bmatrix} = \begin{bmatrix} \mathbf{S}_{11} & \mathbf{S}_{12} \\ \mathbf{S}_{21} & \mathbf{S}_{22} \end{bmatrix} \begin{bmatrix} \mathbf{c}^+(z_\mathrm{L}) \\ \mathbf{c}^-(z_\mathrm{R}) \end{bmatrix}, \tag{27}$$

where we obtain the complete scattering matrix elements for propagation over the entire "cell", i.e., from z_L to z_R, in the form

$$\mathbf{S}_{11} = \mathbf{P}_\mathrm{L} \mathbf{S}'_{11} \mathbf{P}_\mathrm{L}, \quad \mathbf{S}_{12} = \mathbf{P}_\mathrm{L} \mathbf{S}'_{12} \mathbf{P}_\mathrm{R}, \quad \mathbf{S}_{21} = \mathbf{P}_\mathrm{R} \mathbf{S}'_{21} \mathbf{P}_\mathrm{L}, \quad \mathbf{S}_{22} = \mathbf{P}_\mathrm{R} \mathbf{S}'_{22} \mathbf{P}_\mathrm{R}. \tag{28}$$

The cascading of one cell denoted by a, with scattering matrix $\mathbf{S}^a$ and situated in the interval $z_1 \leq z \leq z_2$, with a neighboring cell denoted by b, with scattering matrix $\mathbf{S}^b$ and situated in the interval $z_2 \leq z \leq z_3$, gives the following scattering equation:

$$\begin{bmatrix} \mathbf{c}^-(z_1) \\ \mathbf{c}^+(z_3) \end{bmatrix} = \mathbf{S}^c \begin{bmatrix} \mathbf{c}^+(z_1) \\ \mathbf{c}^-(z_3) \end{bmatrix} = \begin{bmatrix} \mathbf{S}_{11}^c & \mathbf{S}_{12}^c \\ \mathbf{S}_{21}^c & \mathbf{S}_{22}^c \end{bmatrix} \begin{bmatrix} \mathbf{c}^+(z_1) \\ \mathbf{c}^-(z_3) \end{bmatrix}, \tag{29}$$

where

$$\mathbf{S}_{11}^c = \mathbf{S}_{11}^a + \mathbf{S}_{12}^a (\mathbf{I} - \mathbf{S}_{11}^b \mathbf{S}_{22}^a)^{-1} \mathbf{S}_{11}^b \mathbf{S}_{21}^a \tag{30}$$

$$\mathbf{S}_{12}^c = \mathbf{S}_{12}^a (\mathbf{I} - \mathbf{S}_{11}^b \mathbf{S}_{22}^a)^{-1} \mathbf{S}_{12}^b \tag{31}$$

$$\mathbf{S}_{21}^c = \mathbf{S}_{21}^b (\mathbf{I} - \mathbf{S}_{22}^a \mathbf{S}_{11}^b)^{-1} \mathbf{S}_{21}^a \tag{32}$$

$$\mathbf{S}_{22}^c = \mathbf{S}_{22}^b + \mathbf{S}_{21}^b (\mathbf{I} - \mathbf{S}_{22}^a \mathbf{S}_{11}^b)^{-1} \mathbf{S}_{22}^a \mathbf{S}_{12}^b \tag{33}$$

Using the cascading formula (29), it is possible to cascade together any number of cells by iteration.

4. RESULTS AND DISCUSSION

The computer simulation geometry of our two-dimensional transformer winding model is shown in Fig. 2. The transformer is modeled as a two-dimensional parallel plate waveguide, where the upper plate represents the wall of the transformer tank and the lower plate represents the iron core that conducts the magnetic flux. Since at this stage we are mainly concerned with investigating the principle, the chosen dimensions are not supposed to mimic any particular real transformer.

The inverse problem to determine the studied parameters $\mathbf{x} = (x_1, x_2, \ldots, x_n)$ is based on minimizing the optimization function J, defined by

$$J(\mathbf{x}) = \sum_{i,j} \left| \mathbf{S}_{ij}^{\mathrm{calc}}(\mathbf{x}) - \mathbf{S}_{ij}^{\mathrm{meas}} \right|^2, \tag{34}$$

where $\mathbf{S}_{ij}^{\text{calc}}(\mathbf{x})$ are the elements of the calculated scattering matrix and $\mathbf{S}_{ij}^{\text{meas}}$ are the corresponding elements of the measured scattering matrix. In the present paper the studied parameters are the vertical positions of the winding segments. Two graphs of the optimization function J are shown in Figs. 3 and 4. These graphs are obtained when the middle conductor (see Fig. 2) is moved in the vertical direction. However, similar results are obtained when we move any other of the conductors in the vertical direction. The global minimum (here zero, due to the perfect model) is attained at the correct position of the middle conductor. It should be noted that our simulations are performed in the presence of blurred-noisy data which amounts to 10–20 percent of of the mean value of $\mathbf{S}$. The scattering matrix is calculated in the frequency range $2\,\text{MHz} \leq f \leq f_{\text{max}}$ in steps of $2\,\text{MHz}$ up to the maximum frequencies $f_{\text{max}} = 150\,\text{MHz}$ (blue line), $f_{\text{max}} = 300\,\text{MHz}$ (green line) and $f_{\text{max}} = 400\,\text{MHz}$ (red line). The graph in Fig. 3 is obtained when the scattering data are obtained from the dominant (TEM=TM_0) mode only. The graph in Fig. 4 is obtained using the dominant mode, the first higher mode (starting to propagate at $f = 150\,\text{MHz}$) and the second higher mode (starting to propagate at $f = 300\,\text{MHz}$). The blue curves in both graphs are identical, since in that case only the dominant mode propagates in the waveguide model.

In Figs. 3 and 4 we see that as we expand the frequency region upward, the global minimum becomes narrower, which means reduced sensitivity to measurement errors. Comparing the two graphs, we also see that if scattering data is retrieved from all modes which can propagate in the frequency area (Fig. 4) rather than just the dominant mode (Fig. 3) the number of local minima of the J function is substantially reduced. In both cases, local minima occur some distance away from the global minimum. Thus a good initial guess, which lies in the global well can make a local optimization method converge towards the global minimum.

The results of the one-parameter study were encouraging enough to proceed to develop an algorithm to minimize $J(\mathbf{x})$ with respect to variation of all the conductor locations instead of just one. The multi-parameter algorithm is developed for only *one frequency at a time*. As single frequencies, used in the present analysis, we have chosen frequencies in the upper end of the frequency range, notably $f = 150\,\text{MHz}$ and $f = 250\,\text{MHz}$. Despite the proven advantages of expanding the algorithm to sweep over a wide band of frequencies, we limit the present analysis to one frequency at the time, in order to limit the computation time.

In order to minimize $J(\mathbf{x})$ with respect to variation of multiple conductor locations, we use a modified steepest-descent optimization method where we first compute the gradient of J, and then seek a minimum of the function by stepping from an initial guess x_0 in the direction of the negative of the gradient. The developed method is programmed to be quasi-genetic, so that if the number of iterations is exceeded and the gradient of J hasn't reached a value near zero, the algorithm restarts itself with a new initial guess. All restarts are saved, and the one with the lowest J-value is printed. Our optimization algorithm is similar to the memetic algorithm presented in [11]. As explained above, we employ an iteration procedure that vaguely resembles the iteration procedure of the
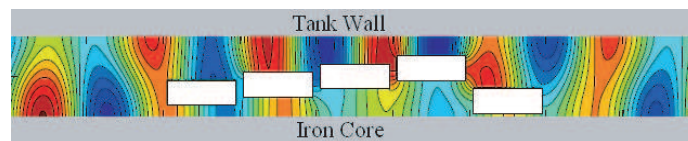

Figure 2: The computer simulation geometry with a distance between the tank wall and iron core $a = 1\,\text{m}$ and five winding segments each of length $\Delta z = 1\,\text{m}$. The colors indicate the magnitude of the resulting magnetic field when the dominant TEM-mode of frequency $f = 200\,\text{MHz}$ is incident from the left.
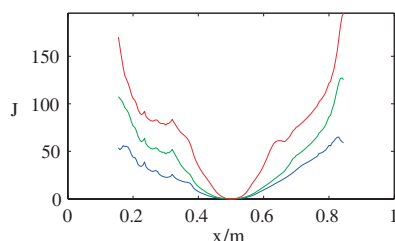

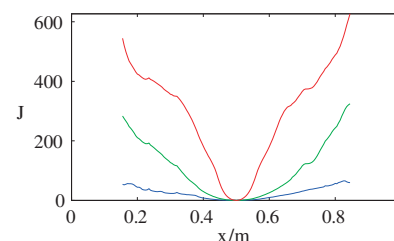Figure 3: Optimization functions with the dominant (TEM) mode only.

Figure 4: Optimization functions including the first three modes.

Table 1: Recreation of 5 cell positions, with 20% offset.

Conductor	1	2	3	4	5
True $\mathbf{x}$ value	0.3000	0.4000	0.5000	0.6000	0.2000
Computed $\mathbf{x}$ value	0.2994	0.3985	0.5028	0.5979	0.2000

Table 2: Recreation of 10 cell positions, with 10% offset.

Conductor	1	2	3	4	5	6	7	8	9	10
True $\mathbf{x}$ value	0.3000	0.4000	0.5000	0.6000	0.2000	0.3000	0.7000	0.6000	0.5000	0.7000
Computed $\mathbf{x}$ value	0.3024	0.3935	0.4941	0.6019	0.1996	0.2986	0.7056	0.6106	0.4972	0.6994

Table 3: Recreation of 5 cells in Fig. 1, using HFSS data at $f = 250\,\text{MHz}$.

Conductor	1	2	3	4	5
True $\mathbf{x}$ value	0.3000	0.4000	0.5000	0.6000	0.2000
Computed $\mathbf{x}$ value	0.2627	0.4382	0.5354	0.6101	0.1943

memetic algorithm shown in Fig. 2. in [11]. However, in comparison to the memetic algorithm of [11], our optimization algorithm is a simpler and less structured quasi-genetic algorithm.

In Table 1, results for recreating the positions of the 5 cells in Fig. 2 are shown. The three lowest modes are used at $f = 150\,\text{MHz}$. In the optimization model, a partially randomized offset matrix has been added to S, corresponding to about 20% of the mean value of S.

The model can in general handle any number of conductor cells. In Table 2, a simulation of ten cells is shown. The three lowest modes are used at $f = 150\,\text{MHz}$ and the added offset is 10% of the mean value of S. Although the results obtained for ten cells are relatively accurate, we note that as the cell number increases, it is likely that more modes and a wider frequency band are needed to ensure a good optimization accuracy.

The optimization model is also tested by comparing our calculated scattering data with the synthetic measurement data from the commercial program HFSS. The S-parameters are determined directly using HFSS by defining two ports at the two sides of the waveguide. The three lowest modes are used and a frequency band of $10\,\text{MHz}$ to $300\,\text{MHz}$ in steps of $10\,\text{MHz}$ is swept. The accuracy is increased as much as possible while the simulation is time efficient, such that the numerical errors are small. The results of the comparison of our calculated scattering data with the HFSS synthetic measurement data, for $f = 250\,\text{MHz}$, are shown in Table 3.

The present optimization method is very sensitive to the choice of the initial guess and it easily stops at the local minima. The randomized initial guess x_0 sometimes reproduces very good results, but sometimes it does not. Therefore, the present algorithm needs to be improved, such that the genetic search bases the next initial guess depending on the success of the previous. Alternatively, other efficient optimization methods can be considered to improve efficiency and accuracy of the calculations (e.g., the method of conjugate gradients based on the quadratic polynomial fit of J etc.). Furthermore, the difficulties experienced in performing the multi-parameter algorithm with HFSS-data may also be a consequence of the fact that we run the algorithm with one frequency at the time, as discussed above. The sensitivity analysis indicates that expanding the algorithm to sweep over a wide band of frequencies may be a way to remedy these difficulties.

Generally speaking, the optimization techniques may be classified into deterministic and stochastic methods. An extensive lists of publications can be found in [12] with various optimization methods [12, 13]. For example the steepest-descent-, the greedy- and the tree search algorithms belong to the former class. Although effective in terms of convergence speed, these methods generally require a 'domain knowledge', since for nonlinear and multi-minima optimization functions the initial trial solution must lie in the so-called 'attraction basin' of the global solution to avoid the convergence solution being trapped into local minima (i.e., wrong solutions of the problem at hand).

In contrast, stochastic algorithms are inherently global and search approaches are potentially able to find the global optimum of the functional whatever the initial point(s) of the search. The goal of optimization is the knowledge of the global solution [12, 13]. The solution is fully described

when its descriptors (i.e., its descriptive features), which quantify the information content of the solution itself, are defined. Since on one hand the descriptors are different (e.g., discrete/continuous variables) and the number of unknowns to be determined can vary among the optimization problems, the choice of a proper optimization algorithm is a key issue and a general rule for this choice does not exist.

From a practical point of view, the main features necessary for an optimization algorithm are the ability to deal with complex optimization functions, the 'simplicity of use', a limited number of control parameters, good convergence properties and the exploitation of the parallelism offered by modern PC clusters. In this sense, evolutionary algorithms (EAs) like the memetic algorithms of [11] seem to be good candidates. Thus as an alternative strategy, it may be of interest to investigate some more structured stochastic optimization algorithms. The study of the potential improvements of the present analysis, as discussed above, will be the objective of our continued efforts.

5. CONCLUSION

We investigated a proposed new principle to diagnose power transformers while in operation. The idea of the present approach is to insert antennas inside the transformer tank to radiate and measure microwave fields that interact with the metallic structure and the insulation. We have studied the responses from the radiated waves, which are expected to be sensitive to material properties that reflect the effects of various degradation mechanisms. We employed a model of a transformer as a two-dimensional parallel plate waveguide where one plate represents the wall of the transformer tank and the other plate represents the iron core that conducts the magnetic flux. In between we placed a set of parallel conductors representing the winding segments. The propagation problem was solved accurately and efficiently by conventional waveguide theory, including mode-matching and cascading techniques.

We have solved the inverse electromagnetic problem for a number of winding configurations using an optimization procedure. From a parametric study of the optimization function, we have found an agreement between the theory and measured data. We have also found that wide-band data may stabilize reconstructions and that information from multiple modes is likely to decrease the occurrence of local minima. Hence, it is important that several waveguide modes can be transmitted and received with high accuracy, which implies that many antennas are needed in the measurement system.

ACKNOWLEDGMENT

REFERENCES

1. ABB Group, *Transformer Service Handbook*, 2006.
2. Wang, M., A. J. Vandermaar, and K. D. Srivastava, "Review of condition assessment of power transformers in service," Feature Article, *IEEE Electrical Insulation Magazine*, Vol. 18, No. 6, 12–25, November/December 2002.
3. Tenbohlen, S., D. Uhde, J. Poittevin, H. Borsi, P. Werle, U. Sundermann, and H. Matthes, "Enhanced diagnosis of power transformers using on- and off-line methods: Results, examples and future trends," *Cigre*, Session 2000, paper 12–204, 2000.
4. Mackenzie, E. A., J. Crossey, A. de Pablo, and W. Ferguson, "On-line monitoring and diagnostics for power transformers," *Conference Record of IEEE International Symposium on Electrical Insulation (ISEI)*, 1–5, San Diego, CA, June 6–9, 2010.
5. Vaessen, P. T. M. and E. Hanique, "A new frequency response analysis method for power transformers," *IEEE Trans. on Power Delivery*, Vol. 7, No. 1, 384–391, January 1992.
6. Shao, Y., Z. Rao, and Z. Jin, "Online state diagnosis of transformer windings based on time-frequency analysis," *WSEAS Transactions on Circuits and Systems*, Vol. 8, No. 2, 227–236, February 2009.
7. Abeywickrama, N., Y. V. Serdyuk, and S. M. Gubanski, "High-frequency modeling of power transformers for use in frequency response analysis," *IEEE Trans. on Power Delivery*, Vol. 23, No. 4, 20420–2049, 2008.
8. Colton, D. and R. Kress, *Inverse Acoustic and Electromagnetic Scattering Theory*, Springer, Berlin, 1992

9. Masterman, P. H. and P. J. B. Clarricoats, "Computer field-matching solution of waveguide transverse discontinuities," *Proc. IEE*, Vol. 118, 51–63, 1971.

10. Cheng, D. K., *Field and Wave Electromagnetics*, Addison-Wesley, Reading Massachusets, 1989.

11. Caorsi, S., A. Massa, M. Pastorino, M. Raffetto, and A. Randazzo, "Detection of buried inhomogeneous elliptic cylinders by a memetic algorithm," *IEEE Trans. Antennas Propag.*, Vol. 51, 2878–2884, 2003.

12. Rocca, P., G. Oliveri, and A. Massa, "Differential evolution as applied to electromagnetics," *IEEE Antennas Propag. Mag.*, Vol. 53, 38–49, 2011.

13. Rocca, P., M. Benedetti, M. Donelli, D. Franceschini, and A. Massa, "Evolutionary optimization as applied to inverse scattering problems," *Inverse Problems*, Vol. 25, 1–41, 2009.

Shape Reconstruction of a Buried Perfectly Conducting Cylinder by Inverse Schemes

Wei Chien[1], Chi-Hsien Sun[2], Chien-Ching Chiu[2],
Szu-Chi Shen[2], and Chung-Hsin Huang[3]

[1]Electronic Engineering Department
De Lin Institute of Technology, Tu-Cheng, Taipei, Taiwan, R.O.C.
[2]Electrical Engineering Department
Tamkang University, New Taipei City, Taiwan, R.O.C.
[3]Department of Computer and Communication Engineering
Taipei College of Maritime Technology
Danshui Town, New Taipei City, Taiwan, R.O.C.

Abstract— Dynamic differential evolution (DDE) for shape reconstruction of perfect conducting cylinder (PEC) buried in a half-space is presented. Assume that a conducting cylinder of unknown shape is buried in one half-space and scatters the field incident from another half-space where the scattered filed is measured. Based on the boundary condition and the measured scattered field, a set of nonlinear integral equations is derived and the imaging problem is reformulated into an optimization problem. The inverse problem is resolved by an optimization approach, and the global searching scheme DDE is then employed to search the parameter space. Numerical results demonstrate that even when the initial guess is far away from the exact one, good reconstruction can be obtained by using DDE.

1. INTRODUCTION

The object of inverse electromagnetic scattering is to reconstruct the profile of unknown objects using measurement data. The inverse scattering problem has many applications in diverse fields such as nondestructive testing, medical imaging, geophysics, remote sensing, and ground penetrating radar [1–4].

As known, the inverse scattering problem is generally nonlinear and ill-posedness [5]. One way for solving the nonlinear inverse problem is solving the forward scattering problem iteratively to minimize an error function known as the cost function. This function represents the error between the measured scattered fields and the simulated fields during the updates of the evolving objects in each inversion. Recently, several papers for inverse scattering problems have been published on the subject of 2-D object about deal with shape reconstruction problems by using genetic algorithms (GAs) [6–10], differential evolution (DE) [11–13], particle swarm optimization (PSO) [14–18] and Neural network [19].

In the 2010, the dynamic differential evolution (DDE) was first proposed to deal with the shape reconstruction of homogenous dielectric objects [11]. DDE algorithm is potentially able to obtain the global optimum of a functional whatever the initial guesses are. It is also found that DDE algorithms have good convergences compared with PSO methods in the inverse scattering problems [20]. To the best of our knowledge, there is still no investigation on using the DDE to reconstruct the electromagnetic imaging of buried perfect conducting cylinders.

In this paper, the goal of the current work is to reconstruct 2-D buried PEC target with arbitrary cross sections, and dynamic differential evolution (DDE) is employed to recover the shape of a buried perfectly conducting cylinder. In Section 2, a theoretical formulation for the inverse scattering is presented. The general principles of DDE, we applied them to the inverse problem are described in Section 3. Numerical results for reconstructing objects of different shapes with noise are given in Section 4. Finally, some conclusions are drawn in Section 5.

2. THEORETICAL FORMULATION

Let us consider a perfectly conducting cylinder which is buried in a lossy homogeneous half-space, as shown in Figure 1. Media in regions 1 and 2 are characterized by permittivity and conductivity $(\varepsilon_1, \sigma_1)$ and $(\varepsilon_2, \sigma_2)$, respectively and the permeability in both regions are μ_0, i.e., non magnetic media are concerned here. The cross section of the cylinder are described in polar coordinates in xy plane by the equation $\rho = F(\theta)$. The cylinder is illuminated by a plane wave with time dependence $e^{j\omega t}$.
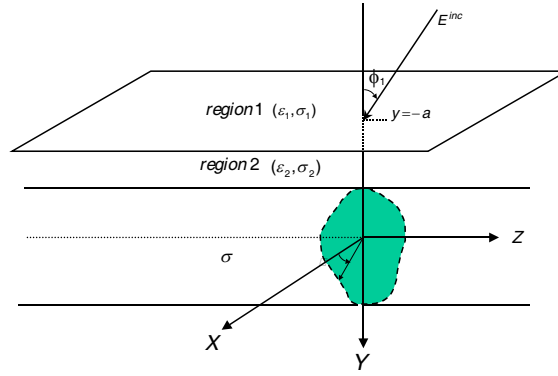
Figure 1: Geometry of the problem in (x, y) plane.

For simplicity, the electric field vector is assumed to be parallel to the z-axis (i.e., transverse magnetic or TM polarization). Let E^{inc} denote the incident field from region 1 with incident angle ϕ_1. Owing to the interface between region 1 and region 2, the incident plane wave generates two waves which would exist in the absence of the conducting object: a reflected wave (for $y \leq -a$) and a transmitted wave (for $y > -a$). Thus unperturbed field is given by

$$\vec{E}_i(\vec{r}) = E_i(x, y)\hat{z} \tag{1}$$

For a TM incident wave, the scattered field can be expressed as

$$E_s(x, y) = - \int_0^{2\pi} G(x, y; F(\theta'), \theta') J(\theta') d\theta' \tag{2}$$

with

$$J(\theta) = -j\omega\mu_0 \sqrt{F^2(\theta) + F'^2(\theta)} J_s(\theta)$$
$$G(x, y; x', y') = \begin{cases} G_1(x, y; x', y'), & y \leq -a \\ G_2(x, y; x', y') = G_f(x, y; x', y') + G_s(x, y; x', y'), & y > -a \end{cases} \tag{3}$$

where

$$G_1(x, y; x', y') = \frac{1}{2\pi} \int_{-\infty}^{\infty} \frac{j}{\gamma_1 + \gamma_2} e^{j\gamma_1(y+a)} e^{-j\gamma_2(y'+a)} e^{-j\alpha(x-x')} d\alpha \tag{3a}$$

$$G_f(x, y; x', y') = \frac{j}{4} H_0^{(2)} \left[k_2 \sqrt{(x-x')^2 + (y-y')^2} \right] \tag{3b}$$

$$G_s(x, y; x', y') = \frac{1}{2\pi} \int_{-\infty}^{\infty} \frac{j}{2\gamma_2} \left(\frac{\gamma_2 - \gamma_1}{\gamma_2 + \gamma_1} \right) e^{-j\gamma_2(y+2a+y)} e^{-j\alpha(x-x')} d\alpha \tag{3c}$$

$$\gamma_i^2 = k_i^2 - \alpha^2, \quad i = 1, 2, \quad \text{Im}(\gamma_i) \leq 0, \quad y' > a$$

Here $J_s(\theta)$ is the induced surface current density which is proportional to the normal derivative of electric field on the conductor surface. $G(x, y; x', y')$ is the Green's function which can be obtained by Fourier transform. In (3b), $H_0^{(2)}$ is the Hankel function of the second kind of order zero.

Let us consider the following inverse problem: giving the scattered electric field E_s measured outside the scatterer determine the shape $F(\theta)$ of the object. Assume the approximate center of the scatterer, which in fact can be any point inside the scatterer, is known. Then the shape function $F(\theta)$ can be expanded as:

$$F(\theta) \cong \sum_{n=0}^{\frac{N}{2}} B_n \cos(n\theta) + \sum_{n=1}^{\frac{N}{2}} C_n \sin(n\theta) \tag{4}$$

where B_n and C_n are real coefficients to be determined, and $N + 1$ is the number of unknowns.

For the inverse scattering problem, the shape of the PEC is reconstructed by the given scattered electric field measured at the receivers. This problem is resolved by an optimization approach, for

which the global searching scheme DDE is employed to minimize the following objective function (OF):

$$OF = \left\{ \frac{1}{M_t} \sum_{m=1}^{M_t} \left| E_s^{\exp}(\bar{r}_m) - E_s^{cal}(\bar{r}_m) \right|^2 / |E_s^{\exp}(\bar{r}_m)|^2 \right\}^{1/2} \tag{5}$$

where M is the total number of measured points. $E_s^{\exp}(\vec{r}_m)$ and $E_s^{cal}(\vec{r}_m)$ are the measured scattered field and the calculated scattered field respectively. Therefore, the maximization of OF can be interpreted as the minimization of the least-squares error between the measured and the calculated fields. It should be noted that the shape function used to describe the shape of the cylinder will be determined by the DDE scheme.

3. DYNAMIC DIFFERENTIAL EVOLUTION (DDE)

DDE algorithm starts with an initial population of potential solutions that is composed by a group of randomly generated individuals which represents shape function of the cylinders. Each individual in DDE algorithm is a D-dimensional vector consisting of D optimization parameters. The initial population may be expressed by $\{x_i : \quad i = 1, \ 2, \cdots, Np\}$, where Np is the population size. After initialization, DDE algorithm performs the genetic evolution until the termination criterion is met. DDE algorithm, like other EAs, also relies on the genetic operations (mutation, crossover and selection) to evolve generation by generation.

The key distinction between a DDE algorithm and a typical DE [21] is on the population updating mechanism. In a typical DE, all the update actions of the population are performed at the end of the generation, of which the implementation is referred as static updating mechanism. Alternatively, the updating mechanism of a DDE algorithm is carried out in a dynamic way: each parent individual will be replaced by his offspring if the offspring has a better objective function value than its parent individual does. Thus, DDE algorithm can respond the progress of population status immediately and to yield faster convergence speed than the typical DE. Based on the convergent characteristic of DDE algorithm, we are able to reduce the numbers of objective function evaluation and reconstruct the microwave image efficiently.

4. NUMERICAL RESULTS

Let us consider a perfectly conducting cylinder which is buried in a lossless half-space ($\sigma_1 = \sigma_2 = 0$). the permittivity in region 1 and region 2 is characterized by $\varepsilon_1 = \varepsilon_0$ and $\varepsilon_2 = 2.7\varepsilon_0$, respectively. A TM polarization plane wave of unit amplitude is incident from region 1 upon the object as shown in Fig. 1. The frequency of the incident wave is chosen to be 3 GHz, i.e., the wavelength λ_0 is 0.1 m. The object is buried at a depth $a = \lambda_0$ and the scattered field is measured on a probing line along the interface between region 1 and region 2. Our purpose is to reconstruct the shape of the object by using the scattered field at different incident angles. To reconstruct the shape of the object, the object is illuminated by incident waves from three different directions and 8 measurement points at equal spacing are used along the interface $y = -a$ for each incident angle. There are 24 measurement points in each simulation. To save computing time, the number of unknowns is set to be 7. The parameters and the corresponding searching ranges are listed follows: The operational coefficients are set as below: The crossover rate CR is set to be 0.8. Both parameters F and λ are set to be 0.8. The population size Np is set to be 110. The search range for the unknown coefficient of the shape function is chosen to be from 0 to 0.1. The extreme value of the coefficient of the shape function can be determined by the prior knowledge of the objects. Here DR, which is called shape function discrepancies, is defined as

$$DR = \left\{ \frac{1}{N'} \sum_{i=1}^{N'} [F^{cal}(\theta_i) - F(\theta_i)]^2 / F^2(\theta_i) \right\}^{1/2} \tag{6}$$

In the example, the shape function is chosen to be $F(\theta) = 0.03 + 0.01\cos(2\theta)$ m. The reconstructed images for different generations and the relative error of the example are shown in Figure 2 and Figure 3, respectively. Figure 3 shows that the relative errors of the shape decrease quickly and good convergences are achieved within 50 generation. The DR value is about 0.5% in the final generation.
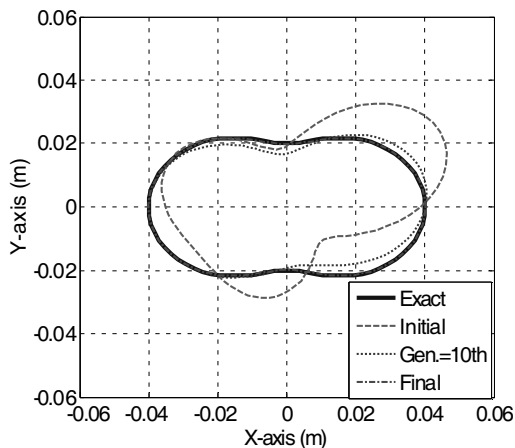
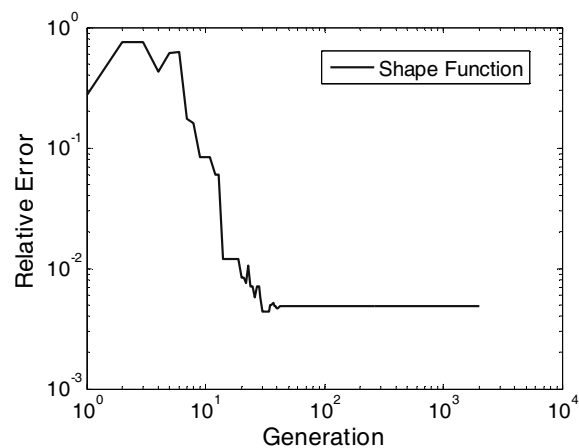Figure 2: The reconstructed shape of the cylinder at different generations for the example.

Figure 3: Shape function error versus generation for the example.

5. CONCLUSION

We have presented a study of applying the DDE to reconstruct the shape of a buried conducting cylinder. These approaches are applied to two-dimensional configurations. After an integral formulation, a discretization using the method of moment (MoM) is applied. Considering that the microwave imaging is recast as a nonlinear optimization problem, objective function is defined by the norm of a difference between the measured scattered electric field and the calculated scattered field for an estimated the shape of metallic cylinder. Thus, the shape of metallic cylinder can be obtained by minimizing the objective function.

ACKNOWLEDGMENT

REFERENCES

1. Mudanyalı, O., S. Yıldız, O. Semerci, A. Yapar, and I. Akduman, "A microwave tomographic approach for nondestructive testing of dielectric coated metallic surfaces," *IEEE Geoscience and Remote Sensing Letters*, Vol. 5, No. 2, 180–184, Apr. 2008.

2. Benedetti, M., D. Lesselier, M. Lambert, and A. Massa, "Multiple-shape reconstruction by means of multiregion level sets," *IEEE Transactions Geoscience and Remote Sensing*, Vol. 48, No. 5, 2330–2342, May 2010.

3. Sun, C. H., C. C. Chiu, and C. J. Lin, "Image reconstruction of inhomogeneous biaxial dielectric cylinders buried in a slab medium," *International Journal of Applied Electromagnetics and Mechanics*, Vol. 34, No. 1–2, 33–48, Nov. 2010.

4. Sun, C. H., C. L. Li, C. C. Chiu, and C. H. Huang, "Time domain image reconstruction for a buried 2D homogeneous dielectric cylinder using NU-SSGA," *Research in Nondestructive Evaluation*, Vol. 22, No. 1, 1–15, Jan. 2011.

5. Sabatier, P. C., "Theoretical considerations for inverse scattering," *Radio Science*, Vol. 18, 629–631, Jan. 1983.

6. Sun, C. H., C. L. Liu, K. C. Chen, C. C. Chiu, C. L. Li, and C. C. Tasi, "Electromagnetic transverse electric wave inverse scattering of a partially immersed conductor by steady-state genetic algorithm," *Electromagnetics*, Vol. 28, No. 6, 389–400, Aug. 2008.

7. Pastorino, M., A. Massa and S. Caorsi, "A microwave inverse scattering technique for image reconstruction based on a genetic algorithm," *IEEE Transactions on Instrumentation and Measurement*, Vol. 49, No. 3, 573–578, 2000.

8. Caorsi, S., A. Massa, and M. Pastorino, "A computational technique based on a real-coded genetic algorithm for microwave imaging purposes," *IEEE Transactions on Geoscience and Remote Sensing, Imaging and Target Identification*, Vol. 38, No. 4, 1697–1708, 2000.

9. Caorsi, S., A. Massa, and M. Pastorino, "A crack identification microwave procedure based on a genetic algorithm for nondestructive testing," *IEEE Transactions on Antennas and Propagation*, Vol. 49, No. 12, 1812–1820, 2001.

10. Chien, W., C. H. Sun, and C. C. Chiu, "Image Reconstruction for a partially immersed imperfectly conducting cylinder by genetic algorithm," *International Journal of Imaging Systems and Technology*, Vol. 19, 299–305, Dec. 2009.

11. Sun, C. H., C. C. Chiu, C. L. Li, and C. H. Huang, "Time domain image reconstruction for homogenous dielectric objects by dynamic differential evolution," *Electromagnetics*, Vol. 30, No. 4, 309–323, May 2010.

12. Massa, A., M. Pastorino, and A. Randazzo, "Reconstruction of twodimensional buried objects by a hybrid differential evolution method," *Inverse Problems*, Vol. 20, No. 6, 135–150, 2004.

13. Rocca, P., G. Oliveri, and A. Massa, "Differential evolution as applied to electromagnetics," *IEEE Antennas and Propagation Magazine*, Vol. 53, No. 1, 38–49, 2011.

14. Chiu, C. C., C. H. Sun, and W. L. Chang, "Comparison of particle swarm optimization and asynchronous particle swarm optimization for inverse scattering of a two- dimensional perfectly conducting cylinder," *International Journal of Applied Electromagnetics and Mechanics*, Vol. 35, No. 4, 249–261, Apr. 2011.

15. Caorsi, S., M. Donelli, A. Lommi, and A. Massa, "Location and imaging of two-dimensional scatterers by using a Particle Swarm algorithm," *Journal of Electromagnetic Waves and Applications*, Vol. 18, No. 4, 481–494, 2004.

16. Chen, C. H., C. C. Chiu, C. H. Sun, and W. L. Chang, "Two-dimensional finite-difference time domain inverse scattering scheme for a perfectly conducting cylinder," *Journal of Applied Remote Sensing*, Vol. 5, 053522, May 2011.

17. Donelli, M. and A. Massa, "A computational approach based on a particle swarm optimizer for microwave imaging of two-dimensional dielectric scatterers," *IEEE Transactions on Microwave Theory and Techniques*, Vol. 53, No. 5, 1761–1776, Feb. 2006.

18. Donelli, M., G. Franceschini, A. Martini, and A. Massa, "An integrated multi-scaling strategy based on a particle swarm algorithm for inverse scattering problems," *IEEE Transactions on Geoscience and Remote Sensing*, Vol. 44, No. 2, 298–312, 2006.

19. Lee, K. C., "A neural-network-based model for 2D microwave imaging of cylinders," *International Journal of RF and Microwave Computer-aided Engineering*, Vol. 4, No. 5, 398–403, Sep. 2004.

20. Rekanos, I. T., "Shape reconstruction of a perfectly conducting scatterer using differential evolution and particle swarm optimization," *IEEE Transactions on Geoscience and Remote Sensing*, Vol. 46, No. 7, 1967–1974, Jul. 2008.

21. Storn, R. and K. Price, "Differential evolution a simple and efficient adaptive scheme for global optimization over continuous spaces," Technical Report TR-95-012, International Computer Science Institute, Berkeley, 1995.

Study of Compact Thin-film UWB Antenna with Dual Band-notched Characteristics

M. Tangjitjetsada[1], P. Rakluea[2], and C. Benjangkaprasert[1]

[1]Faculty of Engineering, King Mongkut's Institute of Technology Ladkrabang
Ladkrabang, Bangkok 10520, Thailand
[2]Department of Electronic and Telecommunication Engineering, Faculty of Engineering
Rajamangala University of Technology Thanyaburi, Pratumthani 12110, Thailand

Abstract— A study of compact thin-film ultra-wideband (UWB) antenna with dual band-notched characteristics is presented. The proposed antenna operated in the frequency range 2.9–11.3 GHz with 10 dB impedance bandwidth, and reasonable radiation properties. It also exhibit dual band-notched characteristics, one notch frequency band at 3.3–3.7 GHz (WiMax band), and the other at 5.1–5.8 GHz (WLAN-WiMax band). This antenna is printed on Mylar® Polyester Film substrate with thickness of 0.4 mm, and dielectric constant of 3.2. The antenna also demonstrates very compact dimensions, 27.3×34.5 mm in physical size. The antenna is designed for dual band-notched by embedding two separated slots on ground plane. The main aim behind the design methodology of the notch function is to tune the total length of the U-like slot and rectangular slot approximately equal to the half guided wavelength (λ_g) of the desired notch frequency. The antenna is determined using design equation, and simulated the commercial IE3D software, which is based on the method of moments. Good agreement is obtained between simulated and measured antenna characteristics. The results show that proposed antenna is very suitable for various portable UWB applications.

1. INTRODUCTION

Now a day, the wireless communication technology has developed rapidly and become much more important. There are many applications of these technologies such as the internet, mobile phone, teleconference and learning distance, which requires extremely high-speed data transmission. Therefore, there has been extensive research and development of wireless communication technology. In particular, the width of bandwidth and the capacity of channel. The ultra-wideband (UWB) technology has been a lot of attention because of the very wide of bandwidth in a wide range of frequencies between 3.1 GHz to 10.6 GHz. However, the frequency range for UWB systems will cause interference to the existing WiMAX and WLAN networks operating in 3.3–3.7 GHz and 5.15–5.825 GHz, respectively. Thus, a better antenna for UWB applications should be rejected frequency at WiMAX band and WLAN band to prevent interference. Some UWB antennas with dual band-notched characteristic have been reported in the published literature [1, 2]. Nevertheless, most of these antennas have the common deficiency of large size, which may lead to a challenging task in miniaturizing antenna design.

In this paper present the compact UWB antenna size, the design include the ultra-wideband performances of the impedance matching and notch frequency response. The design antennas of using CPW-fed rectangular patch with a fork-like tuning stub which ensures UWB impedance matching from 3.1 GHz to 10.6 GHz. The rectangular slot with first notch frequency response of 5.1 to 5.8 GHz, and the U-like slot with second notch frequency response of 3.3 to 3.7 GHz are proposed. The simulation is conducted using the commercially available Zeland IE3D simulation software. The compact antenna area of 34.5×27.3 mm^2 and thickness 0.3 mm are achieved. Finally, the thin-film UWB antennas with dual band-notched at WiMAX/WLAN frequencies are successfully designed, simulated, and measured, show good characteristics.

2. ANTENNA DESIGN

The compact thin-film ultra-wideband (UWB) antenna with dual band-notched is shown in Figure 1. At first, we design the UWB antenna by using CPW-fed rectangular patch with a fork-like tuning stub which ensures UWB impedance matching from 3.1 GHz to 10.6 GHz. To reduce the impact of interference to WLAN and WiMax networks the rectangular slot and U-shape slot are inserted. Next, the geometry of UWB antenna with first band-notched is designed by inserting rectangular slot at first notch frequency response of 5.1–5.8 GHz (WLAN). The expression for the length of a rectangular slot (L_{n1}) can be calculated by (1). And last, addition the U-like slot on
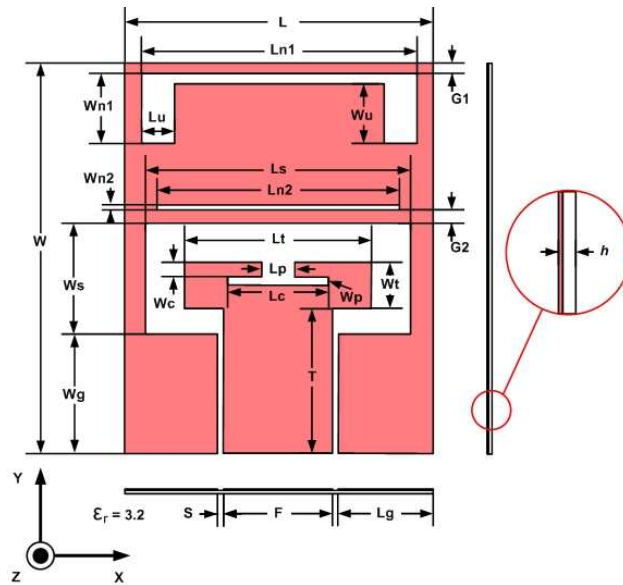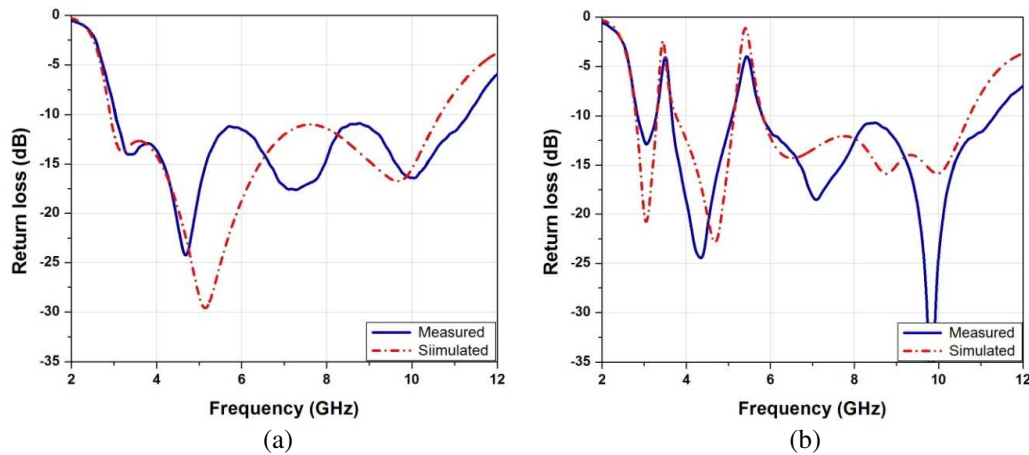
Figure 1: Geometry of antenna.

Figure 2: (a) Return loss of the UWB antenna. (b) Return loss of the UWB antenna with dual band-notched.

ground plate of UWB to be obtained second band-notched at 3.3–3.7 GHz (Wimax) is achieved. The expression for the length of the U-like slot (L_{n2}) can be calculated by (2)

$$f_{n1} = \frac{c}{(4W_{n1} + 2L_{n1} - 4L_u)\sqrt{\varepsilon_{eff}}} \tag{1}$$

$$f_{n2} = \frac{c}{2L_{n2}\sqrt{\varepsilon_{eff}}} \tag{2}$$

where C is the speed of light, and ε_{eff} is the effective dielectric constant.

Which at the desired notch frequencies, the current distribution is around the both slots. Hence, a destructive interference for the excited surface current will occur, which causes the antenna to be non-responsive at that frequency. The compact antenna was fabricated on Mylar® Polyester film with the dielectric constant 3.2, $34.5 \times 27.3\,\text{mm}^2$ of antenna size and thickness of substrate 0.3 mm. The design parameters are $Ws = 9.8\,\text{mm}$, $Ls = 23.3\,\text{mm}$, $Wt = 4\,\text{mm}$, $Lt = 16.5\,\text{mm}$, $Wc = 1.2\,\text{mm}$, $Lc = 9\,\text{mm}$, $Wp = 0.8\,\text{mm}$, $Lp = 3\,\text{mm}$, $Wg = 10.5\,\text{mm}$, $Lg = 8.3\,\text{mm}$, $T = 12.7\,\text{mm}$, $F = 9.7\,\text{mm}$, $S = 0.5\,\text{mm}$, $G1 = 1.35\,\text{mm}$, $Wn1 = 0.5\,\text{mm}$, $Ln1 = 21.47\,\text{mm}$, $G2 = 0.75\,\text{mm}$, $Wn2 = 6.3\,\text{mm}$, $Wu = 5.3\,\text{mm}$, $Ln2 = 24.3\,\text{mm}$, $Lu = 2.75\,\text{mm}$.

(a)   (b)   (c)
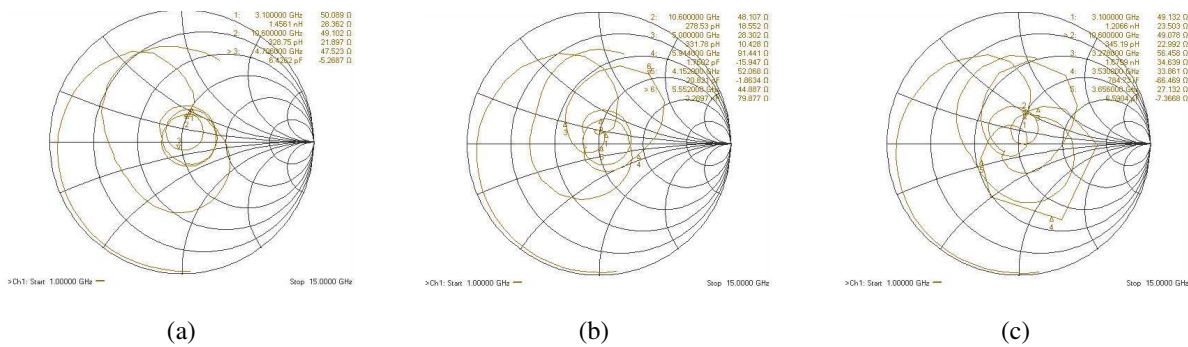
Figure 3: (a) Impedance of UWB antenna; (b) Impedance of UWB antenna with dual band-notched of 5.1–5.8 GHz; (c) Impedance of UWB antenna with dual band-notched of 3.3–3.7 GHz.

(a)   (b)
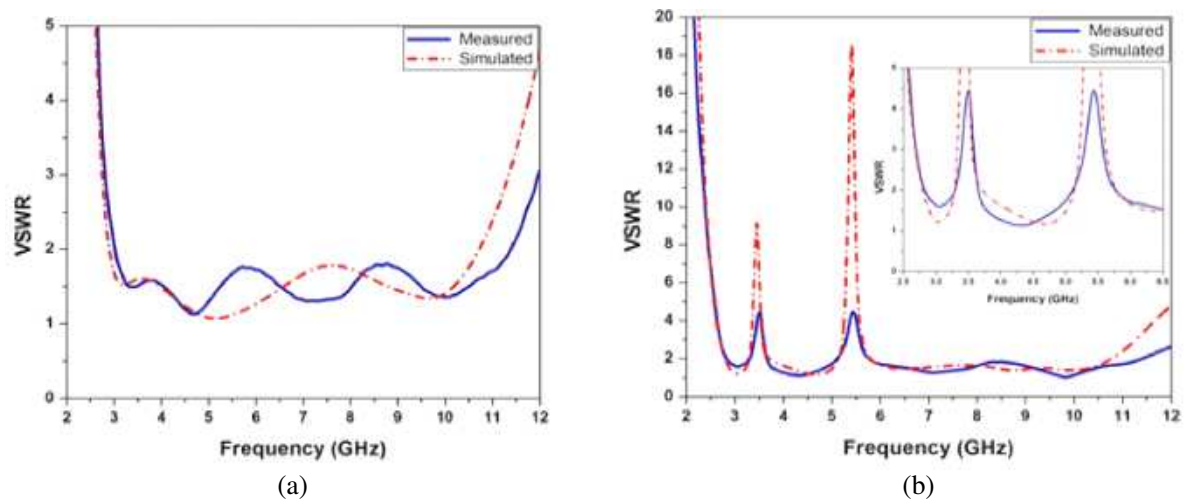
Figure 4: (a) VSWR of the UWB antenna. (b) VSWR of the UWB antenna with dual band-notched.

3. UWB ANTENNA WITH DUAL BAND-NOTCHED CHARACTERISTICS

In this section, we studied the characteristics of UWB antenna with dual band-notched by comparing measuring and simulation result between the designed antenna, UWB antenna and UWB antenna with dual band-notched. The characteristics of proposed antenna are studied including return loss, impedance matching, VSWR, radiation pattern and gain.

3.1. Return Loss

It can be seen that the return loss of the UWB antenna shown in Figure 2(a) is lower than −10 dB cover entire UWB frequency band. In Figure 2(b), the return loss of the UWB antenna with dual band-notched shows that the return loss of band notched positions (5.1–5.8 GHz and 3.3–3.7 GHz) are higher than −10 dB while return loss of the rest of UWB frequency band are lower than −10 dB.

3.2. Impedance Matching

Figure 3(a) shows the matched impedance of UWB antenna. That is the impedance is close to 50 ohms input impedance. Whereas impedance of UWB antenna with band notched of 5.1–5.8 GHz and 3.3–3.7 GHz shown in Figures 3(b) and (c), respectively. There have missmacthed impedance at notch frequency response. The impedance of first band notched is approximately 28 ohms and the impedance of second band notched is approximately 57 ohms. That is the impedance are not close to input impedance due to the notch characteristic.

3.3. VSWR

Figure 4, the comparison of VSWR between UWB antenna and UWB antenna with dual band-notched are shown. Figure 4(a) shows the VSWR of UWB antenna, it can be seen that the VSWR of UWB antenna have wideband performance of 3–11.4 GHz for VSWR less than 2, covering the entire UWB frequency band. On the other hand in Figure 4(b) the VSWR of designed antenna with notch characteristic shows that at the positions of notch frequency response, first band-notched of 5.1–5.8 GHz and second band-notched of 3.3–3.7 GHz, the VSWR are more than 2.

3.4. Radiation Pattern

In considering the radiation patterns of UWB antenna and UWB antenna with dual band-notched in the E-plane (xz-plane) and H-plane (yz-plane) for frequency 4.5 GHz and 7 GHz are shown in Figures 5 and 6, respectively. It is obvious that the radiation patterns of UWB antenna and UWB antenna with dual band- notched are nearly close. That is both antennas are characterized by an omnidirectional pattern in the xz-plane while it is a bidirectional pattern in the yz-plane. And they are acceptable over the UWB bandwidth.

3.5. Gain

Figure 7 shows the performance gain of the antenna. It can be seen in Figure 7(a) that gain of UWB antenna are more than 2 dB and nearly stable over entire the UWB frequency band. Whereas in Figure 7(b) sharp gain decreases occur in the vicinity of 3.5 and 5.5 GHz bands. However, for the other frequencies outside the rejected band, the antenna gain is nearly constant over the entire UWB frequency band.

XZ-Plane   YZ-Plane   XZ-Plane   YZ-Plane
        (a)   (b)
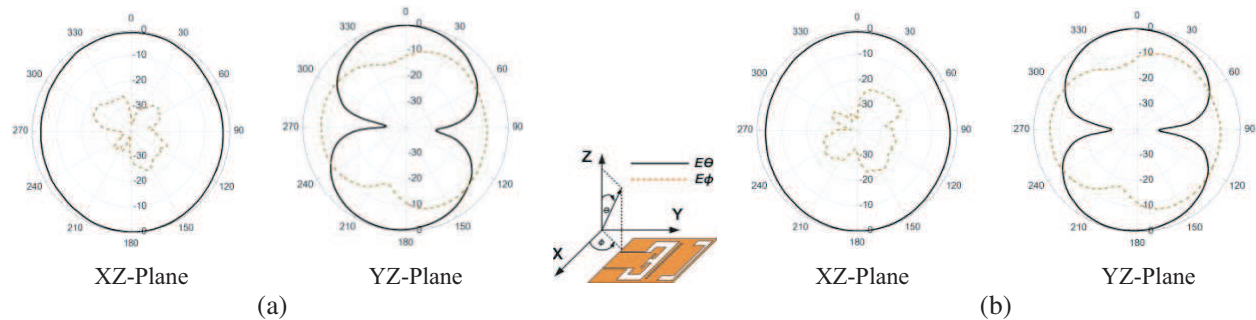
Figure 5: Radiation pattern at 4.5 GHz. (a) Radiation pattern of UWB antenna. (b) Radiation pattern of UWB antenna with dual band-notched.

XZ-Plane   YZ-Plane   XZ-Plane   YZ-Plane
        (a)   (b)
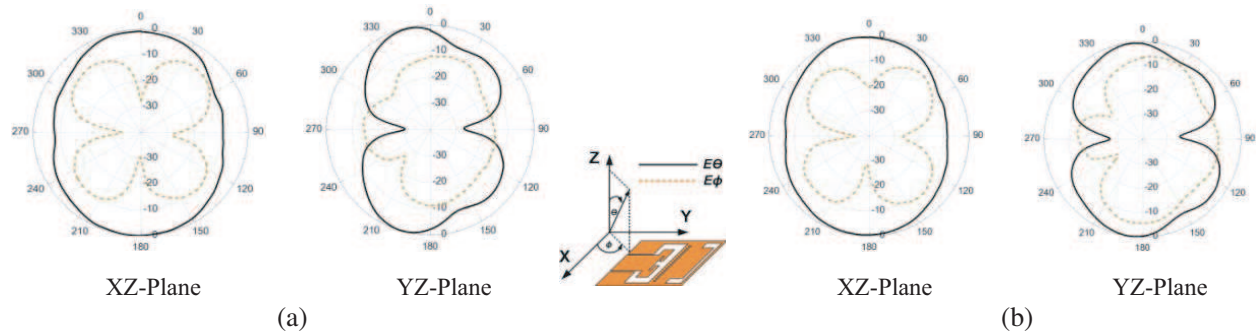
Figure 6: Radiation pattern at 7 GHz. (a) Radiation pattern of UWB antenna. (b) Radiation pattern of UWB antenna with dual band-notched.

        (a)   (b)
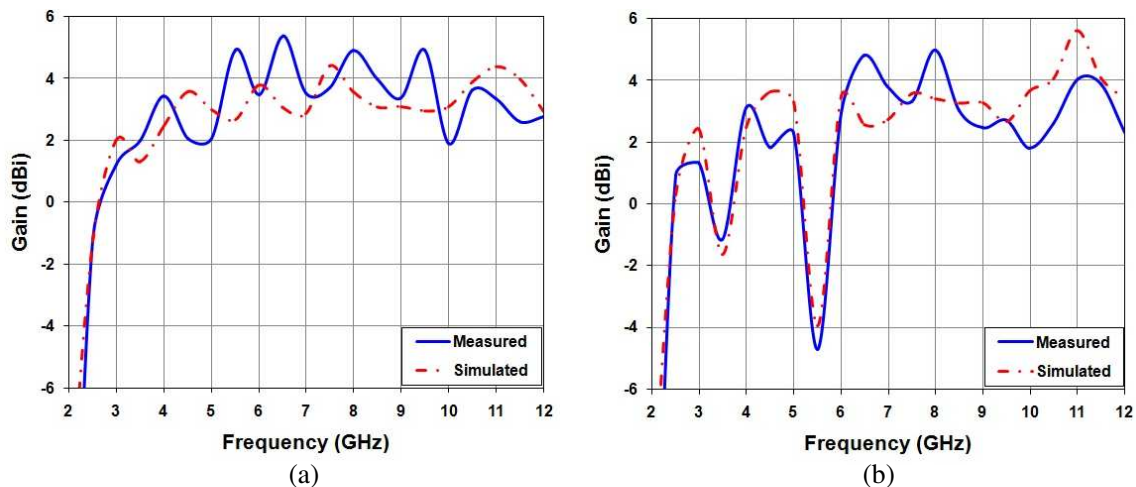
Figure 7: (a) Gain of the UWB antenna. (b) Gain of the UWB antenna with dual band-notched.

4. CONCLUSION

We proposed a compact thin-film ultra-wideband (UWB) antenna with dual band-notched. The antenna is designed to reduce the interference to WLAN and WiMax networks from ground plane effects by cutting a notch from the radiator. The studied of proposed antenna characteristics, with good agreements between the simulated and the measured results, shows that the dual band-notched can avoid interference problem for 5.1–5.8 GHz and 3.3–3.7 GHz. And it has good performance such as good impedance matching, stable gain and good radiation pattern, in addition to the small size.

REFERENCES

1. Panda, J. R., A. S. R. Saladi, and S. K. Rakhesh, "A compact 3.4/5.5 GHz dual band-notched uwb monopole antenna with nested U-shaped slots," *International conference on Computing, Communication and Networking Technologies*, 2010.
2. Natarajamani, S. K. B. and S. K. Patra, "Compact slot antenna for UWB application and band," *International Conference on Computational Intelligence and Communication Networks*, 2010.
3. Rakluea, P. and J. Nakasuwan, "Planar UWB antenna with single band-notched characteristic," *ICCAS*, Oct. 27–30, 2010.
4. Zhang, M., Y. Yin, L. Wen, W. Xiao, and Y. Wang, "A slot antenna with band-notched coupling strips for UWB application," *ISSSE*, 2010.
5. William, J. and R. Nakkeeran, "CPW-fed UWB slot antenna with triangular tuning stub," *International Journal of Computer and Electrical Engineering*, Vol. 2, No. 4, 1793–8163, Aug. 2010.
6. Subbarao, A. and S. Raghavan, "A compact CPW-fed arrow shaped monopole antenna for UWB applications," *International conference on Computing, Communication and Networking Technologies*, 2010.

High-gain Antenna for Base Station Using MSA and Triangular EBG Cavity

P. Kamphikul, **P. Krachodnok**, **and R. Wongsan**

School of Telecommunication Engineering, Institute of Engineering
Suranaree University of Technology, Nakhon Ratchasima, Thailand

Abstract— This paper presents a high-gain antenna using microstrip antenna (MSA) with triangular Electromagnetic Band Gap (EBG) cavity for mobile base station. The advantages of this proposed antenna arelight weight, easy fabrication and installation. Moreover, it provides the moderately high gain compare to the other antennas in the cellular phone system at present. The paper also presents the procedures of the 3-element MSA and triangular EBG cavity design. A Computer Simulation Technology (CST) software has been used to compute the return loss, VSWR, radiation pattern, and gain of the antenna. The azimuth patterns of the proposed antenna can cover 360 degree of user's areas according to our requirement. The bandwidth, at S_{11} (-10 dB), is between 1920 to 2170 MHz with a gain more than 10 dB of each element.

1. INTRODUCTION

Recently, the development of the antennas with new performances becomes currently imperatively essential for the new services and network of telecommunication. It's a matter of the technology of EBG structure, a new technology for the improvement of the performances of antenna, applicable on a frequential spectrum extremely wide covered from the acoustic until the optical frequencies [1] Microstrip antennas (MSA) are an attractive choice for many modern communication systems due to their light weight, low profile with conformability, easy to be integrated with carriers of missile and satellite [2]. Two of the major disadvantages are the low gain and very narrow impedance bandwidth due to the resonant nature of the conventional MSA. By employing, EBG structures are capable to enhance the performance of MSA in terms of gain, side lobe, back lobe level and also mutual coupling. This is due to EBG exhibits frequency band-pass and band-stop that can block surface wave excitation in the operational frequency range of the antennas [3]. The objectives in using EBG were basically either to increase the gain, to reduce the side lobe and back lobe level, to reduce the mutual coupling (S_{21}) or to produce dual band to operate at different frequencies [4]. From such advantages, this paper presents the 3-element MSA with triangular EBG cavity providing the moderately high gain suitable for mobile base station. The simulated results of the return loss, VSWR, radiation patterns, and gain of the antenna are conducted with CST software.

At first, the general approach will be presented which is including the configurations of MSA and EBG structures as shown in Section 2. In Section 3, we apply this approach into the results and discussion. Finally, the conclusions are given in Section 4.

2. MICROSTRIP ANTENNA AND EBG CONFIGULATIONS

The objective of this part is a dual band MSA design that can work in UMTS band of 2100 MHz frequency The antenna is printed on FR4 substrate with the size of 50 mm × 50 mm and the thickness of 1.6 mm as shown in Fig. 1 [5]. The design of a MSA is initiated by determining its patch dimension and adds stubs on original antenna as illustrated in [5]. The simulated result shows that the gain at 2.1 GHz is 2.48 dB.

The woodpile EBG material is a dielectric structure that is periodic in all three dimensions. The unit cell of this material is shown in Fig. 2 [6]. The woodpile EBG material is defined by the lattice constant or repeat distance in the horizontal plane (a), the rod width (w), the rod height (h), and the total height of the unit cell (b). Notice in Fig. 2 that consecutive layers are orthogonal to each other, and the parallel rods are offset from the rods two layers below by half a lattice constant, to obtain a four layer stacking sequence. To implement the woodpile we have used alumina rods ($\varepsilon_r = 8.4$, $\tan\delta = 0.002$) that have a rectangular cross section. The lattice parameters are given as follow [6] with $a = 15.48$ mm, $w = h = 4.42$ mm, and $b = 17.70$ mm.

3. RESULTS AND DISCUSSION

The 3-element MSA, triangular EBG cavity, and PEC reflector were simulated by CST software, which uses the Finite Difference Time Domain Method (FDTD) approach in their modeling equations with the final model as shown in Fig. 3.
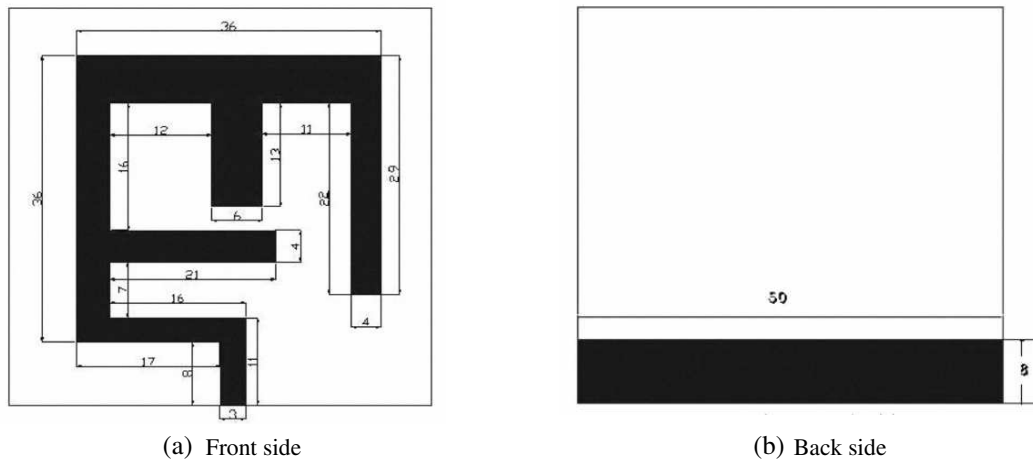
(a) Front side

(b) Back side

Figure 1: The geometry of the dual band MSA.
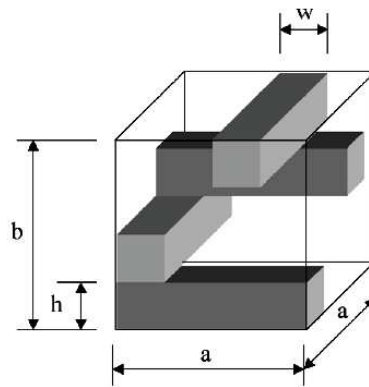
Figure 2: The unit cell for the woodpile EBG material.
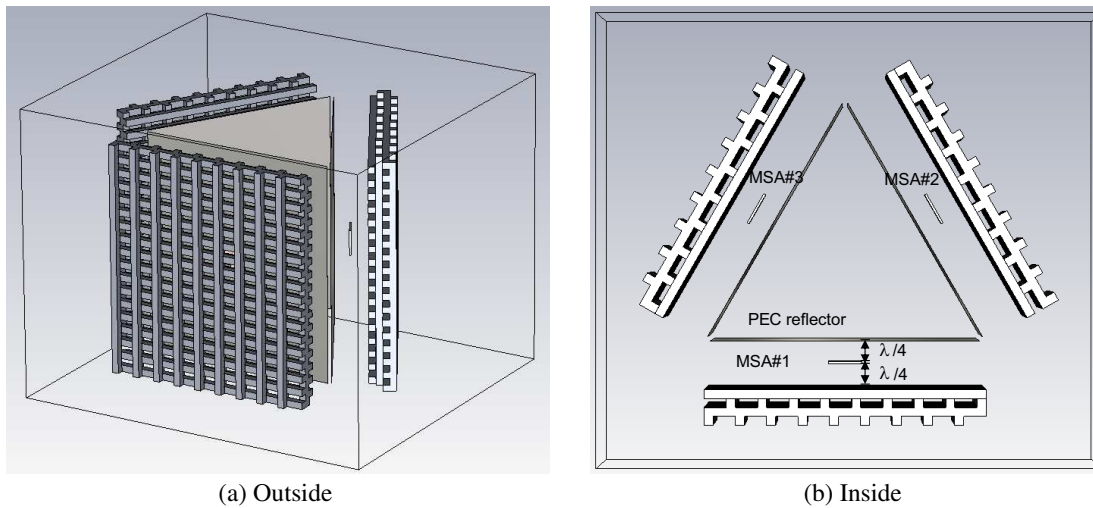

(a) Outside

(b) Inside

Figure 3: The 3-element MSA and triangular EBG cavity model.

The return losses of the antennas are obtained about −15 dB at the frequency of 2.1 GHz as shown in Fig. 4. Moreover as shown in Fig. 5, The VSWRs at 2.1 GHz are lower than 1.5 which are well matched antennas to the cable impedance. Also, the radiation patterns of the antennas are obtained as shown in Fig. 6 which is the azimuth patterns at 2.1 GHz. They can be observed from these radiations that the design syntennas have stable radiation patterns throughout the whole operating band. The simulated results show that the gains at 2.1 GHz are 14.50 dB, 13.48 dB, and 13.43 dB of MSA#1, MSA#2, and MSA#3, respectively.
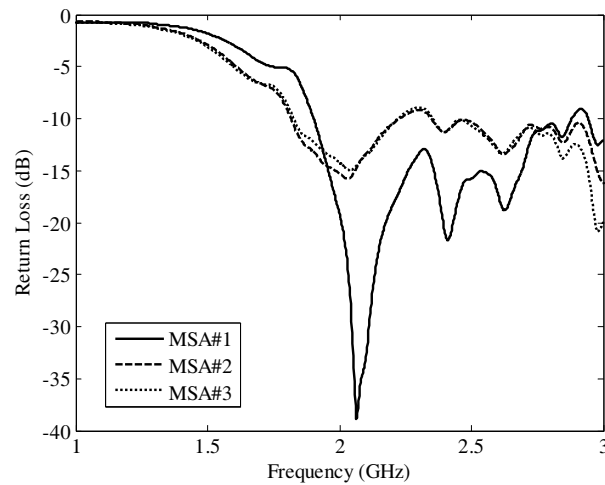
Figure 4: The return loss.
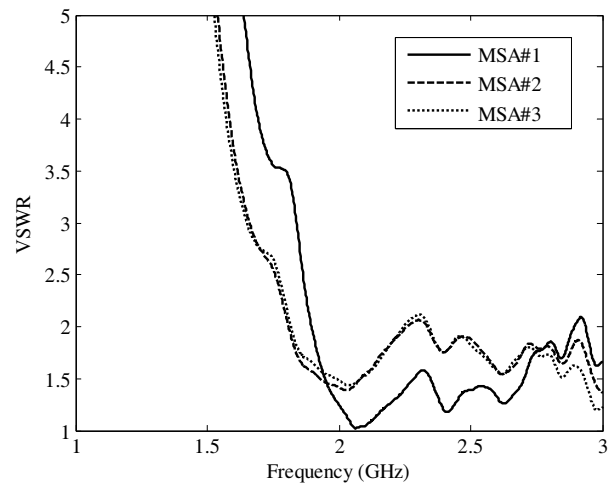
Figure 5: The VSWR.
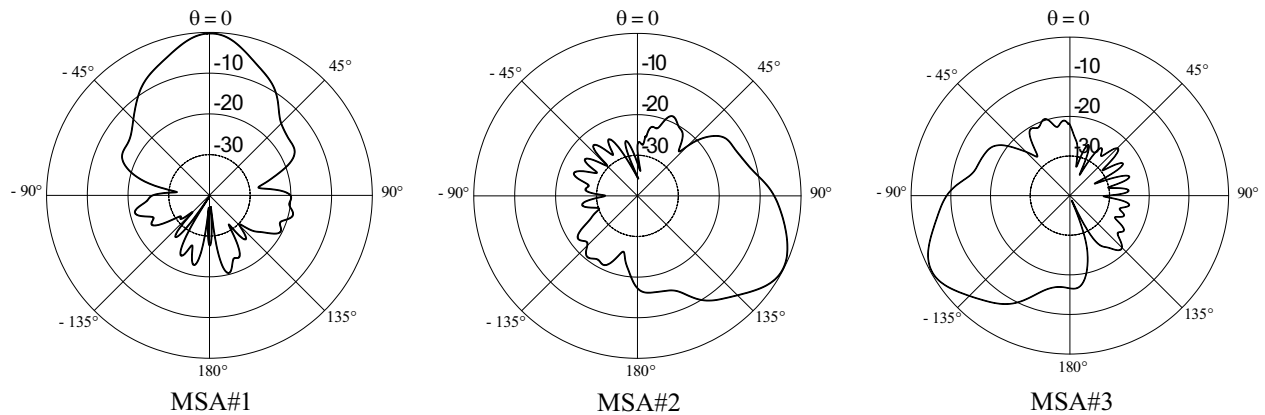
Figure 6: The azimuth pattern.

4. CONCLUSION

This paper has presented a high-gain antenna using the 3-element MSA with triangular EBG cavity. It provides the azimuth patterns that can cover user's areas according to our requirement and a high gain of 10 dB of each element. Therefore, this proposed antenna accords to the requirements and is appropriated for mobile base station. In the future, we will research to change MSA to other antennas that give the good results of gain and bandwidth.

REFERENCES

1. Elayachi, M., P. Brachat, and P. Ratajczak, "EBG identification by the reflection phase method (RPM) design for application WiFi antenna," *Proceedings EuCAP 2006*, Nice, France, Nov. 2006.

2. Zhu, L., G. Wang, X. Gao, and J. Liang, "Design of a new circular polarization broadband microstrip antenna," *Journal of Microwaves in China*, Vol. 24, 21–24, 2008.

3. Illuz, Z., R. Shavit, and R. Bauer, "Micro-strip antenna phased array with electromagnetic band-gap substrate," *IEEE Transactions on Antenna and Propagation*, Vol. 52, No. 6, 1064–1076, 1986.

4. Tan, M. N. M., T. A. Rahman, S. K. A. Rahim, M. T. Ali, and M. F. Jamlos, "Antenna array enhancement using mushroom-like electromagnetic band gap (EBG)," *Antennas and Propagation (EuCAP)*, 2010.

5. Tuan, T. M., "Design dual band microstrip antenna for next generation mobile communication," *The 2010 International Conference on Advanced Technologies for Communication*, 331–335, 2010.

6. Weily, A. R., L. Horvath, K. P. Esselle, B. C. Sanders, and T. S. Bird, "A planar resonator antenna based on a woodpile EBG material," *IEEE Transactions on Antennas and Propagation*, Vol. 53, No. 1, 216–223, 2005.

Statistical Analysis of Microwave Scattering and Attenuation in Randomly Distributed Rainfalls Using Parallel Computation

Yasumitsu Miyazaki[1], **Koichi Takahashi**[1], **and Nobuo Goto**[2]

[1]Department of Media Informatics, Aichi University of Technology
50-2 Manori, Nishihasama-cho, Gamagori 443-0047, Japan
[2]Institute of Technology and Science, The University of Tokushima
2-1 Minamijosanjima-cho, Tokushima 770-8506, Japan

Abstract— Rain measurement system using propagation characteristics of microwave and millimeter wave is very effective disaster prevention system for local strong rainfalls. Measurement technique of electromagnetic scattering and attenuation characteristics by rain is one of useful evaluation methods of rainfall rate. In this study, propagation region is considered as random media with randomly distributed rainfalls. Attenuations of incident beam with 20 GHz carrier frequency in random media corresponding to rainfall rate 5–50 mm/h are evaluated by three-dimensional FDTD method. To obtain accurate relationship between rainfall rate and rain attenuation, analysis of propagation for the incident wave with relatively flat distribution around beam center is considered. For the analysis of large area, parallel computing is studied.

1. INTRODUCTION

Rain measurement system using propagation characteristics of microwave and millimeter wave is very effective for disaster prevention system for local strong rainfalls. Measurement technique of electromagnetic scattering and attenuation characteristics by rain is one of useful evaluation methods of rainfall rate [1]. Incident wave with relatively flat distribution around beam center is transmitted. Attenuations of incident wave with 20 GHz carrier frequency in random media corresponding to rainfall rate 5–50 mm/h are evaluated by three-dimensional FDTD method. Firstly, we show measurement system of rain attenuation using microwave Gaussian beam [2–4]. To obtain accurate relationship between rainfall rate and rain attenuation, precise study of scattering characteristics by single raindrop is indispensable. When the incident wave is microwave with 20 GHz frequency, scattering by single raindrop with 1 mm diameter can be shown by Rayleigh approximation scattering theory. Next, we show comparison of scattering fields of single raindrop by numerical FDTD method with analytical approximate results derived by Rayleigh scattering theory. For single raindrop, scattering properties of cubic and non-cubic raindrop models are evaluated. Also, interference characteristics of scattered fields by two and three raindrops are evaluated by FDTD method and Rayleigh scattering theory. Lastly, the field in the large area which contains hundred raindrops is calculated using parallel and successive FDTD method and specific rain attenuation is evaluated[5–9]. Based on these computer simulations, the optimum measurement systems of raindrop using microwave techniques may be accomplished.
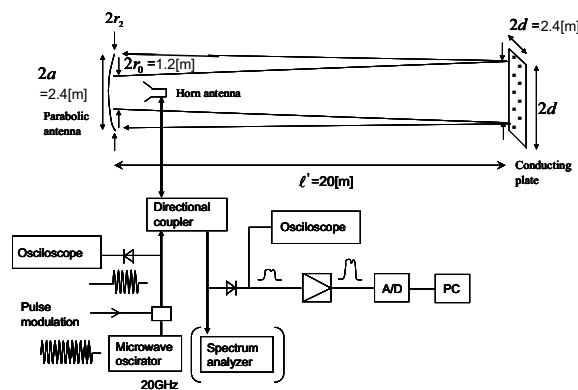

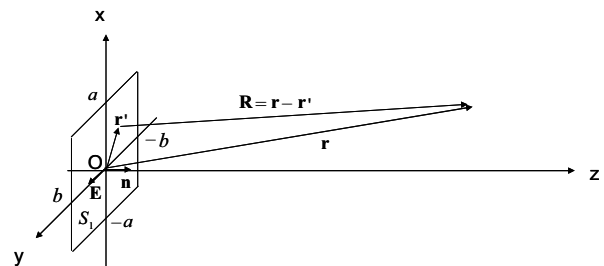Figure 1: Measurement system of rain attenuation using microwave.

Figure 2: Radiation field by rectangular aperture.

2. RAIN MEASUREMENT SYSTEM USING MICROWAVE

Rain measurement system using microwave is shown in Fig. 1. A parabolic antenna with diameter $2a = 2.4$ m is used to transmit and receive microwave of 10–20 GHz. Gaussian beam with beam spot $r_0 = 0.6$ m–$20\lambda \sim 40\lambda$ is transmitted. Reflected wave from a conducting plate is received by the parabolic antenna and specific attenuation A (dB/km) is evaluated by, using propagation losses α along length ℓ

$$A = \alpha \cdot 10^3/\ell, \quad \alpha = -10 \log_{10} \frac{P(\ell)}{P_0(\ell)} \tag{1}$$

where, for example, $\ell' = \ell/2 = 20$ (m) is the distance from the antenna and the conducting plate. Here, P_0 and P are the received powers of incident and total fields, E_{inc} and E in free space and rain region. $\ell = 2\ell'$ is propagation distance. The conducting plate needs sufficiently area to reflect transmitted wave with spreading beam width. Radiated field $E_y(x, y, z)$ is microwave beam given by Eq. (2) when the distribution of electric field on the incident plane S_0 is Gaussian with beam spot size r_{0x} and r_{0y} in x and y coordinate, respectively. Fundamental characteristics of radiated field by parabolic antenna are studied by Gaussian beam radiated from an aperture as shown in Fig. 2. Direction of polarization of the Gaussian beam is y, and sizes of the aperture are $2a$ and $2b$ in x and y directions. Here, $a = 2r_{0x}$ and $b = 2r_{0y}$.

If $\zeta_x = \frac{2z}{kr_{0x}^2}$, $\zeta_y = \frac{2z}{kr_{0y}^2}$

$$E_{inc,y}(x, y, z) = E_0 e^{-jkz} \frac{1}{\sqrt{1 - j\zeta_x}} \frac{1}{\sqrt{1 - j\zeta_y}} e^{-\frac{x^2}{r_{0x}^2}\left(\frac{1}{1-j\zeta_x}\right) - \frac{y^2}{r_{0y}^2}\left(\frac{1}{1-j\zeta_y}\right)} \tag{2}$$

Amplitudes of incident field with $f = 20$ (GHz), $\lambda = 0.015$ (m), $k = 2\pi/\lambda$, $r_{0x} = r_{0y} = r_0 = 0.6$ (m) and $E_0 = 1$ (V/m), at propagation distances $z = 1, 5, 10, 20$ and 30 (m) are shown in Fig. 3. When r_0 is sufficiently larger compared to the wavelength, such as $r_0 = 40\lambda = 0.6$ (m), divergence of the beam due to diffraction is very small. When the sizes of the aperture in x and y directions are $2a = 2b = 2.4$ (m), diffraction angle θ is approximately $\theta \cong \frac{\lambda}{2a} = \frac{\lambda}{2b} = 6.25 \times 10^{-3}$ [rad]. In this case, divergences of the beam Δx and Δy in x and y directions after $\ell' = 20$ (m) propagation are given by $\Delta x = \Delta y = \theta\ell' = 0.125$ (m) and satisfy $\Delta x, \Delta y \ll a, b$. The beam width at $z = 20$ (m) can be covered by conducting plate with a side length $2d = 2.4$ (m) and almost all the transmitted power is reflected by conducting plate. By using conducting plate reflection, rain attenuation can be measured in long propagation distance of $\ell = 2\ell'$ where ℓ' is the distance from the antenna aperture to the conducting plate.

3. ELECTROMAGNETIC SCATTERING BY SINGLE RAINDROP

Scattered field of incident beam wave with the relatively large beam waist by a sphere with diameter a' and dielectric constant $\varepsilon = n_r^{*2}\varepsilon_0$ is approximately obtained by Rayleigh scattering as shown in Eq. (3) when diameter is smaller than $1/10$ of wavelength. The amplitudes of scattered fields by theoretical approximate and numerical analysis are compared to test the accuracy of FDTD
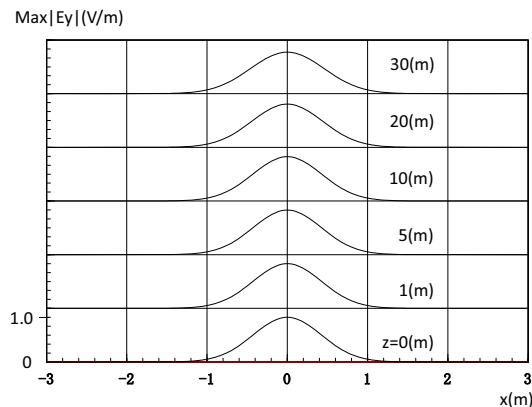

Figure 3: Incident electric field ($f = 20$ GHz, $\lambda = 0.015$ m, $r_{0x} = r_{0y} = r_0 = 0.6$ m, $E_0 = 1$ V/m).
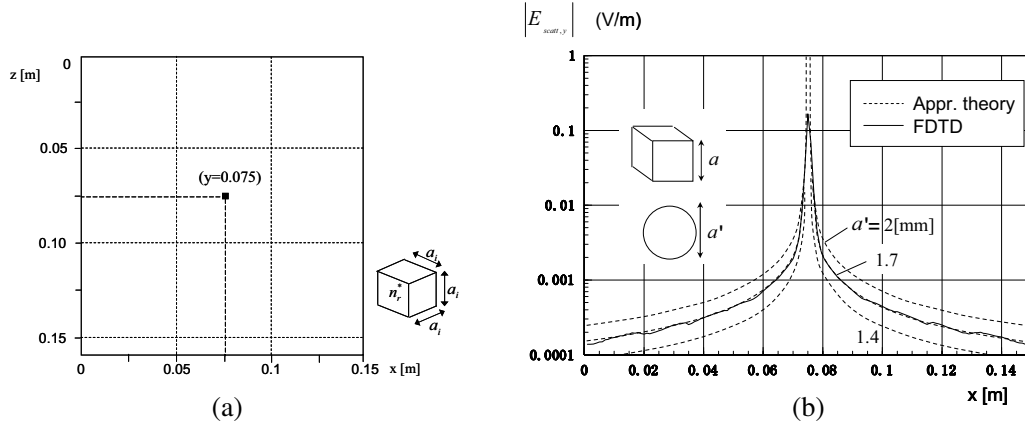
Figure 4: Comparison of scattered field amplitudes of cubic and spherical raindrop ($y = z = 0.075$ m) $N = 1$, $a = 1$ mm, $n_r^* = 6.46 - j2.81$. (a) Analysis model of scattering by single raindrop. (b) Scattered amplitude by FDTD and approximation theory.

analysis. Scattered field at $\mathbf{r} = (x, y, z)$ from a raindrop at $\mathbf{r}_i = (x_i, y_i, z_i)$ is given by

$$\mathbf{E}_{scatt}^{(1)} = \frac{e^{-jkr_i'}}{r_i'} C E_{inc}(\mathbf{r}_i) \left(\cos\theta_i' \sin\phi_i' \mathbf{i}'_{\theta i} + \cos\phi_i' \mathbf{i}'_{\phi i}\right), \quad C = k^2 \left(\frac{a'}{2}\right)^3 \frac{\varepsilon - \varepsilon_0}{\varepsilon + 2\varepsilon_0} \tag{3}$$

where $x_i' = x - x_i$, $y_i' = y - y_i$, $z_i' = z - z_i$, $r_i' = |\mathbf{r} - \mathbf{r}_i| = \sqrt{x_i'^2 + y_i'^2 + z_i'^2}$, $\cos\theta_i' = \frac{z_i'}{r_i'}$, $\cos\phi_i' = \frac{x_i'}{\sqrt{x_i'^2 + y_i'^2}}$, $\sin\phi_i' = \frac{y_i'}{\sqrt{x_i'^2 + y_i'^2}}$.

In FDTD analysis, Gaussian beam is excited at $z = 0$ (m) for the incident wave, and in theoretical study, the incident wave is plane wave characteristics having the uniform amplitude with the Gaussian beam at raindrop position in FDTD analysis. Fig. 4 shows the comparison of scattered field amplitudes of cubic and spherical raindrop model at $\mathbf{r}_i = (x_i, y_i, z_i) = (0.075, 0.075, 0.075)$. In this figure, a is a side length of cubic model and a' is a diameter of spherical model. When $a' \ll \lambda$, theoretical approximate amplitude is given by Eq. (3) and $|E_{scatt,y}(x, y_0, z)| = |\mathbf{i}_y \cdot \mathbf{E}_{scatt}^{(1)}(x, y_0, z)|$, where $y_0 = 0.075$ (m). In FDTD analysis, the incident wave at $z = 0$ (m) is y polarized Gaussian beam with beam spot size $r_0 = 0.03$ (m). E_0 is the amplitude of electric field of incident wave and $E_0 = 0.18$ (V/m) at $(x, y, z) = (0.075, 0.075, 0.075)$. When the volume of a sphere $\frac{4}{3}\pi(\frac{a'}{2})^3 = a^3$ is equal to the volume of a cube, $a = 1$ (mm) and $a' = 1.24$ (mm). Fig. 4 shows scattered results of sphere with $a' = 1.4, 1.7$ and 2 (mm) and scattered characteristics of cubic model with $a = 1$ (mm) in FDTD analysis almost coincides to spherical model with $a' = 1.7$ (mm).

4. MULTIPLE SCATTERING AND INTERFERENCE BY TWO AND THREE RAINDROPS

Multiple scattering and the interference of scattered waves from two and three raindrops are also considered to test the accuracy of FDTD analysis. First iterative approximation theory of scattering field given by Eq. (3) is shown by the equivalent dipole of Rayleigh scattering $\mathbf{p}_i$, and Green's function $\mathbf{G}$ for the free space, as

$$\mathbf{E}_{scatt,i}^{(1)}(\mathbf{r}) = \mathbf{p}_i(\mathbf{E}_{inc})\mathbf{G} \tag{4}$$

Considering the second order scattering terms, scattering field by N raindrops are given by

$$\mathbf{E}_{scatt}^{(2)} = \mathbf{E}_{scatt}^{(1)} + \sum_{j=1}^{N}\sum_{i=1}^{N}\mathbf{p}_j(\mathbf{p}_i(\mathbf{E}_{inc})\mathbf{G})\mathbf{G}, \quad \mathbf{E}_{scatt}^{(1)} = \sum_{i=0}^{N}\mathbf{p}_i(\mathbf{E}_{inc})\mathbf{G} \tag{5}$$

Comparison of FDTD numerical and approximate analytical results for two and three raindrops given in Fig. 5 shows interference patterns around raindrop models.
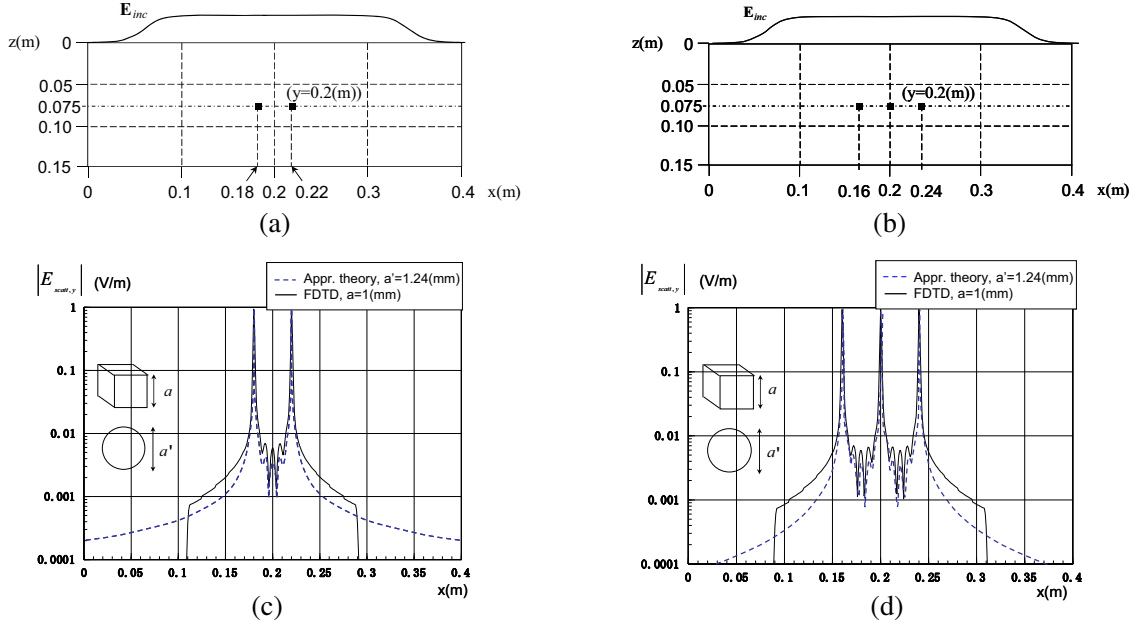
(a)

(b)

(c)

(d)

Figure 5: Comparison of the scattering amplitude on the line $y = 0.2$ m on the x-y plane ($z = 0.075$ m) a: Side length of a cube, a': Diameter of a sphere, $n_r^* = 6.46 - j2.81$. (a) Analysis model of scattering by two raindrops. (b) Analysis model of scattering by three raindrops. (c) Scattering amplitudes by two raindrops. (d) Scattering amplitudes by three raindrops.
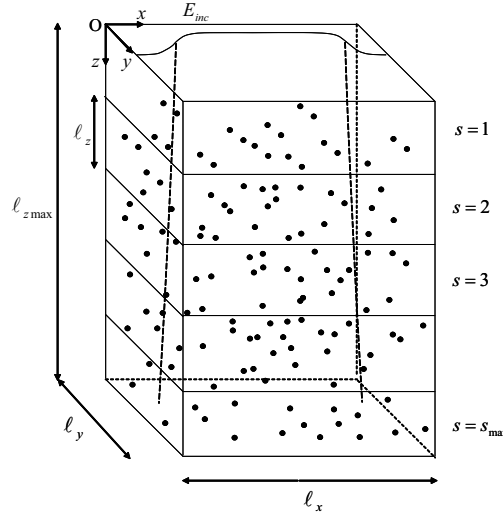

Figure 6: Analysis model for rain attenuation.

5. MULTIPLE SCATTERING AND INTERFERENCE BY MANY RAINDROPS

Three-dimensional analysis model of rain attenuation is shown in Fig. 6. Analysis region is defined as $\ell_x \ell_y \ell_{z\,\text{max}}$. Total analysis space is divided into subspaces with length in z direction ℓ_z. $\ell_{z\,\text{max}} = s_{\text{max}} \ell_z$ and s_{max} is the maximum number of subspaces. Raindrops are distributed randomly in rain region. The incident wave has flat distribution around beam center as shown in Fig. 7. The electric field of the incident wave at $z = 0$ (m) is given by

$$E_y(x, y, 0, t) = E_0 \left\{ \frac{1}{1 + e^{-\beta(x-x_1)}} + \frac{1}{1 + e^{\beta(x-x_2)}} - 1 \right\} \left\{ \frac{1}{1 + e^{-\beta(y-y_1)}} + \frac{1}{1 + e^{\beta(y-y_2)}} - 1 \right\}$$

$$\cdot \left\{ \frac{1}{1 + e^{-\alpha(t-t_1)}} + \frac{1}{1 + e^{\alpha(t-t_2)}} - 1 \right\} \sin(2\pi f t) \tag{6}$$

where, $\beta = 10^2$ (m^{-1}), x_1, $y_1 = 0.06$ (m), x_2, $y_2 = 0.34$ (m), $\alpha = 10^{11}$ (s^{-1}), $t_1 = 0.05$ (ns), $t_2 = 0.45$ (ns) are used. Pulse width is $t_2 - t_1 = 0.4$ (ns) and beam width is $x_2 - x_1 = y_2 - y_1 = 0.28$ (m).
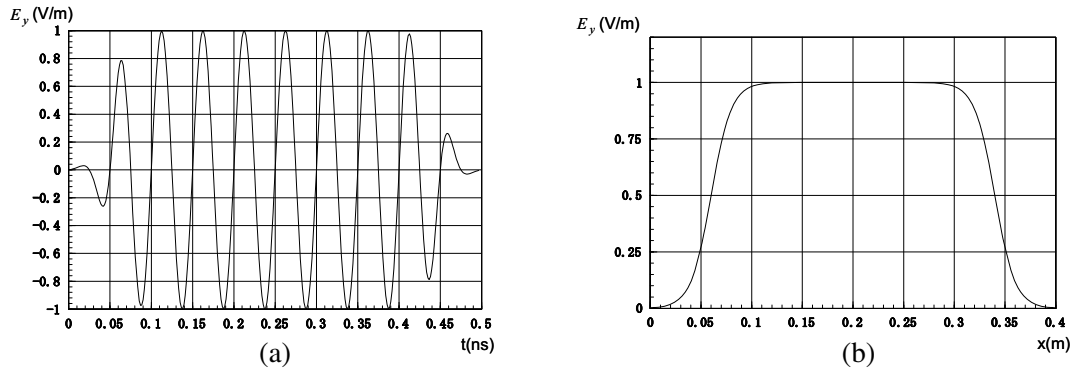
Figure 7: Time waveform and spatial distribution of the electric field of the incident wave. (a) Time waveform of incident wave. (b) Spatial distribution of incident wave.
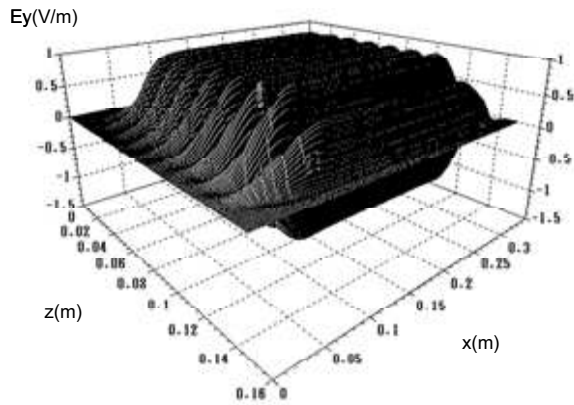

Figure 8: Electric field of incident wave at $t = 333$, $\Delta t = 0.5\,\text{ns}$ $(s = 1)$.
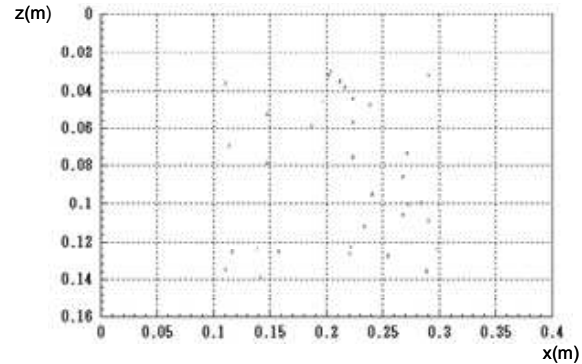
Figure 9: Cross sectional view of raindrop distribution $(N = 33$, $a_i = 1\,\text{mm}$, $s = 1)$.

Pulse width of $0.4\,(\text{ns})$ is sufficiently long so that six stable peaks of the incident wave are shown in Fig. 7(a). Beam width of $0.28\,(\text{m})$ is appropriate because the amplitudes of the incident wave on the boundary of analysis space, at $x = 0$, ℓ_x, $y = 0$, ℓ_y can be negligibly small and the amplitude distribution in a region of $0.1\,(\text{m}) \leq x, y \leq 0.2\,(\text{m})$ is almost uniform constant. When raindrop positions x_i and y_i are restricted as $0.1\,(\text{m}) \leq x_i, y_i \leq 0.2\,(\text{m})$, the incident waves at raindrop positions (x_i, y_i, z_i) with same z_i coordinate have almost constant amplitudes. Simulation parameters are shown in Table 1. The electric field distribution of incident wave is shown in Fig. 8. Fig. 9 shows a random media model of rainfall rate $R = 20\,(\text{mm/h})$, where $N = 33$ is the number of raindrops, $a_i = 1\,(\text{mm})$ is a side length of raindrops and $n_r^* = 6.46 - j2.81$ is complex refractive index of raindrops. Fig. 10 shows the numerical results of field difference ΔE_y between total field and incident field, as scattered field. Spherical scattering waves from raindrops are observed in this figure.

6. COMPARISON OF RAIN ATTENUATION BY FDTD ANALYSIS AND MEASUREMENT

In FDTD simulation, field difference of electric fields $\Delta E_y = E_y - E_{inc,y}$ compared with incident field is shown in Fig. 10. Rain attenuation α for propagation length $\ell\,(\text{m})$ in Eq. (1) is calculated by receiving power $P(\ell)$ and $P_0(\ell)$ given by incident field $\mathbf{E}_{inc}$ in Eq. (1),

$$P(\ell) = \int_S \bar{W}(x, y, \ell)\, dS$$

$$\bar{W}(x, y, \ell) = \frac{1}{T} \int_{t'}^{t'+T} (E_x H_y - E_y H_x)\, dt \tag{7}$$

Table 1: Parameters for long distance simulation using parallel FDTD computation $s = 1 - 5$: Step number of subspaces.

| Parameters	Values
λ : Wavelength of incident wave	0.015m
ℓ_x, ℓ_y, ℓ_z : Length of subspace in x, y, z direction	0.4m (26.7λ), 0.4m (26.7λ), 0.15m (10λ)
$\ell_{z\max}$: Length of total analysis space in z direction	0.75m (50λ)
f : Frequency of incident wave	20GHz
α : Time parameter for incident pulse t_1, t_2 : Time when pulse gets the half amplitude	10^{11} (1/s) 0.05ns, 0.45ns
β : Spatial parameter for incident pulse x_1, x_2 : Point where pulse gets the half amplitude y_1, y_2 : Point where pulse gets the half amplitude	100 0.06m, 0.34m 0.06m, 0.34m
Δs : Length of a cell Δt : Time increment	0.001m 1.5ps
N : Number of raindrops in a subspace	8 (5mm/h), 16 (10mm/h), 33 (20mm/h) 66 (40mm/h), 83 (50mm/h)
a_i : Length of a side of a raindrop n_r : Complex refractive index of raindrops	1mm 6.46-j2.81
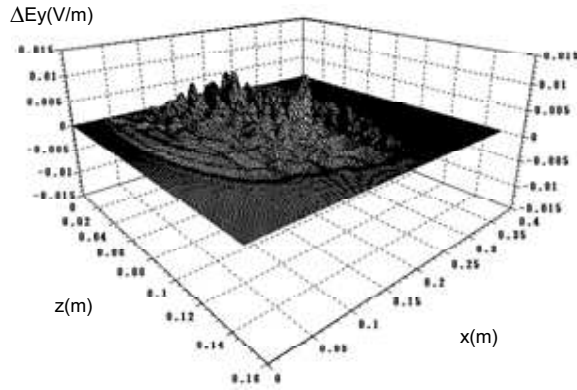
Figure 10: Difference of electric field ΔE_y at $t = 333$, $\Delta t = 0.5$ ns $(s = 1)$.
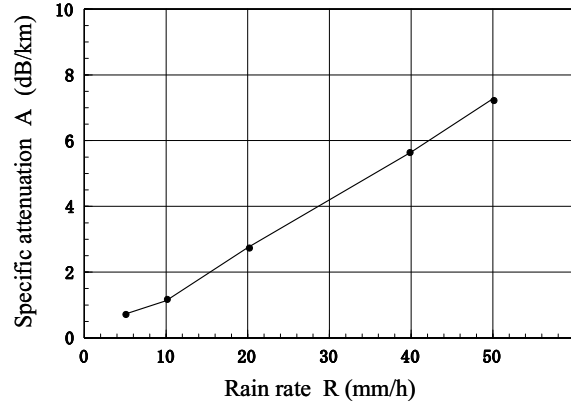
Figure 11: Specific rain attenuation by FDTD.

where $\ell = \ell_{\max} = 0.075$ (m) is propagation distance of total analysis space. Specific attenuation by rain A (dB/km) is given by Eq. (1). Rain rate R (mm/h) is obtained by

$$R = \frac{N}{V} vta^3 \cdot 10^{-6} \tag{8}$$

where N is a number of raindrops in one subspace with volume $V = \ell_x \ell_y \ell_z = 0.024$ (m^3), v is the terminal velocity of raindrops and $t = 1$ (hr) $= 3600$ (sec). When $v = 4$ (m/s), $t = 1$ (hr), $V = 0.024$ (m^3) and $a = 1$ (mm) are assumed, R is given by $R = 0.6N$. Electromagnetic fields in s-th subspace is calculated by using the results of electromagnetic fields at the terminal plane at $z = (s-1)\ell_z$ in $(s-1)$-th subspace as the incident wave. Fig. 11 shows specific rain attenuation obtained by FDTD using these parameters. These numerical simulation discussed by FDTD method will be compared with the measured data in next paper.

7. CONCLUSIONS

In this paper, rain attenuation in large area which contains hundreds of raindrops is shown by using parallel and successive computation of FDTD and successive FDTD method and specific rain attenuation is evaluated. Based on these computer simulations, the optimum measurement systems of raindrop using microwave techniques may be accomplished.

REFERENCES

1. Oguchi, T., "Electromagnetic wave propagation and scattering in rain and other hydrometers," *IEEE Proc.*, Vol. 71, 1029–1078, 1983.

2. Miyazaki, Y., "Light scattering of laser beams by random micro-inhomogeneities in glasses and polymers," *Jpn. J. Appl. Phys.*, Vol. 13, No. 8, 1238–1248, 1974.

3. Takahashi, K., Y. Miyazaki, and N. Goto, "FDTD analysis of scattering and attenuation characteristics for microwave and milli-meter wave due to rainfall," *The Papers of Technical Meeting on Electromagnetic Theory, IEE Japan*, EMT-03-69, 83–87, 2003.

4. Takahashi, K. and Y. Miyazaki, "Scattering and attenuation characteristics of microwave and millimeter wave due to rainfall for ITS and weather measurement system," *Proc. of ISAP'04, Sendai*, POS-B-4, 1081–1084, 2004.

5. Miyazaki, Y., K. Takahashi, and N. Goto, "FDTD parallel computing of microwave scattering and attenuation characteristics due to randomly distributed rainfalls," *PIERS Online*, Vol. 4, No. 2, 245–250, 2008.

6. Rodriguez, G., Y. Miyazaki, and N. Goto, "Matrix-based FDTD parallel algorithm for big areas and its applications to high-speed wireless communications," *IEEE Trans. Antennas and Propagation*, Vol. 54, No. 3, 785–796, 2006.

7. Takahashi, K., Y. Miyazaki, and N. Goto, "FDTD parallel computational analysis of grid-type scattering filter characteristics for medical X-ray image diagnosis," *IEEJ Trans. EIS*, Vol. 127, No. 12, 1973–1981, 2007.

8. Takahashi, K., Y. Miyazaki, and N. Goto, "Statistical scattering and attenuation characteristics of microwaves by randomly distributed rainfalls," *Proc. of 2009 International Symposium on EMC, Kyoto*, 21P4-3, 221–224, 2009

9. Miyazaki, Y., N. Goto, and K. Takahashi, "FDTD parallel computing of microwave scattering and polarization characteristics by raindrop models," *Proc. of AP-RASC 2010*, BEFKb-2, Toyama, 2010.

Calculation of Circular Microstrip Antenna Parameters with a Single Artificial Neural Network Model

S. S. Gultekin[1], **D. Uzer**[1], **and O. Dundar**[2]

[1]Department of Electrical and Electronics Engineering
Faculty of Engineering and Architecture, Selcuk University, Konya, Turkey
[2]Electronic Communication Technology Department
Eregli Kemal Akman Vocational High School, Selcuk University, Turkey

Abstract— A model for the design of circular microstrip antennas, based on Artificial Neural Networks, is presented. The multiple output design parameters are calculated by using a neural network. This neural model is simple and useful for the computer-aided design (CAD) of microstrip antennas. A distinct advantage of neural computation is that, after proper training, a neural network completely bypasses the repeated use of complex iterative processes for new cases presented to it. For engineering applications, this simple model is very usable. Thus the neural model given in this work can also be used for many engineering applications and purposes. In this study, for this neural network model, patch radius, radiation resistance, directivity, total quality factor, bandwidth, efficiency and gain are calculated as output parameters against input parameters as dielectric constant, resonant frequency, dielectric substrate thickness and tangent loss. Extended Delta-Bar-Delta training algorithm by Multilayer Perceptron structure that used popular in literature and gives good approaches is used for training the network. The design results obtained by using the neural model are in very good agreement with the results available in the literature.

1. INTRODUCTION

Microstrip antennas are used in a broad range of applications from communication systems (radars, telemetry, and navigation) to biomedical systems, primarily due to their simplicity, conformability, low manufacturing cost, light weight, low profile, reproducibility, reliability, and ease in fabrication and integration with solid-state devices [1–10]. Several methods [1–6] are available to design the circular microstrip patch antenna, as this is one of the most popular and convenient shapes. These methods have different levels of complexity, require vastly different computational efforts, and can generally be divided into two groups: simple analytical methods and rigorous numerical methods. Simple analytical methods can give a good intuitive explanation of antenna radiation properties. Exact mathematical formulations in rigorous methods involve extensive numerical procedures, resulting in round-off errors, and may also need final experimental adjustments to the theoretical results. They are also time consuming and not easily included in CAD package. In this work, a simple method based on the artificial neural networks (ANNs) is presented to design accurately the circular microstrip antennas. In previous works [11, 12], it was also successfully introduced the artificial neural models to compute the bandwidth, the resonant resistance and the resonant frequencies of various microstrip antennas. In these works [11, 12], again only one output parameter has been computed. In this study, the multiple output parameters for the design of the circular microstrip antennas are computed by using ANNs.

2. DESIGN OF CIRCULAR MICROSTRIP PATCH ANTENNAS

Consider a circular patch of radius a over a ground plane with a substrate of thickness h and a relative dielectric constant ε_r, as shown in Figure 1.

The first design step is to select a suitable dielectric substrate material [1–6]. The major electrical properties to consider are relative dielectric constant ε_r and loss tangent $\tan \delta$. Generally it is best to select a substrate with the lowest possible dielectric constant consistent with the space available for the antenna. Substrate thickness should be chosen as large as possible to maximize bandwidth and efficiency, but not so large as to risk surface-wave excitation. For a maximum operating frequency of f_r, the thickness should satisfy;

$$h \leq \frac{0.3c}{2\pi f r \sqrt{\varepsilon_r}} \tag{1}$$

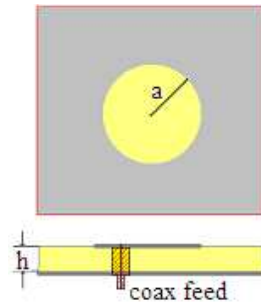where c is the velocity of electromagnetic waves in free space.

Figure 1: Geometry of circular microstrip antenna.

After the selection of a suitable substrate material, the other characteristics parameters of the antenna are determined by using the design methods available in the literature [1–6]. In this work, the design procedure given in [1] was followed. The design results presented here have been obtained assuming that the VSWR = 2, the copper as the patch material, and the dominant TM_{11} mode, which are widely used in circular microstrip antenna applications. Under these conditions, it is clear from [1] that the patch radius, radiation resistance and directivity are determined by ε_r, f_r, and h, and that the total quality factor, bandwidth, efficiency, and gain are determined by f_r, h, a, and $\tan \delta$. Since the patch radius a depends on ε_r, f_r, and h, the total quality factor, bandwidth, efficiency, and gain can also be determined by ε_r, f_r, h, and $\tan \delta$. The neural models can also be easily adopted to design a circular patch antenna for any mode, any patch material and any value of the VSWR.

3. ARTIFICIAL NEURAL NETWORKS

ANNs are biologically inspired computer programs designed to simulate the way in which the human brain processes information. ANNs gather their knowledge by detecting the patterns and relationships in data and learn (or are trained) through experience, not from programming. An ANN is formed from hundreds of single units, artificial neurons or processing elements connected with weights, which constitute the neural structure and are organized in layers. The behaviour of a neural network is determined by the transfer functions of its neurons, by the learning rule, and by the architecture itself.

There are many types of neural networks for various applications available in the literature [14, 15]. Multilayered perceptrons (MLPs) [13–15] are the simplest and therefore most commonly used neural network architectures. In this work, they have been adapted for the design of the circular microstrip antennas. An MLP consists of three layers: an input layer, an output layer and an intermediate or hidden layer. Neurons in the input layer only act as buffers for distributing the input signals x_i to PEs in the hidden layer. Each PE j in the hidden layer sums up its input signals x_i after weighting them with the strengths of the respective connections w_{ji} from the input layer and computes its output y_j as a function f of the summation as;

$$y_j = f \left(\sum w_{ji} x_i \right) \tag{2}$$

where f can be a simple threshold function, a sigmoidal or hyperbolic tangent function. The output of PEs in the output layer is computed similarly. MLPs can be trained using many different learning algorithms [13–19]. A learning algorithm gives the change $\Delta w_{ji}(k)$ in the weight of a connection between PEs i and j. In this work, MLP is trained with the extended delta-bar-delta (EDBD) algorithm. In the following section, the EDBD algorithm has been explained briefly.

The extended delta-bar-delta algorithm [13] is an extension of the delta-bar-delta algorithm [17] and based on decreasing the training time for multilayered perceptrons. The use of the momentum heuristics and avoiding the cause of the wild jumps in the weights are the features of the algorithm. The EDBD algorithm includes a little-used "error recovery" feature which calculates the global error of the current epoch during training. If the error measured during the current epoch is greater than the error of the previous epoch, then the network's weights revert back to the last set of weights (the weights which produced the lower error).

4. APPLICATION OF ARTIFICIAL NEURAL NETWORKS TO THE DESIGN OF CIRCULAR MICROSTRIP ANTENNAS

The proposed method involves training the neural networks to design the circular microstrip antennas when the values of ε_r, f_r, h, and $\tan\delta$ are given. The neural model has been used in the design, as shown in Figure 2. Training an MLP with the use of the EDBD algorithm to design the circular microstrip antenna involves presenting them sequentially/randomly with different (ε_r, f_r, h, $\tan\delta$) sets and corresponding target values (radius of the patch, radiation resistance, quality factor, efficiency, bandwidth, directivity, gain). Differences between the target outputs and the actual outputs of the MLP are trained through the EDBD algorithm to adapt their weights. The adaptation is carried out after the presentation of each set (ε_r, f_r, h, $\tan\delta$) until the calculation accuracy of the network is deemed satisfactory according to some criterion (for example, when the root-mean square (rms) error between the target outputs and the actual outputs for all the training set falls below a given threshold) or the maximum allowable number of epochs is reached.

The cavity model [1] was used to generate data for $1.1 < \varepsilon_r < 12$, $0.01\,\mathrm{cm} < h < 0.38\,\mathrm{cm}$, $0.07\,\mathrm{GHz} < f_r < 11\,\mathrm{GHz}$, and $0.0001 < \tan\delta < 0.01$. For design curves, out of 200 data sets generated, 180 data sets were used for training and the rest were used for testing the network. A set of random values distributed uniformly between -0.1 and $+0.1$ was used to initialize the weights of the networks. However, the input data tuples were scaled between -1.0 and $+1.0$ and the output data tuples were also scaled between -0.8 and $+0.8$ before training. After several trials, it was found that two layers network achieved the task with high accuracy.

The parameters of the network are: the inputs are ε_r, f_r, h and $\tan\delta$. The outputs are the patch radius, radiation resistance, directivity, total quality factor, bandwidth, efficiency and gain. The number of iteration for training is 10,000,000. The root-mean-square (rms) errors for training and testing are 0.0017 and 0.0038, respectively.
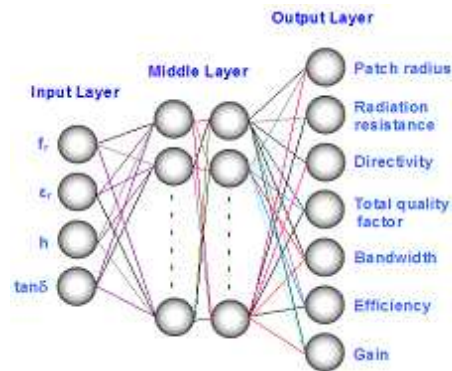

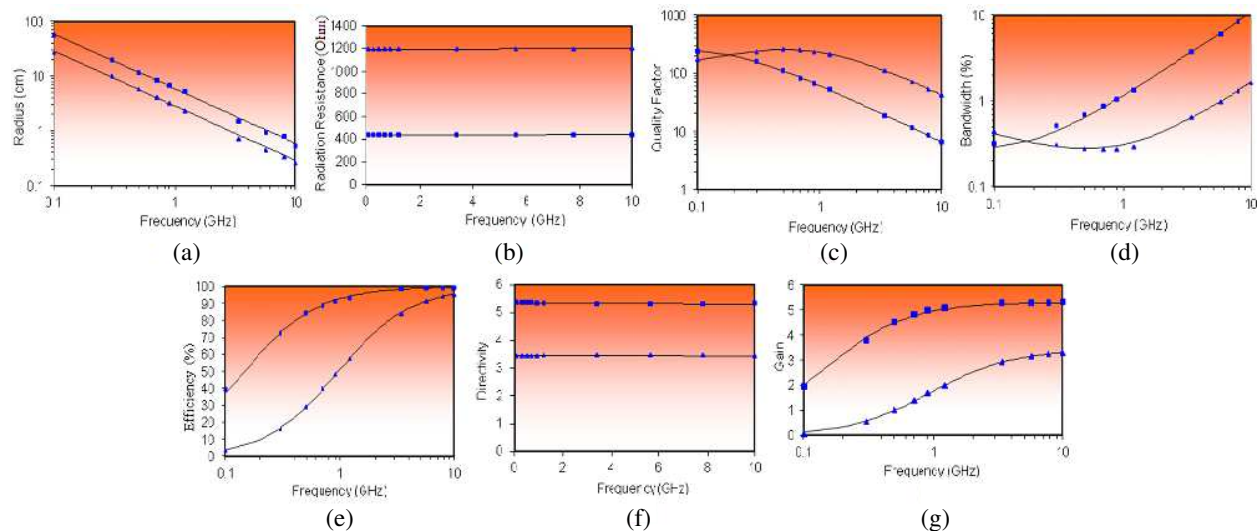Figure 2: Neural model for a circular microstrip antenna.

Figure 3: Design curves for (a) radius, (b) radiation resistance, (c) quality factor, (d) bandwidth, (e) efficiency, (f) directivity and (g) gain.

5. RESULTS AND CONCLUSIONS

As a design aid, test results obtained from the model versus frequency for two different dielectric substrates are in Figure 3. As can be seen from Figure 3 that the test results are in very good agreement with the results of [3]. This good agreement supports the validity of the neural model. The multiple outputs are calculated successfully. In this work, different learning algorithms such as the back propagation [13], the delta-bar-delta [17], and the quick propagation [16] were also used to train the networks. However, the best result was obtained from the EDBD. For this reason, only the results of the EDBD were given in this work. For engineering, the simple models are very usable. Thus the neural model given in this work can also be used for many engineering applications and purposes.

ACKNOWLEDGMENT

REFERENCES

1. Bahl, J. and P. Bhartia, *Microstrip Antennas*, Artech House, Dedham, MA, 1980G.
2. Gupta, K. C. and A. Benalla (Editors), *Microstrip Antenna Design*, Artech House, Canton, MA, 1988.
3. James, J. R. and P. S. Hall, *Handbook of Microstrip Antennas*, IEE Electromagnetic Wave Series No. 28, Vols. 1, 2, Peter Peregrinus Ltd., London, 1989.
4. Bhartia, P., K. V. S. Rao, and R. S. Tomar (Editors), *Millimeter-wave Microstrip and Printed Circuit Antennas*, Artech House, Canton, MA, 1991.
5. Pozar, D. M. and D. H. Schaubert (Editors), *Microstrip Antennas — The Analysis and Design of Microstrip Antennas and Arrays*, IEEE Press, New York, 1995.
6. Sainati, R. A., *CAD of Microstrip Antennas for Wireless Applications*, Artech House, Norwood, MA, 1996.
7. Güney, K., "A new edge extension expression for the resonant frequency of electrically thick rectangular microstrip antennas," *International Journal of Electronics (IJE)*, Vol. 75, 767–770, 1993.
8. Güney, K., "Radiation quality factor and resonant resistance of rectangular microstrip antennas," *Microwave and Optical Technology Letters*, Vol. 7, 427–430, Jun. 20, 1994.
9. Güney, K., "Bandwidth of a resonant rectangular microstrip antenna," *Microwave and Optical Technology Letters*, Vol. 7, 521–524, Aug. 5, 1994.
10. Güney, K., "Closed-form expression for radiation resistance of a resonant rectangular microstrip patch antenna," *International Journal of Microwave and Millimeter-Wave Computer-Aided Engineering (Journal MIMICAE)*, Vol. 5, 31–39, 1995.
11. Sagiroglu, S. and K. Güney, "Calculation of resonant frequency for an equilateral triangular microstrip antenna with the use of artificial neural networks," *Microwave and Optical Technology Letters*, Vol. 14, 89–93, Feb. 1997.
12. Sagiroglu, S., K. Güney, and M. Erler, "Resonant frequency calculation for circular microstrip antennas using artificial neural networks," *International Journal of RF and Microwave Computer-Aided Engineering*, Vol. 8, 270–277, 1998.
13. Rumelhart, D. E. and J. L. McClelland, *Parallel Distributed Processing*, Vol. 1, The MIT Press, Cambridge, 1986.
14. Maren, A., C. Harston, and R. Pap, *Handbook of Neural Computing Applications*, Academic Press, London, 1990.
15. Haykin, S., *Neural Networks: a Comprehensive Foundation*, Macmillan College Publishing Company, New York, 1994.
16. Fahlman, S. E., "An emprical study of learning speed in backpropagation networks," Technical Report CMU-CS-88-162, Carnegie Mellon University, Jun. 1988.
17. Jacobs, R. A., "Increased rate of convergence through learning rate adaptation," *Neural Networks*, Vol. 1, 295–307, 1988.
18. Minai, A. and R. D. Williams, "Acceleration of backpropagation through learning rate and momentum adaptation," *Int. Joint Conf. on Neural Networks*, Vol. 1, 676–679, Washington, DC, Jan. 1990.
19. NeuralWare, Inc., *Neural Computing, a Technology Handbook for Professional II/Plus and Neuralworks Explorer*, Technical Publications Group, Pittsburgh, 1996.

Estimation and Design of U-slot Physical Patch Parameters with Artificial Neural Networks

D. Uzer[1], S. S. Gultekin[1], and O. Dundar[2]

[1]Department of Electrical and Electronics Engineering
Faculty of Engineering-Architecture, Selcuk University, Konya, Turkey
[2]Electronic Communication Program
Eregli Kemal Akman Technical Vocational School of Higher Education
Selcuk University, Konya, Turkey

Abstract— In this study, physical U slot parameters of rectangular microstrip patch antennas as vertical and horizontal slot lengths and widths with the patch lengths and widths are determined by the help of Artificial Neural Networks. The aim of the study is calculation of physical U slot patch parameters without any mathematical expressions or long and complex numeric calculations with a neural network model. Experimental results in the literature are used as the training data for the network by using Gradient Descent with Adaptive Learning Rate Back Propagation learning algorithm. The resonant frequency, dielectric constant of the substrate and the dielectric substrate thickness values are the inputs of the neural network and the patch length, patch width, the lengths and widths of the vertical and horizontal slots are the network outputs. The test output data of the network are used for simulations and the results are confirmed by these simulations. S_{11} responses, simulation frequency, impedance bandwidth, directivity, gain and radiation efficiency values of the antennas are investigated by HFSS. Simulation results are compatible with test outputs. The high training success of the network and R^2 values very close to 1 show that physical patch parameters of U-slot rectangular microstrip antennas can be calculated with this Artificial Neural Network model with high accuracy.

1. INTRODUCTION

Thanks to their various advantages, microstrip antennas have large application fields, but their small bandwidths restrict them. In recent years, lots of studies have been presented and various methods that aimed larger bandwidths have been developed [1–3]. Etching U-slot on the patch is may be the simplest design [4, 5]. This design avoids the use of stacked or coplanar parasitic patches, either of which increases the thickness or the lateral size of the antenna. So, while changing the current distribution on the microstrip patch, enhancing the impedance bandwidth with sometimes more than one resonant frequency are obtained.

In 1995, a broad band single layer probe fed patch antenna with a U-shaped slot was presented by Huynh and Lee and wideband impedance characteristics were obtained by cutting a U-slot on the surface of the rectangular patch in [4] and [5]. In this study, an Artificial Neural Network was modeled with U-slot rectangular microstrip antenna parameters in the literature for calculation of their physical patch parameters. Then, with the Artificial Neural Network results, experimental results from the literature are compared.

2. U-SLOT RECTANGULAR MICROSTRIP ANTENNA

Rectangular microstrip antenna is the easiest geometry for designing and implementation. It is shown that etching U slot on rectangular patches enhance the impedance bandwidth up to 47% [4, 5]. By etching U slot, the impedance seen from the feed point will be changed and realizing impedance matching a larger bandwidth will be obtained. Generally, the enhancement process is realized by obtaining more than one resonant frequency that radiates under $-10\,\mathrm{dB}$ level [6–9]. The first resonance frequency is understood to be generated by the microstrip patch due to the physical parameters, while the second one by the U-shaped slot parameters [4, 5]. The surface currents originate behind the U-slot, and are strong outside the U-slot arms [10]. The U-slot introduces a capacitance and induces a second resonance frequency near the main resonance frequency of the microstrip patch, producing an enhanced frequency response [9]. The basic U-slot rectangular microstrip patch antenna design can be seen in Figure 1. Here, L is the patch length, W is the patch width, F is the feed point, L_S is the vertical slot length, W_S is the horizontal slot length, t_L and t_W are slot widths in the vertical and horizontal, respectively.
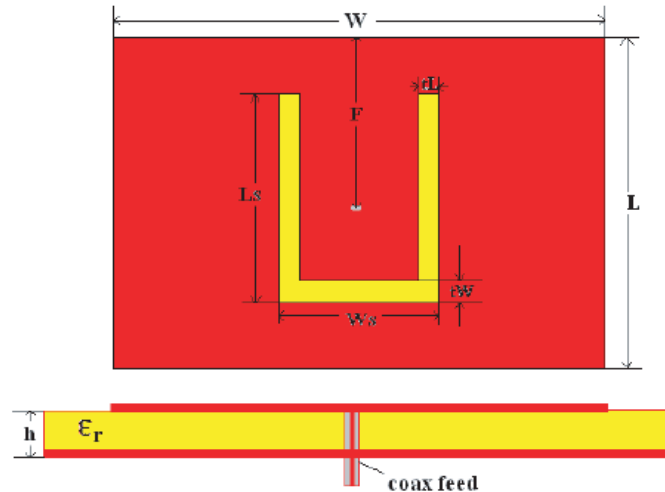
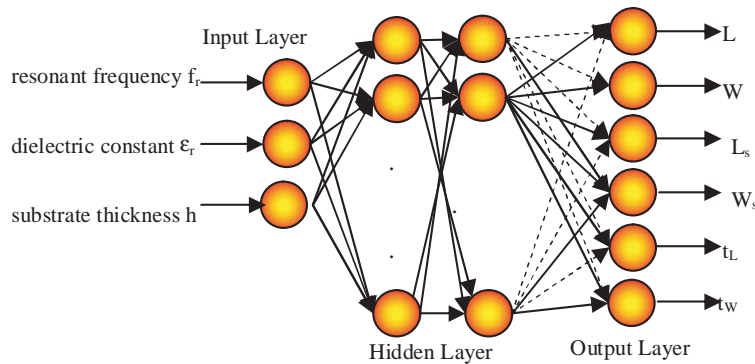Figure 1: U-slot rectangular microstrip patch antenna.

Figure 2: Artificial neural network model for calculation of physical patch parameters.

3. ARTIFICIAL NEURAL NETWORKS

Artificial Neural Networks (ANN) are artificial systems based on vision and learning that are designed in a similar way to human brain working principle. Because of their parallel working ability, results can be produced quickly and they can give useful results for real time problem solution by learning from samples. In general, an ANN is considered as a complicated system developed by connecting simple processors with different effect layers or lots of neurons in human brain [11–14]. Among them, multilayer perceptron (MLP) had been employed in this study for calculations of slot lengths and widths on a U-slot rectangular microstrip antenna.

Gradient Descent with Adaptive Learning Rate Back Propagation (GDA) is a learning function which updates the weights and bias values according to the gradient descent with adaptive learning rate. An Adaptive Learning Rate can be whatever makes the learning stable. The learning rate should be considered as the main reason for the complexity on the local error surfaces [16].

It needs some changes while learning process with adaptive learning rate. First, outputs and biases whose initial values of the network are established and weight values are calculated again. After than new output values and errors are calculated. In case of using the momentum, if new error rate is larger than the error rate of the previous circle that defined before (generally 1.04), new weight and bias values will turn back to the preceding values. Also, the learning rate is decreased. For this aim, the learning coefficient is generally multiple by 0.70 otherwise new weights and other values are hold. If the error is smaller than the older, the learning rate will be increased by multiplying the learning coefficient by 1.05.

In this learning rule, learning rate increases so large error variations should not be seen in the network. Thus, for local learning, an approximate optimum learning rate is determined. For larger learning rates in stable learning, the rate is increased.

Table 1: ANN input and output test parameters with simulation results.

No	Inputs				Outputs					
	f_r (GHz)	f_r HFSS(GHz)	ε_r	h (mn)	L (mm)	W (mm)	L_S (mm)	W_S (mm)	t_L (mm)	t_W (mm)
1	1.8	**1.863727**	6.15	3.18	32.49	40.70	18.95	15.57	2.17	2.00
2	1.8	**1.786774**	6.15	1.27	23.62	24.65	12.78	10.68	1.12	1.07
3	1.8	**1.976754**	4.5	1.57	24.31	25.06	13.30	10.92	1.19	1.16
4	1.8	**1.858918**	3.5	1.52	28.56	29.80	16.40	12.70	1.65	1.68
5	1.9	**2.045491**	6.15	3.18	29.87	35.78	17.13	14.09	1.85	1.73
6	1.9	**1.889178**	6.15	1.27	23.13	23.78	12.43	10.42	1.06	1.01
7	1.9	**1.821844**	3.5	1.52	27.94	29.00	15.95	12.42	1.58	1.61
8	1.9	**1.848297**	10.2	2.54	26.03	28.89	14.51	11.97	1.40	1.33
9	1.9	**1.863727**	1	5	56.38	74.76	36.25	27.48	5.54	4.12
10	3	**3.027054**	6.15	1.27	21.46	21.00	11.24	9.56	0.88	0.82
11	3	**3.465932**	2.33	1.58	28.43	28.86	16.36	12.48	1.56	1.72
12	3	**3.598196**	3.5	1.52	23.08	22.76	12.44	10.23	1.02	1.03
13	3	**2.343687**	3	1.52	24.92	24.81	13.79	11.00	1.20	1.27
14	5.8	**6.1183**	4.1	3.18	21.28	20.84	11.10	9.50	0.87	0.79
15	5.8	**4.546**	2.33	1.58	21.56	21.16	11.30	9.61	0.90	0.82
16	5.8	**3.854709**	3.5	1.52	21.30	20.86	11.12	9.50	0.87	0.79
17	0.9	**0.906313**	1	5	85.37	131.83	55.23	44.71	9.83	6.34
18	5	**4.744489**	1	5	28.27	28.73	16.23	12.42	1.56	1.70

Table 2: Comparison between the perfusion coefficient (B) for the different tissues.

Data				Physical patch parameters					
Number				ANN-GDA R^2					
Train	37	*Test*	18	L	W	L_S	W_S	t_L	t_W
Structure		$3 \times 9 \times 9 \times 6$							
Epoch Number		80.000		0.9547	0.9913	0.9405	0.9845	0.8379	0.9651
Performance		14.8764							

4. METHODOLOGY AND RESULTS

Although there are some design procedures and equivalent circuit model determination studies for U-slot rectangular microstrip antennas recently, the current formulas are experiment based and take so long time, because of complex mathematical calculations they aren't useful for the designers [9, 23]. In this study a solution to the above situation with an ANN model that calculates U-slot rectangular microstrip antenna patch parameters easy and fast was composed that seen in Figure 2.

In the design process, different Matlab training algorithms like Levenberg-Marquardt (LM) [13–15], Gradient descent with momentum back propagation (GDM), Extended Delta-Bar-Delta (ED BD) [14], Gradient descent with adaptive learning rate back propagation (GDA), Gradient descent with momentum and adaptive learning rate back propagation (GDM), Scaled conjugate gradient back propagation (SCG) BFGS quasi-Newton back propagation (BFGS), Conjugate gradient back propagation with Polak-Ribiere (PR), One step secant back propagation (OSS) [28], etc. were used and GDA which gives the best results was chosen. For training ANN, 37 experimental data from the literature were used [4, 9, 17–27]. After the network was trained, for f_r, ε_r and h inputs belong to 18 antenna, L, W, L_S, W_S, t_L and t_W patch parameters were obtained as the network outputs. The input and output parameters can be seen in Table 1. In Table 2 train algorithm structure was given with train R^2 output values. In parameter producing with ANN ε_r and h from input data were chosen between 1–10.2 and 1.27–5 mm, respectively considering the most common substrate materials used in the literature. In simulations, some antennas had only one resonant frequency, in spite of others had two or more. The bandwidths of the antennas were between 0.9% and 33.

5. CONCLUSIONS

In this study patch parameters of U-slot rectangular microstrip antennas were determined by using experimental data in the literature in Artificial Neural Networks. With these parameters the designed antennas were verified in simulation media and it was observed that the results were compatible with desired values. It can be said that the design model was successful for determining the U-slot antenna parameters due to the simulation results and high training success of the Artificial Neural Network. In the future work, improving the network structure for getting better results is aimed.

ACKNOWLEDGMENT

REFERENCES

1. Lee, R. Q., K. F. Lee, and J. Bobinchak, "Characteristics of a two-layer electromagnetically coupled rectangular patch antenna," *Electron. Lett.*, Vol. 23, No. 20, 1070–1072, 1987.
2. Fong, K. S., H. F. Pues, and M. J. Withers, "Wideband multilayer coaxial fed microstrip antenna element," *Electron. Lett.*, Vol. 21, No. 11, 497–499, 1985.
3. Pues, H. G. and A. R. Van De Capelle, "An impedance matching technique for increasing the bandwidth of microstrip antennas," *IEEE Trans. on Ant. and Propa.* Vol. 37, No. 11, 1345–1354, 1989.
4. Huynh, T. and K. F. Lee, "Single-layer single-patch wideband microstrip antenna," *Electron. Lett.*, Vol. 31, No. 16, 1310–1312, 1995.
5. Lee, K. F., K. M. Luk, L. Tongy, Y. L. Yung, and T. Huynh, "Experimental study of the rectangular patch with a U shaped slot," *IEEEIAP-S International Symposium Dig.*, 10–13, 1996.
6. Kumar, G. and K. P. Ray, *Broadband Microstrip Antennas,* Artech House, Waterhouse, R.B., 2002.
7. Uzer, D., "Bandwidth enhancement techniques on microstrip antennas," *Teknikleri, Doct. Seminar, Selcuk Uni. Gradu. Sch. of Nat. and App.Sci.*, Konya, Turkiye, 2010.
8. Uzer, D., "Investigation on favorable methods for wideband microstrip patch antenna designs, geniş band, mikro Şerit yama anten tasarimlari için uygun yöntemlerin araştirilmasi," Ph.D. thesis, Selcuk Uni. Gradu. Sch. of Nat. and App. Sci., Konya, Turkiye, (in progress).
9. Weigand, S., G. H. Huff, K. H. Pan, and J. T. Bernhard, "Analysis and design of broad-band single-layer rectangular U-slot microstrip patch antennas," *IEEE Trans. on Ant. and Prop.*, Vol. 51, No. 3, 457–468, Mar. 2003.
10. Tong, K. F., K. M. Luk, and K. F. Lee, "Design of a broadband U-slot patch antenna on a microwave substrate," *Asia Pacific Microwave Conference*, 221–224, 1997.
11. Rumelhart, D. E. and J. L. McClelland, *Parallel Distributed Processing, Explorations in the Microstructure of Cognition,* The MIT Press, Cambridge, Mass., 1986.
12. Haykin, S., *Neural Networks: A Comprehensive Foundation,* Macmillan College Publishing Company, 1994.
13. Levenberg, K., "A method for the solution of certain non-linear problems in least squares," *The Quart. Appl. Math*, Vol. 2, 164–168, 1944.
14. Minai, A. and R. D. Williams, "Acceleration of backpropagation through learning rate and momentum adaptation," *Int. Joint Conf. on Neural Networks*, Vol. 1, 676–679, 1990.
15. Marquardt, D., "An algorithm for least-squares estimation of nonlinear parameters," *SIAM J. Appl. Math.*, Vol. 11, 431–441, 1963.
16. Hagan, M. T., H. B. Demuth, and M. Beale, *Neural Network Design,* Boston PWS Publishing Company, 1996.
17. Choltiar, E., V. Nalarajan, and D. Chatterjee, "Comparison of resonant frequency calculations for wideband U-slot antennas on microwave substrates," *IEEE Antennas and Propagation Society International Symposium*, Vol. 4, Nos. 20–25, 13713–3716, Jun. 2004.
18. Khodaei, G. F., J. Nourinia, and C. Ghobadi, "A practical miniaturized U-slot patch antenna with enhanced bandwidth," *Progress In Electromagnetics Research B*, Vol. 3, 47–62, 2008.
19. Houari, O., *Wireless Sensor Systems Design Course Book,* 13–20, University of South Florida, Tennessee Technological University, Spring, 2001.

20. Zhang, S., G. Huff, and T.J. Bernhard, "Antenna efficiency and gain of two new compact microstrip antennas," *Proc. Antenna Applications Symposium*, 108–116, Allerton Park, Monticello, Illinois, 2001. .

21. Clenet, M. and L. Shafai, "Multiple resonances and polarization of U-slot patch antenna," *Electron. Lett.*, Vol. 35, No. 2, 101–103, 1999.

22. Lee, K. F., S. Lung, S. Yang, A. A. Kishk, and K. M. Lu, "The versatile U-slot patch antenna," *IEEE Antennas and Propagation Magazine*, Vol. 52, No. 1, 71–88, Feb. 2010.

23. Bhalla, R. and L. Shafai, "Resonance behavior of single U-slot microstrip patch antenna," *Microwa. and Optic. Techn. Lett.*, Vol. 32, No. 5, 333–335, Mar. 5, 2002.

24. Mahmoud, M., "Improving the bandwidth of U-slot microstrip antenna using a new technique (trough-slot patch)," *IEEE Region 5 Conference*, 1–6, Kansas City, MO, Apr. 17–20, 2008.

25. Lee, K. F., K. M. Luk, K. F. Tong, S. M. Shum, T. Huynh, and R. Q. Lee, "Experimental and simulation studies of the coaxially fed U-slot rectangular patch antenna," *IEE Proc. — Microw Antennas Propag.*, Vol. 144, No. 5, 354–358, Oct. 1997.

26. Shackelford, A. K., K. F. Lee, and K. M. Luk, "Design of small-size wide-bandwidth microstrip-patch antennas," *IEEE Anten. and Propa. Mag.*, Vol. 45, No. 1., 75–83, Feb. 2003.

27. Tong, K. F., K. M. Luk, K. F. Lee, and S. M. Shum, "Analysis of broadband u-slot microstrip antenna," *10th International Conference on Antennas and Propagation, Conference Publication*, No. 436, 1.10–1.13, Apr. 14–17, 1997.

28. MATLAB 7.04, http://www.mathworks.com/products/matlab/.

29. HFSS v 12., http://www.ansoft.com/products/hf/hfss.

Effect of U-slot Applications on Circular Microstrip Patches Modeling with Artificial Neural Networks on Impedance Bandwidth

D. Uzer, **M. S. Uzer**, **S. S. Gultekin**, **and N. Yilmaz**

Electrical and Electronics Engineering Department
Faculty of Engineering and Architecture, Selcuk University, Konya, Turkey

Abstract— In this study, effects of etching U-slot on circular patches on their bandwidths are investigated. The study is carried out by etching U-slots on the present microstrip patches in the literature by simulating them with HFSS. Simulation results are used for training and testing of an Artificial Neural Network model for different microstrip patches' bandwidth predictions. The obtained simulation results are compared with Artificial Neural Network results. In comparison of the simulation and Artificial Neural Network results, accuracy rates of training and testing were found as 93.28% and 94.19%, respectively. It is obtained that by etching U-slot, the bandwidths can be enhanced for the present circular microstrip patches. It is shown that possible the bandwidth behavior of U-slot circular microstrip disc antenna with this Artificial Neural Network model is powerfully estimated.

1. INTRODUCTION

Recently, most applications need larger bandwidths, so in these application areas, microstrip antennas' biggest handicap is the narrow bandwidth. Because of this, there are lots of studies going on and various bandwidth enhancement techniques are found [1–9]. These techniques to increase bandwidth include introducing multiple resonances into the structure. This may take the form of stacked patches, coplanar parasitic patches, or patches that have novel shapes such as the U-shaped slot patch [1–9]. Using special feed networks or feeding techniques to compensate for the natural impedance variation of the patch is another method [7]. Etching U-slot on the patch is may be the simple design [1–3]. This design avoids the use of stacked or coplanar parasitic patches, either of which increases the thickness or the lateral size of the antenna. So, while changing the current distribution on the microstrip patch, enhancing the impedance bandwidth with sometimes more than one resonant frequency are obtained.

In this study, U slots with various dimensions etched on present circular disc antennas in literature are tested and it is seen that their bandwidths can be enhanced by sacrificing a bit from the initial resonant frequencies. The simulation measurement without U slots give near resonant frequencies to the experimental results; but all the bandwidths are under %10. U-slot loading enhances the bandwidth up to %55; but there are little shifting from resonant frequencies due to the alternations of slot dimensions.

2. CIRCULAR DISC MICROSTRIP PATCH ANTENNA WITH U-SLOT

Circular disc antennas have better performance than rectangular ones, because they are smaller and can use easily in array applications. U-slot loaded circular disc antenna can be represented with an equivalent circuit that the slots are modeled by two impedances parallel to the classic RLC circuit of circular disc microstrip patch. Then, for calculating slot dimensions, input impedance of the patch and feed line impedance will be effective [8, 9].

From Figure 1(a), r is the patch radius, a is the feed point, L_s is the vertical slot length, L_b is the horizontal slot length, T_s and T_b are slot widths in the vertical and horizontal, respectively. From Figure 1(b), Z_{Uh} is the horizontal slot impedance, Z_{Uv} is the impedance of vertical slots, L_p is the coaxial feed line impedance, R, L and C are the resistance, inductance and capacitance of the circular patch. By etching U slot, the impedance seen from the feed point will be changed and realizing impedance matching for a larger bandwidth will be obtained [10].

3. ARTIFICIAL NEURAL NETWORKS

Artificial Neural Networks (ANN) are biologically-inspired, intelligent techniques and they have a number of simple and highly interconnected layers of neurons. Multilayered perceptron neural networks (MLPNNs) are the simplest ANN architectures, and therefore most commonly used [11–13]. A MLPNN has mainly three layers: an input layer, an output layer, and an intermediate or

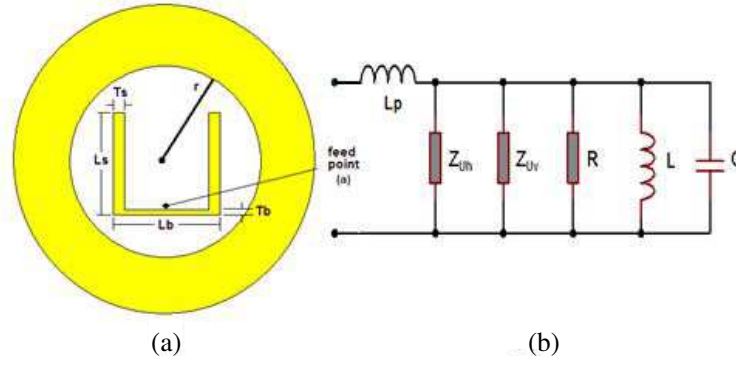(a)   (b)

Figure 1: (a) U slot loaded circular microstrip disc antenna. (b) Equivalent circuit of antenna fed by a 50-ohm coaxial probe.

hidden layer. The input layer neurons distribute the input signals x_i to neurons in the hidden layer(s). Each hidden layer neuron j sums up its input signals x_i after weighting them with the strengths of the respective connections w_{ji} from the input layer and computes its output y_j as a function f of the sum:

$$y_j = f\left(\sum w_{ji} x_i\right) \tag{1}$$

where f is a sigmoid or hyperbolic tangent function. The output of neurons in the output layer is computed similarly.

Training a network consists of adjusting weights of the network using a learning algorithm. The Back-Propagation [14] learning algorithm is used in this study. It is a gradient descent algorithm that gives the change $\Delta_{w_{ij}}(k)$ in the weight of a connection between neurons i and j as follows:

$$\Delta w_{ji}(k) = \alpha \delta_j x_i + \mu \Delta w_{ji}(k-1) \tag{2}$$

where x_i is the input, α is the learning coefficient, μ is the momentum coefficient, and δ_i is a factor depending on whether neuron j is an output neuron or a hidden neuron. For output neurons,

$$\delta_j = \frac{\partial f}{\partial net_j}\left(y_j^T - y_i\right) \tag{3}$$

Here $net_j = \sum x_i w_{ji}$ and y_j^T is the target output for neuron j. For hidden neurons,

$$\delta_j = \frac{\partial f}{\partial net_j}\sum_q w_q \delta_q \tag{4}$$

As there are no target outputs for hidden neurons in Eq. (4), the difference between the target and actual output of a hidden neuron j is replaced by the weighted sum of the δ_q terms already obtained for neurons q connected to the output of j. Thus, iteratively beginning with the output layer, the δ term is computed for all neurons in all layers except the input layer and weights were then updated according to Eq. (2).

In the training of neural network, gradient descent with adaptive learning rate algorithm is used and K-fold cross-validation is used for the test result to be more valuable [15, 16]. We used this method for finding the best ANN architecture. After training and test phase, the mean absolute error (MAE) and mean square error (MSE) calculation given in Eq. (5) and Eq. (6) was used as performance criterion. Expressions in Eqs. (5)–(8) can be suggested for different ANN applications. In this study Eq. (9) was arranged aiming to compare other literature studies.

$$\% \, MAE = \left(\frac{1}{n}\sum_{n=1}^{n}|t_i - t_h|\right) * 100 \tag{5}$$

$$\% \, MSE = \left(\frac{1}{n}\sum_{n=1}^{n}(t_i - t_h)^2\right) * 100 \tag{6}$$

Here, t_i is the desired outputs values, t_h is the ANN output values and n is the data number.

In addition, the test results satisfying the minimum errors were subjected to r-square correlation test given in Eq. (7) and Eq. (8). These correlation values were used as another criterion for the determination of optimum ANN structure:

$$r = \frac{\sum (t_i - \bar{t}_i)(t_h - \bar{t}_h)}{\sqrt{\sum (t_i - \bar{t}_i)^2 (t_h - \bar{t}_h)^2}} \tag{7}$$

$$\text{RSQ} = r^2 \tag{8}$$

Accuracy rates of training and testing were calculated in Eq. (9) [17].

$$\text{The accuracy rate} = (100 - \%\text{MAE}) \tag{9}$$

4. DESIGN SPECIFICATIONS

In this study, for an antenna that was designed on Rexolite 2200 dielectric substrate ($\varepsilon_r = 2.62$, $h = 1.6$, 3.2 and 4.7 mm) and had three different patch dimensions (14.1, 13.5 and 13 mm) the effects of etching U slots about the bandwidth were investigated [18, 19]. While designing the circular disc, classic circular disc antenna formulas and design steps fin the literature were used [4]. The U-slot designs were simulated with HFSS software and from S_{11} graphics in dB; bandwidth values were taken [20]. For each time, only one parameter was changed systematically and searched the effect of each dimension on bandwidth of the antenna. At first, L_s was changed between 4.29 and 24 mm with 1 mm steps. L_b was tested for 4, 6 and 8 mm values. The best results were taken for 8 mm, so for later designs it was taken constant and other parameters were changed in order. T_s and T_b dimensions were changed between 0.5 and 2 mm with 1 mm steps, and then the best results were taken for $T_s = 0.5$ and $T_b = 1$ mm values.

At the end of simulations, 63 data were produced. 2 experimental data from literature were added to them and the whole data set has 65 elements. 20% of this set is left for testing and the rest of the data are used for training. The experimental data are in the training set. The inputs were L_s, L_b, T_s, T_b, ε_r and h. The bandwidth was the ANN output. Consequently, the number of nodes for input ANN and output ANN were formed as 6 and 1, respectively. The developed ANN structure included one hidden layer. MLP feed forward back-propagation was used as an ANN structure. Hidden layer node numbers of optimum ANN structure was found as 12, experimentally. For this hidden node, minimum training and test errors were obtained.
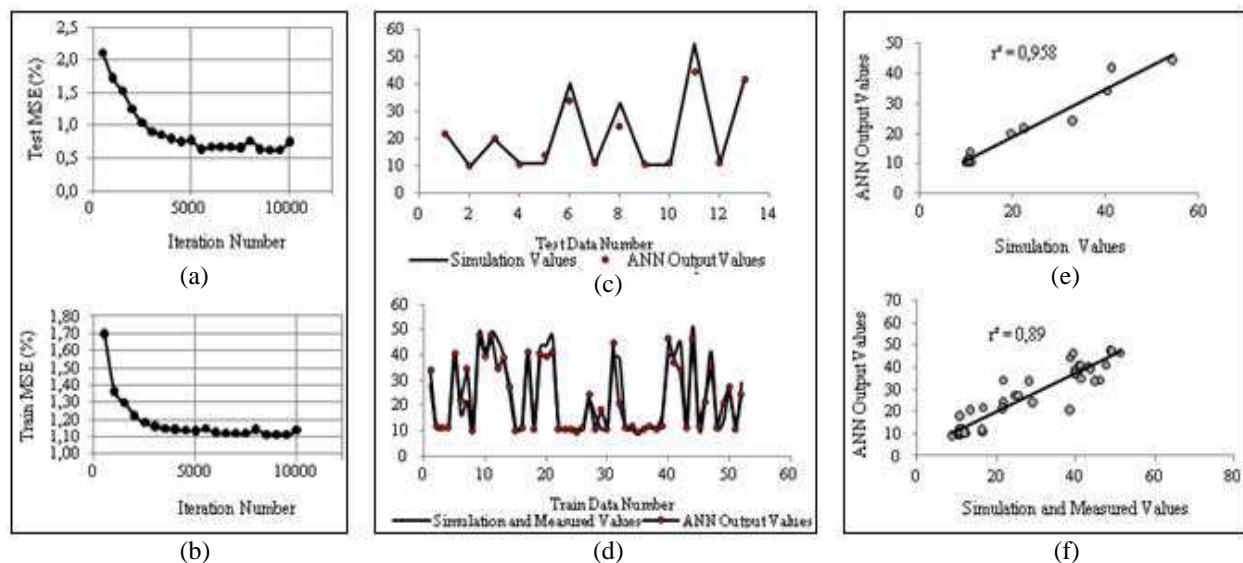
Figure 2: (a) System average error at testing phase. (b) System average error versus iteration number at training phase. (c) ANN test output results comparison with simulation values. (d) ANN train output results comparison with simulation-measurement values. (e) Correlation between ANN outputs antenna bandwidth outputs for testing. (f) ANN train output results comparison with simulation-measurement values.

Table 1: Circular microstrip disc antennas ANN Test parameters and results.

No	ε_r	h	L_s	L_b	T_s	T_b	BW Sim	BW ANN
		\multicolumn{5}{c}{(mm)}				(%)	
1	2.62	1.6	17	8	0.5	0.5	10.090	10.288
2	2.62	1.6	21	8	1	1	10.330	11.150
3	2.62	1.6	19	8	0.5	1	10.650	11.263
4	2.62	1.6	20	8	0.5	1	10.760	11.267
5	2.62	1.6	18	8	1	1	11.150	10.515
6	2.62	3.2	19	8	1	0.5	19.730	20.201
7	2.62	3.2	21	8	1	1	22.540	21.815
8	2.62	3.2	24	8	0.5	0.5	33.040	24.284
9	2.62	3.2	21	8	0.5	0.5	54.580	44.484
10	2.62	4.7	16	8	1	0.5	40.500	34.033
11	2.62	4.7	21	8	0.5	1	11.060	14.048
12	2.62	4.7	18	8	0.5	0.5	41.430	41.935
13	2.62	4.7	22	8	0.5	0.5	10.580	10.449

5. RESULTS

Simulation results show if $L_s \approx 1.45r$, for all three patch dimensions, large bandwidths are obtained. When L_s is increasing, the bandwidth increases, too, but for the resonant frequency, there is a small shifting toward to lower values. For $T_b = 0.5\,\text{mm}$ and $T_b = 1\,\text{mm}$, the bandwidth is enhanced to better results. In the training, first a scan process for finding the best hidden node number and best iteration number was run random search where the iteration number is adjusted from 500 to 10000 with 500 intervals and the hidden nodes number is adjusted from 3 to 30. After this process, the iteration number and node number of hidden layer was found to be 9500 and 12, respectively, while initial learning coefficient of the network as $\varepsilon = 0.9$, initial momentum coefficient adjusting the learning speed as $\alpha = 0.7$ was selected. In Table 1, ANN test parameters of circular disc antennas and results are given.

The mean square errors of training and testing at the best ANN architecture were found to be 1.11% and 0.62%, respectively. Correlation analysis was performed. The results of this analysis of train and test phase were found to be $r^2 = 0.89$ and 0.958, respectively. The above given average error and average correlation values of testing and training phases versus iteration number were determined by the help of measured and simulated antenna bandwidths for U-slot circular disc antennas and developed ANN model outputs, and they were presented graphically in Figure 2, the correlation between outputs of ANN and simulation outputs are given for testing and training, respectively.

6. CONCLUSION

By etching U slot on conventional circular disc microstrip patch antennas in the literature an enhancement for bandwidth of them is carried out. There can be more applicable antennas designed by giving some sacrificing from the resonant frequency. From the analysis of simulation and ANN results, it is seen that U-slot loaded disk patch exhibit wide bandwidth characteristics and the antenna bandwidth depends on the various parameters of U-slot.

In the training of neural network, K-fold cross-validation is used for test results to be more valuable. The measurement values obtained from experimental studies and the results of trained and tested ANN model are compatible with each other in great proportion. The accuracy ratios of training and testing stages in obtained optimum ANN were found to be 93.28% and 94.19%, respectively. Our subsequent studies will be about the measuring of simulation bandwidths and some other parameters like resonant frequencies and radiation patterns, experimentally.

ACKNOWLEDGMENT

REFERENCES

1. Huynh, C. and K. F. Lee, "Single-layer single-patch wideband microstrip antenna," *Electron. Lett.*, Vol. 31, No. 16, 1310–1312, 1995.
2. Lee, K. F., K. M. Luk, L. Tongy, Y. L. Yung, and T. Huynh, "Experimental study of the rectangular patch with a U-shaped slot," *IEEE IAP-S Int. Symp. Dig.*, 10–13, 1996.
3. Luk, K. M., K. F. Lee, and W. Tam, "Circular U-slot patch with dielectric superstrate," *Electron. Lett.*, Vol. 33, No. 12, 1001–1002, 1997.
4. Ramesh, G., B. Prakash, B. Inder, and I. Apisak, *Microstrip Antenna Design Handbook*, Artech House, USA, 2001.
5. Uzer, D., "Bandwidth enhancement techniques of microstrip antennas," *Doct. Seminar*, Selcuk Uni. Gradu. Sch. of Nat. and App. Sci., Konya, Turkiye, 2010.
6. Uzer, D., "Investigation of suitable methods for wideband microstrip antenna designs", Ph.D. Thesis, Selcuk Uni. Gradu. Sch. of Nat. and App. Sci., Konya, Turkiye, (In Progress).
7. Yadav, N. P., A. Mishra, P. Singh, J. A. Ansari, B. R. Vishvakarma, "A broadband U-slot loaded circular disk patch antenna," *International Conference on Emerging Trends in Electronic and Photonic Devices & Systems (ELECTRO-2009)*, 317–319, 2009.
8. Deshmukh, A. A. and G. Kumar, "Various slot loaded broadband and compact circular microstrip antennas," *Micr. and Opti. Tech. Lett.*, Vol. 48, No. 3, 435–439, Mar. 2006.
9. Kumar, G. and K. P. Ray, "Broadband microstrip antennas," *Artech House*, Waterhouse, R.B., 2002.
10. Sharma, V., V. K. Saxena, D. Bhatnagar, J. S. Saini, and K. B. Sharma, "Compact dual frequency wide band circular patch antenna with U-slot," *IEEE APSURSI'09, Antennas and Propagation Society International Symposium*, 1–4, Jun. 1–5, 2009.
11. Maren, A., C. Harston, and R. Pap, *Handbook of Neural Computing Applications*, Academic Press, London, 1990.
12. Haykin, S., *Neural Networks: A Comprehensive Foundation*, Macmillan College Publishing Company, New York, 1994.
13. Gultekin, S. S., K. Guney, and S. Sagiroglu, "A comparative study of neural networks for resonant frequency computation of electrically thin and thick circular microstrip antennas," *Second International Conference on Electrical and Electronics Engineering (ELECO'2001)*, 204–208, Bursa, Turkey, Nov. 2001.
14. Rumelhart, D. E. and J. L. McClelland, *Parallel Distributed Processing*, The MIT Press, Cambridge, 1986.
15. Francois, D., F. Rossi, V. Wertz, and M. Verleysen, "Resampling methods for parameter-free and robust feature selection with mutual information," *Neurocomp.*, Vol. 70, 1276–1288, 2007.
16. Diamantidis, N. A., D. Karlis, and E. A. Giakoumakis, "Unsupervised stratification of cross-validation for accuracy estimation," *Artif. Int.*, Vol. 116, 1–16, 2000.
17. Baykan Akhan, N. and N. Yilmaz, "Mineral ientification using color spaces and artificial neural networks," *Computers & Geosciences*, Vol. 36, No. 1, 91–97, 2010, DOI 10.1016/j.cageo.2009.04.009.
18. Koçer, D., "Simulation of circular and rectangular microstrip antennas and determination of their resonant frequencies by artificial neural networks," M.S. Thesis, Selcuk Uni. Gradu. Sch. of Nat. and App. Sci., Konya, Turkiye, 2009.
19. Davidovitz, M. and Y. Lo, "Input impedance of a probe-fed circular microstrip antenna with thick substrate," *IEEE Transactions on Antennas and Propagation*, Vol. 34, No. 7, 905–911, 1986.
20. HFSS Simulation Software, Ansys, v12 version. http://www.ansoft.com/products/hf/hfss/.

Bandwidth Modeling of U-slot Rectangular Microstrip Antennas with Artificial Neural Networks

M. S. Uzer, **D. Uzer**, **N. Yilmaz**, and **S. S. Gultekin**

Electrical-Electronics Engineering Department
Faculty of Engineering and Architecture, Selcuk University, Konya, Turkey

Abstract— In this study, rectangular U-slot microstrip antennas are modeled by an Artificial Neural Network structure and their bandwidth values are calculated with the model. The antenna parameters are taken from in the literature. The experimental results are compared with Artificial Neural Network results. In comparison of the experimental and Artificial Neural Network results, accuracy rates of training and testing were found to be 96.6% and 91.3%, respectively. It is obtained that Artificial Neural Network results are compatible with experimental bandwidth results from the literature. It is shown that possible bandwidth behavior of U-slot rectangular microstrip patch antennas with this Artificial Neural Network model is powerfully estimated.

1. INTRODUCTION

Microstrip antennas suffer from low impedance bandwidth characteristics by the reason of increasing wideband applications. To overcome this handicap, there have been lots of studies on various bandwidth enhancement techniques like stacked patches, coplanar parasitic patches, or patches that have novel shapes such as the U and H-shaped patches [1–3]. Using special feed networks or feeding techniques to compensate for the natural impedance variation of the patch is another method [4–6]. Etching U-slot on the patch is may be the simple design [1, 2]. This design avoids the use of stacked or coplanar parasitic patches, either of which increases the thickness or the lateral size of the antenna. So, while changing the current distribution on the microstrip patch, enhancing the impedance bandwidth with sometimes more than one resonant frequency are obtained.

In 1995 a broad band single layer probe fed patch antenna with a U-shaped slot was presented by Huynh and Lee and wideband impedance characteristics were obtained by cutting a U-slot on the surface of the rectangular patch in [1, 2]. In this study, an Artificial Neural Network (ANN) is modeled with U-slot rectangular microstrip antenna parameters in the literature for calculation of their bandwidths. Then, with the ANN results, experimental results from the literature are compared.

2. RECTANGULAR MICROSTRIP PATCH ANTENNA WITH U-SLOT

Rectangular microstrip antenna is the easiest geometry for designing and implementation. It is shown that etching U slot on rectangular patches enhance the impedance bandwidth up to 47% [1, 2]. By etching U slot, the impedance seen from the feed point will be changed and realizing impedance matching a larger bandwidth will be obtained. Generally, the enhancement process is realized by obtaining more than one resonant frequency that radiates under $-10\,$dB level [4–6]. The first resonance frequency is understood to be generated by the microstrip patch due to the physical parameters, while the second one by the U-shaped slot parameters [1, 2]. The surface currents originate behind the U-slot, and are strong outside the U-slot arms [7]. The U slot introduces a capacitance and induces a second resonance frequency near the main resonance frequency of the microstrip patch, producing an enhanced frequency response [6].

The basic U-slot rectangular microstrip patch antenna design is seen in Figure 1. Here, L is the patch length, W is the patch width, F is the feed point, L_s is the vertical slot length, W_s is the horizontal slot length, t_L and t_W are slot widths in the vertical and horizontal, respectively.

3. ARTIFICIAL NEURAL NETWORKS

Artificial Neural Networks are biologically-inspired, intelligent techniques and they have a number of simple and highly interconnected layers of neurons. Multilayered perceptron neural networks (MLPNNs) are the simplest ANN architectures, and therefore most commonly used [8–10]. A MLPNN has mainly three layers: an input layer, an output layer, and an intermediate or hidden layer. The input layer neurons distribute the input signals x_i to neurons in the hidden layer(s). Each hidden layer neuron j sums up its input signals x_i after weighting them with the strengths of
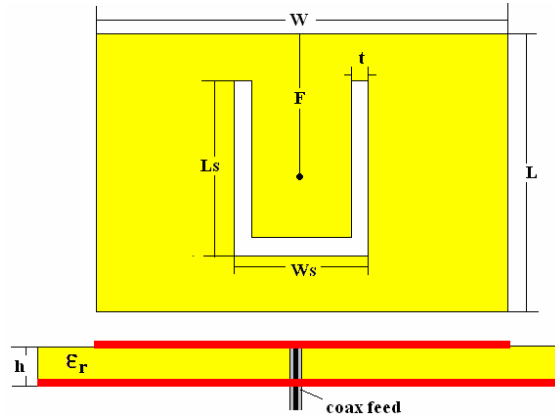
Figure 1: U slot loaded rectangular microstrip antenna.

the respective connections w_{ji} from the input layer and computes its output y_j as a function f of the sum:

$$y_j = f\left(\sum w_{ji}x_i\right) \tag{1}$$

where f is a sigmoid or hyperbolic tangent function. The output of neurons in the output layer is computed similarly.

Training a network consists of adjusting weights of the network using a learning algorithm. The Back-Propagation [11] learning algorithm is used in this study. It is a gradient descent algorithm that gives the change $\Delta w_{ij}(k)$ in the weight of a connection between neurons i and j as follows:

$$\Delta w_{ji}(k) = \alpha\delta_j x_i + \mu\Delta w_{ji}(k-1) \tag{2}$$

where x_i is the input, α is the learning coefficient, μ is the momentum coefficient, and δ_i is a factor depending on whether neuron j is an output neuron or a hidden neuron. For output neurons,

$$\delta_j = \frac{\partial f}{\partial net_j}\left(y_j^T - y_i\right) \tag{3}$$

Here $net_j = \sum x_i w_{ji}$ and y_j^T is the target output for neuron j. For hidden neurons,

$$\delta_j = \frac{\partial f}{\partial net_j}\sum_q w_q \delta_q \tag{4}$$

As there are no target outputs for hidden neurons in Equation (4), the difference between the target and actual output of a hidden neuron j is replaced by the weighted sum of the δ_q terms already obtained for neurons q connected to the output of j. Thus, iteratively beginning with the output layer, the δ term is computed for all neurons in all layers except the input layer and weights were then updated according to Equation (2).

In the training of neural network, gradient descent with adaptive learning rate algorithm is used and K-fold cross-validation is used for the test result to be more valuable [12, 13]. We used this method for finding the best ANN architecture. After training and test phase, the mean absolute error (MAE) and mean square error (MSE) calculation given in Equations (5) and (6) was used as performance criterion. Expressions in Equations (5)–(8) can be suggested for different ANN applications. In this study Equation (9) was arranged aiming to compare other literature studies.

$$\% \, MAE = \left(\frac{1}{n}\sum_{n=1}^{n}|t_i - t_h|\right) * 100 \tag{5}$$

$$\% \, MSE = \left(\frac{1}{n}\sum_{n=1}^{n}(t_i - t_h)^2\right) * 100 \tag{6}$$

Here, t_i is the desired outputs values, t_h is the ANN output values and n is the data number.

In addition, the test results satisfying the minimum errors were subjected to r-square correlation test given in Equations (7) and (8). These correlation values were used as another criterion for the determination of optimum ANN structure:

$$r = \frac{\sum \left(t_i - \overline{t_i}\right)\left(t_h - \overline{t_h}\right)}{\sqrt{\sum \left(t_i - \overline{t_i}\right)^2 \left(t_h - \overline{t_h}\right)^2}} \tag{7}$$

$$\mathrm{RSQ} = r^2 \tag{8}$$

Accuracy rates of training and testing were calculated in Equation (9) [14].

$$\text{The accuracy rate} = (100 - \%\,\mathrm{MAE}) \tag{9}$$

4. ANN MODELLING RESULTS

In this study, the data in Table 1 are used for the ANN model seen from Figure 2. The length of the whole data was 25 lines. First 5 lines of the data were separated for test. More than patch
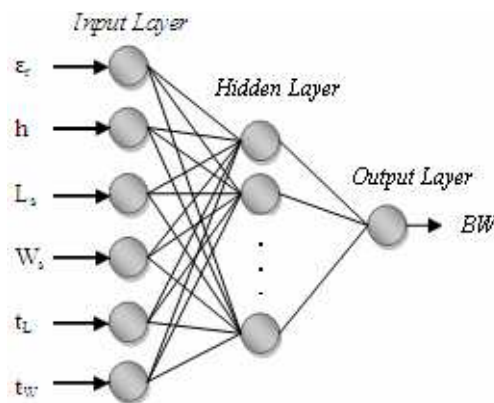
Figure 2: ANN structure used for modeling.

Table 1: Rectangular microstrip antennas ANN test parameters and results.

No	r	h	L$_S$	W$_S$	t$_L$	t$_w$	BW-Exp.	BW-ANN
				(mm)			(%)	
1•	2.20	3.175	6.60	6,00	0.60	0.60	39,00	39.07
2•	2.20	3.175	9,30	12,00	0.80	0.80	15,00	14.51
3•	2.20	5,000	12,00	16,00	2,00	2,00	13,00	15.64
4•	2.20	6.350	23.30	25.90	2.30	2.30	13.50	13.97
5º	1,00	5,000	20,00	12,00	2,00	2,00	25,00	27.04
6º	1,00	5,000	18,00	10,00	2,00	2,00	28,00	26.87
+7	2.20	12.160	27.65	21.48	3.09	3.09	29.52	31.02
8	2.35	12.160	39.54	26.04	4.42	4.42	21.36	21.27
9	2.94	12.160	25.86	20.09	3.72	3.72	28.71	29.00
10	3.00	12.160	26.15	20.31	2.93	2.93	29.21	28.74
11	3.27	12.700	27.77	21.38	3.06	3.06	27.70	27.58
12	3.48	12.500	32.83	25.51	3.67	3.67	21.40	21.61
+13	4.50	12.700	24.5	19,00	2.74	2.74	23,00	27.62
14	6.00	12.700	22.47	17.30	2.50	2.5	23.26	23.11
15	6.15	12.700	27,00	20.98	3.02	3.02	20.77	20.99
16	9.80	8,000	17.50	13.16	1.96	1.96	39.58	39.58
17*	1,00	5,000	20,00	12,00	2,00	2,00	25,00	27.04
18▲	2.33	6.400	18,00	14,00	2,00	2,00	2500,	22.27
19▲	2.33	8,000	18,00	14,00	2,00	2,00	25.30	27.48
20■	2.32	8,000	14,00	18,00	2,00	2,00	26.54	25.73
21*	1,00	5,000	19.50	12,0	2.10	2.10	32.40	28.14
22*	1,00	5,000	18,00	10,00	2.10	2.10	26.40	27.73
+23*	1,00	5,000	16.50	14,00	2.10	2.10	30,00	28.93
+24▼	1,00	26.924	82.17	68.58	10.16	8.89	47,00	44.51
+25▼	1,00	13.462	82.17	68.58	10.16	8.89	12.40	18.27

The parameters are taken from : •[6], º[18], *[16], ▲[17], ■[7], ▼[1] and the rest [15]. The data with "+"symbols are used as test set.
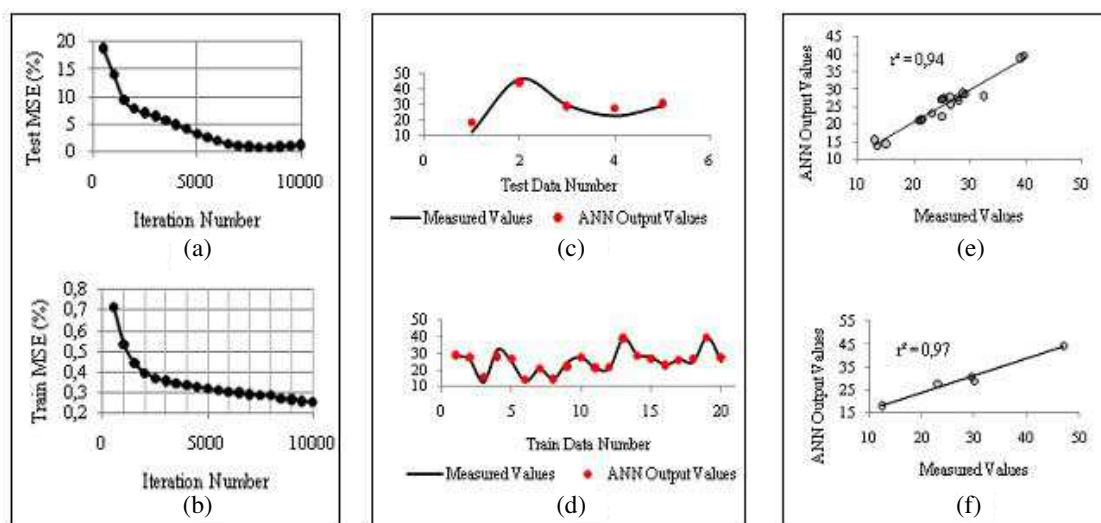
Figure 3: (a) System average error versus iteration number at testing phase. (b) System average error versus iteration number at training. (c) ANN test output results comparison with simulation values. (d) ANN train output results comparison with simulation-measurement values. (e) Correlation between ANN output values and antenna bandwidth outputs for training. (f) Correlation between ANN output values and antenna bandwidths for test.

dimensions, the substrate specifications and U-slot dimensions are important on the bandwidth of the microstrip antenna [6, 7] so for the ANN model, L_s, W_s, ε_r, h, t_L and t_W are used as inputs, after the bandwidth was calculated as the network output. Consequently, the number of nodes for input ANN and output ANN were formed as 6 and 1, respectively. The developed ANN structure included one hidden layer. MLP feed forward back-propagation was used as an ANN structure.

The hidden layer node numbers of optimum ANN structure was found as 18, experimentally. For this hidden node, minimum training and test errors were obtained. In the training, first a scan process for finding the best hidden node number and best iteration number was run random search where the iteration number was adjusted from 500 to 10000 with 500 intervals and the hidden nodes number was adjusted from 3 to 30. After this process, the iteration number and node number of hidden layer was found to be 8000 and 18, respectively, while initial learning coefficient of the network as $\varepsilon = 0.9$, initial momentum coefficient adjusting the learning speed as $\alpha = 0.7$ was selected. ANN diagram was trained and tested with 5-fold cross validation methods under the best optimum structure determined by trials. The mean square errors of training and testing at the best ANN architecture were found to be %0.88 and %0.23, respectively. Correlation analysis was performed. The results of this analysis of train and test phase were found to be $r^2 = 0.94$ and 0.97, respectively. The above given average error and average correlation values of testing and training phases versus iteration number were determined by the help of measured and simulated antenna bandwidths for U-slot rectangular microstrip antennas and developed ANN model outputs, the correlation between outputs of ANN and simulation outputs for testing and training then they were presented graphically in Figure 3, respectively. Rectangular microstrip antennas used as ANN test parameters and the obtained results are given in Table 1. 7, 13, 23, 24 and 25. data are selected for test set and pointed with "+" symbols in from of the datum number.

5. CONCLUSIONS

In this study, bandwidth calculation of rectangular U-slot microstrip antennas are achieved by the help of an Artificial Neural Network model trained with GDX algorithm. In the training of neural network, K-fold cross-validation is used for test results to be more valuable. The measurement values obtained from experimental studies and the results of trained and tested ANN model are compatible with each other in great proportion. The accuracy ratios of training and testing stages in obtained optimum ANN were found to be 96.6% and 91.3%, respectively. These results show that the ANN network is studied successfully for calculation of the bandwidth values of rectangular U-slot microstrip antennas.

REFERENCES

1. Huynh, C. and K. F. Lee, "Single-layer single-patch wideband microstrip antenna," *Electron. Lett.*, Vol. 31, No. 16, 1310–1312, 1995.
2. Lee, K. F., K. M. Luk, L. Tongy, Y. L. Yung, and T. Huynh, "Experimental study of the rectangular patch with a U-shaped slot," *IEEEIAP-S International Symposium Dig.*, 10–13, 1996.
3. Tong, K. F., K. M. Luk, K. F. Lee, and S. M. Shum, "Analysis of broadband U-slot microstrip antenna," *IEE 10th International Conference on Antennas and Propagation*, No. 436, 1.110–1.113, Apr. 14–17, 1997.
4. Kumar, G. and K. P. Ray, *Broadband Microstrip Antennas*, Artech House, Waterhouse, R.B., 2002.
5. Uzer, D., "Investigation of suitable methods for wideband microstrip antenna designs," Ph.D. Thesis, Selcuk Uni. Gradu. Sch. of Nat. and App. Sci. Konya, Turkiye, (in progress).
6. Weigand, S., G. H. Huff, K. H. Pan, and J. T. Bernhard, "Analysis and design of broad-band single-layer rectangular U-slot microstrip patch antennas," *IEEE Trans. on Ant. and Prop.*, Vol. 51, No. 3, 457–468, Mar. 2003.
7. Tong, K. F., K. M. Luk, and K. F. Lee, "Design of a broadband U-slot patch antenna on a microwave substrate," *Asia Pacific Microwave Conference*, 221–224, 1997.
8. Maren, A., C. Harston, and R. Pap, *Handbook of Neural Computing Applications*, Academic Press, London, 1990.
9. Haykin, S., *Neural Networks: A Comprehensive Foundation*, Macmillan College Publishing Company, New York, 1994.
10. Shackelford, A. K., K. F. Lee, and K. M. Luk, "Design of small-size wide-bandwidth microstrip-patch antennas," *IEEE Antennas and Propagation Magazine*, Vol. 45, No. 1, 76–83, Feb. 2003.
11. Rumelhart, D. E. and J. L. McClelland, *Parallel Distributed Processing*, The MIT Press, Cambridge, 1986.
12. Francois, D., F. Rossi, V. Wertz, and M. Verleysen, "Resampling methods for parameter-free and robust feature selection with mutual information," *Neurocomp.*, Vol. 70, 1276–1288, 2007.
13. Diamantidis, N. A., D. Karlis, and E. A. Giakoumakis, "Unsupervised stratification of cross-validation for accuracy estimation," *Artif. Int.*, Vol. 116, 1–16, 2000.
14. Baykan Akhan, N. and N. Yilmaz, "Mineral ientification using color spaces and artificial neural networks," *Computers & Geosciences*, Vol. 36, No. 1, 91–97, 2010, DOI 10.1016/j.cageo.2009.04.009.
15. Tong, K. F., K. M. Luk, K. F. Lee, and R. Q. Lee, "A broad-band U-slot rectangular patch antenna on a microwave substrate," *IEEE Trans. on Ant. and Prop.*, Vol. 48, No. 6, 954–960, Jun. 2000.
16. Lee, K. F., K. M. Luk, K. F. Tong, S. M. Shum, T. Huynh, and R. Q. Lee, "Experimental and simulation studies of the coaxially fed U-slot rectangular patch antenna," *IEE Proc. — Microw. Ant. Propag.*, Vol. 144, No. 5, 354–358, Oct. 1997.
17. Choltiar, E., V. Nalarajan, and D. Chatterjee, "Comparison of resonant frequency calculations for wideband U-slot antennas on microwave substrates," *IEEE Antennas and Propagation Society International Symposium*, Vol. 4, 3713–3716, Jun. 20–25, 2004.
18. Gültekin, S. S., K. Güney, and Ş. Sağıroğlu, "Resonant frequency calculation of electrically thin and thick rectangular microstrip antennas with artificial neural networks trained by different algorithms," *Electrical-Electronisc-Computer Engineering Symposium (ELECO'2002)*, 171–175, Bursa, Turkey, Apr. 2002.

A Metamaterial Antenna with Reduced Radiation Hazards towards Human Head

D. Laila, **R. Sujith**, **C. M. Nijas**, **V. A. Shameena**, **R. Dinesh**, and **P. Mohanan**

Centre for Research in Electromagnetics and Antennas(CREMA), Department of Electronics
Cochin University of Science and Technology, Cochin, Kerala 682022, India

Abstract— A modified coplanar wave guide (CPW) fed printed monopole antenna with reduced radiation hazards for mobile application is presented and discussed. Directional radiation pattern of a CPW fed monopole antenna in the elevation plane is modified with a single null in the azimuth plane by using metamaterial substance like Split Ring Resonator (SRR).The antenna resonates at 1.8 GHz when printed on a substrate of dielectric constant (εr) 4.4 and thickness 1.6 mm with an overall dimension of $42 \times 31.7 \, \text{mm}^2$. Experimental and simulation studies of the antenna radiation characteristics of the proposed antenna are also discussed. A 25 dB reduction of radiated power in one quadrant of the radiation pattern offers a reduction of radiation towards the users head.

1. INTRODUCTION

The use of cellular phones and mobile wireless communication systems has been growing rapidly during the past few years. And, there is public concern for safety exposure from these devices. Therefore, it is necessary to decrease the interaction of electromagnetic energy between the antenna and the human head when mobile handset is in use. This is achieved in different ways. A ferrite sheet attached [1] to the front side, close to head can reduce radiation, however, the parameters such as attaching location, size and material properties of ferrite sheet played an important role in the reduction effectiveness. Highly directive antennas [2] can also reduce radiation towards human head significantly. However, the adoption of highly directive antennas certainly causes degradation in signal reception from other directions. Parasitic elements are also used to get end fire pattern. Complicated truncated ground plane is used in [3] to get end fire pattern throughout the operating band. In [4] a folded vertical copper wire of length 0.48λ as a reflector is used. But the very large reflector is a major problem in compact devices. PIFA (Planar Inverted F Antenna) with EBG (Electromagnetic Band Gap) surface [5] on the ground plane is also reported to reduce electromagnetic radiation.All of the above methods deteriorate the structure simplicity and compactness.

Recently, metamaterials have inspired great interests due to their unique physical properties and novel application [6, 7]. Metamaterials denote artificially constructed materials having electromagnetic properties not generally found in nature. Two important parameters, electric permittivity and magnetic permeability determine the response of the materials to the electromagnetic propagation. Mediums with negative permittivity can be obtained by arranging the metallic thin wires periodically [8]. On the other hand, an array of split ring resonators (SRRs) can exhibit negative effective permeability [9]. When one of the effective medium parameters is negative and the other is positive, the medium will display a stop band. An array of Split Ring Resonators (SRRs) [10] are placed between the antenna and human head to reduce the electromagnetic interaction between them.

The electromagnetic interaction between the antenna and the human head can be reduced by modifying the radiation pattern of the monopole antenna by printing single SRR with the proper geometrical parameters on the backside of a planar monopole antenna is presented in this paper.

2. ANTENNA DESIGN

Antenna is basically a monopole strip fed by coplanar waveguide (CPW) feed. The antenna geometry and the associated parameters are shown in Fig. 1. The main radiating element is a vertical stripe of length $L_1 = 25$ mm and width $W_1 = 3$ mm. This is acting as a $\lambda g/4$ monopole, where λg is the wavelength in the substrate. The ground plane dimension are $L_2 = 17$ mm and $W_2 = 14$ mm.The gap between monopole strip and ground plane (g) is 0.35 mm. Fig. 1(b) shows the back side view of the antenna. Split ring resonator (SRR) with dimension of $r1$ (outer ring radius) $= 6.3$ mm, Width of the ring $W = 0.9$ mm, distance between the two rings $d = 0.6$ mm, split gap (t) $= 0.5$ mm is offset by a distance (a) $= 1.7$ mm from the right edge of the feed and $b = 1.3$ mm from the top edge of the right ground is printed at back side. By properly choosing the

parameters and position of printed SRR, the radiation pattern can be modified. The prototype was fabricated on a substrate of dielectric constant (εr) 4.4 and $h = 1.6$ mm with an overall dimension of $42 \times 31.7 \times 1.6$ mm^3.

3. RESULTS AND DISCUSSION

The experimental and simulated return loss characteristic of the SRR loaded monopole antenna is illustrated in Fig. 2 It is seen from the return loss characteristics that the antenna operates from 1.75 GHz to 1.91 GHz with a fractional bandwidth of 8.7% centered at 1.8 GHz. By loading the SRR structure at the optimum position, it is observed that the monopole resonance shifts to a lower resonance value at 1.8 GHz. Therefore, SRR structure reduces the overall size of the antenna. It also modifies the directional pattern of the monopole antenna in the elevation plane to a pattern suitable for mobile hand set. The simulation result is in good agreement with the measured values. The measured value is validated by Ansoft HFSS simulation tool and all antenna measurements were carried out with HP8510C network analyzer.

The simulated 3D far field radiation pattern at 1800 MHz of the proposed antenna along $\phi = 90$ plane is shown in Fig. 3. The figure shows that the antenna is radiating in the negative Y direction and offers a null along the positive Y direction. Moreover, there is only one null appeared in the pattern.

Measured 2D radiation patterns of the antenna in YZ and XY plane at the resonance frequency are shown in Figs. 4(a) and (b) respectively. It is observed that the radiation pattern of the conven-
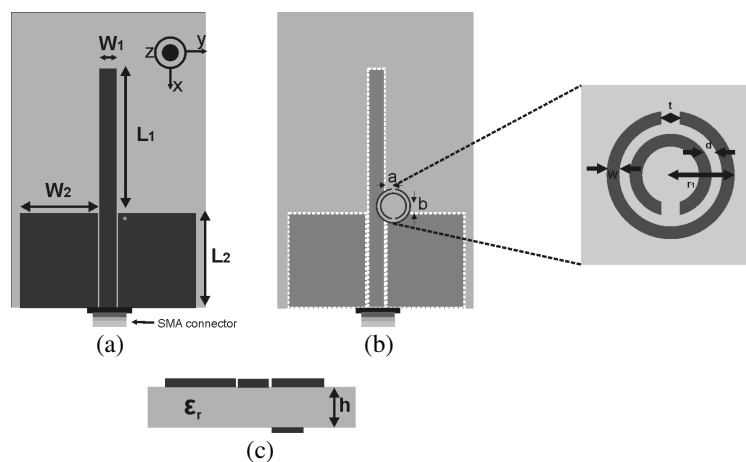
Figure 1: Geometry of the proposed antenna, (a) front view, (b) bottom view, (c) side view. ($L1 = 25$ mm, $W1 = 3$ mm, $L2 = 17$ mm, $W2 = 14$ mm, $g = 0.35$ mm, $r1 = 6.3$ mm, $W = 0.9$ mm, $d = 0.6$ mm, $t = 0.5$ mm $a = 1.7$ mm, $b = 1.3$ mm, $h = 1.6$ mm, $\varepsilon r = 4.4$.).
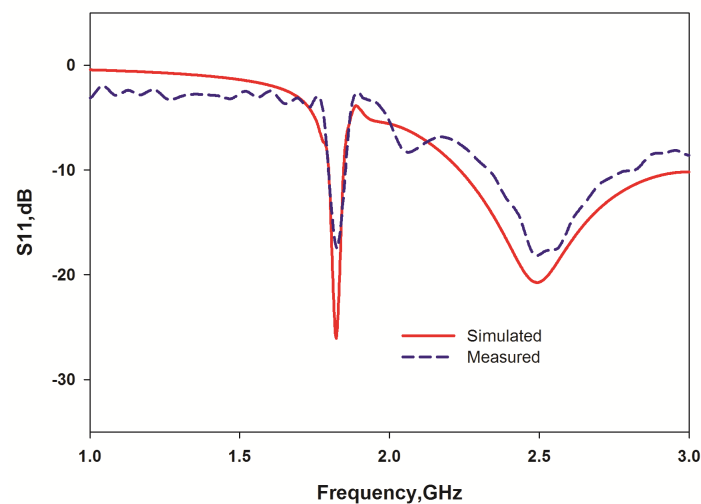
Figure 2: Return loss characteristics of the antenna.

tional monopole gets modified by the addition of the SRR structure. The fringing field between the monopole and any of the lateral ground plane is affected by adding the SRR, but the coupling on the other lateral ground plane remains same. As a result the electric field gets redistributed giving a null along positive Y direction and filling the original two nulls of the conventional monopole. This change in radiation pattern can be conveniently employed to reduce the EM interaction towards the head of a mobile phone user.

A nearly 25 dB reduction in radiated power is observed at the beam minima, with appreciable power in all other directions. Fig. 5 shows the measured gain plot of the proposed antenna. The antenna shows an average gain of 1.22 dBi.

4. SAR CALCULATION WITH PHANTOM HEAD MODEL

The simulation model of SAM phantom head model provided by CST Microwave Studio® (CST MWS) with planar monopole antenna with and without printed SRR for a distance of 10 mm from head model is also studied and are shown in Figs. 6(a) and (b) respectively.

The SAR [11] in human head is defined as follows,

$$\text{SAR} = \frac{\sigma |E|2}{\rho} \, \text{W/kg.} \tag{1}$$

where σ = conductivity of the tissue (S/m), ρ = mass density of the tissue (kg/m^3), E = rms electric field strength (V/m).

Simulated SAR value of the proposed antenna is compared with monopole antenna of same dimension for different distances are shown in Table 1.
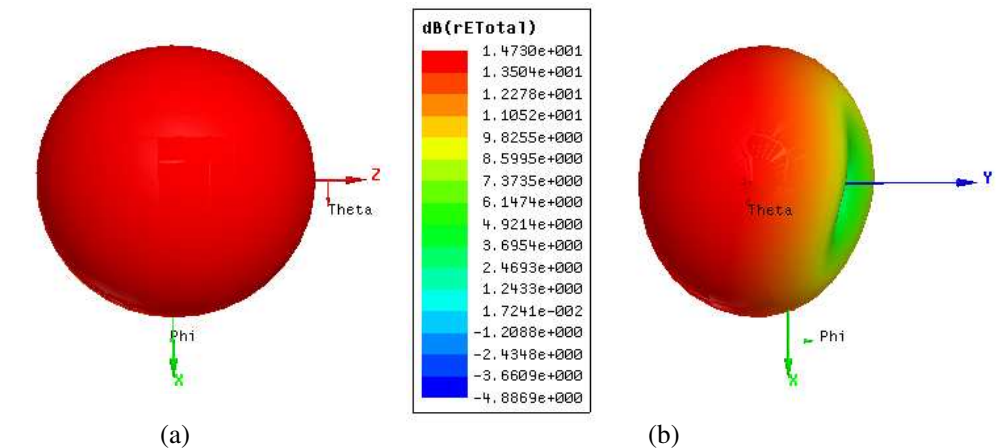
Figure 3: Simulated 3D pattern of the antenna.
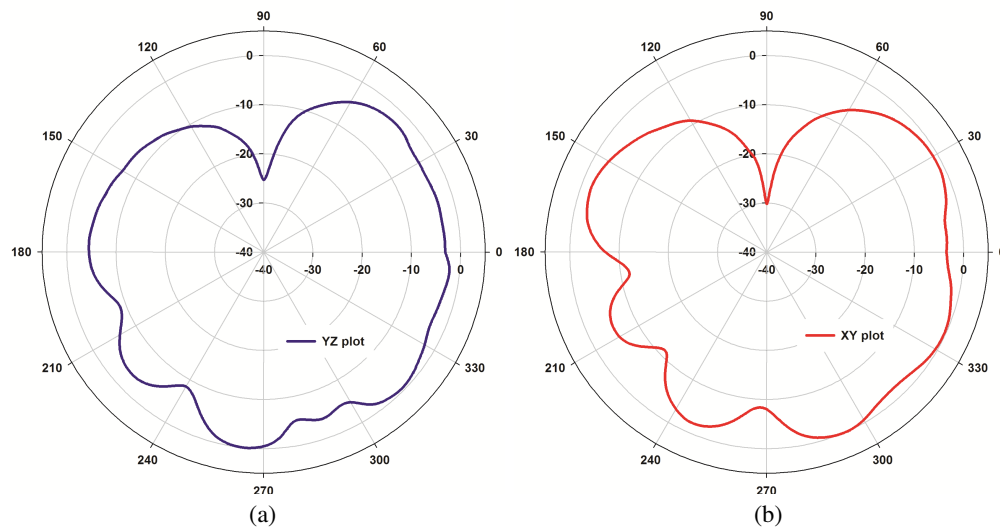
Figure 4: (a) and (b) Measured radiation pattern of the proposed antenna in YZ and XY plane.
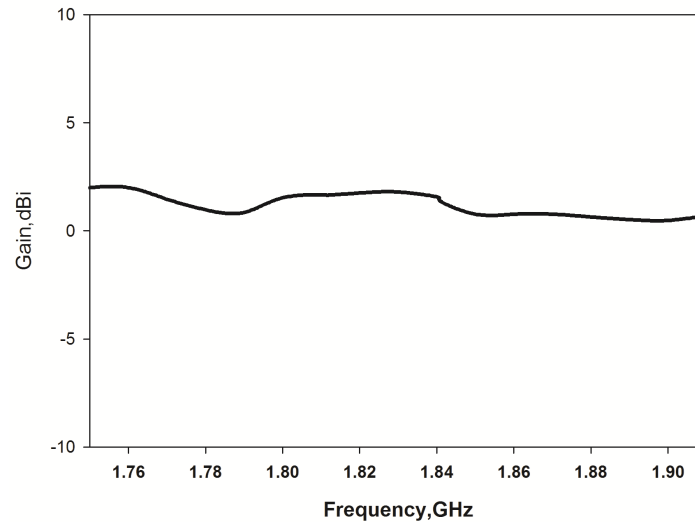
Figure 5: Measured gain of the antenna.

(a)   (b)
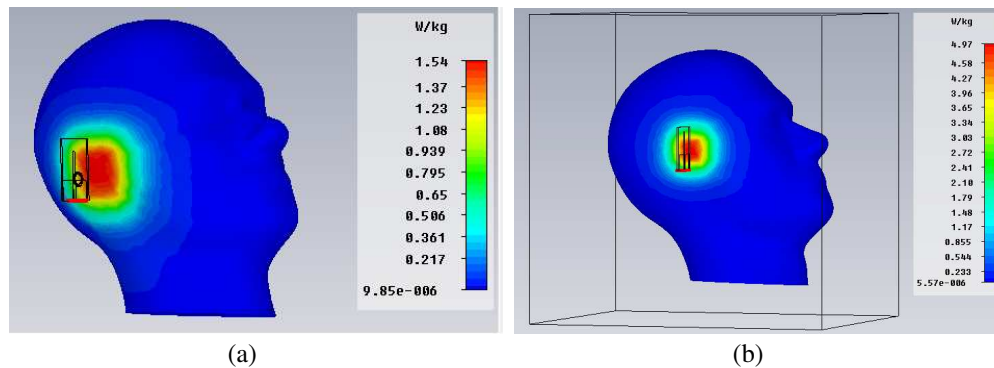
Figure 6: Planar monopole antenna with (a) and without (b) printed SRR for a distance of 10 mm from head model.

Table 1: Simulated SAR value of the antenna with distance.

Distance from phantom model to antenna	SAR w/kg (1 gm) Planar monopole antenna	SAR w/kg (1 gm) Planar monopole antenna with printed metal SRR at the back
10 mm	4.97	1.54
20 mm	2.616	1.22
30 mm	1.074	0.623
40 mm	0.707	0.509

From the SAR value of the proposed antenna with phantom head model for different distance as shown in Table 1. It is observered that SAR value decreases with distance and for the proposed antenna. SAR value is less than FCC recommended value, even for a distance of 10 mm.

5. CONCLUSION

A CPW fed monopole antenna with printed SRR at the back side, producing radiation characteristics suitable for a mobile handset is presented. The proposed antenna operates at GSM 1800 band. A good agreement between measurement and simulation is obtained. This antenna structure is very simple with single null and can efficiently be used in mobile handset.

REFERENCES

1. Wang, J. and O. Fujiwara, "Reduction of electro magnetic absorption in the human head for portable telephones by a ferrite sheet attachment," *IEICE Trans. Commun.*, Vol. 80, 1810–

1815, 1997.

2. Rowley, J. T. and R. B. Waterhouse, "Performance of shorted microstrip patch antennas for mobile communication handset at 1800 MHz," *IEEE Trans. Antennas Propag.*, Vol. 47, 815–822, 1999.

3. Sor, J., Y. X. Qian, and T. Itoh, "Coplanar waveguide fed quasi yagi antenna," *Electron. Lett.*, Vol. 36, 1–2, 2000.

4. Lim, S. and H. Ling "Design of a closely spaced folded yagi antenna," *IEEE Antennas Wireless Propag.*, Vol. 5, 302–305, 2006.

5. Kwak, S. I., D.-U. Sim, and J. H. Kwon, "SAR reduction on mobile phone antenna using the EBG structures," *Pro. 38th European Microwave Conference*, 1308–1311, The Netherlands, 2008.

6. Ozbay, E., K. Aydin, E. Cubukcu, and M. Bayindir, "Transmission and reflection properties of composite double negative metamaterials in free space," *IEEE Trans. Antennas Propag.*, Vol. 51, No. 10, 2592–2595, Oct. 2003.

7. Ziolkowski, R. W., "Design, fabrication, and testing of double negative metamaterials," *IEEE Trans. Antennas Propag.*, Vol. 51, No. 7, 1516–1529, Jul. 2003.

8. Sigalas, M. M., C. T. Chan, K. M. Ho, and C. M. Soukoulis, "Metallic photonic band gap materials," *Phys. Rev. B.*, Vol. 52, No. 16, 11744–11751, Oct. 1995.

9. Pendry, J. B., A. J. Holen, D. J. Robbins, and W. J. Stewart, "Magnetism from conductors and enhanced nonlinear phenomena," *IEEE Trans. Microwave Theory Tech.*, Vol. 47, No. 11, 2075–2084, Nov. 1999.

10. Hwang, J.-N. and F.-C. Chen, "Reduction of the peak SAR in the human head with metamaterials," *IEEE Trans. Antennas Propag. Lett.*, Vol. 54, No. 12, 3763–3770, Dec. 2006.

11. Lin, J. C., "Cellular mobile telephones and children," *IEEE Antennas and Propagation Magazine*, Vol. 44, No. 5, 142–145, 2002.

Polarization Diversity Unidirectional Antenna for IEEE 802.11a Applications

S. Vongsack[1], C. Phongcharoenpanich[2], S. Kosulvit[2], K. Hamamoto[3], and T. Wakabayashi[4]

[1]International College, King Mongkut's Institute of Technology Ladkrabang, Thailand
[2]Faculty of Engineering, King Mongkut's Institute of Technology Ladkrabang, Thailand
[3]School of Information and Telecommunication Engineering, Tokai University, Japan
[4]Malaysia-Japan International Institute of Technology (MJIIT)
University of Technology Malaysia (UTM), Jalan Semarak, Kuala Lumpur 54100, Malaysia

Abstract— The polarization diversity unidirectional antenna is proposed for IEEE 802.11a applications by using two-probe excited circular ring antenna above square reflector. The purpose of this investigation is to design a polarization diversity unidirectional antenna to resonate at the center frequency of 5.5 GHz to cover the frequency range from 5.2 to 5.8 GHz for wireless LAN system following IEEE 802.11a standard. The performances of the antenna such as the return loss, the isolation between two-probes, the radiation pattern and the gain, are analyzed by using Computer Simulation Technology (CST) Microwave Studio. The proposed antenna has a polarization diversity unidirectional pattern with maximum gain of 8.34 dBi. Moreover, the proposed antenna yields the front-to-back ratio better than 20 dB and the isolation between the two-probes better than 20 dB as well. Besides, the proposed antenna is useful for wireless local area network (WLAN) communication systems.

1. INTRODUCTION

Recently, the wireless communications have progressed rapidly. Wideband antenna designs have become an important part for wireless communications. Thus, the demand for using a mobile telephone is increased everywhere. The numbers of base stations are very large. Therefore, the developments of the cost effective base-station antennas are of great importance. Generally, the conventional omnidirectional antenna is employed to cover the approximated circular area. Nevertheless, on long and narrow areas, such as subway station, tunnel, corridors or long rows of objects, a unidirectional or bidirectional antenna is more suitable than conventional omnidirectional one to apply serving these demands. Some ring antennas which are excited by an electric probe were proposed [1–6]. Also, the probe excited different ring shapes such as circular ring, elliptical and rectangular rings were introduced [7, 8]. Hence, this paper proposes the simple and cost-effective polarization diversity unidirectional antenna that can be designed easily and straightforwardly by choosing appropriate antenna parameters. It is also providing high gain, good radiation pattern and isolation between the two-probes. Futhermore, the impedance bandwidth is obtained over which the return losses for both feed are less than -10 dB and cover the frequency range from 5.2 to 5.8 GHz. For the specified operating frequency, the dimension of rectangular ring is first chosen to achieve the condition that only the dominant mode can be propagated inside the circular ring. Otherwise, this antenna structure has the unidirectional radiation characteristics in XZ- and XY-planes. It is obvious that the maximum radiated field directs along the circular ring aperture in $+x$ direction. The content of this paper is organized as follows: The geometry of the proposed antenna is described in Section 2. In Section 3, the design procedure of the antenna is discussed. The antenna parametric study results are obtained by using CST Microwave Studio [9] as presented in Section 4. Final section is conclusions.

2. GEOMETRY OF THE PROPOSED ANTENNA

The proposed antenna structure is polarization diversity unidirectional antenna by using two-probe excited circular ring above square reflector to cover the frequency of 5.2–5.8 GHz for wireless applications. The geometry of antenna structure consists of two parts such as circular ring fed by two probes and square reflector as illustrated in Figure 1. The two probes are perpendicular to each other and are located at the center of the circular ring of the length l and aligned along the z and y axes. The dimension of square reflector is $W \times H$, and the distance from probe is h, and it is surrounded by a circular ring of the radius r_a and circular ring length d with thickness t. Furthermore, the dimension of the circular ring is reasonably chosen to perform the dominant mode.
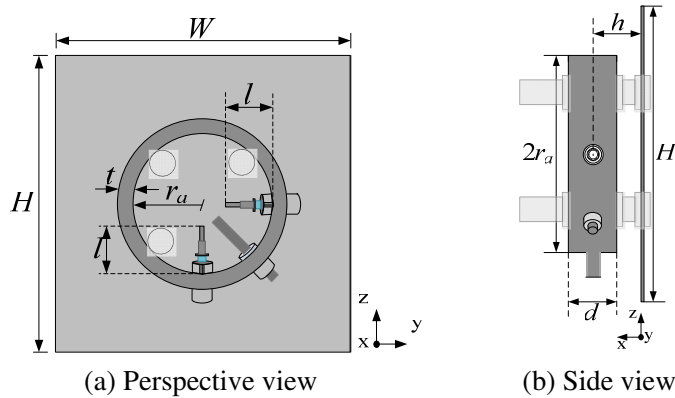
Figure 1: Antenna structure.
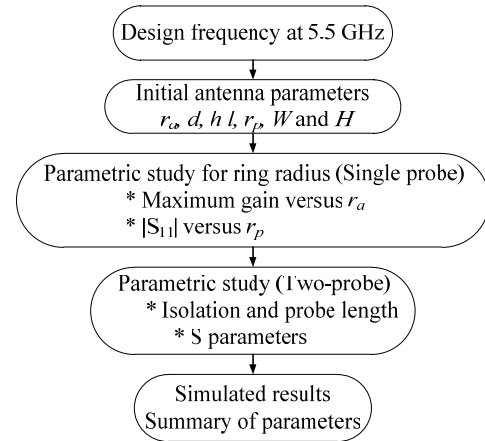
Figure 2: The flowchart of antenna design procedure.

3. THE DESIGN PROCEDURE

According to the flowchart of antenna design procedure in Figure 2, this antenna is designed to be operated along the frequency band of 5.2–5.8 GHz. In order to design the antenna, the circular ring radius is first chosen to operate at the desired frequency of 5.5 GHz. The circular ring is chosen such that the lowest cutoff frequency is the dominant mode TE_{11}. The other initial parameters; r_a, d, h, l, H and W are also determined to operate at the center frequency. The circular ring length d, the distance between probe and reflector h and the probe length l are also chosen such that the amplitudes of the higher modes are fractionally small at the aperture ring. Then, the circular ring radius r_a is desired to be as small as possible.

$$0.293\lambda < r_a < 0.48\lambda, \tag{1}$$

where λ is the wavelength at the operating frequency of 5.5 GHz.

To obtain the diversity unidirectional antenna with maximum gain, good radiation pattern, resonance ($|S_{11}| < -10$ dB) and isolation at 5.5 GHz, the parametric study are done for various r_a, r_p and l. The design process is to choose a suitable radius of the ring r_a for a single probe antenna. In addition, a parametric study of the probe radius r_p is carried out to improve the impedance matching. Therefore, the suitable ring radius r_a, ring length d and the distance between probe and reflector h are determined for the two-probe antenna and are presented in the fourth step. Moreover, the design of the diversity unidirectional antenna by insertion the second probe to perpendicular to each other is carried out. To achieve the good performance, it can be done by insertion the isolator length l_i and probe length l as discussed in fourth step. Finally, from the simulation to parametric study of antenna parameters we can summarize the parameters used in this paper. The investigation of two-probe excited circular ring antenna with square reflector can provide the maximum gain, good radiation pattern and wide frequency band by using the optimum parameters.

4. PARAMETRIC STUDY

According to the design procedure described in the previous section, the initial antenna parameters are determined as the two probes which are perpendicular to each other with the length l of 13 mm and distance from reflector h of 14 mm, and it is surrounded by a circular ring radius r_a of 13 mm and circular ring length d of 15 mm. The dimension of square reflector $W \times H$ is 80×80 mm, respectively. The circular ring is made of aluminum with thickness 3 mm for small size and light weight. The proposed antenna is fed by a probe at the center of the inner ring. The dimension of the ring is reasonably chosen to perform the dominant mode propagation inside the cylindrical waveguide as well. To obtain the suitable parameters, the circular ring radius r_a are varied from 0.25λ to 0.50λ whereas the other parameters are fixed as initial parameters. It can be obtained that the optimum r_a of 0.40λ is suitable for the antenna design because this provides the maximum gain as shown in Figure 3.

For the third step, it is important to perform impedance matching by performing a parametric study of the influence of the probe radius r_p when varied from 0.65 mm to 0.95 mm as illustrated
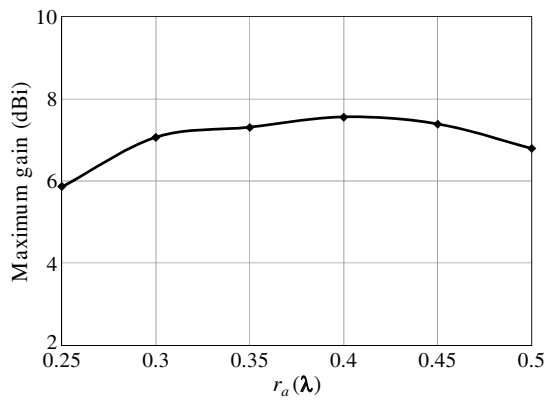
Figure 3: Maximum gain versus circular ring radius.
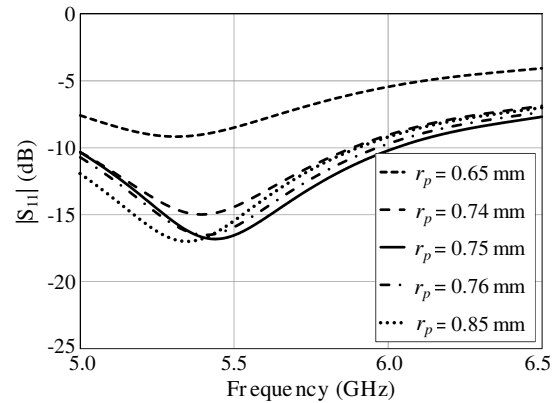
Figure 4: $|S_{11}|$ versus frequency as a function of probe radius r_p.
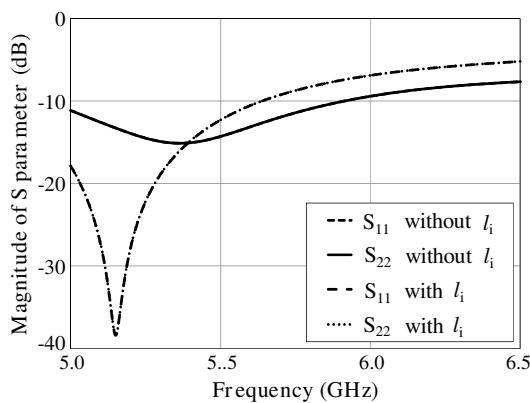
(a) The S parameter versus frequency with and without l_i
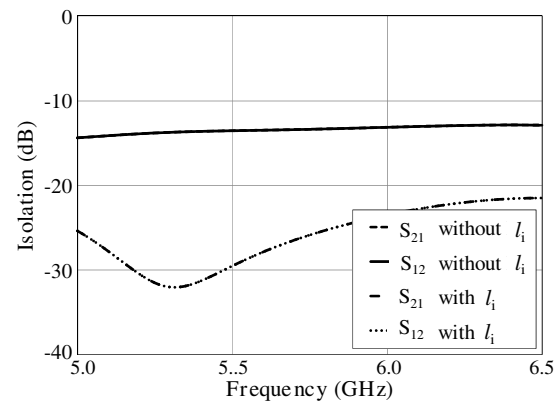
(b) The isolation versus frequency with and without l_i

Figure 5: The magnitude of S parameter versus frequency with and without the isolator.
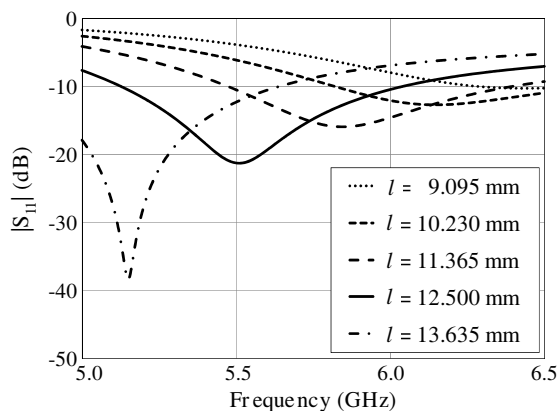
Figure 6: $|S_{11}|$ versus frequency as a function of l.
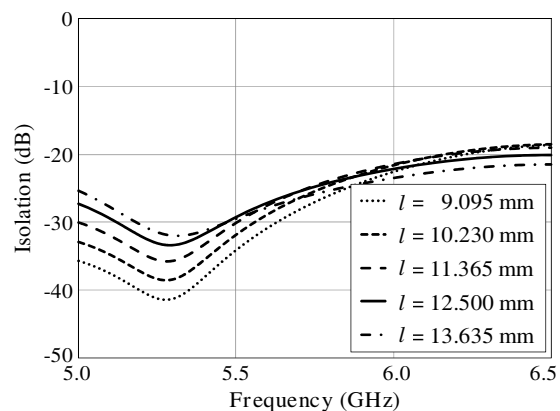
Figure 7: The isolation versus frequency as a function l.

in Figure 4. The next step is to determine a suitable circular ring radius r_a, ring length d, the distance between probe and reflector h, probe length l and the radius of probe r_p for the two-probe antenna. From the simulated results, it is found that the magnitude of S parameter can cover the frequency range from 5 GHz to 5.91 GHz, but the isolation between two probes is lower than 20 dB. In addition, to improve the isolation between two probes, an isolator length of l_i with the length of 0.44λ is inserted between two probes. As seen from the results, the isolation between two probes is larger than 20 dB but the impedance bandwidth with magnitude of S parameter curves cannot cover the frequency band of 5.2–5.8 GHz as shown in Figures 5 (a) and (b), respectively.

Furthermore, an enhancement of the impedance bandwidth can be achieved after a parametric
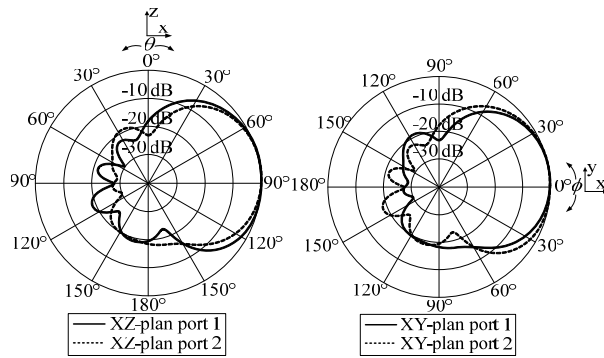
Figure 8: The radiation pattern in XZ and XY-planes.
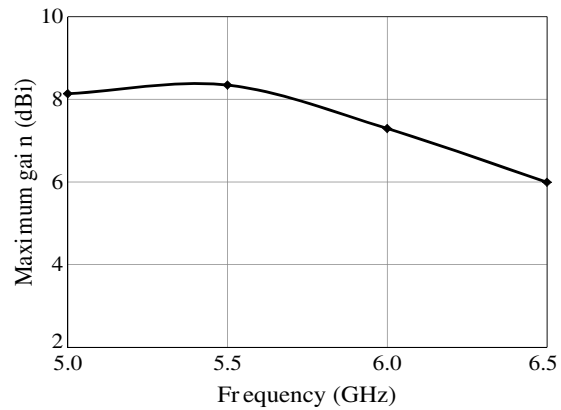
Figure 9: The maximum gain versus frequency.

study of the probe lengths which are varied from 9.095 to 13.635 mm. It is shown in the simulation that the operating bandwidth of the probe length fed the circular ring antenna with square reflector critically depending on the probe length l. It is noted that these parameters should be optimized for maximum gain, radiation pattern, impedance bandwidth and isolation between two probes as well. Finally, the frequency response curves of $|S_{11}|$ and $|S_{22}|$, the isolation between two probes, $|S_{21}|$ and $|S_{12}|$, the radiation pattern in both planes when excited by two probes and the maximum gain are illustrated in Figures 6, 7, 8 and 9, respectively.

5. CONCLUSION

The purpose of this paper is to present a two-probe excited circular ring antenna with square reflector and its design to being used for base stations of wireless local area network systems. The proposed antenna is designed easily and straightforwardly by choosing the appropriate parameters. The $|S_{11}|$, $|S_{22}|$ characteristics and the isolation between two-probes, $|S_{21}|$ and $|S_{12}|$, the radiation pattern and the maximum gain are obtained by antenna parametric study. This antenna possesses a maximum simulated gain of 8.34 dBi at 5.5 GHz over the impedance bandwidth of 16.32%, over which the return losses for both feed ports are less than -10 dB ranging from 5.12 to 6.03 GHz. Moreover, the isolation between two probes is greater than 20 dB. It is noted that the proposed antenna design possesses the advantage of compact size that can promise the good radiation performance when used with wireless local area network (WLAN) communication systems.

ACKNOWLEDGMENT

REFERENCES

1. Keowsawat, P., C. Phongcharoenpanich, S. Kosulvit, and M. Krairiksh, "Achievable diversity performance and range improvement from polarization diversity bi-directional antenna using two-probe excited circular ring," *TENCON*, Vol. 3-C, 208–211, Nov. 21–24, 2004.

2. Keowsawat, P., C. Phongcharoenpanich, S. Kosulvit, and M. Krairiksh, "Characteristics of polarization diversity bi-directional antenna in expressway environment," *IEEE Antennas and Propagation Society International Symposium*, Vol. 3, 3199–3202, Jun. 20–25, 2004.

3. Vaughan, R. G., "Polarization diversity in mobile communications," *IEEE Trans. Veh. Technol.*, Vol. 39, 177–186, Aug. 1990.

4. Krairiksh, M., P. Keowsawat, C. Phongcharoenpanich, and S. Kosulvit, "Two-probe excited circular ring antenna for MIMO APPLIcation," *Progress In Electromagnetics Research*, Vol. 97, 417–413, 2009.

5. Keowsawat, P., "A bi-directional atenna using two-perpendicular-probe excited ring for polarization diversity, master thesis (in Thai)," Faculty of Engineering, King Mongkut's Institute of Technology Ladkrabang, Thailand, 2001.

6. Kosulvit, S., M. Krairiksh, C. Phongcharoenpanich, and T. Wakabayashi, "A simple and cost effective bidirectional antenna using a probe excited circular ring," *IEICE Trans. Electronics*, Vol. E84-C, No. 4, 443–450, Apr. 2001.

7. Chawanonphitak, K., C. Phongcharoenpanich, S. Kosulvit, and M. Krairiksh, "Characteristics of an elliptical ring antenna excited by a linear electric probe," *International Journal of Electronics*, Vol. 94, No. 10, 973–984, Oct. 2007.

8. Ammann, M. J. and Z. N. Chen, "Wideband monopole antennas for multi-band wireless systems," *IEEE Antennas and Propagation Magazine*, Vol. 45, No. 2, Apr. 2003.

9. CST-Microwave Studio, User's Manual, 2006.

10. Khaleghi, A., A. Azoulay, and J. C. Bolomey, "Polarization diversity performance of a circular patch antenna for wireless LANs applications," *11th European Next Generation Wireless and Mobile Communication and Services (European Wireless)*, 1–4, Apr. 10–13, 2005.

11. Kozono, S., T. Tsuruhara, and M. Sakamoto, "Base station polarization diversity reception for mobile radio," *IEEE Trans. Veh. Technol.*, Vol. 33, No. 4, 301–306, Nov. 1984.

A New Seljuk Star Shape Microstrip Antenna Design

D. Uzer and S. S. Gultekin

Electrical and Electronics Engineering Department, Faculty of Engineering and Architecture
Selcuk University, Turkey

Abstract— A new star shape microstrip patch antenna in the form of Seljuk star is designed on a circular shape Foam substrate that has a thickness of 5 mm. It is simulated using by HFSS simulator. Electrical parameters of the antenna like bandwidth, radiation pattern, and return loss, exc. are investigated. The relationship between geometric sizes of the patch and the electrical parameter specifications of the antenna is researched. It is concluded that this new antenna design can be used for different applications and widespread bandwidth enhancement techniques can be adapted to this type of patch antenna.

1. INTRODUCTION

Conventional microstrip patch antennas basically have a conducting patch that made of copper or gold, printed on a grounded dielectric substrate, and have the attractive features of low profile, light weight, easy fabrication, and conformability to mounting hosts that allows choosing these types of antennas for lots of applications. Although there are more commonly used patch shapes especially that can be expressed geometrically like rectangular, circular, triangular, exc., if it has desired specifications, the microstrip patch antennas can be realized at any regular or irregular shapes [1, 2].

In this study, microstrip patch antennas are designed in a shape of Seljuk star which is one of the basic figures of Seljuk culture, named as Rub El Hizb in Arabic [3–6]. Seljuk star has eight corners and can be easily obtained with combining two same dimension squares located 45° relative to each other. Calculating all its geometric characteristics easily make this shape usage advantageous in microstrip patch antenna design.

Although star shape patch designs in various forms are available in literature, the eight corner star hasn't used before [7–12]. Also, in other star shape antenna studies, rather than a simple, single layer design with a single coaxial feed line, like shorting pin, aperture-coupled feed, stacked geometry exc. different and more complex techniques are preferred. In addition, except [7], there isn't any design formulation study for star shape patches, only geometric associations are examined.

2. ANTENNA GEOMETRY

Owing to there isn't any design formula, the resonant frequencies of the star shape microstrip antennas were predicted by using conventional circular microstrip patch antenna design formulas and these frequencies were used for simulations in HFSS [14]. In this study, all designs were fed by coaxial lines. After dimension calculations with circular microstrip antenna formulas, an optimum feed point determination for coaxial feed line of the antennas were realized starting from the corner of the star shape and going 1 mm steps to the center of the patch for impedance matching and improving the antenna performance. As a result of different feed line locations it was obtained that the best impedance matching is provided by feeding the patch at the corner of the star. The designed Seljuk star shape antenna can be seen in Figure 1.

At first, the study was started in mind, such as designing a 10 mm radius circular patch antenna on a Foam substrate that has a thickness of 5 mm and a dielectric constant of 1.03 then effective radius value r_{eff} was calculated, instead of r, aiming to increase the patch dimensions systemathcially at the end of multiple simulation studies and this value was assumed as the length between one corner and the center of the star shape antenna. With using r_{eff}, one edge length of the squares expressed with a can be calculated by multipling $\sqrt{2}$. Patch radii were increased by 5 mm steps till $r = 50$ mm and at total, nine different star microstrip antennas were designed. After patch dimensions were determined, resonant frequencies of the patches were predicted with using the conventional circular microstrip patch antenna formulas in [13]. Due to the chosen dimensions, resonant frequencies of the antennas were calculated between 1530 and 6280 MHz.

3. RESULTS

The designed patches were realized by using HFSS simulator and electrical parameters of these patch antennas were investigated [14]. Design parameters of star shape antennas are given in Table 1. Resonant frequencies and bandwidth values of the antennas obtained from S_{11} response compared with theoretical calculation results can be seen in Table 2. It is seen in Table 2 that most designs have two resonant frequencies under $-10\,\mathrm{dB}$ level and all antennas have a bandwidth over 10%.
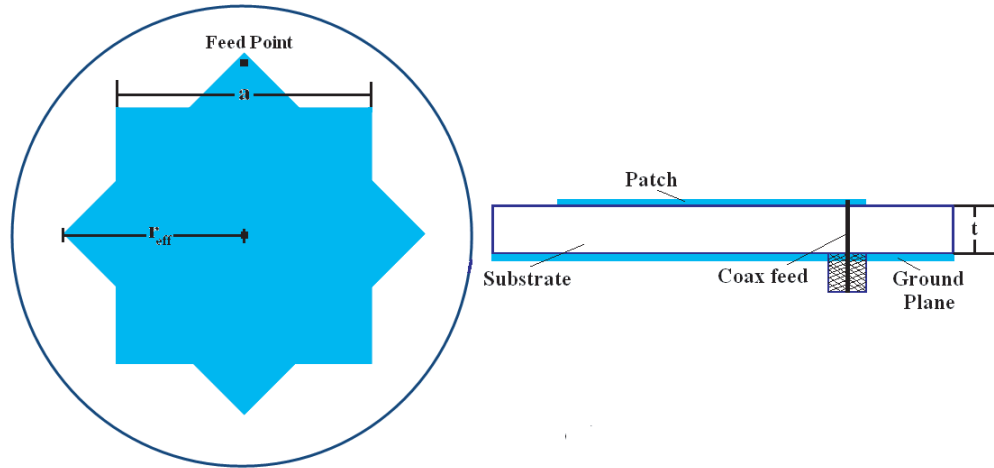

Figure 1: Seljuk star shape microstrip patch antenna.

Table 1: Design parameters of Seljuk star microstrip patches.

Design			1	2	3	4	5	6	7	8	9
Parameters	f_r	(MHz)	6280	4450	3470	2850	2430	2120	1880	1690	1530
	ε_r	-	1.03	1.03	1.03	1.03	1.03	1.03	1.03	1.03	1.03
	t	(mm)	5	5	5	5	5	5	5	5	5
	r		10	15	20	25	30	35	40	45	50
	a		19.52	27.54	35.3	43	50.45	57.9	65.3	72.66	80

Table 2: Comparison of theoretical and simulation resonant frequency and impedance bandwidth results.

Design	$f_{r\,design}$	$f_{r\,HFSS\text{-}1}$	$f_{r\,HFSS\text{-}2}$	$f_{r\,HFSS\text{-}3}$	$BW_{HFSS\text{-}1}$	$BW_{HFSS\text{-}2}$	$BW_{HFSS\text{-}3}$
	(MHz)						
1	6280	5960	-	-	1.07	-	-
2	4450	5990	-	-	1.06	-	-
3	3470	4640	7120	-	0.85	0.51	-
4	2850	2750	4330	-	0.47	0.43	-
5	2430	2410	3790	-	0.36	0.2	-
6	2120	2080	3010	4810	0.31	0.22	0.26
7	1880	1860	2950	-	0.24	0.1	-
8	1690	1630	2650	-	0.21	0.45	-
9	1530	1530	2450	-	0.17	0.16	-

In Table 3, S_{11} response peak directivity, peak gain, radiation power and radiation efficiency values of the patches from simulations are given. As an example of the obtained simulation results, S_{11} response and 2D radiation pattern of the patch No. 5 are shown in Figure 2.

Table 3: Some electrical parameters of antenna from simulations.

Design	S_{11} Response (dB)	Peak Directivity	Peak Gain	Radiated Power (W)	Radiation Efficiency
1	$-18,05$	1,889	2,2204	0,42425	1,1754
2	$-17,41$	3,243	3,1698	0,5474	0,9774
3	$-20,60$	2,427	2,6207	0,7322	1,0800
4	$-23,37$	0,167	0,3048	0,3471	1,8279
5	$-20,39$	0,205	0,3511	0,2762	1,7100
6	$-21,86$	0,258	0,4658	0,2700	1,8046
7	$-19,58$	0,042	0,0930	0,3400	2,200
8	$-22,66$	0,032	0,0840	0,3500	2,6374
9	$-18,46$	0,025	0,0560	0,2469	2,2214

(a)   (b)
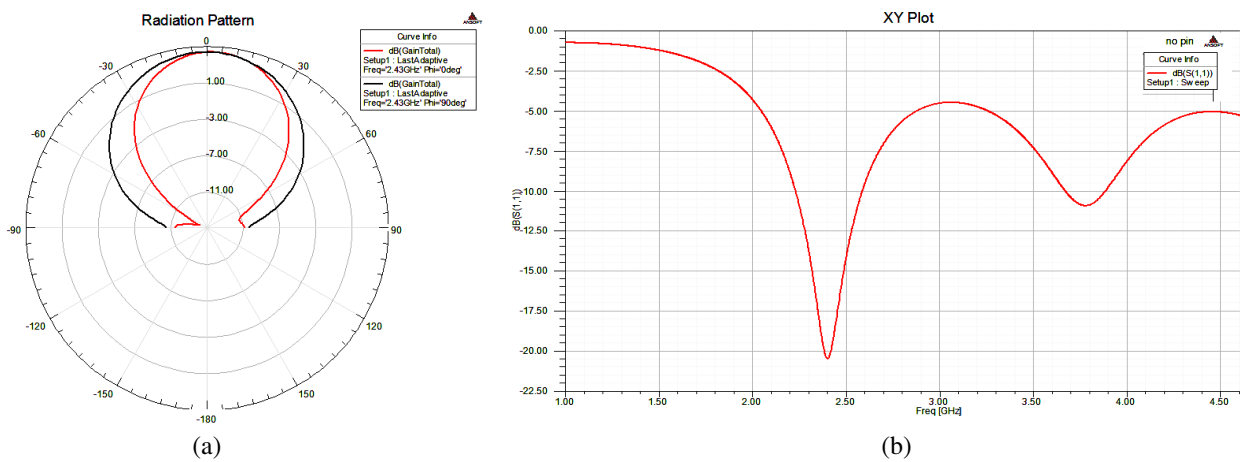
Figure 2: Result graphics of patch 5 (a) radiation pattern (b) S_{11} response.

4. CONCLUSION

In this study, parameters on the basis of S_{11}, electrical parameters like resonant frequency, bandwidth, gain, directivity and radiation efficiency of the patches with current distribution and radiation patterns are investigated. Most of the antennas have more than one resonant frequency. The studies on formulations of Seljuk star that allow directly design due to the resonant frequency and dielectric material parameters are going on. All antennas have a bandwidth over 10% and performance optimizations are expected by using bandwidth enhancement techniques on these antennas [15–17]. In future studies the formulas used for designing the star shape microstrip patch antennas will arrange to give a direct result of the star arm length and resonant frequency.

REFERENCES

1. Bahl, I. J. and P. Bhartia, *Microstrip Anrennas*, Artech House, 1980.
2. Garg, R., P. Bhartia, I. Bahl, and A. Ittipiboon, *Microstrip Antenna Design Handbook*, Artech House, 1995.
3. Yetkin, S. K., "Islamic architecture, islam mimarisi," *Ank. Uni. İah. Fak. Turk ve Islam San. Tar. Ens. Yay.*, Ankara, Turkiye, 1965.
4. Öney, G. and Ü. Erginsoy, "Architectural decoration and minor arts in seljuk anatolia, anadolu selçuklu mimari süslemesi ve el sanatları," *Turkiye Is Bankası Kultur Yay.*, Ankara, 1992.
5. Mulayim, S., "Geometric ornaments in anatolian turkish architecture-seljuk era, anadolu türk mimarisinde geometrik süslemeler — Selçuklu çagı," *Kültür ve Turizm Bakanlıgı Yayınları.*, Ankara, Turkiye, 1982.

6. Büyükçanga, M., "Eight corner star themes in Turkish Architecture, Türk mimarisinde sekiz köşeli yıldız motifleri," *6th of International Turkish World Congress of Social Sciences*, 1230–1234, Calalabat, Kyrgyzstan, May 25–28, 2008.

7. Parasnis, K., L. Shafai, and G. Kumar, "Performance of star microstrip as a linearly and circularly polarised TM_{21} mode radiator," *Electronic Letters*, Vol. 22, 463–464, 1986.

8. Mehta, A., D. Mirshekar-Syahkal, P. J. Massey, and H. Nakano, "A switched beam star patch antenna," *Antennas and Propagation Society International Symposium*, 1–4, San Diego, CA, USA, July 2008.

9. Abbaspour, M. and H. R. Hassani, "Wideband star-shaped microstrip patch antenna," *Progress In Electromagnetics Research Letters*, Vol. 1, 61–68, 2008.

10. Mehta, A., D. Mirshekar-Syahkal, and H. Nakano, "A star patch antenna for generating multiple radiation patterns," *Microwave and Optical Technology Letters*, Vol. 50, No. 7, 1908–1910, 2008.

11. Costantine, J., Y. Tawk, C. G. Chrnstodouloou, and S. B. Barbint, "A star shaped reconfigurable patch antenna," *IEEE MTT-S International Microwave Workshop Series on Signal Integrity and High-Speed Interconnects (JMWS)*, 97–100, Guadalaj'aral, Mexico, February 2009.

12. Montrose, A. B., D. Popovic, B. Popovic, and Z. Popovic, "Dual-polarization star microstrip antennas," *31st European Microwave Conference*, September 2001.

13. Dahele, J. S. and K. F. Lee, "Effect of substrate thickness on the performance of a circular-disk microstrip antenna," *IEEE Transactions on Antennas and Propagation*, Vol. 31, No. 2, 358–360, 1983.

14. HFSS v12., http://www.ansoft.com/products/hf/hfss.

15. Uzer, D., "Bandwidth enhancement techniques on microstrip antennas, mikroşerit antenlerde bandgenişligini arttırma teknikleri," *Doct. Seminar*, Selcuk Uni., Gradu. Sch. of Nat. and App. Sci., Konya, Turkiye, 2010.

16. Uzer, D., "Investigation on favourable methods for wideband microstrip patch antenna designs, geniş band mikro şerit yama anten tasarımları için uygun yöntemlerin araştırılması," Ph.D. Thesis, Selcuk Uni., Gradu. Sch. of Nat. and App. Sci., Konya, Turkiye, (in progress).

17. Kumar, G. and K. P. Ray, *Broadband Microstrip Antennas*, *Artech House*, R. B. Waterhouse, 2002.

A Novel Radiation Enhancement Technique for Multilayer Microwave Circuits

K. M. Lum

University of Surrey, Guildford, Surrey, GU2 7XH, United Kingdom

Abstract— Design and measurement data are presented that shows how a single strip of low permittivity, thick film dielectric material beneath the radiating edges of the microstrip patch antenna can be employed to improve the fringing field of the radiating edges and thus the efficiency of radiation. Design and practical data are provided for two prototype antennas working at 5 GHz. The radiation enhanced patch antennas demonstrated return loss below −30 dB and improvement in radiation efficiency. This simple yet efficient technique is particularly suitable for use with patch antenna under consideration, because of the general suitability of the whole structure for implementation in multilayer thick film, or LTCC formats.

1. INTRODUCTION

Patch antennas are widely used in a variety of communication systems because of their low profile, high efficiency, and increased mechanical reliability [1]. The substrate dielectric constant, ε_r, plays an important role in the efficiency of the patch antenna. A low value of ε_r for the substrate will increase the fringing field at the periphery, and thus the radiated power. However, other performance requirements may also dicate the use of substrate materials whose dielectric constants can be high and lead to reduction of antenna efficiency. External substrate perforation was introduced in the past to improve the far field radiation pattern of a patch antenna on a relatively thick and high dielectric constant substrate without any reduction in bandwidth or increase in patch size [2] and concept of soft-and-hard surface was reported to improve the radiation performance of a patch antenna on a high dielectric constant substrate [3]. Some approaches employed in the past to improve the performance of an antenna laid on a high dielectric constant substrate are [4, 5].

In this paper, with the development of thick film multilayer fabrication technique, a technique is proposed to increase the fringing fields and thus the associated radiation efficiency of a microstrip patch antenna on a substrate of high dielectric constant. Two prototypes 5 GHz antenna were designed and tested to establish the validity of the proposed technique. Practical data are presented that verify the principle of the radiation enhanced microstrip patch antenna.

2. ANTENNA STRUCTURE

Figure 1 shows the configuration of the proposed radiation enhanced patch antenna. The structure is composed of a single planar rectangular radiating patch with dimensions L_{pa} and W_{pa}, where L_{pa} is the resonant length dimension for the fundamental mode, and W_{pa} is the width of the patch. Two thin strips of low permittivity, thick film dielectric material, of width W_{st}, and length L_{st}, are arranged in parallel and beneath the radiating edges of the patch. A slotline channel, of width W_{sl},
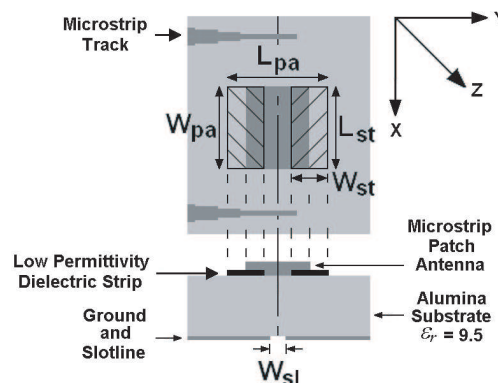
Figure 1: Configuration of microstrip patch antenna with low permittivity dielectric strips to improve radiation efficiency.

(a)   (b)
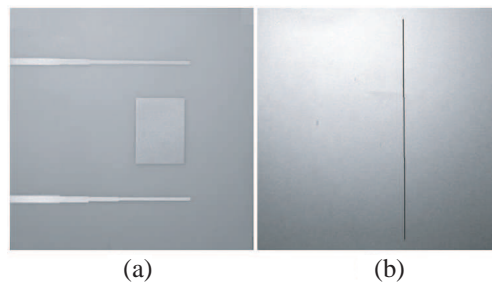
Figure 2: Fabricated (a) top plane, (b) bottom plane.

runs in the ground plane beneath the patch antenna. Traveling-wave propagating in the slotline channel will excite the patch [6] and propagating traveling-wave in the slotline channel was excited through a microstrip-to-slotline transition [7].

The test antenna was fabricated on Alumina substrate having the following parameters: substrate thickness, $h_{sub} = 1.270$ mm; panel size $= 50.800$ mm $\times 50.800$ mm; substrate dielectric constant, $\varepsilon_r = 9.5$; loss tangent $= 0.004$. Microstrip tracks, patch antenna and ground plane were printed using screen printable thick film silver conductor paste, C8710. C8710 is a mixed bond silver conductor that yields a smooth dense film with fired thickness of 10–14 µm per layer. It exhibits high adhesion, excellent solder-ability and good solder leach resistance. Drying profile should be process at 150°C for time duration of 10 minutes and peak temperature of firing profile is 850°C with a dwell time of 8 to 12 minutes. Strips of low permittivity thick film dielectric material were printed using low loss screen printable dielectric, KQ150. KQ150 is an advanced thick film dielectric, which offers a very low loss factor of 0.0005 and dielectric constant of 3.9 with fired thickness of 10–12 µm per layer. 150°C is maintained for 10 minutes during the drying profile and loss factor of 0.0005 can be achieved with a 925°C peak temperature lasting for 10 minutes. A single print thickness is designed for the microstrip tracks, rectangular patch, ground plane and the two strips in this proposed structure.

The circuit was fed from $50\,\Omega$ microstrip track. However, the width of the slotline channel, W_{sl} would be very small to give a characteristics impedance of $50\,\Omega$ and so, to avoid etching problems, the impedance of the slotline channel was increased to $67\,\Omega$ so that a wider channel could be used. Two-section quarter-wave microstrip transformers were used to convert the microstrip impedance from $50\,\Omega$ to $67\,\Omega$ [8].

A portion of the signal traveling in slotline will excite the patch, providing that the slotline channel is offset from center of the patch. The amount of offset will determine the amount of coupling. In the first prototype, the offset was chosen to be 1000 µm, in order to provide reasonable coupling to the patch to demonstrate the concept of the proposed low permittivity strip for radiation enhancement. In order to further establish the validity of the new technique, a second prototype with 2000 µm was built. Traveling-wave in the offset slotline channel was previously employed to excite an array of patch antenna for circular polarization [9–12].

The key antenna dimensions were: $L_{pa} = 09.730$ mm, $W_{pa} = 13.090$ mm, $L_{st} = 13.090$ mm, $W_{st} = 04.000$ mm and $W_{sl} = 00.200$ mm. The photographs of the fabricated patch antenna with 1000 µm offset on Alumina substrate are shown in Figure 2, where (a) is the top view and (b) is the bottom view of the substrate.

3. RADIATION MECHANISM

Figure 3(a) displays a classical behavior of charge distribution and current density beneath and above a microstrip patch [13]. Based on this behavior of charge distribution and current density, a technique is proposed to increase the concentration of charges beneath the radiating edges and henceforth, the current density that will lead to more fringing fields at the edges. Figure 3(b) shows the charge distribution of the proposed configuration for the radiation enhanced patch antenna.

Two thin strips of low permittivity, thick film KQ150 dielectric material, are printed beneath and in parallel with the radiating edges of the patch antenna laying on a high dielectric constant substrate. Like charges underneath the strips along the inter-section plane (IP) will treat the low permittivity KQ150 strip region as a less resistant channel of movement and henceforth, will create a burst of charges moving into the strips with increased repulsive force beneath the radiating edges
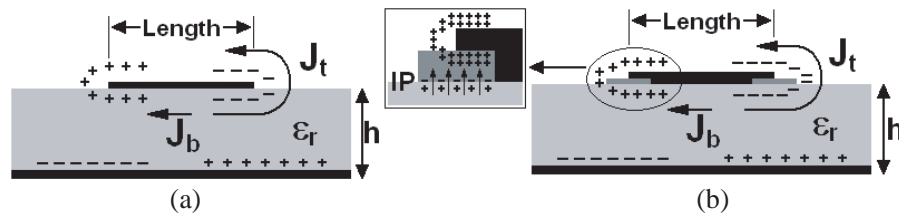
Figure 3: Charge distribution and current density on (a) conventional microstrip patch, and (b) radiation enhanced microstrip patch.
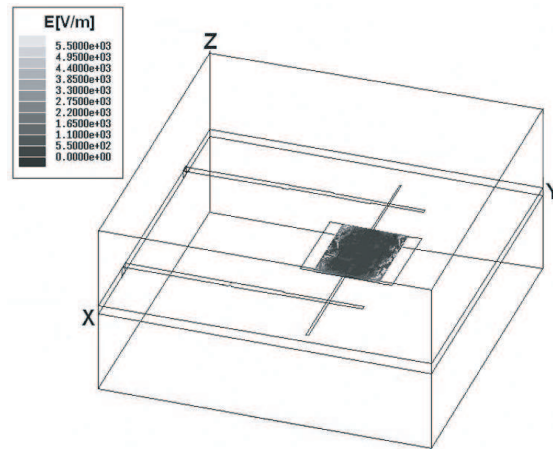
Figure 4: HFSS simulation model for patch antenna with low permittivity KQ150 strips at 1000 μm offset.

of the patch antenna. This will lead to more like charges on the top surface of the radiating patch and result in greater current density and the associated fringing field that will improve the radiation efficient of the patch.

In this case, the dependence of the performance of the antenna on the dielectric strips parameters is based on appropriate theoretical analysis. The length of the dielectric strip, L_{st}, is arranged to cover the entire radiating width, W_{pa}, of the patch and the width of the dielectric strip, W_{st}, is extended by approximately $0.1\lambda_g$ on both sides of the radiating edge of the patch to facilitate the ease of movement for the charges to the top surface of the patch. In this prototype, a dielectric material with permittivity of comparatively lower value than the main substrate is used for the dielectric strip. A single print of the KQ150 dielectric paste beneath the patch is chosen to minimize the change in the shape orientation of the patch.

Rule of employing this low dielectric strips has not been considered in this prototype design, which was intended merely to demonstrate the principle. In further work it is intended to control the dimension of the low dielectric strip for optimum radiation performance. Initial verification of the proposed technique is carried out using Ansoft High Structure Frequency Simulator (HFSS) package. Figure 4 shows the model employed to demonstrate the behavior of the electric field magnitude of the patch with the permittivity strips.

The patch structure was modeled with the radiating patch, microstrip tracks and the ground plane being perfect conductors to avoid the existence of fields inside the conductors. Low permittivity KQ150 strips are modeled by adding a new dielectric material with $\varepsilon_r = 3.9$ and loss tangent of 0.0005. Free space boundary is added above and below the structure to allow examination of the fields in the immediate vicinity of the patch and low permittivity KQ150 strips when excited by the energy coupled from the slotline. Only the dominant mode is considered in the simulation.

Figure 5 shows the magnitude of the electric field distribution on the surface of the radiating patch. Examination of the field distribution clearly indicates that the field concentration at the radiating edges of patch antennas with low permittivity KQ150 strips has increased. Without the presence of the low permittivity KQ150 strips, more like charges are confined within the high dielectric constant Alumina substrate beneath the patch radiating edges and results in less like charges flow to the top surface of the radiating patch. However, with the presence of the low
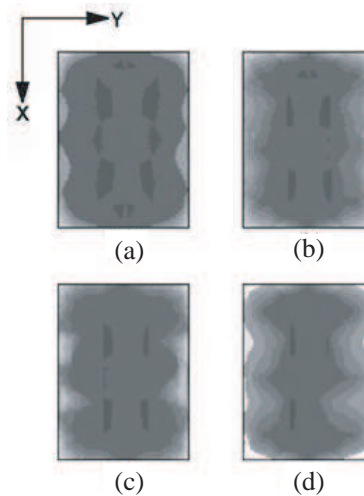
Figure 5: Simulated electric field (magnitude) for patch antennas, (a) #1, 1000 μm offset, (b) #2, 1000 μm offset with KQ150 strips, (c) #3, 2000 μm offset, and (d) #4, 2000 μm offset with KQ150 strips.
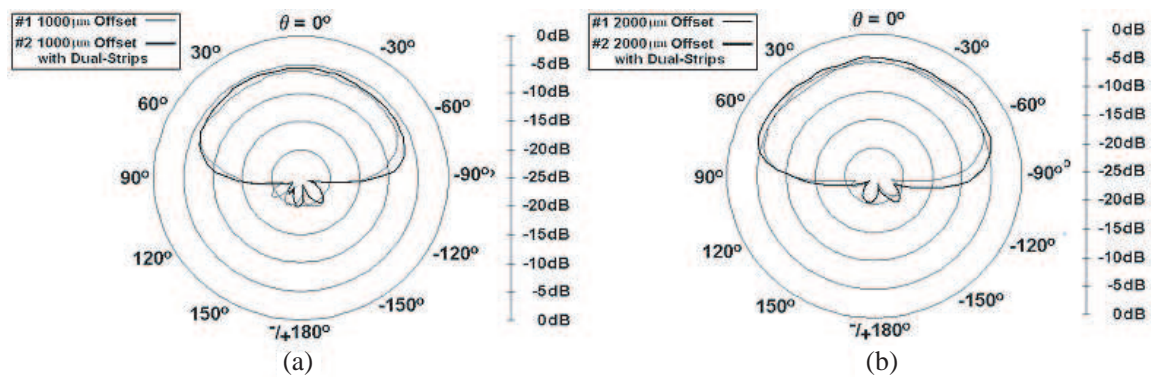
Figure 6: Measured elevation pattern for patch antennas #1 #2 #3 and #4 at $\Phi = 0°$.

permittivity KQ150 strips, it enhances the flow of like charges from the Alumina substrate to the surface beneath the radiating edges.

4. EXPERIMENTAL REULTS AND DISCUSSION

Measured elevation pattern for patch antennas #1 and #2 at $\Phi = 0°$ are presented in Figure 6(a). Around 0.5 dB of improvement in the measured radiation strength is achieved with the presence of low permittivity KQ150 strips. It should be noted that since the slotline is relatively narrow, and the slotline is matched, there would not be significant radiation from the slotline.

It is further proven in Figure 6(b). Due to a greater slotline offset of 2000 μm for patch antenna #3, more traveling-wave signal in the slotline channel is coupled to the patch as compared with patch antenna #1. Henceforth, more charges are expected to flow to the bottom and top surface of the radiating edge of patch antenna #4 with the presence of the low permittivity strips. Improvement of 0.7 dB is obtained with the KQ150 strips arrangement. It is apparent that improvement in the radiation efficiency exists and the key performance of the proposed technique has been established practically. It is to be noted that a 50 Ω load is used to terminate the second port during measurement as shown in Figure 1.

5. CONCLUSION

The concept of a novel technique to increase the fringing field of a patch antenna on a high dielectric constant substrate has been established through practical measurement of two prototypes designed at 5 GHz. Measured return loss below -30 dB and radiation efficiency improvement between 0.5 dB and 0.7 dB in the two respective prototypes with KQ150 strips are achieved. The proposed technique is particularly suitable for use in multilayer microwave circuits, and particularly highly integrated

multilayer transceiver packages used for localization applications [14–17].

REFERENCES

1. Pozar, D. M. and D. H. Schaubert, *Microstrip Antenna: The Analysis and Design of Microstrip Antennas and Arrays,* Wiley, New York, 1995.
2. Colburn, J. S. and Y. R. Samii, "Patch antennas on externally perforated high dielectric constant substrates," *IEEE Trans. Antennas. Propag.*, Vol. 47, No. 12, 1785–1794, Dec. 1999.
3. Li, R. L., G. D. Jean, M. M. Tentzeris, J. Papapolymerou, and J. Laskar, "FDTD analysis of patch antennas on high dielectric constant substrates surrounded by soft-and-hard surface," *IEEE Trans. Magnetics*, Vol. 40, No. 2, 1444–1447, Mar. 2004.
4. Waterhouse, R. B., "Stacked patches using high and low dielectric constant material combination," *IEEE Trans. Antennas Propag.*, Vol. 47, 1767–1771, Jun. 1999.
5. Zavosh, F. and J. T. Aberle, "Improving the performance of microstrip-patch antennas," *IEEE Mag. Antennas Propag.*, Vol. 38, No. 4, 7–12, Aug. 1996.
6. Tang, K. P., C. E. Free, and G. F. Goldspink, "A novel slotline-fed microstrip patch antenna," *IEEE Antennas and Propagation Conf.*, Vol. 1, No. 407, 235–238, Apr. 1995.
7. Knorr, J. B., "Slot-line transitions", *IEEE Trans. Micro. Theory Tech.*, Vol. 22, No. 5, 548–554, May 1974.
8. Colin, R. E., *Foundations for Microwave Engineering,* McGraw-Hill, New York, 1992.
9. Lum, K. M. , C. Laohapensaeng, and C. E. Free, "A novel traveling-wave feed technique for circularly polarized planar antennas, *IEEE Micro. and Wireless Components Letters,* Vol. 15, No. 3, 180–182, Mar. 2005.
10. Lum, K. M., T. Tick, C. Free, and H. Jantunen, "Design and measurement data for a microwave CP antenna using a new travelling-wave feed concept," *European Microwave Conf.*, Paris, France, Oct. 2005.
11. Lum, K. M. and C. Free, "A novel traveling-wave feed technique for circularly polarized planar microstrip antennas," *IEEE Antennas and Propag. International Symposium*, Vol. 2A, 250–253, Oct. 2005.
12. Lum, K. M. and C. E. Free, "A novel dual circularly polarized planar and multi-layer LTCC antenna arrays using traveling-wave feed system," *IEEE Trans. Micro. Theory Tech.*, Vol. 54, No. 6, 2880–2886, Jun. 2006.
13. Balanis, C. A., *Antenna Theory: Analysis and Design,* Wiley, New York, 1997.
14. Seow, C. K. and S. Y. Tan, "Non-line-of-sight localization in multipath environment," *IEEE Trans. Mobile Computing*, Vol. 7, No. 5, 647–660, May 2008.
15. Seow, C. K. and S. Y. Tan, "Localization of omni-directional mobile device in multipath environments," *Progress In Electromagnetic Research*, Vol. 85, 323–348, 2008.
16. Seow, C. K. and S. Y. Tan, "Localisation of mobile device in multipath environment using bi-directional estimation," *Electronics Letters*, Vol. 44, No. 7, 485–487, Mar. 2008.
17. Seow, C. K. and S. Y. Tan, "Non-line-of-sight unidirectional mobile localisation in multipath environment," *Electronics Letters*, Vol. 44, No. 2, 141–142, Jan. 2008.

Novel M-shaped Defected Ground Structure for Spurious Suppressed Dual Mode Bandpass Filter Design

J. W. Lau and K. M. Lum

School of Electrical Engineering and Computer Science
University of Newcastle, Callaghan, NSW 2308, Australia

Abstract— This paper presents a spurious suppressed microstrip dual mode bandpass filter (BPF). High selectivity and good adjacent channel interference rejection are required of modern transmitting and receiving devices. Conventionally, square resonator with orthogonal input and output feedlines is employed to achieve a quasi-elliptic type of bandpass response with two transmission zeros near its passband edges. However, this resulted in spurious response of unwanted harmonics at higher frequencies. The proposed spurious suppressed dual mode BPF utilized novel M-shaped defected ground structures (DGS) etched in the ground plane beneath a square resonator input and output feedlines to attain spurious suppressed bandpass responses. The presence of DGS leads to the increment in the current path and effective permittivity, and also decrement of the effective phase velocity and effective wavelength. In addition, DGS of different sizes, patterns and positioning, equivalent L-C ratio, coupling coefficients and other electrical parameters will result in various spurious suppression responses. It can be represented by a parallel tuned circuit arranged in series with the main circuit transmission line to which it is coupled. The prototyped BPF is fabricated on a Ro4003C substrate with relative permittivity of 3.38 and loss tangent of 0.0021. The center frequency is 2.55 GHz. The best measured S_{11} is obtained at 2.58 GHz with a value of -23.76 dB and the corresponding S_{21} is -3.7 dB which is slightly lower as compared to the simulated response. This is mainly due to fabrication tolerance and misalignment loss. One transmission zero is obtained at 2.25 GHz and 2.85 GHz respectively. The lower and upper stopband attenuation is greater than 20dB/GHz. The bandwidth of the passband response at -3 dB level is 3.2%. Validation of the BPF design is obtained via good agreement between the simulated and measured results.

1. INTRODUCTION

In modern communications systems, BPF with high, selectivity and adjacent channel interference rejection abilities are required. To attain this requirement, a quasi-elliptic bandpass response is highly recommended. A conventional square resonator integrated with square perturbation stub and orthogonally oriented gap-coupled feedlines is proposed. This configuration allows the BPF to obtain a dual mode, quasi-elliptic frequency response with two transmission zeros near the edge of the passband. This however, leads to spurious response of unwanted harmonics. In order to remove this imperfection, DGSs are studied and adopted in the BPF design to achieve better interference rejection.

2. BANDPASS FILTER DESIGN

Design specifications of the proposed spurious suppressed dual mode BPF are highlighted in Table 1 and the layout is presented in Fig. 1.

The BPF comprises a square loop resonator, square perturbation stub and orthogonally oriented feedlines. It is further integrated with a novel M-shaped DGS laid in the ground plane beneath the $50\,\Omega$ input and output feedlines respectively. The following sections will detail the concept of the resonator and DGS designs.

3. SQUARE RESONATOR BANDPASS FILTER DESIGN AND CONCEPT

In this section, we shall look at the design of the square resonator BPF without the M-shaped DGS. The square resonator also known as ring resonator is a transmission line formed in a closed loop. The mean circumference of the ring resonator is equivalent to multiple guided wavelengths.

The ring resonator supports two degenerate modes and in microwave cavity resonators, degenerate modes coexist independently. Based on the Maxwell's equation, and boundary conditions, sine and cosine functions are considered as orthogonal functions. Hence the two modes can be interpreted as two waves, travelling clockwise and anti-clockwise along the ring. If circular symmetrical ring resonators are used with co-linear feed lines, only one mode will be excited. If coupling lines are arranged asymmetrically, both modes should be excited [1].

Table 1: Design specifications of bandpass filter.

Parameter	Value
Centre Frequency, f_o	2.55 GHz
Passband Bandwidth, $f_{3\,dB}$	0.2 GHz
Return Loss, S_{11}	< -10 dB
Insertion Loss, S_{21}	> -3 dB
Stopband attenuation (L_{AS})	> 20 dB/GHz
Substrate type	Ro4003C
Substrate relative permittivity	3.38
Substrate loss tangent	0.0021
Substrate thickness	1.524 mm
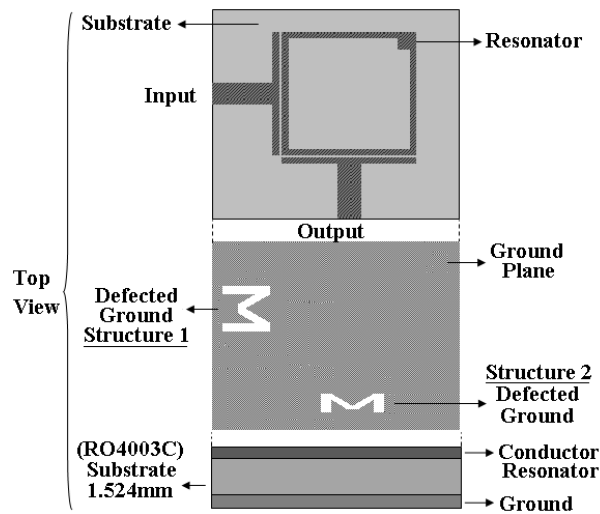
Figure 1: Layout of proposed spurious suppressed dual mode square resonator bandpass filter with M-shaped defected ground structures.
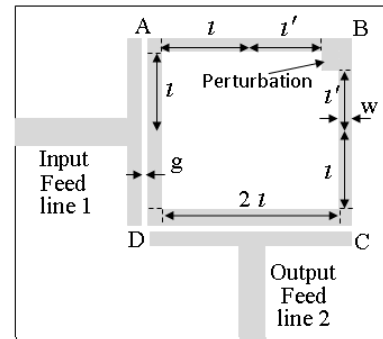
Figure 2: Geometrical layout of dual mode square resonator bandpass filter without M-shaped DGS.

Typically asymmetrical feed lines, perturbing stubs, notches or slits created on the width of the ring, will lead to excitation of two degenerate modes or splitting resonant frequencies. Ring resonator generates dual mode for odd modes only, if the perturbing stub or notch is positioned at $\Phi = 45°$, $135°$, $225°$ or $315°$ on the horizontal plane [2]. In this BPF design, a square perturbation stub of dimension 1.8 mm by 1.8 mm is placed at $45°$ orientation.

Figure 2 shows the geometrical layout of the dual mode BPF using square resonator and coupled feedlines. W refers to the width of the square resonator, g is the size of the coupling gap, and ι' is the length of the resonator from point A, C and D to the center of the square resonator. ι' is the length from the edge of the perturbation stub located at point B to the center of the square resonator.

The geometrical layout can be modeled base on the equivalent circuit as shown in Fig. 3. The circuit is determined using microstrip transmission line and discontinuities concepts. Each corner of the square resonator, points A, B, C and D are right-angle bends. Right-angle bends in microstrip line are considered as discontinuities and can be modeled using inductors, L and capacitors, C elements. As detailed in Fig. 3, point B is modeled using equivalent L-C circuit that consists of capacitors C_s, C_{pf} and inductor L_p which are adopted from [3–4]. Fig. 4 shows the dimensional layout of the dual mode square resonator bandpass filter without M-shaped DGS.

Simulation is done using Agilent Advanced Design System (ADS). The simulated response of S_{11} and S_{21} of the dual mode square resonator bandpass filter without DGS are shown in Fig. 5 and the frequency response is similar to the quasi-elliptic type. It also has one transmission zero at 2.35 GHz and 2.85 GHz respectively. The best S_{11} is obtained at 2.55 GHz with a value less than -15 dB. The corresponding S_{21} has a value of -2 dB and the lower and upper stopband attenuation

is greater than 20 dB/GHz. However, it is also observed that the presence of the spurious response at 5.3 GHz will degrade the suppression performance of the filter. Hence, in order to suppress any existing harmonics at 5.3 GHz, the novel M-shaped DGS is proposed and integrated with the dual mode square resonator BPF which will be discussed in the following section.

4. M-SHAPED DEFECTED GROUND STRUCTURE FOR BANDPASS FILTER

Defected ground structure is slot pattern created in the ground plane. Typically DGS is laid beneath microstrip transmission line. The presence of DGS is known to lead to the increment of the path of current and effective permittivity, and also decrement of the effective phase velocity, and effective wavelength [5]. DGS of different sizes, patterns and positioning, equivalent L-C ratio, coupling coefficients and other electrical parameters will result in various spurious suppression responses. The DGS can be represented by a parallel tuned circuit arranged in series with the main circuit
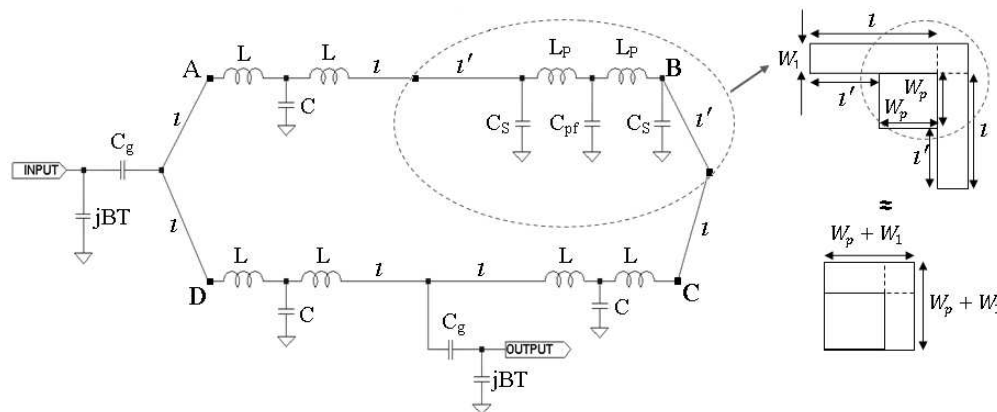
Figure 3: Equivalent circuit of dual mode square resonator bandpass filter without M-shaped DGS.

Notations	Dimension (µm)
L1	20,000
L2	20,000
L3	18,000
L4	20,000
L5	20,000
L6	18,000
L7	18,000
w1	1,000
w2	1,000
w3	3,500
w4	3,500
g1	400
g2	400
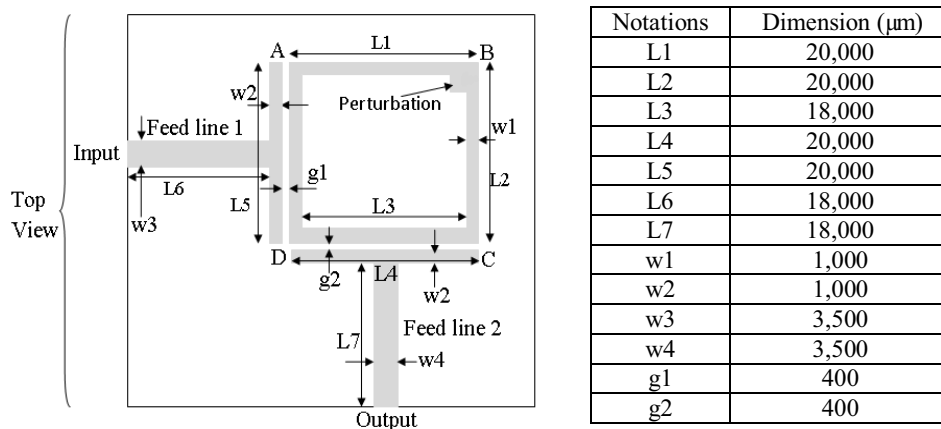
Figure 4: Key dimension data of dual mode square resonator bandpass filter without M-shaped DGS.
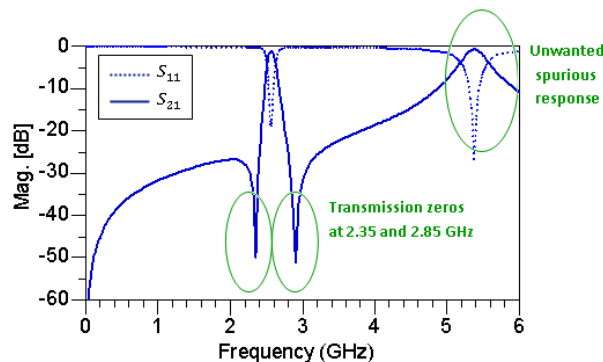
Figure 5: Simulated S_{11} and S_{21} response of dual mode square resonator bandpass filter without DGS.

transmission line to which it is coupled.

A novel M-shaped DGS is proposed and integrated with the dual mode square resonator BPF to provide suppression of unwanted harmonics. Figs. 6 and 7 show the key dimensional data of the M-shaped DGS. The M-shaped DGS is being etched in the ground plane below the $50\,\Omega$ input and output microstrip feedlines respectively. Through proper design of the M-shaped DGS, the frequency at which the transmission zero is present can be determined.

5. SIMULATED AND MEASURED RESULTS OF SQUARE RESONATOR BANDPASS FILTER WITH M-SHAPED DEFECTED GROUND STRUCTURE

The effectiveness of the M-shaped DGS in achieving suppression of unwanted harmonic is examined through the simulated S_{21} response. As shown in Fig. 8, the centered frequency of the passband is observed at 2.57 GHz. The corresponding S_{11} has a value less than $-10\,\text{dB}$ and S_{21} is $-2\,\text{dB}$. The lower and upper stopband attenuation is greater than $20\,\text{dB/GHz}$. One transmission zero is located at 2.35 GHz and 2.92 GHz respectively. The unwanted harmonic response at 5.3 GHz as highlighted in Section 3, is being suppressed by an $20\,\text{dB}$ attenuation with the presence of the M-shaped DGS. The bandwidth of the passband at $-3\,\text{dB}$ level is 3.1%.

Figure 9 shows the fabricated BPF with DGS. Measurement is carried out using Rohde & Schwarz VL6 Vector network analyzer and the measured results are presented in Fig. 10. The best measured S_{11} is obtained at 2.58 GHz with a value of $-23.76\,\text{dB}$. The S_{21} is $-3.7\,\text{dB}$ which is slightly lower as compared to the simulated response in Fig. 8. This is mainly due to fabrica-

Notations	Dimensions (μm)
L1	10,000
L2	3,110
L3	1,400
L4	7,760
L5	4,440
L6	1,400
L7	7,500

Notations	Dimensions (μm)
L1	3,000
L2	2,780
L3	1,600
L4	1,990
L5	3,730
L6	1,600
L7	9,500
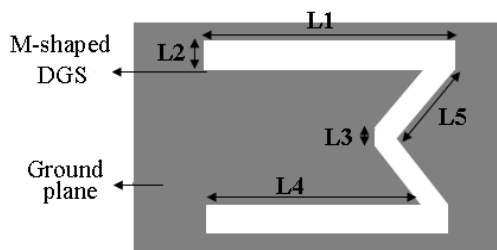
Figure 6: Key dimension data of M-shaped DGS beneath $50\,\Omega$ input feedline.
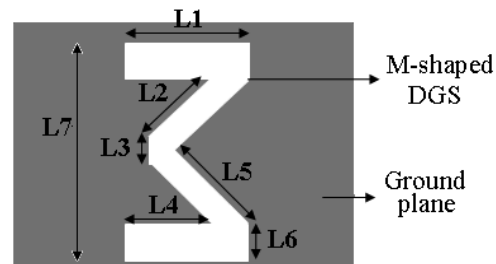
Figure 7: Key dimension data of M-shaped DGS beneath $50\,\Omega$ output feedline.
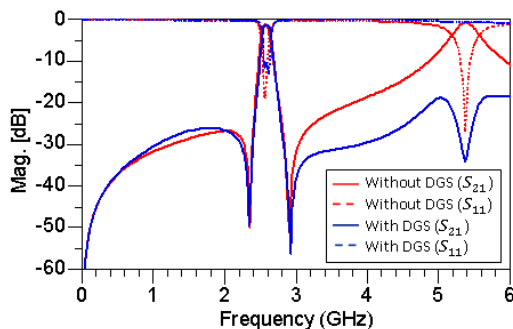
Figure 8: Simulated S_{11} and S_{21} response of dual mode square resonator bandpass filter with and without DGS.
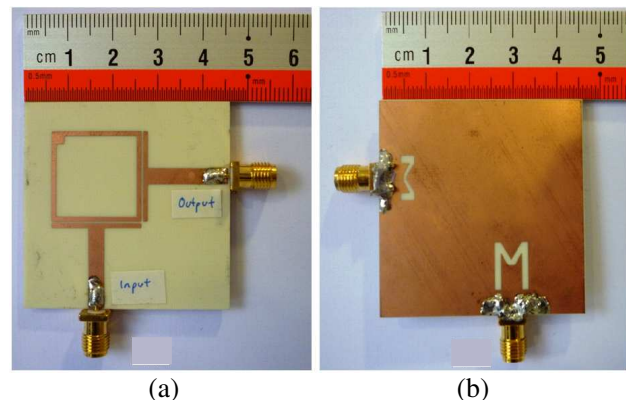
Figure 9: Fabricated BPF. (a) Square resonator and (b) defected ground structure.
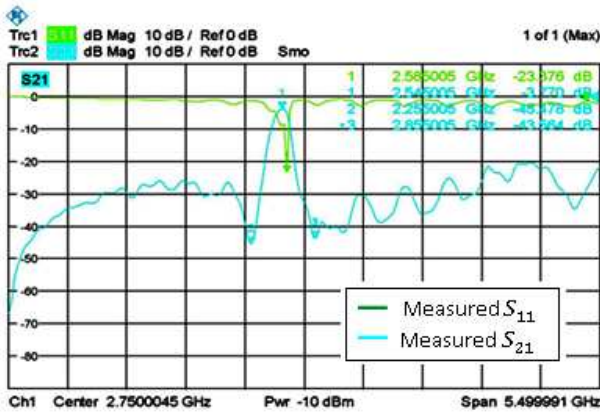
Figure 10: Measured S_{11} and S_{21} response of dual mode square resonator bandpass filter with M-shaped DGS.
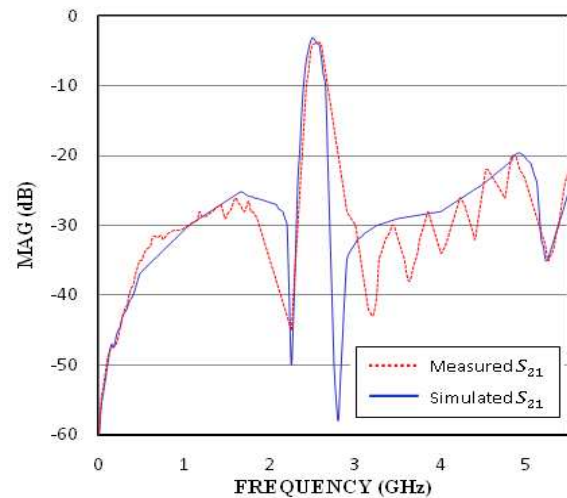
Figure 11: Simulated and measured S_{21} response of dual mode square resonator bandpass filter with M-shaped DGS.

tion tolerance, alignment and connector loss. One transmission zero is obtained at 2.25 GHz and 2.85 GHz respectively. The lower and upper stopband attenuation is greater than 20 dB/GHz. The bandwidth of the passband at -3 dB level is 3.2% which is quite similar to the simulation. It is clearly evident that the simulated and measured S_{21} response presents reasonably good agreement as shown in Fig. 11.

6. CONCLUSION

The concept of a dual mode quasi elliptic bandpass filter using novel M-shaped defected ground structure has been established through simulation and practical measurement. The spurious suppression of unwanted harmonics are achieved with the presence of the highly attenuated transmission zeros in the stopband response.

It is also clearly shown that with the implementation of the M-shaped DGS, wider stopband bandwidth is obtained. The measured results are in good agreement with the simulated results. The proposed configuration seems particularly suitable for use in multilayer microwave circuits, and particularly highly integrated multilayer transceiver packages used for localization applications [6–9].

REFERENCES

1. Wolff, I., "Microstrip bandpass filter using degenerate modes of a microstrip ring resonator," *Electron. Lett.*, Vol. 8, No. 12, 302–303, June 1972.
2. Chang, K. and L. H. Hsieh, *Microwave Ring Circuits and Related Structures*, 2nd Edition, A Wiley-Interscience Publication, Canada, 2004.
3. Kirschning, M., R. H. Jansen, and N. H. L. Koster, "Measurement and computer aided modeling of microstrip discontinuities by an improved resonator method," *IEEE MTT-S Int. Microwave Symp. Dig.*, 495–497, 1983.
4. Wadell, B. C., *Transmission Line Design Handbook*, 321, Artech House, MA, 1991.
5. Oraizi, H. and M. S. Esfahlan, "Miniaturization of Wilkinson power dividers by using defected ground structures," *Progress In Electromagnetics Research Letters*, Vol. 4, 113–120, 2008.
6. Seow, C. K. and S. Y. Tan, "Non line of sight localization in multipath environment," *IEEE Trans. Mobile Computing*, Vol. 7, No. 5, 647–660, May 2008.
7. Seow, C. K. and S. Y. Tan, "Localization of omni-directional mobile device in multipath environments," *Progress In Electromagnetic Research*, Vol. 85, 323–348, 2008.
8. Seow, C. K. and S. Y. Tan, "Localisation of mobile device in multipath environment using bi-directional estimation," *Electronics Letters*, Vol. 44, No. 7, 485–487, Mar. 2008.
9. Seow, C. K. and S. Y. Tan, "Non-line-of-sight unidirectional mobile localisation in multipath environment," *Electronics Letters*, Vol. 44, No. 2, 141–142, Jan. 2008.

Stepped Impedance Key-shaped Resonator for Bandpass and Bandstop Filters Design

K. C. Lek and K. M. Lum

School of Electrical Engineering and Computer Science
University of Newcastle, Callaghan, NSW 2308, Australia

Abstract— In this paper, a bandpass filter (BPF) and bandstop filter (BSF) designs using Key-shaped resonators are presented. The filter designs comprise stepped impedance resonators (SIR) and defective ground structure (DGS). The presence of the DGS creates a coupling capacitor in the ground plane which provides a filtering channel for improving the insertion loss and bandwidth performances. In addition, the DGS leads to reduction of overall circuit size, suppression of harmonic response and high selectivity of the filter response. Conversely, the SIR resonators are laid on the top conductor layer and the structure topology can be varied to obtain the desired performance of the filter. Furthermore, the stopband characteristics can be controlled by arranging the attenuation poles of the passband response. The proposed BPF is fabricated on FR4 substrate having a thickness of 1.6 mm, loss tangent of 0.027 and relative permittivity of 4.7. The best measured S_{11} response was observed at 2.6 GHz with a value of -20 dB. The corresponding S_{21} is -4.2 dB, with a stopband attenuation of 21.8 dB/GHz. As an extension of the SIR concept, a BSF is further proposed which consists of an open-ended stepped impedance quarter-wavelength stub. The best measured S_{11} response was obtained 3.22 GHz with a value of -0.2 dB. The stopband attenuation is 19.4 dB/GHz and the corresponding S_{21} is -28 dB. The BSF is prototyped using FR4 substrate. The dimensions of both BPF and BSF are 23.5 mm by 25.2 mm and 25.5 mm by 22.5 mm respectively. Validation of the BPF design is obtained via good agreement between the simulated and measured results.

1. INTRODUCTION

Microwave filters are essential circuits in the wireless communication systems such as wireless LAN and cellular telephone. To fulfil the current technology needs, a compact and high performance filter had to be designed. Stepped Impedance Resonator (SIR) filter has been widely use because of its low cost, light weight and simple structure [1–3].

In addition, defective ground structure (DGS) is introduced. DGS leads to reduction of overall circuit size, suppression of harmonic response and high selectivity of the filter response [4, 5]. In this paper, a BPF and BSF operating in the S-band are proposed using stepped impedance resonators and DGS.

2. BANDPASS FILTER DESIGN AND CONCEPT

Design specifications of the proposed BPF are highlighted in Table 1. Fig. 1 depicts the BPF design which comprises a single layer of FR4 substrate having a thickness of 1.6 mm. The top resonators
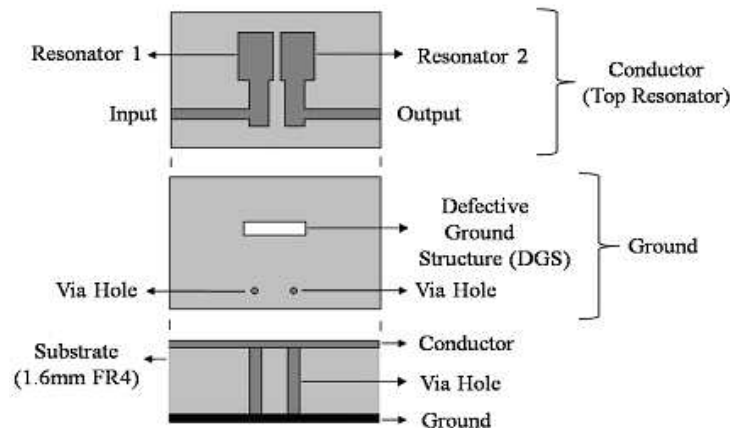
Figure 1: Configuration of proposed bandpass filter.

1 and 2 are laid on the FR4 substrate. The structure of the resonators can be varied to obtain the desired performance of the filter. Furthermore, the stopband characteristics of the BPF can be controlled by arranging the attenuation poles of the passband response [6, 7].

3. BANDPASS FILTER SIMULATION AND MEASUREMENT RESULT

Figure 2 detailed the dimensional data of the proposed BPF. Advanced Design System (ADS) simulation software was used to simulate the BPF design. Fig. 3 shows the simulated S_{11} and S_{21} results of the proposed BPF. The best match for the BPF is obtained at 2.62 GHz with a S_{11} value of less than −25 dB. In the passband response, the corresponding S_{21} is approximately −3 dB with an attenuation of 26.5 dB/GHz. The proposed BPF was fabricated on FR4 substrate as shown in Fig. 4. Measurements were carried out using Network Analyzer.

As presented in Fig. 5, the best measured S_{11} was observed at 2.6 GHz with a value of −20 dB. The corresponding S_{21} is −4.2 dB, with a stopband attenuation of 21.8 dB/GHz. The measured −5 dB bandwidth over the passband is about 200 MHz. It is evident that the measured result agrees well with the simulation results.

Table 1: Design specifications of bandpass filter.

Key Parameter	Value
Operating Frequency (GHz)	2.6
Return Loss, S_{11} (dB)	< -10
Passband Insertion loss, S_{21} (dB)	> -10
Passband (MHz) at −5 dB	200
Stopband Attenuation	> 20 dB/GHz
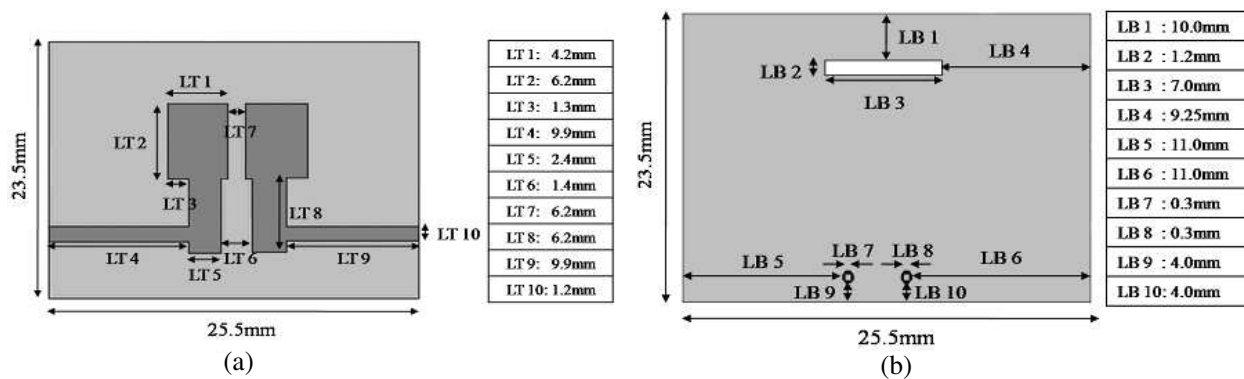
Figure 2: Key dimensional data of (a) top resonator and (b) defected ground plane.
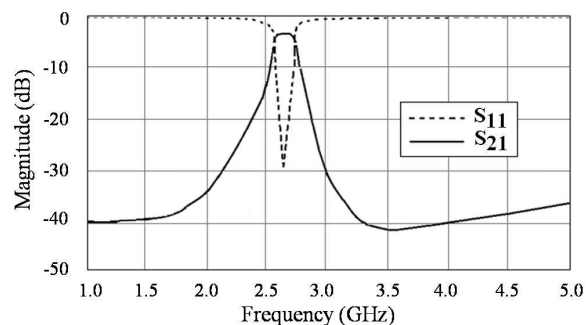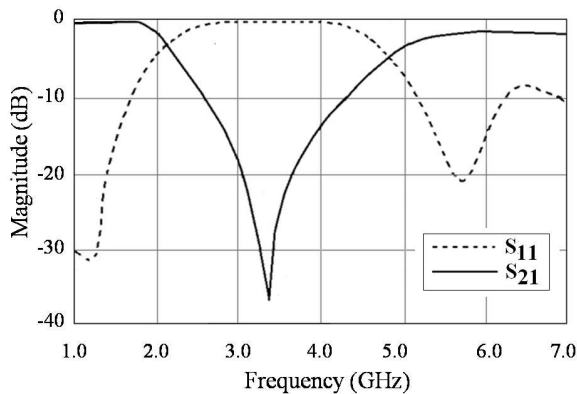

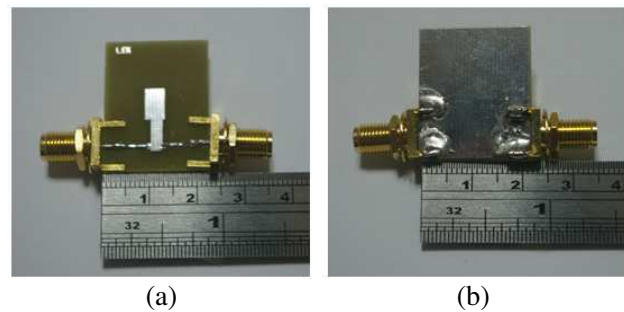Figure 3: Simulated S$_{11}$ and S$_{21}$ response of bandpass filter.
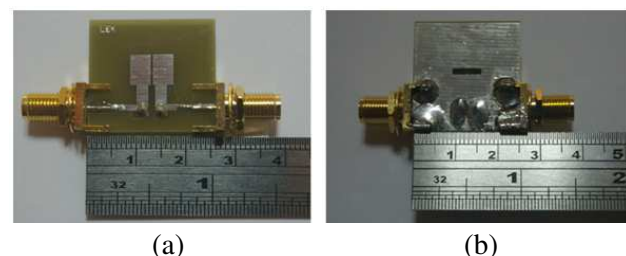
Figure 4: Fabricated bandpass filter. (a) Top resonators. (b) Ground plane.
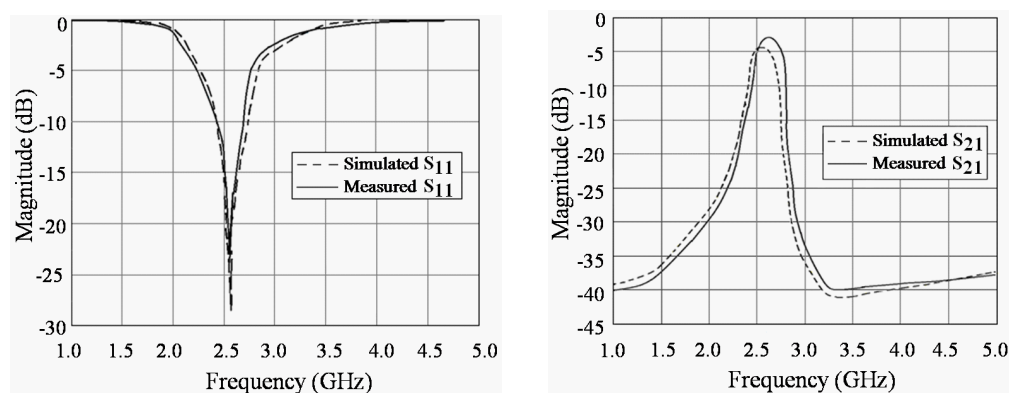
Figure 5: Simulated and measured S_{11} and S_{21} response of bandpass filter.

Table 2: Design specifications of bandstop filter.

Key Parameter	Value
Operating Frequency	3.2 GHz
Return Loss	> -1 dB
Stopband Insertion Loss, S_{21}	< -10 dB
Stopband (MHz) at -10 dB	2000
Stopband Attenuation	> 10 dB/GHz
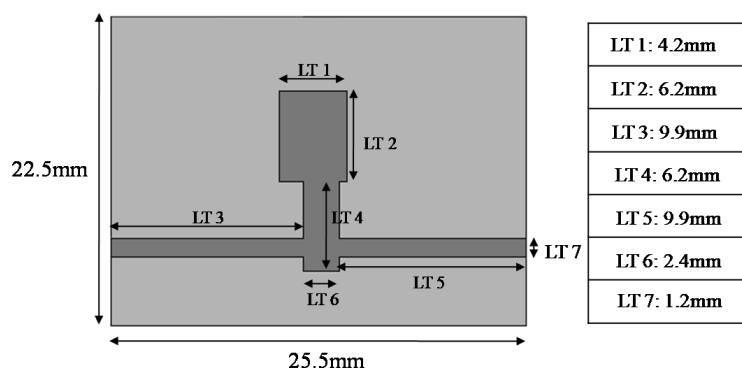
Figure 6: Key dimensional data of top resonator.

4. BANDSTOP FILTER DESIGN AND CONCEPT

As an extension of the SIR concept, a BSF is proposed. Design specifications of the proposed BPF are highlighted in Table 2. As shown in Fig. 6, the BSF design consists of an open-ended stepped impedance quarter-wavelength stub which comprises two characteristic impedances (Z_1, Z_2) and electrical lengths (Q_1, Q_2) that leads to the resonating of two different frequencies (w_f and w_c).

As illustrated in Fig. 7, the components encircled indicate the resonate circuits of the filter at frequencies w_f and w_c. At the resonant frequencies, w_f and w_c, the circuits are able to exhibit a stopband response that rejects unwanted signal thus enabling the filter to operate as a BSF [8–10].

5. BANDSTOP SIMULATION AND MEASUREMENT RESULT

Figure 8 shows the simulated S_{11} and S_{21} response of the proposed BSF. The best return loss, S_{11} for the BSF is obtained at 3.28 GHz with a corresponding S_{11} value of -0.1 dB. The stopband attenuation is 17.4 dB/GHz. In the stopband response, S_{21} is approximately -38 dB.

The proposed BSF was prototyped using one FR4 substrate with the SMA connectors soldered onto the microstrip feed line as shown in Fig. 9. Measurements were carried out using Network Analyzer.

As presented in Fig. 10, the best measured S_{11} was obtained at 3.22 GHz with a value of
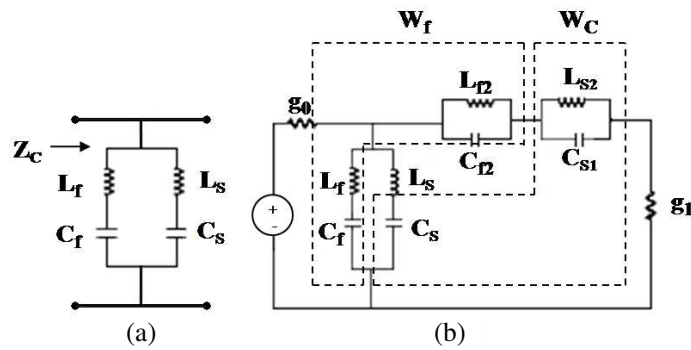
Figure 7: Equivalent circuit of (a) configuration of stepped impedance resonator, (b) bandstop filter.

Figure 8: Simulated S_{11} and S_{21} response of band-stop filter.

Figure 9: Fabricated bandstop filter. (a) Top resonator. (b) Ground plane.
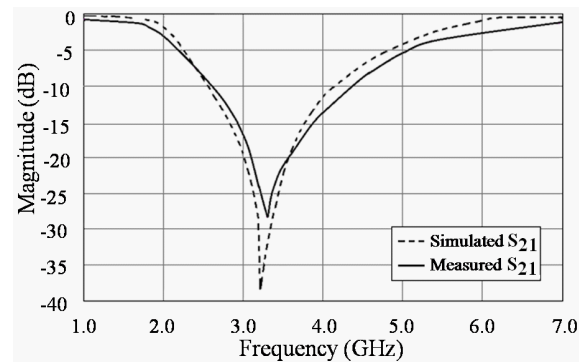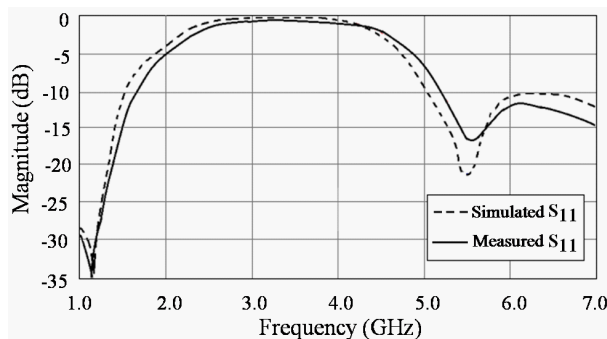
Figure 10: Simulated and measured S_{11} and S_{21} response of bandstop filter.

-0.2 dB. The stopband attenuation is 19.4 dB/GHz and the corresponding S_{21} is -28 dB. The measured -10 dB bandwidth over the stopband is about 1800 MHz. Despite of the slight variance in the results due to unexpected fabrication tolerance, material losses and parasitic effect of the SMA connectors, it is evident that the measured result agrees well with the simulation results.

6. CONCLUSION

The design of a bandpass filter based on the configuration of stepped impedance key-shaped resonators with defected ground structure has been validated through simulation and practical measurement. It has also been demonstrated that the stepped impedance key-shaped resonator topology of the proposed bandpass filter design can be further modified to obtain a bandstop filter response. The proposed filters have the advantages of providing reasonably acceptable filtering function using simple resonator and defected ground structure topology and are easy to be fabricated. The proposed configuration seems particularly suitable for use in multilayer transceiver designs [11–14] and localization applications [15–18].

REFERENCES

1. Zhang, J., J.-Z. Gu, B. Cui, and X.-W. Sun. "Compact and harmonic suppression open-loop resonator bandpass filter with tri-section sir," *Progress In Electromagnetics Research*, Vol. 69, 93–100, 2007.

2. Velazquez-Ahumada, M. D. C., J. Martel, F. Medina, and F. Mesa, "Application of stub loaded folded stepped impedance resonators to dual band filter design," *Progress In Electromagnetics Research*, Vol. 102, 107–124, 2010.

3. Liu, Y., W. B. Dou, and Y.-J. Zhao, "A tri-band bandpass filter realized using tri-mode t-shape branches," *Progress In Electromagnetic Research*, Vol. 105, 425–444, 2010.

4. Lin, W.-J., C.-S. Chang, J.-Y. Li, D.-B. Lin, L.-S. Chen, and M.-P. Houng, "A new approach of dual-band filters by stepped impedance simplified cascaded quadruplet resonators with slot coupling," *Progress In Electromagnetic Research letters*, Vol. 9, 19–28, 2009.

5. Zhang, J., J.-Z. Gu, B. Cui, and X. W. Sun, "Compact and harmonic suppression open-loop resonator bandpass filter with tri-section sir," *Progress In Electromagnetic Research*, Vol. 69, 93–100, 2007.

6. Bahrami, H., M. Hakkak, and A. Pirhadi, "Analysis and design of highly compact bandpass waveguide filter using complementary split ring resonators (CSRR)," *Progress In Electromagnetics Research*, Vol. 80, 107–122, 2008.

7. Yang, X., Y. Fan, B. Zhang, and M. Zhao, "A novel compact suspended double side CMRC millimeter bandpass filter with wide stopband," *Progress In Electromagnetics Research Letters*, Vol. 21, 59–66, 2011.

8. Yang, R.-Y., M.-H. Weng, C.-Y. Hung, H.-J. Chen, and M.-P. Houng, "Novel compact microstrip interdigital bandstop filter," *IEEE Transactions Ultrasonics, Ferroelectrics, and Frequency Control*, Vol. 51, No. 8, Aug. 2004.

9. Guo, L., Z.-Y. Yu, and L. Zhang, "Design of a dual-mode dual-band filter using stepped impedance resonators," *Progress In Electromagnetics Research Letters*, Vol. 14, 147–154, 2010.

10. Chin, K.-S. and C.-K. Lung, "Miniaturized microstrip dual-band bandstop filters using tri-section stepped-impedance resonators," *Progress In Electromagnetics Research C*, Vol. 10, 37–48, 2009.

11. Lum, K. M., C. Laohapensaeng, and C. E. Free, "A novel traveling-wave feed technique for circularly polarized planar antennas," *IEEE Micro. and Wireless Components Letters*, Vol. 15, No. 3, 180–182, Mar. 2005.

12. Lum, K. M., T. Tick, C. Free, and H. Jantunen, "Design and measurement data for a microwave CP antenna using a new travelling-wave feed concept," *European Microwave Conf.*, Paris, France, Oct. 2005.

13. Lum, K. M. and C. Free, "A novel traveling-wave feed technique for circularly polarized planar microstrip antennas," *IEEE Antennas and Propag. International Symposium*, Vol. 2A, 250–253, Oct. 2005.

14. Lum, K. M. and C. E. Free, "A novel dual circularly polarized planar and multi-layer LTCC antenna arrays using traveling-wave feed system," *IEEE Trans. Micro. Theory Tech.*, Vol. 54, No. 6, 2880–2886, Jun. 2006.

15. Seow, C. K. and S. Y. Tan, "Non line of sight localization in multipath environment," *IEEE Trans. Mobile Computing*, Vol. 7, No. 5, 647–660, May 2008.

16. Seow, C. K. and S. Y. Tan, "Localization of omni-directional mobile device in multipath environments," *Progress In Electromagnetic Research*, Vol. 85, 323–348, 2008.

17. Seow, C. K. and S. Y. Tan, "Localisation of mobile device in multipath environment using bi-directional estimation," *Electronics Letters*, Vol. 44, No. 7, 485–487, Mar. 2008.

18. Seow, C. K. and S. Y. Tan, "Non-line-of-sight unidirectional mobile localisation in multipath environment," *Electronics Letters*, Vol. 44, No. 2, 141–142, Jan. 2008.

Multilayered Miniaturized Hairpin Resonator for Bandpass Filter Design

M. L. Lee and K. M. Lum

School of Science and Technology, SIM University, Singapore

Abstract— This paper present a multilayered bandpass filter (BPF) operating at 2 GHz. Four miniaturized hairpin resonators are positioned in pairs, laid on two different conductor layers to obtain the BPF response. The multilayer configuration allows more flexibility in controlling the variation on the coupling effect of the resonators, namely the horizontal coupling effect between resonators on the same layer and vertical coupling effect between the top and bottom overlaid resonators. The overall dimensions of the prototyped BPF are 65 mm by 26 mm. It is fabricated on two FR4 substrates with relative permittivity, $\varepsilon_r = 4.7$. Validation of the BPF design is obtained via good agreement between the simulated and measured results.

1. INTRODUCTION

With the increasing demand on wireless communication devices, being the key component, improving the performance and reducing the circuit size of filter had become a key challenge in the emerging market. Many designs had been studied and look into in recent year to reduce the circuit size and improve the circuit performance. Some of the design used was hairpin resonator, ring resonator; step impedance resonator, defected ground structure, and short circuit stub [1–5].

Due to its ease of fabrication and compact in circuit size, hairpin resonator is one of the commonly used filter design technology. Hairpin resonator is an evolved form of a common microstrip resonator, by bending the strip into a "U" shape pattern. This technique allows the resonator length to be significantly reduced, thus making this kind of design very attractive. In addition, the U-shaped hairpin resonator can be further miniaturize by bending the open-ended terminates of the microstrip inwards within the open area of the U-shaped pattern.

Fabrication limitation on a single layer structure, where the gap between two resonators on the same layer could not be too closed is one of the challenges faced for microstrip filter design. This is a major setback as stronger coupling effect could only be achieved with smaller gap between the two resonators. Therefore multilayer structure had been introduced which allow stronger coupling effect and further reduction in circuit area. In this paper, the overall size of the proposed filter is smaller as compared with existing designs [6].

2. BANDPASS FILTER DESIGN AND CONCEPT

Table 1 and Fig. 1 present the design specification and configuration of the proposed BPF respectively. The BPF consists of two FR4 materials with a thickness of 0.8 mm and 1.6 mm, and are stacked together using adhesive. The modified miniaturized hairpin resonators 1 and 2, 3 and 4 are arranged on conductor layer 1 and 2. Both pairs are subjected to a 180 degree difference in the angle orientation. It should be noted that an overlapping region is created between resonators 1 and 3, and resonators 2 and 4. The filter is fed with a 50 ohm microstrip feedline on conductor layer 1 for the input and output ports respectively.

Table 1: Design specification of proposed bandpass filter.

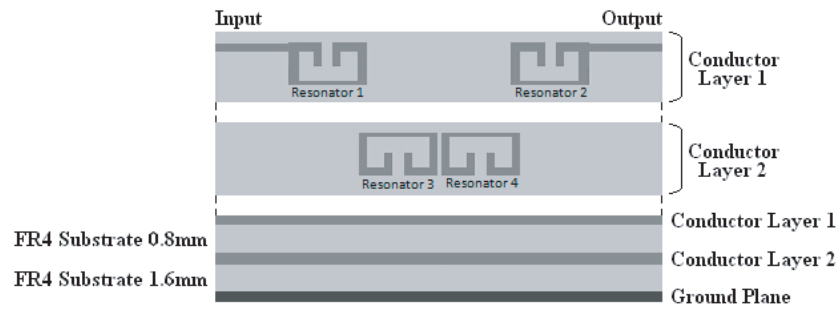| Parameters	Value
Center Frequency, f_o	2 GHz
Return Loss, S_{11}	< -10 dB
Passband Insertion Loss, S_{21}	> 2 dB
Passband Bandwidth at -20 dB	500 MHz
Stopband Rejection	> 20 dB/GHz

Figure 1: Configuration of proposed bandpass filter.

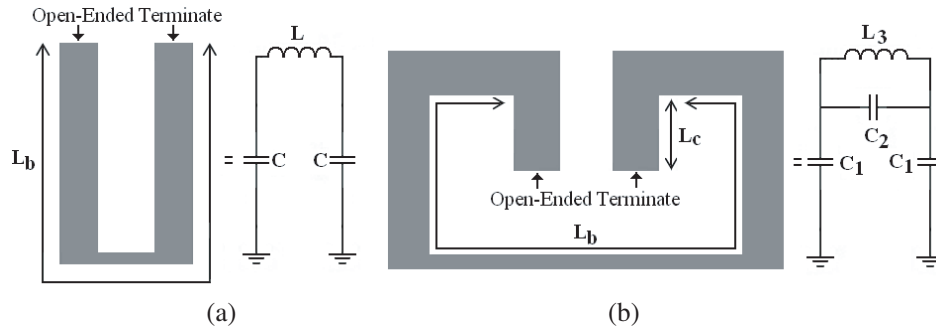(a)   (b)

Figure 2: (a) Conventional hairpin resonator and equivalent circuit. (b) Modified miniaturized hairpin resonator and equivalent circuit.
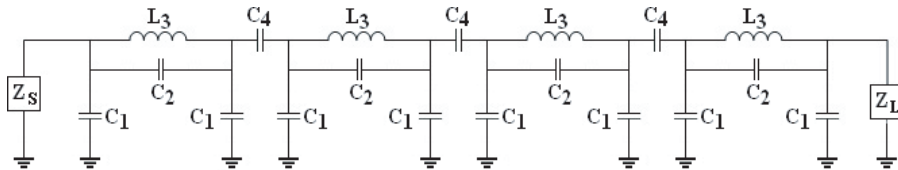

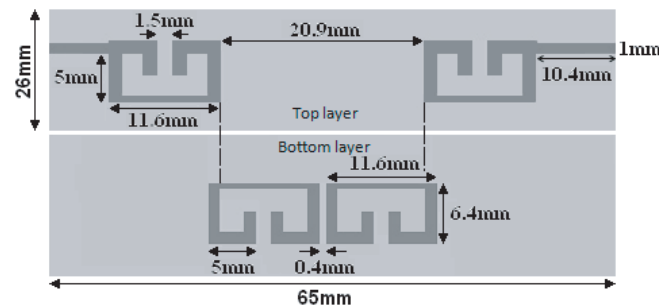Figure 3: Equivalent circuit of proposed bandpass filter.

Figure 4: Key dimensional data of proposed bandpass filter.

Figure 2 shows a conventional hairpin resonator and a modified miniaturized hairpin resonator topology. C_2 is the capacitance due to the inter-coupling effect between the two open-ended terminates. Multilayer structure is further implemented to create a stronger cross-coupling effect between resonators 1 and 3, and resonators 2 and 4. The value of L, C, C_1, C_2, and L_3 are obtained using Equations (1)–(4). β_b, β_c and w are the phase constant and angular frequency of the transmission line [7].

$$L_3/L = \frac{Z_{01} \sin(\beta_b L_b)}{w} \tag{1}$$

$$c = \frac{1 - \cos(\beta_b L_b)}{w Z_{01} \sin(\beta_b L_b)} \tag{2}$$

$$c_1 = \frac{1}{wZ_e \cot(\beta_c L_c)} + \frac{1 - \cos(\beta_b L_b)}{wZ_o \sin(\beta_b L_b)} \tag{3}$$

$$c_2 = \frac{Z_e - Z_o}{2wZ_e Z_o \cot(\beta_c L_c)} \tag{4}$$

Figure 3 shows the equivalent circuit of the proposed BPF, where C_2 represents the inter-coupling capacitance and C_4 represents the cross-coupling capacitance. Key dimensional data of the BPF are presented in Fig. 4. The overall circuit size is $65\,\text{mm} \times 25\,\text{mm}$.

3. BANDPASS FILTER SIMULATION AND MEASUREMENT RESULT

The proposed BPF is modeled using Agilent's Advance Design System (ADS). Fig. 5 illustrates the simulated results. The best matching response is observed at $2\,\text{GHz}$ with a return loss S_{11} value less than $-30\,\text{dB}$. The corresponding passband insertion loss S_{21} is greater than $-2\,\text{dB}$. The lower and upper stopband rejection is $27\,\text{dB/GHz}$ and $74\,\text{dB/GHz}$ respectively. Fig. 6 shows the fabricated BPF.
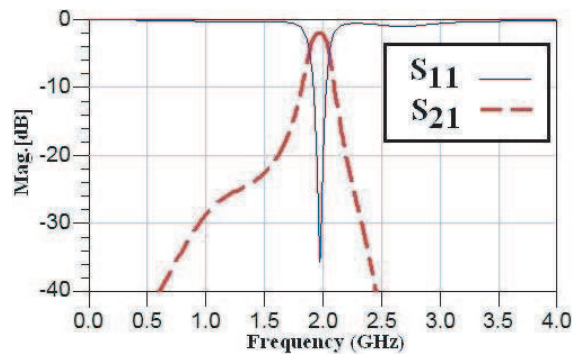
Figure 5: Simulated result of proposed bandpass filter.

(a)   (b)
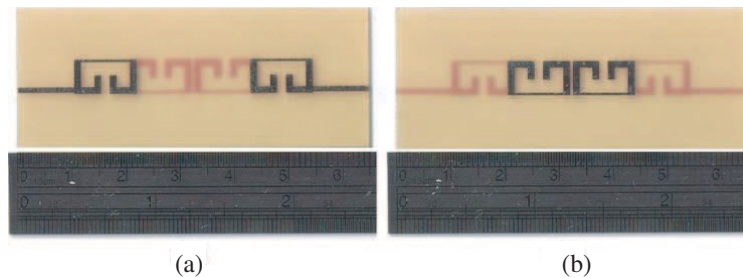
Figure 6: Fabricated bandpass filter. (a) Conductor layer 1. (b) Conductor layer 2.
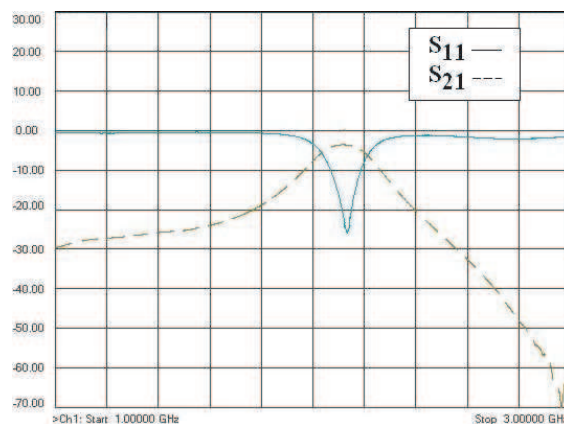
Figure 7: Measured result of proposed bandpass filter.

Table 2: Simulation and measurement results of proposed bandpass filter.

Parameter	Simulated Results	Measured Results
Center Frequency, f_o (GHz)	2	2.17
Return Loss, S_{11} (dB)	-35	-26
Passband Insertion Loss, S_{21} (dB)	-2.4	-3.44
Lower Stopband Rejection (dB/GHz)	27	23
Upper Stopband Rejection (dB/GHz)	74	72

Measurement is done using network analyzer. The measured results are shown in Fig. 7 and the best matched return loss S_{11} is obtained at 2.7 GHz with a value less than -25 dB. The passband insertion loss S_{21} is greater than -4 dB. The lower and upper stopband rejection is 23 dB/GHz and 72 dB/GHz respectively. It is apparent that the simulated and measured passband response is closely identical. The difference between the simulated and measured results may be attributed by the mis-alignment between the two substrates. As the desire BPF response is critically dependent on the arrangement of the resonators on the two conductor layers, thus any inaccurate placement would inevitably affect the filter response. Table 2 detailed the simulation and measurement results.

4. CONCLUSION

In conclusion, a multilayered bandpass filter using modified miniaturized hairpin resonators had been proposed and implemented. The simulated and measured results have shown excellent matching return loss value below -20 dB. The corresponding passband insertion loss is reasonably acceptable at value above -4 dB. The stopband rejection can be further improved with better technique of stacking the two substrates together. The prototyped bandpass filter at this stage is merely used to demonstrate the concept of the new design. Further work would be carried out to control the coupling mechanism between the multilayered resonators. The proposed configuration seems particularly suitable for integration with multilayer transceiver antenna modules [8–11] and localization applications [12–15].

REFERENCES

1. Rahman, A. A., A. R. Ali, S. Amari, and A. S. Omar, "Compact bandpass filter using defected ground structure (DGS) coupled resonators," *IEEE MTT-S Int. Dig.*, 1479–1482, 2005.

2. Adam, H., A. Ismail, M. A. Mahdi, M. S. Razalli, A. Alhawari, and B. K. Esfeh, "X-band miniaturized wideband bandpass filter utilizing multilayered microstrip hairpin resonator," *Progress In Electromagnetic Research*, Vol. 93, 177–188, 2009.

3. Hong, J.-S. and M. J. Lancaster, "Theory and experiment of novel microstrip slow-wave open-loop resonator filters," *IEEE Transaction on Microwave Theory and Techniques*, Vol. 45, No. 12, Dec. 1997.

4. Velazquez-Ahumada, M. D. C., J. Martel-Villagr, F. Mediana, and F. Mesa, "Application of stub loaded folded stepped impedance resonators to dual band filters," *Progress In Electromagnetic Research*, Vol. 102, 107–124, 2010.

5. Chiou, Y.-C., P.-S. Yang, J.-T. Kuo, and C.-Y. Wu, "Transmission zero design graph for dual-mode dual-band filter with periodic stepped-impedance ring resonator," *Progress In Electromagnetic Research*, Vol. 108, 23–36, 2010.

6. Hong, J.-S. and M. J. Lancaster, *Microstrip Filters for RF/Microwave Applications*, John Wiley & Sons, Inc, 2001.

7. Nosrati, M. and A. Najafi, "Bandwidth enhancement and further size reduction of a class of elliptic-function low-pass filter using modified hairpin resonators," *Progress In Electromagnetics Research C*, Vol. 5, 187–194, 2008.

8. Lum, K. M., C. Laohapensaeng, and C. E. Free, "A novel traveling-wave feed technique for circularly polarized planar antennas," *IEEE Micro. and Wireless Components Letters,* Vol 15, No. 3, 180–182, Mar. 2005.

9. Lum, K. M., T. Tick, C. Free, and H. Jantunen, "Design and measurement data for a microwave CP antenna using a new travelling-wave feed concept," *European Microwave Conf.*, Paris, France, Oct. 2005.

10. Lum, K. M. and C. Free, "A novel traveling-wave feed technique for circularly polarized planar microstrip antennas," *IEEE Antennas and Propag. International Symposium*, Vol. 2A, 250–253, Oct. 2005.

11. Lum, K. M. and C. E. Free, "A novel dual circularly polarized planar and multi-layer LTCC antenna arrays using traveling-wave feed system," *IEEE Trans. Micro. Theory Tech.*, Vol. 54, No. 6, 2880–2886, Jun. 2006.

12. Seow, C. K. and S. Y. Tan, "Non line of sight localization in multipath environment," *IEEE Trans. Mobile Computing*, Vol. 7, No. 5, 647–660, May 2008.

13. Seow, C. K. and S. Y. Tan, "Localization of omni-directional mobile device in multipath environments," *Progress In Electromagnetic Research*, Vol. 85, 323–348, 2008.

14. Seow, C. K. and S. Y. Tan, "Localisation of mobile device in multipath environment using bi-directional estimation," *Electronics Letters*, Vol. 44, No. 7, 485–487, Mar. 2008.

15. Seow, C. K. and S. Y. Tan, "Non-line-of-sight unidirectional mobile localisation in multipath environment," *Electronics Letters*, Vol. 44, No. 2, 141–142, Jan. 2008.

A Stepped Impedance Comb-line Filter Design Using Defective Ground Structure for Wireless Applications

Y. T. Lim and K. M. Lum

School of Science and Technology, SIM University, Singapore

Abstract— This paper presents a novel bandpass filter (BPF) design using stepped impedance comb-line resonator and defected ground structure (DGS) for S-band application. Two microstrip stepped impedance resonators (SIR) lay on the top conductor layer, are grounded using VIA hole. A $50\,\Omega$ microstrip line is connected to each resonator to act as the input and output feedlines respectively. DGS is widely and commonly exploited for its advantage of producing compact and simple design procedures, as well as mutual coupling between elements of the arrays. The proposed DGS is implemented by using a square-shaped capacitor represented by slots into the ground plane. The coupling effect of the slot to the microstrip stepped impedance resonators laid above it is further enhanced by adding stub and cavity structures around the border. Charges are accumulated within the slots which will in turn increases the effective capacitance of the microstrip resonators. The prototyped BPF is fabricated using FR4 substrate with a relative permeability of 4.7, loss tangent of 0.027 and thickness of 1.6 mm. The center frequency of the designed BPF is 3 GHz and the dimensional size is 2.56 cm by 2.56 cm. The measured best match for the BPF is obtained at 3.12 GHz with a S_{11} value of less than -35 dB. In the passband response, the corresponding S_{21} is approximately -4 dB with rejection rate at 10 dB/GHz. Both simulation and measurement results are presented and discussed for the proposed BPF.

1. INTRODUCTION

Microwave BPF are used in many radio frequency (RF)/microwave applications, it is also fundamentally the backbone component that contributes to the overall performance of various communication systems. As filters can be designed and fabricated on various materials, using the commonest standard; printed circuit technologies is most preferred since cost of manufacturing should be kept as low as possible.

Filters with microstrips acting as resonators should pay attention to space limitation, thus reducing design size is always the main challenge of such filter designs. Numerous researchers have proposed various configurations for reducing filter size yet improving filter performance. Some of the common filter configurations are using DGS, Step Impedance Resonator (SIR), hairpin resonator, ring resonator and short circuit stub [1]. Among diverse avenues of configurations of filter designs, DGS is widely and commonly exploited for its advantage of producing compact and simple design procedures, as well as mutual coupling between elements of the arrays [2]. In this paper, a BPF using SIR and unique DGS is presented. The proposed filter is smaller in size as compared to existing designs [3] and is particularly suitable for integration with multilayer transceiver antenna modules [4, 5] and localization applications [8–11].

2. BANDPASS FILTER DESIGN AND CONCEPT

Two microstrip SIR were arranged on the top conductor layer and grounded using a through VIA hole of diameter 0.5 mm. A microstrip feedline with characteristic impedance of $50\,\Omega$ is connected to each resonator. A square-shaped DGS is introduced by inserting slots into the ground plane. The slots are further modified by adding stubs and cavities structures. Charges are accumulated

Table 1: Design specifications of bandpass filter.

Key Parameters	Values
Center Frequency, f_o	3 GHz
Return Loss, S_{11}	< -10 dB
Insertion Loss, S_{21}	> 3 dB
Passband Bandwidth at -10 dB	500 MHz
Rejection	20 dB/GHz
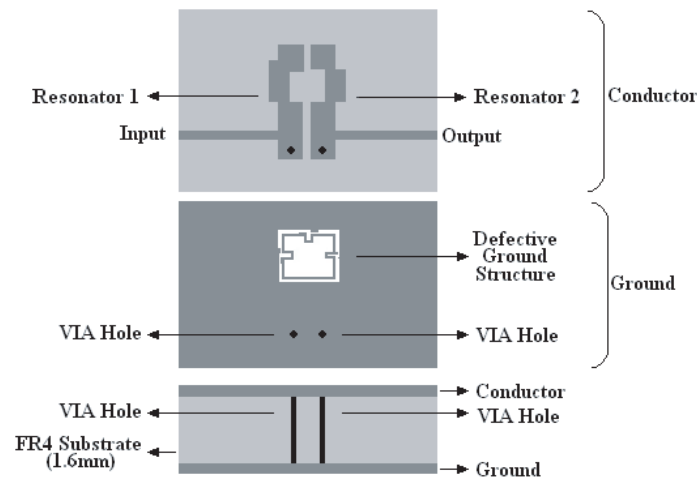
Figure 1: Design configuration of bandpass filter.

Notations	Value	Notations	Value
LB1	5.4 mm	WB4	1 mm
LB2	0.6 mm	WB5	2 mm
LB3	14.6	WB6	0.8 mm
LB4	1 mm	WB7	4.72 mm
LB5	1.2 mm	WB8	0.8 mm
LB6	0.8 mm	WB9	6 mm
LB7	0.6 mm	WB10	2.9 mm
LB8	14.2 mm	WB11	0.8 mm
LB9	6 mm	WB12	2 mm
WB1	9.8 mm	WB13	1.2 mm
WB2	10 mm	WB14	0.8 mm
WB3	0.4 mm	WB15	10 mm

Figure 2: Key dimensional data of DGS.

Notations	Value
L1	25.6 mm
L2	1.63 mm
L3	4.57 mm
L4	3 mm
L5	2 mm
L6	7.4 mm
L7	8.4 mm
L8	2.56 mm
L9	2.55 mm
L10	3.65 mm
L11	1.2 mm
W1	25.6 mm
W2	2.4 mm
W3	2.6 mm
W4	3 mm
W5	2.2 mm
W6	3.2 mm
W7	13.2 mm
W8	10 mm

Figure 3: Key dimensional data of top resonators.

within the modified slots which increase the effective capacitance of the microstrip line laid on the conductor layer.

Figure 1 and Table 1 detailed the design configuration and specification of the proposed 3 GHz BPF respectively. Figs. 2 and 3 present the key dimensional data of the DGS and top resonators.

3. SIMULATION AND MEASUREMENT RESULTS

Agilent Advanced Design System (ADS) was used to model the proposed BPF. Fig. 4 shows the simulated S_{11} and S_{21} results of the BPF. The best matched S_{11} is obtained at 3.14 GHz with a value of less than -40 dB. In the passband response, the corresponding S_{21} is approximately -0.5 dB with lower and upper rejection at 20 dB/GHz and 38 dB/GHz respectively. The proposed BPF was fabricated on FR4 substrate having a dielectric constant of 4.7 and thickness of 1.6 mm. Measurements were done using Network Analyzer.
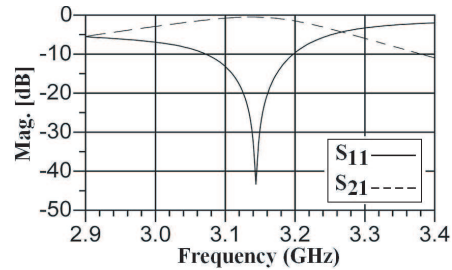
Figure 4: Simulated results of bandpass filter.

(a)   (b)
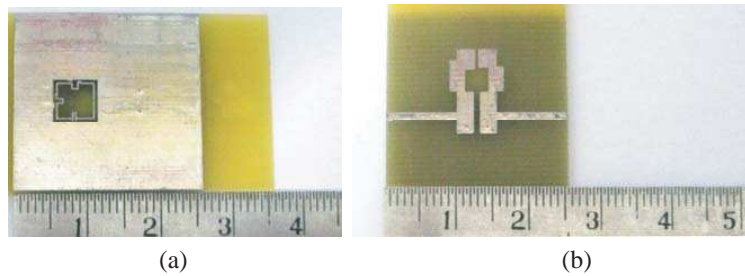
Figure 5: Fabricated bandpass filter. (a) DGS. (b) Top resonators.
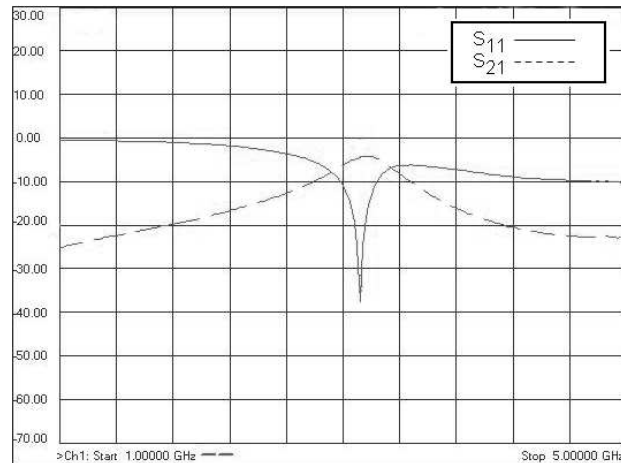
Figure 6: Measured S_{11} and S_{21} of bandpass filter.

Table 2: Comparison of simulation and measurement results.

Key Parameters	Simulation Results	Measurement Results
Center Frequency, f_o (GHz)	3.14	3.12
Return Loss, S_{11} (dB)	-43	-37
Insertion Loss, S_{21} (dB)	-0.5	-4
Lower Rejection dB/GHz	20	9
Upper Rejection dB/GHz	38	10

Figure 6 shows the measured results of the BPF. The best matched return loss is obtained at 3.12 GHz with a value of -37 dB. The insertion loss is -4 dB and lower and upper rejection are approximately 9 dB/GHz and 10 dB/GHz respectively. It is evident that the simulated and measured return loss is approximately similar. However, it can be observed that the simulated and measured passband insertion loss and rejection rates are degraded by about 3 dB and 20 dB respectively. The degradation could be attributed to the mis-alignment between the top resonators and DGS. Table 2 highlights the comparison between the simulation and measurement results.

4. CONCLUSION

A stepped impedance bandpass filter with unique DGS is proposed in this paper. The novel DGS comprises modified stubs and cavities structures. The 3 GHz BPF is validated through simulation and practical measurement. The proposed configuration seems particularly suitable for integration with multilayer transceiver antenna modules [3–6] and localization applications [7–10].

REFERENCES

1. Adam, H., A. Ismail, M. A. Mahdi, M. S. Razalli, A. R. H. Alhawari, and B. K. Esfeh, "X-band miniaturized wideband bandpass filter utilizing multilayered microstrip hairpin resonator," *Progress In Electromagnetic Research*, Vol 93, 177–188, 2009.
2. Zainud-Deen, S. H., M. E. S. Badr, E. Hassan, K. H. Awadalla, and H. A. Sharshar, "Microstrip antenna with defected ground plane structure as a sensor for landmines detection," *Progress In Electromagnetics Research B*, Vol. 4, 27–39, 2008.
3. Hong, J.-S. and M. J. Lancaster, *Microstrip Filters for RF/Microwave Applications*, John Wiley & Sons, Inc, 2001.
4. Lum, K. M., C. Laohapensaeng, and C. E. Free, "A novel traveling-wave feed technique for circularly polarized planar antennas," *IEEE Micro. and Wireless Components Letters,* Vol. 15, No. 3, 180–182, Mar. 2005.
5. Lum, K. M., T. Tick, C. Free, and H. Jantunen, "Design and measurement data for a microwave CP antenna using a new travelling-wave feed concept," *European Microwave Conf.*, Paris, France, Oct. 2005.
6. Lum, K. M. and C. Free, "A novel traveling-wave feed technique for circularly polarized planar microstrip antennas," *IEEE Antennas and Propag. International Symposium*, Vol. 2A, 250–253, Oct. 2005.
7. Lum, K. M. and C. E. Free, "A novel dual circularly polarized planar and multi-layer LTCC antenna arrays using traveling-wave feed system," *IEEE Trans. Micro. Theory Tech.,* Vol. 54, No. 6, 2880–2886, Jun. 2006.
8. Seow, C. K. and S. Y. Tan, "Non line of sight localization in multipath environment," *IEEE Trans. Mobile Computing*, Vol. 7, No. 5, 647–660, May 2008.
9. Seow, C. K. and S. Y. Tan, "Localization of omni-directional mobile device in multipath environments," *Progress In Electromagnetic Research*, Vol. 85, 323–348, 2008.
10. Seow, C. K. and S. Y. Tan, "Localisation of mobile device in multipath environment using bi-directional estimation," *Electronics Letters*, Vol. 44, No. 7, 485–487, Mar. 2008.
11. Seow, C. K. and S. Y. Tan, "Non-line-of-sight unidirectional mobile localization in multipath environment," *Electronics Letters*, Vol. 44, No. 2, 141–142, Jan. 2008.

Miniaturized Multilayered Bandpass Filter Using Microstrip Hairpin Resonator for C-band Application

C. Y. Wong and K. M. Lum

School of Science and Technology, SIM University, Singapore

Abstract— This paper presents a miniaturized multilayered bandpass filter (BPF) using U-shaped and W-shaped hairpin resonators. The proposed BPF consisted of five microstrip hairpin resonators arranged on two separate conductor layers and being placed by design to control the vertical and horizontal coupling effect in order to obtain the desired bandpass filter performance. Resonator 1, 2 and 3 are arranged on the top conductor layer of the substrate. Resonator 4 and 5 are buried between the first and second substrate with a 180 degree change in the orientation of the position. In addition, the buried U-shaped resonators are attached together which result in the implementation of a unique W-shape resonator structure. $50\,\Omega$ microstrip input and output feedlines are joined together with resonator 1 and 3 on the top conductor layer respectively. The proposed BPF is fabricated on two FR4 substrates with a dielectric constant of 4.7, loss tangent of 0.027 and thickness of $0.8\,\text{mm}$. Epoxy adhesive loss is used to laminate the two substrates collectively. The dimension of the prototyped BPF is $33\,\text{mm}$ by $21\,\text{mm}$. The best matching measured return loss S_{11} is observed at $5.18\,\text{GHz}$ with a value less than $-15\,\text{dB}$. The corresponding passband response S_{21} is approximately $-3\,\text{dB}$ with an upper and lower stopband attenuation of more than $10\,\text{dB/GHz}$. Both simulation and measurement results are presented and discussed.

1. INTRODUCTION

Communication technologies such as wireless and radar systems require high performances bandpass filters in microwave frequency spectrum. The usage of hairpin resonator filter in designs is becoming popular because of the ease of design and relatively eases of fabrication. Typically, hairpin resonators are modified from parallel coupled lines, where the half-wavelength resonator is bent into a U-shape pattern, thus making it more compact [1–3]. To suit the demands of compact modern wireless mobile communication, further reduction of the filter dimension is required by implementing multilayer substrates configuration. In addition, multilayer technique also improves the control of coupling coefficient by allowing gaps to be inserted between resonators positioned on different conductor layers. In this paper, the overall size of the proposed filter is smaller as compared with existing designs [4]. The filter seems particularly suitable for integration with multilayer transceiver antenna modules [5–8] and useful in designing pulse or waveform for mission critical applications such as indoor localization [9–12].

2. BANDPASS FILTER DESIGN AND CONCEPT

As illustrated in Fig. 1, the BPF comprises five hairpin resonators being separated into two conductor layers. The resonators are placed strategically to adjust the coupling effect in order to obtain the desired bandpass filter performance. Fig. 2 depicted the multilayer configuration of the proposed BPF. Resonator 1, 2 and 3 were arranged on the conductor layer 1. Resonator 4 and 5 were joined together to form a unique W-shaped pattern and was placed on conductor layer 2. A $50\,\Omega$ microstrip feed line is integrated with resonator 1 and 3 to create the input and output port.

The design specifications of the proposed BPF are detailed in Table 1.

Table 1: Design specifications.

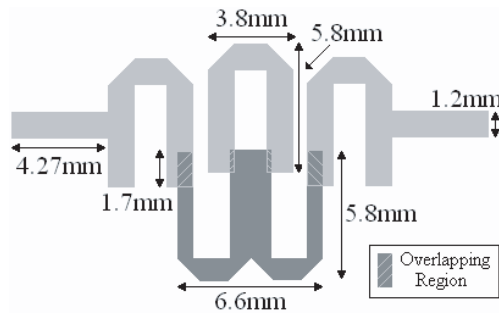| Parameters	Values
Center Frequency, f_o	$4\,\text{GHz}$
Return loss, S_{11}	$< -20\,\text{dB}$
Passband Insertion loss, S_{21}	$> -3\,\text{dB}$
Passband Bandwidth at $-10\,\text{dB}$	$500\,\text{MHz}$
Stopband Attenuation	$> 10\,\text{dB/GHz}$

Figure 1: Top view topology of proposed BPF and key dimensions.
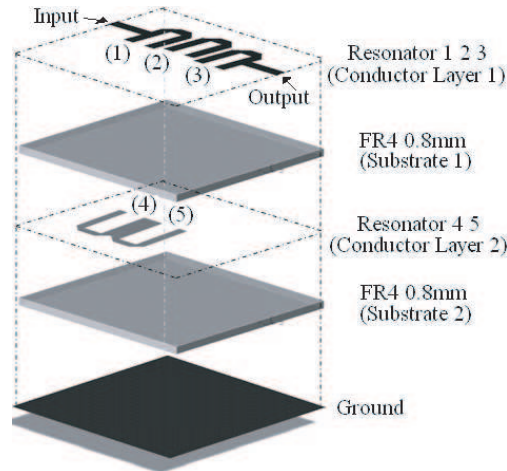

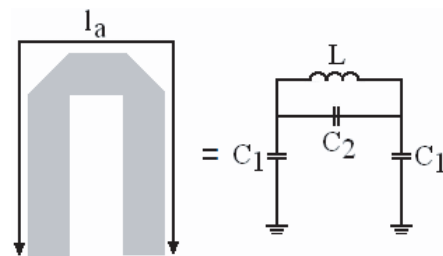Figure 2: Multilayer configuration of proposed BPF.

Figure 3: Equivalent π-network circuit of the conventional hairpin resonator.

The equivalent circuit of a conventional hairpin resonator is shown in Fig. 3. Using the following Equations (1)–(3), the value of components C_1, C_2 and L can be calculated. The equivalent circuit of the proposed BPF is presented in Fig. 4.

$$c_1 = \frac{1 - \cot(\beta_a l_a)}{\omega Z_o \sin(\beta_a l_a)} \tag{1}$$

$$L = \frac{Z_o \sin(\beta_a l_a)}{\omega} \tag{2}$$

$$c_2 = \frac{Z_e - Z_o}{2\omega Z_e Z_o \cot(\beta_c L_c)} \tag{3}$$

3. BANDPASS FILTER SIMULATED AND MEASURED RESULTS

The bandpass filter is simulated using Agilent Advanced Design System. As observed in Fig. 5 the simulated return loss S_{11} is best matched at 4.16 GHz with a value of -31.7 dB. The passband insertion loss S_{21} is about 0 dB. The lower and upper stopband attenuation is approximately 10 dB/GHz and 18 dB/GHz respectively.

Two FR4 substrates with dielectric constant of 4.7 and a thickness of 0.8 mm each, were used to prototyped the proposed BPF. The two substrates were attached together using a fine layer of epoxy adhesive, Nitto Denko double-coated adhesive tape (No. 500) with a thickness of 0.17 mm. The fabricated BPF is shown in Fig. 6 and measurement is done using network analyzer. The overall dimension is 33 mm by 21 mm.

The measured response of the BPF is presented in Fig. 7. The measured return loss S_{11} is below -10 dB from 5.09 GHz to 5.26 GHz. The best matching frequency is observed at 5.18 GHz with a S_{11} value of -17 dB. The passband insertion loss is -3 dB. Lower and upper attenuation is 17 dB/GHz and 12 dB/GHz respectively. A comparison is made between the modeled and practical results as detailed in Table 2.
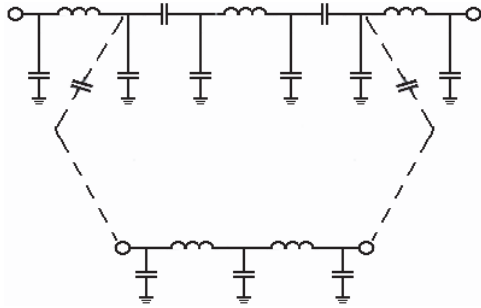
Figure 4: Equivalent circuit of proposed BPF.
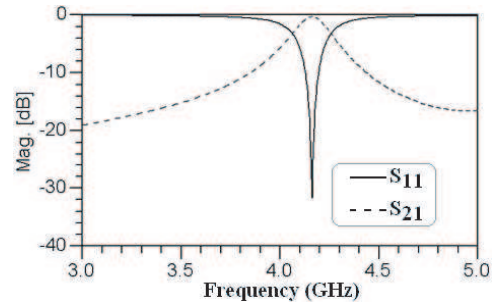
Figure 5: Simulated results of proposed bandpass filter.
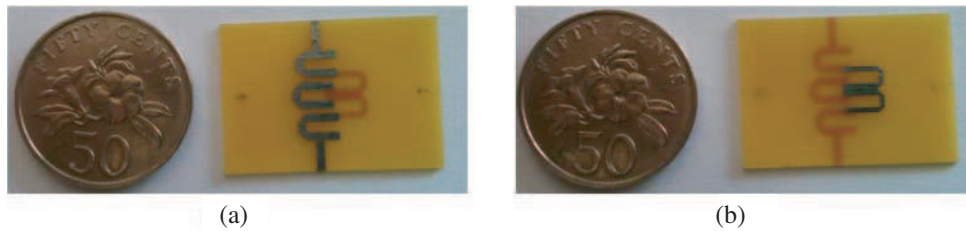
Figure 6: Fabricated proposed bandpass filter. (a) Resonator 1, 2 and 3. (b) Resonator 4 and 5.
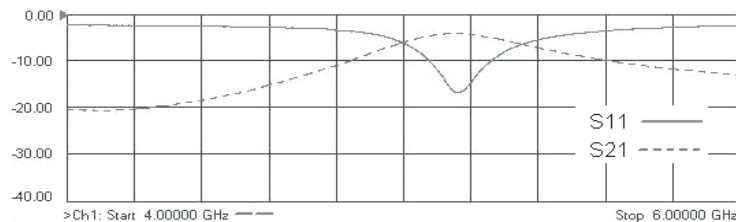
Figure 7: Measured results of proposed BPF.

Table 2: Comparison of simulated and measured results for bandpass filters.

Parameters	Simulated	Measurement
Operating Frequency, f_o (GHz)	4.16	5.18
Return loss, S_{11} (dB)	-31.7	-17
Passband Insertion loss, S_{21} (dB)	0	-3
Passband Bandwidth at -10 dB (MHz)	505	595
Lower Stopband Attenuation (dB/GHz)	10	17
Upper Stopband Attenuation (dB/GHz)	18	12

4. CONCLUSION

A multilayered hairpin bandpass filter operating at C-Band has been proposed and validated via simulation and measurement results. It is apparent that close resemble exists between the simulation and measurement results. The variance in the S-parameters response may be due to the mis-alignment between the resonators on conductor layer 1 and 2. The proposed configuration seems particularly suitable for integration with multilayer transceiver antenna modules [5–8] and localization applications [9–12].

REFERENCES

1. Sulaiman, A. A., M. H. Mokhtar, M. H. Jusoh, N. H. Baba, R. A. Awang, and M. F. Ain, "Simple multilayer hairpin bandpass filter," *European Journal of Scientific Research*, Vol. 42, No. 4, 604–613, 2010, ISSN 1450-216X.

2. Hong, J. S. and M. J. Lancaster, *Microstrip Filters for RF/Microwave Applications*, John Wiley & Sons, Inc., New York, 2001.

3. Hasan, A. and A. E. Nadeem, "Novel microstrip hairpinline narrowband bandpass filter using via ground holes," *Progress In Electromagnetics Research*, Vol. 78, 393–419, 2008.

4. Hong, J. S. and M. J. Lancaster, *Microstrip Filters for RF/Microwave Applications*, John Wiley & Sons, Inc., New York, 2001.

5. Lum, K. M. and C. E. Free, "A novel dual circularly polarized planar and multi-layer LTCC antenna arrays using traveling-wave feed system," *IEEE Trans. Micro. Theory Tech.,* Vol. 54, No. 6, 2880–2886, Jun. 2006.

6. Lum, K. M., T. Tick, C. Free, and H. Jantunen, "Design and measurement data for a microwave CP antenna using a new travelling-wave feed concept," *European Microwave Conf.*, Paris, France, Oct. 2005.

7. Lum, K. M. and C. Free, "A novel traveling-wave feed technique for circularly polarized planar microstrip antennas," *IEEE Antennas and Propag. International Symposium*, Vol. 2A, 250–253, Oct. 2005.

8. Lum, K. M., C. Laohapensaeng, and C. E. Free, "A novel traveling-wave feed technique for circularly polarized planar antennas," *IEEE Micro. and Wireless Components Letters,* Vol. 15, No. 3, 180–182, Mar. 2005.

9. Tai, C. S., S. Y. Tan, and C. K. Seow, "Robust non-line-of-sight localization system in indoor environment," *Electronics Letters*, Vol. 46, No. 8, 593–595, Apr. 2010.

10. Seow, C. K. and S. Y. Tan, "Localization of omni-directional mobile device in multipath environments," *Progress In Electromagnetic Research*, Vol. 85, 323–348, 2008.

11. Seow, C. K. and S. Y. Tan, "Localisation of mobile device in multipath environment using bi-directional estimation," *Electronics Letters*, Vol. 44, No. 7, 485–487, Mar. 2008.

12. Seow, C. K. and S. Y. Tan, "Non-line-of-sight unidirectional mobile localisation in multipath environment," *Electronics Letters*, Vol. 44, No. 2, 141–142, Jan. 2008.

Compact Lowpass Filter Design Using Cavity Resonator and Ladder-shaped Defected Ground Structure

K. X. Ng and K. M. Lum

School of Science and Technology, SIM University, Singapore

Abstract— A compact lowpass filter (LPF) design using cavity resonator and ladder-shaped defected ground structure (DGS) is presented in this paper. A cavity resonator is implemented on the top conductor layer with orthogonally oriented input and output feedlines for the proposed LPF filter. The cavity resonator has identical electrical function as of a square resonator. By proper design of the cavity structure, coupling coefficients and electrostatics parameters which influence the cutoff frequency can be controlled. The ladder-shaped DGS is etched on the ground plane directly beneath the $50\,\Omega$ input and output feedlines in order to manipulate the filter response. The DGS structure is effective for accurate transmission cutoff values, which ensure proper multiple spurious suppressions. The proposed LPF is prototyped using FR4 substrate with a dielectric constant of 4.7, loss tangent of 0.027 and thickness of 0.8 mm. The fabricated LPF has a compact dimensional size of 26 mm by 26 mm. The measured attenuation rate is 10 dB/GHz. Both simulation and measurement data are presented and discussed for the proposed LPF with and without the unique ladder-shaped DGS.

1. INTRODUCTION

In modern communication systems, high selective filter is usually required to prevent adjacent channel interference. The filter uses a full length resonator which results in the suppressing of spurious frequencies [1, 2]. The low pass filter (LPF) attenuates the frequencies that is higher than the cutoff frequency, but does not affect the characteristic of frequencies that are below cutoff frequency. Typically, full wavelength resonator will lead to degrading of the interference rejection as there will be several spurious responses at the center frequency. Lately defected ground structure (DGS) has been used in suppressing spurious response [3]. In certain situations, a few units of the DGS have to be used to achieve the desired results, causing the circuitry to be oversized. A ladder-shaped DGS design has been proposed in this paper. The proposed filter is relatively smaller as compared with existing designs [4] and configuration seems particularly suitable for integration with multilayer transceiver antenna modules [5–8] and localization applications [9–12].

2. LOWPASS FILTER DESIGN

As shown in Fig. 1, the proposed LPF includes a cavity resonator structure with orthogonally oriented $50\,\Omega$ input and output terminates on the top conductor layer. A ladder-shaped DGS is etched on the ground plate directly beneath the input and output feedlines. Table 1 describes the technical specification of the LPF. The prototyped LPF is fabricated using FR4 substrate with a dielectric constant of 4.8 and thickness of 0.8 mm.

3. CAVITY RESONATOR DESIGN

Cavity filters are structure with stairway topology located at the corner of a resonator. Generally, cavity resonator has identical electrical function as of a square-loop resonator. As illustrated in Fig. 2, a 1.8 mm by 1.8 mm cavity topology is introduced at position B and C respectively to improve the roll-off factor of the LPF response. The cavity structure at position A and D are used to vary the cutoff frequency value. The cutoff frequency is regulated by making fine adjustments of the steps size dimension or changing the steps count.

Table 1: Design specification of proposed lowpass filter.

Parameters	Value
Cutoff Frequency, f_o	2.4 GHz
Cutoff dB Level, S_{21}	> -20 dB
Rejection Rate	> 10 dB/GHz
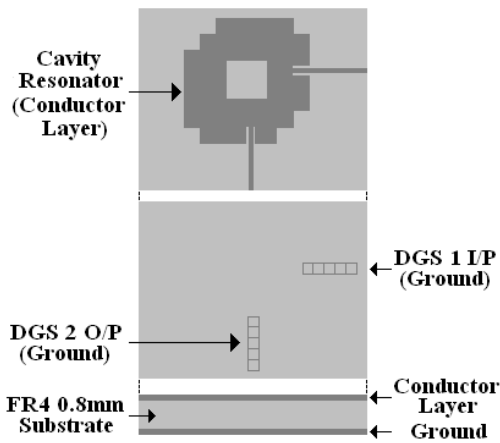
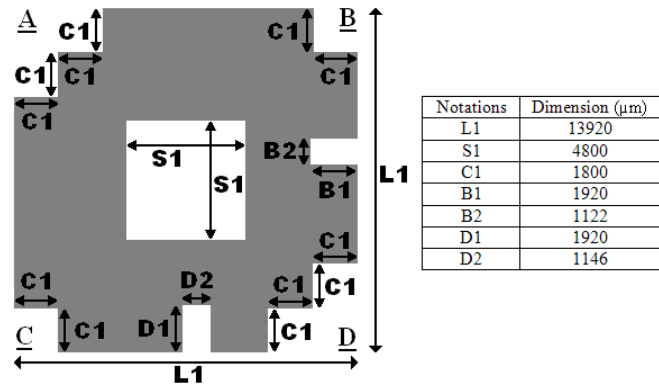Figure 1: Design configuration of proposed low-pass filter.

Notations	Dimension (µm)
L1	13920
S1	4800
C1	1800
B1	1920
B2	1122
D1	1920
D2	1146

Figure 2: Key dimensional data of cavity resonator.
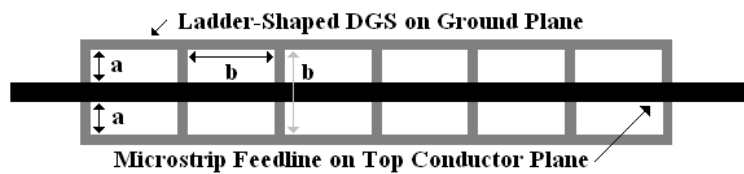
Figure 3: Arrangement of feedlines and DGS.

Notations	Dimension (µm)
L1	6600
L2	1200
L3	960
L4	120
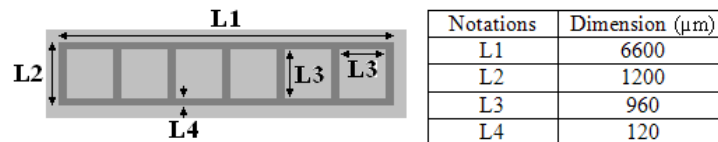
Figure 4: Key dimensional data of ladder-shaped DGS below input feedline.

Notations	Dimension (µm)
L1	7680
L2	1200
L3	960
L4	120
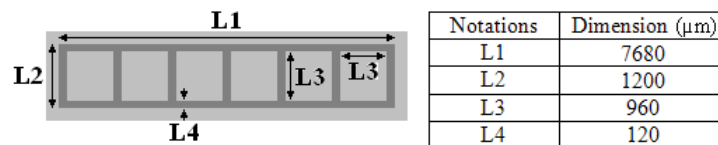
Figure 5: Key dimensional data of ladder-shaped DGS below output feedline.

4. LADDER-SHAPED DEFECTED GROUND STRUCTURE DESIGN

Defective ground structure (DGS) is slot opening situated on the ground plane. In most cases, the DGS is placed directly under microstrip transmission line and presents itself as a parallel resonance circuit. The introduction of DGS on the ground plane affects the current and permittivity characteristic of the transmission line above. DGS with different patterns, locations and dimensions will affect the equivalent L-C ratio, coupling coefficients and the related electrical parameters.

A ladder-shaped DGS is proposed in this paper. It is integrated with the stairway resonator as highlighted in Section 3 to offer suppression for unwanted harmonics. The unbiased DGS is etched off on the ground plane directly below the $50\,\Omega$ input and output feedlines. Fig. 3 illustrates the arrangement of the microstrip feedlines and the DGS. Figs. 4 and 5 detailed the dimensional data of the ladder-shaped DGS.

5. SIMULATED AND MEASURED RESULTS OF LOWPASS FILTER

To analyse the effectiveness of the proposed LPF, modelling is carried out using Agilent Advanced Design System (ADS). The simulation result of the LPF with and without DGS is shown on Fig. 6. The best matched return loss S_{11} with DGS is obtained at $0.88\,\text{GHz}$ with a value of $-54\,\text{dB}$. Attenuation response S_{21} is $12\,\text{dB/GHz}$ The lowest S_{11} without DGS is located at about $1\,\text{GHz}$ with
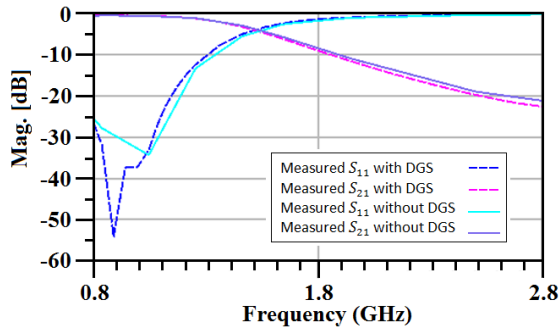
Figure 6: Simulated S_{11} and S_{21} response for lowpass filter with and without ladder-shaped DGS.
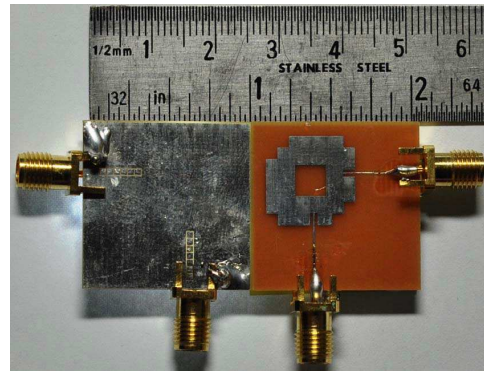
Figure 7: Fabricated lowpass filter (left) defected ground structure and (right) cavity resonator.
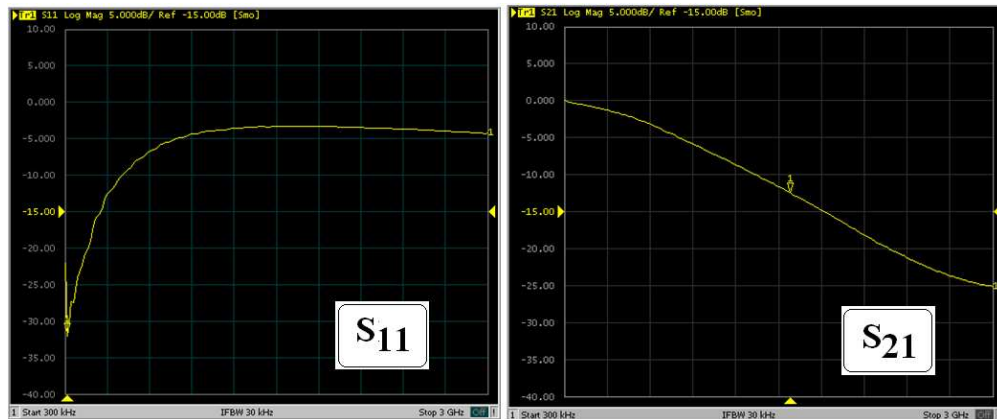
Figure 8: Measured S_{11} and S_{21} response for lowpass filter with ladder-shaped DGS.

a value of -34 dB. Attenuation response S_{21} is 10 dB/GHz. At cutoff frequency of 2.4 GHz, S_{21} is -20 dB. It is apparent that with the presence and the appropriate positioning of the ladder-shaped DGS, it will have a constructive effect on the filter response.

The fabricated LPF with ladder-shaped DGS is shown in Fig. 7. Measurement is done using Network Analyzer. As depicted in Fig. 8, the best matched return loss S_{11} is obtained at approximately 0.3 GHz with a reasonably good value of -32 dB. The measured S_{21} is about 10 dB/GHz. The cutoff level is -22 dB at 2.4 GHz.

6. CONCLUSION

In this paper, a lowpass filter with unique cavity resonator and ladder-shaped defected ground structure is proposed. Simulation and measurement data are presented and discussed. The best matched return loss is obtained at values below -30 dB and attenuation rate is about 10 dB/GHz. The proposed configuration seems particularly suitable for integration with multilayer transceiver antenna modules [5–8] and localization applications [9–12].

REFERENCES

1. Jenq, F. L., K. K. Chong, and L. Q. Zeng, "Overcoupled response improvement with miniaturing of rectangular dual-mode filter by slow-wave modified resonator," *Journal of Applied Sciences*, Vol. 9, No. 15, 2841–2846, 2009.

2. Singhal, P. K., "Compact narrow band non-degenerate dual-mode microstrip filter with etched square lattices," *Journal of Electromagnetic Analysis and Applications*, Feb. 2010.

3. Moyra, T., S. K. Parui, and S. Das, "Design of a quasi-elliptic lowpass filter using a new defected ground structure and capacitively loaded microstrip line," *International Journal on Electrical Engineering and Informatics*, Vol. 3, No. 1, 61–73, 2011.

4. Hong, J.-S. and M. J. Lancaster, *Microstrip Filters for RF/Microwave Applications*, John Wiley & Sons, Inc, 2001.

5. Lum, K. M. and C. E. Free, "A novel dual circularly polarized planar and multi-layer LTCC antenna arrays using traveling-wave feed system," *IEEE Trans. Micro. Theory Tech.*, Vol. 54, No. 6, 2880–2886, Jun. 2006.

6. Lum, K. M. and C. Free, "A novel traveling-wave feed technique for circularly polarized planar microstrip antennas," *IEEE Antennas and Propag. International Symposium*, Vol. 2A, 250–253, Oct. 2005.

7. Lum, K. M., T. Tick, C. Free, and H. Jantunen, "Design and measurement data for a microwave CP antenna using a new travelling-wave feed concept," *European Microwave Conf.*, Paris, France, Oct. 2005.

8. Lum, K. M., C. Laohapensaeng, and C. E. Free, "A novel traveling-wave feed technique for circularly polarized planar antennas," *IEEE Micro. and Wireless Components Letters*, Vol. 15, No. 3, 180–182, Mar. 2005.

9. Tai, C. S., S. Y. Tan, and C. K. Seow, "Robust non-line-of-sight localization system in indoor environment," *Electronics Letters*, Vol. 46, No. 8, 593–595, Apr. 2010.

10. Seow, C. K. and S. Y. Tan, "Localisation of mobile device in multipath environment using bi-directional estimation," *Electronics Letters*, Vol. 44, No. 7, 485–487, Mar. 2008.

11. Seow, C. K. and S. Y. Tan, "Localization of omni-directional mobile device in multipath environments," *Progress In Electromagnetic Research*, Vol. 85, 323–348, 2008.

12. Seow, C. K. and S. Y. Tan, "Non-line-of-sight unidirectional mobile localisation in multipath environment," *Electronics Letters*, Vol. 44, No. 2, 141–142, Jan. 2008.

A Novel Bandpass Filter Design Using E-shaped Resonator and Dual Square-loop Defected Ground Structure

P. L. Lim and K. M. Lum

School of Science and Technology, SIM University, Singapore

Abstract— This paper presents a bandpass filter (BPF) using two E-shaped microstrip resonators and a dual open square-loop defected ground structure (DGS). The proposed novel DGS structure is realized by implementing two opened square loop topologies on the ground plane. The etched DGS structure interferes with the shield current distribution in the ground plane which affects the characteristics of the two E-shaped resonators laid above it. This disturbance creates beneficial capacitance and inductance effect on the filter design, which results in the desired filter response. Two E-shaped resonators are laid on the top conductor layer. The behavior of the E-shaped resonators can be represented using even and odd mode analysis. For odd mode analysis, an electric wall is inserted between the two E-shaped resonators to enable a quasi quarter wavelength to be extracted. In the case of even mode analysis, a magnetic wall is added in between the two E-shaped resonators. Thus the resonators can be associated with a folded quasi half-wave resonator. By manipulating the E-shaped resonator and dual open square-loop DGS design, the desired BPF response can be achieved. The proposed BPF is fabricated on FR4 substrate with a relative permittivity of 4.7 and thickness of 0.8 mm. The center frequency is 2.4 GHz and the dimensions of the prototyped BPF are 12.41 mm by 13.70 mm. The best matching return loss S_{11} response is obtained at 2.2 GHz with a value less than -10 dB. The corresponding insertion loss S_{21} is -2.2 dB. The lower and upper stopband attenuation is 10 dB/GHz and 15 dB/GHz respectively. Both simulation and measurement results are presented and discussed for the proposed BPF.

1. INTRODUCTION

Research in defected ground structure (DGS) has been highly prominent in radio frequency/microwave circuits, as it aids in the development of a compact circuitry and spurious response suppression. DGS is realized by etching a defected pattern in the ground plane, this etched pattern interfers with the shield current distribution in the ground plane which affects the characteristics of the transmission line. This disturbance creates beneficial capacitance and inductance effect on the structure, which results in a stopband and slow wave effect [1, 2].

Another area of concern is to fabricate a filter which is compact in size and comes in lighter weight. Usage of microstrip line would be the perfered choice, reason being the ease of fabrication by photolithographic processes and comes in a low cost. It is one of the most popular type of planar transmission lines which is easily integrated with passive and active microwave devices. It enables miniturization of circuitry with improved performance. Two E-shaped microstrip resonators and a novel dual open square-loop DGS structure are proposed in this paper to achieve a bandpass responses. The E-shaped resonators are jointed to a 50 ohm microstrip line to construct the input and output ports respectively [3–5].

2. BANDPASS FILTER DESIGN AND CONCEPT

Design specifications of the proposed bandpass filter (BPF) are highlighted in Table 1. Fig. 1 illustrates the design configuration of the proposed BPF. Two E-shaped microstrip resonators are laid on the top conductor layer and a dual open square-loop DGS is etched on the bottom ground

Table 1: Design specification of proposed bandpass filter.

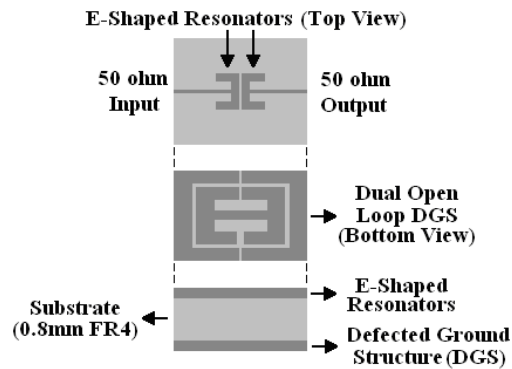| Parameters	Values
Center Frequency	2.4 GHz
Return Loss, S_{11}	< -10 dB
Passband Insertion Loss, S_{21}	> -3 dB
Stopband Attenuation	> 10 dB/GHz

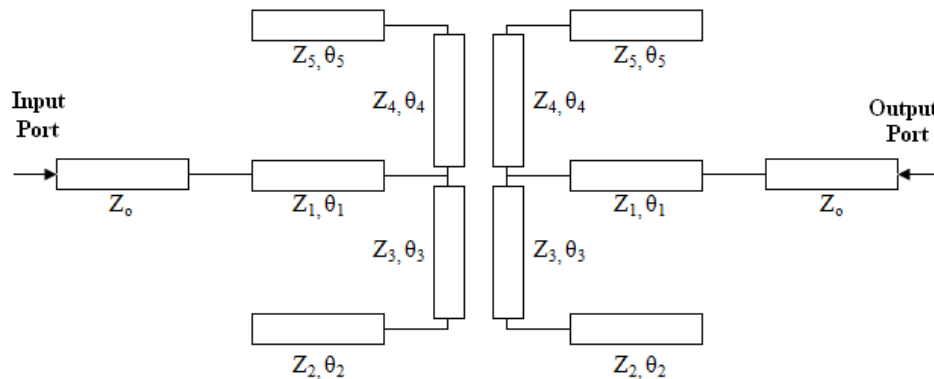Figure 1: Configuration of proposed bandpass filter.

Figure 2: Equivalent circuit of E-shaped resonators on top conductor layer.

Table 2: Characteristic impedance of even and odd mode of E-shaped microstrip resonators.

J	$(Zo_e)_{jj+1}$	$(Zo_o)_{jj+1}$
0	0.068	0.023
1	0.089	0.032
2	0.068	0.023

layer of the substrate. FR4 is used as the substrate which has a thickness of 0.8 mm and dielectric constant of 4.7.

$$(Z_{0e})_{j,j+1} = \frac{1}{Y_0} \left[1 + \frac{j_{j,j+1}}{Y_0} \right] \quad \text{for} \quad j = 0 \quad \text{to} \quad n \tag{1}$$

$$(Z_{0o})_{j,j+1} = \frac{1}{Y_0} \left[1 + \frac{j_{j,j+1}}{Y_0} \right] \quad \text{for} \quad j = 0 \quad \text{to} \quad n \tag{2}$$

$$\frac{w}{h} = \frac{8e^A}{e^{2A} - 2} \tag{3}$$

$$A = \frac{Z_o}{60} \left(\frac{\varepsilon_r + 1}{2} \right)^{0.5} + \frac{\varepsilon_r - 1}{\varepsilon_r + 1} \left(0.23 + \frac{0.11}{\varepsilon_r} \right) \tag{4}$$

Characteristic impedance of the even and odd mode of the E-shaped microstrip resonators are tabulated from Equations (1), (2) and results are tabulated in Table 2. The physical dimensions of the top resonators are theoretically determined from Equations (3), (4) as proposed by Harold A. Wheeler and Hammerstad [6–8]. Fig. 2 shows the equivalent circuit of the E-shaped resonators.

Figure 3 presents the layout of the proposed BPF. The top conductor layer shows the E-shaped microstrip resonators connected to the input and output microstrip feedline. The characteristic impedance Z_o of the feedline is 50 ohm. The gap between the two E-shaped resonators is used for
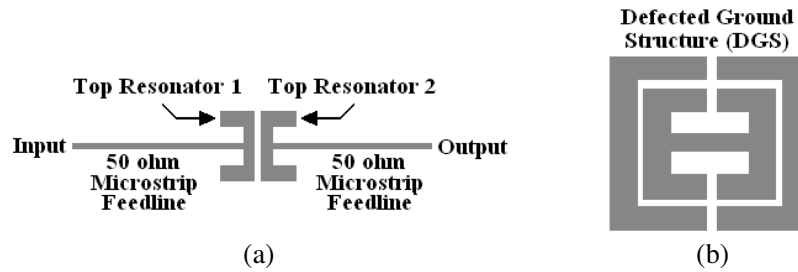
Figure 3: Layout of proposed bandpass filter. (a) Top conductor layer. (b) Bottom ground layer.

Notations	Dimensions (mm)
LR1=LR11	1.835
LR2=LR10	0.550
LR3=LR9	6.176
LR4=LR8	1.248
LR5=LR7	0.625
LR6	0.212

Figure 4: Key dimensional data of top resonator 1 and 2.

Notations	Dimensions (mm)
LB1	13.700
LB2	6.685
LB3	4.735
LB4	4.485
LB5	3.185
LB6	6.700
LB7=LB10	1.950
LB8=LB9	1.300
LB11	7.809
LB12	8.509
LB13	12.410
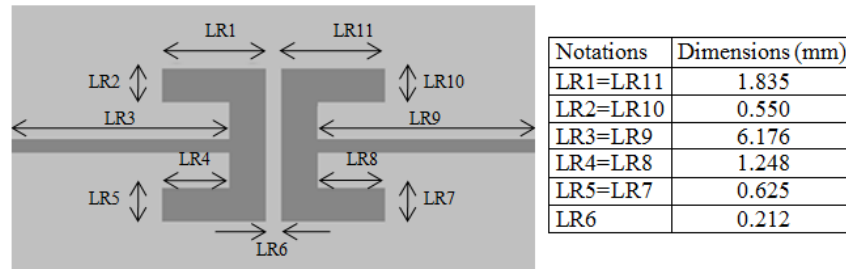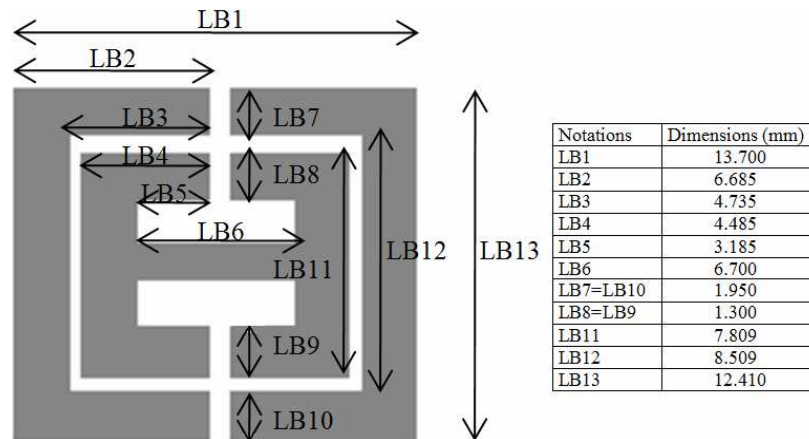
Figure 5: Key dimensional data of DGS.

appropriate coupling effects. The bottom layer shows the dual open square-loop DGS structure.

Figures 4 and 5 present the key dimensional data of top resonators and bottom DGS respectively. The effect of varying the feed line LR3 and LR9 of the top E-shaped resonators create a wider or narrower passband response. In addition, the effect of varying stub length LR2 and LR5 increases or decreases the center frequency. A dual open square-loop DGS creates a passband response.

3. BANDPASS FILTER SIMULATION AND MEASUREMENT RESULT

Figure 6 shows the simulated S-parameters of the proposed BPF. Simulation is done using Agilent Advanced Design System (ADS) software. The best matched S_{11} is approximately $-11\,\text{dB}$ and the corresponding stopband insertion loss S_{21} is about $-2.5\,\text{dB}$. The lower and upper stopband attenuation is around $10\,\text{dB/GHz}$ and $15\,\text{dB/GHz}$ respectively.

The fabricated BPF are shown in Fig. 7. The overall size is $13.70\,\text{mm}$ by $12.41\,\text{mm}$. Simulated and measured S-parameter results are presented in Fig. 8 and a comparison is tabulated in Table 3. The measured center frequency is closed to the simulated result with a return loss S_{11} value of less than $-10\,\text{dB}$. The corresponding passband insertion loss S_{21} is above $-2\,\text{dB}$. The lower and upper stopband attenuation are $10\,\text{dB/GHz}$ and $15\,\text{dB/GHz}$ respectively. It is apparent that the simulation and measurement results exhibit a close resemble. The slight difference in the results may be due to the losses attributed by the mis-alignment between the E-shaped resonators on the top conductor layer and DGS on the bottom ground layer.
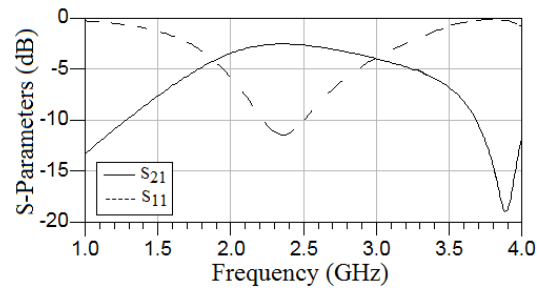
Figure 6: Simulated S-parameters of proposed BPF.
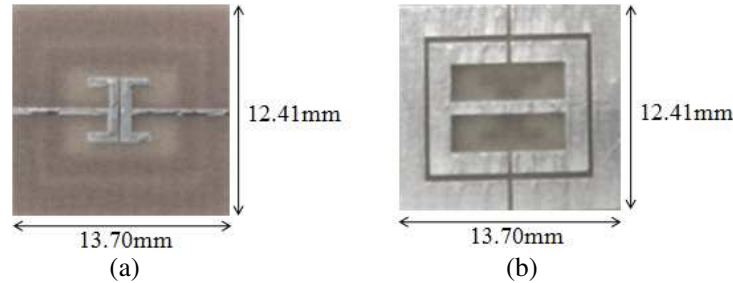
Figure 7: Fabricated BPF. (a) E-shaped resonators on top conductor layer. (b) DGS on bottom ground layer.
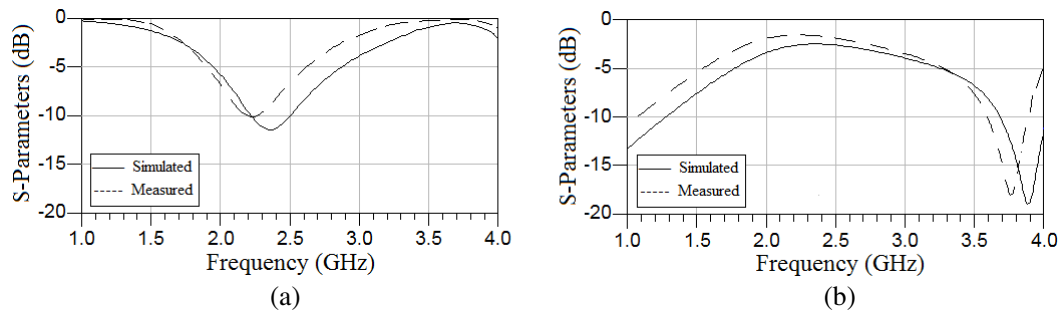
Figure 8: Simulated and measured S-parameters of BPF. (a) S_{11}. (b) S_{21}.

Table 3: Comparison of simulated and measured results of BPF.

Parameters	Simulation	Measurement
Center Frequency (GHz)	2.352	2.230
Return Loss (dB), S_{11}	-11.475	-10.115
Passband Insertion Loss, S_{21}	-2.590	-2.250
Lower Stopband Attenuation	10 dB/GHz	10 dB/GHz
Upper Stopband Attenuation	15 dB/GHz	15 dB/GHz

4. CONCLUSION

A second-order chebyshev bandpass filter using two E-shaped resonators and a dual open square-loop defected ground structure has been presented in this paper. The proposed topology presents a compact circuitry which has the flexibility of achieving a wide or narrow passband response. The bandpass filter response is validated through fabrication and practical measurements. Measured return loss and insertion loss responses are in fairly good agreement with the simulation results. Further improvement can be achieved with better fabrication technique of ensuring high alignment accuracy between the resonators on the top conductor layer and defected ground structure on the bottom ground layer. The proposed configuration seems particularly suitable for integration with

multilayer transceiver antenna modules [9–12] and localization applications [13–16].

REFERENCES

1. Ahn, D., J.-S. Park, C.-S. Kim, J. Kim, Y. Qian, and T. Otoh, "A design of the low-pass filter using the novel microstrip defected ground structure," *IEEE Trans. Microwave Theory Tech.*, Vol. 49, No. 1, 86–93, Jan. 2001.

2. Ting, S.-W., K.-W. Tam, and R. P. Martins, "Miniaturized microstrip lowpass filter with wide stopband using double equilateral U-shaped defected ground structure," *IEEE Microw. Wireless Compon. Lett.*, Vol. 16, No. 5, 240–242, May 2006.

3. Wei, C.-L., B.-F. Jia, Z.-J. Zhu, and M.-C. Tang, "Design of different selectivity dual-mode filters with E-shaped resonator," *Progress In Electromagnetics Research*, Vol. 116, 517–532, 2011.

4. Wu, Y.-L., C. Liao, and X.-Z. Xiong, "A dual-wideband bandpass filter based on E-shaped microstrip SIR with improved upper-stopband performance," *Progress In Electromagnetics Research*, Vol. 108, 141–153, 2010.

5. Hong, J.-S. and M. J. Lancaster, "Theory and experiment of novel microstrip slow-wave open-loop resonator filters," *IEEE Trans. Microwave Theory Tech.*, Vol. 45, No. 12, 2358–2365, Dec. 1997.

6. Matthaei, L. Y. and E. M. T. Jones, *Microwave Filters, Impedance-matching Networks, and Coupling Structures*, Artech House, Boston, MA, 1980.

7. Wheeler, H., "Transmission line properties of parallel strips separated by a dielectric sheet," *IEEE Trans. MTT*, Vol. 13, 172–185, 1965.

8. Hammerstad, E. O., "Equations for microstrip circuit design," *Proceedings of the European Microwave Conference*, 268–272, Hamburg, Germany, 1975.

9. Lum, K. M., C. Laohapensaeng, and C. E. Free, 'A novel traveling-wave feed technique for circularly polarized planar antennas," *IEEE Micro. and Wireless Components Letters*, Vol. 15, No. 3, 180–182, Mar. 2005.

10. Lum, K. M., T. Tick, C. Free, and H. Jantunen, "Design and measurement data for a microwave CP antenna using a new travelling-wave feed concept," *European Microwave Conf.*, Paris, France, Oct. 2005.

11. Lum, K. M. and C. Free, "A novel traveling-wave feed technique for circularly polarized planar microstrip antennas," *IEEE Antennas and Propag. International Symposium*, Vol. 2A, 250–253, Oct. 2005.

12. Lum, K. M. and C. E. Free, "A novel dual circularly polarized planar and multi-layer LTCC antenna arrays using traveling-wave feed system," *IEEE Trans. Micro. Theory Tech.*, Vol. 54, No. 6, 2880–2886, Jun. 2006.

13. Seow, C. K. and S. Y. Tan, "Non line of sight localization in multipath environment," *IEEE Trans. Mobile Computing*, Vol. 7, No. 5, 647–660, May 2008.

14. Seow, C. K. and S. Y. Tan, "Localization of omni-directional mobile device in multipath environments," *Progress In Electromagnetic Research*, Vol. 85, 323–348, 2008.

15. Seow, C. K. and S. Y. Tan, "Localisation of mobile device in multipath environment using bi-directional estimation," *Electronics Letters*, Vol. 44, No. 7, 485–487, Mar. 2008.

16. Seow, C. K. and S. Y. Tan, "Non-line-of-sight unidirectional mobile localisation in multipath environment," *Electronics Letters*, Vol. 44, No. 2, 141–142, Jan. 2008.

Study on New Ultrasonic Positioning and Movement Detection Installed in Sensor Network

Mitsutaka Hikita, **Akira Nakano, and Natsuki Tobita**

Faculty of Global Engineering, Kogakuin University, Shinjuku-Ku, Tokyo 163-8677, Japan

Abstract— Sensor network which connects many sensors via small-scale private wireless network such as ZigBee has been researched all over the world. This system consists of many sensors (sensor nodes) which measure environmental parameters such as temperature, humidity, brightness etc. and one controller (center node) which processes the data gathered from all sensor nodes via wireless communications medium. In near future, the sensor network will provide home/office-circumstance monitoring functions such as taking care of old people, preventing crime and maintaining security. Therefore, it is necessary for the system to install not only sensing functions for temperature, humidity etc. but also those for distance measurement and movement detection. In this paper, we will present new method for distance measurement and movement detection.

1. INTRODUCTION

Cellular-phone systems have spread all over the world and their technologies continue to be developed during the first half of the twenty-first century. On the other hand outstanding technical innovations have been observed in a sensor area. A new concept called "Sensor Network" has been proposed recently by combining sensor technologies together with such mobile communications system as cellular-phone, radio LAN and Bluetooth [1, 2]. Sensing signals from many sensor nodes distributed in a certain area such as home, office and public places are collected to a center node by the technology similar to that used in mobile communications. Sensor network enables home/office circumstance control, environment monitoring and protection based on the collected data. It is also thought to have a big impact on our lives and to grow to be a giant industry like the cellular-phone systems in the future. In our laboratory, we have been studying the sensor network to achieve comfortable living circumstances by home/office sensing and control.

We have proposed an accurate novel ultrasonic positioning method and based on it invented a new movement detection technique which can be installed in sensor network. Sensor nodes require long-term operation with extremely low-power supply, such as several-year operation with a single battery. However, such conventional accurate ultrasonic measurement methods as a code-division method [3] and a chirp-signal method [4] require complicated and heavy signal processing procedures for both the transmitter and receiver. Therefore, their devices cannot be included in sensor nodes due to the power consumption. Our proposed method can provide not only the low-power consumption but also removal of the complicated signal processing procedures, which overcomes the limitation for devices used in sensor nodes.

Ultrasonic continuous waves (CWs) at discrete frequencies within the transducer bandwidth which correspond to those of the Inverse Fast Fourier Transform (IFFT) procedure are transmitted [5]. Based on the relative amplitudes and phases between the received and transmitted CWs, the impulse response can be calculated in the center node, which can provide accurate distance information without any sophisticated procedures such as the pulse compression or the correlation between the received and replica signals [3, 4]. If we subtract the impulse responses at present from those at the preceding time, we can obtain the change of distances between objects and nodes at two different points in time. By this procedure, we can exclude effects of inactive objects and can emphasize only moving objects [6]. Therefore as shown in Fig. 1 the sensor network, ZigBee [7] in this case, which includes our positioning and movement detection devices will possibly be applied not only to home/office monitoring but also to care for old people, prevention of crime and watch in hospitals. In this paper, both theoretical investigation and experimental results will be presented.

2. THEORETICAL INVESTIGATION FOR DISTANCE MEASUREMENT

Figure 2's simple model which consists of a transmitter and a receiver is considered. In general, ultrasonic transducers have frequency bandwidth from f_1 to f_2 and single-peaked characteristics. We divide this bandwidth into $n + 1$ of discrete frequencies, i.e., $f(1) = f_1$, $f(2) = f_1 + (f_2 - f_1)/n, \ldots, f(n + 1) = f_2$. These frequencies also correspond to discrete frequencies of
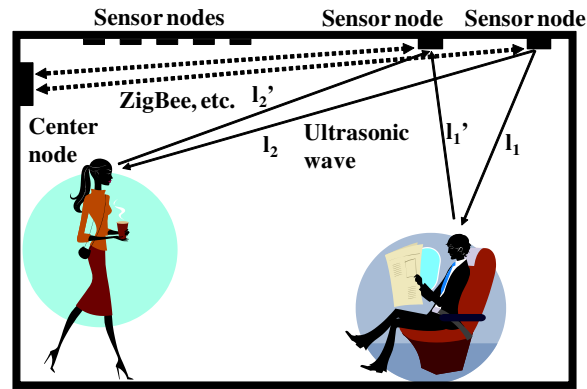
Figure 1: Example of sensor network installing ultrasonic positioning and detection.
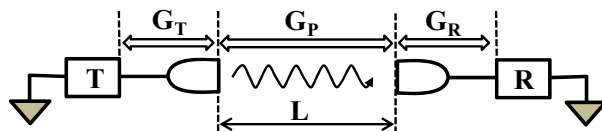

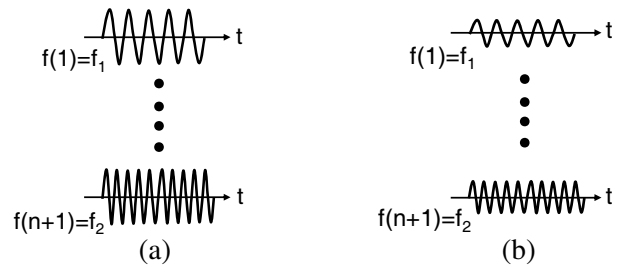Figure 2: Basic measurement system with transmitter and receiver transducers.

Figure 3: Ultrasonic continuous waves at $n+1$ discrete frequencies. (a) Transmitted CWs. (b) Received CWs.
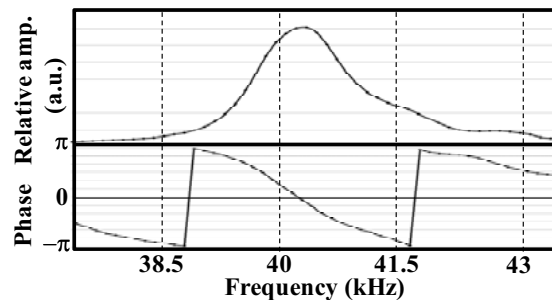

Figure 4: Amplitude and phase characteristics of transmitter/receiver transducers, $G_T(\omega) \cdot G_R(\omega)$.

IFFT procedure. The CWs at these frequencies are transmitted as shown in Fig. 3(a). Relative amplitudes and phases of the received CWs (Fig. 3(b)) to the transmitted CWs are measured and stored, which corresponds to the transfer function $G(\omega) = G_T(\omega) \cdot G_P(\omega) \cdot G_R(\omega)$. IFFT results of $G(\omega)$ can provide an impulse response between the transmitter and the receiver. However, we have found that $G_T(\omega) \cdot G_R(\omega)$ caused by the transmitter and receiver transducer characteristics has significant effect on the impulse response.

Measured amplitude/phase characteristics of $G_T(\omega) \cdot G_R(\omega)$, i.e., $L = 0$ in Fig. 2, for general 40kHz transducers are shown in Fig. 4. In the figure, a frequency division is $\Delta f = 0.125\,\text{kHz}$. The amplitude bandwidth is about 5% and the phase has inclined and distorted characteristics. The impulse response calculated by IFFT procedure based on Fig. 4's data is shown in Fig. 5(a), which reveals that time delay equivalent to about 10 cm is generated in the transmitter/receiver transducers. This delay is caused by the energy storage effect of a transducer, because most ultrasonic transducers consist of piezoelectric vibrators and their vibration inertia is very large. Using the relations of $G_T(\omega) = |G_T(\omega)| \cdot \exp(j\theta_T)$ and $G_R(\omega) = |G_R(\omega)| \cdot \exp(j\theta_R)$, we compensate phase characteristics of $G_T(\omega) \cdot G_R(\omega)$ by multiplying $\exp\{-j(\theta_T + \theta_R)\}$. Results of IFFT for the compensated values are shown in Fig. 5(b), which achieves an ideal symmetrical impulse response with peak at 0 cm.

3. EXPERIMENT TO CONFIRM PROPOSED METHOD

In the experiment to verify our proposal, we arranged the transmitter and the receiver exactly 50 cm apart to each other. Relative amplitudes and phases are measured with same frequency division of $\Delta f = 0.125$ kHz, which corresponds to the maximum measurable distance is about 270 cm [5]. Characteristics of phase-compensated transfer function between the transmitter and the receiver, $G(\omega) \cdot \exp\{-j(\theta_T + \theta_R)\} = |G_T(\omega)| \cdot G_P(\omega) \cdot |G_R(\omega)|$, are shown in Fig. 6. Results of IFFT for Fig. 6's data are shown in Fig. 7(a). A magnified view near the center of the impulse response is shown in Fig. 7(b). An error between the peak of the impulse response and the distance of 50 cm is less than 1 mm, which is about ten-percent of the ultrasonic wavelength at 40 kHz [6].

(a)

(b)
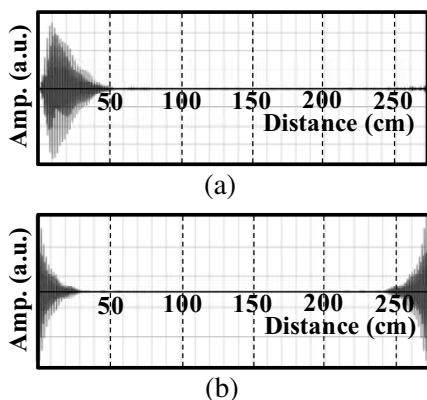
Figure 5: IFFT results for $G_T(\omega) \cdot G_R(\omega)$. (a) Impulse response without phase compensation. (b) Impulse response with phase compensation.
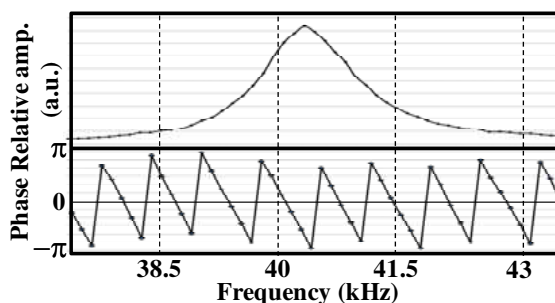
Figure 6: Measured amplitude and compensated-phase characteristics between transmitter and receiver transducers, $|G_T(\omega)| \cdot G_P(\omega) \cdot |G_R(\omega)|$, with $L = 50$ cm.

(a)

(b)
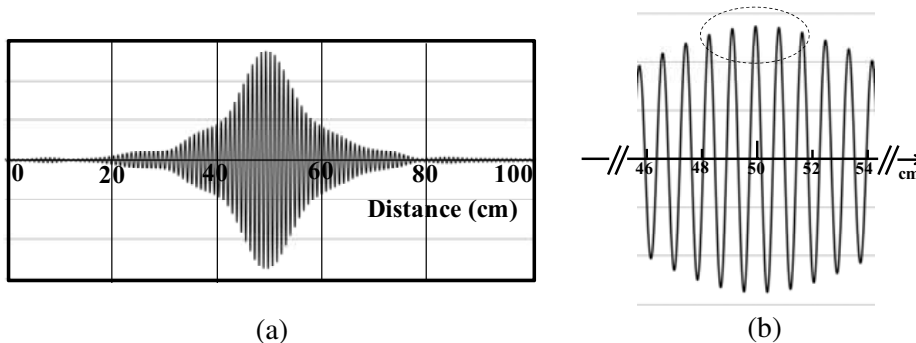
Figure 7: IFFT results for Fig. 6's $|G_T(\omega)| \cdot G_P(\omega) \cdot |G_R(\omega)|$. (a) Impulse response. (b) Magnified view at center of impulse response.

(1): 4.8 m
(2): 4.9 m
(3): 5.05 m
(4): 5.2 m
(5): 5.35 m
(1'): 5.5 m
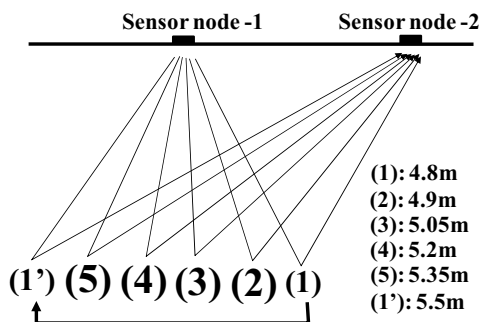
Figure 8: Simulation model with moving object from position (1) to (1').

4. SIMULATION RESULTS FOR DETECTION OF MOVEMENT

If we introduce the proposed method to sensor network as shown in Fig. 1, the impulse responses between transmitters and receivers (sensor nodes) include distance information from nodes to objects. However there are many reflecting objects, which reveals that exact distances between them and nodes cannot be obtained. If we subtract the impulse responses at present from those at the preceding time, we can obtain the change of distances between objects and nodes at two different points in time. By this procedure, we can exclude effects of inactive objects and can emphasize only moving objects.

A simulation model is shown in Fig. 8, where one object at the position (1) with 4.8 m distance moves to the position (1') with 5.5 m distance. There are other 4 reflecting objects in this model. The simulated impulse responses at the positions with 4.8–5.5 m distances are shown in Figs. 9(a)–(h). Subtracting to each other between two impulse responses at two different points in time clearly illustrates movement of the object as shown in Figs. 10(a)–(g).
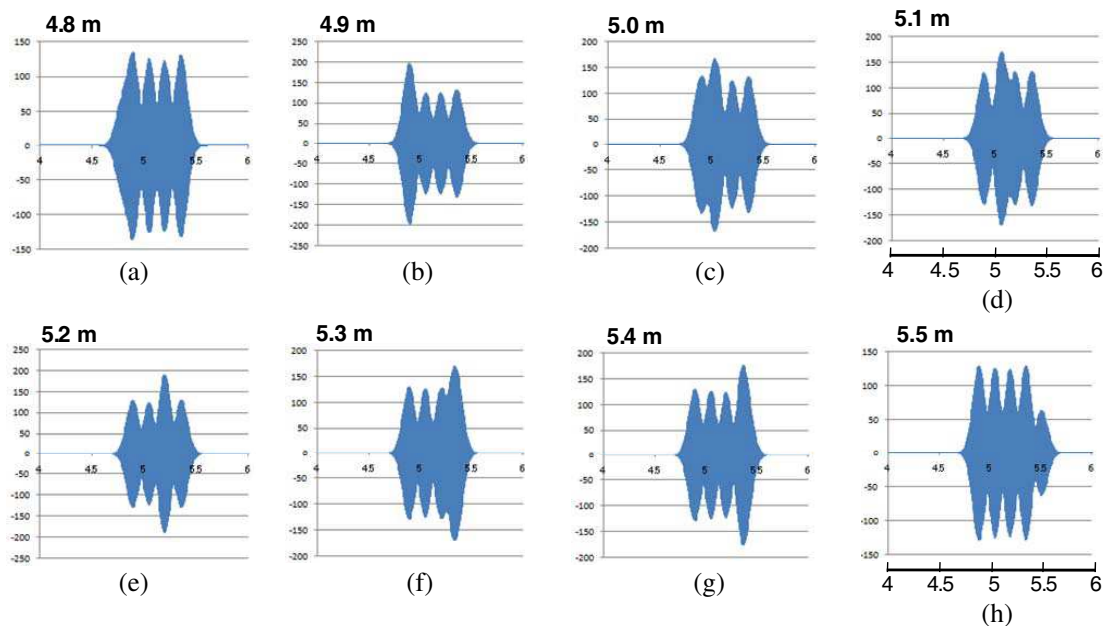
Figure 9: Impulse response for moving object with distances from (a) 4.4 m to (h) 5.5 m.
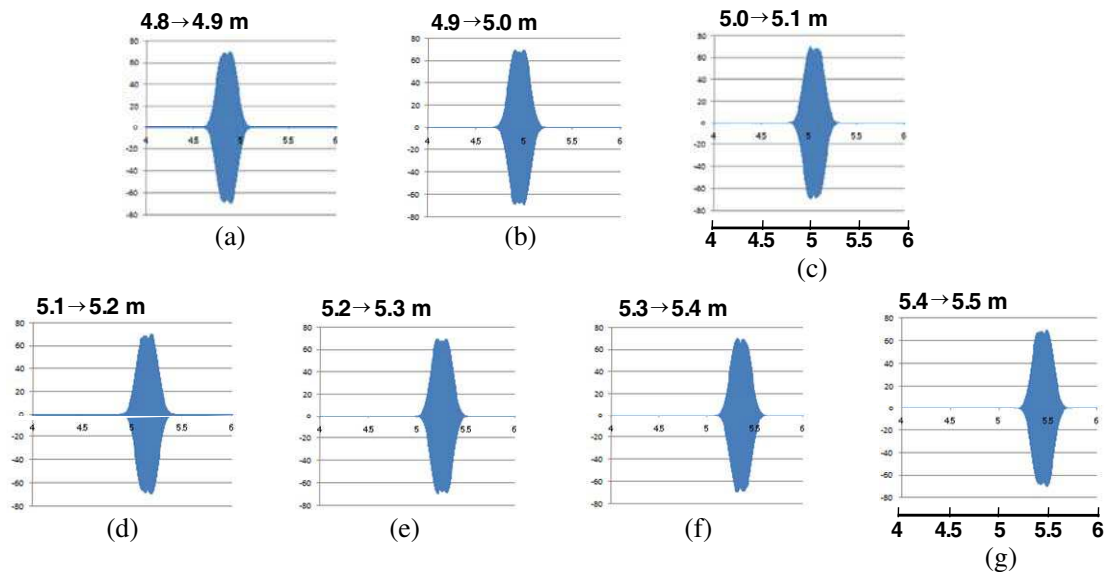
Figure 10: Subtraction of Fig. 8's impulse responses between two points in time. (a)–(g) Correspond to movements of object.

5. CONCLUSIONS

Sensor network which consists of small-sized radio-communication infrastructures has been investigated as most promising means to monitor and control home/office circumstances. We proposed a novel ultrasonic distance measuring method based on impulse responses calculated by IFFT, which can be used as ultrasonic positioning installed in sensor network. The fundamental experiments with the transmitter and the receiver facing to each other showed validity of the proposed method. Simulation results show that if they are installed in sensor network it is possible to detect only moving objects.

REFERENCES

1. Home Page of Kogakuin University (http://www.ns.kogakuin.ac.jp/~wwa1022/).
2. Dargle, W., et al., *Fundamentals of Wireless Sensor Networks*, John Wiley and Sons, 2010.
3. Dixon, R. C., *Spread Spectrum Systems*, John Wiley & Sons, 1976.
4. De Witte, E. and H. D. Griffiths, "Improved ultra-low range side lobe pulse compression waveform design," *Electronics Letters*, Vol. 40, No. 22, 1448–1450, Oct. 2004.
5. Japanese Patent (Tokugan2008-125735) pending.
6. Japanese Patent (Tokugan2010-269436) pending.
7. IEEE Standard 802.15.4: Wireless Medium Access Control (MAC) and Physical Layer (PHY) Specifications for Low Rate Wireless Personal Area Networks (LR-WPANs), 2003.

Evaluation of Site Diversity Effectiveness Using Weather Radar Data for Singapore

See Chuan Leong, **Wan Jing Loh**, **Yanjuan Chen**, **Peng Hon Yip**, and **Boon Tiong Koh**

Defence Science & Technology Agency, Singapore

Abstract— Long term weather radar data from open source are used for the determination of rainfall exceedance distributions for Singapore. Using an empirical model and methodology, the τ-min to 1-min time sampling of rainfall values is achieved so that accurate and high spatial resolution rain rate, attenuation maps and site diversity measurements can be computed in accordance to ITU-R recommendations. Rainfall contour maps within Singapore show a difference of about $40\,\mathrm{mmhr}^{-1}$. Site diversity gain dependence with distance shows a different relationship as compared to ITU-R Hodges model for Singapore. Site diversity methodology provides at least 10 dB of gain at 99.99% availability Ku band frequencies. The diversity gain is also highly dependent on the combination of site used in addition to the site separation distances.

1. INTRODUCTION

Satellite communication links are known to be severely attenuated by rain. In tropical regions such as Singapore, where rainfall at 0.01% exceedance reaches $135\,\mathrm{mmhr}^{-1}$ [1], a single path attenuation due to rainfall at Ku (12 GHz) band frequencies can reach 20 dB at 99.99% availability. Site diversity using 2 or more earth stations, can be used to provide the diversity gain necessary to counter rain fade events. Preliminary site diversity experiments [2] in Singapore utilized satellite beacon signals over a period of 297 days to evaluate the achievable diversity gain between 2 selected sites. Site diversity gain relationship with distance is not evaluated due to the limited availability of sites. In a recent study [3] utilizing weather radar data to correlate the rainfall cumulative distributions to attenuation, the site diversity gains and its relationship with site distances, elevation angle and frequency are evaluated. However, in these two studies, long term attenuation distributions are not obtained and therefore the published diversity gains will be subjected to yearly variations.

In this paper, we utilize long term (Jan. 2003–Oct. 2011) weather radar data, available from public domain, to extract the rainfall cumulative distributions for Singapore. Since different sources of weather radar data have different time-sampling intervals, an empirical model and methodology is proposed to convert the τ-min sampling to a 1-min sampling rainfall rate in accordance to ITU-R [4] recommendations. Following which, the equivalent 1-min rainfall at percentage of time, $P = 0.01\%$ or 99.99% availability Ku band attenuation maps are presented for the first time for Singapore. With the attenuation figures computed, the long term diversity gain is spatially evaluated for Singapore. Diversity gain relationships with distance comparisons are also made with comparisons from the Hodge model [5] used ITU-R.

Section 2 provides a description of the source weather radar data used. Section 3 provides the modeling approach to determine the 1-min period data for used in attenuation calculations. Section 4 provides the rain rate and attenuation contour maps. Section 5 provides the site diversity figures and effectiveness evaluation for Singapore.

2. DESCRIPTION OF WEATHER RADAR DATA

A weather radar system usually implements full volume 360° scans in loops to detect reflectivity. Based on the Marshall and Palmer [6] relationship, the radar reflectivity signal is then converted to rainfall values. Weather radar plots, representing a range of rainfall values over a region at a particular sampled time, can be obtained from public domain, such as the Singapore weather radar [7] (located at 103.97°E, 1.3512°N) as shown in Figure 1 and the regional weather radar plots [8] with larger coverage area but lower spatial and temporal resolutions as compared to the Singapore weather radar. For this study, the source of weather radar information used and their data availability is as shown in Table 1.

The extraction of useful digitized rainfall amount information starts from saving of the GIF89a /JPEG images from the web server. As some of the images are not geo-referenced properly, rainfall values at specific locations cannot be directly read at fixed x-y pixel locations in the image. To perform image geo-referencing, 3 reference control points containing the reference area of interest are first formulated. Pattern recognition is applied to detect the presence of the reference points.

Table 1: Source data and their availability. A low availability is due to the downtime of the data logger.

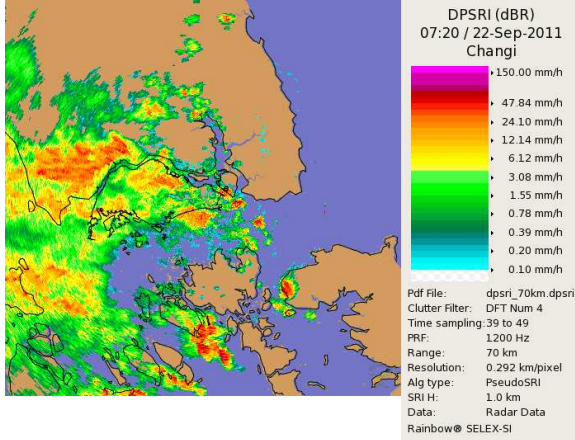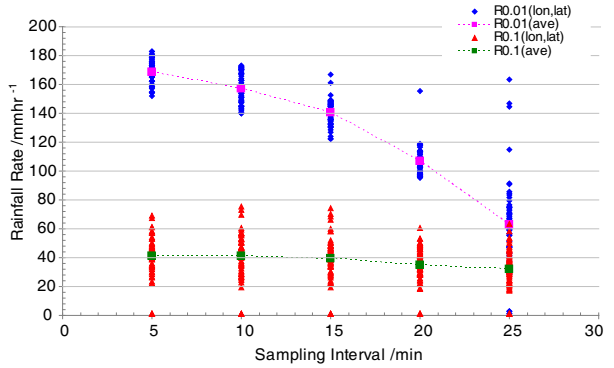| Duration	Source Data	Availability	Sampling Interval
Jan. 2003–Dec. 2003	SG [7]	95%	5 min
Jan. 2004–Dec. 2008	MY [8]	74%	20 min
Jan. 2009–Oct. 2011	SG [7]	43%	5 min

Figure 1: Regional rainfall plot from Singapore weather radar. A 70 km radial data is provided.

Figure 2: Relationship between the rainfall rate at ($P = 0.01\%$ (Blue/Magenta), $P = 0.1\%$ (Red/Green)) versus the sampling interval. The distribution of data at each sampling interval is obtained with $n = 64$ locations.

These 3 reference control points form a delaunay triangle following which a piecewise linear affine transformation is applied to interpolate and determine the required x-y point. The 3 control points are situated not far away from the region of interest to reduce the second order transformation errors. In this way, an x-y pixel to real world latitude-longitude registration is obtained. The color index at each location is subsequently matched using nearest color algorithm to the color bin in the legend. The actual rainfall value for the color bin is determined by a randomized continuous probability distribution function of the rainfall bin ranges.

3. DERIVATION OF τ-MIN TO 1-MIN SAMPLING INTERVAL

ITU-R recommends long term 1min integration time rain rate statistics for the preliminary design of both terrestrial and earth-satellite microwave links. Subsequently, the use of the 1-min integration time rate rates is statistically used to compute the percentage of time the rainfall value is exceeded distribution curve using long-term data. The use of sampled interval data (e.g., weather radar) differs from integrated data in the way that sampled data may lose information on high rainfall rates for long sampling interval. A conversion factor on the rainfall exceedance value is therefore required for sampling intervals greater than 1min.

Assuming the rainfall rate at fixed sampling interval, τ (min) is uncorrelated spatially, the discrete point rainfall exceedance value, R_P, can be computed at each spatial location and sampling interval. The longitude and latitude points are first computed based on the detection range of the weather radar as shown in Equation (1).

$$\mathrm{lon}(i) = \frac{i}{n}\left[\mathrm{lon}2 - \mathrm{lon}1\right] + \mathrm{lon}1$$
$$\mathrm{lat}(j) = \frac{j}{n}\left[\mathrm{lat}2 - \mathrm{lat}1\right] + \mathrm{lat}1$$

(1)

where $n > i, j \in \mathrm{Z}^+$, $n > 1$. lat1, lat2, lon1, lon2 are constants, ± 60 km from weather radar origin in the vertical and horizontal direction. Distance is converted to lat, lon using the inverse haversine formula.

At each of these locations, the rainfall exceedance value, $R_P(\mathrm{lon}(i), \mathrm{lat}(j), \tau)$ can be extracted

and an average value over these locations is defined as $R_{(P)(\tau)}$ as shown in Equation (2).

$$R_{(P)(\tau)} = \frac{\sum\limits_{i=1,j=1}^{n} R_P\left(\text{lon}(i), \text{lat}(j), \tau\right)}{2n} \tag{2}$$

The 2003 weather radar data [7] at 5 min sampled interval is used to derive the $R_{0.01}$ and $R_{0.1}$ values with $n = 64$. As shown in Figure 2, at higher sampling interval, the spread of exceedance values increases and also decreases in magnitude. The decrease is more pronounced at probabilities, $P = 0.01\%$ than at $P = 0.1\%$. Using the averaged R_P values, power law model with regression coefficients is developed to fit the averaged rainfall exceedance values. Equation (3) shows the regression variable results and equations for $P = 0.01\%$ and $P = 0.1\%$ respectively using the Levenberg-Marquardt fitting technique. The power law model is chosen so that it is continuous for different sampling interval and probabilities.

$$R_{(0.01)(\tau)} = 170.51 - 4.64 \times 10^{-2}\tau^{2.41}$$
$$R_{(0.1)(\tau)} = 41.59 - 4.93 \times 10^{-3}\tau^{2.36} \tag{3}$$

With the coefficient of multiple determination of at least 0.99 for both fits, the 1-min sampling rainfall exceedance value, as a function of P and sampling interval, τ, can be obtained as shown in Equation (4).

$$R_{(P)(1)} = R_{(P)(\tau)} + 4.785 \times 10^{(-\lg(P)-4)}\tau^{2.385} \tag{4}$$

Using Equation (4), the appropriate factor can be applied directly to rainfall values extracted from weather radar data or onto the rainfall exceedance values for correction to 1-min sampled data. The 1-min sampled data is subsequently assumed to be equivalent to the 1-min integrated data as defined by ITU-R.

4. RAIN RATE AND ATTENUATION CONTOUR MAPS

Using the weather radar data sources highlighted in Table 1 and the τ-min to 1-min conversion methodology, the rain rate contour maps for Singapore is developed. 60 location points are used to extract the rain rate and generate the contour lines using the kriging method. Figure 3 shows the $P = 0.01\%$ rain rate contour plot for Singapore. Several observations on the rain rate contours can be deduced. The rain rates in the north eastern area are lower than other parts of Singapore while the central location is higher. The variation of rain rates in the north western area is lower than other parts of Singapore. The $P = 0.01\%$ rain rate for Singapore is about $154\,\text{mmhr}^{-1}$ and this is within 20% [1] of the reported figures. Using the mean annual rainfall contour plots obtained from past Singapore statistics [9] and the scaling model provided by Chebil [10], the $P = 0.01\%$ rain rate variation across Singapore is about $20\,\text{mmhr}^{-1}$ while the current study suggests a variation of about $40\,\text{mmhr}^{-1}$.

The path attenuation model in ITU-R is based on a semi-empirical model involving specific attenuation [11] and effective path length, L_E. The specific attenuation, dependent on the reference
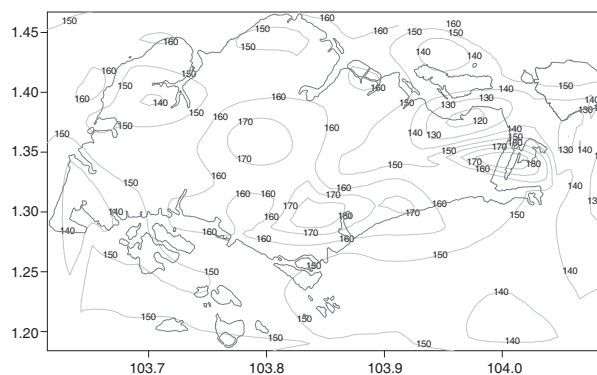

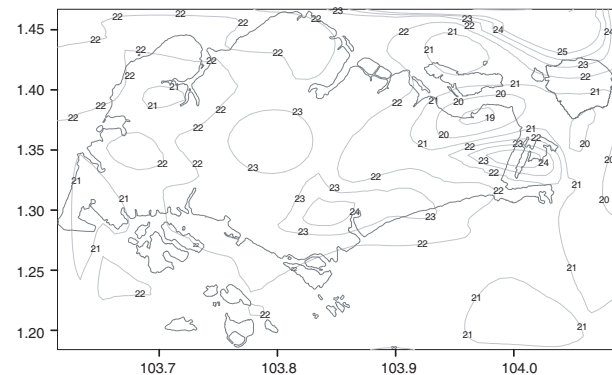Figure 3: Rain rate (mm/hr) contour maps for $P = 0.01\%$.

Figure 4: Rain attn (dB) contour maps for $P = 0.01\%$.

point rainfall rate, is replaced with an integrated path geometry attenuation involving rain height difference contour maps [12, 13] From the weather radar plots, the rainfall value is assumed to be constant in the vertical columnar direction and the path to the satellite can exit through the side of a storm cell or it can exit through the top. The total path attenuation, A, is therefore calculated accordingly through a numerical summation of path lengths as shown in Equation (5). The effective path length is a function of the rain rate.

$$A = \sum_{i=0}^{n} k R_{P,i}^{\alpha} L_E(R_P) \tag{5}$$

where $i \in \mathbb{Z}^{+}$, $n = \left\lceil \frac{\text{RainHeight} \cdot Pix(x)}{D \cdot \tan(elev)} \right\rceil$, $Pix(x)$ is the number of pixels in the x-direction for a distance, $D = 60$ km. k, α are frequency dependent coefficients defined in [11].

The satellite link is simulated by assuming earth stations located in Singapore are pointed to the WINDS geostationary satellite located at longitude 143°E, with elevation, *elev*, equal to 44°, Ku band (12 GHz), vertical linear polarization. The cumulative distribution function for attenuation, A, is statistically computed and the rain attenuation contour map at $P = 0.01\%$ is shown in Figure 4. There is an attenuation variation of about 7 dB across Singapore.

5. DIVERSITY GAIN EFFECTIVENESS

The separation distance between two diverse sites is a major factor that influences the performance of the site diversity technique. Using the single site attenuation defined in Equation (5), site diversity calculations involving 2 sites are computed. In Figure 6, the selection combination of sites Tuas (103.643°E, 1.323°N) and Changi (104.025°E, 1.323°N) provides a diversity gain of at least 14 dB at $P = 0.01\%$ as compared to a single site at Tuas (Attn = 21.924 dB). By interpolating 8 locations between Tuas and Changi in the east west direction, the diversity gain with respect to the distance apart can be calculated and shown in Figure 5. The site diversity performance monotonically increase with increasing distance and for large distances, the site diversity gain approaches its single site attenuation figure. The diversity gain in the vertical south to north direction is also evaluated with reference to single site at Sentosa (103.832°E, 1.245°N). Diversity gain in the *S-N* direction is higher than the *W-E* direction as shown by the larger gradient in Figure 5. In Figure 7, the Hodge's model is used and it did not provide good diversity gain estimates; the diversity gain at 20 dB single site attenuation is about 13.06 dB and 13.87 dB for distances of 5.55 km to 42.44 km apart respectively. This deviates significantly with the measured attenuation of about 7.29 dB and 15.79 dB for similar distances apart. One possible reason for the difference is that Hodge's model used climatic data from temperate regions.

The 2-site selection combining site diversity of 4 fixed locations (Tuas, Sentosa, Woodlands (103.817°E, 1.457°N), Changi) in Singapore are evaluated at $P = 0.01\%$. It is observed that high
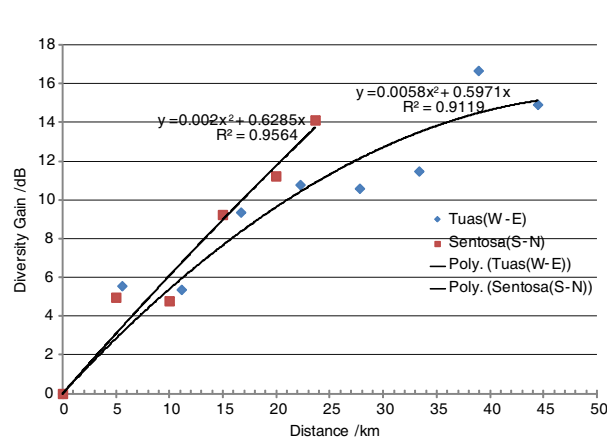

Figure 5: Diversity gain for West-East (ref to Tuas) and South-North (ref to Sentosa) directions versus distance.
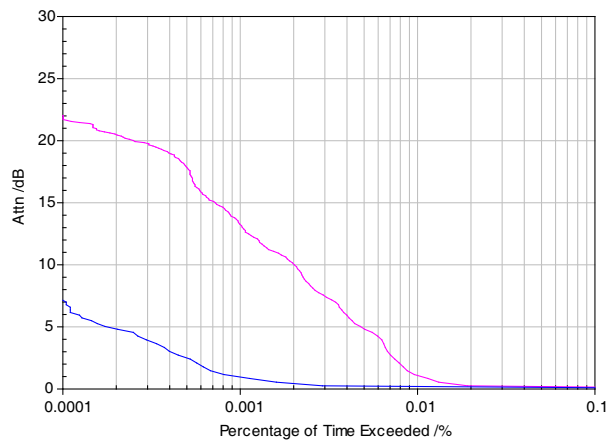
Figure 6: Attenuation distribution of single site Tuas and selection combining of two sites (Tuas-Changi).
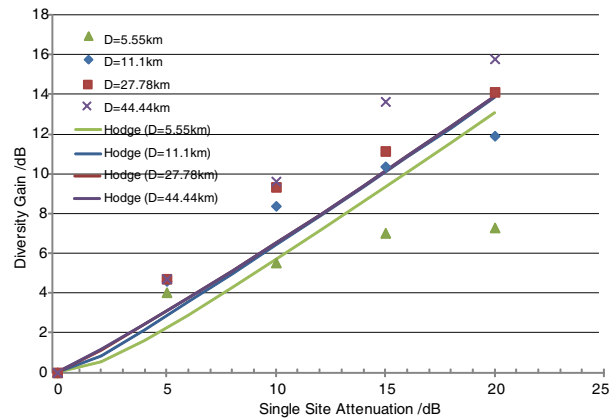
Figure 7: Relationship between single site attenuation on diversity gain at different site separations.

Table 2: Attenuation at 99.99% ($P = 0.01\%$) for 2-site selection combination. Diversity gain is referenced to the site on the left.

Selection Combination	Attn/dB	Div Gain/dB	Dist/km
Tuas-Sentosa	10.9	11.2	22.72
Tuas-Woodlands	11.22	10.1	24.40
Sentosa-Woodlands	7.82	13.9	23.62
Sentosa-Changi	10.38	8.8	23.13
Woodlands-Changi	9.55	12.0	27.49
Tuas-Changi	7.1	14.8	42.44

diversity gains (e.g., Sentosa-Woodlands, Tuas-Changi) is dependent not just on the distance apart but also on the selection of sites. The Sentosa-Woodlands sites combination provides comparable diversity gains as compared to Tuas-Changi combination even though their distance ratio is about two times. This observation strongly suggests that the rain cells move in the *S-N* direction more than the *W-E* direction and provides the observable diversity improvement.

6. CONCLUSION

8 years of long term weather radar data has been used for the first time to extract the rainfall cumulative distribution for attenuation studies and site diversity performance estimation for Singapore. A new proposed empirical model converts τ-min sampled data to 1-min integrated rainfall information so that accurate and high spatial rainfall information can be used. It is observed that there is statistically difference in rainfall exceedance values and Ku band attenuation figures obtained for different locations in Singapore. Using the same weather radar data with a reference satellite vertical polarization link at Ku band (12 GHz), site diversity methodology can provide at least 10 dB of gain at 99.99% availability for Singapore. The diversity gain is also highly dependent on the combination of sites in additional to the site separation distance factor predicted by the Hodges ITU-R model. The Hodges model did not estimate the site diversity gains with respect to site separation distance compared to the observations provided in this paper.

REFERENCES

1. Leong, S. C. and Y. C. Foo, "Singapore rain rate distributions," *6th Int. Conf. on Information, Comms and Signal Processing*, 1–5, Dec. 2007.
2. Timothy, K. I., J. T. Ong, and E. B. L. Choo, "Performance of the size diversity technique in Singapore: Preliminary results," *IEEE Communications Letters*, Vol. 5, No. 2, 49–51, Feb. 2001.
3. Yeo, J. X., Y. H. Lee, and J. T. Ong, "Performance of site diversity investigated through radar derived results," *IEEE Trans. on Antennas and Propagation*, Vol. 59, No. 10, 1–9, Oct. 2011.
4. ITU-R, "Propagation data and prediction methods required for the design of Earth-space telecommunication systems," Recommendation ITU-R P.618-10, Geneva, 2009.

5. Hodge, D. B., "An improved model for diversity gain in earth-space propagation paths," *Radio Science*, Vol. 17, No. 6, 1393–1399, 1982.
6. Marshall, J. S. and W. Palmer, "The distribution of raindrops with size," *Journal of Atmospheric Sciences*, Vol. 5, No. 4, 165–166, 1948.
7. http://www.weather.gov.sg/wip/c/portal/layout?p_l_id=PUB.1023.5, Meteorological Service Singapore, 2011.
8. Regional Weather Radar Information, http://www.ulfp.com/ulfp/mod_animate/view.asp?ID= 1, Ulfpettersson.com, 2011.
9. "Summary of observations," *Meteorological Service Singapore*, 1993.
10. Chebil, "Rain rate and rain attenuation distribution for microwave propagation study in Malaysia," Ph. D. Thesis, Universiti Teknologi Malaysia, 1997.
11. ITU-R, "Specific attenuation model for rain for use in prediction methods," Recommendation ITU-R P.838-3, Geneva, 2007.
12. ITU-R, "Rain height model for prediction methods," Recommendation ITU-R P.839-3, Geneva, 2007.
13. ITU-R, "Topography for earth-to-space propagation modeling," Recommendation ITU-R P.1511, Geneva, 2007.

Realization and Characterization of a High-performance SOA-based Multi-wavelength Fiber Ring Laser

Peng-Chun Peng[1], An-Li Tsou[2], Hoshin H. Yee[2], and Hai-Han Lu[1]

[1]Department of Electro-Optical Engineering
National Taipei University of Technology, Taipei 106, Taiwan, R.O.C.
[2]Department of Electrical Engineering
National Taipei University of Technology, Taipei 106, Taiwan, R.O.C.

Abstract— This investigation demonstrates a novel multi-wavelength fiber ring laser with ultra-narrow wavelength spacing and with very stable optical power output. The high-performance ring laser was realized based on a semiconductor optical amplifier (SOA), a delay interferometer (DI) and a mirror, and then characterized in the aspects of lasing wavelengths, output power stability, signal to noise ratio (SNR), as well as wavelength selectivity and tunability. Up to 181 stable lasing wavelengths, from 1574.91 to 1591.25 nm, with a wavelength spacing of 10.7 GHz and a signal-to-noise ratio of over 24 dB, were obtained at room temperature.

1. INTRODUCTION

Fiber ring lasers have had a great progress in recent decades and becomes very attractive for use in wavelength division multiplexed (WDM) communication systems as one such device can produce numerous wavelength channels, eliminating the need for several wavelength-specific light sources and greatly reducing costs in the implementation and operation of WDM networks [1] Recently, multi-wavelength fiber lasers have been extensively studied using various gain media, such as erbium-doped fiber amplifiers (EDFAs) [2], semiconductor optical amplifiers [3] and hybrid gain media [4]. However, because of the homogeneous gain broadening of the Er-doped fiber, the realization of stable multi-wavelength oscillations is difficult [5]. While various methods such as cryogenic cooling, frequency shifting, and intracavity four-wave mixing in nonlinear fibers [6–8] have been utilized to overcome this limit, they make the lasers more complex and therefore costly. In contrast, SOA is an inhomogeneous broadening gain medium, which can suppress mode competition in multi-wavelength oscillations and provide stable multi-wavelength lasing output with narrow channel spacing. Hence, the SOA has become a key device in the construction of multi-wavelength fiber lasers. An SOA-based fiber ring laser, with an ultra-narrow wavelength spacing of 50 pm but only has three fixed wavelengths, has been reported using a fiber Bragg grating [9]. Multiwavelength oscillations with a wavelength spacing of 0.08 nm can be generated using a Sagnac loop mirror filter as a multichannel filter that is incorporated into an SOA-based fiber ring cavity [10]. However, the signal-to-noise ratio of the lasing wavelength is fairly low of about 10 dB.

In this work, a multi-wavelength SOA-based fiber laser with ultra-narrow wavelength spacing, incorporating a double-pass interferometer, is demonstrated. The laser configuration is based on an SOA, a DI, and a reflection mirror. The DI and the mirror are used as a double-pass interferometer to increase the mode suppression ratio and reduce the output spectral linewidth. More than 181 simultaneous lasing lines, with a bandwidth of 5 dB, a signal-to-noise ratio over 24 dB, and a wavelength spacing of 10.7 GHz, are produced.

2. EXPERIMENTAL SETUP

Figure 1 schematically depicts the proposed multiwavelength fiber ring laser, which consists of an SOA, a DI, a polarization controller (PC), a circulator, a mirror, and an optical coupler. The SOA is responsible for the inhomogeneous broadened gain of the laser operated under a driving current of 300 mA at an operating temperature of 25°C. On these operating conditions, the SOA has a saturation output power of 11 dBm and a peak wavelength of 1517.82 nm.

The optical circulator transfers the ASE of the SOA to DI. And the DI is used as a comb-like filter in the ring cavity. When the ASE of SOA passes through the DI, it generates a comb-like transmission spectrum. The mirror is used to reflect the light back to the DI with a mirror loss of 0.6 dB. The optical coupler is used to direct the output of the ring laser to an optical spectrum analyzer. The polarization controller (PC) is for optimizing the polarization state of the light into the SOA.
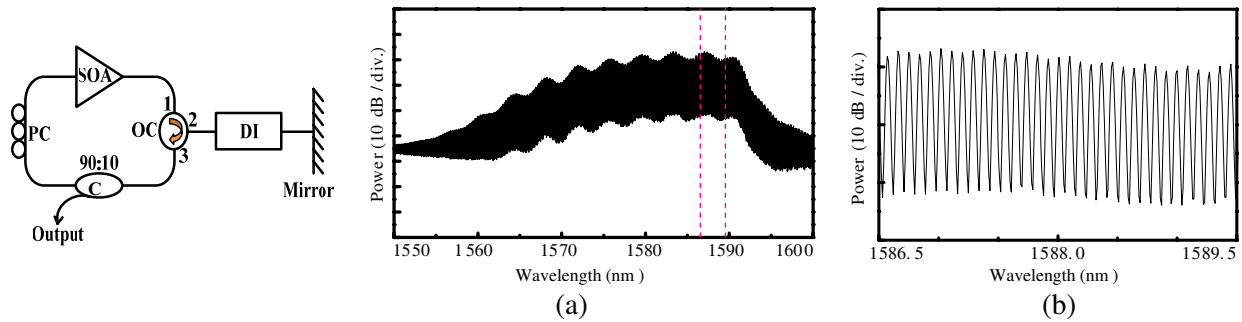
Figure 1: The fiber ring laser configuration in this work.

Figure 2: (a) Multi-wavelength output spectrum with a wavelength spacing of 10.7 GHz. (b) Magnified part surrounded by dashed lines in Fig. 2(a).

The DI is based on a free-space optical Michelson interferometer with a free spectral range (FSR) of 10.7 GHz. It comprises an optical beam splitter (BS) and two reflection mirrors. The incident beam from a BS is split into two beams, which travel along separate paths with different lengths and are reflected back to the BS by two reflection mirrors. The optical beam that travels along the longer path reaches the BS later than that travels along the shorter one, producing a phase difference between the longer-traveling and the shorter-traveling beams at the BS. These two optical beams interfere with each other at the BS, and finally couple to the output.

3. LASER CHARACTERISTICS

3.1. Lasing Wavelength and Its Spacing

Figure 2(a) presents the output spectrum of the multi-wavelength fiber laser. The number of lasing wavelengths is 181 with a spacing of 10.7 GHz and with a 5-dB bandwidth of 16.34 nm, ranging from 1574.91 nm to 1591.25 nm. The SOA, which has an inhomogeneous gain characteristics ensures stable multi-wavelength lasing. The apparatus comprising a DI and a mirror reshapes the transmission spectrum and produces narrow-linewdith lasing lines.

3.2. Signal to Noise Ratio

Figure 2(b) magnifies a part of the dashed line from 1586.5 nm to 1589.5 nm, from which it is clear that the SNR exceeds 24 dB. This value is much higher than that obtained (10 dB) from another similar study [13], in which SOA was also used as the gain medium. It is thus evident that the implementation of the DI and the mirror in this work will significantly increase the SNR and improve the lasing characteristics.

3.3. Output Power Stability

Stable multi-wavelength output is crucial, for example, in high-bite rate data transmissions. To observe the wavelength stability, the optical spectra were measured, six times for 40 minutes in an interval of 0.63 nm, scanning from 1574.91 to 1591.25 nm. There are two main probable factors resulting in the operation instability: (i) mode competition in the laser cavity, and (ii) drift of the emission spectrum caused by thermal fluctuation. In the SOA-based multi-wavelength configuration, the inhomogeneous linewidth broadening of the gain medium considerably reduces the mode competition within the cavity. Therefore, the multi-wavelength operation can be self-stabilized when SOA is adopted as the gain medium of the system.

Since the DI is relatively insensitive to the variations in power, temperature and polarization, a well-packed DI is utilized to eliminate the effects resulting from thermal fluctuation. Based upon the above arrangements, typical multi-channel peak power variations were mostly smaller than 0.5 dB.

3.4. L-I Curve

The optical power output depending on the SOA driving current is shown in Fig. 3. The insets of which illustrate different output spectra at two driving currents. It can be found that the spectrum will be broadened as the driving current is enhanced.
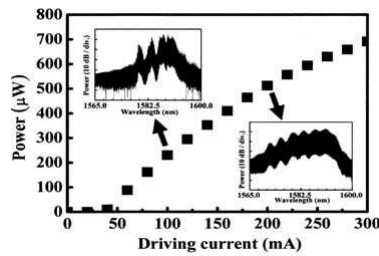
Figure 3: Output power of the SOA-based fiber ring laser as a function of driving current.
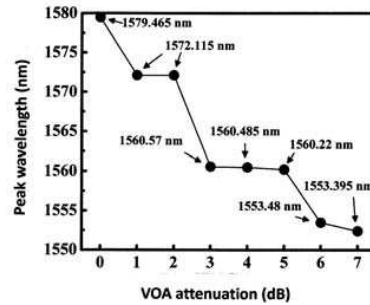
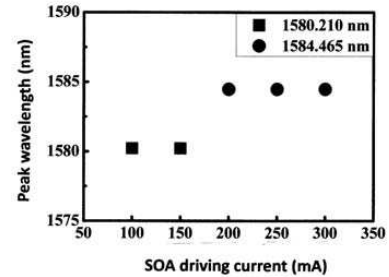Figure 4: Power peak wavelength dependence on attenuation of the cavity.

Figure 5: The evolution of power peak wavelengths upon SOA driving current.

3.5. Wavelength Selectivity and Tunability

Furthermore, the selectivity of lasing peaks at different wavelengths was systematically investigated by incorporating a variable optical attenuator (VOA) into the laser ring structure (not shown here). By changing the magnitude of VOA, from 0 to 7 dB, the wavelength of lasing power peak was monotonously decreased, i.e., from 1579.47 to 1553.40 nm as shown in Fig. 4. It is crystal clear that the addition of the VOA into the laser configuration will greatly vary the mechanism of gain-loss competition in the cavity and significantly change the wavelength of the lasing peak.

Moreover, in order to observe the tunability of this specific laser source, the driving current of SOA was deliberately varied from 100 to 250 mA. Fig. 5 demonstrates the peak wavelength dependence upon the SOA driving current. In which it is found that the laser experiences a red shift when the injection current is increased to 200 mA. We believed that this red shift is resulting from the carrier-induced plasma effect on the refractive index change of the semiconductor optical amplifier in the laser configuration.

4. CONCLUSION

In conclusion, this investigation experimentally demonstrated a stable multi-wavelength SOA-based fiber ring laser with ultra-narrow wavelength spacing. The SNR of the ring laser is improved herein by the use of a DI and a mirror as a double-pass interferometer. Up to 181 stable lasing wavelengths with a spacing of 10.7 GHz, a signal-to-noise ratio of over 24 dB, and a small power variation below 0.5 dB are achieved at room temperature. It is believed that this high performance multi-wavelength fiber laser will be a very promising light source for WDM optical communications.

ACKNOWLEDGMENT

REFERENCES

1. Staring, A. A. M., L. H. Spiekman, J. J. M. Binsma, E. J. Jansen, T. V. Dongen, P. J. A. Thijs, M. K. Smit, and B. H. Verbeek, "A compact nine-channel multiwavelength laser," *IEEE Photon. Technol. Lett.*, Vol. 8, 1139–1141, 1996.
2. Zhang, A., H. Liu, M. S. Demokan, and H. Y. Tam, "Stable and broad bandwidth multiwavelength fiber ring laser incorporating a highly nonlinear photonic crystal fiber," *IEEE Photon. Technol. Lett.*, Vol. 17, 2535–2537, 2005.
3. Dong, H., G. Zhu, Q. Wang, H. Sun, N. K. Dutta, J. Jaques, and A. B. Piccirilli, "Multiwavelength fiber ring laser source based on a delayed interferometer," *IEEE Photon. Technol. Lett.*, Vol. 17, 303–305, 2005.
4. Peng, P. C., K. M. Feng, C. C. Chang, H. Y. Chiou, J. H. Chen, M. F. Huang, H. C. Chien, and S. Chi, "Multiwavelength fiber laser using S-band erbium-doped fiber amplifier and semiconductor optical amplifier," *Opt. Communications*, Vol. 259, 200–203, 2006.
5. Hayashi, R., S. Yamashita, and T. Saida, "16-wavelength 10-GHz actively mode-locked fiber laser with demultiplexed outputs anchored on the ITU-T grid," *IEEE Photon. Technol. Lett.*, Vol. 15, 1692–1694, 2003.

6. Bellemare, A., M. Karasek, M. Rochette, S. L. Rochelle, and M. Tetu, "Room temperature multifrequency erbium-doped fiber lasers anchored on the ITU frequency grid," *IEEE J. Lightwave Technol.*, Vol. 18, 825–831, 2000.

7. Han, Y. G., T. V. A. Tran, and S. B. Lee, "Wavelength-spacing tunable multiwavelength erbium-doped fiber laser based on four-wave mixing of dispersion-shifted fiber," *Opt. Lett.*, Vol. 31, 697–699, 2006.

8. Xia, L., L. P. Shum, Y. X. Wang, and T. H. Cheng, "Stable triple-wavelength fiber ring laser with ultranarrow wavelength spacing using a triple-transmission-band fiber Bragg grating filter," *IEEE Photon. Technol. Lett.*, Vol. 18, 2162–2164, 2006.

9. Zhang, Z., J. Wu, K. Xu, X. Hong, and J. Lin, "Tunable multiwavelength SOA fiber laser with ultra-narrow wavelength spacing based on nonlinear polarization rotation," *Opt. Express*, Vol. 17, 17200–17205, 2009.

10. Hsieh, J., A. Chiayu, V. Chien, X. Liu, A. Gnauck, and X. Wei, "Athermal demodulator for 42.7-Gb/s DPSK signals," *31st European Conference on Optical Comm.*, Vol. 4, 827–828, 2005.

180 GHz Microstrip Ring Resonator Bandpass Filter on Micromachined Silicon Substrate

H. R. Lin[1], K. B. Ng[2], C. H. Chan[3], E. Y. B. Pun[3], F. J. Hsieh[1], and W. C. Wang[1, 4, 5]

[1]Department of Mechanical Engineering, University of Washington, Seattle, Washington, USA
[2]State Key Laboratory of Millimeter Waves, City University of Hong Kong, China
[3]Department of Electrical Engineering, City University of Hong Kong, China
[4]Department of Electrical Engineering, University of Washington, Seattle, Washington, USA
[5]Medical Device Innovation Center, National Cheng-Kung University, Tainan, Taiwan, R.O.C.

Abstract— A 180 GHz bandpass filter utilizing dual mode stepped impedance ring resonator is reported. A monolithic integrated microstrip design is proposed and fabricated on a silicon substrate. To excite appropriate resonant mode and to alleviate difficulties in micro-fabrication process, the second-order resonance of the circular ring resonator is adopted in the filter design. The whole design includes a conductor-backed coplanar waveguide (CBCPW) to guide signals into and out of the filter. Coplanar waveguide (CPW)-microstrip transition structure between CBCPW and central ring is considered for grounding to avoid having via metal layers bridging the top and bottom electrodes. This design also eliminates the need for wire bonding. Between the microstrip and ring resonator is a capacitive coupling gap for its simple design and easy to modify for different frequency operation. Aluminum is used for the top and bottom electrodes and the thickness is controlled at 600 nm. A (110) p-type 150 μm double side polished silicon wafer is used as the substrate. The thickness of the wafer is etched down to 100 μm from backside by inductively coupled plasma (ICP) dry etching to insure optimal waveguide transmission at the operation frequency. Since the backside surface roughness of substrate is shown to be much less than 600 nm, the thin film quality of subsequent conductor layer is guaranteed. The result from the CST simulation shows that a 3.5 dB insertion loss at 181 GHz and 3 dB passband from 176 to 186 GHz can be obtained.

1. INTRODUCTION

Many attractive applications operated over 100 GHz are forecasted. They include airplane landing aid system, imaging, wireless office and high-data rate long-distance communication systems [1, 2]. Short-distance application, for example, millimeter wave imaging system, is proposed for frequency bands with higher attenuation, including 120 GHz, 180 GHz, 320 GHz and 380 GHz. On the contrary, long-distance communication system for frequency bands with lower attenuation is also suggested [2]. For any one of these systems, filter will be required to avoid interference when there are more and more different applications squeezed into one frequency band.

Recently, various sub-terahertz CMOS integrated circuits are proposed [3]. A 300 GHz oscillator based on 65 nm CMOS technology is also reported [4]. Since microstrip and coplanar waveguide (CPW) have been applied in monolithic microwave integrated circuits (MMIC) for decades [5], these transmission lines are supposed to integrate with the emerging sub-terahertz solid state circuits. To achieve this goal, a bandpass filter constructed by microstrip ring resonator on silicon substrate is proposed.

Microstrip ring resonator has been applied in material constitutive parameter extraction [6] and bandpass filter. As a bandpass filter, the bandwidth of passband could be manipulated by introducing asymmetric structure and perturbation. The perturbation could be realized by step impedance change or connecting the ring resonator with an external active device [7]. For simplicity, the stepped impedance perturbation is adopted in this design. Meanwhile, an all-planar design is considered to reduce the complexity in the fabrication stage. Based on this later design, wire bonding or conducting via layers are eliminated. However, a CPW-microstrip transition [8] must be implemented. With this new waveguide coupling system, the whole fabrication process is simplified to one mask process. The following section will introduce the detail of each section of the design.

2. DESIGN AND SIMULATION

The system consists of a conductor-backed coplanar waveguide (CBCPW), CBCPW-microstrip transition, microstrip and ring resonator (Figure 1). The thickness of substrate and dimensions of CPW are trimmed to match the dimensions of GSG probe and to provide good impedance matching.

The length of CBCPW-microstrip transition is one-quarter of guided wavelength [9]. Besides, the capacitive coupling gap between microstrip and ring resonator should be trimmed to provide sufficient coupling. The circumference of ring dominates the resonant frequency. At the preliminary stage, existing publication [10] provides equations for determining the guided wavelength. This value is $600\,\mu m$ based on the calculation. However, it is later found from the simulation that the value is $584\,\mu m$. According to reference [7], the width of ring is suggested to be less than 20% of the mean radius of the ring. If circumference is $600\,\mu m$, the ring width should be less than $20\,\mu m$ which is approaching the limit of our fabrication capability. To avoid potential problems in fabrication, the circumference is doubled and second-order resonance is adopted for filter design.

The simulation software is CST® microwave studio. The simulation results are shown in Figure 2. Please note that S_{21} is equivalent to S_{12} (blue line) and S_{11} is equivalent to S_{22} (purple line) because of the symmetry of layout. The insertion at $181\,GHz$ is $3.5\,dB$ and $3\,dB$-bandwidth is from 176 to $186\,GHz$.

3. FABRICATION PROCESS

The physical structure consists of three layers: top electrode, silicon substrate and bottom electrode. The fabrication process is divided into three parts as shown below.

In the first step, aluminum top electrode is evaporated onto the silicon and then patterned by wet etching. The thickness of this layer is $600\,nm$ which is three times thicker of skin depth at $180\,GHz$. After that, the $150\,\mu m$ silicon substrate is thinned down to $100\,\mu m$ by SF_6/O_2 plasma. Thinning of substrate is to provide better matching of GSG waveguide. Finally, the etched backside is deposited again with aluminum bottom electrode. As mentioned above, the simplification of fabrication process is reflected on the careful design of dimensions of ring resonator and CPW-microstrip transition structure. To guarantee proper mode propagating over the ring, the width is tailored to $28\,\mu m$ which is 15% of the mean radius. The expected length of transition structure is
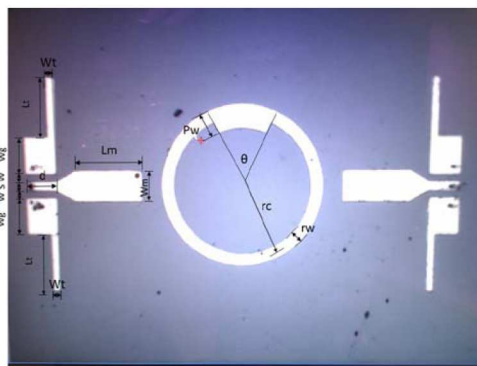
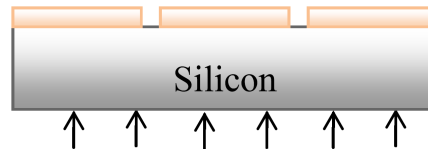Figure 1: The fabricated ring resonator filter.
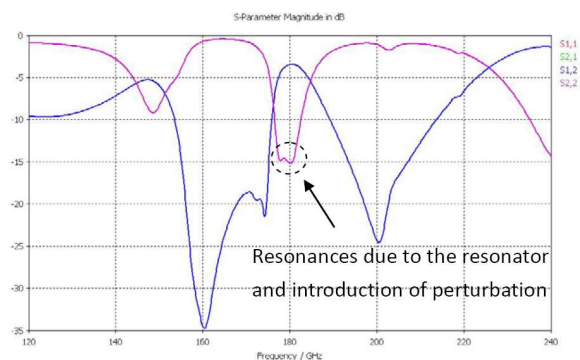
Figure 2: S-parameters of the ring filter: insertion loss is $3.5\,dB$ at $181\,GHz$ and $3\,dB$ passband between 176 and $186\,GHz$ is discovered from S_{11}.

2) Patterning of 600 nm thick aluminum top electrode.

1) ICP dry etching (SF_6/O_2) from backside of (110) 150 um thick silicon substrate.

3) Deposition of 600 nm thick aluminum bottom electrode on backside of silicon substrate.

Figure 3: Fabrication process of the ring filter.

Table 1: Dimensions of each component (unit: micron meter).

CBCPW					Microstrip		CPW-microstrip transition		Ring Resonator			
Wg	W	S	d	t	Wm	Lm	Wt	Lt	rc	rw	Pw	θ^*
90	19	21	75	0.6	75	163	16	143	186	28	42	47.5

*The perturbation angle unit is in degree.

Table 2: List of filter parameters.

	f_c	Insertion loss	Passband (3 dB)	Return Loss
Simulation	181 GHz	3.5 dB	176–186 GHz	−15 dB
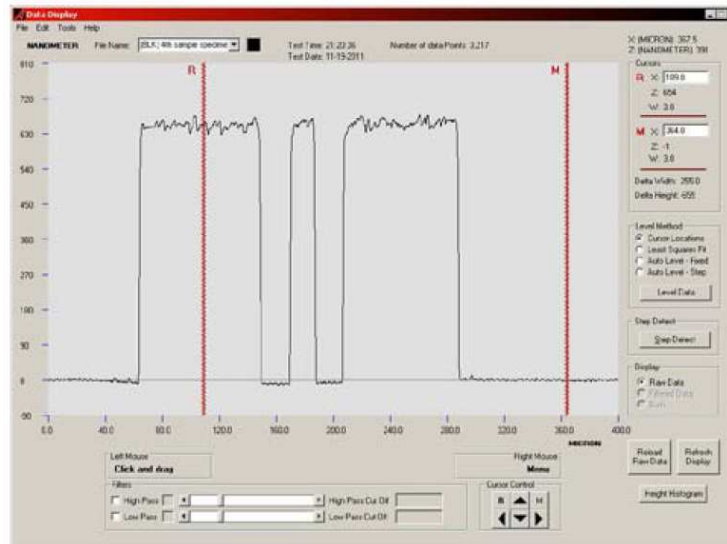
Figure 4: Profiling of CBCPW: surface roughness is within 60 nm.

later optimized to 143 μm. All design parameters are listed in Table 1, in which Wg is the width of finite grounding plane of CBCPW, S is the width of signal of CBCPW, W is the gap between signal and grounding, d is the length of CBCPW, t is the thickness of top electrode, Wm is the width of microstrip, Lm is the length of microstrip, Wt is the width of transition structure, Lt is the length of transition structure, rc is the mean radius of ring, rw is the width of ring, Pw is the width of perturbation and θ is the angle of perturbation (Figure 1).

4. MEASUREMENT AND DISCUSSION

The measurement is conducted through Agilent N5245A vector network analyzer (VNA) incorporating OML frequency extension modules. With this combination, the measurement frequency is raised up to 220 GHz. The GSG probe is calibrated with open-short-through (OST) over an impedance standard substrate (ISS) provided by the vendor.

5. CONCLUSIONS

The ring resonator filter is fabricated on silicon substrate. The surface roughness is controlled down to less than 60 nm. With the aid of CST, the insertion loss is estimated to be 3.5 dB at 180 GHz. The VNA measurement will be conducted to verify several design concepts: the function of CBCPW-transition structure and the operation of ring resonator filter incorporating such via-less transition structure. The results will be demonstrated in the following work.

ACKNOWLEDGMENT

REFERENCES

1. Wallace, H. B., "Analysis of RF imaging applications at frequencies over 100 GHz," *Applied Optics*, Vol. 49, 38–47, 2010.
2. Rappaport, T. S., et al., "State of the art in 60-GHz integrated circuits and systems for wireless communications," *Proceedings of the IEEE*, Vol. 99, 1390–1436, 2011.
3. Seok, E., et al., "Progress and challenges towards Terahertz CMOS integrated circuits," *IEEE Journal of Solid-State Circuits*, Vol. 45, 1554–1564, 2010.
4. Razavi, B., "A 300-GHz fundamental oscillator in 65-nm CMOS technology," *IEEE Journal of Solid-State Circuits*, Vol. 46, 894–903, 2011.
5. Houdart, M. and C. Aury, "Various excitation of coplanar waveguide," *The Symposium of 1979 IEEE MTT-S International*, presented, 1979.
6. Thompson, D. C., et al., "Characterization of liquid crystal polymer (LCP) material and transmission lines on LCP substrates from 30 to 110 GHz," *IEEE Transactions on Microwave Theory and Techniques*, Vol. 52, 1343–1352, 2004.
7. Chang, K., Ed., *Microwave Ring Circuits and Antennas (Wiley Series in Microwave and Optical Engineering*, Wiley-Interscience, New York, 1996.
8. El-Gibari, M., et al., "Ultra-wideband GCPW-MS-GCPW driven electrode for low-cost and wide range application electro-optic modulators," *Microwave and Optical Technology Letters*, Vol. 52, 1078–1082, 2010.
9. Raskin, J. P., et al., "Mode conversion at GCPW-to-microstrip-line transitions," *IEEE Transactions on Microwave Theory and Techniques*, Vol. 48, 158–161, 2000.
10. Wadell, B. C., Ed., *Transmission Line Design Handbook*, Artech House, Norwood, MA, 1991.

Novel Tunable Band-reject Filter Using Modified C-shaped Defected Ground Structure

Rajab M. Begenji and M.-H. Neshati

Department of Electrical Engineering, Ferdowsi University of Mashhad, Iran

Abstract— In this paper, a novel tunable DGS filter is proposed to provide a frequency-rejection property at centre frequency of 2.4 GHz. The new structure has a simple and compact shape and its rejection characteristic is sharp at stop band. Different parameters of the DGS have been adjusted for the best frequency response to reject the desired frequency. The proposed filter is numerically investigated using HFSS and a parametric study was carried out. Results show that for capacitor values of 0.35 pF to 3 pF, the centre frequency of the band reject filter is varied from 2.512 GHz to 2.292 GHz. Transmission coefficient of the proposed DGS filter is at least −16.59 dB, which attenuates the desired frequency very well. It exhibits a minimum Q-factor of 67.40, whereas maximum impedance bandwidth is 36 MHz.

1. INTRODUCTION

In recent years, microstrip lines with defected ground patterns have offered many applications at microwave frequencies as a filter due to their compact size and better frequency characteristics. Also, using these novel structures, one can achieve attractive features at the design frequency. Moreover, for integrating with other active and passive device, various research results have dealt with Defected Ground Structures DGS [1–4]. DGS structures offer a few resonance properties in transfer characteristics such as RLC circuits. Corresponding to the shape and size of the defect pattern, parallel or series resonance are obtained which can be used in microwave band reject filters. Using DGS, the effective inductance of a micro strip line could be enlarged lead to a longer electrical length of transmission line than that of a conventional line, and so compact microwave circuits can be implemented [5].

Photonic band gap (PBG) structures have a periodic structure and only supply rejection at certain frequencies. Moreover, too many design parameters such as number of lattice, spacing between lattices, lattice shapes, and relative volume fraction effect on the band gap properties of PBGs. As a result, it is difficult to find the PBG structure's equivalent circuit and parameters; and also it is difficult to use a PBG circuit for the design of the microwave or millimeter-wave components [6]. Conversely, the DGS structures can be modeled by simple resonant circuits and their parameter extraction is simple and they can be useful in the design of microwave and millimeter-wave circuits. Finding the equivalent circuit and parameters of a DGS, various efforts have been reported [7].

In microwave applications, the band rejection property and the slow-wave effect of the DGS can be used in the design of microwave circuits such as dividers and filters [5–7]. It is necessary to use a high Q-factor filter to suppress an undesired signal, which is closely located from the desired signal. The dumbbell or spiral shapes have been used as a conventional defect of DGS. But, for narrowband rejection applications, their frequency characteristics are not adequate. The spiral DGS provides steeper rejection property than the dumbbell DGS, but the Q factor of the spiral DGS is usually smaller than 10.

In this paper, a C-shaped DGS is presented to provide a high Q-factor at 2.4 GHz as a band reject filter and provide adjusting the centre frequency of the filter. A parametric study is carried out and the effects of variable capacitor are numerically investigated on the frequency response of the filter using HFSS.

2. DGS FILTER CONFIGURATION

The proposed filter including a variable capacitor C_V is shown in Fig. 1. Rogers RO3003 with dielectric constant of 3.5 and height of 60 mils is used as the filter substrate. A 50 Ω line, as a feed line is designed by line width of $W = 3.45$ mm. The C-shaped DGS is etched at the backside of the PC-board and its size are $l_2 = 3$ mm, $t = k = g = 0.2$ mm and $g_1 = 1$ mm. Although, tuning capability of the DGS band-stop filter by lumped elements is reported in literature [8], using a rectangular patch in the ground plane, as shown in Fig. 1, leading to adding a varactor diode with its bias network to obtain an electronically tunable filter. So, a parasitic patch with size of $l \times 0.6$ mm^2 is also added at the proper for adding the diode, which l is the length of parasitic patch, and its value is determined by simulation and is presented in next part.
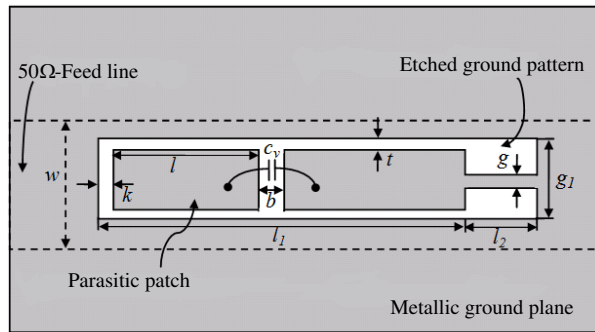
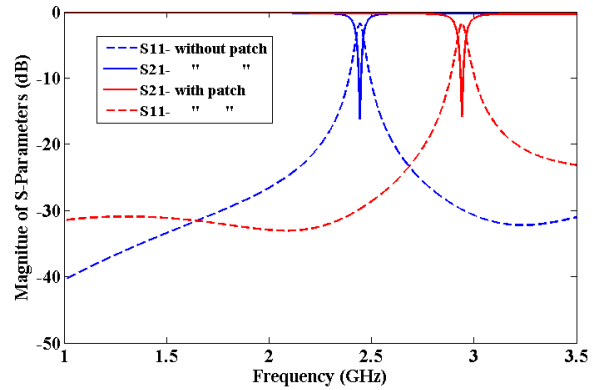Figure 1: Bottom view of the proposed DGS filter with a variable capacitor.

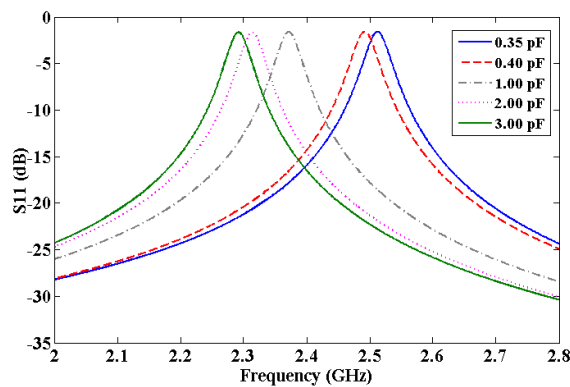Figure 2: Numerical results of the propsed filter with and without parasitic patch.

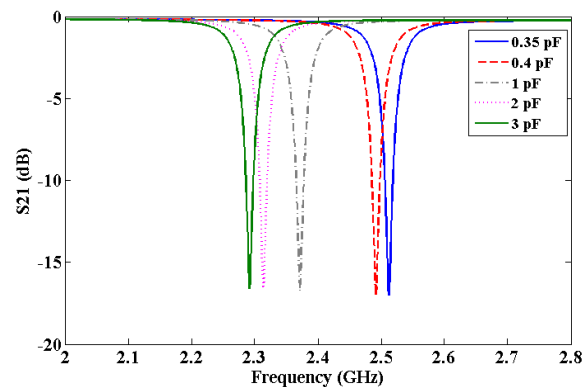Figure 3: Numerical results of S_{11} for different values of C_V with patch.

Figure 4: Numerical results of S_{21} for different values of C_V with patch.

3. NUMERICAL RESULTS

3.1. Without Capacitor

The proposed filter is numerically simulated using HFSS. Simulation results for reflection coefficient S_{11} and transmission coefficient S_{21} are shown in Fig. 2. First of all, the DGS filter is simulated $l = 0$ and l_1 equal to 15.2 mm. Results show that the band reject filter illustrate the resonance frequency of 2.44 GHz. To ease adding a varactor diode to obtain an electronically tunable filter, a narrow gap with size of b equal to 1.4 mm is created in the defected pattern; as a result a patch with size of $l \times 0.6$ mm^2 is also obtained. Numerical results show that with $l = 2$ mm, as shown in Fig. 2, the rejected frequency is around 2.9 GHz.

3.2. With Capacitor

To adjust the centre frequency of the band reject DGS filter, a variable capacitor is added at the proper place as shown in Fig. 1. A parametric study was carried out and the effect of different values of the capacitor on the frequency response of the filter was studied. The exact value of the centre frequency by mounting variable capacitor is summarized in Table 1.

For a specified varactor diode, which its tuning capacitor is varied from 0.35 pF to 3 pF, the length of parasitic patch and the arm length of DGS are adjusted to 4 mm and 17 mm, respectively. The numerical results for S_{11} and S_{21} are shown in Fig. 3 and Fig. 4. It can be seen that for capacitor values between 3 pF to 0.35 pF, the centre frequency is varied from 2.292 GHz to 2.512 GHz. The complete numerical results including resonance frequency, impedance bandwidth, quality factor and S-parameter of the proposed DGS filter are summarized in Table 2. It can be concluded that the attenuation of the filter at the centre frequency is at least -16.59 dB, which shows that the desired frequency is reduced. Moreover, the DGS filter exhibits a minimum Q-factor of 67.47, which shows bandwidth of 34 GHz at 2.292 GHz.

Table 1: Tuning of resonance frequency of the proposed filter for different values of C_V.

C_V (PF)	0	0.20	0.40	1.00	2.00	4.00	8.00	16.0	∞
f (GHz)	2.94	2.653	2.573	2.508	2.478	2.461	2.452	2.447	2.44

Table 2: Characteristics of band-reject filter for various values of capacitor C_V.

C_V (PF)	f (GHz)	BW (MHz)	Q	S_{12} (dB)	S_{11} (dB)
0.35	2.512	36	69.77	-17.01	-1.616
0.40	2.492	36	69.22	-17.00	-1.609
1.00	2.372	35	67.77	-16.75	-1.629
2.00	2.314	34	68.06	-16.59	-1.663
3.00	2.292	34	67.40	-16.59	-1.656

4. CONCLUSION

In this paper, a new novel tunable band reject filter using a C-shaped DGS is proposed and its frequency characteristics are reported. A parametric study of the different values of a capacitor is numerically investigated by HFSS. Simulation results show that foe capacitor values of 0.35 pF to 3 pF, the centre frequency of the band reject filter is varied from 2.512 GHz to 2.292 GHz. It provides at least -16.59 dB suppression at the centre frequency of the filter, while minimum Q-factor of 67.40 is obtained. The maximum band reject filter bandwidth is also 36 MHz. The proposed filter may have wide applications in the design of microwave systems.

ACKNOWLEDGMENT

REFERENCES

1. Park, J.-S. and M.-S. Jung, "A novel defected ground structure for an active device mounting and its application to a microwave oscillator," *IEEE Microwave and Wireless Components Letters*, Vol. 14, No. 5, 198–200, 2004.
2. Safwat, A. M.-E., F. Povedin, P. Ferrari, and A. Vilcot, "Tunable bandstop defected ground structure resonator using reconfigurable dumb-bell-shaped coplanar waveguide," *IEEE Trans. on MTT*, Vol. 54, No. 9, 3559–3564, 2006.
3. Huang, S.-Y. and Y.-H. Lee, "A compact E-shaped patterned ground structure and its applications to tunable bandstop resonator," *IEEE Trans. on MTT*, Vol. 57, No. 3, 657–666, 2009.
4. El-Shaarawy, H.-B., F. Cocceti, R. Plana, M. El-Said, and E.-A. Hashish, "Novel reconfigurable defected ground structure resonator on coplanar waveguide," *IEEE Trans. on MTT*, Vol. 58, No. 11, 3622–3628, 2010.
5. Lim, J.-S., Y.-C. Jeong, and D. Ahn, "A technique for reducing the size of microwave amplifiers using defected ground structure," *IEEE International Microwave Symposium Digest (MTT-S)*, 1153–1156, 2002.
6. Kim, C.-S., J.-S. Park, D. Ahn, and J.-B. Lim, "A novel 1-D periodic defected ground structure for planar circuits," *IEEE Microwave Guided Wave Letters*, Vol. 10, No. 4, 131–133, 2000.
7. Abdel-Rahman, A.-B., A. K. Verma, A. Boutejdar, and A. S. Omar, "Control of bandstop response of hi-lo microstrip low-pass filter using slot in ground plane," *IEEE Trans. on MTT*, Vol. 52, No. 3, 1008–1013, 2004.
8. El-Dain, A.-Z., A.-B. Abdel-Rahman, R.-E. Fat-Helbary, and A. M. Montaser, "Tunable-compact bandstop defected ground structure (DGS) with lumped element," *7th Intenational Multi-Conference on Systems, Signals and Devices (SSD)*, 1–3, 2010.

Miniaturization and Harmonic Suppression of a Novel Rat-race Coupler

Wei Song, **Hiroyuki Deguchi**, **and Mikio Tsuji**

Department of Electronics, Doshisha University, Kyotanabe, Kyoto 610-0321, Japan

Abstract— A 0.9 GHz conventional rat-race coupler has been miniaturized in three steps: First, characteristic impedance and electrical lengths of microstrip section has been adequately modified by using even and odd method to form a novel rat-race coupler. Second, T-shaped stub has been implemented to diminish the strip length. Third, a defected ground structure (DGS) is applied to the coupler to realize further miniaturization due to slow-wave effect. Besides, by using DGS, 30-dB suppression for the second and third harmonics are achieved while the fourth harmonic is suppressed below 30 dB by the T-shaped stub. The fabricated coupler occupies only 21.3% of a conventional one. The coupler characteristics remain comparable to that of a conventional coupler at the fundamental operating frequency.

1. INTRODUCTION

Rat-race hybrid couplers (RRC) are one of the basic components in microwave and millimeter wave applications such as power amplifiers, mixers and antenna front ends. Total electrical length of the conventional coupler is 1.5λ at fundamental operating frequency (f_0) and therefore it occupies a large circuit area [1]. It also has spurious passbands at harmonic frequencies of f_0. In order to remove passbands, generally a lowpass filter should be cascaded which will further increases occupying area as well as insertion loss. In [2], a periodic stepped-impedance ring has been proposed. Though the designed coupler occupies only 21.5% of the conventional rat-race coupler and has no passband up to the sixth harmonic, the second harmonic is not suppressed. The branch-line coupler proposed in [3] can realize up to the fourth harmonic suppression by introducing the defected ground structure (DGS). However, the extra microstrip section with DGS just below at each port further increases the volume and make it impossible to use.

In this paper, based on the rat-race coupler proposed in [4], a combination method of T-shaped stub [5] and spiral DGS [6] which can realize both miniaturization and harmonic suppression is taken into consideration. Using transmission-line theory, with each $\lambda/4$ section of a conventional rat-race coupler replaced by T-shaped stub and DGS on the ground, a novel rat-race coupler is proposed and fabricated. The newly designed coupler in compactness has the advantages of harmonic suppression has verified numerically and experimentally.

2. HEPTAGONAL COUPLER

The conventional rat-race coupler occupies a large area due to the six $\lambda/4$ section with the impedance $70.7\,\Omega$ as depicted in Fig. 1(a), especially at low operating frequency. From the conclusion proposed in [4], the rat-race coupler circuit can be singularly decided concerning the electrical length and characteristic impedance of each section. After setting the power division ratio equal
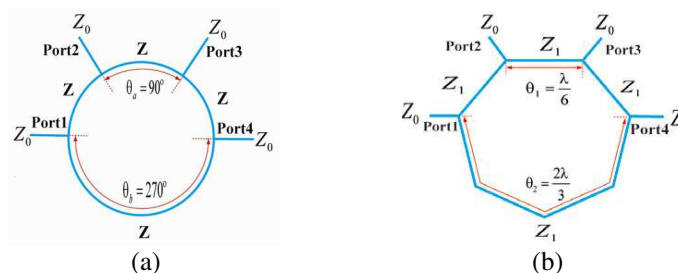

Figure 1: Configurations of rat-race couplers ($Z_0 = 50\,\Omega$): (a) conventional ($Z = 70.7\,\Omega$) and (b) reduced heptagonal coupler ($Z_1 = 70.7\,\Omega$).

in two output ports, the design formulas can be given as follows:

$$\theta_2 = 180° + \theta_1 \tag{1}$$

$$Z_1 = Z_0\sqrt{\left\{3 - \frac{1}{2}\left(\cot^2\frac{\theta_1}{2} + \tan^2\frac{\theta_1}{2}\right)\right\}} \tag{2}$$

Here, $50\,\Omega$ for the port impedance. One possible solution is chosen and depicted in Fig. 1(b). To make it easy to introduce the T-shaped stub design step, the $2\lambda/3$ section is divided into four $\lambda/6$ sections. Now a heptagonal rat-race coupler is proposed. With the modification, the area of the heptagonal coupler is only 60% of a conventional one.

3. IMPLICATION OF T-SHAPED STUB

In order to realize further miniaturization, here T-shaped stub is introduced in place of the $57.7\,\Omega$ section, as depicted in Fig. 2(a). The $ABCD$ matrix of the T-shaped stub can be obtained by multiplying the $ABCD$ matrix of each component together to get:

$$\begin{bmatrix} A & B \\ C & D \end{bmatrix} = \begin{bmatrix} \cos\theta_2 & jZ_2\sin\theta_2 \\ j\frac{1}{Z_2}\sin\theta_2 & \cos\theta_2 \end{bmatrix}\begin{bmatrix} 1 & 0 \\ j\frac{1}{Z_3}\sin\theta_3 & 1 \end{bmatrix}\begin{bmatrix} \cos\theta_2 & jZ_2\sin\theta_2 \\ j\frac{1}{Z_2}\sin\theta_2 & \cos\theta_2 \end{bmatrix} \tag{3}$$

The $ABCD$ matrix of $a\lambda/6$ microstrip section is:

$$\begin{bmatrix} A & B \\ C & D \end{bmatrix} = \begin{bmatrix} \cos\theta_1 & jZ_0\sin\theta_1 \\ j\frac{1}{Z_1}\sin\theta_1 & \cos\theta_1 \end{bmatrix}_{\theta_1=\frac{\lambda}{6},Z_1=57.7\Omega} \tag{4}$$

By equating the matrix of (3) and (4)

$$Z_2 = \cot\theta_2 \cdot \frac{1-\cos\frac{\lambda}{6}}{\sin\frac{\lambda}{6}} \cdot Z_1 \tag{5}$$

$$Z_3 = \tan\theta_3 \cdot \frac{\cos^2\theta_2}{\cos 2\theta_2 - \cos\frac{\lambda}{6}} \cdot \frac{1-\cos\frac{\lambda}{6}}{\sin\frac{\lambda}{6}} \cdot Z_1 \tag{6}$$

θ_3 is fixed 22.5 degree so that the T-shaped stub works like a bandstop filter at the fourth harmonic. Fig. 2(b) shows the curve of Z_2 and Z_3 as a function of θ_2. Due to the limitation of the microstrip-line impedance, θ_2 should be between 18 degree and 27 degree.
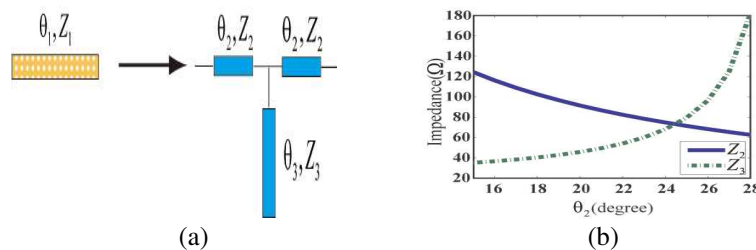
Figure 2: (a) Proposed T-shaped stub and (b) Z_2, Z_3 variation with θ_2 when $\theta_3 = 22.5°$.
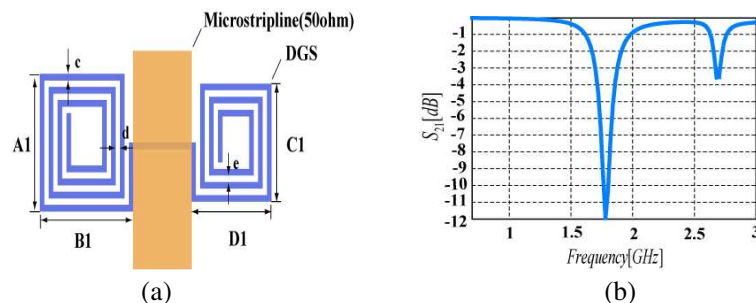

Figure 3: (a) Geometry of the proposed spiral DGS and (b) simulated transfer characteristics of asymmetric DGS.

4. DUAL-BAND REJECTION SPIRAL DGS

In Fig. 3(a), the geometry of an asymmetric spiral DGS on the ground is shown. Simulation result indicates this single asymmetric DGS provides two resonant frequencies corresponding to the left side defect structure and the right side defect structure [5]. The characteristic impedance of the line is assumed to be $50\,\Omega$ here and the simulation is performed by HFSS. As it can be seen in Fig. 3(b), S_{21} is below 12 dB at the operating frequency 1.8 GHz and below 4 dB at the operating frequency 2.7 GHz. The two resonant frequencies can be adjusted by changing the dimensions of the spiral DGS. Obviously, it can be used to suppress the second and third harmonics if the fundamental operating frequency is set at 0.9 GHz.

5. FABRICATION AND MEASUREMENT

Under the above investigation, a novel rat-race coupler with spiral DGS and T-shaped stub is designed and fabricated on a 1 mm substrate of dielectric constant $\varepsilon_r = 2.8$, shown in Fig. 4(a). $\theta_2 = 22.5°$ is chosen. Correspondingly, impedance values are $Z_1 = 71.31\,\Omega$ and $Z_2 = 79.24\,\Omega$. With the existence of DGS, due to the slow-wave effect, the practical values of L_2, L_3, W_2 and W_3 depicted in Fig. 4(b) are 10.4 mm, 13.5 mm, 2.6 mm and 1.14 mm, respectively. Open end effects and junction discontinuity are compensated by adjusting the length of the stubs and the arms of this coupler [6]. Fig. 4(c) shows photographs of the fabricated coupler. Fig. 5(a), Fig. 5(b), Fig. (5) and Fig. 5(d) compare the measured results with the simulated ones. The measured centre frequency is 0.91 GHz which has a little frequency shift due to the fabrication error. The second, third and fourth harmonic are all suppressed below 30 dB. The power imbalance and phase difference between S_{21} and S_{31} is 0.1 dB and -182.7 degree. The power imbalance and phase difference between S_{21} and S_{32} is 0.15 dB and 1.7 degree. The fifth harmonic is also suppressed below 20 dB in the measurement

(a)   (b)   (c)   (d)
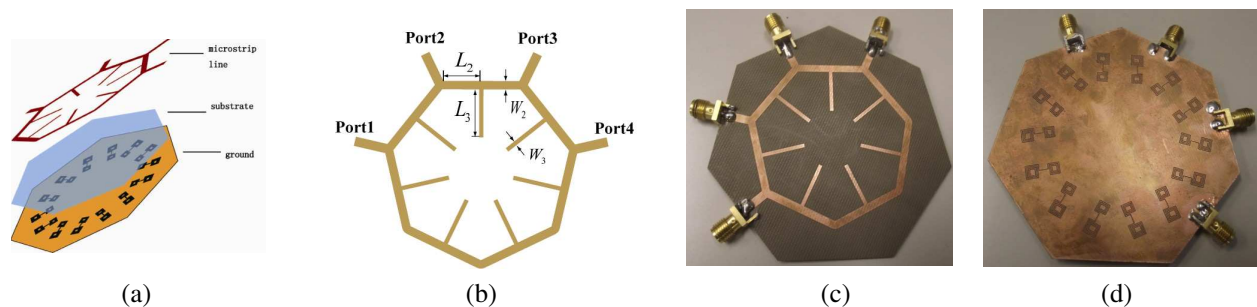
Figure 4: (a) Geometry of the top, middle and bottom layer of the coupler, (b) the dimension of the top layer, (c) photograph of the top side and (d) photograph of the bottom side.
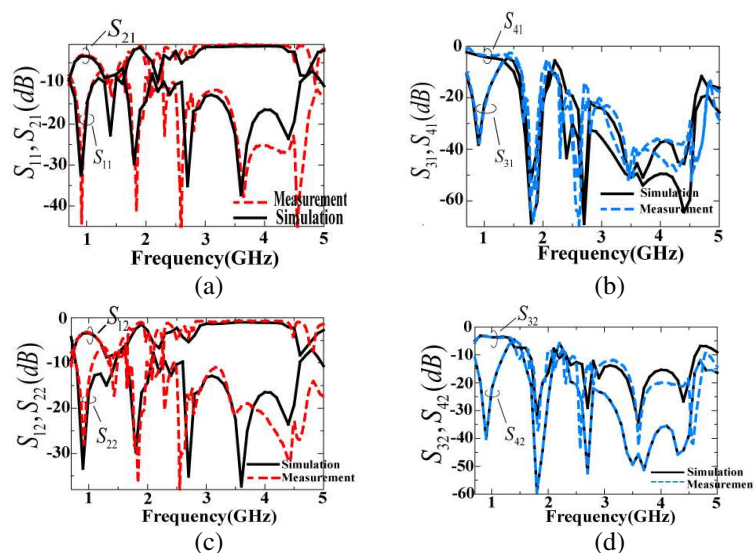

(a)   (b)

(c)   (d)

Figure 5: S-parameters variation of the coupler (a) S_{11} and S_{21} (b) S_{31} and S_{41} (c) S_{12} and S_{22} (d) S_{32} and S_{42}.

result. After some analysis, it is mainly due to the third frequency resonant point of the DGS. Fig. 4(c) and Fig. 4(d) show the photos of the fabricated coupler.

6. CONCLUSION

This paper presents a combination method of spiral DGS and T-shaped structure which can realize harmonic suppression and miniaturization to rat-race coupler. Up to the fourth harmonic is deeply suppressed by the effect of spiral DGS and T-shaped structure. The function of this new coupler remains comparable to the conventional rat-race coupler at the fundamental frequency. Besides, the novel coupler occupies only 21.3% area of a conventional one. As no holes and lumped elements are used in the design procedure, it's easy to fabricate and cost less. This method can also be used in other microwave components.

ACKNOWLEDGMENT

Thank Mr. Nakatsukasa for offering help in measurement.

REFERENCES

1. Pozar, D. M., *Microwave Engineering*, J. Wiley & Sons, New York, 1988.
2. Kuo, J.-T., J.-S. Wu, and Y.-C. Chiou, "Miniaturized rat race coupler with suppression of spurious passband," *IEEE Microwave and Wireless Components Letters*, Vol. 17, No. 1, 46–48, Jan. 2007.
3. Tong, J.-Z., X.-Q. Chen, and X.-W. Shi, "A wide stopband branch-line coupler using defected ground structure," *Microwave and Millimeter Wave Technology of International Conference*, 66–69, Chengdu, China, May 2010.
4. Mandal, M. K. and S. Sanyal, "Reduced-length rat-race couplers," *IEEE Transactions on Microwave Theory and Techniques*, Vol. 55, No. 12, 2593–2598, Dec. 2007.
5. Tu, W.-H. and K. Chang, "Compact second harmonic-suppressed bandstop and bandpass filters using open stubs," *IEEE Transactions on Microwave Theory and Techniques*, Vol. 54, No. 6, 2497–2502, Jun. 2006.
6. Woo, D.-J. and T.-K. Lee, "Suppression of harmonics in wilkinson power divider using dual-band rejection by asymmetric DGS," *IEEE Transactions on Microwave Theory and Techniques*, Vol. 53, No. 6, 2139–2144, Jun. 2006.
7. Gupta, K. C., R. Garg, I. Bhal, and P. Bhartia, *Microstrip Lines and Slot Lines*, Artech House, Boston, 1996.

MAGIC2D Implicit Particle Pusher Description and Test

Andrew J. Woods and Lars D. Ludeking

Alliant Techsystems (ATK), 8560 Cinderbed Road, Suite 700, Newington, VA 22122, USA

Abstract— The MAGIC2D electromagnetic computer code [1] has been upgraded to include an implicit particle-in-cell (PIC) update scheme (particle "pusher") for increased time steps and stability in beam-plasma simulations. The adjustable damping implicit update method of Friedman [2] allows selectable attenuation of modes in a plasma. The particle update method and testing within MAGIC2D are described, and a dramatically improved low temperature plasma calculation is presented.

1. INTRODUCTION

The MAGIC2D finite-difference time domain (FDTD) electromagnetic (EM) computer code [1] has been modified to include an implicit particle-in-cell (PIC) update scheme (particle "pusher") designed to enable increased time steps and stability in beam-plasma simulations. The adjustable damping implicit update method of Friedman [2, 3] has been incorporated. This treatment allows greater economy in charged particle plasma simulations through increased time steps and stability. The method also enables selectable attenuation of EM modes so that longer term plasma oscillations of interest can be emphasized.

2. APPROACH

Our approach has been to first develop a simple particle pusher one-dimensional (1D) finite-difference code model, named PPUSH1, which incorporates implicit PIC as outlined in [3]. Particles are started with initial energy and applied electric field, and the motion computed with FDTD update using an adjustable damping parameter. We have replicated the electron motion reported in [3] for a potential well with electric field linear in electron excursion distance from the origination point. This model represents the simplest form of plasma oscillation where the particles oscillate about the stationary positive charge left behind. The essential result is that for a given $\omega_0 \Delta t$ $(= 0.42$ in the test case) where ω_0 is the frequency of oscillation and Δt is the time step, the damping parameter θ can be chosen between 0 (no damping) and 1.0 ($10\times$ damping in 16 periods for our test problem). Hence, for a mix of frequencies in a complex many-particle system, unwanted higher frequency oscillations can be adjustably diminished while preserving the lower values of greater interest.

Subsequent to verification against [3], the implicit PIC model was extended to three dimensions and relativistic dynamics, tested for magnetic field effects, and incorporated into MAGIC2D. Several validation tests against the 1D code and the original reference were conducted and reported [4].

3. IMPLICIT METHOD

The implicit particle update method employs fields in the current time step for the particle properties of acceleration, velocity and positions. Numerical analysis shows this method is stable [5–7] as contrasted to the explicit particle method where only fields from the previous time step are employed.

The default particle update method in MAGIC2D is the Boris split time step explicit scheme described elsewhere [8]. The newly-implemented implicit treatment is presented here. In the following, the nomenclature of the original references has been largely retained in each case. Bold characters signify vectors in this publication. The particle velocity is $\mathbf{v}$, acceleration is $\mathbf{a}$, electric field is $\mathbf{E}$, magnetic induction is $\mathbf{B}$, q/m is the electron charge to mass ratio, mc^2 is the rest mass, and $\gamma = [1 - (v/c)^2]^{-1/2}$ is the relativistic mass expansion factor. MKS units are employed here, and the original expressions modified for relativistic effects.

The implicit method, which also uses the Boris split time step treatment, follows Friedman's algorithm #1 [2, 3]. It uses the damping parameter theta (θ) for the implicit PIC c0-to-d1 fraction $(0.0 (= c0$ method) to 1.0 (= d1 method)). In between values of θ combine the c0 and d1 treatments giving the analyst some control over the degree of damping of unwanted high frequency modes. Both c0 and d1 methods are implicit as described in [3, 5] and their references. As is detailed in [5], the methods differ in that c0 is entirely conservative (no damping), while d1 damps high frequencies

owing to the retention of higher order terms in the expansion for acceleration versus position on the finite difference grid.

The current time step n is entered with particle quantities $\underline{\mathbf{x}}_n$, $\underline{\mathbf{v}}_{n-1/2}$, $\underline{\mathbf{a}}_{n-2}$, $\Omega_{n-1} = q\mathbf{B}_{n-1}/(m\gamma_{n-3/2})$, $\gamma_{n-1/2}$, and with $\mathbf{E}_n(\underline{\mathbf{x}}_n)$ and $\mathbf{B}_n(\underline{\mathbf{x}}_n)$ interpolated from the mesh to the particle positions. The final push is:

$$\mathbf{a}_n = (q/m)\mathbf{E}_n(\underline{\mathbf{x}}_n)/\gamma_{n-1/2} \tag{1}$$

$$\Delta\mathbf{v}_{n-1/2} = (\Delta t/2)(\mathbf{a}_n + \Delta\mathbf{v}_{n-1/2} \times \Omega_{n-1}) \tag{2}$$

$$\mathbf{v}_{n-1/2} = \underline{\mathbf{v}}_{n-1/2} + \Delta\mathbf{v}_{n-1/2} \tag{3}$$

$$\mathbf{x}_n = \underline{\mathbf{x}}_n + \Delta t\mathbf{v}_{n-1/2} \tag{4}$$

$$\underline{\mathbf{A}}_{n-1} = (\theta/2)\mathbf{a}_n + (1-\theta/2)\underline{\mathbf{a}}_{n-2} \tag{5}$$

$$\underline{\mathbf{a}}_{n-1} = (1-\theta/2)\mathbf{a}_n + (\theta/2)\underline{\mathbf{a}}_{n-2} \tag{6}$$

$$\Omega_n = q\mathbf{B}_n(\underline{\mathbf{x}}_n)/(m\gamma_{n-1/2}) \tag{7}$$

$$\underline{\mathbf{v}}_{n+1/2} = \mathbf{v}_{n-1/2} + (\Delta t/2)(\underline{\mathbf{A}}_{n-1} + \mathbf{v}_{n-1/2} \times \Omega_n) \tag{8}$$

$$\gamma_{n+1/2} = \gamma_{n-1/2} + [q\Delta t/(2mc^2)]\mathbf{E} \cdot (\underline{\mathbf{v}}_{n+1/2} + \underline{\mathbf{v}}_{n-1/2}) \tag{9}$$

(Optional) corrector pass:

$$\mathbf{v}^+ = \underline{\mathbf{v}}_{n+1/2} \tag{10}$$

$$\underline{\mathbf{v}}_{n+1/2} = \gamma_{n-1/2}/\gamma_{n+1/2}\{\underline{\mathbf{v}}_{n-1/2} + [q\Delta t/(m\gamma_{n-1/2})][\mathbf{E} + 0.5(\mathbf{v}^+ + \underline{\mathbf{v}}_{n-1/2}) \times \mathbf{B}]\} \tag{11}$$

$$\gamma^{++} = \gamma_{n+1/2} + [q\Delta t/(mc^2)]\mathbf{E} \cdot (\underline{\mathbf{v}}_{n+1/2} + \underline{\mathbf{v}}_{n-1/2}) \tag{12}$$

$$\gamma_{n+1/2} = \gamma^{++} \tag{13}$$

$$\underline{\mathbf{x}}_{n+1} = \mathbf{x}_n + \Delta t\underline{\mathbf{v}}_{n+1/2} \tag{14}$$

The positions $\underline{\mathbf{x}}_{n+1}$ are the free-streaming pre-push results for the next step. Note that matrix inversions are required in steps 2 and 8. The quantities $\underline{\mathbf{v}}_{n+1/2}$ and $\underline{\mathbf{x}}_{n+1}$ provide the information for the current densities required by Maxwell's equations on the grid.

4. IMPLEMENTATION

Several modifications of the basic method have been employed in MAGIC2D. Differences from time step to time step in the relativistic factor have been ignored in the matrix inversion process in steps 2 and 8. Equations (2) and (7) above have been listed as in [3], but in our case, $\mathbf{B}_n$ is only supplied for the particle positions $\underline{\mathbf{x}}_n$ at the beginning of the step as opposed to $\mathbf{x}_n$. We have found the optional corrector iteration step to be effective in reducing unwanted artificial particle heating. It is based on the methodology detailed in [9] for the ABORC code which has been widely employed for a variety of analytical and experimental electron beam, spacecraft charging, x-ray, and air plasma projects [9–12].

5. VERIFICATION TESTS

Subsequent to verification against [3], the implicit PIC routine was extended to three dimensions and relativistic dynamics, tested for magnetic field effects, and incorporated into MAGIC2D. The Lorentz equation particle update code closely resembles the 1D subroutine checked out previously. Additional successful tests included particle deceleration in self fields to analytically solvable positions, and acceleration through known potentials to relativistic levels. The new method agrees with the previous explicit treatment in these simple tests where both have sufficiently small time step.

The new implicit particle pusher in MAGIC2D has been described and tested as summarized in [4]. Verification tests have shown: 1) agreement with the original author of the method, 2) agreement between one- and two-dimensional implementations for an electric field-driven case, 3) agreement with analysis for gyro motion in a relativistic magnetic field-driven case, and 4) agreement with the baseline explicit treatment when both have adequate numerical grids with some slight improvement seen for the new method.

A more rigorous example test problem configuration is shown in Fig. 1. A volume bounded by symmetry conditions left and right, top and bottom is filled with movable negatively charged

particles and effectively stationary ions. The density is $n_e = 3.3 \times 10^{13}$ #/cc leading to an expected plasma oscillation frequency of

$$\omega = (n_e e^2 / \varepsilon_0 m_e)^{1/2} \sim 3.2 \times 10^{11} \text{ radians/s.} \tag{15}$$

The electron charge e and mass m and the permittivity of freespace are used in the above expression. The approximate initial temperature T_e is between 4 and 6 keV depending on whether the average or most probable velocity squared is used to relate our initial mono-energetic particles' velocity to temperature. The particles move only in their self fields generated by the charge separation. The Debye length is $\lambda \sim 0.14$ mm compared to the zone sizes Δr, $\Delta z = 0.5$ mm leading to the
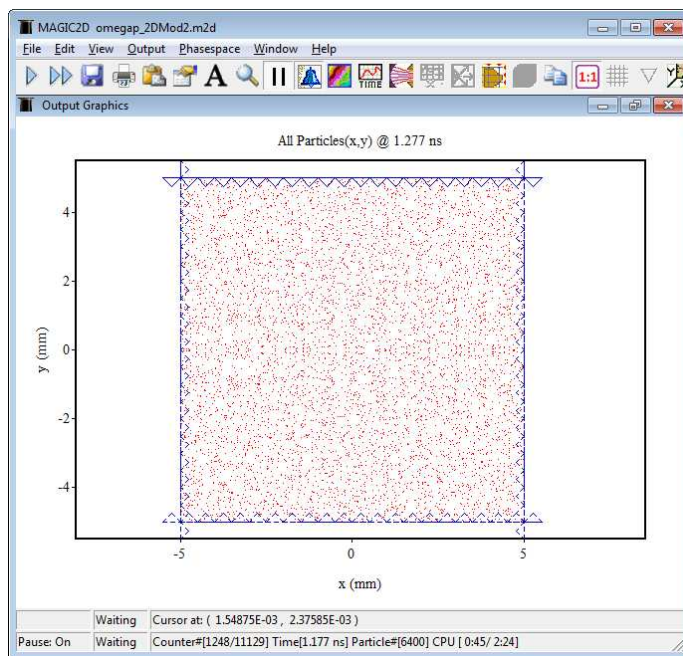
Figure 1: Cross section of volume filled with initial population of charged particles.
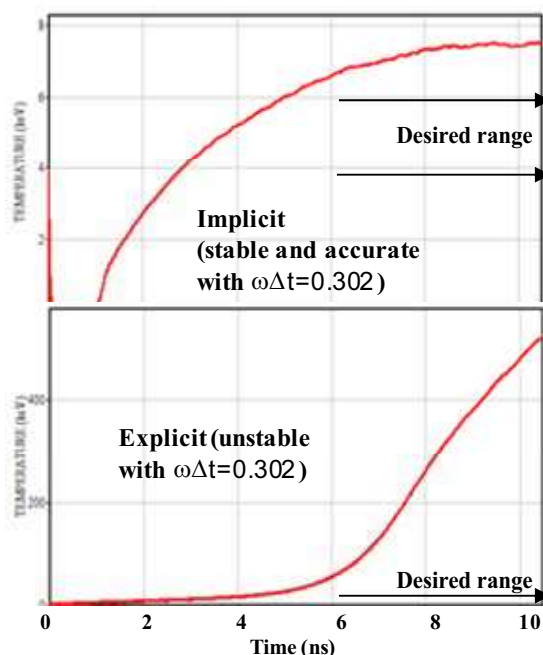
Figure 2: MAGIC2D plasma temperature results showing stability of implicit particle update (top) compared to unphysical values from the explicit model (bottom).

expectation of numerical instability for the explicit treatment. The default code time step of 80% of the centered-difference Courant criterion was used in all the calculations presented here. This resulted in $\omega\Delta t = 0.302$ for the time step $\Delta t = 9.43 \times 10^{-13}$ s which was employed.

Benefits of the implicit treatment are seen in Fig. 2, where the electron temperature versus time is plotted. The implicit model results with $\theta = 1.0$ are shown on the top and standard explicit on the bottom. The implicit curve reaches steady state at $T_e \sim 7.5$ keV reasonably close to the expected range of 4 and 6 keV. The artificial heating of the explicit results is $\sim 100\times$ the desired value in the short simulation time.

The unwanted temperature in Fig. 2 (bottom) is due to failure to resolve the Debye length; it is largely avoided with the implicit capability even with the coarse grid (top). As a further illustration of explicit grid requirements, a dramatically improved explicit result was obtained with zone sizes Δr, $\Delta z = 0.15$ mm $\sim \lambda \sim 0.14$ mm (5.9 keV for the improved grids in the same short time interval — versus the erroneous 520 keV of the larger grid). The execution time increased greatly ($30\times$) in this more highly resolved case, however.

Only minor sensitivity to the damping parameter was observed in this test problem ($T_e = 7.64$ keV with $\theta = 0.0$ versus 7.59 keV with $\theta = 1.0$). Much greater differences occurred when the optional corrector pass (Equations (10)–(13)) was not used ($T_e > 21$ keV in the same short time interval with $\theta = 1.0$ and > 294 keV with $\theta = 0.0$).

6. SUMMARY AND CONCLUSIONS

The new implicit particle pusher in MAGIC2D has been described here, and validation tests summarized. The method has been further exercised on an important class of low energy plasma problems and found to produce a superior result compared to the explicit method. The temperature of a population of electrons in a plasma was maintained at nearly the correct value in less than 3% the computational time required by the conventional explicit treatment.

We conclude the implicit particle pusher in MAGIC2D is ready for export, and useful to users. The new algorithm, available for both 2D and 3D simulations in MAGIC version 3.2.0 [13], will enable users to select damping of high-frequency plasma modes thus concentrating on fundamental frequencies of interest. This additional user tool can prevent instabilities resulting from ionization growth beyond the time step limit for explicit particles, for example.

Important improvements to the MAGIC code suite are planned which will more fully utilize the implicit update scheme. Particle transport through more than one spatial zone per time step will allow greater time steps for a given cell size. Greater accuracy for simulations of thin atmosphere ionizing plasmas will be possible with particle coalescing improvements underway in our combined particle-fluid plasma treatment. This method, in which macro-particles can migrate between the particle and fluid representations, has been previously shown to be effective for problems of low energy plasmas subjected to high fields creating runaway electrons [10, 11, 14].

REFERENCES

1. Goplen, B., et al., "User-configurable MAGIC for electromagnetic PIC calculations," *Computer Physics Comm.*, 87, 1995, http://www.magictoolsuite.com.

2. Friedman, A., "Implicit multiscale PIC and related topics," *Workshop on Multiscale Processes in Fusion Plasmas*, UCLA, Jan. 2005, http://hifweb.lbl.gov/public/slides/.

3. Friedman, A., "A second-order implicit particle mover with adjustable damping," *Journal of Computational Physics*, Vol. 90, No. 2, 292–312, Oct. 1990.

4. Woods, A. J. and L. D. Ludeking, "MAGIC implicit particle pusher description and validation," *18th IEEE International Pulsed Power Conference*, Chicago, IL, Jun. 19–23, 2011, http://ppc.missouri.edu/. *Pulsed Power Conference, PPC '11, IEEE*, 2011, ieeexplore.ieee.org.

5. Cohen, B. I., A. B. Langdon, and A. Friedman, "Implicit time integration for plasma simulation," *Journal of Computational Physics*, Vol. 46, 15–38, 1982.

6. Birdsall, C. K. and A. B. Langdon, *Plasma Physics via Computer Simulation*, McGraw-Hill, 1985, ISBN 0-07-005371-5.

7. Langdon, A. B., "Electromagnetic direct implicit PIC simulation," UCRL-88979, March 1983.

8. Boris, J. P., "Relativistic plasma simulation-optimization of a hybrid code," *Proceedings of the 4th Conference on Numerical Simulation of Plasmas*, 3–67, Naval Research Laboratory, Washington, D.C., Nov. 1970.

9. Woods, A. J. and T. N. Delmer, "The Arbitrary Body of Revolution Code (ABORC) for SGEMP/IEMP," DNA-4348-T, Jul. 1976.

10. Chan, P. C. and A. J. Woods, "Computation of vacuum and 3-Torr IEMP responses and comparison with benchmark experiments," *IEEE Transactions on Nuclear Science*, Vol 32, No. 6, 4441–4443, Dec. 1985.

11. Woods, A. J., W. E. Hobbs, and E. P. Wenaas, "Air effects on the external SGEMP response of a cylinder," *IEEE Transactions on Nuclear Science*, Vol. 28, No. 6, Dec. 1981.

12. Woods, A. J. and E. P. Wenaas, "Spacecraft discharge electromagnetic interference coupling models," *Journal of Spacecraft and Rockets*, Vol. 22, No. 3, May–Jun. 1985.

13. Woods, A. J. and L. D. Ludeking, "MAGIC3D EM-PIC code implicit particle pusher description and test," abstract prepared for *Progress In Electromagnetics Research Symposium*, Suzhou, China, Sept. 12–16, 2011, withdrawn, re-submitted to *Progress In Electromagnetics Research Symposium*, Kuala Lumpur, Malaysia, Mar. 27–30, 2012.

14. Welch, D. R., T. C. Genoni, R. E. Clark, and D. V. Rose, "Adaptive particle management in a particle-in-cell code," *J. Comp. Phys.*, Vol. 227, 143, 2007.

Synthesis of Composite Materials with Conductive Aligned Cylindrical Inclusions

M. H. Nisanci, **F. de Paulis**, **D. Di Febo**, and **A. Orlandi**

UAq EMC Laboratory, University of L'Aquila, L'Aquila, Italy

Abstract— Composite materials are largely studied due to their mechanical and electrical performances. The characterization of a composite material usually goes toward the development of an equivalent homogeneous model. This study is based on the Maxwell Garnett homogenization theories, and it is focused on synthesizing a composite material starting from the equivalent dielectric permittivity of a homogeneous material. The approach considers a composite made by an host material with constant permittivity and aligned conductive cylindrical inclusions. The proposed approach can be feasible for synthesizing carbon fiber based materials, and achieving a desired shielding effectiveness. The proposed procedure is validated through numerical simulations of three synthesized composite materials.

1. INTRODUCTION

Many of our modern technologies today require materials with complex performances in terms of both electric and mechanical properties [1–3]. These features can be achieved with unusual combinations of properties that cannot be met by conventional homogeneous materials, but they are rather obtained combining different materials together, obtaining the so called composite structures. These materials have many advantages allowing for high design flexibility, since they can be adapted to achieve complex shapes and ad-hoc strength levels, as well as providing electromagnetic protection.

Electromagnetic shielding is one of the main concerns for electrical engineers designing enclosures containing complex electronic systems [1–3]. The electronics, in fact, can be sensible to the surrounding EM environment, and also because it can act as noise source, to be dampened for avoiding EM interference toward other systems around it. Previous studies are mainly focused on the analysis of the composite EM properties; the target is to get the effective electrical permittivity ε_{eff} of an equivalent homogeneous medium from the physical dimensions and electrical properties of the composite ingredients, by using some mixing rules, i.e., the Maxwell Garnett approximation [4]. Then the obtained frequency dependent ε_{eff} can be employed in 3D EM simulators to evaluate the electromagnetic behavior of the composite, and thus its shielding performances [1–3]. This work is focused on the synthesis of composites consisting of a host material with aligned cylindrical inclusions. The aim of this study is to extract the geometrical properties of the composite constituents such as the inclusion diameter, length, and its conductivity starting from the known frequency-dependent effective dielectric permittivity. The relationships between a specific shielding effectiveness value and a homogeneous material are well known [1, 2, 5]; however the synthesis of an homogeneous material could lead to parameters such as panel thickness, material conductivity etc. that are not associated to any feasible product, or they do not satisfy the project requirements. The larger flexibility offered by composite materials provides more degrees of freedom in the material design, allowing the variation of several parameters to meet the desired requirements.

2. SYNTHESIS PROCEDURE

The synthesis procedure of the composite material is based on the specifications in terms of shielding effectiveness (SE) properties associated to a homogeneous material. Thus the panel size and the frequency-dependent effective permittivity ε_{eff} are used as constrains for designing the composite material that will have the same shielding performances as the homogeneous counterpart. The study assumes that ε_{eff} can be described by a Debye model, as in (1), along each direction, x, y, and z. The composite panel to be derived will be characterized by a constant permittivity host material, and by conductive aligned cylindrical inclusions with $\varepsilon_i(\omega)$, as described by (2), where σ_i denotes the conductivity of the inclusion material, $\varepsilon_{i\infty}$ is the high frequency ("optic limit") relative permittivity and $\varepsilon_0 = 8.85 \cdot 10^{-12}$ F/m is the permittivity of free space. The synthesis procedure
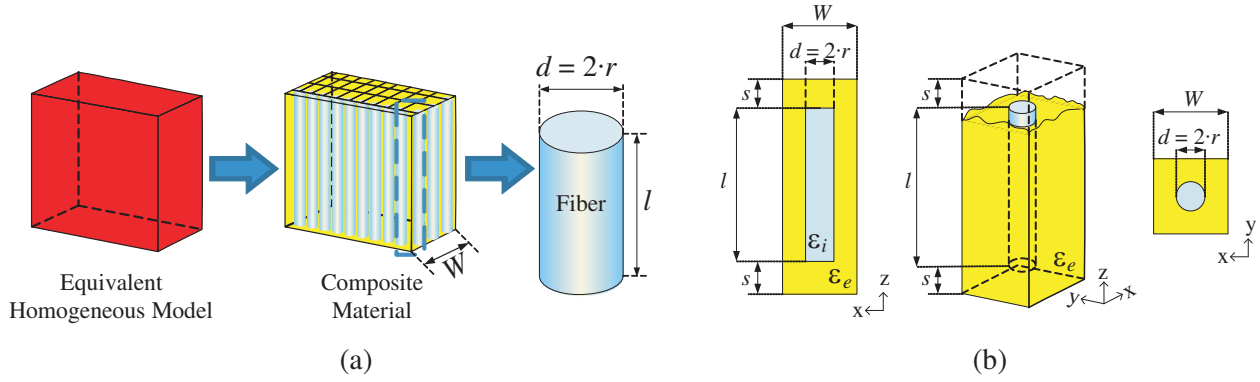
Figure 1: (a) Flowchart to synthesize a composite with aligned cylindrical inclusions. (b) Model views of one volume.

of composite structure is shown in Figure 1(a).

$$\varepsilon_{eff(x,y,z)}(\omega) = \varepsilon_{\infty Dx,y,z} + \frac{\varepsilon_{sDx,y,z} - \varepsilon_{\infty Dx,y,z}}{1 - j\omega\tau_{Dx,y,z}} \tag{1}$$

$$\varepsilon_i(\omega) = \varepsilon_{i\infty} + \frac{\sigma_i}{j\omega\varepsilon_0} \tag{2}$$

In [2, 3] the analytical derivation for extracting the Debye dependent $\varepsilon_{eff}(\omega)$ associated to a homogeneous model is provided, starting from the electrical and geometrical properties of a composite material with aligned cylindrical inclusions. They depend on the volume fraction f (percentage of inclusion volume with respect to the overall material volume), on the host and inclusion permittivity parameters, ε_e and ε_i, respectively, and on the depolarization factors $N_{x,y,z}$. The depolarization factors depend on the aspect ratio a, the ratio between inclusion length l and diameter d. The analytical relationships in (3), derived in [2, 3], are employed herein for achieving the inverse procedure. The study carried out is based on a SE specified only along the inclusion direction (i.e., along the z axes), that allows to synthesize a composite panel with one layer of oriented inclusions; thus the effect of the composite along the x and y directions will be neglected. The three equations in (3), taking into account only the characterization of the equivalent homogeneous model along the z direction, contains six unknowns, f, N_z, W, ε_e, $\varepsilon_{i\infty}$, σ_i. Usually some additional constrains coming from mechanical and electrical specifications force to fix some of these unknowns. Thus the following proposed procedure assumes W, ε_e and $\varepsilon_{i\infty}$ to be fixed. The Figure 1(b) shows the details of one volume of the material of interest with aligned cylindrical inclusions.

$$\varepsilon_{sDx,y,z} = \frac{\varepsilon_e(fN_{x,y,z} - N_{x,y,z} - f)}{N_{x,y,z}(f-1)} \tag{3a}$$

$$\varepsilon_{\infty Dx,y,z} = \frac{\varepsilon_e(\varepsilon_e(fN_{x,y,z} - N_{x,y,z} - f + 1) + \varepsilon_{i\infty}(-fN_{x,y,z} + N_{x,y,z} + f))}{\varepsilon_e(fN_{x,y,z} - N_{x,y,z} + 1) + \varepsilon_{i\infty}(-fN_{x,y,z} + N_{x,y,z})} \tag{3b}$$

$$\tau_{Dx,y,z} = \frac{\varepsilon_0(\varepsilon_e(-fN_{x,y,z} + N_{x,y,z} - 1) + \varepsilon_{i\infty}N_{x,y,z}(f-1))}{\sigma N_{x,y,z}(f-1)} \tag{3c}$$

Two equations for the volume fraction f can be derived from (3a) and (3b), $(f\varepsilon_{sDz}, N_z)$ and $(f\varepsilon_{\infty Dz}, N_z)$; then they can be compared and solved for N_z, achieving (4). The depolarization factor N_z can be put into either $(f\varepsilon_{sDz}, N_z)$ or $(f\varepsilon_{\infty Dz}, N_z)$ to obtain the expression for f, as in (5). The volume fraction is defined as the ratio between inclusion volume $(V_i = \pi l r^2)$ and the overall volume $(V_{tot} = (l + 2s)W^2)$; assuming that $l \gg s$, then f can be approximated as $\pi r^2/W^2$. After the volume fraction f is computed using (5), the inclusion radius r can be evaluated as in (6), having the thickness of the composite panel W fixed from the mechanical specifications. The relationship between the depolarization factor N_z and the aspect ratio a in (7) cannot be solved for a; therefore a graphical solution can be employed. Once a is known, the inclusion length l can be obtained from $l = 2 \cdot r \cdot a$. The last unknown is the inclusion conductivity. The parameter

σ_i can be extracted from (3c) using the N_z and f values previously computed.

$$N_z = \frac{\varepsilon_e \left(\varepsilon_e - \varepsilon_{\infty Dz} \right)}{\varepsilon_{sDz} \left(\varepsilon_{\infty Dz} - \varepsilon_{\infty i} \right) + \varepsilon_{\infty Dz} \left(\varepsilon_{\infty i} - 2\varepsilon_e \right) + \varepsilon_e^2} \tag{4}$$

$$f = \frac{N_z \cdot \left(\varepsilon_{sDz} - \varepsilon_e \right)}{\varepsilon_e N_z - \varepsilon_e - \varepsilon_{sDz} N_z} \tag{5}$$

$$r = W \sqrt{\frac{f}{\pi}} \tag{6}$$

$$N_z = \frac{1}{2} \frac{\ln \left(\frac{a + \sqrt{a^2 - 1}}{a - \sqrt{a^2 - 1}} \right) a - 2\sqrt{a^2 - 1}}{\left(\sqrt{a^2 - 1} \right)^3} \tag{7}$$

$$\sigma_i = \frac{\varepsilon_0 \left(\varepsilon_e \left(-f N_z + N_z - 1 \right) + \varepsilon_{i\infty} N_z \left(f - 1 \right) \right)}{\tau_{Dz} N_z \left(f - 1 \right)} \tag{8}$$

3. RESULTS AND DISCUSSION

The proposed procedure is applied to synthesize three different composite materials starting from a panel made by an anisotropic homogeneous model. Since the composite panel to be synthesized will have inclusions aligned along one direction, the assumption that $\varepsilon_{eff(z)} \gg \varepsilon_{eff(x,y)}$ is considered, and the panel performances will take into account only the SE_z. The panel made by the homogenous material is characterized by the following parameters: $W = 0.6\,\mathrm{mm}$, $\varepsilon_{sDz} = 39330$, $\varepsilon_{\infty Dz} = 5.9$, $\tau_{Dz} = 1.714 \cdot 10^{-8}\,\mathrm{s}$ ($\varepsilon_{sDx,y} = 6.245$, $\varepsilon_{\infty Dx,y} = 5.8$, $\tau_{Dx,y} = 6.50 \cdot 10^{-14}\,\mathrm{s}$). This panel is able to achieve $\mathrm{SE}_z \approx 10\,\mathrm{dB}$ in the range of interest $100\,\mathrm{MHz}$–$20\,\mathrm{GHz}$, as computed from the analytical approach described in [1, 5], based on the transmission line approximation. The SE_z of the homogeneous panel is also evaluated by a 3D simulation using the time domain solver in CST MicroWave Studio [6]. In these simulations, the modeled structure is excited by a plane wave source $1\,\mathrm{mm}$ before the composite panel (at $x = -1\,\mathrm{mm}$) with the E-field linearly polarized along the z-direction; the E_z-field is evaluated $20\,\mathrm{mm}$ behind the composite layer (at $x = W + 20\,\mathrm{mm}$). The periodic boundary conditions are applied along the y and z axis to emulate an infinite structure along these directions. These boundary conditions allow to simulate just one material brick, as the one in Figure 1(b). The host material covers entirely the inclusions along the z direction for avoiding adjacent inclusions to touch each other (as emulated by the periodic boundary conditions applied along the z direction); thus the extra length $s = r/2$ is added to the host material. The thickness of the composite panel is assumed to come from a design requirement, thus is kept constant to $W = 0.6\,\mathrm{mm}$. The values of the input parameters ε_e and $\varepsilon_{i\infty}$ are varied, generating three different models described in Table 1. The goal is to derived three composites that employ different host and inclusion materials that are able to achieve the same shielding performances as the original homogeneous material ($\mathrm{SE} \approx 10\,\mathrm{dB}$). The step described in Section 2 and the Equations (4)–(8) are applied to the Model 1–3, obtaining the host and inclusion parameters listed in the right side of Table 1.

The three composite models are simulated and the SE_z is evaluated as the ratio between the $|E_z|$ without and with the panel [5]. The same 3D simulation is run for the case of the original panel made by the homogeneous model. The SE_z is also analytically evaluated as described in [1, 5], for the homogenous panel. The resulting SE_z values are shown in Figure 2. Beside same differences before $300\,\mathrm{MHz}$, all the three synthesized composite panels are able to achieve the $10\,\mathrm{dB}$ shielding associated to the original homogeneous model.

Table 1: Model description and derived parameters of the three composite materials.

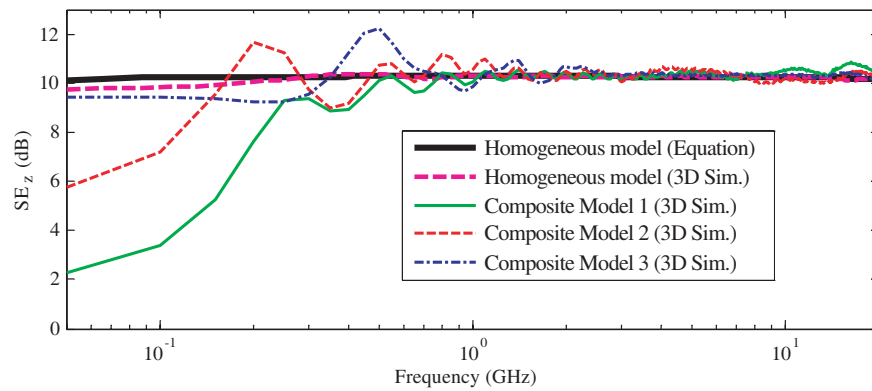| MODEL	Fixed Parameters			Obtained Parameters				
	W (mm)	ε_e	$\varepsilon_{i\infty}$	$N_z(a)$	f (%)	σ_i (S/m)	l (mm)	r (mm)
Model 1	0.6	9	5	$7.6 \cdot 10^{-4}$ (72.1)	77.08	26.353	42.8777	0.2972
Model 2	0.6	9	1.1	$1.41 \cdot 10^{-4}$ (186.9)	39.04	52.0483	79.0669	0.2115
Model 3	0.6	6	5	$1.22 \cdot 10^{-5}$ (716.8)	8.30	244.74	139.774	0.0975

Figure 2: Shielding effectiveness result comparison of the simulation models for conductive case.

4. CONCLUSIONS

A quick and efficient analytical procedure is proposed for synthesizing composite materials starting from an homogenous material. The derived approach can be used for composites characterized by constant permittivity host material, and conductive inclusions (such as carbon fibers). The shielding performances of a panel made by an homogenous material can be easily obtained through the analytical evaluation of the SE or by 3D simulations. Based on the knowledge of such material, the proposed synthesis procedure can be applied efficiently for achieving the electrical and geometrical parameters of a biphasic composite material with aligned cylindrical inclusions. This procedure is very flexible since it has many degrees of freedom; the designer can fix some parameters according to the design specifications (i.e., values given by commercial products, mechanical requirements etc.), and derive the other parameters to achieve the desired shielding performances. The procedure is validating through the synthesis of three composite materials with different inclusion geometry and conductivity values; the models are simulated with a 3D electromagnetic solver. The panels made by these materials are able to achieve the desired shielding effectiveness set by the initial homogeneous material.

REFERENCES

1. Koledintseva, M. Y., et al., "'Engineering of composite media for shields at microwave frequencies," *Proc. Int. IEEE Symp. Electromag. Compat.*, Vol. 1, 169–174, Chicago, August 2005.
2. Nisanci, M. H., F. de Paulis, M. Y. Koledintseva, and A. Orlandi, "Full-wave EMC simulations using Maxwell Garnett model for composites with cylindrical inclusions," *Proc. Int. IEEE Symp. Electromag. Compat.*, Long Beach, CA, USA, August 2011.
3. De Paulis, F., M. H. Nisanci, M. Y. Koledintseva, J. L. Drewniak, and A. Orlandi, "Derivation of homogeneous permittivity of composite materilas with aligned cylindrical inclusions for causal electromagnetic simulations," accepted for publication at *PIER B*.
4. Koledintseva, M. Y., R. E. DuBroff, and R. W. Schwartz, "A Maxwell Garnett model for dielectric mixtures containing conducting particles at optical frequencies," *Progress In Electromagnetics Research,* Vol. 63, 223–242, 2006.
5. Pozar, D. M., *Microwave Engineering*, 3rd Ed., John Wiley & Sons Inc, 2005.
6. Computer Simulation Technology, CST Studio Suite, 2011, http://www.cst.com/.

Analyzing Effects of Mobile Dipole Speed on Survey Data via Forward Modeling Technique

Nazabat Hussain, Norashikin Yahya, M. N. Karsiti, and Zainal A. Burhanuddin

Department of Electrical and Electronic Engineering, Universiti Teknologi Petronas
Bandar Seri Iskandar, Tronoh 31750, Perak, Malaysia

Abstract— Data collected from marine controlled-source electromagnetic (CSEM) survey has been used for hydrocarbon exploration in marine environment. The collected data is used to map the spatial distribution of seabed layers through inversion techniques. However, the accuracy of the seabed mapping depends on the quality of the survey data. There are several factors affecting the survey data; such as source-receiver geometry, source signal strength, seawater depth and geological complexities. This paper presents a method of finding optimum speed of mobile dipole source in marine CSEM survey, one of the factor affecting the survey data. The technique involved numerical solution of forward modelling using staggered-grid finite difference in spatial domain and forward time central space in temporal domain. The results show that the optimal speed obtained from the forward model can significantly improve the quality of survey data.

1. INTRODUCTION

The area of interest for geophysical exploration has now extended from continents and shallow water to deeper water. For many years, seismic has been quite successful in mapping the spatial distribution of earth layers. However, in marine geological terrain, high reflections in seismic data produce irregularities in survey data and introduce difficulty in data interpretation [1]. In such scenario, electromagnetic (EM) survey data is complementary to the existing seismic data which is proved to be give more reliable map then the seismic or EM data alone [11–13].

Controlled source electromagnetic (CSEM) is an EM geophysical survey which utilizes a mobile horizontal electric dipole (HED) as an active signal source [2]. In marine CSEM, the mobile dipole source is towed by a water vessel and moved along a certain traverse line. This is illustrated by Figure 1 where the moving direction of mobile HED is along the Traverse Line I while the receivers are located along the Traverse Line II.

The mobile dipole source is moved at a certain speed along the Traverse Line I while receivers continuously record the measurement of EM field. The EM field values are dependent on the geological conditions and the position of dipole source and the target depth is a function of signal frequency and the source-receiver position [3]. Therefore it is important for survey operators to follow the basic EM survey rule that is to have the source-receiver separation distance larger than the depth of the target area. This will guaranteed that the reflected EM field to be more dominant than the direct field.

Now, consider an inline survey set up as in Figure 1. Let t_0 and t_1 be the time at location point p_0 and p_1 respectively. The radiated EM energy at time t_0 will propagate through earth layers and
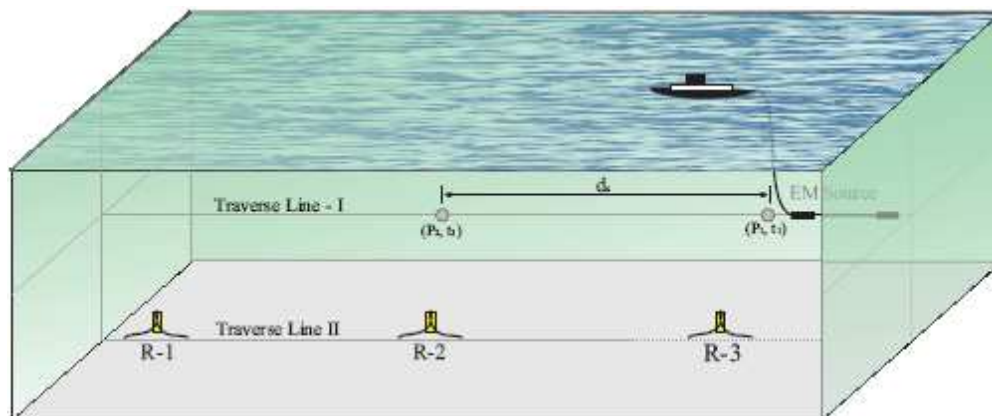
Figure 1: Plane view of inline profiling technique.

got reflected towards the seafloor. The receiver will record the reflected field at time t_1. If t_d is the time taken for the reflected EM signals to travel from point p_0 through the medium to reach at p_1, then t_1 can be expressed as

$$t_1 = t_0 + t_d. \tag{1}$$

The magnitude of t_d is dependent on electrical property of the medium and mobile dipole frequency. In order to calculate the source location at point p_1, the source should be at the same position until reflected signals are recorded by the receivers. However, in practical scenario the dipole source will not remained at the same position and this will caused inaccuracy in calculating the source location. This problem can be minimized if the dipole source travels at a low speed so here, our objective is to determine the optimal speed of mobile dipole source in marine CSEM.

In this paper, we used 1D forward modeling solved by finite difference method (FDM) and forward time centered space (FTSC) to find optimal speed of a mobile dipole source. This paper is organized as follows. In Section 2, we cover the principle of CSEM method and discuss the FDM and FTSC solution to the governing equations. In Section 3, we present simulation setup for three different isotropic models and subsequently present the result of 1D modeling. Finally, conclusion are given in Section 4.

2. METHODOLOGY

The E-field and H-field components of EM survey can be expressed by the quasi-static model of Maxwell's equations in frequency domain [4, 9, 10],

$$\nabla \times H = \sigma E + J_s, \tag{2}$$
$$\nabla \times E = -i\omega\mu H, \tag{3}$$

where σ is electrical conductivity of the medium, J_s is an external source, and μ is the magnetic permeability of the medium. The solution for general wave equation can be obtained for electric field by using the divergence operator on (3),

$$\nabla \times \nabla \times E = -i\omega\mu \left(\nabla \times H\right). \tag{4}$$

Using vector identity, in 1D modeling, Equation (4) can be cast in the form of

$$\nabla^2 E_z + \sigma\mu \frac{\partial E_z}{\partial t} = -i\omega\mu J_s. \tag{5}$$

Equation (5) is the general wave equation for electric field. The numerical solutions for this type of partial differential equation are discussed by Recktenwald [15]. The field governing equation of 1D geological model for spatial and temporal domain can be written as,

$$\nabla^2 E_z + \sigma\mu \frac{\partial E_z}{\partial t} = 0, \tag{6}$$

where $E_z = E\left(z, t\right)$ is a function of space and time. The solution of (6) is obtained for finite time interval and will be solved using Forward Time Centered Space (FTCS) scheme as outlined in [8] in which is used for discrete approximation in time and space domain. The FTSC scheme is a temporal derivative form and is given as

$$\frac{\partial E_z}{\partial t}\big|_{(t_n+1, x_k)} = \frac{E_k^{n+1} - E_k^n}{\Delta t} + O\left(\Delta t\right), \tag{7}$$

where Δt corresponds to time step size. Similarly, in spatial domain, the centrel difference approximation can be written as,

$$\frac{\partial^2 E_z}{\partial z^2}\big|_{(x_k)} = \frac{E_{k+1}^n - 2E_k^n + E_{k-1}^n}{\Delta z^2} + O\left(\Delta z^2\right). \tag{8}$$

By substititing Equations (7) and (8) into (6), the solution to E-field can be casted in the form of

$$E_z^{n+1} = E_z^n + \eta \left(E_{k+1}^n - 2E_k^n + E_{k-1}^n\right) + O\left(\Delta t\right) + O\left(\Delta z^2\right), \tag{9}$$

where the term $\eta = \Delta t / \left(\sigma \mu \Delta z^2 \right)$ is the stability factor affecting the amplitude of the EM field. Poor selection of η could result in oscilatory behaviour of EM field which leads to instability. For stable behaviour of EM field, η value should be less than 0.5 [10]. This value is derived from skin depth, δ and phase velocity, C_p equations in conductive medium,

$$\delta = 503.3 \left(\frac{1}{\sqrt{\sigma f}} \right), \tag{10}$$

$$C_p = 3162 \sqrt{\frac{f}{\sigma}}. \tag{11}$$

The skin depth is defined as a distance covered by the EM wave in a medium at which its amplitude fall to $1/e$ of its original value at the entry point of the medium [6]. The penetration depth for different conducting mediums at various skin depth are given in Table 1. The electrical conductivity for seawater, sediment and hydocarbon are assumed to be $3.2\,\text{S/m}$, $1\,\text{S/m}$ and $0.5\,\text{S/m}$ respectively.

The phase velocity, C_p of a wave travelling in a conducting medium is a function of electrical conductivity and frequency given in Equation (11). At frequency of $0.25\,\text{Hz}$, the phase velocity of EM signals in seawater, sediments and hydrocarbon are at $883\,\text{m/s}$, $1581\,\text{m/s}$ and $2236\,\text{m/s}$ respectively.

Now, Equation (9) can be simplified by considering that the term $O\left(\Delta t\right)$ and $O\left(\Delta z^2\right)$ to be small and negligible so Equation (9) can be written as

$$E_z^{n+1} = E_z^n + \eta \left(E_{k+1}^n - 2E_k^n + E_{k-1}^n \right). \tag{12}$$

Figure 2 shows the model domain mesh points for computation of EM fields using FTSC technique. The terms Δz and Δt are the spatial and time step of the numerical computations and can be obtained as,

$$\Delta z = \frac{l}{N - 1}, \tag{13}$$

$$\Delta t = \frac{t_{\max}}{M - 1}, \tag{14}$$

where l is the length of 1D medium and $t_{\max}$ is the maximum time. As indicated earlier, the magnitude of EM fields are reduced to less than 1% of its actual value at the surface of conducting medium in $3.186\,\text{sec}$. Therefore, the value of $t_{\max}$ should be less than $3.186\,\text{sec}$ and will be chosen to be at $3\,\text{sec}$.

In FTCS scheme, the solution existed if the value of stability factor η is is less than 0.5. For Δz set at $500\,\text{m}$, the range of Δt and η are given in Table 2. In Table 2, the value of permeability is considered to be same as in vacuum which is a valid assumption for EM geophysical surveys.

Table 1: Maximum penetration depth of EM wave in conducting medium.

Skin depth (δ)	Penetration depth (m)		
	Seawater	Sediment	Hydrocarbon
δ	562	1006	1423
2δ	1125	2012	2847
3δ	1688	3018	4270
4δ	2250	4024	5694
5δ	2813	5030	7117

Table 2: Values of stability factor in conducting medium.

Parameters	Seawater	Sediment	Hydrocarbon
Δt	$0 < t \leq 0.49$	$0 < t \leq 1.4$	$0 < t \leq 3$
η	xx	xx	xx
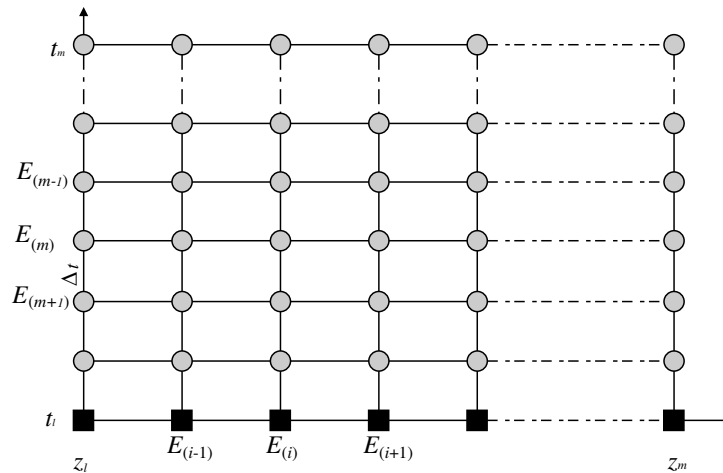
Figure 2: Discretization of model domain for solution to one-dimensional equation using FTSC method.
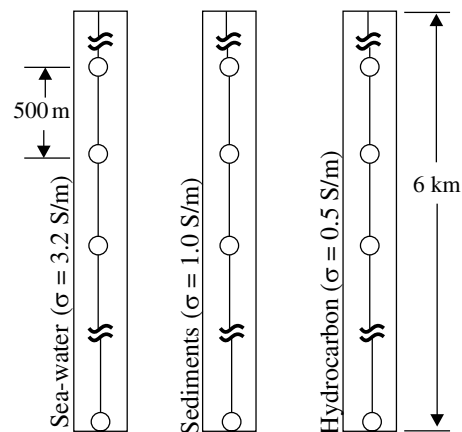
Figure 3: 1D isotropic geological model.

The ranges of time step size Δt varies for different conductive medium to meet the conditions of stability factor.

The field values in space and time domain for each node in Figure 2 can be computed by solving Equations (7) and (8). This is equivalent to solving a set of linear algebraic equations and can be written in a matrix form as

$$E^{n+1} = ME^n, \tag{15}$$

where M is a tri-diagonal matrix, and the E^{n+1} and E^n are column matrices at time $n + 1$ and n respectively.

3. RESULTS

Three different isotropic models shown in Figure 3 will be used to investigate the effect of dipole speed on the survey data. The isotropic models for hydrocarbon, sediment and seawater are of 10 km length along the z-axis and the spatial step size is set at 100 m. The electrical conductivity for layers of hydrocarbon, sediments and seawater are 0.5 S/m, 1.0 S/m and 3.2 S/m respectively while value of electrical permittivity is assumed to be negligible due to the low frequency signal. In here, we again assumed that the magnetic permeability to be the same as in vacuum.

The computed electric fields at time $t = 0$ and $t = 3$ sec for the three model are shown in Figure 4. The graphs show that on average, the magnitude of electric field reduces by 90% of its original value in 3 sec. Similarly, the distance d_s (In reference to Figure 1) is function of source moving speed, medium electrical properties and signal frequency. Figure 5 shows, if moving speed dipole source is fast than the distance d_s will be more.
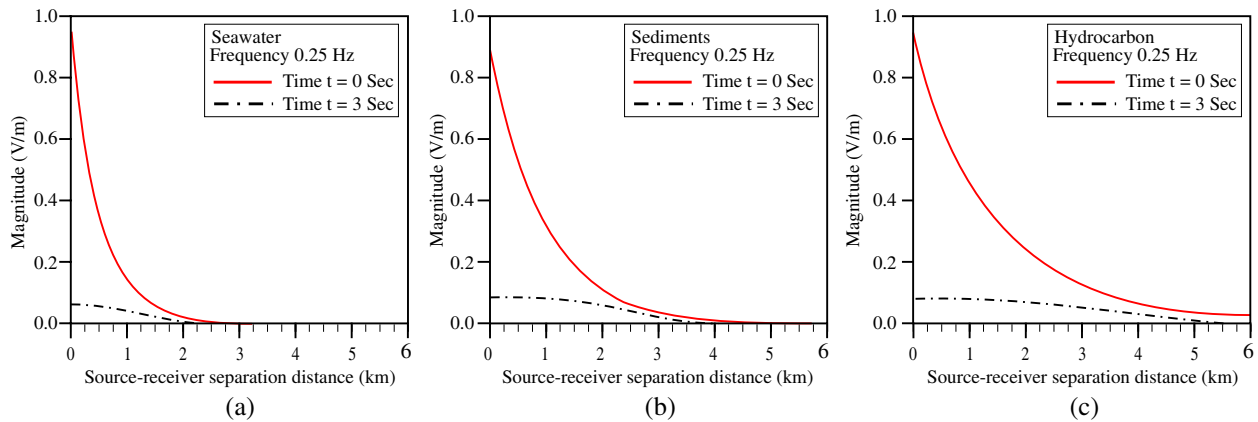
Figure 4: Inline fields computed for 1D isotropic model at frequency of 0.25 Hz. (a) Seawater. (b) Sediment. (c) Hydrocarbon.
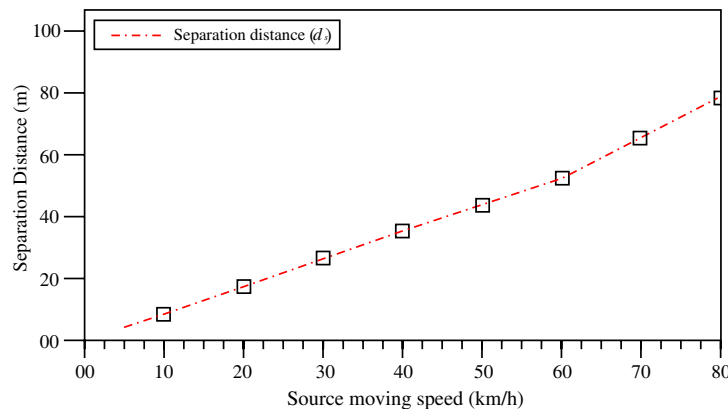
Figure 5: Separation distance between points p-1 and point p-2.

4. CONCLUSION

Marine EM survey requires careful planning on survey geometry setup in order to collect high quality data and this includes proper selection of dipole speed. The effect of dipole speed on survey data can be studied via forward modeling solved using finite difference method (FDM) and forward time centered space (FTSC) method. The 1D modeling of isotropic geological models has shown that at a relatively high speed, the collected data do not give a correct physical location which can lead to intepretation error in the later stage of data inversion. The results indicate that for isotropic model, the choice of dipole speed should be less than x km/s [DO WE HAVE THIS VALUE?]. Further work in this area is to develop 3D forward model in order to gain more insight into the effect of dipole speed on EM data.

ACKNOWLEDGMENT

REFERENCES

1. Nabighian, N., "Electromagnetic methods in applied geophysics," Vol. 2, Application, Parts A and B, Society of Exploration Geophysics, 2008.
2. Chave, A. D. and C. S. Cox, "Controlled electromagnetic sources for measuring electrical conductivity beneath the oceans 1. Forward problem and model study," *Journal of Geophysical Research*, Vol. 87, No. B7, 5327–5338, July 1982.
3. Constable, S., "Hydrocarbon exploration using marine EM techniques," *Offshore Technology Conference OTC*, 17168, 2005.
4. Zhdanov, M. S., *Geophysical Inverse Theory and Regularization Problem*, Vol. 36, Elsevier, Amsterdam, 2002.

5. Weitemeyer, K. A., "Marine electromagnetic methods for gas hydrate characterization," Ph.D. Dissertation, Department of Earth Science, University of California, San Diego, 2008.

6. Guru, B. S. and H. Hiziroglu, *Electromagnetic Field Theory Fundamentals*, Cambridge University Press, 2004.

7. Sadiku, M. N., *Numerical Techniques in Electromagnetics*, 2nd Edition, CRC Press, Washington DC, 2000.

8. Loseth, L. O., "Modelling of controlled source electromagnetic data," Ph.D. Dissertation. Department of Phy., Norwegian University of Science and Technology, 2007.

9. Berdichevsky, M. N. and M. S. Zhdanov, *Advanced Theory of Deep Geomagnetic Sounding*, 408, Elsevier, Amsterdam, New York, 1984.

10. Jackson, J. D., *Classical Electrodynamics*, 3rd Edition, New York, John Wiley & Sons, 1998.

11. Chen, J., G. M. Hoversten, D. Vasco, Y. Rubin, and Z. Hou, "A Bayesian model for gas saturation estimation using marine seismic AVA and CSEM data," *Geophysics*, Vol. 72, No. 2, WA85–WA95, 2007.

12. Hu, W., A. Abubakar, and T. M. Habashy, "Integrated imaging and inversion of multi-physics data for exploration geopysics applications," *2nd IEEE International Workshop on Computational Advances in Multi-sensor Adaptive Processing (CAMPSAP 2007)*, 2007.

13. Harris, P. E., Z. Du, L. MacGregor, W. Olsen, R. Shu, and R. Cooper, "Joint interpretation of seismic and CSEM data using well log constraints: An example from the Luva field," *First Break*, Vol. 27, No. 5, 2009.

Numerical Solution of BLT Equation for Inhomogeneous Transmission Line Networks

M. Oumri, Q. Zhang, and M. Sorine

INRIA Paris-Rocquencourt, France

Abstract— In this paper, a numerical solution is presented for the generalized BLT equation with inhomogeneous transmission lines. In particular, a fully automatized method is developed for the computation of the transmission line propagation matrices and the junction scattering matrices from network structural specification and from transmission line characteristic parameters. Two numerical examples are presented, one for a tree-shaped network, and the other for a network involving a circuit loop.

1. INTRODUCTION

The Baum-Liu-Tesche (BLT) equation [1] is widely used for the modeling and analysis of complex transmission line networks, such as wired telecommunication networks and power lines in automotive vehicles, railway infrastructures, aircrafts, etc.. The original BLT equation for networks with homogeneous transmission lines has been generalized to the case of inhomogeneous transmission lines in [2]. This generalized BLT equation is parameterized by the propagation matrices of inhomogeneous transmission lines and by the scattering matrices at network junctions. However, it is not indicated in [2] how these propagation and scattering matrices can be computed from the structural specification of a network and from the inhomogeneous characteristic parameters of the transmission lines constituting the network. In this paper, a fully automatized method is presented for the computations of the propagation matrices and of the scattering matrices from the specification of the topological structure of a network and from the *inhomogeneously* distributed resistance, inductance, capacitance and conductance (RLCG) characteristic parameters of all the transmission lines. It is shown that the propagation and scattering matrices are independent of the choice of the directions of the currents in transmission lines, despite the fact that the definition of the two opposite waves on each line (as linear combinations of voltage and current) depends on the chosen current direction. It is then possible to compute the propagation and scattering matrices with some *local* convention for current directions on each line and at each junction, without taking care of the consistency between all the local choices in a network. The automatized computation method is greatly simplified thanks to these well defined local conventions. The computation of the scattering matrices has been partially inspired by the results reported in [3]. A new convention for the notations involved in the generalized BLT equation is also introduced to facilitate the implementation of the automatized approach to network simulation through the construction and numerical solution of the generalized BLT equation.

2. MATHEMATICAL MODEL

We consider an electrical network of lossy transmission lines, formed by N_J junctions J_n for $n \in \{1, \ldots, N_J\}$ and N_B branches. Each branch B_{nm} is delimited by two junctions J_n and J_m[1]. The branch B_{nm} is parameterized by its distributed per-unit-length resistance R_{nm}, inductance L_{nm}, capacitance C_{nm} and conductance G_{nm} and its length ℓ_{nm}. Each branch B_{nm} is also illuminated by an electromagnetic wave which is represented by equivalent current $I^s_{n \to m}$ and voltage $V^s_{n \to m}$ sources distributed along the branch. Let us denote by $I_{n \to m}$ the current leaving J_n to J_m along the branch B_{nm} and by $V_{n \to m}$ the voltage along the same branch. The voltage and current waves along a branch driven by a harmonic source of angular frequency ω are solutions of the following frequency domain Telegrapher's equations,

$$
\begin{cases}
\dfrac{dV_{n \to m}(z, \omega)}{dz} = -Z_{nm}(z, \omega) I_{n \to m}(z, \omega) + V^s_{n \to m}(z, \omega) \\[2mm]
\dfrac{dI_{n \to m}(z, \omega)}{dz} = -Y_{nm}(z, \omega) V_{n \to m}(z, \omega) + I^s_{n \to m}(z, \omega)
\end{cases}
\quad, \quad \forall z \in [0, \ell_{nm}]
\tag{1}
$$

---

[1]If there are more than one branches connecting J_n and J_m, an indexing exponent can be added to the notation B_{nm} to distinguish them. For notation simplicity it is assumed in this paper that there is no multiple branches connecting two junctions.

where z is the coordinate along the branch and $Z_{nm}(z, \omega) = R_{nm}(z) + j\omega L_{nm}(z)$, $Y_{nm}(z, \omega) = G_{nm}(z) + j\omega C_{nm}(z)$ are the per-unit-length series impedance and shunt admittance respectively. We define the characteristic impedance ζ_{nm} and the propagation constant γ_{nm} of each branch B_{nm} as follows:

$$\zeta_{nm}(z, \omega) \triangleq \sqrt{Z_{nm}(z, \omega)Y_{nm}^{-1}(z, \omega)}, \qquad \gamma_{nm}(z, \omega) \triangleq \sqrt{Z_{nm}(z, \omega)Y_{nm}(z, \omega)} \tag{2}$$

On each branch, two power waves [5] of opposite directions are defined as linear combinations of the voltage and current along the branch. We denote by $w_{n \to m}$ and $w_{m \to n}$ the wave traveling from J_n to J_m and from J_m to J_n respectively.

$$w_{n \to m}(z, \omega) \triangleq \zeta_{nm}^{-\frac{1}{2}}(z, \omega)V_{n \to m}(z, \omega) + \zeta_{nm}^{\frac{1}{2}}(z, \omega)I_{n \to m}(z, \omega) \tag{3}$$

$$w_{m \to n}(z, \omega) \triangleq \zeta_{nm}^{-\frac{1}{2}}(z, \omega)V_{n \to m}(z, \omega) - \zeta_{nm}^{\frac{1}{2}}(z, \omega)I_{n \to m}(z, \omega) \tag{4}$$

In the same way, we define sources waves $w_{n \to m}^s$ and $w_{m \to n}^s$ in terms of $I_{n \to m}^s$ and V_n^s.

Let $\tilde{w}_{nm}(z, \omega) = [w_{m \to n}(z, \omega), w_{n \to m}(z, \omega)]^T$ and $\tilde{u}_{nm}(z, \omega) = [w_{m \to n}^s(z, \omega), w_{n \to m}^s(z, \omega)]^T$. The combined waves vector $\tilde{w}_{nm}$ satisfies the following differential equation,

$$\frac{d\tilde{w}_{nm}(z, \omega)}{dz} = A_{nm}(z, \omega)\tilde{w}_{nm}(z, \omega) + \tilde{u}_{nm}(z, \omega), \quad \forall z \in [0, \ell_{nm}] \tag{5}$$

where $A_{nm}(z, \omega)$ is defined accordingly in terms of γ_{nm} and the potential function q_{nm} which expresses the heterogeneity of the characteristic impedance along the branch B_{nm}.

$$q_{nm}(z, \omega) \triangleq -\frac{1}{2}\frac{d\ln(\zeta_{nm}(z, \omega))}{dz}, \qquad A_{nm}(z, \omega) \triangleq \begin{bmatrix} \gamma_{nm}(z, \omega) & q_{nm}(z, \omega) \\ q_{nm}(z, \omega) & -\gamma_{nm}(z, \omega) \end{bmatrix}$$

Equation (5) is equivalent to (1) and will be useful for the definition propagation matrices.

3. WAVE PROPAGATION EQUATIONS

The two equations of (5) cannot be solved separately and no closed form of the solution is available because A_{nm} depends on z. In order to numerically solve Equation (5), we introduce a state transition matrix Φ_{nm} related to A_{nm}. This matrix satisfies the following differential equation, for any $z, z' \in [0, \ell_{nm}]$,

$$\frac{d\Phi_{nm}(z, z'; \omega)}{dz} = A_{nm}(z, \omega)\Phi_{nm}(z, z'; \omega), \qquad \Phi_{nm}(z, z; \omega) = \Phi_{nm}(z', z'; \omega) = I_d \tag{6}$$

where I_d is the identity matrix. If $\Phi_{nm}(z, z'; \omega)$ was known, then given the value of $\tilde{w}_{nm}(z, \omega)$ for z equal to any $z_0 \in [0, \ell_{nm}]$, the unique solution of (5) would be given by

$$\tilde{w}_{nm}(z, \omega) = \Phi_{nm}(z, z_0; \omega)\tilde{w}_{nm}(z_0, \omega) + \int_{z_0}^{z} \Phi_{nm}(z, s; \omega)\tilde{u}_{nm}(s, \omega)ds \tag{7}$$

As the state transition matrix $\Phi_{nm}(z, z'; \omega)$ is generally unknown, we do not really use it to solve (5), but it will be used to derive the equations for the computation of the wave propagation matrices defined as follows. For each branch B_{nm}, the propagation matrix $\Gamma_{nm}(\omega)$ relates the values of the waves two opposite waves $w_{m \to n}$, $w_{n \to m}$ at the two ends of the branch through the equation

$$\begin{bmatrix} w_{m \to \text{\textcircled{n}}}(\omega) \\ w_{n \to \text{\textcircled{m}}}(\omega) \end{bmatrix} = \begin{bmatrix} \Gamma_{n,m}(\omega) & \Gamma_{n,n}(\omega) \\ \Gamma_{m,m}(\omega) & \Gamma_{m,n}(\omega) \end{bmatrix} \begin{bmatrix} w_{\text{\textcircled{m}} \to n}(\omega) \\ w_{\text{\textcircled{n}} \to m}(\omega) \end{bmatrix} + \begin{bmatrix} d_{n,m}(\omega) \\ d_{m,n}(\omega) \end{bmatrix} \tag{8}$$

where $w_{m \to \text{\textcircled{n}}}(\omega)$ is the value of $w_{m \to n}(z, \omega)$ at the end of the branch connected to junction J_n (the index n is circled), the other similar notations can be easily understood, and $d_{n,m}(\omega)$, $d_{m,n}(\omega)$ are due to voltage and/or current sources distributed along the branch B_{nm}. Using Equations (6) and (7), we show that the components of $\Gamma_{nm}(\omega)$ and $[d_{n,m}(\omega), d_{m,n}(\omega)]^T$ can be computed by solving

the following differential equations:

$$
\begin{cases}
\dfrac{d\Gamma_{m,m}(z,\omega)}{dz} = q_{nm}(z,\omega) - 2\gamma_{nm}(z,\omega)\Gamma_{m,m}(z,\omega) - q_{nm}(z,\omega)\Gamma_{m,m}^2(z,\omega) \\[2mm]
\dfrac{d\Gamma_{n,m}(z,\omega)}{dz} = \Gamma_{n,m}(z,\omega)\left[q_{nm}(z,\omega)\Gamma_{m,m}(z,\omega) - \gamma_{nm}(z,\omega)\right] \\[2mm]
\dfrac{d\Gamma_{m,n}(z,\omega)}{dz} = -\Gamma_{m,n}(z,\omega)\left[\gamma_{nm}(z,\omega) + q_{nm}(z,\omega)\Gamma_{m,m}(z,\omega)\right] \\[2mm]
\dfrac{d\Gamma_{n,n}(z,\omega)}{dz} = -\Gamma_{n,m}(z,\omega)q_{nm}(z,\omega)\Gamma_{m,n}(z,\omega) \\[2mm]
\dfrac{dd_{n,m}(z,\omega)}{dz} = -\Gamma_{n,m}(z,\omega)\left[q_{nm}(z,\omega)d_{m,n}(z,\omega) + w_{m\to n}^s(z,\omega)\right] \\[2mm]
\dfrac{dd_{m,n}(z,\omega)}{dz} = -d_{m,n}(z,\omega)\left[\gamma_{nm}(z,\omega) + q_{nm}(z,\omega)\Gamma_{m,m}(z,\omega)\right] - w_{m\to n}^s(z,\omega) \\[1mm]
\qquad\qquad\qquad -w_{m\to n}^s(z,\omega)\Gamma_{m,m}(z,\omega) + w_{n\to m}^s(z,\omega) \\[2mm]
\Gamma_{m,m}(0,\omega) = \Gamma_{n,n}(0,\omega) = 0\,,\ \Gamma_{n,m}(0,\omega) = \Gamma_{m,n}(0,\omega) = 1\,,\ d_{n,m}(0,\omega) = d_{m,n}(0,\omega) = 0
\end{cases}
$$

Then we have $\Gamma_{n,m}(\omega) = \Gamma_{n,m}(l_{nm},\omega)\,,\ \Gamma_{n,n}(\omega) = \Gamma_{n,n}(l_{nm},\omega)\,,\ \Gamma_{m,m}(\omega) = \Gamma_{m,m}(l_{nm},\omega)$
$\Gamma_{m,n}(\omega) = \Gamma_{m,n}(l_{nm},\omega)\,,\ d_{n,m}(\omega) = d_{n,m}(l_{nm},\omega)$ and $d_{m,n}(\omega) = d_{m,n}(l_{nm},\omega)$.

4. SCATTERING MATRIX

Let $w_n^{\circ\to}(\omega)$ be the vector composed of all the waves getting out of junction J_n and evaluated the end connected to junction J_n, or more formally $w_n^{\circ\to}(\omega) \triangleq [w_{\textcircled{n}\to m}(\omega)]_{m\in C_n}$ with C_n being the set of indices of the junctions adjacent to J_n. Similarly let $w_n^{\to\circ} \triangleq [w_{m\to\textcircled{n}}(\omega)]_{m\in C_n}$ be the vector composed of all the waves getting into junction J_n and evaluated the end connected to J_n. In the literature of BLT equation, the scattering of a signal at junction J_n is described by the scattering parameter S_n (scalar or matrix) relating incoming waves to outgoing waves.

$$w_n^{\circ\to}(\omega) = S_n(\omega)w_n^{\to\circ}(\omega) \tag{9}$$

Suppose that each terminal junction, say J_n, is not connected to any lumped source and is characterized by a generalized Thévenin equivalent as

$$V_{\textcircled{n}\to m}(\omega) = -Z_{T,n}(\omega)I_{\textcircled{n}\to m}(\omega) \tag{10}$$

where $Z_{T,n}$ is a load connected to the same junction, $V_{\textcircled{n}\to m}(\omega)$ is the value of $V_{n\to m}(z,\omega)$ evaluated at the end of B_{nm} connected to J_n. When the junction is open-circuited, we replace relation (10) by $I_{\textcircled{n}\to m}(\omega) = 0$. In this case, the waves vectors $w_n^{\circ\to}(\omega)$ and $w_n^{\to\circ}(\omega)$ are scalars and are defined as a combination of voltage $V_{\textcircled{n}\to m}(\omega)$, current $I_{\textcircled{n}\to m}(\omega)$ and the characteristic impedance $\zeta_{\textcircled{n}}(\omega)$ of branches B_{nm} evaluated at J_n. The scattering parameter $S_n(\omega)$ is given by

$$S_n = \frac{Z_{T,n} - \zeta_{\textcircled{n}}(\omega)}{Z_{T,n} + \zeta_{\textcircled{n}}(\omega)} \tag{11}$$

In the case of intermediate junctions[2], we suppose that all currents in the branches connected to J_n have their negative directions pointing to junction J_n. This choice of the current directions is only used for the computation of the scattering matrix at the junction J_n, hence there is no problem of conflict between the local choices for different junctions. The scattering matrix at a junction is independent of the chosen current directions, and the above particular choice is for the purpose of simplifying the computation of the scattering matrix. Kirchhoff's laws at such a junction are expressed by:

$$C_I I_n(\omega) = 0\,,\ \ C_V V_n(\omega) = 0 \tag{12}$$

where $V_n(\omega)$ and $I_n(\omega)$ represent the voltage and the current vectors on the branch connected to the junction J_n and evaluated at this junction. The matrices C_I and C_V are filled with ± 1 and 0 so that Equation (12) describes that fact that the sum of the currents is equal to zero and the

---

[2]An intermediate junction is a junction connected to more than one branches. It is assumed in this paper that no load or lumped source is connected to intermediate junctions.

(a)

(b)
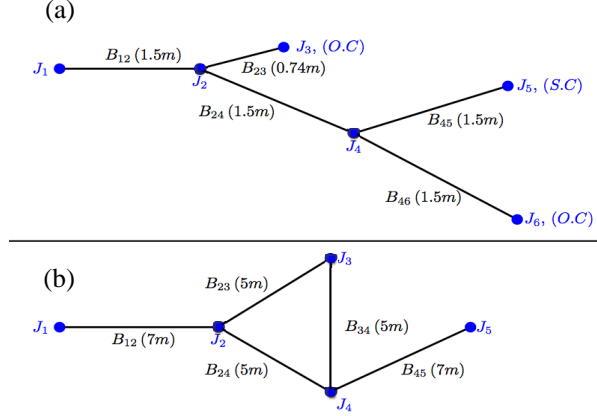
Figure 1: Example of two electric networks.
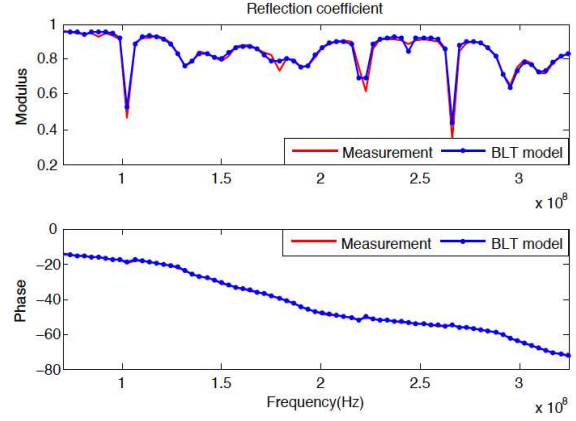
Figure 2: Measured reflection coefficient compared to simulated reflection coefficient for a star shaped network.

voltages at the ends of the branches connected to J_n are all equal. Using (3) and (12), the waves vectors $w_n^{\circ\to}(\omega)$ and $w_n^{\to\circ}(\omega)$ are given as follows:

$$w_n^{\circ\to}(\omega) = Z_n^{-\frac{1}{2}}(\omega)V_n(\omega) + Z_n^{\frac{1}{2}}(\omega)I_n(\omega), \qquad w_n^{\to\circ}(\omega) = Z_n^{-\frac{1}{2}}(\omega)V_n(\omega) - Z_n^{\frac{1}{2}}(\omega)I_n(\omega) \qquad (13)$$

where Z_n is a diagonal matrix filled with the characteristic impedance of branches connected to the junction J_n. By inverting (13), the voltage $V_n(\omega)$ and the current $I_n(\omega)$ vectors can be computed as:

$$V_n(\omega) = \frac{1}{2}Z_n^{\frac{1}{2}}(\omega)\left[w_n^{\circ\to}(\omega) + w_n^{\to\circ}(\omega)\right], \qquad I_n(\omega) = \frac{1}{2}Z_n^{-\frac{1}{2}}(\omega)\left[w_n^{\circ\to}(\omega) - w_n^{\to\circ}(\omega)\right] \qquad (14)$$

Combining (12) and (14) and using the definition of the scattering matrix (9), we obtain,

$$S_n(\omega) = \begin{bmatrix} C_V Z_n^{\frac{1}{2}}(\omega) \\ C_I Z_n^{-\frac{1}{2}}(\omega) \end{bmatrix}^{-1} \begin{bmatrix} -C_V Z_n^{\frac{1}{2}}(\omega) \\ C_I Z_n^{-\frac{1}{2}}(\omega) \end{bmatrix} \qquad (15)$$

The BLT equation is the collections of the Equations (8) and (9) for all branches and all junctions constituting a network, usually written in a compact form with super wave vectors, super propagation matrices and super scattering matrices.

5. NUMERICALS SIMULATIONS

The generalized BLT network numerical simulator is implemented in Matlab. With this numerical simulator, we can compute the reflection coefficient at any junction of the simulated network, the current and the voltage at any junction or at any point on a transmission line. In this section, we present the results of simulation examples and compare these results with real measurements which provides a validation of simulator.

Example 1:   For the tree-shaped network illustrated in Figure 1(a) made of coaxial cables with the characteristic impedance $\zeta(\omega) = 50\,[\Omega]$ and wave propagation velocity $c = 2.478.10^8\,[\text{m/s}]$, we simulate the reflection coefficient at junction J_1 and the voltage at the same junction. These results are then compared with the real measurements made on a laboratory test bed. Two terminal branches (J_3 and J_6) are open-circuited, and another one (J_5) is short-circuited. The ohmic loss of $(10^{-13} + 4.5 \times 10^{-5}\sqrt{\omega})\,[\Omega/\text{m}]$ depending on ω but independent of z is added to each branch in the numerical simulator. After having solved the BLT equation for the power waves, we compute the reflection coefficient at J_1 as the ratio between the two waves, and deduce the current and voltage values through (14). Figure 2 and Figure 3 present a good agreement between measurements and simulations, both for the reflection coefficient and for the voltage $V_{\text{①}\to 2}(\omega)$ at junction J_1 when the network is powered with lumped voltage source $V_s(\omega) = 1[V]$ for $\omega \in [0, 2.1[\text{rad} \cdot \text{GHz}]]$. The
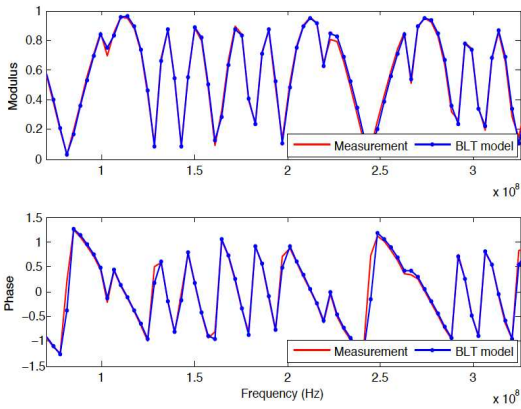
Figure 3: Measured voltage compared to simulated voltage for a tree-shaped network.
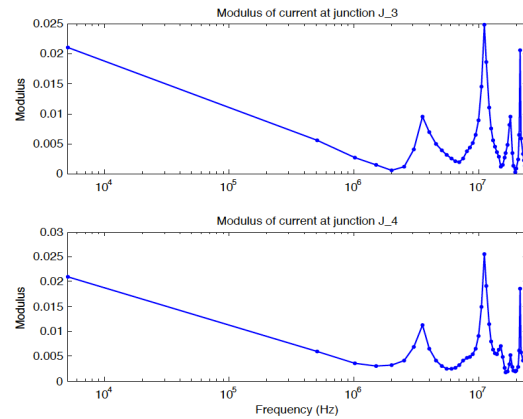
Figure 4: Simulated currents at two ends of branch $B_{3,4}$ (Figure 1(b)).

small difference in the modulus may come from measurements noises and losses in the connectors. This example has also been used in [4] where a simulator specialized for tree-shaped networks was presented.

Example 2: We consider an electric network of lossless transmission lines, composed of 5 junctions and 5 branches, as illustrated in Figure 1(b). Each branch B_{nm} is parametrized by its capacitance $C_{nm}(z) = 0.1 \, [\mathrm{nF/m}]$ and inductance $L_{nm}(z) = (0.08 e^{-5(z-2.3)^2} + 0.9) \, [\mu\mathrm{H/m}]$. The network is supplied with a lumped voltage source $V_s(\omega) = 1 \, [\mathrm{V}]$ at junction J_1 and the terminal junction J_5 is short-circuited. The modulus of currents at the two ends of branch $B_{3,4}$ are shown in Figure 4, with a logarithmic scale.

6. CONCLUSION

To summarize, this paper presents a numerical solution of the BLT equation generalized to inhomogeneous transmission lines networks. Despite the inhomogeneous nature of the transmission lines, the propagation matrix for each network branch is computed by solving simple differential equations. The computation of the scattering matrices at network junctions is also fully automatized.

ACKNOWLEDGMENT

REFERENCES

1. Baum, C. E., T. K. Liu, and F. M. Tesche, "On the analysis of general multiconductor transmission line networks," *Interaction Notes*, Note 350, 1978.
2. Baum, C. E., "Generalization of the BLT equation," *Interaction Notes*, Note 511, 1995.
3. Parmantier, J. P., "An efficient technique to calculate ideal junction scattering parameters in multiconductor transmission line networks," *Interaction Notes*, Note 536, 1998.
4. Oumri, M., Q. Zhang, and M. Sorine, "A reduced model of reflectometry for wired electric networks," *Proceedings of the 19th International Symposium on Mathematical Theory of Networks and Systems — MTNS 2010*, 2213–2218, 2010.
5. Kurokawa, K., "Power Waves scattering matrix," *Microwave Theory and Techniques*, Vol. 13, No. 2, 194–202, 1965.

Improvised PEEC Method in the Modeling of the Near-field Coupling with Electrical Cable

E. R. Rajkumar, **M. Bensetti**, **B. Ravelo**, and **M. Kadi**

Institut de Recherche en Systèmes Electroniques Embarqués (IRSEEM)
EA 4353, 76801 Saint Etienne du Rouvray, France

Abstract— To study the susceptibility of these cables due to external electromagnetic (EM) perturbation, several numerical methods have been developed. This paper describes a technique for obtaining integrated near-field (NF) coupling Partial Element Equivalent Circuit (PEEC) model for the electromagnetic compatibility (EMC) issues. It incorporates EM coupling due to electronic components and cables with/without ground plane along with its capabilities of transforming field based problem into the circuit domain. Elementary dipoles are used to calculate the EM field, which represents modeling of electronic components radiation. The proposed approach is demonstrated by analyzing a cable above the ground plane and with elementary dipoles as source of disturbances. It is being carried over with Finite Element Method (FEM) and then Finite Integration Technique (FIT). The results obtained by both the methods are in good agreement. In order to validate the obtained results, the test set up is being built by analytical TLM models. The developments of 2D and 3D dimensional dipole are being integrated into the PEEC method. As perspective, coupling PEEC model could be developed considering inductive and capacitive coupling between the cable, ground plane and devices.

1. INTRODUCTION

In the modern automotive electronic system cables play a major role for the reliability due to the integration density. In power electronic system transmission and energy conversion, electrical cabling is an indispensable part. The advent of inexpensive memory and processing power also renders numerical methods very attractive. General numerical methods, such as the finite element method (FEM), the Method of Moments (MoM), and Finite-Difference (FD) methods, Partial Element Equivalent Circuit (PEEC) methods give acceptable accuracy when the size of the structure is not much larger than the excitation wavelength and the number of numerical unknowns is sufficiently small for present-day computers [1]. Unfortunately, these two requirements are often violated in real-world applications. Parallelization of numerical algorithms has achieved some success in extending modeling scale [2]. However, the required processing hardware is often not within easy reach of typical scientists and engineers.

This paper develops efficient hybrid method to overcome the difficulty of large simulation scale. This hybrid method can capture accuracy of exact numerical solvers on scales that far exceed their native capability. It also depicts the application of the hybrid method to a general large-scale EM modeling problem. The method must analyze the given structure and produce the required induced electrical components. The study setup is analyzed by dividing the structure into a number of small segments. In every simulation model, an analysis combines key information from previous models with knowledge about the coupling phenomenas and physical structure to apply proper inputs. This hybrid method employs many tools which are not new to the EM engineering/modeling discipline: radiated emission, FEM, finite-difference methods (FDM), field extraction and network analysis. The main contribution of this paper is the innovative combination of FEM methods and Analytical methods along with dipole source as perturbation source. The final significant contribution of this work is an extended understanding of time and frequency domain analysis and proposed methodology for full wave solution analysis.

2. HYBRID METHOD FORMULATION

In the calculation of radiated coupling with analytical model, the methodology has the above steps. Normally in the calculation of E and H field, we used to consider the total field to obtain the complete radiated field, whereas in the case of analytical method we are not obliged to include the scattering field due to the fact that the model is considered in the absence of the cable and also with the ground plane condition [3–5].

This proposed hybrid method considers the limitations posed by the previous researchers where the coupling between the cable and ground plane, the coupling between the dipole and cable and

then coupling between the dipole and ground plane are also considered for the calculation. Another advantage is that there is no need of matched load conditions in the calculation of coupling [6–8].

To study, the coupling between the cable and external electromagnetic field several numerical methods are developed and used to predict the disturbance induced on the cables; with the help of analytical formulations, it is possible to predict the voltage induced on the cable. These formulations are used to calculate the field excitation. The near-field coupling of a cable above the ground plane can be studied using differential techniques based on transmission line theory. In this study, we are representing the non-uniform electromagnetic field interference between electronic components and the cable when placed close to each other.

This model consists of three sections. In Section 1, it deals with radiation emission model; Section 2 with transmission line models; Section 3 deals with integration of PEEC models in the coupling modeling under study is examined. In this paper we focus on feasibility study of the PEEC implementation.

3. PEEC METHOD

The PEEC method, developed by A. Ruehli, is like the MoM based integral formulation of Maxwell's equations making the technique is well suited for free space simulations. The main feature with PEEC method is the combined circuit and EM simulation that is performed with the same equivalent circuit in both time and frequency domain [9–12].

The starting point of theoretical derivation is the total electric field, at the observation point expressed in terms of vector magnetic potential $\vec{A}$, and the scalar electric potential as:

$$E(\vec{r}, \omega) = -j\omega \vec{A}(\vec{r}, \omega) - \nabla \Phi(\vec{r}, \omega). \tag{1}$$

and the vector potential is given by:

$$\vec{A}(\vec{r}, \omega) = \mu \int_{v'} G(\vec{r}, \vec{r'}) J(\vec{r'}, \omega) \, dv', \tag{2}$$

where J is the volume current density at a source point $\vec{r'}$ and G is the Green's free-space function:

$$G(\vec{r}, \vec{r'}) = \frac{e^{-j\beta \cdot R}}{4\pi R}, \tag{3}$$
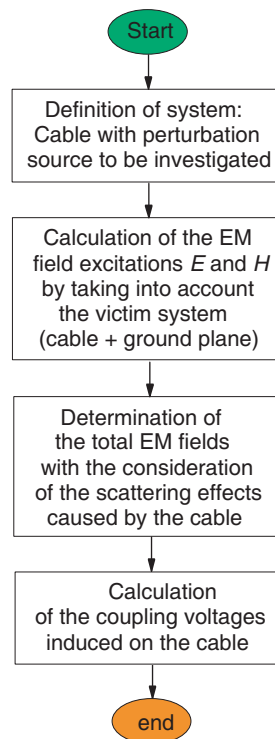
Figure 1: Flow chart summarizing the hybrid method understudy.
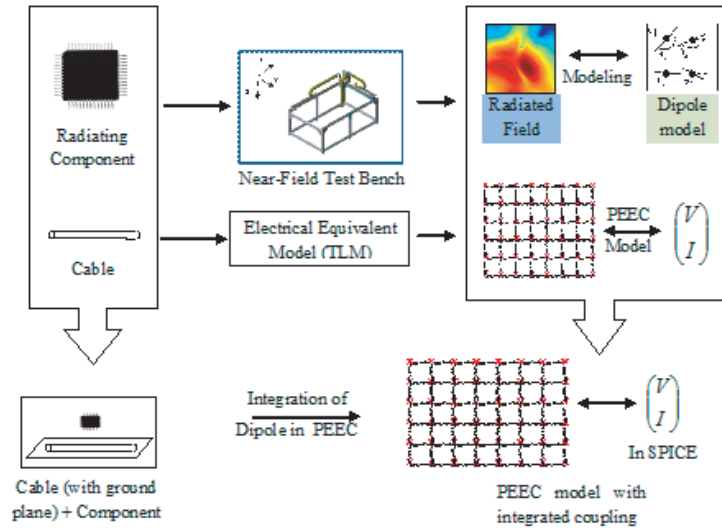
Figure 2: Proposed radiated coupling model.
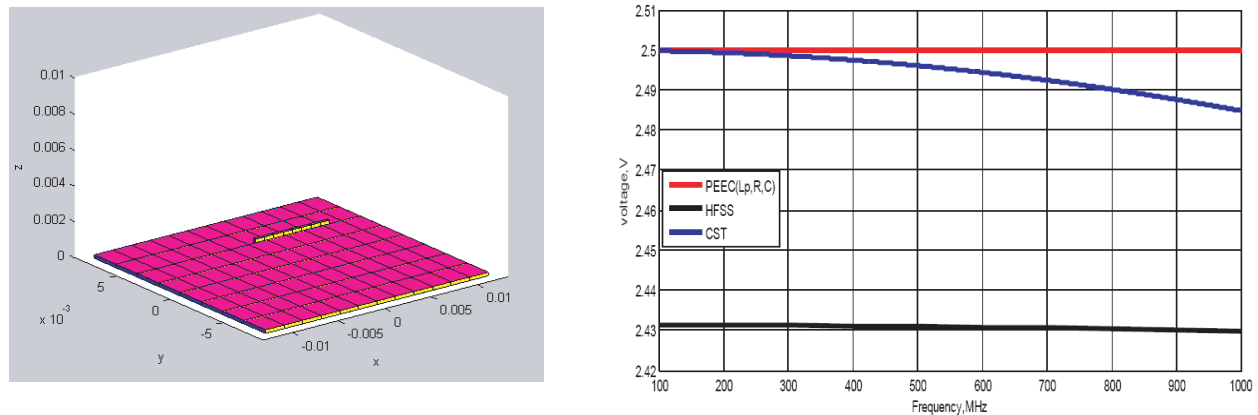
Figure 3: Test setup radiated coupling model & comparison results.

where R is given by $R = |\vec{r} - \vec{r'}|$. The scalar potential term is given by:

$$\Phi(\vec{r}, \omega) = \frac{1}{\varepsilon} \int_{v'} G\left(\vec{r}, \vec{r'}\right) q(\vec{r}, \omega) \, dv', \tag{4}$$

where v' is the volume of the conductor and q is the charge density at the conductor. If above equations are substituted into an electric field integral equation (EFIE) in the unknown variables $\vec{J}$ and q is obtained as:

$$\vec{E}(\vec{r}, \omega) = j\omega\mu \int_{v'} G\left(\vec{r}, \vec{r'}\right) \vec{J}\left(\vec{r'}, \omega\right) dv' - \frac{\nabla}{\varepsilon} \int_{v'} G\left(\vec{r}, \vec{r'}\right) \vec{J}\left(\vec{r'}, \omega\right) dv', \tag{5}$$

The above equation is then solved by expanding each unknown, $\vec{J}$ and q, into a series of pulse basis functions with unknown amplitude.

4. RESULTS

The test setup is calculated with the HFSS, CST and PEEC method. The configuration is given as follows. The ground plane of (length $= 28$ mm, breadth $= 20$ mm and thickness $= 0.2$ mm) and the cable (length $= 8$ mm, radius $= 0.1$ mm) is kept above 2 mm height from the ground plane. At the end 221 Ω of impedance with lumped RLC port is used for termination at the ends.

5. CONCLUSIONS

From the results of Fig. 3, we observed that the results are in good agreement in FEM, FIT and PEEC models. As the relative error is below 1%, with this agreement in the results prompted us to proceed further with integration of dipole in the PEEC method and compare the results with FEM and FIT methods. Further currently we are working with the implementation of dipole setup with the same setup. with the validation of simulation setup, the same can be done with the measurement setup targeting the industrial oriented problem.

REFERENCES

1. Shin, J., "Automotive EMC standards and testing," *2011 APEMC Tutorial Workshop Digests on 'Introduction to Automotive EMC Testing'*, Jeju, S. Korea, May 2011.
2. Liu, K., "An update on automotive EMC testing," *Microwave Journal*, Vol. 54, No. 7, 40–46, Jul. 2011.
3. Taylor, C. D., R. S. Sattewhite, and C. W. Harrison, "The response of a terminated two-wire transmission line excited by a nonuniform electromagnetic field," *IEEE Trans. Antennas Propagat.*, Vol. 13, No. 6, 987–989, Nov. 1965.
4. Agrawal, A. K. and H. J. Price, "Transient response of multiconductor transmission lines excited by a non uniform electromagnetic field," *IEEE Trans. Antennas Propagat.*, Vol. 18, 432–435, Jun. 1980.
5. Rachidi, F., "Formulation of the field to transmission line coupling equations in terms of magnetic excitation field," *IEEE Trans. EMC*, Vol. 35, No. 3, 404–407, Aug. 1993.
6. Fernández López, P., A. Ramanujan, Y. Vives Gilabert, C. Arcambal, A. Louis, and B. Mazari, "A radiated emission model compatible to a commercial electromagnetic simulation tool," *20th Int. Symp. EMC*, 369–372, Zurich, Switzerland, Jan. 2009.
7. Atrous, S., D. Baudry, E. Gaboriaud, A. Louis, B. Mazari, and D. Blavette, "Near-field investigation of the radiated susceptibility of printed circuit boards," *2008 Int. Symp. EMC Europe*, Hamburg, Germany, Sep. 8–12, 2008.
8. Leseigneur, C., P. F. Lopez, C. Arcambal, D. Baudry, and A. Louis, "Near-field coupling model between electronic systems and transmission line," *IEEE Int. Symp. EMC*, 22–27, Fort Lauderdale, FL, USA, Jul. 25–30, 2010.
9. Kantartzis, N. V., "Multi-frequency higher-order ADI-FDTD solvers for signal integrity predictions and interference modeling in general EMC applications," *ACES Journal*, Vol. 25, No. 12, 1046–1060, Dec. 2010.
10. Antonini G., G. Miscione, and J. Ekman, "PEEC modeling of automotive electromagnetic problems," *ACES Newsletter*, Vol. 23, No. 1, 39–50, 2008.
11. Antonini, G., "The partial element equivalent circuit method for EMI,EMC, and SI analysis," *ACES Newsletter*, Vol. 21, No. 1, 8–32, 2006.
12. Ekman, J., G. Antonini, and A. E. Ruehli, "Toward improved time domain stability and passivity for full-wave PEEC models," *Special Session at the IEEE Int. Symp. on EMC*, Portland, USA, 2006.

The Scattering Property Analysis of Metamaterials-coated Object Based on FDTD

Shi-Quan Zhang

Engineering University of CAPF, Xi'an, Shaanxi 710086, China

Abstract— The Maxwell equations combined with Drude model medium are discretized and two-dimensional recursive formulas are derived. FDTD programs for metamaterial-coated target is compiled in this paper. The radar cross sections (RCS) of metamaterial-coated metallic circular cylinder is computed. Numerical examples of metamaterial-coated metallic circular cylinder for both TM and TE wave incidence are given to verify the feasibility and effectiveness of the scheme and the stealth property of metamaterials. It is demonstrated that metamaterials take an active role in stealth applications.

1. INTRODUCTION

In recent years, there has been a growing interest for the study of target stealth technique, while the special properties of left-handed metamaterials with negative values of permittivity and permeability exhibit potential prospect for applications such as stealth and so on. In 1968 Soviet scientist Veselago V. G. indicated that media with negative permittivity ε and permeability μ would have distinct electromagnetic characteristics such as negative refraction and so on. Smith et al. [1–3], inspired by the work of Pendry et al. constructed a composite medium in the microwave regime by arranging periodic arrays of small metallic wires and split ring resonators and demonstrated the negative diffraction in this artificial medium. Since then many aspects of this class or other types of artificial materials, now termed metamaterials are being investigated by several researchers worldwide and various ideas for potential applications of these media have been demonstrated. The discovery of metamaterials was considered as one of the ten greatest scientific and technological breakthroughs in 2003 by the famous American journal, *Science*. It was once again regarded as one of the ten greatest scientific and technological achievements in 2006 by *Science* due to its applications in electromagnetic stealth [4–6]. The study of metamaterials has become a hot topic in the international science field. In this paper, the electromagnetic scattering properties of the object such as metamaterial-coated metallic circular cylinder are analyzed and discussed by using finite-difference time-domain method (FDTD) based on Drude model.

2. MEDIUM MODEL

The constitutive parameters of metamaterials are the function of frequency, hence, metamaterials are surely dispersive media. Their effective permittivity and permeability can be expressed in terms of lossy Drude model [7] as follows:

$$\varepsilon(\omega) = \varepsilon_0 \varepsilon_r(\omega) = \varepsilon_0 \left(1 - \frac{\omega_{pe}^2}{\omega(\omega + \mathrm{j}\Gamma_e)} \right) \tag{1}$$

$$\mu(\omega) = \mu_0 \mu_r(\omega) = \mu_0 \left(1 - \frac{\omega_{pm}^2}{\omega(\omega + \mathrm{j}\Gamma_m)} \right). \tag{2}$$

where ω_{pe}, ω_{pm}, Γ_e and Γ_m are the electric plasma angular oscillating frequency, the magnetic plasma oscillating angular frequency, and their electron collision frequencies, respectively.

3. FDTD RECURSIVE FORMULAS

Applying Maxwell's vortex equations, constitutive relations for metamaterials and time-frequency relation, we can derive and obtain the following electromagnetic field equations:

$$\nabla \times H = \varepsilon_0 \frac{\partial E}{\partial t} + J_e \tag{3}$$

$$\nabla \times E = -\mu_0 \frac{\partial H}{\partial t} - J_m \tag{4}$$

$$\frac{\partial J_e}{\partial t} + \Gamma_e J_e = \varepsilon_0 \omega_{pe}^2 E \tag{5}$$

$$\frac{\partial J_m}{\partial t} + \Gamma_m J_m = \mu_0 \omega_{pm}^2 H. \tag{6}$$

It shoud be noted that the above equations are valid for sourceless case. If we need to consider source electric current, we can insert J directly into Eq. (3)

$$\nabla \times H = \varepsilon_0 \frac{\partial E}{\partial t} + J_e + J \tag{7}$$

The above equations are discretized and the two-dimensional recursive formulas can be derived for TE and TM cases. For TE case, we have the following derivation:

$$H_z^{n+1/2}(i+1/2, j+1/2) = H_z^{n-1/2}(i+1/2, j+1/2) - \frac{\Delta t}{\mu_0} J_{mz}^{n-1/2}(i+1/2, j+1/2)$$

$$-\frac{\Delta t}{\mu_0}\left[\frac{E_y^n(i+1, j+1/2) - E_y^n(i, j+1/2)}{\Delta x} - \frac{E_x^n(i+1/2, j+1) - E_x^n(i+1/2, j)}{\Delta y}\right] \tag{8}$$

$$E_x^{n+1}(i+1/2, j) = E_x^n(i+1/2, j) - \frac{\Delta t}{\varepsilon_0} J_{ex}^{n+1/2}(i+1/2, j)$$

$$+\frac{\Delta t}{\varepsilon_0}\left[\frac{H_z^{n+1/2}(i+1/2, j+1/2) - H_z^{n+1/2}(i+1/2, j-1/2)}{\Delta y}\right] \tag{9}$$

$$E_y^{n+1}(i, j+1/2) = E_y^n(i, j+1/2) - \frac{\Delta t}{\varepsilon_0} J_{ey}^{n+1/2}(i, j+1/2)$$

$$-\frac{\Delta t}{\varepsilon_0}\left[\frac{H_z^{n+1/2}(i+1/2, j+1/2) - H_z^{n+1/2}(i-1/2, j+1/2)}{\Delta x}\right] \tag{10}$$

$$J_{mz}^{n+1/2}(i+1/2, j+1/2) = \frac{1 - 0.5\Gamma_m \Delta t}{1 + 0.5\Gamma_m \Delta t} J_{mz}^{n-\frac{1}{2}}(i+1/2, j+1/2)$$

$$+\frac{\mu_0 \omega_{pm}^2 \Delta t}{1 + 0.5\Gamma_m \Delta t} H_z^{n+\frac{1}{2}}(i+1/2, j+1/2) \tag{11}$$

$$J_{ex}^{n+1}(i+1/2, j) = \frac{1 - 0.5\Gamma_e \Delta t}{1 + 0.5\Gamma_e \Delta t} J_{mx}^n(i+1/2, j) + \frac{\mu_0 \omega_{pe}^2 \Delta t}{1 + 0.5\Gamma_e \Delta t} E_x^{n+1}(i+1/2, j) \tag{12}$$

$$J_{ey}^{n+1}(i, j+1/2) = \frac{1 - 0.5\Gamma_e \Delta t}{1 + 0.5\Gamma_e \Delta t} J_{ey}^n(i, j+1/2) + \frac{\mu_0 \omega_{pe}^2 \Delta t}{1 + 0.5\Gamma_e \Delta t} E_y^{n+1}(i, j+1/2). \tag{13}$$

For TM incidence the FDTD formulas can be derived in terms of duality principle [7, 8], that is, the duality relations, $\varepsilon \to \mu$, $\mu \to \varepsilon$, $E \to H$, $H \to -E$ can be used. In order that the discretized formulas for TM wave have the similar form with that of TE wave, we can move the coordinates (x, y) in the x and y directions by half a grid. In the mean time, we also move the time step by half a grid. Therefore, we have

$$E_z^{n+1}(i, j) = E_z^n(i, j) - \frac{\Delta t}{\varepsilon_0} J_{mz}^n(i, j)$$

$$-\frac{\Delta t}{\varepsilon_0}\left[\frac{H_y^{n+\frac{1}{2}}(i+1/2, j) - H_y^{n+1/2}(i-1/2, j)}{\Delta x} - \frac{H_x^{n+1/2}(i, j+1/2) - H_x^{n+\frac{1}{2}}(i, j-1/2)}{\Delta y}\right] \tag{14}$$

$$H_x^{n+1/2}(i, j+1/2) = H_x^{n-1/2}(i, j+1/2) - \frac{\Delta t}{\mu_0} J_{mx}^{n-1/2}(i, j+1/2) - \frac{\Delta t}{\mu_0}\left[\frac{E_z^n(i, j+1) - E_z^n(i, j)}{\Delta y}\right] \tag{15}$$

$$H_y^{n+1/2}(i+1/2, j) = H_y^{n-1/2}(i+1/2, j) - \frac{\Delta t}{\mu_0} J_{my}^{n-1/2}(i+1/2, j) + \frac{\Delta t}{\mu_0}\left[\frac{E_z^n(i+1, j) - E_z^n(i, j)}{\Delta x}\right] \tag{16}$$

$$J_{ez}^{n+1}(i, j) = \frac{1 - 0.5\Gamma_e \Delta t}{1 + 0.5\Gamma_e \Delta t} J_{ez}^n(i, j) + \frac{\varepsilon_0 \omega_{pe}^2 \Delta t}{1 + 0.5\Gamma_e \Delta t} E_z^{n+1}(i, j) \tag{17}$$

$$J_{mx}^{n+1/2}(i, j+1/2) = \frac{1 - 0.5\Gamma_m \Delta t}{1 + 0.5\Gamma_m \Delta t} J_{mx}^{n-1/2}(i, j+1/2) + \frac{\varepsilon_0 \omega_{pm}^2 \Delta t}{1 + 0.5\Gamma_m \Delta t} H_x^{n+1/2}(i, j+1/2) \quad (18)$$

$$J_{my}^{n+1/2}(i+1/2, j) = \frac{1 - 0.5\Gamma_m \Delta t}{1 + 0.5\Gamma_m \Delta t} J_{my}^{n-1/2}(i+1/2, j) + \frac{\varepsilon_0 \omega_{pm}^2 \Delta t}{1 + 0.5\Gamma_m \Delta t} E_y^{n+1/2}(i+1/2, j) \quad (19)$$

In FDTD computation of metamaterials, we use 4-point-average method [9, 10] to deal with the coupling between electric field and magnetic field. When calculating $H_x^{n+1}(i, j+1/2)$ and $H_y^{n+1}(i+1/2, j)$ at the total field boundary, we only need to calculate the field in the region which is one grid away from the boundary, and use free space to carry out calculation. Other cases can be handled in the similar way.

4. NUMERICAL EXAMPLES

FDTD programs for metamaterial-covered targets are compiled. The radar cross sections (RCS) for metamaterial-coated metallic circular cylinders are computed. The plane wave is supposed to strike the target from the left side. The incident wave is choosed to be Guaussian pulse in the following calculation

$$E_i(t) = \exp\left[-4\pi(t - t_0)^2 / \tau^2\right]$$

where τ is pulse width. δ and Δt refer to the cell size and time step of FDTD, respectively. $\Delta t = \delta/(2c)$, where c is the speed of light in free space.

The radius of the metamaterials-coated cylinder is $2\,\mathrm{cm}$, and the radius of the cylinder is $1.5\,\mathrm{cm}$. The parameters of the metamaterials are chosen as: $\omega_{pe} = 5.595 \times 10^{10}\,\mathrm{rad/s}$, $\omega_{pm} = 8.43 \times 10^{10}\,\mathrm{rad/s}$, $\Gamma e = \Gamma m = \Gamma = 1.0 \times 108\,\mathrm{rad/s}$. The space and time discritized intervals for FDTD
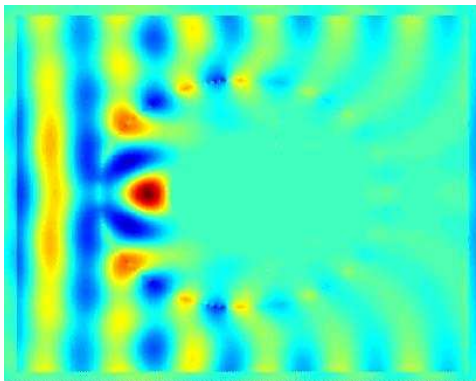
Figure 1:   The   near-field   distribution   of metamaterial-coated   metallic   circular   cylinder for TM incidence.
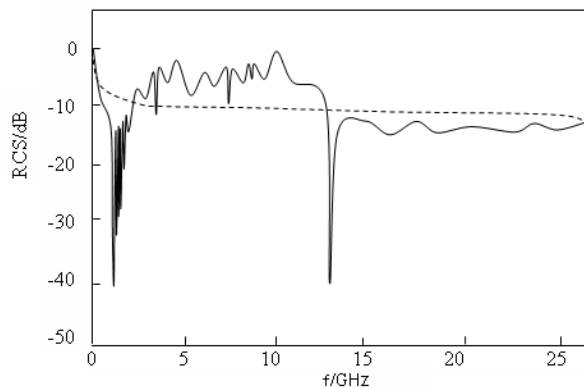
Figure 2: The backward scattering of metamaterial-coated metallic circular cylinder for TM incidence.
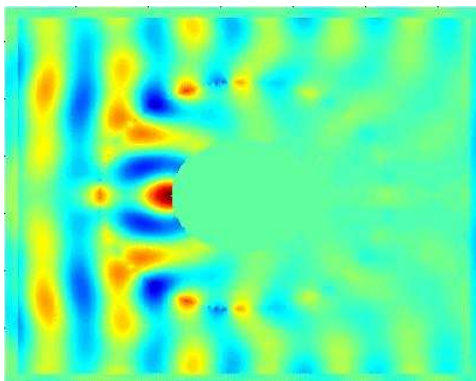
Figure 3:   The   near-field   distribution   of metamaterial-coated   metallic   circular   cylinder for TE incidence.
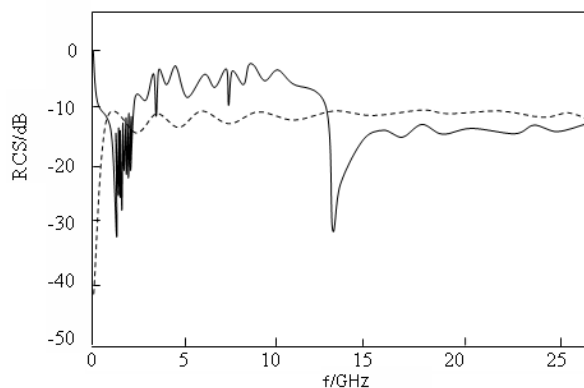
Figure 4: The backward scattering of metamaterial-coated metallic circular cylinder for TE incidence.

calculation are, $\delta = \lambda/50 = 0.02\,\text{cm}$, $\Delta t = \delta/(2c)$, respectively. The observation time interval is $t = 5000\Delta t$. The near-field distribution and bistatic RCS of metamaterial-coated metallic circular cylinder for TM wave incidence case are shown in Fig. 1 and Fig. 2, and the near-field distribution and backward scattering bistatic RCS of metamaterial-coated metallic circular cylinder for TE wave incidence case are shown in Fig. 3 and Fig. 4. It is demonstrated that the backward scattering is reduced within a wide range of frequency band and the RCS resonance region in the vicinity of the backward field is greatly expanded. Therefore, it is obvious that the metamaterials take an active role in stealth applications.

5. CONCLUSION

We derived the two-dimensional recursive formulas for Maxwell's vortex equations and the constitutive relations. The radar cross sections (RCS) for and metamaterial-coated metallic circular cylinder is computed. Numerical examples indicate that the feasibility and effectiveness of FDTD programs and the stealth property of metamaterials.

ACKNOWLEDGMENT

REFERENCES

1. Pendry, J. B., A. J. Holden, W. J. Stewart, et al., "Extremely low frequency plasmas in metallic structure," *Phys. Rev. Lett.*, Vol. 76, No. 2, 4773–4776, 1996.
2. Pendry, J. B., A. J. Holden, D. J. Robbins, et al., "Magnetism from conductors and enhanced nonlinear phenomena," *IEEE Trans. Microwave Theory and Tech.*, Vol. 47, No. 11, 2075–2084, 1999.
3. Smith, D. R., W. J. Padilla, D. C. Vier, et al., "Composite medium with simultaneously negative permeability and permittivity," *Phys. Rev. Lett.*, Vol. 84, No. 18, 4184–4187, 2000.
4. Schurig, D., J. J. Mock, B. J. Justice, et al., "Metamaterial electromagnetic cloak at microwave frequencies," *Science*, Vol. 314, No. 5801, 977–980, 2006.
5. Lezec, H. J., J. A. Dionne, and H. A. Atwater, "Negative refraction at visible frequencies," *Science*, Vol. 316, No. 5823, 430–432, 2007.
6. Cai, W. S., U. K. Chettiar, A. V. Kildishev, et al., "Optical cloaking with metamaterials," *Nature Photonics*, Vol. 1, No. 4, 224–227, 2007.
7. Talfove, A., *Advance in Computational Electrodynamics: The Finite-difference Time-domain Method*, Artech House, Inc., Norwood, MA, 1998.
8. Ge, D.-B. and Y.-B. Yan, *The Finite Difference Time-domain Method for Electromagnetic Waves*, Xidian University Publishing House, Xi'an, China, 2005.
9. Bing, W., D.-B. Ge, and M.-Y. Wang, "Wideband scattering of perfectly conducting object coated with DNM," *Systems Engineering and Electronics Technology*, Vol. 28, No. 6, 840–843, 2006.

Analysis of Near-field Optical Disk with a Circular Aperture

T. Kitamura

Faculty of Engineering Science, Kansai University, Japan

Abstract— A phase change disk illuminated by a near-field optical light through a ridgedcircular nano-aperture is analyzed by using three-dimensional FDTD method. The motion equations of free electrons are installed to analyze a metallic material. The electromagnetic field distributions of optical near-field around the aperture and the far-field scattering patterns from the phase change disk are investigated. The crosstalk characteristics between plural marks are also studied.

1. INTRODUCTION

The recording density of conventional optical recording systems has an optical diffraction limit. Recently, there has been a lot of interest in the field of optical storage technologies for the recording methods that are based on near-field optical principles. This is because they have the potential to overcome the limitation by using the localized optical near-field for writing and reading recorded marks. Many types of nano-apertures and nano-antennas have been proposed to achieve the high throughput of the optical near field [1–4]. This study focuses on the scattering characteristics from a phase change disk illuminated by the optical near field through a nano-aperture. First, the electromagnetic field distributions of optical near-field around the aperture are analyzed. Next, the scattering characteristics from a phase change disk with a ridged-circular nano-aperture are studied. Finally, the crosstalk characteristics between plural marks are discussed.

2. FDTD FORMULATION

In the FDTD method, special handling of the metallic material is required because the permittivity is dispersive and has a negative value in the optical frequency. In this study, the following motion equation is introduced into the FDTD method to evaluate the conducting current.

$$m\frac{\partial \mathbf{u}}{\partial t} = -e\mathbf{E} - m\nu\mathbf{u}, \tag{1}$$

where $\mathbf{u}$ is the electron velocity, $\mathbf{E}$ is the electric field, e is the elementary electric charge, m is the electron mass, and ν is the collision frequency. The collision frequency ν is expressed as follows.

$$\nu = \frac{2n_1 n_2 \omega}{1 - n_1^2 + n_2^2}, \tag{2}$$

where ω is the angular frequency of a light wave, and n_1 and n_2 are the real and imaginary parts, respectively, of the complex refractive index N of a metallic material ($N = n_1 - jn_2$).

Maxwell's equations are expressed as follows by representing the current density using the electron velocity $\mathbf{u}$ and the electron density n_0.

$$\varepsilon_0 \frac{\partial \mathbf{E}}{\partial t} = \nabla \times \mathbf{H} + n_0 e\mathbf{u} \tag{3}$$

$$u_0 \frac{\partial \mathbf{H}}{\partial t} = -\nabla \times \mathbf{E}, \tag{4}$$

where $\mathbf{H}$ is the magnetic field, and ε_0 and μ_0 are the electric permittivity and magnetic permeability of free space, respectively. The finite difference equations corresponding to Eqs. (1), (3), and (4) are used for the analysis. The perfect matched layer (PML) absorbing boundary conditions are applied to truncate the computational domain.

3. NUMERICAL RESULTS

Figures 1(a) and (b) show the side view and cross section, respectively, of a ridged-circular nanoaperture. Silver, which has a complex refractive index $N = 0.07 - 4.2j$ and a thickness $t = 150\,\text{nm}$, is assumed to be the metallic material used. The plane wave with a wavelength $\lambda = 650\,\text{nm}$, whose

electric field is polarized in the x direction, is illuminated vertically to the aperture. In the FDTD analysis, the 5-nm cubic cells are used. The near-field intensity when $g = 100$ nm (circular aperture) and 30 nm are shown in Figures 2(a) and (b), respectively. The near-field is observed on the plane 15 nm below the bottom surface of the aperture as shown in Figure 1(a). In these figures, the solid and dashed lines show the near-field intensity along the x and y axes, respectively, and the vertical axes are normalized by the maximum intensity of a circular nano-aperture. By using the ridged-circular aperture, we can obtain the strong and sharp optical near-field around the aperture.

The maximum intensity and full-width half-maximum (FWHM) as a function of g are shown in Figures 3(a) and (b), respectively. The maximum intensity has the highest value when the gap g is about 30 nm. The FWHM becomes smaller when using the smaller gap.

Figure 4 shows the structure of a near-field optical disk that consists of a metallic nano-aperture, a phase change disk, two protective films and a substrate. Here, the ridged-circular nano-aperture shown in Figure 1(b) is used. The refractive index of the phase change disk is $4.6 - 4.2j$ (crystalline) and the center of the phase change disk is assumed to be the cylindrical recorded mark with a diameter of w_R, a thickness of 15 nm, and a refractive index of $4.2 - 1.9j$ (amorphous). The refractive indexes of the protective films and the substrate are assumed to be 2.2 and 1.5, respectively. The numerical aperture of the objective lens NA is assumed to be 0.6. The incident light is a Gaussian beam polarized in the x direction whose electromagnetic field components in the frequency domain are expressed as follows when the focus plane is $z = z_0$ and the center of the light beam is $(x_0,$
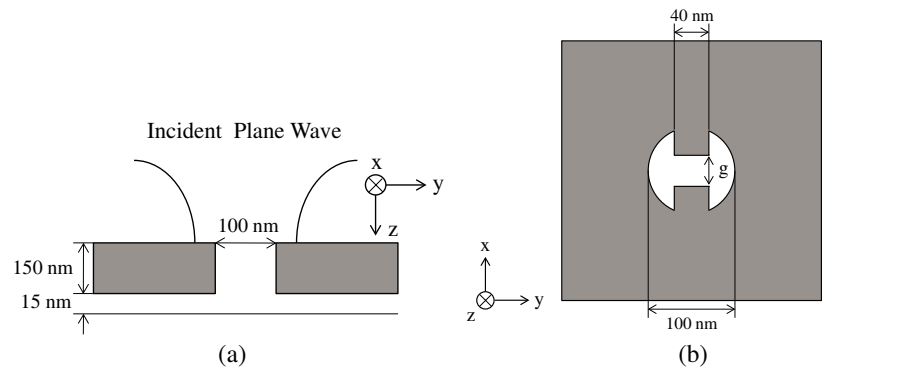
Figure 1: Ridged-circular nano-aperture. (a) Side view. (b) Cross section.
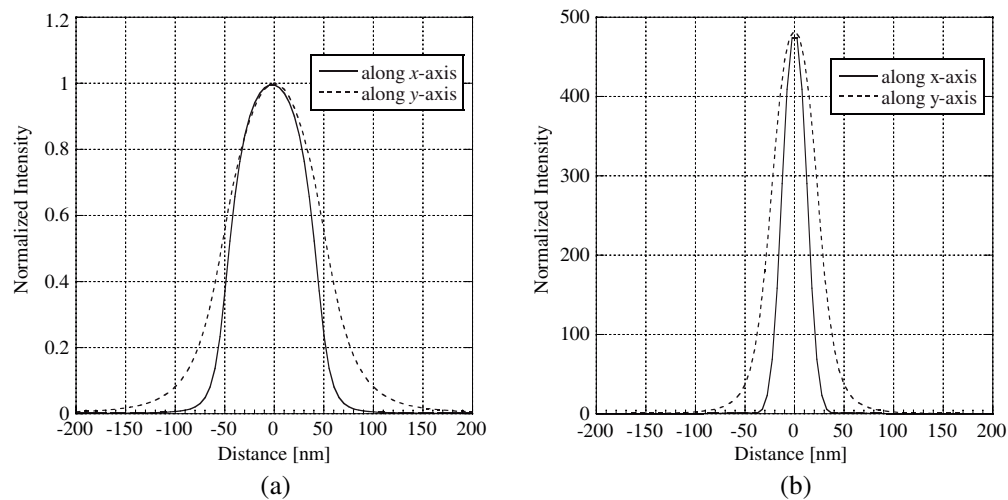
Figure 2: Near-field intensity. (a) Circular nano-aperture. (b) Ridged-circular nano-aperture ($g = 30$ nm).
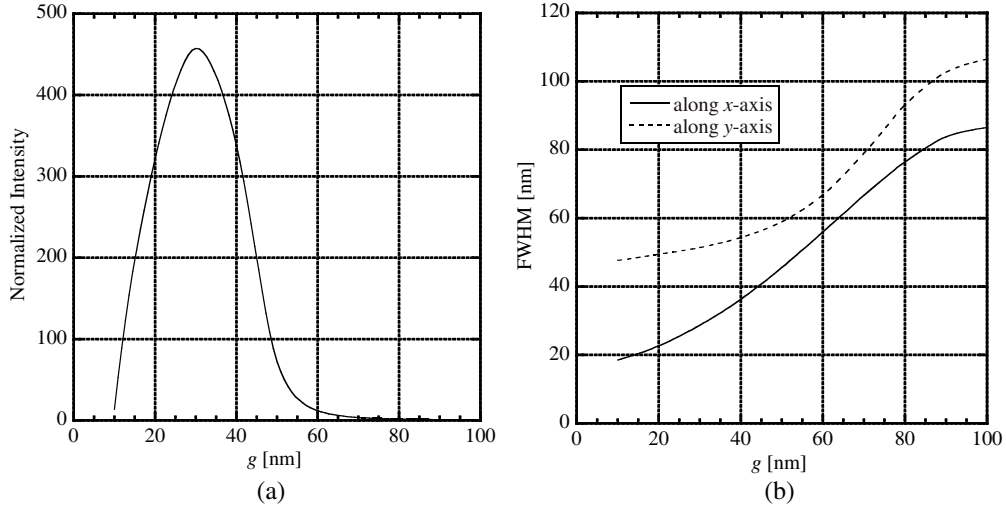
Figure 3: Near-field characteristics as function of g. (a) Maximum intensity. (b) FWHM.
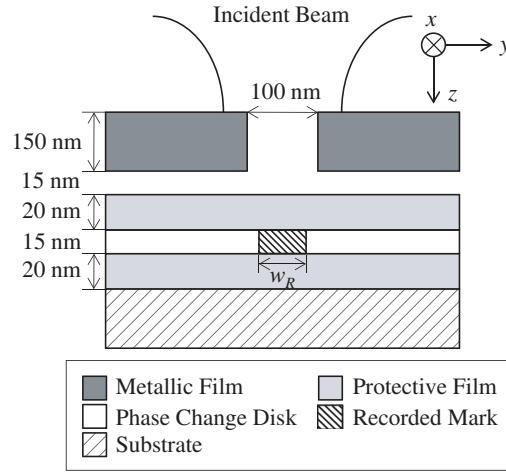
Figure 4: Disk structure.

y_0) [5].

$$E_x^{inc} = \frac{W_0}{W(z)} \exp\left[j\left\{ k(z - z_0) + \frac{kr^2}{2R(z)} - \theta(z) \right\} - \frac{r^2}{W(z)^2} \right] \tag{5}$$

$$H_y^{inc} = -\frac{1}{j\omega\mu_0} \frac{\partial E_x^{inc}}{\partial z}, \tag{6}$$

where, r, $W(z)$, $R(z)$, and $\theta(z)$ are written as

$$r = \sqrt{(x - x_0)^2 + (y - y_0)^2} \tag{7}$$

$$W(z) = W_0 \sqrt{1 + \left\{ \frac{2(z - z_0)}{kW_0^2} \right\}^2} \tag{8}$$

$$R(z) = (z - z_0)\left[1 + \left\{ \frac{kW_0^2}{2(z - z_0)} \right\}^2 \right] \tag{9}$$

$$\theta(z) = \tan^{-1}\left\{ \frac{2(z - z_0)}{kW_0^2} \right\}. \tag{10}$$

Here, the wavelength λ is 650 nm, and k ($= 2\pi/\lambda$) and $2W_0$ are the wave number and spot size of the light beam, respectively. In this analysis, the focus plane is set on the upper plane of the metallic film shown in Figure 4, and the center of the light beam is equal to that of the aperture.
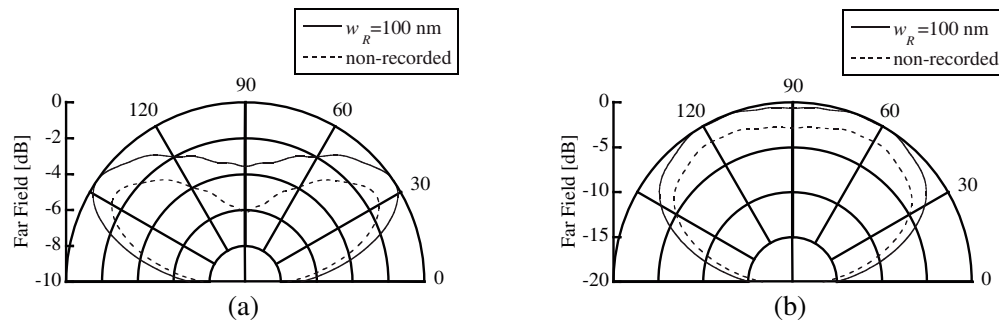
Figure 5: Far-field scattering patterns. (a) xz plane. (b) yz plane.
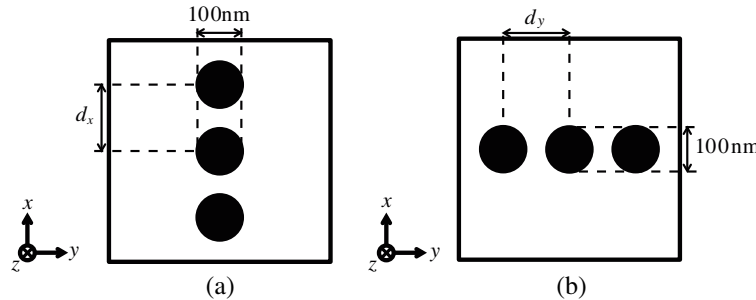
Figure 6: Plural recorded marks. (a) Along x axis. (b) Along y axis.
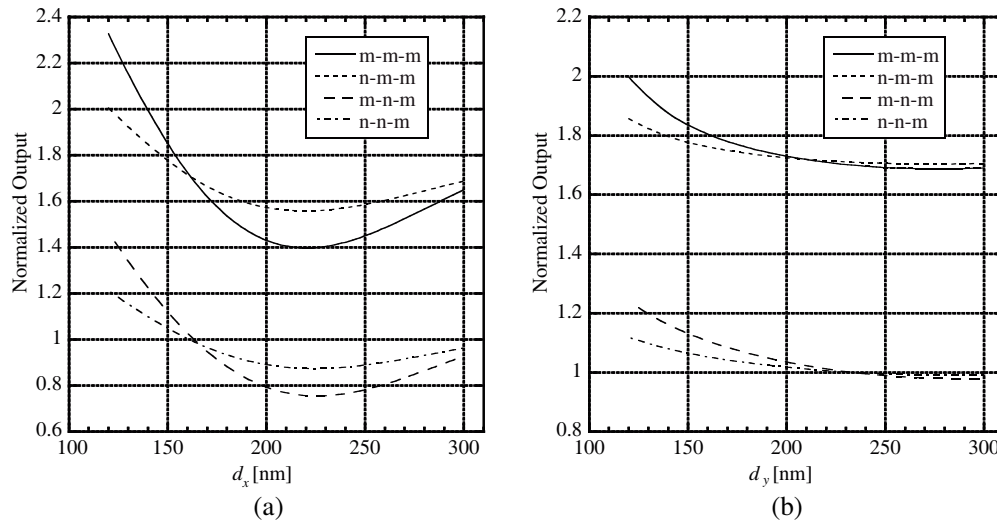
Figure 7: Crosstalk characteristics. (a) Along x axis. (b) Along y axis.

Figures 5(a) and (b) show the far-field scattering patterns of the transmitted wave from the phase change disk in the xz and yz planes, respectively. In these figures, the solid and dashed lines show the results when $w_R = 100$ and 0 nm (non-recorded mark), respectively, and they are normalized by using the maximum value in the xz plane when $w_R = 100$ nm. We deal with the transmitted wave because the reflected far-field barely changes when varying the recorded-mark size [6, 7]. It is understood that the light beam, whose electric field is polarized in the x direction, is scattered more widely in the x direction.

Next, the crosstalk characteristics between plural marks were evaluated. Figures 6(a) and (b) show the arrangements of three neighboring recorded marks along the x and y axes, respectively. Here, the ridged-circular nano-aperture ($g = 30$ nm) was used. The diameters of the recorded marks are equally 100 nm and the distances between the marks (d_x, d_y) are the parameters.

Figures 7(a) and (b) show the normalized output as a function of d_x and d_y, respectively. The The arrangements of the three neighboring marks are denoted by m-m-m, n-m-m, m-n-m, and n-n-m, where 'm' and 'n' represent the recorded and non-recorded marks, respectively. Along the x

axis the influence of the neighboring marks exists when d_x is much larger than the recorded-mark size. On the other hand, the variation in output with regard to d_y is smaller.

4. CONCLUSION

The scattering characteristics from the phase change disk illuminated by the optical near field through a ridged-circular nano-aperture were analyzed by using the FDTD method into which the motion equations of free electrons were installed. The near-field around the aperture and the farfield scattering patterns were investigated. The crosstalk characteristics between the plural marks were also studied. It was demonstrated that the output of the plural marks differs depending on the arrangement direction of the marks.

REFERENCES

1. Omodani, S., T. Saiki, and M. Obara, "Metallic slit aperture as a near-field optical head for heat-assisted magnetic recording," *J. Appl. Phys.*, Vol. 105, 013101, 1–5, Jan. 2009.
2. Wu, Y. M., L. W. Li, and B. Liu, "Gold bow-tie shaped aperture nanoantenna; wide band nearfield resonance and far-field radiation," *IEEE Trans. Magn.*, Vol. 46, No. 6, 1918–1921, Jun. 2010.
3. Scorrano, L., F. Bilotti, and L. Vegni, "Achieving power transmission enhancement by using nano-rings made of silver spheres," *IEEE Photon. Technol. Lett.*, Vol. 22, No. 21, 1595–1597, Nov. 2010.
4. Nakagawa, K., Y. Ashizawa, S. Ohnuki, A. Itoh, and A. Tsukamoto, "Confined circularly polarized light generated by nano-size apeture for high density all-optical magnetic recording," *J. Appl. Phys.*, Vol. 109, 07B735, 1–3, Mar. 2011.
5. He, Y., T. Kojima, T. Uno, and S. Adachi, "FDTD analysis of three-dimensional light-beam scattering from the magneto-optical disk structure," *IEICE Trans. Electron.*, Vol. E81-C, No. 12, 1881–1888, Dec. 1998.
6. Kagawa, S., Y. He, and T. Kojima, "Two-dimensional FDTD analysis of the readout characteristics of an optical near field disk," *IEICE Trans. Electron.*, Vol. E91-C, No. 1, 48–55, Jan. 2008.
7. Kitamura, T. and S. Iwata, "Analysis of a near-field optical disk with an acute-edged metallic nano-aperture," *IEICE Trans. Electron.*, Vol. E93-C, No.9, 1474–1477, Sept. 2010.

GMI Effect in Thin Amorphous Microwires for Sensors and Tuneable Metamateriales Applications

A. Zhukov[1, 2]**, M. Ipatov**[1]**, and V. Zhukova**[1]

[1]Dpto. Fís. Mater., Fac. Químicas, UPV/EHU, San Sebastián 20018, Spain
[2]IKERBASQUE, Basque Foundation for Science, Bilbao 48011, Spain

Abstract— We present the results on GMI effect in thin microwires at elevated frequencies paying special attention to tailoring the GMI effect and achievement of low hysteretic GMI behavior. We measured magnetic field, H, dependence of real part, Z_1 of the longitudinal wire impedance Z ($Z = Z_1 + iZ_2$) till 4 GHz in Co-rich microwires. We observed considerable GMI effect at GHz frequencies. General features of these dependences are that the magnetic field of maximum shifts to the higher field region increasing the f. Both $\Delta Z/Z$, and hysteresis loops of nearly-zero $Co_{67.1}Fe_{3.8}Ni_{1.4}Si_{14.5}B_{11.5}Mo_{1.7}$ microwires magnetostrictive exhibit strong sensitivity to the ratio, ρ, of the metallic nucleus diameter to the total microwire diameter. On the other hand field dependence of the off-diagonal voltage response of nearly zero magnetostriction ($\lambda_s \approx -3 \times 10^{-7}$) $Co_{67.1}Fe_{3.8}Ni_{1.4}Si_{14.5}B_{11.5}Mo_{1.7}$ with metallic nucleus diameter of 6.0, 7.0 and 8.2 μm exhibits anti-symmetrical shape with almost linear growth within the field range from $-H_m$ to H_m associated with the anisotropy field. Current annealing significantly affects the off-diagonal GMI curves of $Co_{67.1}Fe_{3.8}Ni_{1.4}Si_{14.5}B_{11.5}Mo_{1.7}$ microwires with vanishing magnetostriction constant: under DC current annealing the H_m decreases from 480 A/m in as-cast state to 230 A/m after 5 min annealing with 50 mA current. We found, that if the surface anisotropy is not circumferential, then the magnetization and, consequently, the MI curve $Z(H)$ present hysteresis. This hysteresis can be suppressed by application of sufficiently high DC bias current I_B that creates a circumferential bias field H_B. Applications of thin microwires in tuneable metamaterials are discussed.

1. INTRODUCTION

Magnetically soft glass coated microwires (typically of 5–30 μm in diameter) exhibit a number of outstanding magnetic properties such as magnetic bistability and giant magneto-impedance, GMI, effect [1, 2]. Recent studies allowed improvement of magnetically soft properties and GMI effect of glass coated microwires [2, 3].

Giant magneto-impedance effect (GMI), consisting of large sensitivity of the impedance of magnetically soft conductor on applied magnetic field, attracted great attention in the field of applied magnetism [2–6] especially because of excellent magnetic field sensitivity suitable for low magnetic field detection. Such GMI effect is especially high in ferromagnetic magnetically soft wires (especially of amorphous and nanocrystalline origin) [2, 5, 6]. It is worth mentioning, that the cylindrical shape is quite suitable for achieving of high GMI effect [2, 5, 6]. General tendency on miniaturization of magnetic sensors requires development of thin soft magnetic materials, like thin wires and thin films. Owing to its thin dimensions, glass-coated microwires gained special interest in the filed of applied magnetism for designing of the sensors based on GMI effect [2, 3].

In this paper, we studied the GMI effect (GMI ratio, $\Delta Z/Z$, diagonal Z_{zz} and off-diagonal impedance tensor $\zeta_{\phi z}$ components) and hysteretic magnetic properties in ultra-thin amorphous glass-coated microwires with vanishing magnetostriction constant.

2. EXPERIMENTAL

We have measured dependences of the diagonal Z_{zz} and off-diagonal $Z_{\varphi z}$ impedance components on external axial magnetic field H in Co-rich microwires, as described elsewhere [2, 7, 8]. The microwires with nominal composition $Co_{67.1}Fe_{3.8}Ni_{1.4}Si_{14.5}B_{11.5}Mo_{1.7}$ and $Co_{66}Cr_{3.5}Fe_{3.5}B_{16}Si_{11}$ different diameters of metallic nucleus, d, and total diameters, D, have been fabricated by the Taylor-Ulitovsky method [2, 9].

The microwires were placed in a specially designed microstrip cell. One wire end was connected to the inner conductor of a coaxial line through a matched microstrip line while the other was connected to the ground plane. The components Z_{zz} and $Z_{\varphi z}$ were measured simultaneously using vector network analyzer. The diagonal impedance of the sample $Zw = Zzzl$, where l is the wire length, was obtained from reflection coefficient S_{11} and the off-diagonal impedance $Z_{\varphi z}$ was

measured as transmission coefficient S_{21} as a voltage induced in a 2-mm long pick-up coil wounded over the wire. The static bias field H_B was created by the dc current I_B applied to sample through the bias-tee element. The other experimental details are given in Ref. [7]. The frequency range for the off-diagonal component $Z_{\varphi z}$ was 10–300 MHz, while diagonal impedance component has been measured till 7 GHz.

For practical sensor it is essential to have the anti-symmetrical dependence on magnetic field, so off-diagonal MI components could be more suitable. In the sensor application, pulse excitation is preferred over sinusoidal because of simple electronic design and low power consumption, therefore we used also pulsed excitation scheme, as described elsewhere [2, 8].

3. RESULTS AND DISCUSSION

Magnetic field, H, dependence of real part, Z_1 of the longitudinal wire impedance Z_{zz} ($Z_{zz} = Z_1 + iZ_2$), measured till 4 GHz in $Co_{66}Cr_{3.5}Fe_{3.5}B_{16}Si_{11}$ microwire is shown in Fig. 1. General features of these dependences is that the magnetic field of maximum shifts to the higher field region increasing the f. High enough magnetic field sensitivity, i.e., GMI effect till GHz-range frequencies should be also underlined.

Off-diagonal and low field diagonal components of GMI, measured in $Co_{67}Fe_{3.85}Ni_{1.45}B_{11.5}Si_{14.5}Mo_{1.7}$ microwire are shown in Fig. 2. Important feature of Fig. 2 is a considerable hysteresis for both off-diagonal and longitudinal impedance.

Figure 3 shows field dependence of the off-diagonal voltage response, V_{out} measured using pulsed scheme, described elsewhere [2, 8] in $Co_{67.1}Fe_{3.8}Ni_{1.4}Si_{14.5}B_{11.5}Mo_{1.7}$ ($\lambda_s \approx 3 \cdot 10^{-7}$) microwire with different geometry: metallic nucleus diameter and total diameter with glass coating are 6.0/10.2,
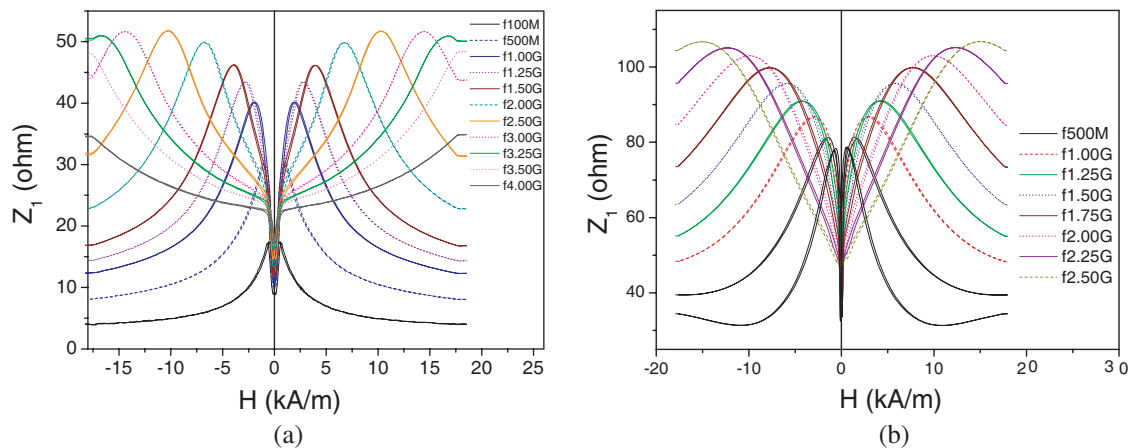
Figure 1: $Z(H)$ dependence of (a) $Co_{66}Cr_{3.5}Fe_{3.5}B_{16}Si_{11}$ and (b) $Co_{67}Fe_{3.85}Ni_{1.45}B_{11.5}Si_{14.5}Mo_{1.7}$ microwires measured at different frequencies.
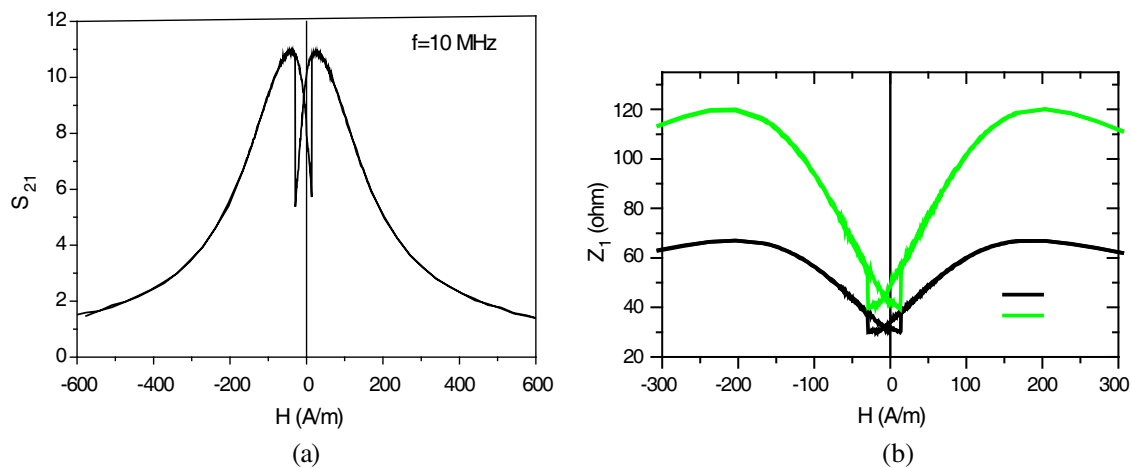
Figure 2: Magnetic field dependences of (a) the coefficient S_{21} at 10 MHz and (b) $Z_1(H)$ dependences at different frequencies measured in $Co_{66}Cr_{3.5}Fe_{3.5}B_{16}Si_{11}$ microwire.
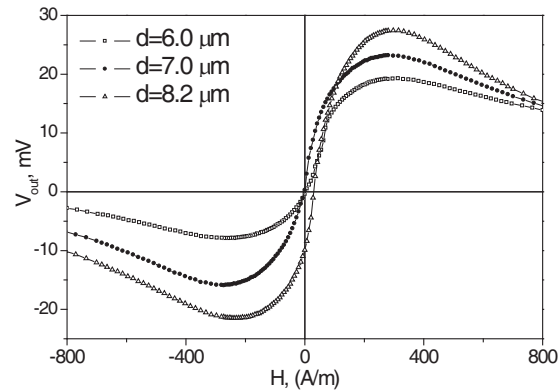
Figure 3: $V_{out}(H)$ response of $Co_{67.1}Fe_{3.8}Ni_{1.4}Si_{14.5}B_{11.5}Mo_{1.7}$ microwires with different diameters, d.

(a)	(b)
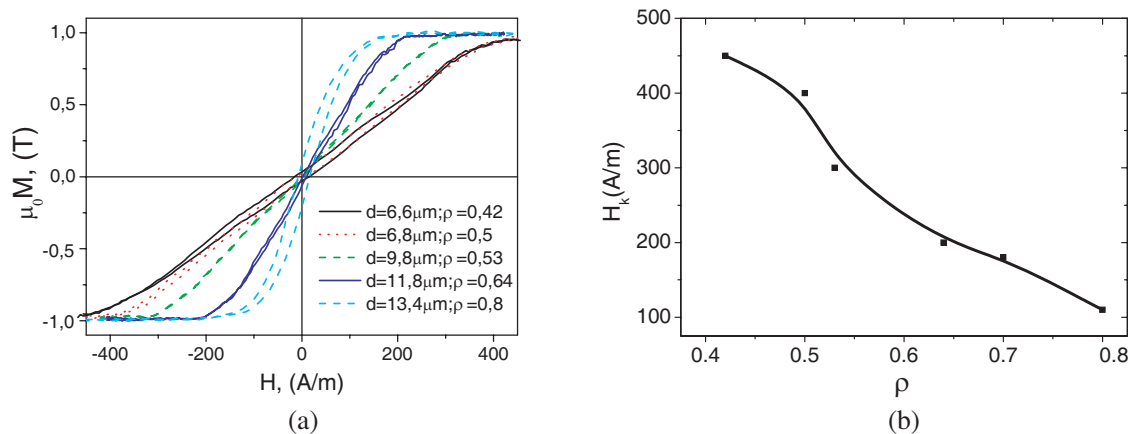
Figure 4: Hysteresis loops of (a) $Co_{67.1}Fe_{3.8}Ni_{1.4}Si_{14.5}B_{11.5}Mo_{1.7}$ microwires with different geometry and (b) dependence of H_k on ρ-ratio.

7.0/11.0 and 8.2/13.7 μm.

The off-diagonal components exhibit anti-symmetrical magnetic field dependence, suitable for determination the magnetic field direction in real sensor devices [2, 8]. It should be noted from Fig. 3 that the $V_{out}(H)$ curves exhibit nearly linear growth within the field range from $-H_m$ to H_m. The H_m limits the working range of MI sensor to 240 A/m and should be associated with the anisotropy field. The effect of the ρ-ratio on $V_{out}(H)$ (Fig. 3) should be attributed to the effect of internal stresses on the magnetic anisotropy field. It must be underlined, that all studied samples exhibited excellent magnetically soft properties with inclined hysteresis hoops and extremely low coercivities (between 4 and 10 A/m). Magnetic anisotropy field, H_k, is found to be determined by the ρ-ratio, decreasing with ρ (Fig. 4), as also has been reported earlier [2, 11].

On the other hand, it is well established, that strength of internal stresses, σ_i, arising during simultaneous rapid quenching of metallic nucleus surrounding by the glass coating can be controlled by the ρ-ratio: strength of internal stresses increases decreasing ρ-ratio (i.e., increases with increasing of the glass volume). Consequently magnetic field dependences of both Z_{zz} and $Z_{\varphi z}$ can be controlled by ρ-ratio.

Additionally, we recently found, that the nature of observed low field hysteresis on $Z_1(H)$ and $Z_{\varphi z}(H)$ is directly related with deviation of the anisotropy easy axis from transversal direction [7]. Therefore, application of circular bias magnetic field H_B produced by DC current I_B running through the wire affects the hysteresis and asymmetry of the MI dependence, suppressing this hysteresis when I_B is high enough (see Fig. 5, where effect of bias voltage on diagonal impedance, Z_1, and on S_{21} parameter proportional to off-diagonal GMI component is shown). In fact in pulsed exciting scheme when the sharp pulses with pulse edge time about 5 ns are produced by passing square wave multi-vibrator pulses through the differentiating circuit, overall pulsed current contains a DC component that produces bias circular magnetic field [6, 7]. In this way low field hysteresis can be surpassed selecting adequate pulse amplitude.

Traditional way to tailor magnetoelastic anisotropy is the thermal treatments The influence of Joule heating on off-diagonal field characteristic of nearly zero magnetostriction $Co_{67.1}Fe_{3.8}Ni_{1.4}Si_{14.5}B_{11.5}Mo_{1.7}$ microwire with diameters $9.4/17.0\,\mu m$ is shown in Fig. 6. One can see that the thermal annealing with 50 mA DC current reduces the H_m from 480 A/m in as-cast state to 240 A/m after 5 min annealing.

Observed $H_k(\rho)$ dependence has been attributed to the magnetoelastic energy contribution given by

$$K_{me} \approx 3/2\lambda_s\sigma_\iota, \tag{1}$$

where λ_s is the saturation magnetostriction and σ_i is the internal stress. The magnetostriction constant is mostly determined by the chemical composition and achieves almost nearly-zero values in amorphous alloys based on Fe-Co with $Co/Fe \approx 70/5$ $\lambda_s \approx 0$ [2, 12]. On the other hand, the estimated values of the internal stresses in these glass coated microwires arising from the difference in the thermal expansion coefficients of simultaneously solidifying metallic nucleus and glass coating are of the order of 100–1000 MPa, depending strongly on the ratio between the glass coating thickness and metallic core diameter [2, 13, 14], increasing with decreasing ρ-ratio. Consequently, magnetoelastic anisotropy of glass-coated microwires can be controlled by the geometrical ratio ρ through the strength of internal stresses.

Application of stress during stress annealing of $Fe_{74}B_{13}Si_{11}C_2$ microwires resulted in induction of considerable stress induced anisotropy [15]. In this case the easy axis of magnetic anisotropy has been changed from axial to transversal [15]. Origin of such stress-induced anisotropy is related
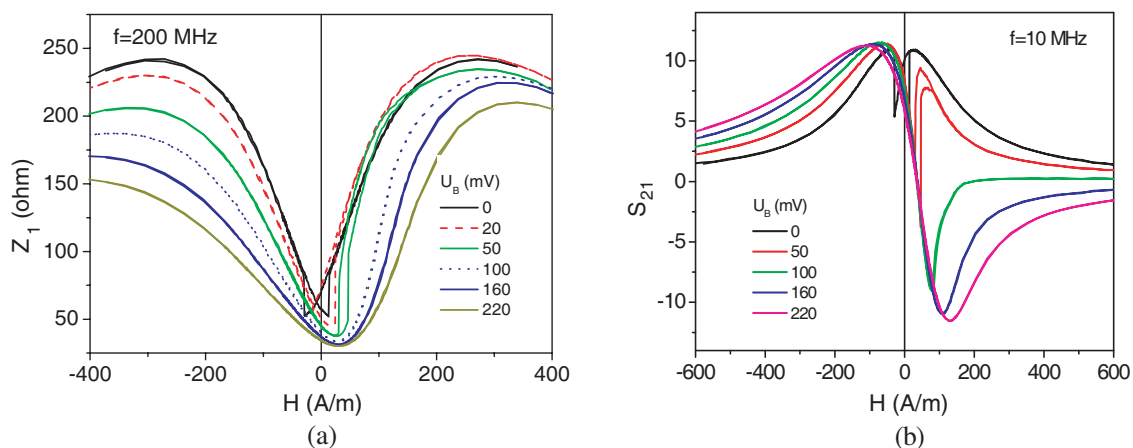
Figure 5: Effect of bias voltage U_B on magnetic field dependence of (a) diagonal impedance and (b) S_{21} parameter of $Co_{67}Fe_{3.85}Ni_{1.45}B_{11.5}Si_{14.5}Mo_{1.7}$ microwire.
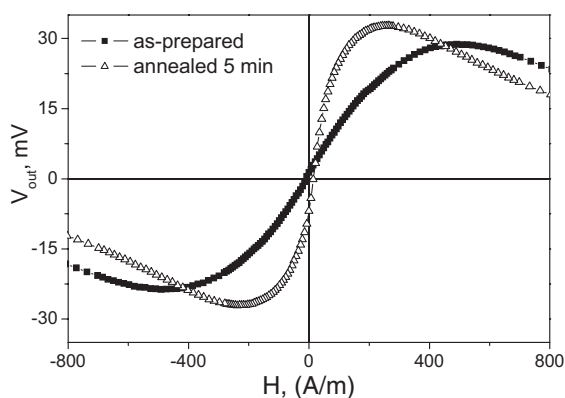
Figure 6: $V_{out}(H)$ of as — prepared and Joule-heated $Co_{67}Fe_{3.85}Ni_{1.45}B_{11.5}Si_{14.5}Mo_{1.7}$ microwire (current annealing with 50 mA current intensity).
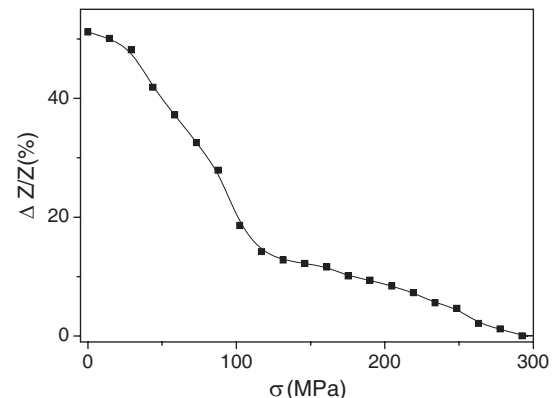
Figure 7: Stress impedance effect of stress annealed $Fe_{74}B_{13}Si_{11}C_2$ glass-coated microwire under stress (468 MPa) at 275°C for 0.5h measured at frequency, $f = 10\,MHz$ for the driving current amplitude of 2 mA.

with so-called "Back stresses" originated from the composite origin of glass-coated microwires annealed under tensile stress: compressive stresses compensate axial stress component and under these conditions transversal stress components are predominant [15].

Consequently, these stress annealed samples exhibit stress-impedance effect, i.e., impedance change ($\Delta Z/Z$) under applied stress, σ, observed in samples with stress induced transversal anisotropy (see Fig. 7).

It should be assumed that the internal stresses relaxation after heat treatment should drastically change both the soft magnetic behavior and $\Delta Z/Z(H)$ dependence due to stress relaxation, induced magnetic anisotropy and change of magnetostriction constant under annealing.

Obtained stress and magneto-impedance effects are demonstrated to be quite suitable for applications for development of tuneable metamaterials containing ferromagnetic microwires [16, 17]. The potential applications for metamaterials based on microwires with high magneto-impedance effect can be divided in two categories. The first one, where the MI effect in wires is used to control the metamaterials properties. Applying the magnetic field or other stimulus will cause the change of reflection, transition and absorption in the MTM. For example, an "active microwave window" can be realized which state can be changed from transparent (open) to opaque (close) for the microwaves waves. Other applications are transmission signal modulation, deferent frequency selective surfaces and reconfigurable absorbers.

The second category includes different sensing applications that use the high sensitivity of the wire's impedance to external stimuli. They include non-destructive testing and structure health monitoring for detection of invisible structural damages and defects, local measurements of the stress and temperature distribution. The measurement can be conducted in the waveguide and in the free-space. The later being non-contact remote method is of special interest as it allows in-situ health monitoring of objects such as infrastructure (bridges, buildings, etc.), pipeline and pressure vessel structural integrity monitoring and other.

4. CONCLUSIONS

In thin amorphous wires, produced by the Taylor-Ulitovski technique, magnetic softness and magnetic field dependence of GMI effect (both longitudinal and off-diagonal) and GMI hysteresis are determined the magnetoelastic anisotropy. This magnetoelastic anisotropy can be tailored by the sample geometry and adequate annealing. There are a number of interesting effects, such as induction of the transversal anisotropy in Fe-rich microwires allowing creating extremely stress sensitive elements. Studies of diagonal and off-diagonal MI tensor components of glass-coated microwires have shown the grate potential of these materials for microminiaturized magnetic field sensor application. Their main advantages are high sensitive low-hysteresis field dependence. By varying the alloys composition and applying post fabrication processing it is possible to control the sensor's operating range. Low field GMI hysteresis has been observed and explained in terms of helical magnetic anisotropy of microwires. Applications of thin microwires in tuneable metamaterials is discussed.

REFERENCES

1. Jiles, D. C., *Acta Materialia*, Vol. 51, 5907–5939, 2003.
2. Zhukova, V., M. Ipatov, and A. Zhukov, *Sensors*, Vol. 9, 9216–9240, 2009.
3. Cobeño, A., F. A. Zhukov, J. M. Blanco, and J. Gonzalez, *J. Magn. Magn. Mater.*, Vol. 234, L359–L365, 2001.
4. Honkura, Y., *J. Magn. Magn. Mater.,* Vol. 249, 375–381, 2002.
5. Panina, L. V. and K. Mohri, *Appl. Phys. Lett.*, Vol. 65, 1189–1191, 1994.
6. Beach, R. and A. Berkowitz, *Appl. Phys. Lett.*, Vol. 64, 3652–3654, 1994.
7. Ipatov, M., V. Zhukova, A. Zhukov, J. Gonzalez, and A. Zvezdin, *Phys. Rev. B*, Vol. 81, 134421-8, 2010.
8. Sandacci, S. I., D. P. Makhnovskiy, L. V. Panina, K. Mohri, and Y. Honkura, *IEEE Trans. Magn.*, Vol. 35, 3505–3510, 2004.

9. M. Vazquez, J. M. García-Beneytez, J. M. García, J. P. Sinnecker, and A. Zhukov, *J. Appl. Phys.*, Vol. 88, 6501–6505, 2000.

10. Zhukova, V., N. A. Usov, A. Zhukov, and J. Gonzalez, *Phys. Rev B*, Vol. 65, 134407-1-7, 2002.

11. Zhukov, A., M. Ipatov, J. Gonzalez, J. M. Blanco, and V. Zhukova, *J. Magn. Magn. Mater.*, Vol. 321, 822–825, 2009.

12. Fujimori, H., K. I. Arai, H. Shirae, H. Saito, T. Masumoto, and N. Tsuya, *Japan. J. Appl. Phys.*, Vol. 15, 705–706, 1976.

13. Zhukov, A. and V. Zhukova, *Magnetic Properties and Applications of Ferromagnetic Microwires with Amorphous and Nanocrystalline Structure*, 162, Nova Science Publishers, Inc., 400 Oser Avenue, Suite 1600 Hauppauge, NY 11788, 2009, ISBN: 978-1-60741-770-5.

14. Chiriac, H., T. A. Ovari, and G. Pop, *Phys. Rev. B*, Vol. 42, 10105–10113, 1995.

15. Zhukov, A., *Adv. Func. Mat.*, Vol. 16, 675–680, 2006.

16. Panina, L., M. Ipatov, V. Zhukova, J. Gonzalez, and A. Zhukov, "Tuneable composites containing magnetic microwires," *Composite Materials/Book 2*, InTech-Open Access Publisher, University Campus STeP Ri, Slavka Krautzeka 83/A, 51000 Rijeka, Croatia, www.intechweb.org ISBN 978-953-307-1098-3.

17. Panina, V., M. Ipatov, V. Zhukova, A. Zhukov, and J. Gonzalez, *J. Appl. Phys.*, Vol. 109, 053901, 2011.

Effect of Ionospheric Macroscale Inhomogeneities on Radiosignals under Conditions of High-frequency Oblique Heating

Yu. K. Kalinin[1] and N. P. Sergeenko[2]

[1]Fedorov Institute of Applied Geophysics, Moscow, Russia
[2]Pushkov Institute of Terrestrial Magnetism
Ionosphere and Radiowaves Propagation, Moscow, Troitsk, Russia

Abstract— The basic properties of macroscale ionospheric inhomogeneities with horizontal sizes of the order of 1 thousand km and lifetime of more than 10^4 s, traveling over a distance of up to 10 thousand km at a nearly sonic velocity, are considered. The occurrence frequency of such objects varies from 0.05 to 0.3 and is characterized by the Poisson law. The results characterizing the effect of macroscale inhomogeneities on various radiosignals during sounding of the ionosphere in the HF ranges are presented. Some results of high-frequency oblique heating of the ionosphere are interpreted in terms of macroscale inhomogeneities originating as a result of anthropogenic effects on near-Earth space.

1. INTRODUCTION

The formation of macroscale ionospheric inhomogeneities with horizontal sizes of the order of 1 thousand km and a lifetime of more than 10^4 s can now be accepted as an established fact after the series of works [1, 2]. These objects are independently observed in the topside ionosphere with an occurrence frequency of 0.1 and in the region of the main ionization maximum with an occurrence frequency of up to 0.3.

The presence of macroscale inhomogeneities in the ionosphere can explain a series of characteristic features of various signals of ionospheric vertical sounding. One of the objectives of the present paper is to analyze these effects. At the same time, under the oblique action of a narrow powerful high-frequency (HF) radiowave beam on the ionosphere, several new features of the listed signals may arise. These features can be interpreted in terms of macroscale inhomogeneities in the ionosphere. What we mean here are the series of unique experiments (which have not yet been repeated completely) carried out in 1971–1973. Powerful transmitters ($\bar{P} = 0.1$–5 MW) in the decameter range ($f = 10$–23 MHz) and large-format antennas ($G = 500$–2000) of broadcasting and radiolocation systems located in southern Ukraine were used as emitters. These systems produced intensities of the HF-wave field of up to 0.3 V/m at distances of 1–1.5 thousand km in the region of the first hop. The present publication is aimed at a more representation of the results of the study of the oblique HF heating of the ionosphere as was done in [3]. It should be noted that the cycle of investigations (1971–1973) was carried out by many groups of collaborators of the Scientific Research Institute of Long-Range Radiocommunication; Bauman Moscow State Technical University; Institute of Terrestrial Magnetism, Ionosphere, and Radiowave Propagation and other organizations.

In the past years, the results of these experiments have been reanalyzed, and their updated version is presented here. To a greater extent, this refers to standpoints and hypotheses.

2. VERTICAL SOUNDING

As is known, the critical frequency fc of the ionospheric F2 region is one of the basic parameters at vertical sounding by the sufficiently well known method. This also holds true for the theory of sounding of the horizontally stratified ionosphere. The presence of macroscale inhomogeneities of the electron density n_e near the main ionization maximum determines the fact that the statistics of the ionosphere virtually always has a non-Gaussian character. Phenomenologically, this means that the condition of small moduli of the statistical invariants (asymmetry A and excess E) of the relative variations in the critical frequency fc is invalid. The sample statistical invariants A and E can be compared to the parameters of a random impulse process [4], where proper macroscale inhomogeneities of electron density are impulses. Data on the ionosphere sounding by the VS method make it possible to estimate the occurrence probability of macroscale inhomogeneities with a contrast $|\delta n_{e.}/n_e| \geq 0,3$ equal to ~ 0.1. These data can be matched to the estimate of the rms deviation (RMSD) of the critical-frequency $\delta fc_{.}/fc$ relative variation, which is also equal to
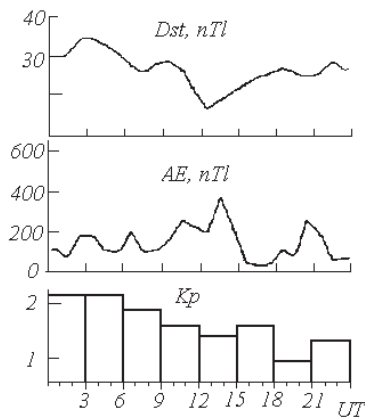
Figure 1: Variations of geomagnetic indexes on December 24, 1971.
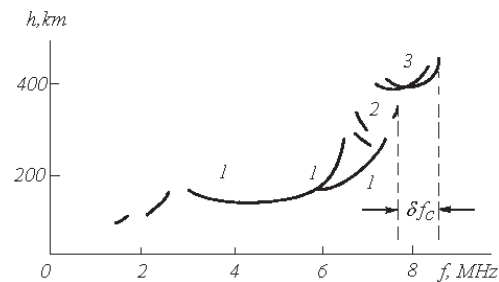

Figure 2: (1) Fragments of the undisturbed ionosphere ionogram; (2) and (3) additional ionogram fragments arising at oblique HF heating.

0.1. For matching, we should use a multicomponent model of random variations $fc_./fc$. Since the horizontal sizes of the macroinhomogeneities $l_r \sim 1$ thousand km exceed by an order of magnitude the sizes of the Frenel zone at vertical sounding, the presence of macroinhomogeneities in this case means that fc varies in the wide vicinity of a VS station. In other words, no variations in the ionogram structure registered by the VS stations will occur, save for the boundary effects. Only an increment δfc of the quantity fc will be registered. The situation will slightly change when oblique heating by a powerful beam of HF radiowaves is carried out. Fig. 1 represents the typical simplified scheme of the VS ionograms registered at Moscow station on December 24, 1971, during the experimental heating of the ionosphere by a powerful oblique beam of HF radiowaves.

Let's notice, that this day was absolutely quiet in the geomagnetic relation. On Fig. 1 the variations of geomagnetic indexes Kp, Dst and AE, presenting geomagnetic activity is resulted. It is visible, that was not classical storms, ionospheric substorms, index AE did not exceed 400 nTl.

The heating was realized at the frequency $fc = 12$ MHz, which is close to the MUF-F2-2000 value in daytime when the emission is directed from southen Ukraine toward Moscow. Heating was carried out from 12:00 to 16:00 Moscow Legal Time for 20 min at the beginning of every hour. Fig. 1 displays the frequency (abscissa) and VS-signal delay recalculated to the effective altitudes. The heating was realized at the frequency $fc = 12$ MHz, which is close to the MUF-F2-2000 value in daytime when the emission is directed from southen Ukraine toward Moscow. Heating was carried out from 12:00 to 16:00 Moscow Legal Time for 20 min at the beginning of every hour. Fig. 1 displays the frequency (abscissa) and VS-signal delay recalculated to the effective altitudes. Before the beginning of the heatting intervals, the ionograms contained the usual traces denoted by 1 in Fig. 2. They were used for determining an undisturbed value of the critical frequency fc. By the end of the 20-min intervals of heating, the form of the ionograms became more complicated. Omitting insignificant details, "falling" traces (2) and traces (3) corresponding to the origination of the new region with the critical frequency $fc + \delta fc$ above F2 appeared in the ionograms. The ratio $\delta fc/fc$, as determined from the ionograms, is about 0.05. This value corresponds to an electron-density increment $\delta n_e/n_e = 0.1$ in the main ionization maximum. The estimates performed ignoring absorption in the E region indicate that, at the apex of the first hop, the field intensity in antinodes of the interfering incident and reflected waves should be about ~ 0.3 V/m. The squared ratio of this value to the value of the characteristic plasma-field intensity E_p can be used as an expected estimate of the $\delta n_e/n_e$ order of magnitude. It is characteristic that this estimate coincides with the independent estimate of the $\delta n_e/n_e = \delta fc/fc$ value.

Now, we should examine the complex questions associated with the deformation of the $n_e(h)$ profile as a result of the oblique HF heating. In Fig. 3, the abscissa represents the value of $\log[\delta n_e/(n_e)_0]$, where $(n_e)_0$ is expressed in cm-3, and the height (in km) is plotted on the y-axis. The solid line represents the undisturbed profile, and the dashed line corresponds to the result of heating. The decrease in the height scale near the main maximum from H_0 to H_x is also shown here. The $n_e(h)$ variation obtained as a result of direct VS-data processing can be interpreted in a rather simple manner, based on the model notions of the presence of a hotter interspersion with
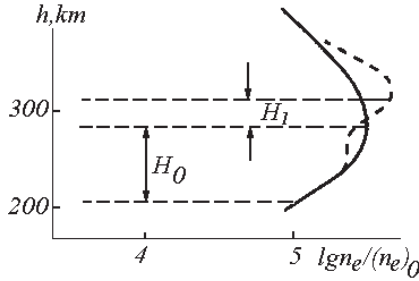
Figure 3: The scheme of transformation of the undisturbed $n_e(h)$ profile with the scale H_0 (solid line) into the profile changed by oblique HF heating with the scale H_1 (dashed line).
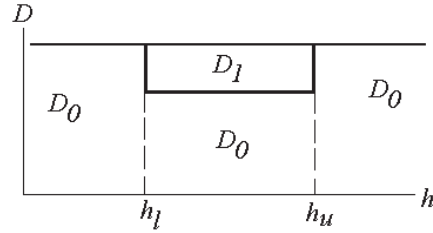
Figure 4: Model height profile of the diffusion coefficient in the interval (h_l, h_u), a fraction-of the medium is characterized by the diffusion coefficient D_1.

the diffusion coefficient D_0 in the medium with a diffusion coefficient D_x.

Let us assume that, at the time instant $t = 0$, the interspersion is characterized by the geometry presented in Fig. 4; i.e., the whole medium outside the height range $h \in [h_l, h_u]$ corresponding to the powerful HF-wave beam is characterized by the diffusion coefficient D_0. Inside the range $[h_l, h_u]$, part of the medium (say, $p\%$) is also characterized by the value D_0, while D_1, characterizes the remaining part $(1-p)\%$. Let then the pattern described in Fig. 3 be "rest in itself." It is evident that diffusion mixing and respective spreading of boundaries will begin. Since $1 - p \ll p(\delta n_e \ll n_e)$, the model diffusion processes can be regarded as independent. For modeling, solution of the following parabolic equation will be required:

$$\frac{\partial n_e}{\partial t} = D \frac{\partial^2 n_e}{\partial h^2} \tag{1}$$

at the initial time instant, Eq. (1) has the form of the integral of the δ-function. Such solutions can be obtained in the form of the respective integrals:

$$U(x) = \frac{1}{\sqrt{2\pi}} \int_z^\infty e^{-\frac{y^2}{2}}, \quad V(x) = \frac{1}{\sqrt{2\pi}} \int_{-\infty}^z e^{-\frac{y^2}{2}} \tag{2}$$

where $z = x/Dt$. Functions U and V are the solution to Eq. (1), as can be proved by direct differentiating. It is not difficult to obtain $U(x, D) + V(x, D) = 1$ and $U(0) = V(0) = 1/2$. If we consider now the dynamics of mixing near only one of the boundaries presented in Fig. 3, it will be evident that the desired variation $\delta n_e/n_e$ can be represented in the form

$$\frac{\delta n_e}{n_e} = 1 - U(x, D_0) + V(x, D_1) \tag{3}$$

where D_1, is the diffusion coefficient inside the beam. Let us note that relationship (3) at $D_1 = D_0$ is vanishing. Solution (3) has important model properties. In particalar, it is possible to derive the extrema of the function $\frac{\delta n_e}{n_e}(x)$ in the explicit form. The respective equation has the form

$$\sqrt{\frac{D_1}{D_0}} = \exp\left[-\frac{x}{4t}\left(\frac{1}{D_1} - \frac{1}{D_0}\right)\right] \tag{4}$$

From this it follows that the extrema are located symmetrically with respect to the beam boundary and are moved away from it proportionally to $t^{1/2}$. For a not very big difference between D_1 and D_0, the relationship $|x| \approx \sqrt{2D_0 t}$ is valid. For example, for $D_0 \sim 10^9 \, \text{cm}^2/\text{s}$ and $t \sim 10^3 \, \text{s}$, $|x| = 10 \, \text{km}$, as can be seen in Fig. 3, where the scale H is presented. Fig. 5 displays the height $|h|$ (the abscissa) counted off from the boundary of the HF-radiowave beam, which heats up the ionosphere. Various functions $F_i(h)$ are plotted on the y-axis, ($i = 1, 2, 3$ correspond to the curve nos.): $i = 1$ corresponds to $V(h)$; $i = 2$, $U(h)$. Functions F_1 and F_2 are taken for the same instant. However, since $D_1 > D_0$ (hot plasma occupies the region $h > 0$), curve 2 at a zero point has a derivative that is less than the modulus of curve 1 derivative. As a result, the sum $F_1 + F_2 = F_3$ (presented by curve 3 in Fig. 5) has two extrema: the maximum in the region of colder plasma
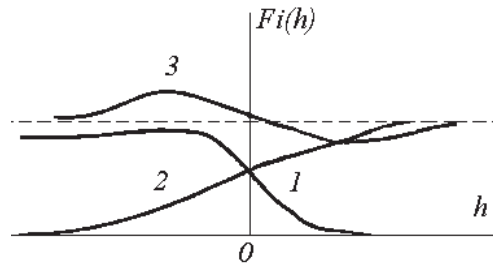
Figure 5: Various solutions of the model diffusion problem.

$(h < 0)$ and the minimum at $h > 0$. Less movable cold plasma has no time to completely compensate the hot plasma outflow from the region $h > 0$. The proposed scheme has an illustrative character and can be improved by summarizing the effect of the upper and lower boundaries of the beam (h_u and h_l in Fig. 4). It is also possible to take into account the fact that the values of D_0 are different at heights h_u and h_l and the formation of the extrema is more effective near the upper boundary of the beam. It could also be taken into account that the dependence $D_0(h)$ for the longitudinal coefficient of the ambipolar diffusion admits a good approximation:

$$D_0(h) = D_0(h_m) \exp\left[\frac{h - h_m}{H_D}\right], \tag{5}$$

where h_m is the reference level (e.g., the height of the ionization main maximum), and H_D is the diffusion scale. In the presence of dependence (5), the diffusion equation is more complex than Eq. (1). However, in this case, the model problem also admits a solution in quadratures. In this case, all improvements will not fundamentally change the order of magnitude of the estimates obtained on the basis of Eqs. (1)–(4).

It is also important that the stratification of the ionospheric F2-region, which apparently was first observed on December 24, 1971, at oblique heating of the ionosphere by a powerful HF beam (at the frequency chosen according to the long-term prediction), was not observed in the other two experiments with a similar heating regime, which were carried out on December, 1971. The technique used in these experiments did not admit an operative re-tuning at a frequency of the powerful radiowave. The question remains open as to whether, for example, a partial shielding by the semitransparent sporadic Es layer took place in the mentioned two unfortunate cases, or the real operating frequencies were higher than the current MUF on the path with the first-hop located above the Moscow station. In this case, the region of heating would have moved further to the north.

3. CONCLUSIONS

In the present paper, we mainly succeeded in considering the radiophysical effects of the presence of macroscale inhomogeneities in the ionosphere using, as an example, vertical sounding, under natural conditions and under conditions of disturbance by oblique HF heating. The framework of the paper did not enable us to cover a number of other aspects in this area. Let us mention some of them. For example, it is the movement of objects that causes the space-time shift of the cross-correlation function of the critical-frequency relative variations. Further, it is possible to mention one effect of practical importance for the HHF signals. Since macroscale inhomogeneities occur independently in different ionospheric regions, a percentage of the duration of the period, when the stability of transiono-spheric signals can be lowered, should be summarized over all regions. This operation yields the values 30–40%, which is significantly higher than in the case of the topside ionosphere only.

For oblique HF heating of the ionosphere, it should be stressed that the ionogram deformations (similar to those presented in Fig. 2) take place also after chemical explosions in the ionosphere (the Firefly project [5]) and after earthquakes [1, 2]. In all cases, the ionospheric critical frequency varies. Naturally, this leads to a variation in the sample statistical invariants of the critical-firequency relative variations in the ionospheric F2 region. In addition, sample invariants (the mean, dispersion, asymmetry, and excess) are variable from year to year. For example, the anthropogenic component caused by the launches of satellites with special-type orbits is identified in this variability [4].

Thus, the hypothesis of a macroscale instability of the ionosphere takes hold; i.e., the ionosphere can form macroscale long-living inhomogeneities of the electron density spontaneously and under the action of "shock" external sources.

REFERENCES

1. Kalinin, U. K. and N.P. Sergeenko, "Mobile solitary macroinhomogeneities appearing in the ionosphere several hours before catastrophic earthquakes," *Doklady of Russian Akademy of Sciences/Earth Science Section*, Vol. 387, No. 1, 105, 2002.
2. Kalinin, U. K., A. A. Romanchuk, N. P. Sergeenko, and V. N. Shubin, "The large-scale isolated disturbances dynamics in the main peak of electronic concentration of ionosphere," *Journal of Atmospheric and Solar Terrestrial Physics*, Vol. 65, No. 11–13, 1175, 2003.
3. Kalinin, Yu. K. and N. P. Sergeenko, "Propagation of decametric radio waves along transpolar parths," *Radiophysics and Quantum Electronics*, Vol. 52, No. 2, 2009.
4. Dzvonkovskaya, A. L., V. A. Kuznetsov, and N. P. Sergeenko, "Planetary statistics of the critical frequency of the ionospheric F2 region during catastrophic earthquakes," *Geomagn. Aeron.*, Vol. 46. No. 4, 552, 2006.
5. Gallagher, Ph. B. and R. A. Barnes, "Radio-frequency backscatter of artificial electron clouds," *J. Geophys. Res.*, Vol. 68, No. 10, 2987, 1961.

UHF Propagation Prediction in Smooth Homogenous Earth Using Split-step Fourier Algorithm

Seyyed Reza Hosseini[1], **Reza Sarraf Shirazi**[1], **A. Kiaee**[1],
P. Pahlavan[2], **and M. Sharifi Sorkherizi**[3]

[1]Wave Propagation & Microwave Measurement Research Lab., Department of Electrical Engineering
Amirkabir University of Technology, 424 Hafez Avenue, Tehran 15914, Iran
[2]Sharif University of Technology, Iran
[3]Khajenasir University of Technology, Iran

Abstract— The electromagnetic wave propagation prediction in smooth homogenous earth is studied. This estimation employs Fourier Split-Step algorithm. The process of how parabolic equation and Fourier Split Step algorithm achieved, is investigated. Error resulted from this approximation is studied. Source modeling is analyzed. Simulations based on this method are illustrated on different values of frequency, range and antenna height.

1. INTRODUCTION

There are several methods for predicting electromagnetic wave propagation in the atmosphere such as geometric optics (GO), Finite Difference Time Domain (FDTD) [1], modal analysis and even combinations of them [2].

One of the most important and efficient methods for electromagnetic wave propagation prediction is solving parabolic equation that is an approximation of Helmholtz equation [3].

A good introduction to the parabolic equation (PE) method and its application to radio wave propagation together with the approximations involved is given in [4].

For problems having large computation domains, the domain decomposition technique has been presented to solve the problem of a double-sided impedance boundary by the Fourier split-step method [5].

This approximation leads to Fourier split-step algorithm that has two kinds, narrow angle and wide angle. Unfortunately, in the process of approximation, backscattered field component is neglected and simulations show that the algorithm accuracy will be decreased if propagation angle be greater than approximately 10° of the horizontal plane [2] but for angles smaller than 10°, the created error is tolerable [6]. For implementing Fourier Transform in Split Step Parabolic Equation (SSPE) algorithm, we use Fast Fourier Transform (FFT) method that reduces program run time.

In this paper, we first represent a brief review of parabolic equation that leads to Fourier split-step algorithm, source modeling, and at the end the numerical simulations are illustrated. This method predicts the propagation factor, receiver power pattern and path loss for line of sight propagation.

2. PARABOLIC EQUATION

Parabolic equation method is a kind of wave equation approximation that models energy propagation in a cone with specified axis called paraxial direction as shown in Figure 1.
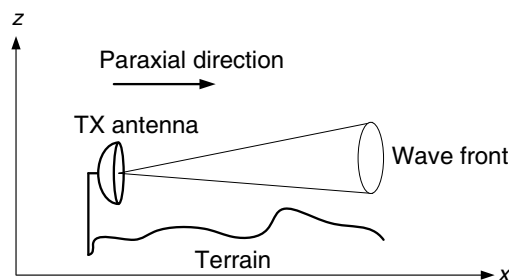
Figure 1: Wave paraxial propagation.
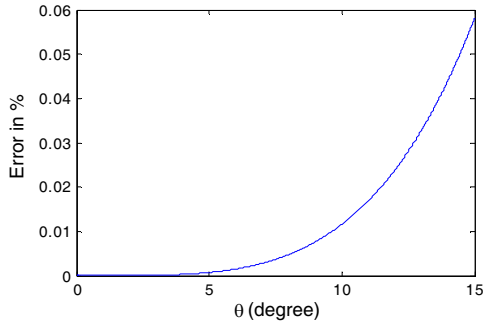
Figure 2: Error percentage caused by parabolic equation approximation.
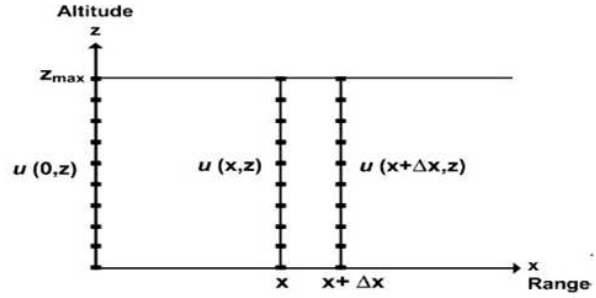
Figure 3: Fourier split-step.

In tropospheric propagation analysis, we deal with the two-dimensional (2D) electromagnetic problem, which is managed by the scalar Helmholtz equation as presented here [7]:

$$\nabla^2 \varphi + k^2 n^2 \varphi = 0 \tag{1}$$

which can be expressed as:

$$\frac{\partial^2 \varphi}{\partial x^2} + \frac{\partial^2 \varphi}{\partial z^2} + k^2 n^2 \varphi = 0 \tag{2}$$

where $\varphi = \varphi(x, z)$ is the wave function that shows electric or magnetic fields in vertical or horizontal polarization. x, represents range and z, represents altitude. Furthermore, $n = n(x, z)$ is refractive index that generally is not constant and is dependent to range and altitude variations. k is wave number in free space. Field component $\varphi(x, z)$ is equal to $E_y(x, z)$ in horizontal polarization and is equal to $H_y(x, z)$ in vertical polarization. We assume the time dependence of φ to be $\exp(-i\omega t)$. By choosing x direction as paraxial direction, function $u(x, z)$ is defined as [8]

$$u(x, z) = e^{-ikx} \varphi(x, z). \tag{3}$$

For propagated waves in paraxial direction according to (3), $u(x, z)$ variations toward x are slow, so this function has appropriate numerical features. By using (3) we can express Helmholtz equation according to $u(x, z)$:

$$\frac{\partial^2 u}{\partial x^2} - 2ik\frac{\partial u}{\partial x} + \frac{\partial^2 u}{\partial z^2} + k^2(n^2 - 1)u = 0 \tag{4}$$

Equation (4) describes waves propagating along both positive and negative x directions. We can factorize (4) into

$$\left(\frac{\partial}{\partial x} - ik + ik\sqrt{1 + (n^2 - 1) + \frac{1}{k^2}\frac{\partial}{\partial z^2}} \right) \times \left(\frac{\partial}{\partial x} - ik - ik\sqrt{1 + (n^2 - 1) + \frac{1}{k^2}\frac{\partial}{\partial z^2}} \right) u = 0 \tag{5}$$

where the first and second bracket are forward and backward waves, respectively.

If we assume that there is only the forward wave component in the medium we achieve to [9]

$$\left(\frac{\partial}{\partial x} - ik + ik\sqrt{1 + (n^2 - 1) + \frac{1}{k^2}\frac{\partial}{\partial z^2}} \right) u = 0. \tag{6}$$

The differential operator under square root sign is not in usual form, it can be understood if it is represented in formal sense. So, we should use some approximations to express pseudo differential operator in usable form. We rewrite (6) as:

$$\frac{\partial u}{\partial x} = ik\left(1 - \sqrt{1 + (n^2 - 1) + \frac{1}{k^2}\frac{\partial}{\partial z^2}} \right) u \equiv ik\left(1 - \sqrt{1 + Q(x, z)} \right) u \tag{7}$$

in which $Q(x, z) = n^2 - 1 + \frac{1}{k^2}\frac{\partial}{\partial z^2}$.

The narrow-angle parabolic equation can be obtained from (7) by taking only the first two terms of the Taylor series expansion of the square-root operator [3].

$$\sqrt{1 + Q(x, z)} \cong 1 + \frac{Q(x, z)}{2} \tag{8}$$

Finally the narrow-angle parabolic equation is obtained as:

$$\frac{\partial u}{\partial x} = \frac{1}{2ik} \left(\frac{\partial^2 u}{\partial z^2} + k^2 (n^2 - 1) u \right). \tag{9}$$

This is a first-order partial differential equation in x and can, therefore, be marched numerically if $u(z)$ is known on some initial plane x_0 [9]. The created error using above approximation is

$$e_{PE} = 1 - \cos\theta - \frac{\sin^2\theta}{2} \tag{10}$$

where θ is angle of propagation with respect to x-axis. The error plot is ascending with θ. But in small ranges of θ, error is tolerable.

It is clear that for small ranges of propagation angles the error can be easily neglected. The split-step Fourier technique searches the solution using Fourier transform:

$$U(x, p) = F\{u(x, z)\} = \int_{-\infty}^{\infty} u(x, z) e^{-ipz} dz. \tag{11}$$

The split-step Fourier Transform solution at $x + \Delta x$ is given by:

$$u(x + \Delta x, z) = e^{\frac{ik(n^2 - 1)\Delta x}{2}} F^{-1} \left\{ e^{\frac{-ik_z^2 \Delta x}{2k}} F\{u(x, z)\} \right\} \tag{12}$$

in which F represents the Fourier Transform, k_z is transform variable defined by $k_z = k \sin\theta$ and n is refractive index and in general is not constant, but in an infinite and homogeneous medium, n is constant. SSPE algorithm calculates field magnitude in each range according to field magnitude in last range by step Δx. The Fourier Transform is implemented in MATLAB by Fast Fourier Transform (FFT).

3. SOURCE MODELING

For starting SSPE algorithm procedure we need to know the initial field $u(0, z)$. This field is easily determined using image theory and antenna pattern far field approximation. So, the initial field at $x = 0$ is constructed in the Fourier domain and can be obtained as follows

$$U(0, p) = G \left[f(p) e^{-ipa_t} + |\Gamma| f(-p) \exp(ipa_t) \right] \tag{13}$$

where $f(p)$ is antenna pattern, a_t is the height of antenna, Γ is the Fresnel reflection coefficient, and G is normalized factor. The initial field and antenna aperture distribution are Fourier Transform pairs, according to different boundary conditions (Dirichlet or Neumann), the initial fields can be found by the following equation [10]

$$u_H(0, z) = G \int_0^{\infty} \left[U(0, p) e^{-ipa_t} + \Gamma_H U(0, -p) e^{ipa_t} \right] \sin(pz) dp \tag{14}$$

$$u_V(0, z) = G \int_0^{\infty} \left[U(0, p) e^{-ipa_t} - \Gamma_V U(0, -p) e^{ipa_t} \right] \cos(pz) dp \tag{15}$$

The initial field of an antenna with Gaussian pattern is given by:

$$u(0, z) = G \frac{k\beta}{2\sqrt{2\pi \log 2}} e^{-ik\theta_0 z} e^{-\left(\frac{\beta^2}{8 \log 2} k^2 (z - a_t)^2 \right)} \tag{16}$$

where β is beam width, θ_0 is elevation angle, G is a normalization factor related to β and θ_0 [8, 11].
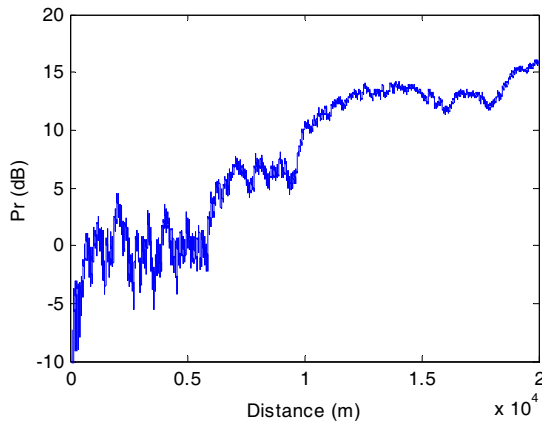
Figure 4: Received power in range 20 km, at 1 GHz, transmitter antenna height is 40 m, propagation angle is 30, receiver antenna height is 100 m, G is normalization factor assumed 10.8.
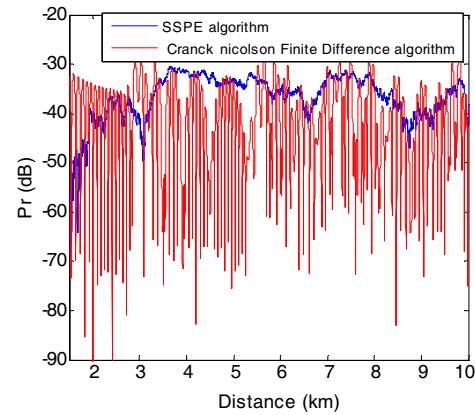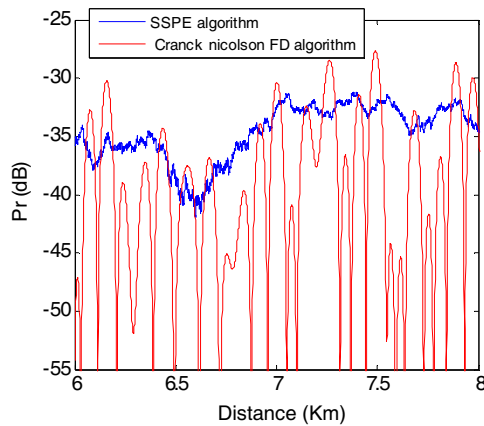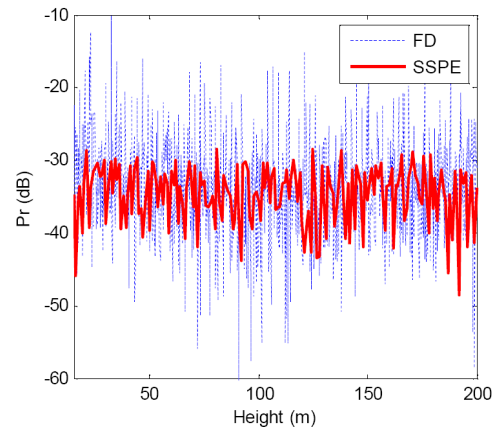

Figure 5: Received power in range 10 km, operating frequency is 1 GHz, transmitter antenna height is 40 m, propagation angle is 50, receiver antenna height is 100 m, G is normalization factor assumed 10.8.

Figure 6: Received power in range [6 8] km, operating frequency is 1 GHz, transmitter antenna height is 40 m, propagation angle is 5°, receiver antenna height is 100 m, G is normalization factor assumed 10.8.

Figure 7: Received power in height to 200 m, operating frequency is 1 GHz, transmitter antenna height is 40 m, propagation angle is 5°, G is normalization factor assumed 10.8.

The accuracy of SSPE method depends on accuracy of choosing parameters. Range (x), range step size (Δx), height step size (Δz) and propagation angle (θ) are some important parameters for accurate implementing of SSPE method. The general conditions are presented [2]

$$\Delta z \to 0 \quad \Delta x \to 0 \quad \Delta p \to 0 \quad 0 < x < \infty \tag{17}$$

More exact conditions that we use for simulations are listed below

$$\Delta x = \frac{4\pi}{\lambda} (\Delta z)^2 \quad x > \frac{100\lambda}{2\pi} \quad \Delta z \leq \frac{\lambda}{10}. \tag{18}$$

We calculate received power based on Split-Step Fourier algorithm, which is shown in Figures 4 and 5.

If we look at the desired range it can be seen that the received power variation is approximately like sine function as shown in Figures 6 and 7.

Parabolic equation approximation has been studied as an appropriate way to analyze wave propagations and SSPE algorithm has been presented as a recursive method for predicting far field receiving power pattern.

SSPE method simulations have shown the receiver power has a kind of periodic pattern that can be changed by distance.

REFERENCES

1. Funda, A. and L. Sevgi, "A novel finite-difference time-domain wave propagator," *IEEE Transactions in Antenna & Propagation*, Vol. 48, No. 3, Mar. 2000.
2. Dockery, G. D., "Modeling electromagnetic wave propagation in the troposphere using the parabolic equation," *IEEE Transactions in Antenna & Propagation*, Vol. 36, No. 10, Oct. 1988.
3. Kutller, J. R., "Differences between the narrow-angle and wide-angle propagators in the split-step fourier solution of the parabolic wave equation," *IEEE Transactions in Antenna & Propagation*, Vol. 47, No. 7, Jul. 1999.
4. Kuttler, J. R. and G. D. Dockery, "Theoretical description of the parabolic approximation/Fourier split-step method of representing electromagnetic propagation in the troposphere," *Radio Sci.*, Vol. 26, No. 2, 381–393, Mar./Apr. 1991.
5. Valtr, P. and P. Pechac, "Domain decomposition algorithm for complex boundary modeling using the Fourier split-step parabolic equation," *IEEE Antenna and Wireless Propagation Letters*, Vol. 6, 2007.
6. Lee, D. and S. T. McDaniel, "Ocean acoustic propagation by finite difference methods," *Comput. Math. Applicat.*, Vol. 14, No. 5, 1987.
7. Ozgun, O., "Recursive two-way parabolic equation approach for modeling terrain effects in tropospheric propagation," *IEEE Transactions in Antenna & Propagation*, Vol. 57, No. 9, Sep. 2009.
8. Levy, M. F., *Parabolic Equation Methods for Electromagnetic Wave Propagation*, IEEE Press, London, UK, 2000.
9. Barcley, L., *Propagation of Radiowaves*, 2nd Edition, Institution of Engineering & Technology, London, 2003.
10. Yang, C., L. Guo, and H. Li, "Modelling the radio wave propagation in the troposphere with discrete mixed fourier method," *Antenna, Propagation and EM Theory*, 2008.
11. Li, Y., C. Liu, M. Zhong, Y. Wang, and M. Yang, "Radio wave propagation path loss in the irregular terrain environments," *Microwave, Antenna, Propagation and EMC Technologies for Wireless Communications, 3rd IEEE International Symposium*, 2009.

Radio-frequency Spectrum of Radar Return Signal from Extended Targets

B. S. Yurchak

Goddard Earth Sciences & Technology Center
University of Maryland, Baltimore County, USA

Abstract— This paper presents results of measurements and simulations of the radio frequency spectrum of radar echo-signals from spatially extended geophysical targets such as clouds and rain. The measurements were carried out by X-band weather radar and analog dispersive spectrum analyzer. A quantitative interpretation of the results was carried out based on the representation of an individual meteorological echo-signal as a group of adjoining radio frequency pulses with random initial phases. Simulation of RF-spectrums verified the theoretical assessment the cause of spectrum envelope oscillations as due to the intersignal phase statistics. The results obtained can be applicable to improve calibration and diagnostic aspects of the radar remote sensing.

1. INTRODUCTION

Radar return signal from spatially extended geophysical target (SEGT) $U(t)$ is a convolution of the radar probing pulse with the radial distribution of Slice Equivalent Length (SREL) of the SEGT $b(\frac{2r}{c})$ [1]:

$$U(t) \propto U_0(t) \otimes b\left(\frac{2r}{c}\right) \tag{1}$$

where r is the distance, c is the speed of electromagnetic wave propagation. SREL is the arithmetic sum of square roots of the radar cross section of scatterers located close to the spherical wavefront of the radar irradiance within a so-called slice at a given moment of time [1]. Correspondingly, the radio frequency spectrum (RFS) of a radar return signal $F(\omega)$ is a product of the probing pulse's RFS $F_0(\omega)$ and Fourier transform of the SREL $F\{b(\frac{2r}{c})\}$:

$$F(\omega) \propto F_0(\omega) \cdot F\left\{b\left(\frac{2r}{c}\right)\right\} \tag{2}$$

The features of $F\{b(\frac{2r}{c})\}$ and, consequently, of $F(\omega)$ are commonly unknown. On the other hand, its study is expedient for optimal instrumental calibration of the geophysical (weather) radars and for determination of the information capacity of the radar spectral analysis [2].

2. MEASUREMENTS OF RADIO-FREQUENCY SPECTRUMS OF RETURN SIGNALS FROM METEOROLOGICAL TARGETS

Measurements of RFS were carried out with the standard X-band weather radar MRL-2 that used probing pulse duration of 1 and 2 μs. Radar receiver has Gaussian-shape frequency-response characteristic with "−3 dB" passband of 1.5 MHz. To perform the spectrum analysis, the radio-frequency signal was taken from the intermediate-frequency amplifier output, and directed to dispersive spectrum analyzer C4-47 [3, 4]. The output device of the spectrum analyzer can register spectrums of individual signals and the overlapping envelopes resulting from a number of consecutive signals with radar sounding repetition period during the photo recorder's exposition time of 1–2 seconds.

3. EXPERIMENTAL RADIO-FREQUENCY SPECTRUMS OF RETURN SIGNALS FROM METEOROLOGICAL TARGETS

An illustrative example of the RFS from a point target (a relay broadcast station mast) and a meteorological target (cumulus cloud) is shown in Fig. 1. The spectrum from the point target looks like the same of the probing pulse (Fig. 1(a)). The typical "mean" RFS, as a result of overlapping of many individual RFSs during an exposition time ($\sim$ 1 second) of photo recorder, is shown in Fig. 1(b) and again its envelope looks like the same of the probing pulse. The RFS patterns of individual echo-signals (Figs. 1(c)–(f)) from the meteorological target (cumulus cloud) has a predominately peak-like shape which widely varies from a single peak with a pair of matching
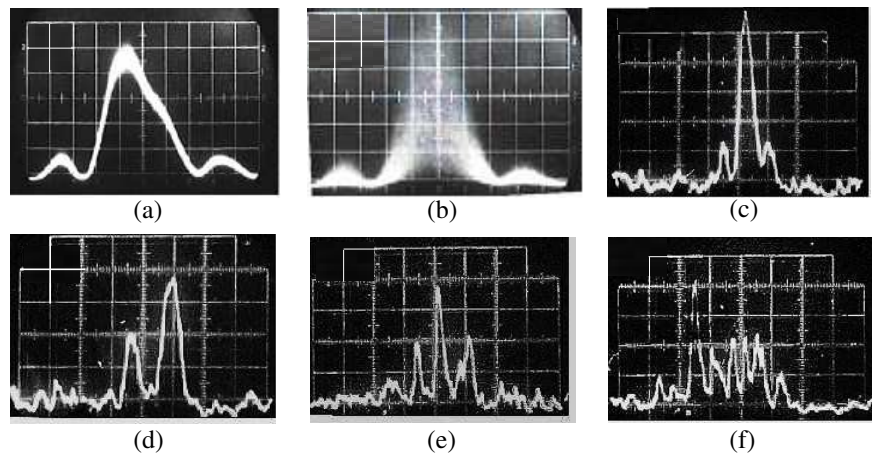
Figure 1: Radio-frequency spectrum of return signals from (a) a point target and (b)–(f) cumulus cloud. (b) is "mean' RFS, (c)–(f) are RFS of several individual signals; horizontal axis is frequency with scale 1 unit equals to 0.5 MHz; duration of probing pulse is 1 μs, duration of the echo-signal section analyzed is 6 μs.

side peaks (Fig. 1(c)) to a multi-peak shape (Fig. 1(f)). The bandwidth of the individual RFS is equal or less of the same of the probing pulse. Measurements of the RFSs from the broad class of meteorological targets, which included clouds of different forms and with different rainfall intensities, indicate that on average the RFSs have a bandwidth (by the first nulls) usually equal to the bandwidth of the probing pulse (Fig. 1(b)), independently of the spatial extension of the meteorological object [5]. Thus the product of the spectrum bandwidth ($\Delta\omega$) and the duration of meteorological echo-signals (τ_e) is much more than unit ($\frac{\Delta\omega}{2\pi} \cdot \tau_e \gg 1$). Therefore meteorological targets can be classified as dispersive targets [6].

4. QUALITATIVE INTERPRETATION OF RESULT OBTAINED

It is possible to show that the spectrum wideness of the meteorological echo-signal is caused by the random phase modulation of the carrier frequency with correlation interval close to the duration of probing pulse [5]. To interpret RFS envelope oscillations observed, it is reasonable to represent the meteorological echo-signal as a group of adjoined radio-frequency pulses with random initial phases and duration equals to the duration of probing pulse (τ_0). In general, the RFS of such random pulse process equals to [7]:

$$S(\omega) = \frac{|F_0(\omega - \omega_0)|^2}{2\tau_0} [1 + K(\omega - \omega_0)] \tag{3}$$

where $F_0(\omega)$ is the RF-spectrum of the typical pulse of the process (group), $K(\omega)$ is a function depended on the correlation among the features of the pulse series, and ω_0 is the central angular frequency of a spectrum. In the case of zero correlation between the initial phases, the RFS of such pulse process will be equal to the RFS of the typical pulse, i.e., to spectrum of the probing pulse. In the case when phase correlation is not negligible, the component $K(\omega)$ is an oscillation function, and depth of its oscillation increases in accordance with the increase of the phase correlation rate [8]. The oscillation pattern (number and the order of alternation of minor and major peaks) depends on the correlation interval $N_0\tau_0$ (N_0 is integer). In the extreme case, when all pulses of a group have the same initial phase, the echo-signal is a long RF-pulse without phase disturbances. The corresponded RFS has a single main peak with bandwidth less than the same of the probing pulse. An example of this case is represented in Fig. 1(c) and corresponds to conditions of high spatial homogeneity of the meteorological target.

5. SPECTRUM SIMULATION

Simulation procedure included a generation of random spatial distribution of the SREL and the probing pulse, calculations their convolution and the spectrum of the "return signal". The phase structure of simulated return signals was analyzed as well. Some stages of the analysis are illustrated in Figs. 2–4. An illustrative example of comparison of RF spectrums of simulated probe pulse with
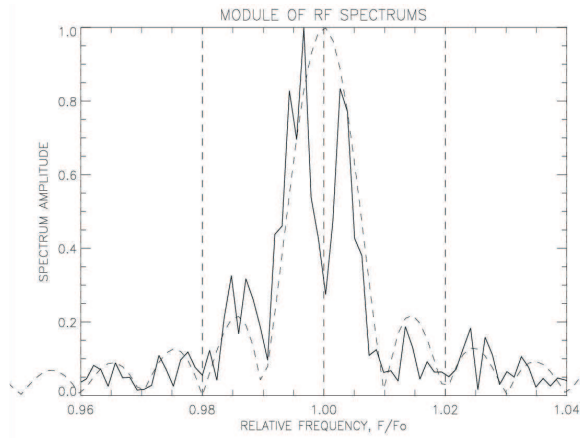
Figure 2: Typical RF-spectrum of the simulated return signal (solid line), spectrum of the probing pulse is shown by dashed line.
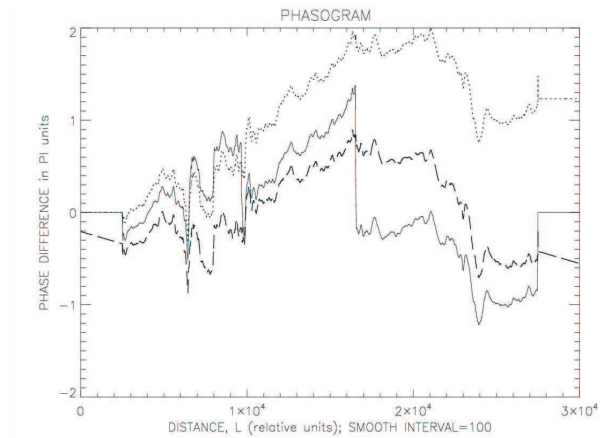

Figure 3: Phasograms of a carrier wave (solid line — original, dotted — unwrapped, long dash — unwrapped & untrended).
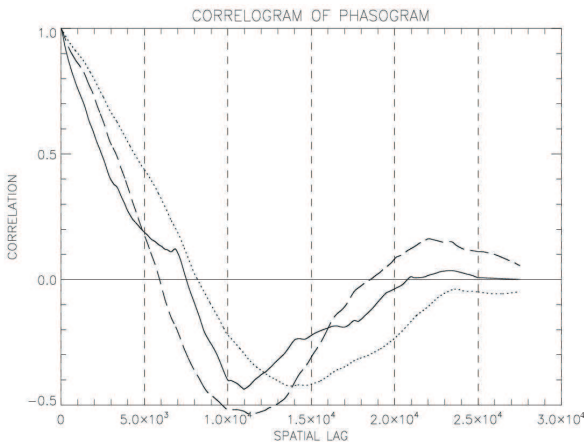

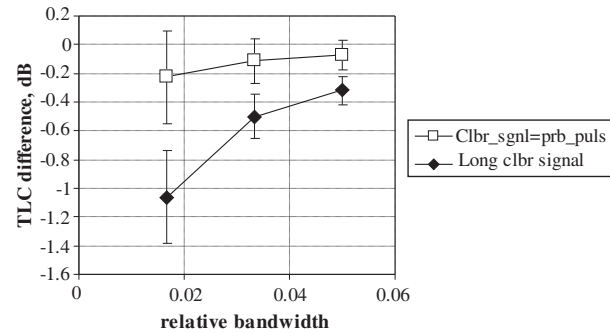Figure 4: Correlation functions of the phasograms shown in Fig. 3; curve marking is the same of Fig. 3.

Figure 5: Mean calibration error versus relative bandwidth for random return signal; error bars indicate the standard deviation.

duration of $1\,\mu s$ (5000 relative units) and return signal of duration $6\,\mu s$ (30000 relative units) is presented in Fig. 2.

Notable feature of return spectrum is its significant unevenness within a main lobe as well as within sidelobes close to the same of the experimental spectrums shown in Fig. 2. In Fig. 3, a phasogram of the same return signal is depicted. To calculate statistical characteristics of this function the unwrapping and untrended procedures were applied to the original phasogram.

Correlation functions of phasograms shown in Fig. 3 are illustrated in Fig. 4.

The plot related to the unwrapped and untrended phasogram verifies, in particular, that the length of the phase correlation interval is equal approximately to the duration of the probing pulse.

6. APPLICATION TO CALIBRATION ISSUE

Primarily calibration principal states: during the passing of a receiver stages the calibration signal should have the same distortion as real signal. Let us take the Transformation Loss Coefficient (TLC) as a ratio of a signal power at the output of a receiver with bounded bandwidth and real non square amplitude-frequency response function (AFRF) to the power at the output of an ideal receiver with evenly distributed AFRF. For calibration and return signals the TLC can be written

in the form:

$$\mu_{c,r} = \frac{\int\limits_{-\infty}^{\infty} |F(\omega)|_{c.r}^2 |K(\omega)|^2 \, d\omega}{\int\limits_{-\infty}^{\infty} |F(\omega)|_{c.r}^2 \, d\omega} \tag{4}$$

where indexes c an r are related to calibration and return signals, respectively. To satisfy the primarily calibration principal the equality $\mu_c = \mu_r$ should be satisfied. In real situation this equality does not fulfilled that causes the relative calibration error:

$$\delta = \frac{\mu_r}{\mu_c} \tag{5}$$

The error (5) has been calculated for calibration signal equal to the probe pulse and to a signal with length much longer compare with the probe pulse length. AFRF was assumed to be Gaussian. Return signal spectrum was simulated as was described above. Estimates were carried out for each of 50 realizations, and then averaged. The calculations were performed for three values of relative bandwidth ($\frac{\Delta\omega}{\omega_0}$) and are shown in Fig. 5. As follows from the plot the usage of long calibration signals causes notable calibration errors that verifies theoretical estimates provided in [2].

7. SUMMARY

In this study the characteristics of the radio frequency spectrums of the meteorological radar echo-signals have been obtained. The study included theoretical, experimental and simulation stages. On average, the envelopes and bandwidth of RFSs of the meteorological echo-signals and probing radar pulse are coincided roughly, although individual spectrums demonstrate significant oscillations of its envelope. A qualitative interpretation of the RFS is that the oscillations are caused by the correlation between the phases of the carrier wave over intervals equal to the probing pulse duration. The depth and pattern of the oscillations depend on the rate and interval of the phase correlation and can be used as indicators of the spatial homogeneity of a meteorological object. The features of the RFSs obtained can be used for the development of optimal techniques of the instrumental calibration of the different kinds of geophysical radar as well.

REFERENCES

1. Yurchak, B. S., "Radar volume backscatter from spatially extended geophysical targets in a "slice" approach," *IEEE Transactions on Geoscience and Remote Sensing*, Vol. 47, No. 11, 3690–3696, November 2009.
2. Yurchak, B. S., "About optimal measurement of radar features of meteorological targets," *Meteorology and Hydrology*, No. 4, 117–121, 1981 (in Russian).
3. Tverskoi, V. I., "Dispersive-time methods of measurements of radio-frequency signals' spectrums," *Sov. Radio*, Moscow, USSR, 1974 (in Russian).
4. Mardin, V. V. and A. I. Krivonosov, *Textbook on Electronic Measurement Devices*, Svyaz, Moscow, USSR, 1978 (in Russian).
5. Yurchak, B. S., "Radio-frequency spectrums of meteorological echo-signals," *Proceedings of IEM*, Vol. 38, No. 141, 40–47, 1985 (in Russian).
6. Van Trees, H. L., *Detection, Estimation, and Modulation Theory, Part III, Radar-sonar Processing and Gaussian Signals in Noise*, John Wiley & Sons, Inc. 2001.
7. Levin, B. R., "Theoretical foundation of statistical radio engineering," *Sov. Radio*, Vol. I, Moscow, USSR, 1974 (in Russian).
8. Bityutski, V. I. and A. I. Ermakov, "Phase correlation impact on the shape of radio-frequency pulse signals' spectrum," *Izvestia Vuzov SSSR-radio Electronics*, Vol. XXI, No. 9, 35–39, 1978 (in Russian).

Specular Radar Backscatter from a Planar Surface

Boris S. Yurchak

Goddard Earth Sciences & Technology Center
University of Maryland, Baltimore County, MD 21228, USA

Abstract— Satellite and airborne radar altimetry return signals often contain the specular component primarily in Polar Regions due to the backscatter from a relatively smooth and planar water/ice surface. This paper introduces the radar equation rigorously derived using the physical optics approach and describes the backscatter as a function of the spatial distribution of the complex Fresnel reflection coefficient across a planar surface. The closed form of the radar equation was obtained for the constant reflection coefficient for an infinite surface and an annulus.

1. INTRODUCTION

Although the principal objective of satellite and airborne radar altimeters is to measure the elevation of Earth's surface, the backscatter information can be used for other geophysical purposes as well. Since altimeter probing is performing in close to the nadir incidence, the altimeter backscatter from calm water or new ice surface contains the specular component [1]. Such geophysical targets are extended widely over space and completely fill the entire radar beamwidth. The surface is illuminated by a spherical electromagnetic wave and is in the near zone regardless of the radar range (e.g., [2]). It means that the problem should be considered under the physical optics approach.

2. ELECTRIC FIELD GENERATED BY TRANSMITTING ANTENNA APERTURE AT A PLANAR SURFACE

The scheme of the radar sounding is implemented such that a circle aperture antenna is elevated stationary over the infinite partially reflecting surface, Figure 1. The geometric center of the radar antenna is at the origin of a Cartesian coordinate system $\{X_a, Y_a, Z_a\}$. The antenna irradiates continuous spherical electromagnetic wave in the positive direction (down) along the axis Z_a. Transmitting and receiving antennas are combined. The electric field of this wave is at point $P_s\,(x_s,\,y_s,\,z_s)$ on the surface in the plane perpendicular to the incidence irradiation, i.e., in the plane $Z_a = z_s$. If the region of interest at the observation plane (S_s) is restricted to a relatively narrow region about the Z_a — axis such that the condition $\frac{(x_s-x_a)^2+(y_s-y_a)^2}{z_s^2} \ll 1$ is valid and a distance r for the phase term may be represented in accordance with the Fresnel approximation $r \approx z_s[1 + \frac{1}{2}(\frac{x_s-x_a}{z_s})^2 + \frac{1}{2}(\frac{y_s-y_a}{z_s})^2]$. This is valid for all radar applications that exploit a relatively narrow beam width, such as in radar altimetry. Polarization features can be ignored due to nadir sounding. In this case, taking the fundamental radar equation for the surface illumination in Cartesian coordinates (e.g., [3]), the illuminating electric field strength at point P_s created by the electric field strength $E_a\,(x_a,\,y_a)$ can be written through cylindrical coordinates in the following form

$$
\dot{E}_s(\varphi_s, \rho_s, z_s) \;=\; \frac{j}{\lambda z_s} e^{-j\left(kz_s + \frac{k}{2z_s}\rho_s^2\right)}
$$
$$
\int\limits_0^{2\pi} d\varphi_a \int\limits_0^{r_a} d\rho_a \rho_a E_a(\rho_a, \phi_a) e^{-j\frac{k}{2z_s}\rho_a^2} e^{j\frac{k}{z_s}(\rho_s \cos\varphi_s \cdot \rho_a \cos\varphi_a + \rho_s \sin\varphi_s \cdot \rho_a \sin\varphi_a)} \tag{1}
$$

where $x_a^2+y_a^2=\rho_a^2$, $x_s^2+y_s^2=\rho_s^2$, $r \approx z_s$ (for the amplitude term). To make further transformations simpler, the distribution of the electric field strength across the aperture is assumed to be axis-symmetric and it is Gaussian:

$$
E_a(\rho_a, \varphi_a) = E_a(\rho_a) = E_a F(\rho_a) \tag{2}
$$

where E_a is the on-axis electric field strength, and

$$
F(\rho_a) = \exp(-\alpha^2 \rho_a^2) \tag{3}
$$

is the aperture distribution function (ADF), $\alpha = k_a/r_a$ is the antenna parameter, r_a is the effective radius of the antenna aperture, and k_a is the fitted coefficient that depends on the definition of
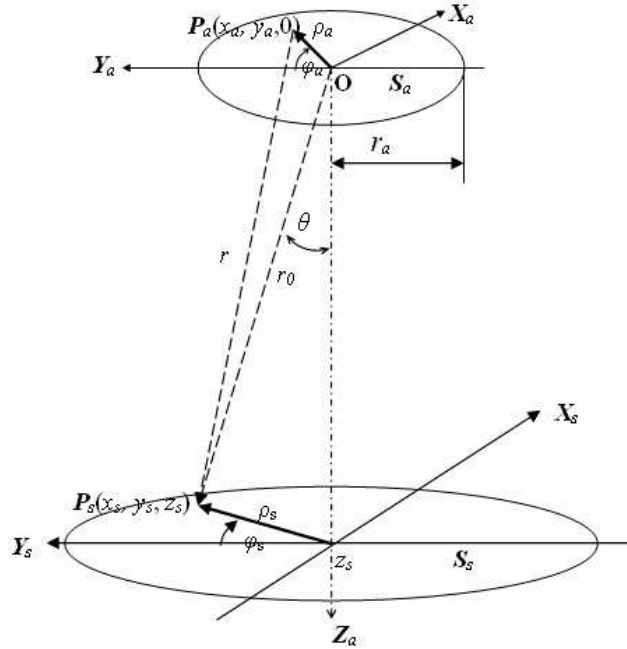
Figure 1: Geometry of the illumination of a flat surface (S_s) by the circular aperture (S_a) of radius r_a; P_a (x_a, y_a, 0) is the aperture point and P_s (x_s, y_s, z_s) is the observation point.

the effective radius. The phase distribution is uniform within the entire aperture. We define the effective radius as the aperture radius that generates $y\%$ of the total emitted power. It is easy to show, if $y = 90\%$ then $k_a \approx 1$, and $r_a \approx \alpha^{-1}$. Thus, the total power emitted by the antenna with aperture S_a and the amplitude-phase distribution of the exited electric field $\dot{E}_a(\rho_a, \varphi_a)$ is (e.g., [3]):

$$P_t = \frac{1}{2Z_0} \int\limits_{S_a} \left| \dot{E}_a(\rho_a, \varphi_a) \right|^2 dS_a = \frac{\pi}{4Z_0} E_a^2 \frac{1}{\alpha^2} \tag{4}$$

where Z_0 is the intrinsic impedance of the free space. By neglecting the impact of $\sim 10\%$ contribution of the antenna periphery parts in the emitted power, we can substitute the upper limit of the integral over ρ_a to infinity and write (1) by taking into account (2) in the following form:

$$\dot{E}_s(\varphi_s, \rho_s, z_s) = \frac{j}{\lambda z_s} e^{-j\left(kz_s + \frac{k}{2z_s}\rho_s^2\right)} E_a \int\limits_0^\infty e^{-\alpha^2 \rho_a^2} e^{-j\frac{k}{2z_s}\rho_a^2} \rho_a d\rho_a \int\limits_0^{2\pi} e^{j\frac{k}{z_s}\rho_s\rho_a \cos(\varphi_s - \varphi_a)} d\varphi_a \tag{5}$$

Taking the table values of the integrals $\int\limits_0^{2\pi} e^{j\frac{k}{z_s}\rho_s\rho_a \cos(\varphi_s - \varphi_a)} d\varphi_a = 2\pi J_0(\frac{k\rho_s}{z_s}\rho_a)$ and $\int\limits_0^\infty \rho_a e^{-t\rho_a^2} J_0(m\rho_a)$ $d\rho_a = \frac{1}{2t} e^{-\frac{m^2}{4t}}$, where $J_0(\dots)$ is the Bessel function of the first kind and order 0, using so-called quadratic phase factor (QPF) [3]: $g = \frac{k}{2z_s\alpha^2} = \frac{\pi}{\lambda z_s\alpha^2}$, and denoting $A = \frac{g^2}{1+g^2}$, $B = A \cdot g$, we get:

$$\dot{E}_s(\varphi_s, \rho_s) = jE_a\sqrt{A}e^{-jkz_s}e^{-\alpha^2 A\rho_s^2}e^{-j[\text{arctg}(g) - (B-g)\alpha^2\rho_s^2]} \tag{6}$$

From the above expression, the size of an illuminated area is determined by the width of envelope of the illumination field expressed through the term $\exp(-A\alpha^2\rho_s^2)$. Its effective illumination radius for 90% power is

$$r_{ill} \approx \frac{1}{\alpha\sqrt{A}}\Big|_{g<1} \approx \frac{1}{\alpha g} = \frac{2}{\pi}\alpha r_F^2 \tag{7}$$

where $r_F = \sqrt{\frac{1}{2}z_s\lambda}$ is the radius of the First Fresnel zone (FFZ) and that is roughly by $\sim \frac{2}{\pi}(\frac{r_F}{r_a})^2$ times larger than the effective radius of the aperture r_a.

3. RADAR EQUATION FOR A PLANAR SURFACE

3.1. Backscattered Electric Field in a Plane of Receiving Antenna Aperture

The main idea of the current evaluation is to consider the target (surface) as a secondary antenna with the electric field distribution (7) modified by the reflection properties of air/surface interface:

$$\dot{E}_r(\rho_s, \varphi_s, z_s) = \dot{E}_s(\rho_s, z_s) \cdot \dot{\Gamma}(\rho_s, \varphi_s, z_s) \tag{8}$$

where $\dot{\Gamma}(\ldots)$ is the Fresnel reflection coefficient (complex in a general case) depended on electric surface properties. The origin of the coordinate system should be placed at point $Z_a = z_s$. Thus, the reflected electric field in a plane of receiving antenna aperture can be written by analogy with (1), by substituting the antenna exiting field for the illumination field $\dot{E}_s(\rho_s, \phi_s, z_s)$, in the form:

$$\dot{E}_r(\rho_a, \varphi_a, 0) = \frac{j}{\lambda z_s} e^{-j\left(kz_s + \frac{k}{2z_s}\rho_a^2\right)}$$
$$\int_0^{2\pi} \int_0^\infty \dot{E}_s(\rho_s, \varphi_s, z_s)_r e^{-j\frac{k}{2z_s}\rho_s^2} e^{j\frac{k}{z_s}(\rho_a \cos\varphi_a \cdot \rho_s \cos\varphi_s + \rho_a \sin\varphi_a \cdot \rho_s \sin\varphi_s)} \rho_s d\rho_s d\varphi_s \tag{9}$$

Using previous inputting denotes and expression (6) for $\dot{E}_s(\rho_s, \varphi_s, z_s)$, Equation (9) becomes:

$$\dot{E}_r(\rho_a, \varphi_a, 0) = -E_a \frac{\alpha^2}{\pi} g\sqrt{A} e^{jg\alpha^2\rho_a^2} e^{-jarctg(g)}$$
$$\int_0^{2\pi} \int_0^\infty \dot{\Gamma}(\rho_s, \varphi_s, z_s) e^{-[A-j(B-2g)]\alpha^2\rho_s^2} e^{j2g\alpha^2\rho_a\rho_s \cos(\varphi_a-\varphi_s)} \rho_s d\rho_s d\varphi_s \tag{10}$$

3.2. General Radar Equation for Arbitrary Distributed Fresnel Reflection Coefficient

Radar equation in a general form for arbitrary spatial distribution of the Fresnel coefficient can be written through the power flux density $\Pi_r(\rho_a, \varphi_a, 0)$ that is created by the reflected field (10) from a surface and corrected with the antenna sensitiveness (3) for a power:

$$P_r = \int_0^{2\pi} d\varphi_a \int_0^\infty \Pi_r(\rho_a, \varphi_a, 0) \rho_a e^{-2\alpha^2\rho_a^2} d\rho_a \tag{11}$$

where (under $g < 1 \Rightarrow A \approx g^2$)

$$\Pi_r(\rho_a, \varphi_a, 0) = \frac{1}{2Z_0} \left| \dot{E}_r(\rho_a, \varphi_a, 0) \right|^2$$
$$= P_t \frac{2g^4\alpha^6}{\pi^3} \left| \int_0^{2\pi} \int_0^\infty \dot{\Gamma}(\rho_s, \varphi_s, z_s) e^{-[A-j(B-2g)]\alpha^2\rho_s^2} e^{j2g\alpha^2\rho_a\rho_s \cos(\varphi_a-\varphi_s)} \rho_s d\rho_s d\varphi_s \right|^2 \tag{12}$$

Relationship (4) was taken into account for denoting P_t. Equation (11) with the power flux density definition expressed through the arbitrary distributed Fresnel reflection coefficient (12) is the fundamental equation to calculate the backscatter from a planar geophysical surface.

3.3. Radar Equation for Constant Fresnel Reflection Coefficient

To compare the radar equation obtained (11) with known result in the geometrical optics approach for the constant reflection coefficient, we should resolve Equation (12) with $\dot{\Gamma}(\rho_s, \varphi_s, z_s) = \Gamma_0$. Following the previous way of transformations, we obtain from (10):

$$\dot{E}_r(\rho_a, \varphi_a, 0) \approx -E_a \Gamma_0 T e^{-T^2\alpha^2\rho_a^2} e^{-jM\alpha^2\rho_a^2} e^{jL} \tag{13}$$

where

$$T = \frac{g}{\sqrt{A}} \frac{1}{\sqrt{1 + \left(\frac{B-2g}{A}\right)^2}} = g\sqrt{\frac{1+g^2}{4+5g^2+g^4}} \underset{g<1}{\approx} \frac{g}{2} \tag{14}$$

$L = \text{arctg}(\frac{B-2g}{A}) - \text{arctg}(g)$, $M = (\frac{B-2g}{A}) \cdot T^2 - g$. Consequently,

$$\left| \dot{E}_r(\rho_a, \varphi_a, 0) \right| \approx E_a \Gamma_0 T e^{-T^2 \alpha^2 \rho_a^2} \tag{15}$$

As follows from (15), an envelope of the backscattered electric field at the antenna plane is proportional to $\exp(-T^2 \alpha^2 \rho_a^2)$. It means that under $g < 1$ when $T \approx g/2$ the field spatial distribution is by $2/g = \frac{1}{\pi}(\frac{r_F}{r_a})^2$ times wider in comparison with the initial antenna field distribution (3). It means that the electric field distribution is practically unvarying within the effective aperture of radius r_a. Substitution (15) in (12) gives the radar equation in closed form (expressed through the QPF) to estimate the backscattered power from the infinite smooth planar surface under constant reflection coefficient:

$$P_r = P_t H_g \Gamma_0^2 \tag{16}$$

where

$$H_g = \frac{1}{1 + T^{-2}} \underset{g<1}{\approx} \left(\frac{g}{2}\right)^2 \tag{17}$$

is the scaling factor, and parameter T is (14). An approximation error of this factor with the square power function for real altimeter conditions with $g \sim 10^{-2}$–10^{-6} is a negligible quantity. The consideration provided above used a radar antenna with the Gaussian infinite electric strength distribution. Although such antenna cannot be practically realized, this approach allowed obtaining the physically considerable features regarding the radar probing of the infinite planar surface. Any real finite amplitude distributions for the circular antenna can be represented by a series of the Laguerre-Gaussian functions (e.g., [4]).
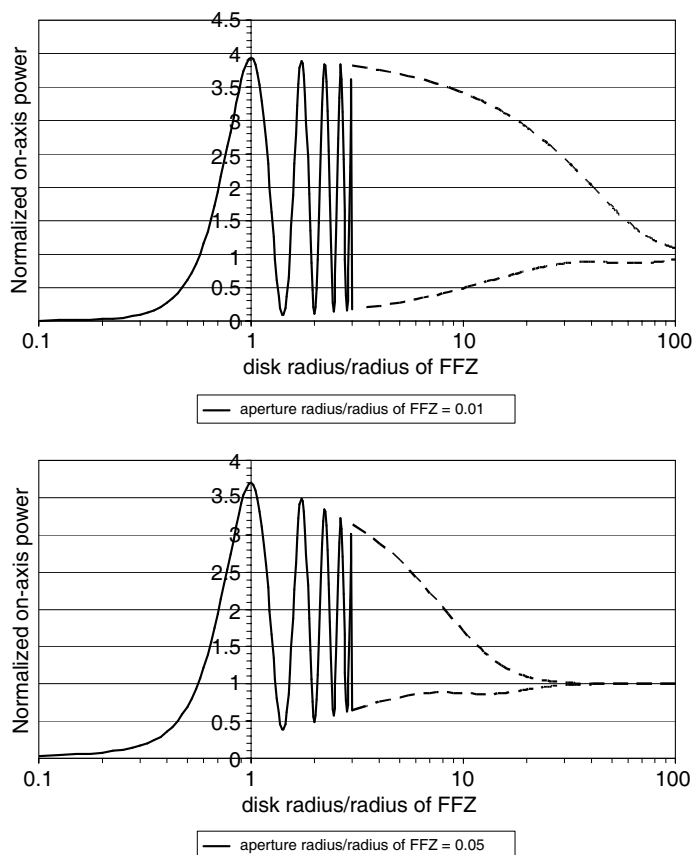
Figure 2: Dependence of the normalized on-axis power versus the relative disk radius for two relative aperture radii of 0.01 (upper plot) and of 0.05 (bottom plot); only the envelope of the oscillated function is shown with dashed curves for great values of the argument.

4. RADAR EQUATION FOR FINITE SYMMETRICAL AREAS

To verify our evaluation, we compare the general equation obtained (11) modified for a homogeneous disk with calculation of the backscatter from a metallic disk in the near-field region [5]. We assume in (12) $\dot{\Gamma}(\rho_s, \varphi_s, z_s) = \Gamma_0$, and substitute limits in integral over ρ_s by inside ($r_{\min}$) and outer ($r_{\max}$) radii to model an annulus. Particular cases of an annulus are a disk ($r_{\min} = 0$, $r_{\max} = r_d$) and the infinite surface ($r_{\min} = 0$, $r_{\max} \to \infty$). We have:

$$\Pi_r(\rho_a, \varphi_a, 0) = P_t \Gamma_0^2 \frac{2^3 g^4 \alpha^6}{\pi} \left| \int_{r_{\min}}^{r_{\max}} \rho_s J_0 \left(2g\alpha^2 \rho_a \rho_s \right) e^{-[A-j(B-2g)]\alpha^2 \rho_s^2} d\rho_s \right|^2 \tag{18}$$

This equation cannot be resolved through the elementary functions. Nevertheless, there is a way to get an analytical solution by estimating "on-axis" backscatter (e.g., [5]). It means the substitution of the real distribution of the return power flow density across an aperture by its value at the aperture center. We can do that based on the previous notes to expression (15) where it was stated that the distribution pattern of the backscattered field at the antenna plane is practically constant within the effective aperture radius r_a. At that, we set $\rho_a = 0$ in the argument of the Bessel function. Thus, $J_0(0) = 1$ and (18) is reduced to:

$$\Pi_0 = P_t \Gamma_0^2 \frac{2^3 g^4 \alpha^6}{\pi} \left| \frac{1}{2\alpha^2 [A - j(B - 2g)]} \left\{ e^{-[A-j(B-2g)]\alpha^2 r_{\max}^2} - e^{-[A-j(B-2g)]\alpha^2 r_{\min}^2} \right\} \right|^2 \tag{19}$$

Evaluating the square of the module and assuming $g < 1$ that causes $B \ll 2g$, we obtain the closed-form solution for the on-axis power flow density from an annulus:

$$\Pi_0 \approx P_t \Gamma_0^2 \frac{1}{2\pi} (\alpha g)^2 \left\{ e^{-2g^2 \alpha^2 r_{\max}^2} + e^{-2g^2 \alpha^2 r_{\min}^2} - 2 e^{-g^2 \alpha^2 (r_{\max}^2 + r_{\min}^2)} \cos \left[2g\alpha^2 \left(r_{\max}^2 - r_{\min}^2 \right) \right] \right\} \tag{20}$$

Substituting (20) in (12) we obtain the on-axis power from an annulus:

$$P_0 = \int_0^{2\pi} d\varphi_a \int_0^{\infty} \Pi_0 \rho_a e^{-2\alpha^2 \rho_a^2} d\rho_a = \Pi_0 \frac{\pi}{2\alpha^2} \tag{21}$$

It is convenient to express parameters $(g\alpha r_m)^2$ and $g(\alpha r_m)^2$ in (20) through the relative quantities normalized by the radius of the FFZ: $(g\alpha r_m)^2 = (\frac{\pi}{2} \frac{r_a}{r_F} \frac{r_m}{r_F})^2$, $2g(\alpha r_m)^2 = \pi (\frac{r_m}{r_F})^2$ and to write the radar equation in the form normalized to the return power from the infinite surface (16). That results the general equation for the radar backscatter from an annulus:

$$\begin{aligned} \frac{P_{0,a}}{P_{0,\inf}} &= \exp \left[-2 \left(\frac{\pi}{2} \frac{r_a}{r_F} \frac{r_{\min}}{r_F} \right)^2 \right] + \exp \left[-2 \left(\frac{\pi}{2} \frac{r_a}{r_F} \frac{r_{\max}}{r_F} \right)^2 \right] \\ &\quad - 2 \exp \left[- \left(\frac{\pi}{2} \frac{r_a}{r_F} \right)^2 \left(\frac{r_{\max}^2}{r_F^2} + \frac{r_{\min}^2}{r_F^2} \right) \right] \cos \left[\pi \left(\frac{r_{\max}^2}{r_F^2} - \frac{r_{\min}^2}{r_F^2} \right) \right] \end{aligned} \tag{22}$$

The particular case of (22) is the equation for a disk ($r_{\min} = 0$, $r_{\max} \equiv r_d$)

$$\frac{P_{0,d}}{P_{0,\inf}} = 1 + \exp \left[-2 \left(\frac{\pi}{2} \frac{r_a}{r_F} \frac{r_d}{r_F} \right)^2 \right] - 2 \exp \left[- \left(\frac{\pi}{2} \frac{r_a}{r_F} \frac{r_d}{r_F} \right)^2 \right] \cos \left[\pi \left(\frac{r_d}{r_F} \right)^2 \right] \tag{23}$$

The plot of (23) for two relative aperture sizes is depicted in Figure 2. As follows from the figure, the relative backscatter from a disk (23) versus the relative disk radius (r_d/r_F) grows monotonously up to 4 (6 dB) until the disk radius becomes equal to the radius of the FFZ. Further, it begins to oscillate with reducing peak to peak amplitude and oscillation period, and bringing near to 1 under the great relative disk radius. For a small disk with $\frac{r_d}{r_F} \ll 1$ we can obtain from (23): $\frac{P_{0,d,\text{small}}}{P_{0,\inf}} \approx (\frac{\pi}{2} \frac{r_a}{r_F} \frac{r_d}{r_F})^4$.

It means that the backscatter is proportional to the fourth power of the disk's size that coincides with the classical estimate of the RCS for this case [6].

5. SUMMARY

In the current paper, an attempt to derive the radar equation to probe a smooth and planar infinite surface was undertaken based on solving the general diffraction problem under a spherical wave (physical optics) approach. To calculate the backscatter, the illuminated area on a surface was represented as a circular surface "aperture" that is excited by irradiation of elevated radar. The radar equation in general form for an arbitrary distributed Fresnel reflection coefficient and a Gaussian main lobe of antenna pattern was derived using the Kirchhoff approach and the Fresnel approximation (11). The particular result for a large disk (23) coincides with the known results validated by the field experiments.

ACKNOWLEDGMENT

REFERENCES

1. Fetterer, F. M., M. R. Drinkwater, K. C. Jezek, S. W. Laxon, R. G. Onstott, and L. M. H. Ulander, "See ice altimetry," *Geophysical Monograph Series*, Vol. 68, 111–135, 1992.
2. Atlas, D., "Possible key to the dilemma of meteorological "angel" echoes," *Journal of Meteorology*, Vol. 17, No. 2, 95–103, 1960.
3. Ulaby, F. T., R. K. Moore, and A. K. Fung, *Microwave Remote Sensing, Fundamentals and Radiometry*, Vol. I, Addison-Wesley Publishing Company, Inc., Advanced Book Program/World Science Division, 1981.
4. Bogush, Jr., A. J., *Radar and the Atmosphere*, 452, Artech House, Inc., Norwood, MA, 1989.
5. Pouliguen, P., R. Hémon, C. Bourlier, J.-F. Damiens, and J. Sailard, "Analytical formulae for radar cross section of flat plates in near field and normal incidence," *Progress In Electromagnetic Research B*, Vol. 9, 263–279, 2008.
6. Knott, E. F., J. F. Shaeffer, and M. T. Tuley, *Radar Cross Section*, 2nd Edition, SciTech Publishing, Inc., Raleigh, 2004.

A New Compact Size Fractal Based Microstrip Slot Antenna for GPS Applications

Jawad K. Ali[1], Zaid A. Abed AL-Hussain[2], Ammer A. Osman[2], and Ali J. Salim[1]

[1]Department of Electrical and Electronic Engineering, University of Technology, Baghdad, Iraq
[2]Department of Electrical Engineering, Al-Mustansiriya University, Baghdad, Iraq

Abstract— A circularly polarized single feed microstrip slot antenna has been introduced in this paper as a candidate for use in GPS applications. The slot structure of the proposed antenna has been created on the radiating patch in two steps. At first, a 45 degree rotated square has been etched at the center of the patch, and then a Sierpinski gasket type of the 3rd iteration occupies the resulting slot. The presented antenna has been fed with a single 50 Ohm probe. The feed position has been allocated in such away to produce the dual orthogonal modes required to produce the circular polarization radiation. The antenna has been designed to resonate at 1.575 GHz, L1 GPS band. Finite element simulations have been carried out to evaluate the performance of the modeled antenna using the HFSS v.11 EM simulator, from Ansoft. The resulting antenna has a slotted square patch with side length of about 40 mm. Simulation results show that it possesses impedance and axial ratio bandwidths of about 27 MHz and 22 MHz respectively, which meet the GPS L1 band requirement. Furthermore, the proposed antenna possesses satisfactory circular polarization radiation characteristics and gain. The antenna can be used for a wide variety of communication applications adopting circular polarization.

1. INTRODUCTION

Circularly polarized (CP) microstrip antennas with a small size, low profile, and light weight are required in mobile, wireless communication system, global positioning system (GPS), satellite communications, etc.. In these applications, the circular polarization contributes to the high link reliability and spectral efficiency [1]. However, microstrip patch antennas, when used for circular polarization application, suffer from the poor axial ratio (AR) bandwidths; which are typically less than 1% (AR < 3 dB) [2, 3].

On other hand, the application of fractal geometries on microstrip antennas makes them more attractive for antenna designers. Fractal geometry based antennas are characterized by the compact size and the multiband performance. Several research works, [4–10], have successfully applied many fractal geometries to produce antennas with good circular polarization radiation. Koch fractal based structures have proposed for CP antennas in [4, 5]. A CP patch antenna based on hi-impedance surface electromagnetic bandgap (EBG) structure has been reported in [6], where Minkowski fractal geometry has been applied to reduce the size of the EBG cells. Fractal structures based on the square and triangular shapes, as generators in fractal generation process, have been also examined to be used for CP antenna applications [7–10]. Most of the reported research works, an AR bandwidth of more than 1% has been reached, but certainly there are some exceptions [5].

However, the application of fractal geometries to design circularly polarized antennas for GPS applications is still limited to several works, to name a few [11, 12]. The same concept used in [6], has been reproduced to design an antenna for use in GPS applications [11]. Koch fractal structure is employed in the design of a GPS antenna piezoelectric substrate [12].

In this paper, a new compact size, circularly polarized microstrip fractal based slot antenna is presented. This antenna slot structure is based upon the inverted Sierpinski gasket fractal geometry of the 3rd iteration. The presented antenna is fed with a single 50 Ω probe. The antenna is supposed to be used for GPS L1 applications.

2. THE PROPOSED ANTENNA STRUCTURE

The steps of generating the proposed antenna structure are shown in Figure 1. The first step is to cut a 45° rotated square patch as depicted in Figure 1(a), where it is clear that the resulting slot structure is divided into two similar triangles. The subsequent steps are to make use of inverted Sierpinski gaskets of the first, second and third iterations to occupy the depicted two triangles slot, as shown in Figures 1(b) to 1(d) respectively. It is clear that the resulting structures have increasing number of sub slot, according to the fractal iteration levels, which consequently increase the equivalent radiating edge lengths. This considerably contributes in the resulting antenna to
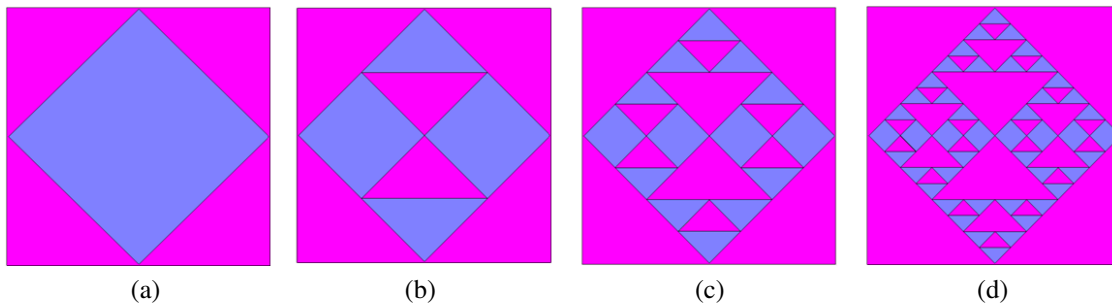
Figure 1: Steps of the fractal generation process of the proposed slot antenna structure.
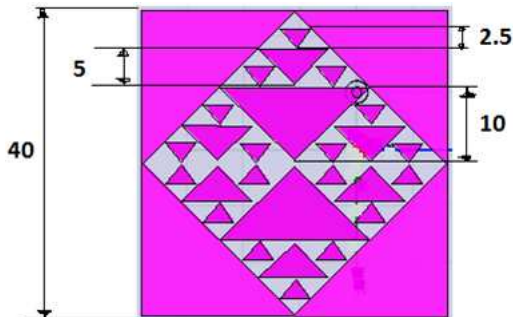

Figure 2: Summary of the dimensions (in mm) of the modeled antenna at 1.575 GHz.
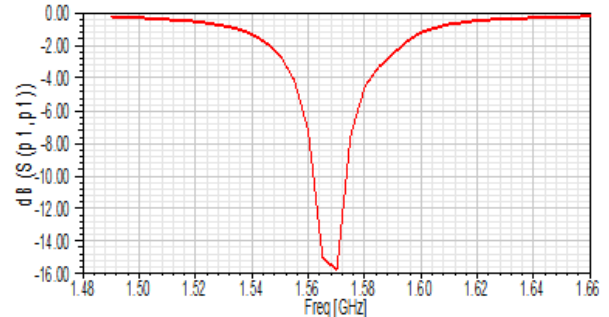
Figure 3: The simulated return loss response of the modeled antenna over the resonant band.

become smaller and smaller. In addition, the geometric symmetry of the resulting structure makes the possibility of the corresponding antenna more probable.

3. THE PROPOSED ANTENNA DESIGN

Many antennas based on the structures, depicted in Figure 1, have been modeled in an attempt to design a compact size circularly polarized antenna meeting the requirements of the GPS L1 applications. The results of the modeled antennas, corresponding to the structures shown in Figures 1(b) and 1(c), are not so encouraging in both size reduction and the performance as well. To save space, only the antenna with slot structure based on the 3rd inverted Sierpinski gasket, Figure 1(d), will be considered here.

The slot structure has been supposed to be etched using the Rogers RT/Duriod 5880 substrate, with relative permittivity of 2.2, and thickness of 2.3 mm. A single 50 Ω probe has been used to feed the modeled antenna. The modeled antenna had been located parallel to XY-plane and centered at the origin. Modeling and theoretical performance of the modeled antenna structure have been carried out using the finite element based electromagnetic simulator, HFSS v11, from Ansoft [13].

4. PERFORMANCE EVALUATION

It has been found that, the proposed antenna offers considerable return loss response with an impedance bandwidth of about 27 MHz, centered at the design frequency, 1.575 GHz. For this, the antenna has an overall size of 40 mm × 40 mm. Figure 2 summarizes all the detailed dimensions of the proposed antenna at resonance.

Figure 3 demonstrates the simulated return loss (S_{11}) response, for the 3rd iteration based slot antenna. It can be noted that at the resonant frequency, 1.576 GHz, the antenna input return loss is of about −15.75 dB, and the realized impedance bandwidth is of about 1.64%.

Figure 4 shows the axial ratio response for the proposed antenna. It can be seen that the axial ratio in the broadside direction is below 3 dB throughout a bandwidth of about 21.04 MHz. Minimum value of AR, 0.578 dB, takes place at 1.575 GHz. Computed antenna gain, throughout this bandwidth, is found to be around 3.86 dB. It is clear that this antenna meets the requirements for GPS L1 standard communication applications [14, 15].

The simulated 3D and the RHCP far field radiation patterns of the modeled antenna have been shown in Figures 5 and 6 respectively at 1.575 GHz. The proposed antenna supports an electric
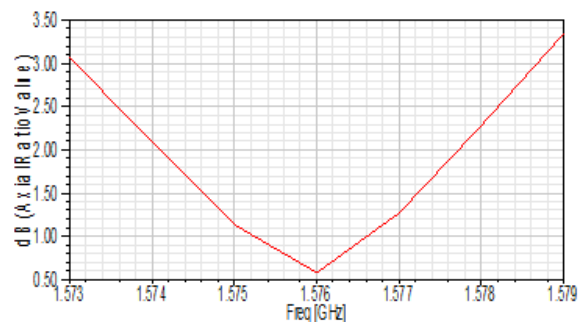
Figure 4: The axial ratio response of the antenna over the resonant band.
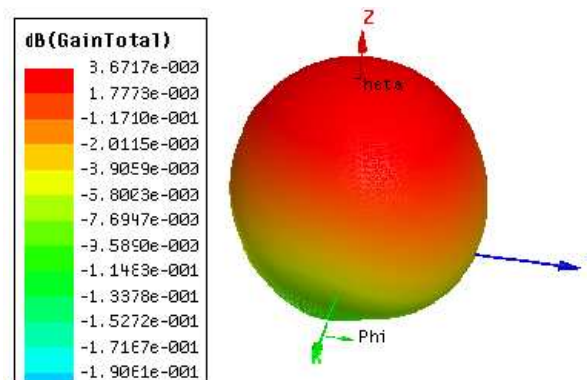
Figure 5: The simulated 3D E-field radiation pattern at 1.575 GHz.
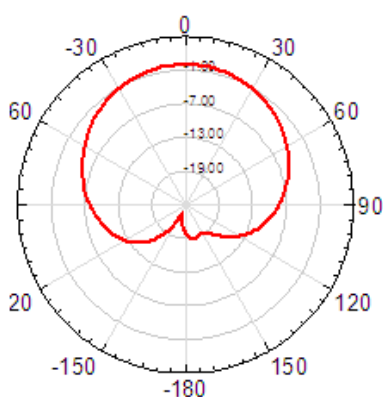
Figure 6: The simulated RHCP E-field radiation pattern at 1.575 GHz.
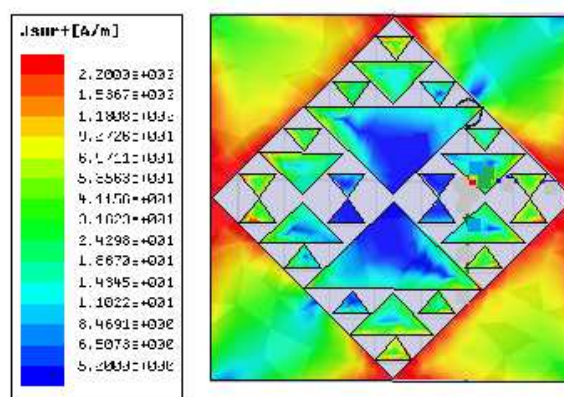
Figure 7: Surface current distribution on the slot patch of the modeled antenna at 1.575 GHz.

field radiation pattern that occupies the upper hemispheric shape required for the GPS operation.

The simulated current distribution, at the surface of the modeled antenna, has been presented at 1.575 GHz as shown in Figure 7. Largest values of the surface currents have been found to take place along the edges corners of antenna structure.

It indicates that, the resonance at 1.575 GHz is mainly attributed by the smaller triangles that constitute the 3rd iteration inverted Sierpinski gasket based fractal slot patch antenna. It is worth to say, here, that symmetrical distribution of these small structures about the feed primarily supports producing the RHCP requirement of the GPS antenna radiation pattern. The fact has been assured from the simulation results (not shown due to limited space) of the previous iterations depicted in Figures 1(b) and 1(c), where the values of the AR become better as the smaller sub structures start to appear.

5. CONCLUSION

In this paper, a new fractal based circularly polarized slot microstrip antenna has been presented as a candidate for use in GPS L1 applications. The proposed antenna offers a size reduction of about 61.6% as compared with the conventional square patch. In addition, the proposed antenna has been found to offer reasonable circular polarization performance. It offers a good 3 dB axial ratio bandwidth of about 1.34% and an impedance bandwidth of about 1.63%, covering the bandwidth requirements of the standard GPS L1 application. Furthermore, the antenna has a hemispherical radiation pattern with an average gain of about 3.86 dB throughout the operating bandwidth. This makes the proposed antenna design suitable for use in the GPS L1 applications.

REFERENCES

1. Waterhouse, R. and D. Novak, *A Printed Antennas for Wireless Communications*, John Wiley and Sons, Ltd., 2007.

2. Matthias, K. and R. Vahldieck, "A novel concept for slot coupled circularly polarized patch antenna," *Proceedings of IEEE Ant. and Propag. Soc. Symp.*, Vol. 3, 490–493, Boston, USA, Aug. 2001.

3. Vlasits, T., E. Korolkiewwicz, A. Sambell, and B. Robinson, "Performance of a cross-coupled single feed circularly polarized patch antenna," *Electronic Lett.,* Vol. 32 , No. 7, 612–613, 1996.

4. Nageswara Rao, P. and N. V. S. N. Sarma, "A single feed circularly polarized fractal shaped microstrip antenna with fractal slot," *PIERS Proceedings*, 195–197, Hangzhou, China, Mar. 24–28, 2008.

5. Yusop, M. A. M., M. K. A. Rahim, M. F. Ismail, and A. Wahid, "Circular polarization fractal koch microstrip patch antenna using single-fed EM coupled ring resonators," *Proceedings of IEEE Asia-Pacific Conf. on Appl. Electromag.*, Port Dickson, Nov. 2010.

6. Bao, X., M. Ammann, G. Ruvio, and M. John, "High performance circularly polarized antenna based on fractal EBG structure," *Proceedings of IEEE International Workshop on Antenna Technology, Small Antennas, and Novel Metamaterials*, Mar. 2006.

7. Hojjat-Kashani, F., N. Komjani, J. Ghalibafan, and S. Bahrami, "A novel circularly polarized fractal microstrip antenna," *Proceedings of 2009 5th IEEE GCC Conf. and Exhibition*, IEEEGCC, Kuwait City, Mar. 2009.

8. Hojjat-Kashani, F. and J. Ghalibafan, "A circularly polarized fractal microstrip antenna for RFID applications," *Proceedings of IEEE Int. Symp. on Radio Freq. Integ. Technology, RFIT 2009*, Singapore, Dec. 2009.

9. Cheng, H., L. Tian, and B. Hu, "Compact circularly polarized square microstrip fractal antenna with symmetrical T-slits" *Proceedings of Int. Conf. on Wireless Communications, Networking and Mobile Computing, WiCom,* Shanghai, China, Sep. 2007.

10. Raj Kumar, J., P. Shinde, and P. Malath, "The design of CP triangular fractal patch antenna with slit," *Proceedings of ISAP2007*, Niigata, Japan, 2007.

11. Bao, X., G. Ruvio, M. Ammann, and M. John, "A novel GPS patch antenna on a fractal hi-impedance surface substrate," *IEEE Ant. and Wireless Propag. Lett.*, Vol. 5, 323–326, 2006.

12. Tang, T., C. Tsai, K. Lin, Y. Huang, and C. Chen, "Fractal GPS antenna design on piezoelectric substrate," *Proceedings of 2010 Asia-Pacific Microwave Conference*, Yokohama, Dec. 2010.

13. HFSS version 11.0, Ansoft Software Inc., 2007.

14. Chia-Hsien, L., J. Wu, T. Chiou, C. Chen, and C. Wang, "A microstrip-fed circularly-polarized loop-like antenna," *Proceedings of IEEE Int. Workshop on Antenna Technology, iWAT 2009*, Santa Monica, Mar. 2009.

15. Ali, J. K., "A new compact size microstrip patch antenna with irregular slots for handheld GPS applications," *Engineering and Technology*, Vol. 26, No. 10, 1241–1246, 2008.

Simulation and Verification of Methods for Partial Discharge Source Localization

R. Myška and P. Drexler

Department of Theoretical and Experimental Electrical Engineering
Brno University of Technology, Kolejni 2906/4, Brno 612 00, Czech Republic

Abstract— This article deals with possibilities of localization of partial discharges (PD) in oil power transformers. Localization can be performed by means of analysis of UHF waveforms which are measured during activity of the partial discharges. The time differences of arrival (TDOA) of the waveforms related to transient process occurrence in the signals are the main input parameters for localization methods. In order to estimate the position of the signal source in 3D space a minimum of four antennas has to be used, since the time of the PD occurrence is unknown. For localization purposes the system of nonlinear equations has to be solved. This can be performed by means of analytical or numerical methods. Both of the methods have their own advantages and disadvantages. The application of both approaches for signal source localization in measurement model will be presented in this paper. The methods will be compared in view of their suitability for a given configuration of antenna system.

1. INTRODUCTION

In order to prevent the transformer failure the observation of pulse activity of PD is necessary. The occurrence of discharge with substantial charge transport level can be localized in critical areas of the transformers. Having possibility to localize the increased discharge activity in some of critical areas allows undertaking precautions in order to avoid the critical transformer failure. The discharge activity localition can be estimated by processing of signals from suitable installed sensors [1].

2. PRINCIPLE OF LOCALIZATION

In case when sensors are realized as antennas, it is possible to determine the TDOA from antennas output signals. For this situation, the propagation time of the signal from source of discharge activity to antenna, which is closest, is unknown. The TDOA of signals arriving on each of antennas can be determined only. Therefore, there are four unknowns, source coordinates x, y, z and propagation time of the signal from the source to the first antenna t_0. It is possible to write a system of four equations in order to found four unknowns

$$(x - x_1)^2 + (x - y_1)^2 + (z - z_1)^2 = \left(\frac{c}{\sqrt{\varepsilon_r}} t_0 \right)^2, \tag{1}$$

$$(x - x_2)^2 + (y - y_2)^2 + (z - z_2)^2 = \left(\frac{c}{\sqrt{\varepsilon_r}} (t_0 + t_{12}) \right)^2, \tag{2}$$

$$(x - x_3)^2 + (y - y_3)^2 + (z - z_3)^2 = \left(\frac{c}{\sqrt{\varepsilon_r}} (t_0 + t_{13}) \right)^2, \tag{3}$$

$$(x - x_4)^2 + (y - y_4)^2 + (z - z_4)^2 = \left(\frac{c}{\sqrt{\varepsilon_r}} (t_0 + t_{14}) \right)^2, \tag{4}$$

where x_n, y_n, z_n are coordinates of nth antenna and t_{1n} is TDOA between the first and nth antenna, $t_{1n} = t_1 - t_n$. Position of the source is determined by solution of equation system (1)–(4), where defined antennas coordinates and measured TDOA parameters are used.

The system (1)–(4) is a non-linear equation system. This system can be solved by numerical or analytical methods. The basic numerical method for non-linear equation system solution is the Newton's method. This method and other numerical methods are based on finding of roots of non-linear vector equations

$$\mathbf{F}(\mathbf{X}) = 0, \tag{5}$$

where $\mathbf{F}(\mathbf{X})$ is non-linear vector function which components are given by system (1)–(4). The components are modified into homogenous form. $\mathbf{X}$ is a vector variable which components consist

of x, y, z, t_0. Vector function $\mathbf{F(X)}$ is possible to expand according to Taylor's series in vicinity of root iteration $\mathbf{X}_n$

$$\mathbf{F}\left(\mathbf{X}_{n+1}\right) = \mathbf{F}\left(\mathbf{X}_n\right) + \frac{\partial \mathbf{F}\left(\mathbf{X}_n\right)}{\partial \mathbf{X}}\left(\mathbf{X}_{n+1} - \mathbf{X}_n\right) + \frac{1}{2}\frac{\partial^2 \mathbf{F}\left(\mathbf{X}_n\right)}{\partial \mathbf{X}^2}\left(\mathbf{X}_{n+1} - \mathbf{X}_n\right)^2. \tag{6}$$

The Equation (6) can be reduction to first order

$$\mathbf{F}\left(\mathbf{X}_{n+1}\right) = \mathbf{F}\left(\mathbf{X}_n\right) + \frac{\partial \mathbf{F}\left(\mathbf{X}_n\right)}{\partial \mathbf{X}}\left(\mathbf{X}_{n+1} - \mathbf{X}_n\right). \tag{7}$$

The solution of the vector equation is achieved by means of iterative procedure. The starting point in Equation (7) is estimation of vector $\mathbf{X}_0$. The following root iterations are determined by

$$\mathbf{X}_{n+1} = \mathbf{X}_n + \mathbf{D}_n = \mathbf{X}_n - \frac{\mathbf{F}\left(\mathbf{X}_n\right)}{\frac{\partial \mathbf{F}\left(\mathbf{X}_n\right)}{\partial \mathbf{X}}}, \tag{8}$$

where

$$\mathbf{J}\left(\mathbf{X}_n\right) = \frac{\partial \mathbf{F}\left(\mathbf{X}_n\right)}{\partial \mathbf{X}}, \tag{9}$$

is a Jacob's matrix (Jacobian) of equation system in point $\mathbf{X}_n$. A modification of the Newton's method or other methods for solution of non-linear equation system can be used also.

The second approach to localization problem exploits analytical solution of the non-linear equation system. The analytic methods are based on direct solution of non-linear set of equations. The important issue in the analytical solution of system (1)–(4) is the non-symmetry due to character of Equation (1). However, it is possible to overcome this by suitable linear combination of equations containing time of arrival parameters only (TOA) [3].

3. NUMERICAL METHOD APPLICATION

The application of numerical method for source localization has been experimentally examined on a measurement model. The model consists of four receiving antennas connected to acquisition device and one pulsed signal source. The arrangement of the model is shown in Fig. 1(a)). The antennas positions are marked as A1, A2, A3 and A4. The antennas arrangement has been chosen similar to the arrangement in target application. The given arrangement is determined by construction possibilities of the transformer. The pulsed signal source has been placed in position marked as $1, 2, 3, \ldots, 7$. The coordinates system in relation to the antennas positions is shown in Fig. 1(b)). The coordinates of antennas in direction x and z are $x = 0$ and $z = 0$. The TDOA parameters between acquired signals from antennas A1, A2, A3 and A4 have been determined by means of threshold crossing algorithm [4].

Further, the TDOA parameters have been forwarded to localization algorithm. In order to source position determination a Newton's method has been chosen. This method is included in numerical tools of Optimization Toolbox in MATLAB system. The Newton's method is utilized in case of Large-scale problems solution.

In first computation trials the algorithm wasn't converging. Large order difference between the input parameters has been suspected as one of the reasons. Since the propagation velocity is in order of 10^8 m/s and the TDOA values are in order of 10^{-9} s, the order difference is 10^{17}, which is an extreme value. While the numerical methods are using finite numerical steps between the iterations, the extreme value of order difference may cause the algorithm to fail.

Therefore the reduction of the order difference has been proposed in order to reduce this extreme value. Using this reduction no influence on the results should occur. The reduced order difference which has been found for stable and fast convergence was 10^{11}. The values of the TDOA for signal positions 1, 3, 4, 6, 7 only have been processed by MATLAB algorithm due to symmetry of the measurement model. The exact results have been found for positions 1 and 3 only. Therefore, another order differences have been examined. It has been found that order difference 10^{-1} provided convergence for almost all source positions 1, 3, 4, 6. However the algorithm wasn't converging for source position 7. It is evidently caused by poor geometric dilution of precision for this position. Based on the results of numerical method verification it may be concluded that its application is potentially problematic due to convergence problem. The significant factor on the convergence and results precision is antennas arrangement, which was subject to transformer construction possibilities.
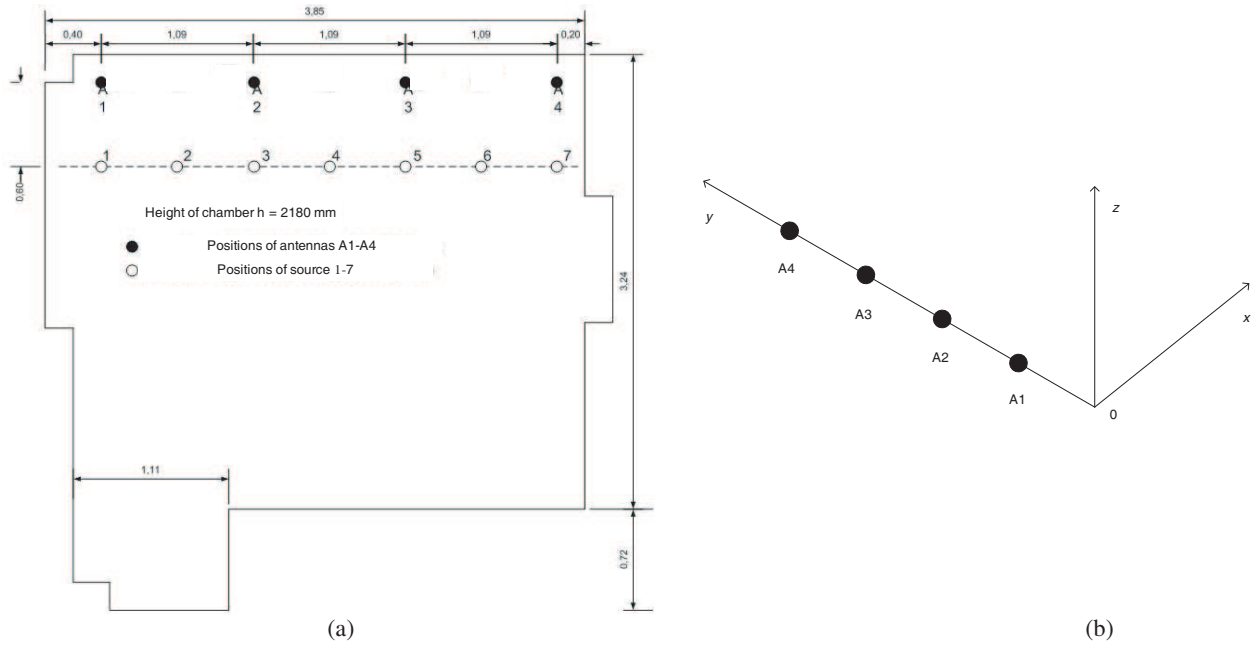
Figure 1: (a) The antennas positions in measurement model, (b) system of coordinates related to antennas positions.

4. ANALYTICAL METHOD APPLICATION

An example approach to analytical solution of non-linear set of equations has been published in [3]. The approach is based on subtraction of TOA equations which are similar to (1)–(4). Therefore the TDOA parameters can be used instead of the TOA parameters and the set symmetry is provided also.

Due to given antennas arrangement the solution and therefore the source position is ambiguous. For a given set of TDOA parameters the solution (source position) lies on circle, which's plane is perpendicular to the straight line join of antennas. Therefore the solution in 2D space may be sought only. Then, the source of signal may be found as an intersection of the circle with relevant part of inner transformer structure. A new proposed method suppose the source position in plane xy and the position of the first antenna is $x_1 = 0$, $y_1 = 0$. The initial equation system defines source position towards three antennas

$$x^2 + y^2 = v^2 t_0^2, \tag{10}$$

$$x^2 + (y - y_2)^2 = v^2 (t_0 + t_{12})^2, \tag{11}$$

$$x^2 + (y - y_3)^2 = v^2 (t_0 + t_{13})^2, \tag{12}$$

where v is the propagation velocity and t_{ij} are input TDOA parameters. By direct solution of equation set (10)–(11) it is possible to deduce solution t_0, y, x

$$t_0 = \frac{v^2 \left(y_2 t_{13}^2 - y_3 t_{12}^2 \right) + y_3 y_2^2 - y_2 y_3^2}{2 v^2 \left(y_3 t_{12} - y_2 t_{13} \right)}, \tag{13}$$

$$y = \frac{y_2}{2} - \frac{v^2 \left(y_2 t_{13}^2 - y_3 t_{12}^2 \right) + \left(y_3 y_2^2 - y_2 y_3^2 \right)}{2 y_2 \left(y_3 t_{12} - y_2 t_{13} \right)} t_{12} - \frac{v^2 t_{12}^2}{2 y_2}, \tag{14}$$

$$x = \sqrt{ v^2 \left(\frac{v^2 \left(y_2 t_{13}^2 - y_3 t_{12}^2 \right) + y_3 y_2^2 - y_2 y_3^2}{2 v^2 \left(y_3 t_{12} - y_2 t_{13} \right)} \right)^2 - \left(\frac{y_2}{2} - \frac{v^2 \left(y_2 t_{13}^2 - y_3 t_{12}^2 \right) + \left(y_3 y_2^2 - y_2 y_3^2 \right)}{2 y_2 \left(y_3 t_{12} - y_2 t_{13} \right)} t_{12} - \frac{v^2 t_{12}^2}{2 y_2} \right)^2 }. \tag{15}$$

It is possible to found the source position using (13)–(14) when antennas coordinates y_2, y_3, propagation velocity v and TDOA parameters t_{12}, t_{13} are known. Results of analytical method application are presented in Table 1. The analytical solutions p1, p2 and p3 in Table 1 are valid for various

Table 1: Comparison of analytically calculated and real source coordinates.

source position	time difference of the si gnals [ns]		analytical solutions						Mean of the solutions		real position of the source	
			p1		p2		p3		p			
			x	y	x	y	x	y	x	y	x	y
01	t_{12}	2.2	0.7895	−0.1393	0.6614	−0.0559	0.3591	0.1673	0.6033	−0.0093	0.6000	0.0000
	t_{13}	5.5										
	t_{14}	9.1										
03	t_{12}	−2.2	0.5713	1.0900	0.5743	1.0918	0.5900	1.0900	0.5785	1.0906	0.6000	1.0900
	t_{13}	0										
	t_{14}	3.4										
04	t_{12}	−3.1	0.6050	1.6350	0.6050	1.6350	0.6050	1.6350	0.6050	1.6350	0.6000	1.6400
	t_{13}	−3.1										
	t_{14}	0										
06	t_{12}	−3.5	0.5922	2.7062	0.5971	2.7231	0.6032	2.7250	0.5975	2.7181	0.6000	2.7250
	t_{13}	−6.6										
	t_{14}	−6.6										
07	t_{12}	−3.6	0.2499	2.3668	0.3591	3.1027	0.6614	3.3259	0.4235	2.9318	0.6000	3.2700
	t_{13}	−6.9										
	t_{14}	−9.1										

combinations of 4 antennas (only 3 antennas are used). The calculated results of the source positions are in a good accordance to the real source positions. In case of position 7 the accuracy is poor, probably to poor geometric dilution of precision.

5. CONCLUSION

In this paper, the verification of methods for partial discharge source localization has been presented. The methods have been applied on specific antennas arrangement which is identical to arrangement of antennas in target application −300 MVA high voltage power transformer [5]. The numerical and analytical methods have been briefly described and applications of these methods have been shown. An approach based on analytical method for discharge activity localization in transformer seems to be more suitable than numerical method. This conclusion is based on better accordance of analytical results to the real source positions. However, this is given by specific antennas arrangement, which doesn't dispose with a significant geometric dilution of precision. Another advantage is the calculation time, which is generaly shorter in compare to numerical methods.

ACKNOWLEDGMENT

REFERENCES

1. Markalous, S. M., S. Tenbohlen, and K. Feser, "Detection and location of partial discharges in power transformers using acoustic and electromagnetic signals," *IEEE Transactions on Dielectrics and Electrical Insulation*, Vol. 15, No. 6, 1576–1583, 2008.
2. Bucher, R. and D. Misra, "A synthesizable VHDL model of the exact solution for three-

dimensional hyperbolic positioning system," *VLSI Design*, Vol. 15, No. 2, 507–520, 2002, ISSN: 1563-5171.

3. Bucher, R. and D. Misra, "A synthesizable VHDL model of the exact solution for three-dimensional hyperbolic positioning system," *VLSI Design*, Vol. 15, No. 2, 507–520, 2002, ISSN: 1563-5171.

4. Myska, R. and P. Drexler, "The development of methods for estimation of time differences of arrival of pulse signals," *Progress In Electromagnetics Research Symposium*, Malaysia, Kuala Lumpur, March 27–30, 2012.

5. Fiala, P., T. Jirku, and P. Drexler, "Detection of partial discharge inside of hv transformer, modeling, sensors and measurement," *PIERS Proceedings*, 1013–1016, Cambridge, USA, July 5–8, 2010.

The Development of Methods for Estimation of Time Differences of Arrival of Pulse Signals

R. Myška and P. Drexler

Department of Theoretical and Experimental Electrical Engineering
Brno University of Technology, Kolejni 2906/4, Brno 612 00, Czech Republic

Abstract— This article deals with possibilities of processing of the pulse signals which are produced by partial discharges (PD) in oil power transformers. Possible methods of signal processing are examined in the paper. One of the possibilities is electromagnetic waves sensing radiated by partial discharges in UHF range. Suitable sensors can be realized in a form of antennas. Detected signals may be used for PD source localization, which is based on method of signal time differences of arrival (TDOA). Hence, it is important to determine the front transient process in analyzed signals. The basic method for transient identification is to track the crossing of threshold level. However, this method may fail in case when obtained waveform doesn't contain expressive front transient. One of the solutions can be the modification of the basic method which consists in the observation of immediate power waveform of the signal. The second possibility is to calculate rate of energy accumulation waveform. The energy of the signal is transferred from the sensing space through the antenna on the input impedance of the recording instrument. Another group of methods is based on the signals cross-correlation which can also provide the TDOA of signal waveforms. The topic of the paper is focused on the application of suitable methods on data, which were acquired in a model of partial discharge detection system. The methods will be compared in view of their reliability and accuracy.

1. INTRODUCTION

One of the problematic phenomena in the field of high-voltage technology is the occurrence of partial discharge (PD). Several other effects have combined with this notion over time. In consequence of these effects there emerge short electromagnetic pulses with a defined and measurable spectrum in the characteristic frequency band. This fact is used for measurement of electromagnetic pulse signal by antennas. Once the signals are detected, it is possible to determine their TDOA parameters and localization procedure may follow. Output signals can be processed by various methods, which are presented in this paper.

2. METHODS OF TOA DETERMINATION

The TDOA parameters are calculated as differences of signal time of arrivals (TOA) on the antennas. The signal TOA parameters can be found by signal waveform processing. The first method consists in tracking of threshold level crossing by the voltage signal. This method is unsuitable for signals without considerable front transients because is hard to chose threshold level, which will be correct for all signals. The modification is calculation of immediate power p_i of the signal according to equation [1]

$$p_i = \frac{u_i^2}{Z_0} = \frac{u_i^2}{50}, \quad i = 1 \ldots N \tag{1}$$

where u_i is sample of voltage signal, Z_0 is input impedance of acquisition instrument and N is number of signal samples. Therefore, the front transient is emphasized due to the square of voltage samples in p_i sequence. Threshold level setting is still problematic, while risk of wrong threshold level setting is reduced. Influence of un-suitable threshold level on results may be substantial also.

The second method is a modification of the first. However the calculation of energy accumulation curve (EAC) is performed [3]. Curve samples w_i are given by equation

$$w_i = \frac{t_s}{Z_0} \sum_{k=0}^{i} u_k^2, \quad k = 1 \ldots N \tag{2}$$

where t_s is sampling period. Fast increase in the energy accumulation curve indicates the signal arrival. The time of this moment can be found by calculation of difference value between neighbouring samples. Utilization of threshold level crossing is possible also. In this case, the threshold

level up to 10% of EAC maximal value is chosen. This method is possible to modify by introduction of the negative trend δ into Equation (2) [2]

$$w'_i = \frac{t_s}{Z_0} \sum_{k=1}^{i} \left(u_k^2 - i\delta\right), \quad i = 1 \ldots N \tag{3}$$

The result of waveform calculation according to Equation (3) is a modified EAC curve. The TOA of the signal is determined by the minimum of the curve.

Another approach to TOA estimation is the waveform cross-correlation method. The TDOA parameter of two signals waveforms is determined by calculation of their cross-correlation sequence [4]

$$c_{12}(i) = \sum_{k=1}^{N} u_1(k) u_2(k-i), \quad i = 1 \ldots N. \tag{4}$$

If the two signals are in best correlation during the sequence (4) calculation, the sequence reaches its maximum. The index of the sequence maximum i_{max} determines the TDOA of the two signals

$$\tau = i_{max} \cdot t_s. \tag{5}$$

The cross-correlation method has the advantage that no threshold level has to be chosen in comparison to above described methods. The TDOA of the signals is determined by the analysis of the cross-correlation sequence in way of its maximum evaluation.

The cross-correlation method is suitable only if the two signals are similar in view of their waveforms character and shape. In case when the signals waveforms have considerable mutual divergence, the method fails. However, this a frequent case due to the stochastic character of PD signal origin, multi-path signal propagation, different attenuation of both signals and so on.

In order to deal with these issues, an advanced combination of cross-correlation and threshold crossing method may be used. Its principle consists in the statistical approach to multiple signal processing. Several acquisitions of the signals from each antenna are taken. Further, cross-correlation coefficients for all acquisitions from each of the antennas are calculated. Acquisitions, whose cross-correlation coefficients don't reach a rated value (e.g., 0.8) are disqualified from following processing. In this way, the abnormal signal acquisitions are excluded. The cross-correlation coefficient for signal sequences u_1 and u_2 is calculated as

$$\rho(u_1, u_2) = \frac{C(u_1, u_2)}{\sigma(u_1)\sigma(u_2)} = \frac{\frac{1}{N}\sum_{i=1}^{N} u_1(i) u_2(i) - \overline{u_1} \cdot \overline{u_2}}{\sqrt{\frac{1}{N}\sum_{i=1}^{N}\left(u_1(i) - \overline{u_1}\right)^2} \cdot \sqrt{\frac{1}{N}\sum_{i=1}^{N}\left(u_2(i) - \overline{u_2}\right)^2}}, \tag{6}$$

where $C(u_1, u_2)$ is covariance of u_1 and u_2, $\sigma(u_1)$ a $\sigma(u_2)$ are standard deviation of the sequences and $\overline{u_1}$ a $\overline{u_2}$ are mean values of sequences u_1 and u_2. The second step is a superposition of signal sequences in acquisition collection. This procedure improves signal to noise ratio (SNR) in final sequence. Then, the following threshold level crossing method will give more reliable results due to the clearer moment of signal arrival in the processed signals.

3. EXAMINATION OF SELECTED METHOD

The method based on the EAC calculation has been chosen for estimation of TOA (TDOA) parameters of signals, taking into account the issue of threshold level setting. This method is universal and can be used even for signals where methods based on cross-correlation fail. Further, by exploitation of statistical approach as described above, the mean value of TOA can be determined. Acquisitions with high dispersion of TOA compared to the mean value can be removed from the statistical processing in order to improve the estimation accuracy.

Experimental measurement has been realized in a chamber, which indoor walls, roof and floor are made from stainless steel. Four antennas and signal source were placed in the chamber according to Figure 1. In this experimental workplace the measurement by four antennas has been performed. Antenna signals were recorded by means of high-speed digitizer with 1 GHz bandwidth. The pulse
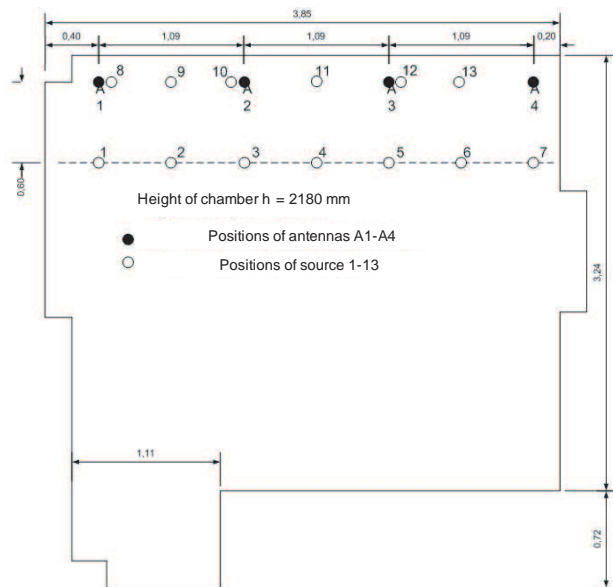
Figure 1: Test setup with marked position of antennas and signal source.
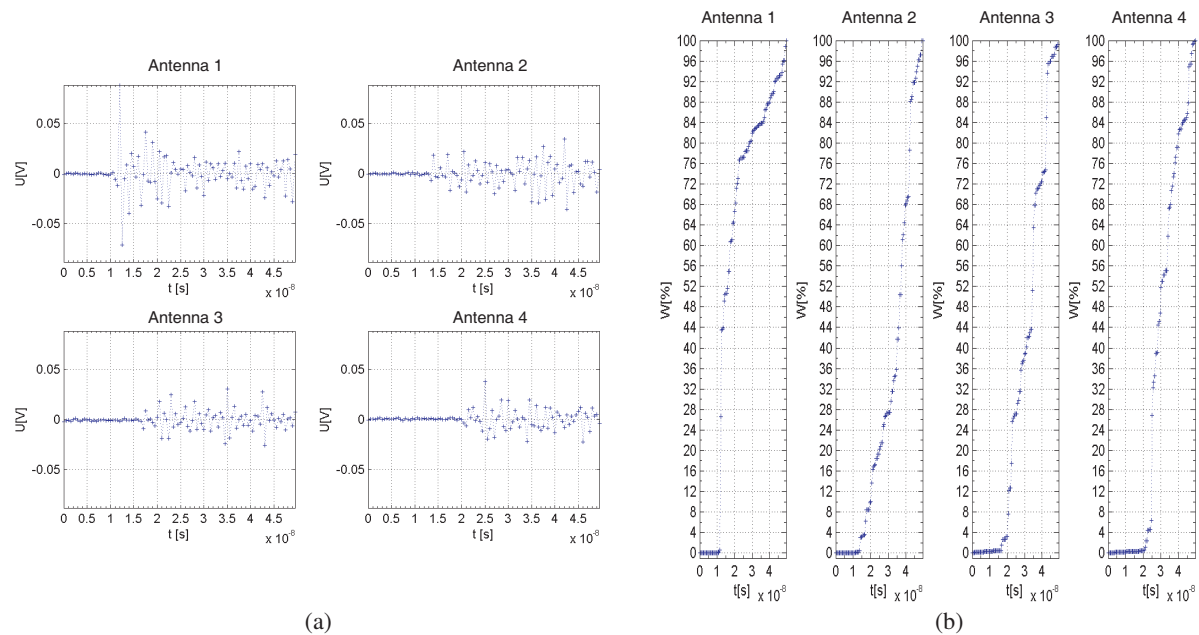
Figure 2: Recorded signal waveforms for (a) source position 1 and (b) computed EACs.

source emitted signals with rise time close to 1 ns. Signal waveforms for source position 1 are shown in Figure 2(a)). Calculated EACs are shown in Figure 2(b)). The EACs are expressed in percents in order to illustrative threshold level expression. Final points of the curve have value of 100% of total signal energy. EACs were calculated by means of MATLAB script. Another script served to tracking the threshold level crossing by the EAC samples. Further, the TDOA parameters has been calculated by subtraction of TOA parameters.

In order to verify the accuracy of the script results it is possible to compare them with expected values. Expected values can be determined from the known electromagnetic wave velocity in air and geometrical relations of the antennas-source arrangement. For example, the TDOA parameter t_{12} for antenna A1 and A2 and source position 1 is

$$t_{12} = \frac{\Delta d}{c} = \frac{\sqrt{0.6^2 + 1.09^2} - 0.6}{c/n_{air}} = 2.149\,\text{ns}, \tag{7}$$

where Δd is the difference in signal paths and $n_{air} = 1{,}0003$ is refractive index of air. Results

Table 1: Calculated and expected time differences for various source position.

Source position	Time difference	Calculation values in [ns]											from geom.
		algorithm										mean value	
		acq.1	acq.2	acq.3	acq.4	acq.5	acq.6	acq.7	acq.8	acq.9	acq.10		
01	t_{12}	2.0	2.0	2.0	2.0	2.0	4.0	2.0	2.5	2.0	2.0	2.3	2.2
	t_{13}	5.0	5.0	6.0	6.0	5.0	5.5	5.0	5.5	6.0	5.0	5.4	5.5
	t_{14}	9.0	9.5	9.0	9.5	8.5	9.0	8.5	9.5	9.5	9.5	9.2	9.1
03	t_{12}	−2.0	−2.5	−1.5	−2.0	−1.5	−1.0	−1.5	−2.0	−1.5	−2.0	−1.8	−2.2
	t_{13}	−0.5	−0.5	−0.5	−0.5	0.0	−0.5	−0.5	−0.5	−0.5	1.0	−0.3	0
	t_{14}	3.0	2.5	3.5	3.5	4.0	3.5	3.0	3.0	4.5	3.0	3.4	3.4
04	t_{12}	−2.5	−2.5	−2.5	−2.5	0.5	−3.0	−2.5	−2.5	−3.5	−3.0	−2.4	−3.1
	t_{13}	−0.5	−2.5	−3.0	−2.5	1.0	−0.5	−3.0	−2.5	−3.5	−3.0	−2.0	−3.1
	t_{14}	0.5	0.0	0.0	0.0	-1.0	1.0	0.0	2.0	0.5	1.5	0.5	0
06	t_{12}	−3.5	−3.5	−3.5	−3.5	−3.5	−3.5	−3.5	−3.5	−3.5	−3.5	−3.5	−3.5
	t_{13}	−6.0	−6.0	−6.0	−5.5	−5.5	−6.0	−6.0	−6.0	−6.5	−6.5	−6.0	−6.6
	t_{14}	−6.0	−4.5	−4.5	−5.5	−5.5	−4.0	−6.0	−6.0	−6.0	−5.0	−5.3	−6.6
07	t_{12}	−3.5	−3.5	−3.5	−4.0	−3.5	−3.5	−2.0	−4.0	−3.5	−3.5	−3.5	−3.6
	t_{13}	−6.5	−6.5	−6.5	−7.0	−6.5	−6.5	−5.5	−7.0	−6.5	−6.5	−6.5	−6.9
	t_{14}	−8.5	−8.5	−8.5	−9.0	−8.5	−8.5	−8.0	−9.0	−8.5	−8.0	−8.5	−9.1
08	t_{12}	3.0	3.0	2.5	3.0	3.0	3.0	3.0	3.0	3.0	3.0	3.0	3.6
	t_{13}	6.5	6.0	6.5	7.0	7.0	7.0	6.5	7.0	7.0	7.0	6.8	7.3
	t_{14}	10.5	11.5	10.0	10.5	11.0	10.5	10.0	10.5	10.5	10.5	10.6	10.9
12	t_{12}	−0.5	−3.0	−3.0	−4.0	−3.0	−4.0	−3.5	−3.0	−3.5	−4.5	−3.2	−3.6
	t_{13}	−4.5	−6.5	−6.5	−7.0	−6.5	−7.0	−7.0	−7.0	−7.5	−8.0	−6.8	−7.3
	t_{14}	−1.5	−3.0	−3.0	−4.0	−3.5	−4.0	−4.0	−4.0	−4.5	−5.0	−3.7	−3.6
13	t_{12}	−4.0	−4.5	−4.0	−4.0	−4.0	−3.5	−4.0	−3.5	−4.0	−4.0	−4.0	−3.6
	t_{13}	−7.0	−8.0	−7.0	−7.5	−7.5	−7.5	−7.5	−7.5	−7.5	−7.5	−7.5	−7.3
	t_{14}	−7.5	−7.5	−7.5	−7.5	−7.5	−7.5	−7.5	−7.0	−7.5	−7.5	−7.5	−7.3

for threshold level 1% are shown in Table 1. For each position of the source ten acquisitions have been acquired. In Table 1 the calculated TDOA parameters for each acquisition are shown. The mean value of TDOA is calculated in the table also. In order to verify the computed results, the expected values are shown also. They are presented in outside right column as TDOA parameters computed from the arrangement geometry. It is obvious, that the computed results are very close to the expected values. Therefore, this method appears as a suitable one for the TDOA parameters estimation.

4. CONCLUSION

The methods for estimation of TDOA parameters of pulse signals have been presented in this paper. The method based on the calculation of energy accumulation curve has been chosen for experimental verification. This method is robust and universal and can be used for signals where methods based on cross-correlation may fail. Experimental measurement has been performed. Recorded signals have been processed by means of MATLAB scripts. Results of the MATLAB script were compared to expected values. The comparison exhibits a good match between the calculated and the expected TDOA parameters.

REFERENCES

1. Yang, L., M. D. Judd, and C. J. Bennoch, "Time delay estimation for UHF signal in PD location of transformers," *Proceedings of Annual Report Conference on Electrical Insulation and Dielectric Phenomena*, Boulder, USA, 2004, ISBN: 0-7803-8584-5.

2. Markalous, S. M., S. Tenbohlen, and K. Feser, "Detection and location of partial discharges in power transformers using acoustic and electromagnetic signals," *IEEE Transactions on Dielectrics and Electrical Insulation*, Vol. 15, No. 6, 1576–1583, 2008, ISSN: 1070-9878.

3. Judd, M. D., L. Yang, and I. B. B. Hunter, "Partial discharge monitoring for power transformers using UHF sensors part 1: Sensors and signal interpretation," *IEEE Electrical Insulation Magazine*, Vol. 21, No. 2, 5–14, 2005, ISSN: 0883-7554.

4. Tang, J. and Y. Xie, "Partial discharge location based on time difference of energy accumulation curve of multiple signals," *IET Electric Power Applications*, Vol. 5, No. 1, 175–180, 2011, ISSN: 1751-8660.

A Time Domain Analytic Solution for Finite and Perfectly Conducting Ellipsoidal Surface Illuminated by Transient Impulsive Plane Wave

Shih-Chung Tuan[1] and Hsi-Tseng Chou[2]

[1]Department of Communication Engineering, Oriental Institute of Technology, Pan-Chiao, Taiwan
[2]Department of Communication Engineering, Yuan Ze University, Chung-Li 320, Taiwan

Abstract— This paper presents an analytical and closed-form solution, based on a time domain (TD) physical optics (PO) approximation, for the fast analysis of transient scattering from a finite and perfectly conducting ellipsoidal surface when it is illuminated by a transient impulsive plane wave. An ellipsoidal surface is selected because it may resemble a variety of realistic surface such as spherical or parabolic surfaces. The integration of various finite ellipsoidal surfaces may be used to model a realistic scattering object such as an aircraft, which makes this solution more applicable to treat realistic problems in an effective fashion. This TD-PO solution can be further applied via a convolution to derive the early time transient fields scattered from the same scatterer that is illuminated by a realistic astigmatic finite-energy pulse. Physical appealing interpretation of wave phenomena in terms of reflection and diffraction mechanisms is also provided in the solution. Numerical examples are presented to demonstrate its physical phenomenon of the scattering mechanisms.

1. INTRODUCTION

A time domain (TD) analytical and closed-form solution of electromagnetic (EM) fields scattered from a perfectly conducting ellipsoidal surface with a finite edge truncation contour is developed by using the approximation of TD physical optics (TD-PO) when the surface is illuminated by a transient-step plane wave. This work is motivated by the interests of ultra wideband or short pulse target identification and remote sensing applications. In this case, a direct TD analysis provides more physically appealing interpretation of wave phenomena. An ellipsoidal surface is selected because it may resemble a variety of realistic surface such as spherical, parabolic and planar surfaces. The integration of these various finite ellipsoidal-like surfaces may be used to model a realistic scattering object such as an aircraft, which makes this solution very applicable to treat realistic problems in an effective fashion. Furthermore this TD solution can also be employed via the convolution theorem to obtain the early-time transient scattering fields generated by the same scatterer when illuminated by a plane wave with a realistic astigmatic finite-energy pulse. In the past, most of TD EM analysis employed TD numerical analysis techniques, such as finite difference time domain (FDTD) and TD integral approaches, which provided exact analytical solutions, but suffered from computational inefficiency to treat the scattering problems of electrically large objects when the pulse widths of the incident waves are very narrow in comparison with the sizes of the scattering/radiating objects. Thus, recent efforts tend to develop quasi-analytical TD solutions [1–7] that appear in closed-forms and have the abilities to provide physical interpretations of wave behaviors. The past work most related to the current one is the development of TD analytic solution of scattering from a parabolic surface. The current work can be considered as its extension to treat an ellipsoidal surface. However, the current solution appears more superior and completed than that previous works because an ellipsoidal surface is more sophisticated, and may be used to more accurately model realistic and general scatters which can not be achieved by simply using parabolic ones, such as a sphere. Furthermore, the current solution will reduce to the previous one because an ellipsoidal surface will reduce to a parabolic one when the radius of the ellipse approaches to an infinite. Figure 1 illustrates several realistic scatterers modeled by truncating ellipsoidal surfaces with finite edge contours including a sphere, a parabolic surface, an ellipsoidal body, a finite cylinder and a planar surface, which appear in many practical objects.

2. TRANSIENT STEP RESPONSE

Consider an ellipsoidal surface described by

$$\left(\frac{z'}{b_z}\right)^2 + \left(\frac{x'}{b_x}\right)^2 + \left(\frac{y'}{b_y}\right)^2 = 1, \tag{1}$$

(a) A Realistic Aircraft

Finite Ellipsoidal Surface

Finite Parabolic Surface

Finite Cylinder

Finite Plane

Finite Sphere

Finite Cone Shape

(b) Realistic Models to Form the Scatter
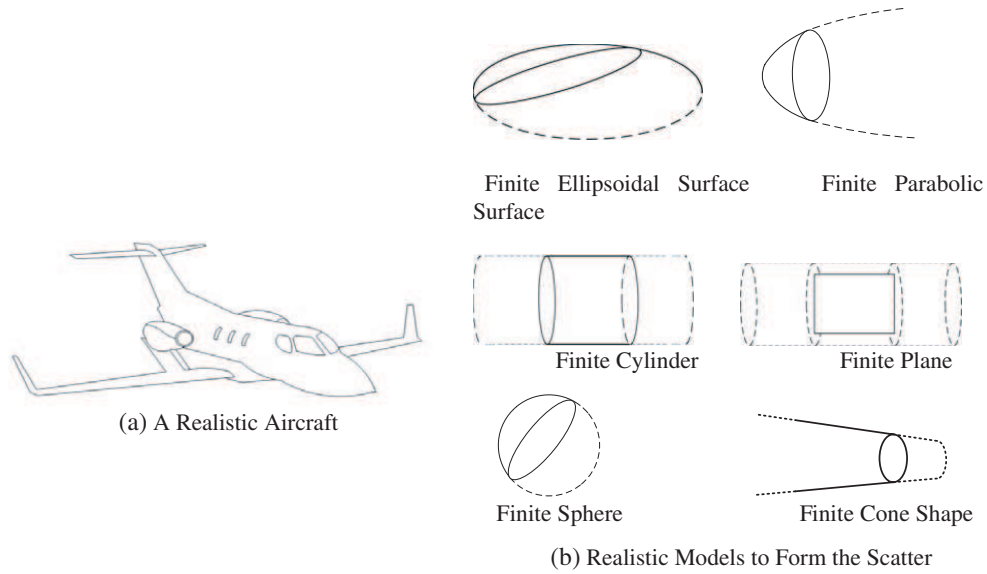
Figure 1: Typical structures of scatters to assemble a realistic structure of scatter such as aircraft. (a) Shows a realistic aircraft model. (b) Shows a variety of shaped surfaces that can be used to approximate the model in (a).

where $\bar{r}' = (x', y', z')$ is a position vector on the surface with b_z, b_x and b_y being its radii along z-, x- and y-axis, respectively. The actual surface is formed by taking a part from the ellipsoidal surface described in (1) with an edge contour, which is then illuminated by a plane wave incident from the direction $\hat{k}_i$. It is noted that since PO is employed in this study, which considers only the induced currents on the part of surface in the lit region of the incident field, an effective edge contour, C_e, is formed by the original edge contour and the shadow boundary of the incident field such that the surface under examination is a part of the original surface in the lit region of the incident field. It is noted that (1) may approximately model a variety of realistic surfaces such as these shown in Figure 1. For example, when $b_z = b_x = b_y$, it reduces to a sphere. The electrical field of the incident plane wave in TD is described by

$$\bar{\mathcal{E}}_i(\bar{r}', t) = \bar{E}_0 \, U(t - \frac{\hat{k}_i \cdot \bar{r}'}{c}), \tag{2}$$

where the time reference, $t = 0$, is selected at $\bar{r}' = (0, 0, 0)$, which allows $t < 0$ for a negative value of $(\hat{k}_i \cdot \bar{r}')/c$. Also $U(\cdot)$ is a step function defined by

$$U(\xi) = \left\{ \begin{array}{ll} 1, & \xi \geq 0 \\ 0, & \xi < 0 \end{array} \right\}. \tag{3}$$

The fields scattered from the ellipsoidal surface due to the illumination of the transient-step incident field in (2) can be obtained by TD-PO. At $\bar{r} = (x, y, z)$ in the far zone of the scatter, it can be approximated by

$$\bar{\mathcal{E}}_s^u(\bar{r}, t) \cong \frac{1}{2\pi rc} \hat{r} \times \hat{r} \times \left\{ \iint_{S_a} \hat{n} \cdot \delta \left(t - \frac{(\hat{k}_i - \hat{r}) \cdot \bar{r}' + r}{c} \right) ds' \right\} \times \hat{k}_i \times \bar{E}_0 \tag{4}$$

Also in (4), the delta function, $\delta(t) = dU(t)/dt$, which may reduce (4) to a line integral at the conditions that the delta function has a nonzero value at t, by

$$\delta \left(t - \frac{(\hat{k}_i - \hat{r}) \cdot \bar{r}'}{c} - \frac{r}{c} \right) \neq 0, \tag{5}$$

which occurs at

$$(\hat{k}_i - \hat{r}) \cdot \bar{r}' = ct - r \equiv L \tag{6}$$

(a) Illustration of PO Edge Contour

(b) Illustration of Integration Contour
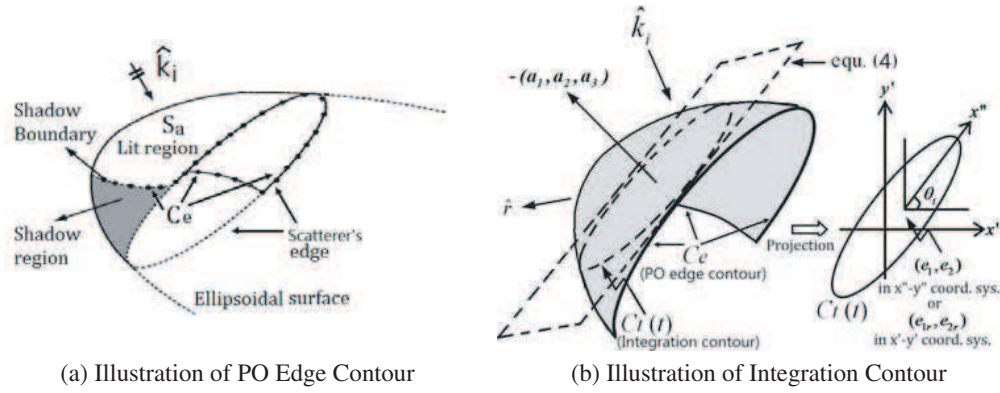
Figure 2: The relation of integration contour to the ellipsoidal surfaces with finite edges. C_e is formed by the edges in the lit region and the shadow boundary of scatterer, s_a is the surface in the lit region to the incident field, and $C_t(t)$ is the intersection of and the plane.

that corresponds to a line contour $C_t(t)$ on S_a as illustrated in Figure 2.

$$\bar{P}(t) = \bar{P}_r(t)\,T(t) + \bar{P}_d(t, \varphi_e) - \bar{P}_d(t, \varphi_b) \tag{7}$$

where $\bar{P}_r$ and $\bar{P}_d$ are referred to reflected and edge diffracted components, respectively. In particular,

$$\bar{P}_r(t) = -2\pi|a_3|AB\left(\hat{x}\frac{b_z^2}{b_x^2}e_{1,r} + \hat{y}\frac{b_z^2}{b_y^2}e_{2,r} + \hat{z}e_{3,r}\right), \tag{8a}$$

$$\begin{aligned}
\bar{P}_d(t, \varphi_a) = -|a_3|ABb_z^2\bigg(&\hat{x}\frac{1}{b_x^2}\left[A\rho_t\cos\theta_t\sin\varphi_a + B\rho_t\sin\theta_t\cos\varphi_a\right] \\
&+\hat{y}\frac{1}{b_y^2}\left[A\rho_t\sin\theta_t\sin\varphi_a - B\rho_t\cos\theta_t\cos\varphi_a\right] \\
&+ \hat{z}\frac{1}{b_z^2}\left[-\frac{\alpha_1}{a_3}A\rho_t\sin\varphi_a + \frac{\alpha_2}{a_3}B\rho_t\cos\varphi_a\right]\bigg) = |a_3|ABb_z^2\bar{\Phi}(t)
\end{aligned} \tag{8b}$$

3. REDUCED FORMULATIONS FOR SPECIAL CASES

3.1. A Rotationally Symmetric Ellipsoidal Surface

In this case, one considers $b_x = b_y$ results in the field solutions by

$$\bar{\mathcal{E}}_r^u(\vec{r}, t) = \frac{(ct - r)b_z(1 - \hat{r}\cdot\hat{k}_i)}{rb_x\left(a_3^2\frac{b_z^2}{b_x^2} + a_1^2 + a_2^2\right)^{3/2}} \cdot \left[\bar{E}_0\cdot\left(\hat{e}_\parallel^i\hat{e}_\parallel^r - \hat{e}_\perp\hat{e}_\perp\right)\right] \tag{9a}$$

at any t, and

$$\bar{\mathcal{E}}_d^u(\vec{r}, t) = \frac{b_zb_x^2\left\{\hat{r}\times\hat{r}\times\bar{\Phi}(t)\times\hat{k}_i\times\bar{E}_0\right\}}{2\pi r\sqrt{a_3^2b_z^2 + b_x^2(a_1^2 + a_2^2)}} \tag{9b}$$

3.2. Spherical Surface

In this case, $b_z = b_x = b_y$, The field solutions now become

$$\bar{\mathcal{E}}_r^u(\vec{r}, t) = \bar{E}_0\cdot\left(\hat{e}_\parallel^i\hat{e}_\parallel^r - \hat{e}_\perp\hat{e}_\perp\right)\frac{(ct - r)(1 - \hat{r}\cdot\hat{k}_i)}{r\left(a_3^2 + a_1^2 + a_2^2\right)^{3/2}}, \tag{10a}$$

and

$$\bar{\mathcal{E}}_d^u(\vec{r}, t) = \frac{b_z^2\left\{\hat{r}\times\hat{r}\times\bar{\Phi}(t)\times\hat{k}_i\times\bar{E}_0\right\}}{2\pi r\sqrt{a_3^2 + a_1^2 + a_2^2}} \tag{10b}$$

(a) Illustration of t_1 and t_2 on the x-z plane

(b) Transient Responses
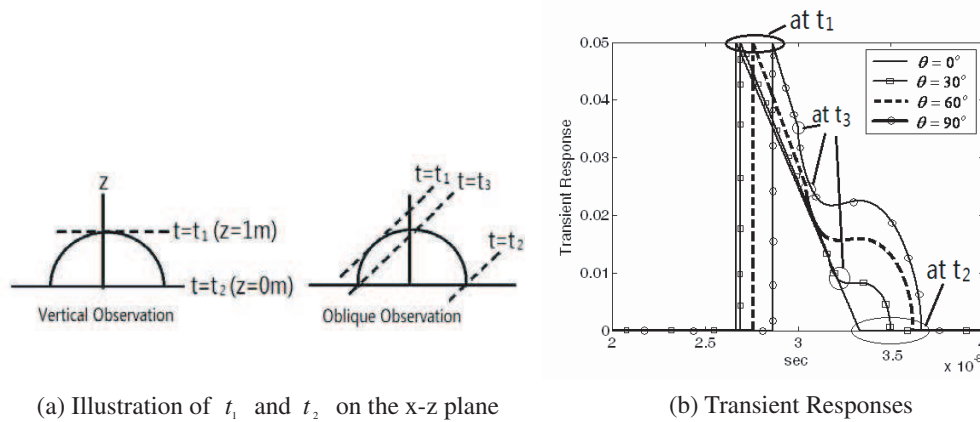
Figure 3: Illustration of transient scattering from a half sphere, and its transient responses for various observation angles. The plane wave is incident from z-axis.

3.3. Finite Cylindrical Surface

In this case, one assumes $b_y \to \infty$, and makes $\hat{y}$ being the axis of the cylinder. Results will shows on the presentation.

3.4. Finite Planar Surface

In this case, one makes $b_x = b_y \to \infty$. Results will shows on the presentation.

4. NUMERICAL EXAMPLES

One considers the cases of observation in the oblique angles on the x-z plane, where $\theta = 30°$, $60°$, and $90°$ are considered. As illustrated in Figure 3(a), three times of t_1, t_2 and t_3 need to be considered, which are the time that the plane of $(\hat{k}_i - \hat{r}) \cdot \vec{r}' = ct - r \equiv L$ touches the surface (reflection point), the edge point at $x = -1\,\text{m}$ and the edge point at $x = 1\,\text{m}$, respectively. At $t_1 < t < t_3$, only the reflection term exists, which exhibits the phenomena of transient response identical to these exhibited in the case of $\theta = 0°$ as demonstrated in Figure 3(b). At $t > t_3$, the transient function and diffraction term come into effects. In this case, both the reflection term and transient function ($T(t) = 1 \to 0$) continue to decrease and become zero at $t = t_2$, while the diffraction term starts to increase its effect. It is noted that the diffraction term increases initially, reaches a maximum, and then decreases to zero at $t = t_2$. Many numerical results will shows on the presentation.

5. CONCLUSIONS

A time domain (TD) analytical and closed-form solution of electromagnetic (EM) fields scattered from a perfectly conducting ellipsoidal surface with a finite edge truncation contour is developed by using the approximation of TD-PO when the surface is illuminated by a transient-step plane wave. The integration of these various finite ellipsoidal-like surfaces may be used to model a realistic scattering object such as an aircraft, which makes this solution very applicable to treat realistic problems in an effective fashion.

REFERENCES

1. Heyman, E., "Pulsed beam propagation in inhomogeneous medium," *IEEE Trans. Antennas Propag.*, Vol. 42, No. 3, 311–319, March 1994.

2. Heyman, E. and L. B. Felsen, "Gaussian beam and pulsed-beam dynamics: Complex-source and complex-spectrum formulations within and beyond paraxial asymptotics," *J. Opt. Soc. Am. A*, Vol. 18, No. 7, 1588–1611, July 2001.

3. Heyman, E. and L. B. Felsen, "Complex-source pulsed-beam fields," *J. Opt. Soc. Am. A*, Vol. 6, No. 6, 806–817, June 1989.

4. Ianconescu, R. and E. Heyman, "Pulsed field diffraction by a perfectly conducting wedge: A spectral theory of transients analysis," *IEEE Trans. Antennas Propag.*, Vol. 42, No. 6, 781–789, June 1994.

5. Chou, H.-T. and S.-C. Tuan, "Analytic analysis of transient scattering from a finite second-order surface illuminated by an incident plane wave," *IEEE Trans. Antennas Propag.*, Vol. 54, No. 9, 2463–2471, September 2006.
6. Chou, H.-T. and P. H. Pathak, "Analytic solution for early-time transient radiation from pulse-excited parabolic reflector antennas," *IEEE Trans. Antennas Propag.*, Vol. 45, 829–836, May 1997.
7. Tyo, J. S., E. G. Farr, and D. I. Lawry, "Effect of defocus on the prompt response of a reflector IRA," *IEEE Trans. Antennas Propag.*, Vol. 53, No. 10, 3247–3254, October 2005.

Omega-K Algorithm for Bistatic SAR Image Formation

C. Y. Dai and X. L. Zhang

University of Electronic Science and Technology of China, China

Abstract— Comparing to the common monostatic synthetic aperture radar (SAR), the bistatic SAR data are more challenging to process because of its complicated flight geometry. This paper proposes an Omega-K algorithm to handle a general case of bistatic SAR data. The two-dimensional frequency spectrum expression derived by the method of series reversion is rewritten to a new form with explicit geometric significance. Based on this new frequency spectrum expression, the frequency mapping function can be derived by making use of the multi-variable Taylor's theorem. After data mapping operation, the coupling between the range and azimuth can be eliminated, and the final focused image can be obtained using FFT technology. Numerical simulations are performed to validate the proposed algorithm.

1. INTRODUCTION

The imaging algorithms of monostatic synthetic aperture radar (SAR) use monostatic point target reference spectrum (PTRS), which is based on the hyperbolic range history [1]. However, in the bistatic system, the range history is the sum of two hyperbolic range equations, known as the double-square-root (DSR) term [2]. This implies that it is difficult to obtain the bistatic point target reference spectrum (BPTRS) using the method of stationary phase directly [3]. Therefore, monostatic SAR processing algorithms must be modified if they are to be used to handle bistatic data.

Several algorithms have been proposed to focus on the BiSAR data. In [4], an accurate BPTRS has been derived by basing on the reversion of a power series for the general bistatic case. It is known as the method of series reversion (MSR). The prominent property of MSR is controlled by the number of terms used in the power series. Thus the point target spectrum of the MSR is more accurate analytical spectrum than LBF [5]. Based on MSR, in [6], an Omega-K algorithm was formulated for the azimuth-invariant case. It assumes that the coefficients of BPTRS vary only with the range of the target point.

This paper further develops the Omega-K algorithm for BiSAR with arbitrary geometry configuration based on the method of series reversion. We rewrite the BPTRS derived by MSR to a new function form with explicit geometric significance. Based on this new frequency spectrum expression, the frequency mapping function is derived by making use of the multi-variable Taylor's theorem. Due to the space-variant feature in BiSAR with arbitrary configuration, the frequency spectrum does not only vary with the range, but also varies with the azimuth. Thus the frequency mapping is a two-dimensional process.

2. SIGNAL MODEL

The data acquisition geometry of the general bistatic SAR is described in Fig. 1. Without loss of generality, the center of the scene to be imaged is located at the origin of coordinates, and the ground plane is the $z = 0$ plane. A scatterer within that scene is located at $\mathbf{P}(x, y, 0)$. The instantaneous position of the transmitter is denoted by $\mathbf{P}_{\mathrm{T}}(u)$ and that of the receiver by $\mathbf{P}_{\mathrm{R}}(u)$, where u represents the slow time. $R_{\mathrm{T}}(u; \mathbf{P})$ and $R_{\mathrm{R}}(u; \mathbf{P})$ denote the slant ranges from scatterer
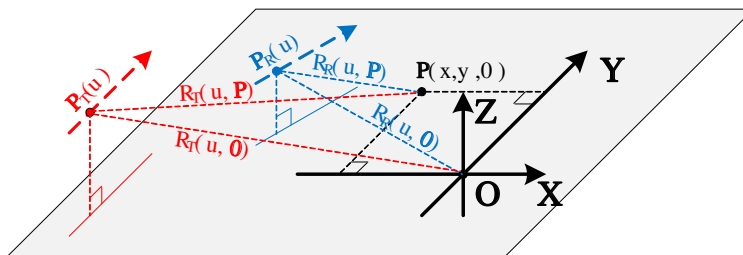
Figure 1: Imaging geometry for the general bistatic SAR configuration at slow-time u.

$\mathbf{P}$ to the transmitter and the receiver, respectively. Thus the slant range $R(u; \mathbf{P})$ of scatterer $\mathbf{P}$ is the sum of the slant ranges form point $\mathbf{P}$ to the T/R platforms, i.e.,

$$
\begin{aligned}
R(u; \mathbf{P}) &= R_{\mathrm{T}}(u; \mathbf{P}) + R_{\mathrm{R}}(u; \mathbf{P}) \\
&= \|\mathbf{P}_{\mathrm{T}}(u) - \mathbf{P}\| + \|\mathbf{P}_{\mathrm{R}}(u) - \mathbf{P}\| \\
&= k_0 + k_1 u + k_2 u^2 + k_3 u^3 + k_4 u^4 + \ldots
\end{aligned}
\tag{1}
$$

where coefficients k_0, k_1, k_2, ..., in (1) are given as

$$
k_n = \frac{1}{n!} \left. \frac{dR(u; \mathbf{P})}{du} \right|_{u=0} \quad (n = 0, 1, 2, \ldots)
\tag{2}
$$

Similarly, the slant range of the reference point $\mathbf{0}$ of the scene space is given by

$$
\begin{aligned}
R(u; \mathbf{0}) &= R_{\mathrm{T}}(u; \mathbf{0}) + R_{\mathrm{R}}(u; \mathbf{0}) \\
&= \|\mathbf{P}_{\mathrm{T}}(u) - \mathbf{0}\| + \|\mathbf{P}_{\mathrm{R}}(u) - \mathbf{0}\| \\
&= k_{0\_\mathrm{ref}} + k_{1\_\mathrm{ref}} u + k_{2\_\mathrm{ref}} u^2 + k_{3\_\mathrm{ref}} u^3 + k_{4\_\mathrm{ref}} u^4 + \ldots
\end{aligned}
\tag{3}
$$

where coefficients k_{0_ref}, k_{1_ref}, k_{2_ref}, ..., in (3) are given as

$$
k_{n\_\mathrm{ref}} = \frac{1}{n!} \left. \frac{dR(u; \mathbf{0})}{du} \right|_{u=0} \quad (n = 0, 1, 2, \ldots)
\tag{4}
$$

By using MSR, the 2-D spectrum of received signal $s(t, u; \mathbf{P})$ can be derived. For simplicity, we directly give the result as

$$
S(f_t, f_u; \mathbf{P}) = \exp\left[j\phi(f_t, f_u; \mathbf{P}) \right]
\tag{5}
$$

where f_t and f_u denote the range and azimuth frequency, respectively. The phase $\phi(f_t, f_u; \mathbf{P})$ is given by [4]

$$
\begin{aligned}
\phi(f_t, f_u; \mathbf{P}) =\ & -\pi \frac{T_p}{B} f_t^2 - 2\pi \frac{f_c + f_t}{c} k_0 \\
& + 2\pi \frac{1}{4k_2} \frac{c}{f_c + f_t} \left(f_u + \frac{f_c + f_t}{c} k_1 \right)^2 \\
& + 2\pi \frac{k_3}{8k_2^3} \frac{c^2}{(f_c + f_t)^2} \left(f_u + \frac{f_c + f_t}{c} k_1 \right)^3 \\
& + 2\pi \frac{9k_2^2 - 4k_2 k_4}{64k_2^5} \frac{c^3}{(f_c + f_t)^3} \left(f_u + \frac{f_c + f_t}{c} k_1 \right)^4
\end{aligned}
\tag{6}
$$

where B and T_p denote the bandwidth and the pulse length of the transmitted signal, c denotes the wave propagation speed and f_c denotes the carrier frequency.

3. OMEGA-K ALGORITHM FOR GENERAL BISTATIC SAR

After polynomial expansion in (6), the phase $\phi(f_t, f_u; \mathbf{P})$ can be rearranged as

$$
\phi(f_t, f_u; \mathbf{P}) = -\pi \frac{T_p}{B} f_t^2 - 4\pi \frac{f_c + f_t}{c} R_{\mathrm{b}} + 2\pi f_u \tau + \sum_{k=2}^{4} 2\pi A_k \left(\frac{c}{f_c + f_t} \right)^{k-1} f_u^k
\tag{7}
$$

where

$$R_{\mathrm{b}} = \frac{1}{2}\left(k_0 - \frac{k_1{}^2}{4k_2} - \frac{k_1{}^3 k_3}{8k_2{}^3} - \frac{k_1{}^4\left(9k_3{}^2 - 4k_2 k_4\right)}{64k_2{}^5}\right) \tag{8}$$

$$\tau = \frac{k_1}{2k_2} + \frac{3k_1{}^2 k_3}{8k_2{}^3} + \frac{k_1{}^3\left(9k_3{}^2 - 4k_2 k_4\right)}{16k_2{}^5} \tag{9}$$

$$A_2 = \frac{1}{4k_2} + \frac{3k_1 k_3}{8k_2{}^3} + \frac{3k_1{}^2\left(9k_3{}^2 - 4k_2 k_4\right)}{32k_2{}^5} \tag{10}$$

$$A_3 = \frac{k_3}{8k_2{}^3} + \frac{k_1\left(9k_3{}^2 - 4k_2 k_4\right)}{16k_2{}^5} \tag{11}$$

$$A_4 = \frac{9k_3{}^2 - 4k_2 k_4}{64k_2{}^5} \tag{12}$$

From (7) we can see that, the existence of coefficients A_2, A_3 and A_4 represent the coupling between the range frequency f_t and azimuth frequency f_u. If this coupling relation is eliminated, the focused SAR image in (R_{b}, τ) space can be obtained using FFT operation.

Therefore, after performing the reference function multiply (RFM) on $S(f_t, f_u; \mathbf{P})$, i.e., multiplying $S(f_t, f_u; \mathbf{P})$ with $S^*(f_t, f_u; \mathbf{0})$, we have

$$S_{\mathrm{RFM}}\left(f_t, f_u\right) = S\left(f_t, f_u; \mathbf{P}\right) \cdot S^*\left(f_t, f_u; \mathbf{0}\right) = \exp\left\{j\phi_{\mathrm{RFM}}\left(f_t, f_u\right)\right\} \tag{13}$$

where

$$\begin{aligned}\phi_{\mathrm{RFM}}\left(f_t, f_u\right) &= \phi\left(f_t, f_u; \mathbf{P}\right) - \phi\left(f_t, f_u; \mathbf{0}\right) = -4\pi\frac{f_c + f_t}{c}\left(R_{\mathrm{b}} - R_{\mathrm{b\_ref}}\right) + 2\pi f_u\left(\tau - \tau_{\mathrm{ref}}\right) \\ &\quad + 2\pi\left(A_2 - A_{2\_\mathrm{ref}}\right)\frac{c}{f_c + f_t}f_u{}^2 + 2\pi\left(A_3 - A_{3\_\mathrm{ref}}\right)\frac{c^2}{\left(f_c + f_t\right)^2}f_u{}^3 \\ &\quad + 2\pi\left(A_4 - A_{4\_\mathrm{ref}}\right)\frac{c^3}{\left(f_c + f_t\right)^3}f_u{}^4 \end{aligned} \tag{14}$$

where coefficients $R_{\mathrm{b\_ref}}$, τ_{ref}, A_{2_ref}, A_{3_ref} and A_{4_ref} can be calculated by substituting $\mathbf{P}$ to $\mathbf{0}$ in (2).

According to the multi-variable Taylor's theorem, we can express coefficients $A_k(k = 2, 3, 4)$ in (10)–(12) over $R_{\mathrm{b\_ref}}$ and τ in terms of bilinear regression:

$$A_k - A_{k\_\mathrm{ref}} \approx \alpha_k \cdot \left(R_{\mathrm{b}} - R_{\mathrm{b\_ref}}\right) + \beta_k \cdot \left(\tau - \tau_{\mathrm{ref}}\right) \tag{15}$$

where

$$\alpha_k = \left.\frac{\partial A_k}{\partial R_{\mathrm{b}}}\right|_{R_{\mathrm{b}}=R_{\mathrm{b\_ref}}; \tau=\tau_{\mathrm{ref}}} \tag{16}$$

$$\beta_k = \left.\frac{\partial A_k}{\partial \tau}\right|_{R_{\mathrm{b}}=R_{\mathrm{b\_ref}}; \tau=\tau_{\mathrm{ref}}} \tag{17}$$

By substituting (15) into (14), phase $\phi_{\mathrm{RFM}}(f_t, f_u)$ can be rewritten as

$$\begin{aligned}\phi_{\mathrm{RFM}}\left(f_t, f_u\right) &= -4\pi\frac{f_c + f_t}{c}\left[1 - \frac{1}{2}\sum_{k=2}^{4}\alpha_k\left(\frac{cf_u}{f_c + f_t}\right)^k\right]\left(R_{\mathrm{b}} - R_{\mathrm{b\_ref}}\right) \\ &\quad + 2\pi f_u\left[1 + \sum_{k=2}^{4}\beta_k\left(\frac{cf_u}{f_c + f_t}\right)^{k-1}\right]\left(\tau - \tau_{\mathrm{ref}}\right) \end{aligned} \tag{18}$$

It is evident that the coupling between the range frequency f_t and azimuth frequency f_u can be

removed if we rescale the 2-D frequency domain data by the frequency mapping:

$$f_t{}' = (f_c + f_t) \left[1 - \frac{1}{2} \sum_{k=2}^{4} \alpha_k \left(\frac{cf_u}{f_c + f_t} \right)^k \right] - f_c \tag{19}$$

$$f_u{}' = f_u \left[1 + \sum_{k=2}^{4} \beta_k \left(\frac{cf_u}{f_c + f_t} \right)^{k-1} \right] \tag{20}$$

After mapping the data from (f_t, f_u) space to (f_t', f_u') space, we have

$$\phi_{\mathrm{RFM}} \left(f_t{}', f_u{}' \right) = -4\pi \frac{f_c + f_t'}{c} \left(R_\mathrm{b} - R_\mathrm{b\_ref} \right) + 2\pi f_u{}' \left(\tau - \tau_{\mathrm{ref}} \right) \tag{21}$$

Then, performing a 2-D inverse Fourier transform, we can get the focused image of target point **P** in the (R_b, τ) space.

4. NUMERICAL SIMULATION

To verify the validity of the proposed image formation method, the numerical simulation is carried out in this section. In this simulation, the carrier frequency $f_c = 10\,\mathrm{GHz}$, the bandwidth of transmitted signal $B = 150\,\mathrm{MHz}$, the Doppler bandwidth of the reference point $B_a \approx 175\,\mathrm{Hz}$. The sampling frequency in range is $200\,\mathrm{MHz}$ and the pulse repetition frequency is $400\,\mathrm{Hz}$. The rest of the parameters for the simulation are shown in Table 1.

The simulated scene consists of five point targets in the ground plane $z = 0$. The reference point O is located in the center of the scene, and the other four points are located on the vertices of a $200\,\mathrm{m} \times 200\,\mathrm{m}$ square. The corresponding coordinates in (R_b, τ) space can be calculated using (9)–(13): O $(11.773\,\mathrm{km}, -0.927\,\mathrm{s})$, A $(11.799\,\mathrm{km}, -2.007\,\mathrm{s})$, B $(11.733\,\mathrm{km}, -1.545\,\mathrm{s})$, C $(11.748\,\mathrm{km}, 0.153\,\mathrm{s})$ and D $(11.815\,\mathrm{km}, -0.308\,\mathrm{s})$.

Imaging results are shown in Fig. 2. From this figure, we can see that, five targets are arranged in their correct position in (R_b, τ) space. To quantify the precision of the presented processing

Table 1: Simulation parameters.

Parameter	Transmitter	Receiver
initial position in x direction	−5 (km)	−3 (km)
initial position in y direction	0 (km)	1.5 (km)
initial position in z direction	12 (km)	10 (km)
velocity in x direction	0 (m/s)	50 (m/s)
velocity in y direction	120 (m/s)	86.6 (m/s)
velocity in z direction	0 (m/s)	0 (m/s)
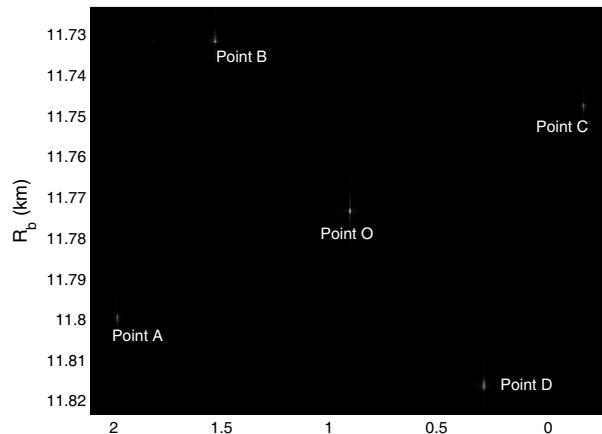
Figure 2: Imaging result of five target points.
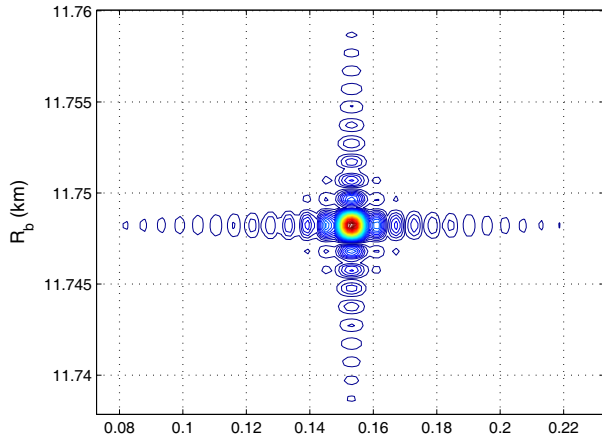
Figure 3: The response of point target C.

Table 2: Results of point target analysis of Point C.

	Range	Azimuth
Resolution calculated	$0.886\,\mathrm{m}$	$5.051 \times 10^{-3}\,\mathrm{s}$
Resolution measured	$0.903\,\mathrm{m}$	$5.126 \times 10^{-3}\,\mathrm{s}$
PSLR (dB)	-12.91	-13.18
ISLR (dB)	-9.65	-9.73

method, point C is chosen to analyse the performance of boundary point target response. Fig. 3 indicates the output response of the chosen point target C. Results of the point target response of point C are shown in Table 2.

The ideal focusing result has PSLR $\approx -13.3\,\mathrm{dB}$ and ISLR $\approx -9.8\,\mathrm{dB}$. Comparing with the ideal performance, the resolution broadening is less than 2% in range and 1.5% in azimuth; PSLR rising is less than $0.5\,\mathrm{dB}$ and ISLR rising is less than $0.2\,\mathrm{dB}$. Thus, the proposed algorithm can well meet the requirement of moderate focusing accuracy [3].

5. CONCLUSION

This paper has proposed an effective Omega-K image formation algorithm for bistatic SAR with arbitrary geometry configuration. The frequency spectrum expression derived by MSR is rewritten as a novel function form with explicit geometric significance. Within this new expression, parameters R_b and τ represent the position in the image space, and parameters A_k represent the coefficients of coupling between the range and azimuth. After performing the RFM operation, the remained phase can be expressed as the linear combination of R_b and τ, thus the frequency mapping function is derived to correct the coupling effect. Consequently, the ultimate focused image in (R_b, τ) space can be obtained using FFT technology. To validate the proposed algorithm, numerical simulation are performed for a typical arbitrary geometry configuration. The simulation results prove that the presented algorithm is effective in image formation processing in arbitrary bistatic SAR imaging configurations.

ACKNOWLEDGMENT

REFERENCES

1. Raney, R. K., "A new and fundamental Fourier transform pair," *Proc. IGARSS*, 106–107, Clear Lake, TX, May 1992.
2. D'Aria, D., A. Guarnieri, and F. Rocca, "Focusing bistatic synthetic aperture radar using dip move out," *IEEE Trans. Geosci. Remote Sens.*, Vol. 42, No. 7, 1362–1376, Jul. 2004.
3. Cumming, I. G. and F. Wong, *Digitial Processing of Synthetic Aperture Radar: Algorithms and Implementation*, Artech House, Norwood, MA, 2005.
4. Neo, Y. L., F. H. Wong, and I. G. Cumming, "A two-dimensional spectrum for bistatic SAR processing using series reversion," *IEEE Geosci. Remote Sens. Lett.*, Vol. 4, No. 1, 93–96, Jan. 2007.
5. Neo, Y. L., F. H. Wong, and I. G. Cumming, "A comparison of point target spectrum derived for bistatic SAR processing," *IEEE Trans. Geosci. Remote Sens.*, Vol. 46, No. 9, 2481–2492, Sep. 2008.
6. Liu, B., T. Wange, Q. Wu, and Z. Bao, "Bistatic SAR data focusing using an Omega-K algorithm based on method of series reversion," *IEEE Trans. Geosci. Remote Sens.*, Vol. 47, No. 8, 2899–2912, Aug. 2009.

Implementation of Space-time Adaptive Processing (STAP) for Target Detection in Passive Bi-static Radar

Zia Ul Mahmood[1], Mubashir Alam[1], Khalid Jamil[2], and Mohammed Elnamaky[2]

[1]Department of Electrical Engineering, King Saud University, Riyadh, KSA
[2]Prince Sultan Advanced Technologies Research Institute (PSATRI)
King Saud University, Riyadh, KSA

Abstract— This paper presents the implementation of Space Time Adaptive Processing (STAP) algorithm for Passive Bi-static Radar (PBR) using commercial FM transmitter as illuminator of opportunity. A simulated target was inserted in the real-time recorded FM eight channel data signal. The simulated target was detected after effective zero Doppler frequency clutter removal with the help of STAP processing. Before finding the actual target the system performs different steps involved in STAP processing. Finally, some initial FPGA implementation of the STAP processor was developed using Xilinx Virtex-6 platform.

1. INTRODUCTION

Radars using illuminators of opportunity like FM, GSM, DVB-T etc., available in the environment are called Passive Bi-static Radars (PBR). PBR exploits existing commercial radio transmitters as illuminators of opportunity to perform target detection and localization. The illuminators of opportunity are selected due to their high power and excellent border-border coverage performance [1]. Another advatage of PBR radar is its stealth nature, which is impossible to detect. PBR systems are currently being developed for detecting both air and ground targets.

A basic passive radar system works in such a way that it establishes unsynchronized connections from the nearby illuminators of opportunity, to detect and track targets of interest. Most of the moving target indication (MTI) active radars with stationary platform usually encounter slow moving targets. The two dimensional nature of the ground clutter makes the detection process complicated because the reflections from ground clutter can be many orders of magnitude greater than the potential targets of interest. The jammer also provides the similar problem in conventional active radar systems. Space-Time Adaptive Processing (STAP) algorithm has the capability of multidimensional (space and time) filtering of ground clutters and also jammers using phased array antennas in order to detect the weak targets [8].

Previous contributions of PBR using signals from FM radio broadcast towers [2], digital video broadcast (DVB-T) [3], and Global System for mobile communications (GSM) base stations [4] have been studied in order to identify the suitable signal for this scenario. Also some more contributions include the implementation of STAP on PBR with GSM base station [5], with DVB-T transmitters [6] while using amplitude and phase estimation (APES) method to reject ground clutter was proposed.

In this paper we have considered FM transmitters as illuminator of opportunity, and actual FM signal is recorded. A simulated target at specific angle and Doppler frequency is then inserted in this actual recorded data. After this the target signature is detected using the STAP algorithm. This paper mainly focuses on the FPGA implementation of kronecker-delta product which will be used in STAP algorithm. Firstly the system model explaining the data reception scenario and the pre-signal processing steps are explained in Section 2. Secondly the simulation results of these signal processing steps are described in Section 3. Section 4 explains the FPGA implementation of the kronecker product.

2. SYSTEM MODEL

The data reception scenario used in this paper consists of an antenna array which will record an actual commercial FM signal and then a simulated target will be inserted to complete the scenario as shown in Fig. 1. Later on, this setup will be used with actual targets. In Fig. 2, a block diagram is shown, explaining the signal processing steps involved in the detection of the simulated target. Firstly we perform the post processing of the eight channel real-time FM data by calibrating the data, which includes correction of phase and amplitude errors. For effective STAP processing we need a pure reference signal from the FM transmitter. This signal can be obtained by Direction-of-Arrival (DOA) estimation and adaptive beamforming.
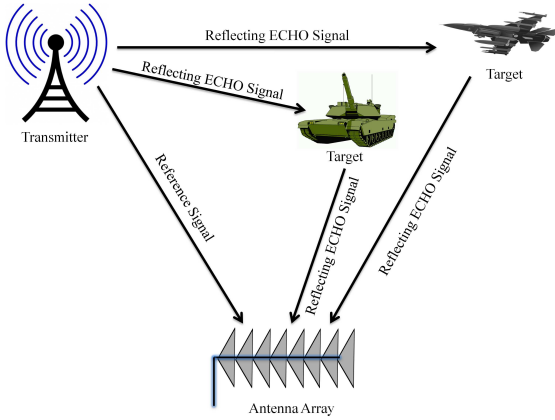
Figure 1: Data reception scenario.
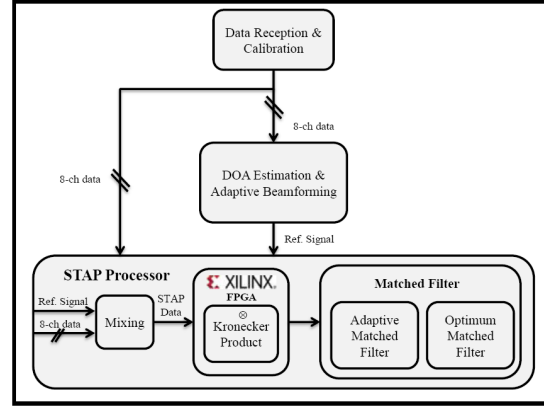
Figure 2: Signal processing block diagram.

The STAP process starts after obtaining the pure reference signal and the eight channel data signal, by mixing the data signal from each channel with the time delayed version of the reference signal $x_{ref}(k-n)$ known as the mixing product as given in Eq. (1) [5].

$$x_m(k;n) = x(k) \circ (1 \otimes x_{ref}(k-n)) * \tag{1}$$

Let N denote the number of channels, then $x(k)$ denotes the eight channel data matrix. The element 1 in Eq. (1) is the $Nx1$ column vector with unit elements, $\circ$ denotes the Hadamard (element-wise product) and $\otimes$ denotes the Kronecker product. This processing is done at a specific range n. For the specific case of a uniform linear array, the spatio-temporal steering vector is given in Eq. (2) [5].

$$v(v_s, v_d) = a(v_s) \otimes b(v_d) \tag{2}$$

The size of this spatio-temporal steering vector depends on the number of channels N used in $a(v_s)$ and the temporal samples M used in $b(v_d)$. After obtaining the spatio-temporal steering vector the next step is to subsample the mixing product in Eq. (1) at some specific range n, to obtain the subsampled signal. The matched filter output y_m containing the transmitter and simulated target returns can be obtained by using the spatio-temporal steering vector and subsampled signal as shown in Eq. (3) [5].

$$y_m(v_s, v_d; n) = v^\dagger(v_s, v_d) x_s(n) \tag{3}$$

3. SIMULATION RESULTS

The simulation of these signal processing steps in Fig. 2 was performed in MATLAB. The real-time data used for simulation was recorded at 94 MHz, while capturing the signal from the commercial FM transmitter installed at around 12 miles away from the receiving eight element FM antenna array with inter-element spacing of 104 cm. The result of the adaptive matched filter output in Eq. (3) is shown in Fig. 3(a). In this figure the FM transmitter was found out to be at 20 deg. with zero Doppler frequency. Other peaks at zero Doppler are appeared due to the multipath and other ground clutter. For this experiment we have inserted a simulated target echo at -30 deg. with Doppler frequency of 200 Hz. This small ridge of simulated target is appeared at the output as shown in Fig. 3(a).

Now the next signal processing step is to filter out the contributions of zero Doppler frequency clutter in order to get pure target signal at the output. For this purpose we need an interference and noise covariance matrix R, required to compute the optimum filter w which will help in removing the zero Doppler clutter and noise effectively. The optimum matched filter output is given by Eq. (4) below [5].

$$y(v_s, v_d; n) = w^\dagger(v_s, v_d) x_s(n) \tag{4}$$

where, w is the optimum filter weight vector and x_s is the recorded subsampled signal. The optimum matched filter output as shown in Fig. 3(b), shows the single target ridge which is found to be at -30 deg. and 200 Hz Doppler frequency.

(a) Matched filter output   (b) Optimum matched filter output
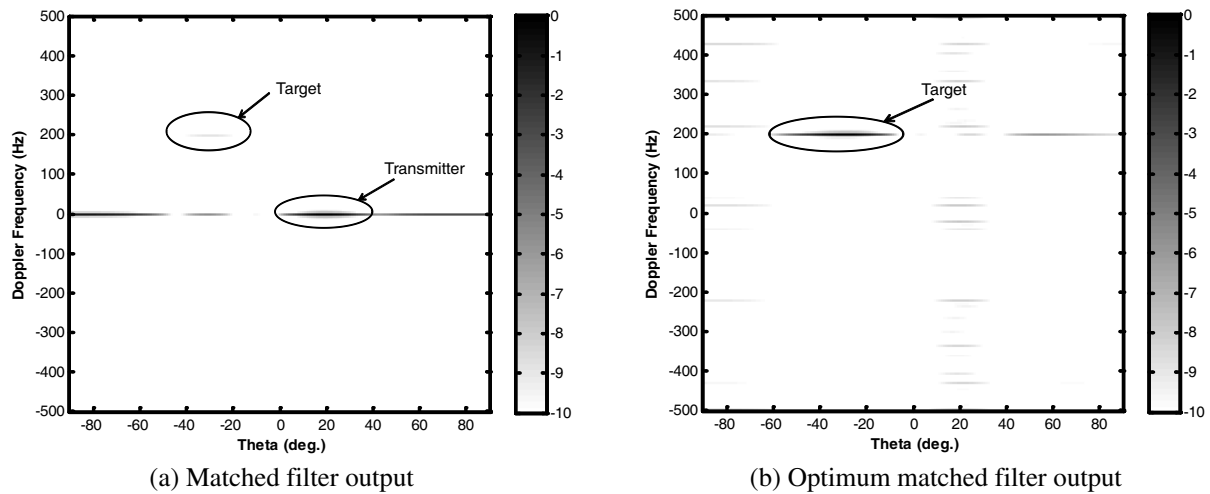
Figure 3: Angle-Doppler plot of Matched Filter containing transmitter and simulated target DOA with Doppler frequency.

4. FPGA IMPLEMENTATION

In this paper, Xilinx Virtex-6 ML605 FPGA platform is used for hardware implementation of the initial STAP Processing containing the kronecker product unit (KPU). The KPU unit has two data vectors containing spatial and temporal samples. Apart from directly loading the required data of kronecker function and filling up the memory space with repeated samples, the data vector needs to be generated in an intelligent way so that it requires very less memory for the same operation. Fig. 4 below shows the designed FPGA model generating the kronecker product at the output with the help of channel A and channel B subsystem.

For this scenario, we used dual-port RAM and ROM blocks along with some couple of counters for different types of data loading operations [7]. High-performance and optimized complex multipliers were used to complete the multiplication process. Finally, the sub-blocks contain the loading mechanism along with the associated control unit.
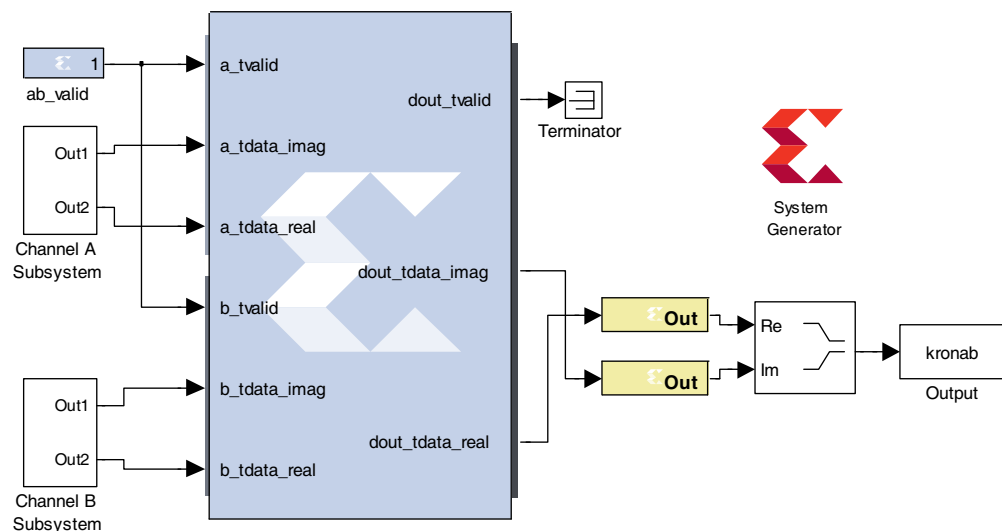
Figure 4: FPGA model.

5. CONCLUSIONS

In this paper we presented the simulation and partial FPGA implementation of Space Time Adaptive Processing (STAP) algorithm for Passive Bi-static Radar (PBR) using commercial FM transmitter as illuminator of opportunity. The simulation results show that the zero-Doppler clutter can be effectively filtered out by using optimum matched filtering. Finally, some necessary hardware

blocks of Xilinx System Generator$^{\text{TM}}$ were developed to obtain kronecker product from FPGA under virtex-6 platform. Future work will be continued to further optimize the kronecker product with some advanced FPGA blocks and to implement more signal processing steps in order to satisfy the real-time requirements for the STAP processor functionality.

REFERENCES

1. Howland, P. E., D. Maksimiuk, and G. Reitsma, "FM radio based bistatic radar," *IEE Proceedings of Radar, Sonar and Navigation*, Vol. 152, No. 3, 107–115, Jun. 2005.
2. Li, F., J. Luo, J. Lu, and H. Zheng, "Bistatic radar experiment based on FM broadcast transmitter," *Proc. RADAR'04*, Toulouse, France, Oct. 2004.
3. Saini, R., M. Cherniakov, and V. Lenive, "Direct path interference suppression in bistatic system: DTV based radar," *Proc. of the International Radar Conference 2003*, 309–314, Sept. 2003.
4. Tan, D. K. P., H. Sun, Y. Lui, M. Lesturgie, and H. Chan, "Passive radar using global system for mobile communication signal: Theory, implementation and measurements," *IEE Proceedings — Radar, Sonar and Navigation*, Vol. 152, 116–123, Jun. 2005.
5. Neyt, X., et al., "Feasibility of STAP for passive GSM-based radar," *IEEE Conference on Radar*, 6, Apr. 2006.
6. Raout, J., A. Santori, and E. Moreau, "Space-time clutter rejection and target passive detection using the APES method," *Signal Processing, IET*, Vol. 4, No. 3, 298–304, Jun. 2010.
7. (2012, Jan) Xilinx, Inc., [Online], http://www.xilinx.com/.
8. Richards, M. A., *Fundamentals of Radar Signal Processing*, McGraw Hill, 2005.

Performance Improvement of a Switched Reluctance Motor

Jawad Faiz[1], F. Tahvilipour[2], and G. Shahgholian[2]

[1]Center of Excellence on Applied Electromagnetic Systems, School of Electrical and Computer Engineering
University College of Engineering, University of Tehran, Tehran, Iran
[2]Department of Electrical Engineering, Islamic Azad University, Najafabad Branch, Isfahan, Iran

Abstract— In this paper, impacts of different operating factors of switched reluctance motors (SRM) upon vibrations and noise in the motor are reviewed. The noise in the motor may be reduced by applying a suitable control strategy or modifying design technique. Attempt is made to minimize the noise by creating a hole in the rotor poles of the motor. It is shown that a circular shape hole is preferred to rectangular one. A proper rotor and stator pole arcs are adjusted and optimal hole radius is determined.

1. INTRODUCTION

Switched reluctance motor (SRM) operates based on magnetic reluctance variations and its application is economical due to its high efficiency and low maintenance. However, acoustic noise and high torque ripples reduce its wide application and its noise reduction is essential. In [1], impact of stator yoke shape and in [2] effect of pole number of SRM on the noise has been investigated. Using different materials in the motor leads to different level of noise and rotor pole shape affect the noise level [3].

The origins of the noise in SRM are due to magnetic, mechanical, aero-dynamic and electrical characteristics of the motor. Magnetic noise crossing the air gap almost radially leads to radial forces on the teeth and motor vibrations. Dominant noise generating factor is radial deformation of the stator due to magnetic variation of radial magnetic attraction by rotor [4]. Shape, dimensions, materials and winding type are among the factors influencing these forces. If natural frequency of SRM stator interferes one of the excitation winding switching frequencies the resonance occurs which generates the noise. Dominant vibrating mode frequency as a function of sheet dimensions and materials has been given in [5]. Movement of air and other fluids are aero-dynamic origin of noise generating in the motor. Interaction between SRM, power electronics converters and its control system are electrical origin of the noise. Torque ripple is the major factor in noise generation which can be mitigated by controller and its switching pattern. Optimal design of magnetic structure [1, 6] can reduce resonance effect during motor operation. Holes inside rotor pole may decrease the radial forces and noise; however this may lead to a lower efficiency [7].

Generally radial forces, torque ripples and switching pattern play dominant roles in the noise generation in SRM. In the case of radial forces and torque ripples, there are two major procedures for noise reduction: 1) control strategy and 2) design technique. Control strategies are active techniques and they propose the windings supply type and shaping input current waveform. Design techniques as passive methods concentrate on the motor structural design. This paper deals with the noise reduction based on the structural design techniques.

2. DESIGN-BASED TECHNIQUES FOR NOISE REDUCTION

The radial force in 6/4 SRM is almost twice that of 12/8 SRM while deformation of 12/8 SRM is 1.26 times that of 6/4 SRM [2]. Modal analysis shows that the noise and vibration in 12/8 SRM is very smaller than that of 6/4 SRM. A very robust dielectric or non-magnetic material of slot wedge, called spacer, can mitigate the noise level in SRM [8]. Trapezoidal poles on a yoke with external hexagonal shape and internal circular shape can lead to a low noise SRM [6]. To damp vibration and oscillation in SRM, Piezoelectric material has been recommended [9]. The optimum location for the piezoelectric material placement has been determined by Genetic algorithm [10], Deformation of rotor pole tips and asymmetry of stator pole (non-uniform air gap) are optimized to reduce the torque ripples [3]. Simultaneous optimization of stator and rotor poles arc and switching patterns of converter may decrease the noise level in SRM [11]. Stator slots internal spans have been optimized to minimize the vibration of SRM [12]. A multi-objective optimization technique has been presented for a 4/2 SRM [13] using rotor and stator dimensions as optimization variables and the noise of the proposed SRM has been mainly reduced by optimal rotor configuration.

A rectangular hole inside rotor teeth can reduce the noise. FE analysis shows that the width of the hole has impact on the noise reduction compared to that of the height of the hole [7]. Trapezoidal fins with wide upper part and narrow lower part have influence on the noise reduction with no negative impact on the heat transfer [14]. Multi-layer design can reduce noise and increase the starting torque [15]. Some modifications of the rotor and stator pole head shape may be applied and then dimensions optimized in order to reduce the torque ripple [16].

3. ESTIMATION OF RADIAL FORCES, TORQUE RIPPLE, VIBRATION AND ACOUSTIC NOISE

Prior to the manufacturing SRM, it is essential to estimate radial forces and torque ripples. Analytical method is appropriate when optimizing large number of parameters. Coupled mechanical-electromagnetic FEM is first applied to estimate electromagnetic forces exerted on the motor and then forces data is transferred for mechanical and modal analysis [1, 14]. Combination of Matlab-Simulink and FEM can be used to model noise and vibration in SRM [17]. A microscopic-based method has been employed in [18] to analyze the force in SRM. First FE analysis with pulse waveform excitation is carried out and the response is analyzed by Fourier series, then all excitations are modeled by Canvolution. This method provides proper excitation for reduction of radial forces.

Using Maxwell stress method, the radial forces and tangential flux densities in any node are calculated and then force density is estimated as follows [5]:

$$F_n = (B_n^2 - B_t^2)/2\mu_0 \tag{1}$$
$$F_t = B_n B_t/\mu_0 \tag{2}$$

where B_t, B_n, F_t and F_n are the tangential, radial flux densities, and force densities respectively. Thus tangential force is as follows:

$$F_t = \int\limits_0^{2\pi} \frac{1}{2\mu_0}(B_n^2 - B_t^2)r_{gap}d\varphi \tag{3}$$

An external voltage source is applied to each phase of the motor and transient analysis is used in which the back emf is calculated. For simulation purpose, the slipping surface between the rotor and stator is employed and each stage following motor move and placing it on arbitrary location, the Lagrenge equations on the nodes between rotor and stator nodes applied by CE command in Ansys. Fig. 1 shows phase connection in the software. Inductance of the winding is calculated by the 2D-FEM. If the 3D or end-winding inductance was known, it can be put in series with supply. Every phase of SRM consists of two coils (in series or parallel) and each coil has two levels. One coil element is defined in Ansys. for each level.

Parameters	Value
No. of stator/rotor poles	8/6
Stator outer diameter (mm)	125
Stator slot bottom diameter (mm)	100
Rotor outer diameter (mm)	63
Rotor slot bottom diameter (mm)	41
Air gap length (mm)	0.35
Shaft Diameter (mm)	21
Stack length (mm)	90
Stator and rotor pole arc (°)	21
Turn per coil	124
Rotor resistance (Ω)	0.69

Table 1. Specifications of proposed SRM.
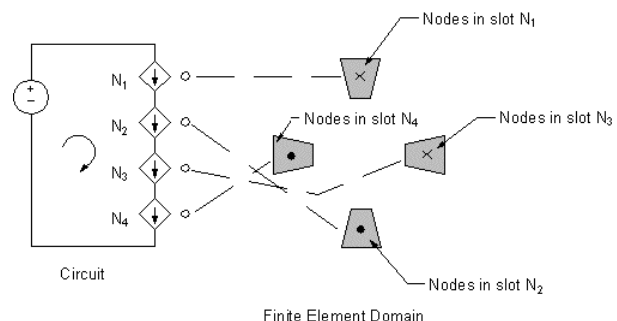
Figure 1. Procedure for applying phase voltage in software.
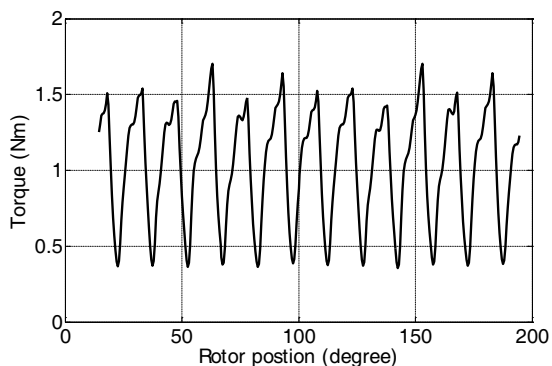
Figure 2. Developed torque of SRM phase versus rotor angular position.
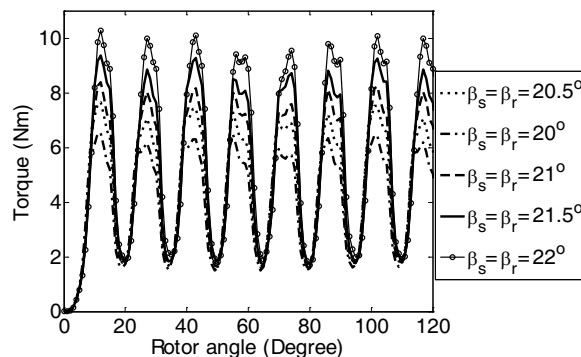
Figure 3. Torque of SRM versus rotor angle for different pole arcs.
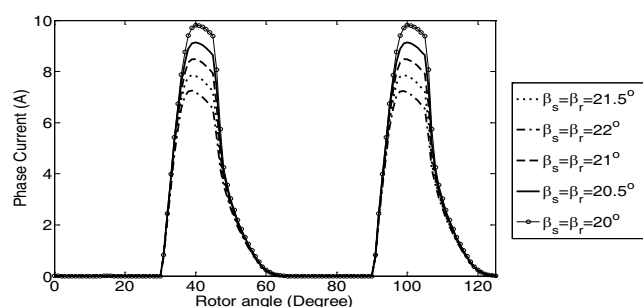
Figure 4. Current of SRM versus rotor angle for different pole arcs.
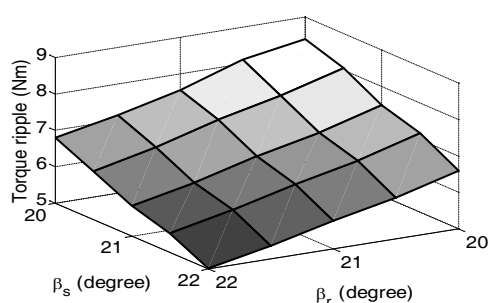
Figure 5. Torque ripples variations versus rotor and stator poles arcs.

Specifications of the proposed SRM have been summarized in Table 1. The motor is simulated for rated speed of 1500 rpm with 0.5 step and half rotation. The developed torque of the SRM with considerable ripples has been shown in Fig. 2.

4. IMPACT OF POLES ARCS ON TORQUE AND CURRENT WAVEFORMS

The poles arc of rotor and stator of the proposed SRM is 21 degrees. To investigate the impact of the poles arc on the performance of the motor, poles arc of 20, 20.5, 21.5 and 22 degrees are also considered and the torque versus rotor angular position has been presented in Fig. 3. The corresponding current waveforms have been shown in Fig. 4. As seen in Fig. 3, smaller pole arc increases the torque ripples, however in this case the average torque rises which is an advantage. Fig. 4 indicates that for smaller pole arc, current is higher and this the reason for larger average torque. If the pole arc is reduced further the current may increase beyond its permissible value. In such a case a hysteresis controller is needed. Therefore, the minimum pole arc is determined by the maximum phase current and its maximum pole arc by minimum average torque. Fig. 5 exhibits the torque ripple variations versus rotor and stator poles arc. Considering contradictory effects of pole arc on the performance indexes of the SRM a 22 degrees arc has been recommended as optimum value.

5. IMPACT OF CIRCULAR HOLE ON RADIAL FORCES REDUCTION

Figure 6 shows the total radial forces exerted on the SRM over different rotor positions which is almost the same for pole arcs 21 and 22 degree. Radial forces in SRM with optimum pole arcs are estimated. The impact of a rectangular hole inside the rotor teeth in radial force reduction has been demonstrated [7]. However, the circular hole has some advantages such as simplicity of manufacturing, structural stability and preventing from the local saturation in sharp corners.

The circular hole is inserted in the rotor teeth as such that the distance between the hole center and shaft center is chosen to have enough mechanical robust, far enough from the pole tip, as shown in Fig. 7. The holes radius, r_h, is optimized based on FEM. This distance would be 1 mm and hole radius 2 mm. Figs. 8 to 9 show the magnetic flux lines and forces exerted on the pole with peak radial forces. Fig. 10(a) presents the radial forces due to excitation of one phase for

70 degrees rotation of SRM and different radius. As seen the radial force decreases by increasing radius of the hole and tend to 71% at 4 mm radius. Fig. 10(b) shows the developed torque for one excited phase with different hole radius which has the largest drop at radius 4 mm. If unidirectional SRM is considered the impact of the circular hole displacement from center to the left of teeth (in rotation direction) can be studied. For radiuses 1.5, 2 and 2.5 mm the radial forces approach 70%, 64% and 57% that of the initial value. There is no considerable reduction of the force for larger radius. However, the mean torque also decreases and this reduction is considerable for 4 mm radius. This reduction is about 10% up to radius 2.5 mm which is negligible against 43% reduction of their forces. So the hole with radius 2.5 mm is the optimal one.
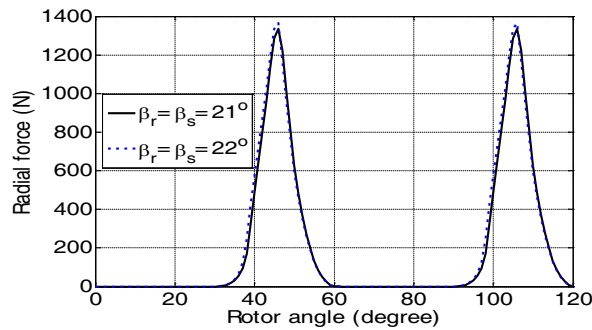
Figure 6. Radial force exerted on SRM with optimum poles arc.
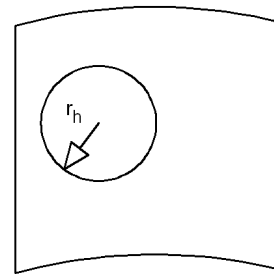
Figure 7. Pole with circular hole.
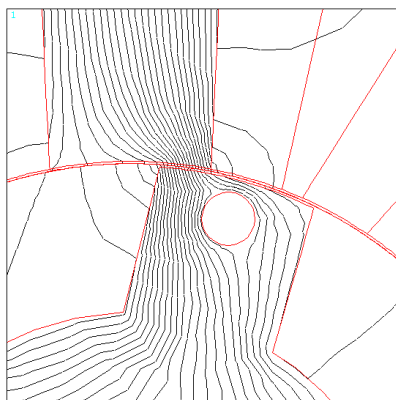
Figure 8. Flux distribution at angle with peak radial forces.
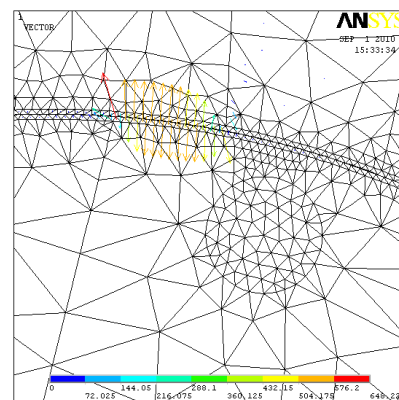
Figure 9. Forces exerted on SRM at angle with peak radial forces.

(a)

(b)
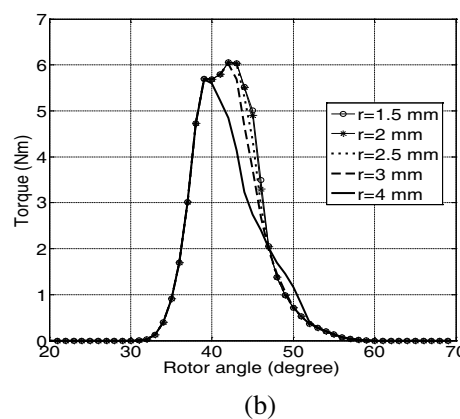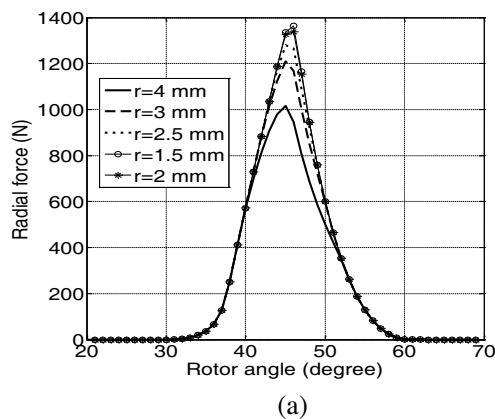
Figure 10. Radial forces (a) and developed torque (b) of SRM with radius of hole 1.5 mm to 4 mm.

6. CONCLUSION

Acoustic noise reduction based of design technique of the SRM was discussed and implemented in this paper. Radial force as a dominant factor on the acoustic noise generation is reduced by circular holes inside of the rotor teeth. The holes with radius 1.5, 2, 2.5, 3 and 4 mm were examined and it was found that a 2.5 mm radius hole is the optimal one reducing the force by 43%. Combination of the optimal rotor poles arc and the circular holes reduce both radial forces and torque ripples. Advantages of the circular hole compared to rectangular hole include higher average torque and better reduction of the radial force. Two-dimensional FEM was applied to estimate precisely the magnetic flux distribution, current waveforms, forces and developed torques within the motor.

REFERENCES

1. Cai, W., et al., "Low-vibration design of switched reluctance motors for automotive applications using modal analysis," *IEEE Trans. Industry Applications*, Vol. 39, No. 4, 971–977, 2003.
2. Li, J., X. Song, and Y. Cho, "Comparison of 12/8 and 6/4 switched reluctance motor: Noise and vibration aspects," *IEEE Trans. Magnetics*, Vol. 44, No. 11, 4131–4134, Nov. 2008.
3. Choi, Y. K. and C. S. Koh, "Pole-shape optimization of a switched-reluctance motor for torque ripple reduction," *IEEE Trans. on Magnetics*, Vol. 43, No. 4, 1797–1800, 2007.
4. Cameron, D. E., J. H. Lang, and S. D. Umans, "The origin and reduction of acoustic noise in doubly salient variable-reluctance motor," *IEEE Trans. on Industry Applications*, Vol. 28, No. 6, 1250–1255, 1992.
5. Colby, R. S., F. M. Mottier, and T. J. E. Miller, "Vibration modes and acoustic noise in a four-phase switched reluctance motor," *IEEE Trans. on Industry Applications*, Vol. 32, No. 6, 1357–1364, 1996.
6. Hong, J. P., K. H. Ha, and J. Lee, "Stator pole and yoke design for vibration reduction of switched reluctance motor," *IEEE Trans. on Magnetics*, Vol. 38, No. 2, 929–932, 2002.
7. Sanada, M., et al.,"Radial force and acoustic noise reduction for switched reluctance motor with hole inside pole," *Trans. of the Institute of Electrical Engineers of Japan*, Vol. 123, No. 12, 1438–1445, 2003.
8. Rasmussen, P. O., J. H. Andreasen, and J. M. Pijanowski, " Structural stator spacers-A solution for noise reduction of switched reluctance motors," *IEEE Trans. on Industry Applications*, Vol. 40, No. 2, 574–581, 2004.
9. Mininger, X., et al., "Modeling of magneto-elastic and piezoelectric coupling: Application to SRM noise damping," *IEEE Trans. on Magnetics*, Vol. 45, No. 3, 1218–1221, 2009.
10. Ojeda, X., et al., "Piezoelectric actuator design and placement for switched reluctance motors active damping," *IEEE Trans. on Energy Conv.*, Vol. 24, No. 2, 305–313, Jun. 2009.
11. Choi, J. H., et al., "Geometric and electrical optimization design of SR motor based on progressive quadratic response surface method," *IEEE Trans. on Magnetics*, Vol. 39, No. 5, 3241–4243, 2003.
12. Besbes, M., et al., "Influence of stator geometry upon vibratory behaviour and electromagnetic performances of switched reluctance motors," *IEE Proc. Elect. Power Appl.*, Vol. 145, No. 5, 462–468, 1998.
13. Nabeta, S. I., et al., "Mitigation of the torque ripple of a switched reluctance motor through a multiobjective optimization," *IEEE Trans. on Magnetics*, Vol. 44, No. 6, 1018–1021, 2008.
14. Sin, J., et al., "A novel radiating rib structure in switched reluctance motors for low acoustic noise," *IEEE Trans. on Magnetics*, Vol. 43, No. 9, 3630–3637, 2007.
15. Daldaban, F. and N. Ustkoyuncu, "Multi-layer switched reluctance motor to reduce torque ripple," *Journal of Energy Conversion and Management*, Vol. 49, No. 5, 974–979, 2008.
16. Ozoglu, Y., M. Garip, and E. Mese, "New pole tip shapes mitigating torque ripple in short pitched and fully pitched switched reluctance motors," *Journal of Electric Power Systems Research*, Vol. 74, No. 1, 95–103, 2005
17. Tang, Z., et al., "Prediction of electromagnetic forces and vibrations in SRMs operating at steady-state and transient speeds," *IEEE Trans. on Industry Applications*, Vol. 41, No. 4, 927–934, 2005.
18. Chris, S., et al., "Investigation of electromagnetic force components in SRM under single and multi-phase excitation," *IEEE Trans. on Industry Applications*, Vol. 41, No. 4, 978–988, 2005.

Monitoring of Mid-ocean Eddies in the Northeastern Atlantic

Shigehisa Nakamura
Kyoto University, Japan

Abstract— This work concerns on mid-ocean eddies in the North Atlantic. Eddies in the ocean are frequently found as a result of an undulation of the ocean front. The author notes about a meddy formed by contact of the Gulf Stream water and the Mediterranean water in the area around the Azores. Then, the author notices about the ocean front formed by the two water masses with his hydrodynamic understanding of problems.

1. INTRODUCTION

The author introduces a problems on mid-ocean eddies in the ocean. In the NW Pacific, the eddy formed after undulation of the ocean front in the ocean current extension of the Kuroshio as one of the western boundary intensified ocean currents. In the North Atlantic, researches and surveys related to the eddy, named as "mid-ocean eddy" were left to be continued beyond the year of 2000 for realizing the meddy in a scope of hydrodynamics.

First, a review note is introduced for a primary understanding what is eddy in the ocean. Then, an ocean front evolution is considered as a key to realize ocean eddy formation. In this case, the ocean front formed between the two waters in the North Atlantic, i.e., the water in the Gulf Stream extension and the Mediterranean water in the Atlantic.

Present status of the related research on meddy must be aimed to see whether the Gulf Stream crosses the Atlantic mid-ocean ridge and to find the interaction of the interested two waters in the ocean. Some remarks could be given for a more advanced research in the related fields to the oceanography.

2. REVIEW NOTE

Eddy in the ocean had been found around the Japanese Islands in the NW Pacific in the early age of 1900s. Robinson [1] published his "Eddies in Maine Science" to show local scale eddies observed in the ocean and to notice "mid-ocean eddies" in relation to biological processes. He introduced Armi's preliminary hydrographic data report including transient tracers, which was appeared in 1981. Research papers on Meddy had been reported to describe the physical pattern.

In the year of 2008, the author had a chance to know a project for Ocean research with observation promoting by the University of Azores (the leader Professor Anna Martine). The research group under the leader is working to see ocean pattern in the surface layer covering the process of thee meddys and of the ocean front, by using the survey ships and the satellite monitoring.

Marchuk has evaluated highly in 2008 by EGU for his long-time life work on the overturn process of the ocean water off the south of Greenland.

3. MEDITERRANEAN WATER OUTFLOW INTO ATLANTIC

A shear flow field model is considered for helping our understanding of eddy evolution as shown in Figure 1(a). This can be taken as a simplified model of Gibraltar. When the Mediterranean water flows out into the Atlantic water, an ocean front is formed between the two waters, for example, as shown in Figure l(b).

The front evolution can be detected by the satellite monitoring. The pattern of the front on the sea surface varies in time and space.

Hydrodynamics tells us that the pattern of the front on the sea surface can be a glimpse of the two waters contact in motion.

4. SALINITY AND TEMPERATURE

Sverdrup et al. [2] introduced a typical illustrations of the temperature and salinity vertical sections through the Gibraltar. These look to be illustrating a stable stratification of the North Atlantic water and the Mediterranean water nevertheless the budget of the Mediterranean Sea tells us that the inflow from the Atlantic is l,750,000 m^3/sec, and the outflow to the Atlantic is l,680,000 m^3/sec respectively. The minor factors are the budget of the Black Sea, precipitation and evaporation, and,

(a)   (b)
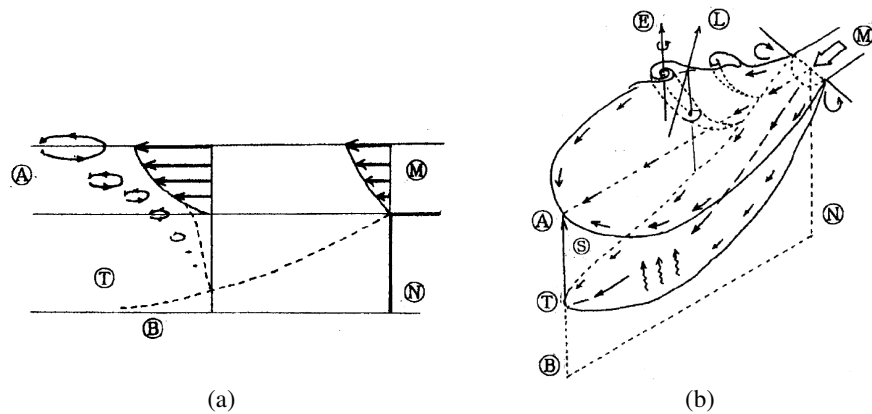
Figure 1: Schematic model for ocean eddy evolution. (a) Ocean eddy evolution in a shear flow field. (1) An outflow from M to A in the surface layer. (2) A dense down-flow from M to T in deep. (3) A tongue shaped interface between M and T. (4) A reference in deep at B and/or at N. (b) A model structure of an ocean eddy in a field [cf. (a)]. (1) An outflow from mark M to mark A. (2) A down-flow along mark M to mark T in deep. (3) A tongue shaped interface between M and T. (4) A reference in deep from B to N. (5) An intermediate water layer S between marks T and A. (6) A reference in deep for a horizontal line from B to N. (7) An eddy evolution found on the ocean front. Formed between the outflow water M and the ocean water. (8) Mark L for a log line on the ocean surface for a eddy suurvey.

(a)   (b)
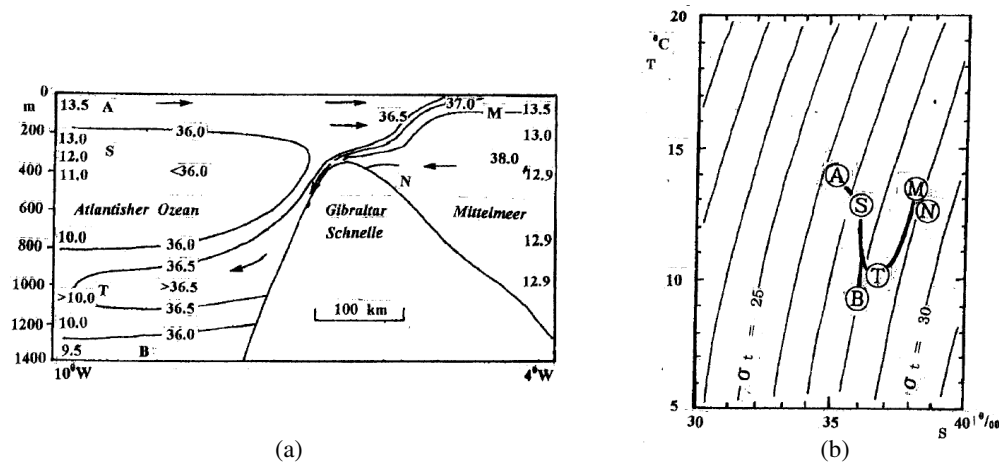
Figure 2: (a) A vertical section between the Mediterranean Sea and the Atlantic. (1) Marks for M, N, B, T, S, and A are corresponding to those found in Figure 1(b). (2) The Atlantic Ocean for the notated Atlantischer Ozean. (3) The Mediterranean Sea for the notated Mittelmeer. (4) The Gibraltar Strait for the notated Gibraltar Schnelle. (b) S-T diagram. (1) Notations S and T for salinity and temperature. (2) A densimetric parameter sigma-t (σt) is in the S-T diagram, where, sigma-t = [difference of density of ocean water and of fresh water] $\times 10^3$. (3) Marks for M, N, T, B, S, and A should be referred to those in (a).

runoff. The above budget is referred to Schott. In this case, the average velocity of the total inflow is evaluated to be ca 100 cm/sec (or 2 knot. For a convenience for our understand, the illustration of the oceanographic patterns of salinity temperature along 36°N is shown in a modified form of G. Schott in 1942 referring to the figure introduced by Dietrich [3], that is, Figure 1. Looking at the Gibraltar in Figure 1, the flow of the upper layer (surface to 200 m deep) is driven as a geostrophic tidal flow to and fro the Mediterranean, and, the now of the lower (200 m to 500 m under the sea surface) is taken as a thermo-haline water motion.

In order to clarify the relation of salinity temperature and density the S-T diagram with a parameter of sigma-t (where, sigma-$t = D_{st} \times 10^{-3}$, for D_{st} = [sea water density minus fresh water density]), the S-T diagram is obtained by the author referring to the data obtained by this time on the bases of the oceanographic data obtained during the expedition in the early age of 1900s.

Looking at Figure 2, it can be seen that the water M flow out of the Mediterranean into the Atlantic to be modified as the water T in a shape of tongue. The upper part of the tongue is in

an inversion state, so that a densimetric unstable condition is settled, though the lower part is in a ordinal and stable state.

On the upper surface of the tongue T a physical processes of thermal energy exchange and of salinity potential adjustment though the saline exchange must be seen in order to form a stable state even alter the intrusion of the water tongue. During the intrusion, the water M exchanges thermal energy and salinity for densimetric adjustment.

Some part of the upper surface water of the tongue T forms a small droplet by the buoyant erect caused by the density difference if the two waters above and under the surface of the tongue. The buoyancy make to accelerate to move the droplet up to the balanced state to intrude and mix up in the intermediate water in the intermediate water in the Atlantic.

5. CONCLUSIONS

In a case of the Mediterranean water out flow into the Atlantic water, an ocean front is formed between the two waters. The ocean front can be monitored by satellites though it is necessary to see three dimensional structures of salinity, temperature and density in a scope of hydrodynamics on the rotating earth.

REFERENCES
1. Robinson, A. R., *Eddies in Marine Science*, 609, Springer-Verlag, Berlin, 1983.
2. Sverdrup, H. U., M. W. johnson, and R. H. Fleming, *The Oceans*, 1059, Prentice-Hall,Inc., Englewood Cliffs, N.J., 1942.
3. Dietrich, G., *Allgemeine Meereskunde*, 492, Gebruder Borntraeger, Berhn, 1957.

Satellite Monitoring in Relation to Ekman Transport and Kelvin-Helmholz Billows in Ocean

Shigehisa Nakamura
Kyoto University, Japan

Abstract— As for the water motion in the upper layer of the ocean, there are two kinds of the water flows. These two flows are known as "geostrophic current" as a part of ocean circulation and "currents" found around an ocean front which Could be an evolution of a Kelvin-Helmholtz instability in the field of physical ocean science. In this work, an outline Of these two flows is introduced in relation to the existing satellite monitoring of the earth surface. A brief review note is given for helping a dynamical understanding of these historical backgrounds with the striking pattern found alter the observation during the oceanographic expeditions in the early age of the ocean science. After a review of the two flows in the ocean, it might be found a key to introduce the existing satellite monitoring in order to promote research works on the motions of the ocean flows as inertia motion in a global scale with a polar orbital path.

1. INTRODUCTION

This work concerns a problem on satellite monitoring in relation to Ekman transport observed in the ocean.There are two kinds of ocean flows, i.e., the one is "geostrophic current", and the other is "Ekman transport" around an ocean front to be induced as a result of evolution of Kelvin-Helmholtz instability. These two kinds of flows have been outside of the interest of the satellite monitoring. In this work, an outline of these two flows in the ocean are introduced first for helping a dynamical understanding of the flows in the historical backgrounds with the striking pattern found during the oceanographic expeditions in the early age of the ocean science. After a review of the two flows, it might be found a key to introduce the existing satellite monitoring techniques in order to promote research works on the motions of the ocean flows as inertia motion in a global scale with a polar orbital path.

2. FORMULATION

The equatin of motion for the ocean water is expressed an equation fluid motion on the rotating earth. Generally, the ocean water is compressible though an approximated solution can be obtained when the equation of fluid motion for an incompressible fluid.

In order to describe the ocean water motion bounded by the ocean surface and the ocean floor covering a part of the earth surface, a spherical co-ordinate system is usually introduced. As for a local problem, the equation of motion is referred to a local rectangular co-ordinate system for convenience.

In case of the ocean water flows, an ultimate brief expression must be written as follow for a steady state under a hydrostatic condition, that is (for example, [1]),

$$\rho[fv,\, -fu,\, -g] = [\partial p/\partial x,\, \partial p/\partial y,\, \partial p/\partial z], \tag{1}$$

where, velocity vector is $(u(x),\, v(y),\, w(z)) = (u,\, v,\, 0)$ for the fluid density ρ in a field of pressure p. The Coriolis parameter is expressed as $f = 2\Omega \sin \phi$ for the interested latitude ϕ in the co-ordinate system of $(r,\, \theta,\, \phi)$.

For many cases of local ocean flow problem, the parameter f is taken as a constant only for the problem of the interested local area, for convenience. In some cases of numerical ocean modeling, the parameter is taken as a constant though mathematical singularity is at the equator, i.e., singularity at $\phi = 0$.

When time derivatives of $(u,\, v,\, 0)$, the above equation of motion is rewritten as many scientists have had expressed in their formulation, that is (for example, [2]),

$$[\partial u/\partial t,\, \partial v/\partial t] + f[-v,\, u] = (-1/\rho)[(\partial p'/\partial x + \partial X/\partial x),\, (\partial p'/\partial y + \partial Y/\partial z)], \tag{2}$$

where, the pressure p' and the stress $[X(x,y,z',t),\, Y(x,y,z',t)]$ for geostrophic velocity, $[u,\, v] = [u_P + 0,\, v_P + 0]$. In the ocean, the interested layer is thick in the range of $10\,\mathrm{m}$ to $100\,\mathrm{m}$).

3. EKMAN TRANSPORT

In any case of application for the actual ocean processes, the problem is not so simple to obtain the solution in any simple form, say, even in a case of any processes formulated in a linear equation. When the velocity vector is $(u, v, w) = (u_E, v_E, 0)$ only for $[X, Y]$, then, the problem for the Equation (2) can be taken as the problem of the case for the velocity field $[u, v] = [u_P + u_E, v_P + v_E]$.

So that, we have Ekman's theory (1905) about the velocity in the boundary layer (for example, [3]) when $[u, v] = [0 + u_E, 0 + v_E]$. Gill has a brief note about this Ekman's theory in 1982 [2]. In a case Of steady current field, the Ekman volume transport is directed at right angles to the surface stress when the integral about z of the velocity $[u_E, v_E]$ is obtained.

The author has had found that there are many works on the ocean currents assuming the condition of steady flow in a stratified ocean layer. This assumption must be proper when the approximation fit well to the interested flow field.

Nevertheless, the author has to notice here that the concept of the Ekman transport has had been used for researches on the ocean currents without any confirmation of the assumed conditions to be appropriate for the purpose. As Gill (1982) pointed out it [2], Ekman transport is used many times though there has had been left that the difficulty is left yet after the observational confirmation for the purpose.

4. INERTIA MOTION

As for a case of that the ocean is at rest and a wind stress in the x direction (i.e., a westery wind) suddenly rises and is maintained at a constant value $X = X_s$, the Equation (2) can be rewritten as follows, that is,

$$(\partial/\partial t)(U_E + iV_E) + if(U_E + iV_E) = (X_s/\rho) \tag{3}$$

where, $i^2 = -1$.

The solution of the Equation (3) can easily obtained in following form (for example, Gold in 1908 [2]).

$$U_E + iV_E = -i(X_{S/\rho}f)[1 - \exp(-ift)] \tag{4}$$

At first, the Ekman transport is in the direction of the wind, but as time elapse the Coriolis effect causes it to veer (in the northern hemisphere). Finally the transport is given by the sum of a steady Ekman transport at right angle to the wind plus an anticyclonic rotation with the same amplitude around inertial circles. For a particle moving with the average velocity for the layer, the result gives a cycloidal path as expected (for example, [2]).

One of the illustrations for the above cycloid trajectory is introduced by Sverdrup [4] and by Hidaka [5]. This is obtained as a rotating currents of period one-half pendulum day observed in Baltic and represented by a progressive vector diagram for the period, August 17 to August 24 in 1933, and by a central vector diagram between 6 h and 20 h on August 21 (according to Gustafson and Kullenberg. The measurements were at a station between the coast of Sweden and the island of Gotland in a locality where the depth to the bottom was a little over 100 m. On August 17 in 1933, when the measurements began, a well-defined stratification of the water was found. From the surface to a depth of about 24 m the water had a nearly constant density, but between 24 and 30 m a slow increase continued toward the bottom.

The cycloidal trajectory pattern were confirmed by Pollard and Millard in 1970 [6], by Kundu in 1976 [7], and by Käse and Olbers in 1979 [8], after a modified equation is introduced. That is,

$$(\partial/\partial t)[U_E, V_E] - f[V_E, -U_E] = -r[U_E, V_E] + (1/\rho)[X_S, Y_S] \tag{5}$$

where, the notation r is a decay constant (or Rayleigh friction). This form of friction was used Airy (1845) in his canal theory of tides.

The inertia motion in the above sections is for model of an ocean water layer in a range of 10 m to 100 m thick for 5 inertia cycles corresponding to 4 days [4].

5. TURBULENCE AND KELVIN-HELMHOLTZ BILLOWS

Bell [9] introduced a model for seeing the decay of inertia oscillations in the mixed layer in 1978. Turbulent motions advected by the mixed-layer currents cause motions of the base of the mixed layer that radiate energy in the form of internal waves at a rate that gives ($1/r$ of order 3–4 days. The layer also act as a significant source of internal waves with frequencies of order N and wave

numbers of order NH_{MIX}/U_E, U_E/H_{MIX} being taken as a typical value of the current at the base of the mixed layer.

The presence of inertia oscillations in the mixed layer of the ocean represents also a possible source of mechanical energy that can be used to entrain water from below the mixed layer, they cause a large shear at the base of the mixed layer that can produce turbulent mixing in the form of turbulent Kelvin-Helmholtz billows such as those observed in the laboratory and in a lake by Thorpe in 1973 [10] and in 1977 [11].

6. PLANETARY INERTIA MOTION

Whipple [12] developed a theory of inertia motion of air particle in a planetary scale on the rotating earth of low latitude in 1917. Sasaki [13] had obtained seven solutions in a advanced model of inertia motion in a planetary scale. Shono [14] digested Sasaki model of inertia motion of air particles in 1954. Sasaki obtained an inertia motion on a polar orbital path in the solutions.

The author [15] presented a note on satellite thermal monitoring of ocean water front formation referring to satellite thermal monitoring of an intruding of Bering Sea water into the Arctic Sea in order to see a link of the ocean waters in the north Pacific, the Arctic Sea, and the north Atlantic. For this work, it was taken as reference when Perovich and Richter-Menge published the loss of sea ice in Arctic in 2009 [16].

Marzke's works ([17] and [18]) are effective references as much as those works appeared in Stommel's text [1] and Sverdrup's publication [4] for the author in this work. The other observation data obtained in the past were also taken as the author's references though no details noted in this work.

The author could not find any published materials which noted on inertia motion after Whipple [12] except the theoretical solution of inertia motion in a global scale solved by Sasaki [13]. So that, the author decided to introduce his dynamical understanding on the inertia motion with a global scale surely be existing. The author would not introduce many related physical processes obtained by the scientific observations. Nevertheless, no details is described in this work for completing this work in a simple form.

7. CONCLUSIONS

A linealized equation of motion is analyzed in order to see the Ekman transport whether observable or not. This problem is closely related to inertia motion of ocean water. Some examples in the past are reviewed to realize a wind-induced inertia motion which can be reduced to form an illustration of trajectory which agrees well to the simplified theoretical model. A brief note is given for problem on mixed layer and for turbulent Kelvin-Helmholtz billows. It is stressed to note about an inertia motion of water particle with a polar orbital motion which could take part of a link of the north Pacific, the Arctic, and the north Atlantic. It may supported to consider a polar orbital inertia circulation of the ocean waters on the bases of the theoretical model and the satellite thermal monitoring of the ice front in the Arctic.

REFERENCES

1. Stommel, H., *Gulf Stream*, University of California Press, Berkley and Los Angeles, 1958.
2. Gill, A. E., *Atmosphere-Ocean Dynamics*, International Geophysics Series, Vol. 30, Academic Press, New York, 1982.
3. Ekman, V. M., "On the influence of the earth's rotation on ocean-currents," *Arkiv fur Mathematik, Astronomy och Fysik*, Vol. 2, No. 11, Stockhplm, 1905.
4. Sverdrup, H. U., M. W. Johnson, and R. H. Fleming, *The Ocean*, 1060, Prentice-Hall, Englewood Clirs, New Jergey, 1942.
5. Hidaka, K., *Ocean Currents*, Iwanalli Science Series, Vol. 182, 291, 1955.
6. Pollard, R. T. and R. C. Millard, "Compaison between observed and simulated wind-generated inertia oscillations," *Deep-Sea Research*, Vol. 17, 813–821, 1970.
7. Kundu, P. K., "An analysis ofinertia oscillations observed near Oregon coast," *Journal of Physical Oceanography*, Vol. 6, 879–893, 1976.
8. Käse, R. H. and D. J. Olbers, "Wind-driven inertial waves obsetted during phase III of GATE," *Deep-Sea Research*, Vol. 26, Supplement-1, 191–216, 1979.
9. Bell, T. H., "Radiation damping of inertia oscillations in the upper ocean," *Journal of Fluid Mechanics*, Vol. 88, 289–308, 1978.

10. Thorpe, S. A., "Experiments on instability and turbulence in a stratified shear flow," *Journal of Fluid Mechanics*, Vol. 32, 693–704, 1973.
11. Thorpe, S. A., "Billows in loch ness," *Deep-Sea Research*, Vol. 24, 371–379, 1977.
12. Whipple, F. J. W., "The inotion of a particle on the surface of a smooth rotating globe," *Philosophical Magazine*, Vol. 33, 457–471, 1917.
13. Sasaki, Y., "On the trajectory of the inertia motion of an parcel of air," *Geophysical Notes*, Vol. 3, No. 32, 1–16, University of Tokyo, 1950.
14. Shono, S., *Introduction to Meteorological Dynamics*, Iwanami, Tokyo, 1954.
15. Nakamura, S., "Satellite thermal monitoring of ocean water front formation after an intruding Bering Sea water into the Arctic Sea," *PIERS Proceedings*, 100–103, Xi'an, China, March 22–26, 2010.
16. Perovich, D. K. and J. A. Richter-Menge, "Loss of sea ice in the Arctic," *Annual Review of Marine Sciences*, Vol. 1, 417–441, 2009.
17. Marzke, J. and J. W. Lebrand, "Multiple equibria of global thermohaline circulation," *Journal of Physical Oceanography*, Vol. 21, 1372–1385, 1991.
18. Marzke, J., "Boundary mixing and the dynamics of the three-diinensional thernohaline circulation," *Journal of Physical Oceanography*, Vol. 21, 1372–1385, 1997.

Satellite Monitoring of the Ocean in Relation to Structure of the North Atlantic

Shigehisa Nakamura
Kyoto University, Japan

Abstract— Ocean front which can be monitored by the existing satellite is a glimpse of the two water masses in the ocean. In this work, a basic problem about the ocean front in relation to the density of the ocean water. The typical ocean water motion is geostrophic under the effect of the earth's rotation. The ocean water is essentially stratified in densimetric stratification. The density of the ocean water is determined by salinity temperature and depth under the ocean surface. In brief, the Water is specified by a function of salinity temperature and depth. For demonstrate the waters in the ocean Surface layer, intermediate layer and deep water layer (abyssal layer). For the author's convenience, a special reference is taken for the structure of the North Atlantic.

1. INTRODUCTION

Ocean front which can be monitored by satellite,is a glimpse of the two water masses in the ocean. In order to realize ocean front evolution, it is essential to see about density of ocean water as a function of salinity, temperature and water depth. A special reference is taken for the structure of the North Atlantic, in this work, for the author's convenience.

2. EQUATION OF MOTION

Ocean front evolution is generally induced between the two ocean waters where the two kinds of ocean water motions are found on the one side and on the other side. This ocean front evolution can be monitored by the satellite.

The ocean front is on the ocean surface as a part of the interface of the two ocean water masses. Ocean water is specified by density as a Function of salinity temperature and water depth.

In the ocean, a forcing of F generates a motion of the ocean water mass m to move with an acceleration a, that is,

$$F = ma \tag{1}$$

When a corresponding displacement of the water is r, then, it can be written as follow.

$$a = [d/dt(dr/dt)], \quad \text{then,} \quad a = [dv/dt] \quad \text{for} \quad v = dr/dt, \tag{2}$$

then, equation of motion for a unit mass ρ of an unit volume can be written as,

$$F = \rho(dv/dt). \tag{3}$$

When the above ρ is taken as density as a function of salinity s, temperature T and depth D at a position r, then, the above equation is rewritten as,

$$F = [d(\rho v)dt]/dt \quad \text{for} \quad \rho = \rho(s, T, D) \tag{4}$$

Now, the above equation is rewritten as follows, that is.

$$F = \rho dv/dt + vd\rho/dt \tag{5}$$

As for a case of $d\rho/dt = 0$ (the condition of the mass conservation), the equation can be taken as the equation of motion for the ocean water with in terms of the pressure gradient, the effect of the earth's rotation, and the stress. Generally, the stress should be a tensor though it is assumed here a vector could be replaced for a convenience.

Many scientists have had reduced the solution for the equation of motion under some given conditions in space and in time.

Strictly, the equation of motion is a nonlinear equation. Nevertheless, there have been many kinds of solutions for the linear equation or for the nonlinear equation in an approximated expression. Some of them are expressed in a form of an asymptotic solution.

3. DOUBLE DIFFUSION EQUATION

The double diffusion equation for $\rho(s, T, D)$, can be written as

$$d\rho/dt = \partial\rho/\partial t + v\nabla_\rho = \Phi, \quad \text{and} \quad \Phi = -\nabla_\rho + \nabla(\kappa\nabla_\rho), \tag{6}$$

under some specific condition of the ocean water motions. Generally, κ is a tensor nevertheless it is taken as a diffusion coefficient, for a convenience. The values of κ for s and for T are not same to each other. Diffusion of salinity is a process for simply saline contents nevertheless thermal diffusion is a process of fluid motion of a water mass as a heat carrier.

In the ocean, the water motions after the effect of viscosity, are so complicated that as if it were a dye-streak rather than a diffusion precesses. The observed results during the ocean expeditions had been introduced first to note a specified ocean water masses, for example, Defant [1], Sverdrup et al. [2], and, Dietrich [3]. Although, the diffusion process modeling was developed by Taylor for describe a smoke in the atmospheric surface layer. The diffusion does not mean the molecular diffusion but the eddy diffusion or turbulent diffusion. Any one of the ocean waters is not isotropic and not uniform. Nevertheless, the concept of the eddy diffusion is convenient at discussing a macroscopic process in the ocean as well as in the atmospheric layer.

4. EQUATION FOR DENSITY

In the ocean, the water density is determined by salinity and temperature even in any case holding above diffusion equation.

When the ocean water in a conservative system, the equation for conservation of ρ can be written as, for example, in a rectangular co-ordinate system,

$$\partial\rho/\partial t + u[\partial\rho/\partial x] + v[\partial\rho/\partial y] + w[\partial\rho/\partial z] = A, \tag{7}$$

or, in a cylindrical co-ordinate system,

$$\partial\rho/\partial t + u[\partial\rho/\partial r] + (v/r)[\partial\rho/\partial\theta] + w[\partial\rho/\partial z] = A. \tag{8}$$

Referring to the above equation, several specific tendencies can be seen in a form of a mathematical expression.

(A) When any one of velocity components is trivial to be possible to neglect, then,

$$\partial\rho/\partial t = A, \tag{9}$$

now, the solution is reduced to write as

$$\rho = A_o \exp(pt), \quad \text{or}, \quad (\rho = A_o + A_1 t, \text{ as an approximation for small value of } t). \tag{10}$$

(B) When a very slow motion with a small horizontal speed (no radial component),

$$(v/r)[\partial\rho/\partial\theta] = A, \tag{11}$$

then, the solution is written as follows,

$$\rho = \oint (A/v)rd\theta, \tag{12}$$

(C) When the motion is a very slow vertical motion (no radial component),

$$w(\partial\rho/\partial z) = A, \tag{13}$$

then, the solution is written as,

$$\rho = \int (A/w)dz, \tag{14}$$

These three solutions might be helpful at considering the water motions just around an interface between the stratified water motion in a small column in the ocean.

When these cases are happened just in the ocean subsurface, the satellite might monitor the trends of the density variation pattern which can be specified boldly.

5. S-T DIAGRAM

In order to specific property of the ocean waters, it has been widely used a S-T diagram with a sigma-t in the field of oceanography. The sigma-t (σt) is a parameter for an index of the density of the ocean water. This sigma-t is defined as the difference of the ocean water density and the fresh water density. This difference has a dependency of salinity and temperature. For a convenience, one of the illustrations is introduced in Figure 1 [2]. In Figure 1, no data were, included for the surface layer between the ocean surface layer about 200 m thick which is taken to be understood as a wind generated mixing layer [4].

Looking at the illustration in Figure 1, it is easily found that the following which has not clearly described by the ocean scientists. That is,

1) The Mediterranean out flow (G) spreads to form an intermediate layer in the sub-surface areas covering (E) to the north, (S) to the south and (M) to the mid ocean area. The intermediate water is well stratified stable layer between the surface layer and the deep layer with transitional layers as the interfaces between the surface layer and the intermediate layer, and between the intermediate layer and the deep layer.

2) The Mediterranean out flow must have been pooled for a long years (say, more than ten thousand years) to form the stable intermediate layer by the thermohaline exchange at meeting the water of the primitive North Atlantic ocean water.

3) The intermediate water must have a faint flow in a thermohaline stable balance.

4) In the interfaces, the diffusion coefficient of salinity can be taken to be proportional to the diffusion coefficient for temperature.

5) The Gulf Stream extension in the area at the south of Greenland (C) shows cooled well to form a stable stratification. This area is just neighbor of the over turn area of the Gulf Stream water [5]. Nevertheless, the S-T diagram tells us nothing about the water transport at the over turn from the surface layer to the deep layer [2].

6) The origin of the Gulf Stream must be in the area (S). The track of the Gulf Stream can be along a line through the areas (W), (H), (G), and (C).

7) The Arctic surface water (P) has a contact with the Mediterranean water (E), though the diffusion coefficients of salinity and of temperature in the two interfaces are different from those in the areas (E), (G), and (S), but looks to be similar to that in the area (M) at the south of Iceland.
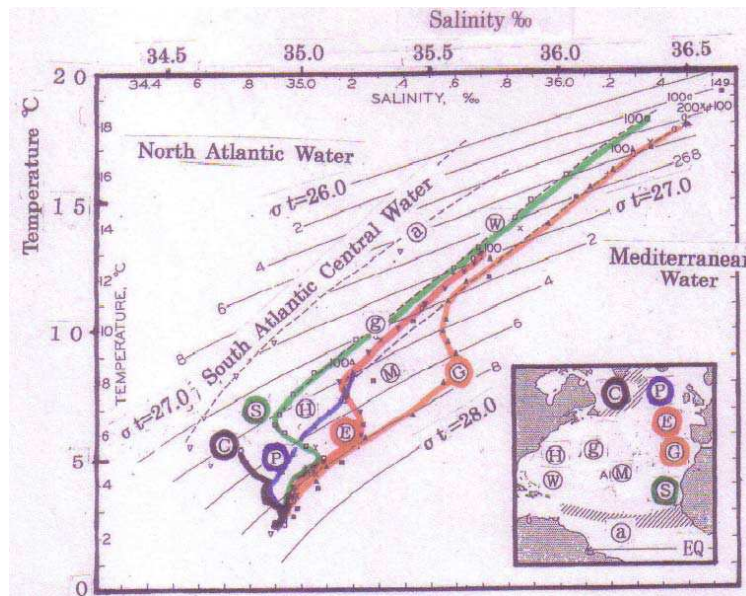
Figure 1: Double diffusion pattern of S-T diagram in the North Atlantic. (a) Mark (G) — [Orange line] for Mediterranean water in Atlantic. (b) Mark (E) — [Red line] for water in the north area of Gibraltar. (c) Mark (S) — [Green line] for water in the south area of Gibraltar. (d) Mark (C) — [Black line] for water in the south area of Greenland. (e) Mark (P) — [Thin line] for water in the south area of Iceland. (f) The other marks — refer to the inset map. Modified from [2].

8) The deep water layers have a common thermohaline property in the S-T diagram. This shows that the strong effect of the Arctic Sea water (C) to the waters in the areas (E), (G), (S), (W), (H), (g), and (M). A water transport in the area of the over turn, meets to the Arctic Sea water (P) and (C) in the deep layer to form a kick of curve in the S-T diagram. This face supports that the author's proposal of the meridional ocean inertia circulation in a global scale with a polar orbital path [6–8].

6. CONCLUSIONS

The ocean front evolution is a glimpse of the ocean water circulation in the satellite thermal monitoring. The author proposed a meridional ocean inertia circulation in a global scale with a polar orbital path. Reviewing the observed results obtained during the Expeditions in the early stage of the 1900s, and referring the Marzke's recent work about over turn of the Gulf Stream extension, the author found that both of the Expedition data and the over turn model [5] support the existence of the meridional ocean inertia circulation a global scale with a polar orbital path which had ever been reduced in a mathematical model.

REFERENCES

1. Defant, A., "Die abschiede Topographie des physikalischen Meeres-niveaus und der Drueck-flaechen, So wie die Wasser beweguggen im Atlantiscen Ozean," Deutschen Atlantische Expedition des Meteor, 1925–1927; Wissenschaftlicher Ergebnisses, Bund VI, 2Teil, 5Lief, 191–260, 1941.
2. Sverdrup, H. U., M. W. Johnson, and R. H. Flemig, *The Oceans*, Prentice-Hall, Englewood Chifs, N.J., 1942.
3. Dietrich, G., *Allgemeine Meereskunde*, Gebrueder Borntraeger, Nikolassee, Berlin, 1957.
4. Munk, W. H., "On the wind driven ocean circulation," *Journal of Meteorology*, Vol. 7, 79–93, 1950.
5. Kuhlbrot, T., A. Griesel, M. Momtoya, A. Levermann, M. Hoffimann, and S. Rahmstorf, "On the driving processes of the Atlantic meridional overturn circulation," *Reviews of Geophysics*, Vol. 45, RG2001, 1032, 2007, doi:10.1029/2004RG000166.
6. Nakamura, S., "Satellite thermal monitoring of arctic ice front in relation to dynamics of a polar orbital ocean circulation," *PIERS Proceedings*, 97–99, Xi'an, China, March 22–26, 2010.
7. Nakamura, S., "Satellite thermal monitoring of ocean water front formation after an intruding Bering Sea Water into the Arctic Sea," *PIERS Proceedings*, 100–103, Xi'an, China, March 22–26, 2010.
8. Nakamura, S., "Satellite thermal monitoring of ocean front evolution in relation to ocean climate in the North Atlantic, Pacific and Arctic Sea," *PIERS Proceedings*, 104–108, Xi'an, China, March 22–26, 2010.

Improvement of Signal Integrity with Active Metamaterial for Microwave Applications

B. Ravelo and E. R. Rajkumar

IRSEEM, EA 4353, Graduate School of Engineering ESIGELEC, Av. Galilée, BP 10024
76801 Saint-Etienne-du-Rouvray Cedex, France

Abstract— This letter introduces an LC-effect cancellation method based on the use of active left-handed (ALH) circuit. This latter is formed by an FET in cascade with LH-circuit formed by a series-capacitor and parallel inductance. Via S-parameter analysis, ALH-circuit synthesis relations are established. To verify the relevance of the synthesis method introduced, a microwave LC-circuit compensation is proposed at 1 GHz with the sensitivity analysis and the influence of the used FET parameters. As expected in theory, equalization of the LC-circuit transmission loss and phase was performed.

1. INTRODUCTION

Because of the operating speed and integration density increases, the reliability and the integrity of modern electronic components used in the measurement become less and less efficient [1]. These limitation effects can be investigated with the spectral analysis of the interaction between the operating signals and the electronic systems used. The basic parameters considered for such investigation are based on the gain and the phase qualities. In the microwave frequency bands, the S-parameters are generalized used to interpret the different behaviors of the structures. The correction techniques of these microwave parameters are always one of the most attractive topics of the researchers working in the electronic and microwave instrumentations. In [2, 3], an innovative technique based on the use of the negative group delay (NGD) was proposed. The NGD circuits present a particular function enabling to compensate the delay in the electronic systems [4–6]. But in this case, the behaviors of the phase remains degraded. So, it seems interesting to exploit the concept of the metamaterial (MM) or left-handed (LH) passive devices [7–11] which are capable to generate phase in opposite sign to the classical circuit like the interconnect lines. The MM concept was introduced in 1968 by Veselago [12] and validated fifty years later by Pendry and Smith with 3D artificial material [13, 14]. Then, 2D- and 1D-circuits were implemented thanks to the analogy between the frequency responses of the structures.

But these passive circuits [4–7] present significant losses due to the absorption phenomenon linked to the LH effect. To overcome such an effect, the use of active MMs can be a good solution in the future. In this letter, innovative concept of microwave device integrity corrections is introduced by using the active MM circuits. To illustrate the feasibility of the principle, one focuses on the association of the LH cell proposed in [7, 8] and a field effect transistor (FET). An analytical approach for the synthesis of the circuit is established knowing the characteristics of the FET transconductance and the Drain-Source resistance. Then, numerical analyses performed with the Advance Design System electronic microwave circuit simulators were realized to explain the validity of the principle. The results from the analyses realized around some GHz confirm the effectiveness of the principle.

2. THEORY ON THE LC-EFFECT CANCELLATION WITH ALH-CIRCUIT

To cancel out the LC-effect represented by the circuit composed of a series inductance L ended by a parallel capacitance C, passive LH-cells can be used [7–9]. But in this case, the whole compensated circuit can generate unwanted losses and unmatching effects. To overcome such effects, in this letter, a development of association of this LC-circuit with an ALH-cell is proposed as depicted in Fig. 1. The ALH-circuit is comprised of an FET ended by a LH- or CL-circuit.

For the theoretical approach, the transistor is supposed comprised of a voltage controlled current with its conductance gm in cascade with its drain-source resistance R_{ds}, and $\omega_0 = 1/\sqrt{L \cdot C}$. According to the desired value of gain S_{21} at the given frequency denoted $\omega_1 = 2\pi f_1$, one establishes the following synthesis formulae:

$$R_d = Z_0 \cdot L^2 / \left[Z_0^2 \cdot \omega_1^2 / \left(\omega_1^2 - \omega_0^2 \right) + L^2 \right] \tag{1}$$

$$g_m = S_{21} \cdot \sqrt{Z_0^2 \cdot \omega_1^2 + L^2 \cdot \left(\omega_1^2 - \omega_0^2 \right)^2} / \left(L \cdot \omega_0^2 \sqrt{Z_0 \cdot R_d} \right), \tag{2}$$
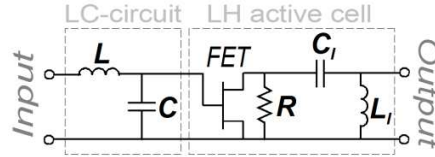
Figure 1: LC-circuit compensated with ALH circuit.
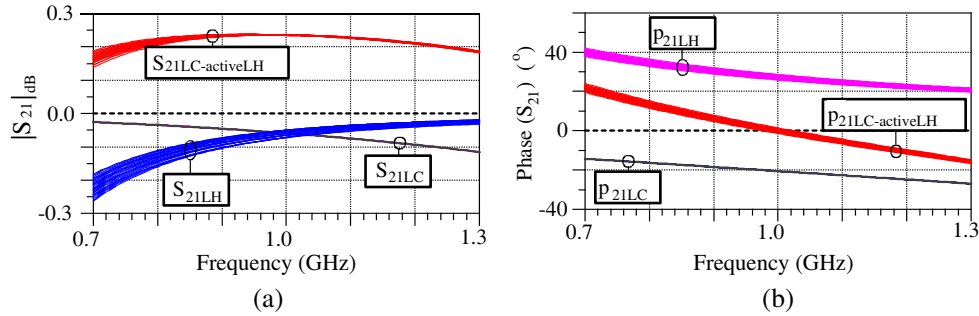
Figure 2: Transmission parameters of the LC-circuit, LH-cell and compensated circuit. (a) Magnitudes and (b) phases.
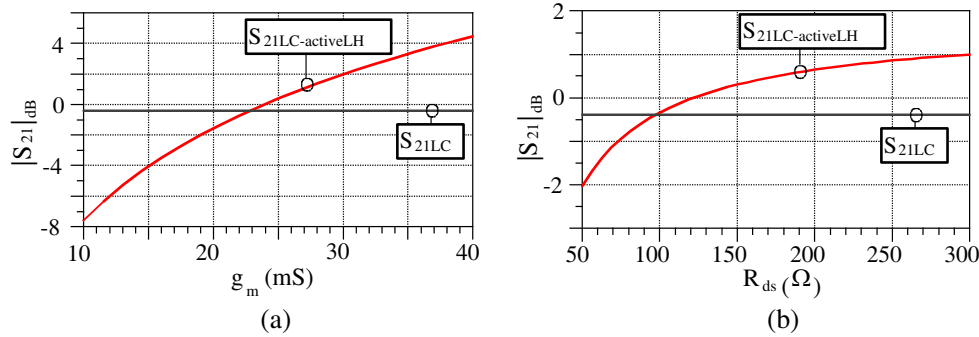
Figure 3: Variation of S_{21} in function of the FET parameters. (a) S_{21} ($f = 1\,\text{GHz}$) vs g_m and (b) S_{21} ($f = 1\,\text{GHz}$) vs R_{ds}.

with $Z_0 = 50\,\Omega$ represents the reference impedance, $1/R_d = 1/R_{ds} + 1/R$. Meanwhile, the matching resistance can be defined with the equation $R = R_{ds} \cdot R_d/(R_{ds} - R_d)$. To annihilate the LC-circuit transmission phase with the output matching $S_{22}(\omega_1) = 0$, the LH-cell parameters can be determined with the following expressions:

$$L_1 = Z_0\sqrt{R_d}/\left(\omega_1\sqrt{Z_0 - R_d}\right),\tag{3}$$

$$C_l = 1/\left(L_i \cdot \omega_1^2\right).\tag{4}$$

To verify the relevance of this synthesis method, an illustrating application is presented in the next section.

3. APPLICATION RESULTS

For starting, one underlines that the results presented in this section was run with the ADS simulator from AgilentTM. To cancel the LC-effect, an arbitrary LC-circuit with parameters $L = 2\,\text{nH}$ and $C = 2.2\,\text{pF}$ was considered. At the given frequency $f_1 = 1\,\text{GHz}$, the expressions of previous section were applied, thus, one synthesizes the ALH elements $L_l = 15\,\text{nH}$, $C_l = 7.8\,\text{pF}$ and $R_m = 62\,\Omega$. Then, after sensitivity studies of these parameters with $\pm10\%$-tolerances, the results displayed in Fig. 2 were obtained.

These graphs illustrate the feasibility of transmission gain (S_{21}) and phase (p_{21}) compensations simultaneously. One can see that with 10-%-variations of ALH-circuit parameters, relative variations only of about 1.5% are found. In addition, an analysis of the transistor parameter influences was also performed by varying first, g_m and fixing $R_{ds} = 100\,\Omega$, and then, varying R_{ds} and fixing $g_m = 20\,\text{mS}$. Therefore, the results shown in Fig. 3 were realized.

These explain that the gain compensations can be carried out from certain values of the used FET parameters.

4. CONCLUSION

A compensation technique enabling to cancel out the LC-effect is presented by using an ALH-cell. This later is comprised of an FET cascaded with a series capacitor ended by a parallel inductance. Synthesis expressions enabling to determine the compensator are established according to the operating frequency and the LC-parameters. To validate the synthesis method, results in excellent agreement with the theory were realised. In the continuation of this work, the application of the ALH-cell for the improvement of the signal integrity in the communication systems is in progress.

REFERENCES

1. http://www.itrs.net/links/2010itrs/2010Update/ToPost/2010_Update_Overview.pdf.
2. Ravelo, B., A. Perennec, and M. Le Roy, "New technique of inter-chip interconnect effects equalization with negative group delay active circuits," *VLSI*, Vol. 20, 409–434, INTECH Book, Z. Wang, Ed., Feb. 2010.
3. Ravelo, B., A. Perennec, and M. Le Roy, "Equalization of interconnect propagation delay with negative group delay active circuits," *11th IEEE Workshop on Signal Propagation on Interconnects*, 15–18, Genova, Italy, May 2007.
4. Ravelo, B., "Demonstration of negative signal delay with short-duration transient pulse," *Eur. Phys. J. Appl. Phys. (EPJAP)*, Vol. 55, 1–8, 2011.
5. Ravelo, B., "Baseband NGD circuit with RF amplifier," *Electronic Letters*, Vol. 47, No. 13, 752–754, Jun. 2011.
6. Ravelo, B., "Investigation on microwave NGD circuit," *Electromagnetics*, Vol. 31, No. 8, 537–549, Nov. 2011.
7. Caloz, C., A. Sanada, and T. Itoh, "A novel composite right/left-handed coupled-line directional coupler with arbitrary coupling level and broad bandwidth," *IEEE Trans. MTT*, Vol. 52, 980–992, Mar. 2004.
8. Lai, A., C. Caloz, and T. Itoh, "Composite right/left-handed transmission line metamaterials," *IEEE Microwave Magazine*, Vol. 5, 34–50, Sep. 2004.
9. Islam, R. and G. V. Eleftheriades, "Phase-agile branch-line couplers using metamaterial lines," *IEEE MWC Lett.*, Vol. 14, No. 7, 340–342, Jul. 2004.
10. Eleftheriades, G. V., O. Siddiqui, and A. K. Iyer, "Transmission line for negative refractive index media and associated implementations without excess resonators," *IEEE MWC Lett.*, Vol. 13, No. 2, 51–53, Feb. 2003.
11. Veselago, V., "The Electrodynamics of substances with simultaneously negative values of ε and μ," *Soviet Physics Uspekhi*, Vol. 10, No. 4, 509–514, 1968.
12. Pendry, J. B., "Negative refraction make a perfect lens," *Phys. Rev. Lett.*, Vol. 85, 3966–396, 2000.
13. Shelby, R. A., D. R. Smith, and S. Schultz, "Experimental verification of a negative index of refraction," *Science*, Vol. 292, 77–79, Apr. 2001.

Signal Processing for High Resolution RCS Measurement

E. S. Kashani and Y. Norouzi

Electrical Engineering, Amirkabir University of Technology, Tehran, Iran

Abstract— The interfering signal is the main difficulty in high resolution RCS measurement. Besides, using the network analyzer with a limited output power as the signal source reduces the attainable SNR. In this paper we have examined several different signal processing methods that can cure both above problems. Our proposed signal processing methods are based on some famous radar signals such as LFM, Non Linear FM and Costas.

1. INTRODUCTION

Radar Cross Section (RCS) of a radar target is a presumed area with isotropic scattering pattern which its scattered power equals that of the radar target. Before designing any radar system it is quit necessary to know the RCS of the objects that system encounters. So, over time many methods for measuring and estimating radar cross section have developed. Despite several methods have been considered for measuring RCS in lab, each of these methods have some disadvantages. Modern radio frequency generation technology available in network analyzers makes it possible to synthesize high resolution measurements using frequency-stepping techniques. In this method, the radiated frequency is stepped across a specified band at specified intervals. At each frequency received signal is sampled and its phasor relative to transmitted sinusoid is calculated. After appropriate processing — which is described in the next sections — the RCS of the object is determined. Despite its simplicity, the method has some difficulties.

Network analyzers have limited output power usually between 10 and 20 dBm. So a short duration pulse produced by these systems cannot provide enough SNR necessary for RCS measurement. As a result long pulses should be transmitted by the system. These long pulses reduce the range resolution of the measurement which is a necessity for today's high resolution RCS measurement. As was mentioned earlier to cure this problem usually stepped frequency waveform is applied by the network analyzer. After the phasor of the received signal at each frequency step is determined, inverse Fourier Transform is used to convert the signal to the frequency domain. Nevertheless, the important matter in laboratory methods is separation of real reflected signals from disturbing signals. However simple Fourier Transform produces signals with great side lobes which forbid detection of a small scattering centre in vicinity of a greater one. Usually windowing is used to reduce the side lobes of the signal; however windowing also widens the main lobe of the signal so reducing the range resolution.

In this paper, we will examine different signal processing methods to find which method is more suitable when fine range resolution is the goal and which one is more suitable when higher dynamic range is required. The proposed methods are based on the radar signal design which will be mentioned in the next sections.

The remainder of this paper is organized as follows: in Section 2, different radar signals are mentioned. In Section 3, we have demonstrated how these signals and appropriate processing could be accomplished using laboratory network analyzers. Finally in Section 4, the results of our simulations are presented and discussed and the best waveform for each application is suggested.

2. RADAR SIGNALS

In modern radar systems usually signal modulation is used to achieve fine resolution while using long duration pulses [1]. While many different signal modulation methods are proposed for radar systems [2], not all of them are applicable while using network analyzer for RCS measurement.

It can be said while all frequency modulations proposed for radar signals are applicable for RCS measurement, phase modulation and multi-carrier methods could not be used in this way. Here we will describe three main frequency modulation methods that can be used in network analyzer based RCS measurement.

2.1. Linear Frequency Modulation

Linear Frequency Modulation (LFM) is the first and probably still is the most popular pulse compression method. The basic idea is to sweep the frequency band linearly during pulse duration

T. The complex envelope of a linear-FM pulse is given by

$$u\left(t\right) = \frac{1}{\sqrt{T}} rect\left(\frac{t}{T}\right) \exp\left(jk\pi t^2\right) \quad \left(k = \pm\frac{B}{T}\right) \tag{1}$$

Here T is the signal transmission duration and B is the total swept bandwidth. In RCS measurement, all objects are stationary. So the zero Doppler cut of the ambiguity function should be used to find the range resolution of the signal. For LFM signal the zero Doppler cut of the ambiguity function is equal to:

$$\left|\chi\left(\tau, 0\right)\right| = \left|\left(1 - \frac{|\tau|}{T}\right) \frac{\sin\left[\pi B\tau\left(1 - |\tau|/T\right)\right]}{\pi B\tau\left(1 - |\tau|/T\right)}\right|, \quad |\tau| \leq T \tag{2}$$

Usually B is many times greater than $1/T$. In this case (2) can be approximated as:

$$\left|\chi(\tau, 0)\right| \approx \left|\frac{\sin \pi B\tau}{\pi B\tau}\right| \tag{3}$$

This function is sketched in Figure 2 for the case of $B = 10/T$. It can be shown that irrelevant to T, the main lobe width of the ambiguity function is almost equal to $1/B$. So fine range resolution can be achieved using long duration LFM pulses.

Referring to Figure 2, the ambiguity function of LFM signal has powerful side lobe levels. The main to side lobe level for LFM signal is only $13\,\text{dB}$. This fact makes it impossible to detect a weak object in vicinity of a greater one. Non-Linear FM and Costas modulations are proposed to reduce the side lobe level.

LFM modulation cannot be directly applied by a network analyzer. However any network analyzer can change it transmitted frequency in step by step manner. The stepped frequency is discretized version of the LFM signal and its properties are almost the same as LFM. The Fourier Transform is the equivalent matched filter that can compress the stepped frequency signal.

2.2. Non-linear Frequency Modulation

As was mentioned earlier, LFM signal has considerable side lobe level. So a great scattering point will cover a weaker nearby point. Non-Linear FM signal is proposed by the authors to cure this problem [3]. In NLFM signal the spectrum is shaped by deviating from the constant rate of frequency change and by spending more time at frequencies that need to be enhanced. While NLFM is a favourable signal in radar systems, it is not possible to use this method directly in network analyzers. The main idea behind the NLFM signal is to use time windowing before transmitting the signal. Using time window the spectrum of the signal can be shaped so that its ambiguity function has completely reduced sidelobe levels [4].

The idea of windowing can be used in network analyzer based RCS measurement. In this way after the phasor for all frequency steps are calculated by the network analyzer, these phasors are multiplied by the window coefficients and then *ifft* of the resultant signal is calculated to convert the signal to time domain.
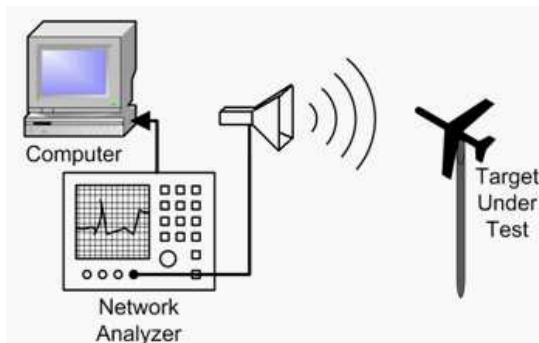
Figure 1: RCS measurement using network analyzer.
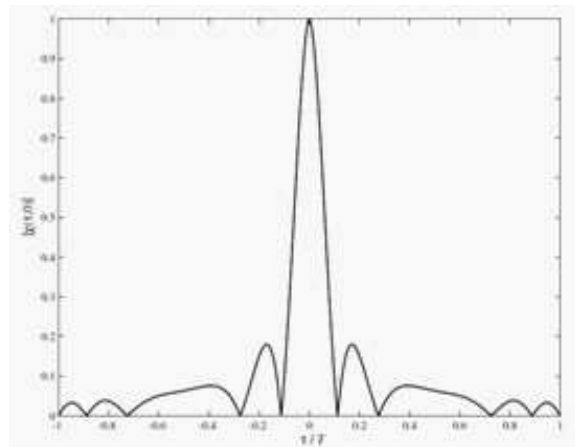
Figure 2: Zero Doppler cut of the ambiguity function of LFM signal ($BT = 10$).
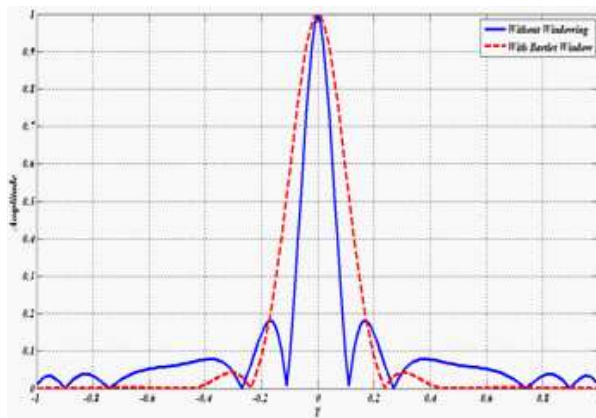
Figure 3: Comparison between the ambiguity function of LFM signal with and without windowing.
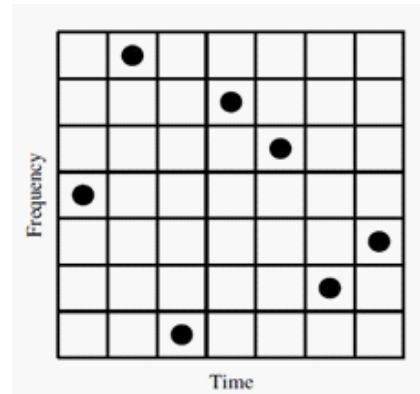
Figure 4: The Costas time-frequency matrix.

2.3. The Costas Signal

In frequency modulation methods, Costas coding results in a rather randomlike frequency evolution. According to this method the transmitted pulse is divided in to M parts of t_b seconds length. In each part a specific frequency is used. Costas has suggested theses specific frequencies so to achieve in favourable ambiguity function [5]. Costas signal is demonstrated by the binary matrix. At any one of the M time slices, only one frequency is transmitted and each frequency is used only once.

The Costas signal has a complicated Ambiguity function which can be found in [6]. It is not possible to create a Coastas using network analyzer. However the saved samples can be processed according to the Coastas method.

3. EXPERIMENTAL AND SIMULATION RESULTS

The test setup is shown in Figure 4. Here a network analyzer is used to find the RCS of a target placed on the top of the white column.

The transmitted signal can be assumed as a complex waveform:

$$X_T(t) = e^{j2\pi ft} \tag{4}$$

The received signal, assuming two separate scattering centres, is

$$X_r(t) = e^{j2\pi ft} + A_1 e^{j2\pi f(t-T_1)} + A_2 e^{j2\pi f(t-T_2)} = e^{j2\pi ft} \left(1 + A_1 e^{-j2\pi fT_1} + A_2 e^{-j2\pi fT_2}\right) \tag{5}$$

Here the first term is the part of signal reflected back from antenna feed point. This signal has no delay. The other two sections are reflection from two scattering centers located $cT_1/2$ and $cT_2/2$ meters in front of the antenna. Here the amplitude of these two signals is normalized to that of the first term. Therefore usually A_1 and A_2 are many times smaller than unity. Comparing (4) and (5) equations, the phasor of the received signal is equal to:

$$X_r = 1 + A_1 e^{-j2\pi fT_1} + A_2 e^{-j2\pi fT_2} \tag{6}$$

The LFM signal can be generated using step frequency. The frequency span of 2 to 18 GHz is divided to 400 points (network analyzer's sampling rate is either 400 or 1600 points). The output of the matched filter for LFM signal can be calculated using inverse Fourier transforms of the X_r of these 400 frequencies. The result of this process is represented in Figure 6.

As it is seen in this figure, both targets have great side lobes. These side lobes can be reduced by shaping the power spectrum according to one of the many sidelobe reduction windows. In our simulations we used 16 famous windows. Usage of these windows is almost equivalent to using NLFM Signal.

In Costas signal case, the received signal in time interval $(i-1)\Delta t$ to $i\Delta t$ is

$$u(t) = \exp\left(j2\pi f_i\left(t - (i-1)\Delta t\right)\right) \tag{7}$$

The phasor of this signal is equal to:

$$X_i = \exp\left(-j2\pi\left(i-1\right)f_i\right) \tag{8}$$

If the phasor of the received signal for f_i frequency is equal to Y_i, then Z_i is calculated as:

$$Z_i = Y_i \exp\left(-j2\pi\left(i-1\right)f_i\right) \tag{9}$$

Then fast fourier transform is used over Z_i samples. The result is the output signal assumeing Coastas transmitted signal.

Figure 5: Test setup at electromagnetic laboratory of AUT using ZVK R&S network analyzer.
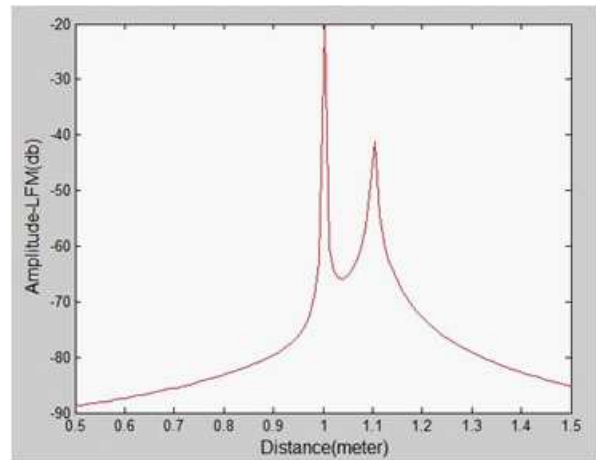
Figure 6: *ifft* of the received phasors for two targets separated by 10 cm.

Table 1: Comparing different waveforms.

#	Group	Waveform	Resolution	SLL (dB)	Loss (dB)
1	LFM	LFM	1	−13.3	0
2		Bartlett-Hann	1.4	−35.9	1.642
3		Bartlett	1.4	−26.5	1.26
4		Blackman	1.8	−58.2	2.383
5		Blackman-Harris	2	−98.9	3.02
6		Bohman	1.8	−46	2.529
7		Chebyshev	2	−100.3	2.889
8		Flattop	3.8	−98	4.438
9	NLFM	Gaussian	1.4	−43.5	1.609
10		Hamming	1.4	−44.5	1.352
11		Hann	1.6	−31.5	1.772
12		Kaiser	1	−13.7	0.001
13		Nuttall	2	−98.2	2.958
14		Parzen	2	−53.1	2.827
15		Taylor	1.2	−30.4	0.689
16		Triangular	1.4	−26.6	1.239
17		Tukey	1.2	−15.1	0.882
18	Coastas	Coastas	1	−26	0
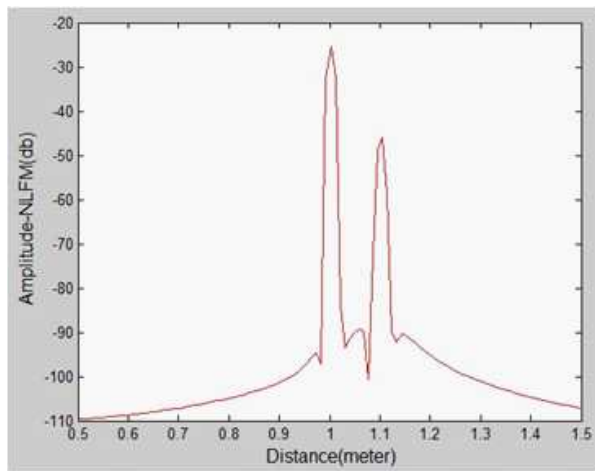
Figure 7: The target return using frequency windowing (Nuttall NLFM signal).
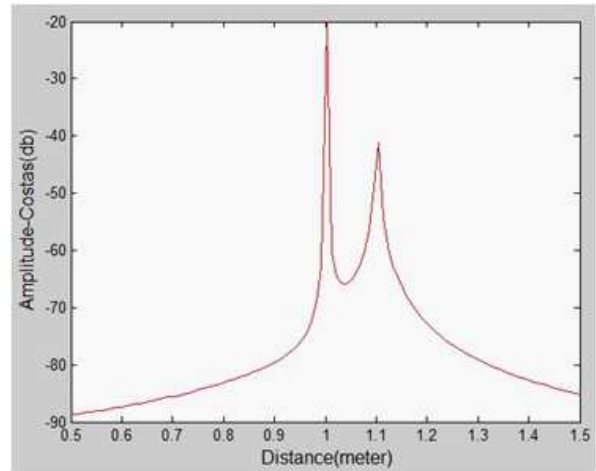
Figure 8: Output signal assuming Coastas transmitted signal.

4. DISCUSSION

In our simulations two targets separated by 10 cm, were assumed, the RCS of the second target was assumed ten times smaller than the first one. LFM, 16 different NLFM and Coastas signals were used in our simulations. The results of the simulation are presented in Table 1

According to this table, the lowest side lobe level can be achieved using Chebyshev, Nuttall, and Blackman-Harris or Flattop windows. However all these windows have considerable loss. Regarding these four windows Chebyshev has the least loss. If the aim is higher resolution, then LFM, Coastas and Kaiser Windowing are the best cases. Comparing these three windows, Coastas has the least side lobe level.

The results of these simulations can be used to select proper signal processing while measuring RCS using Network Analyzer.

REFERENCES

1. Skolnik, M. I., *Introduction to Radar Systems*, 3rd Edition, McGraw-Hill, 2000.
2. Levanon, N. and E. Mozeson, *Radar Signals*, 1st Edition, Wiley-Interscience, 2004.
3. Johnston, J. A. and A. C. Fairhead, "Waveform design and Doppler sensitivity analysis for nonlinear FM chirp pulses," *IEE Proceedings*, Vol. 133, No. 2, Part F, 163–175, April 1986.
4. Oppenheim, A. V. and R. W. Schafer, *Discrete Time Signal Processing*, 3rd Edition, Prentice Hall Signal Processing, 2009.
5. Costas, J. P., "A study of a class of detection waveforms having nearly ideal range — Doppler ambiguity properties," *Proceedings of the IEEE*, Vol. 72, No. 8, 996–1009, August 1984.
6. Golomb, S. W. and H. Taylor, "Constructions and properties of Costas arrays," *Proceedings of the IEEE*, Vol. 72, No. 9, 1143–1163, September 1984.

Quasi-normal Modes and Strong Coupling in a Plasmonic Nanocavity

A. Castanié and D. Felbacq

Laboratoire Charles Coulomb UMR-CNRS 5221, Université de Montpellier 2
34095 Montpellier Cedex 05, France

Abstract— The confinement of plasmons in a planar nanocavity was studied. It was shown that the dispersion curves partly result from the strong coupling of photon-like and plasmon-like modes. The Green function was constructed from the generalized modes.

1. INTRODUCTION

Surface Plasmon Polaritons are electromagnetic modes localized at the air-metal interface. They can be confined in regions much smaller than their wavelength. This strong confinement results in a huge Purcell effect [1], hybrid excitonic modes [2], quantum dots luminescence [3] or spasers [4]. In this work, we study the effect of confinement on surface plasmons in a planar cavity [5] with a wall coated with a lossy metal. It is shown that the modes result from the strong coupling of photon-like modes with plasmon-like modes. Modes strongly concentrated at the air-metal interface can be obtained.

2. THE MODES OF THE STRUCTURE

Time harmonic modes with the magnetic field linearly polarized along a direction transverse to the direction of propagation z are considered. The time dependence is e^{-ik_0ct} (c is the speed of light in vacuum). The magnetic field is denoted $H(x, y) = u(x)e^{i\gamma y} e^{-ik_0ct} e_z$. The total heigth of the waveguide is h and the thickness of the metal is d ($\tau = d/h$). The field $u(x)$ satisfies the following equation:

$$\partial_x \left(\varepsilon^{-1}\partial_x u \right) + \left(k_0^2 - \gamma^2 \varepsilon^{-1} \right) u = 0 \tag{1}$$

where $\varepsilon(x)$ is equal to 1 for $x \in [d, h]$ and to $\varepsilon_m = 1 - \frac{\omega_p^2}{\omega(\omega+i\Gamma)}$ for $x \in [0, d]$, that is, the metal is described by a Drude model. For numerical computations, the parameters of silver will be used (the plasma wavelength is $\lambda_p = 137\,\text{nm}$). As a simple model of confinement, Neumann conditions $\partial_x u = 0$ on the boundaries of the cavity ($x = 0, h$) are used.

The plasma wavelength $\lambda_p = \frac{2\pi c}{\omega_p}$ allows to define a unit of length and a unit of spatial frequency by $k_p = \frac{2\pi}{\lambda_p}$. Upper case letters denote the normalized quantities: $H = k_p h$ the normalized height of the waveguide, $D = k_p d$ the normalized width of the metal layer, $X = k_p x$ the normalized transversal position, $K_0 = k_0/k_p$, $G = \gamma/k_p$ the normalized wavenumber and propagation constant respectively.

A straightforward computation leads the following dispersion relations:

$$F(K_0^2, G^2) = \frac{\beta_m}{\varepsilon_m} \tan(\beta_m H\tau) - \beta_g \tan(\beta_g H(\tau - 1)) = 0 \tag{2}$$

where

$$\beta_g^2 = K_0^2 - G^2, \qquad \beta_m^2 = K_0^2 \varepsilon_m - G^2 \tag{3}$$

In order to give a specific example of dispersion curves, we choose the following parameters: $h = 150\,\text{nm}$, $d = 50\,\text{nm}$ (i.e., $\tau = 1/3$). A colorplot of $F(K_0^2, G^2) = 0$ is given in Fig. 1. Two set of curves can be distinguished: a lower branch, below the plasma frequency of the metal (i.e., $K_0 < 1$) and below the light cone ($K_0 = G$); and an upper branch made of several curves, above the plasma frequency and above the light cone. The curves above the light cone correspond to the usual guided modes, while the mode below the light cone correspond to fields localized at the air-metal interface. As τ varies in $[0, 1]$, the variation of the curves is given in Fig. 2. The part of the curve above 1 corresponds to those frequencies above the plasma frequency ω_p, where the real part of the permittivity of the metal is positive. When losses are small enough quasi-modes exist in the guide, leading to the above branch of the dispersion curve. The branch is thus the photon-like curve. The lower branch corresponds to the frequencies below the plasma frequency, where the real part of the permittivity of the metal is negative. It corresponds to modes essentially localized at the interface of the metal with air, that is, confined surface plasmons.

3. THE GREEN FUNCTION

In view of dealing with quantum dots embedded in the dielectric waveguide, the Green function of the system is studied. The permittivity of the waveguide is denoted $\varepsilon_g(\omega)$. An electric dipole is embedded in the waveguide at the position (x_0, y_0). Remark that: $\delta(x - x_0, y - y_0) = \delta_{x_0} \otimes \delta_{y_0}$. The electric dipole is denoted: $\vec{P} = \vec{p}\,\delta_{x_0} \otimes \delta_{y_0}$ and $\vec{p} = (p_x, p_y)$ is contained in the (x, y) plane. All the field are harmonic with a time dependence of $e^{-i\omega t}$ and p-polarized fields are looked for. The magnetic field reads as: $\vec{H}(x, y) = u(x, y)\vec{e_z}$. Maxwell equations read as:

$$\nabla \times \vec{E} = i\omega\mu_0 u(x, y)\vec{e_z}, \qquad \nabla \times \vec{H} = -i\omega\varepsilon_0\omega\vec{E} - i\omega\vec{P}$$

The function u satisfies the following equation in the Schwartz distributional meaning:

$$\nabla \cdot \left(\eta^{-1}\nabla u\right) + k_0^2 u = i\omega\eta_g^{-1}\left(\partial_x \mathcal{P}_y - \partial_y \mathcal{P}_x\right)$$

Let us denote, for a distribution $f(x, y)$: $\partial_z f = \frac{1}{2}\left(\partial_x f - i\partial_y f\right)$, $\partial_{\bar{z}} f = \frac{1}{2}(\partial_x f + i\partial_y f)$ and $p_z = p_x + ip_y$, $p_{\bar{z}} = p_x - ip_y$ then:

$$\partial_x \mathcal{P}_y - \partial_y \mathcal{P}_x = p_y \partial_x \delta - p_x \partial_y \delta = -i\left(p_z \partial_z \delta - p_{\bar{z}} \partial_{\bar{z}} \delta\right)$$
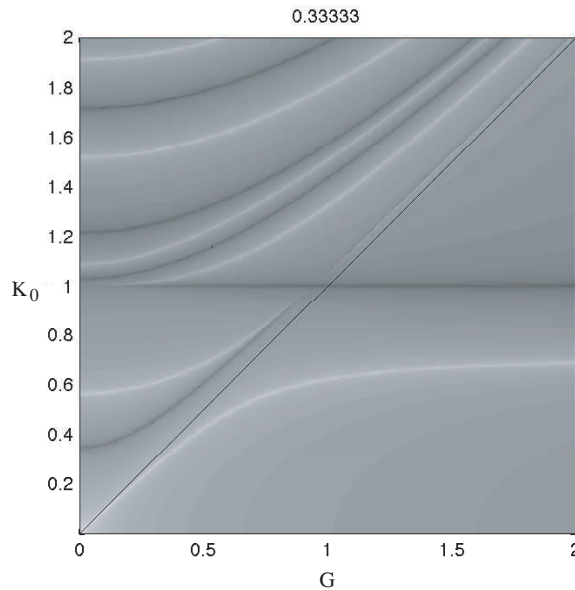
Figure 1: Dispersion relation of the waveguide for $h = 150$ nm, $\tau = 1/3$. The modes appear as white lines.
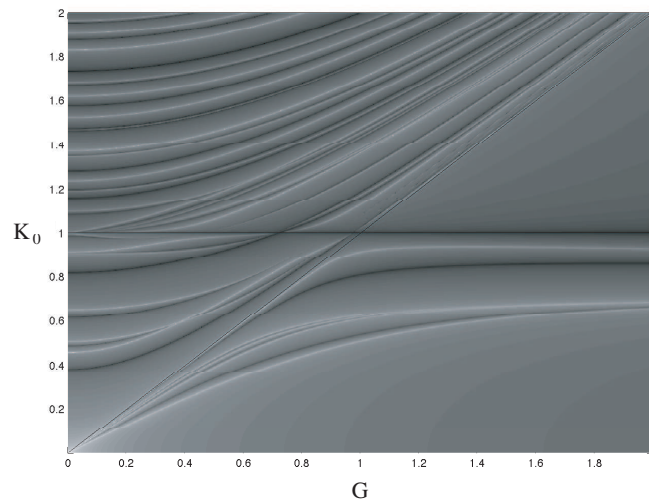
Figure 2: Bundle of the dispersion curves for a varying τ between 0 and 1.

the equation to be solved is:

$$\nabla \cdot \left(\varepsilon^{-1}\nabla u\right) + k_0^2 u = \omega\varepsilon_g^{-1}\left(p_z\partial_z\delta - p_{\bar{z}}\partial_{\bar{z}}\delta\right) \tag{4}$$

This can be decomposed into:

$$\nabla \cdot \left(\varepsilon^{-1}\nabla g_z\right) + k_0^2 g_z = \omega\varepsilon_g^{-1}\partial_z\delta \tag{5}$$

$$\nabla \cdot \left(\varepsilon^{-1}\nabla g_{\bar{z}}\right) + k_0^2 g_{\bar{z}} = \omega\varepsilon_g^{-1}\partial_{\bar{z}}\delta \tag{6}$$

in a homogeneous domain $\mathbb{R} \times U$ containing (x_0, y_0) with permittivity $\varepsilon_{m,g}$, the functions $g_z, g_{\bar{z}}$ satisfy:

$$\Delta g_z + k_0^2\varepsilon_{m,g}g_z = \omega\partial_z\delta \tag{7}$$

$$\Delta g_{\bar{z}} + k_0^2\varepsilon_{m,g}g_{\bar{z}} = \omega\partial_{\bar{z}}\delta \tag{8}$$

Particular solutions of these equations read locally:

$$g_z = \omega\partial_z H_0(k_0\sqrt{\varepsilon_{m,g}}r), \qquad g_{\bar{z}} = \omega\partial_{\bar{z}}H_0(k_0\sqrt{\varepsilon_{m,g}}r)$$

These solutions can be made explicit by noting the following result:

$$H_1(r)e^{i\theta} = -2\partial_{\bar{z}}H_0(r), \qquad H_1(r)e^{-i\theta} = -2\partial_z H_0(r)$$

Hence:

$$\partial_{\bar{z}}H_0(r) = \frac{-x-iy}{r}H_1(r) = -H_1(r)e^{i\theta}$$

We denote: $\beta^2 = k^2\varepsilon_{m,g} - \alpha^2$, and β is defined using the square root function with a cut along $\mathbb{R}^-$ and $\sqrt{1} = 1$. Weyl formula for the Hankel function provides a plane wave expansion:

$$H_0(r) = \frac{1}{\pi}\int\frac{1}{\beta}e^{i\beta|y|}e^{i\alpha x}d\alpha$$

From which it follows that:

$$H_1(r)e^{i\theta} = \frac{1}{\pi}\int\frac{i\alpha - \text{sign}(y)\beta}{\beta}e^{i\beta|y|}e^{i\alpha x}d\alpha$$

We denote $\mathcal{K}_{\mp}(\alpha) = (i\alpha \mp \beta)/\pi\beta$. Using this result, in the waveguide, a Green function has the form:

$$\begin{aligned}
y_0 < y \quad & g_z(y, y_0) = \left(\mathcal{K}_+(\alpha)\frac{e^{-i\beta y_0}}{2i\beta} + A\right)e^{i\beta y} + Be^{-i\beta y} \\
y < y_0 \quad & g_z(y, y_0) = Ae^{i\beta y} + \left(\mathcal{K}_-(\alpha)\frac{e^{i\beta y_0}}{2i\beta} + B\right)e^{-i\beta y}
\end{aligned} \tag{9}$$

that is, the sum of a regular field $Ae^{i\beta y} + Be^{-i\beta y}$ and the green function for a uniform medium. This form leads to a quantization scheme described in [6] and opens the way to the study of quantum plasmonics in this context. Also the extraction of light could be performed by corrugating the exterior surface of the waveguide. Work is in progress in that direction to modelize the coupling of light to the continuum of exterior modes by means of the Fourier Modal Method [7–9].

ACKNOWLEDGMENT

REFERENCES

1. Iwase, H., et al., "Analysis of the purcell effect in photonic and plasmonic crystals with losses," *Opt. Express*, No. 18, 16546, 2010.
2. Bellessa, J., et al., "Strong coupling between surface plasmons and excitons in an organic semiconductor," *Phys. Rev. Lett.*, Vol. 93, 036404, 2004.
3. Tanaka, K., et al., "Multifold enhancement of quantum dot luminescence in plasmonic meta-materials," *Phys. Rev. Lett.*, No. 105, 227403, 2010.

4. Bergman, D. J. and M. I. Stockman, "Surface plasmon amplification by stimulated emission of radiation: Quantum generation of coherent surface plasmons in nanosystems," *Phys. Rev. Lett.*, Vol. 90, 027402, 2003.

5. Dionne, J. A., et al., "Planar metal plasmon waveguides: Frequency-dependent dispersion, propagation, localization, and loss beyond the free electron model," *Phys. Rev. B*, Vol. 72, 075405, 2005.

6. Matloob, R., R. Loudon, S. M. Barnett, and J. Jeffers, "Electromagnetic field quantization in absorbing dielectrics," *Phys. Rev. A*, Vol. 52, 4823–4838, 1995.

7. Guizal, B., et al., "Electromagnetic beam diffraction by a finite lamellar structure: An aperiodic coupled-wave method," *J. Opt. Soc. Am. A*, Vol. 20, 2274–2280, 2003.

8. Granet, G. and B. Guizal, "Analysis of strip gratings using a parametric modal method by fourier expansions," *Opt. Comm.*, Vol. 255, 1–11, 2005.

9. Edee, K., et al., "Beam implementation in a nonorthogonal coordinate system: Application to the scattering from random rough surfaces," *J. Opt. Soc. Am. A*, Vol. 25, 796–804, 2008.

Photon-plasmon Strong Coupling in a Layered Structure

B. Guizal and A. Castanié

Université de Montpellier 2, Laboratoire Charles Coulomb UMR CNRS-UM2 5221
34095 Montpellier Cedex 05, France

Abstract— We, theoretically, show that it is possible to realize the strong coupling of a guided mode with a surface plasmon in a waveguide coated by a lossy metal. The dispersion relation of such a structure is obtained through the T-matrix algorithm combined with the the Cauchy integral technic that allows for rigorous computations of the complex poles. The strong coupling is identified by the anticrossing in the dispersion diagram and simultaneously by the crossing in the loss diagram (circular frequency vs. the imaginary part of the wave vector). The spatial structures of the different modes (original and hybridized) are computed and it is shown that spatial Rbbi oscillations appears for one of them. This last feature can be exploited to reduce losses in the propagation of surface plasmons.

1. INTRODUCTION

The strong coupling of plasmons with excitons in a layered structure was investigated in [1–3]. The interrest of such a phenomenon is twoflod: from the point of view of fundamental quantum physics since it can perform spatial Rabi oscillations [4, 5] and from the point of view of technology since it can prove useful for efficient extraction of light. In the present work, we investigate, numerically, the strong coupling of a surface plasmon with a guided mode in a multilayered planar structure. The study is based on the so-called trasfert matrix algorithm for multilayered planar structures. It allows the computation of the complex dispersion relation as well as the computation of the spatial structures of the related modes. With such a technic, one usually ends up with a determinant of a matrix whose zeros are the eigenfrequencies of the structure. It is of fundamental importance to emphasize that the problem of determining the dispersion relation is far from beeing obvious even for such simple structures. Indeed, the common methods used to handle this problem are based on the use of Muller algorithm or equivalently the Newton method which are efficient only if initial guessed values are available. Here, we use a more efficient algorithm based on the use of: (i) the S-matrix algorithm thant that of the T-matrix; and (ii) Cauchy integrals, combined with a *tetrachotomy* strategy, to compute the poles (rather than the zeros) of the determinant of the S-matrix .

In the following, after the presentation of the formalism related to the problem and a brief description of the numerical procedure used in the study, we discuss the modes of the proposed structure and show the appearance of the strong coupling. Finally we give the fields maps for these modes and discuss the spatial oscillations the structure supports.

2. THEORY

We consider a multilayedred structure made of N films of widths e_p and dielectric permittivities ϵ_p. Under TM plarization, the magnetic field is parallel to the y axis and can be represented as:

$$
\begin{cases}
H_0(x,z) = Ie^{i(\alpha x + \beta_0 y)} + Re^{i(\alpha x - \beta_0 y)}, & \text{for } z \leq 0 \\
H_p(x,z) = a_p e^{i(\alpha x + \beta_p y)} + b_p e^{i(\alpha x - \beta_p y)}, & \text{for } z_{p-1} \leq z \leq z_p \\
H_N(x,z) = Te^{i(\alpha x + \beta_N y)} + I'e^{i(\alpha x - \beta_N y)}, & \text{for } z \geq z_N
\end{cases}
$$

α is the parallel component of the incoming wave vector and $\alpha^2 + \beta_p^2 = (\omega/c)^2 \epsilon_p$ for each medium. The different constants I, I', R, T, a_p and b_p represent the amplitudes of the different waves (cf. Figure 1). Writing the boundary conditions (i.e., continuity of $H_p(x,z)$ and $\partial_z H_p$) over the $N+1$ interfaces ($z = z_p$) leads to a system of $2N+2$ algebraic equations relating the $2N+2$ unknowns R, T, a_p and b_p ($1 \leq p \leq N$). It is of common use to solve this system through the T-matrix algorithm that relates he amplitudes of the fields and their normal derivatives between the interfaces of each layer. However we prefer to use the more stable S-matrix algorithm that relates the outgoing ampitudes to the incoming ones throug the scattering matrix of the structure:

$$
\begin{pmatrix} R \\ T \end{pmatrix} = S(\omega, \alpha) \begin{pmatrix} I \\ I' \end{pmatrix}
$$
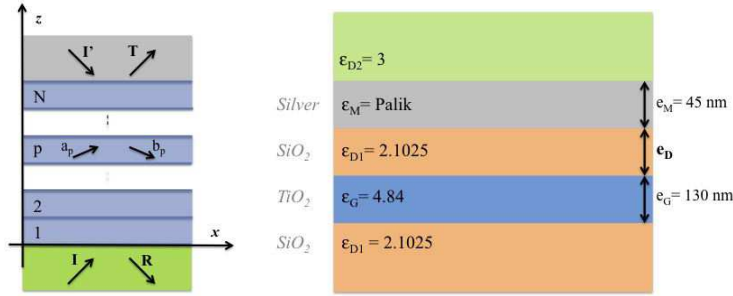
Figure 1: General scheem of a multilayered structure and the particular case studied here: a dielectric waveguide (ϵ_G) and a metallic film (ϵ_M) inserted in between two dielectric hosts (ϵ_{D1} and ϵ_{D2}) and separated by a dielectric layer.

The modes of the structure correspond to $detS^{-1}(\omega, \alpha) = 0$ and can be found by searching for the poles of $detS(\omega, \alpha)$. For each ω, we look for the corresponding poles α_0 in the complex plane by using Cauchy integrals:

$$\alpha_0 = \int_\gamma \alpha S(\omega, \alpha)d\alpha / \int_\gamma S(\omega, \alpha)d\alpha$$

where γ is a closed loop of the complex plane containing the seeked pole. In order to find the right loop, containing only α_0, we begin by a first arbitrary rectangular loop and compute the number of poles it contains. If there is only one pole then we compute it by Equation (3) and if not we devide the rectangle in four sub-rectangles to which we apply the same procedure; this is what we call: the *tetrachotomy* strategy.

3. RESULTS

We consider the structure depicted in Figure 1; made of a dielectric waveguide and a metallic film embedded between two dielectric hosts and separated by a dielectric layer of thickness e_D. There are three different modes supported by the constituents of this structure: a guide mode GM in the waveguide (e_G is chosen such that only one guided mode do exist) and two surface plasmons SP1 and SP2 over the interfaces of the metal. To reveal the interactions between these original modes, we computed the dispersion diagram of the whole structure where the permittivity of the metal (silver in this case) has been taken from [6]. As we are looking for a strong coupling between GM and SP1/2, we choosed a value of $e_D = 98$ nm for which this effect is fostered. Indeed, the numerous numerical computations we performed showed that: (i) if e_D is large enough, then there is no coupling between GM and SP1/2 and their orginal dispersion curves just cross; which means that the modes do not see each other; (ii) if e_D is too small, then the coupling between the modes is weak.

In Figure 2, we show the computed real part of the dispersion relation of the multilayered stack (black circles) as well as those of the guided mode alone (blue circles) and the surface plasmons alone (red circles). The aniticrossing arround $\alpha_R = 0.029$ is clearly the result of hybridization of the GM and the SP2 and indicates the presence of a strong coupling (SC) between these two modes. To confirm that is the case, we check the imaginary part of the dispersion diagram (ω/ω_p versus α_I). Indeed, we know that for this particular state, there should be a crossing between the imaginary dispersion curves of GM and SP2. Figure 3 gives the loss diagram that exhibits a clear crossing of these curves, confirming, thus the presence of strong coupling. Otherwise, it is interesting to notice that for the particular frequency around which the SC occurs, the losses of the hybrid part of GM and PS2 are minimum. This characteristic could be exploited to reduce the losses inherent to surrface plasmons by replacing them by their hybridized conterparts.

We wish, now, to look at the spatial structure of the hybrid mode. For that, we excite, artefactually, the structure by an evanescent gaussian beam centered at $\alpha_R = 0.3$, launched at $x = 0 = z$ and just wide enough to excite the mode in the lower part of the anticrossing.

Figure 4, shows the map of the magnetic under such an excitation computed with ϵ_G taken from [6] (left). Once excited from the bottom, the mode oscillates between the waveguide and the lower interface of the metallic layer. In order to better see these oscillations, we emplyed a Drude model with less losses. On the left part of Figure 4, Spatial Rabi oscillation are now more pronounced.
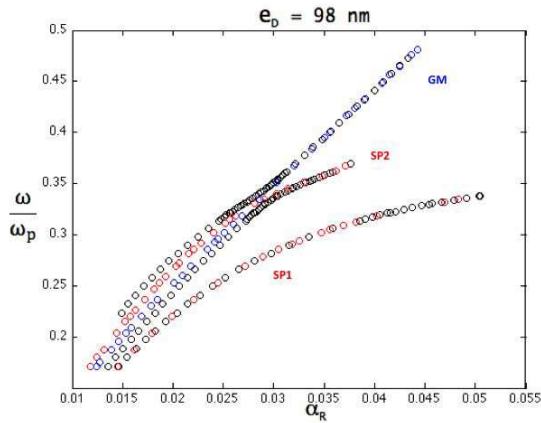
Figure 2: Dispersion relation: the normalized frequency (to the plasma frequency ω_p) vs. the real part of α.
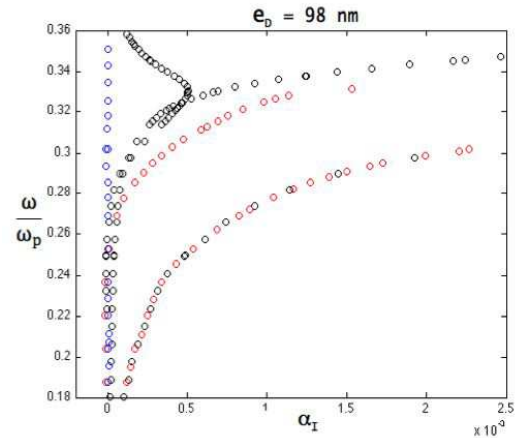
Figure 3: Loss diagram: the normalized frequency (to the plasma frequency ω_p) vs. the imaginary part of α.
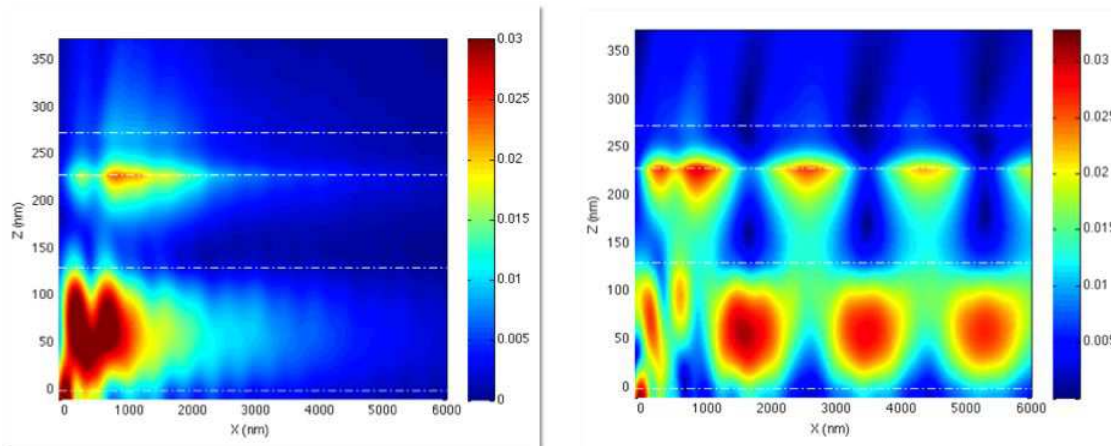
Figure 4: Map of the magnetic field arround the SC computed with different parameters of siver: Palik-left and Drude-right.

4. CONCLUSION

We presented a multilayered structure that demonstrates a strong coupling between a guided mode and a surface plasmon. The numerical study is based on a rigorous computation of the dispersion and loss diagrams. A suitable excitation of the structure by an evanecent gaussian beam revealed the spatial structure of the hybridized mode showing spatial Rabi oscillations. This phenomenon can be observed for more complicated structures for which efficient semi-analytic numerical tools delivering S-matrices are available; as it is the case photonic crystals [7], photonic quasi-crystals [8] or aperiodic structures [9].

REFERENCES

1. Bellessa, J., et al., "Giant Rabi splitting between localized mixed plasmon-exciton states in a two-dimensional array of nanosize metallic disks in an organic semiconductor," *Phys. Rev. B*, Vol. 80, 033303, 2009.
2. Bellessa, J., et al., "Strong coupling between surface plasmons and excitons in an organic semiconductor," *Phys. Rev. Lett.*, Vol. 93, 036404, 2004.
3. Chern, R. L. and D. Felbacq, "Artifcial magnetism and anticrossing interaction in photonic crystals and split-ring structures," *Phys. Rev. B*, Vol. 79, 075118, 2009.

4. Centeno, E. and D. Felbacq, "Characterization of defect modes in finite bidimensional photonic crystals," *J. Opt. Soc. Am. A*, Vol. 16, 2705–2712, 1999.
5. Centeno, E. and D. Felbacq, "Rabi oscillations in bidimensional photonic crystals," *Phys. Rev. B*, Vol. 62, 10101, 2000.
6. Palik, E., *Handbook of Optical Constants of Solids*, Academic Press, Inc., New York, 1985.
7. Bouchitte, G. and D. Felbacq, "Homogenization of a wire photonic crystal: The case of small volume fraction," *SIAM Journal*, Vol. 6, 2061–2084, 2006.
8. Zolla, F.. et al., "A remarkable diffractive property of photonic quasi-crystals," *Opt. Comm.*, Vol. 148, 6–10, 1998.
9. Felbacq, D., et al., "Localization of light by a set of parallel cylinders," *Journal of Modern Optics*, Vo. 42, 473–482, 1985.

Exchange Splitting of Backward Volume Spin Wave Configuration Dispersion Curves in a Permalloy Nano-stripe

G. Venkat[1], A. Prabhakar[1], M. Franchin[2], and H. Fangohr[2]

[1]Department of Electrical Engineering
Indian Institute of Technology, Madras, Chennai 600036, India
[2]Engineering and Environment, University of Southampton, Southampton, UK

Abstract— Micromagnetic simulations of spin wave (SW) propagation in a permalloy film are used to extract the SW dispersion relation. The SWs are excited using the Oersted fields around a current carrying microstrip. Strong exchange interactions yield forward volume dispersion, despite using a backward volume configuration. Edge effects cause the formation of standing longitudinal waves, which manifest themselves as resonance peaks in the SW transmission spectrum. By studying the frequency separation between adjacent resonance peaks, we extract an effective exchange length for the SW excitations in the nano-stripe geometry. The interaction length is in good agreement with the values used in the simulation, thus validating the underlying theoretical approximations. The radiation resistance for the structure is also obtained from the dispersion curve. It shows a minimum at 217 GHz.

1. INTRODUCTION

The dispersion relation of SWs, in magnetic structures, has been a matter of investigation for quite some time [1, 2]. The dispersion relation, $\omega(k)$, is a valuable source of information for structures of various geometries and various materials [3, 4]. Traditionally, these relations have been obtained by experimental means, which often have to be run multiple times. Recent advancements in computational methods have enabled us to obtain these dispersion relations numerically [5–7].

The Landau-Lifshitz-Gilbert (LLG) equation [8] is the governing differential equation that describes the dynamics of the magnetization in a magnonic waveguide. There are various packages which can be used for this. We rely on the finite element method based package NMAG [9]. We compare simulation against analytically obtained results. We are also interested in a study of SW excitation due to a microstrip. This has important ramifications for actual device fabrication, and we model a current pulse, applied to a microstrip transducer above the permalloy stripe, to excite SWs. The chosen geometry allows us to demonstrate the use of micromagnetic simulations to extract the frequency dependence of the radiation resistance, paving the path for studies that involve the interaction of magnetic nano-structures coupled to external circuitry [10].

2. PROBLEM SPECIFICATIONS

The problem, which was considered, is a modification of the one which has been proposed as a standard problem for micromagnetic simulations [11]. The geometry of the problem (shown in Fig. 1(a)), was a permalloy stripe of dimension $(1000 \times 50 \times 1) \, \text{nm}^3$. Further specifications of the problem are given in Table 1.
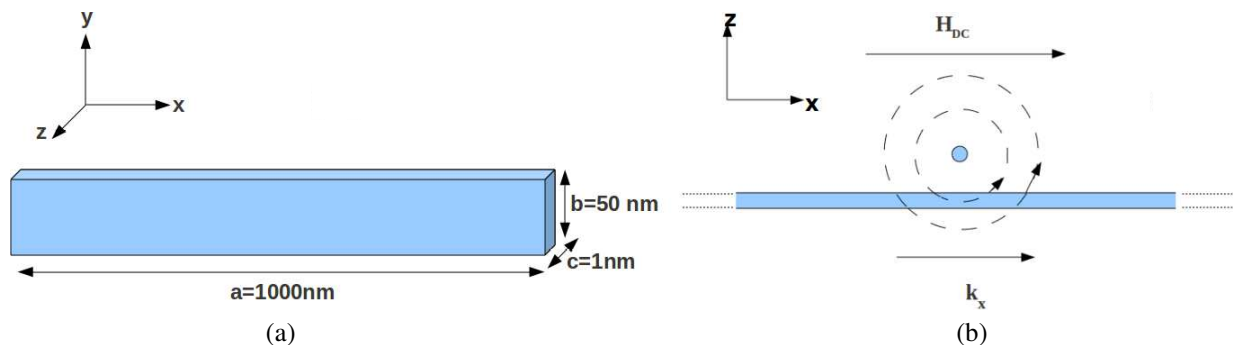
Figure 1: (a) The geometry of the nano stripe and (b) the applied excitation along with the DC bias field and the direction of wave propagation. Figures are not to scale.

The excitation, which was used for inducing spin waves, had the following features:

1. A cylindrical current carrying conductor, of radius $5\,\text{nm}$ was assumed to be placed at $(500, y, 6)$ nm, in the x-z plane (shown in Fig. 1(b)).
2. A sinc excitation pulse was applied to the current conductor. The maximum amplitude of the excitation pulse $(I = 160\,\mu\text{A})$ was chosen so that a field of about $5\,\text{kOe}$ was obtained at the circumference of the wire.
3. The Oersted fields were calculated for each finite element cell in the geometry based on its distance from the axis of the wire.

Thus the excitation, $h_{\text{exc}}(r, t)$, at a point can be expressed as:

$$h_{\text{exc}}(r, t) = \frac{\mu_0 I}{2\pi r} \frac{\sin(2\pi f t)}{2\pi f t}, \tag{1}$$

where r is the radial distance of the point from the centre of the conductor, and f is the cutoff frequency and was taken to be $500\,\text{GHz}$. The $\omega(k)$ curve is obtained by viewing a surface plot of $m_y(k_x, \omega)$, which is obtained by taking the two dimensional Fourier transform of $m_y(x, t)$, after allowing the simulation to run for $5\,\text{ns}$.

3. SIMULATION RESULTS

The spatial and temporal variation in the excitation field excites only the dominant lowest order SW mode, which is easily visible in Fig. 2. To facilitate a comparison with analytic models, we fit the points on the dispersion curve to a polynomial (in rad/s)

$$\omega(k_x) = (-1.76 \times 10^{-24}) k_x^4 + (5.54 \times 10^6) k_x^2 + 2.36 \times 10^{11}. \tag{2}$$

Table 1: Fields and constants used in the simulation.

Sr. No.	Parameter	Value
1	Saturation Magnetization (M_s)	$8.6 \times 10^5\,\text{A/m}$
2	Exchange Coupling Constant (A)	$1.3 \times 10^{-11}\,\text{J/m}$
3	Anisotropy Constant (K)	0
4	Gyromagnetic ratio (γ)	$1.7 \times 10^9\,\text{m/A-s}$
5	Damping coefficient (α)	0
6	DC bias field (H_{DC})	$10.1\,\text{kOe}$
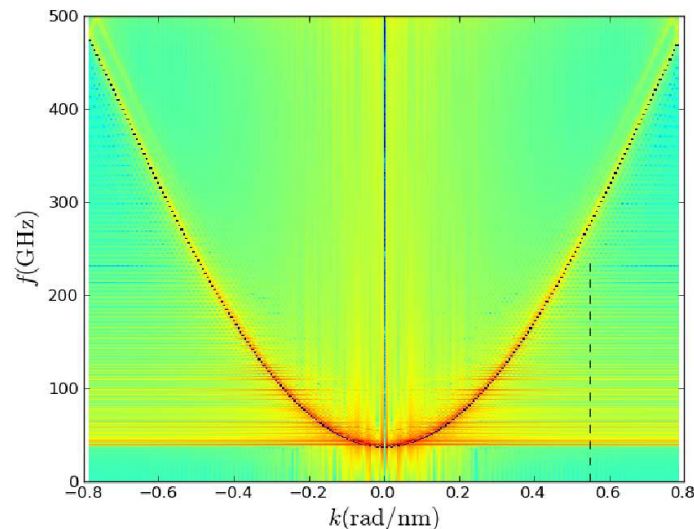
Figure 2: Dispersion curve for a BVSW configuration in a permalloy nano-stripe excited by Oersted fields from a current carrying filament along with the polynomial fit (2) (dotted line). The vertical dashed line corresponds to $k = 0.55\,\text{rad/nm}$.

Figure 2 shows (2) superimposed, as black dots, on a surface color plot of $m_y(k_x, \omega)$. A number of horizontal lines are also seen in Fig. 2. These are a manifestation of the exchange splitting of the dispersion relation due to interactions between the lowest and higher order longitudinal modes [12]. One such mode is shown schematically in Fig. 3.

The resonances due to standing wave modes will follow a relation of the form [13]

$$\omega_n = \omega_0 + \omega_M \lambda_{\text{ex}} \left(\frac{n\pi}{d} \right)^2, \tag{3}$$

where d is the length along the dimension of interest. The exchange constant (λ_{ex}) is given by

$$\lambda_{\text{ex}} = \frac{2A}{\mu_0 M_s^2}. \tag{4}$$

In our case, we are exciting longitudinal modes that have a maxima at the centre of the film and a particular width mode. Hence, (3) gets modified to

$$\omega_n = \omega_0 + \omega_M \lambda_{\text{ex}} \left(\frac{(2n+1)\pi}{a} \right)^2, \tag{5}$$

$$\text{or} \quad \Delta f = \frac{1}{2\pi} (\omega_{n+1} - \omega_n) = \frac{4\omega_M \lambda_{\text{ex}} \pi}{a^2} (n+1). \tag{6}$$

Resonance peaks in the power spectrum, for $k_x = 0.55\,\text{rad/nm}$ (which corresponds to the dashed vertical line in Fig. 2), are shown in Fig. 4(a). We fit the data to a line, shown in Fig. 4(b). The slope is found to be $57.53 \pm 0.76\,\text{MHz}$, from which, using (6), we extract $\lambda_{\text{ex}} = 2.59 \times 10^{-17}\,\text{m}^2$. This is in reasonable agreement with the values given in Table 1 that yield $\lambda_{\text{ex}} = 3.23 \times 10^{-17}\,\text{m}^2$.
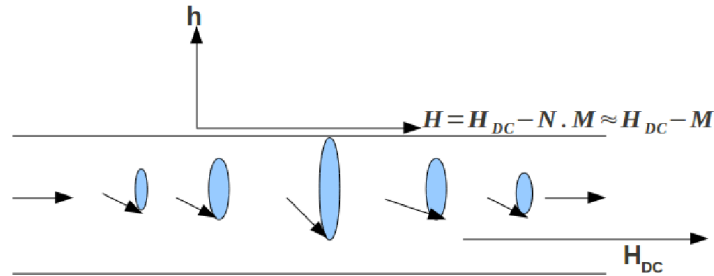
Figure 3: Standing spin wave resonance in a magnetic thin film. The precession cone angle of the magnetization has been exaggerated for clarity. N is the demagnetizing tensor. It was assumed that the applied field, H_{DC}, is strong enough to saturate the stripe so that M_s is parallel to H_{DC}, everywhere.
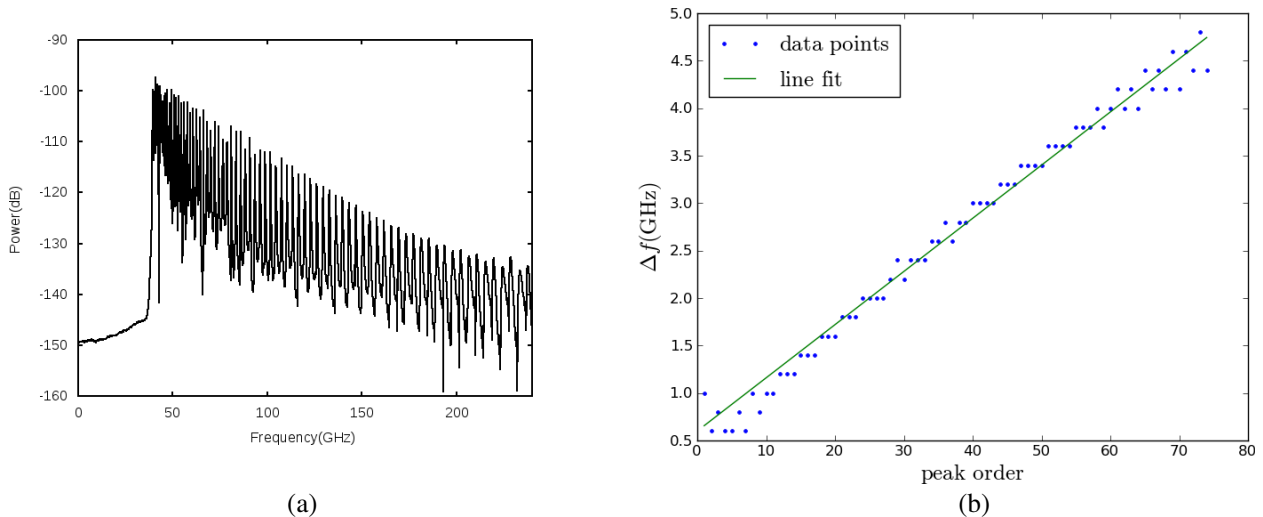
Figure 4: (a) The power spectrum at $k = 0.55\,\text{rad/nm}$ and (b) frequency separation (Δf) dependence on mode order (n_x) with a linear fit to the equation $\Delta f = 57.53n + 523.88\,\text{MHz}$, with $R^2 = 0.98$.

4. RADIATION RESISTANCE

Radiation resistance determines the amount of power transferred between the current in a microstrip transducer and the excited SWs. For the lowest order BVSW mode [13],

$$r_{\text{rad}}(\omega) = \frac{\omega \mu_0}{k_x c} \sin^2 \left[\frac{k_x c}{2 \sqrt{-(1+\chi)}} \right] \left| \frac{F}{I} \right|^2. \tag{7}$$

The array factor

$$F = I e^{-k_x s} J_0 \left(\frac{k_x w'}{2} \right), \tag{8}$$

where J_0 is the zeroth Bessel function, $s = 6\,\text{nm}$ is the spacing of the of the current filament from the film, I is the current carried by the conductor, $w' = 10\,\text{nm}$ is the width of the current filament and the susceptibility χ is given by

$$\chi = \frac{\omega_{\text{ex}} \omega_M}{\omega_{\text{ex}}^2 - \omega^2}. \tag{9}$$

To calculate $r_{\text{rad}}(\omega)$, we must first estimate ω_0 and λ_{ex}.

The dispersion curve for the lowest order BVSW, in an infinite film, is approximated as [14]

$$\omega = \sqrt{\omega_{\text{ex}} \cdot \left(\omega_{\text{ex}} + \omega_M \frac{1 - e^{-k_x c}}{k_x c} \right)}, \tag{10}$$

where

$$\omega_{\text{ex}} = \gamma \mu_0 H_{\text{DC}} + \frac{2\gamma A}{M_s} k_x^2 = \omega_0 + \lambda_{\text{ex}} \omega_M k^2. \tag{11}$$

When can fit the (ω, k_x) dispersion curve in Fig. 2, to (10), we obtain the values $\omega_0 = 2.21 \times 10^{11}\,\text{rad/s}$ and $\lambda_{\text{ex}} = 2.61 \times 10^{-17}\,\text{m}^2$.

Figure 5 shows a minima in $r_{\text{rad}}(f)$ at 217 GHz. This corresponds to the zero of the Bessel function in (8). The position of this zero can be shifted by considering current filaments of different widths.

The return loss, for a microstrip transducer (in our case the current carrying conductor), is defined as [13]

$$RL = -10 \log \left[\frac{(R_c + R_{\text{rad}} - R_g)^2 + (X_l + X_{\text{rad}})^2}{(R_c + R_{\text{rad}} + R_g)^2 + (X_l + X_{\text{rad}})^2} \right], \tag{12}$$
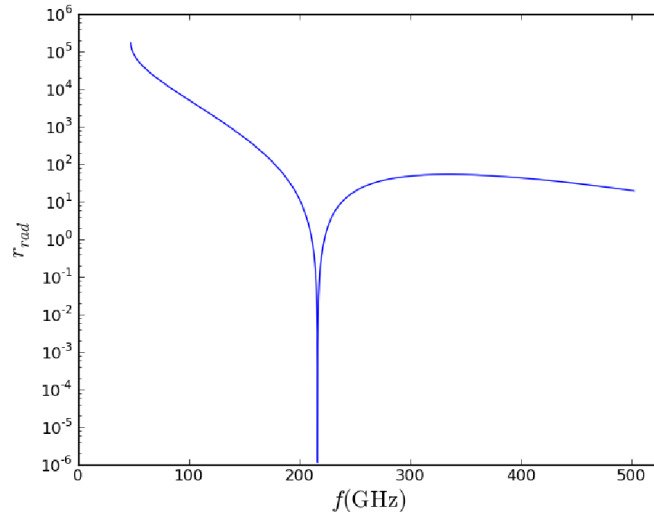
Figure 5: Frequency dependence of radiation resistance per unit length for exchange dominated BVSWs.

where R_c is the resistance from the finite conductivity of the transducer, R_{rad} and X_{rad} are the radiation resistance and reactance resulting from coupling to spin waves, X_l is the inductive reactance of the microstrip transducer in the absence of dipolar spin wave coupling and R_g is the input impedance if the transducer is modelled as a transmission line. Here $R_{\text{rad}} = r_{\text{rad}} \times L_{\text{fil}}$ where L_{fil} is the length of the microstrip transducer. With $L_{\text{fil}} = b = 50\,\text{nm}$, $R_{\text{rad}} \ll \{R_c, R_g\}$. Therefore, RL shows no significant frequency dependence and the return loss will be largely determined by the impedance characteristics of the external circuitry connected to the microstrip transducer.

5. CONCLUSION

We have shown how micromagnetic simulations can be used to obtain valuable information about the exchange splitting of the dispersion curve and the radiation resistance of the structure. The effects of exchange can be extracted by looking at SW resonances in the transmission characteristics, and the value of λ_{ex} thus extracted seems to agree with the values used as input to the simulation. This provides a validation of the method used to obtain the SW dispersion relation.

Excitation of SWs using an Oersted field would be a possible experimental geometry. The radiation resistance of SWs helps design transducers with proper impedance matching characteristics. r_{rad} was estimated from $\omega(k)$, and was found to have a minimum at 217 GHz. However, we would need to know the impedance characteristics of the microstrip transducer fairly accurately before we can estimate return and insertion losses in an experiment.

ACKNOWLEDGMENT

REFERENCES

1. Damon, R. and J. Eshbach, "Magnetostatic modes of a ferromagnet slab," *J. Phys. Chem. Solids*, Vol. 19, 308–320, 1961.
2. Damon, R. W. and H. Van De Vaart, "Propagation of magnetostatic spin waves at microwave frequencies in a normally-magnetized disk," *J. Appl. Phys.*, Vol. 36, 3453–3459, 1965.
3. Khitun, A., M. Bao, and K. Wang, "Spin wave magnetic nanofabric: A new approach to spin-based logic circuitry," *IEEE Trans. Magn.*, Vol. 44, 2141–2152, 2008.
4. Khitun, A., D. E. Nikonov, M. Bao, K. Galatsis, and K. L. Wang, "Feasibility study of logic circuits with a spin wave bus," *Nanotechnology*, Vol. 18, 465202, 2007.
5. Kim, S.-K., "Micromagnetic computer simulations of spin waves in nanometre-scale patterned magnetic elements," *J. Phys. D: App. Phys.*, Vol. 43, 264004, 2010.
6. Kruglyak, V. V. and R. J. Hicken, "Magnonics: Experiment to prove the concept," *J. Magn. Magn. Mater.*, Vol. 306, 191–194, 2006.
7. Dvornik, M. and V. V. Kruglyak, "Dispersion of collective magnonic modes in stacks of nanoscale magnetic elements," *Phys. Rev. B*, Vol. 84, 140405, Oct. 2011.
8. Gilbert, T., "A phenomenological theory of damping in ferromagnetic materials," *IEEE Trans. Magn.*, Vol. 40, 3443–3449, 2004.
9. Fischbacher, T., et al., "A systematic approach to multiphysics extensions of finite-element-based micromagnetic simulations: N_{mag}," *IEEE Trans. Magn.*, Vol. 43, 2896–2898, 2007.
10. Kajiwara, Y., et al., "Transmission of electrical signals by spin-wave interconversion in a magnetic insulator," *Nature*, Vol. 464, 262–266, 2010.
11. Venkat, G., et al., "Proposal for a standard micromagnetic problem: Spin wave dispersion in a magnonic waveguide," *IEEE Trans. Magn.*, submitted for publication.
12. Kalinikos, B. and A. N. Slavin, "Theory of dipole-exchange spin wave spectrum for ferromagnetic films with mixed exchange boundary conditions," *J. Phys. C: Solid Sate Phys.*, 19, 1986.
13. Stancil, D. D. and A. Prabhakar, *Spin Waves Theory and Applications*, 1st Edition, Springer, New York, 2008.
14. Kalinikos, B. A., "Excitation of propagating spin waves in ferromagnetic films," *IEE Proc.*, Vol. 127, 4, 1980.

A Computational Study of the Coupled Emissions between Flurophores and Gold Triangular Prism Bow Tie

A. Centeno, **F. Xie**, and **N. Alford**

Department of Materials, Imperial College London, SW7 2AZ, United Kingdom

Abstract— Amplification of light from reporter fluorophores is a promising strategy to further increase the sensitivity of fluorescence based biosensing. One such enhancement system is metal induced fluorescence enhancement (MIFE). The enhanced fluorescence intensity due to the presence of metal nanostructures makes it possible to detect much lower levers of proteins tagged with fluorescence molecules. This paper reports work undertaken on the emission enhancement possible from triangular elements in the bow-tie configuration. The results show that emission enhancement is possible over a long distance ($\sim 50\,\mathrm{nm}$).

1. INTRODUCTION

There has been much recent interest and large amounts of literature on localized surface plasmon resonance (LSPR) in metal nanoparticles and their applications (see for example [1–6]), whilst Fluorescence based approaches are gaining prominence for clinical assays due to their sensitivity and the increasing availability of various fluorescent molecules capable of biospecific recognition. Amplification of light from reporter fluorophores is a promising strategy to further increase the sensitivity of fluorescence based biosensing. One such enhancement system is metal induced fluorescence enhancement (MIFE) [7–12]. The enhanced fluorescence intensity due to the presence of metal nanostructures makes it possible to detect much lower levels of proteins tagged with fluorescence molecules.

There are three mechanisms involved in MIFE; electric field enhancement at the absorption wavelength, emission enhancement and quenching, both at the emission wavelength of the fluorophore. The metal nanostructures are chosen with dimensions and materials such that the LSPR is close to the absorption and emission of the fluorophore. In this paper, we report on the calculated emission enhancement when a fluorophore is located between the tips of two Au triangular prisms in a bow-tie configuration and compare with the extinction spectrum. Figure 1 depicts the bow tie configuration with the dimensions considered in our calculations.

The calculations were carried out using the Finite Difference Time Domain (FDTD) technique [13]. The Au was modeled using the complex dielectric function $\varepsilon(\omega)$:

$$\varepsilon(\omega) = \varepsilon_1(\omega) + \varepsilon_2(\omega) \tag{1}$$

The intraband part of the dielectric function $\varepsilon_1(\omega)$ is described by the Drude model for conductors and the interband part $\varepsilon_2(\omega)$ by the Lorentz model for insulators. The combined Drude-Lorentz model for metal permittivity can be described by [14]:

$$\varepsilon(\omega) = \varepsilon_\infty + \sum_{i=1}^{n} \frac{\sigma_i \omega_p^2}{\omega_i^2 - \omega^2 - \omega \Gamma_j} \tag{2}$$

We have considered spheres of Au using five terms in the summation, where $\varepsilon_\infty = 1$, the plasma frequency $\omega_p = 9.03$, the oscillators' strength $f = [0.760, 0.024, 0.010, 0.071, 0.604, 4.384]$, the damping frequency of each oscillation Γ in eV $= [0.053, 0.241, 0.345, 0.870, 2.494, 2.214]$ and the resonant frequency of each oscillator in eV $= [0.000, 0.415, 0.0830, 2.969, 4.304, 13.32]$.

2. SCATTERING AND EFFICIENCY CALCULATIONS

If we now define a surface that fully encloses the scattering object then by considering the total field flowing though it we can calculate Q_{abs} [15]:

$$Q_{abs} = \frac{-\int\limits_{s} \mathrm{Re}\left(\frac{1}{2}\vec{E} \times \vec{H}^*\right) d\vec{a}}{|S_i|} \tag{3}$$
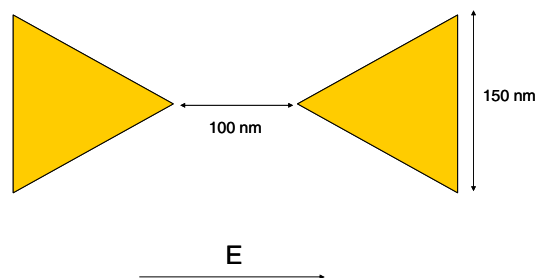
Figure 1: Bow-tie configuration considered. The incident electric field is normal to the upper surface and polarized in the direction shown.
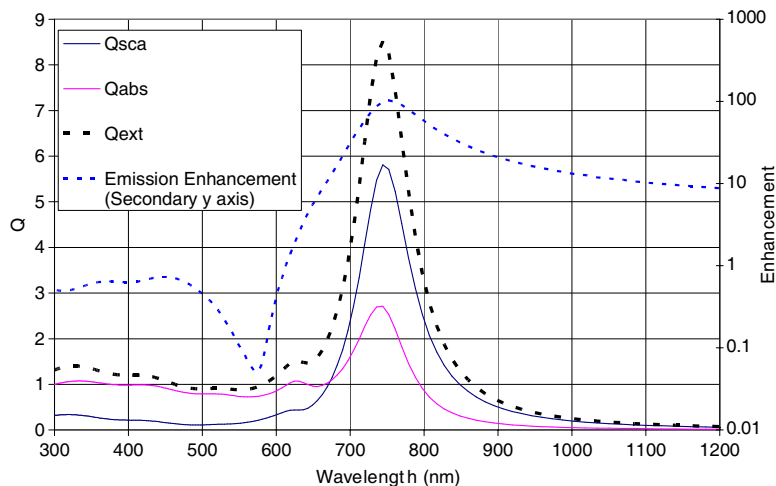
Figure 2: FDTD calculations of scattering (Qsca), absorption (Qabs), extinction (Qext = Qsca + Qabs) and radiated emission enhancement, secondary y-axis (Logarithmic scale).

and by considering the scattered field [15]:

$$Q_{sca} = \frac{\int\limits_s \mathrm{Re}\left(\frac{1}{2}\vec{E}_s \times \vec{H}_s^*\right) d\vec{a}}{|S_i|} \qquad (4)$$

Using computational electromagnetics to calculate the power flow (Poynting vector) through a surface enclosing the triangles Equations (3) and (4) can be solved. Our FDTD algorithm uses a total field formulism so to obtain Q_{sca} the power flow through the surface must be found without the scattering objects present and subtracted from the total field through the surface.

3. RADIATED EMISSION CALCULATIONS

When calculating the radiated emission enhancement the fluorophore is considered to be a small dipole, 1 nm in our calculations, which is in the proximity of the one or both of the triangular elements. The procedure used in our calculations considers the normal power flow out of a closed surface around the triangles, as described in detail in reference [16]. The radiated emission enhancement is given by the ratio of radiated power with the dipole in the proximity of the nanoparticle to the power radiated when the point dipole is isolated in free space, P_r/P_o [16]. In our calculations we place the dipole midway between the two triangles and polarize normal to the tips of the triangles, as depicted in Figure 1.

4. RESULT AND DISCUSSION

The computed results obtained using FDTD modeling between 300 and 1200 nm, for both scattering and absorption efficiencies and radiated emission from a dipole are shown in Figure 2. They show that the emission enhancement is a maximum at the same wavelength as the peak scattering efficiency and so couples strongly with what could be considered a dipole like Localised Surface

Plasmon Resonance (LSPR) mode in the triangle. It can also be seen that there is a sharp minima at around 580 nm where $P_r/P_o < 1$. This mode is not seen on the scattering or absorption efficiency plots.

It is interesting to note that even for this quite large separation of triangles (100 nm) and relatively long distance from the triangle surfaces there is maximum emission enhancement of more than 10^2. This indicates that using bow-tie elements the MIFE mechanisms can be over comparatively long distances; more than 50 nm compared and could be quite large.

ACKNOWLEDGMENT

REFERENCES

1. Atwater, H. A. and A. Polman, "Plasmonics for improved photovoltaic devices," *Nature Materials*, Vol. 9, 205–213, 2010.
2. Centeno, A., B. Ahmed, J. D. Breeze, H. Reehal, and N. Alford, "Scattering of light into silicon by spherical and hemispherical silver nanoparticles," *Optics Letters*, Vol. 35, No. 1, Vol. 76–78, 2010.
3. Willets, K. A. and R. P. V. Duyne, "Localised surface plasmon resonance spectroscopy and sensing," *Annu. Rev. Phys. Chem.*, Vol. 58, 267–297, 2007.
4. Evanoff, D. D. and G. Chumanov, "Synthesis and optical properties of silver nanoparticles and arrays," *Chem. Phys. Chem.*, Vol. 6, 1221–1231, 2005.
5. Centeno, A., F. Xie, J. D. Breeze, and N. Alford, "Electromagnetic design of solar collectors," *PIERS Online*, Vol. 7, No. 4, 376–379, 2011.
6. Centeno, A., F. Xie, and N. Alford, "Localized field and absorption due to two dimensional arrays of noble metal nanoparticles," *Journal Optical Society of America B: Optical Physics*, 2011.
7. Geddes, C. D. and J. R. Lakowicz, "Metal-enhanced fluorescence," *Journal of Fluorescence*, Vol. 12, No. 2, 121–129, 2002.
8. Goldys, E. M. and F. Xie, "Metallic nanomaterials for sensitivity enhancement of fluorescence detection," *Sensors*, Vol. 8, 886–896, 2008.
9. Cheng, Y., T. Stakenborg, P. van Dorpe, L. Lagae, M. Wang, H. Chen, and G. Borghs, "Fluorescence near gold nanoparticles for DNA sensing," *Anal. Chem.*, Vol. 83, 1307–1314, 2011.
10. Xie, F., M. S. Baker, and E. M. Goldys, "Enhanced fluorescence detection on homogeneous gold colloid self-assembled monolayer substrates," *Chem. Mater.*, Vol. 20, 1788–1797, 2008.
11. Zhang, Y., A. Dragan, and C. D. Geddes, "Wavelength dependence of metal-enhanced fluorescence," *J. Phys. Chem. C*, Vol. 113, 12095–12100, 2009.
12. Xie, F., M. S. Baker, and E. M. Goldys, "Homogeneous silver-coated nanoparticle substrates for enhanced fluorescence detection," *J. Phys. Chem.*, Vol. 110, 23085–23091, 2006.
13. Oskooi, A. F., D. Roundy, M. Ibanescu, P. Bermel, J. D. Joannopoulos and S. G. Johnson, "MEEP: A flexible free-software package for electromagnetic simulations by the FDTD method," *Comput. Phys. Commun.*, Vol. 181, 687–702, 2010.
14. Rakic, A. D., A. B. Djurisic, J. M. Elavar, and M. L. Majewski, "Optical properties of metallic films for vertical-cavity optoelectronic devices," *Appl. Opt.*, Vol. 37, 5271–5283, 1998.
15. Camacho, L. M., L. Mingyu, and S. Tjuatja, "Study of emissions from finite-size objects using FDTD," *IEEE International Symposium on Geoscience and Remote Sensing*, Vol. 1, 1153–1156, 2008.
16. Chowdhury, M. H., J. Pond, S. K. Gray, and J. R. Lakowicz, "Systematic computational study of the effect of silver nanoparticle dimmers on the coupled emissions from nearby fluorophores," *J. Phys. Chem. C*, Vol. 112, 11236–11249, 2008.

Blocking Oscillation Due to Combination of Discrete and Continuous Charge/Flux Transfer in Systems Including Nano/Josephson Tunnel Junctions

Yoshinao Mizugaki

The University of Electro-Communications (UEC Tokyo), Japan

Abstract— Nanotechnology enables us to manipulate a single electron in solid-state circuits. Single-electron tunneling is known to transfer electric charge in units of the fundamental charge e through tiny (nano-scale) tunnel junctions. So far, many single-electron devices, such as a single-electron transistor, a single-electron turnstile, and a single-electron pump, have been proposed and demonstrated. The author proposes a blocking oscillator composed of tiny tunnel junctions and a dissipative element (resistor). The key is the combination of the discrete and continuous charge transfer. Monte-Carlo simulation demonstrates blocking oscillation of an island charge. Similar blocking oscillation occurs in a superconducting loop including Josephson junctions and a resistor. Electromagnetic duality between single-electron devices and superconducting Josephson devices are observed in these results. In this paper, the author numerically demonstrates these blocking oscillation phenomena and discuss the possibility of experimental observation.

1. INTRODUCTION

It is commonly understood that electric current in a metal wire is carried by electrons. Because the number of electrons is huge, electric current is considered to be continuous. It is valid if the system is macroscopic. However, if the system is microscopic or mesoscopic, we sometimes need to handle not continuous electric current but discrete electrons.

In fact, recent progress of nanofabrication techniques has enabled us to manipulate a single electron in solid-state circuits [1]. Single-electron tunneling based on the Coulomb blockade is realized in tiny (nano-scale) tunnel junctions when the following conditions are satisfied: $e^2/2C \gg k_B T$ and $R_t \gg R_Q \equiv h/e^2$, where e, C, k_B, T, R_t, R_Q, and h are the fundamental charge, tunnel capacitance, Boltzmann constant, absolute temperature, tunnel resistance, quantum resistance, and Planck constant, respectively. A single-electron transistor composed of two tiny tunnel junctions and a capacitive gate is known as a ultra-sensitive charge sensor [2]. Systems including more than three tiny tunnel junctions can transfer a single-electron one by one, known as a single-electron turnstile [3] and a single-electron pump [4].

On the other hand, a single flux quantum in a superconducting loop can be used as a bit carrier in superconducting Josephson electronics [5]. Interestingly, electromagnetic duality can be found between single-electron devices and single-flux-quantum devices [2]. Although the duality is phenomenological and imperfect, it sometimes helps us to develop a new device. Examples are an RF single-electron transistor [6] dual to an RF superconducting quantum interference device (RF-SQUID), a single-flux-quantum pump [7] dual to a single-electron pump, and a single-electron current mirror [8] dual to a single-flux-quantum voltage mirror.

In this paper, the author describes numerical results of a single-electron blocking oscillator [9] and a single-flux-quantum blocking oscillator [10], both of which have been proposed recently. The key is the combination of the discrete and continuous charge/flux transfer.

2. CONFIGURATION OF BLOCKING OSCILLATORS

2.1. Single-electron Blocking Oscillator

The author has proposed a blocking oscillator composed of tiny tunnel junctions and a dissipative element (resistor) [9], of which configuration is shown in Figure 1(a). Because of charge leakage through the resistive path, the island charge Q_0 becomes continuous, whereas single-electron tunneling events through the junctions carry fundamental charges into/from the island electrode discretely. Combination of continuous and discrete charge transfer eventually shifts the operation point into the Coulomb blockade, resulting in blocking oscillation.
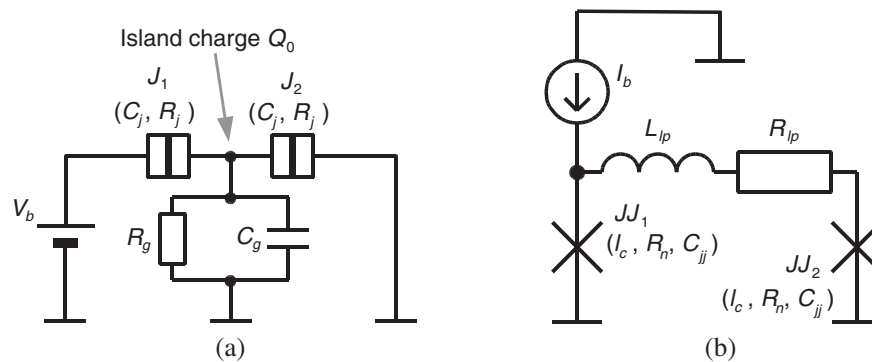
Figure 1: Blocking oscillators utilizing combination of discrete and continuous chrage/flux transfer. (a) Single-electron blocking oscillator comprising series array of two tiny tunnel junctions with capacitive and resistive ground paths from its island electrode. C_j and R_j are the junction capacitance and junction resistance, respectively. (b) Single-flux-quantum blocking oscillator comprising parallel array of two Josephson junctions connected via a superconducting inductor and a resistor. I_c, R_n, and C_{jj} are the superconducting critical current, junction resistance, and junction capacitance, respectively.
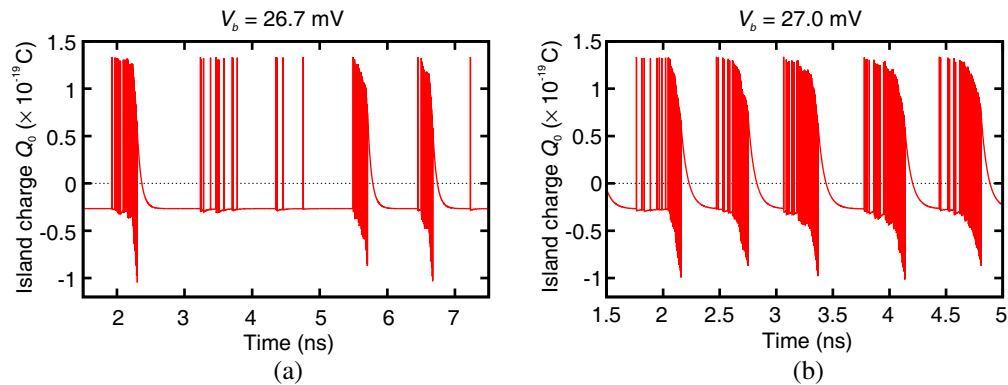
Figure 2: Numerical waveforms of the island charge. C_j, R_j, C_g, and R_g are set at $1\,\mathrm{aF}$, $100\,\mathrm{k\Omega}$, $1\,\mathrm{aF}$, and $20\,\mathrm{M\Omega}$, respectively. Absolute zero temperature and no cotunneling processes are assumed. V_b is set at (a) $26.7\,\mathrm{mV}$ and (b) $27.0\,\mathrm{mV}$.

2.2. Single-flux-quantum Blocking Oscillator

A single-flux-quantum blocking oscillator [10] dual to the single-electron blocking oscillator is presented in Figure 1(b). The flux in the JJ_1-L_{lp}-R_{lp}-JJ_2 loop is continuously changing toward zero due to the resistive element R_{lp}, whereas switching events of the Josephson junctions (JJ_1 and JJ_2) transfer flux quanta into/from the loop discretely. Combination of continuous and discrete flux transfer eventually moves the operation point into the superconducting state, resulting in blocking oscillation.

3. NUMERICAL RESULTS

3.1. Waveforms of Island Charge in Single-electron Blocking Oscillator

Two examples of the island charge evolution in the single-electron blocking oscillator are shown in Figure 2. Simulation was carried out using a simulator for single-electron devices and circuits (SIMON) on the basis of the Monte Carlo method [11].

Blocking oscillation can be confirmed in both results, whereas sporadic single-electron tunneling events are seen for the lower bias condition in Figure 2(a), at the time durations from $3\,\mathrm{ns}$ to $5\,\mathrm{ns}$ and from $7\,\mathrm{ns}$ to $7.5\,\mathrm{ns}$. Since single-electron tunneling events are stochastic, intervals among events are not constant in both Figures 2(a) and 2(b). Especially at low bias conditions, time intervals vary widely, resulting in sporadic events.

3.2. Waveforms of Junction Voltages in Single-flux-quantum Blocking Oscillator

Waveforms of the junction voltages in the single-flux-quantum blocking oscillator are shown in Figure 3. For discussion on the voltages across the junctions below, not the magnetic flux in the loop but the junction voltages are presented. Simulation was carried out using a Josephson integrated circuit simulator (JSIM) [12]. The voltage V across a Josephson junction is expressed

as $V = (\Phi_0/2\pi)(\partial\phi/\partial t)$, where Φ_0 and ϕ are the flux quantum and the quantum phase difference across the junction, respectively.

The numbers of junction switching in JJ_1 and JJ_2 in one period of blocking oscillation are rather small in these conditions: the numbers of switching in one period are 2 in JJ_1 and 1 in JJ_2 for Figure 3(a), and those are 3 in JJ_1 and 2 in JJ_2 for Figure 3(b). The switching number in JJ_1 is one greater than that in JJ_2, which is a feature of the single-flux-quantum blocking oscillator [10].

Differently from the results in Figure 2, the blocking oscillation is deterministic and periodic, which demonstrates imperfect duality between single-electron devices and single-flux-quantum devices.

4. EVIDENCE OF BLOCKING OSCILLATION OBTAINED FROM STATIC CHARACTERISTICS

It can be seen in Figures 2 and 3 that the signals from the blocking oscillators are rather small and fast. The RF-SET technique [6] and the Josephson sampling technique [13, 14] would be applied to detect such signals, although each of them is a challenging task.

Here, the author proposes an indirect measurement method of blocking oscillation in the single-flux-quantum blocking oscillator. A voltage waveform across a Josephson junction is a pulse train as shown in Figure 3. In experiments, however, pulses are smeared through conventional low-bandwidth equipments, and the average voltage expressed as $\langle V \rangle = \Phi_0 f$ is measured, where f is the number of pulses per unit time (the pulse repetition frequency). In other words, the number of pulses per unit time can be obtained by measuring the average voltage. Thus, the average voltage across JJ_1 in Figure 3(a) is twice as large as that across JJ_2. In Figure 3(b), the average voltage ratio for JJ_1 to JJ_2 becomes $3/2 (= 1.5)$.

The current (I_b)-average voltage ($\langle V \rangle$) characteristics, calculated using the device parameters described in Figure 3, are shown in Figure 4(a). These characteristics are those obtained by means of quasi-static (low-bandwidth) measurements. Several step structures can been seen, which will be explained later.
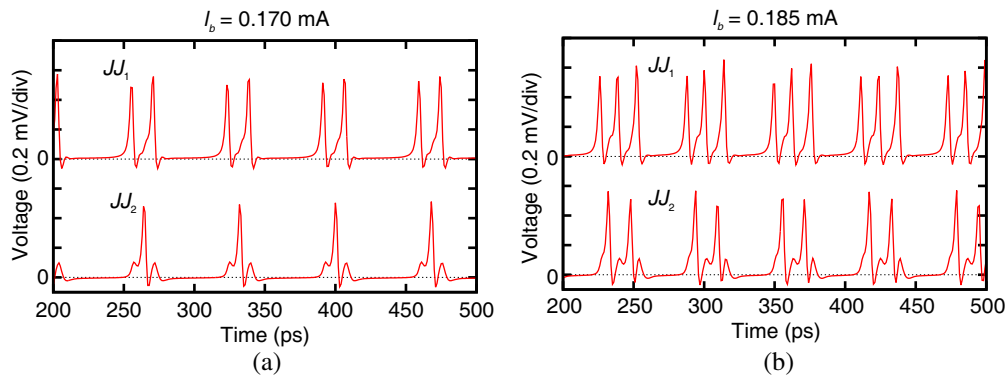
Figure 3: Numerical waveforms of the junction voltages. I_c, R_n, C_{jj}, L_{lp}, and R_{lp} are $0.10\,\text{mA}$, $3.8\,\Omega$, $0.22\,\text{pF}$, $20\,\text{pH}$, and $0.38\,\Omega$, respectively. Absolute zero temperature is assumed. I_b is set at (a) $0.170\,\text{mA}$ and (b) $0.185\,\text{mA}$.
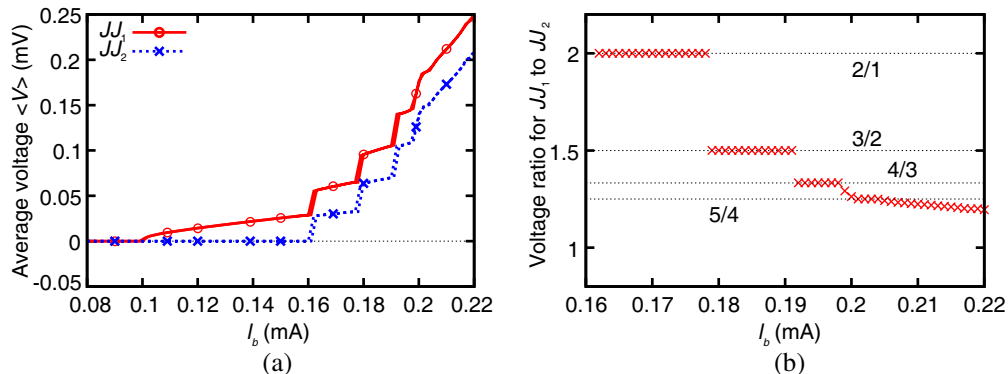
Figure 4: (a) Current (I_b)-average voltage ($\langle V \rangle$) characteristics across JJ_1 and JJ_2. (b) The voltage ratio for JJ_1 to JJ_2 plotted as functions of I_b.

The voltage ratio for JJ_1 to JJ_2 is plotted in Figure 4(b) as functions of I_b. The constant voltage ratios of 2/1, 3/2, 4/3, and 5/4 can be confirmed. These voltage ratios directly correspond to the ratios of the pulse numbers per unit time. That is, the blocking oscillation in the mode of "2 switching events in JJ_1 and 1 switching event in JJ_2" appears as the voltage ratio of 2/1, that of "3 in JJ_1 and 2 in JJ_2" appears as the voltage ratio of 3/2, and so on. The step structures in Figure 4(a) correspond to the boundaries between the oscillation modes.

According to these results, it is possible to obtain an evidence of blocking oscillation in the single-flux-quantum blocking oscillator by means of quasi-static measurements.

5. CONCLUSION

In this paper, the author presented the single-electron blocking oscillator and the single-flux-quantum blocking oscillator. Numerical simulation demonstrated the waveforms of blocking oscillation in both. Some electromagnetic duality was confirmed between the two blocking oscillators, although it was not perfect. Since the blocking oscillation in the single-flux-quantum blocking oscillator was deterministic and periodic, it would be confirmed by measuring quasi-static current-voltage characteristics using conventional low-bandwidth equipments.

REFERENCES

1. Likharev, K. K., "Single-electron devices and their applications," *Proc. IEEE*, Vol. 87, 606–632, 1999.
2. Likharev, K. K., "Single-electron transistors: Electrostatic analogs of the dc SQUIDs," *IEEE Trans. Magn.*, Vol. 23, 1142–1145, 1987.
3. Geerligs, L. J., V. G. Anderegg, P. A. M. Holweg, J. E. Mooij, H. Pothier, D. Esteve, C. Urbina, and M. H. Devoret, "Frequency-locked turnstile device for single electron," *Phys. Rev. Lett.*, Vol. 64, 2691–2694, 1990.
4. Pothier, H., P. Lafarge, C. Urbina, D. Esteve, and M. H. Devoret, "Single electron pump based on charging effects," *Europhys. Lett.*, Vol. 17, 249–254, 1992.
5. Hayakawa, H., N. Yoshikawa, S. Yorozu, and A. Fujimaki, "Superconducting digial electronics," *Proc. IEEE*, Vol. 92, 1549–1563, 2004.
6. Schoelkopf, R. J., P. Wahlgren, A. A. Kozhevnikov, P. Delsing, and D. E. Prober, "The radio-frequency single-electron transistor (RF-SET): A fast and ultrasensitive electrometer," *Science*, Vol. 280, 1238–1242, 1998.
7. Mizugaki, Y., J. Chen, S. Nishikata, K. Sugi, K. Nakajima, and T. Yamashita, "Single-flux-quantum pump based on a three-junction superconducting quantum interference device," *Appl. Phys. Lett.*, Vol. 80, 4585–4587, 2002.
8. Mizugaki, Y., M. Itoh, and H. Shimada, "Current correlation in single-electron current mirror electromagnetically dual to josephson voltage mirror," *Jpn. J. Appl. Phys.*, Vol. 46, Part 1, 6237–6242, 2007.
9. Mizugaki, Y., "Blocking charge oscillation in a series array of two tiny tunnel junctions with a resistive ground path from its island electrode," *IEEE Trans. Nanotechnol.*, (to be published. DOI: 10.1109/TNANO.2011.2169984).
10. Mizugaki, Y., "Numerical demonstration of relaxation oscillation in a resistive superconducting quantum interference device with two nonhysteretic Josephson junctions," *IEEE Trans. Appl. Supercond.*, Vol. 20, 2322–2326, 2010.
11. Wasshuber, C., *Computational Single-Electronics*, Springer-Verlag, Heidelberg, 2001.
12. Fang, E. S. and T. Van Duzer, "A Josephson integrated circuit Simulator (JSIM) for superconductive electronics application," *Extended Abstracts of 1989 International Superconductivity Electronics Conference*, 407–410, Tokyo, Japan, Jun. 1989.
13. Faris, S. M., "Generatin and measurement of ultrashort current pulses with Josephson devices," *Appl. Phys. Lett.*, Vol. 36, 1005–1007, 1980.
14. Tuckerman, D. B., "A Josephson ultrahigh-resolution sampling system," *Appl. Phys. Lett.*, Vol. 36, 1008–1010, 1980.

Calculation of the Acoustomagnetoelectric Field in a Rectangular Quantum Wire with an Infinite Potential in the Presence of an External Magnetic Field

N. V. Nghia, **N. Q. Bau**, **N. V. Nhan**, and **D. Q. Vuong**

Department of Physics, College of Natural Sciences, Hanoi National University, Hanoi, Vietnam

Abstract— The acoustomagnetoelectric (AME) effect in a rectangular quantum wire (RQW) with an infinite potential is investigated in the presence of an external magnetic field (EMF). The analytic expression for the AME field in a RQW with an infinite potential is calculated by using the quantum kinetic equation for the distribution function of electrons interacting with external phonons. The dependence of AME field on the acoustic wave number q, the temperature of the system T and the intensity of the external magnetic field H are obtained. The analytic expression for the AME field is numerically evaluated, plotted and discussed for the specific RQW with an infinite potential GaAs. The dependence of the AME field on the temperature of the system is significantly reduced in the low temperature region and it is approximately constant in the high temperature region. In the dependence of the AME field on the intensity of the EMF, the AME field can get the small peaks corresponding to the resonance frequency of the cyclotron-electron-acoustic phonon. The results are compared with those for normal bulk semiconductors and superlattices to show the difference.

1. INTRODUCTION

In recent times, there have been more and more interests in studying and discovering the behavior of low-dimensional system, in particular, one-dimensional systems, such as quantum wire. In quantum wires, the motion of electrons is restricted in two dimensions, so that they can flow freely in one dimension. The confinement of electron in these systems has changed the electron mobility remarkably. This has resulted in a number of new phenomena, which concern a reduction of sample dimensions. These effects differ from those in bulk semiconductors, for example, electron-phonon interaction and scattering rates [1] and acoustic-electromagnetic wave interaction [2].

It is well known that the propagation of the acoustic wave in conductors is accompanied by the transfer of the energy and momentum to conduction electrons. This leads to the emergence of a longitudinal acoustoelectric effect, i.e., a stationary electric current running in a sample in the direction opposite to that of the wave. Presently this effect has been studied in detail both theoretically and experimentally and has found wide application in radioelectrionic systems [3–10]. In the presence of an EMF the acoustic wave is propagated in the conductor can produce another effect called the acoustomagnetoelectric (AME) effect. It was predicted by Galperin and Kagan [11] and later observed experimentally in bismuth [12]. In addition, the quantum AME effect due to the Rayleigh sound waves was investigated in a bulk semiconductor [13, 14], the AME effect was also studied in a monopolar semiconductor [15] for both the case of the weak magnetic field region and the quantizing magnetic field region, a superlattice [16] and a cylindrical quantum wire (CQW) with an infinite potential [17] only the case of the weak magnetic field region. However, the AME effect in the RQW with an infinite potential has not been studied yet. Therefore, the purpose of this work is to examine this effect in the RQW with an infinite potential for the case the quantizing magnetic field region.

In this paper, we present a calculation of the AME field in a RQW with an infinite potential by using the quantum kinetic equation for the distribution function of electrons interacting with external phonons. We assumed the deformation mechanism of electron-acoustic phonon interaction. We have obtained the AME field in the RQW with an infinite potential in the presence of an EMF. The dependence of the expression for the AME field on acoustic wave numbers q, the temperature of the system T and the intensity H of the EMF has been shown. Numerical calculations are carried out a specific the RQW with an infinite potential GaAs to clarify our results.

2. ANALYTIC EXPRESSION FOR THE ACOUSTOMAGNETOELECTRIC FIELD IN A RECTANGULAR QUANTUM WIRE WITH AN INFINITE POTENTIAL

Let us suppose that the acoustic wave of frequency ω_q is propagating along the RQW with an infinite potential axis (Oz) and the magnetic field is oriented along the Ox axis. We consider the most

realistic case from the point of view of a low-temperature experiment, when $\omega_q/\eta = \nu_s|q|/\eta \ll 1$ and $ql \gg 1$, where v_s is the velocity of the acoustic wave, q is the acoustic wave number and l is the electron mean free path. The compatibility of these conditions is provided by the smallness of the sound velocity in comparison with the characteristic velocity of the Fermi electrons.

When the magnetic field is applied in the x-direction, in the case of the vector potential is chose $A = A_y = -zH$, the eigenfunction of an unperturbed electron is expressed as

$$\psi_{n,N,\vec{p}}(\vec{r}) = \frac{2}{\sqrt{abL}} \sin\left(\frac{n\pi}{a}x\right) \sin\left(\frac{N\pi}{b}y\right) \exp\left(i\frac{p_z}{\hbar}z\right). \tag{1}$$

where a and b are, respectively, the cross-sectional dimensions along x- and y-directions, n, N are the subband indexes, L is the length of the wire, and $\vec{p} = (0, 0, p_z)$ is the electron momentum vector along z-direction The electron energy spectrum takes the form

$$\varepsilon_{n,N,\vec{p}} = \frac{\hbar^2\pi^2 n^2}{2ma^2} + \frac{\hbar^2\pi^2 N^2}{2mb^2} + \frac{p_z^2}{2m}. \tag{2}$$

If the conditions $\omega_q/\eta = \nu_s|q|/\eta \ll 1$ and $ql \gg 1$ are satisfied, a macroscopic approach to the description of the acoustoelectric effect is inapplicable and the problem should be treated by using quantum mechanical methods. We also consider the acoustic wave as a packet of coherent phonons. Therefore, we have to first find the Hamiltonian describing the interaction of the electron-phonon system in the RQW with an infinite potential, which can be written in the secondary quantization representation as

$$H = \sum_{n,N,\vec{k}} \varepsilon_{n,N,\vec{p}} a^+_{n,N,\vec{k}} a_{n,N,\vec{k}} + \sum_{n,N,n',N'} C_{\vec{q}} U_{n,N,n',N'}(q) a^+_{n',N',\vec{k}} a_{n',N',\vec{k}+\vec{q}} b_{\vec{q}} \exp(-i\omega_{\vec{q}}t). \tag{3}$$

where $C_{\vec{q}}$ is the electron-external phonon interaction factor and takes the form [14]

$$C_{\vec{q}} = \frac{i\Lambda c_l^2}{q} \left(\frac{\hbar\omega_{\vec{q}}^3}{2\rho S}\right)^{\frac{1}{2}} \left[\frac{1+\sigma_l^2}{2\sigma_t} + \left(\frac{\sigma_l}{\sigma_t} - 2\right)\frac{1+\sigma_t^2}{2\sigma_t}\right]^{-1}, \tag{4}$$

with $\sigma_l = (1 - v_s^2/c_l^2)^{1/2}$, $\sigma_t = (1 - v_s^2/c_t^2)^{1/2}$, is the deformation potential constant, $a^+_{n,N,\vec{k}}$ and $a_{n,N,\vec{k}}$ are the creation and the annihilation operators of the electron, respectively, and $b_{\vec{q}}$ is the annihilation operator of the external phonon. $|n, \vec{k}\rangle$ and $|n', \vec{k} + \vec{q}\rangle$ are electron states before and after interaction, $U_{n,N,n',N'}(q)$ is the matrix element of the operator $U = \exp(iqy - k_l z)$, $k_l = (q^2 - (\omega_q/c_l)^2)^{1/2}$ is the spatial attenuation factor of the potential part the displacement field, c_l and c_t are the velocities of the longitudinal and the transverse bulk acoustic wave, ρ is the mass density of the medium and $S = ab$ is the surface area.

Using Eq. (1) it is straightforward to evaluate the matrix elements of the operator U. The result is

$$U_{n,N,n',N'}(q) = \frac{4n^2\pi^2}{k_l bL^2} \left(e^{ibq} - 1\right) \frac{e^{-k_l L}\delta_{\vec{k},\vec{k}'}\delta_{n,n'}\delta_{N,N'}}{q[(bq)^2 - (2n\pi)^2]}, \tag{5}$$

here δ is the Kronecker delta symbol.

The acoustic wave will be considered as a packet of coherent phonons with the delta-like distribution function $N(\vec{k}) = (2\pi)^3 \phi\delta(\vec{k} - \vec{q})/\left(\hbar\omega_{\vec{q}}v_s\right)$ in the wave vector $\vec{k}$ space, ϕ is the sound flux density. Using Eqs. (1)–(3), we obtained the basic equation of the problem which is that the quantum kinetic equation for the distribution function of electrons interact with external phonons in presence an EMF

$$\frac{\vec{R}(\varepsilon)}{\tau(\varepsilon)} + \Omega_c\left[\vec{h}, \vec{R}(\varepsilon)\right] = \vec{Q}(\varepsilon) + \vec{S}(\varepsilon), \tag{6}$$

where $\Omega_c = eH/mc$ is the cyclotron frequency, $\vec{h} = \vec{H}/H$ is unit vector along the direction of the

EMF,

$$\vec{R}(\varepsilon) = \sum_{n',N',\vec{p}} e \frac{\vec{p}}{m} f_{n',N',\vec{p}} \delta(\varepsilon - \varepsilon_{n',N',\vec{p}}), \quad \vec{Q}(\varepsilon) = -e^2 \sum_{n',N',\vec{p}} \frac{\vec{p}}{m} \left(\vec{E}, \frac{\partial f_{n',N',\vec{p}}}{\partial \vec{p}} \right) \delta(\varepsilon - \varepsilon_{n',N',\vec{p}}), \quad (7)$$

$$\vec{S}(\varepsilon) = \frac{(2\pi)^3 |C_{\vec{q}}|^2 \phi}{\hbar^3 \omega_{\vec{q}} v_s} \sum_{n,N,n',N',\vec{p},\vec{k}} |U_{n,N,n',N'}(q)|^2 \frac{\vec{p}}{m} \delta(\varepsilon - \varepsilon_{n',N',\vec{p}})$$

$$\times \left[(f_{n',N',\vec{p}+\vec{k}} - f_{n,N,\vec{p}}) \delta(\varepsilon_{n',N',\vec{p}+\vec{k}} - \varepsilon_{n',N',\vec{p}} - \hbar\omega_{\vec{k}}) \right.$$

$$\left. + (f_{n',N',\vec{p}-\vec{k}} - f_{n,N,\vec{p}}) \delta(\varepsilon_{n',N',\vec{p}-\vec{k}} - \varepsilon_{n',N',\vec{p}} + \hbar\omega_{\vec{k}}) \right]. \quad (8)$$

Here $f_{n,N,\vec{p}}$ is the distribution function of the electron in the absence of an EMF.

Solving the Eq. (6), we obtained the partial current $R(\varepsilon)$ and the total current density is generally expressed as

$$\vec{j} = \int_0^\infty \frac{\tau}{1+\Omega_c^2\tau^2} \left\{ \left(\vec{Q}(\varepsilon) + \vec{S}(\varepsilon) \right) \tau - \Omega_c \tau \left(\left[\vec{h}, \vec{Q}(\varepsilon) \right] + \left[\vec{h}, \vec{S}(\varepsilon) \right] \right) + \Omega_c^2 \tau^2 \left(\vec{Q}(\varepsilon) + \vec{S}(\varepsilon), \vec{h} \right) \vec{h} \right\} d\varepsilon, \quad (9)$$

we find the current density

$$j_i = \alpha_{ij} E_j + \beta_{ij} \phi_j. \quad (10)$$

where α_{ij} and β_{ij} are the electrical conductivity and the acoustic conductivity tensor, respectively

$$\alpha_{ij} = \frac{e^2 m}{\hbar} \left\{ a_1 \delta_{ij} - \Omega_c a_2 \varepsilon_{ijk} h_k + \Omega_c^2 a_3 h_i h_j \right\}, \quad \beta_{ij} = A \left\{ b_1 \delta_{ij} - \Omega_c b_2 \varepsilon_{ijk} h_k + \Omega_c^2 b_3 h_i h_j \right\}. \quad (11)$$

Here ε_{ijk} is the unit antisymmetric tensor of third order, and al, bl ($l = 1, 2, 3$) are given as

$$a_l = \int_0^\infty \frac{\tau^l}{1+\Omega_c^2\tau^2} \left(\varepsilon - \frac{\pi^2\hbar^2}{2m} \left(\frac{n^2}{a^2} - \frac{N^2}{b^2} \right) \right) \frac{\partial f_0}{\partial\varepsilon} d\varepsilon, \quad b_l = \int_0^\infty \frac{\tau^l}{1+\Omega_c^2\tau^2} \frac{\partial f_0}{\partial\varepsilon} d\varepsilon, \quad (12)$$

$$A = \frac{8e |C_q|^2 \pi^5}{3\hbar\omega_q v_s m^2 q^2} \sum_{n,n',N,N'} \left(\frac{4\pi^2 n^2}{k_l b L^2} \right)^2 \frac{\left(e^{-ibq} - 1 \right)^2 e^{-2k_l L}}{\left[(qb)^2 - (2\pi n)^2 \right]^2} \left[\frac{n^2}{a^2} + \frac{N^2}{b^2} \right]^{3/2}$$

$$\times \left\{ \delta \left(\frac{\pi^2\hbar^2}{2m} \left(\frac{(n'^2 - n^2)}{a^2} + \frac{(N'^2 - N^2)}{b^2} \right) - \hbar\omega_q \right) \right.$$

$$\left. - \delta \left(\frac{\pi^2\hbar^2}{2m} \left(\frac{(n'^2 - n^2)}{a^2} + \frac{(N'^2 - N^2)}{b^2} \right) + \hbar\omega_q \right) \right\}. \quad (13)$$

We considered a situation whereby the sound is propagating along the Ox axis and the magnetic field H is parallel to the Oz axis and we assume that the sample be opened in all directions, so that $j_i = 0$. Therefore, from Eq. (10) we obtained the expression of the AME field E_{AME}, which appeared along the Oy axis of the sample

$$E_y = E_{AME} = \frac{\beta_{zz}\alpha_{zy} - \beta_{yz}\alpha_{yy}}{\alpha_{yy}^2 + \alpha_{zy}^2} \phi. \quad (14)$$

Eq. (14) is the general expression to calculate the AME field in a RQW with an infinite potential in the case of the relaxation time of carrier, τ, depends on carrier energy. We can see that Eq. (14) in the general case is very complicated, so that we only examined the relaxation time of carrier τ depending on carrier energy as follows

$$\tau = \tau_0 \left(\frac{\varepsilon}{k_B T} \right)^v, \quad (15)$$

where τ_0 is constant, k_B is Boltzmann constant and T is the temperature of the system. By using the Eqs. (11)–(14) and carrying out manipulations, we derived the expression for the AME field as

follows

$$E_{AME} = \frac{\hbar\Omega_c A \tau_0 \phi}{me^2 k_B T} \left\{ F_{v,2v} F_{2v+1,2v} - F_{2v,2v} F_{v+1,2v} \right\}$$

$$\times \left\{ \left(F_{v+1,2v} - \frac{\pi^2 \hbar^2}{2mk_B T} \left(\frac{n^2}{a^2} + \frac{N^2}{b^2} \right) F_{v,2v} \right)^2 + \Omega_c^2 \tau_0^2 \left(F_{2v+1,2v} - \frac{\pi^2 \hbar^2}{2mk_B T} \left(\frac{n^2}{a^2} + \frac{N^2}{b^2} \right) F_{2v,2v} \right)^2 \right\}^{-1} \quad (16)$$

with $F_{m,n} = \int_0^\infty \frac{x^m}{1+\Omega_c^2 \tau_0^2 x^n} \frac{\partial f_0}{\partial x} dx$.

Equation (16) is the AME field in a RQW with an infinite potential in the case of the EMF. We can see that the dependence of the AME field on the EMF and the frequency $\omega_{\vec{q}}$ is nonlinear.

We will carry out further analysis of the expression (16) for the case of quantizing magnetic field region. In this case of the quantizing magnetic field $\hbar\Omega_c \gg k_B T$, we also calculated for $f_0 = [1 - \exp(\beta(\varepsilon - \varepsilon_F))]^{-1}$ the Fermi-Dirac distribution function, $\beta = 1/k_B T$, ε_F is the Fermi energy, and by carrying out a few manipulation we obtained an analysis expression for the AME field as follows

$$E_{AME} = \frac{64 \tau_0 \phi \left| C_{\vec{q}} \right|^2 \pi^7 \hbar^3}{3e^2 m^3 q^2 b^2 L^4} \sum_{n,n',N,N'} \left(\frac{n^2}{k_l} \right)^2 \frac{(e^{-ibq}-1)^2 e^{-2k_l L}}{\left[(qb)^2 - (2\pi n)^2 \right]^2} \left[\frac{n^2}{a^2} + \frac{N^2}{b^2} \right]^{\frac{3}{2}} \cos \left(\frac{2}{\Omega_c \tau_0} \right) \frac{1}{B}$$

$$\times \left\{ \delta \left(\frac{\pi^2 \hbar^2}{2m} \left(\frac{(n'^2 - n^2)}{a^2} + \frac{(N'^2 - N^2)}{b^2} \right) - \hbar\omega_q \right) - \delta \left(\frac{\pi^2 \hbar^2}{2m} \left(\frac{(n'^2 - n^2)}{a^2} + \frac{(N'^2 - N^2)}{b^2} \right) + \hbar\omega_q \right) \right\} \quad (17)$$

with

$$B = \left\{ \left[ci^2 \left(\frac{1}{\Omega_c \tau_0} \right) + si^2 \left(\frac{1}{\Omega_c \tau_0} \right) \right] \frac{\hbar^3 \pi^2 \tau_0^2 \Omega_c}{2mk_B T} \left(\frac{n^2}{a^2} + \frac{N^2}{b^2} \right) - 2ci \left(\frac{1}{\Omega_c \tau_0} \right) si \left(\frac{1}{\Omega_c \tau_0} \right) \cos \left(\frac{2}{\Omega_c \tau_0} \right) \right.$$

$$\left. - \frac{\hbar \tau_0 \pi^2}{m} \left(\frac{n^2}{a^2} + \frac{N^2}{b^2} \right) \left[ci^2 \left(\frac{1}{\Omega_c \tau_0} \right) - si^2 \left(\frac{1}{\Omega_c \tau_0} \right) \right] \sin \left(\frac{1}{\Omega_c \tau_0} \right) \right\} \left\{ ci^2 \left(\frac{1}{\Omega_c \tau_0} \right) - si^2 \left(\frac{1}{\Omega_c \tau_0} \right) \right\}^{-1}. \quad (18)$$

$$si(x) = -\frac{\pi}{2} + \sum_{k=1}^\infty \frac{(-1)^k x^{2k-1}}{(2k-1)(2k-1)!}; \qquad ci(x) = -\ln(x) + \sum_{k=1}^\infty \frac{(-1)^k x^{2k}}{2k(2k)!}. \quad (19)$$

From Eq. (17), we see that in case the quantizing magnetic field, the dependence of AME field on the intensity H of the EMF is non-linear. These results are different compared to those obtained in bulk semiconductor [13–15], the superlattice [16] and the CQW with an infinite potential [17].

3. NUMERICAL RESULTS AND DISCUSSIONS

To clarify the results that have been obtained, in this section, we considered the AME field in the quantizing magnetic field region in a RQW with an infinite potential. This quantity is considered as a function the external magnetic field H, the frequency ω_q of ultrasound, the temperature of system T, and the parameters of the RQW with an infinite potential GaAs. The parameters used in the numerical calculations are as follow: $\tau_0 = 10^{-12}$ s, $\phi = 10^4$ Wm^{-2}, $a = b = 100$ Å, $m = 0.067m_e$, m_e being the mass of free electron, $\rho = 5320$ kgm^{-3}, $c_l = 2 \times 10^3$ ms^{-1}, $c_t = 18 \times 10^2$ ms^{-1}, $v_s = 5370$ ms^1, $\Lambda = 13.5$ eV, $\omega_q = 10^9$ s^{-1}.

In the Figure 1, we show the dependence of the AME field on the temperature T of the RQW with the acoustic wave number $q = 2.23 \times 10^6$ cm^{-1}, theintensity of the external magnetic field $H = 2.0 \times 106$ A^{-1}, $H = 3.0 \times 10^6$ A^{-1} and $H = 4.0 \times 10^6$ A^{-1}. The value of the AME field strongly decreases with the temperature when the temperature increases in the small value range the low temperature. This value isapproximately constant in the high temperature region.

Figure 2 was investigated the dependence of AME field on the intensity of the magnetic field H in the quantum magnetic field region, which have many small peaks. The result showed the different behavior from results in the bulk semiconductor [13–15] and the CQW with an infinite potential [17]. Unlike the CQW [17], in the RQW with an infinite potential the AME field is non-linear. Unlike the bulk semiconductor, these peaks in this case are much more acute. According to the result in [13–15] in the case of strong magnetic field E_{AME} is proportional to $1/H$, the cause of the difference between our result and other results is because of two reasons: one is the presence
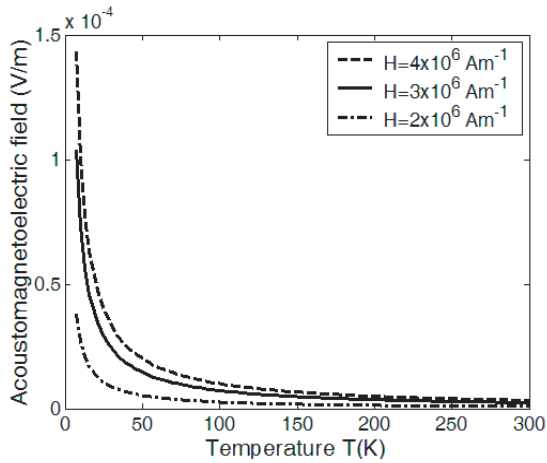
Figure 1: The dependence of the AME field on the temperature of system T.
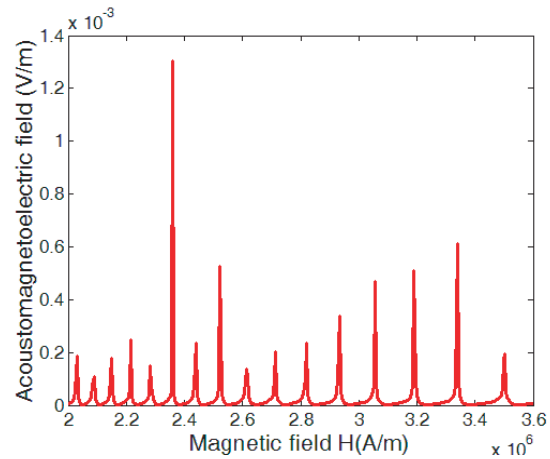
Figure 2: The dependence of the AME field on the intensity of the external magnetic field H.

of the quantum magnetic field, the electron energy spectrum was affected by quantizing magnetic field and the other is the effect of the one-dimensional systems characteristic, it is obvious that carriers in the samples satisfy the quantum limit conditions: $h\Omega_c \gg k_B T$ and $\Omega_c \tau \gg 1$, and in the low-dimensional systems the energy spectrum of electron is quantized.

4. CONCLUSIONS

In this paper, we have analytically investigated the possibility of the AME effect in the RQW with an infinite potential. We have obtained analytical expressions for the AME field in the RQW with an infinite potential for the quantum limit case. The strong dependences of AME field on the acoustic wave number q, the cyclotron frequency Ω_c of the magnetic field, and the temperature T of system. The result showed that the cause of the AME effect is the existence of partial current generated by the different energy groups of electrons, and the dependence of the electron energy due to momentum relaxation time. In addition, the absorption of acoustic quanta by electrons is accompanied by the displacement of the cyclotron orbit centers in the direction perpendicular both to the magnetic field and to the acoustic wave vector which led to the increase of the AME effect.

The numerical result obtained for RQW with an infinite potential GaAs shows that in the quantum magnetic field region, the dependence of the AME field on the temperature of the system is significantly reduced in the low temperature region and it is approximately constant in the high temperature region. In the dependence of the AME field on the intensity of the EMF is non-linea, there are many distinct maxima. This dependence has differences in comparison with that in normal bulk semiconductors [13–15], superlattice [16] and CQW with an infinite potential [17]. The results show a geometrical dependence of AME field due to the confinement of electrons in RQW with an infinite potential.

ACKNOWLEDGMENT

REFERENCES

1. Mori, N. and T. Ando, "Electron-optical-phonon interaction in single and double heterostructures," *Phys. Rev. B*, Vol. 40, No. 9, 6175–6188, 1989.
2. Lawrence, D. E. and K. Sarabandi, "Acoustic and electromagnetic wave interaction: Analytical formulation for acousto-electromagnetic scattering behavior of a dielectric cylinder," *IEEE Transactions on Antennas and Propagation*, Vol. 49, No. 10, 1382–1393, 2001.
3. Shilton, J. M., D. R. Mace, V. I. Talyanskii, Y. Galperin, M. Y. Simmons, M. Pepper, and D. A. Ritchie, "On the acoustoelectric current in a one-dimensional channel," *J. Phys.*, Vol. 8, No. 24, 337–341, 1996.
4. Enti-Wohlman, O., Y. Levinson, and Y. M. Galperin, "Acoustoelectric effect in a finite-length ballistic quantum channel," *Phys. Rev. B*, Vol. 62, 7283–7288, 2000.

5. Zimbovskaya, N. A. and G. Gumbs, "The effect of a magnetic field on the acoustoelectric current in a narrow channel," *J. Phys.*, Vol. 13, No. 20, 409–416, 2001.

6. Galperin, Y. M., O. Entin-Wohlman, and Y. Levinson, "Quantized acoustoelectric current in a finite-length ballistic quantum channel: The noise spectrum," *Phys. Rev. B*, Vol. 63, No. 15, 153309–153313, 2001.

7. Reulet, B., A. Y. Kasumov, M. Kociak, R. Deblock, I. I. Khodos, Y. B. Gorbatov, V. T. Volkov, C. Journet, and H. Bouchiat, "Acoustoelectric effects in carbon nanotubes," *Phys. Rev. Lett.*, Vol. 85, 2829–2832, 2000.

8. Mensah, S. Y., F. K. A. Allotey, and S. K. Adjepong, "Acoustoelectric effect in a semiconductor superlattice," *J. Phys.*, Vol. 6, No. 34, 6783–6787, 1994.

9. Mensah, S. Y., F. K. A. Allotey, N. G. Mensah, H. Akrobotu, and G. Nkrumah, "The influence of external electric field on acoustoelectric effect in a superlattice," *J. Phys.*, Vol. 37, No. 2, 87–97, 2005.

10. Astley, M. R., M. Kataoka, C. J. B. Ford, C. H. W. Barnes, M. D. Godfrey, I. Farrer, D. A. Ritchie, D. Anderson, G. A. C. Jones, M. Pepper, and S. N. Holmes, "Quantized acoustoelectric current in an InGaAs quantum well," *J. Appl. Phys.*, Vol. 103, No. 9, 096102–096105, 2008.

11. Galperin, M. Y. and V. D. Kagan, "On the acoustoelectric effect in a strong magnetic field," *Fiz. Tverd. Tela Sov. Phys. Solid. State*, Vol. 10, 2038–2045, 1968.

12. Salaneck, W., Y. Sawada, and E. Burstein, "The magneto-quantum-electric effect," *J. Phys. Chem. Solids*, Vol. 32, No. 10, 2285–2300, 1971.

13. Margulis, A. D. and V. A. Margulis, "The quantum acoustomagnetoelectric effect due to Rayleigh sound waves," *J. Phys.*, Vol. 6, No. 31, 6139–6150, 1994.

14. Kogami, M. and S. Tanaka, "Acoustomagnetoelectric and acoustoelectric effects in n-InSb at low temperatures," *J. Phys. Soc. Japan*, Vol. 30, 775–784, 1971.

15. Shmelev, G. M., G. I. Tsurkan, and N. Q. Anh, "Photostimulated planar acoustomagnetoelectric effect in semiconductors," *Phys. Stat. Sol.*, Vol. 121, No. 1, 97–102, 1984.

16. Bau, N. Q. and N. V. Hieu, "Theory of the acoustomagnetoelectric effect in a superlattice," *PIERS Proceedings*, 342–346, Xi'an, China, Mar. 22–26, 2010.

17. Bau, N. Q., N. V. Nhan, and N. V. Nghia, "The dependence of the acoustomagnetoelectric current on the parameters of a cylindrical quantum wire with an infinite potential in the presence of an external magnetic field," *PIERS Proceedings*, 1452–1456, Suzhou, China, Sep. 12–16, 2011.

Microwave Reflectometry for the Diagnostic of Cultural Heritage Assets

**L. Capineri[1], P. Falorni[1], C. Frosinini[2], M. Mannucci[3], N. Macchioni[4], R. Olmi[7],
S. Palanti[4], S. Penoni[5], S. Pieri[7], S. Priori[7], C. Riminesi[6], A. Santacesaria[2], and C. Todaro[5]**

[1]Dipartimento Elettronica e delle Telecomunicazioni, Università di Firenze, Firenze 50139, Italy
[2]Opificio delle Pietre Dure, Via degli Alfani 78, Firenze 50100, Italy
[3]LegnoDOC, Via Pier della Francesca, b39, Prato 59100, Italy
[4]CNR, IVALSA, Via Madonna del Piano 10, Sesto Fiorentino 50019, Italy
[5]Faberestauro, piazza Ginori 13, Sesto Fiorentino 50019, Italy
[6]ELab Scientific, 17 Fra' D. Bartolomeo Street, Firenze 50132, Italy
[7]CNR, IFAC, Via Madonna del Piano 10, Sesto Fiorentino 50019, Italy

Abstract— A non destructive diagnostic method for cultural heritage assets based on microwave reflectometry has been studied and developed. This new method is implemented with a ridged antenna operating in the range 1.5–3 GHz for the detection of reflected wave amplitude and phase variation due to the dielectric properties of the materials under investigation. Particular interest has been devoted to wood structures attacked by fungi and insects and to mural paintings with delaminations due to subsurface humidity. A simplified model of the antenna coupled to the material has been implemented in terms of a cascade of transmission lines in order to investigate the response of the system in presence of dielectric discontinuities. A series of laboratory models have been developed to assess the capability of the method to display in real time images of a calculated parameter which includes both amplitude and phase variation respect to a reference response taken from a homogeneous portion of the investigated item. A novel compact easy to use in-situ optical system mounted on the antenna has been developed to correlate the positions of the antenna on the surface with the optical digital picture, avoiding cumbersome wheel optical encoding which need flat surfaces and raster lines for guiding the manual scan.

1. INTRODUCTION

Microwaves can penetrate up to several centimetres in dry wood [1] or plaster and brick or stone walls [2]. In the operating frequency range of the instrument (1.5–3 GHz) there is also a good sensitivity to the moisture content, that can be a source of degradation both in wooden structures and in mural paintings, favouring the development of biotic decay in the former and the development of detachment of the painted layer in the latter [3, 4]. Preliminary experience with the holographic radar have pointed out that using single emitting frequency and two antenna polarizations it is possible to get high resolution images of impedance discontinuities at shallow depth by using the phase variation information. Moreover the investigation of cultural heritage assets like paintings on wood or frescos often implies to work on thickness of the order of a few wavelengths. Then the use of high frequency pulsed radar becomes difficult due to the overlapping of the finite pulse length reflected from the item interfaces [5–7]. This research work is aimed to a new microwave reflectometry system for the investigation for several materials like stone, plaster and wood. The depth analysis is performed thanks to a modulated continuous wave operating in the 1.5–3 GHz frequency range. The electromagnetic wave penetration in a medium depends on the dielectric characteristics of the material: moisture, presence of cavities, and material inhomogeneities can be detected exploiting the dielectric "contrast" among different regions. The specifications of the system should take into account the application requirements in not easy areas, such as restoration sites, including portability (weight and reduced size) and autonomy (battery operation). These features should be added to the responsiveness, reliability and, possibly, the low cost. The implementation of the microwave reflectometer prototype consisted in:

(1) The development of a generator/receiver that complies with electromagnetic compatibility issues. The prototype described in this paper has been based on a commercial Vectorial Network Analyzer.

(2) An optical compact low cost system for tracking the scan head with accuracy better than 1 cm that takes into account different environmental illumination conditions.

(3) The development of models to study the interaction between the electromagnetic signal and the different media — e.g., wood, stone, plaster.

(4) The development of software for signal analysis and imaging of the reflectometric response.

The results of the prototype applied to several case studies will be presented for two areas of interest in the cultural heritage: diagnostics of frescoes and mural paintings, diagnostics of wooden structures and artefacts. In both cases the objective is the detection of material discontinuities (voids, delaminations, knots) and inhomogeneities (in particular, moisture), by analysing images obtained by scanning the head of the microwave reflectometer on the object under investigation.

With regard to the study of wall paintings, the analysis should also give information about the texture of the support layer.

Concerning wooden artefacts, two types of structures are of interest: structural elements (beams) and panel paintings. For both structures, laboratory models have been developed: the presence of fungal decay and pockets of moisture have been simulated in wooden beams, as well as painted woods boards attacked by xylophageous insects.

These activities should hopefully lead to the creation of a database of "signatures" that will later be used to interpret the results of on site diagnostic case studies that will be discussed in the presentation.

2. THE TRANSMISSION LINE MODEL

The interpretation of the reflection measurements requires the development of a model of the interaction between the antenna and the material under investigation. A full-wave model can be implemented using well known numerical approaches, e.g., the finite element method, but the solution is quite time consuming and not very flexible.

An analytical approach is very desirable, as it allows studying the dependence of the response on the geometry and on the dielectric properties. A zero-order approximation is therefore assumed, consisting in representing the material under investigation as a layered medium excited by a plane wave. Such a system is described by an equivalent circuit consisting in a series of transverse electromagnetic (TEM) lines with characteristic impedances depending on the dielectric constant of each layer. As an example, Figure 1 represents a wooden structure with a cavity inside, represented by the line section identified by the characteristic impedance Z_2.

The reflection coefficient Γ at the wood surface is defined in the following equation:

$$\Gamma = (f, d_1, d_2) = \frac{Z_0 - Z_{i1}(f, d_1, d_2)}{Z_0 + Z_{i1}(f, d_1, d_2)} \tag{1}$$

where Z_{i1} is the impedance at the air-material interface, defined by:

$$Z_{i1}(f, d_1, d_2) = Z_1 \frac{Z_{i2}(f, d_2) + iZ_1 \tan(k_1 d_1)}{Z_1 + iZ_{i2}(f, d_2) \tan(k_1 d_1)} \tag{2}$$

d_i is the thickness of the layer i, f is the operating frequency and k_i the wavenumber in the i-th material.

We can observe that the reflection coefficient can be measured at different discrete frequencies in order to get the information about impedance variation (amplitude and phase) into the material.

3. EXPERIMENTAL APPARATUS

The experiments have been done by using a set-up consisting of a portable reflectometer model Anritsu S331E using a double-ridged antenna as a probe head, shown in Figure 2. In our experiments the antenna has been manually scanned over the surface of the investigated item without air gap. This is not a limitation for the investigation of paintings or frescos because a thin (few mm thickness) protective layer can be used to couple the antenna to the surface.
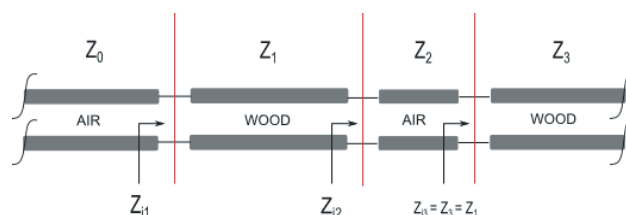
Figure 1: The TEM model of a wooden structure under investigation.

(a)   (b)
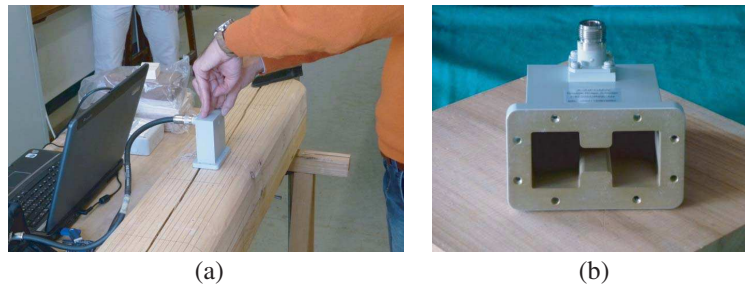
Figure 2: Measurement setup on (a) a wood beam and (b) a particular of the double-ridged antenna.
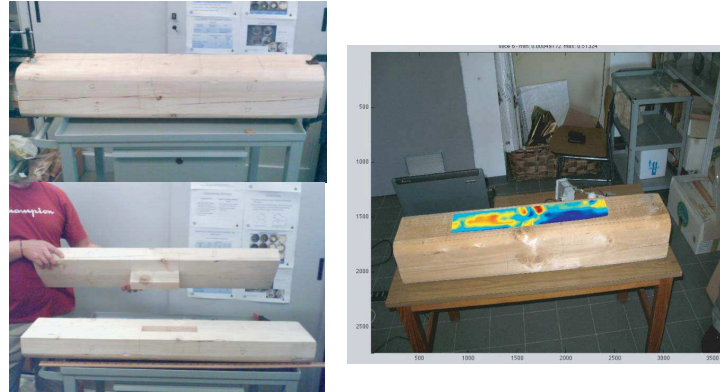
Figure 3: Wood beam utilized for measurement, internal cavity in the centre of the beam and image obtained through elaboration of the signals obtained with the double-ridged antenna on wood surface with optical positioning system.

4. IMAGING OF THE PARAMETER $K\varepsilon$

For each antenna position the reflection parameter is acquired together with the antenna position. A parameter called $K\varepsilon$ has been defined (see Equation (3)) to obtain a single display representation of the amplitude and phase variation of the reflection coefficient respect to a homogeneous portion of the material assumed as reference response (Γref).

$$K\varepsilon = \frac{|\Gamma ref|}{|\Gamma|}\cos\left[\arg\left(\Gamma\right) - \arg\left(\Gamma rif\right)\right] \tag{3}$$

where $\Gamma ref = \frac{Z_0 - Z_1}{Z_0 + Z_1}$ is the reference reflection coefficient.

A preliminary experiment has been carried out to test the feasibility of the method on a wood beam where in the central position a cavity was excavated. Different wood blocks, artificially attacked by insect, positioned inside the cavity simulated different grade of biotic decay. (see Figure 3(a)).

On the investigated surface the wood beam shows some knots and vein patterns. On the Figure 3(b) the image of $K\varepsilon$ in false color (yellow and red) where all above features can be described accurately. The position of the ridged antenna has been acquired with an optical system with position accuracy better than 1 cm that is a fraction of the wavelength.

5. CONCLUSION

The developed microwave reflectometry have been tested on laboratory models and has demonstrated sufficient sensitivity to detect dielectric variations inside the material. The imaging of a calculated parameter which includes both amplitude and phase variation is investigated with the perspective of facilitating the interpretation of acquired images by a final user when operating in-situ or in a restoration laboratory.

ACKNOWLEDGMENT

REFERENCES

1. Bucur, V., "Techniques for high resolution imaging of wood structure: A review," *Meas. Sci. Technol.*, Vol. 14, 91–98, 2003.
2. Capineri, L., P. Falorni, G. Borgioli, T. Bechtel, S. Ivashov, A. Zhuravlev, I. Vasiliev, M. Paradiso, and G. Cartocci, "Application of the holographic radar RASCAN to cultural heritage inspection," *Archaeological Prospection, Archaeol. Prospect.*, Vol. 16, 1–13, 2009.
3. Olmi, R., S. Priori, D. Capitani, N. Proietti, L. Capineri, P. Falorni, R. Negrotti, and C. Riminesi, "Innovative techniques for sub-surface investigations," *Materials Evaluation, Materials Evaluation*, Vol. 69, No. 1, 89–96, 2011.
4. Bison, P., G. Cadelano, L. Capineri, D. Capitani, U. Casellato, P. Faroldi, E. Grinzato, N. Ludwig, R. Olmi, S. Priori, N. Proietti, E. Rosina, R. Ruggeri, A. Sansonetti, L. Soroldoni, and M. Valentini, "Limits and advantages of different methods and techniques for moisture content evaluation in masonry," *Materials Evaluation*, Vol. 69, No. 1, 111–116, 2011.
5. Razevig, V. V., S. I. Ivashov, I. A. Vasiliev, A. V. Zhuravlev, T. Bechtel, and L. Capineri, "Advantages and restrictions of holographic subsurface radars experimental evaluation," *XIII International Conference on Ground Penetrating Radar*, 657–662, Lecce, Jun. 21–25, 2010.
6. Capineri, L., P. Falorni, M. Inagaki, T. D. Bechtel, V. V. Razevig, and C. G. Windsor, "Validation of a theoretical model for quantitative interpretation of holographic radar response from an inclined plane reflector," *XIII International Conference on Ground Penetrating Radar*, Lecce, 657–662, Jun. 21–25, 2010.
7. Ivashov, S. I., V. V. Razevig, I. A. Vasiliev, A. V. Zhuravlev, T. Bechtel, L. Capineri, P. Falorni, and T. Lu, "Holographic subsurface radar as a device for NDT of construction materials and structures," *International Symposium on Nondestructive Testing of Materials and Structures*, 28, Istanbul, Turkey, May 15–18, 2011.

Investigation of Holographic Radar Capabilities for the Detection of Shallow Buried Plastic Antipersonnel Landmines

T. Bechtel[1], **L. Capineri**[2], **P. Falorni**[2], **M. Inagaki**[3], **S. Ivashov**[4], **and C. Windsor**[5]

[1]Department of Earth and Environment, Franklin & Marshall College, Lancaster, PA, USA
[2]Department of Electronics and Communications, University of Florence, Florence 50139, Italy
[3]Walnut Ltd., 1-19-13, Saiwaicho, Tachikawa, Tokyo 190-0002, Japan
[4]Remote Sensing Laboratory, Bauman Moscow State Technical University, Moscow, Russia
[5]116, New Road, East Hagbourne, OX11 9LD, UK

Abstract— The RASCAN holographic subsurface radar [1] has been investigated for the detection of small plastic antipersonnel landmines buried at shallow depth in soil. The investigation consists of the comparison of data obtained by surface scans in an outdoor test bed with two RASCAN systems operating at different discrete frequencies near 2 GHz and 4 GHz, each with receiving antennae both parallel and perpendicular to the polarization of the transmitter. The two systems have different signal penetrations (up to 20 cm in dry soil for the 2 GHz), different antenna radiation patterns and different sensitivities for the parallel and perpendicular polarization images. RASCAN has the capability to record small phase changes in the received signals due to electromagnetic impedance discontinuities. This high sensitivity is an advantage to detect small (5 cm diameter) plastic targets but introduces also clutter signals due to surface irregularities and the other clutter objects commonly found in a battlefield. The choice of the operating frequency, the coupling of the antenna with the soil surface and the scanning spatial sampling is important to get enough information for the efficient detection of small plastic targets. Thanks to the high spatial resolution of the RASCAN images, the detection of targets by direct image interpretation is still possible, but is time consuming, is limited to the sensitivity of the human eye grey scale variations, and may be subjective based on different operators experience and level of expertise.

This paper is a comparison of the output of experiments made in Italy, Japan and USA using RASCAN holographic radar to identify the presence of plastic mine simulants buried in soil. Experiments covered the response variability due to surface conditions in Italian experiments, moisture level in Japan experiments and a feature of PMA-2 mines in USA experiments.

1. AIM OF THE EXPERIMENTS

Aim of these experiments is to study the effect of moisture, surface condition and target features on holographic radar response. In particular, experiments made in Japan considered the same target at different moisture levels, experiments made in USA considered the effect of the trigger on the detectability of a PMA-2 antipersonnel mine and experiments made in Italy considered different surface conditions in a outdoor setup.

The comparison is made against a elaboration algorithm [2] that considers response variations along spatial coordinate or along frequency coordinate. The algorithm take the output of RASCAN as input and produces two images, one based on frequency variations and the other based on spatial variations. Other than the classic geometric correlation (shape), targets can be identified on the two images by a normalized color scale: the higher is the value the higher is the probability of target response.

2. DESCRIPTION OF THE EXPERIMENTS

All experiments have been carried out by a joint team of researchers from Italy, USA and Japan. Each member of the team exploited a different facet of the general problem of buried mine simulants detection using RASCAN, from moisture effect on the background response to the constructional details of antipersonnel mines.

2.1. Experiments from Japan

In the first experiment two targets was buried in a sandbox at depths of about 3–4 cm and separated by 9 cm (see Figure 1). The aim of the experiments is to see which is the effect of different trigger type combined with different moisture level.

Measurements was performed with dry sandbox (humidity 0% of mass water) and wet sandbox (humidity 3% of mass water).
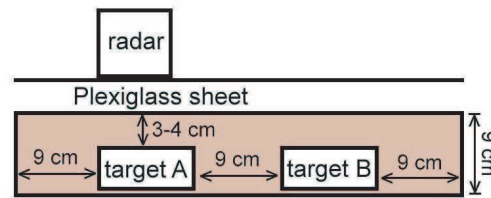
Figure 1: Layout of experiment from Japan.

(a)   (b)

Figure 2: (a) Target A with big trigger, filled with granulated sugar (dielectric constant from 2.5 to 3.2). (b) Target B with small trigger.
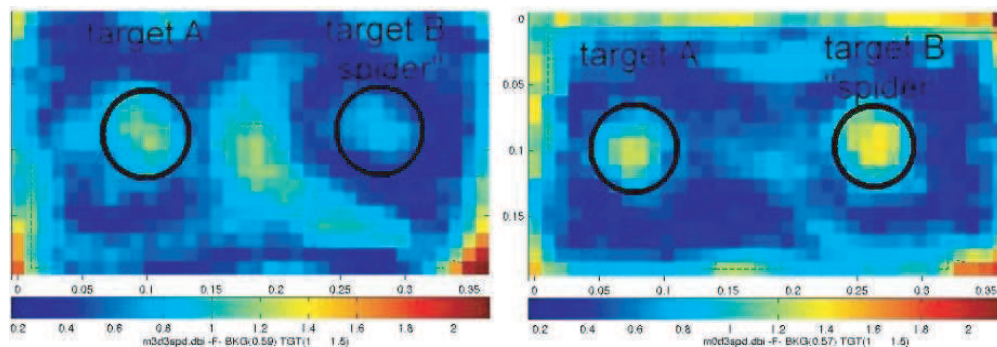
(a)   (b)

Figure 3: (a) Results for moisture level 3%. (b) Results for moisture level 0%.

Two cylindrical plastic boxes, one with big trigger and the other with small trigger, was used as targets (see Figure 2).

Results shows a little variation with spider type and a significant reduction in detectability when moisture level rise to 3% mass water.

2.2. Experiments from the USA

In this experiment was tested the effect of the presence of the spider trigger above a small plastic antipersonnel mine named PMA-2. These scans were done in air to avoid soil effects.

One scan is with the trigger while the other is without the trigger. The mine body was not moved at all (see Figure 4 for the experiment layout).

The target was a PMA-2 mine simulant filled with granulated sugar (dielectric constant 2.9). Size of the simulant is 61 mm height by 68 mm diameter (see).

Results in Figure 5 show little variations between the two tests with or without trigger. Notice that the two images don't have the same color scale but from the color bar it can be seen that the two target areas share about the same values.

(a)   (b)
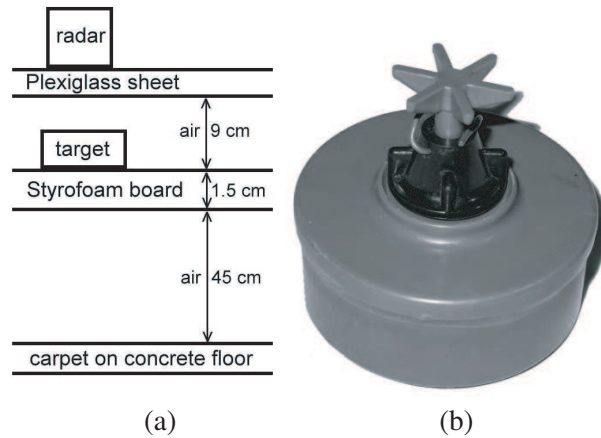
Figure 4: (a) Layout of experiment from USA. (b) View of the PMA-2 mine simulant.

(a)   (b)
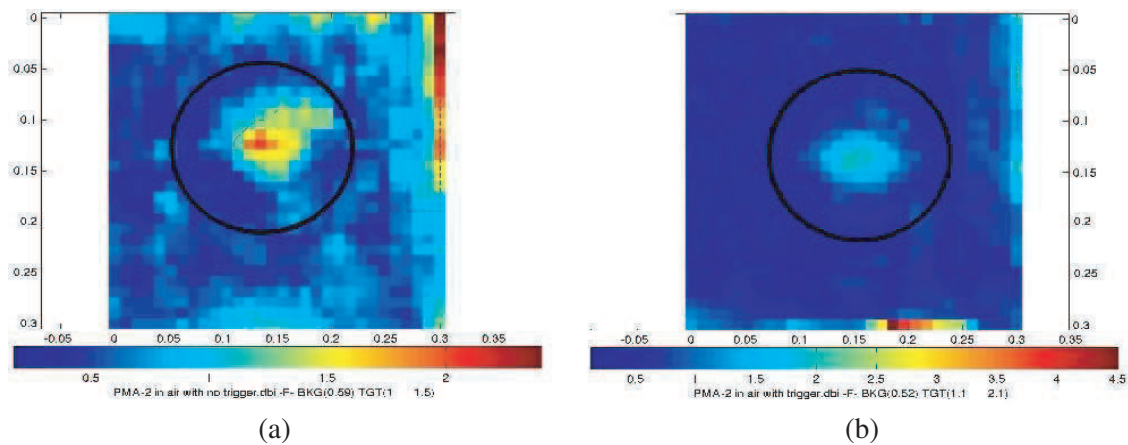
Figure 5: (a) Results with no trigger. (b) Results with trigger.
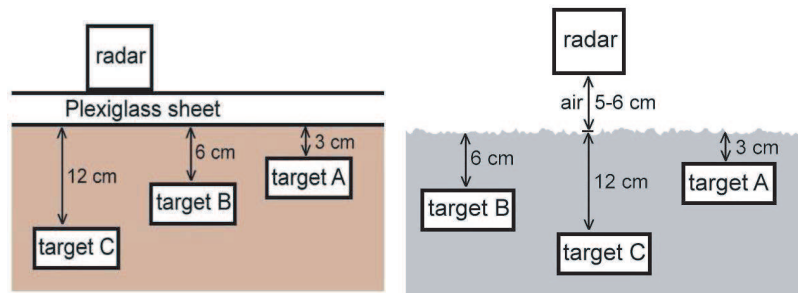
Figure 6: Section view of the layout of Italian experiment.

2.3. Experiments from Italy

In these experiments it was tested the effect a real outdoor environment, with vegetation and uneven surface and soil composition. The test field is a squared area of about 3 m side where test objects are buried from long time (about two years).

One corner of the area is reserved for new tests and has been excavated to perform these tests. In the first test scanning was performed coupling the antenna with the ground by using a plexyglass sheet while the second test was performed by scanning with a air gap of about 5–6 cm (see Figure 6 for details).

The three targets are circular boxes (radius $R = 6$ cm, thickness $H = 3$ cm) filled with epoxy (dielectric constant from 2.9 to 3.7) and buried on a straight line at various depths (see Figure 6 for details). Results in Figure 7 show that the air gap significantly reduce the detectability of targets in a outdoor field test environment.

(a)

(b)
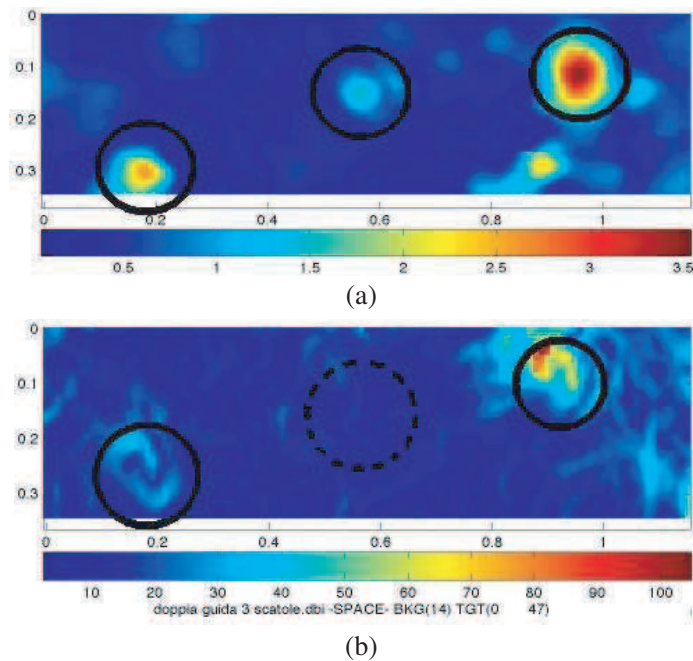
Figure 7: (a) Scanning in contact with ground. (b) Scanning with air gap. (Left) target C, (Middle) target B, (Right) target A.

3. ELABORATION ALGORITHM

All comparisons have been carried out by using an algorithm that takes all ten RASCAN images (two polarizations by five frequencies) and produces a single image based on image variations with respect to HSR frequency. The algorithm normalize each single image (identified by polarization and frequency) subtracting mean value and dividing by standard deviation. After this phase, for each polarization, the standard deviation along frequency dimension is evaluated. Finally the two images are square-summated and the resulting image is normalized. The rationale of this calculation is that a target will have a frequency response that is more complicated with respect to the background.

Values in the final image can be subdivided into two parts: one (background) made by values that are close to their mean value and the other (target) made by highly scattered values.

4. CONCLUSIONS

An algorithm that apply variations of received signal along frequency abscissa has been developed and used as a comparison mean.

Experiments from Japan and Italy showed that moisture level highly influence the detectability of buried objects because it tends to create a confused (foggy) background.

Experiments from the USA and Japan show that the detectability of a PMA-2 antipersonnel mine in air is quasi independent on the presence and type of trigger.

Experiments from Italy showed that there can be the case where the same object in the same medium can be better detected at higher depths.

ACKNOWLEDGMENT

REFERENCES

1. Ivashov, S., V. V. Razevig, I. A. Vasiliev, A. V. Zhuravlev, T. D. Bechtel, and L. Capineri, "Holographic subsurface radar of RASCAN type: Development and applications," *IEEE Journal of Selected Topics in Earth Observations and Remote Sensing*, Accepted on June 5, In Print Digital Object Identifier JSTARS-2010-00097, 2011.
2. Windsor, C. G., A. Bulletti, L. Capineri, P. Falorni, S. Valenini, G. Borgioli, M. Inagaki, T. D. Bechtel, E. Bechtel, A. V. Zhuravlev, and S. I. Ivashov, "A single displays for RASCAN 5-frequency 2-polarisation holographic radar scans," *PIERS Online*, Vol. 5, No. 5, 496–500, 2009.

Microwave Imaging System for the Detection of Buried Objects Using UWB Antenna — An Experimental Study

Elizabeth Rufus and Zachariah C. Alex

School of Electronics Engineering, VIT University, Vellore, India

Abstract— In this paper, we have developed a microwave imaging experimental set up using a 1-D beamforming algorithm for the detection of buried object using UWB antenna operating at 1–11 GHz, and done the experimental validation. The experiment consists of a mechanical scanner with 3.6 mm resolution in the X and Y directions, UWB horn antenna which sweeps over the frequency range. The antenna transmits the microwave signal and receives the backscatters from all the objects. These backscatters are passed through the 1-D bean former designed to image the backscatter energy as a function of location. Object of size 4 mm embedded in the sand bath has been detected using the developed microwave imaging set up.

1. INTRODUCTION

The studies conducted in the past have proved the potential of microwave imaging technique for many applications in the field of non destructive evaluation. Different types of microwave imaging systems are currently being used for imaging in areas such as ground penetrating radar and remote sensing. Depending on the objects and medium to be imaged, different antennas are needed; these range from small antennas used for near field measurements in ground penetrating radar to large airborne system used in remote sensing.

Microwave imaging using the subsurface UWB radar technique do not attempt to reconstruct the dielectric properties profile of the object, instead seeks to identify the presence and location of significant scatterers in the medium. To create images from microwave measurements, it is necessary to construct a microwave imaging system which is able to transmit microwaves and measure the scattered waves at one or more antennas.

There are two key issues to address while designing a microwave imaging system. One is the increase of the signal to noise ratio in the system and the other is to assure that the system has a large dynamic range. These are important because of the fact that the scattered signal is often weak in comparison with the transmitted signal. This implies that any noise in the system will have large impact on the image quality and then the system must be able to distinguish even small difference in the received signals.

Microwave imaging can be done in two ways. One based on analysis of the transmitted signals from the target, and another is by analyzing the scattered signals. The latter technique is used in many applications because it can be done with one antenna or both antennas at nearby distances. UWB based radar technique is used in this work to detect the embedded objects to locate the position and size In radar based techniques, the wide bandwidth is a prerequisite to achieving high fidelity of the radiated pulse. The multi-frequency approach allows for the reconstruction of the permittivity distribution with higher fidelity compared to a single frequency or narrow band reconstruction [1].

2. MICROWAVE IMAGING SYSTEM

The components of the experimental set up includes the microwave source and detector pair, UWB antenna, the mechanical scanner for the movement of antenna and the test samples to be imaged. A UWB horn antenna (1 GHz to 11 GHz) designed [5] is connected to a mechanical scanner to illuminate the object to be imaged with microwaves and also to collect the scattered radiation with the help of the Agilent network analyzer PNA N5230A calibrated for 1 port reflection measurement The horn antenna was connected to a mechanical scanner to illuminate the object to be imaged with a UWB signal. It can be moved in X and Y directions with a resolution of 3.6 mm. The experimental setup is shown in Figure 1. The targets to be imaged are embedded in sand for experimental purpose. The reflection coefficients are collected and passed through the 1-D beamformer which synthesizes the effect of the antenna receiving all the returns due to different scatterers present at the same time.

Figure 1: Experimental set up of the Microwave imaging system.

3. BEAMFORMING ALGORITHM

Beamforming is a spatially filtering method that focuses the array data toward a specified direction of arrival. Successful adoption of UWB radar technology requires, spatially focusing the back scattered signals to discriminate against clutter and backscatters. The antenna transmits the UWB signal into the medium at a particular location and records the backscatter from that location. The focus can be achieved synthetically by applying signal processing techniques to the recorded backscattered signals. Microwave imaging via time shift and sum beamforming, microwave imaging via space time beamforming are the proven procedures which are available in the literature (Bond E. J. et al., 2003), which operates in the time domain. We have used a frequency domain approach to design a one dimensional beamforming procedure that requires much less computational complexity than required by the time domain approaches. The designed beamformer first removes the contributions due to the heterogeneity of the medium and due to the antenna reverberations by making measurements without any target in the medium and the reflections measured by the antenna only without any medium and finding the average and thereby subtracting this average from every measurement that is made. Secondly the designed beamformer applies the phase compensation. Consider the scattering range to be r. If the antenna were to receive all the returns at the same time then there has to be a phase compensation included so as to account for the phase shift between the signals received from the different scattering distances while operating in the frequency domain. This phase compensation term can be given by, $e^{-j\frac{4\pi}{\lambda}r_i}$. Adding the phase shift to each received component in the frequency domain, is the same as delaying the received signal by the time of flight without actually requiring time domain operation. For a particular distance r, the real part of the phase-compensated reflection coefficient will add up over all frequencies coherently only when a scattering source is present. In case no scatterer is present, the contributions of all frequencies will cancel out resulting in a relatively low resultant value.

The energy at each antenna location is obtained by taking the sum of the squares of the received signal.

$$E\left(d\right) = \sum_{k}\left[y_1'(f)e^{-j\frac{4\pi}{\lambda_i}r_k}\right]^2$$

If a scattering object exists at the candidate location, a relatively large energy results. The beamformer is scanned at different locations by appropriately changing the antenna location and the display of energy as a function of location provides the image of the back scattered signal strength.

4. EXPERIMENTAL RESULTS

In the first experiment, metal targets are embedded in bulk sand medium at the coordinates $(5, 4)$, $(9, 13)$ and $(18, 4)$. Figure 2(a) shows the surface plot with the reflection coefficient plotted without applying beamforming, the presence of target cannot be identified properly due to the returns consisting of the incident signal, antenna reverberations, and reflections from the inhomogeneities in the medium, and any objects present. The surface plot of the resultant data shows a peak at $(5, 4)$ indicating the presence of a strong reflector at the location where one of the target was buried. The other buried targets could not be detected from this result. Hence, beamforming is applied to improve the performance of the imaging system. Figure 2(b) shows the presence of all the targets.

Shows the presence of the metal target at the coordinates $(5, 5)$ and the vertical slice taken at $y = 5\,\text{mm}$ in Figure 3(c) shows the target present at the coordinate $x = 5\,\text{mm}$ and the depth information is obtained in the z direction.
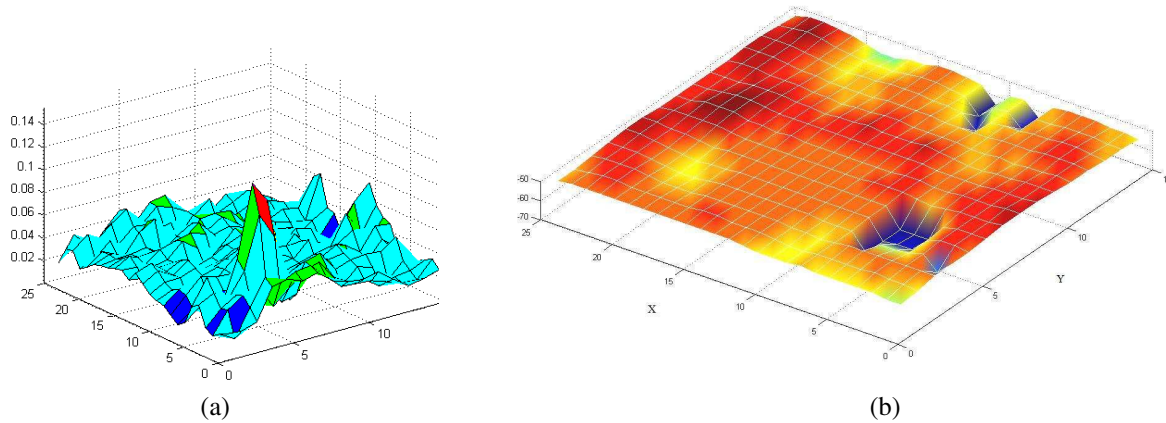
Figure 2: Reflection coefficients plotted as the surface plot (a) before beamforming, (b) beamformer output.
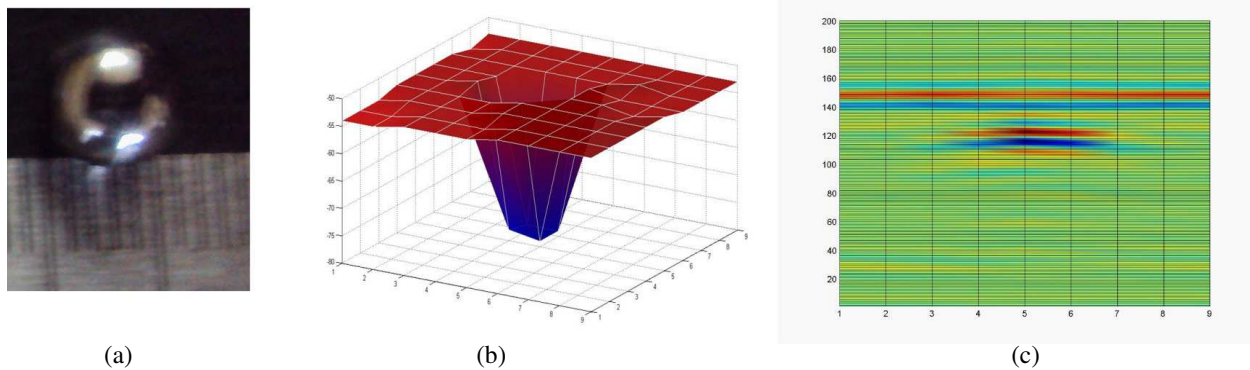
Figure 3: (a) metal target of radius 2 mm, (b) beamformer output, (c) vertical slice where the target was buried.

5. CONCLUSION

The beamformer was tested on sand bath containing metallic objects embedded in it. The beamformer uses a phase compensation technique which obviously does not involve much computational effort and takes less time for its implementation. The smallest size of the object that can be detected using this microwave imaging system developed is 4 mm.

REFERENCES

1. Chew, W. C. and J. H. Lin, "A frequency hopping approach for microwave imaging of large inhomogenous bodies," *IEEE Microwave Guided Wave Letters*, Vol. 5, 439–441, 1955.

2. Chen, X., K.-M. Huang, and X.-B. Xu, "Microwave imaging of buried inhomogenous objects using parallel genetic algorithm combined with FDTD method," *Progress In Electromagnetics Research*, Vol. 53, 283–298, 2005.

3. Meany, P. M., K. D. Paulsen, A. Hartov, and R. K. Crane, "An active microwave imaging system for reconstruction of 2-D Electrical property distributions," *IEEE Trans. Biomed. Eng.*, Vol. 42, 1017–1025, 1995.

4. Shakti, K. D., B. D. van Veen, S. C. Hagness, and K. Frederick, "Breast tumor characterization based on Ultrawideband microwave backscatter," *IEEE Trans. Biomed. Eng.*, Vol. 55, 237–246, 2008.

5. Xie, Y., B. Guo, L. Xu, J. Li, and P. Stoica, "Multistatic adaptive microwave imaging for early breast cancer detection," *IEEE Trans. Biomed. Eng.*, Vol. 53, 1647–1657, 2006.

A Review on the Migration Methods in B-scan Ground Penetrating Radar Imaging

Caner Özdemir[1, 2]**, Sevket Demirci**[2]**, and Enes Yiğit**[2]

[1]Department of Electrical and Electronics Engineering, Zirve University
Kızıllhisar Campus, Gaziantep 27260, Türkiye
[2]Department of Electrical-Electronics Engineering, Mersin University
Yenişehir, Mersin 33343, Türkiye

Abstract— Ground penetrating radar (GPR) has been a pioneering electromagnetic tool for detecting and locating subsurface objects with high imaging fidelities [1, 2]. The main defocusing effect in the GPR imagery is occurred due to the well-known hyperbolic distortion of the subsurface scatterers in the resultant space-time B-scan GPR image [1–3]. Although many migration/focusing methods have been proposed by various researchers, the focusing problem in the measured GPR images remains to be a challenging task. In this work, we review the recent migration methods of the B-scan GPR images that are popular among the GPR researchers. These methods are the hyperbolic summation (HS), the Kirchhoff migration, the $f - k$ migration and the SAR-based focusing techniques. The brief formulation of these methods together with their algorithms is presented. The applications of the algorithms to both the numerical and the measurement data are provided and the corresponding B-scan focused GPR images are presented.

1. INTRODUCTION

Ground Penetrating Radar (GPR) is a non-destructive remote sensing tool that is aimed to detect objects buried beneath the Earth's surface or situated interior to a visually opaque medium. In a typical space-time B-scan GPR image, any scatterer within the image region shows up as a hyperbola because of the different trip times of the EM wave while the antenna is moving along the B-scan path. Therefore, one of the most applied problem for the B-scan GPR image is to transform or migrate the unfocused space-time GPR image to a focused one showing the object's correct placement and size with its EM reflectivity. The common name for this task is called *migration* or *focusing* [4–6]. Kirchhoff wave-equation [4] and frequency-wave number ($\omega - k$) based [6, 7] migration algorithms are widely accepted and applied. The wave number domain focusing techniques; for instance, was first formulated for seismic imaging applications [6] and then adapted to the modern synthetic aperture radar (SAR) imaging practices [7]. These algorithms are also named as seismic migration and $\omega - k$ (or $f - k$) migration [8] by different researchers. In this paper, we present a brief review of the B-scan GPR migration/focusing methods that are commonly used by GPR research community.

2. MIGRATION TECHNIQUES

In this section, we will review the basic steps of the mostly applied GPR algorithms; namely hyperbolic summation (HS), the Kirchoff migration, $\omega - k$ (Stolt) migration and the SAR based focusing.

2.1. Hyperbolic (Diffraction) Summation

Let us assume a perfect point scatterer situated at (x_o, z_o) in the 2D plane where x-axis corresponds to the B-scan direction and the z-axis is the depth as illustrated in Figure 1. If the propagating medium is homogeneous, the parabolic hyperbola in the GPR image can be characterized by $\mathbf{R} = \sqrt{z_o^2 + (\mathbf{X} - x_o)^2}$ when the radar is moving on a straight path along X-axis. Here, $\mathbf{X}$ is the synthetic aperture vector along the B-scan and $\mathbf{R}$ represents the path length from the antenna to the scatterer. Assuming that the resultant B-scan GPR image can be regarded as the contribution of finite number of hyperbolas that correspond to different points on the object(s) below the surface, the following methodology can be applied to migrate the defocused image structures; i.e., hyperbolas to the focused versions:

1. For each pixel point; (x_i, z_i) in the 2D original B-scan space-depth GPR image; find the corresponding hyperbolic template using (1) and trace the pixels under this template.

2. Record the image data for the traced pixels under the template. This step provides 1D field data; E^s whose length; N is the same as the total number of sampling points in $\mathbf{X}$.

3. Then, take the root-mean-square (rms) value of the total energy contained within this 1D complex field data as follows:

4.

$$\{rms \text{ at } (x_i, z_i)\} = \sqrt{\frac{\left(|\mathbf{E^s}|^2 |(\mathbf{E^s})^*|^2\right)}{N}} = \frac{1}{\sqrt{N}} \sum_{i=1}^{N} |\mathbf{E_i^s}|^2 \tag{1}$$

5. The calculated rms value is recorded in the new GPR image at the point (x_i, z_i). This procedure is repeated until all pixels in the original GPR image are covered.

The concept of HS is illustrated through an example as shown in Figure 1. In this example, the measured data is collected from a subsurface scene where a thick iron pipe with 16.5 cm in diameter and 47 cm in length was buried flat about 15 cm below the ground. For the data collection, a stepped-frequency continuous radar (SFCWR) set-up by the help of vector network analyzer is utilized to measure the back-scattered field data along a straight line of discrete measurement points. The ground medium is occupied by dry and homogeneous sand. First, the classical space-depth B-scan GPR image is obtained by applying an IFT operation to the frequency domain back-scattered data as plotted in Figure 1(a). The major scattering from air-to-ground surface can be easily seen in the B-scan GPR image along the synthetic aperture direction for the depth of $z = 0$ m. The pipe below the surface manifests itself as a hyperbola in the image as expected. Second, we apply the methodology listed above for the hyperbolic summation realization of the GPR image. As depicted from the image in Figure 1(b), the hyperbolic defocusing is transformed to a more focused pattern in the migrated image.

2.2. Frequency-wavenumber (Stolt) Migration

The algorithm behind the frequency-wavenumber $(\omega - k)$ method works faster than the previously presented migration methods. Below is the brief explanation of the algorithm.

The algorithm begins with the 3D scalar wave equation for the wave function; $\varphi(x, y, z, t)$ within the constant-velocity propagation medium

$$\left(\frac{\partial^2}{\partial x^2} + \frac{\partial^2}{\partial y^2} + \frac{\partial^2}{\partial z^2} - \frac{1}{v_m^2} \frac{\partial^2}{\partial t^2}\right) \varphi(x, y, z, t) = 0 \tag{2}$$

In the Fourier space, spatial wave-numbers and the frequency of operation are related with the following equation

$$\varphi(x, y, z, t) = \left(\frac{1}{2\pi}\right)^{\frac{3}{2}} \iiint_{-\infty}^{\infty} E(k_x, k_y, \omega) e^{-j(k_x x + k_y y + k_z z - \omega t)} dk_x dk_y d\omega \tag{3}$$
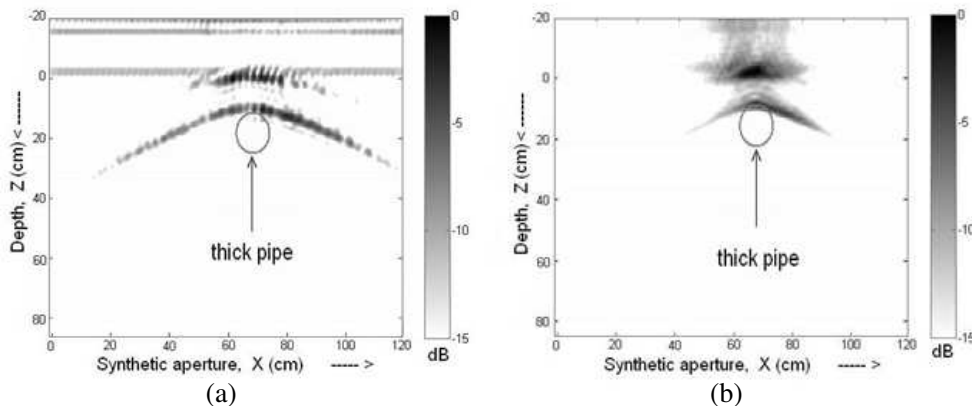
Figure 1: Measured B-scan GPR images: (a) hyperbolic B-scan image of a buried pipe, (b) focused image after applying the HS method.

For the GPR operation; the scattered field is taken to be measured on the $z = 0$ plane above the surface. When carefully treated, the above equation offers a Fourier transform pair where $e(x, y, t)$ can be regarded as the time-domain measured field on the $z = 0$ plane.

$$\varphi(x, y, 0, t) \triangleq e(x, y, t) = \left(\frac{1}{2\pi}\right)^{\frac{3}{2}} \iiint_{-\infty}^{\infty} E(k_x, k_y, \omega) e^{-j(k_x x + k_y y - \omega t)} dk_x dk_y d\omega \tag{4}$$

It is very important to notice that this equation designates a 3D forward FT relationship between $e(x, y, t)$ and $E(k_x, k_y, \omega)$ for the negative values of time variable; t. Then, the inverse FT can be dually defined as the following way:

$$E(k_x, k_y, \omega) = \left(\frac{1}{2\pi}\right)^{\frac{3}{2}} \iiint_{-\infty}^{\infty} e(x, y, t) e^{j(k_x x + k_y y - \omega t)} dx dy dt \tag{5}$$

Afterwards, we now use the ESM to focus the image by setting $t = 0$ in (4) and using

$$E(k_x, k_y, \omega) = e^{jk_z z} E(k_x, k_y, \omega, z = 0) \tag{6}$$

Therefore, one can get the time-domain measured field via

$$e(x, y, z, 0) = \left(\frac{1}{2\pi}\right)^{\frac{3}{2}} \iiint_{-\infty}^{\infty} E(k_x, k_y, \omega) e^{-j(k_x x + k_y y + k_z z)} dk_x dk_y d\omega \tag{7}$$

The above equation presents a focused image. However, the data in (k_x, k_y, ω) domain should be transformed to (k_x, k_y, k_z) domain to be able to use the FFT. Therefore, a mapping procedure from ω domain to k_z domain is required for fast processing. The relationship between the ω-and-k_z and $d\omega$-and-dk_z can be easily get as

$$e(x, y, z) = \left(\frac{1}{2\pi}\right)^{\frac{3}{2}} \iiint_{-\infty}^{\infty} \frac{v_m^2 k_z}{\omega} E^m(k_x, k_y, k_z) e^{-j(k_x x + k_y y + k_z z)} dk_x dk_y dk_z \tag{8}$$

Here $E^m(k_x, k_y, k_z)$ is the mapped version of the original data $E(k_x, k_y, \omega)$. After this mapping, the new data set does not lie on the uniform grid due to non-linear feature of the transformation. Therefore, an interpolation procedure should also be applied to be able to use the FFT for fast processing of the collected data set. The above focusing equation is valid for the 3D GPR geometry or the C-scan problem. Therefore, the focusing equation in (19) can be easily reduced to 2D B-scan GPR problem in the space-depth domain via the following equation:

$$e(x, z) = \left(\frac{1}{2\pi}\right) \iint_{-\infty}^{\infty} \frac{v_m^2 k_z}{\omega} E^m(k_x, k_z) e^{-j(k_x x + k_z z)} dk_x dk_z \tag{9}$$

2.3. SAR Based Focusing

In this work, we will present a SAR based focusing algorithm based on the plane wave decomposition of spherical wave-fronts in the 2D frequency-wavenumber domain. Assuming that the 2D scattered electric field $E^s(x, \omega)$ is recorded for different synthetic aperture points and frequencies for the B-scan GPR geometrical layout, the frequency domain back-scattered field from a point scatterer at r distance from the antenna will have the form of $E^s(\omega) = \rho \cdot e^{-j2\omega r/v_m}$ where $\omega = 2\pi f$ is the angular frequency, ρ is the strength of the scattered from the point target and v_m is the velocity of the wave. In the above equation, the propagation medium is assumed to be homogeneous. The number "2" in the exponential stands for the two-way propagation between the radar and the point scatterer on the object.

The general steps for SAR-based algorithm migration for the B-scan GPR operation can be summarized as the followings:

1. First, the scattered field data is collect the either in time domain to have $E^s(x, t)$ or in frequency domain to have $E^s(x, \omega)$.
2. Then, 2D FT of $E^s(x, t)$ or 1-D FT of $E^s(x, \omega)$ of taken to transform the data onto wave number–frequency plane to have $E^s(k_x, \omega)$. As demonstrated in [9], the data can be normalized as to be $\bar{E}_s(k_x, \omega)$.

(a)   (b)
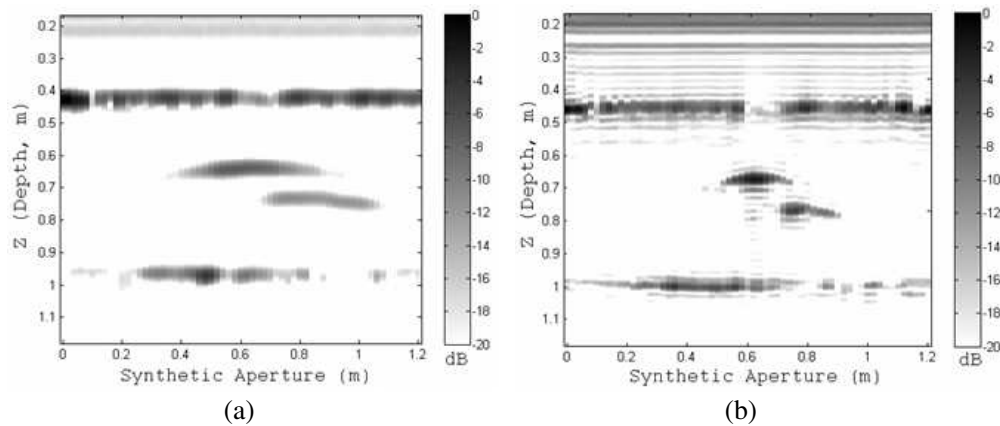
Figure 2: Measured B-scan images of two closely placed pipes buried in sand (a) classical GPR image, (b) focused image after SAR based $\omega - k$ focusing.

3. In the next step, $\bar{E}_s(k_x, \omega)$ is mapped from $k_x - \omega$ domain to $k_x - k_z$ domain to transform the data spatial frequency domains to have $\tilde{E}^s(k_x, k_z)$.

4. In the final step, 2D IFFT of $\tilde{E}^s(k_x, k_z)$ is taken to get the final focused image in the Cartesian coordinates as $e^s(x, z)$.

An example of presented SAR based $\omega - k$ migration imaging algorithm is demonstrated through the results given in Figure 2. Two metal pipes that were buried flat around $z = 30\,\text{cm}$ and $z = 40\,\text{cm}$ in a dry and homogeneous sand environment as the geometry is seen in Figure 2(a). Using a vector network analyzer that can be used as stepped frequency continuous wave radar (SFCWR), a B-scan measurement was acquired along a straight path while the frequency is changed from 4.0 to 7.1 GHz. The classical space-depth B-scan GPR image is depicted in Figure 2(b) where the hyperbolic image distortion of the pipe responses can be clearly seen. Then, we apply the above presented SAR based $\omega - k$ migration algorithm in aiming to get a better focused image. The resultant migrated image is displayed in Figure 2(c) where the pipe responses are more localized around their correct locations.

3. CONCLUSION

In this paper, we have reviewed some fundamental algorithms for migrating the B-scan GPR data by presenting the algorithms steps of, HS, $\omega - k$ (Stolt) migration and SAR-based focusing algorithms. HS technique has been shown to be conceptually very simple to implement; but the computation time for completing the whole focusing procedure could be quite long if the image size is big. Stolt migration algorithm tries to constitute a 3D Fourier transform relationship between the image at the object space and the collected scattered field. Before applying FFT routine, a mapping procedure from frequency-wavenumber domain to wavenumber-wavenumber domain is needed. Although this mapping procedure may slow down the computation time, the algorithm is still fast thanks to the FFT step. SAR based focusing technique make use of the fact that the B-scan geometry is very similar to the stripmap SAR geometry. SAR based focusing algorithm also requires the same mapping in Stolt algorithm to be able to use two dimensional inverse FFT.

REFERENCES

1. Daniels, D. J., *Surface-penetrating Radar*, IEE Press, London, 1996.
2. Peters, Jr., L., D. J. Daniels, and J. D. Young, "Ground penetrating radar as a subsurface environmental sensing tool," *Proc IEEE*, Vol. 82, No. 12, 1802–1822, 1994.
3. Ozdemir, C., S. Demirci, E. Yigit, and A. Kavak, "A hyperbolic summation method to focus B-Scan ground penetrating radar images: An experimental study with a stepped frequency system," *Microwave Opt. Tech. Letters*, Vol. 49, No. 3, 671–676, 2007.

4. Schneider, W. A., "Integral formulation for migration in two and three dimensions," *Geophysics*, Vol. 43, 49–76, 1978.
5. Gazdag, J., "Wave equation migration with the phase-shift method," *Geophysics*, Vol. 43, 1342–1351, 1978.
6. Stolt, R. H., "Migration by Fourier transform," *Geophysics*, Vol. 43, 23–48, 1978.
7. Cafforio, C., C. Prati, and F. Rocca, "Full resolution focusing of seasat SAR images in the frequency-wave number domain," *J. of Robotic Systems*, Vol. 12, 491–510, 1991.
8. Zhang, A., Y. Jiang, W. Wang, and C. Wang, "Experimental studies on GPR velocity estimation and imaging method using migration in frequency-wavenumber domain," *Proceedings ISAPE*, 468–473, Beijing, China, 2000.
9. Demirci, Ş, E. Yiğit, İ. H. Eskidemir, and C. Özdemir, "Ground penetrating radar imaging of water leaks from buried pipes based on back-projection method," *Independent Nondestructive Testing and Evaluation*, Vol. 47, 35–42, 2012.

Topology Optimization Procedure to Minimize Radar Cross Section of Perfectly Electric Conductive Structures

H. Yigit

Gebze Institute of Technology, Turkey

Abstract— In this paper, we introduce level set based optimization framework to find optimum shape and topology of perfectly electric conductive (PEC) structure for achieving minimum radar cross section (RCS). The geometry of the structure and it's domain implicitly expressed by scalar level set function and corresponding shape boundary is updated via Hamilton-Jacobi differential equation through optimization iterations. In differential equation boundary propagation speed is determined with the solution of sensitivity analysis of electric field integral equation over PEC surface. Derived integral and differential equations are solved using method of moments (MOM) and upwind scheme techniques respectively. The suggested algorithm is exampled on two dimensional RCS problem and results will be introduced during presentation. This study shows us method can be successfully applicable other electromagnetic problems where optimal shape and topology is looked for.

1. INTRODUCTION

Since the World War II scattering phenomena specifically RCS analysis are studied extensively among electromagnetic community. Questions arises mostly about the best shape for vehicle in order to make it invisible through electromagnetic spectrum. Although design of such vehicle or object should be done with a multidisciplinary work, we see that people in electromagnetics prefer analyze design draft and then make some final contributions. However these attempts usually relies on try-and-error processes [1, 2]. So generally speaking, although fundamentals and solution algorithms of RCS widely studied and documented in literature, there is still few works for an automatic determination of optimum shape of structures.

Genetic algorithms are widespread method in electromagnetics within optimization manner [3, 4]. It is used not for only scattering problems and also many other subjects in electromagnetics. Because such evolutionary design optimization procedure is more general, it needs many design variables and iterations to achieve objective value. On the other hand, specifically for boundary integral formulations-like our problem-gradient based optimization methods are also presented in the past [5]. These methods naively can handle evolving of shape using penalty functions but it's sensitivity analysis need to be done for all design variables.

In this work, we set up a framework for RCS minimization of PEC structures. We will review well studied level set optimization method and adopt it to our problem. Level set method first revealed by Osher and Sethian as a fast marching method of moving boundaries [6]. It is successfully employed at stress analysis optimization problems in mechanical engineering. Method first requires sensitivity analysis of objective function over elastic object boundary. Such formulations are derived for most cases of engineering problems in the literature [7]. Object boundary, which is represented by zero level set function, propagates to achieve minimum objective with solution of Hamilton-Jacobi equation. Fortunately, in recent some few studies are done in electromagnetic within this scope; meta-materials [8], dipole antenna [9], inverse problem [10], resonators [11] are example to them. All these show us level set method can rigorously applicable to electromagnetic problems. Especially [9] gives us an idea that, it is also possible to use the algorithm minimize scattered field from PEC boundary.

The outline of the paper will be in the following form; First we go over well known scattering problem of PEC boundaries in 2D, secondly we declare sensitivity analysis of electric field integral equation (EFIE) for both topology and shape optimization, after that level set algorithm is formulated. Finally beyond the discussion of framework we will put forward some ideas about future implementations of level set method in electromagnetics.

2. SCATTERING PROBLEM

We consider cylindrical PEC boundary, infinitely long through $-z$ axis. Supposing such object is illuminated by TMz polarized plane wave, and with time dependence $e^{-i\omega t}$ it is in the form.

$$\vec{E}^i(q) = \hat{z}e^{ik(x\cos\phi^i + y\sin\phi^i)} \qquad \phi^i : incident\ angle \tag{1}$$
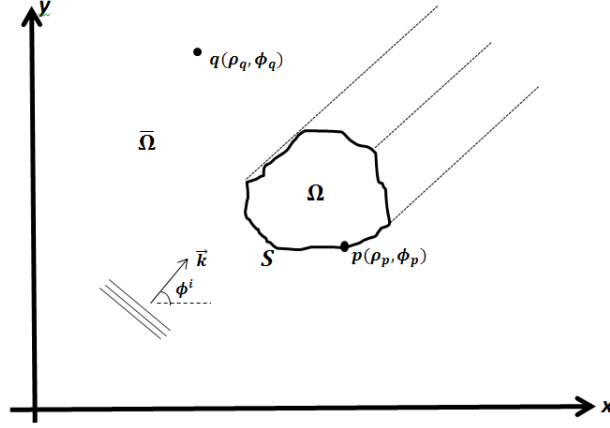
Figure 1: Problem environment.

On the boundary incident field and scattered field satisfy condition:

$$\vec{n} \times [\vec{E}^s + \vec{E}^i] = 0$$
$$E_z^s = -E_z^i \tag{2}$$

Scattered field can be expressed by means of potentials.

$$\vec{E}^s(q) = i\omega \vec{A}(q) - \nabla \Phi(q) \tag{3}$$

Because of the excitation only $-z$ vector components induced on boundary along $-z$ direction there is no change respect to location. So with substituting magnetic potential's explicit form and taking into account boundary condition (2), we obtain well known electric field integral equation (EFIE) for our problem.

$$A_z = \mu \int_S J_z(p)G(q,p)dS_p \qquad G(q,p) = \frac{-i}{4}H_0^{(1)}(k|q-p|)$$

$$i\omega A_z = -E_z^i$$

$$\frac{k\eta}{4}\int_S J_z(p)H_0^{(1)}(k|q-p|)dS_p = -E_z^i(q) \qquad q,p \in \partial\Omega \tag{4}$$

Once we calculate surface current J_z from above, bistatic RCS can be computed using far field approximation.

$$\sigma = \lim_{\rho_q \to \infty} \left\{ 2\pi\rho_q \frac{|E^s|^2}{|E^i|^2} \right\} \simeq C \left| \int_S J_z(p)e^{-ik(\rho_p \cos(\phi_q - \phi_p))}dS_p \right|^2 \qquad C : some\ constant \tag{5}$$

3. SENSITIVITY ANALYSIS

In order to embed our function (5) into an optimization problem we need to determine it's change respect to elastic boundary or boundary movement, which is called shape derivative. In the literature some gradient analysis already done using Frechet derivative, for integral functions like (5). In this aspect, referring to Lemma 5 in [7] we can find shape derivative of our RCS function.

$$Let's\ say\ (5)\ is\ in\ the\ from \qquad \sigma = \int_S K(p)dS_p \qquad then;$$

$$\sigma' = \int_S \theta \cdot \mathbf{n} \left(\frac{\partial K(p)}{\partial n} + HK(p) \right) dS_p \tag{6}$$

Here θ is small enough descent vector, $\mathbf{n}$ represents surface normal and H is mean curvature. Similarly area and perimeter constraint functions shape derivatives can be also derived like following

Remark 6 in [7].

$$
\begin{aligned}
A = \int_\Omega d\Omega = C_1 \quad &\to \quad g_1 = \int_\Omega d\Omega - C_1 \quad &\to \quad g_1' = \int_S \theta \cdot \mathbf{n} dS_p \\
P = \int_S dS_p = C_2 \quad &\to \quad g_2 = \int_S dS_p - C_2 \quad &\to \quad g_2' = \int_S \theta \cdot \mathbf{n} M dS_p
\end{aligned}
\tag{7}
$$

As a result we can review our problem in the optimization problem in the following form,

$$
\begin{aligned}
Min \quad &\sigma = \int_S K(p) dS_p & objective\ function \\
Subject\ to: \quad &\int_\Omega d\Omega = C_1 & area\ constraint \\
&\int_S dS_p = C_2 & perimeter\ constraint
\end{aligned}
\tag{8}
$$

and using fixed Lagrange multipliers (λ_1, λ_2) we reconstruct objective function and it's shape derivative as below:

$$
\begin{aligned}
F &= \int_S K(p) dS_p + \lambda_1 \left(\int_\Omega d\Omega - C_1 \right) + \lambda_2 \left(\int_S dS_p - C_2 \right) \\
F' &= \int_S (\theta \cdot \mathbf{n_p}) \left(\frac{\partial K(p)}{\partial n_p} + H K(p) + \lambda_1 + \lambda_2 H \right) dS_p
\end{aligned}
\tag{9}
$$

4. LEVEL SET ALGORITHM

We see that, change in the boundary of the structure is bound to objective function by means of sensitivity. However boundary evolution needs to be handled through optimization iterations. For such purpose Osher and Sethian proposed an algorithm for fast propagating curves, based on Hamilton-Jacobi equation [6]. This study shows that closed elastic boundary, represented by level set function, can be altered to converge an optimal shape with speed factor which is derived from objective function. Scalar zero level set function of the medium $D = \overline{\Omega} \cup S \cup \Omega$ occupying material Ω can be written by setting boundary as zero level,

$$
\begin{cases}
\psi(q) = 0; & q \in S \cap D \\
\psi(q) < 0; & q \in \Omega \\
\psi(q) > 0; & q \in \overline{\Omega}
\end{cases}
\tag{10}
$$

Now normal to the surface $\mathbf{n}$ can defined as $\nabla\psi/|\nabla\psi|$ and mean curvature H is $\nabla \cdot \mathbf{n}$. After implicit definition boundary, level set function satisfies Hamilton-Jacobi equation:

$$
\frac{\partial \psi}{\partial t} - v|\nabla\psi| = 0
\tag{11}
$$

in this differential form t stands for not actual time, but instead optimization steps. v is speed of shape change can be easily determined from sensitivity analysis, like it is shown in [7].

$$
A\ problem \quad Min \left\{ F = \int_S \dots dS \right\} \quad derivative\ will\ be\ in\ the\ form \quad F'(\Omega) = \int_S v(\theta \cdot \mathbf{n}) dS
$$

Therefore our speed term v equivalent to sensitivity analysis of the functions under RCS integral and constraints in addition.

$$
v = \frac{\partial K(p)}{\partial n_p} + H K(p) + \lambda_1 + \lambda_2 H
\tag{12}
$$

After substituting propagation speed into [11], differential equation can be solved numerically using upwind scheme. And the result yields updated implicit representation of evolving boundary of the structure. To sum up we can list steps of iterative optimization process as below:

   1. *Initialize the level set function.*

2. Till the convergence of objective function (5) to some limit value, repeat the following steps:

   i Solve EFIE and find current distribution. (MOM preferred for our analysis).

   ii Compute speed function using Equation (12).

   iii Update level set function via solution of Hamilton-Jacobi equation (using upwind scheme).

5. CONCLUSION

In this work, we introduce a new approach to achieve optimum RCS of PEC bodies. Numerical results will be discussed during presentation. Although example problem has rather simple integral formulation ($EFIE - 2D$), algorithm is nearly same for 3 dimensional scattering analysis and there is no difficulty implicit representation of level set function since it is scalar simply. Main advantage of this algorithm is, process steps are decoupled. For example one can investigate another integral equation formulation and solve it with various numerical techniques, while general aspects of sensitivity and level set method formulations remain same. On the other hand, sensitivity analysis can be done differently like Zhou et al. in [12], while other procedures done as usual. Also, some additional terms can be considered to increase the stability of Hamilton-Jacobi equation. Therefore, these all show us level set based optimization method gains it's main advantage with serving great flexibility, while handling shape or topological change of structure.

REFERENCES

1. Peoroni, M. B. and S. E. Barbin, "A study on RCS of missile models using the method of moments," *IMOC 2007*, 492–495, 2007.

2. Motevasselian, A. and B. L. G. Jonsson, "Radar cross section reduction of aircraft wing front End," *ICEAA'09*, 237–240, 2009.

3. Johnson, J. M. and Y. Rahmat-Samii, "Genetic algorithms in engineering electromagnetics," *IEEE Antennas and Propogation Magazine*, Vol. 39, No. 4, 7–25, 1997.

4. Veremev, A. and A. J. Ferraro, "Genetic algorithm optimization of radar cross section of cylindrical scatterers," *IEEE APS'98*, Vol. 2, 1288–1291, 1998.

5. Bondeson, A., Y. Yang, and P. Weinerfelt, "Optimization of radar cross section by a gradient method," *IEEE Transaction on Magnetics*, Vol. 40, No. 2, 1260–1263, 2004.

6. Osher, S. and Sethian, "Fronts propagating with curvature-dependent speed: Algorithms based on Hamilton-Jacobi formulations," *Journal of Computational Physics*, Vol. 79, 12–49, 1988.

7. Gregoire, A., J. Francois, and T. Anca-Maria, "Structural optimization using sensitivity analysis and a level-set method," *Journal of Computational Physics*, Vol. 194, 363–393, 2004.

8. Zhou, S., W. Li, G. Sun, and Q. Li, "A level-set procedure for the design of electromagnetic meta-materials," *Optics Express*, Vol. 18, No. 7, 2010.

9. Zhou, S., W. Li, G. Sun, and Q. Li, "Level-set based topology optimization for electromagnetic dipole antenna design," *Journal of Computational Physics*, Vol. 229, 6915–6930, 2010.

10. Ivan, C. and V. K. Roger, "Level Set method for the inverse elliptic problem in nonlinear electromagnetism," *Journal of Computational Physics*, Vol. 229, 9269–9283, 2010.

11. Khalil, H., S. Bila, M. Aubourg, D. Baillargeat, S. Verdeyme, and F. Jouve, "Shape and topology optimization of microwave components," *ACTEA 2009*, 275–278, Zouk Mosbeh, Lebanon, 2009.

12. Zhou, S., W. Li, and Q. Li, "Sensitivity analysis for electromagnetic topology optimization problems," *WCCM/APCOM 2010*, Vol. 10, No. 1, Sydney, Australia, 2010.

Radar Cross Section Analysis of a Square Plate Modeled with Triangular Patch

N. Altın[1] and E. Yazgan[2]

[1]Turkish Aerospace Industries, Inc., Fethiye Mah., No. 17 Havacılık Bulvarı, Kazan Ankara 06980, Türkiye
[2]Electrical & Electronics Engineering Department, Hacettepe University, Beytepe, Ankara 06532, Türkiye

Abstract— In this study, monostatic Radar Cross Section (RCS) of targets which are modeled with different number of triangular patches were analyzed by using Shooting and Bouncing Ray (SBR) method based on geometric optics which is one of the high frequency techniques. Numerical results obtained by SBR method are compared with Physical Optics (PO) results. This study showed that monostatic RCS value is not changed when smooth-surface targets are modeled with different number of triangular patches but computation time increased with increasing the number of triangular patch.

1. INTRODUCTION

Nowadays, when the electronic warfare technology is growing rapidly in, the stealth technology in radar systems became one of the indispensable factors of the defence industry and is used widely in air, land, sea and undersea platforms. Usuage of these techniques that reduces the detection probability of vehicles such as ship, plane, helicopter, submarine, etc. are very important in defence industry.

Complex shaped targets can't be easily identified analytically; therefore they may be modeled as triangular patches. In this study, the change in the radar cross section is examined for any model composed of different number of flat and triangular patches, furthermore by using triangular patches model, Scattering Field is calculated by SIY method. Therefore, a target of any size in the triangular patch model can be used. This approach gives better results at targets consisting of flat surfaces such as ship and building.

2. RADAR CROSS SECTION

Radar cross section is the measure of a target's ability to reflect radar signals in the direction of the radar receiver, i.e., it is a measure of the ratio of backscatter power per steradian (unit solid angle) in the direction of the radar (from the target) to the power density that is intercepted by the target [6]. RCS express the size of the target as seen by radar. RCS of the target is not the same with its physical cross-sectional area. RCS is a parameter which depends on the target frequency and polarization of incident plane wave, illumination and observation geometry, the shape of the target and the function of the material from which it is fabricated [1]. The radar cross section is expressed mathematically in the following way.

$$RCS = \lim_{R \to \infty} 4\pi R^2 \frac{|E^{scat}|^2}{|E^{inc}|^2} \tag{1}$$

where $|E^{inc}|^2$ is the electric-field strength of the incident wave impinging on the target $|E^{scat}|^2$ is the electric-field strength of the scattered wave at the radar and R is typically taken to be the range from the radar to the target. Eq. (1) is valid when the target is illuminated with plane waves in the far field. Calculation of the scattered field from a target is complex by using Eq. (1) but analytical solution of this equation is available for simple geometries.

Modeling complex shaped targets by triangular patches facilitates SBR application and accelerates RCS analysis.

3. SHOOTING AND BOUNCING RAY (SBR) METHOD

High frequency technique called shooting and bouncing ray was examined by Ling, Chou and Lee [2–4] and this method is applied in electromagnetic scattering and antenna radiation problems.

It is assumed that plane wave is from the far field to the target and scattering field from target is calculated by SBR which is one of the high frequency techniques and RCS value of target is determined [2, 5]. Shadowing and multiple reflections are important, SBR gives very accurate results.

SBR is based on geometric optic method. Complex shaped targets are modeled with triangular patches by using graphics program in the SBR method. RCS analyses with SBR method helps to accelerate composed of triangular patches of target. Targets composed of triangular patches accelerate the RCS analyses using the SBR method.

At an observation point (r, θ, ϕ) in the far field, scattering field is expressed by

$$\overrightarrow{E_s} = \frac{e^{-jkr}}{r}[\hat{\theta}A_\theta + \hat{\phi}A_\phi] \tag{2}$$

To calculate scattering field on the aperture, Huygens principle is used. According to Huygens principle, after incident ray is reflected multiply on the surface, scattering field is calculated the last hit point from surface.

When the SBR method is used, the contribution of the existing rays to the scattered field is given by:

$$\begin{bmatrix} A_\theta \\ A_\phi \end{bmatrix} = \frac{jk}{4\pi} \int\limits_{\substack{raytube \\ projection \\ on \, S}} e^{j\vec{k}_0 \cdot r} \left(\begin{bmatrix} -\hat{\phi} \\ \hat{\theta} \end{bmatrix} \times \vec{E}(r) + \eta \begin{bmatrix} \hat{\theta} \\ \hat{\phi} \end{bmatrix} \times \vec{H}(r) \right) \cdot \hat{n} \, ds' \tag{3}$$

$$\begin{bmatrix} A_\theta \\ A_\phi \end{bmatrix} = \frac{jk}{4\pi} \begin{bmatrix} A_\theta \\ A_\phi \end{bmatrix} = \sum_{i \, rays} \begin{bmatrix} B_\theta \\ B_\phi \end{bmatrix} \left(\frac{jk}{2\pi} \right) (\Delta A)_{exit} S(\theta, \phi) e^{jk \cdot r_A} \tag{4}$$

In the above expression, r_A is the position vector of point A where the ray-tube integration is carried out. Point A is usually chosen to be the last hit point on the target for the ray. $(\Delta A)_{exit}$ is the cross section of the exit ray tube at A and $S(\theta, \phi)$ is the shape function corresponding to the radiation pattern from the ray tube. $S(\theta, \phi)$ can usually be assumed to be unity if the ray tube area is sufficiently small, since the radiation from the ray tube will be nearly isotropic. B_θ, B_ϕ are explicitly related to the aperture fields at A as:

$$B_\theta = 0.5[-s_1 \cos\phi E_3 - s_2 \sin\phi E_3 + s_3(\cos\phi E_1 + \sin\phi E_2)] + 0.5Z_0[s_1(\cos\theta\sin\phi H_3 + \sin\theta H_2)$$
$$+ s_2(-\sin\theta H_1 - \cos\theta\cos\phi H_3) + s_3(\cos\theta\cos\phi H_2 - \cos\theta\sin\phi H_1)] \tag{5}$$
$$B_\phi = 0.5[s_1(\cos\theta\sin\phi E_3 + \sin\theta E_2) + s_2(-\sin\theta E_1 - \cos\theta\cos\phi E_3) + s_3(\cos\theta\cos\phi E_2 - \cos\theta\sin)$$
$$+ 0.5Z_0[s_2\cos\phi H_3 + s_2\sin\phi H_3 + s_3(-\cos\phi H_1 - \sin\phi H_2)] \tag{6}$$

where $E(A) = E_1\hat{x} + E_2\hat{y} + E_3\hat{z}$ and $H(A) = H_1\hat{x} + H_2\hat{y} + H_3\hat{z}$ are respectively the electric and magnetic field associated with each ray at A, and $\hat{s} = s_1\hat{x} + s_2\hat{y} + s_3\hat{z}$ is the exit ray direction.

In summary, the far field contribution from a ray tube is given in Eq. (4) and Eq. (6). This result is obtained by applying the PO theory to the scattered field over the scatterer surface.

4. MODELING OF TARGETS

Computer Aided Design (CAD) models of targets are produced by using CATIA modeling program. After producing CAD model of target, target surface is divided triangular patches by generating automatically mesh. Sizes of triangular patches are selected to produce optimal results in the simulation: generally, triangular patches sizes are 0.1. Targets divided into triangular patches are imported to radar cross section software program for simulation. In this study, computer aided design models obtained stereolithography (stl) format is used.

5. NUMERICAL RESULTS

$1\,m \times 1\,m$ square plate composed of Fig. 1(a) two triangular patches, Fig. 1 (b) four triangular patches and Fig. 1(c) 322 triangular patches. For a square plate when θ elevation angle changes between $[-90°, 90°]$ and the ϕ azimuth angle is $0°$, Figs. 1(a), (b) and (c) show the Monostatic RCS value in the vertical polarization.

RCS values in figures are given in dB square meter. Ray window illuminated to square plate is created by $\lambda/20$ intervals in SBR method and square plate is illuminated with rays of the number 4356 in the 1 GHz frequency value.

As shown in Figs. 2 (a), (b) and (c), RCS values of square plate modeled with different number of triangular patches are the same. It is also showed that RCS value is independent of the number

(a)   (b)   (c)
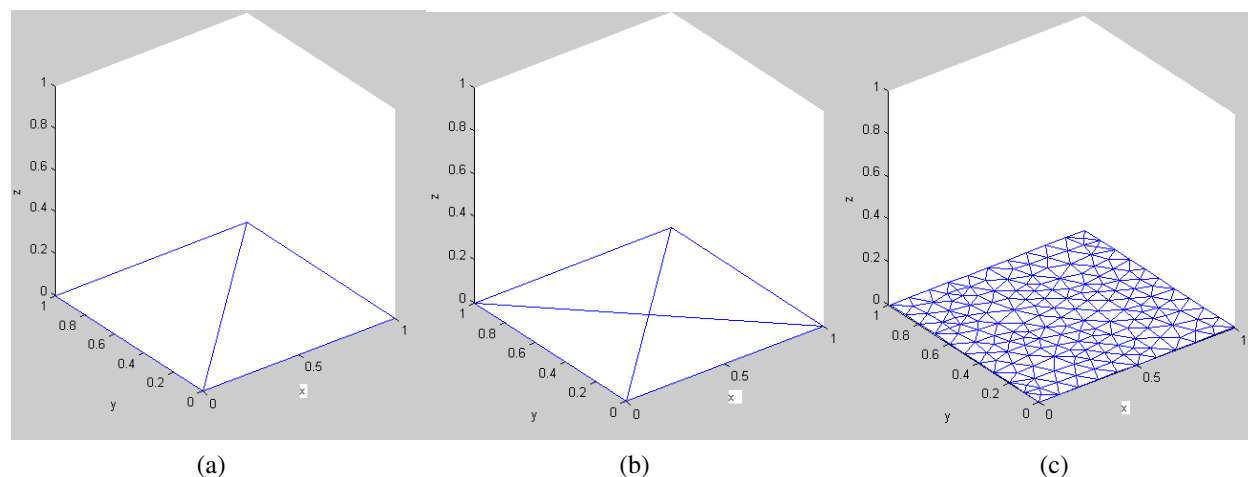
Figure 1: (a) Square plate modeled with two triangular patches, (b) square plate modeled with four triangular patches and (c) square plate modeled with 322 triangular patches.

(a)   (b)   (c)
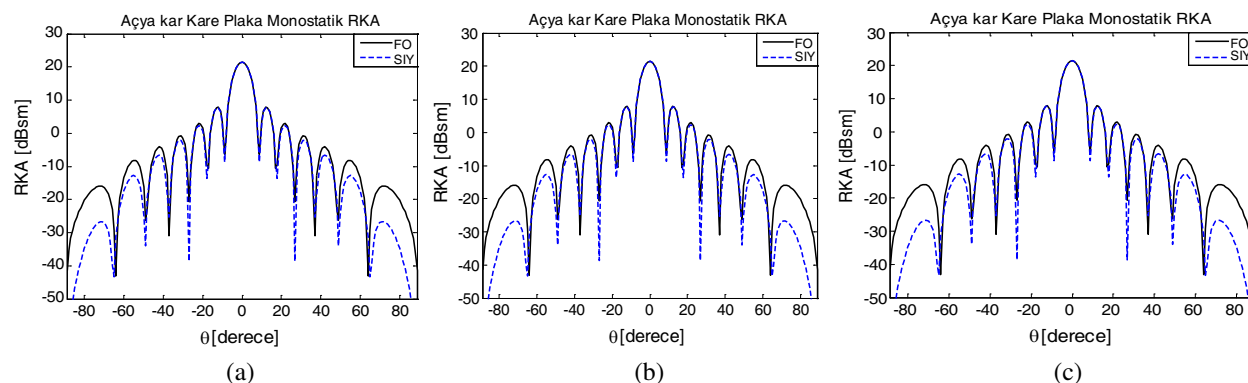
Figure 2: Monostatic RCS of square plate for vertical polarization according to angle comparison physical optics and SBR results.

Table 1: The running time of square plate.

RCS analyses of square plate with SBR	The number of triangular patches	Running time (sc)
Fig. 1(a)	2	34
Fig. 1(b)	4	37
Fig. 1(c)	322	593

of triangular patches composed of square plates. If the target surface is flat, target surface is divided by great triangular patches as properties of target surface (surface normal vector, surface empedance v.b.) have not changed throughout the plate. to take physical optics integral over the large surface does not change the Computational complexity because samples should be taken during the integration in order to describe the phase change of a single triangle. As shown in Table 1, when the number of triangular patches is more, program running time increases.

6. CONCLUSION

In this study, when triangular patch number in the flat surface as a plate changes, it is examined whether RCS value change. As a result of analyses, it is seen that RCS value is independent of the number of triangular patches. But when there are curved surfaces in the model, it is expected that RCS value changes according to the sensitivity of modeling. As the number of triangular patches in the curved surfaces change, modification in the model geometry may occur. Changes of the geometry model will cause to changes in RCS values and graphics. For flat surfaces when the number of triangular patches increases in the flat surfaces, RCS value does not change but the time of RCS analysis increases.

REFERENCES

1. Ergin, A., *Gorunmezlik Teknolojileri: Radar Kesit Alanı Nedir?*, No. 120, Savunma ve Havacılık, 2007.
2. Ling H., R. Chou, and S. W. Lee, "Shooting and bouncing rays: Calculating the RCS of an arbitrarily shaped cavity," *IEEE Trans. on Antennas and Propagat.*, Vol. 37, No. 2, 194–205, 1989.
3. Lee, S. W., H. Ling, and R. Chou, "Ray-tube integration in shooting and bouncing ray method," *Microwave and Optical Technology Letters*, Vol. 1, No. 8, 286–289, October 1988.
4. Ling, H., S. W. Lee, and R. C. Chou, "High frequency RCS of open cavities with rectangular and circular cross section," *IEEE Trans. on Antennas and Propagat.*, 648–654, 1989.
5. Ling H. and R. Bhalla, "Image-domain ray-tube integration formula for the shooting and bouncing ray technique," Air Force Wright Laboratory through NASA Grant NCC 3-273, July 1993.
6. Knott, E. F., J. F. Shaeffer, and M. T. Tuley, *Radar Cross Section*, Artech House, Inc., USA, 1985.

Dual Wideband CPW Fed Dieletric Resonator Antenna

Sriparna Bhattacharya (Mitra)[1] and Bhaskar Gupta[2]

[1]Department of Electronics and Communication Engineering
Heritage Institute of Technology, Kolkata 700107, India
[2]Department of Electronics and Tele-Communication Engineering
Jadavpur University, Kolkata 700 032, India

Abstract— This paper presents the design of a hybrid dual wideband dielectric resonator antenna. The DRA is parallelepiped in shape and is fed by a coplanar wave guide slot. The slot acts both as the feeding structure and an effective radiator. A substrate with $\varepsilon_r = 2.5$ has been chosen for etching the slot and the DRA consists of material with $\varepsilon_r = 6$. The structure parameters are optimized using HFSS(v.11) to get two independent operating frequency range. Performance parameters such as resonant frequencies, impedance parameters and radiation pattern have been studied. The simulated bandwidths are 23% and 12.9% in the two bands. The antenna has been fabricated and measured results are awaited for.

1. INTRODUCTION

Dielectric resonator antenna has become very popular as an effective radiating element in the field of wireless communication. High radiation efficiency because of absence of conductor loss is the main reason of its popularity. Apart from that it also has a number of other advantages like low loss, light weight, compact size, and good compatibility with other structures etc.

DRA comes in many shapes and sizes like rectangular, circular, hemispherical, cylindrical etc. The design of an antenna becomes more flexible with rectangular shape because it has two degrees of freedom [1] whereas other common shapes like cylindrical, hemispherical etc. have less. Moreover the rectangular shape is easier to fabricate compared to other shapes.

Matching of the DRA to the feedline is very important in order to excite the desired mode and to get proper radiation pattern. A DRA can be excited by many ways like using a probe [2, 3] or an aperture coupled microstrip [4] or CPW [5]. The coplanar waveguide fed antenna has become a promising candidate due to its uniplaner structure, wide bandwidth, and easy integration with RF front-end circuitry.

As the field of wireless communication is expanding demand for more and more broad band antennas is also increasing. Recently much focus has been given on the band width enhancement of DRA and many techniques have been proposed to broaden their operational bandwidth. One type of effective methods uses some special composite DR structures such as stacked DRs with different materials [6] and embedded DRs [7]. Other types of methods adopt special feeding mechanisms or utilize multisegment DRAs [8–13] or use parasitic elements [14] or air gap in DRA [15]. However all of these either include complex design or a combination of different dielectric materials.

In this paper a very simple and novel design is proposed for dual wideband operation. Keeping in mind the design flexibility a parallelepiped shaped DRA is chosen and it is excited by a CPW
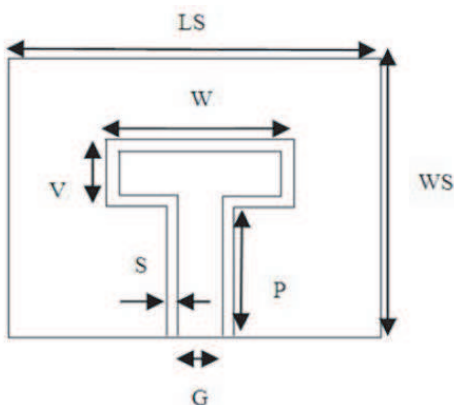
Figure 1: The loop shaped slot.
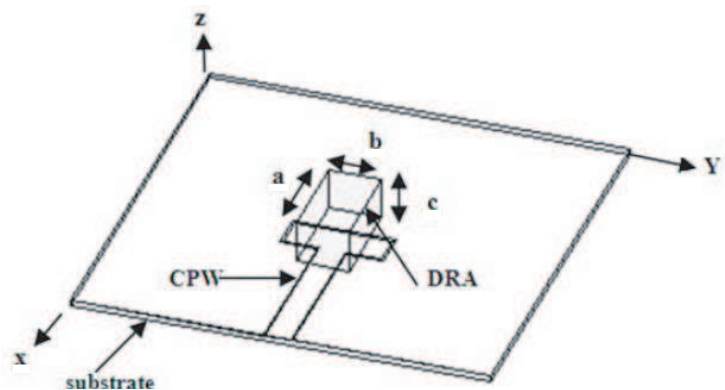
Figure 2: The Loop with the DRA.
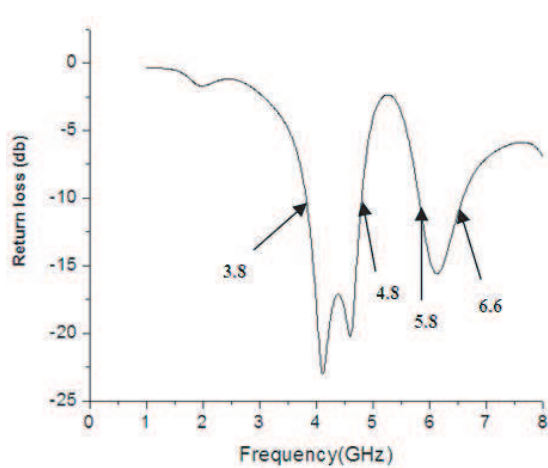
Figure 3: Plot of S_{11} vs. frequency of the designed antenna.
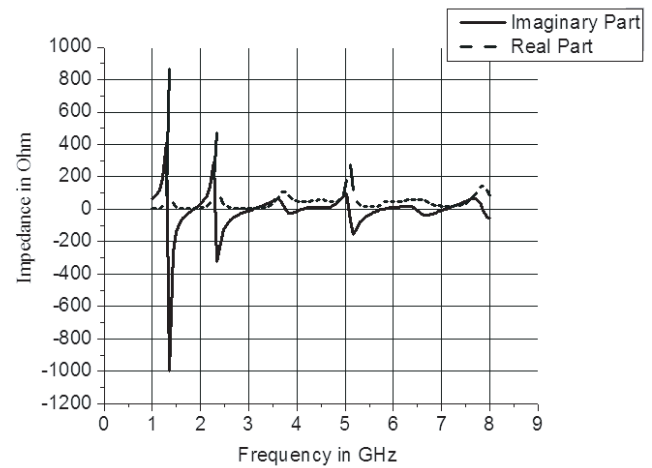
Figure 4: Impedance Plot vs. Frequency of the proposed antenna.
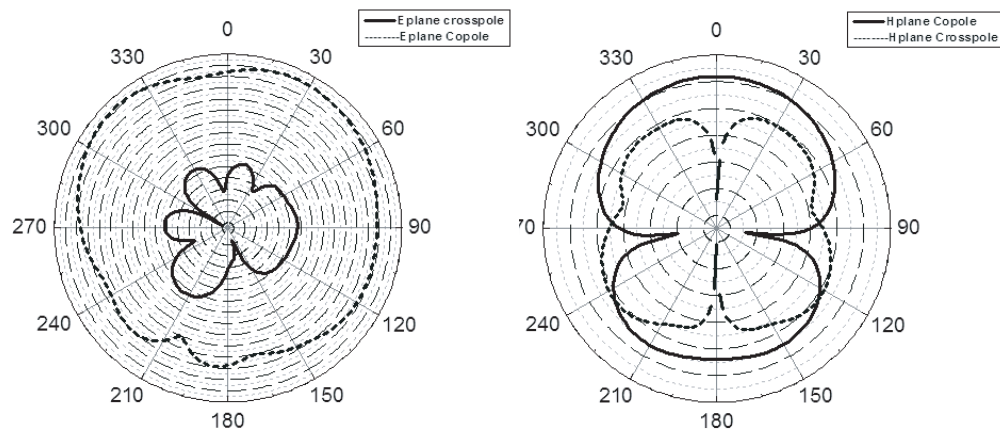
Figure 5: Radiation patterns at 4.3 GHz.

feed. The antenna is a hybrid structure consisting of a CPW slot and a dielectric resonator placed on the loop shaped slot (Fig. 2).

2. DESIGN

An approximate and quick design procedure is followed according to [16]. A substrate with $\varepsilon_r = 2.5$ and thickness of 60 mils has been chosen for etching the CPW slot on it. The shape of the substrate is a perfect square with $LS = WS = 120$ mm and it is without a back conductor. The dimensions of the CPW are found out so that it provides $50\,\Omega$ characteristic impedance and is centrally placed on the substrate. The dimensions are further optimized using HFSS and the final design comes with $S = 0.3$ mm and $G = 7.8$ mm where G is the central conductor and S is the gap. The resonant frequency of the loop shaped radiating slot is chosen to be 4.4 GHz and the dimensions of the slot are optimized again using HFSS. The Final design of the slot is as follows: $V = 10.525$ mm, $W = 29.4$ mm and $P = 46.075$ mm. The DRA consists of material with $\varepsilon_r = 6$ and is parallelepiped in structure. After thorough parametric studies, the DRA dimensions are optimized as $a = 28$ mm, $b = 15$ mm, $c = 12$ mm as shown in Fig. 2.

The antenna thus behaves as a hybrid radiator with two radiating structures being predominant at the two frequency bands of operation. Parasitic loading enhances the bandwidth in both bands.

3. RESULTS

Dual wideband operation has been observed through simulation using HFSS, one ranging from 3.8 GHz to 4.8 GHz and another ranging from 5.8 GHz to 6.6 GHz. The 10-dB simulated return loss band widths are 23% (3.8–4.8 GHz) and 12.9% (5.8–6.6 GHz). A very good impedance match has
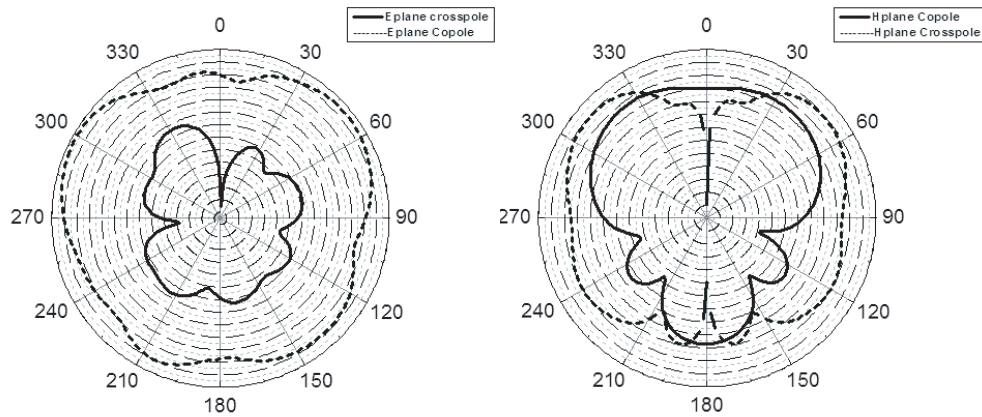
Figure 6: Radiation patterns at 6.2 GHz.

been obtained in both bands as is evident from the simulated return loss plot (Fig. 3). Both bands satisfy the Ultra Wide Band (UWB) requirements according to IEEE definition. The frequency vs. impedance plot is also shown in Fig. 4. We find that the real part of the input impedance is 50 ohms and its imaginary part is zero in both the frequency bands, thus showing excellent impedance match.

The radiation patterns at centre frequencies of the two bands are shown in Fig. 5 & Fig. 6. The radiation patterns are omnidirectional in E plane and monopole like in H plane. The peak gain of the antenna in the first frequency band 3.8–4.8 GHz is 4.75 dB and in the second frequency band 5.8–6.6 GHz is −2.6 dB. The antenna has been fabricated and measured results are awaited for.

4. CONCLUSION

In this paper a dual wideband antenna has been designed. The antenna is a hybrid structure consisting of a resonating slot and a dielectric resonator fed by a coplanar waveguide. All the design parameters have been optimized using HFSS. We have obtained two independent frequency bands ranging from 3.8–4.8 GHz and 5.8–6.6 GHz. The S_{11} in both the frequency range lies well below −10 dB The radiation patterns in both E plane and H plane have been studied and are quite regular. The antenna is quite simple in nature and easy to fabricate and hence can be used in various fields.

REFERENCES

1. Antar, Y. M. M. and Z. Fan, "Theoretical investigation of aperture-coupled rectangular dielectric resonator antenna," *Proc. Inst. Elect. Eng.*, Part H, Vol. 143, No. 2, 113–118, Apr. 1996.
2. Long, S. A., M. W. McAllister, and L. C. Shen, "The resonant cylindrical dielectric cavity antenna," *IEEE Trans. Antennas Propagat.*, Vol. 31, 406–412, May 1983.
3. Leung, K. W., K. M. Luk, and K. Y. A. Lai, "Theory and experiment of a coaxial probe fed hemispherical dielectric resonator antenna," *IEEE Trans. Antennas Propagat.*, Vol. 41, 1390–1398, Jun. 1993.
4. St.-Martin, J. T. H., Y. M. M. Antar, A. A. Kishk, A. Ittipiboon, and M. Cuhaci, "Dielectric resonator antenna using aperture coupling," *Electron. Lett.*, Vol. 26, No. 24, 2015–2016, Nov. 1990.
5. Ghosh, B., Y. M. M. Antar, A. Petosa, and A. Ittipibon, "CPW feed to rectangular DRA," *Microwave and Optical Technology Letters*, Vol. 45, No. 3, May 2005.
6. Shum, S. M. and K. M. Luk, " Stacked annular-ring dielectric resonator antenna excited by axi-symmetric coaxial probe," *IEEE Trans. Antennas Propagat.*, Vol. 43, No. 8, 889–892, Aug. 1995.
7. Walsh, A. G., S. D. Young, and S. A. Long, "An investigation of stacked and embedded cylindrical dielectric resonator antennas," *IEEE Antennas Wireless Propag. Lett.*, Vol. 5, 130–133, 2006.
8. Petosa, A., N. Simons, R. Siushansinan, A. Ittipiboon, and M. Cuhaci, "Design and analysis of multisegment dielectric resonator antennas," *IEEE Trans. Antennas Propagat.*, Vol. 48, No. 5, 738–742, May 2000.

9. Coulibaly, Y., T. A. Denidni, and L. Talbi, "Wideband impedance bandwidth hybrid dielectric resonator antenna for X-band applications," *Proceedings of IEEE Antennas and Propagation Society Symposium*, 2429–2432, Albuquerque, NM, 2006.

10. Lapierre, M., et al., "Ultra wideband monople/dielectric resonator antenna," *IEEE Antennas Wireless Propag. Lett.*, Vol. 15 , No. 1, 7–9, Jan. 2005.

11. Guha, D., et al., "Improved design guidelines for the ultra wideband monopole-dielectric resonator antenna," *IEEE Antennas Wireless Propag. Lett.*, Vol. 5, 373–376, 2006.

12. Kumar, A. V. P., V. Hamsakutty, J. Yohannan, and K. T. Mathew, "A wideband conical beam cylindrical dielectric resonator antenna," *IEEE Antennas Wireless Propag. Lett.*, Vol. 6, 15–17, 2007.

13. Liang, X.-L., T. A. Denidni, and L.-N. Zhang, "Wideband L-shaped dielectric resonator antenna with a conformal inverted-trapezoidal patch feed," *IEEE Trans. Antennas Propagat.*, Vol. 57, No. 1, 272–274, 2009.

14. Fan, Z., et al., "Parasitic coplanar three element dielectric resonator antenna subarray," *Electron. Lett.*, Vol. 32, No. 9, 789–790, Apr. 1996.

15. Wong, K. L., et al., "Analysis of a hemispherical dielectric resonator antenna with an airgap," *IEEE Microw Guide Wave Lett.*, Vol. 3, No. 9 , 355–357, Oct. 1993.

16. Al Salameh, M. S., Y. M. M. Antar, and G. Séguin, "Coplanar-waveguide-fed slot-coupled rectangular dielectric resonator antenna," *IEEE Trans. Antennas Propagat.*, Vol. 50, No. 10, 1415–1419, Oct. 2002.

Design of a Wide Dual-band Microstrip Antenna for WLANs Applications

Abdulkareem S. Abdullah and Nabil E. Abdulhussein

Department of Electrical Engineering, College of Engineering
University of Basrah, Basrah, Iraq

Abstract— This paper presents a new design to obtain wide dual-band operation from a single-feed microstrip antenna loaded with a chip resistor and two cross-slots in ground plane. The lower band of the proposed antenna has a bandwidth of 12.5% around 2550 MHz, and the upper band has a bandwidth of 6.3% around 5263 MHz and 6.41% around 5651 MHz. The obtained bandwidths cover WLANs operations in both the 2.4 GHz (2400–2483.5 MHz) and 5.2 GHz (5150–5350 MHz) or 5.6 GHz (5470–5825 MHz) bands. A three dimensional finite-difference time-domain (3-D FDTD) method is employed to analyze the proposed structure and find its performance.

1. INTRODUCTION

Some applications such as satellite links, wireless local networks (WLAN), cellular telephones and global positioning system (GPS) require wide-band dual-frequency antennas, and microstrip patch antennas can be used to satisfy these requirements due to their low profile structure, light weight, ease of integration with microwave integrated circuits (MICs), and capability of producing dual frequency operations [1, 2].

Various methods have been used to achieve dual frequency operation such as excitation of orthogonal modes [3], using slots in the patch [4, 5], loading the patch with shorting pins [6, 7], using stacked patch [8, 9] and using planner antennas with special geometries to create several resonance paths [10]. Using these methods achieve very narrow bandwidth, 0.5%–1.5% (SWR = 2), so it is necessary to use additional techniques to improve it.

In this paper, a technique of adding a resistive load between patch and ground plane at suitable position is used to achieve acceptable return losses at desired frequencies. A two cross slots in ground plane is created to control the two resonant frequencies and for antenna size reduction. A full-wave method of a three dimensional finite- difference time-domain (3-D FDTD) method is employed to analyze the proposed structure and find its performance. A proposed antenna provides two bands, the lower band covers ISM band (2400–2483.5 MHz) which is required by WLAN IEEE 802.11b,g standard, Bluetooth, and the higher band covers one of U-NII1 (5150–5350 MHz), U-NII2 (5470–5725 MHz) and U-NII3/ISM (5725–5825 MHz) which is required by IEEE 802.11a and HiperLAN2 standards [11].

In Section 2 the details of the design considerations of the proposed antenna are described. The simulation results are presented in Section 3. Conclusion is presented in Section 4.

2. ANTENNA DESIGN

Figure 1 shows the structure of the proposed antenna. The patch has a width of 13 mm and length of 10 mm which is approximately equal to the half-wavelength at 6 GHz. The patch is fabricated on $(23 \times 20)\,\mathrm{mm}^2$ FR4 substrate with a thickness of 1.6 mm, a relative permittivity of 4.4 and a loss tangent of 0.02. A chip resistor is connected between the patch and ground plane at 1 mm above patches center. A chip resistor presence causes the antenna to operate at two frequencies with wide bandwidth. A two cross-slots in ground plane are existed to control the two resonant frequencies and to reduce the antenna size. The vertical arm of the lower cross-slot has a length of (L) mm and the vertical arm of the upper cross-slot has a length of $(L-2)$ mm. The horizontal arms of upper and lower cross-slot have length of $(d\,\mathrm{mm})$, a width of all arms are 1 mm.

A 50 Ω probe feed is used for feeding the antenna. The optimal feed position is found to be 3 mm left of the chip resistor along x-axis to ensure acceptable values of return loss at the two bands.

3-D FDTD method is used for the simulation of the complete structure of the antenna including the resistive load. The FDTD problem space is composed of cells with $\Delta x = 0.5\,\mathrm{mm}$, $\Delta y = 0.5\,\mathrm{mm}$ and $\Delta z = 0.533\,\mathrm{mm}$ which are selected to be smaller than $(1/20)$ wavelength of maximum frequency (6 GHz) in order to ensure the accuracy of the computed results [12, 13]. These cell sizes make the volume of object to be $(40\Delta x, 46\Delta y$ and $3\Delta z)$. The boundaries are terminated by 8 cells conventional perfect match layers (CPML) and 10 cells air gap is left between the object in the problem space and CPML boundaries.

(a) Patch side view   (b) Ground plane view
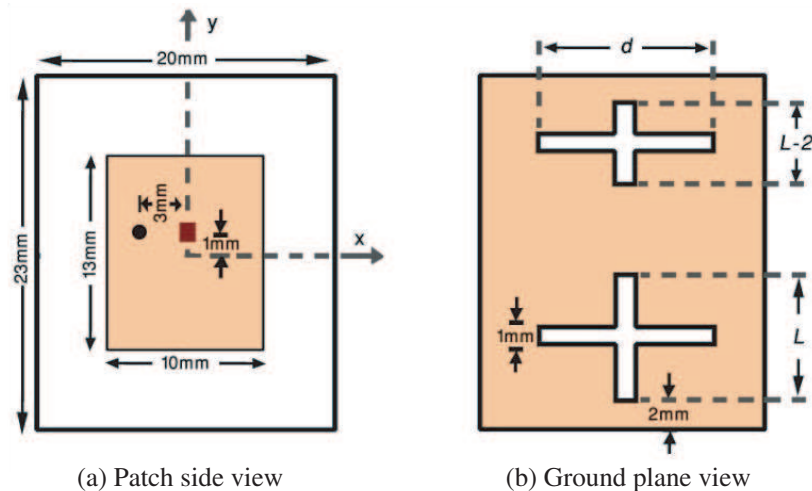
Figure 1: Proposed configuration for dual-band microstrip antenna.
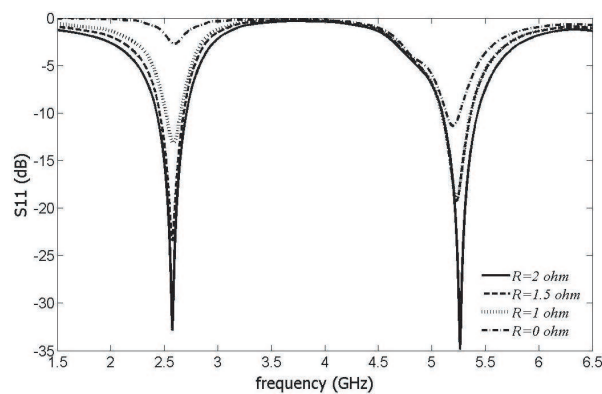
Figure 2: Return losses of the proposed antenna for different R values at $L = 9$ mm and $d = 8$ mm.
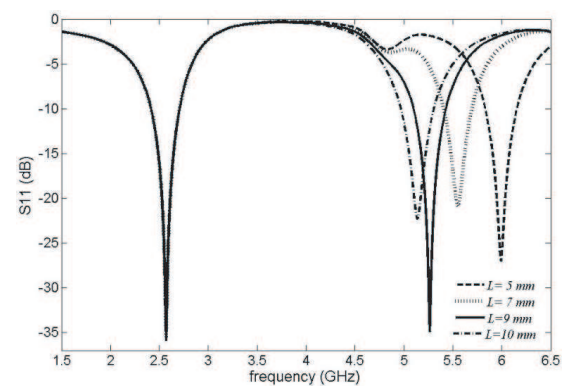
Figure 3: Return losses of the antenna for different value of L at $d = 8$ mm.

3. RESULTS AND DISCUSSION

3.1. Effect of Chip Resistor R

The effects of chip resistor loading are studied first. In order to obtain minimum return losses at the desired two frequency bands, the chip resistor is placed at 1 mm above the patches centre, and its value is changed from $0\,\Omega$ (shorting case) to $2\,\Omega$. For the case of using chip resistor of larger value, the ohmic loss of the antenna quickly increases and the radiation efficiency decreases [14]. Fig. 2 shows the calculated return losses of the proposed antenna at different values of chip resistor and the corresponding results are given in Table 1. It is noticeable that as the value of the chip resistor increases from 0 to $2\,\Omega$ the bandwidth of the two bands increases. The positions of two resonant frequencies are very slightly affected by variation of chip resistor value.

The optimal feed position need to be moved further from the chip resistor when the loading resistance increases. It is seen that at the shorting case the distance between the feed position and chip resistor is 1 mm, and at the $2\,\Omega$ case the distance is 3 mm.

3.2. Effect of Vertical Arms Length L

To find the effect of the vertical arms of the two cross-slots on the two operating frequencies, the length of the two vertical arms (L) and $(L-2)$ is varied at fixed length of horizontal arms of the two cross-slots $(d = 8$ mm$)$ and $R = 2\,\Omega$. Fig. 3 shows the calculated return losses for two frequencies at different values of L.

Figure 4 shows the two resonant frequencies and the frequency ratio (f_{r2}/f_{r1}) against L. The corresponding calculated dual-frequency performance is listed in Table 2. The results clearly show that, upon the increasing of the slot length L, the lower frequency f_{r1} is not affected by the variation of L and it remains at 2550 MHz. On the other hand, the higher frequency f_{r2} is decreased and

Table 1: Performance of the antenna for different values of a chip resistor at $L = 9\,\text{mm}$ and $d = 8\,\text{mm}$.

$R\ (\Omega)$	f_{r1} MHz	BW_1 MHz, %	f_{r2} MHz	BW_2 MHz, %
0	-	-	5197	127, 2.04
1	2571	142, 5.52	5231	273, 5.22
1.5	2554	224, 8.77	5232	272, 5.20
2	2550	307, 12.04	5263	332, 6.30

Table 2: Performance of the proposed antenna for different values of L at $R = 2\,\Omega$ and $d = 8\,\text{mm}$.

L mm	f_{r1} MHz	BW_1 MHz, %	f_{r2} MHz	BW_2 MHz, %	(f_2/f_1)
5	2550	307, 12.04	5991	325, 5.45	2.35
7	2550	307, 12.04	5550	290, 5.23	2.18
9	2550	307, 12.04	5263	332, 6.30	2.06
10	2550	307, 12.04	5136	340, 6.62	2.01
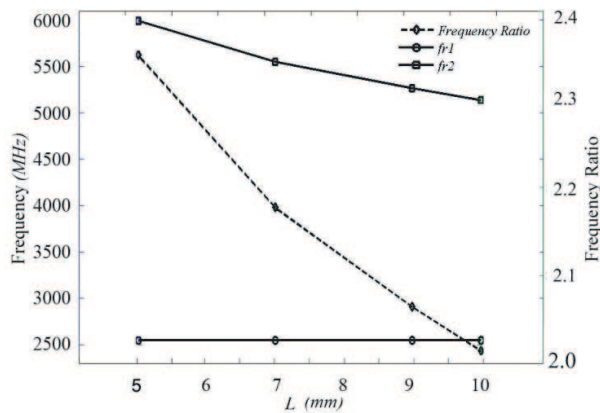
Figure 4: Calculated resonant frequencies f_{r1} and f_{r2} and frequency ratio (f_{r2}/f_{r1}) against L.
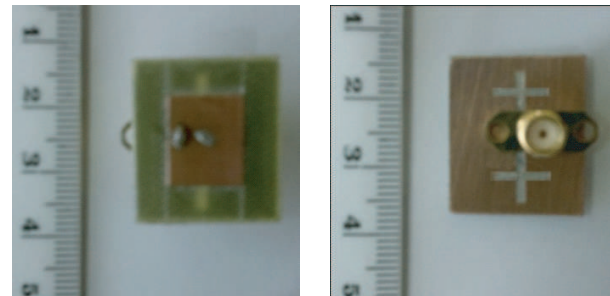
(a) Patch side view　　(b) Ground plane view

Figure 5: A photograph of the proposed dual-band microstrip antenna.

is lower than $6000\,\text{MHz}$. Also, from the results, it is found that the optimal feed positions for the present design are almost about the same, which indicate that the feed position is not affected by the variation of L.

From Table 2, at $L = 9\,\text{mm}$, the lower mode of the proposed design has a $10\,\text{dB}$ bandwidth of $307\,\text{MHz}$ (2398–$2705\,\text{MHz}$), and the upper mode has a bandwidth of $332\,\text{MHz}$ (5097–$5429\,\text{MHz}$). The obtained bandwidths cover WLAN operations in two bands, the first band is ISM band (2400–$2483.5\,\text{MHz}$) which is required by WLAN IEEE 802.11b,g and Bluetooth standards, and the second band is U-NII1 (5150–$5350\,\text{MHz}$) band which is required by IEEE 802.11a and HiperLAN2 standards.

The photograph of the proposed design with $L = 9\,\text{mm}$, $d = 8\,\text{mm}$ and $R = 2\,\Omega$ is shown in Fig. 5. The measured and simulated return losses are shown in Fig. 6.

Figure 6 shows the simulated bandwidth is $307\,\text{MHz}$ at $2550\,\text{MHz}$ while the measured bandwidth is $366\,\text{MHz}$ at $2590\,\text{MHz}$.

3.3. Effect of Horizontal Arms Length d

The horizontal arms length d is varied with fixed L ($L = 8\,\text{mm}$) and $R = 2\,\Omega$. Fig. 7 shows the calculated return losses for two frequencies at different values of d. The two resonant frequencies (f_{r1} and f_{r2}) and the frequency ratio (f_{r2}/f_{r1}) against d variation are shown in Fig. 8. The corresponding antenna performance listed in Table 3.

From the above result, the increasing in slot length d has same effect on the two resonant frequencies and causes decreasing in both of them, so that the frequency ratio approximately
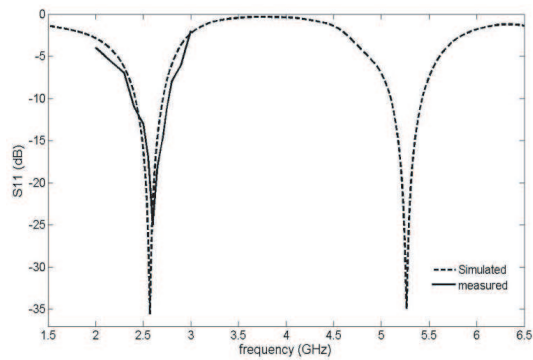
Figure 6: Measured and simulated return losses for $L = 9\,\text{mm}$, $d = 8\,\text{mm}$ and $R = 2\,\Omega$.
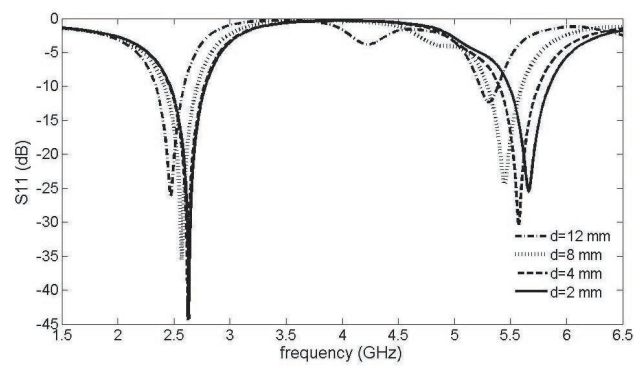
Figure 7: Calculated return losses for different values of d at $L = 8\,\text{mm}$.
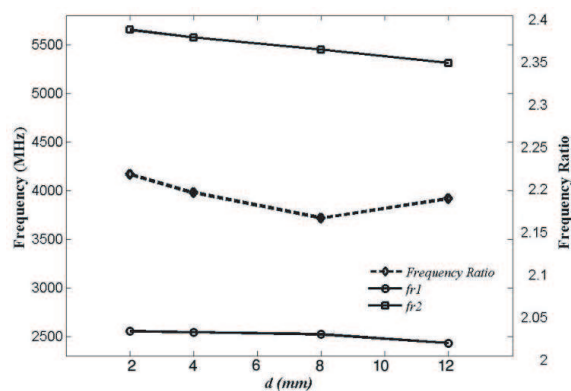
Figure 8: Resonant frequencies f_{r1} and f_{r2} and frequency ratio (f_{r2}/f_{r1}) against d.
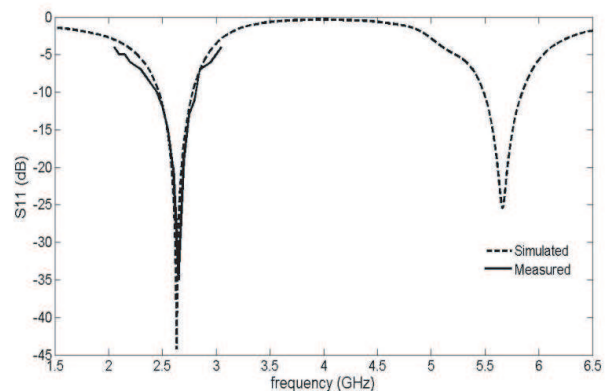
Figure 9: Measured and simulated return losses for $L = 8\,\text{mm}$, $d = 2\,\text{mm}$ and $R = 2\,\Omega$.

Table 3: Performance of the proposed antenna for different values of d at $R = 2\,\Omega$ and $L = 8\,\text{mm}$.

| d | f_{r1} | BW_1 | f_{r2} | BW_2 | (f_2/f_1) |
mm	MHz	MHz, %	MHz	MHz, %	
2	2553	319, 12.5	5651	362, 6.41	2.21
4	2543	311, 12.23	5573	351, 6.30	2.19
8	2520	294, 11.67	5447	307, 5.64	2.16
12	2431	253, 10.41	5311	158, 2.97	2.18

remains constant compared with the case of varying L. It is clear that, the increasing in d causes longer paths for two modes.

From Table 3, it is shown that, by set $d = 2\,\text{mm}$ the lower mode of the proposed design has a bandwidth of 319 MHz (2394–2713 MHz), and the upper mode has a bandwidth of 362 MHz (5467–5829 MHz). The obtained bandwidths cover WLAN operations in two bands, the first band is ISM band (2400–2483.5 MHz) which is required by IEEE 802.11b,g and Bluetooth standards and the second band is U-NII2 (5470–5725 MHz) and U-NII3/ISM (5725–5825 MHz) bands which is required by IEEE 802.11a standard.

The proposed design with $L = 8\,\text{mm}$, $d = 2\,\text{mm}$ and $R = 2\,\Omega$ has been fabricated, and the measured and simulated return losses of designed antenna are shown in Fig. 9.

It is shown that the simulated bandwidth is 319 MHz at 2553 MHz while the measured bandwidth is 341 MHz at 2580 MHz.

4. FAR-FIELDS CALCULATIONS

With the FDTD technique, the direct evaluation of the far field calls for an excessively large computational domain, which is not practical. Instead, the far-zone electromagnetic fields are computed

(a) 2.45 GHz   (b) 5.2 GHz   (c) 5.6 GHz
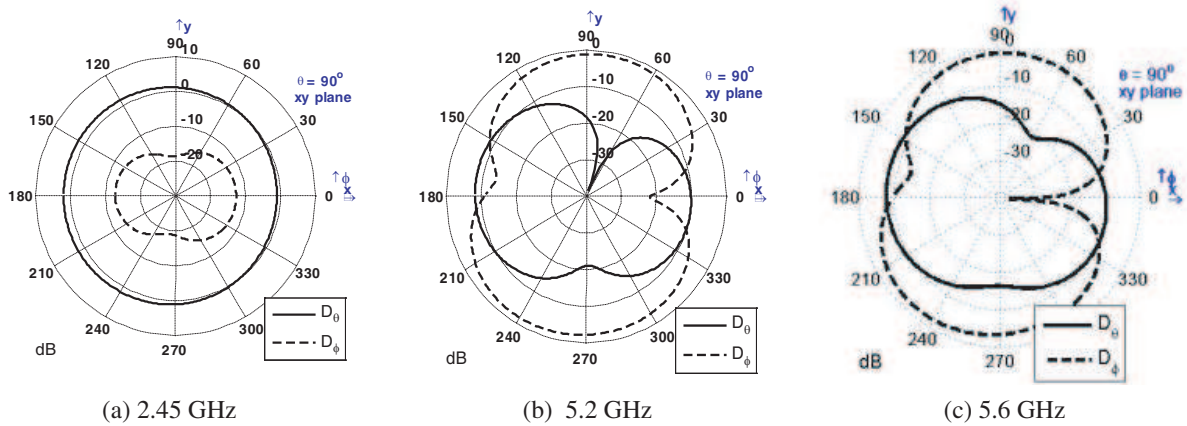
Figure 10: Radiation patterns in the xy plane cut.

(a) 2.45 GHz   (b) 5.2 GHz   (c) 5.6 GHz
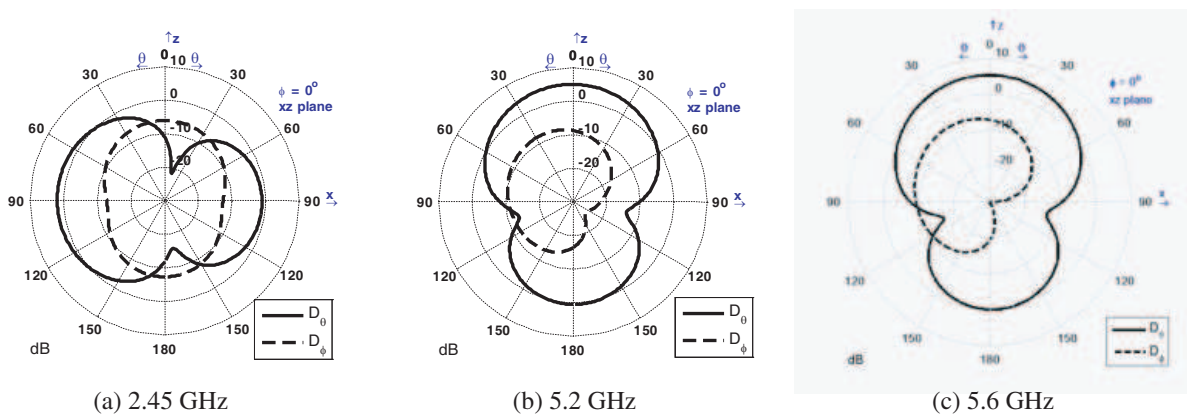
Figure 11: Radiation patterns in the xz plane cut.

(a) 2.45 GHz   (b) 5.2 GHz   (c) 5.6 GHz
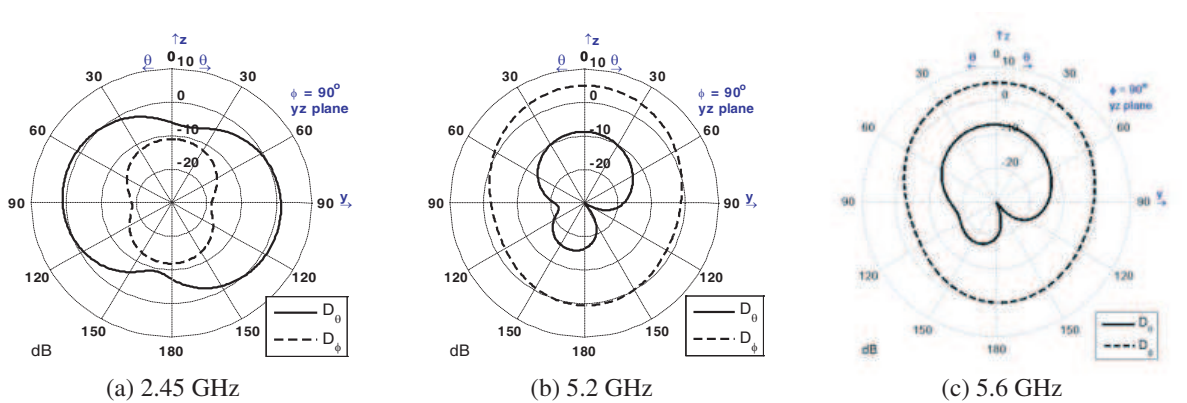
Figure 12: Radiation patterns in the yz plane cut.

from the near-field FDTD data through a near-field to far-field transformation technique [15].

The directivity patterns are calculated in the xy, xz, and yz plane cuts at 2.45 GHz, 5.2 GHz, and 5.6 GHz. These patterns are plotted in Fig. 10, Fig. 11, and Fig. 12, respectively.

5. CONCLUSION

A new microstrip patch antenna is proposed in this paper to obtain a wide-band dual-band operation. The proposed antenna is loaded by a chip resistor between patch and ground plane and two cross-slots in the ground plane are created. The proposed structure is analyzed by the 3D-FDTD method, and the chip resistor values and dimensions of the two cross-slots are varied to control the two resonant frequencies and their bandwidths. The calculated results of the proposed antenna

agree well with experimental results. It is found that antenna can operate at two bands, the first band covers ISM (2400–2483.5 MHz) band, and the second band covers U-NII1 (5150–5350 MHz) band. The antenna also can cover U-NII2 (5470–5725 MHz) and U-NII3/ISM (5725–5825 MHz) bands.

REFERENCES

1. Garg, R., P. Bhrtia, I. Bahl, and A. Ittipitoon, *Microstrip Antenna Handbook*, Artech House, 2001.
2. Balanis, C. A., *Antenna Theory: Analysis and Design*, 2nd Edition, Wiley, New York, 1997.
3. Wong, K. L., *Compact and Broadband Microstrip Antennas*, John Wiley & Sons, New York, 2002.
4. Maci, S., G. B. Gentili, P. Piazzesi, and C. Salvador, "Dual band slot loaded patch antenna," *Proc. Inst. Elect. Eng. Microw. Antennas Propagation*, Vol. 142, 225–232, Jun. 1995.
5. Wang, B. F. and Y. T. Lo, "Microstrip antennas for dual frequency operation," *IEEE Transactions on Antenna and Propagation*, Vol. 32, 938–943, Sep. 1984.
6. Wong, K. L. and W. S. Chen, "Compact micostrip antenna with dual frequency operation," *IEEE Electronic Letters*, Vol. 33, No. 8, 646–647, Apr. 1997.
7. Pan, S. C. and K. L. Wand, "Dual frequency triangular microstrip antenna with shorting pin," *IEEE Transactions on Antenna and Propagation*, Vol. 45, 1889–1891, Dec. 1997.
8. Lee, C. S., V. Nalbandian, and F. Schwering, "Planner dual-band microstrip antenna," *IEEE Transactions on Antenna and Propagation*, Vol. 43, No. 8, 892–894, Aug. 1995.
9. Anguera, J., C. Puente, C. Borga, and J. Soler, "Dual-frequency broadband-stacked microstrip antenna using a reactive loading and a fractal-shaped radiating edge," *IEEE Antenna and Wireless Propagation Letters*, Vol. 6, 309–312, 2007.
10. Chen, Z. N. and M. Y. W. Chia, *Broadband Planar Antennas: Design and Applications*, John Wily & Sons, New York, 2006.
11. Balanis, C. A., *Modern Antenna Handbook*, John Wiley & Sons, New York, 2008.
12. Chuang, H. R. and L. C. Kuo, "3-D FDTD design analysis of a 2.4 GHz polarization-diversity printed dipole antenna with integrated balun and polarization — Switching circuit for WLAN and wireless communication application," *IEEE Transactions on Microwave Theory and Technology*, Vol. 51, No. 2, Feb. 2003, 374–381.
13. Sullivan, D. M., *Electromagnetic Simulation Using the FDTD Method*, IEEE Press Series on RF and Microwave Technology, New York, 2000.
14. Kumar, G. and K. P. Ray, *Broadband Microstrip Antennas*, Artech House, 2003.
15. Elsherbeni, A. and V. Demir, *The Finite Difference Time Domain Method for Electromagnetics with Matlab Simulations*, SciTech Publishing, United States of America, 2009.

Relevant Electromagnetic Details for a Couple Antenna-vehicle

M. Sossouhounto and Thierry Gilles

Royal Military Academy of Brussels, Belgium

Abstract— In the choice of a CAD model for a vehicle, it is important to identify the geometrical details that are relevant for the electromagnetic simulation. Their importance could depend on the application, the location of antenna, the frequency. The vehicle under consideration in this paper is the Light Multirole Vehicle of the Belgian Defense, and the antenna is a monopole.

1. INTRODUCTION

The numerical analysis of the near and far field radiation of an antenna mounted on a vehicle is a time consuming task, both to establish the CAD model and to run the simulations. Minimizing the amount of structural elements to account for in the geometrical model while maintaining reliable electromagnetic simulation results is the objective of this paper.

2. THE CAD MODEL

The vehicle of interest is depicted in Figure 1. Its overall dimensions are $L = 5.215\,\text{m}$, $W = 2.407\,\text{m}$ and $H = 2.247\,\text{m}$. Only its outer contour was modeled. Nine structural elements are under consideration: (1) the 3 mm thick fenders ($\mu_r = 100$, $\sigma = 3.3 * 10^6\,\text{S/m}$, $\tan\delta_\mu = 0$), (2) the steps, (3) the rear view mirrors, (4) the back elements, (5) the radiator holes, (6) the hinges, modeled as metallic cylinders ensuring the electric continuity between doors and frame, (7) the roof elements, (8) the 7 mm thick glass windows ($\varepsilon_r = 7$, $\tan\delta = 0.02$), (9) the 5 mm rubber tires ($\varepsilon_r = 4$, $\tan\delta = 0$).

The three simulation frequencies are 150, 300 and 600 MHz. The antenna is a $\lambda/4$ monopole antenna whose length is adjusted to exhibit at least $S_{11} < -18\,\text{dB}$ when mounted on the vehicle.

We have modeled two types of ground: perfectly conducting ground for near field simulations and a dielectric ground ($\varepsilon_r = 10$, $\sigma = 0.002\,\text{S/m}$) for far field simulations.

3. SIMULATIONS

The simulations have been performed with the commercial software FEKO$^{\text{TM}}$. The numerical methods used are the MOM (Method of Moments) and the MLFMM (Multi Level Fast Multipole Method). To assess the influence of a given structural element, we first simulate the whole vehicle, then we remove the element from the vehicle and measure the modification to the Near Electric Field (in a plane located $\lambda/10$ above the ground, below the vehicle and up to 3 m all around the vehicle) and the Far Field Gain (between 0° and 20° elevation all around the vehicle). If a difference of more than 1 dB is observed in the whole area of interest between the full vehicle model and the model less one structural element, then the element is considered relevant. For the far field, we also require that the gain in every directions where the 1 dB threshold is exceeded be higher than $-4\,\text{dBi}$.
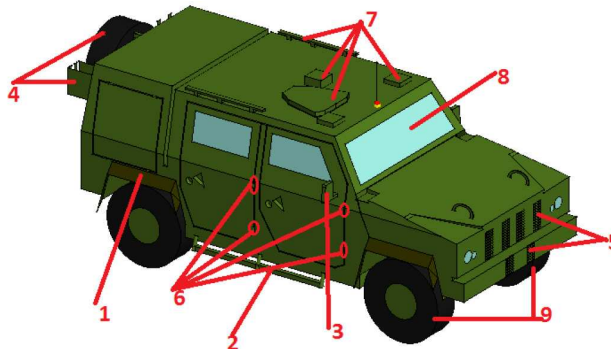
Figure 1: Structural detail elements of the Light Multipurpose Vehicle (LMV).
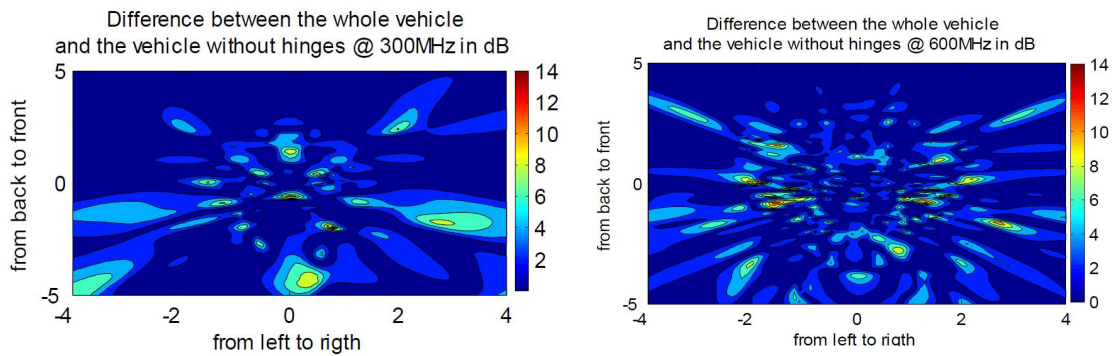
Figure 2: Hinges influence on near field at 300 and 600 MHz.
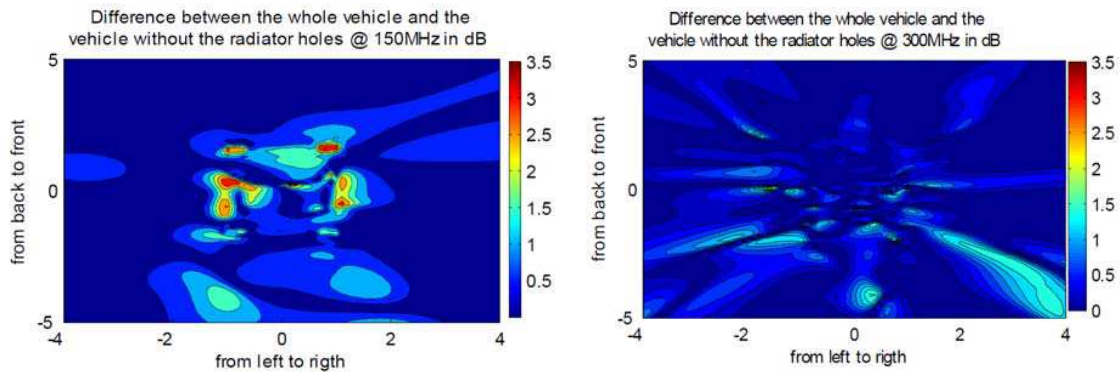
Figure 3: Radiator holes influence on near field at 150 and 300 MHz.
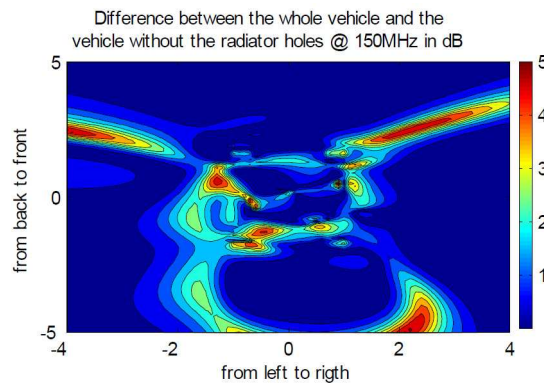
Figure 4: Difference due to the radiator holes in presence of a perfectly conducting ground.

4. RESULTS

4.1. Near Field in Free Space

According to our threshold and decision rule, all nine structural elements have been found relevant at all three frequencies. Among them, the hinges and radiator holes are respectively the most and least important, as can be seen in Figure 2 and Figure 3.

4.2. Near Field with Ground

The presence of the perfectly conducting ground does not alter our conclusions regarding the relevance of the structural elements: the observed differences are generally higher than in the free space case. As an example, we show the radiators holes relevance in Figure 4.

4.3. Far Field in Free Space

Only the roof elements, the hinges and the windows are found relevant at all three frequencies. We illustrate in Figure 5 the relevance of the roof elements and in Figure 6 the irrelevance of the rear view mirrors.
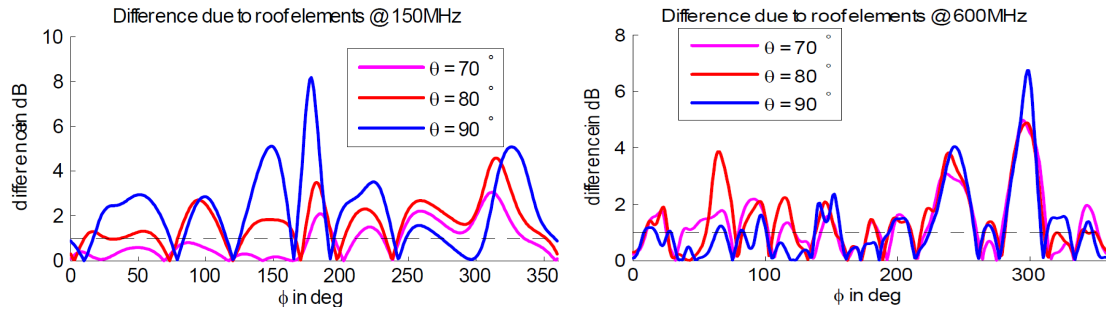
Figure 5: Difference in Gain for three elevations θ (roof elements).
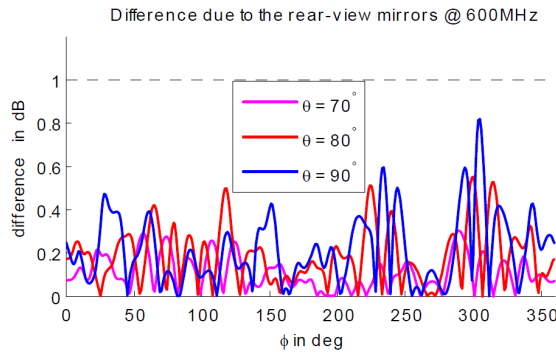
Figure 6: Difference in Gain for three elevations θ (rear-view mirrors).
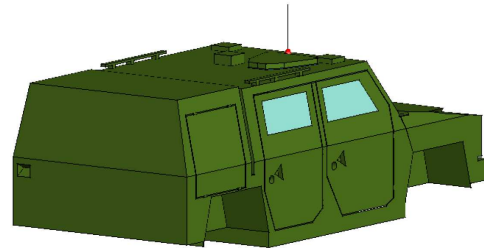
Figure 7: Side view of the shell model of the LMV.
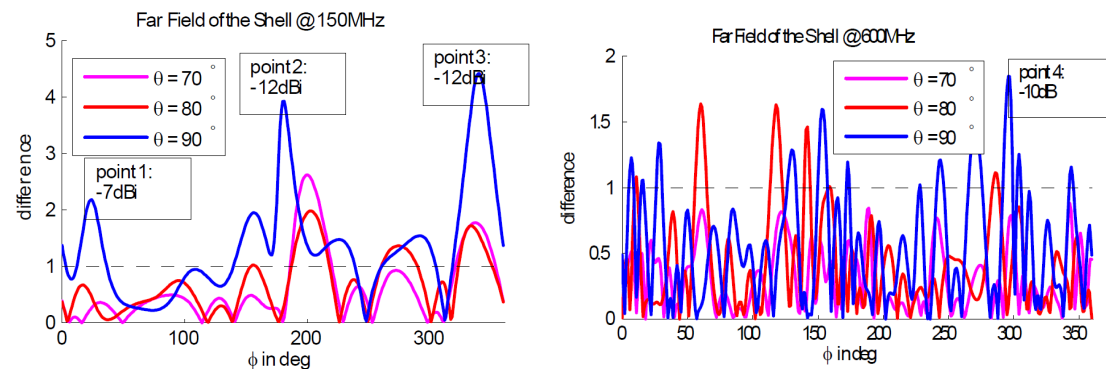
Figure 8: All irrelevant structural elements influence at 150 and 600 MHz.

Next we have verified if all six irrelevant structural elements could be removed together, leading to the shell model of the vehicle depicted in Figure 7.

We see in Figure 8 that the points 1 to 4 exceed the threshold, but the gain of the radiation pattern at these points is weak enough to conclude that the shell can be used to represent the LMV in far field application without ground, according to our decision rule.

4.4. Far Field with Ground

Identical conclusions can be made if a dielectric ground is added to the far field simulation: the shell is still an appropriate simplified model for the LMV.

5. WINDOWS AND TIRES

The previous simulations show that even if the windows and the tires have the same dielectric properties, the former are much more important than the latter. We assumed that the main reason is the position of the tires away from the radiation. To check this hypothesis we have placed the antenna close to the tires (see Figure 9). The results in Figure 10 show that the positioning of the windows away from the radiation has reduced their importance whereas the tires have become important.
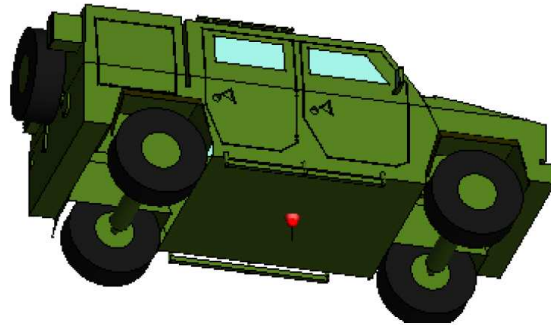
Figure 9: The position of antenna was changed to put tires close the antenna radiation.
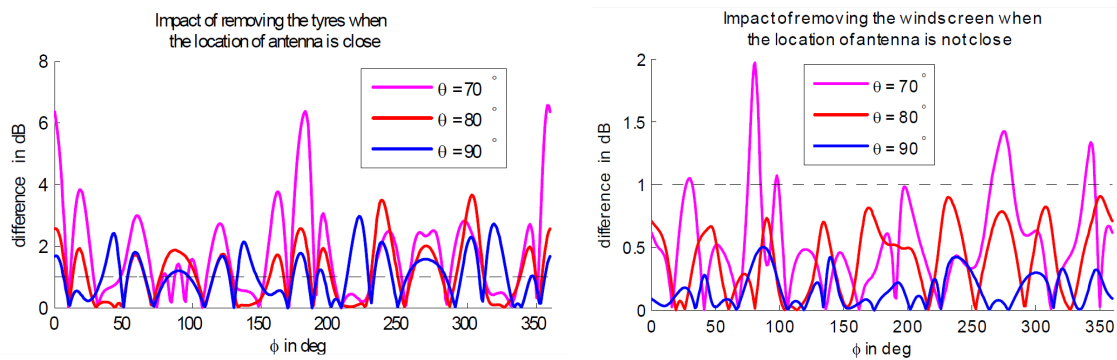
Figure 10: Impact of removing the windscreen when the location of the antenna is not close.

6. CONCLUSION

Outside near field simulations require all nine elements considered in this study, whereas a reduced shell model can be used for far field simulations. It should be noted though that these conclusions depend on the antenna location and the chosen threshold and decision rules.

REFERENCES

1. *Nec 2 Manual*, 1996.
2. *Feko Example Guide*, Example 32, 2005.
3. *Feko User's Manual*, 2005.
4. Feko Reference Guide.
5. Miroslav, L. J. D. and B. M. Notaros, "Highly efficient large-domain moment-method analyis and cad of radio-frequency antenna mounted on or situated in vehicles," *52nd Vehicular Technology Conference, 2000. IEEE VTS-Fall VTC 2000*, Vol. 5, 2373–2377, 2000.
6. Batchelor, J. C., R. J. Langley, and H. Endo, "On-glass mobile antenna perfomance modelling," *IEE Proceedings of Microwaves, Antennas and Propagation,* Vol. 148, No. 4, 233–238, 2001.
7. Saveskie, P. N., "Earth Constants," *TAI Inc Consuletter International*, Vol. 6, No. 5.

Reconfigurable E-shaped Antenna with Bandwidth Control for Wideband Applications

Hattan F. Abutarboush[1] and R. Nilavalan[2]

[1]Electrical Engineering, Physical Science and Engineering
King Abdullah University of Science and Technology (KAUST), Saudi Arabia
[2]School of Engineering and Design, Electrical and Electronics Engineering
Brunel University, London, UK

Abstract— A reconfigurable antenna based on E-shaped structure with bandwidth controlled is proposed in this paper. The bandwidth of the antenna can be increased and controlled from 3.4% to 23% by varying the capacitance of the varactor diodes. The bandwidth can cover the frequency range from 1.85 GHz–2.33 GHz. The antenna consists of four E-Shaped connected to 50 ohm GCPW line, varactor diodes and 10 pF ship capacitances. The total size of the antenna is $80 \times 80\,\text{mm}^2$. The performances of the proposed antenna, in terms of return losses and radiation patterns, with different DC bias voltages across the varactor diode, have been studied using computer simulation and measurement. Simulated and measured results are in good agreements.

1. INTRODUCTION

There have been interests in the field of reconfigurable antennas where the multiband capabilities can be further enhanced to incorporate multiple wireless standards [1]. Future cognitive communication systems will also require antennas capable of operating over wide bandwidth [2]. Modern wireless communication systems relying on multiband reconfigurable antennas are becoming more popular for their ability to serve multiple standards using a single compact antenna, allowing a reduction in the dimensions of the wireless device and more space to integrate with other electronic components [3–6].

Frequency reconfigurable antennas can be classified into two categories, namely continuous tuning and coarse tuning. Continuous tuning can be achieved using varactors and the antennas are allowed for smooth transitions within or between operating bands [7]. Coarse tuning can be achieved using PIN diode switches and the operating frequency is switched among different services, depending on the switching states [8].

In this paper, the proposed antenna has E-shaped radiators, a GCPW and four varactor diodes connecting the E-Shapes. Through the use of DC bias voltage across the varactor diodes, the bandwidth of the antenna can be controlled to be wide or narrow.

2. DESIGN CONCEPT

The structure of the proposed reconfigurable E-shape antenna is shown in Fig. 1(a), where four radiators are optimized to allow the bandwidth of the antenna to be controlled over a wide range. The varactors operate like variable capacitors. The positions of the varactor on the structure are optimized using the HFSS simulator software to achieve the widest controlled range. The antenna was fabricated using an FR-4 substrate with thickness of 1.57 mm and a relative permittivity of 4.4, as shown in Fig. 1(b). To prove our design concept, a practical varactor diode, BB184 from NXP with a capacitance value ranging from 2 pF to 14 pF controlled by a DC bias voltage varying from 1 V to 14 V was employed. The dimension of the varactor diode is approximately $1 \times 1\,\text{mm}^2$. In the simulations, the varactor diodes were modelled using Resistance, Inductance and Capacitance (RLC) boundary sheet when the capacitance of the varactor diodes varied from 2 pF to 14 pF. The characteristic of Fig. 2 are used for the varactor diode in the simulation tests.

3. SIMULATED AND MEASURED RESULTS

Results in Fig. 3 show that, when all the varactors are fixed at 2 pF, the bandwidth of the antenna is 3.4% (for reflection coefficient $S_{11} < -10\,\text{dB}$). The bandwidth of the antenna can be further increased to 5%, 8% and 23% when increasing the varactor diodes to 4, 5 and 10 pF respectively. This is summarized in Table 1. 10 pF chip capacitance is used to prevent the DC signal from flowing to the main feed line but allow the RF current to pass through.
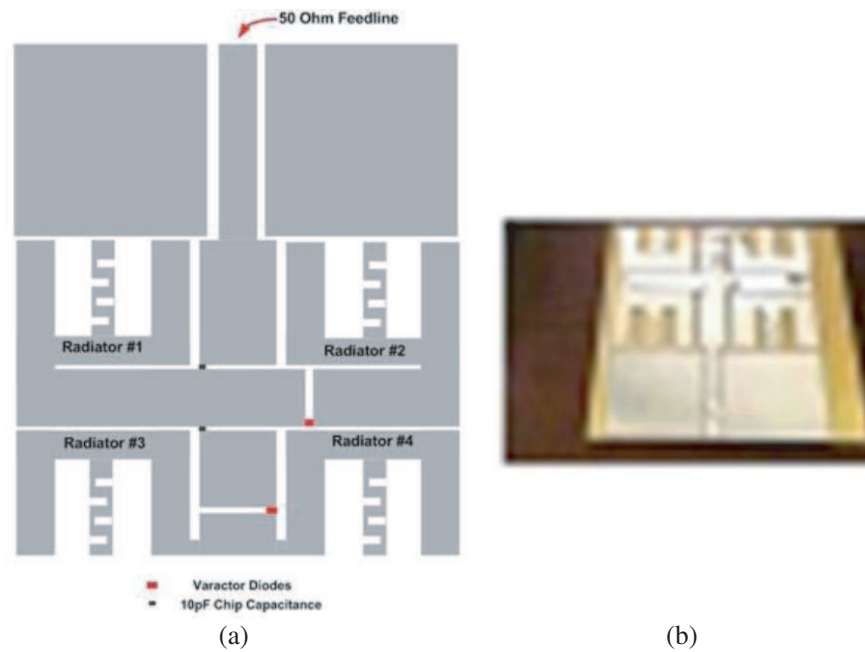
Figure 1: (a) Layout of proposed antenna and (b) fabricated prototype.
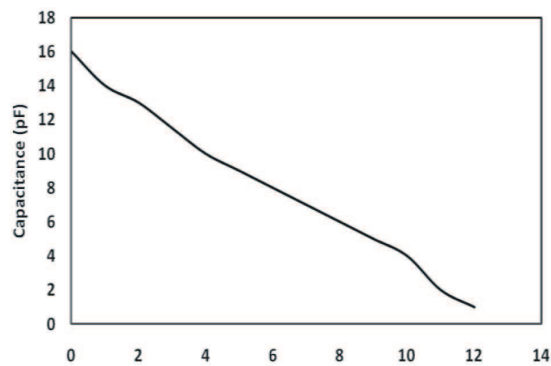
Figure 2: Capacitance versus DC bias voltage for varactor BB184 (obtained from BB184 data sheet).
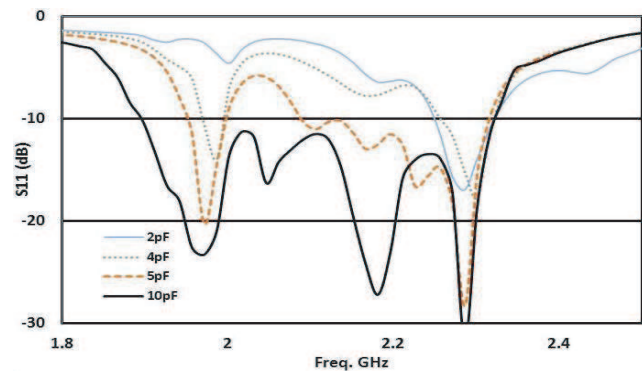
Figure 3: Effect of varactor capacitance on the bandwidth.

Table 1: The achieved bandwidth VS value of varactor diodes.

Varactor diodes	Bandwidth (-10 dB)
2 pF	3.4%
4 pF	5%
5 pF	8%
10 pF	23%

To validate the simulation results, the proposed antenna has also been fabricated as shown in Fig. 1(b) and the S_{11} in have been measured using Agilent N5230A vector network analyzer. Results of the measured S_{11} are shown in Fig. 3. The simulated and measured results were in acceptable agreements. There were small discrepancies between the simulated and measured results and this could be attributed to the fabrication accuracy of the prototype and the losses of the varactor diodes. Further results of simulations have reviewed that varying the capacitance values of the varactor diodes alters the surface current distributions of the antenna, hence changing the bandwidth. It can be seen that, meandered line technique has been used in part of the E-shape in the four radiators to allow the antenna to operate at lower frequencies without using larger radiators.

(a)   (b)
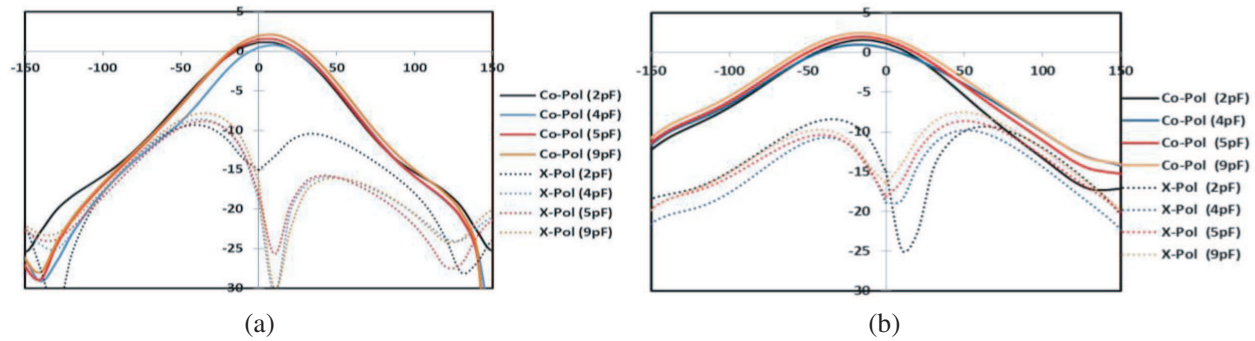
Figure 4: Simulated radiation patterns with different biasing values (a) E-plane and (b) H-plane.

It should be noted that the bandwidth-tuning concept proposed here can be extended to cover more bands or to serve the lower frequencies by using meandered line in all the E-shape. Since our target is for the mobile and Wireless applications, we have limited the meandered line structure to just in a single arm of the E-shape.

Figure 4 shows the simulated co- and cross-polarization patterns for E- and H-planes of the antenna in different biasing state at 2.3 GHz with results normalized to the maximum values. It can be seen that the shape of the radiation patterns does not change when applying different biasing voltage. The cross polarization is lower than -10 dB at the broadside.

4. CONCLUSIONS

A reconfigurable wideband antenna, employing four E-shapes and meandered structure with a compact volume of $80 \times 80 \times 1.57\,\text{mm}^3$, has been presented and studied using simulation and measurement. Four varactor diodes are used to control the operating bandwidth of the antenna over a wide range. The bandwidth of the antenna can be increased to a maximum of 23%. The simulated results have shown that radiation patterns at 2.3 GHz are stable in different modes. The main advantages of the proposed antenna include low profile, lightweight and easy to fabricate simple structure targeting future smaller wireless communication devices and cognitive radio applications.

REFERENCES

1. Abutarboush, H. F., R. Nilavalan, S. W. Cheung, K. Nasr, T. Peter, and D. Budimir "A reconfigurable wideband and multiband antenna using dual-patch elements for compact wireless devices," *IEEE Transaction on Antennas and Propagation*, Aug. 2011.
2. Tawk, Y., J. Costantine, K. Avery, and C. Christodoulou, "Implementation of a cognitive radio front-end using rotatable controlled reconfigurable antennas," *IEEE Transactions on Antennas and Propagation*, Vol. 59, No. 5, 1773–1778, May 2011.
3. Hu, Z. H., C. T. P. Song, J. Kelly, P. S. Hall, and P. Gardner, "Wide tunable dual-band reconfigurable antenna," *Electronics Letters*, Vol. 45, No. 22, 1109–1110, Oct. 22, 2009.
4. AbuTarboush, H. F., R. Nilavalan, H. S. Al-Raweshidy, and D. Budimir, "Reconfigurable dual-band and wideband antenna for cognitive radio applications," *Loughborough Antennas and Propagation Conference, LAPC*, 141–144, 2009.
5. Abutarboush, H. F., R. Nilavalan, K. Nasr, S. W. Cheung, H. Al-Raweshidy, and D. Budimir, "Reconfigurable tri-band H-shaped antenna with frequency selectivity feature for compact wireless communication systems," *IET Microwave Antennas and Propagation*, Aug. 2011.
6. Abutarboush, H. F., R. Nilavalan, S. W. Cheung, T. Peter, and D. Budimir, "Reconfigurable penta-band PIFA for small and slim mobile handsets," *Microwave and Optical Technology Letters*, Nov. 2011.
7. Abutarboush, H. F., R. Nilavalan, K. Nasr, H. Al-Raweshidy, and D.Budimir, "Widely tunable multiband reconfigurable patch antenna for wireless applications," *Proceedings of the Fourth European Conference on Antennas and Propagation (EuCAP 2010)*, 1–3, Apr. 2010.
8. Tawk, Y., M. Bkassiny, G. El-Howayek, S. K Jayaweera, K. Avery, and C. Christodoulou, "Reconfigurable front-end antennas for cognitive radio applications," *IET Microwave Antennas and Propagation*, Vol. 5, No. 8, 985–992, Jun. 6, 2011.

Frequency-tunable Antenna for Dual-band WLAN Applications

X. L. Sun, **S. W. Cheung**, and **T. I. Yuk**

Department of Electrical and Electronic Engineering
The University of Hong Kong, Hong Kong, China

Abstract— In this paper, a frequency-tunable dual-band antenna for WLAN applications is proposed. The antenna consists of two microstrip branches serving as radiating elements for two frequency bands at 2.4 and 3.5 GHz and two variable capacitors on the radiating elements for individually tuning the frequency bands. The antenna is designed on a 40 mm × 40 mm substrate with a thickness of 0.8 mm, relative permittivity of 3.5 and loss tangent of 0.02. The reflection coefficient S_{11} of the antenna with different capacitance values is studied. Simulation results suggest that the two frequency bands have a tuning range of 2.4–3.5 GHz and 3.5–5.9 GHz separately. Moreover, simulated radiation patterns, efficiencies and gains of the proposed antenna are also presented.

1. INTRODUCTION

The rapid development in personal and computer communications technologies demands integration of more than one communication system into a single compact module. This trend leads to the increasing requirement of using a single antenna to cover multiple frequency bands for different wireless standards. In literature, many techniques have been proposed for multiband antenna designs. Among these designs, planar monopoles are most often used [1–5], where multiple-mode operations are obtained by modifying the radiators so that multiple current paths are formed. This requires large antenna sizes. Designing a small antenna to operate in several frequency bands is formidably challenging because of the difficulties in impedance matching and volume reduction. Tunable antenna is one of the ways to overcome such problems. Recently tunable antennas have been studied on different types of antenna such as patch antennas [6], loop antennas [7, 8] and Planar-Inverted-F antennas (PIFA) [9, 10].

In this paper, a frequency-tunable dual-band antenna is proposed. Two microstrip lines are used as the radiating elements of the antenna to create resonances in two different bands, 2.4 and 3.5 GHz. Two variable capacitors, each being placed in the proper locations of two radiating elements, are used to achieve the frequency-tunable feature. The performance of the antenna is evaluated using the commercial EM simulation tool CST. Simulation results on the reflection coefficient S_{11} with different capacitance values suggest that the two resonant frequencies can be tuned independently with the tuning ranges of 2.4–3.5 GHz and 3.5–5.9 GHz.
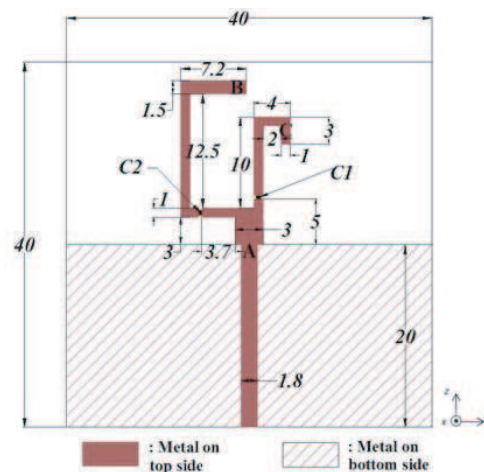
Figure 1: Geometry of the proposed antenna (unit: mm).

2. ANTENNA STRUCTURE

The geometry of the proposed antenna is shown in Fig. 1. The two branches, AB and AC, are quarter-wavelength structures at the frequencies of 2.44 GHz and 3.5 GHz, respectively, and serve as the radiating elements for dual-band resonances. Branches AB and AC are for the lower and higher frequency bands, respectively. A slot with the width of 0.3 mm is etched on each of the two radiating elements. Two variable capacitors (C_1 and C_2) are placed over the slots and used to individually tune the two frequency bands. The radiator is fed using a 50-ohm feed line with a width of 1.8 mm. The antenna is designed on a substrate with the relative permittivity (ε_r) of 3.5, a loss tangent ($\tan \delta$) of 0.02 and a thickness of 0.8 mm. The parameters of the antenna are optimized using computer simulation.

3. RESULTS AND DISCUSSIONS

Computer simulation is used to study the tuning performance of the antenna. In the simulation studies, the value of C_2 in branches AB for the low frequency band is first fixed with C_1 in branch
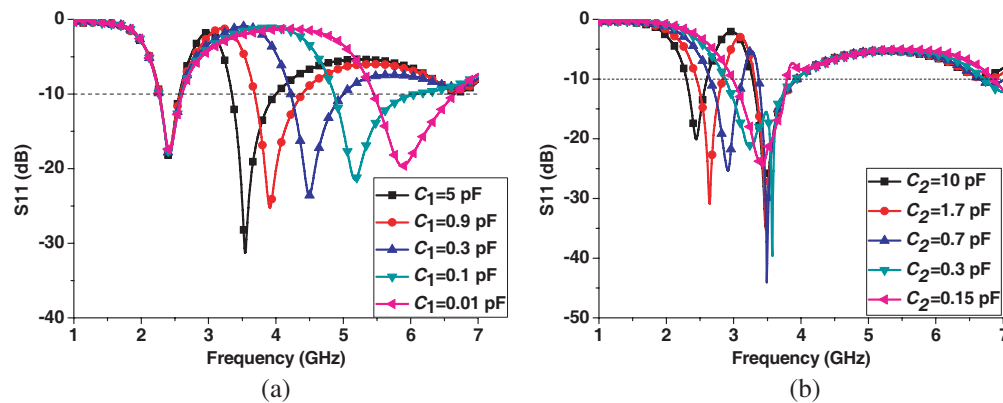
Figure 2: Simulated S_{11} for different values of (a) C_1 and $C_2 = 10$ pF, and (b) C_2 and $C_1 = 5$ pF.
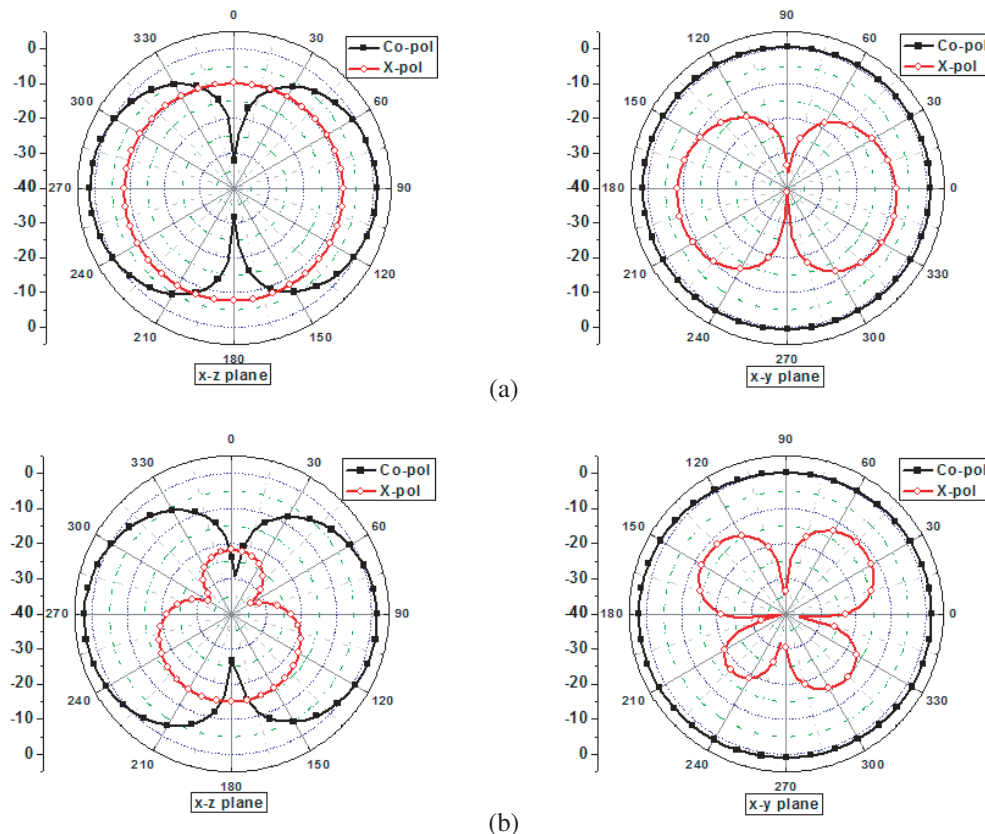
Figure 3: Radiation patterns with $C_1 = 5$ pF and $C_2 = 10$ pF at (a) 2.4 GHz and (b) 3.5 GHz.

AC for the higher frequency band being varied to see the tuning range. Then the value of C_1 in branch AC is fixed with C_2 in branch AB being varied.

With C_2 fixed at 10 pF, the simulated S_{11} of the antenna with the capacitor $C_1 = 5, 0.9, 0.3, 0.1$ and 0.01 pF are shown in Fig. 2(a). It can be observed that, as C_1 in branch AC decreases from 5 to 0.01 pF, the higher frequency band shifts from 3.5 to 5.9 GHz. That is because the length of the branch AC is responsible for the resonance of the higher frequency band.

With $C_1 = 5$ pF, the simulated S_{11} with different values of C_2 is shown in Fig. 2(b). The lower frequency band is designed to be at 2.4 GHz which is determined by the total length of the branch AB. It can be seen that, as C_2 decreases from 10 pF to 0.15 pF, the higher frequency band shifts from 2.4 to 3.5 GHz and then overlaps with the higher frequency band. Again, it can be seen that the higher frequency band is not affected by the capacitor value in branch AB, indicating that the lower frequency band can be tuned independe.

Figure 2(a) shows that the higher frequency band can be shifted from 3.5 to 5.9 GHz by changing the capacitance pairs from $(C_1 = 5$ pF and $C_2 = 10$ pF) to $(C_1 = 0.01$ pF and $C_2 = 10$ pF). Figure 2(b) shows that the lower frequency band can be shifted from 2.4 GHz to 3.5 GHz by changing
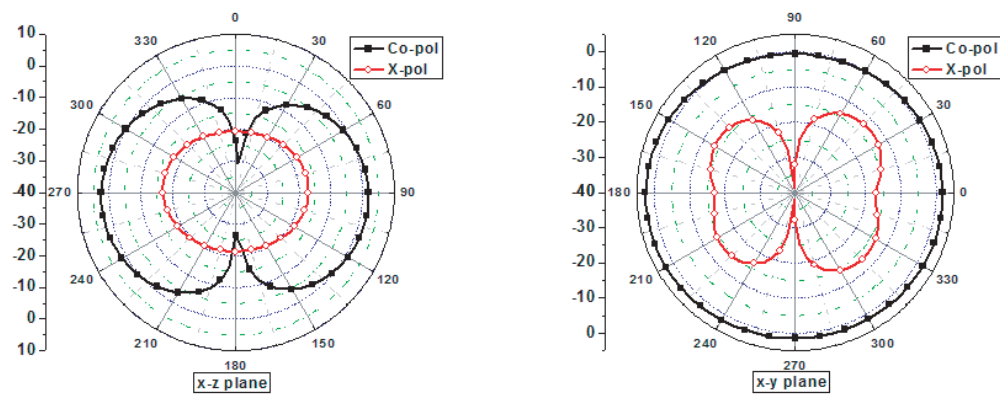
Figure 4: Radiation patterns with $C_1 = 5$ pF and $C_2 = 0.15$ pF at 3.5 GHz.
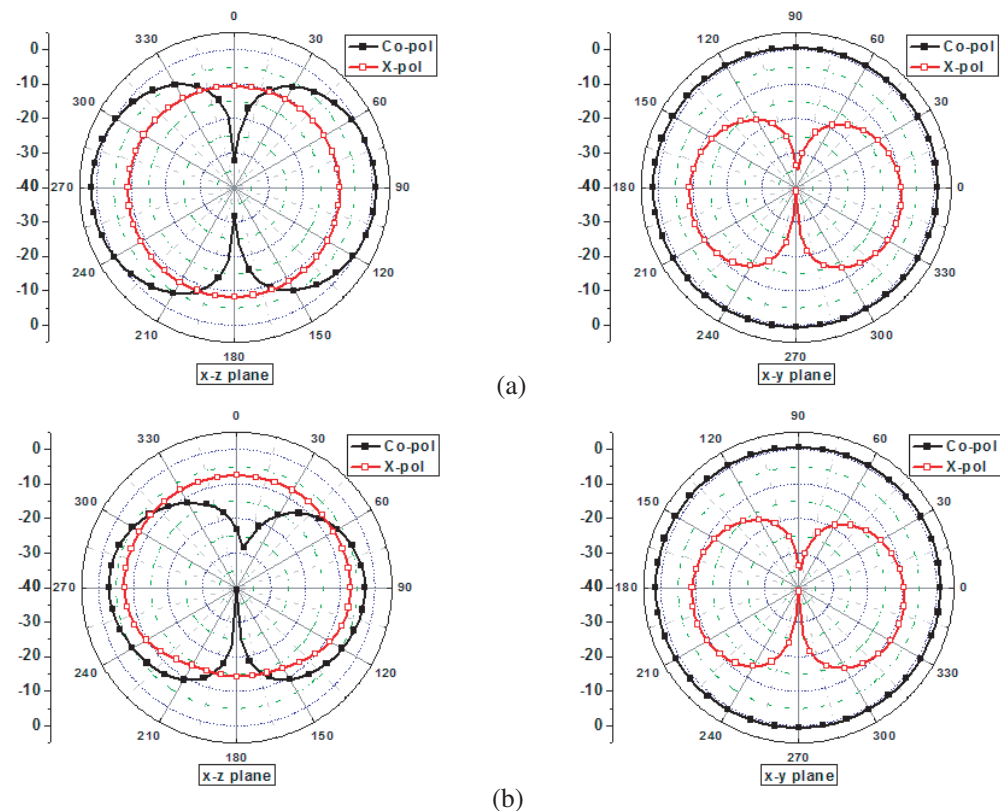
Figure 5: Radiation patterns with $C_1 = 0.01$ pF and $C_2 = 10$ pF at (a) 2.4 GHz and (b) 5.9 GHz.
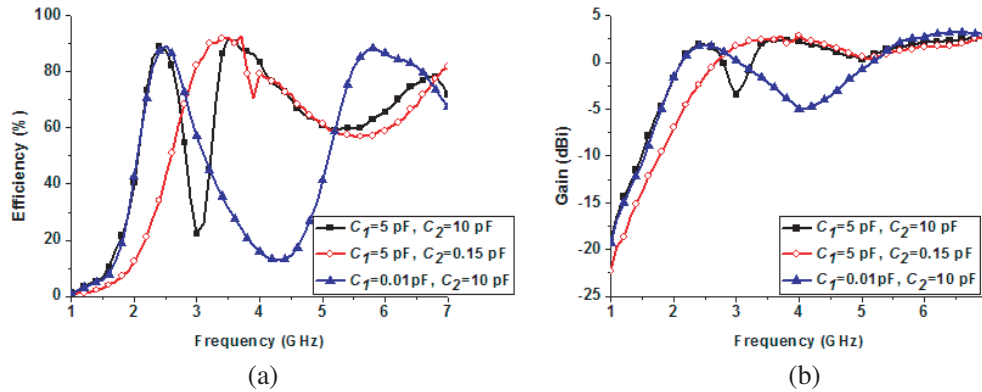
Figure 6: (a) Efficiencies and (b) gains. $C_1 = 5\,\text{pF}$ and $C_2 = 10\,\text{pF}$ (resonances at 2.4 and 3.5 GHz), $C_1 = 5\,\text{pF}$ and $C_2 = 0.15\,\text{pF}$ (resonance at 3.5 GHz), and $C_1 = 5\,\text{pF}$ and $C_2 = 10\,\text{pF}$ (resonances at 2.4 and 5.9 GHz).

the capacitance pairs from ($C_1 = 5\,\text{pF}$ and $C_2 = 10\,\text{pF}$) to ($C_1 = 5\,\text{pF}$ and $C_2 = 0.15\,\text{pF}$) and then overlapping with the higher frequency band. Consequently, the radiation patterns in these extreme cases are studied by computer simulation and results are shown in Figs. 3, 4 and 5. It can be seen that the antenna has monopole-like radiation patterns in all these cases. The efficiencies and gains with these three variable capacitance pairs are shown in Fig. 6. At the frequencies 2.4, 3.5 and 5.9 GHz, the antenna achieves the efficiencies of more than 85% and gains of larger than 1.5 dBi.

4. CONCLUSIONS

A simple tunable dual-band antenna has been designed and studied. The antenna has two microstrip branches serving the quarter-wavelength monopoles at the frequency bands of 2.4 and 3.5 GHz. Two variable capacitors placed on these two branches are used to achieve the tuning feature. Simulation results have shown that the two frequency bands can be tuned independently.

REFERENCES

1. Chu, Q.-X. and L.-H. Ye, "Design of compact dual-wideband antenna with assembled monopoles," *IEEE Trans. Antennas Propag.*, Vol. 58, No. 12, 4063–4066, 2010.
2. Thomas, K. G. and M. Sreenivasan, "Compact triple band antenna for WLAN/WiMAX applications," *Electronic Letters*, Vol. 45, 811–813, 2009.
3. Yeh, S.-H. and K.-L. Wong, "Dual-band F-shaped monopole antenna for 2.4/5.2 GHz WLAN application," *2002 IEEE Antenna and Propagation Society International Symposium Digest*, Vol. 4, 72–75, 2002.
4. Lin, Y. F., H. D. Chen, and H. M. Chen, "A dual-band printed L-shaped monopole for WLAN applications," *Microwave Opt. Technology Lett.*, Vol. 37, 214–216, 2003.
5. D'Souza, R. and R. K. Gupta, "Printed dual band WLAN antenna," *2006 IEEE International Conference on Electro/Information Technology*, 539–543, 2006.
6. Fayyaz, N., S. Safavi-Naeini, E. Shin, and N. Hodjat, "A novel electronically tunable rectangular patch antenna with one octave bandwidth," *IEEE Canadian Conference on Electrical and Computer Engineering*, Vol. 1, 25–28, 1998.
7. Chi, P.-L., R. Waterhouse, and T. Itoh, "Compact and tunable slot-loop antenna," *IEEE Trans. Antennas Propag.*, Vol. 59, No. 4, 1394–1397, 2011.
8. Lee, D. H., A. Chauraya, Y. Vardaxoglou, and W. S. Park, "A compact and low-profile tunable loop antenna integrated with inductors," *IEEE Antennas and Wireless Propagation Letters*, Vol. 7, 621–624, 2008.
9. Oh, S.-K., Yo.-S. Shin, and S.-O. Park, "A novel PIFA type varactor tunable antenna with U-shaped slot," *International Symposium on Antennas, Propagation & EM Theory*, 1–3, 2006.
10. Nguyen, V.-A., R.-A. Bhatti, and S.-O. Park, "A simple PIFA-based tunable internal antenna for personal communication handsets," *IEEE Antennas and Wireless Propagation Letters*, Vol. 7, 130–133, 2008.

CPW-coupled-fed Elliptical Monopole UWB Antenna with Dual-band Notched Characteristic

J. Zhang, **S. W. Cheung**, and **T. I. Yuk**

Department of Electrical and Electronic Engineering
The University of Hong Kong, Hong Kong, China

Abstract— This paper presents the results of a coplanar-waveguide (CPW)-coupled-fed elliptical monopole UWB antenna (CCFEMUA) with a dual band-notched characteristic. The antenna has a large bandwidth covering the frequency band from 2.4 GHz to 152 GHz with the return loss larger than 10 dB. Two band notches at 3.7 GHZ and 4.8 GHz are realized by cutting two half-elliptical-arc slots on the radiation patch The return loss, radiation pattern, peak gain and efficiency of the antenna are studied using computer simulation.

1. INTRODUCTION

The FCC (Federal Communications Commission) released an unlicensed frequency band of 3.1–10.6 GHz for ultra-wideband (UWB) applications in 2002 [1]. Since then design of UWB antennas has been attracting much attention. UWB commonly refers to signals or systems that either have a large relative or a large absolute bandwidth [2]. Such large bandwidth offers specific advantages of low power consumption and high data rate which promise solutions for short-range and high-speed indoor mobile communications. The design of UWB antennas is quite challenging because it has to satisfy the requirements of wide impedance bandwidth, omnidirectional radiation pattern, constant gain, high radiation efficiency, constant group delay, low profile and easy manufacturing [3]. Besides these, the UWB antennas should also have notch characteristic to prevent interfering with other systems using frequency bands with the UWB.

UWB antennas with different radiator shapes such as square [4], circular [5], pentagonal [6], hexagonal [7], elliptical [8], ring [9] and trapezoidal [10], different types such as monopoles [6–8, 10–12], dipoles [13] and slot antennas [9], different feeding structures such as microstrip [6, 7, 10, 11], co-planar-waveguide (CPW) [8, 9, 12] and coaxial [14], and different methods for creating the band-notched characteristics have been studied [8, 15, 16]. In this paper, we propose a very simple design of a CPW-coupled-fed elliptical monopole UWB antenna (CCFEMUA) with dualband notched characteristic The two band notches are achieved by cutting two arc slots on the radiator. The return loss, radiation pattern, peak gain, and efficiency are studied using the EM simulation tool CST.

2. ANTENNA DESIGN

The configuration of the proposed dualband notched CCFEMUA is shown in Fig. 1. The antenna is composed of a feeding structure on one side of the substrate and a radiating patch on the other side of it. The antenna is designed in a substrate with a dielectric constant of ε_r and thickness of h. The radiating patch has a simple elliptical shape with the major and minor axes having lengths of $2rx$ and $2ry$ in the y and z directions, respectively. The feeding structure is a CPW terminated with a trapezium patch with a topline of $w3$, baseline of $w2$ and height of d as shown in Fig. 1. The trapezium patch is used to couple the signal from the CPW to the radiating patch on the other side of the substrate. The width of the CPW tapers from $w1$ to $w2$ for achieving good impedance match. Two notch bands at 3.7 GHz and 4.8 GHz are generated by cutting two half-elliptical-arc slots on the radiating patch as shown in Fig. 2. The lower arc slot in Fig. 2(a) and upper arc slot in Fig. 2(b) are responsible for the notch bands at 3.7 GHz and 4.8 GHz, respectively.

3. RESULTS AND DISCUSSIONS

The proposed dual-band notched CCFEMUA is optimized in terms of impedance bandwidth using the EM simulation tool, CST The simulated return loss in Fig. 3 show that the antenna has an impedance bandwidth (return loss > 10 dB) from 2.4 to 15.2 GHz, covering the bandwidth from 3.1–10.6 GHz for UWB applications. The two notch bands are created at 3.7 GHZ and 4.8 GHz.

The simulated radiation patterns of the antenna in the x-y, x-z and y-z planes at 2.4, 3.0, 3.7, 4.8, 10.0 and 15.2 GHz are shown in Fig. 4. Due to the wavelength is much larger than the antenna

size at 2.4 and 3.0 GHz, the patterns in the x-y plane are approximately omnidirectional. The radiation patterns in the x-z and y-z planes are approximately symmetrical along the y-axis. As the electrical length of the radiator increases at the higher frequencies of 10 GHz and 15.2 GHz, the radiation patterns in the y-z plane are still symmetrical along the y-axis, but side lobes appear. The radiation patterns in the x-z plane become asymmetrical because the front (with the feed-line structure) and back (with the radiator) of the antenna structure are not symmetrical. At the notch frequencies of 3.7 GHz and 4.8 GHz, it can be seen that the peak gains are suppressed by about 6 and 5 dB, respectively, compared to that at 3 GHz.

The simulated peak gain and efficiency of the antenna are shown in Fig. 5. It can be seen that there are two notches occurring at the notched frequencies of 3.7 and 4.8 GHz, with the gains
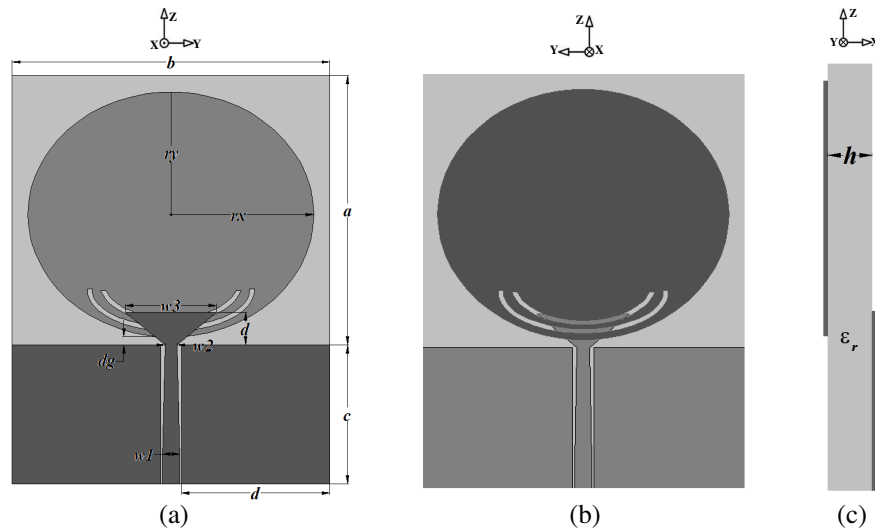
Figure 1: Geometry of antenna. (a) Front view, (b) back view and (c) side view. $\varepsilon_r = 3.5$, $h = 0.8$ mm, $rx = 18$ mm, $ry = 15$ mm, $w1 = 2.2$ mm, $w2 = 1.5$ mm, $w3 = 11.5$ mm, $d = 4$ mm, $dg = 1$ mm, $a = 33$ mm, $b = 40$ mm, $c = 17$ mm, $d = 18.7$ mm.
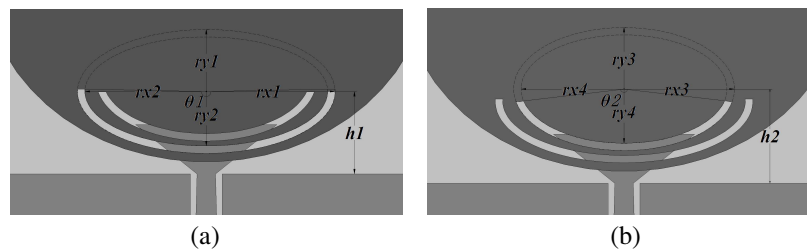
Figure 2: Half-elliptical-arc slots with large scale Dimensions of (a) lower slot with $h1 = 6.7$ mm, $\theta1 = 185°$, $rx1 = 10.5$ mm, $ry1 = 5$ mm, $rx2 = 9.9$ mm, $ry2 = 4.4$ mm, and (b) upper slot with $h2 = 7.7$ mm, $\theta2 = 155°$, $rx3 = 9$ mm, $ry3 = 5$ mm, $rx4 = 8.4$ mm, $ry4 = 4.4$ mm.
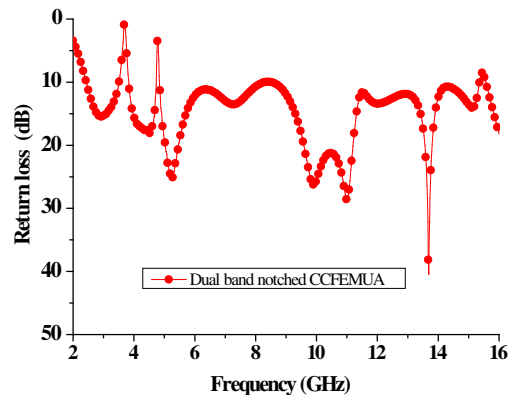
Figure 3: Return loss.
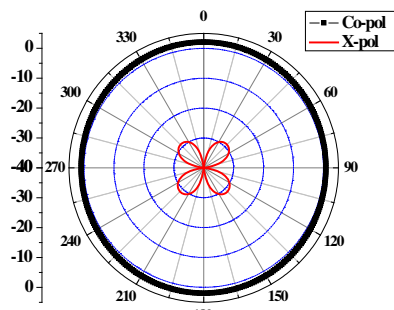
(a)
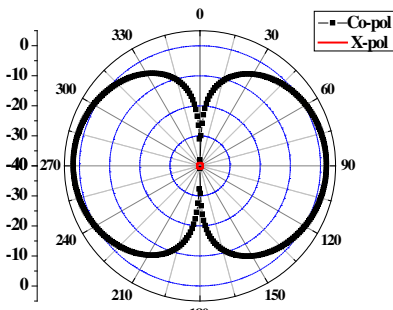
(b)
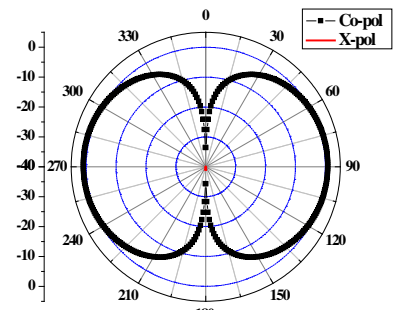
(c)
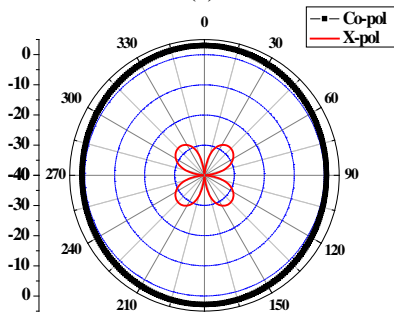
(d)
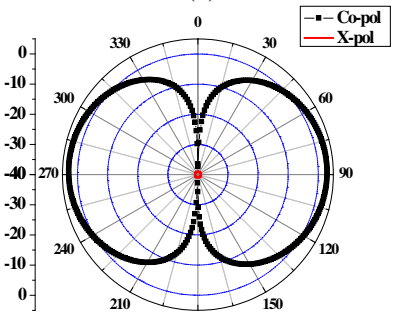
(e)
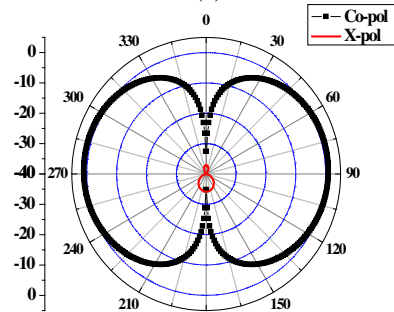
(f)
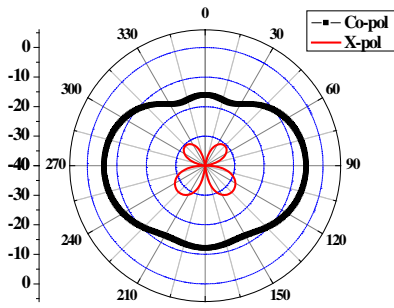
(g)
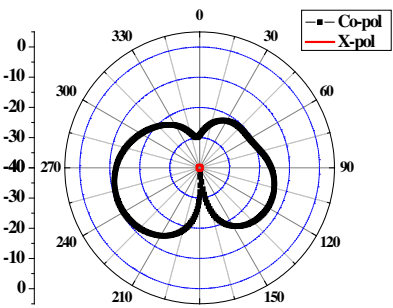
(h)
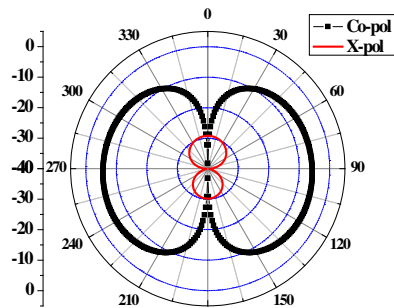
(i)
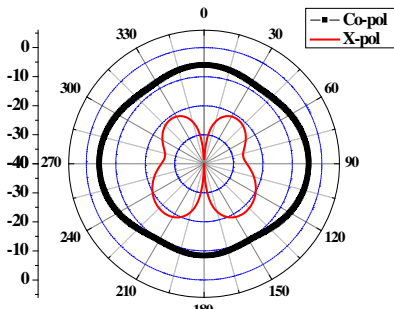
(j)
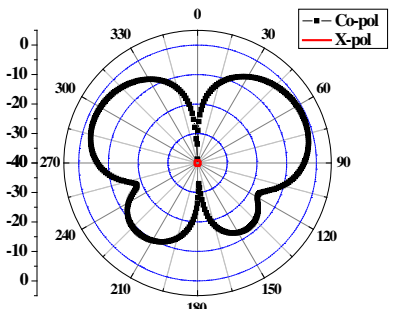
(k)
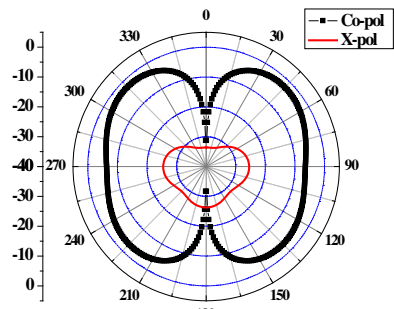
(l)
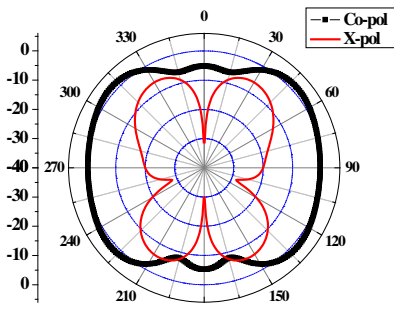
(m)
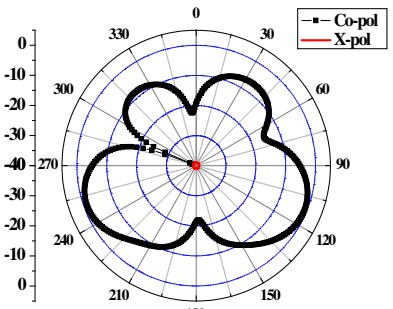
(n)
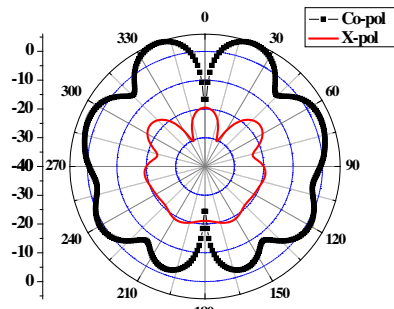
(o)
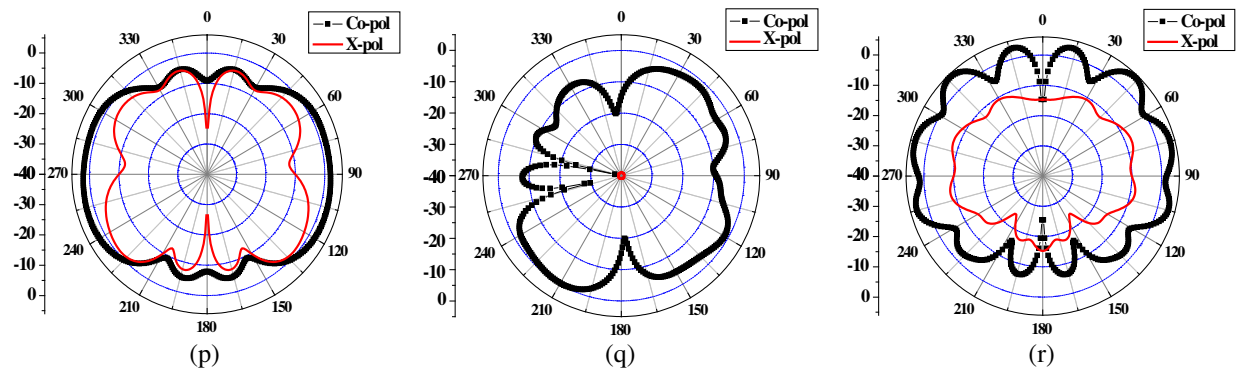
Figure 4: Simulated radiation patterns. 2.4 GHz in (a) x-y, (b) x-z and (c) y-z plane; 3 GHz in (d) x-y, (e) x-z and (f) y-z planes; 3.7 GHz in (g) x-y, (h) x-z and (i) y-z planes; 4.8 GHz in (j) x-y, (k) x-z plane and (l) y-z planes; 10 GHz in (m) x-y, (n) x-z plane and (o) y-z planes; 15.2 GHz in (p) x-y, (q) x-z plane and (r) y-z.
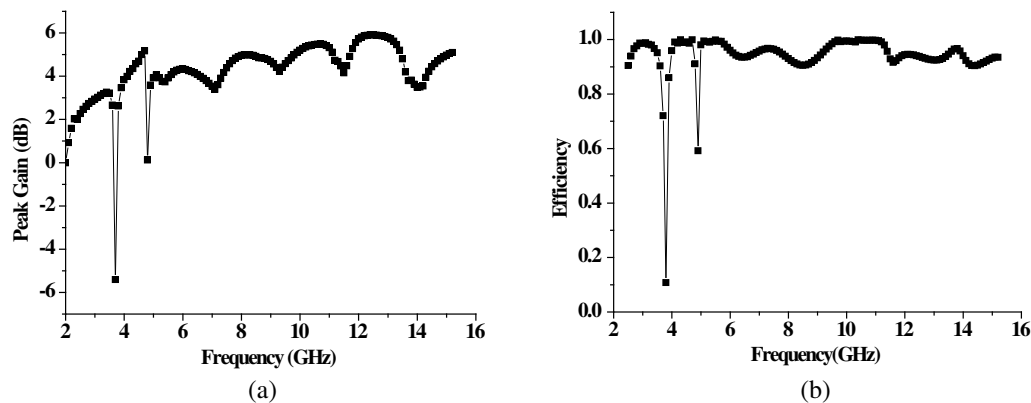
Figure 5: Efficiency and peak gain. (a) peak gain, (b) efficiency.

suppressed to -5 dBi and 0.1 dBi and radiation efficiencies reduced to 10% and 60%, respectively.

4. CONCLUSIONS

The design of a CCFEMUA with a dual band-notched characteristic has been presented. The antenna is simple and has a CPW-coupled-fed structure with an elliptical patch for radiation. Two half-elliptical-arc slots are cut on the radiator to generate two band notches at 3.7 GHz and 4.8 GHz. Simulation results have shown that it has a wide operation bandwidth of 2.4–15.2 GHz and approximately omnidirectional radiation patterns, and so is suitable for UWB applications.

REFERENCES

1. Federal Communications Commission, First Report and Order, Revision of Part 15 of the Commission's Rules Regarding Ultra-wideband Transmission Systems, FCC 02-48, Apr. 2002.
2. Schantz, H., *The Art and Science of Ultra Wideband Antennas*, Artech House Inc., 2005.
3. Ghavami, M., L.B. Michael, and R. Kohno, *Ultra Wideband Signals and Systems in Communication Engineering*, John Wiley and Sons, New York, USA, 2004.
4. Ojaroudi, M., C. Ghobadi, and J. Nourinia, "Small square monopole antenna with inverted T-shaped notch in the ground plane for UWB application," *IEEE Antennas and Wireless Propagation Letters*, Vol. 8, 728–731, 2009.
5. Chiaw, C. C. and M. R Kamarudin, "Novel design of circular UWB antenna," *Asia Pacific Microwave Conference*, Singapore, 1977–1979, 2009.
6. Shrivastava, V. and Y. Ranga, "Ultra wide band CPW-fed printed pentagonal antenna with modified ground plane for UWB applications," *IET International Conference on Wireless Mobile and Multimedia Networks*, 1–2, Beijing, China, 2008.
7. Panda, J. R. and R. S. Kshetrimayum, "A compact CPW-fed hexagonal 5 GHz/6 GHz band-notched antenna with an U-shaped slot for ultrawideband communication systems," *International Conference on Signal Processing and Communications*, Bangalore, India, 1–5, 2010.

8. Weng, Y. F., S. W. Cheung, and T. I Yuk, "Compact ultra-wideband antennas with single band-notched characteristic using simple ground stubs," *Microwave and Optical Technology Letters*, Vol. 53, No. 3, Mar. 2011.

9. Azim, R., M. T. Islam, and N. Misran, "Printed circular ring antenna for UWB application," *International Conference on Electrical and Computer Engineering*, 361–363, Dhaka, Bangladesh, 2010.

10. Lee, S. H., J. K. Parka, and J. N. Lee, "A novel CPW-fed ultra-wideband antenna design," *Microwave and Optical Technology Letters*, Vol. 44, No. 5, Mar. 2005.

11. Nazli, H., E. Bicak, B. Turetken, and M. Sezgin, "An improved design of planar elliptical dipole antenna for UWB applications," *IEEE Antennas and Wireless Propagation Letters*, Vol. 9, 264–267, 2010.

12. Zhang, Z. C., C. J. Guo, J. Ding, and Y. Su, "A novel printed UWB monopole antenna fed by coaxial cable," *International Conference on Microwave and Millimeter Wave Technology*, 25–27, 2010.

13. Chu, Q.-X. and Y.-Y. Yang, "A compact ultrawideband antenna with 3.4/5.5 GHZ dual band-notched characteristics," *IEEE Transactions on Antennas and Propagation*, Vol. 56, No. 12, 3637–3644, Dec. 2008.

14. Eshtiaghi, R., J. Nourinia, and C. Ghobadi, "Electromagnetically coupled band-notched elliptical monopole antenna for UWB applications," *IEEE Transactions on Antennas and Propagation*, Vol. 58, No. 4, 1937–1402, Apr. 2010.

15. Weng, Y. F., W. J. Lu, S. W. Cheung, and T. I. Yuk, "UWB antenna with single or dual-band notched characteristic for WLAN band using meandered ground stubs," *Loughborough Antennas & Propagation Conference*, 767–760, Nov. 2009.

16. Weng, Y. F., S. W. Cheung, and T. I. Yuk, "An antenna for UWB and bluetooth standards with band-notched characteristic," *International Conference on Ultra-wideband*, 170–174, Sep. 2009.

Deep Band-notched Characteristic Using Meander Lines for UWB Monopole Antennas

L. Liu[1], Y. F. Weng[1], S. W. Cheung[1], T. I. Yuk[1], and T. Peter[2]

[1]Department of Electrical and Electronic Engineering
The University of Hong Kong, Hong Kong, China
[2]Department of Electronics and Computer Engineering
Brunel University, Kingston Lane, Uxbridge, UB8 3PH, UK

Abstract— The paper proposes using two pairs of meander lines (MLs) with different structures to design a deep single band notch for planar monopole ultra-wide band (UWB) antennas. The center frequency and bandwidth of the deep notch in the characteristic of the UWB antennas can be adjusted by using the dimensions of the ML structures. For illustration, the single band notch is designed in the wireless local area network (WLAN) band from 5.15 GHz to 5.825 GHz. The band-notched characteristics such as radiation patterns and peak gains of the antenna are studied using computer simulation.

1. INTRODUCTION

Ultra-wide band (UWB) technology has caught great interest since the first release of the unlicensed frequency band of 3.1–10.6 GHz for UWB communications in 2002 [1]. The unique characteristics of low-power consumption and high-data rate make the UWB technology very suitable for high-speed indoor mobile communications. However, there are other communications systems such as the wireless local area networks (WLANs) already using some frequency bands with the UWB. Preventing the UWB communication systems from interfering with these systems becomes a challenging task for the system designer. One of the simple methods to achieve this task is to have a band-notched characteristic for the antenna.

Many methods have been proposed to implement band-notched characteristics for UWB antenna. The most common method is etching different shapes of $\lambda/2$- or $\lambda/4$-slots on the radiators, such as the V-shape [2], U-shape [3, 4], hat-shape [5], circular arc [6] and split ring [7]. Other approaches include cutting a slot on the feed line [8] and using meander lines [9–11]. In most of these designs, the peak gains drop by less than 10 dB at the notched frequency, which is not enough in the environments having high interference. In this paper, we propose to design a deep notch for UWB antennas by placing two pairs of meander lines (MLs) with different structures, one on the ground plane and the other next to the feed line. For illustration, we design a microstrip-fed UWB monopole antenna with a notched characteristic in the wireless local area network (WLAN) band from 5.15 to 5.825 GHz. Simulation results show a 15-dB deep notch can be achieved at the notch frequency.

2. ANTENNA DESIGN

The planar monopole antenna proposed in our design for UWB operation is shown in Fig. 1. It consists of an elliptical radiator fed by a 50-Ω microstrip line on one side of the substrate and a partial ground plane on the other side. The feed line tapers toward the radiator end to achieve good impedance matching for the UWB antenna. Two pairs of meander lines (MLs) with different structures, as shown in Fig. 1, are employed to introduce a single deep notch for the antenna in the WLAN band. One pair of MLs is placed at the upper edge of the ground plane and symmetrically on both sides of the feed line. Another pair of MLs is placed closely to the feed line and having one of their ends shorted to the ground plane. These MLs serve as $\lambda/4$-resonators or bandstop filters which have high impedances at resonances. The dimensions of these MLs can be designed to have the same resonating frequency, hence generating a deep notched characteristic for the UWB antenna. The antenna is designed on a Rogers substrate, RO4350B, with a compact size of 30 mm × 39.3 mm, thickness of 0.762 mm and dielectric constant of 3.48. In our design, all the MLs are designed using computer simulation to generate a notch band in the WLAN band of 5.15 to 5.825 GHz. The dimensions of the band-notched antenna are listed in Table 1.
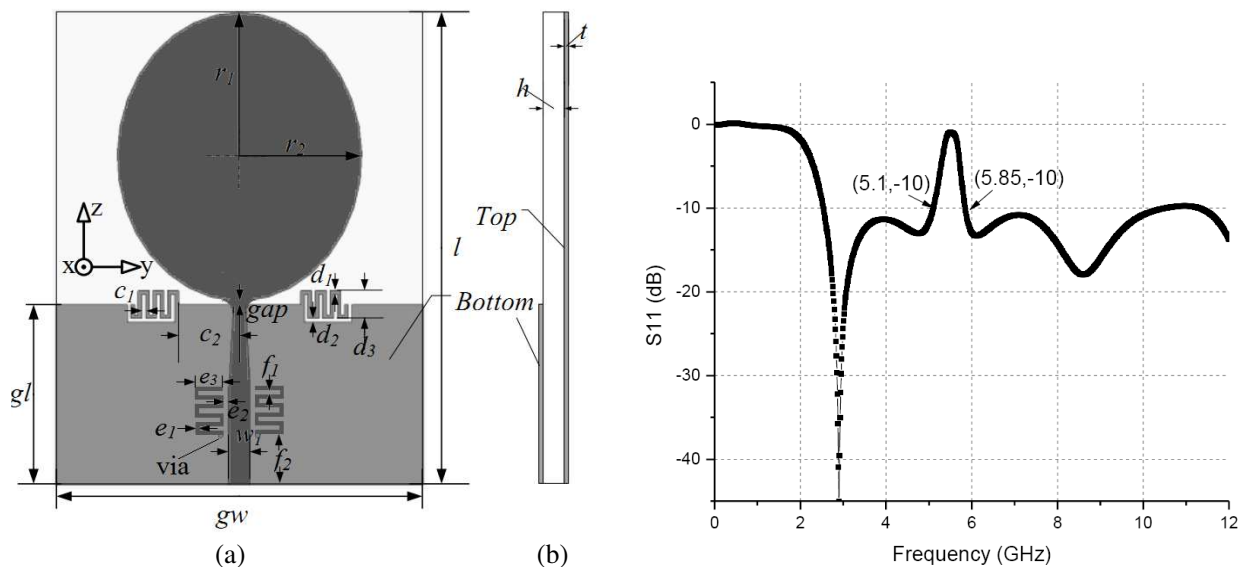
Figure 1: (a) Top view and (b) side view of antenna.

Figure 2: Simulated S_{11} of deep notched antenna.

Table 1: Dimensions of deep notched antenna (in mm).

Parameter	Value	Parameter	Value	Parameter	Value	Parameter	Value
gl	15	c_1	0.3	e_1	0.3	w_1	1.8
gw	30	c_2	4.5	e_2	0.2	T	0.035
l	39.3	d_1	0.3	e_3	2.1	H	0.762
r_1	12	d_2	0.3	f_1	0.3	gap	0.3
r_2	9	d_3	2.3	f_2	6.3		
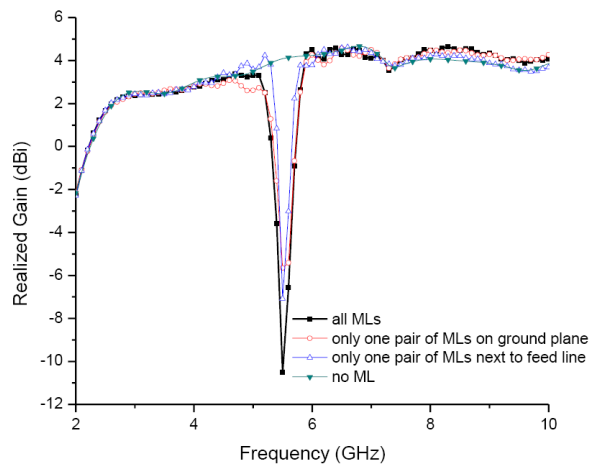
Figure 3: Simulated peak gains of the antenna.

3. RESULTS AND DISCUSSIONS

The performance of the proposed antenna is studied using the EM simulation tool, CST Microwave Studio. The simulated S_{11} is shown in Fig. 2. It can be seen that the antenna has a bandwidth from 2.5 GHz to more than 12 GHz, except in the notch band from 5.1 to 5.85 GHz which is the WLAN band.

The peak gain of the antenna is shown in Fig. 3. For comparison, the peak gains of the antenna having only the pair of MLs on the ground plane and only the pair of MLs next to the feed line, and without having any ML are also shown in the same figure. Without having the MLs, the peak

gain at 5.5 GHz is about 4 dBi. The pair of MLs on the ground plane alone or the pair of MLs next to the feed line alone can cause the gain to drop to −5.5 or −7 dBi, respectively. With the two pairs of MLs working together, the peak gain drops from 4 dBi to −11 dBi, resulting in a deep notch of 15 dB.

The simulated radiation patterns at 3, 5.5, and 10 GHz of the proposed single band-notched antenna are shown in Fig. 4. In these frequencies, the antenna has almost omnidirectional radiation patterns in the x-y plane (or H-plane) and the radiation is much smaller at the notched frequency of 5.5 GHz.
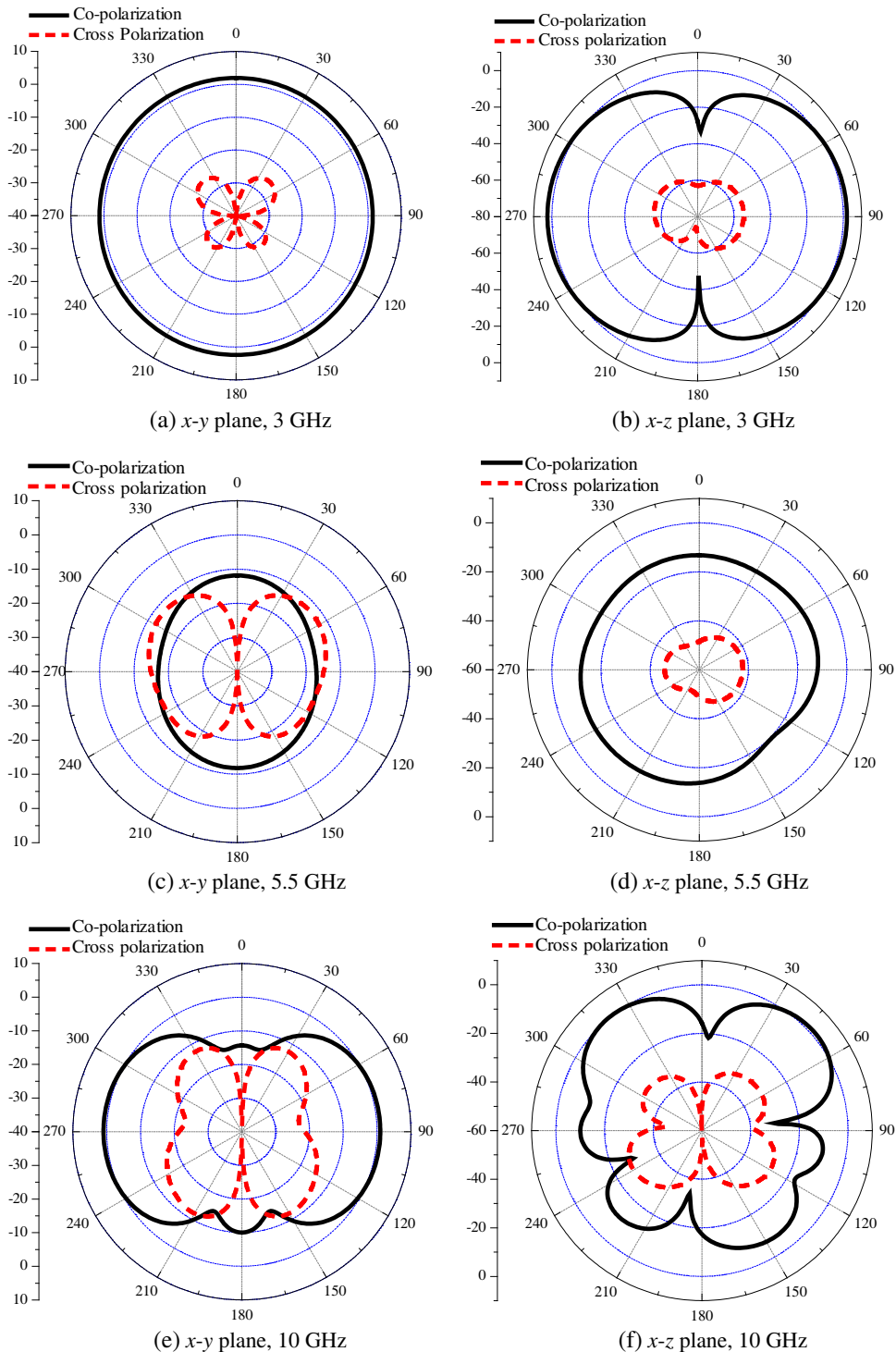
Figure 4: Radiation patterns of band-notched antenna at 3 GHz in (a) x-y plane and (b) x-z plane, at 5.5 GHz in (c) x-y plane and (d) x-z plane, and at 10 GHz in (e) x-y plane and (f) x-z plane.

4. CONCLUSION

In this paper, two pairs of MLs with different structures have been employed to create a deep band notch for the UWB antenna to prevent interference from other systems. One pair of MLs is placed at the upper edges of the ground plane, and the other pair is next to the feed line. Simulation results have shown that, by designing all these MLs to resonate at the WLAN frequency of 5.5 GHz, a deep notch of 15 dB can be achieved.

REFERENCES

1. "Federal communications commission revision of Part 15 of the commission's rules regarding ultra-wideband transmission systems," FCC, First Report and Order FCC, 2002.
2. Kim, Y. and D.-H. Kwon, "CPW-fed planar ultra wideband antenna having a frequency band notch function," *Electron. Lett.,* Vol. 40, No. 7, 403–405, Apr. 2004.
3. Cho, Y. J., K. H. Kim, D. H. Choi, S. S. Lee, and S. O. Park, "A miniature UWB planar monopole antenna with 5 GHz band-rejection filter," *IEEE Trans. Antennas and Propag.*, Vol. 54, No. 5, 1453–1460, Oct. 2005.
4. Lee, W. S., W. G. Kim, and J. Y. Yu, "Multiple band-notch planar monopole antenna for multiband wireless system," *IEEE Microw. Wireless Compon. Lett.*, Vol. 15, No. 9, 576–578, Sep. 2005.
5. Lee, J. N., J. K. Park, and S. S. Choi, "Design of a compact frequency notched UWB slot antenna," *Microw. Opt. Technol. Lett.*, Vol. 48, No. 1, 105–107, Jan. 2006.
6. Liu, G., C. Guo, and P. Zheng, "A new band notched UWB monopole antenna," *Proceedings of 2010 IEEE Asia-Pacific Conference on Applied Electromagnetics*, 2010.
7. Kim, J., C. S. Cho, and J. W. Lee, "5.2 GHz notched ultra-wideband antenna using slot-type SRR," *Electron. Lett.*, Vol. 42, No. 6, 315–316, Mar. 2006.
8. Qu, S. W., J. L. Li, and Q. Xue, "A band-notched ultrawideband printed monopole antenna," *IEEE Antennas and Wireless Progag. Lett.*, Vol. 5, 495–498, 2006.
9. Weng, Y. F., S. W. Cheung, and T. I Yuk, "Compact ultra-wideband antennas with single band-notched characteristic using simple ground stubs," *Microw. Opt. Technol. Lett.*, Vol. 53, No. 3, Mar. 2011.
10. Weng, Y. F., W. J. Lu, S. W. Cheung, and T. I. Yuk, "UWB antenna with single or dual-band notched characteristic for wlan band using meandered ground stubs," *Loughborough Antennas & Propagation Conference*, 767–760, Nov. 2009.
11. Weng, Y. F., S. W. Cheung, and T. I. Yuk, "An antenna for UWB and bluetooth standards with band-notched characteristic," *International Conference on Ultra-wideband*, 170–174, Sep. 2009.

Planar UWB Monopole Antenna with Tunable Notch Band

X. L. Sun[1], C. Wang[1], S. W. Cheung[1], T. I. Yuk[1], and H. F. Abutarboush[2]

[1]Department of Electrical and Electronic Engineering
The University of Hong Kong, Hong Kong, China
[2]Electrical Engineering, King Abdullah University of Science and Technology (KAUST)
Saudi Arabia

Abstract— In this paper, a planar monopole antenna with a tunable notch band for ultra wideband (UWB) applications is proposed. The antenna consists of an elliptical radiator, a microstrip-feed line and a ground plane. A meander-defected-ground structure (meander-DGS) etched on the ground plane is used to create a notch. A variable capacitor placed on the meander-DGS structure is used to tune the frequency of the notch band. The antenna is designed on a $30 \, \text{mm} \, (W) \times 39.1 \, \text{mm} \, (L) \times 0.762 \, \text{mm} \, (h)$ substrate with a relative permittivity of 3.48 and a loss tangent of 0.004. The antenna is studied by using computer simulation. The results show that the notch band can be tuned from 5.5 to 9.6 GHz by varying the capacitance from 1.7 to 0.07 pF, respectively.

1. INTRODUCTION

Ultra wideband (UWB) communications systems have recently received much attention in the wireless world for the advantages of higher data rates, immunity to multi-patch cancelation and increase of communication operational security, etc.. However, within the UWB from 3.1 to 10.6 GHz allocated by the US FCC, there are other communications standards such as the Wireless Local Area Networks (WLANs) operating in 5.2-GHz (5.15–5.35 GHz) and 5.8-GHz (5.725–5.825 GHz) bands [1]. To avoid interference from these communications systems operating in the frequency bands within the UWB, employing an UWB antenna with a band-notched characteristic for the system is a good method to suppress the interference signals. Different designs for implementing the band-notched features have been studied [2–7]. However, in these designs, the notch bands are fixed and cannot be tuned according to the frequency of interference.

In this paper, an UWB monopole antenna with a tunable notch band is proposed. An elliptical radiator and a tapered microstrip-feed line are used to achieve a wide band operation. A meander-defected-ground structure (meander-DGS) is employed to create a notch band in the UWB. A variable capacitor, placed on the meander-DGS, is used to achieve a tunable band-notched feature. The antenna is studied using the commercial EM simulation tool CST. Simulation results on the S_{11}, efficiency and gain with different capacitance values suggest that the notch band can be tuned with a frequency range of 5.5–9.6 GHz.

2. ANTENNA STRUCTURE

The geometry of the proposed antenna is shown in Fig. 1(a), which consists of an elliptical radiator fed by a 50-Ω microstrip line on one side of the substrate and a rectangular ground plane on the other side. The antenna is designed on a substrate with a size of $30 \, \text{mm} \, (W) \times 39.1 \, \text{mm} \, (L) \times 0.762 \, \text{mm} \, (h)$, a relative permittivity of 3.48 and a loss tangent of 0.004. For good impedance matching across the UWB, the 50-Ω microstrip-feed line is tapering gradually from $W_1 = 3 \, \text{mm}$ to $W_2 = 1.4 \, \text{mm}$. To create a notch band for the antenna, a meander-DGS is placed under the feed line and close to the upper edge of the ground plane. A slot with a width of 0.2 mm is etched on the meander-DGS and a variable capacitor C is then placed over it as shown in Fig. 1(c). The resonant frequency of the meander-DGS is tuned by varying the capacitance value. The dimensions of the antenna have been optimized in terms of a wide impedance bandwidth ($S_{11} < -10 \, \text{dB}$) by using computer simulation. Results have showed that the antenna can achieve an impedance bandwidth from 2.8 GHz to over 12 GHz which is more than the UWB allocated by the US FCC. The meander-DGS has been designed to resonate at 5.5 GHz using computer simulation. The optimized dimensions of the antenna and meander-DGS are listed in Table 1.

3. RESULTS AND DISCUSSIONS

Computer simulation is used to study the band-notched antenna. The simulated S_{11} of the antenna with different capacitances are shown in Fig. 2. It can be seen that the frequency of the notch band
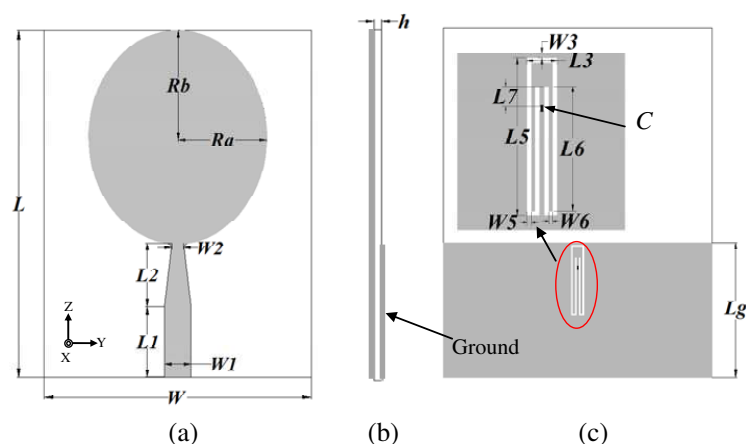
Figure 1: (a) Top and (b) side view of antenna, and (c) meander-DGS.
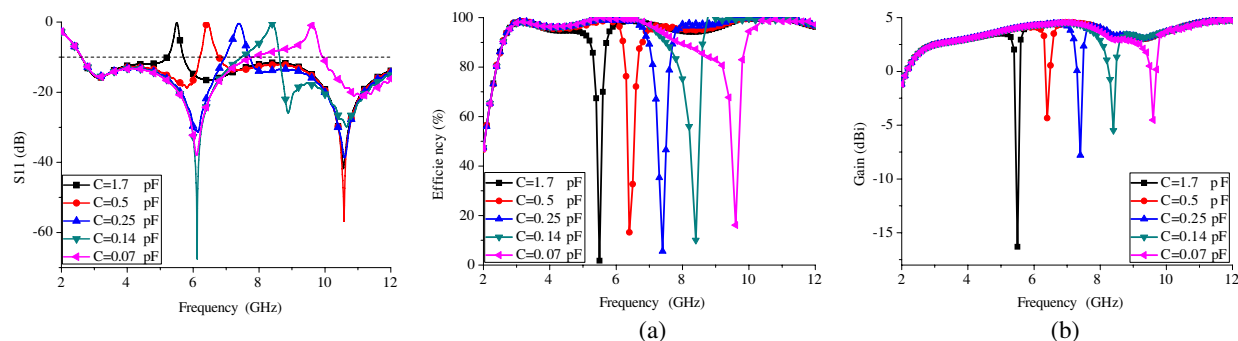
Figure 2: Simulated S_{11} for different values of C.

Figure 3: Simulated (a) efficiencies, and (b) gains for different values of C.

(c)

(d)
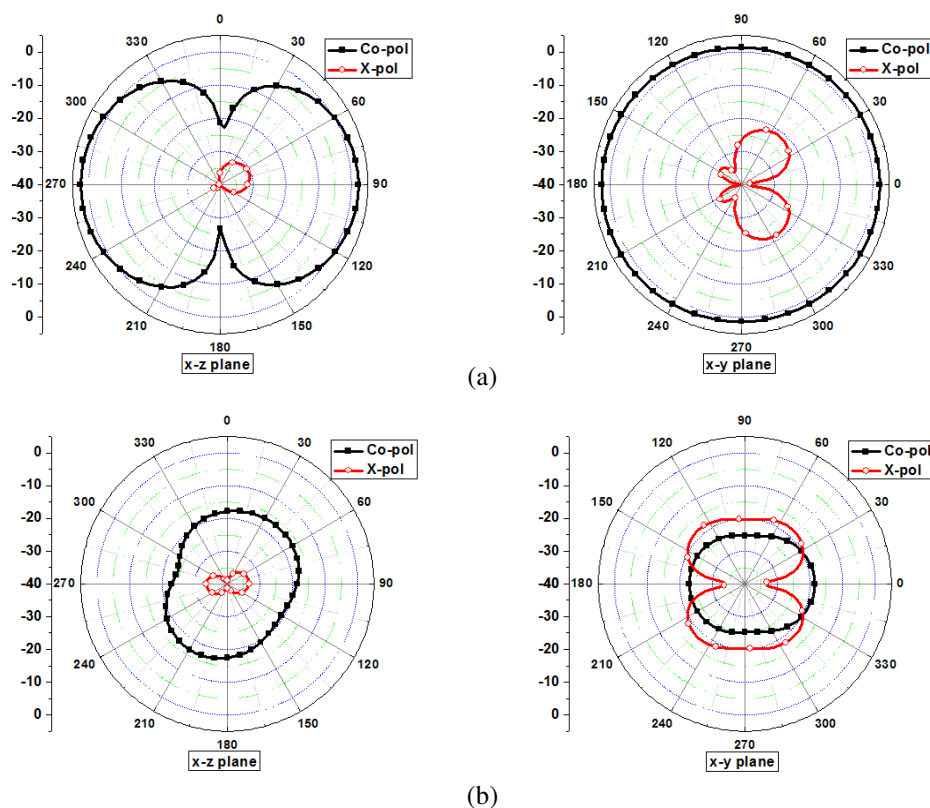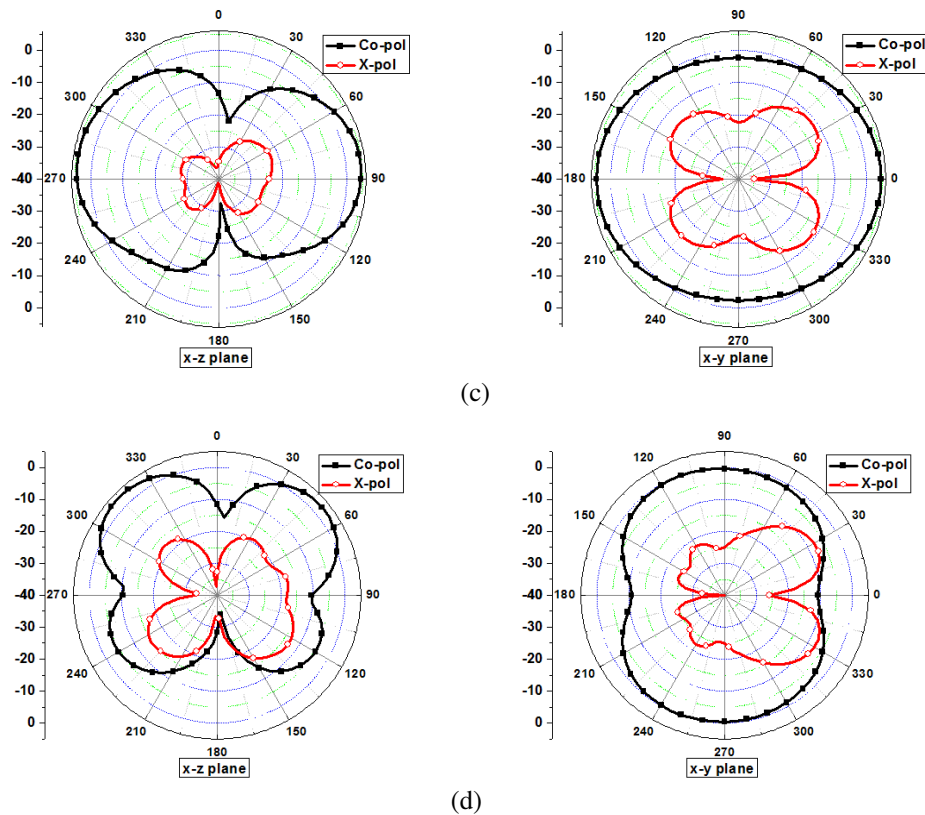
Figure 4: Simulated radiation patterns at (a) 3 GHz, (b) 5.5 GHz, (c) 7 GHz, and (d) 11 GHz.

Table 1: Optimized parameters of antenna (in mm).

L	W	R_a	R_b	L_1	L_2	W_1	W_2	L_3	L_5	L_6	L_7	W_3	W_5	W_6	L_g	h
39.1	30	10	12	8	7.1	3	1.4	1.5	7.96	6.27	1	0.2	0.23	0.17	15	0.762

can be shifted by using different capacitance values of C. With by using $C = 1.7$, 0.5, 0.25, 0.14 and 0.07 pF, the notch frequency can be tuned to 5.5, 6.4, 7.4, 8.4 and 9.6 GHz, respectively.

Figure 3 shows the simulated efficiencies and gains of the antenna with different values of C. It can be observed in Fig. 3(a) that the efficiencies are all above 90% over the UWB from 3.1–10.6 GHz, except in the notch bands which have the efficiencies dropped to below 20%. Figure 3(b) shows that the simulated gain varies from 2.5 to 4 dBi across the UWB. However, the gain drops significantly in the notch bands.

To evaluate the radiation patterns of the antenna at different passband frequencies across the UWB, the frequencies of 3, 7 and 11 GHz are used. To study the radiation patterns in the notch band, the capacitance is set to 1.7 pF to have the notch band at 5.5 GHz (using the results in Fig. 2). The simulated radiation patterns of the antenna at these frequencies in the x-z and x-y planes (or vertical and horizontal planes, respectively) are shown in Fig. 4. At the passband frequencies of 3, 7 and 11 GHz, Figs. 4(a), (c) and (d), respectively, show that the antenna has relatively omnidirectional radiation patterns. At the notch frequency of 5.5 GHz, Fig. 4(b) shows that the radiation pattern is suppressed significantly in all directions.

4. CONCLUSION

A planar UWB monopole antenna with microstrip-fed having a tunable band-notched characteristic has been proposed and studied using computer simulation. A meander-DGS is etched on the ground plane to generate a notch band. A variable capacitor is placed on a slot of the meander-DGS to control the frequency of the notch band. Simulation results have showed that with the capacitance varied from 1.7 to 0.07 pF, the notch band can be shifted from 5.5 to 9.6 GHz.

REFERENCES

1. http://www.fcc.gov/pshs/techtopics/techtopics10.html.
2. Chu, Q. X. and Y. Y. Yang, "A compact ultrawideband antenna with 3.4/5.5 GHz dual band-notched characteristics," *IEEE Transactions on Antennas and Propagation*, Vol. 56, No. 12, 3637–3644, Dec. 2008.
3. Lee, S. H., J. W. Baik, and Y. S. Kim, "A coplanar waveguide fed monopole ultra-wideband antenna having band-notched frequency function by two folded-stripline," *Microw. Opt. Tech. Lett.*, Vol. 49, No. 11, 2747–2750, Aug. 2007.
4. Weng, Y. F., W. J. Lu, S. W. Cheung, and T. I. Yuk, "UWB antenna with single or dual-band notched characteristic for WLAN band using meandered ground stubs," *Loughborough Antennas & Propagation Conference*, 767–760, Nov. 2009.
5. Weng, Y. F., S. W. Cheung, and T. I. Yuk, "An antenna for UWB and bluetooth standards with band-notched characteristic," *International Conference on Ultra-wideband*, 170–174, Sep. 2009.
6. Li, Z. Q. and C. L. Ruan, "A small integrated bluetooth and UWB antenna with WLAN band-notched characteristic," *International Symposium on Signals, Systems and Electronics*, Vol. 1, 1–4, Sep. 2010.
7. Dong, Y. D., W. Hong, Z. Q. Kuai, and J. X. Chen, "Analysis of planar ultrawideband antennas with on-ground slot band-notched structures," *IEEE Trans. Antennas and Propag.*, Vol. 57, No. 7, 1886–1893, Jul. 2009.

A Novel Transparent TSA for Laptop and UWB Applications

T. Peter[1], R. Nilavalan[1], and S. W. Cheung[2]

[1]Brunel University, Uxbridge, Middlesex, UK
[2]The University of Hong Kong, Pokfulam Road, HK, China

Abstract— A novel transparent Tapered Slot Antenna is proposed in this paper. Since the approval by the FCC in 2002, much research has been undertaken on UWB especially for wireless communications. Often times especially for devices where internet services are required, UWB is complemented with the 2.4 GHz WLAN service like in Laptops or notebooks instead of being filtered out. In this paper, a transparent Tapered Slot Antenna (TSA) covering the frequency range from 2.1 GHz to 10.8 GHz is designed and fabricated using AgHT-8 for use in Laptop applications. The antenna provides sufficient gain, reasonable efficiency and a good return loss.

1. INTRODUCTION

Since the approval by the FCC in 2002, much research has been undertaken on UWB especially for wireless communications. Often times especially for devices where internet services are required, UWB is complemented with the 2.4 GHz WLAN service like in Laptops or notebooks [1] since the UWB antenna is usually designed to cover the FCC frequency range of 3.1 GHz to 10.6 GHz.

Also, antennas for Laptops are normally desired to be conformal and discrete. In this regard, a transparent Tapered Slot Antenna (TSA) is designed covering the frequency range from 2.1 GHz to 10.8 GHz and fabricated using AgHT-8. The antenna is compact and miniature in size to comply with the small size demands of current day laptop computers. As per [1], an antenna with a height greater than 25 mm is too large for the Laptop computer UWB applications. Research on transparent antennas for UWB applications only surfaced in the last few years [2–6]. However, pioneering work on narrow band transparent antennas was done as early as 1997 by Simons et al. [7] from the National Aeronautics and Space Agency (NASA). Transparent antennas have also since found potential use in body centric applications and energy harvesting. Work on this is currently being made ready for future publications by the authors.

2. ANTENNA DESIGN

The geometry of the antenna along with its parameters is as shown in Figure 1 and Table 1. It is a coplanar waveguide (CPW) fed tapered slot antenna inscribed on a thin transparent conductive oxide (TCO) polymer film, AgHT-8. The overall size of the antenna is $16 \times 23 \, \text{mm}^2$. The feed gap is 0.1 mm, and the feed is designed to slowly taper and merge into the radiator. The prototype of the antenna is shown in Figure 1(b). The SMA connector is connected to the antenna using conductive epoxy. The DC resistance of the conductive portion of the AgHT-8 is around 25 Ohms and has a conductivity of 125,000 S/m. The surface resistivity of the AgHT-8 as noted from its trademark name is 8 Ohm per square. The AgHT film has a thickness of 0.175 mm making it suitable for use in very slim devices.

3. EXPERIMENTAL RESULTS

The simulated and measured return loss of the antenna prototype is as given in Figure 2. The measured $-10 \, \text{dB}$ bandwidth was 8.7 GHz ranging from 2.1 GHz to 10.8 GHz. The measured gain is shown in Figure 3. The gain is noticed to increase exponentially above 16 GHz and may provide potentials for its use in other higher frequency applications.

The measured efficiency and radiation patterns are given in Figures 4 and 5 respectively. The TSA prototype antenna has an average efficiency of 10% over the FCC UWB bandwidth of 3.1 to

Table 1: Dimensions of the antenna geometry in Figure 1.

Parameters	L	W	L$_1$	L$_2$	W$_1$
Size (mm)	23.0	16.0	15.95	11.96	17.0
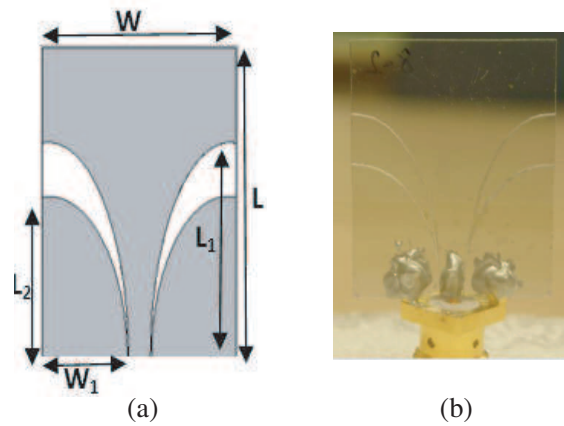
Figure 1: (a) Geometry of proposed transparent UWB TSA. (b) Prototype of the proposed TSA.
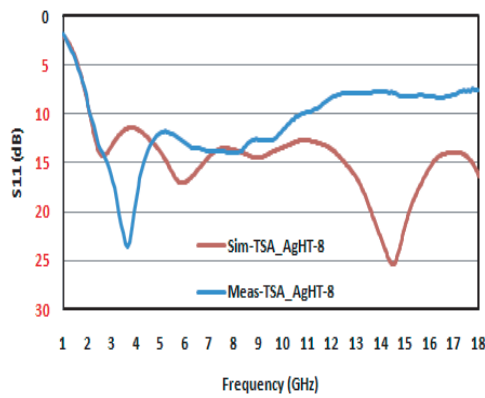
Figure 2: Return loss of the TSA.
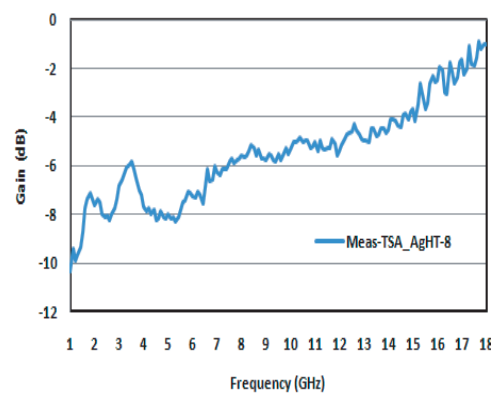
Figure 3: Gain of the TSA.
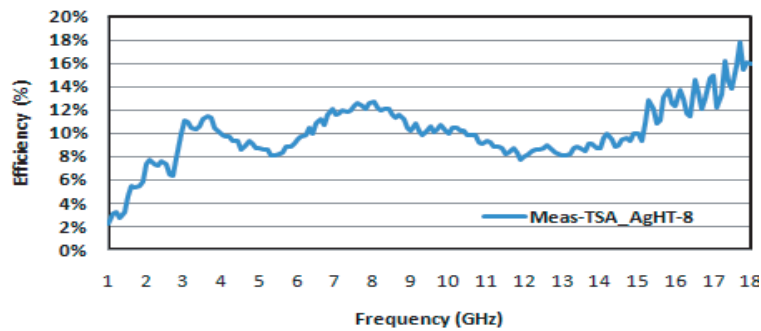
Figure 4: Efficiency of the transparent TSA.
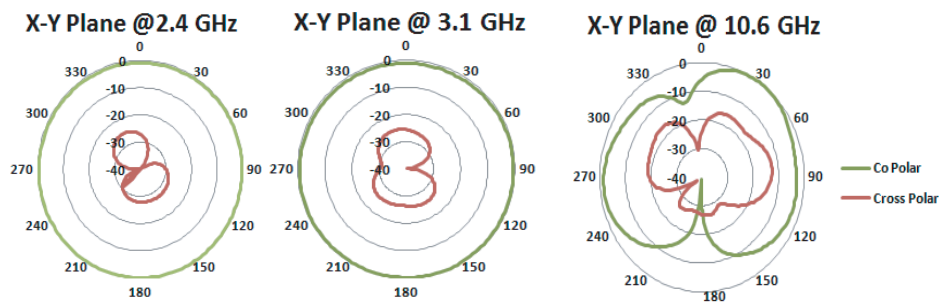
Figure 5: Measured radiation patterns of the antenna at 2.4 GHz, 3.1 GHz & 10.6 GHz.

10.6 GHz. The efficiency is noticed to increase above 16 GHz. This explains the increase in gain above 16 GHz. The gain and efficiency could be effectively improved if the antenna is designed using AgHT-4 which has a higher conductivity and lesser surface resistance of 4 Ohms per square. The
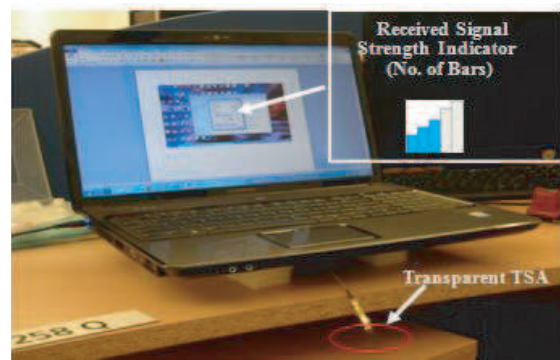
Figure 6: Transparent TSA connected to a laptop to receive 2.4 GHz WIFI signal.

transparent UWB TSA antenna has an omni-directional radiation pattern at 2.4 GHz and 3.6 GHz. It however demonstrates a quasi-omni directional pattern at 10.6 GHz.

Figure 6 shows the transparent TSA connected to a laptop to receive the 2.4 GHz Wi-Fi network signal from the University's Computer Centre. The signal strength is 3 bars in the received signal strength indicator (RSSI) as depicted in the picture This is the same strength observed when the laptop is directly connected to its existing internal 2.4 GHz WLAN antenna.

4. CONCLUSIONS

A miniature and transparent UWB tapered slot antenna capable of receiving and transmitting signals at the WLAN frequency of 2.4 GHz as well as in the UWB range of 3.1 GHz to 10.6 GHz has been proposed and presented. The antenna has the potential to be incorporated into laptop computers to provide WLAN internet connections, as well as fast and high data rate video transmission and reception through its UWB capability.

ACKNOWLEDGMENT

REFERENCES

1. Chen, Z. N., D. Liu, and B. Gaucher, "A planar dualband antenna for 2.4 GHz and UWB laptop applications," *IEEE 63rd Vehicular Technology Conference, 2006, VTC 2006-Spring*, Vol. 6, 2652–2655, May 7–10, 2006.
2. Katsounaros, A., Y. Hao, N. Collings, and W. A. Crossland, "Optically transparent antenna for Ultra Wide-Band applications," *3rd European Conference on Antennas and Propagation, 2009, EuCAP 2009*, 1918–1921, March 23–27, 2009.
3. Peter, T. and R. Nilavalan, "Study on the performance deterioration of flexible UWB antennas," *Antennas and Propagation Conference Loughborough (LAPC'09)*, 669–672, 2009.
4. Peter, T., R. Nilavan, H. F. AbuTarboush, and S. W. Cheung, "A novel technique and soldering method to improve performance of transparent polymer antennas," *IEEE Antennas and Wireless Propagation Letters*, Vol. 9, 918–921, 2010.
5. Peter, T., Y. Y. Sun, T. I. Yuk, H. F. AbuTarboush, R. Nilavalan, and S. W. Cheung, "Miniature transparent UWB antenna with tunable notch for green wireless applications," *2011 International Workshop on Antenna Technology (iWAT)*, 259–262, March 7–9, 2011.
6. Peter, T., T. I. Yuk, R. Nilavalan, and S. W. Cheung, "A novel technique to improve gain in transparent UWB antennas," *Antennas and Propagation Conference Loughborough (LAPC'11)*, 2009.
7. Simons, R. N. and R. Q. Lee, "Feasibility study of optically transparent microstrip patch antenna," *International Symposium and Radio Science Meeting Cosponsored by IEEE, AP-S, and U.R.S.I.*, Montreal, Canada, July 13–18, 1997.

Planar Monopole Ultra-wideband Antennas with Different Radiator Shapes for Body-centric Wireless Networks

Y. Y. Sun, **S. W. Cheung**, **and T. I. Yuk**
Department of Electrical and Electronic Engineering
The University of Hong Kong, Pokfulam Road, Hong Kong, China

Abstract— This paper is a further study on the performances of planar UWB monopole antennas using a radiator of different shapes such as triangle, rectangle, square, circle, annual ring, ellipse (both horizontal and vertical), pentagon and hexagon, for body-centric wireless networks. The planar antennas consist of a radiator and a microstrip-feed line on one side of the substrate and a ground plane on the other side. Previous simulation studies showed that the elliptical and hexagonal antennas appeared to have the best performances in terms of bandwidth, gain, efficiency and radiation pattern. Studies using measurements of these two antennas on a liquid-body phantom are presented in this paper. Results show that the elliptical antenna achieves a wide impedance bandwidth of 3.1–12 GHz, an average peak gain of nearly 2.3 dBi and good radiation patterns, making it a good candidate for UWB body-centric wireless networks.

1. INTRODUCTION

Ultra-wideband (UWB) technology [1], with the advantages of low cost, low complexity, low spectral power density, high precision ranging, low interference and extremely high data rates, has attracted much attention [2–9]. One of the most promising areas in UWB applications is body-centric wireless networks where various sensors are connected together by UWB devices which have to be low power, low-profile and unobtrusive to the human body [10, 11]. Due to the presence of human body, the design of UWB antennas for body-centric wireless networks is complicated. Several fundamental requirements such as wide impedance bandwidth, small size and low profile, good on-body propagation and radiation characteristics in the proximity of the body have to be fulfilled [10–15].

The studies on planar UWB monopole antennas using a radiator of different shapes such as rectangle, square, circle, ellipse, pentagon and hexagon, for body-centric wireless networks using computer simulation were carried out in [16]. Results showed that among all proposed antennas studied the elliptical and hexagonal antennas had the best performances for UWB body-centric wireless networks In this paper, further studies are carried out on the elliptical and hexagonal antennas by using measurements. The antennas are fabricated using FR-4 substrate placed on a body model and measured inside an echoic chamber. Results show that the antenna with an elliptical radiator appears to be the best choice for UWB body-centric wireless networks.

2. ANTENNA STRUCTURE

2.1. Structure of Planar Antennas with Different Radiators

The proposed UWB monopole antennas with radiators of different shapes, including rectangle, square, circle, ellipse, pentagon and hexagon, for computer simulation studies are shown in Fig. 1. Each antenna consists of a radiator fed by a microstrip line, with a width of wm to achieve $50\,\Omega$ characteristics impedance, printed on one side of the substrate and a rectangular ground plane on the other side of the substrate. The antennas are designed on lowcost FR4-substrates with a thickness of 1.6 mm, a relative permittivity of 4.6 and a total size of $W \times L$ optimized in terms of impedance bandwidth ($S_{11} < -10\,\text{dB}$) using computer simulation. In Fig. 1, the antennas have the following parameters: $W = 30\,\text{mm}$, $L = 35\,\text{mm}$, $w_f = 3\,\text{mm}$ and $h_g = 12\,\text{mm}$. Other parameters for these antennas are listed in Table 1.

2.2. Body Model

Human body has a significant influence on the antenna characteristics, so it is important to include the human-body model in the antenna design process. Two types of human-body models are often used. One type is the three-tissue model consisting of skin, fat and muscle tissue, while the other type is a homogeneous model composing of muscle tissue only [10]. Here, the homogeneous model is used due to its simpler structure and shorter simulation time than those of the three-tissue model. Simulation results have shown that there are only slight differences between them. In our
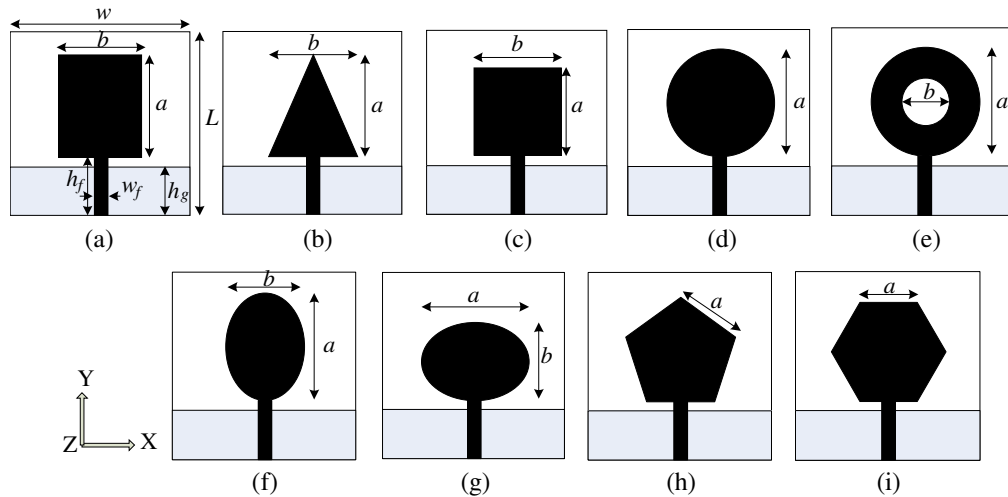
Figure 1: Geometries of antennas: (a) rectangle, (b) triangle, (c) square, (d) circle, (e) annual ring, (f) ellipse (vertical), (g) ellipse, (h) pentagon and (i) hexagon.
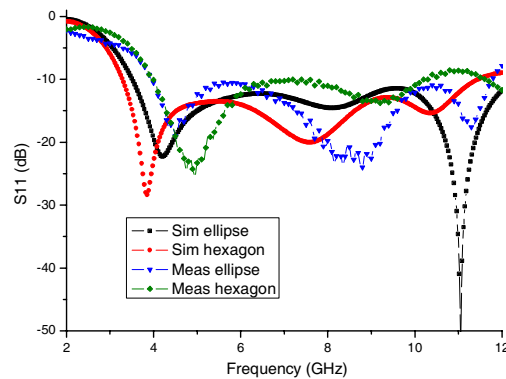
Figure 2: Simulated and measured S_{11} of ellipstical and hexgonal antennas in free space.

simulation studies, the dimension used for the body model is $100 \times 100 \times 30 \, \text{mm}^3$ with a relative permittivity of 53.58 and a loss tangent 0.2.

3. RESULTS AND DISCCUSIONS

3.1. Simulation Results in Previous Study

In free space, the simulated results in [16] showed that the elliptical antenna had the widest impedance bandwidth (for $S_{11} < -10 \, \text{dB}$) of 3.1–12 GHz and the triangular antenna had the narrowest bandwidth. The hexagonal antenna had an average peak gain of about 3.82 dBi and an average efficiency of about 81% throughout the whole UWB bandwidth which were the best among all antennas studied. The elliptical antenna had an average peak gain of about 3.78 dBi and an average efficiency of 80%, which was quite close to the hexagon one. The radiation patterns of all the antennas in the H-plane were almost omnidirectional and in the E-plane had obvious nulls which are typical for monopole antennas. Note that for body-centric wireless networks, the radiation in the E-plane plays a more important role.

When the antennas were place on a human body (with body model in simulation) the simulated results in [16] showed that the hexagon antenna also was the best in terms of average peak gain and efficiency. However, compared with the results in free space the average efficiency dropped from about 80% to 30% and the average peak gain increased a little to 4.18 dBi which was due to reflections of the body. The elliptical antenna had an average peak gain of 4.15 dBi and an average efficiency of 31%.
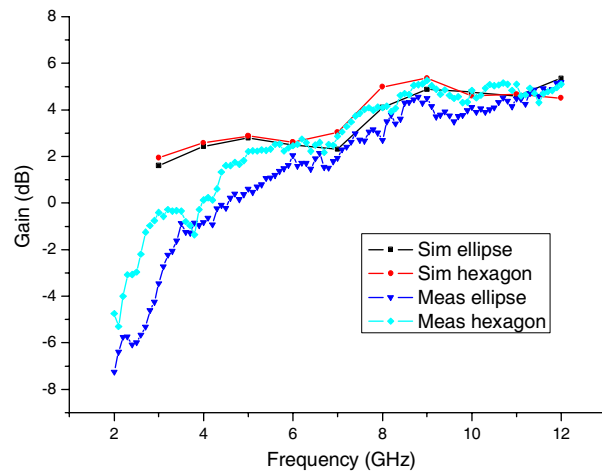
Figure 3: Simulated and measured peak gains.
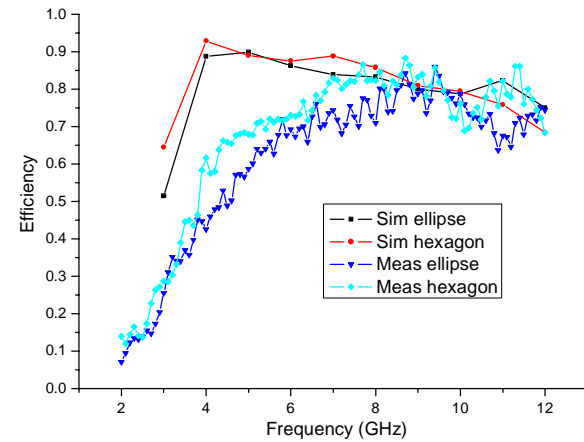
Figure 4: Simulated and measured radiation efficiencies.

(a) 4 GHz

(b) 7 GHz

(c) 11 GHz

(d) 4 GHz

(e) 7 GHz

(f) 11 GHz
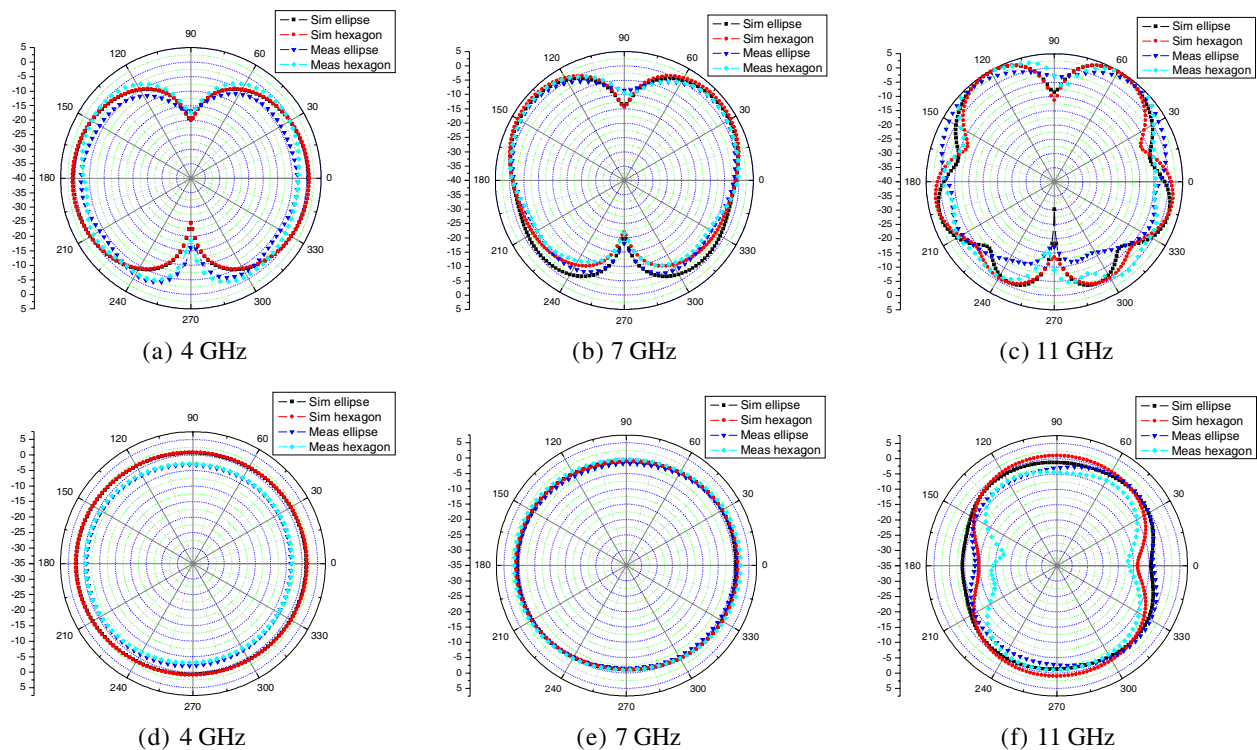
Figure 5: Simulated and measured radiation patterns in (a), (b) & (c) xy-plane and (d), (e) & (f) xz-plane in free space.

3.2. Measurement Results

The simulated and measured reflection coefficients S_{11} of the two antennas in free space are shown in Fig. 2, while the simulated and measured peak gains and radiation efficiencies are shown in Figs. 3 and 4 The elliptical and hexagonal antennas have impedance bandwidths ($S_{11} < -10$ dB) from about 3.5 GHz to more than 12 GHz. The elliptical antenna has an average peak gain of about 2.3 dBi and an average efficiency of about 66% while the hexagonal antenna has an average peak gain of 3.1 dBi and an average efficiency of 72%. The simulated and measured radiation patterns of the antennas in free space at 4, 7 and 11 GHz agree very well, as can be seen in Fig. 5.

A liquid phantom with a dimension of $260 \times 80 \times 60\,\text{mm}^3$ has been used for measurement. It is a cuboidal container filled with liquid provided by SATIMO which has the same electrical characteristics as the tissues in the human body. In measurements, the phantom was placed vertically inside an anechoic chamber with the antenna reflector lying on the surface of it.

    The peak gains and radiation efficiencies of the antennas on body from 3 to 12 GHz are shown
in Figs. 6 and 7 respectively. The elliptical antenna has the better average peak gain of −0.37 dBi
and efficiency of 17%. Fig. 8 shows the radiation patterns at 4, 6 and 9 GHz. It can be seen
that there are obvious discrepancies between simulation and measurement results in peak gains
and radiation efficiencies. These are due to the high loss of FR4-substrate at high frequencies and
unstable relative permittivity across the frequency band, the difference between body model in
simulation and measurement and the measurement errors. These also lead to the discrepancies in
the radiation patterns of Fig. 8. It can be seen that the radiations are directional, with the front-
to-back ratios of about 20–30 dB. Since the radiation in the E-plane plays an important role in
body-centric communications, the results in Fig. 8 show that the elliptical antenna has the slightly
larger radiation patterns in the E-plane at all these frequencies and so appears to be better than
the other antenna.
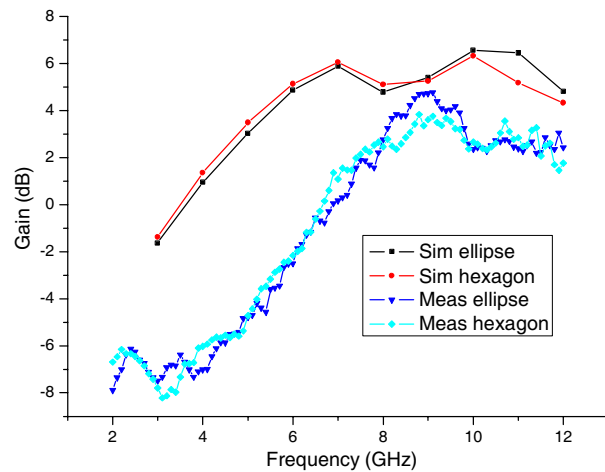
Figure 6: Simulated and measured on-body peak gains.
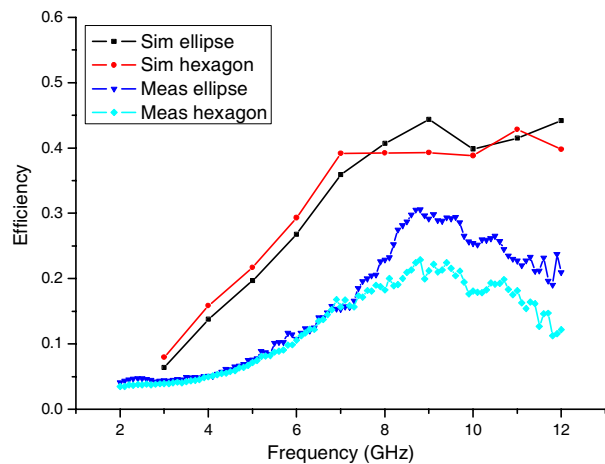
Figure 7: Simulated and measured on-body efficiencies.

(a) 4 GHz

(b) 7 GHz

(c) 11 GHz

(d) 4 GHz

(e) 7 GHz

(f) 11 GHz
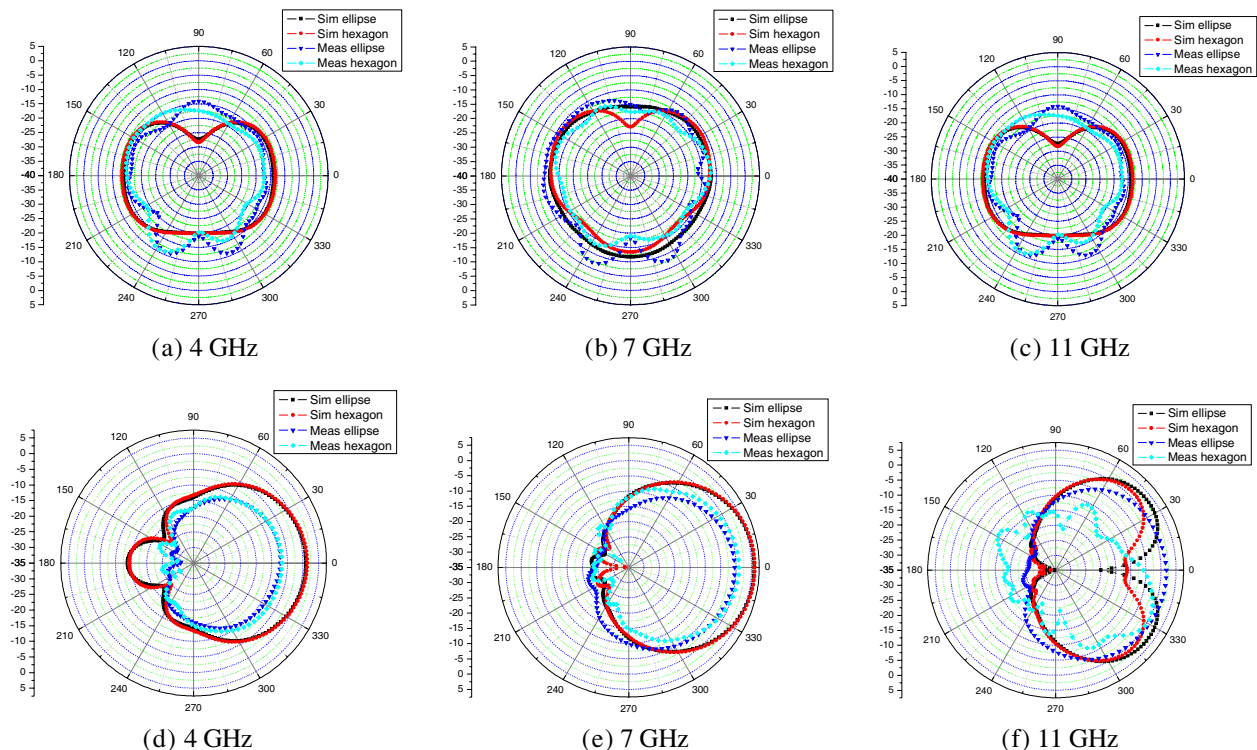
Figure 8: Simulated and measured on-body radiation patterns in (a), (b) & (c) xy-plane and (d), (e) & (f) xz-plane.

Table 1: Dimensions of different radiators of antennas.

	Rectangle	Triangle	Square	Circle	Annual ring	Ellipse	Ellipse h	Pentagon	Hexagon
h_f (mm)	13.65	14	13.7	13	13	13.1	13	13.1	13.2
a (mm)	16	16	13	16	16	16	16	10.4	9.24
b (mm)	12.88	12	13		6	12	12		

4. CONCLUSION

This paper has presented the measured results for further study on the performances of planar UWB monopole antennas using different shapes of radiators. A liquid body phantom has been used in measurements. Results of the simulation and measurement have showed that the antenna with an elliptical radiator has a better overall performance in terms of bandwidth, gain and radiation pattern, both in free space and on body. The antenna can achieve a bandwidth from 3.1 to 12 GHz, an average peak gain of about 2.3 dBi, an average efficiency of 66% and good radiation patterns in the E-plane, making it a good candidate for UWB body-centric wireless networks.

REFERENCES

1. Federal Communications Commission, "Revision of part 15 of the commission's rules regarding ultra-wideband transmission system from 3.1 to 10.6 GHz," 98–153, Federal Communications Commission, Washington, DC, ET-Docket, 2002.
2. Kiminami, K., A. Hirata, and T. Shiozawa, "Double-sided printed bow-tie antenna for UWB communications," *IEEE Antennas Wireless Propag. Lett.*, Vol. 3, No. 1, 152–153, 2004.
3. Liang, J., C. C. Chiau, X. Chen, and C. G. Parini, "Printed circular ring monopole antennas," *Microw. Opt. Technol. Lett.*, Vol. 45, 372–375, 2005.
4. Jung, J., W. Choi, and J. Choi, "A small wideband microstrip-fed monopole antenna," *IEEE Microw. Wireless Compon. Lett.*, Vol. 15, No. 10, 703–705, 2005.
5. Ren, Y. J. and K. Chang, "Ultra-wideband planar elliptical ring antenna," *Electron. Lett.*, Vol. 42, No. 8, 447–449, 2006.
6. Ren, Y. J. and K. Chang, "An annual ring antenna for UWB communications," *IEEE Antennas Wireless Propag. Lett.*, Vol. 5, No. 1, 274–276, 2006.
7. Lin, D. B., I. T. Tang, and M. Y. Tsou, "A compact UWB antenna with CPW-fed," *Microw. Opt. Technol. Lett.*, Vol. 49, 372–375, 2007.
8. Zhang, J. S. and F. J. Wang, "Study of a double printed UWB dipole antenna," *Microw. Opt. Technol. Lett.*, Vol. 50, 3179–3181, 2008.
9. Xiao, J. X., M. F. Wang, and G. J. Li, "A ring monopole antenna for UWB application," *Microw. Opt. Technol. Lett.*, Vol. 48, No. 1, 179–182, 2010.
10. Hall, P. S. and Y. Hao, *Antennas and Propagation for Body-centric Wireless Communications*, Artech House, Norwood, MA, 2006.
11. Alomainy, A., A. Sani, Y. Hao, et al., "Transient characteristics of wearable antennas and radio propagation channels for ultrawideband body-centric wireless communications," *IEEE Trans. Antennas Propag.*, Vol. 57, No. 4, 875–883, 2009.
12. Low, X. N., Z. N. Chen, and T. S. P. See, "A UWB dipole antenna with enhanced impedance and gain performance," *IEEE Trans. Antennas Propag.*, Vol. 57, No. 10, 2959–2966, 2009.
13. Alomainy, A., Y. Hao, P. S. Hall, et al., "Comparison between two different antennas for UWB on-body propagation measurements," *IEEE Antennas Wirel. Propag. Lett.*, Vol. 4, No. 1, 31–34, 2005.
14. Cai, A., T. S. P. See, and Z. N. Chen, "Study of human head effects on UWB antenna," *IEEE International Workshop on Antenna Technology: Small Antennas and Novel Metamaterials*, 310–313, Mar. 7–9, 2005.
15. Chen, Z. N., A. Cai, T. S. P. See, and M. Y. W. Chia, "Small planar UWB antennas in proximity of the human head," *IEEE Trans. Microw. Theory Tech.*, Vol. 54, No. 4, 1846–1857, 2006.
16. Sun, Y. Y., S. W. Cheung, and T. I. Yuk, "Studies of planar antennas with different radiator shapes for ultra-wideband body-centric wireless communications," *PIERS Proceedings*, 1415–1419, Suzhou, China, Sep. 12–16, 2011.

Energy Consumption Reduction by Multi-hop Transmission in Cellular Network

Pengty Ngor, **Siya Mi**, **and Peter Han Joo Chong**

School Electrical and Electronic Engineering, Nanyang Technological University, Singapore

Abstract— Adding relay stations between base station and mobile stations in a cellular network can extend network coverage, overcome multi-path fading and increase the capacity of the system. With the increase of data traffic, more and more energy is needed to support communication. Hence, it is challenging to design an optimal relay network that minimizes the average energy consumption. In this paper, a 3-tier-chitecture with two-hop relay network consisting of a source, a destination and multiple relay nodes is proposed to decrease the consumed energy for a given QoS requirement.

1. INTRODUCTION

As wireless communication develops, higher requirements are demanded of wireless networks. In 2003, the International Telecommunication Union Radio communication sector (ITU-R) proposed that next generation networks should achieve a total cell capacity of up to 1 Gbps for slow-moving users and 100 Mbps for moving mobile stations (MS). However, the limitation on radio resource is the real bottleneck for developing high-speed wireless networks. Research on future wireless system to provide higher capacity, yet retaining efficient use of power, can be divided into two aspects. (1) Advanced technology in the physical layer, such as multiple inputs multiple outputs (MIMO) [1], which provides spatial reuse. And (2) new network architectures, such as adding relay stations between the base station (BS) and mobile stations (MS) [2], or with MESH networks [3]. In future wireless systems, each user will expect a high throughput so they can access different multimedia services regardless of their location and mobility. However, the traditional cellular architecture is not well-suited to provide uniform data rate coverage. Additionally, if the radio propagation is non-line-of-sight (NLOS) (as is likely) the pathloss will be higher than that of line-of-sight (LOS) [4], so that the effect on an MS near the cell boundary will be worse, making it more difficult to achieve a power efficiency comparable to that seen by an MS near the BS that has LOS transmission. A simple way to handle the pathloss problem is to divide a long path into multiple shorter paths and use relay stations (RS) for data forwarding. RSs can also be used for temporary coverage in applications such as disaster relief as well as being deployed in hotspot areas to save energy. In this paper, a 3-Tier Architecture (3TA) is proposed in relay-based cellular networks based on TDD-CDMA to achieve more efficient energy consumption of wireless relay networks through considering the allocation of relay stations. The remainder of article is organized as following. Section 2 elaborates on related work. Section 3 describes 3TA. Section 4 depicts simulation settings and results. Section 5 concludes the paper and suggests future works.

2. RELATED WORKS

Adding relay station to cellular network has drawn much attention and is considered to be a most promising architecture for the very high throughput and coverage requirements of future systems as it can extend network coverage, overcome multi-path effect and increase the capacity of the system [5, 6]. Song [7] has proved that the two-hop transmission saves energy. The RS will be used, if the angle formed by MS and BS via RS is greater than 90°. In this paper, a 3-Tier Architecture is proposed in relay-based cellular networks to achieve more efficient energy consumption of wireless relay networks through considering the allocation of relay stations.

3. THREE-TIER ARCHITECTURE (3TA)

The proposed 3-tier architecture is shown in Figure 1. There are two tier relay stations each of which has its own influenced area. The inner relay station tier controls Tier 2, and the other relay station tier controls Tier 3. Tier 1 is managed directly by the base station. The three radii of Tier 1, Tier 2 and Tier 3 are with the ratio of 1 : 2 : 3 which use the equality of radii model in [8]. The following is the mathematical model to find the boundaries and influenced area. The base station
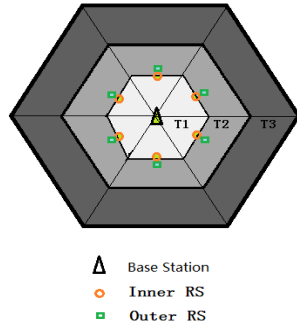
Figure 1: Multi-tier architecture.
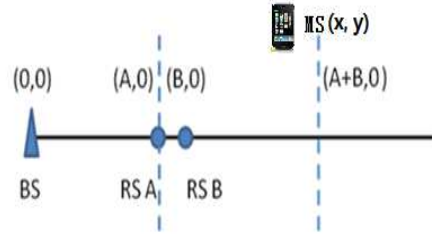
Figure 2: Base station and two relay stations.
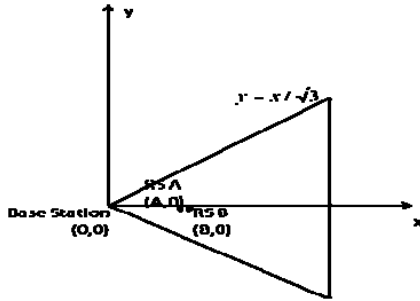
Figure 3: One sector of cellular cell.
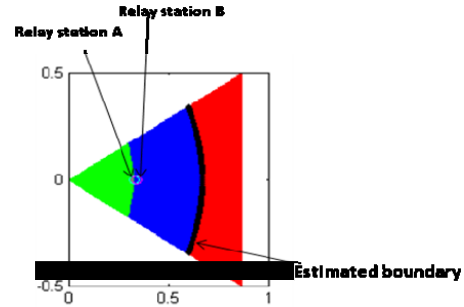
Figure 4: Estimated second tier boundary for $l = 3$.

is set as origin point $(0, 0)$, and the relay stations are $(A, 0)$ and $(B, 0)$. Set the coordination of mobile station as (x, y) as shown in Figure 2. The received power can be calculated via:

$$P_t = P_r \times d^l, \quad P_r = P_t \times d^{-l} \tag{1}$$

where d is the distance between receiver and transmitter. l is the path loss exponent.

Then, the transmission power for using relay station A and B is:

$$P_A = (\sqrt{(x - A)^2 + y^2})^l + A^l \tag{2}$$
$$P_B = (\sqrt{(x - B)^2 + y^2})^l + B^l \tag{3}$$

For $l = 2$, if $P_A > P_B$, the mobile station will use the relay station B to connect with the base station. $(x - A)^2 + A^2 > (x - B)^2 + B^2$, or $x > A + B$. Thus, the boundary of the influenced areas for relay station A and relay station B is $x = A + B$. In other words, if $x > A + B$, it should use relay station B. if $A < x < A + B$, it should use relay station A. The second tier boundary is the curve on which the mobile stations cost equivalent power to transfer information to relay station A and relay station B, which means $P_A = P_B$.

For any l, the second tier boundary is

$$\left[(x - A)^2 + y^2\right]^{l/2} + A^l - \left[(x - B)^2 + y^2\right]^{l/2} - B^l = 0 \tag{4}$$

In order to make the problem clearly, we just consider one sector of the cellular cell as shown in Figure 3. To estimate the second tier boundary, we do the following. For $y = 0$, (4) becomes

$$(x - A)^l + A^l - (x - B)^l - B^l = 0 \tag{5}$$

From (5), we get $x = (A + B)$. So the boundary curve always goes through the fixed point $(A + B, 0)$. Then the intersection point of the boundary curve and the line $y = x/\sqrt{3}$ will be found. As $y = x/\sqrt{3}$, (4) can be rewritten as

$$\left(\frac{4}{3}x^2 - 2Ax + A^2\right)^{l/2} + A^l - \left(\frac{4}{3}x^2 - 2Bx + B^2\right)^{l/2} - B^l = 0 \tag{6}$$
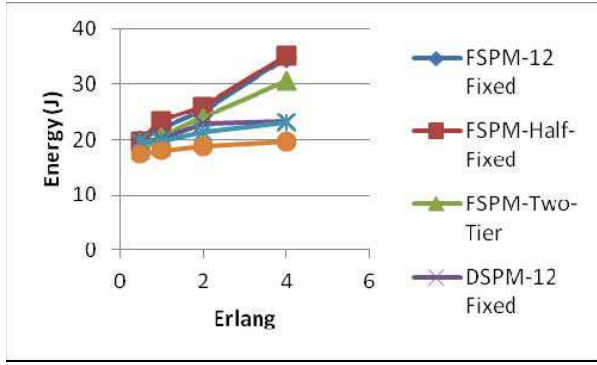
Figure 5: Consumed energy per mobile station for low traffic class.
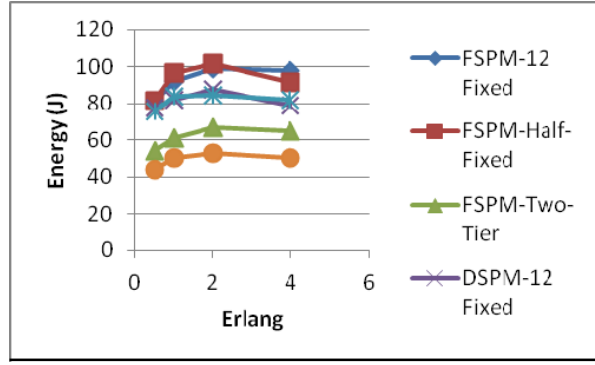
Figure 6: Consumed energy per mobile station for high traffic class.
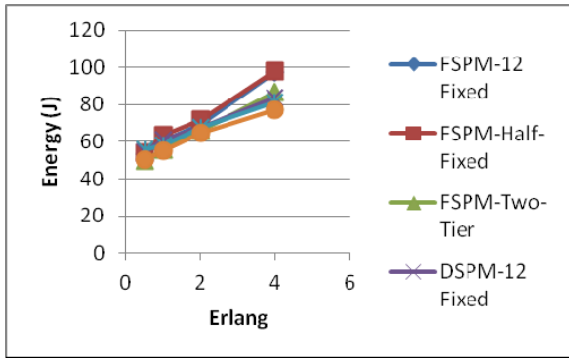
Figure 7: Consumed energy per link station for low traffic class.
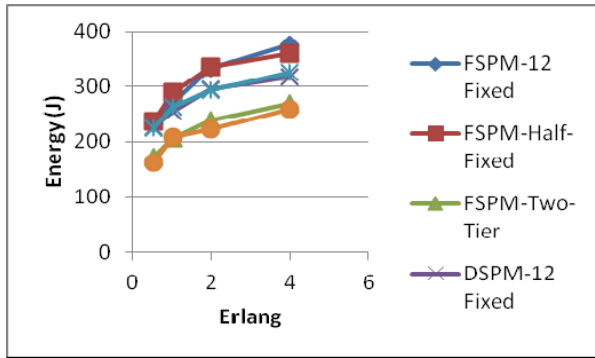
Figure 8: Consumed energy per link station for high traffic class.

Use Taylor Series to generate the power series for function.

$$f(x) = \sum_{n=0}^{\infty} \frac{f^{(n)}(0)}{n!} x^n \tag{7}$$

$$x \cong \frac{2(A^l - B^l) + \frac{1}{5.89l - 4.29} l \left(l - \frac{2}{3}\right) \left(A^{l-2} - B^{l-2}\right)}{l \left(A^{l-1} - B^{l-1}\right)} \tag{8}$$

Let $m = x$, then the intersection point is $(m, m/\sqrt{3})$. Assume that the boundary curve is a parabola, and then the curve can be approximated as:

$$x = \frac{3(m - 0.67)}{m^2} y^2 + 0.67 \tag{9}$$

In order to prove the above estimation is correct, the influenced area and their boundarie of $l = 3$ are plotted and shown in Figure 4.

4. SIMULATION RESULTS AND SETTINGS

Table 1 shows simulation setting. Figure 5 and Figure 6 show the energy consumed per mobile station for both low traffic case and high traffic case. And the consumed energy per link is shown in Figure 7 and Figure 8. By comparing the cases using FSPM and DSPM, it can be seen that the DSPM costs less than FSPM. From Figure 5, Figure 6, Figure 7 and Figure 8, it can be seen that the 3TA consumes the least energy. The simulation result supports the proposed structure, 3TA.

5. CONCLUSION

This paper investigated a new structure, 3TA, in relay based TDD-CDMA cellular network. The aim of 3TA is to save energy consumed by both the mobile stations and the links. The simulation has shown that 3TA can save the energy for the whole system. Future work can be done to extend

this work in term of resource radio management for different QoS service categories. The best dimension of the right height for multi-tier architecture should be identified.

REFERENCES

1. Kaye, A., D. George, and M. Eric, "Analysis and compensation of bandpass nonlinearities for communications," *IEEE Transactions on Communications*, Vol. 20, 965–972, Oct. 1972.
2. C802.16x-07, I., "Integrated relay architecture for IEEE 802.16m systems," Nov. 2007.
3. Akyildiz, I. F. and W. Xudong, "A survey on wireless mesh networks," *IEEE Communications Magazine*, Vol. 43, 23–30, 2005.
4. Jiang, L. and S. Y. Tan, "A simple analytical path loss model for urban cellular communication systems," *Journal of Electromagnetic Waves and Applications*, Vol. 18, No. 8, 1017–1032, 2004.
5. Pabst, R., B. H. Walke, D. C. Schultz, P. Herhold, H. Yanikomeroglu, S. Mukherjee, H. Viswanathan, M. Lott, W. Zirwas, M. Dohler, H. Aghvami, D. D. Falconer, and G. P. Fettweis, "Relay-based deployment concepts for wireless and mobile broadband radio," *IEEE Communications Magazine*, Vol. 42, 80–89, 2004.
6. Li, X. J., B. C. Seet, and P. H. J. Chong, "Multihop cellular networks: Technology and economics," *Computer Networks*, Vol. 52, 1825–1837, Jun. 2008.
7. Song, J. Y., H. Lee, and D. H. Cho, "Power consumption reduction by multi-hop transmission in cellular networks," *IEEE Vehicular Technology Conference*, Vol. 5, 3120–3124, Los Angeles, CA, Sep. 2004.
8. Salov, A. D., K. K. Lee, and H. S. Park, "Energy-efficient topology control algorithm based on location awareness for wireless sensor networks," *International Conference on Control, Automation and Systems*, 2606–2611, 2007.

Routing Performance of Mobile Ad Hoc Network in Urban Street-grid Environment by Using Peer-to-Peer Propagation Model

Pengty Ngor and Peter Han Joo Chong

School of Electrical and Electronic Engineering, Nanyang Technological University, Singapore

Abstract— In this paper, effect of non-line of sight propagation in an urban-street environment on routing performance in mobile ad hoc network is investigated. We implement a reliable propagation model in network simulator (NS2) named peer to peer propagation model which has been shown to be suitable for our street-grid environment by taking into account non-line of sight paths. Our simulation result shows that multiple reflected signals in an urban street grid environment have significant impacts on routing performance.

1. INTRODUCTION

Mobile ad hoc network (MANET) is a self-organizing and self-creating network which requires no fixed infrastructure [1]. Nodes are able to directly communicate with each other if they are in communication range. Multi-hops transmission is required to deliver packet from sources to destinations. Hence, routing protocol and realistic propagation model are imperative and challenging in MANET. Many network simulation tools [2–4] have been used to analyze the routing performance of MANET by assuming that the link between two nodes is in line-of-sight (LOS). However, this LOS assumption is not valid especially in an urban environment where the received signals in non-line-of-sight (NLOS) region are dominated by reflections along the streets-referred to as NLOS propagation [5–7]. However, most of the MANET papers reported in the literature review ignore such propagation paths [8–10]. Also it is assumed that there will be no communication link among nodes if direct LOS path is blocked [11, 12]. In this paper, we integrate into NS2 a reliable propagation model which takes into account reflected signals along street in an urban street environment [13]. To investigate the effects of NLOS propagation on MANET routing performance, AODV routing metrics including packet delivery ratio, normalized routing load, and average end to end delay are examined. The remainder of article is organized as following. Section 2 elaborates on related work. Section 3 describes our implemented peer to peer propagation model. Section 4 depicts simulation setting and result. Section 5 concludes the paper and suggests future works.

2. RELATED WORKS

Effect of non-line of sight propagation on routing performance has been studied and shown to have a significant impact on routing performance in MANET [14, 15]. [14] gave insights on the effect of different propagation models for MANET in indoor and outdoor environments by using three available propagation models in NS2, namely free space, two ray ground and shadowing propagation models. However, the three propagation models did not address the effects of reflected, refracted and diffracted signals from obstacles in free space and two ray ground. Furthermore, the parameter of shadowing propagation model was chosen arbitrarily. [15] proposed an algorithm to take into account the non LOS propagation paths and shadowing effect by modifying the available propagation model in NS2 namely modified free space, modified two ray ground and modified shadowing propagation models. In modified free space and two ray ground models, there would be no received power in NLOS region as the existence of reflected, diffracted and scattered signals are neglected. In the modified shadowing propagation model, the power received was calculated by choosing arbitrarily the value of path loss exponent β and the standard deviation α_{dB} of a Gaussian random variable.

3. PEER-TO-PEER PROPAGATION MODEL FOR MANET

In this paper, a peer-to-peer propagation model [13] is propose to be integrated in NS2 for MANET simulation in a street grid environment. The theoretical path loss formula has been shown to have good agreement with experimental data collected in Tokyo and New York Cities. The following is the list of assumption for our proposed propagation model.

- Width of the streets is assumed to be known.

● Reflection loss is assumed known and constant at all building surfaces. In other words, propagation path with the minimum number of reflection is considered as the dominant signal path.

For the urban street-grid environment as shown in Figure 1, the minimum number of reflections N between two nodes, e.g., A and B for signal path undergoes reflections along the main street W_m and side street W_s can be derived [13]:

$$N_{\min} = \left\lfloor 2\sqrt{\frac{r_m r_s}{W_m W_s}} \right\rfloor$$

The total path loss for reflection is given by:

$$\left[\frac{P_r}{P_t}\right]_{\mathrm{dB}} = 10\log\left(\frac{\lambda}{4\pi(r_m + r_s)}\right)^2 + L_w N_{\min} + X'_{\mathrm{dB}} \tag{1}$$

where $L_w = 20\log R_0$ in dB. R_0 is loss per reflection and λ is the wavelength of the operating signal, X'_{dB} is Gaussian random variable with zero mean and standard deviation α'_{dB}.

Likewise, the minimum number of reflections N between two nodes, e.g., A and C for signal path undergoes reflections along the main street W_m and parallel street W_p can be derived as [17]:

$$N_{\min} = \left\lfloor \frac{r_m}{W_m}\sqrt{\frac{r_s W_m W_p}{W_s(r_m W_p + r_p W_m)}} + \frac{r_s}{W_s}\sqrt{\frac{W_s(r_m W_p + r_p W_m)}{r_s W_m W_p}} + \frac{r_p}{W_p}\sqrt{\frac{r_s W_m W_p}{W_s(r_m W_p + r_p W_m)}} \right\rfloor \tag{2}$$

The total power loss is given by:

$$\left[\frac{P_r}{P_t}\right]_{\mathrm{dB}} = 10\log\left(\frac{\lambda}{4\pi(r_m + r_s + r_p)}\right)^2 + L_w N_{\min} + X'_{\mathrm{dB}} \tag{3}$$

If two nodes are in line of sight with one another and their distance is less than cross-over distance, e.g., node A and B, (1) is used; if their distance is more than cross-over distance, e.g., node A and C, (2) is deployed. If they are in non-line of sight, e.g., node A and D, received power is determined by (6).

4. SIMULATION RESULTS AND SETTINGS

AODV is used as a routing protocol and Manhattan mobility model is employed to govern the node movement with 4 vertical and 4 horizontal streets. We compare our proposed peer to peer propagation model with the modified shadowing model propagation models proposed in [15]. Table 1 shows the parameters for simulation. From Figure 2 to Figure 4, the routing performance of AODV is higher when peer-to-peer to propagation model is used. In Figure 2, the packet delivery ratio
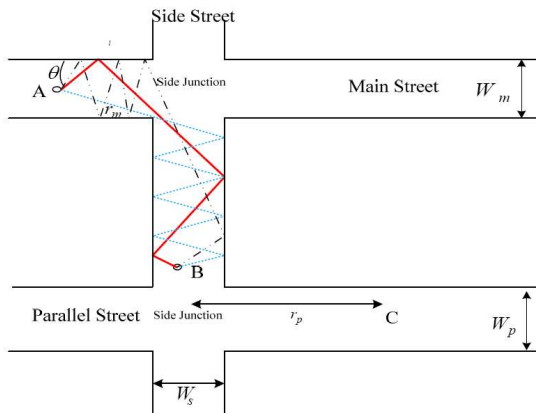
Figure 1: Illustration of side and parallel street scenario showing typical reflection paths.
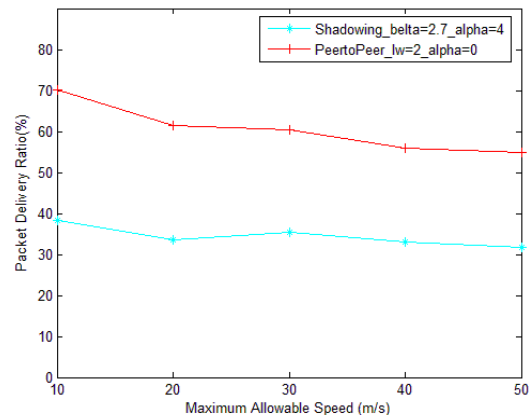
Figure 2: Comparison between peer-to-peer and shadowing models of packet delivery ratio.

Table 1: Simulation settings.

MAC Protocol	IEEE802.11DCF
Traffic model	4 CBR connections
Packet sending rate	1 packets/second
Power received threshold	3.65262×10^{10} W
Number of nodes	100
Simulation area	$1500\,\text{m} \times 1500\,\text{m}$
Node maximum allowable speed	10 m/s to 50 m/s (in the step of 10 m)
G_t, G_r, L, d_0	1
λ	$0.328\,\text{m}$
α_{dB}	$4\,\text{dB}$
β	2.7
L_w	2 dB (loss per reflection)
W_s	10 meters
W_m	35 meters
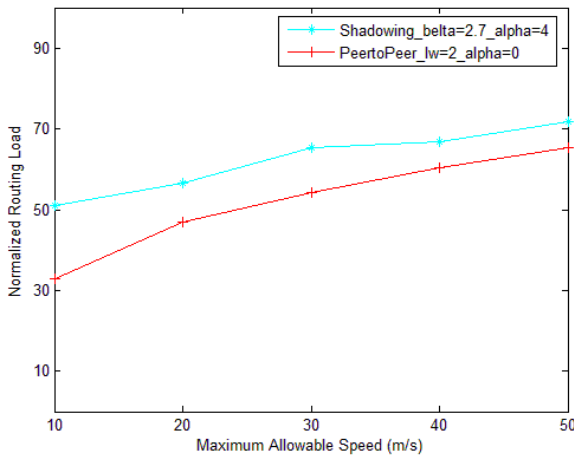
Figure 3: Comparison between peer-to-peer and shadowing models of normalized routing load.
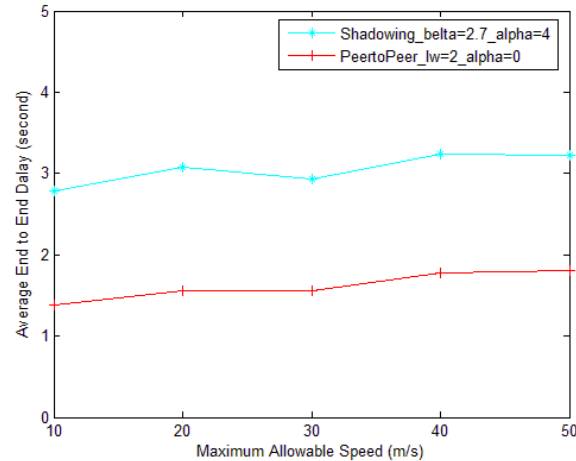
Figure 4: Comparison between peer-to-peer and shadowing models of average end to end delay.

increases from around 39% to 70% when modified shadowing and peer-to-peer propagation model are used respectively. It is because the received the power of the peer to peer propagation model is higher that of modified shadowing when distance between receiver and transmitter is more than cross in distance. Thus, it leads to more connectivity. In Figure 3, it is observed the normalized routing packet of peer to peer propagation model is less than that of modified shadowing model. This is as expected because the data received of peer-to-peer propagation model is higher than that of modified shadowing model. In Figure 4, it can be seen that the average end to end delay of the peer-to-peer propagation model is slightly less than that of modified shadowing propagation model. It is due the fact that the connectivity of peer-to-peer propagation model is more stable than that of shadowing model.

5. CONCLUSION

In this paper, we implemented a more realistic propagation model in an urban street environment. From simulation result, the effect of NLOS propagation model has a significant impact on routing performance in MANET. It can be observed that the received signal strength cannot be arbitrarily chosen or underestimate. Based on our implemented wireless propagation model, the authors are currently researching a new routing protocol in such urban street environment.

REFERENCES

1. Corson, S. and J. Macker, "Mobile ad hoc network (MANET): Routing protocol performance issues and and evaluation considerations," 2501, RFC, 1999.
2. Network Simulator (ns-2), Available: http://www.isi.edu/nsnam/ns/.
3. OPNET Simulator, Available: http://www.opnet.com/.
4. QualNet Network Simulator, Available: http://www.scalable-networks.com/.
5. Jiang, L. and S. Y. Tan, "Geometrical-based statistical channel model for outdoor and indoor propagation environments," *IEEE Trans. Vehicular Technology*, Vol. 56, No. 6, 3587–3593, Nov. 2007.
6. Chen, S. W., S. Y. Tan, and C. K. Seow, "Peer-to-peer localization in urban and indoor environments," *Progress In Electromagnetics Research B*, Vol. 33, 339–358, 2011.
7. Tan, S. Y. and H. S. Tan, "A theory for propagation path-loss characteristic in a city-street grid," *IEEE Transactions on Electromagnetic Compatibility*, Vol. 37, No. 3, 333–342, 1995.
8. Perkins, C. E. and E. M. Royer, "Ad-hoc on-demand distance vector routing," *Second IEEE Workshop on Mobile Computing Systems and Applications. Proceedings, WMCSA'99*, 90–100, 1999.
9. Karp, B. and H. T. Kung, *GPSR: Greedy Perimeter Stateless Routing for Wireless Networks*, Boston, MA, USA, 2000.
10. Johnson, D. and D. Maltz, "Dynamic source routing in Ad hoc wireless networks," *Mobile Computing*, 153–181, Springer, US, 1996.
11. Lochert, C., M. Mauve, H. Fubler, and H. Hartenstein, "Geographic routing in city scenarios," *Mobicom Poster Abstract*, 2004.
12. Jerbi, M., S. M. Senouci, R. Meraihi, and Y. Ghamri-Doudane, *An Improved Vehicular ad Hoc Routing Protocol for City Environments*, Glasgow, Scotland, 2007.
13. Sun, Q., S. Y. Tan, and K. C. Teh, "Analytical formulae for path loss prediction in urban street grid microcellular environments," *IEEE Transactions on Vehicular Technology*, Vol. 54, No. 4, 1251–1258, 2005.
14. Eltahir, I. K., "The impact of different radio propagation models for mobile ad hoc networks (MANET) in urban area environment," *The 2nd International Conference on Wireless Broadband and Ultra Wideband Communications, AusWireless 2007*, 30–30, 2007.
15. Ngor, P., S. Y. Tan, and P. H. J. Chong, "Effect of non-line of sight propagation on routing performance in mobile ad hoc network," *8th IEEE Asia Pacific Wireless Communication Symposium*, Singapore, 2011.

Observations of the Effect of Temperature upon Stability of Resource-constrained, Embedded Clocks

M. A. Collett and T. H. Loh

National Physical Laboratory, Teddington, Middlesex, UK

Abstract— Wireless Sensor Networks (WSNs) are being increasingly sought after for critical applications such as security and health care. This is leading to an increased need to understand and quantify the reliability and stability of WSN-based systems when deployed in real environments. Timing synchronization is a vital capability for many WSN functions such as robust communications and data combining. This paper presents measured results of the frequency output of a WSN node clock. The clock incorporates several layers of software and hardware components, which need to function robustly together. We show how counting errors propagate through these layers to affect the resulting output counter frequency. We also observe that there is a strong relationship between the standard deviation in clock frequency and temperature variation; with the standard deviation varying between 2×10^{-5} Hz and 10×10^{-5} Hz (the standard deviation in the mean of a 10 minute rolling window of frequency measurements) as the ambient temperature crosses a threshold of approximately 23.5 degrees Celsius. Quantification of the stability of a clock output is an important factor in any subsequent synchronization, affecting decisions such as the employment of hibernation for energy saving, sensor sample rates and time division multiple access communications. As wireless sensing systems become increasingly complex, both in terms of capability and requirements, it will be increasingly important to optimize every element. When synchronizing clocks it is important to make judgments about the optimum intervals over which to carry out synchronization and to be able to estimate the accuracy achieved. The observations presented here have highlighted that temperature is an important factor in determining both of these.

1. INTRODUCTION

Wireless Sensor Networks (WSNs) are being increasingly sought after as measurement solutions in a wide range of fields, including critical healthcare, civil structural and military applications [1]. The approach by the National Physical Laboratory (NPL) has been to identify the key measurement issues and investigate each in detail. These include sensor and data validation [2], data fusion [3] and localization [4]. Synchronization constitutes one of the key critical issues when employing WSNs for measurement. Multiple sensors must be synchronized to sufficient precision and accuracy to allow comparison of data gathered across the network. Additionally, many WSN capabilities rely on tight synchronization; time division multiplexing to share communications bandwidth [5], reliable hibernation for power saving [6] and time delay of arrival measurements (of, for example, acoustic signals) for node localisation or target tracking [7]. The research community has carried out much valuable work on developing methods for disseminating time signals throughout a WSN, such as in [8] and [9], and building such capability into a routing protocol as described by [10] and [11]. The trade-offs between synchronization accuracy and system resource burden (processing and communications) have also been well treated [12]. There is a lack, however, of robust characterization of the individual node clocks operating under real-world conditions. This paper presents measurements of the stability of the frequency output of a MICAz clock system. Made up of a combination of hardware and software, a number of instabilities and errors are observed (these are summarized here, and described in full detail in [13]). The key observation of this paper is the temperature dependence of the variation of clock frequency. It is shown that there is a strong correlation between the standard deviation of the clock frequency, and the ambient temperature; with the standard deviation varying between 2×10^{-5} Hz and 10×10^{-5} Hz as the ambient temperature crosses a threshold of approximately 23.5 degrees Celsius.

2. MEASUREMENT PROCESS

The Crossbow MICAz [14] node platform was chosen as the system to investigate, and is typical of the type of system available to potential users of WSNs. This platform can also be readily configured to only perform the operations of interest (with minimal background operations which may affect results). The complete details of the hardware and software specifically relating to the node clock are contained in [13] and [14] and so will not be covered here. However, the key points

are as follows: A quartz oscillator governs the node clock with a nominal resonant frequency of 32.768 kHz. This modulates a voltage, which activates a trigger on every rising edge. For every 32 triggers the on-board processor sends a signal to a higher-level node component. Further layers of counting give rise to an accessible output of nominal frequency 1 Hz. The regularity and stability of this switching was measured using a universal Time Interval Counter (TIC) [15] stabilized by a 10 MHz reference source derived from an active Hydrogen MASER related to UTC [16]. This system was chosen due to its high stability and accuracy, providing a standard uncertainty of below 1×10^{-9} Hz, more than sufficient for this measurement. The surface temperature of the nodes main circuit board was measured using standard thermocouple probes.

3. MEASUREMENT RESULTS

The instantaneous frequency of the clock output of the MICAz system was measured once a second for a period of 13 days. As can be seen in Figure 1, the values are highly discretized into bands. This can be explained by understanding that the clock output is based upon a number of nested counting processes (as described in [13]). If an oscillation from the crystal were to be missed, this would give an instantaneous frequency offset of 3×10^{-5} Hz (if one oscillation were missed in a single second of counting). Similarly, if an oscillation was double-counted, then the frequency over a second would appear to increase by 3×10^{-5} Hz. If these effects were to occur repeatedly in a given second, the frequency of the clock would be subjected to multiples of this offset. These observations and their explanation are considered further, through simulation in [13]. It should also be noted that the central frequency of this clock system is 0.999978 Hz, as opposed to 1 Hz. This is due to manufacturing imperfections in the size of the quartz oscillator, meaning it is not exactly at the intended 32.768 kHz. An important new observation is that the size of the spread is not constant. As shown in the upper three plots of Figure 2 it can be seen that the standard deviation of frequency values measured over a moving 10 minute rolling window is highly variable taking values between 2×10^{-5} Hz and 10×10^{-5} Hz. It can be seen from the lower plot that there is a strong relationship between this standard deviation, and the ambient temperature (shown on the lower plot of Figure 2). This is not a direct linear relationship, however (the correlation between the standard deviation and temperature was calculated to be 0.63) and there appears to be some thresholding effect. The standard deviation varies between 2×10^{-5} Hz and 10×10^{-5} Hz as the ambient temperature crosses a threshold of approximately 23.5 degrees Celsius. Deviations from this may result from some difference between the measured probe temperature, and the temperature of the components in question, or that some other intermittent process is also occurring. It should
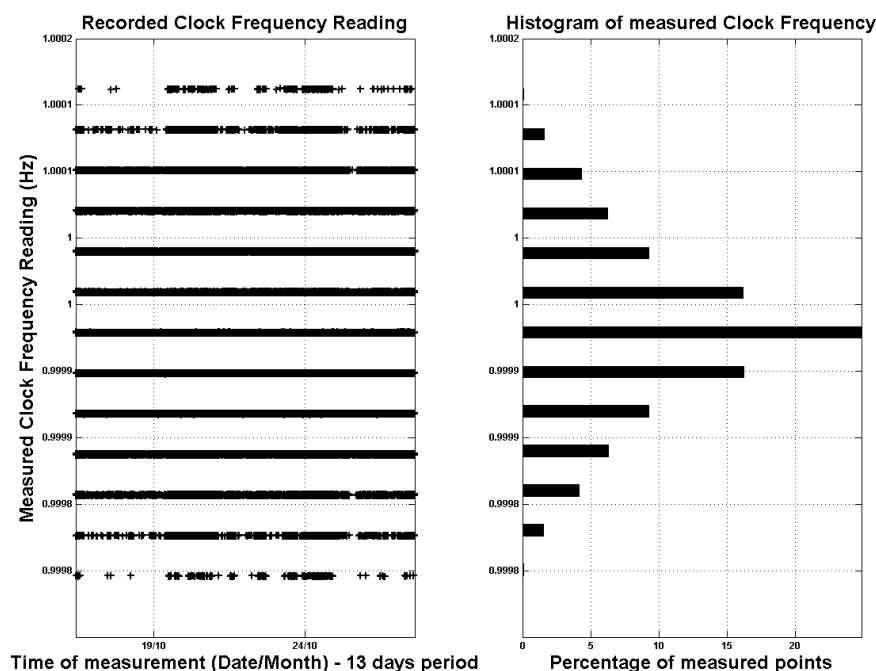
Figure 1: Embedded clock frequency measurement distribution.
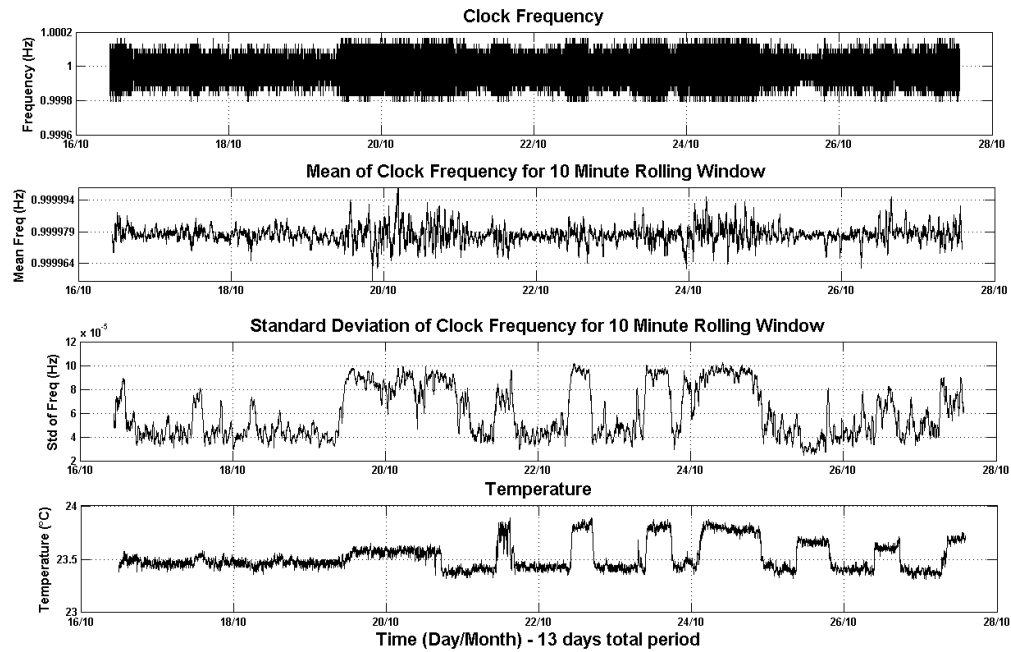
Figure 2: Plots (from top to bottom) of instantaneous frequency, mean frequency over rolling 10 minute window, standard deviation in this mean and temperature. Readings were taken over a 13 day period.

also be noted that this effect was observed over a relatively small temperature variation range (where the temperature in the laboratory only varied between 23 and 24 degrees). This effect may become larger for larger temperature variations. One likely explanation for this behaviour is as follows. The voltage, which is modulated by the quartz oscillator, also has a component of thermal Johnson noise. At a specific temperature, this noise becomes sufficiently large to impact upon the probability of the occurrence of miscounts. This then leads to an increase in the variation of output frequency. Variations in frequency stability with temperature has implications as to the long-term accuracy of remote, embedded clocks. It also has implications as to the necessary regularity of resyncrhonisation required to achieve a given system synchronisation.

4. CONCLUSIONS

This paper has presented the observation of the variation of standard deviation of wireless sensor node embedded clock output with ambient temperature variation. We observe that there is a strong relationship between the standard deviation in clock frequency and temperature variation; with the standard deviation varying between 2×10^{-5} Hz and 10×10^{-5} Hz as the ambient temperature crosses a threshold of approximately 23.5 degrees. Although a relatively small frequency change, this effect could potentially contribute to node clocks becoming unsynchronized over longer periods. It should also be noted that this relationship was observed over relatively small temperature variations of less than 1 degree, and that in outdoor, real world deployments, the effect may be more significant.

There are a number of factors which affect the frequency of a resource constrained, embedded clock system. These include manufacturing tolerances of the governing quartz oscillator and ambient temperature. The stability of such clocks is also affected by many factors. As wireless sensing systems become increasingly complex, both in terms of capability and requirements, it will be increasingly important to optimize every element. When synchronizing clocks it is important to make judgments about the optimum intervals over which to carry out synchronization and to be able to estimate the accuracy achieved. The observations presented here have highlighted that temperature is an important factor in determining both of these. This observation may be of value to developers of high-precision synchronization techniques, where the measurement of the temperature will provide additional information as to the sixe of the standard deviation of the clock frequency. This could be valuable to improve the efficiency of synchronization algorithms, which could potentially reduce the rate at which nodes exchange clock values during cold periods, and increase this during warmer periods. Such a capability would also have to be combined with a model of the quartz oscillator frequency variation with temperature.

REFERENCES

1. Akyildiz, I. F., W. Su, Y. Sankarasubramaniam, and E. Cayirci, "Wireless sensor networks: A survey," *Computer Networks*, March 2002.
2. Collett, M. A., M. G. Cox, T. J. Esward, P. M. Harris, and J. A. Sousa, "Aggregating measurement data influenced by common effects," *Metrologia*, Vol. 44, No. 5, 308–318, 2007.
3. Collett, M. A., M. J. Salter, and D. B. Adamson, "Data fusion for wireless sensor networks: An assisted living case-study," *IET Assisted Living*, March 2009.
4. Collett, M. A., M. G. Cox, M. Duta, T. J. Esward, P. M. Harris, and M. P. Henry, "The application of self-validation to wireless sensor networks," *Meas. Sci. Technol.*, Vol. 19, No. 12, 125201, 2008.
5. Lu, C. Y., B. M. Blum, T. F. Abdelzaher, J. A. Stankovic, and T. He, "RAP: A real-time communication architecture for large-scale wireless sensor networks," Department of Computer Science, University of Virginia, Charlottesville, 2002.
6. Pantazis, N. A., D. J. Vergados, D. D. Vergados, and C. Douligeris, "Energy eficiency in wireless sensor networks using sleep mode TDMA scheduling," *Ad Hoc Netw.*, 2009, ISSN 1570-8705.
7. Sallai, J., G. Balogh, M. Maroti, and A. Ledeczi, "Acoustic ranging in resource constrained sensor networks," Technical Report, ISIS, Vanderbilt University, 2003.
8. Youngtae, J., "Energy effective time synchronization in wireless sensor network," *ICCSA*, 547–553, Aug. 26–29, 2007.
9. He, L. M. and G.-S. Kuo, "A novel time synchronization scheme in wireless sensor networks," *IEEE 63rd VTC*, Vol. 2, 568–572, 2006.
10. Fedor, S. and M. Collier, "Synchronization service integrated into routing layer in wireless sensor networks," *WCNC*, 2905–2910, 2008.
11. Ahn, S., J. Cho, and S. An, "Slotted beacon scheduling using zigbee cskip mechanism," *EN-SORCOMM*, 103–108, Aug. 2008.
12. Ye, Q., Y. C. Zhang, and L. Cheng, "A study on the optimal time synchronization accuracy in wireless sensor networks," *Journal of Computer Networks*, ISSN 1389-1286, 2005.
13. Collett, M. A., C. E. Matthews, T. J. Esward, P. M. Harris, P. Whibberley, "Measurement and simulation of resource-constrained, embedded clocks," *Meas. Sci. Technol.*, 2010.
14. Crossbow MICAz platform data sheet (viewed on 24/08/09), http://www.xbow.com/Products/Product pdf les/Wireless pdf/MICAZ Datasheet.pdf.
15. Stanford Research Systems SR620 Universal Counter Timer (viewed on 24/08/09), http://www.lambdaphoto.co.uk/products/sr620.
16. Szymaniec, K., W. Chalupczak, P. B. Whibberley, S. N. Lea, and D. Henderson, "Evaluation of the primary frequency standard NPL-CsF1," *Metrologia*, Vol. 42, 4957, 2005.

On a Useful Tool to Localize Jacks in Wiring Network

M. Franchet[1], **N. Ravot**[1], **and O. Picon**[2]

[1]CEA, LIST, Embedded Systems Reliability Laboratory
Point Courrier 94, Gif-sur-Yvette, F-91191 France
[2]Université Paris-Est; ESYCOM, Marne-La-Vallée, France

Abstract— With the omnipresence of electronics, the reliability of wiring networks becomes crucial. As they tend to be more and more complex, knowing their topology is of greatful help for monitoring and maintaining them. In order to localize jacks as well as incipient damage, efficient diagnostic tools need to be developed. This article proposes to combine Time Domain Reflectometry (TDR) with time-frequency tools to do so.

1. INTRODUCTION

As automobile, aeronautic and robotic systems more and more rely on electronics, the reliability and a good knowledge of their wiring networks are crucial. To efficiently monitor and maintain these networks, their topology have to be known. Most of the time a wiring network is not made of a single line but of several cables linked to each others with jacks. So knowing where these jacks are, is an important information for going back to the topology. Then once this information is known, the damaged portions of the network can be localized relatively to the jacks, which will facilitate and accelerate the mending. Besides, in a wiring network it can be the jacks themselves that are damaged. So it is important to be able to monitor their condition. Knowing where they are is the first step to study their ageing.

One way to localize jacks in a network is to use reflectometry methods. It consists in injecting a signal into the wiring network and analysing the reflected signals at the injection point. One method is called Time Domain Reflectometry (TDR) (cf. [1–3]). Here a step or a pulse is injected. This method works quite well for detecting hard faults such as open or short circuits. However such as for soft faults (e.g., chafes), the reflections on jacks are of low amplitude (they are not perfectly matched to the line) and TDR may be not efficient enough to detect them. For doing so, some further signal processing tools can be used. In [4, 5] and [6], a method, called Joint Time Frequency Domain Reflectometry (JTFDR), based on the Wigner Ville Transform (WVT) and a normalized Time Frequency Function (TFC) has been proposed. It has shown promising results concerning soft faults (cf. [7]).

This article shows that thanks to the WVT and the TFC, it is possible to localize a jack in a line. The WVT and the TFC will be defined in the first part. Then it will applied on experimental data. The second part exposes the measurement setups. The first line under test is made of two identical coaxial wires linked with a jack. The results are presented in part 4. The second type of line to be tested is made of two identical aeronautic wires (embedded in a set of several other wires) linked with a jack.

2. DEFINITION OF THE TFC

Detecting weak signals, such as pulses reflected on jacks or soft faults, needs a good time and frequency resolution. That's why time frequency tools can be of useful help in reflectometry. Here the chosen method combines the Wigner Ville transform and a normalized Time Frequency Correlation (TFC) between the time frequency distribution of the injected signal $(s(t))$ and the reflected one $(r(t))$. Both the Wigner Ville Transform and the TFC are defined in the next subsections.

2.1. The Wigner Ville Transform

The Wigner Ville Transform (WVT) is a quadratic time frequency tool, often used in detection problems. Due to its quadratic nature, cross-terms arise when computing the WVT of a multi-component signal. As these cross-terms can mask real components or lead to false positives in the detection process, they have to be reduced. For doing so the pseudo Wigner Ville Transform (PWVT) has been used here (cf. [9]). This is a windowed version of the WVT. The WVT and the PWVT of a signal $r(t)$ are defined in Equations (1) and (2).

$$W_r(t,\omega) = \frac{1}{2\pi} \int_{-\infty}^{+\infty} r^* \left(t - \frac{\tau}{2} \right) \cdot r \left(t + \frac{\tau}{2} \right) \cdot \mathrm{e}^{-\mathrm{j}\tau\omega} d\tau \tag{1}$$

Figure 1: Soft Fault on a coaxial line.

where $r^*(t)$ is the conjugate of r and ω the pulsation $(\mathrm{rad} \cdot \mathrm{s}^{-1})$.[1]

$$PW_r(t, \omega) = \int_{-\infty}^{+\infty} w\left(\frac{\tau}{2}\right) \cdot w^*\left(-\frac{\tau}{2}\right) \cdot r^*\left(t - \frac{\tau}{2}\right) \cdot r\left(t + \frac{\tau}{2}\right) \mathrm{e}^{-j\tau\omega} d\tau \tag{2}$$

where $w(t)$ is the chosen window.

In the following a gaussian window has been used. According to [8] the best choice is to use a window of the same size as the ones to be detected.

2.2. Definition of the TFC

The WVT has a good time resolution but it can be not sufficient enough for detecting soft faults or localizing jacks. For this reason, the PWVT is combined with a normalized Time Frequency Cross-correlation function (TFC). The TFC between the time frequency distribution of the injected signal $s(t)$ and the reflected one ($r(t)$) is defined in Equation (3). Here the time frequency distribution of $s(t)$ and $r(t)$ are computed with the PWVT. They are noted $PW_s(t, \omega)$ and $PW_r(t, \omega)$.

$$C_{sr}(t) = \frac{2\pi}{E_r(t) \cdot E_s} \int_{t'=t-T_s}^{t'=t+T_s} \int_{-\infty}^{+\infty} PW_r(t', \omega) \cdot PW_s(t' - t, \omega) d\omega dt' \tag{3}$$

with:

$$E_r(t) = \int_{t'=t-T_s}^{t'=t+T_s} \int_{-\infty}^{+\infty} PW_r(t', \omega) d\omega dt' \tag{4}$$

$$E_s = \int_{-\infty}^{+\infty} \int_{-\infty}^{+\infty} PW_s(t', \omega) d\omega dt' \tag{5}$$

3. EXPERIMENTAL CONDITIONS

3.1. The First Studied Case

3.1.1. The Cable under Test

Here the wiring network under test is made of two identical coaxial cables (RG58), whose characteristic impedance is $Z_c = 50\,\Omega$. The first wire of $1\,\mathrm{m}$ is linked to the other one (of $3.167\,\mathrm{m}$ long) with a jack of $3.3\,\mathrm{cm}$ long (ref: R 141 704). The characteristic impedance of the jack is $50\,\Omega$.

The plastic jacket and the metallic shield have been removed (such a defect can be classified as a soft fault) at $3.133\,\mathrm{m}$ from the beginning of the line (cf. Figure 1) and the far-end of the cable is left open circuited.

3.1.2. The Measurement System

A vector network analyzer (*Agilent E5071c 9 kHz–4.5 GHz*) has been used to inject a signal into the line and to measure the signal reflected at the injection point. The internal impedance of the analyzer is $Z_{in} = 50\,\Omega$. The measurement setup is displayed in Figure 2.

Two kinds of signals have been used: a gaussian pulse of $250\,\mathrm{ps}$ width at half maximum and a gaussian pulse of $500\,\mathrm{ps}$ width at half maximum. In each case the power of the injected signal is $0\,\mathrm{dBm}$.

---

[1] Actually the analytic signal of $s(t)$ is used to compute the WVT. However in order to simplify, both will be written in the same manner.
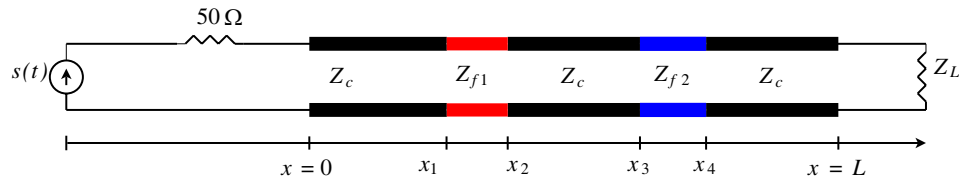
Figure 2: Measurement setup. The red part of the cable corresponds to the jack and the blue one to the defect. $Z_L = +\infty$.
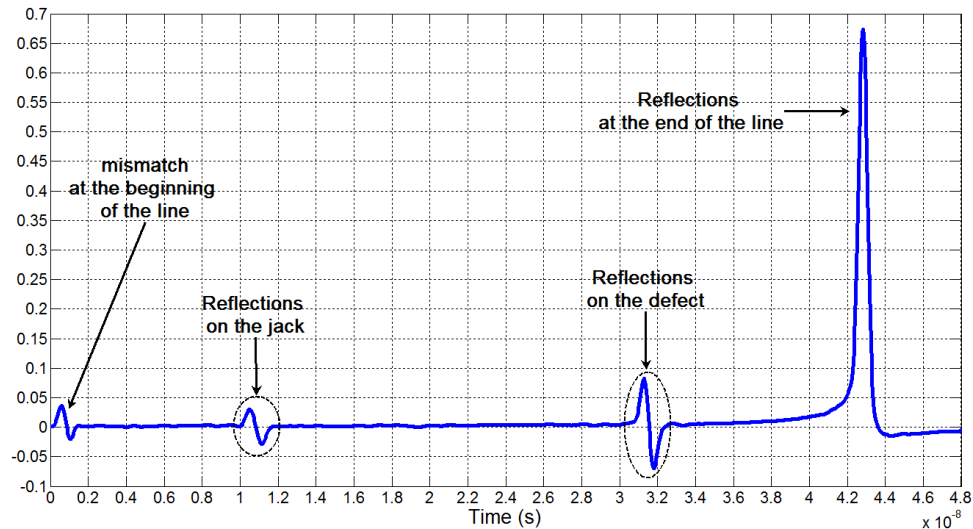
Figure 3: TDR result with a gaussian pulse of 500 ps width at half maximum.

Figures 4 and 3 present the TDR results in each case. Consider first the result for a pulse of 500 ps width. Four interesting areas can be observed. The first one ($t \in [0; 1.4]$ ns) corresponds to the reflections at the beginning of the line because of a slight mismatch between the measurement setup and the line. For $t \in [10; 12]$ ns the reflections at both ends of the jack, which is not perfectly matched with the line, can be seen. The pulses reflected at the beginning and at the end of the defect are visible for $t \in [30.7; 32.6]$ ns. The pulse localized at $t = 42.83$ ns corresponds to the reflection at the far end of the line. Let's now have a look at the result for a injected pulse of 250 ps width. Four areas can be observed too but results are better in term of localization. Indeed in this case we can see for $t \in [9.76; 11]$ ns not only the pulses reflected one time at both end of the jack but also the ones reflected two times at both end of the jack.

Comparing now the amplitudes of the reflections on the jack, the defect and the far end of the line, we can see that although pulses reflected on the jack and the defect can be seen on TDR results their amplitudes are much more smaller than the one reflected on the open circuit. Then the amplitudes of the waves reflected on the soft fault are about 2.7 higher than the one reflected at both end of the jack. So applying some signal processing tools on such data can be useful in order to make the detection of the connector and the soft fault easier.

3.2. The Second Studied Case

Here a line composed of two identical aeronautic wires. It is gathered with several other wires. The first wire of 1.5 m long is linked to the second one (of 5.5 m long) with a jack of 4 cm long.

The measurement setup is displayed in Figure 5. As can be seen, the line is not straight and has two bends. It is left open-circuited at its far-end. Measurements and injection have been done with the vector network analyzer (VNA) previously used. The signal injected into the line is a gaussian pulse of 7 ns width at half maximum, in order to reach a compromise between time resolution and attenuation.

Figure 6 presents the TDR result. Five reflected pulses can be noticed. The first one at $t_0 = 9.5$ ns is due to the mismatch between the line and the measurement setup. The reflected pulse located at $t_1 = 26.84$ ns corresponds to the reflection on the jack, whereas those at $t_2 = 39.1$ ns and
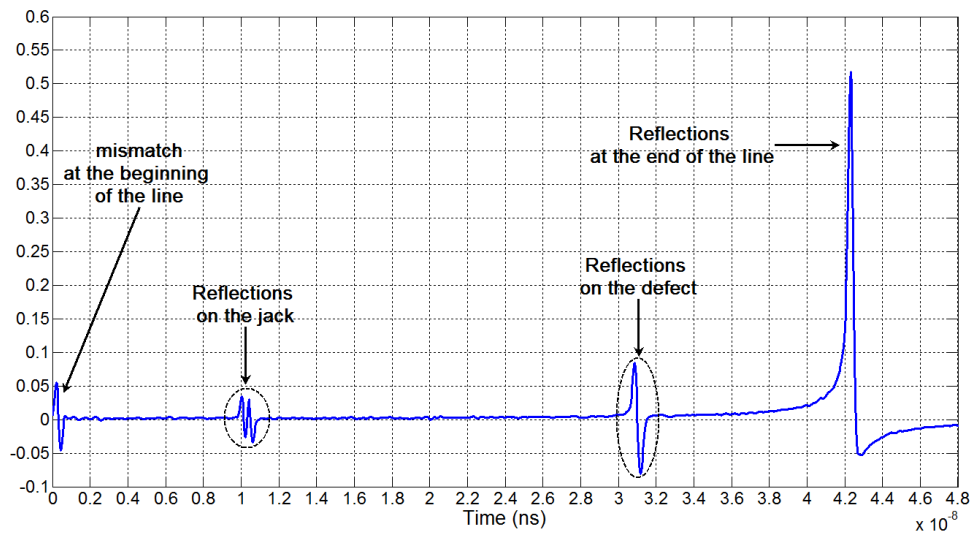
Figure 4: TDR result with a gaussian pulse of 250 ps width at half maximum.
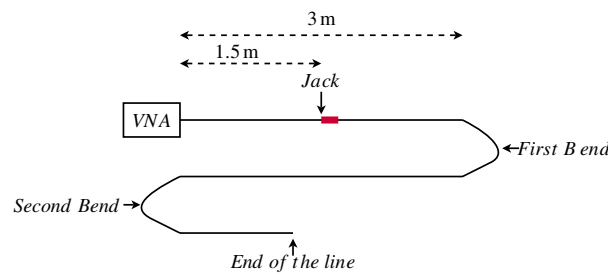
Figure 5: Measurement setup used in the second case.
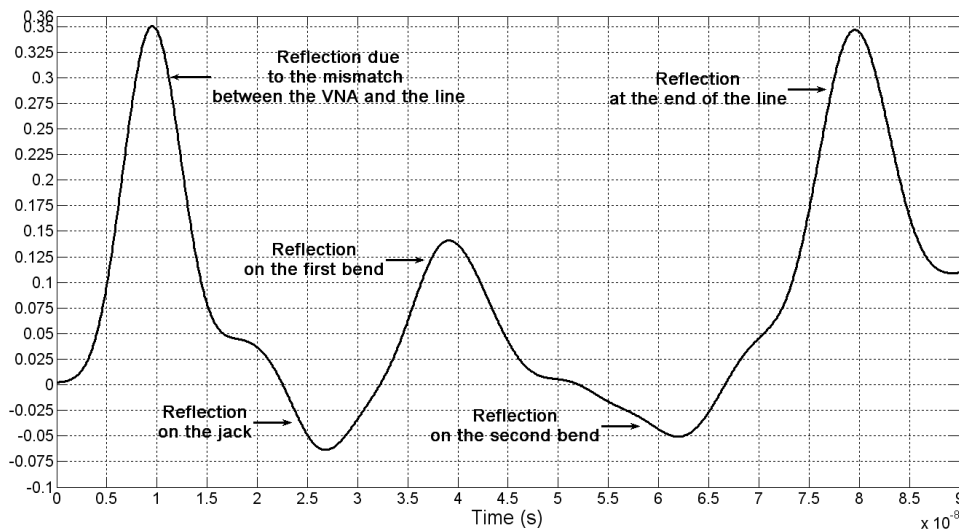
Figure 6: TDR result for the second case.

$t_3 = 62$ ns correspond to the reflections on the first and second bends. The pulse reflected at the end of the line is visible at $t = 79.56$ ns. One can notice that the pulses reflected on the jack and the bends (especially the one reflected on the second bend) are of lower amplitude than the one reflected at the end of the line.

4. RESULTS AFTER COMPUTING THE TFC PROCESS

4.1. Results Obtained in the First Case

Figures 7 and 8 show the results obtained for each kind of injected signal after applying the TFC on the TDR results. For both cases T_s and the width of the gaussian window are equal to the width of the injected signal. This is supposed to be the optimum parameters for computing the TFC. The positions of the peaks, which correspond to the reflections on the jack, the defect and the end of the line are presented in Table 1. Their positions in time have been converted to their positions in meter, considering that the propagating velocity in the line is: $v_p \approx = 2 \cdot 10^8 \mathrm{m} \cdot \mathrm{s}^{-1}$. The corresponding relative errors are displayed in Table 2. The beginning of the jack and the defect (respectively $1\,\mathrm{m}$ and $3.133\,\mathrm{m}$) have been taken as reference to compute these errors.

Considering first the results obtained with a pulse of $500\,\mathrm{ps}$ width, the first remark is that four peaks can be clearly observed. The first one at $t = 0\,\mathrm{ns}$ corresponds to the reflections at the beginning of the line. The other ones correspond to the reflections on the jack, the defect and the far end of the line. One can notice that whereas the reflections on the jack and the defect result in two reflected pulses on the TDR data, only one peak is present on The TFC results. One interesting effect of the TFC is that the amplitudes of the peaks corresponding to the reflections on the defect and the jack are of same range than the one due to the reflection on the open circuit whereas they
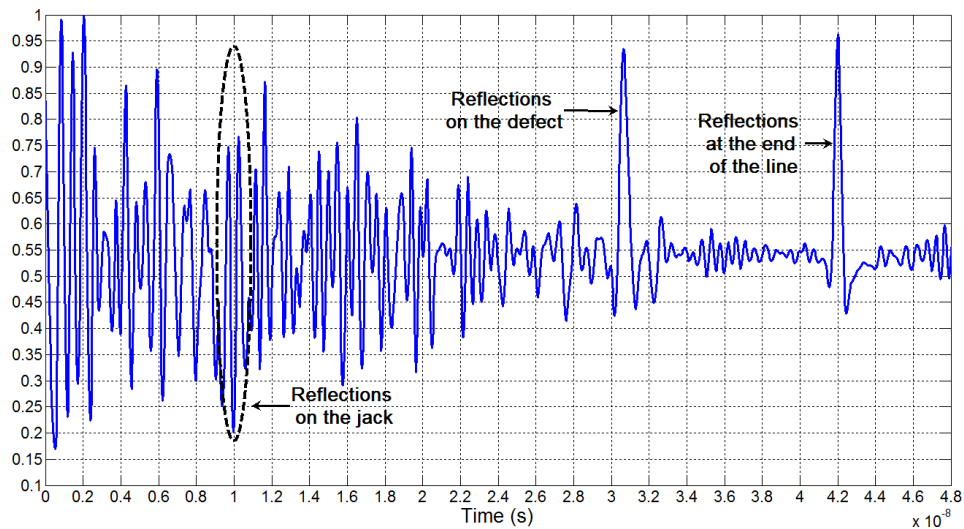
Figure 7: TFC result with a gaussian pulse of $250\,\mathrm{ps}$ width at half maximum.
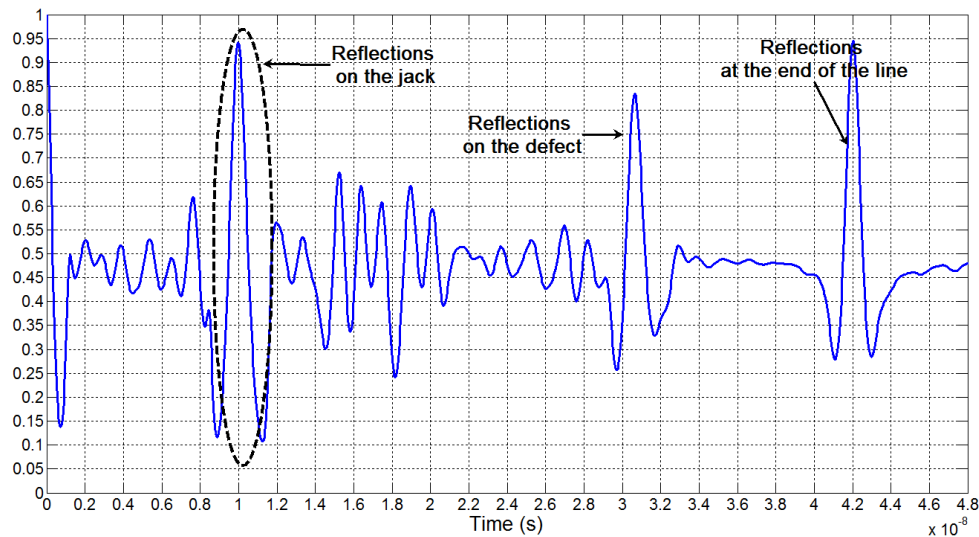
Figure 8: TFC result with a gaussian pulse of $500\,\mathrm{ps}$ width at half maximum.

Table 1: Peaks' positions after computing the TFC.

kind of reflection	position (m) for a pulse of 500 ps width	position (m) for a pulse of 250 ps width	position (m) for a pulse of 250 ps width and the same windowing as the one for a pulse of 500 ps width
on the jack	0.997	ambiguous	1.03
on the defect	3.07	3.06	3.07

Table 2: Relative errors after computing the TFC.

kind of reflection	relative error (%) for a pulse of 500 ps width	relative error (%) for a pulse of 250 ps width	relative error (%) for a pulse of 250 ps width and the same windowing as the one for a pulse of 500 ps width
on the jack	0.3	ambiguous	3
on the defect	2	2.3	2
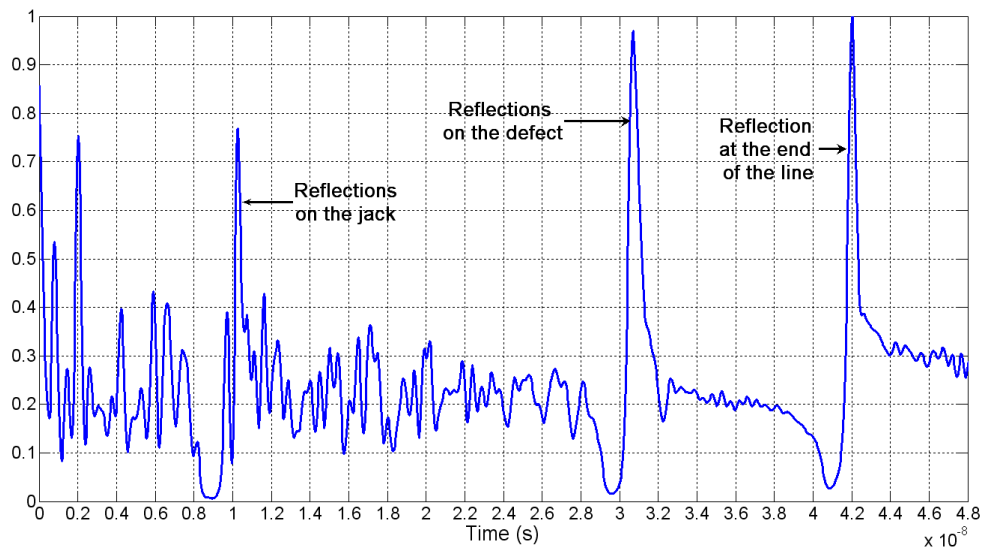
Figure 9: TFC result with a gaussian pulse of 250 ps width at half maximum, computed as if it was for a pulse of 500 ps width.

were far smaller on TDR results. This points out the usefulness of the TFC for the study and the detection of jacks and soft faults in wiring networks.

Let's now have a look at the results obtained with a pulse of 250 ps. One obvious remark is that much more peaks are visible. This makes the interpretation of them more difficult especially for the first portion of the line. These peaks are not artefacts and results from the little variations of the reflectograms. They can be due to the noise and/or the small imperfections of the coaxial cable. So using a narrower pulse improves the time resolution but also leads to more complicated results when applying the TFC, if the cable under test is not of good quality. One can try to find a compromise in using a injected signal signal of 250 ps and computing the TFC as if it was of 500 ps (T_s and the width of the gaussian window are chosen as if a pulse of 500 ps width had been used). The results are displayed in Figure 9. The number of peaks has significantly decreased and the peaks corresponding to the jack, the defect and the end of the line appear more clearly. However the relative error about the localization of the jack has increased. So the time resolution is decreased. In this case using this method makes the jack appear more clearly. But if some other small defects or jacks better matched to the line had been present the corresponding peaks of the TFC may have been reduced as the ones due to the intrinsic imperfections of the cable. So computing the TFC with the same parameters as the ones chosen for a pulse of 500 ps can't be systematically used.
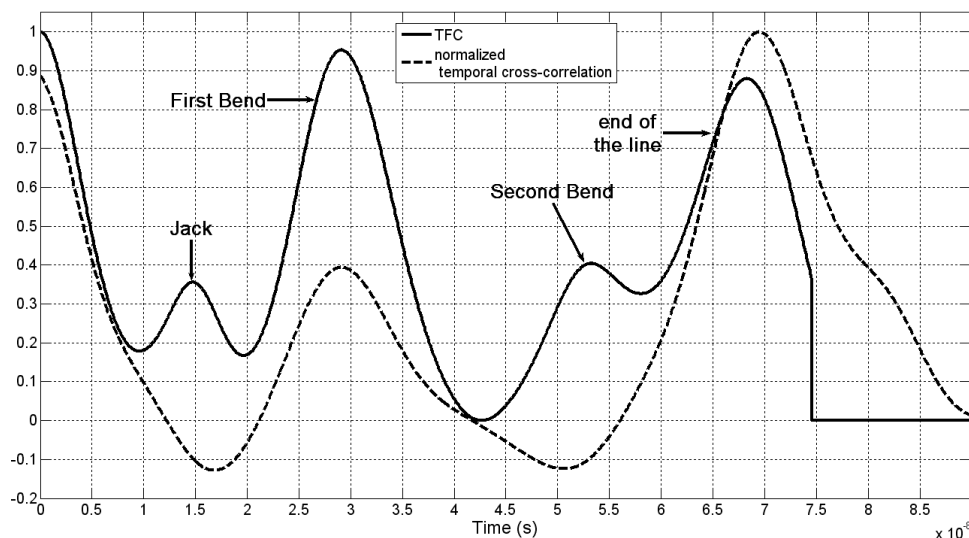
Figure 10: TFC result obtained in the second case.

4.2. Results obtained in the second case

Figure 10 displays the result obtained after applying the TFC on the TDR result. In this case T_s and the gaussian window width are equal to the width of the injected signal. The TFC result is compared with the classical cross-correlation between the reflected signal and the injected one. Such a comparison makes more obvious the advantage of using the TFC. Indeed, whereas only the reflections at the beginning of the line, on the first bend and at the end of the line are visible on the classical cross-correlation result, the pulses reflected on the jack and the second bend become apparent after the application of the TFC. This confirms that the TFC can greatly enhance the capacity of detecting low amplitude signals, as the ones reflected on soft faults, jacks or even bends.

5. CONCLUSIONS

This article has shown that localizing a jack in a wiring network is possible, thanks to TDR. Indeed as the jack is not perfectly matched with the line, if a signal is injected into the wire, a part of its energy is reflected back to the injection point. So this reflected signal is supposed to be visible on the reflectogram. However it has a low amplitude. In order to enhance the presence of the jack, some time frequency tools are of useful help. Here a method which combines the Wigner Ville Transform and the computation of a normalized Time-Frequency Cross-correlation function has been proposed and tested on 2 different kinds of lines. We have seen, in the first case (the coaxial line), that this makes the amplitude of the peaks corresponding to the reflected pulses on a jack and a soft fault be of the same range as the one due to a hard fault (open circuit). The second studied case confirms that the TFC can greatly enhance the presence of jacks and even bends.

Besides whereas using a thiner injected signal improves the time resolution, the results of the TFC are more difficult to interpret. Indeed using a narrower signal makes the small intrinsic imperfections of the line more visible. So the number of peaks present in the TFC result will increase and the peak corresponding to the jack is buried into the others. One way to address this problem is to voluntarily decrease the time resolution when computing the TFC. This can be done in taking the same computation's parameters as for a wider injected signal. However if the amplitude of the reflected pulses on jacks or soft faults are of the same range as for the intrinsic imperfections they won't be detected. So this method has to be used with very good caution.

Thanks to the TFC, jacks can be detected. This enables us to study the topology of the wiring network under test and to find the relative position to the jacks of defects. This will make their maintenance easier. Then knowing where jacks are is also a first step for monitoring their ageing.

REFERENCES

1. Pan, T.-W, C.-W. Hsue, and J.-F. Huang, "Time-domain reflectometry using arbitrary incident waveforms," *IEEE Transactions on Microwave Theory and Techniques*, Vol. 50, No. 11, 2558–

2563, Nov. 2002.

2. Auzanneau, F., M. O. Carrion, and N. Ravot, "A simple and accurate model for wire diagnosis using reflectometry," *PIERS Proceedings*, 232–236, Prague, Czech Repulic, August 27–30, 2007.

3. Ravot, N., F. Auzanneau, Y. Bonhomme, M. O. Carrion, and F. Bouillault, "Distributed reflectometry-based diagnosis for complex wired networks," *EMC: Safety, Reliability and Security of Communication and Transportation Syst.*, June 2007.

4. Shin, Y. J., "Theory and application of time-frequency analysis to transient phenomena in electric power and other physical systems," Ph.D. dissertation, University of Texas, 2004.

5. Wang, J., P. Stone, Y.-J. Shin, and R. Dougal, "Application of joint time-frequency domain reflectometry for electric power cable diagnostics," *Signal Processing, IET*, Vol. 4, No. 4, 395–405, August 2010.

6. Kwak, K. S., T. S. Yoon, and J. B. Park, "Load impedance measurement on a coaxial cable via time-frequency domain reflectometry," *SICE-ICASE International Joint Conference 2006*, October 2006.

7. Wang, J., P. Crapse, J. Abrams, Y. J. Shin, and R. Dougal, "Diagnostics and prognostics of wiring integrity via joint time-frequency domain reflectometry," *10th Joint FAA/DoD/NASA Conference on Aging Aircraft*, April 2007.

8. Shaameri, A. Z., S. Hussain, and S. Salleh, "Window width estimation and the application of the windowed wigner-ville distribution in the analysis of heart sounds and murmurs," *TENCON 2000, Proceedings*, Vol. 2, 114–119, 2000.

9. Franchet, M., N. Ravot, and O. Picon, "The use of the pseudo Wigner Ville transform for detecting soft defects in electric cables," *IEEE/ASME International Conference on Advanced Intelligent Mechatronics*, Budapest, Hungary, July 3–7, 2011.

Shadowing Effect Analysis at Multiple Moving Persons Tracking by UWB Radar

Daniel Urdzík[1], Rudolf Zetík[2], Dušan Kocur[1], and Jana Rovňáková[1]

[1]Technical University of Košice, Košice, Slovak Republic
[2]Ilmenau University of Technology, Ilmenau, Germany

Abstract— Ultra wideband (UWB) radars appear as the suitable technology for detection and tracking of moving people in critical situations and hazardous environments. Our experiences with such applications of UWB radar systems have shown that for the multiple moving person detection and tracking, a single radar with a small antenna array is capable to detect very often the person moving closest to the radar antennas only, whereas the other target (persons) are usually not detected. This is a serious and unsolved problem of UWB radar applications for detection and tracking of multiple moving persons. In this paper, we will outline the results of the series of measurements with short range UWB radar which were dedicated for examination and quantitative description of this negative effect.

1. INTRODUCTION

The short range UWB radar appears to be an attractive and perspective solution for the detection and localization purposes. The UWB radar system is the special type of noise radar and can be used to detect and track moving targets in critical environments with an advantage. One of the possibilities of the UWB radar systems is their use for the various security, rescue and surveillance applications (e.g., through wall and through fire detection and tracking of moving targets during police or military operations, protection of facilities with high industrial or financial importance etc.) Their primary advantage comes from the large bandwidth of the transmitted stimulation signals of up to several GHz (typically between 100 MHz and 5 GHz). The large bandwidth results in an excellent localization precision of such UWB devices and to the ability to penetrate many common materials (e.g., walls, rubble, non-metallic obstacles). Then, such devices are able to detect moving person by measuring changes in the impulse response of the environments [1]. For detection and tracking applications outlined above, the short range UWB devices (range up to 20–25 m) are usually applied.

Our experiences with such applications of UWB radar systems have shown that at multiple moving person scenarios, that a single radar with a small antenna array is able to detect very often the person moving closest to the radar antennas only. The other target (persons) are also detected but usually with a small reliability or none at all. This degradation of radar performance can be explained in such a way that the person located in front of the radar antenna array acts as an obstacle and creates an area with high attenuation of the energy of the electromagnetic waves behind his/her (so-called shadowing person). The area with the additional attenuation is referred to as the shadow zone. The shadowing person absorbs and reflects the energy of electromagnetic waves transmitted by the radar transmitting antenna and/or reflected by the other targets and hence, only a negligible part of the energy of the electromagnetic waves reflected by the other targets can be received by the radar. The presence of such shadowing persons and hence the shadow zones cause that the radar eventually cannot detect and track any of the persons which are located within these zones. This effect is referred to as shadowing effect. The outlined problem of due to shadowing effect has been addressed for the first time in [2], where a qualitative analysis of shadowing effect has been described. The main contribution of this paper is the quantitative analyses of attenuation within the shadow zone due to the person localized in front of the radar transmitting antenna.

2. ANALYSIS OF SHADOWING EFFECT

In order to analyze the additional attenuation caused by the shadowing person the series of measurements had to be performed. The measurements took place in an empty large room (corridor) with dimensions of 5.2 m by 2.6 m. The scenarios were chosen in such a way to examine the additional attenuation in the shadow zone and its spatial shape. The measurements were performed with the UWB pseudo-noise radar using maximum-length-binary-sequence (M-sequence) as the stimulus signal. The system clock frequency of the experimental M-sequence UWB radar was about 7 GHz,

which resulted in the operational base band of about DC-3.5 GHz. The M-sequence order emitted by radar is 12, i.e., the impulse response covers 4095 samples regularly spread over 1170 ns. This corresponds to an observation window of 585 ns leading to an unambiguous range of about 47 m. The radar system was equipped with one transmitting (Tx) and one receiving (Rx) omnidirectional antenna. The radar data acquired by such radar device can be interpreted as a set of impulse responses of the environment $[h(t, \tau)]$, through which the emitted signals were propagated. They are aligned to each other creating 2D picture called radargram, where the vertical axis is related to the time propagation t of the impulse response and the horizontal axis is related to the observation time τ.

The measurement of the spatial shape of the shadow zone and the values of attenuation within was performed according to the scheme of the measurement shown in Fig. 1.

The transmitting antenna (Tx) was placed in the fixed position. The radar receiving antenna (Rx) was situated subsequently in the different positions $P(y, x)$ within the investigated area. At each position, the impulse responses was measured by the antenna without the shadowing person. Then the shadowing person was situated in front of the radar transmitting antenna (P) to analyze the influence of his/her presence. In this position the person was performing a uniform rotating movement along his/her body axis and hence the amount of electromagnetic waves reflected/absorbed by the person. The recorded radargram for each analyzed position of $P(y, x)$ contained a set of impulse responses with and without the information about the presence of the shadowing person. In this manner there was total 55 positions of the investigated area analyzed. By computing the corresponding attenuation for each of the positions of $P(y, x)$, we were able to derive the shape of the shadow zone.

In order to compute the attenuation for one position of $P(y, x)$ the power level of electromagnetic waves had to be calculated from all of the impulse responses of the radargram. Because the impulse responses acquired by the radar device contain only the information about the magnitude of the electromagnetic waves the power level was computed as follows:

$$[P_L(\tau)] = \int_{t_1}^{t_2} (h(t, \tau))^2 dt. \tag{1}$$

The symbol $h(t, \tau)$ denotes the impulse responses of the radargram. The value of $[P_L(\tau)]$ is one dimensional vector of calculated power level of electromagnetic waves for the different time instants of measurement. The power level calculated from all the impulse responses of one radargram is shown in the Fig. 2.

The result obtained by the calculation of the power level contains two parts which corresponds to the measured time intervals. The first part enclosed by the green rectangle $[P_{LDW}(\tau)]_{\tau_1}^{\tau_2}$, represents the values of calculated power level when there was no shadowing person present. The values in the blue rectangle denoted as $[P_{LAW}(\tau)]_{\tau_3}^{\tau_4}$, represent the calculated power level of electromagnetic waves, while the person was present in front of the transmitting antenna and performing a uniform
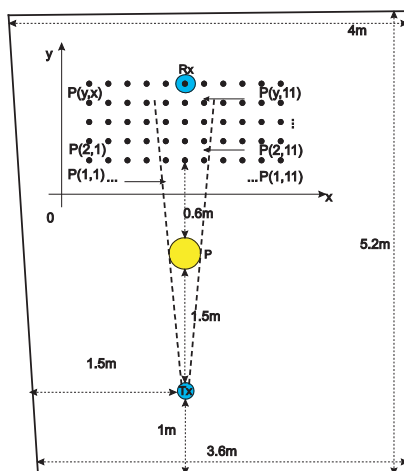
Figure 1: Scheme of the measurement of the shadowing effect.
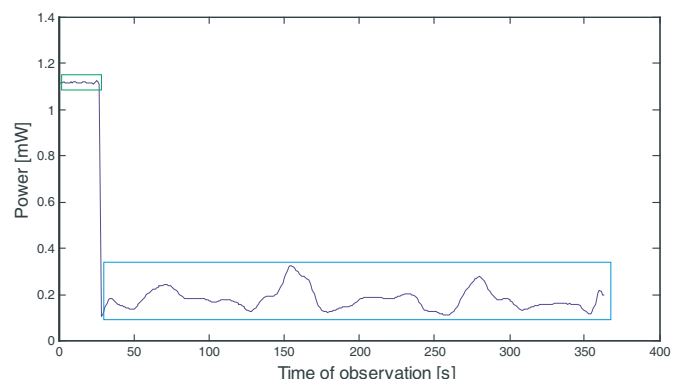
Figure 2: Power level of the direct and attenuated wave.

rotating movement along his/her body axis. Because of the values of the non-shadowed electromagnetic waves appear as nearly constant in measured time interval $\langle \tau_1, \tau_2 \rangle$, one representative value can be estimated from this interval:

$$P_{LDWR} = mean([P_{LDW}(\tau)]_{\tau_1}^{\tau_2}).\tag{2}$$

The level of additional attenuation is then evaluated as the logarithmic ratio of the mean power level of the direct wave and the values of power level of attenuated wave computed for the time instant τ:

$$P_{\mathrm{dB}}(\tau) = 10 \log \left(\frac{P_{LDWR}}{[P_{LAW}(\tau)]_{\tau_3}^{\tau_4}} \right).\tag{3}$$

From the values of $P_{\mathrm{dB}}(\tau)$ which represent the additive attenuation at different time measured instants τ, four quantities were estimated as the representative values of attenuation. These values are estimated by these statistical functions:

$$P_{dBMAX} = \max(P_{\mathrm{dB}}(\tau)),\tag{4}$$
$$P_{dBMIN} = \min(P_{\mathrm{dB}}(\tau)),\tag{5}$$
$$P_{dBMEAN} = mean(P_{\mathrm{dB}}(\tau)),\tag{6}$$

and

$$P_{dBMEDIAN} = median(P_{\mathrm{dB}}(\tau)).\tag{7}$$

Hence we get four different representative values of additional attenuation for one position of the antenna in the investigated area. By computing the additional attenuation for all of the 55 measured positions in the shadow zone we were able to derive its exact shape and the levels of attenuation within.
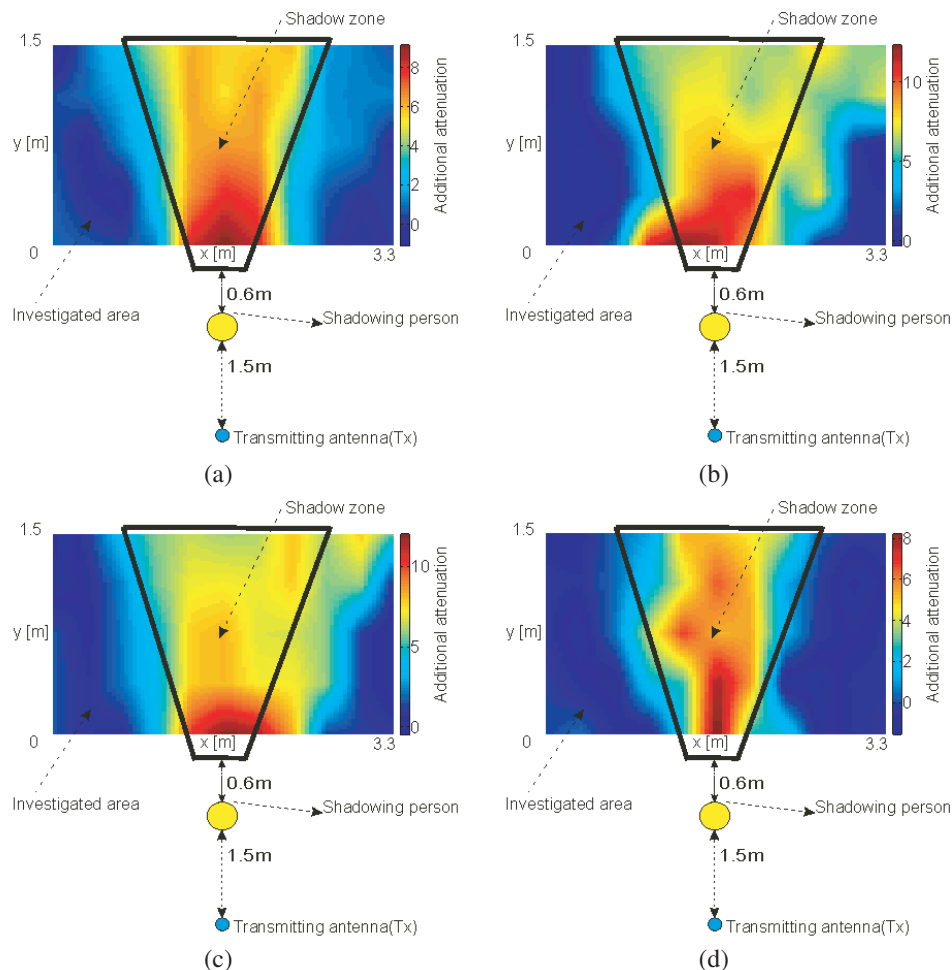
Figure 3: Experimental results of the measurement of the additional attenuation in the shadow zone. (a) P_{dBMAX}. (b) P_{dBMIN}. (c) P_{dBMEAN}. (d) $P_{dBMEDIAN}$.

3. EXPERIMENTAL RESULTS

The experimental results show the values of additional attenuation measured at the height of antenna 1.15 m in the operational base band of UWB radar device of about DC-3.5 GHz. The results are displayed in the Cartesian coordinates to display the attenuation values at different positions in the shadow zone behind the shadowing person. The results show the four cases when the values of the additional attenuation in the investigated area was evaluated as the representation of four different statistical estimations P_{dBMAX}, P_{dBMIN}, P_{dBMEAN} and $P_{dBMEDIAN}$.

From the presented results it can be seen that the person situated in front of the radar transmitting antenna causes significant levels of attenuations behind him/her. The additional attenuation within the shadow zone due to shadowing person can take on values from 1 to +12 dB. By closer inspection of the results it can be also seen that the significant levels of attenuation are focused close behind the shadowing person and are proportionally downsizing with the distance from the person.

4. CONSCLUSIONS

The experimental results obtained by the measurements by UWB radar have confirmed presence of shadowing effect that is caused by a person located in front to the radar antenna apparatus. It was shown that a person situated in front of any of the antennas creates a zone with an additional attenuation within.

The obtained results show that the shape of shadow zones is approximately in the shape of the trapezoid. In the most of analyzed cases it has been found that there is the correlation between the width if the shadow zone and the distance between the antenna and the shadowing person. However the shadow zone properties are needed to be investigated further from different aspects.

With regard to these facts, shadowing effect has to be taken into account in the case of the design of radar systems for multiple moving person detection and tracking. Such solution could lie in the utilization of two or more UWB radar sensor units for multiple target detection and tracking or development of advanced signal processing methods for these purposes.

REFERENCES

1. Withington, P., H. Fluhler, and S. Nag, "Enhancing homeland security with advanced UWB sensors," *Microwave Magazine, IEEE*, Vol. 4, No. 3, 51–58, Sep. 2003.
2. Kocur, D., J. Rovnáková, and D. Urdzík, "Mutual shadowing effect of people tracked by the short-range UWB radar," *The 34th International Conference on Telecommunications and Signal Processing (TSP 2011)*, 302–306, Budapest, Hungary, Aug. 2011.

Human Shadow Effect Assessment when Integrating Inertial Navigation System with Signal Strength Measurements for Pedestrian Dead Reckoning

A. Bahillo[1], **J. Prieto**[1], **S. Mazuelas**[2], **P. Fernández**[1],
R. J. Durán[1], **R. M. Lorenzo**[1], **and E. J. Abril**[1]

[1]Department of Signal Theory and Communications and Telematic Engineering
University of Valladolid, Spain
[2]Laboratory for Information and Decision Systems
Massachusetts Institute of Technology, USA

Abstract— Existing indoor navigation solutions for pedestrian complement Global Navigation Satellite System (GNSS) in GNSS-compromised areas. Recently, these solutions rely on pre-installed wireless sensor networks (WSN) where received signal strength (RSS) based techniques are the most spread due to their availability and cost. However, neither of the RSS based positioning techniques take into account the shadow effect of the human body who carries the RSS meter since the presence of the human body alters the pattern of wave propagation in its immediate proximity. In this paper, we assess the human shadow effect in a theoretical approach based on the finite-difference time-domain (FDTD) method to weight the RSS information that feeds inertial navigation system (INS) based on the human body attitude.

1. INTRODUCTION

The ability to locate the position of the user is an essential part of many applications: electronic travel aids for the visually impaired, context-aware guidance systems for exhibition touring, spatially based applications for a wearable computer, and public and private safety services [1]. The problem of positioning in an open environment is relatively easy to solve using a Global Navigation Satellite System (GNSS). However, GNSS is limited because its inability to provide static heading and its lack of availability due to its signal outages when used in harsh urban areas, and indoors. Existing indoor navigation solutions complement GNSS in GNSS-compromised areas. There are two main research approaches to solve indoor positioning problem: beacon-based solutions, and beacon-free solutions.

The first approach is based on a pre-installed wireless sensor network (WSN). Wireless localization systems determine the position of a mobile target from measurements taken on the signals transmitted by the nodes in the WSN [2–4]. The localization information that can be achieved from measurements is related to distances between the nodes in techniques such as time-of-arrival (TOA) [2] and received-signal-strength (RSS) [3], as well as directions or difference of distances in angle-of-arrival (AOA) or time-difference-of-arrival (TDOA) techniques, respectively [4]. Among the WSN localization solutions, RSS based techniques are the most spread due to their availability and cost [3].

The second approach does not depend on a pre-installed infraestructure. Several applications such as emergency ones are interested in beacon-free solutions since they need to operate independently from the building infrastructure [5]. During the last decade several beacon-free solutions based on inertial measuring units (IMUs) have been proposed for pedestrian navigation [6]. These methodologies, often called pedestrian dead-reckoning (PDR) integrate accelerometer and gyroscope readings of a foot-attached IMU (by strapdown inertial navigation system (INS) mechanization) to compute the position and attitude of the person [7].

However, on the one hand, INS achieves high precision within short time periods but, it has the inconvenient of accumulating errors that grow rapidly. On the other hand, the positioning error of beacon-based positioning is not increasing with time but, less short-term accurate with an absolute error in the range of several meters [6]. Therefore, RSS based positioning techniques have a clear benefit to compensate INS when finding a reliable, continuous and accurate indoor positioning solution for large routes [9]. The integration of RSS information with inertial data has been proposed recently by several authors [10, 11]. However, neither of the RSS based positioning techniques take into account the shadow effect of the human body who carries the RSS meter since the presence of the human body alters the pattern of wave propagation in its immediate

proximity [12]. Hence, there are several problems that remain unsolved related to correctly interpret the RSS readings when the RSS meter is carried by a pedestrian and this information is wanted to be used for positioning [13].

The aim of this paper is to assess the RSS errors caused by the presence of the human body weighting the RSS information that feeds the INS-RSS framework based on the human body attitude. The assessment takes advantage of the fact that the body itself is the only element for sure will be present in the environment. Only the accelerometer and gyroscope sensors will be used to estimate the pedestrian attitude to assess the human body shadow and thus to compensate its effect.

2. FUSIONING INS AND RSS MEASUREMENTS FOR PDR

With the recent trend to integrate micro electro mechanical systems (MEMS) inertial sensors in most devices, research interest in PDR by means of MEMS based IMUs has increased significantly. Most concepts follow a similar approach to the ones presented in [7], in which measurements provided by an IMU mounted on the foot are used to track the position and attitude of the person relative to a known starting point and attitude. IMUs typically contain three orthogonal gyroscopes and three orthogonal accelerometers. It is possible to track the attitude and position of the person by processing signals from the IMU: integrating rate-gyroscopes to keep track of attitude, and double-integrating the accelerometer signals into global coordinates using the known attitude to track the position. However, the main problem of IMU-based PDR systems is that no long-term stability can be provided without additional external reference. Therefore, fusing PDR information from inertial data with RSS localization allows to cope with the RSS inherent fluctuations on the one hand and with the fundamental problem of long-term stability of PDR on the other.

In our approach, we fuse accelerometer and gyroscope data coming from an IMU mounted on the foot, and available RSS data coming form a RSS meter. We follow an integrated INS-RSS methodology similar to the one presented by Jimenez et al. in [10] and depict in Figure 1. This methodology is valid for any kind of motion (forward, lateral or backward walk, at different speeds), and does not require any offline calibration. The methodology is inertial-centric, i.e., the main focus of the estimation is on the inertial processing, while the distance information estimated to the access points (APs) with the RSS method is used to update the position state of the IMU-based PDR estimation. An extended Kalman filter (EKF) is used for the INS estimation, compensating position, velocity and attitude errros as well as IMU biases, and it is fed with the residual between the INS-predicted range to APs, and the range derived from the RSS distance estimation algorithm.

We consider the IMU to be mounted on the foot of the person which allows to perform the so-called zero-velocity updates (ZUPT) to compensate the drift of the acceleration sensors whenever the foot comes to rest on the ground and to correct the estimated velocity [7]. Our approach also includes other drift reduction methods such as zero angular-rate updates (ZARUs) [8] to compensate the drift of the gyroscope sensor when the foot is still. Finally, assuming that the majority of buildings have their corridors parallel to each other, or they intersect at right angles, a
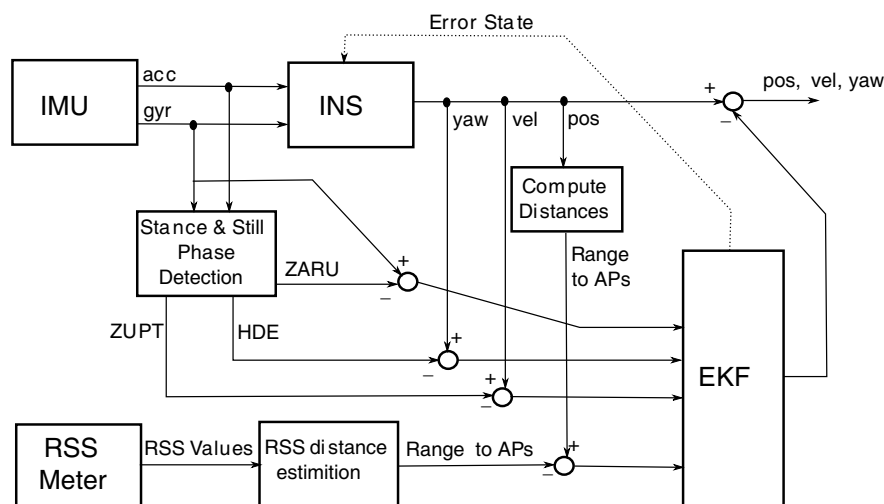
Figure 1: Inertial-centric, INS-RSS methodology.

heuristic drift elimination (HDE) [14] to compensate the heading (yaw) errors is used.

The RSS meter is assumed to be carried by the person in the hands at chest level, and it collects several RSS values acquired from different APs deploy in the building. This RSS data is continuously recorded in a buffer. We process the available RSS information at a 0.5 Hz update rate following the distance estimation algorithm described in [3]. This algorithm consists in dynamically estimate the propagation models that best fit the propagation environments based on maximizing the compatibility of the RSS meter to APs distance estimates by using only the RSS measurements. Once the propagation models are estimated, it is possible to accurately determine the distance between the RSS meter and each AP.

3. THE HUMAN SHADOW EFFECT

The aim of this section is to assess the RSS readings errors caused by the presence of the human body on RSS meters in a theoretical approach with a few simple case studies. In order to perform the assessment, an analysis of field-body interactions near body surface by means of finite-difference time-domain (FDTD) simulations is performed [15]. This method is currently the most acceptable choice if a digital anatomical model of a human has to be analyzed. As the FDTD method is well known, and it is described in more detail in [12, 15], only a brief outline of the implementation is described here.

As a numerical human model, a full 3D human body has been used for simulation purposes [16]. The whole human body has been included inside the computational domain with dimensions $130 \times 130 \times 200 \, \text{cm}^3$, and 2 mm resolution. In order to avoid numerical instabilities, the time step is fixed according to the Courant condition of scheme stability [17]. To calculate the spatial distribution of the E-field, the impulse response of the system has been evaluated in the frequency domain. The tissue in each node is assigned permittivity and conductivity values according to frequency [18]. Frequencies RFID-900 (900 MHz), DCS-1800 (1800 MHz) and ISM-2400 (2400 MHz) are analyzed due to most RSS based localization schemes operate within them. Finally, in order to avoid E-field reflections at the limits of the computational domain, 15 perfectly matched layers haven been used as the absorbing boundary conditions (ABC) [19]. In addition, a total/scattered field formulation has been chosen to minimize the load on the ABC and to avoid any interaction between the incident propagation wave and the ABC [20]. The same implementation has been used in [12] where E-field strength measurements and simulations fit perfectly.

(a) 0° azimuth (b) 45° azimuth (c) 90° azimuth

(d) 135° azimuth (e) 180° azimuth
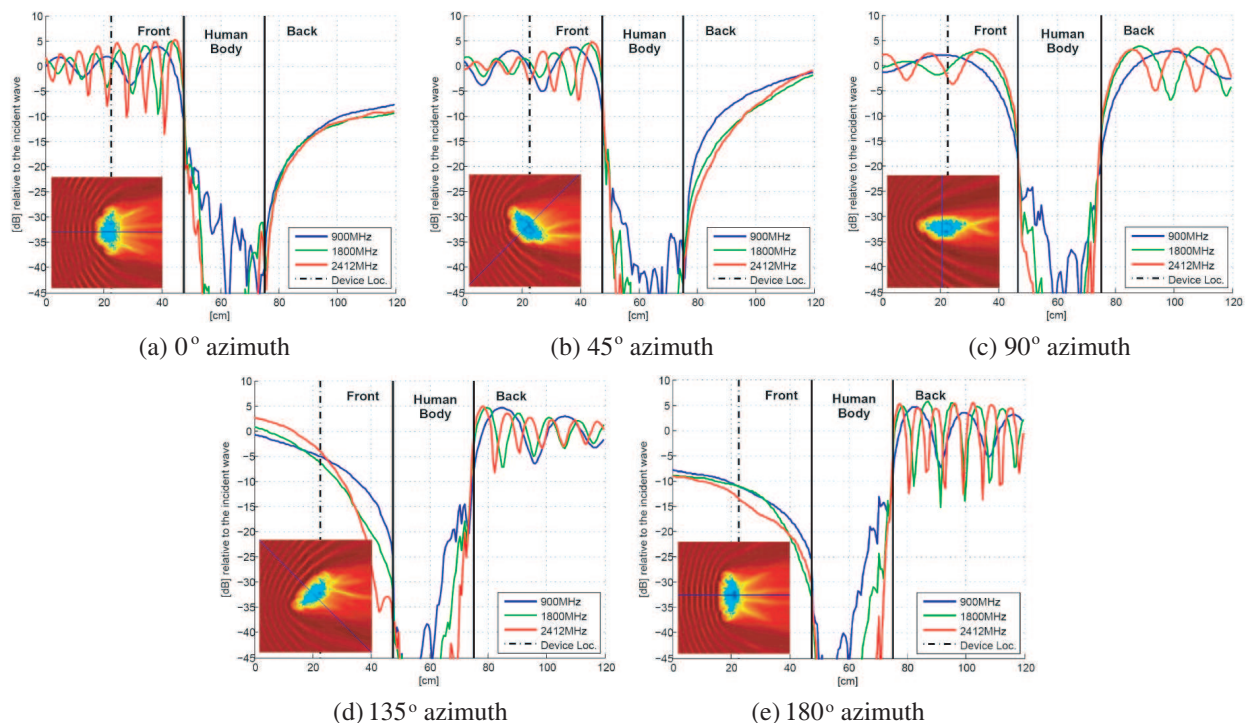
Figure 2: Spatial variability of the E-field due to the presence of the human body through the outcome line at different frequencies and angles of incidence.

Figure 2 shows the spatial variability of the E-field when it is compared to the incident wave through the outcome line. This line is an imaginary segment parallel to the ground which goes approximately through the central part of the human chest (3/4 body height and 1/2 body width). This figure evaluates different scenarios as the human body is illuminated by a monochromatic plane wave with vertical polarization at different frequencies, and from different angles in azimuth. In order to assess the human body shadow, it is assumed that the human carries the RSS meter in the hands at chest level, 25 cm from it. This is a real assumption since the person could be carrying a wireless device where monitoring his own location, but also it is a conservative one since distances nearer to the human body fall in greater RSS differences. Simulation results show that the higher the frequency, the higher the attenuation in the region shaded by the human body. We could observe differences in the RSS meter readings up to 13 dB in RFID-900, 14 dB in DCS-1800 and 19 dB in ISM-2400 bands due to the human body presence.

4. COMPENSATING SHADOW EFFECT BASED ON HUMAN ATTITUDE

In this section, we analyze the performance of the INS-RSS methodology which only uses three accelerometers, three gyroscopes and a RSS meter. To compensate the human body shadow effect we weight the distance estimates obtained from the RSS information based on the human attitude, giving more relevance to the RSS information when the human is facing the APs than when he is giving the back to the AP.

As IMU, we use a Xsens Mtx device from Xsens Technologies B. V. (www.xsens.com). It is configured to provide 100 Hz data rate, and it is placed on the foot. We only use the raw linear acceleration and rate of turn provided by solid state MEMS three orthogonally oriented accelerometers and three gyroscopes, respectively. Magnetometers are not used since magnetic disturbances can be severe and permanent indoors.

As RSS meter, we assume the person carries the RSS meter in the hands at chest level, and we simulate the RSS values from APs accordingly. At 0.5 Hz, 100 RSS values from each AP have been modeled. The input data for the RSS algorithm have been modeled randomly following a Uniform distribution: $n_1 \in U(1.3, 1.7), n_2 \in U(1.7, 2.25)$ and $n_3 \in U(2.25, 3.5)$ where (n_1, n_2, n_3)
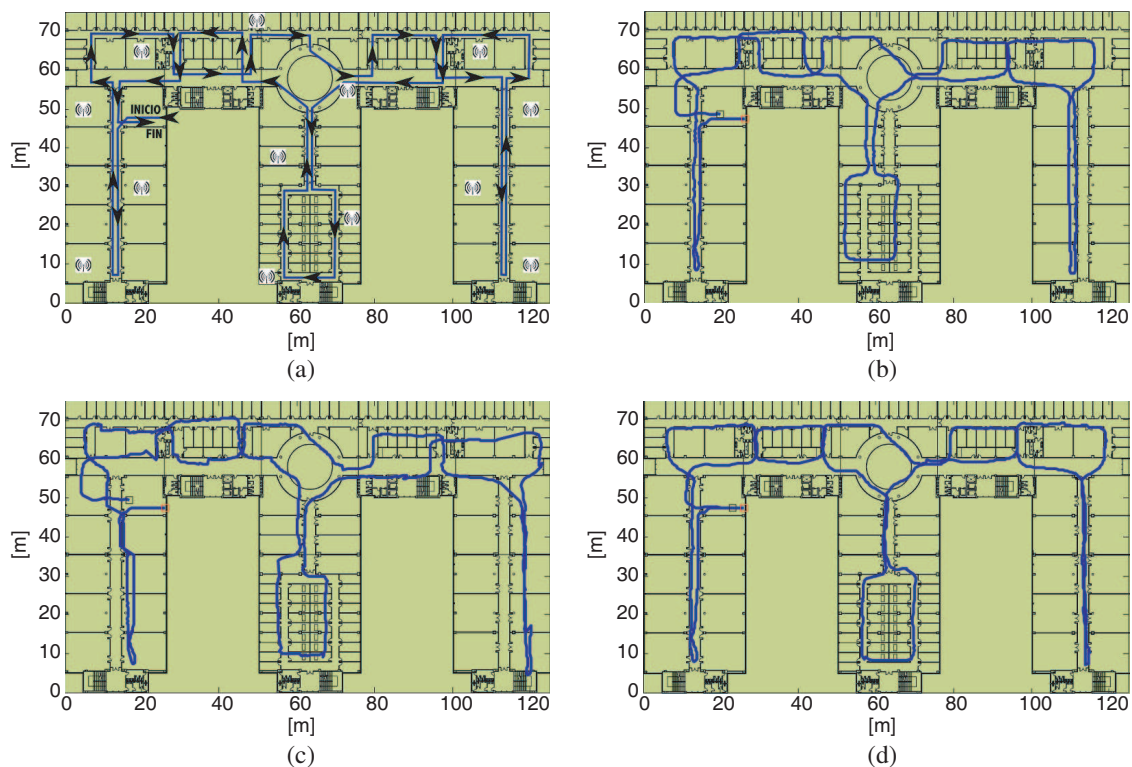
Figure 3: Actual and estimated positions using the integrated INS-RSS methodology in different ways. (a) Actual path and APs deployment. (b) Estimated path with IMU data. (c) Estimated path with IMU and RSS data without taking into account the human body shadow effect. (d) Estimated path with IMU and RSS data compensating human shadow effect.

are the 3 different path-loss exponents that characterize the propagation channel from the 3 APs sorted by their proximity to the RSS meter, and an uniform random value between 2.85 dBm and 3.45 dBm denoting the standard shadowing. Additionally, the effect of the human body shadow has been modeled randomly following a Gaussian distribution as $\epsilon_1 \in N(0, 2.5), \epsilon_2 \in N(-0.5, 1), \epsilon_3 \in N(-1, 1), \epsilon_4 \in N(-5, 0.5)$ and $\epsilon_5 \in N(-13, 0.5)$ where $(\epsilon_1, \epsilon_2, \ldots, \epsilon_5)$ are the effect of the human body shadow added to the RSS values modeled from Figure 2 at each azimuth angle.

Figure 3(a) shows the actual 700 m long path followed by the person who carries the IMU and the RSS meter. The person walked around 9 minutes at constant speed through the corridors of a building at the University of Valladolid. We analyze the integrated INS-RSS methodology in three different ways: (i) without RSS information, (ii) with RSS information provided by the three nearest APs, and (iii) with RSS information provided by the three nearest APs and compensating the human body shadow effect. The three tests are displayed in Figures 3(b), (c) and (d), respectively. The start position is marked with a red square, and the final position with a black one. The accumulated positioning error is computed as the 2-D Euclidean distance between the start and stop positions with respect to the total traveled distance (TTD). As one could expect, as far as the system information increases the accuracy of the methodology should improve. If we only use the IMU data, the total accumulated error is 6 m, i.e., 0.96% TTD, while if we use the IMU and RSS data compensating the body shadow effect, the total accumulated error is 2 m, i.e., 0.32% TTD. If we do not take into account the human body shadow effect, the performance of the integrated INS-RSS methodology decreases with respect to use only IMU data since the human body shadow could cause differences on RSS up to 15 dB. As a consequence, the human body shadow effect degrades the ranging and path-loss exponent estimates. However, thanks to the IMU we know the human body attitude, therefore, we could known the relative orientation between the RSS meter and the angle of arrival of the main RF contribution of each AP, and thus compensate the human body effect on the RSS values accordingly.

5. CONCLUSION

The discussion in this paper has given an overview of the potential error that could be associated with RSS meters for a integrated INS-RSS methodology due to the effect of the human body shadow who carries the meter. As shown, the effect of the human body shadow could cause differences on RSS readings up to 15 dB. As a consequence, this effect degrades the ranging and path-loss exponent estimates, and therefore the integrated INS-RSS methodology. Even a preliminary and conservative study, such as the one reported here, has highlighted the need to weight the RSS information when it is wanted to be used for localization purposes. In conclusion, for those INS schemes whose objective was to locate people, the relative orientation of the human body with respect to the APs based on the attitude information could be used to correctly interpret the RSS meter readings.

REFERENCES

1. Kupper, A., *Location-based Services: Fundamentals and Operation*, John Wiley & Sons, Chichester, UK, 2005.
2. Bahillo Martinez, A., S. Mazuelas Franco, J. Prieto Tejedor, R. M. Lorenzo Toledo, P. Fernandez Reguero, and E. J. Abril, "Indoor location based on IEEE 802.11 round-trip time measurements with two-step NLOS mitigation," *Progress In Electromagnetics Research*, Vol. 15, 285–306, Jun. 2009.
3. Mazuelas, S., A. Bahillo, R.M. Lorenzo, P. Fernandez, F. A. Lago, E. Garcia, J. Blas, and E.J. Abril, "Robust indoor positioning provided by real-time RSSI values in unmodified WLAN networks," *IEEE Journal of Selected Topics in Signal Processing, Special Issue on Advanced Signal Processing for GNSS and Robust Navigation*, Vol. 3, No. 5, 821–831, Oct. 2009.
4. Rappaport, T. S., J. H. Reed, and B. D. Woerner, "Position location using wireless communications on highways of the future," *IEEE Communications Magazine*, Vol. 34, No. 10, 33–41, Oct. 1996.
5. Renaudin, V., O. Yalak, P. Tome, and B. Merminod, "Indoor navigation of emergency agents," *European Journal of Navigation*, Vol. 5, No. 3, Jul. 2007.

6. Lei, F., P. J. Antsaklis, L. A. Montestruque, M. B. McMickell, M. Lemmon, Y. Sun, H. Fang, I. Koutroulis, M. Haenggi, M. Xie, and X. Xie, "Design of a wireless assisted pedestrian dead reckoning system — The NavMote experience," *IEEE Trans. on Instrumentation and Measurement*, Vol. 54, No. 6, Dec. 2005.

7. Foxlin, E., "Pedestrian tracking with shoe-mounted inertial sensors," *IEEE Comput. Graph. Appl.*, Vol. 25, No. 6, 38–46, Nov. 2005.

8. Jimenez, A., F. Seco, J. Prieto, and J. Guevara, "Indoor pedestrian navigation using an INS/EKF framework for Yaw drift reduction and a foot-mounted IMU," *Proc. 7th WPNC*, Vol. 10, No. 6, 135–143, 2010.

9. Retscher, G. and Q. Fu, "Integration of RFID, GNSS and DR for ubiquitous positioning in pedestrian navigation," *Journal of Global Positioning Systems*, Vol. 6, No. 1, 56–64, 2007.

10. Jimenez, A., F. Seco, J. Prieto, and J. Guevara, "Accurate pedestrian indoor navigation by tightly coupling foot-mounted IMU and RFID measurements," *IEEE Trans. on Instrumentation and Measurements*, Vol. 61, No. 1, 178–189, Jul. 2011.

11. Zhu, M., K. Zhang, W. Cartwright, and G. Retscher, "Possibility studies of integrated INS/RFID positioning methods for personal positioning applications," *Proc. Global Navig. Satellite*, 1–9, 2009.

12. Blas, J., F. A. Lago, P. Fernandez, R. M. Lorenzo, and E. J. Abril, "Potential exposure assessment errors associated with body-worn RF dosimeters," *Bioelectromagnetics*, Vol. 28, No. 7, 573–576, 2007.

13. Bahillo, A., J. Prieto, S. Mazuelas, P. Fernandez, R. M. Lorenzo, and E. J. Abril, "*E*-field assessment errors caused by the human body on localization systems," *Proceedings of the IEEE Vehicular Technology Conference (VTC)*, May, Taipei, Taiwan, 2010.

14. Borenstein, J. and L. Ojeda, "Heuristic drift elimination for personnel tracking systems," *The Journal of Navigation*, Vol. 63, 591–606, Sep. 2010.

15. Taflove. A., *Computation Electrodynamics: The Finite-Difference Time-Domain Method*, Artech House, Boston, MA, 2005.

16. Spitzer, V., M. J. Ackerman, A. L. Scherzinger, and D. Whitlock, "The visible human male: A technical report," *J. Am. Med. Inform. Assoc.*, Vol. 2, 118–130, 1996.

17. Kunz, K. S. and R. J. Luebbers, *The Finite Difference Time Domain Method for Electromagnetics*, CRC Press, Boca Raton, FL, 1993.

18. Calculation of the dielectric properties of body tissues in the frequency range 10 Hz–100 GHz, Florence, http://niremf.ifac.cnr.it/tissprop.

19. Sacks, Z. S., D. M. Kingsland, R. Lee, and J-F. Lee, "A perfectly matched anisotropic absorber for use as an absorbing boundary condition," *IEEE Trans. on Antennas Propagation*, Vol. 43, 1460–1463, 1995.

20. Sullivan, D. M., "Electromagnetic simulation using the FDTD method," Wiley-IEEE Press, New York, 2000.

A Novel 3D Ray-tracing Model for Precise Mobile Localization Application

Chee Kiat Seow, **Teng Wah Ang**, **and Kai Wen**

School of Electrical and Electronic Engineering, Nanyang Technological University, Singapore

Abstract— Recent year has seen the need for precise localization for both commercial and government applications. The underlying building block for accessing the performance of the localization algorithm is either the channel measurement data or ray-tracing algorithms that are highly correlated to the empirical channel measurement data. However, the accuracy of ray tracing algorithm is highly related to the simulation of all possible propagation paths traversing through various structures in the realistic environment. Traditionally, most of the rays tracing algorithms have been well researched for planar structures. This paper presents a novel three-dimensional ray-tracing model for building structures with non-planar or curved surfaces. Methodology to overcome the problem in modeling scatterers with non-planar surfaces has been proposed. It takes into all possible propagation paths from any combinations of reflections, diffractions and transmissions from/through planar and non-planar/curved surfaces. Comparisons between proposed model and the measured power delay profile in an environment containing building structure with curved surfaces has shown good agreement and articulate the impact of including scattering phenomenon from curved surfaces on the power delay profile.

1. INTRODUCTION

Due to the advent of antenna array [1, 2], localization has been a prevalent research topic [3, 4]. Usually, experimental campaign is conducted to assess the design performance of the locallization scheme. However, in recent years, ray tracing [5, 6] is used as the simulation tool to mimic the actual environment instead of conducting extensive measurement campaign. As such, to have a holistic comparison of the localization schemes, the ray tracing methodology must able to model the environment and trace out all propagation paths as accurately as possible.

Most of the ray-tracing models make use of multiple-image concept to facilitate the tracking and calculating of the rays which finally arrive at the receiver, provided the location of all the images involved can be determined. Although the image-based ray-tracing model can compute extremely complex ray paths and have shown reasonable prediction accuracy, it is limited to modeling scattering from polygonal scatterers and not curved surfaces. Thus, curved cylindrical scatterers are often approximated using polygonal scatterers [7]. In order to achieve a more realistic model, it is necessary to increase the number of sides of the polygonal scatterers used to approximate the curved cylindrical scatterers. However, the number of sides of the polygonal scatterers have to be limited in order that the computation time is not excessively long and solution based on the UTD are valid. This is because in ray tracing models based on the multiple image theory, an increase in the number of planar surfaces in the environment will result in an exponential rise in the number of reflection images generated, which in turn will result in a large number of ray traced.

The purpose of this paper is to derive a comprehensive three-dimensional ray-tracing model for microcellular communications, which can include all possible propagation paths from any combination of arbitrary number of reflections, transmissions and diffractions from multiple edges and convex surfaces. Furthermore, by incorporating the concept of cones of rays as in [5], the computation time can be shortened by examining whether the receiver is within reach of the cone of rays of a particular image, thus greatly reducing the number of images or rays to be tested.

2. THEORY AND FORMULATION

Figure 1(a) shows the plan view of a point source transmitter T_x in a communication microcell in the campus of the Nanyang Technological University in Singapore. All buildings' surfaces, parapet walls, and floor are constructed of concrete. The transmit antenna T_x is positioned h_t above the ground. A vertically polarized receiving antenna R_x is placed h_r above the ground, and its position is moved around the building corners. In modeling the environment shown in Figure 1(a), the ray-tracing models based on multiple image concept in the literature can only model the semi-cylindrical buildings using polygonal approximation.

Consider now a ray path T_X-R_J-R_K-R_L-R_M-R_X, with reflections from two planar and two convex surfaces. Using the multiple image concept, we can generate the reflection image E_1^J due

to T_x associated with planar surface J. However, we cannot determine the next reflection image associated with convex surface K due to equivalent source E_1^J. If the image associated with a curve cylindrical scatterer cannot be determined, the ray-tracing algorithm will fail when encountering such object because subsequent images can be generated only when the current image location is known.

As such, the concept of our proposed technique is to cascade the positional information of the curved cylindrical scatterers into the images until backward ray tracing is performed. In our new improved ray-tracing algorithm, reflection images for planar surfaces are computed as in [6, 7]. However, when encountering curved cylindrical scatterer, no reflection image associated with the cylindrical scatterer will be computed. Instead, the source illuminating the cylindrical scatterer and the positional information of the scatterer will form the "source" for subsequent scattering events. In general, whenever a curved surface is encountered during the ray tracing procedure, the positional information of the curved surface is combined with the illuminating source to form the new image. By adding the information of the curved surface in the image to generate subsequent images, this technique resolves the deadlock in conventional ray tracing algorithm when modeling curve cylindrical scatterers.

To determine the ray path T_X-R_J-R_K-R_L-R_M-R_X using our proposed technique, we first compute the image E_1^J associated with plane J due to source T_x. Next, instead of computing the image associated with cylindrical scatterer K due to the equivalent source E_1^J which is not possible because the point of reflection on plane L, R_L, has yet to be determined, we combine the curved cylindrical scatterer K and the equivalent source E_1^J to form the reflection image associated with scatterer K. The reflection image associated with plane L is then obtained by reflecting the image of scatterer K about plane L. This image associated with plane L will contain two set of information — E_2^{KL} and E_3^{JL} due to scatterer K and source E_1^J respectively. For the next reflection from cylindrical scatterer M — E_3^{JL}, E_2^{KL} and cylindrical scatterer M are combined to form the reflection image associated with scatterer M.

To determine the path of the ray T_X-R_J-R_K-R_L-R_M-R_X, we proceed to perform backward ray tracing [7]. From the position of receiver R_x and last generated reflection image due to cylindrical scatterer M, we first compute the points of reflection R_M and R'_K on the cylindrical scatterer M and E_2^{KL} respectively. With R_M and R'_K computed, the point of reflection on plane L, R_L, is given by intersection of plane L and ray path $R'_K R_M$. The point of reflection on cylindrical scatterer K, R_K, is given by reflection of R'_K about plane L. Finally, R_J is computed from the intersection of plane J with ray path $E_1^J R_K$. By combining the information of cylindrical scatterers into the images, our proposed technique resolves the difficulty of tracing cylindrical scatterers in conventional ray tracing algorithm.

When implementing the improved technique, an approximation for the points of reflection on the cylindrical scatterers is required. This is because our proposed technique causes all cylindrical scatterers encountered along the ray path to be grouped together when backward ray tracing is performed. As analytical solution to points of reflection on cylindrical surfaces does not exist and numerical solution causes excessive computation time, we use an approximate method, which can be computed efficiently. From Figure 1(b), the approximated point of reflection on cylindrical scatterer K, R_K, is computed by taking half the angle subtended by $T_X O_K$ and $O_K O_M$. Similarly, the point of reflection on cylindrical scatterer M, R_M, makes equal angle with $R_X O_M$ and $O_M O_K$. As can be seen in Figure 1(b), this approximation produces results, which is very close to the actual points of reflection on the cylindrical scatterers.

3. RESULT AND DISCUSSION

Figure 2 shows the predicted and measured power delay profile at point 8 in Figure 1(a). The result shows that our model is able to predict, with reasonable accuracy, the various multipath signal components, i.e., many of the multipath components are predicted by our model and experimentally verified as having the correct delays. The dominant signal paths within the first 70 ns is mainly due to diffractions from the edges of the buildings adjacent to T_x. The results also show that signal components arriving after about 100 ns reach the receiver via transmission paths through the semi-cylindrical building. From Figure 2, it is significant to note that the predicted field strength of ray path T_X-R_J-R_K-R_L-R_M-R_X as illustrated in Figure 1(a), which has a path delay of 180 ns (~ 60 m), is close to the measured signal level around this range of delay time. Thus, the ability to predict such multipath signals improves the prediction accuracy of the propagation model.
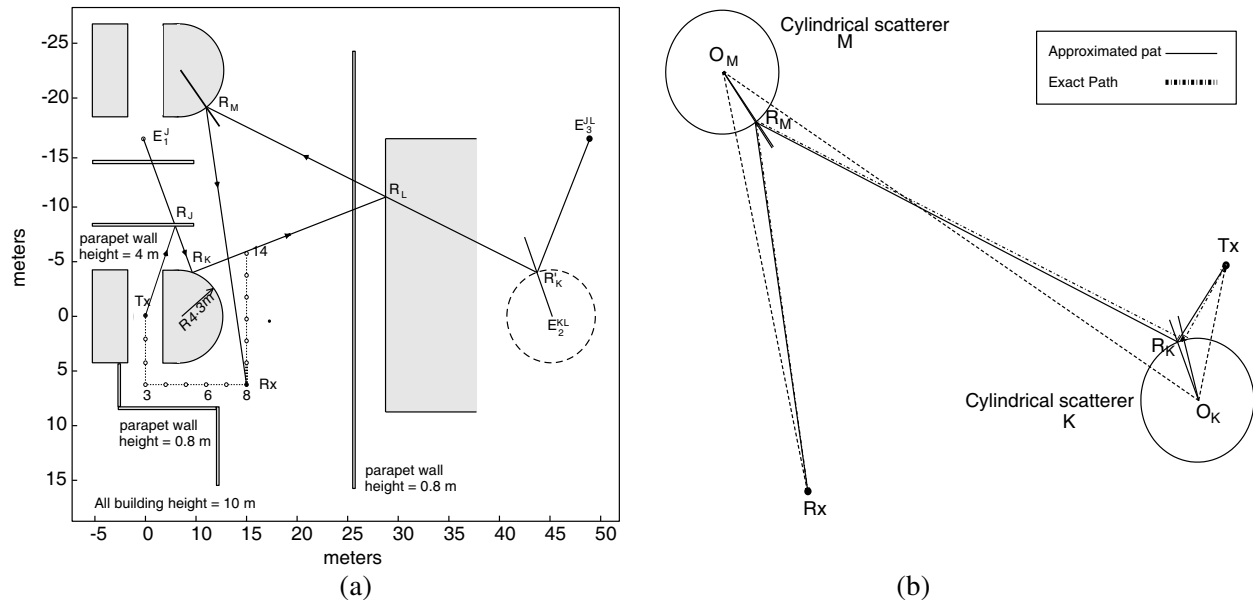
Figure 1: (a) Plan view of measurement site and typical ray path with reflection from cylindrical scatterer. (b) Approximation of reflection points on cylindrical scatterers.
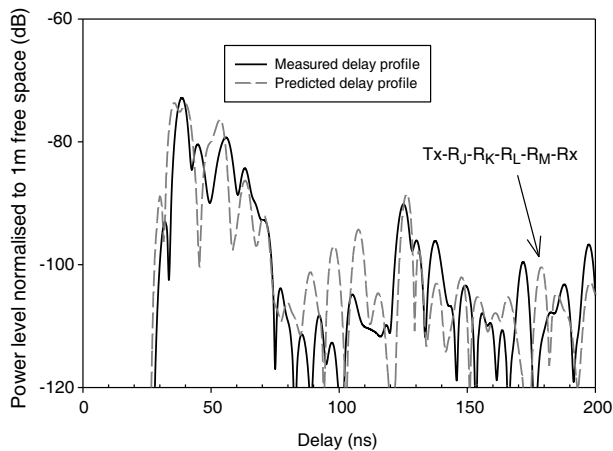
Figure 2: Comparison between predicted and measured delay profile at Point 8 of Figure 1(a).

We have also computed the path loss and rms delay spread τ_{rms} from the delay profiles for the measurement route in Figure 1(a). All τ_{rms} were computed for a dynamic range of 40 dB and delay time of 200 ns. The standard deviation between the measured and predicted path loss obtained using our improved model is 2.8 dB whereas for the model in [6], the standard deviation is 2.9 dB. The good agreement between the measured and predicted results shows the validity of ray-tracing model in predicting path loss coverage, and that diffraction/reflection from cylindrical scatterers may not have much effect on path loss prediction. However, compared to path loss, τ_{rms} is a much more sensitive parameter as it is dependent on both the signal strength and distribution in the delay profile.

4. CONCLUSION

A general three-dimensional ray-tracing model based on the UTD and multiple image theory is presented. This model developed overcomes the major limitation of modeling only polygonal scatterer in image based ray-tracing model. The model also includes convex surface diffraction and diffractions from multiple straight edges. Good agreement between predicted and measured results indicates that the accuracy of the ray-tracing model is a useful prediction tool for microcellular communications.

REFERENCES

1. Lum, K. M., C. Laohapensaeng, and C. E. Free, "A novel traveling-wave feed technique for circularly polarized planar antennas," *IEEE Micro. and Wireless Components Letters*, Vol. 15, No. 3, 180–182, Mar. 2005.
2. Lum, K. M. and C. E. Free, "A novel dual circularly polarized planar and multi-layer LTCC antenna arrays using traveling-wave feed system," *IEEE Trans. Micro. Theory Tech.*, Vol. 54, No. 6, 2880–2886, Jun. 2006.
3. Seow, C. K. and S. Y. Tan, "Non-line-of-sight localization in multipath environment," *IEEE Trans. Mobile Computing*, Vol. 7, No. 5, 647–660, May 2008.
4. Seow, C. K. and S. Y. Tan, "Localization of omni-directional mobile device in multipath enviroments," *Progress In Electromagnetics Research*, Vol. 85, 323–348, 2008.
5. Tan, S. Y., T. W. Ang, and H. S. Tan, "A ray-tracing model for multipath propagation prediction in picocellular environments," *Microwave Opt. Technol. Lett.*, Vol. 25, No. 6, 371–374, 2000.
6. Tan, S. Y. and H. S. Tan, "Improved three-dimensional ray tracing technique for microcellular propagation models," *Electron. Letters*, Vol. 31, No. 17, 1503–1505, 1995.
7. Tan, S. Y. and H. S. Tan, "A microcellular communications propagation model based on the uniform theory of diffraction and multiple image theory," *IEEE Trans. Ant. Propagat.*, Vol. 44, No. 10, 1317–1326, 1996.

Peer-to-peer Non-line-of-sight Localization in Multipath Environment

Si Wen Chen, **Chee Kiat Seow**, **and Kai Wen**

School of Electrical and Electronic Engineering, Nanyang Technological University, Singapore

Abstract— Current localization schemes are able to locate a mobile device using Time-of-Arrival (TOA) and Angle-of-Arrival (AOA) information measured at both the mobile device and reference device. This information is used to derive line of possible mobile device position (LPMD). The intersection points of LPMDs are used to estimate mobile position. However these algorithms do not work well in a dense multipath environment with high level of TOA and AOA noises. In addition, these techniques require at least two paths to locate the mobile position. This paper presents novel methods to find the area of mobile device position and a least square estimator is constructed to find the centroid of mobile position. Furthermore, the proposed technique is able to determine mobile device using one LOS path. Simulation results show that our proposed scheme outperforms previous bidirectional localization schemes by a significant margin especially at high levels of TOA and AOA measurement noise.

1. INTRODUCTION

Wireless localization is an important area that receives significant research interest recently. It is required in many sensor network applications, such as transportation systems, personal tracking and navigation [1–3]. Conventional LOS schemes fail to work when there are insufficient RDs in LOS with the MD or when the signals are dominated by NLOS paths [4, 5]. Several NLOS mitigation techniques [6, 7] have been suggested to identify and discard NLOS signals. These techniques are, however, will not perform satisfactorily as they generally require the number of LOS RDs to be more than the number of NLOS RDs.

With the popularity of Multiple Input Multiple Output (MIMO) system using antenna array [8, 9], Non Line of Sight localization (NLOS) techniques have been proposed to tackle the problem of insufficiency of LOS path. In NLOS schemes, NLOS information, like those of one bounce scattering, is not discarded but used to complement LOS information in determining MD position. So far, NLOS information that is contained within one bounce scattering paths can be used to assist LOS paths [10, 11]. However, these methods do not work well in environments when multipath becomes too dominant and distances travelled by multiple-bounce reflection paths become comparable with those of one-bounce reflection, causing weighting factors of multiple-bounce LPMDs to be comparable with those of one-bounce. Also, these methods is unable to locate MD relying only one signal path and the accuracy will be deteriorated when the TOA and AOA measurement noises become larger.

In this paper, we formulate a novel peer to peer localization technique to improve the robustness of the method presented in [10, 11]. Most importantly, our proposed technique does not require any threshold value to select LPMD for localization. The robustness and accuracy of the technique are greatly enhanced by our proposed making only one LOS signal path. Our simulation results have also shown our proposed localization technique outperforms the existing peer-to-peer localization technique especially for large AOA and TOA measurement noise.

2. NOVEL NLOS SCHEME

The area of mobile device position is able to be derived by leveraging on the TOA and AOA of LOS path that are measured at both RD and MD. The jth RD with known location coordinate (x_j, y_j) has a measured data metric AOA θ_j and TOA t_j for the mth received signal path, where $j = 1, 2, \ldots, N$, with N being the number of RDs. The MD with unknown coordinate (x, y) has a measured AOA ϕ_j and TOA τ_j. The measured TOAs are related to the received path lengths in the following manner:

$$d_j = ct_{j,m}, \quad r_j = c\tau_{j,m} \tag{1}$$

where c is the speed of wave propagation.

The AOA and TOA data value are perturbed by the measurement noise:

$$\theta_j = \theta_j^0 + n_{\theta_j}, \; \phi_j = \phi_j^0 + n_{\phi_j}, \; d_j = d_j^0 + n_{d_j}, \; r_j = r_j^0 + n_{r_j}, \; n_l = N(0, \sigma_l), \; l = \theta_j, \phi_j, d_j, r_j \tag{2}$$

where θ_j^0, ϕ_j^0 and d_j^0, r_j^0 are the true AOA and TOA values of LOS path. n_{θ_j}, n_{ϕ_j} and n_{d_j}, n_{r_j} indicate the measurement noise which are assumed by zero mean Gaussian random variable with known standard deviation σ_l.

Since the noises are assumed to be Gaussian measurement noise, it is possible to know the angular bounds from the statistics of the AOA distribution. That is the LOS path AOA θ_j must in the interval $[\theta_j - 3\sigma_{\theta_j}, \theta_j + 3\sigma_{\theta_j}]$ with confidence level 99.7%. Therefore, the MD position is constrained to an enclosed region overlapped by the two distance and angular bounds, as shown in Fig. 1.

3. RESULT AND DISCUSSION

To test the applicability and accuracy of our proposed localization scheme, we compare our simulation results with those presented in [10]. The authors in [10] presented the accuracy of their algorithm by selecting only the 2 best LOS and NLOS paths based on their weighting factor of LPMD paths. Measurement data metrics (AOA and TOA) were measured by using ray tracing methodology proposed in [12–14]. Three RDs were positioned in the environment at (25, 9), (18, 4), (3, 14). In order to compare with the algorithm in [10], the mobile device was placed at exactly the same position whereby:

For case A, MD is at position (16, 12) in the layout as shown in Fig. 2(a). In this position, the three RDs are in LOS with MD. For case B, MD is at position (14.5, 12) whereby only one RD (3, 14) is in LOS with the MD. Simulation results for case A to B are shown in Fig. 3.

It is observed from the simulation results, as illustrated in Fig. 3, that our proposed technique outperforms the existing peer-to-peer localization technique by a significant margin especially when TOA and AOA measurement noises become large. For example, using $\sigma_d = \sigma_r = 3\,\text{m}$, $\sigma_\theta = \sigma_\phi = 5°$, Fig. 3(a) shows that our proposed scheme achieves an accuracy of 2.6 m for 90% of the time as
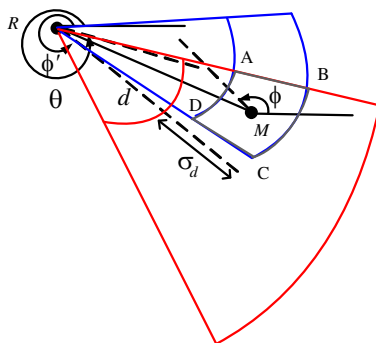
Figure 1: Area of mobile device position.
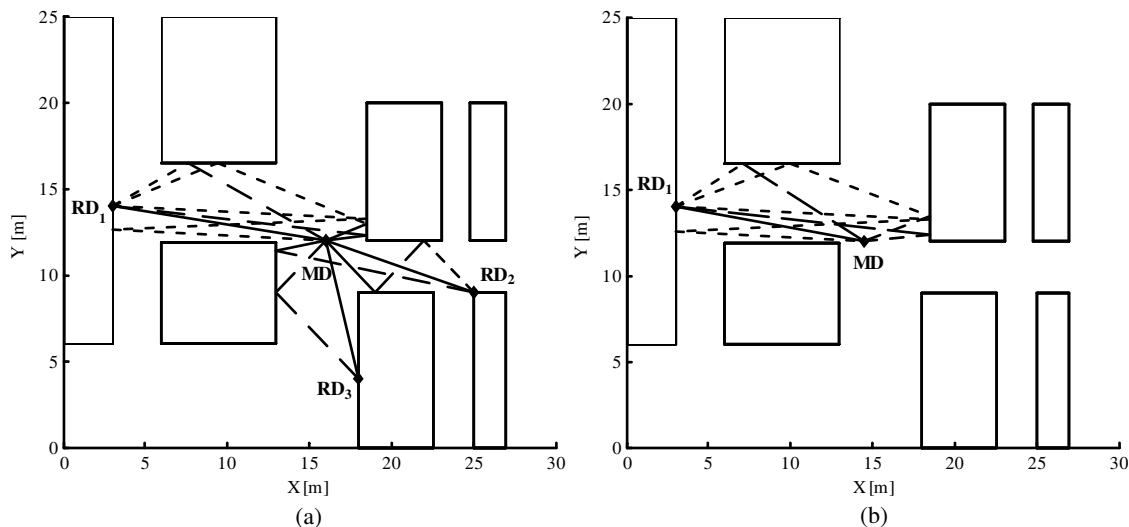
Figure 2: (a) Three RDs are in LOS with MD. (b) One RD is in LOS with MD.
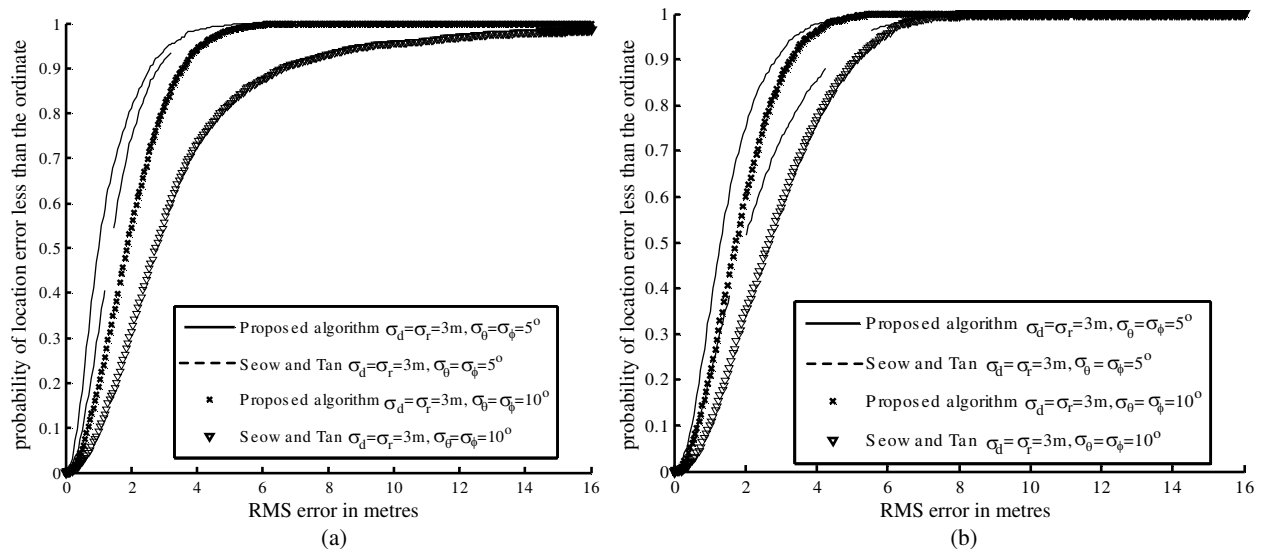
Figure 3: (a) Comparison of the CDF performance for an actual MD located at (16, 12). Three RDs are in LOS with MD. (b) Comparison of CDF performance for an actual MD located at (14.5, 12). One RD is in LOS with MD.

compared 2.8 m of Seow and Tan's method in [10], and improvement of about 7% is shown in Fig. 3(a). This margin increase to 46% using $\sigma_d = \sigma_r = 3\,\text{m}$, $\sigma_\theta = \sigma_\phi = 10°$.

4. CONCLUSIONS

A novel approach to improve the accuracy and robustness of NLOS Peer-to-Peer localization has been proposed. The proposed method was tested and shown to be accurate and robust under various operating conditions. Moreover, the proposed method also significantly outperforms the current NLOS localization technique.

REFERENCES

1. Patwari, N., J. N. Ash., S. Kyperountas, A. O. Hero, III, R. L. Moses, and N. S. Correal, "Locating the nodes: cooperative localization in wireless networks," *IEEE Signal Processing Mag.*, Vol. 22, 54–69, Jul. 2005.

2. Sayed, A. H., A. Tarighat, and N. Khajehnouri, "Network-based wireless location: Challenges faced in developing techniques for accurate wireless location information," *IEEE Signal Processing Mag.*, Vol. 22, 24–40, Jul. 2005.

3. Reed, J. H., K. J. Krizman, B. D. Woerner, and T. S. Rappaport, "An overview of the challenges and progress in meeting the E-911 requirement for location services," *IEEE Commun. Mag.*, 30–37, Apr. 1998.

4. Jiang, L. and S. Y. Tan, "A simple geometrical-based AOA model for mobile communication systems," *IEE Electronics Letters*, Vol. 40, No. 19, 1203–1205, Sept. 2004.

5. Jiang, L. and S. Y. Tan, "Geometrical-based statistical channel model for outdoor and indoor propagation environments," *IEEE Trans. Vehicular Technology*, Vol. 56, No. 6, 3587–3593, Nov. 2007.

6. Cong, L. and W. H. Zhuang, "Nonline-of-sight error mitigation in mobile location," *IEEE Trans. Wireless Commun.*, Vol. 4, 560–572, Mar. 2005.

7. Chan, Y. T., W. Y. Tsui, H. C. So, and P. C. Ching, "Time-of-arrival based localization under NLOS conditions," *IEEE Trans. Veh. Tech.*, Vol. 55, 17–24, Jan. 2006.

8. Lum, K. M., C. Laohapensaeng, and C. E. Free, "A novel traveling-wave feed technique for circularly polarized planar antennas," *IEEE Micro. and Wireless Components Letters*, Vol. 15, No. 3, 180–182, Mar. 2005.

9. Lum, K. M. and C. E. Free, "A novel dual circularly polarized planar and multi-layer LTCC antenna arrays using traveling-wave feed system," *IEEE Trans. Micro. Theory Tech.*, Vol. 54, No. 6, 2880–2886, Jun. 2006.

10. Seow, C. K. and S. Y. Tan, "Non line of sight localization in multipath environment," *IEEE Trans. Mobile Computing*, Vol. 7, No. 5, 647–660, May 2008.

11. Chen, S. W., S. Y. Tan, and C. K. Seow, "Peer-to-peer localization in urban and indoor environments," *Progress In Electromagnetic Research B*, 339–358, 2011.
12. Ang, T. W., S. Y. Tan, and H. S. Tan, "Analytical methods to determine diffraction points on multiple edges and cylindrical scatterers in UTD ray tracing," *Microwave and Optical Technology Letters*, Vol. 22, No. 5, 304–309, Sep. 1999.
13. Tan, S. Y. and H. S. Tan, "Modelling and measurements of channel impulse response for an indoor wireless communication system," *IEE Proceedings, Microwaves, Antennas and Propagation*, Part H, Vol. 142, No. 5, 405–410, London, Oct. 1995.
14. Tan, S. Y., M. Y. Tan, and H. S. Tan, "Multipath delay measurements and modelling for inter-floor wireless communications," *IEEE Trans. Vehicular Technology*, Vol. 49, No. 4, 1334–1341, Jul. 2000.

Multi-user MC-CDMA Using Pseudo Noise Code for Rayleigh and Gaussian Channel

M. F. Ghanim and M. F. L. Abdullah

Department of Communication Engineering, Faculty of Electrical and Electronic Engineering
University Tun Hussein Onn Malaysia, Johor, Malaysia

Abstract— The conventional codedivision multipleaccess (CDMA) technique used in third generation system faced serious limitations by channel dispersion, causing inter symbol interference (ISI), and it requires advanced signal processing algorithms to contain it [1]. Therefore, multi carrier code division multiplexing (MCCDMA) employing multiple stream of data channel can combat channel dispersion, hence ISI, thereby increasing system capability to accommodate a higher number of users This paper presents simulation for the MC-CDMA system using pseudo noise code as spreading code (PN code) to spread data over channel. In this system instead of applying spreading sequences in the time domain, they are applied in the frequency domain, mapping a different chip of a spreading sequence to an individual OFDM subcarrier. The MC-CDMA system is applied in two channel cases, the first one when the used channel is Additive white Gaussian noise (AWGN) channel: the relationship between bit error rate and signal to noise ratio is discussed when the number of the users is increased from 4 to 64 users. Then Rayleigh fading which has four taps with different powers is added to the channel and its effect is simulated. The simulation shows that the fading affects the characteristics of the system sharply and clearly.

1. INTRODUCTION

The multi carrier modulation scheme is easily adaptable to the multiuser environment to provide code division multiplexing. In multicarrier CDMA signatures are formed in the frequency domain, by controlling the amplitudes and phases of subcarriers in a user-specific manner, also combining multi-carrier OFDM transmissions with code division multiple access (CDMA) allows to exploit the wideband channel's inherent frequency diversity by spreading each symbol across multiple subcarriers [2, 3].

In MC-CDMA a data stream from each active user is divided into low rate parallel data streams each being spread by its own chip of the spreading sequence and sent via its own subcarrier. Thus, MC-CDMA is a combination of multicarrier transmission and spreading in the frequency domain [4].

2. MC-CDMA SYSTEM

In MC-CDMA, instead of applying spreading sequences in the time domain, we can apply them in the frequency domain, mapping a different chip of a spreading sequence to an individual OFDM subcarrier. Hence each OFDM subcarrier has a data rate identical to the original input data rate and the multicarrier system "absorbs" the increased rate due to spreading in a wider frequency band [5]. The transmitted signal of the ith data symbol of the jth user $s_i^j(t)$ is written as:

$$s_i^j(t) = \sum_{k=0}^{N-1} b_i^j c_k^j e^{2\pi(f_0 + k f_d)t} p(t - iT), \tag{1}$$

where N is the number of subcarriers.

b_i^j is the ith message symbol of the jth user.

c_k^j represents the kth chip, $k = 0, \ldots, N - 1$, of the spreading sequence of the jth user.

f_0 is the lowest subcarrier frequency.

f_d is the subcarrier separation.

$p(t)$ is a rectangular signalling pulse shifted in time given by:

$$p(t) \triangleq \begin{cases} 1 & \text{for } 0 \leq t \leq T \\ 0 & \text{otherwise.} \end{cases} \tag{2}$$
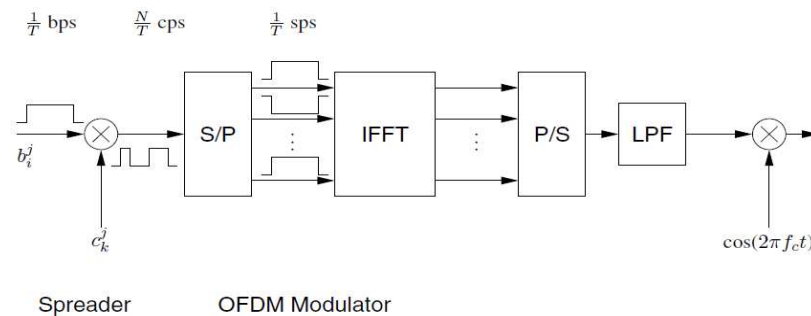
Figure 1: Transmitter schematic of MC-CDMA.
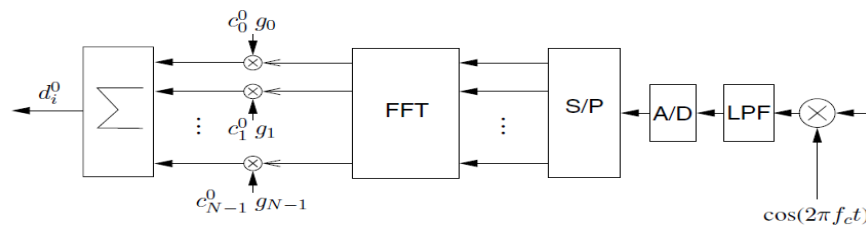
Figure 2: Receiver schematic of MC-CDMA.

If $1/T$ is used for f_d, the transmitted signal can be generated using the IFFT, as in the case of an OFDM system. The overall transmitter structure can be implemented by concatenating a DS-CDMA spreader and an OFDM transmitter, as shown in Figure 1. At the spreader, the information bit, b_i^j, is spread in the time domain by the jth user's spreading sequence, c_k^j, $k = 0, \ldots, N-1$. In this implementation, high speed operations are required at the output of the spreader in order to carry out the chip-related operations. The spread chips are fed into the serial-to-parallel (S/P) block and IFFT is applied to these N parallel chips. The output values of the IFFT in Figure 1 are time domain samples in parallel form. After being parallel to serial (P/S) conversion these time domain samples are low-pass-filtered, in order to obtain the continuous time domain signal. The signal modulates the carrier and is transmitted to the receiver [5].

At the MC-CDMA receiver shown in Figure 2 each carrier's symbol, i.e., the corresponding chip c_k^j of user j, is recovered using FFT after sampling at a rate of N/T samples/sec and the recovered chip sequence is correlated with the desired user's spreading code in order to recover the original information, b_i^j. Let us define the ith received symbol at the kth carrier in the downlink as [5]:

$$r_{k,i} = \sum_{j=0}^{J-1} H_k b_i^j c_k^j + n_{k,i}, \tag{3}$$

where J is the number of users, H_k is the frequency response of the kth subcarrier and $n_{k,I}$ is the corresponding noise sample. The MC-CDMA receiver of the 0-th user multiplies $r_{k,i}$ of Equation (3) by its spreading sequence chip, c_k^0, as well as by the gain, g_k, which is given by the reciprocal of the estimated channel transfer factor of subcarrier k, for each received subcarrier symbol for $k = 0, \ldots, N-1$, and sums all these products, in order to arrive at the decision variable, d_i^0, which is given by:

$$d_i^0 = \sum_{k=0}^{N-1} c_k^0 g_k r_{k,i}. \tag{4}$$

Without the frequency domain equalization of the received subcarrier symbols, the orthogonality between the different users cannot be maintained [5].

3. CHANNEL OF THE SYSTEM

In this paper two types of channels are used:

3.1. AWGN Channel

In reality, transmission is always corrupted by noise. The usual mathematical model is the AWGN (Additive White Gaussian Noise) channel. It is a very good model for the physical reality as long as the thermal noise at the receiver is the only source of disturbance. Nevertheless, because of its simplicity, it is often used to model man-made noise or multiuser interference [6]. The AWGN channel model can be characterized as follows.

The noise $w(t)$ is an additive random disturbance of the useful signal $s(t)$, that is, the receive signal is given by

$$r(t) = s(t) + w(t). \tag{5}$$

The noise is white, that is, it has a constant power spectral density (PSD) [6].

The noise is a stationary and zero mean Gaussian random process. This means that the output of every (linear) noise measurement is a zero mean Gaussian random variable that does not depend on the time instant when the measurement is done.

One must keep in mind that the AWGN model is a mathematical fiction, because it implies that the total power (i.e., the psd integrated over all frequencies) is infinite. Thus, a time sample of the white noise has infinite average power, which is certainly not a physically reasonable property. It is known from statistical physics that the thermal noise density decreases exponentially at (very!) high frequencies. But to understand the physical situation in communications engineering it is better to keep in mind that every receiver limits the bandwidth as well as every physical noise measurement. So it makes sense to think of the noise process to be white, but it cannot be sampled directly without an input device. Each input device filters the noise and leads to a finite power [3].

3.2. Rayleigh Channel

The simplest fading channel from the standpoint of analytical characterization is the Rayleigh channel, whose instantaneous SNR per bit PDF is given by [7]:

$$p_\gamma(\gamma) = \frac{1}{\bar{\gamma}} \exp\left(-\frac{\gamma}{\bar{\gamma}}\right), \quad \gamma \geq 0 \tag{6}$$

where $\bar{\gamma}$ is the average SNR per bit. The Laplace transform of the Rayleigh PDF can be evaluated in closed form with the result

$$M_\gamma(-s) = \frac{1}{1 + s\bar{\gamma}}, \quad s > 0 \tag{7}$$

and

$$I = \frac{1}{\pi} \int_0^{\pi/2} M_\gamma\left(-\frac{a^2}{2\sin^2\theta}\right) d\theta \tag{8}$$

Substituting (7) into (8) gives

$$I \triangleq I_r(a, \bar{\gamma}) = \frac{1}{\pi} \int_0^{\pi/2} \left(1 + \frac{a^2\bar{\gamma}}{2\sin^2\theta}\right) d\theta = \frac{1}{2}\left(1 - \sqrt{\frac{a^2\bar{\gamma}/2}{1 + a^2\bar{\gamma}/2}}\right) \tag{9}$$

4. RESULTS AND DISCUSSION

The MC-CDMA is simulated using Matlab environment. The system was simulated over an Additive White Gaussian Noise (AWGN) channel and Rayleigh multipath fading channel models to show the effect of them on the bit error rate relating to signal to noise ratio.

4.1. MC-CDMA System Performance over AWGN Channel

Figure 3 shows the effect of AWGN channel on MC-CDMA system has users sending 10000 bits on the channel. The data were spread using PN code and modulated by Binary Phase Shift Keying modulation. Figure 3(a) is for system has four users. The data were spread using 4-bit PN code.

The signal to noise ratio values more than 19 dB omit the effect of the additive white Gaussian noise because the bit error rate will be zero and all the received data will be identical with the transmitted data.

The next step is to illustrate the effect of AWGN channel on MC-CDMA system has 16 users. The data were spread using 16-bit PN code and modulated using Binary Phase Shift Keying modulation.

(b) 4 Users

(a) 16 Users

(d) 32 Users

(c) 64 Users
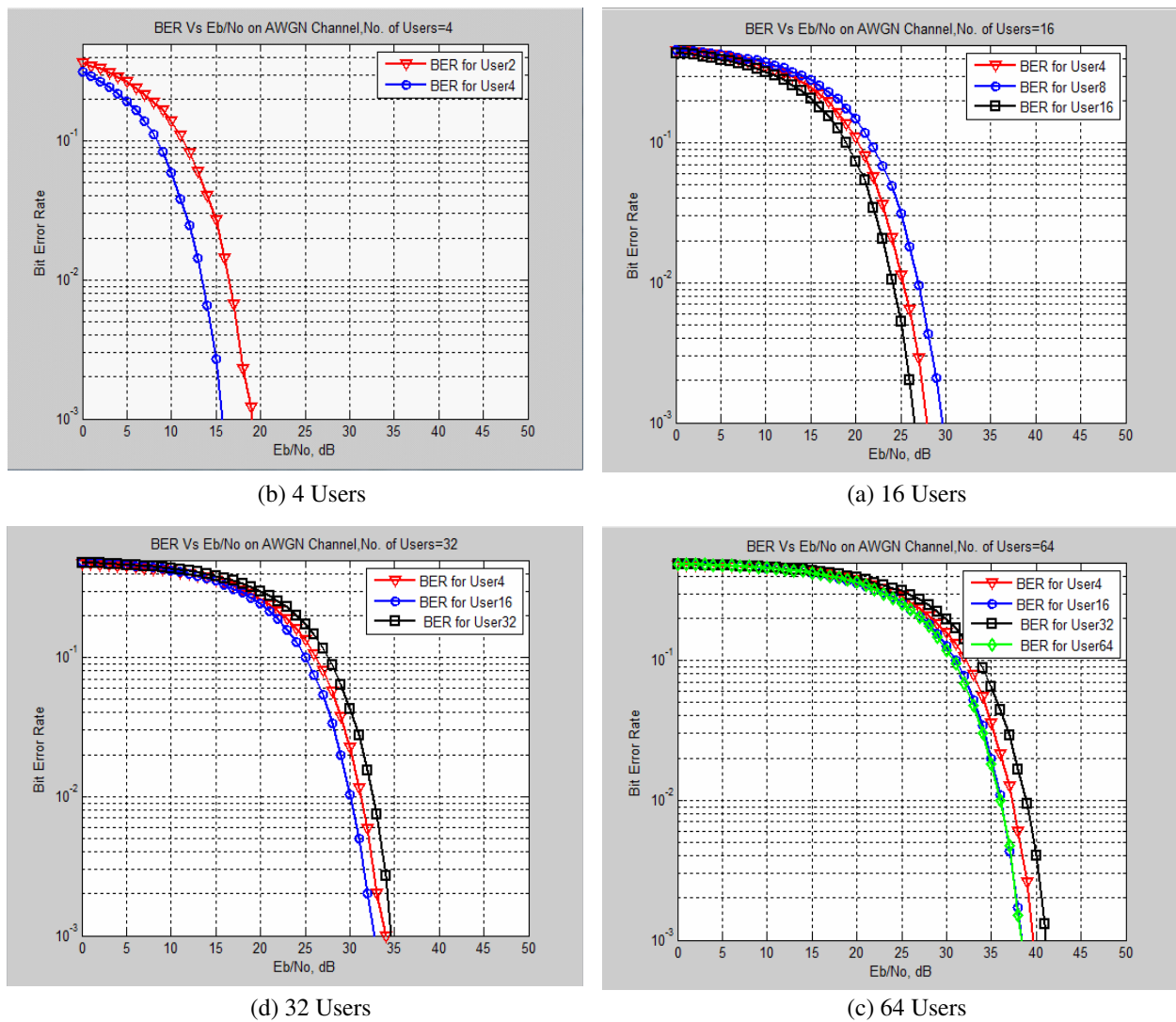
Figure 3: MC-CDMA system broadcasting on AWGN channel.

The bit error rate is direct proportional with the number of users, so increasing the number of users affects the BER as shown in Figure 3(b).

Figure 3(c) illustrates the effect of AWGN channel on MC-CDMA system having 32 users, every user has 10000 bits on the channel. The data were spread using 32-bit PN code and modulated, using Binary Phase Shift Keying modulation.

The requirement for higher SNR is clearly increased to ensure a secure path for the data.

Finally, a MC-CDMA system which has 64 users is simulated to indicate the worst case with the maximum number of users on AWGN channel. The data were spread using 64-bit PN code and modulated using Binary Phase Shift Keying modulation. The system is shown in Figure 3(d).

4.2. MC-CDMA System Performance over Rayleigh and AWGN Channel

This section discusses the results when Rayleigh fading is added to the channel to show the effects of this fading on the BER of the system.

In this paper the Rayleigh fading has four taps with different powers. The following results show that the fading affects the characteristics of the system sharply and clearly.

Figure 4(a) shows the effect of Rayleigh fading channel on MC-CDMA system has four users each one sends ten thousand bits on the channel. The data were spreaded using 4-bit PN code and modulated using Binary Phase Shift Keying modulation.

PN code with 16 bits is used to spread the data of the every user in MC-CDMA system. Ten thousands of data are sent for each SNR value and the BER plot is shown in Figure 4(b). The system has 16 users broadcasting on the Rayleigh fading channel.

(b) 4 Users

(a) 16 Users

(d) 32 Users

(c) 64 Users
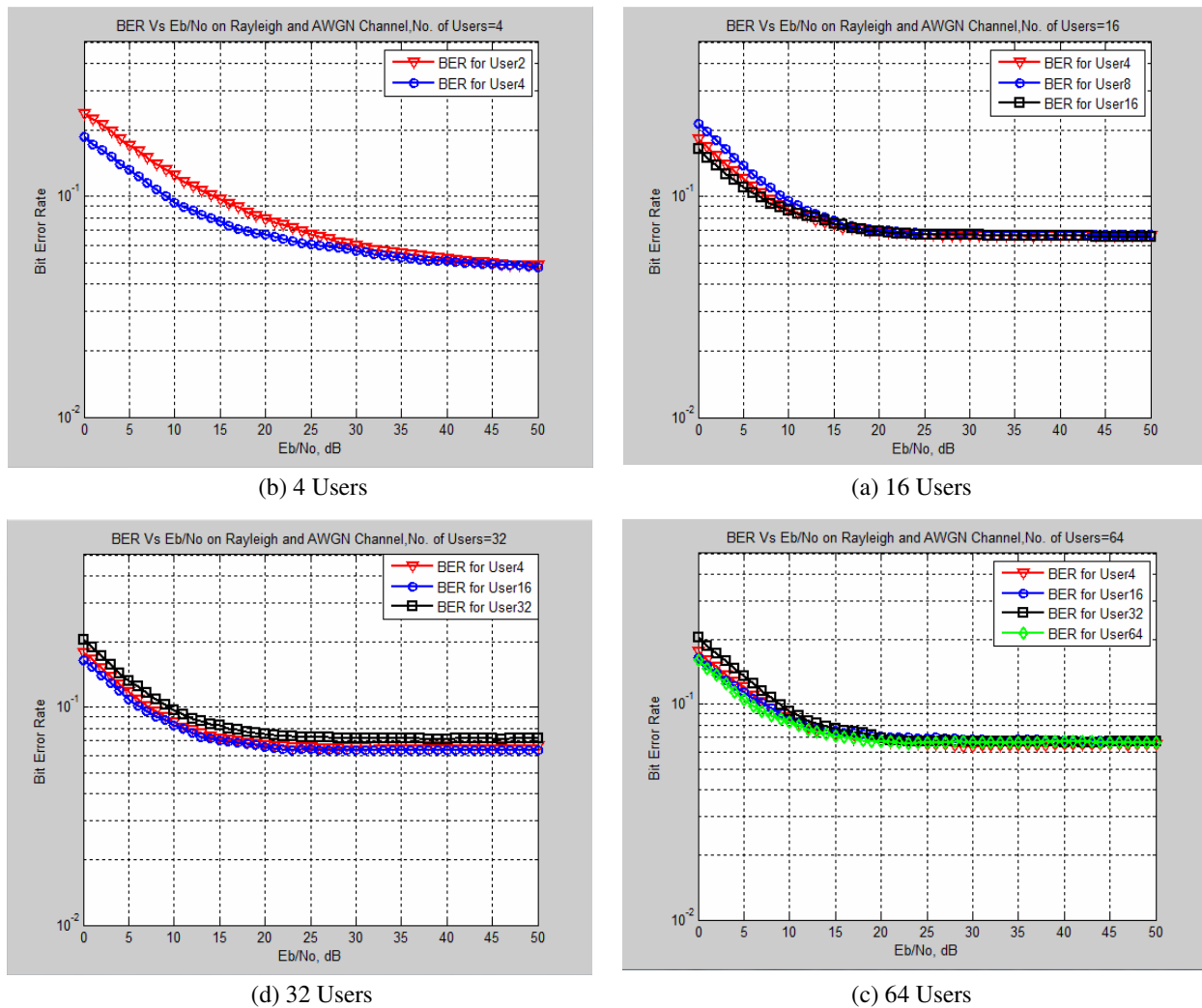
Figure 4: MC-CDMA system broadcasting on Rayleigh fading and AWGN channel.

Figure 4(c) shows the plot of BER for user 4, 16, 32 for different values of SNR. This MC-CDMA system has 32 users sending and receiving data on Rayleigh fading channel. Each user sends and receives 10000 bits with 32-bit PN code and BPSK modulation.

For each SNR between 0 dB and 50 dB the BER values is plotted to show the effect of Rayleigh fading channel on MC-CDMA system has 64 users, every user has 10000 bits. The data were spread using 64-bit PN code and modulated using Binary Phase Shift Keying modulation. BER plot is shown in Figure 4(d).

5. CONCLUSIONS

This paper has showed that PN Codes exhibit Randomness properties and can be suitably used as spreading and scrambling sequences for this reason it is used in this research. The effect of AWGN channel on MC-CDMA system shows that the bit error rate is direct proportional with the number of users, therefore increasing the number of users will increase the required value of SNR to get a secure system with a minimum number of errors. This paper also shows that when, Rayleigh fading was added to the channel the bit error rate is increased with fading in addition to the number of users.

ACKNOWLEDGMENT

REFERENCES

1. Abdullah, M. F. L. and M. F. Ghanim, "An overview of CDMA techniques for mobile communications," *Medwell Journals*, Vol. 5, No. 1, 16–24, 2011.
2. Ipatov, V. P., *Spread Spectrum and CDMA Principles and Applications*, 332, John Wiley & Sons Ltd, England, 2005.
3. Hanzo, L., M. Münster, B. J. Choi, and T. Keller, *OFDM and MC-CDMA for Broadband Multi-user Communications, WLANs and Broadcasting*, 7, John Wiley & Sons Ltd, England, 2003.
4. Krouk, E. and S. Semenov, *Modulation and Coding Techniques in Wireless Communications*, 367, John Wiley & Sons Ltd., 2011.
5. Hanzo, L. and T. Keller, *OFDM and MC-CDMA A Primer*, 211–214, John Wiley & Sons Ltd, England, 2006.
6. Schulze, H. and C. Luders, *Theory and Applications of OFDM and CDMA Wideband Wireless Communications*, 23–24, John Wiley & Sons Ltd, England, 2005.
7. Simon, M. K. and M.-S. Alouini, *Digital Communication over Fading Channels A Unified Approach to Performance Analysis*, 101, John Wiley & Sons, United States, 2000.

Analysis and Design of Triple-band Input Matching for CMOS Low-noise Amplifier

Chun-Yi Lin, **Ching-Piao Liang**, **Pei-Zong Rao**, and **Shyh-Jong Chung**

Institute of Communication Engineering, National Chiao Tung University, Hsinchu, Taiwan

Abstract— This paper presents the analysis and design of a triple-band low-noise amplifier (LNA) fabricated in a 0.18 μm CMOS process. The triple-band operation is achieved by adding a switch component in a dual-band input network of an LNA, so that it can function at 2.5, 3.5, and 5.2 GHz. The proposed method can effectively decrease the chip area as compared to conventional designs. In addition, based on the design procedures provided in this paper, the component values of the triple-band input network can be accurately calculated to reduce the complication of the circuit design.

1. INTRODUCTION

Recently, the widely used wireless communication systems have rapidly expanded the demand for low-cost and low-power RF integrated circuits (RFICs) which can support multi-band operations by a single system. Conventional design strategies have adopted different single-band transceiver circuits in parallel for different frequency bands [1–3]; however, it is unavoidable to result in a high implementation cost because of the large chip area, and simultaneously increase chip current dissipation. In order to improve the above-mentioned drawbacks, the topologies of the wideband LNA have been designed and demonstrated for multi-band application. Unfortunately, the broadband gain response will cause the unwanted interferers to impair the linearity of the receiver. On the other hand, the triple-band LNA has been devised in [4, 5], and it can suppress the out-of-band interferers while maintaining a sufficient in-band property. Nevertheless, the major drawback is the requirement of a higher fabrication cost due to the usage of eight inductors [5]. As a consequence, we propose an approach by using a switch component to reduce the usage of inductors and the significant die area reduction will effectively decrease the cost of a multi-band RF system.

2. THE ANALYSIS OF TRIPLE-BAND LOW NOISE AMPLIFIER

It is known that the noise performance of LNA is dominated to the input stage. The proposed LNA adopts a source-degenerated cascode amplifier, which selects the appropriate device size of M_1 with finger width fixed at 5 μm to achieve input match and good noise figure simultaneously [6, 7]. Traditionally, the design criteria of the multi-band LNA such as that in the WiMAX application may use different LNAs for different frequency bands to accomplish a multi-bands operation. Recently, a concept of triple-band low noise amplifier, as shown in Fig. 1(a), has been proposed [4, 5]. However, the chip area may be consumed while there are eight required inductors in the circuit. Figs. 2(a) and (b) show the conventional dual-band and single-band input matching circuits, respectively. In this paper, we develop a novel manner for triple-band input matching, which is contrived by using dual-band input network with an additional switched component shown in Fig. 2(c). A significant area reduction and better noise figure can be achieved by reducing the usage of inductors in the input network. In the following analyses, it will facilitate the discussions to define that ω_1, ω_2, and ω_3 correspond to 2.5, 5.2, and 3.5 GHz, respectively. When the switch is off, the circuit is equivalent to that shown in Fig. 2(a), and it is to be operated as a dual-band input network at 2.5 GHz and 5.2 GHz. On the other hand, as the switch is on, the circuit becomes that in Fig. 2(b), and it is operated at 3.5 GHz.

3. THE PROPOSED TRIPLE-BAND LOW NOISE AMPLIFIER

The values of the circuit components such as L_s, L_g, L_1, and C_1 should be suitably designed in order to achieve the triple-band input matching, which is discussed in the following analyses. To begin with, the input impedance of the proposed LNA for the switch off status (Fig. 2(a)) can be expressed as

$$Z_{in} = \frac{j\omega L_1}{1 - \omega^2 L_1 C_1} + j\omega(L_s + L_g) + \frac{1}{j\omega C_{gs}} + \frac{g_m L_s}{C_{gs}} \tag{1}$$
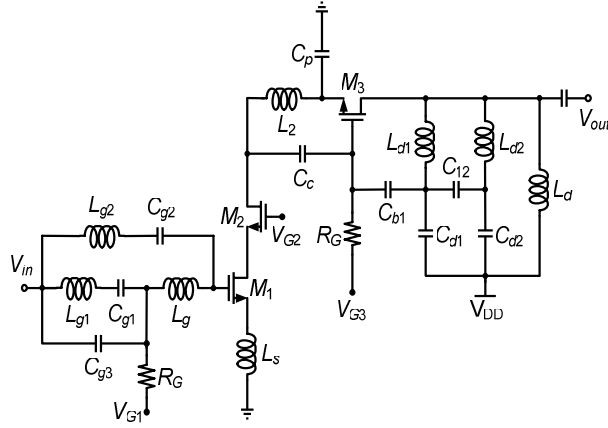
Figure 1: A triple-band low noise amplifier reported in [4, 5].

(a) (b) (c)
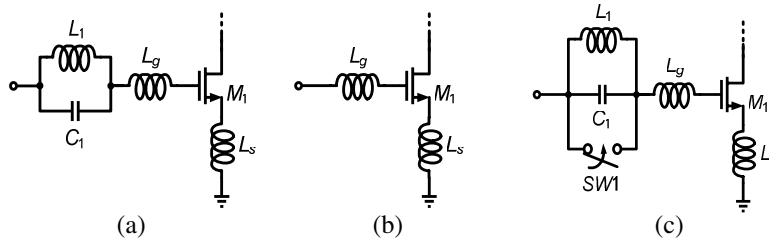
Figure 2: (a) Schematic of a dual-band input matching. (b) Schematic of a single-band input matching. (c) A proposed triple-band input matching with an additional switched component.

To match the input port's impedance, the real term should be equal to $50\,\Omega$ and its imaginary term to zero, which yields

$$L_s = \frac{50 C_{gs1}}{g_{m1}} \qquad (2)$$

and

$$C_1(L_g + L_s)\omega^4 - \left(\frac{L_g + L_s}{L_1} + \frac{C_1}{C_{gs1}} + 1\right)\omega^2 + \frac{1}{C_{gs1}L_1} = 0 \qquad (3)$$

As can be seen in (3), the designed frequencies ω_1 and ω_2 (i.e., 2.5 and 5.2 GHz) satisfies

$$\omega_1^2 \omega_2^2 = \frac{1}{C_1(L_g + L_s)C_{gs1}L_1} \qquad (4)$$

Moreover,

$$\omega_1^2 + \omega_2^2 = \frac{\frac{L_g + L_s}{L_1} + \frac{C_1}{C_{gs1}} + 1}{C_1(L_g + L_s)} \qquad (5)$$

and from (4), L_1 is obtained as

$$L_1 = \frac{1}{\omega_1^2 \omega_2^2 C_1(L_g + L_s)C_{gs1}} \qquad (6)$$

which, upon substitution in (5), yields

$$C_1 = \frac{C_{gs1}}{(L_g + L_s)(\omega_1^2 + \omega_2^2)C_{gs1} - (L_g + L_s)^2 \omega_1^2 \omega_2^2 C_{gs1}^2 - 1} \qquad (7)$$

On the other hand, when the switch is on (i.e., the single-band state for $\omega_3 = 3.5$ GHz, Fig. 2(b)), the criterion of a $50\,\Omega$ input impedance is still required, and L_g can be expressed as

$$L_g = \frac{1}{\omega_3^2 C_{gs1}} - L_s = \frac{1}{\omega_3^2 C_{gs1}} - \frac{50 C_{gs1}}{g_{m1}} \qquad (8)$$

(a)   (b)
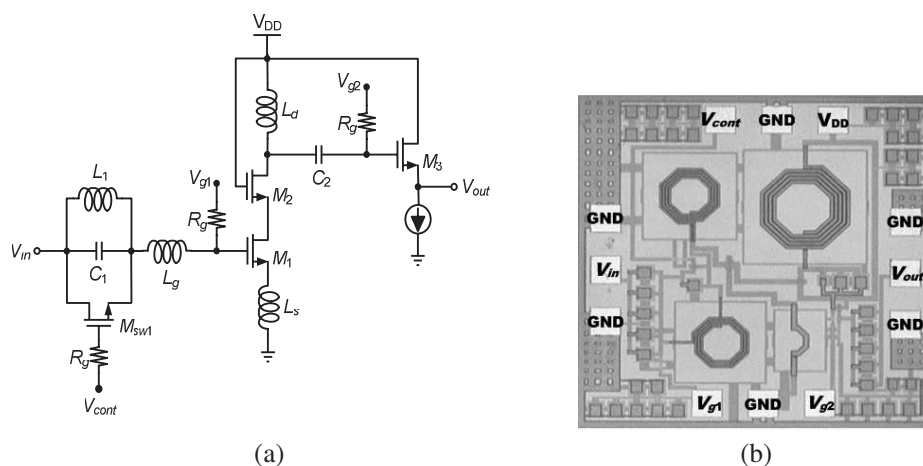
Figure 3: (a) The schematic of the proposed triple-band LNA with input matching design. (b) The microphotograph of the proposed LNA with $0.98 \times 0.94\,\text{mm}^2$ die area.

(a)   (b)
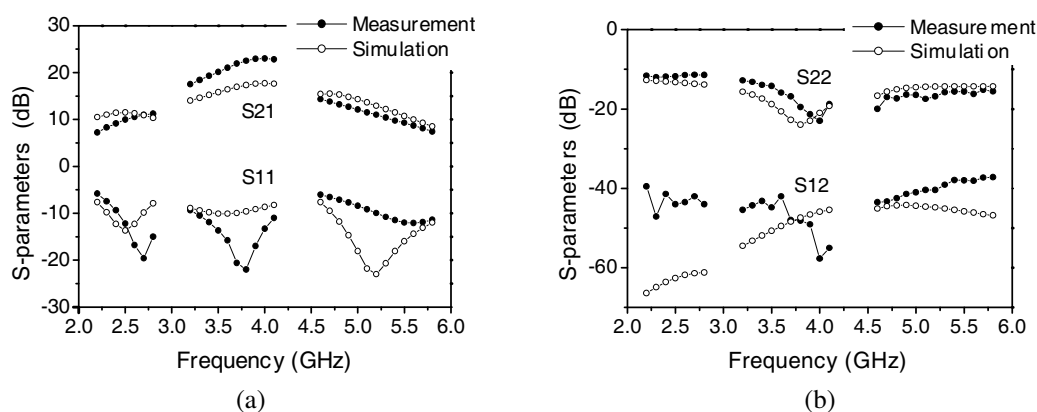
Figure 4: Measured and simulated S-parameters of the proposed LNA.

Table 1: Performance summary of previously published LNA.

Ref.	Tech. [μm]	Freq. [GHz]	S_{11} [dB]	$G_{\max}$ [dB]	$NF_{\min}$ [dB]	P_{diss} [mW]	Area [mm²]
[9]	0.18	2.44/5.76	$< -10/ < -6$	7.6/8.6	5.7/6.8	10.8	1.15
[10]	0.18	0.95/2.4/5.2	$< -7/ < -10/ < -10$	18/ 24/ 23	4.6/ 4.4/ 4.4	32.4	1.34
[5]	0.25	1.8/ 2.45/ 5.25	< -10	10/ 11 /12	3.7/ 4.8/ 6.4	39.1	1.68
This Work	0.18	2.5/ 3.5/ 5.2	< -10	10/ 20/ 11	3.3/ 3.6/ 4.6	10	0.92

where (2) has been incorporated. As we will see, the precise values of $L_s = 0.25\,\text{nH}$, $L_g = 3.5\,\text{nH}$, $L_1 = 2\,\text{nH}$, and $C_1 = 0.9\,\text{pF}$ can be predicted by drawing on (2), (8), (7), and (6) when the width of the transistor $M1$ ($300\,\mu\text{m}$) is chosen with $10\,\text{mW}$ power dissipation. The circuit topology and die microphotographs of the proposed triple-band LNA fabricated by $0.18\,\mu\text{m}$ TSMC CMOS process are shown in Fig. 3(a) and Fig. 3(b). It is noticed that the equivalent circuit of a switched component exists parasitic capacitances, which cause C_1 should be adjusted. In addition, for testing purposes, an output buffer consisted of a source follower is included in the design circuit, which roughly introduces a $6\,\text{dB}$ loss in the signal path [8].

4. MEASUREMENT RESULTS

The proposed LNA is measured by using on-wafer probing. From the $1.8\,\text{V}$ supply voltage the proposed LNA including the output buffer draws a total $6.4\,\text{mA}$ dc current. The simulated and measured results of S-parameters are depicted in Fig. 4. The measured peak gains are $10/20.1/11\,\text{dB}$ at $2.5/3.5/5.2\,\text{GHz}$ while the input and output return losses are better than $10\,\text{dB}$ in the operation frequencies. The simulated and measured noise figures at the same bias condition are depicted in
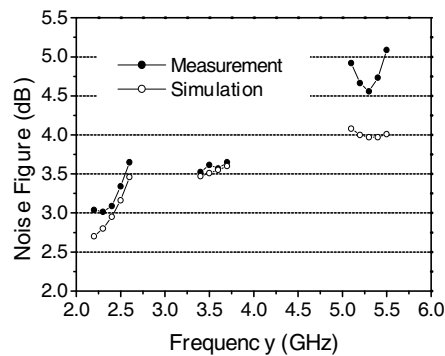
Figure 5: Measured and simulated noise figure of the proposed LNA.

Fig. 5. It is seen that the minimum values of the measured noise figure are equal to $3.3/3.6/4.6$ dB at $2.5/3.5/5.2$ GHz. The proposed LNA is compared with recently published CMOS LNA and summarized in Table 1.

5. CONCLUSION

The analysis and design of triple-band input matching for CMOS LNA is proposed and realized using TSMC 0.18 μm CMOS process. With the proposed method, the triple-band LNA has advantages of the chip cost and circuit complexity.

ACKNOWLEDGMENT

REFERENCES

1. Magoon, R., I. Koullias, L. Steigerwald, W. Domino, N. Vakilian, E. Ngompe, M. Damgaard, K. Lewis, and A. Molnar, "A triple-band 900/1800/1900 MHz low-power image-reject front-end for GSM," *IEEE Int. Solid-State Circuits Conf. Dig. Tech. Papers*, San Francisco, CA, USA, 408–409, Feb. 2001.
2. Kaczman, D., M. Shah, N. Godambe, M. Alam, H. Guimaraes, L. M. Han, M. Rachedine, D. L. Cashen, W. E. Getka, C. Dozier, W. P. Shepherd, and K. Couglar, "A single-chip tri-band (2100, 1900, 850/800 MHz) WCDMA/HSDPA cellular transceiver," *IEEE J. Solid-State Circuits*, Vol. 41, No. 5, 1122–1132, 2006.
3. Bakkaloglu, B., P. Fontaine, A. N. Mohieldin, S. Peng, S. J. Fang, and F. Dülger, "A 1.5-V multi-mode quad-band RF receiver for GSM/EDGE/CDMA2K in 90-nm digital CMOS process," *IEEE J. Solid-State Circuits*, Vol. 41, No. 5, 1149–1159, 2006.
4. Lavasani, S. H. M., B. Chaudhuri, and S. Kiaei, "A pseudo-concurrent 0.18-μm multi-band CMOS LNA," *IEEE MTT-s Int. Microw. Symp. Dig.*, 181–184, Philadelphia, Pennsylvania, USA, Jun. 2003.
5. Jou, C. F., K.-H. Cheng, E.-T. Lu, and Y. Wang, "Design of a fully integrated concurrent triple-band CMOS low noise amplifier," *IEEE Int. Midwest Symposium on Circuits and Systems*, 1239–1242, Cairo, Egypt, Dec. 2003.
6. Shaeffer, D. K. and T. H. Lee, "A 1.5-V, 1.5-GHz CMOS low noise amplifier," *IEEE J. Solid-state Circuits*, Vol. 32, No. 5, 745–759, 1997.
7. Sun, K.-J., Z.-M. Tsai, K.-Y. Lin, and H. Wang, "A noise optimization formulation for CMOS low-noise amplifiers with on-chip low-Q inductors," *IEEE Trans. Microw. Theory Tech.*, Vol. 54, No. 4, 1554–1560, 2006.
8. Bevilacqua, A., C. Sandner, A. Gerosa, and A. Neviani, "A fully integrated differential CMOS LNA for 3–5 GHz ultra-wideband wireless receivers," *IEEE Microw. Wireless Compon. Lett.*, Vol. 16, No. 3, 134–136, 2006.
9. Tang, S.-K., K.-P. Pun, C.-S. Choy, C.-F. Chan, and K. N. Leung, "A fully differential band-selective low-noise amplifier for MB-OFDM UWB receivers," *IEEE Trans. Circuits Syst. II, Exp. Briefs*, Vol. 55, No. 7, 653–657, 2008.
10. Huang, Q.-H., D.-R. Huang, and H.-R. Chuang, "A fully-integrated 2.4/5.7 GHz concurrent dual-band 0.18 μm CMOS LNA for an 802.11 WLAN direct conversion receiver," *Microwave J.*, Vol. 47, No. 2, 76–88, 2004.

A 24 GHz Low-power and High-gain Low-noise Amplifier Using 0.18 μm CMOS Technology for FMCW Radar Applications

Chun-Yi Lin, **Ming-Wei Lin**, **Ching-Piao Liang**, **and Shyh-Jong Chung**

Institute of Communication Engineering, National Chiao Tung University, Hsinchu, Taiwan

Abstract— In this paper, a low power and high gain low-noise amplifier (LNA) is presented for 24 GHz FMCW radar applications fabricated in a 0.18 μm RF CMOS process. The proposed LNA is with the characteristics of the source inductive degeneration type, the current reuse technique, and the invariance of current density in CMOS process. The proposed LNA with a compact size has a gain of 18.95 dB and a noise figure of 5.8 dB, while consuming 11.3 mW. The measured input 1-dB compression point (IP1 dB) and an input third-order intercept point (IIP3) are −26 dBm and −16.5 dBm, respectively.

1. INTRODUCTION

With the development of the FMCW radar system, low power and high gain LNA technologies are required in the radio frequency integrated circuits (RFICs) [1, 2]. There are many LNA presented to realize for the different applications in RFICs. The topologies of the LNA such as the resistive shunt-feedback termination structure [3], shunt-series feedback network [4], common-gate $1/g_m$ termination [5], and the source inductive degeneration [6] have been demonstrated and designed for LNA input stage matching design. However, resistive termination structure and shunt-series feedback network have worse performance on the noise figure, and $1/g_m$ termination topology can merely provide a lower gain to enhance the input signal. Although the source inductive degeneration LNA is subject to a narrow operation frequency, it has a distinguishing characteristic of higher gain and lower noise figure Due to the narrowly 200 MHz bandwidth of 24 GHz FMCW radar system operating between 24.025 ∼ 24.225 GHz, the source inductive degeneration is adopted for the design of the proposed LNA.

2. THE DESIGN AND ANALYSIS OF THE PROSPOSED FMCW RADAR LNA

There are three stages in the proposed LNA circuit as shown in Fig. 1, a current-reusing structure including two common source transistors, a cascode topology with inter-stage matching and gain-boosting designs to further increase the gain, and a source follower as an output buffer for measurements.

On purpose to have an optimum noise figure current density of LNA, the invariance characteristic of current density in the MOSFET is adopted to find out the proper operation point [7, 8]. As a result of the carrier velocity saturation [9], the drain current would be written as

$$I_D = WC_{ox}(V_{GS} - V_{th})v_{sat} \tag{1}$$

v_{sat} is the carrier saturation velocity, and the transconductance g_m would be express as

$$g_m = WC_{ox}v_{sat} \tag{2}$$

As shown in Fig. 2, the minimum noise figure ($\text{NF}_{\min}$) would appear when the width of transistor is chosen as 12 μm, on the other hand, the maximum (Max) available gain would be obtain when width of transistor is chosen as 40 μm. Fig. 3 shows that the first stage of LNA is a current-reusing structure which M_1 and M_2 reuse the same DC current path to save the power consumption [10].
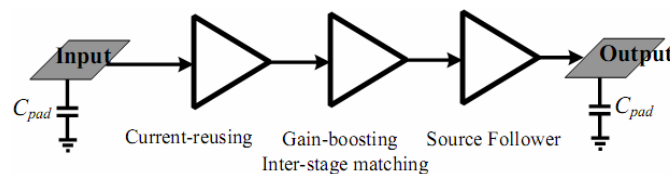
Figure 1: The blocks of the proposed LNA.
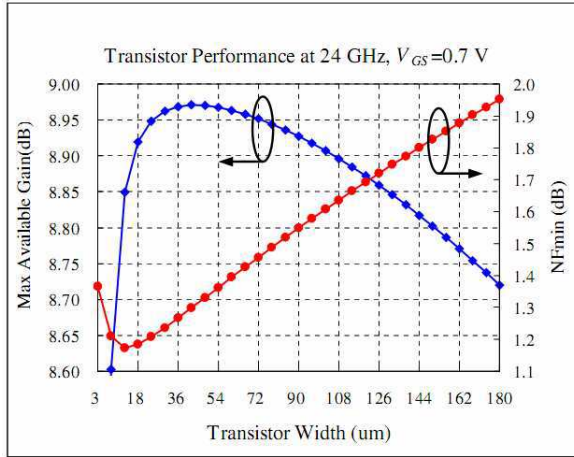
Figure 2: The NF_{min} and Max available gain of LNA.
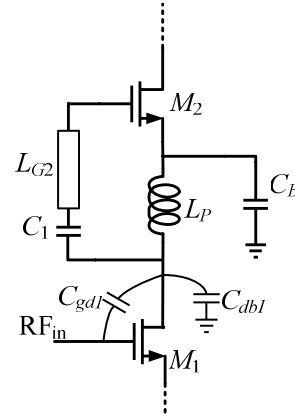
Figure 3: The first stage.
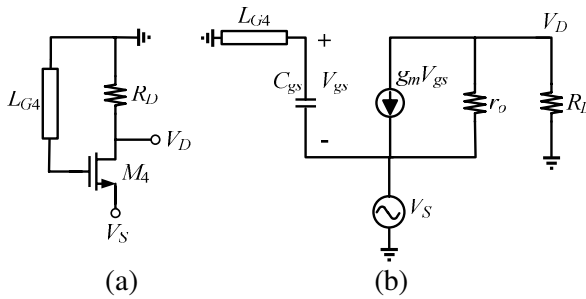
Figure 4: The G_m-boosted stage.
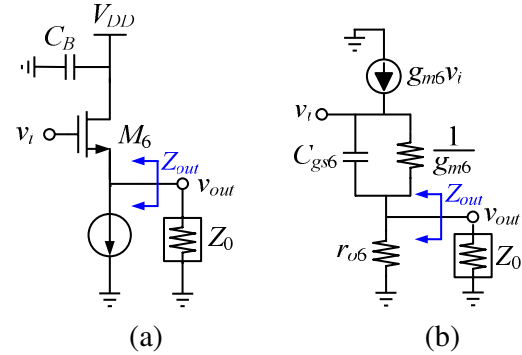
Figure 5: The output stage.

In order to provide an AC short circuit between the drain of M_1 and the gate of M_2, and the open AC path between the drain of M_1 and the source of M_2, an additional capacitor C_1 is added as indicated in Fig. 2.

In order to obtain a higher gain performance, the G_m-boosted stage is used for the second stage of the proposed LNA as shown in Fig. 4. The voltage gain of second stage $A_{v\text{-second}}$ would be written as

$$A_{v\text{-second}} = \frac{V_D}{V_S} = \left(\frac{g_m}{1 - \omega^2 L_g C_{gs}} + \frac{1}{r_o} \right) \frac{r_o \cdot R_D}{r_o + R_D} \tag{3}$$

therefore, the gain would be larger than conventional common-gate amplifier when the operation frequency is less than $1/(L_g C_{gs})^{0.5}$.

In a $50\,\Omega$ measurement system, the output impedance should be matched to avoid the excessive loss. A source follower type is introduced to achieve the matching requirement, and its output impedance Z_{out} and voltage gain of output stage $A_{v\text{-out}}$ is approximated as

$$Z_{out} = \frac{1}{g_{m6}} || r_{o6} || \frac{1}{sC_{gs6}} \approx \frac{1}{g_{m6}} \tag{4}$$

$$A_{v\text{-out}} = \frac{v_{out}}{v_i} \approx \frac{Z_0}{Z_0 + (1/g_{m6})} \tag{5}$$

consequently, the voltage gain is 0.5 when g_{m6} is $20\,\text{mS}$.

3. THE SIMULATED AND MEASURED RESULTS OF THE PROPOSED LNA

The entire schematic of the proposed low power and high gain LNA is presented in Fig. 6, the chip with $0.47\,\text{mm}^2$ is implemented in TSMC $0.18\,\mu\text{m}$ RF CMOS process, and the LNA microphotograph is shown in Fig. 7.

While consuming 11.3 mW, as shown in Fig. 8 and Fig. 9, the proposed LNA has a power gain (S_{21}) of 18.95 dB and a noise figure (NF) of 5.8 dB. As indicated in Fig. 10 and Fig. 11, an input 1-dB compression point (IP1dB) and an input third-order intercept point (IIP3) are -26 dBm and -16.5 dBm, respectively. The performance summary of previously published LNA and the measured results of the proposed LNA are shown in Table 1. According to the measured results of the proposed LNA and the comparison with previously published works, the proposed LNA with compact size has characteristics of low power, high gain (S_{21}) and low noise figure (NF).
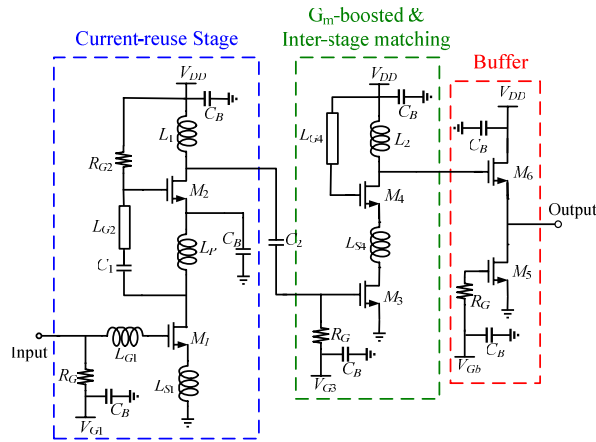
Figure 6: The schematic of the proposed LNA.
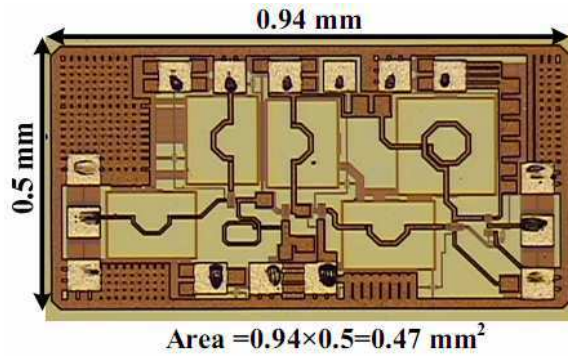
Figure 7: The proposed LNA microphotograph.
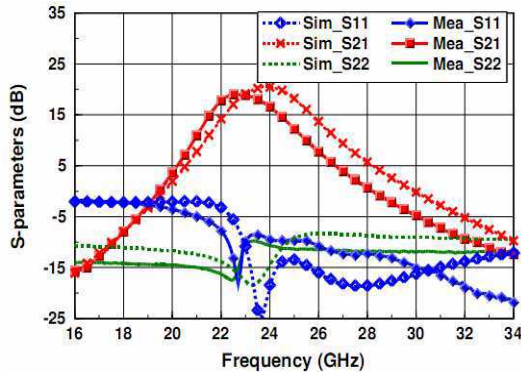
Figure 8: The simulated and measured S-parameter.
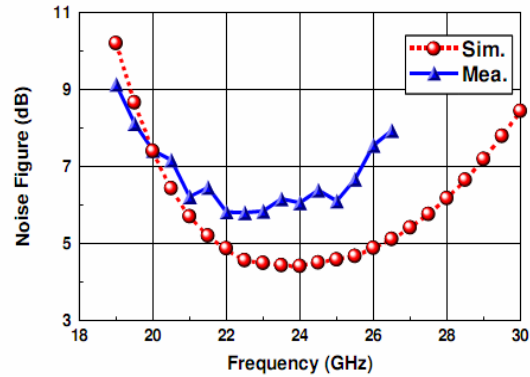
Figure 9: The simulated and measured noise figure.
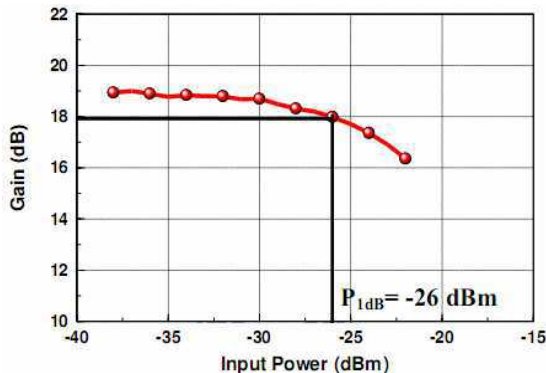
Figure 10: The measured input 1-dB compression point .
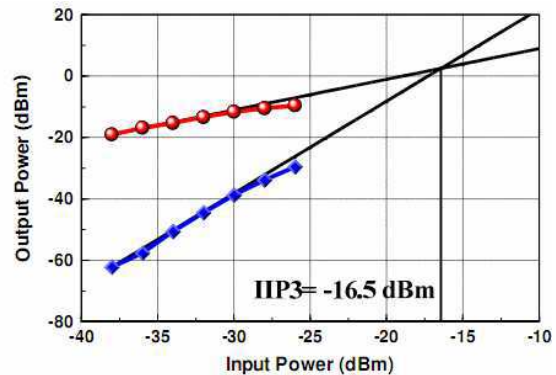
Figure 11: The measured input third-order intercept point.

Table 1: Performance comparison with previously published LNAs.

Ref.	Tech. (μm)	Center Freq. (GHz)	Gain (dB)	NF (dB)	Area (mm2)	Pdiss (mW)	Gain/Pdiss (dB/mW)
This work	0.18	23	18.95	5.8	0.47 (w/i pad)	11.3	1.68
[11]	0.18	24	12.8	3.6	0.55 (w/i pad)	8	1.6
[12]	0.18	28	16	N/A	0.3 (w/i pad)	36	0.44
[13]	0.12	20	18.86	4.26	0.36 (w/i pad)	54	0.35
[14]	0.18	24	10.6	4.9	0.39 (w/o pad)	27	0.39
[15]	0.045	23	7.1	4	0.81 (w/i pad)	3.6	1.97

4. CONCLUSIONS

With taking advantage of the source inductive degeneration, current reuse technique, invariance characteristic of current density, and G_m-boosted stage, the proposed LNA for 24 GHz FMCW radar applications would has balance among power consumption, gain, noise figure, and chip size.

ACKNOWLEDGMENT

REFERENCES

1. Guan, X. and A. Hajimiri, "A 24-GHz CMOS front-end," *IEEE J. Solid State Circuits*, Vol. 39, No. 2, 368–373, 2004.
2. Floyd, B. A., C.-M. Hung, and K. K. O, "A 15-GHz wireless interconnect implemented in a 0.18-μm CMOS technology using integrated transmitters, receivers and antennas," *Symp. VLSI Circuits Dig. Tech. Papers*, 155–158, Kyoto, Japan, Jun. 2001.
3. Chang, C.-P. and H.-R. Chuang, "0.18-μm 3–6 GHz CMOS broad-band LNA for UWB radio," *IET Electron. Lett.*, Vol. 41, No. 12, 696–698, 2005.
4. Hsu, H.-M., C.-J. Hsu, T.-H. Lee, and C.-S. Wang, "Noise analysis of inductive shunt-series feedback technique used in ultra-wideband low noise amplifier," *Proc. IEEE Asia Pacific Microwave Conf.*, 1136–1139, Singapore, Dec. 2009.
5. Cusmai, G., M. Brandolini, P. Rossi, and F. Svelto, "A 0.18-μm CMOS selective receiver front-end for UWB applications," *IEEE J. Solid-State Circuits*, Vol. 41, No. 8, 1764–1771, 2006.
6. Wu, H.-I., R. Hu, and C. F. Jou, "Complementary UWB LNA design using asymmetrical inductive source degeneration," *IEEE Microw. Wireless Compon. Lett.*, Vol. 20, No. 7, 402–404, 2010.
7. Dickson, T. O., K. H. K. Yau, T. Chalvatzis, A. Mangan, R. Beerkens, P. Westergaard, M. Tazlauanu, M. T. Yang, and S. P. Voinigescu, "The invariance of characteristic current densities in nanoscale MOSFETs and its impact on algorithmic design methodologies and design porting of Si(Ge) (Bi)CMOS high-speed building blocks," *IEEE J. Solid-State Circuits*, Vol. 41, No. 8, 1830–1845, 2006.
8. Kuhn, K., R. Basco, D. Becher, M. Hattendorf, P. Packan, I. Post, P. Vandervoorn, and I. Young, "A comparison of state-of-the-art nMOS and SiGe HBT devices for analog/mixed-signal/RF circuit applications," *Symp. VLSI Technology Dig. Tech. Papers*, 224–225, Honolulu, Hawaii, USA, Jun. 2004.
9. Sze, S. M., *Physics of Semiconductor Devices*, 3rd Edition, John Wiley & Sons, New York, 2007.
10. Hsieh, H. H. and L. H. Lu, "Design of ultra-low-voltage RF frontends with complementary current-reused architectures," *IEEE Trans. Microw. Theory and Tech.*, Vol. 55, No. 7, 1445–1458, 2007.

11. Sayag, A., S. Levin, D. Regev, D. Zfira, S. Shapira, D. Goren, and D. Ritter, "A 25 GHz 3.3 dB NF low noise amplifier based upon slow wave transmission lines and the 0.18 μm CMOS technology," *IEEE RFIC Symp. Dig.*, 373–376, Atlanta, GA, USA, Jun. 2008.

12. Nezhad-Ahmadi, M.-R., B. Biglarbegian, H. Mirzaei, and S. Safavi-Naieini, "An optimum cascode topology for high gain micro/millimeter wave CMOS amplifier design," *Proc. IEEE EuMIC Conf.*, 394–397, Munich, German, Oct. 2008.

13. Basaran, U., R. Tao, L. Wu, and M. Berroth, "Low-noise amplifier in 0.12 μm standard CMOS technology for K-band," *IET Electronics Letters,* Vol. 41, No. 10, 592–593, 2005.

14. Yang, H. Y., Y. S. Lin, and C. C. Chen, "0.18 μm 21–27 GHz CMOS UWB LNA with 9.3 ± 1.3 dB gain and 103.9±8.1 ps group delay," *IET Electronics Letters*, Vol. 44, No. 17, 1014–1016, 2008.

15. Wang, W. C., Z. D. Huang, G. Carchon, A. Mercha, S. Decoutere, W. De Raedt, and C. Y. Wu, " A 1 V 23 GHz low-noise amplifier in 45 nm planar bulk-CMOS technology with high-Q above-IC inductors," *IEEE Microw. Wireless Compon. Lett.*, Vol. 19, No. 5, 326–328, 2009.

Design of High Resolution MEMS Accelerometer Using Interdigital Bandpass Filter

Chandan Sharma[1], Chandra Charu Tripathi[2], Santosh Bhagat[3], and Harpreet Singh[4]

[1]Department of Electronics & Communication, Indus International University
Una, Himachal Pradesh, India
[2]Department of Electronics & Communication, Kurukshetra University, Haryana, India
[3]Department of Electronic Science, South Campus, University of Delhi, India
[4]Solid State Physics Laboratory, Defence Research & Development Organisation
Timarpur Lucknow Road, Delhi, India

Abstract— Interdigital band pass filters have been widely used in to the microwave industry because they provide reasonably good pass band characteristics, moderate loss and fairly high attenuation in the stop bands. Now with the advantage of bulk micromachining used in the MEMS fabrication technology, an interdigital band pass filter simultaneously can also be realized as an MEMS accelerometer with a very high capability of finding small changes in the acceleration in comparison to the conventional MEMS based accelerometer. Taking the advantage of a simple arc-length expression commonly used in the mathematics, acceleration is measured as change in the value of central cut off frequency due to the change in coupling of the microstrip resonators by applying the acceleration. Working on X-band region, an interdigital band pass filter of order four with the central pass frequency of 9 GHz is designed. Various structural parameters of the intedigital band pass filter are extracted from the mathematical calculations. As a starting material which should work for both microstrip resonator and also the sensor, Nickel, gold, copper and combination of these three with different thickness is used. Gold has the higher density as compared to nickel and copper and more ductile so it is mechanically more robust for behaving as a cantilever therefore fulfilling the criteria for cantilever based MEMS accelerometer, moreover due to its high conductivity value, in most of RF device metallization is done with gold with ensuring the minimum thickness of 2 μm. Therefore gold with the minimum thickness of 4 μm is optimized for both microstrip resonator as well as accelerometer and shows the best displacement and sensitivity with the applied acceleration as compared to other two materials used. In the normal operation this kind of device will behave as a filter but on applying the acceleration it will behave as a MEMS accelerometer, so it can be used in small g RF-MEMS applications and also for reliability test for the cantilevers. CST MWS-9 tool is used for the RF-part whereas mechanical simulation is carried out in the ANSYS tool. Cost of gold is the factor that plays an important role, so instead of using gold, composites that give sensitivity as comparable to the gold and have high ductile strength will be used for the future analysis.

1. INTRODUCTION

Microelectromechanical systems (MEMS) provide a class of new devices and components which display superior high-frequency performance and enable new system capabilities. For a general definition, MEMS is a miniature device or an array of devices combining electrical and mechanical components and fabricated with integrated circuit (IC) batch-processing techniques. There are several MEMS fabrication techniques, including surface micromachining and bulk micromachining. Bulk micromachining involves the creation of mechanical structures directly in silicon, gallium arsenide (GaAs), or other substrates by selectively removing the substrate materials. Recent developments in these micromachining techniques have resulted in novel high performance, low-loss micromachined filters for microwave and millimeter-wave applications. There are different types of micro machined filters; one among of them is based on the idea of suspending the microstrip on the thin substrate. Interdigital bandpass filter commonly used for microstrip implementation and the filter configuration consists of an array of n TEM-mode or quasi-TEM-mode transmission line resonators, each of which has an electrical length of 90° at the midband frequency and is short-circuited at one end and open-circuited at the other end with alternative orientation. A cantilever based MEMS accelerometers, consist of a cantilever which is fixed at one end and free at the other is used for the acceleration measurement. Now if a micostrip resonator of a filter structure is taken as the analogue for the cantilever as in the case of cantilever based MEMS accelerometer, microstrip resonator has a high resolution capability for measuring the acceleration because a very minute change in the position due to displacement of the resonator creates a large change in

coupling as compared to the conventional MEMS accelerometer in which acceleration is measured in the form of stress generated due to displacement of the cantilever. Taking this idea in account an interdigital band pass filter in addition simultaneously can be realized as the cantilever based MEMS accelerometer with very fine capability of finding the change in acceleration.

2. DESIGN

The filter configuration of an interdigital band pass filter consists of an array of n TEM-mode or quasi-TEM-mode transmission line resonators, each of which has an electrical length of 90° at the midband frequency and is short-circuited at one end and open-circuited at the other end with alternative orientation. In general, the physical dimensions of the line elements or the resonators can be different, as indicated by lengths $l_1, l_2, \ldots, l_n$ and the widths $W_1, W_2, \ldots, W_n$. Coupling is achieved by way of the fields fringing between adjacent resonators separated by spacing $s_{i,i+1}$ for $i = 1 \ldots n-1$. The filter input and output use tapped lines with a characteristic admittance Y_t, which may be set to equal the source/load characteristics admittance Y_0. An electrical length θ_t, measured away from the short-circuited end of the input/output resonators, indicates the tapping position, where $Y_1 = Y_n$ denotes the single microstrip characteristic impedance of the input/output resonator. Now, a micro machined interdigital band pass filter with bandpass center frequency of 9-GHz is designed using CST MWS-9 tool. The order of the filter is four with electrical permittivity of silicon substrate is 11.8. Various structural parameters of the filter are extracted by the mathematical calculation and tabulated below.

2.1. Length & Width of Strip:

$$l_1 = l_n = \frac{\lambda_{g01}}{4} = \Delta l_1, \quad \lambda_{g01} = \lambda_0 \sqrt{\varepsilon_{eff}}$$

$$\varepsilon_{eff} = \frac{\varepsilon_r + 1}{2} + \frac{\varepsilon_r + 1}{2} \left\{ \left(1 + 12\frac{h}{w}\right)^{-0.5} + 0.04 \left(1 - \frac{w}{h}\right)^2 \right\}$$

$$\varepsilon_r = 11.8, \quad h = 300\,\mu m$$

2.2. Spacing Between the Strips:

$$z_{0en-1,n} = \frac{1}{Y_1 - Y_{n,-1\,n}}, \quad z_{0on-1,n} = \frac{1}{Y_1 + Y_{n,-1\,n}}, \quad Y_{i,i+1} = j_{i,i+1} \times \sin\theta$$

$$\theta = \frac{\Pi}{2}\left(1 - \frac{FBW}{2}\right) \quad j_{i,i+1} = \frac{Y}{\sqrt{g_i}\sqrt{g_{i+1}}}$$

3. OPTIMIZATION OF THE STRUCTURE FOR MEMS ACCELEROMETER

As per the mechanical perspective microstrip line can behaves as an analogue for cantilever with very fine thickness that optimized for the filter. For a cantilever based MEMS accelerometer, sensitivity can be increased either by adding a proof mass at one end of the cantilever or cantilever with very fine thickness should be there. Therefore microstrip line of very fine optimized thickness fits suitable in the 2nd criterion of the way to increase the sensitivity. Taking idea from the simple arc-length formula that we commonly use in the mathematics, on applying the acceleration on the interdigital band pass filter change in acceleration can be measured out in the form of the change in the coupling of the resonators. Arc-length formula can be given as:

$$S = R\theta$$

where S = Displacement of the strip from the normal position, R = Length of the arc/strip, θ = Angle formed due to displacement of the resonator from the normal positio.

Figure below shows the structure of the filter in the CST MWS tool and corresponding analogue to the cantilever.

Next diagrams shows commonly used arc-length formula applied on a cantilever structure with proof mass attached, whereas adjacent figure displays the displacement of the resonators in ANSYS tool on applying the acceleration on the structure. Red color shows the maximum displacement whereas blue color displays the minimum displacement.

Table 1: Length and width of resonators calculated from the mathematical calculations.

ith element	length (l_i) in µm	width (w_i) in µm	$i, i+1$ element for spacing	Spacing $S_{i,i+1}$ in (µm)
0	2712	239		
1	2669	320	0	75.00
2	2669	320	1	1850
3	2669	320	2	2125
4	2669	320	3	1850
5	2712	239	4	75.00
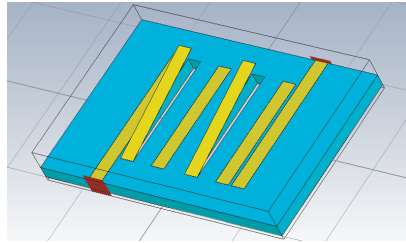
(a)   (b)

Figure 1: (a) Structure in CST MWS tool. (b) Cantilever structure analogue for microstrip.
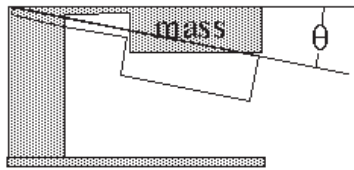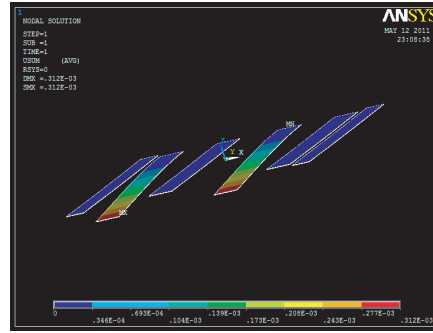
(a)   (b)

Figure 2: (a) Bending of cantilever. (b) Displacement of resonators in ANSYS-tool.
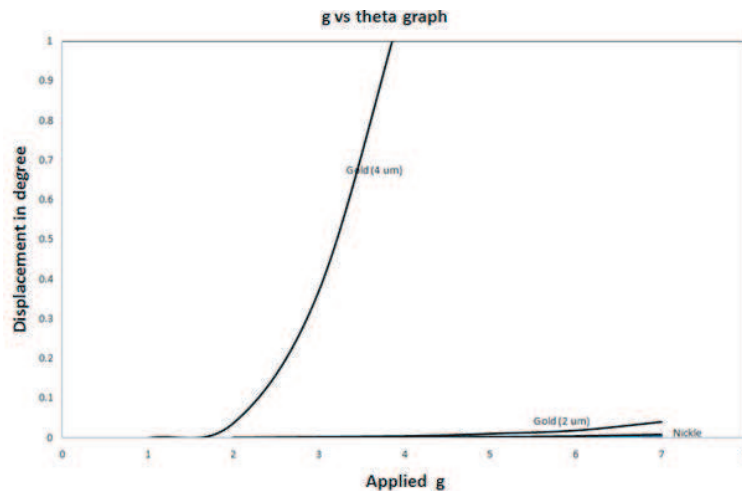
Figure 3: Displacement of the different materials in form of angle with applied acceleration (g).

4. RESULTS AND DISCUSSION

For behaving as a cantilever based MEMS accelerometer, from mechanical perspective cantilever material should be more robust and ductile and from the RF-perspective conductivity should be high. Taking into account above these considerations gold, nickel, copper and their combination materials are taken for consideration. In most of RF device metallization is done with gold with ensuring the minimum thickness of $2\,\mu$m. Therefore gold with the minimum thickness of $4\,\mu$m is optimized by simulation for both microstrip resonator as well as accelerometer and shows the best displacement and sensitivity with the applied acceleration as compared to other two materials used. Graph below shows the displacement of the structure with then applied acceleration. Gold with thickness $4\,\mu$m gives the maximum displacement as compared to nickel and the copper.

Interdigital bandpass filter response is shown in Figure 4 and Figure 5 for FBW of 1% respectively. In above response very sharp response is achieved at central cutoff frequency. In the passband region low (around $3\,$dB) insertion loss (S_{21}) is achieved in micromachined Interdigital bandpass filter with varying angle of resonator. At each central cutoff frequency there is sharp return loss is noticed. At different phases different cutoff frequency shown in tabular form in Table 2.

On applying the $1\,$g acceleration on the resonator structure ANSYS simulation of the resonator gives stress value 10239 Pa and for the $2\,$g acceleration value is almost doubled i.e., 20538 Pa. For very small changes in the value of acceleration for instance $1.5\,$g, $1.7\,$g, $1.9\,$g values of stress remain constant and through simulation and also practically not able to differentiate. But these

Table 2: Cutoff frequency at different phase value.

Angle (Degree)	Center frequency (GHz)	S_{21} (dB)
-1	8.7187	-2.81
-0.9	8.7698	-2.33
-0.8	8.7799	-2.90
-0.7	8.7718	-2.91
-0.6	8.7718	-2.80
-0.5	8.8154	-2.84
-0.4	8.7160	-2.34
-0.3	8.4888	-2.17
-0.2	8.5811	-2.60
-0.1	8.6765	-2.60
0	8.6765	-3.94
0.1	8.7144	-3.99
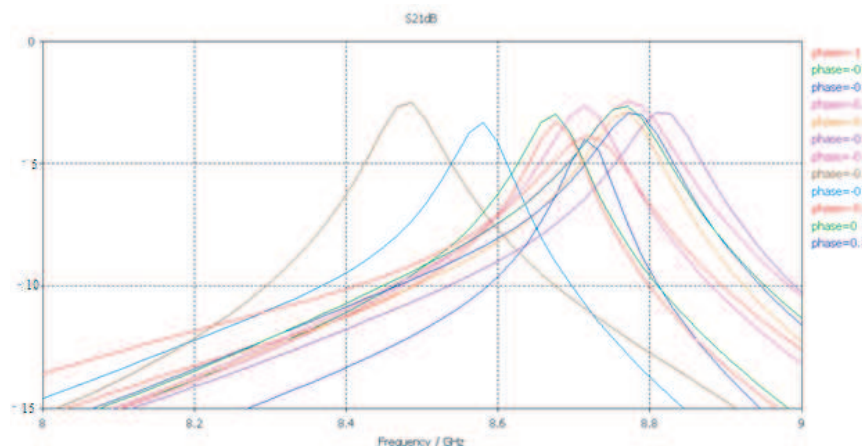
Figure 4: Frequency Response at varying angle $|S_{21}|$ in dB (Angle varying from $+1$ to -1 in a step size of 0.1).
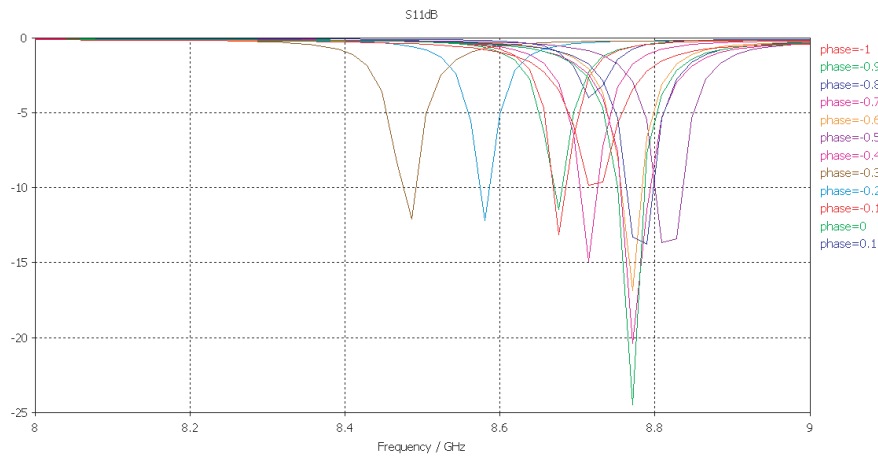
Figure 5: Frequency Response at varying angle $|S_{21}|$ in dB (Angle varying from $+1$ to -1 in a step size of 0.1).

very minute changes of acceleration can be determined due to change in coupling of the resonators cause of the angular variation which changes the central frequency as shown in table below.

5. CONCLUSION

Since with a very little change in the position of the resonators (angular variation/displacement is only 0.1 degree) with applied acceleration, there is a sharp change in the coupling of the resonators, so very fine changes in the acceleration can be detected as compared to the conventional cantilever based MEMS accelerometer where change in acceleration is found out in terms of stress generated at the fixed end of the cantilever. Therefore, in addition to accelerometer and filter purpose this can be used for the reliability test for the cantilevers where there structural deformations can be checked out on applying the pressure. Cost of gold is the factor that plays an important role, so instead of using gold, composites that give sensitivity as comparable to the gold and have high ductile strength will be used/proposed for the future analysis. Moreover design can be enhanced to measure the acceleration from other two Y and Z directions also.

REFERENCES

1. Hong, J.-S. and M. J. Lancaster, *Microstrip Filters for RF/Microwave Application*, John Wiley & Sons, 2001.
2. Matthaei, G. L., *Microwave Filters, Impedance Matching Networks and Coupling Structures*, McGraw-Hill, 1964.
3. Santuria, S. D., *Microsystem Design*, Kluwer Academic, 2001
4. Gardner, J. W. and V. K. Varadan, *Microsensors, MEMS and Smart Devices*, John Wiley & Sons, 2001.
5. Beebay, S., G. Ensell, and M. Kraft, *MEMS Mechanical Sensors*, Artech House, Inc., 2004.

A Novel Defected Microstip Structure (DMS) for Microstrip Gaps

S. R. Hosseini, **R. Sarraf Shirazi**, and **Gh. Moradi**

Wave Propagation & Microwave Measurement Research Lab., Department of Electrical Engineering
Amirkabir University of Technology, 424 Hafez Avenue, Tehran 15914, Iran

Abstract— Microstrip gap is a common discontinuity in planar structures. Circuit modeling of gap as capacitances convert microstrip line to a high pass transmission line. Novel defected microstrip structure (DMS) is presented to model gap discontinuity. 3D full wave simulations show the presented model is valid up to near 30 GHz until higher order modes features will appear.

1. INTRODUCTION

Planar structures have found useful various applications in microwave instruments fabrication and generally microwave engineering.

Producing different types of antennas, filters, couplers and etc are simple models of this increasing interest.

One of bold features of these structures is Flexibility and using changes in their structures to achieve better performance. In this regard, new structures such as defected ground structures (DGS), coupled resonators, defected microstrip structures (DMS) and etc have been developed.

Microwave discontinuity like gap, T-shape, bend, step and etc. are some common changes that apply to microwave structures for leading to specific design performances.

In this paper, gap structure studying in microstrip and presenting new structure using defected mirostrip structures (DMS) has been discussed.

2. MICROSTRIP GAP

A microstrip line can generally be assumed as transmission line. transmission lines are low pass filters that their cutoff frequencies are much higher than our common frequencies. This cut off frequency is limited by higher order modes (non Qausi-TEM).

Two general circuit models were presented for microstrip gap [1, 7]. Equivalent line length Δl_g of Fig. 3 may be calculated as [1]

$$\frac{\Delta l_g}{h} = \frac{C_p}{W} \frac{cZ_0 \dfrac{W}{h}}{\sqrt{\varepsilon_{re}}} \tag{1}$$

where ε_{re} is effective relative permeability. Values of modeled capacitors are calculated in [1].

It was been shown that gap adds capacitor to transmission line structure.since, series capacitors at two port network show high pass filters, so transmission line convert to filter that do not pass low frequencies. Cut off frequency depends on gap distance. using a simple analysis,modeling gap with first order RC high pass filter, the cut off frequency will be

$$f_c = \frac{1}{2\pi RC} \tag{2}$$

where

$$C = \varepsilon_0 \varepsilon_r \frac{A}{d} = \varepsilon_0 \varepsilon_r \frac{wt}{d} \tag{3}$$

Figure 1: Microstrip gap.
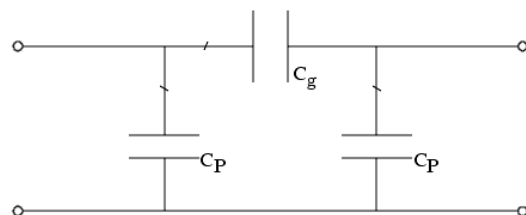
Figure 2: Microstrip gap circuit model type I.

where ε_r is relative permeability, **w** microstrip line width and **t** microstrip thickness.

Equations (2) and (3) show increasing gap distance (**d**) lead to increasing in cut off frequency and vice versa.

3. THEORY I: DMS

Defect on microstrip (DMS) was taken into consideration after developing DGS structures [2].

Disarranging current distribution on micorstrip, leads to resonators structures.theses resonators in combination with microstrip features can realize different filters. Defects circuit modeling has been getting started after [3]. The simplest model for a dumbbell shape DGS/DMS is an one pole Butterworth type filter.

DGS reactance value can be expressed as

$$X_{LC} = \frac{1}{\omega_0 C} \left(\frac{\omega_0}{\omega} - \frac{\omega}{\omega_0} \right) \tag{4}$$

where ω_0 is the resonance angular frequency of the parallel LC resonator [3].

The impedance of two above structures should be equal at certain frequency. The series capacitance C is achieved as

$$C = \frac{\omega_c}{Z_0 g_1} \frac{1}{\omega_0^2 - \omega_c^2} \tag{5}$$

where ω_c is cut off frequency. The L value can be calculated as following [3]

$$L = \frac{1}{4\pi^2 f_0^2 C} \tag{6}$$

various circuit models was expressed for different DGS units in papers [3–6].

The main problem in this type of modeling is the bandwidth that data adaption between circuit model output and full wave simulation output occurred. As a matter of fact circuit model can only be used for structures with narrow bandwidth. This model did not have enough precision for wide band performances.
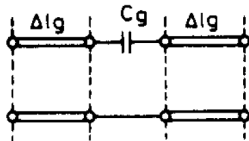
Figure 3: Microstrip gap circuit model type II.
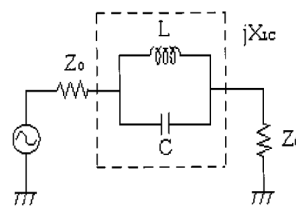
Figure 4: Equivalent circuit of dumbbell DGS.
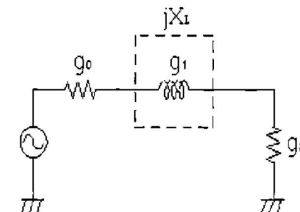
Figure 5: One pole Butterworth type filter.
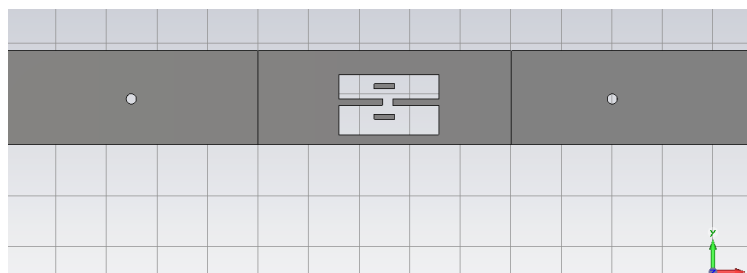
Figure 6: Novel presented DMS.
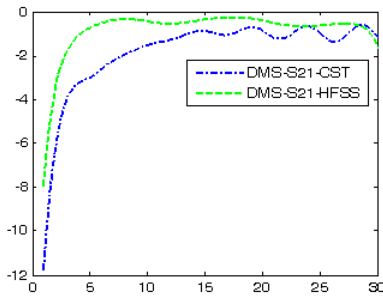
Figure 7: Presented DMS S_{21}.
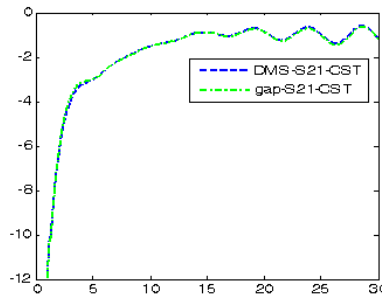
Figure 8: DMS and gap S_{21} comparison.
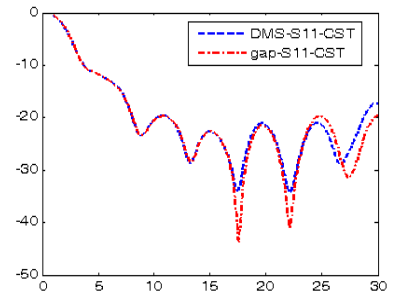
Figure 9: DMS and gap S_{11} comparison.
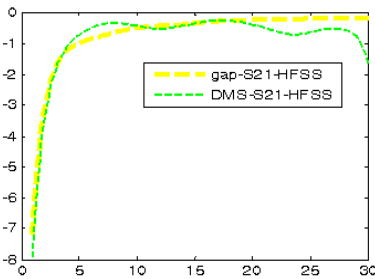
Figure 10: DMS and gap S_{21} comparison.
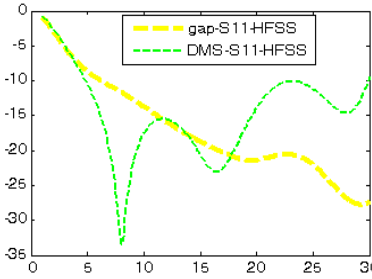
Figure 11: DMS and gap S_{11} comparison.
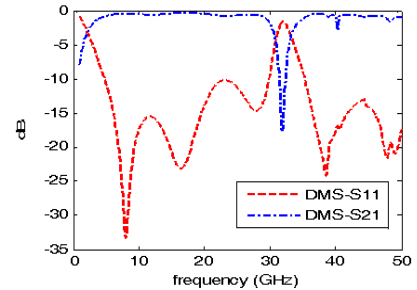
Figure 12: Higher order modes effect on DMS behavior.

4. THEORY II: OUR NOVEL DMS

Novel presented DMS is as shown in Fig. 6.

This structure was analyzed by full wave simulator software (HFSS) and CST Microwave Studio. Its S-parameters are as in Figs. 7 and 8.

It is clearly evident from Fig. 7 our novel DMS acts as high pass filter in wide bandwidth (near 20 GHz). From this point structure can be modeled with simple microstrip gap.

Figures 8 and 9 have compared S-parameters between two structures. Full wave simulation have been shown novel DMS has identical behavior to gap.

Figures 10 and 11 show HFSS simulations confirm CST results.

5. CONCLUSION

A very WB band pass filter using DMS was presented to model microstrip gap structure. this behavioral adaption was continued to approximately 30 GHz where higher order modes eliminate high pass features.

ACKNOWLEDGMENT

REFERENCES

1. Gupta, K. C., R. Grag, and I. J. Bahl, *Microstrip Lines and Slotlines*, Artech House, Norwood, MA, 1979.

2. Kim, C. S., J. S. Park, D. Ahn, and J. B. Lom, "A novel 1-D periodic defected ground structure for planar circuitss," *IEEE Microw. Wireless. Compon. Lett.*, Vol. 10, No. 4, 131–133, 2000.

3. Ahn, D., J. S. Park, C. S. Kim, J. Kim, Y. Qian, and T. Itoh, "A design of the low-pass filter using the novel microstrip defected ground structure," *IEEE Transactions on Microwave Theory and Techniques*, Vol. 49, 86–93, Jan. 2001.

4. Park, J. S., J. Kim, J. Lee, and S. Myung, "A novel equivalent circuit and modeling method for defected ground structure and its application to optimization of a DGS low pass filter," *IEEE Microwave Theory and Tech. Symp. Dig.*, 417–420, 2002.

5. Lim, J.-S., C.-S. Kim, D. Ahn, Y.-C. Jeong, and S. Nam, "Design of low-pass filters using defected ground structure," *IEEE Transactions on Microwave Theory and Techniques*, Vol. 53, No. 8, Aug. 2005.
6. Lim, J. S., C. S. Kim, Y. T. Lee, D. Ahn, and S. Nam, "A new type of low pass filter with defected ground structure," *Proc. 32nd Eur. Microwave Conf.*, 32–36, Sep. 2002.
7. Pozar, D. M., *Microwave Engineering, Reading*, 486–517, Addison-Wesley, MA, 1990.

Frequency Selective Surfaces Based Planar Microwave Absorber

F. Che Seman[1] and R. Cahill[2]

[1]Radio Communication and Antenna Design Laboratory, Faculty Electrical and Electronics Engineering
University of Tun Hussein Onn Malaysia, 86400 Batu Pahat, Johor, Malaysia
[2]The Institute of Electronics, Communications and Information Technology
Queen's University Belfast, Northern Ireland Science Park, Queen's Road, Queen's Island
Belfast BT3 9DT, Northern Ireland, UK

Abstract— In this paper we study the design principle of two types of frequency selective surfaces (FSS) based planar microwave absorber. The first type of the microwave absorber is a high impedance surface (HIS) based microwave absorber, constructed by using a periodic lossy dipoles FSS backed by a metal plate. The second type is the Salisbury screen absorber with a resistively loaded HIS. The performance of these microwave absorbers were analysed using Figure of Merit (FOM) defined as $-10\,\text{dB}$ reflectivity bandwidth divided by physical thickness normalised to the centre operating frequency. The reflectivity predictions over the frequency range 5.38–18 GHz are shown to be in good agreement with experimental results.

1. INTRODUCTION

Modern communications technology employs radio frequency absorbing surfaces for a diverse range of applications, for example to create isolation between antennas and to reduce radar visibility of platforms in military scenarios. For the latter, the absorber material must be placed on or integrated into the surface of the stealthy platform so there is much interest in developing thin, lightweight, RF absorbers which are capable of broadband operation. As is well known, this imposes conflicting requirements on the design because thin stealthy structures normally give narrowband performance and vice versa [1, 2]. Two of the most commonly used classical designs are the Salisbury screen and the Jaumann absorber. The simplest structure is the Salisbury screen which is a quarter wavelength thick [2]. Several layers can be stacked to form a Jaumann absorber which can operate over a wider bandwidth but the disadvantage is that the arrangement is much thicker [3]. More recently, configurations incorporating Frequency Selective Surface (FSS), known as Circuit Analogue (CA) absorbers, have received significant interest due to their ability to reduce the thickness of the screen and/or increase functionality. This arrangement can be further categorized into two major working groups; (i) high impedance surface based microwave absorber where the structure usually incorporates grounded FSS structure and (ii) modified classical designs i.e. Salisbury Screen absorber with FSS [4]. Research has recently been undertaken to use lossy FSS as planar microwave absorbers applied in both groups [4, 5]. In this paper we present two structures of microwave absorbers that incorporate FSS in their designs and each fall under different category. The loss mechanism exploits the terminating impedance property of an open circuit on the surface of the planar absorber which is perfectly match to free space impedance ($377\,\Omega$). The first arrangement consists of the grounded printed lossy dipole. The second arrangement modifies the classical design of the Salisbury screen absorber by replacing the metallic plate with the high impedance surface which is employed in the first arrangement. For quick comparison FOM is used to evaluate the performance of these absorbers. The prototype of the absorber is modeled as an infinite array in CST Microwave Studio. Experimental results are shown to be in very good agreement with numerical predictions.

2. THEORY OF OPERATION

A general equivalent circuit FSS can be represented by components of L, R and C as shown in Figure 1(a) [6]. In general the pattern shape of the FSS determines the value of L and C depending on the plane excitation. The loss incurred in the FSS is represented by component R. Meanwhile a metal backed FSS, which is separated by a dielectric substrate determines component L_h.

In this paper, the dipole array is employed in the design so the component C of the FSS is negligible. By adding a loss component, R to the conducting surface of the dipole array, the HIS can be employed as an absorber where it attenuates the incident signal at the resonance. The structure is usually very thin but high performance operation is only achievable over a very narrow band [5, 7]. The HIS absorber can be embedded in another type of absorber for example Salisbury screen absorber and the equivalent circuit can be represented as shown in Figure 1(b). The present
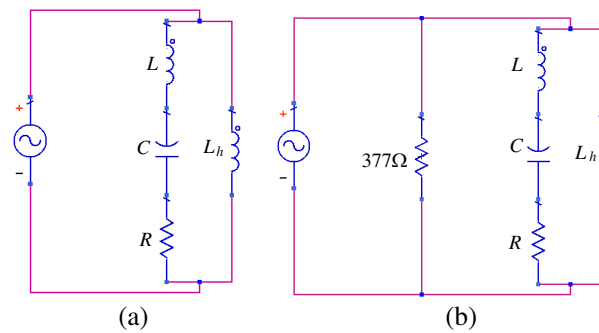
Figure 1: Equivalent circuit of (a) the HIS based absorber (b) the modified Salisbury screen design with a resistively FSS in a unit cell.
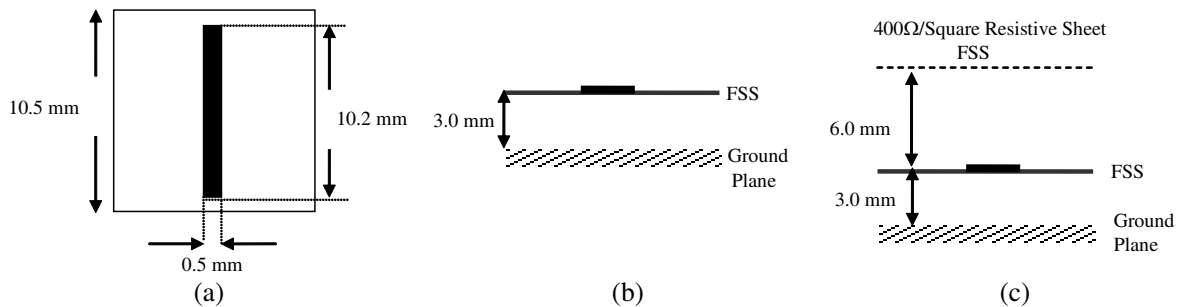

Figure 2: Schematic of FSS based planar microwave absorber. (a) Unit cell dimensions of dipole array. (b) First arrangement using high impedance surface absorber. (c) Second arrangement using modified Salisbury screen design.

of FSS modifies the field distribution in the classical Salisbury screen design and by careful design; it can enhance the overall bandwidth of the Salisbury screen absorber. To demonstrate the capability of the HIS and modified Salibury screen absorber, Figure of merit (FOM) is used and defined as below;

$$\text{FOM} = \frac{-10\,\text{dB reflectivity bandwidth}}{\text{electrical thickness}} \tag{1}$$

where the electrical thickness is normalized to the centre operating frequency of the absorber.

3. PHYSICAL ARRANGEMENT AND NUMERICAL RESULTS

CST Microwave Studio was used to optimize the design and obtain the physical dimensions of the grounded printed dipole FSS which was modeled as a unit cell in an infinite array environment. Figure 2 shows the physical arrangement of the two microwave absorbers. In the numerical arrangement, the lossy periodic array was printed by $5\,\Omega/\text{sq}$ patch resistive ink on a single sided $0.36\,\text{mm}$ thick dielectric substrate with permittivity of 2.31. These values were used to justify the measured parameters obtained in the later section. In both arrangement, the periodic array was separated from the ground plane by foam spacers (Rohacell, $\varepsilon_r = 1.05$) of thickness $3\,\text{mm}$ as shown in Figure 2. In second arrangement, a $400\,\Omega/\text{square}$ resistive sheet was attached to separated from the metal ground plane by a $6\,\text{mm}$ thick Rohacell spacer with permittivity value 1.05 [8].

The predicted reflectivity of the HIS based microwave absorber operating at normal incidence is depicted in Figure 3(a). The dipole array resonates at $9.92\,\text{GHz}$ where the reflection loss is more than $20\,\text{dB}$. This shows that the lossy dipoles generate a significant absorbing band at the resonant frequency. It is demonstrated that reflectivity of the microwave absorber is less than $-10\,\text{dB}$ between 8.85–$10.68\,\text{GHz}$; giving 18.4% at the centre operating frequency of $9.76\,\text{GHz}$. As the frequency increases/decreases away from the centre resonance, the attenuation of the HIS absorber degrades. The electrical thickness of the structure is $\lambda/10.2$ normalized to the centre operating frequency and the FOM is 188. Figure 3(b) shows the predicted $-10\,\text{dB}$ reflectivity of the modified Salisbury screen is 98.4% normalized to the centre frequency of $9.92\,\text{GHz}$ while the electrical thickness of the structure is $\lambda/3.6$. However the FOM of the modified Salisbury screen absorber is 354, nearly double the value obtained by using HIS based absorber. The two absorbing
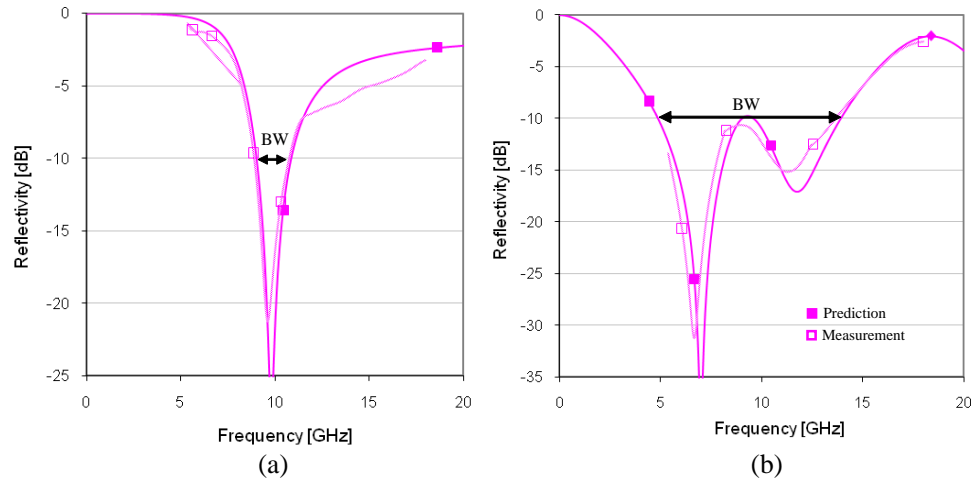
Figure 3: Computed and measure reflectivity of (a) HIS based absorber (b) modified Salisbury screen design.

bands of the modified Salisbury screen are generated when the incident signals are reflected from either the FSS or the ground plane [4]. Here the spectral behavior of the FSS is exploited to suppress the reflection peak so the two absorbing bands are merged and provides wider operating band Furthermore, the FOM is slightly improved compared to the classical design of the Salisbury screen absorber which is 308 [4].

4. EXPERIMENTAL RESULTS

Microwave absorbers were fabricated and measured to experimentally validate the numerical results presented in the previous section. The FSS was prototyped using Y SHIELD HSF-54 electro-conductive shielding paint [9] which was stencil printed on a $0.36\,m$ thick $20\,cm \times 30\,cm$ A4 paper ($\varepsilon_r = 2.31$) and bonded to $3\,mm$ thick backed Rohacell form spacer to form a HIS and consequently the modified Salisbury screen. A mean measured resistance value of approximately $5\,\Omega/sq$ was obtained by fitting predicted spectral reflection coefficients to the experimental data obtained for the HIGP. The manufacture of the Salisbury screen absorbers was completed by glueing the surfaces of a $6\,mm$ thick foam spacer, to the patterned side of the FSS and a $400\,\Omega/square$ resistive textile sheet, EeonyTex^{TM} [10]. Time gated bi-static reflection measurements were made in an anechoic chamber relative to a $20 \times 30\,cm$ metal sheet which was placed $50\,cm$ distance from the aperture of three pairs of standard gain horns which cover the frequency range 5.4–$18\,GHz$. The measured reflectivity plots for the two FSS based planar microwave absorber at normal incidence are plotted in Figure 3. Both the predicted and measured results are in a very good agreement.

5. CONCLUSIONS

This paper has presented two structure of FSS based planar microwave absorber which exploits the spectral response of a resistively loaded dipole FSS. In HIS based absorber, the lossy dipole provides significant absorption band near to the resonant frequency. In the modified Salisbury screen, the losses are required to suppress the reflection peak to significantly increase the reflectivity bandwidth of a Salisbury screen absorber. The modified Salisbury screen is found to have larger FOM compare to the HIS based absorber. The design methodology and numerical results have been validated by measuring the performance of a prototype structure which was manufactured using a low cost carbon loaded paint to print the FSS.

REFERENCES

1. Rozanov, K. N., "Ultimate thickness to bandwidth ratio of radar absorbers," *IEEE Transactions on Antennas and Propagation*, Vol. 48, No. 8, 1230–1234, 2000.
2. Chambers, B., "Optimum design of a Salisbury screen screen radar absorber," *Electronics Letters*, Vol. 30, No. 16, 1353–1354, 1994.
3. Munk, B. A., P. Munk, and J. Pryor, "On designing jaumann and circuit analog absorbers (CA absorbers) for oblique angle of incidence," *IEEE Transactions on Antennas and Propagation*, Vol. 55, No. 1, 186–193, 2007.

4. Seman, F. C. and R. Cahill, "Performance enhancement of Salisbury screen absorber using resistively loaded spiral FSS," *Microwave and Optical Technology Letters*, Vol. 53, No. 7, 1538–1541, 2011.

5. Costa, F., A. Monorchio, and G. Manara, "Analysis and design of ultra thin electromagnetic absorbers comprising resistively loaded high impedance surfaces," *IEEE Transactions on Antennas and Propagation*, Vol. 58, No. 5, 1551–1558, 2010.

6. Munk, B. A., *Frequency Selective Surfaces: Theory and Design*, Wiley-Interscience, New York, 2000.

7. Sievenpiper, D., "High-impedance electromagnetic surfaces," Ph.D. Dissertation, University of California, 1999

8. Y Shield EMR Protection, http://www.yshield.com, accessed Sep. 2010.

9. Taconic Advanced Dielectric Division, www://taconic-add.com, accessed, Jan. 2010.

10. EeonTex Conductive Textiles, http://www.eeonyx.com, accessed Jul. 2010.

Performance Analysis of Complementary and Non-complementary EBG Geometries

Gnanam Gnanagurunathan and Krishnasamy T. Selvan

Department of Electrical and Electronic Engineering
The University of Nottingham, Malaysia Campus
Selangor Darul Ehsan 43500, Malaysia

Abstract— In this work, the bandgap of complementary and non-complementary form of various EBG geometries is characterized. The transmission line analysis method is used for this purpose and the bandgap is observed based on S_{11} and S_{21} measurements across a 2 port transmission line. Five fundamental geometries namely, square, circle, cross, spiral and hexagon are analyzed in both the complementary and non-complementary forms. With the exception of square EBG geometry, an analysis of the rest through simulation and measurement show that the complementary form sees a significant shift in the bandgap to lower frequencies and offers wider bandgap when compared to the non-complementary form.

1. INTRODUCTION

This paper analyses the bandgap occupancy of the Electromagnetic Bandgap (EBG) structures. These structures are currently of interest in the electromagnetic fraternity. These structures are periodic in nature and are able to prevent the propagation of surface electromagnetic waves in a specified band of frequency hereby known as the bandgap.

Planar EBG structures have low profile, low cost and ease of fabrication. Therefore, many researchers have investigated the performance of the planar EBG structure. Increasing the bandgap of the EBG structure [1–3], improving performance by suppressing ripples [4], achieving miniaturization with interdigital structures [5] and parametric analysis on the effect of the EBG shape patterns [6, 7] have been investigated extensively. All these work are carried out by etching the EBG units on the ground plane of a transmission line. This is in fact one of the possible approaches to characterize the EBG bandgap.

In this paper, five fundamental geometries namely, square, circle, cross, spiral and hexagon are analyzed in both the complementary and non-complementary forms. Preliminary simulations are carried out on a commercial simulator, the CST Microwave Studio. Based on the results, the models are fabricated and measurements carried out with an Agilent 8757D Scalar Network Analyzer for verification. Both simulation and experimental results are in good agreement for all cases.

2. METHOD

Five fundamental geometries; square, circle, cross, spiral and hexagon are chosen and analyzed in both the complementary and non-complementary forms. A filling ratio, r/a (r is the EBG size and a is the periodicity of the EBG units backing the transmission line) of approximately 0.5 to 0.6 is maintained for all the geometries.

The RF laminate used is TLY-5, with a dielectric constant of 2.2. The dielectric thickness is 0.79 mm and tangential loss is 0.002. The copper thickness is 0.035 mm. On the top plane, there is a transmission line with a width of 2.4 mm corresponding to a 50 ohm conventional microstrip line. The height and width of the substrate is 20 mm and 140 mm respectively.

These microstrip transmission lines with a deflected ground plane are used for the bandgap analysis. The transmission line is modeled on one side of the RF laminate while the other side is lined with a single row of EBG units. The bandgap is observed based on S_{21} and S_{11} measurements across a 2 port transmission line. Decay on the S_{21} measurement below -20 dB indicates the surface wave bandgap. Meanwhile, this is also reflected by the S_{11} above -10 dB. In this work, bandgap is considered to be identified if both simulation and experimental results are in compliance with the S-parameter threshold. This would be the region over which the surface waves will be substantially attenuated. Measurements for both simulation and experiment are observed over a frequency range of 1 to 20 GHz.
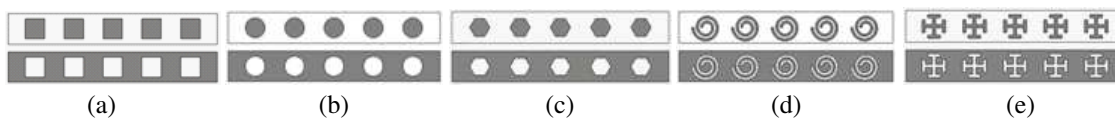
Figure 1: Back profile of the 2-port transmission line with the complementary (bottom) and non-complementary (top) geometries, (a) square, (b) circle, (c)hexagon, (d) spiral and (e) cross (the grey area is PEC).

(a)   (b)
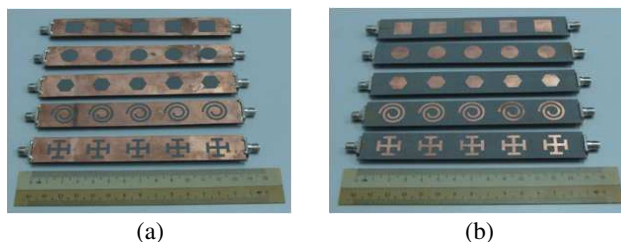
Figure 2: Back profile of the fabricated 2-port transmission line with the (a) complementary and (b) non-complementary geometries.
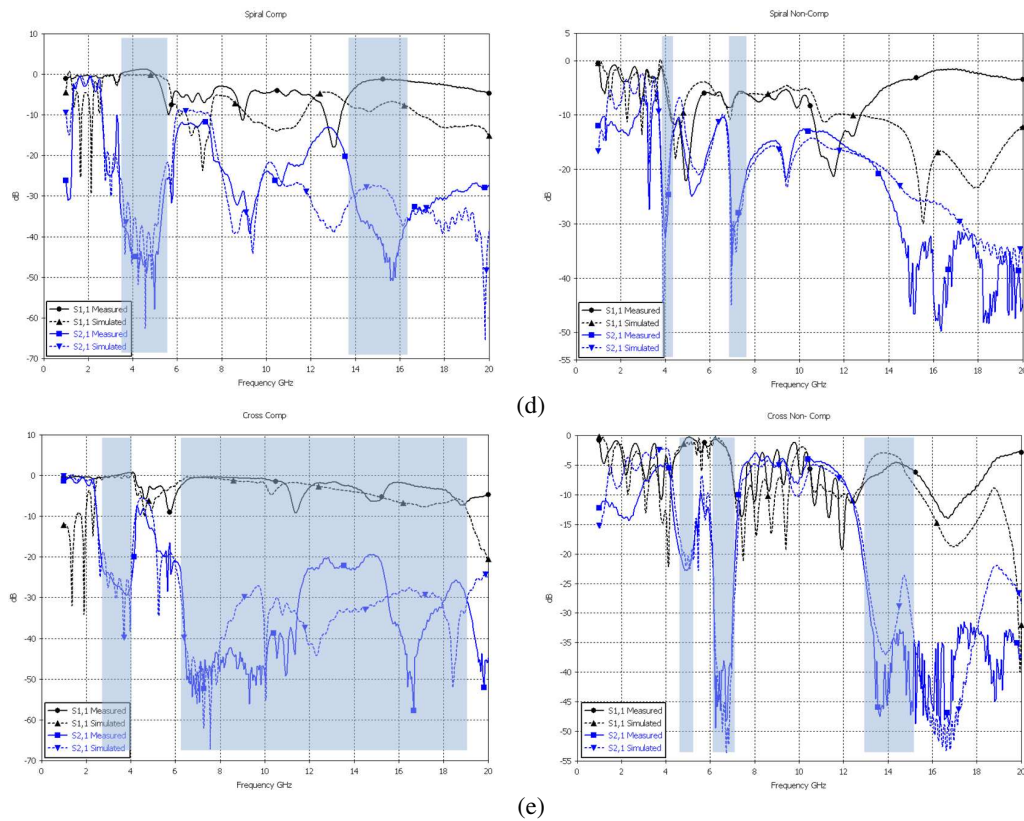

(a)

(b)

(c)
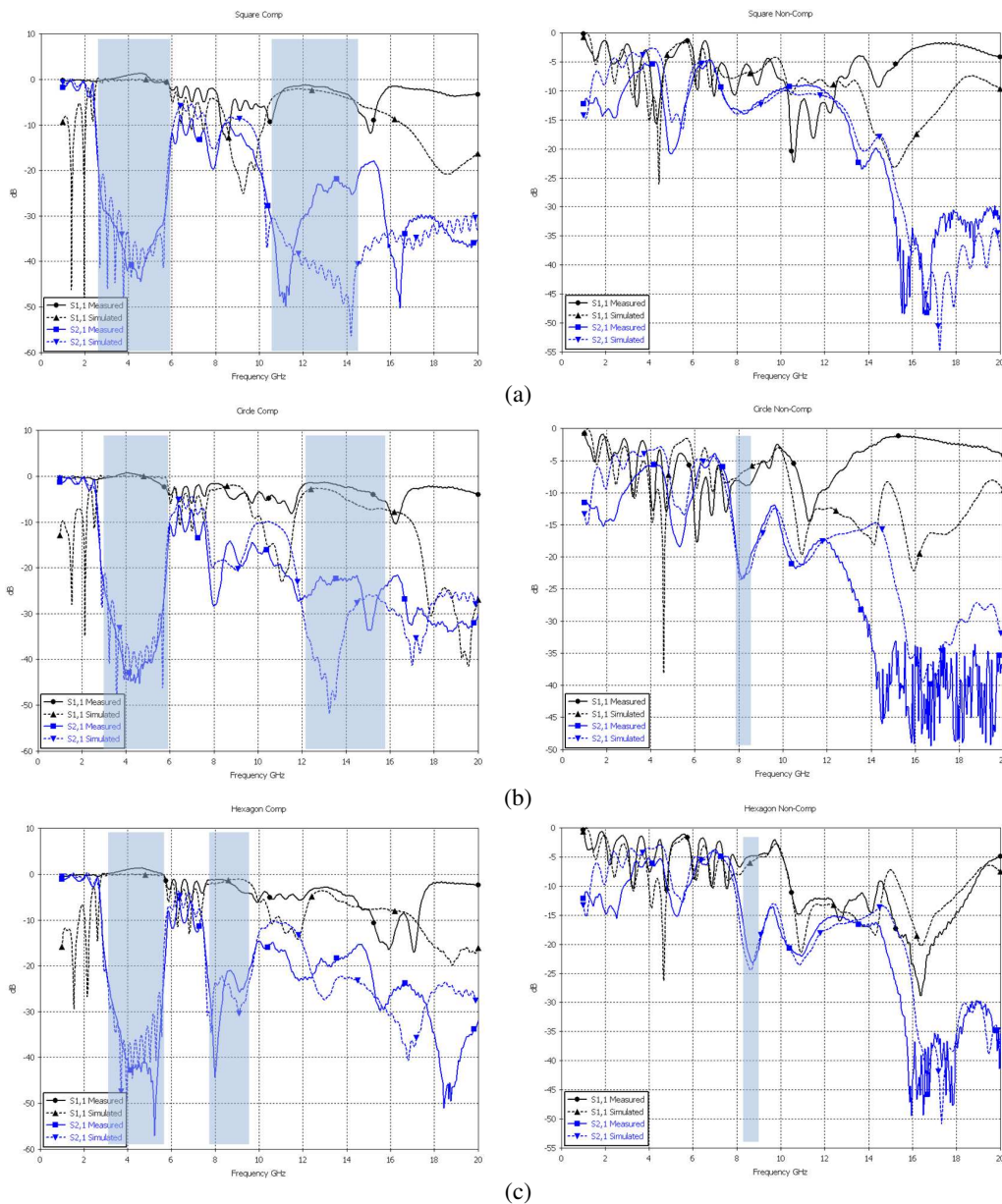
Figure 3: S_{11} and S_{21} simulation and measurements plots of complementary (left; denoted with "comp" in plots) and non-complementary (right; denoted as "non-comp" in plots) geometries, (a) square, (b) circle, (c) hexagon, (d) spiral and (e) cross. The bandgap is shaded.

3. SIMULATION AND EXPERIMENTAL RESULTS

The five geometries are modeled and simulated in CST microwave as studio shown in Figure 1. The gray area is Perfect Electric Conductor (PEC). The square geometry has a side of 13×13 mm. The circular geometry has a diameter of 13 mm. The hexagon has a side of 6.5 mm and diameter of 13 mm. The spiral has 2 turns, thickness of the spiral is 1.5 mm and entire occupancy of the spiral spans over 15 mm. The cross has 4 arms, height and width of 15 mm and thickness of 2 mm. The period of the EBG cells are prefixed at 26 mm. The fabricated models are shown in Figure 2.

Figure 3 shows the simulation and experimental results of all the 5 geometries. All the complementary geometries exhibit two bandgaps throughout the observation range. The first bandgap is all centered approximately at 4 GHz with a bandgap width of about 2–3 GHz. However, the cross's bandgap is centered at 3 GHz. The second bandgap does not have a common center frequency for all the geometries. Interestingly, the complementary cross exhibits the widest second bandgap from 6.2 GHz up to 19 GHz.

The non-complementary geometries, on the other hand, show much narrower bandgap at higher frequencies in comparison to the complementary forms. The non-complementary square exhibits no significant bandgap at all. A very narrow bandgap is observed for the non-complementary circle, hexagon and spiral geometries. The non-complementary cross shows two narrow bandgaps centered at 5 GHz and 6.5 GHz. The third bandgap is wider and centers around 14 GHz.

The measurement and simulation results of the non-complementary geometries (except cross) become insignificant beyond 13–14 GHz. The non-complementary cross's plot becomes insignificant beyond 15 GHz. This is due to the S_{11} and S_{21} plots that are not reflective of one another.

4. CONCLUSIONS

In this paper, the bandgap of complementary and non-complementary EBG unit cells placed on the reverse of a 2-port transmission line was analyzed. Except for the cross geometry, all geometries indicated significant downward shift in the bandgap and wider bandgap width. The complementary cross was observed to have a very wide second bandgap. The performance is qualitatively discussed

thereby enabling EBG based planar antenna, filter and coupler designs to benefit from this study.

REFERENCES

1. Chiau, C. C., X. Chen, and C. Parini, "Multiperiod EBG structure for wide stopband circuits," *IEE Proceedings — Microwaves, Antennas and Propagation*, Vol. 150, 489–492, 2003.
2. Lin, B. Q., X. Y. Ye, X. Y. Cao, and F. Li, "Uniplanar EBG structure with improved compact and wideband characteristics," *Electronics Letters*, Vol. 44, 1362–1363, 2008.
3. Ruiz, J. D., F. L. Martínez, and J. Hinojosa, "1D Koch fractal electromagnetic bandgap microstrip structures with r/a ratios higher than 0.5," *Microwave and Optical Technology Letters*, Vol. 53, 646–649, 2011.
4. Padhi, S. K., "Improved performance of EBGs on a co-planar transmission line using tapered distribution," *Microwave and Optical Technology Letters*, Vol. 42, 128–131, 2004.
5. Lin, B.-Q. and X. Wen, "A novel uniplanar compact EBG incorporated with interdigital structure," *Microwave and Optical Technology Letters*, Vol. 50, 555–557, 2008.
6. Menon, S. K., K. Vasudevan, C. K. Aanandan, and P. Mohanan, "Design and analysis of microstrip lines with EBG-backed ground planes of different geometrical shapes," *Microwave and Optical Technology Letters*, Vol. 46, 544–546, 2005.
7. Moghadasi, S. M., "Compact and Wideband 1-D mushroom-like EBG filters," *Progress In Electromagnetics Research*, Vol. 83, 323–333, 2008.

Simulation of Sensorless Control of Induction Motor Using HIL Method

P. Brandstetter, M. Dobrovsky, and P. Krna

Department of Electronics, VSB-Technical University of Ostrava, Czech Republic

Abstract— The paper deals with simulation of sensorless control of the induction motor using hardware in the loop simulation method (HIL) in Matlab-Simulink. The first part of the paper deals with the description of a vector controlled induction motor with the sensorless control using the model reference adaptive system (MRAS). The second part describes HIL method and its implementation using modern digital signal controller. In the last part, simulation results for different speed changes of the induction motor are shown.

1. INTRODUCTION

Very different methods for supplying three-phase induction motors from a DC voltage source, and for controlling torque and speed as well, have been developed in the past [1–7].

The hardware in the loop simulation method (HIL) was implemented at the Department of Electronics, VSB-Technical University of Ostrava. The drive is simulated by a personal computer while the control algorithm runs in the microcomputer control system with modern digital signal processor. This kind of simulation was used in order to check the control algorithm with the actual control microcomputer and to minimize the number of undesired situations during putting electric drive into operation. The experience with that way of simulation shows that control algorithm debugging is easier and putting electric drive into operation usually does not create any large problems.

2. SENSORLESS CONTROL OF INDUCTION MOTOR

For the sensorless control of the induction motor, the method using MRAS was selected. The MRAS observer structure is shown in Figure 1.

In this system, induction motor state variables are evaluated in the reference model based on the measured variables (stator voltages, stator currents). The reference model is independent of the speed and uses the voltage model of the induction motor. The adaptive model uses the current model and the mechanical angular speed of the motor is one of the input variables of this model.

The difference between state variables (rotor fluxes $\hat{\boldsymbol{\Psi}}_R^S$, $\boldsymbol{\Psi}_R^S$) is adaptive signal (AS) $\Phi_{(e)}$, which is evaluated and minimized by the PI regulator in the block of the adaptation mechanism, which performs the estimate value of the mechanical angular speed ω_m and adapts adaptive model. With feedback, the observer is able to limit the impact of changes in machine parameters on the accuracy of the calculation.

The error signal $\Phi_{(e)}$ corresponding to the deviation of rotor fluxes (Equation (1)) enters to the PI controller, after processing by PI controller, we get estimated angular speed ω_m (Equation (2)).
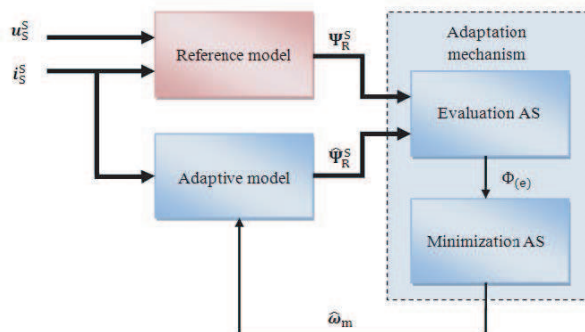
Figure 1: MRAS — basic scheme.
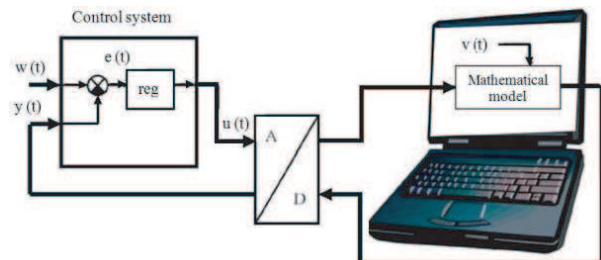
Figure 2: Block scheme of Hardware in the Loop Simulation.

The adaptation algorithm is described with the following equations ($K_1 > 0$, $K_2 > 0$):

$$\Phi_{(e)} = \hat{\mathbf{\Psi}}_R^S \times \mathbf{\Psi}_R^S = \hat{\Psi}_{R\alpha}\Psi_{R\beta} - \hat{\Psi}_{R\beta}\Psi_{R\alpha} \tag{1}$$

$$\hat{\omega}_m = K_1\Phi_{(e)} + K_2 \int_0^t \Phi_{(e)}\, dt \tag{2}$$

3. HARDWARE IN THE LOOP SIMULATION

Hardware in the Loop (HIL) is a tool that connects the hardware (controller) with a mathematical model (controlled system) in a closed feedback loop. To simulate this method, a real microcomputer control system and a mathematical model in an appropriate software environment are required.

The mathematical model is used to configure the control system. The control system generates an actuator variable dependent on the control deviation, which is the difference between desired and actual quantity. The control variable enters to the model, then output variable (actual value) gets off from the mathematical model, and then gets back to the control system. This simulation works in real time.

Results of this simulation approach to reality, because the control system with sensors and actuators is implemented as close as it would be in real. To the fact that the results would match the reality, we need a sufficiently accurate mathematical model, on which simulation accuracy dependents most. As soon as the control system is set up according to the requirements, the mathematical model can be replaced by the real system and the results can be compared.

The Figure 2 shows a general diagram of the simulation using method hardware in the loop. The meaning of values in this picture: $y(t)$ — process value, $w(t)$ — reference quantity, $e(t)$ — control error, $u(t)$ — control variable, $v(t)$ — fault value, reg — regulator.

4. MULTIFUNCTION I/O CARD MF 624

The MF 624 multifunction I/O card is designed for the connection of the PC compatible computer to the real signals from outside. The card contains a fast 8-channel 14-bit A/D converter with simultaneous sampling of multiple channels and function of storage measured values from the A/D conversion, 8 independent 14-bit D/A converter, 8-bit digital inputs, 8 bit digital outputs and quintuple timer/counter.

The card is designed for standard data acquisition and control applications and is optimized for use with the Real Time Toolbox for Simulink. The card offers full 32-bit architecture for fast data processing. The multifunction I/O card MF 624 has no switches or jumpers, and can be installed in any available PCI slot.
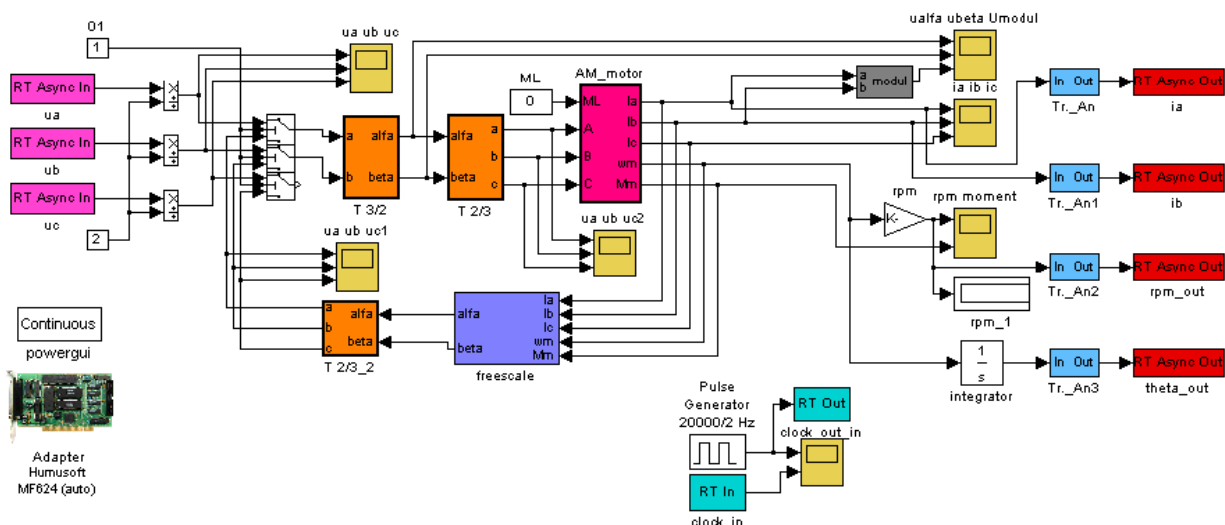
Figure 3: Simulation scheme of the induction motor in Matlab-Simulink.

5. SIMULATION RESULTS

The sensorless control was tested in the different conditions and at different changes of the rotor angular speed. The simulation model of the induction motor was performed in Matlab-Simulink (see Figure 3). The simulation results of sensorless control were recorded by program for setting control variables in LabVIEW environment (see Figure 4). The control variable magnetizing current is set to 4.8 A. The reference speed is set, first at 50 rpm, resp. 200 rpm, and then is changed to −50 rpm, resp. −200 rpm. The Figures 5–8 show the time responses of important quantities.
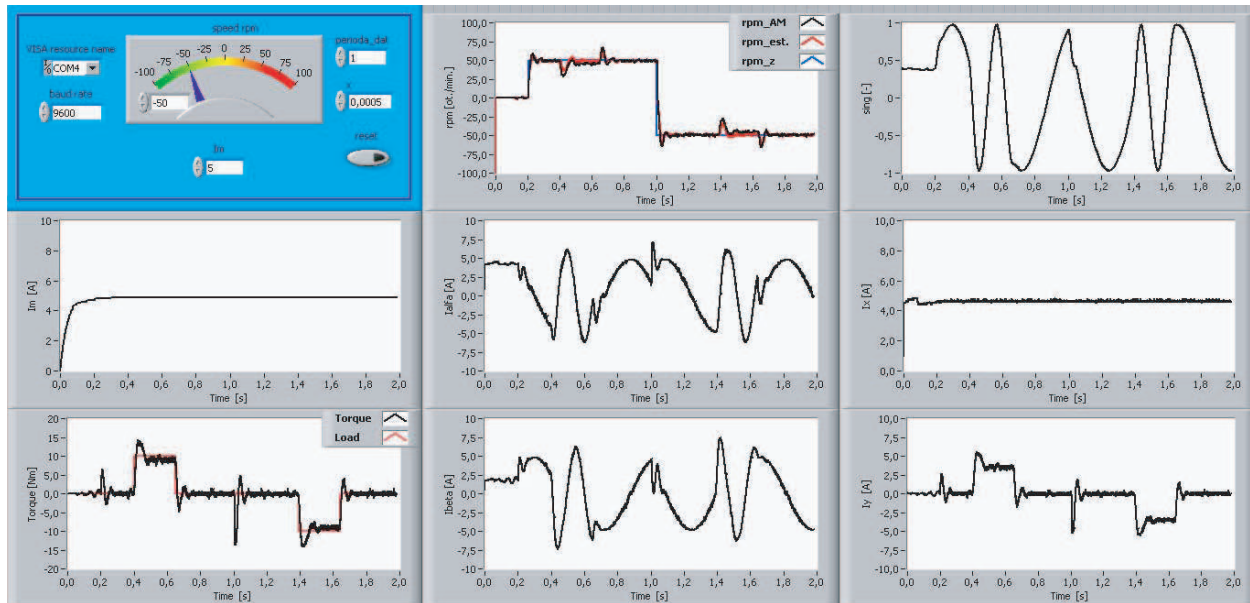
Figure 4: Program in Labview environment for setting control variables and imaging the quantities of the vector contro.
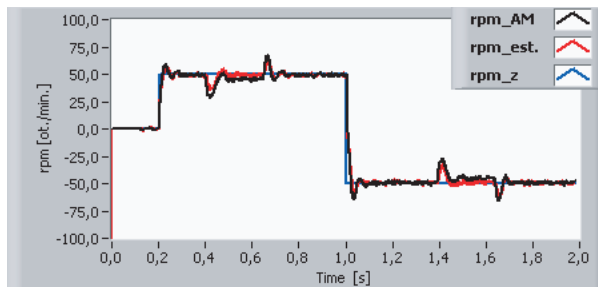
Figure 5: Reference speed 50 rpm (blue), real speed (black) and estimated (red) speed.
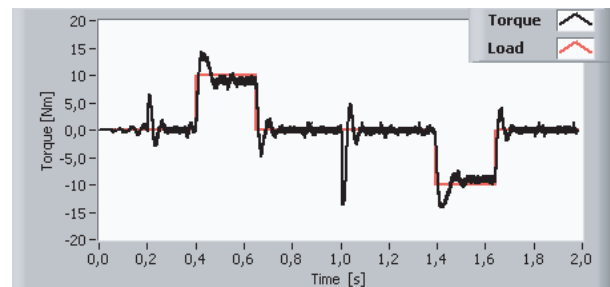
Figure 6: Motor torque (black) and load torque 10 Nm (red).
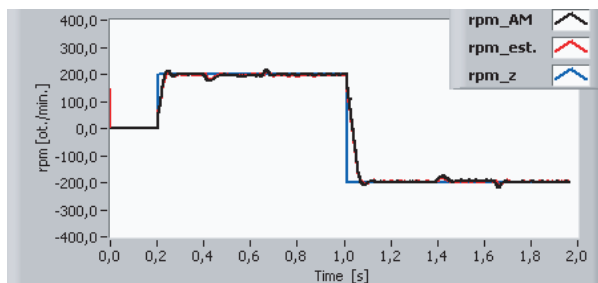
Figure 7: Reference speed 200 rpm (blue), real speed (black) and estimated (red) speed.
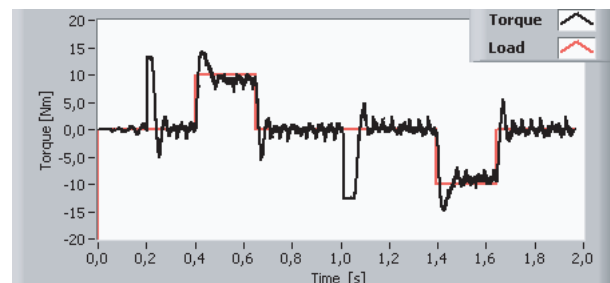
Figure 8: Motor torque (black) and load torque 10 Nm (red).

6. CONCLUSIONS

Hardware in the Loop (HIL) simulation is a technique that is used in the experimental test and development of complex real-time systems. The paper shows a possibility its application in the control of electrical drives with the induction motors. Obtained simulation results confirm expected application possibilities.

ACKNOWLEDGMENT

REFERENCES

1. Holtz, J., "Sensorless control of induction motor drives," *Proceedings of the IEEE*, Vol. 90, No. 8, 1359–1394, 2002.
2. Finch, J. W. and D. Giaouris, "Controlled AC electrical drives," *IEEE Transactions on Industrial Electronics*, Vol. 55, No. 2, 481–491, 2008.
3. Lascu, C., I. Boldea, and F. Blaabjerg, "Comparative study of adaptive and inherently sensorless observers for variable-speed induction-motor drives," *IEEE Transactions on Industrial Electronics*, Vol. 53, No. 1, 57–65, 2006.
4. Orlowska-Kowalska, T. and M. Dybkowski, "Stator-current-based MRAS estimator for a wide range speed-sensorless induction-motor drive," *IEEE Transactions on Industrial Electronics*, Vol. 57, No. 4, 1296–1308, 2010.
5. Sutnar, Z., Z. Peroutka, and M. Rodic, "Comparison of sliding mode observer and extended Kalman filter for sensorless DTC-controlled induction motor drive," *Conference Proceedings, 14th International Power Electronics and Motion Control Conference — EPE/PEMC*, T7-55–T7-62, 2010.
6. Gadoue, S. M., D. Giaouris, and J. W. Finch, "Sensorless control of induction motor drives at very low and zero speeds using neural network flux observers," *IEEE Transactions on Industrial Electronics*, Vol. 56, No. 8, 2009.
7. Yi, L. and H. Mei, "Speed sensorless IM control system based on MRAS and NN flux observers," *Conference Proceedings, 3rd International Conference on Advanced Computer Theory and Engineering (ICACTE)*, V5-163–V5-167, 2010.

Optimization of Indirect Space Vector Modulation Strategy for Matrix Converter

D. Kuzmanovic and J. Lettl

Faculty of Electrical Engineering, Czech Technical University in Prague, Czech Republic

Abstract— Due to the absence of energy storage elements, conventional modulation strategies cannot be applied to the matrix converter. For that reason, a range of modulation strategies specific to the matrix converter have been developed. The selection of the modulation strategy and the switching pattern does not impact only the quality of the input and output quantities, but also the switching losses. In this paper, the analysis of the matrix converter switching losses, when the Indirect Space Vector Modulation (ISVM) is used, is presented. It was shown, how a simple modification of the modulation strategy can lead to a significant decrease of the switching losses. A software tool for the evaluation of the matrix converter losses was designed. The analysis of the matrix converter switching losses performed with this tool has shown that the use of the optimized modulation strategy decreases the switching losses by up to 20%.

1. INTRODUCTION

The matrix converter is a forced commutated converter, which uses an array of controlled bi-directional switches as power elements to create a variable output voltage system (Figure 1). Matrix converter modulation strategies can be classified into the Modulation Duty Cycle Matrix (MDCM) based strategies, and the Space Vector Modulation (SVM) based strategies [1, 2]. MDCM strategies calculate individual bi-directional switches duty cycles by solving the matrix converter input-output equations. SVM strategies can be direct and indirect. The Direct SVM strategy combines all matrix converter switching combinations (vectors) to generate the reference output voltage and the input current vectors.

The Indirect SVM (ISVM) observes the matrix converter as an equivalent combination of an input virtual rectifier and an output virtual inverter, connected by a virtual DC-link [3] (Figure 2). The virtual rectifier is then controlled as the classical current source rectifier, and the virtual inverter as the classical voltage source inverter [4, 5] (Figure 3). The duty cycles are obtained from the following equations

$$d_\alpha = m_U \cdot \sin\left(\frac{\pi}{3} - \theta_{S-U}\right), \quad d_\beta = m_U \cdot \sin\left(\theta_{S-U}\right), \quad d_{0U} = 1 - d_\alpha - d_\beta \tag{1}$$

$$d_\gamma = m_I \cdot \sin\left(\frac{\pi}{3} - \theta_{S-I}\right), \quad d_\delta = m_I \cdot \sin(\theta_{S-I}), \quad d_{0I} = 1 - d_\gamma - d_\delta \tag{2}$$

where m_U and m_I are the output voltage and the input current modulation indexes, and d_{0U} and d_{0I} are the duty cycles of the voltage and current zero vectors.

The selection of the virtual rectifier and the virtual inverter stages switching combinations for each combination of the input current vector and the output voltage vector sectors is illustrated in Table 1.

Unlike the classical AC/AC converters, where the energy storage element in the DC link enables independent operation of the input rectifier and the output inverter, in the case of the matrix
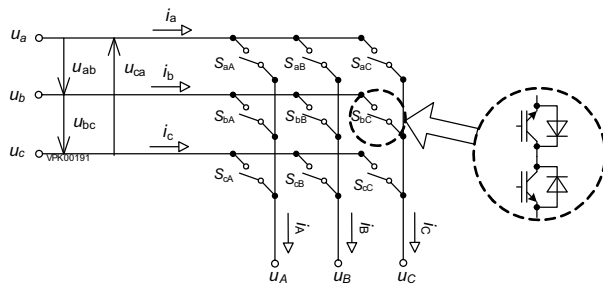
Figure 1: Matrix converter.
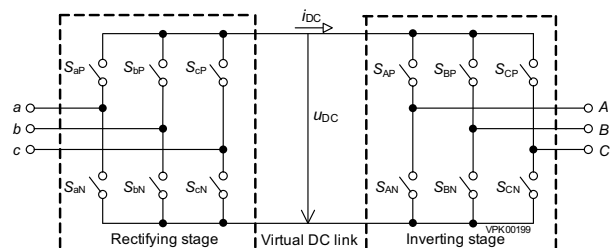
Figure 2: Matrix converter equivalent circuit for indirect modulation.

converter the operation of the input and output stages has to be precisely coordinated. That is achieved by synchronizing the input and output SVM, and by choosing a suitable switching pattern (Figure 4). The upper part of the switching pattern illustrated in Figure 4 shows the switching of the virtual rectifier stage (in this case the virtual DC link voltage is formed by alternating input line voltages u_{ab} and u_{ac}), and the lower part shows the switching of the virtual inverter stage (in this case the virtual inverter output voltage is formed by combining switching combinations 100 — virtual DC link current is equal to the converter output phase current i_A, 110 — virtual DC link current is equal to the converter output phase current $-i_C$, and 111 — virtual DC link current is zero).
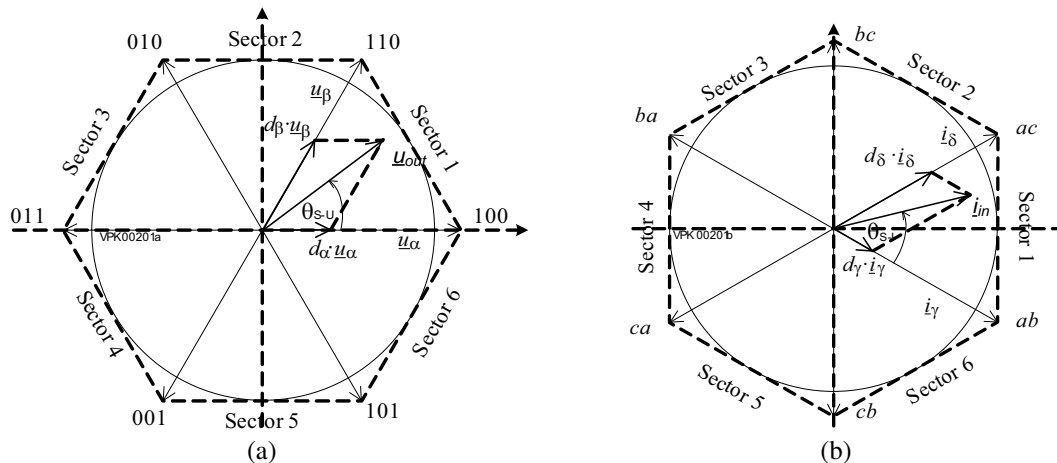
Figure 3: (a) Inverter stage and (b) rectifier stage SVM.
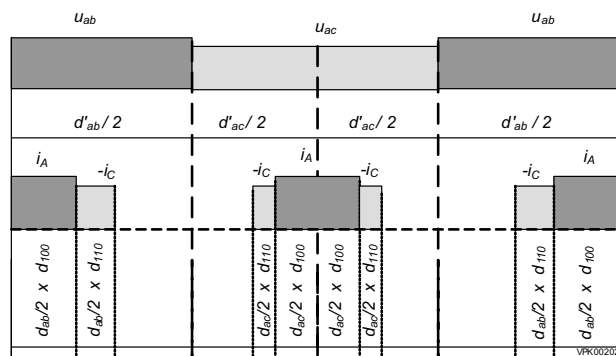
Figure 4: Switching pattern for the first input and the first output sector.
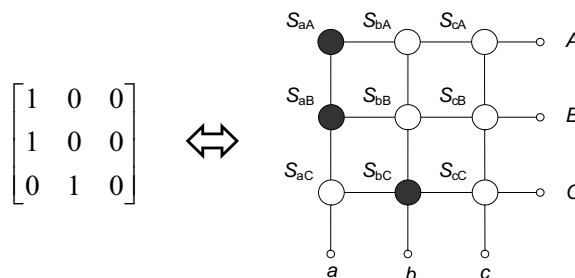
Figure 5: Matrix converter switching combination representation.

Table 1: Virtual rectifier and inverter stages switching states lookup table.

		OUTPUT SECTOR					
		1	2	3	4	5	6
I N P U T S E C T O R	1	ab, ac 100,110,111	ab, ac 110, 010, 000	ab, ac 010, 011, 111	ab, ac 011, 001, 000	ab, ac 001, 101, 111	ab, ac 101, 100, 000
	2	ac, bc 100,110,111	ac, bc 110, 010, 000	ac, bc 010, 011, 111	ac, bc 011, 001, 000	ac, bc 001, 101, 111	ac, bc 101, 100, 000
	3	bc, ba 100,110,111	bc, ba 110, 010, 000	bc, ba 010, 011, 111	bc, ba 011, 001, 000	bc, ba 001, 101, 111	bc, ba 101, 100, 000
	4	ba, ca 100,110,111	ba, ca 110, 010, 000	ba, ca 010, 011, 111	ba, ca 011, 001, 000	ba, ca 001, 101, 111	ba, ca 101, 100, 000
	5	ca, cb 100,110,111	ca, cb 110, 010, 000	ca, cb 010, 011, 111	ca, cb 011, 001, 000	ca, cb 001, 101, 111	ca, cb 101, 100, 000
	6	cb, ab 100,110,111	cb, ab 110, 010, 000	cb, ab 010, 011, 111	cb, ab 011, 001, 000	cb, ab 001, 101, 111	cb, ab 101, 100, 000

2. OPTIMIZATION OF INDIRECT SVM

Let's observe the switching events which occur during one switching cycle for the first output sector and the sixth input sector (Figure 6). It is enough to observe only one half of the cycle, since the switching pattern is symmetrical.

Each matrix in the table shown in Figure 6 represents one matrix switching combination. Columns represent input, and rows output lines. 1 means that the switch that connects the corresponding input and output lines is switched on, as illustrated on the example in Figure 5.

The switching of the virtual rectifier stage is performed during the period when a zero vector is switched at the output. From the indirect representation of the matrix converter it could be concluded that, since a zero vector is switched at the output, there will be zero virtual DC link current, and consequently zero switching losses (Figure 7). However, in reality this switching is carried out by turning three switches off and three switches on (Figure 8). Switching losses which will be generated in this case depend on the magnitudes and directions of the output currents and the input voltage u_{ac}.

By analyzing all combinations from Table 1, it can be seen that in half of the cases, switching losses will occur during the rectifier stage switching. The generation of the switching losses even during the commutation of the input phases is an important disadvantage of the matrix converter.
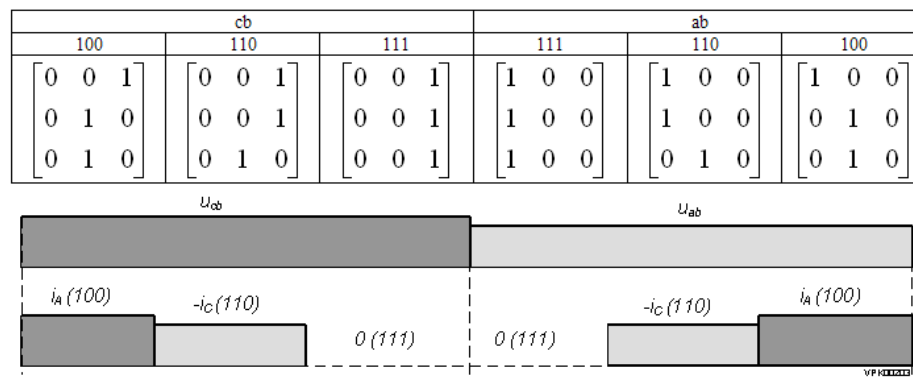
Figure 6: Switching pattern for the first input and the sixth output sector (first half).
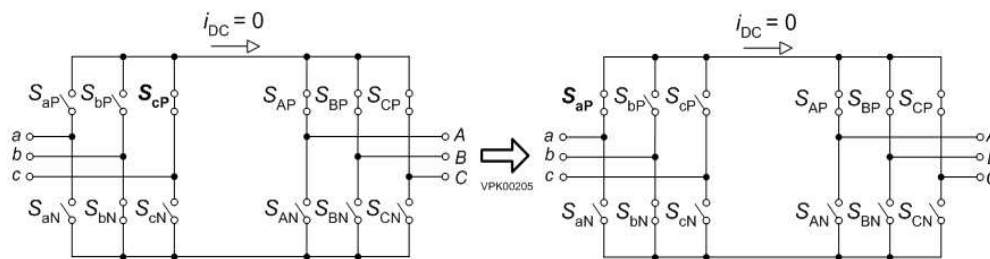
Figure 7: Commutation from input phase c to input phase a in the case of indirect matrix converter representation.
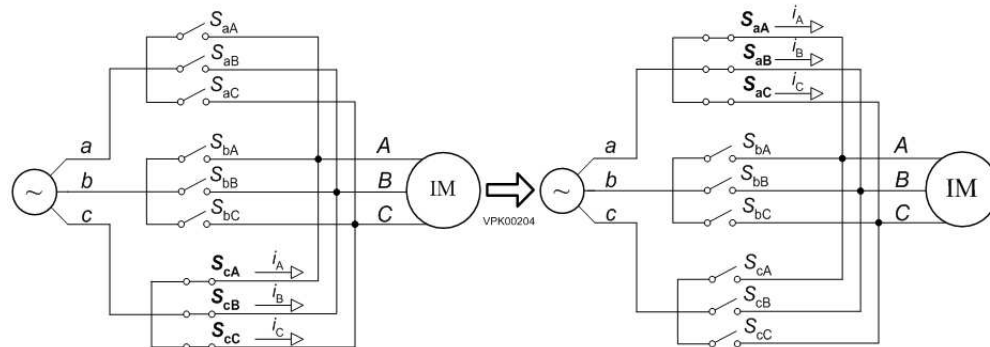
Figure 8: Commutation from input phase c to input phase a in matrix converter.

	cb			ab		
	110	100	000	000	100	110

$$\begin{bmatrix} 0 & 0 & 1 \\ 0 & 0 & 1 \\ 0 & 1 & 0 \end{bmatrix} \quad \begin{bmatrix} 0 & 0 & 1 \\ 0 & 1 & 0 \\ 0 & 1 & 0 \end{bmatrix} \quad \begin{bmatrix} 0 & 1 & 0 \\ 0 & 1 & 0 \\ 0 & 1 & 0 \end{bmatrix} \quad \begin{bmatrix} 0 & 1 & 0 \\ 0 & 1 & 0 \\ 0 & 1 & 0 \end{bmatrix} \quad \begin{bmatrix} 1 & 0 & 0 \\ 0 & 1 & 0 \\ 0 & 1 & 0 \end{bmatrix} \quad \begin{bmatrix} 1 & 0 & 0 \\ 1 & 0 & 0 \\ 0 & 1 & 0 \end{bmatrix}$$
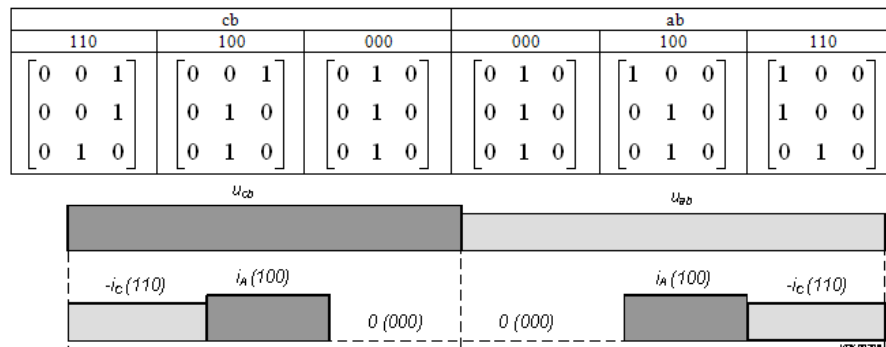
Figure 9: Switching pattern for the first input and the sixth output sector with inverted output vectors order.

Table 2: Optimized virtual rectifier and inverter stages switching states lookup table.

		OUTPUT SECTOR					
		1	2	3	4	5	6
I N P U T S E C T O R	1	ab, ac 100,110,111	ab, ac 010, 110, 111	ab, ac 010, 011, 111	ab, ac 001, 011, 111	ab, ac 001, 101, 111	ab, ac 100, 101, 111
	2	ac, bc 110,100,000	ac, bc 110, 010, 000	ac, bc 011, 010, 000	ac, bc 011, 001, 000	ac, bc 101, 001, 000	ac, bc 101, 100, 000
	3	bc, ba 100,110,111	bc, ba 010, 110, 111	bc, ba 010, 011, 111	bc, ba 001, 011, 111	bc, ba 001, 101, 111	bc, ba 100, 101, 111
	4	ba, ca 110,100,000	ba, ca 110, 010, 000	ba, ca 011, 010, 000	ba, ca 011, 001, 000	ba, ca 101, 001, 000	ba, ca 101, 100, 000
	5	ca, cb 100,110,111	ca, cb 010, 110, 111	ca, cb 010, 011, 111	ca, cb 001, 011, 111	ca, cb 001, 101, 111	ca, cb 100, 101, 111
	6	cb, ab 110,100,000	cb, ab 110, 010, 000	cb, ab 011, 010, 000	cb, ab 011, 001, 000	cb, ab 101, 001, 000	cb, ab 101, 100, 000

Now let's do the same analysis as in Figure 6, but with the inverted order of the output switching combinations: *100* and *110* (Figure 9). In this case, the rectifier stage switching is performed without the generation of the switching losses. By applying the same principle to all relevant combinations from Table 1, the optimized switching states lookup table (Table 2) is obtained. The optimized cells are shadowed.

3. SWITCHING LOSSES CALCULATION

Several papers dealing with the matrix converter losses calculation and measurement have been published recently [6–9]. For the comparison of the switching losses generated with the optimized and unoptimized ISVM, a new approach was used. Special software was developed, which simulates the matrix converter operation and calculates the switching losses of each individual switching event, and conduction losses of each switching state.

At the beginning of the simulation, the configuration parameters are loaded. They define the amplitudes and frequencies of the input and output voltages and the output current, input and output power factors, the simulation duration, the modulation type, and the type of the semiconductor devices. After that the program enters the loop where actual losses calculation takes place. At the beginning of each calculation cycle, the input and output voltages and the output currents are calculated. Each switching cycle is then split into sub cycles based on the selected switching pattern, e.g., for the switching pattern displayed in Figure 6 there will be 12 sub cycles. For each of these sub cycles, a corresponding switching combination is selected from the switching table, and a duty cycle is calculated. Switching losses are calculated based on the comparison of the switching combinations from the present and previous sub cycles. E.g. for the last two sub cycles shown in Figure 6

$$\begin{pmatrix} 1 & 0 & 0 \\ 1 & 0 & 0 \\ 0 & 1 & 0 \end{pmatrix} - \begin{pmatrix} 1 & 0 & 0 \\ 0 & 1 & 0 \\ 0 & 1 & 0 \end{pmatrix} = \begin{pmatrix} 0 & 0 & 0 \\ 1 & -1 & 0 \\ 0 & 0 & 0 \end{pmatrix} \tag{3}$$

where -1 means the switch was turned off and 1 that the switch was turned on. Based on the input line-to-line voltage sign and the current direction through these two switches, the program determines in which of them switching losses have occurred, and calculates these losses from the current and voltage values, and from the device characteristics (Figure 10) [10].
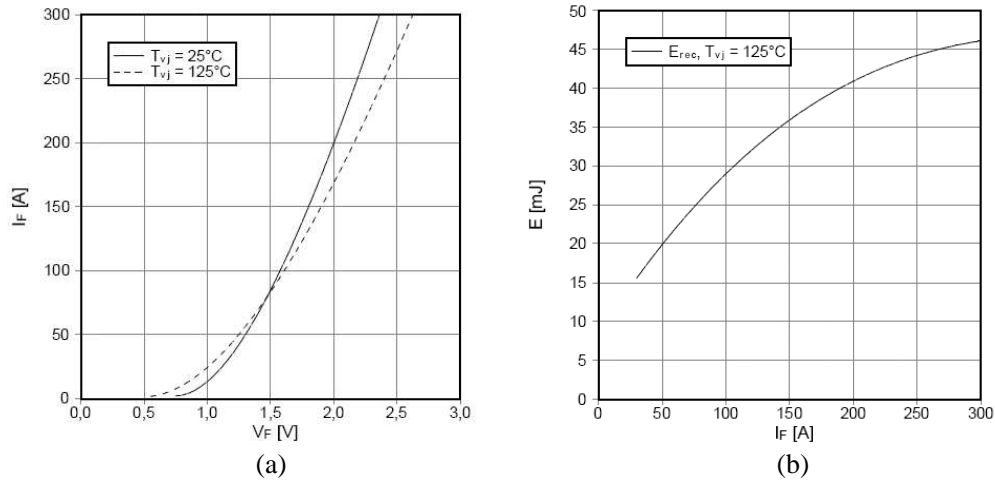
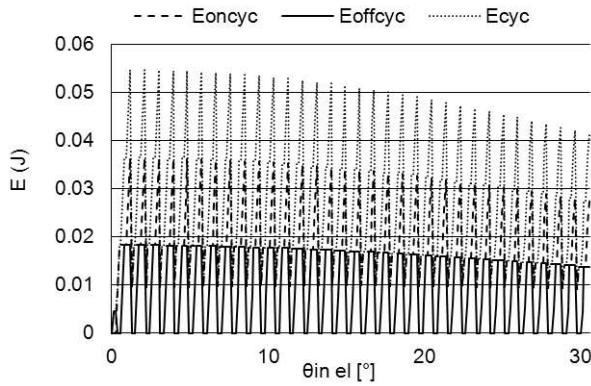Figure 10: (a) IGBT and (b) diode switching losses.

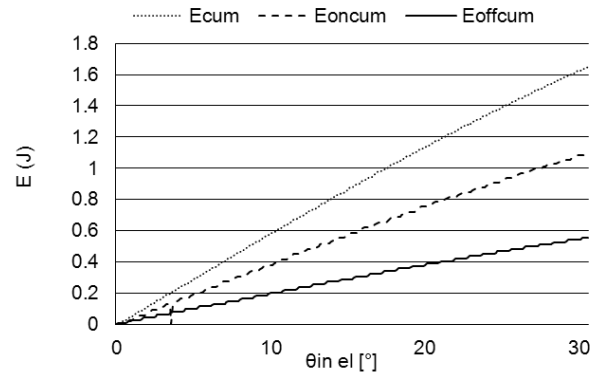Figure 11: Turn-on, turn-off and total switching losses generation per switching cycle.

Figure 12: Cumulative turn-on, turn-off and total switching losses.
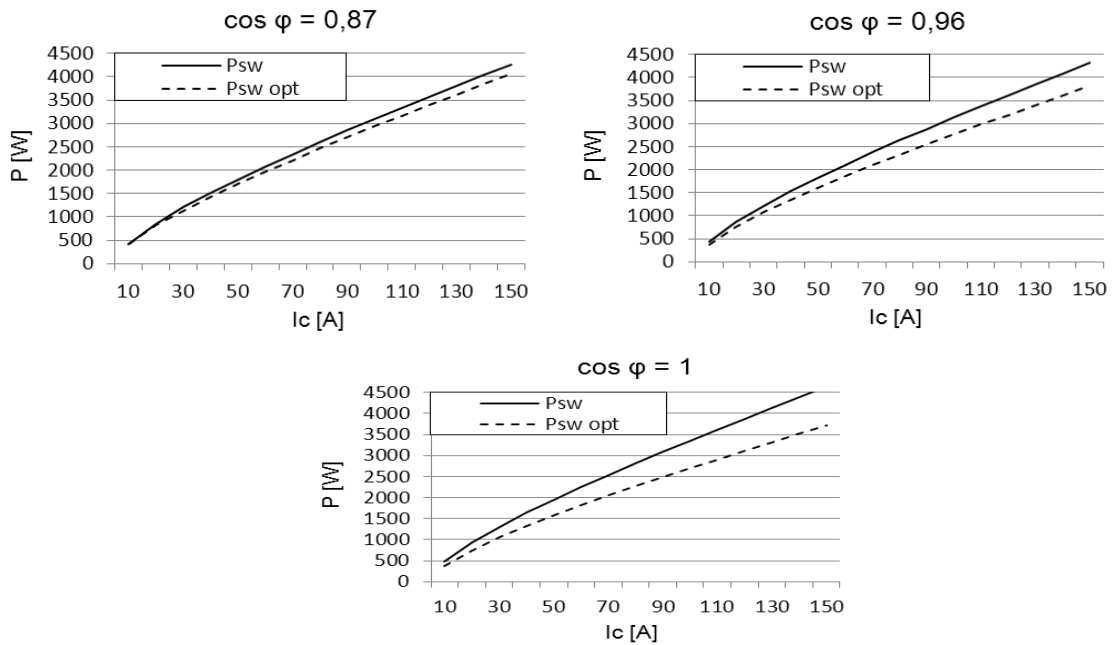

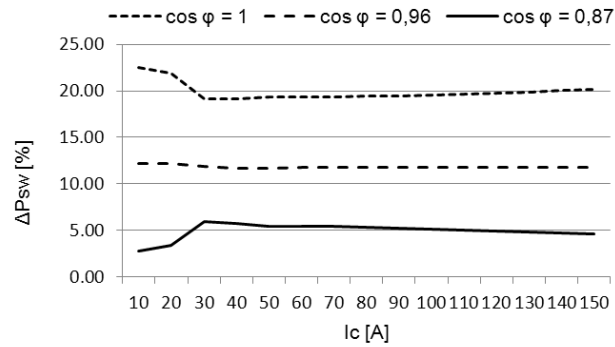Figure 13: Switching losses with optimized and unoptimized modulation.

Figure 14: Switching losses reduction when using optimized modulation for three values of the output power factor.

Table 3: Simulation parameters.

Parameter	Value
Input line-to-line voltage (rms)	500 V
Output line-to-line voltage (rms)	400 V
Input and output frequency	50 Hz
Switching frequency	20 kHz
Input power factor	1

Besides the final results (total switching and conduction losses), various other data (individual IGBTs and diodes switching and conduction losses, voltages, currents, etc.) is generated (Figures 11 and 12). All these data are available in text files, and can easily be imported into the Microsoft Excel for further analysis.

4. SIMULATION RESULTS

The device used in the simulation was the all-in-one matrix converter IGBT module FM35R12KE3 from Eupec. Several simulations for different values of the output current and power factor values have been performed. Simulation parameters there were constants in all simulations are given in Table 3.

The calculated switching losses for optimized and unoptimized modulations are displayed in Figure 13 and the switching losses reduction when the optimized modulation is used in Figure 14. Conduction losses are the same in both modulation strategies, so they were not displayed. The simulation results have shown that the use of the optimized ISVM reduces the switching losses by up to 20%.

5. CONCLUSIONS

The ISVM is the most common matrix converter modulation strategy. It is based on the equivalent representation of the matrix converter as the combination of the virtual rectifier and the virtual inverter stages. Well known rectifier and inverter modulation strategies can then be applied to these stages, similarly like in the conventional VSR/VSI indirect converters. However, unlike the VSR/VSI, where a large DC link capacitor enables independent operation of the input and output stages, in the case of the matrix converter their operations have to be precisely synchronized. The synchronization is carried out by selecting an appropriate switching pattern. Apart from influencing the quality of the converter input and output quantities, the selection of the switching pattern also impacts the switching losses generation. Based on the performed switching losses analysis, an improved ISVM strategy was proposed. A software tool was designed for the matrix converter losses calculation. The calculation results have shown the switching losses reduction of up to 20% when using the proposed optimized ISVM.

REFERENCES

1. Casadei, D., G. Sera, A. Tani, and L. Zarri, "Matrix converter modulation strategies: A new general approach based on space-vector representation of the switch state," *IEEE Transactions on Industrial Electronics*, Vol. 49, No. 2, 370–381, 2002.
2. Wheeler, P. W., J. Rodriguez, J. C. Clare, and L. Empringham, "Matrix converter: A technology review," *IEEE Transactions on Industrial Electronics*, Vol. 49, No. 2, 276–288, 2002.
3. Ziogas, P. D., S. I. Khan, and M. H. Rashid, "Analysis and design of forced commutated cyclo-converter structures with improved transfer characteristics," *IEEE Transactions on Industrial Electronics*, Vol. 33, No. 3, 271–280, 1986.
4. Huber, L. and D. Borojevic, "Space vector modulator for forced commutated cyclo-converters," *IEEE Transactions on Industrial Applications*, Vol. 1, 871–876, 1989.
5. Huber, L. and D. Borojevic, "Space vector modulation with unity input power factor for forced commutated cycloconverters," *IEEE Transactions on Industrial Applications*, Vol. 1, 1032–1041, 1991.
6. Bland, M., P. W. Wheeler, J. C. Clare, and L. Empringham, "Comparison of calculated and measured losses in direct AC-AC converters," *32nd Annual IEEE Power Electronics Specialists Conference*, Vol. 2, 1096–1101, 2001.
7. Bernet, S., S. Ponnulari, and R. Teichmann, "Design and loss comparison of matrix converters and voltage-source converters for modern AC drives," *IEEE Transactions on Industrial Electronics*, Vol. 49, No. 2, 304–314, 2002.
8. Schafmeiser, F., C. Rytz, and J. W. Kolar, "Analytical calculation of the conduction and switching losses of the conventional matrix converter and the (very) sparse matrix converter," *20th Annual IEEE Applied Power Electronics Conference and Exposition (APEC)*, Vol. 2, 875–881, 2005.
9. Gruson, F., P. Le Moigne, P. Delarue, M. Arpilliere, and X. Cimitiere, "Comparison of losses between matrix and indirect matrix converters with and improved modulation," *IEEE Symposium on Industrial Electronics (ISIE)*, 718–723, 2010.
10. "EUPEC IGBT-Module FS150R17KE3G," *Technical Information*, 2004.

Comparison of Gamma and T Models for Convector Controlled Induction Machine Drives

J. Lettl[1], S. Fligl[1], J. Bauer[1], and M. Vlcek[2]

[1]Faculty of Electrical Engineering, Department of Electric Drives and Traction
Czech Technical University in Prague, Czech Republic
[2]Faculty of Nuclear Sciences and Physical Engineering, Department of Mathematics
Czech Technical University in Prague, Czech Republic

Abstract— Nowadays in variable speed drives induction machines are widely used. For the understanding and clear specification of the electromagnetic processes in the induction machines different equivalent circuits can be employed. Traditionally, in order to reduce the complexity of the mathematical model the resistances and inductances are represented as concentrated components and 3 phase winding is assumed to be symmetrical. These equivalent circuits are also used as a starting point for the design of the drive controller. This article strives to compare the two most widely used models and to derive a transformation against each other.

1. INTRODUCTION

In most papers that deal with the problematic of the IM drive control, equation based on the Park's transformation as a T-formed equivalent circuit are used. These models are adequate in many situations. Even though they can seem to be overly simplified, they can serve as a solid basis for an advanced motor control. However other authors tend to use gamma models and there are approaches using both. This paper examines and compares some of the issues of adequate machine modeling and attempts to provide a firmer basis for selection of an appropriate model and to confirm or disprove the equivalence of different approaches.

2. T-CIRCUIT

For the loop 1 and 2 in the T-circuit of the induction machines Equations (1) and (2) can be written.

$$\dot{\underline{\Psi}}_1(t) - \underline{e}_1 + R_1\underline{i}_1(t) + \omega_B \mathrm{j}\,\underline{\Psi}_1(t) = 0 \qquad \dot{\underline{\Psi}}_2(t) + R_2\underline{i}_2(t) + \mathrm{j}\,\underline{\Psi}_2(t)(\omega - \omega_B) = 0 \tag{1}$$

The magnetic fluxes and the the currents themselves can be evaluated from Fig. 1 also. By means of substitution the final Equation (2) is to be obtained.

$$\dot{\mathbf{\Psi}}(t) = \mathbf{g}(t) + \mathbf{C}\Psi(t) \tag{2}$$

where the system matrix and the action vector can be evaluated as

$$
C = \begin{pmatrix}
-\frac{R_1(L_m+L_{\sigma 2})}{\sigma_1} & \omega_B & \frac{L_m R_1}{\sigma_1} & 0 \\
-\omega_B & -\frac{R_1(L_m+L_{\sigma 2})}{\sigma_1} & 0 & \frac{L_m R_1}{\sigma_1} \\
\frac{L_m R_2}{\sigma_1} & 0 & -\frac{R_2(L_m+L_{\sigma 1})}{\sigma_1} & \omega_B - \omega \\
0 & \frac{L_m R_2}{\sigma_1} & \omega - \omega_B & -\frac{R_2(L_m+L_{\sigma 1})}{\sigma_1}
\end{pmatrix}
$$
$$\sigma_1 = L_{\sigma 1} + L_{\sigma 2} + L_m L_{\sigma 1} + L_m L_{\sigma 2}$$
$$g = \begin{pmatrix} e_{1a}(t) \\ e_{1b}(t) \\ 0 \\ 0 \end{pmatrix} \tag{3}$$

The Equation (3) can be considered as basic equation of the T-circuit and any other combination of the IM state matrix for other state variable pairs can be derived from this equation with the help of proper transformation matrix. e.g., (4) is the transformation matrix from the fluxes to the
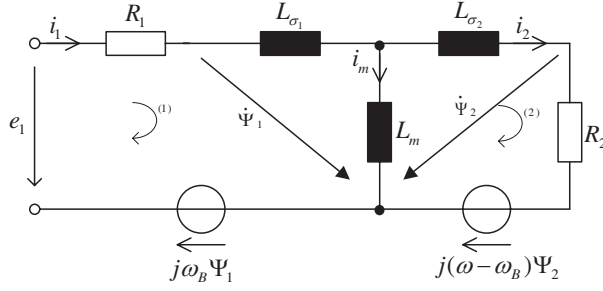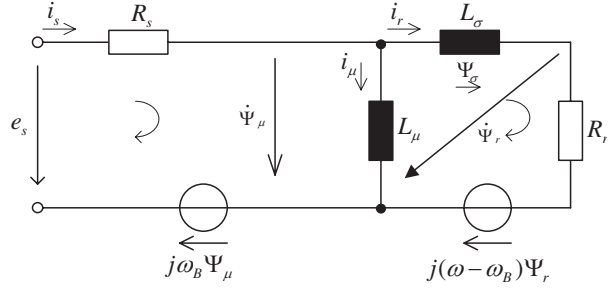
Figure 1: T-circuit of the IM.

Figure 2: Γ-circuit of the IM.

stator flux and stator current vector. Basis values are written in subscript and the new ones are in upper script.

$$T\ \frac{\Psi_1\Psi_2}{\Psi_1 i_1} = \begin{pmatrix} 1 & 0 \\ \frac{L_m+L_{\sigma 2}}{L_m} & -\frac{L_{\sigma 1}L_{\sigma 2}+L_m L_{\sigma 1}+L_m L_{\sigma 2}}{L_m} \end{pmatrix} \qquad \begin{pmatrix} \dot{\underline{\Psi}}_1(t) \\ \dot{\underline{i}}_1(t) \end{pmatrix} = T^{-1}CT \begin{pmatrix} \dot{\underline{\Psi}}_1(t) \\ \dot{\underline{i}}_1(t) \end{pmatrix} + T^{-1}g(t) \quad (4)$$

Then we can express $C_s = \mathbf{T}^{-1}\mathbf{CT}$ a $g_s = \mathbf{T}^{-1}\mathbf{g}$ and finally we obtain (5) and (6)

$$C_S = \begin{pmatrix} 0 & \omega_B & -R_1 & 0 \\ -\omega_B & 0 & 0 & -R_1 \\ \frac{R_2}{\sigma_1} & \frac{\omega(L_m+L_{\sigma 2})}{\sigma_1} & -\frac{R_1 L_{\sigma 2}+R_2 L_{\sigma 1}+L_m R_1+L_m R_2}{\sigma_1} & \omega_B-\omega \\ -\frac{\omega(L_m+L_{\sigma 2})}{\sigma_1} & \frac{R_2}{\sigma_1} & \omega-\omega_B & -\frac{R_1 L_{\sigma 2}+R_2 L_{\sigma 1}+L_m R_1+L_m R_2}{\sigma_1} \end{pmatrix},$$

$$\sigma_1 = L_{\sigma 1}L_{\sigma 2} + L_m L_{\sigma 1} + L_m L_{\sigma 2} \tag{5}$$

$$g_S(t) = \begin{pmatrix} e_{1a}(t) \\ e_{1b}(t) \\ \frac{L_m e_{1a}(t)+e_{1a}(t)L_{\sigma 2}}{\sigma_1} \\ \frac{L_m e_{1b}(t)+e_{1b}(t)L_{\sigma 2}}{\sigma_1} \end{pmatrix}, \qquad \sigma_1 = L_{\sigma 1}L_{\sigma 2} + L_m L_{\sigma 1} + L_m L_{\sigma 2} \tag{6}$$

3. Γ-CIRCUIT

This alternative circuit, the second the most wide spread model can be described by Equations (7) and (8)

$$\dot{\underline{\Psi}}_\mu(t) - e_s(t) + R_s \underline{i}_s(t) + \omega_B \mathrm{j}\,\underline{\Psi}_\mu(t) = 0 \tag{7}$$

$$-\dot{\underline{\Psi}}_r(t) + R_r \underline{i}_r(t) + \mathrm{j}\,\underline{\Psi}_r(t)(\omega-\omega_B) = 0 \tag{8}$$

While using a proper transformation a similar equation set to (2) can be derived

$$\dot{\underline{\Psi}}(t) = b(t) + \mathbf{A}\Psi(t) \tag{9}$$

With the matrix $\mathbf{A}$ defined as and the vector $\mathbf{b}$ is defined as in (10)

$$\mathbf{A} = \begin{pmatrix} -\frac{R_s}{L_\mu} - \frac{R_s}{L_\sigma} & \omega_B & \frac{R_2}{L_\sigma} & 0 \\ -\omega_B & -\frac{R_s}{L_\mu} - \frac{R_s}{L_\sigma} & 0 & \frac{R_3}{L_\sigma} \\ \frac{R_r}{L_\sigma} & 0 & -\frac{R_r}{L_\sigma} & \omega_B-\omega \\ 0 & \frac{R_r}{L_\sigma} & \omega-\omega_B & -\frac{R_r}{L_\sigma} \end{pmatrix} \qquad \mathbf{b} = \begin{pmatrix} e_{sa}(t) \\ e_{sb}(t) \\ 0 \\ 0 \end{pmatrix} \tag{10}$$

The same transformation approach as in (4) leads again to the equation set based on stator variables (12).

$$\mathbf{T}\ \frac{\Psi_\mu i_r}{\Psi_\mu \Psi_r} = \begin{pmatrix} 1 & 0 \\ \frac{1}{L_\sigma} & -\frac{1}{L_\sigma} \end{pmatrix} \qquad \begin{pmatrix} \dot{\underline{\Psi}}_\mu(t) \\ \dot{\underline{i}}_s \end{pmatrix} = \mathbf{A}_s \begin{pmatrix} \Psi_\mu(t) \\ i_s(t) \end{pmatrix} + b_s(t) \tag{11}$$

$$\mathbf{A}_s = \begin{pmatrix} 0 & \omega_B & -R_s & 0 \\ -\omega_B & 0 & 0 & -R_s \\ \sigma_2 & \frac{\omega\sigma_3}{L_\mu L_\sigma} & \sigma_1 & \omega_B-\omega \\ -\frac{\omega\sigma_3}{L_\mu L_\sigma} & \sigma_2 & \omega-\omega_B & -\sigma_1 \end{pmatrix}, \quad \begin{matrix} \sigma_1 = -\frac{R_r L_\mu+R_s L_\mu+R_s L_\sigma}{L_\mu L_\sigma} \\ \sigma_2 = \frac{R_r}{L_\mu L_\sigma} \\ \sigma_3 = L_\mu + L_\sigma \end{matrix} \quad b_s(t) = \begin{pmatrix} e_{sa}(t) \\ e_{sb}(t) \\ \frac{e_{sa}(t)L_\mu+e_{sa}(t)L_\sigma}{L_\mu L_\sigma} \\ \frac{e_{sb}(t)L_\mu+e_{sb}(t)L_\sigma}{L_\mu L_\sigma} \end{pmatrix} \tag{12}$$

4. EQUIVALENCY OF THE ADDITIONALS CIRCUITS

In this chapter, we will strive to prove whether the proper selection of the transformation coefficients between the both circuits leads to the same set of the differential equations. That would mean they are same.

For the prove we suppose for fluxes and the transformation matrix

$$\underline{\Psi}_\mu = \underline{\Psi}_1 \ \text{ and } \ \underline{\Psi}_r = \frac{\underline{\Psi}_2(L_m + L_{\sigma 1})}{L_m} \quad \mathbf{T} = \begin{pmatrix} 1 & 0 & 0 & 0 \\ 0 & 1 & 0 & 0 \\ 0 & 0 & \frac{L_m + L_{\sigma 1}}{L_m} & 0 \\ 0 & 0 & 0 & \frac{L_m + L_{\sigma 1}}{L_m} \end{pmatrix} \quad (13)$$

When we need that (9) and (2) are equivalent, it must be fulfilled, that $\mathbf{T}^{-1}\mathbf{AT} = \mathbf{C}$ a $\mathbf{T}^{-1}\mathbf{b} = \mathbf{g}$. The second condition is fulfilled because of the T. Now we need to calculate the $\mathbf{T}^{-1}\mathbf{AT}$, that can be expressed as:

$$\mathbf{T}^{-1}\mathbf{AT} = \begin{pmatrix} \sigma_1 & \omega_B & \sigma_2 & 0 \\ -\omega_B & \sigma_1 & 0 & \sigma_2 \\ \frac{L_m R_r}{(L_m + L_{\sigma 1})L_\sigma} & 0 & -\frac{R_r}{L_\sigma} & \omega_B - \omega \\ 0 & \frac{L_m R_r}{(L_m + L_{\sigma 1})L_\sigma} & \omega - \omega_B & -\frac{R_r}{L_\sigma} \end{pmatrix},$$

$$\sigma_1 = -\frac{R_s(L_\mu + L_{\sigma 1})}{L_\mu L_\sigma}, \qquad \sigma_2 = -\frac{R_s(L_m + L_{\sigma 1})}{L_m L_\sigma} \qquad (14)$$

The first set of recalculation equations can be expressed as

$$i_s = i_1, \quad i_r = \frac{L_m i_2}{L_m + L_{\sigma 1}}, \quad e_s = e_1, \quad R_s = R_1 \qquad (15)$$

Next we assume that the inductance circuits have the same behaviour, when the right sides of the circuits are opened or short-circuited. From the principle of the superposition then it goes on, that for the opened right side, the same current will flow through the primary circuit (left side). This can be expressed as (38)

$$Z_r = \omega j (L_m + L_{\sigma 1}), \quad Z_r = \omega j L_\mu \quad \rightarrow \quad L_\mu = L_m + L_{\sigma 1} \qquad (16)$$
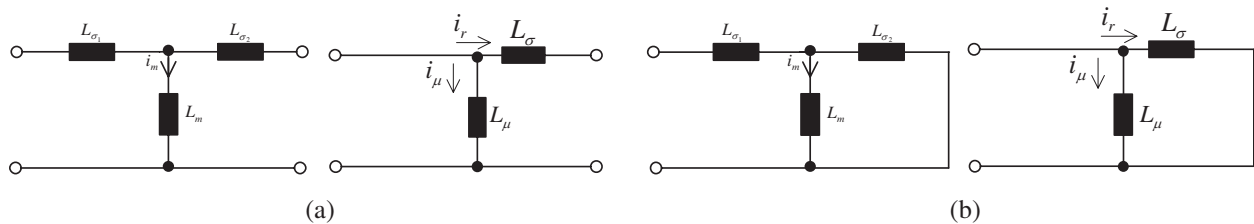
Figure 3: Left/right sides circuit equivalency.
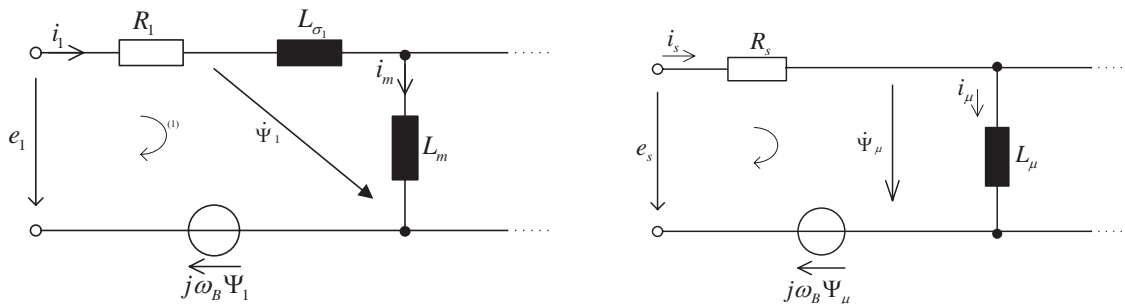
Figure 4: Time constants equivalency.

The same behaviour shall be guarantied in the case of the short-circuit of the right side: Therefore because of parallel connection of the inductors we can write:

$$Z_{\rm r} = \omega {\rm j} \left(L_{\sigma 1} \frac{L_{\rm m} L_{\sigma 2}}{L_{\rm m} + L_{\sigma 2}} \right), \quad Z_{\rm r} = \frac{\omega {\rm j} \, L_\mu \, L_\sigma}{L_\mu + L_\sigma} \quad \rightarrow \quad L_\sigma = \left(\frac{L_{\sigma 1}}{L_{\rm m}} + 1 \right) L_{\sigma 1} + \left(\frac{L_{\sigma 1}}{L_{\rm m}} + 1 \right)^2 L_{\sigma 2} \quad (17)$$

Finally, the very last assumption is the equality of the rotor and stator time constants: $T_1 = T_s$:

$$T_1 = \frac{L_{\rm m} + L_{\sigma 1}}{R_1}, \quad T_s = \frac{L_\mu}{R_s} \tag{18}$$

For the rotor when we suppose $T_2 = T_r$ after several operations we can write:

$$T_2 = \frac{L_{\rm m} + L_{\sigma 2}}{R_2}, \quad T_r = \frac{L_\mu + L_\sigma}{R_r} \tag{19}$$

$$R_r = \frac{R_2 \left(L_{\rm m} + L_{\sigma 1} \right)^2}{L_{\rm m}^2} \tag{20}$$

After all of this we can express the matrix $\mathbf{C}_2$ as:

$$\mathbf{C}_2 = \begin{pmatrix} -\frac{R_1(L_{\rm m}+L_{\sigma 2})}{\sigma_1} & \omega_{\rm B} & \frac{L_{\rm m} R_1}{\sigma_1} & 0 \\ -\omega_{\rm B} & -\frac{R_1(L_{\rm m}+L_{\sigma 2})}{\sigma_1} & 0 & \frac{L_{\rm m} R_1}{\sigma_1} \\ \frac{L_{\rm m} R_2}{\sigma_1} & 0 & -\frac{R_2(L_{\rm m}+L_{\sigma 1})}{\sigma_1} & \omega_{\rm B} - \omega \\ 0 & \frac{L_{\rm m} R_2}{\sigma_1} & \omega - \omega_{\rm B} & -\frac{R_2(L_{\rm m}+L_{\sigma 1})}{\sigma_1} \end{pmatrix},$$

$$\sigma_1 = L_{\sigma 1} L_{\sigma 2} + L_{\rm m} L_{\sigma 1} + L_{\rm m} L_{\sigma 2} \tag{21}$$

That proves the equality of (45) and (17).

5. CONCLUSIONS

The most articles dealing with induction machine control base on the T-formed equivalent circuit. It is an industry and academics widely accepted model. Still there are authors using the Gamma model only or even both. Since the Gamma model brings some simplifications, it is worth to prove whether it is a total replacement or it can be used under more restricted conditions only. It has been shown; it is possible to find recounting equations that deliver the original set of differential equation. This is a proof for the equivalence of both circuits. However size adjustment for rotor state variables must be undertaken if those should be exchanged directly between Gamma and T model running in parallel.

ACKNOWLEDGMENT

REFERENCES

1. Gibo, N., T. Noda, and K. Takenaka, "An induction motor model for transient simulation," *Proceedings XIX International Conference on Electrical Machines (ICEM), 2010*, 2010.
2. Carmona-Sánchez, J. and D. Ruiz-Vega, "Review of static induction motor models," *Proceedings of North American Power Symposium (NAPS)*, 2010.
3. Heising, C., M. Oettmeier, R. Bartelt, F. Jie, V. Staudt, and A. Steimel, "Modelling method for complex induction machines used in naval applications using an advanced simulation concept," *Proc. Electric Ship Technologies Symposium, ESTS 2009*, 2009.
4. Ryvkin, S., R. Schmidt-Obermoeller, and A. Steimel, "Sliding-mode approach to control design for induction motor drive fed by a three-level voltage-source inverter," *Proceedings of 13th International Power Electronics and Motion Control Conference*, EPE-PEMC, Poland, 2008.

Simulation of the Matrix Converter Drive with Sliding Mode Control

J. Lettl[1], S. Fligl[1], J. Bauer[1], and S. Ryvkin[2]

[1]Department of Electric Drives and Traction, Faculty of Electrical Engineering
Czech Technical University in Prague, Czech Republic
[2]Trapeznikov Institute of Control Sciences, Russian Academy of Science, Russia

Abstract— Matrix converter belongs to the direct frequency converter category. In this contribution the name "Matrix Converter" means the symmetrical 3×3 topology made by nine bidirectional switches. Output voltage is produced by direct switching of input phases to output phases.

Very important parts of the converter's controller are used modulation strategy and control algorithm. The common modulation strategies from the area of the indirect frequency converters can not be used because of the absence of the DC-link. Therefore the modulation strategies based on virtual DC-link space vector modulation were developed. It works as a dependency injection. That is why different approaches can be used to control both the output voltage and the input current at the same time. In this paper, the phase control of the input current in the combination with the sliding mode control of the output voltage is presented. This enables us to overcome the traditional limitation of the output voltage without resigning from the input current control.

1. INTRODUCTION

The induction machine is a 4th order system and there are two action inputs that are bundled into seven vectors with predefined direction and value [5]. We can only select a vector among this set of seven action value pairs, since the direction of the vector is given by the inverter construction and the amplitude is given by the dc link and it cannot be changed quickly or not at all (for a matrix converter it can be done in virtual rectifier by adding one switching step). The switching frequency is limited to some hundreds of Hz (for high power drives) or to tens of kHz (for smaller drives). The target point is not given by a value of state variables, but their multiplication (mechanical torque). Moreover, depending on the coordinate system selection the destination point (or the curve) can be steadily moving. In other words, then the aim of the control is not to achieve a certain point in the state space but to produce a never ending movement that delivers the required torque as its side effect.

In order do define criteria for the best control law, we could say: The aim is to move from any current system state (defined by the system state variables) to any target system state by shortest time possible. This can be simplified as the task to find the shortest route to the target point. That is actually defined by a line segment.

Existence and stability can be evaluated by analyzing the employed state space description in order to find limitation boundaries, where the available action vectors cannot produce movement in all directions. In other words the boundary can be defined as system state where the time derivative of one particular state variable is equal zero and at the same time the other available vectors deliver the same sign (the state value achieves its limit and it cannot be increased anymore).

Applying the above mentioned line segment approach will enable us to eliminate the sliding mode reaching phase in the beginning and to obtain comparable performance to the sliding phase. Of course, in the maintenance phase, both the classical sliding mode and the line segment approach can eventually produce unwanted chattering. This can be overcome by additional arrangements, but this is over the scope of this article.

2. MATRIX CONVERTER MODEL

Since the modulation is not the main aim of this article, a simplified model is fully sufficient. Let us use the virtual dc-link concept [3, 4]. This eliminates the rotating and pulsing voltage vectors from the output voltage vector portfolio. This set limitation guaranties the possibility to control the direction of the input current space vector independently from the selected output voltage vector. Based on the power balance and supposing zero losses in the converter, the input current space

Table 1: Virtual inverter output voltage vectors.

u_x	u_0	u_1	u_2	u_3	u_4	u_5
u_α	1	0.5	-0.5	-1	-0.5	0.5
u_β	0	$\sqrt{3}/2$	$\sqrt{3}/2$	0	$-\sqrt{3}/2$	$-\sqrt{3}/2$

vector can evaluated as follows:

$$\frac{3}{2}(u_\alpha i_\alpha + u_\beta i_\beta) = \frac{3}{2}(u_{IN\alpha} i_{IN\alpha} + u_{IN\beta} i_{IN\beta}) \tag{1}$$

$$\frac{i_{IN\alpha}}{i_{IN\beta}} = \frac{u_{IN\alpha}}{u_{IN\beta}} => i_{IN\beta} = \frac{u_{IN\beta}}{u_{IN\alpha}} i_{IN\alpha} \tag{2}$$

When we combine the (1) and (2) we will obtain

$$i_{IN\alpha} = \frac{u_\alpha i_\alpha + u_\beta i_\beta}{u_{IN\alpha} + \frac{u_{IN\beta}^2}{u_{IN\alpha}}} = \frac{u_{IN\alpha}(u_\alpha i_\alpha + u_\beta i_\beta)}{u_{IN\alpha}^2 + u_{IN\beta}^2} \tag{3}$$

In the same way the equation for $i_{IN\beta}$ can be derived. Such sinusoidal switching will cause the virtual DC-link voltage to be constant. Its value corresponds exactly to the lower limit for a diode rectifier supplying a purely resistive load. The same value will be obtained for virtual DC-link and it will be virtually constant:

$$U_{DC\_diode\_min} = U_{DC\_virtual} = \frac{3}{2} u_{IN\,max} \tag{4}$$

At the output side it will be different since in our case one of the six space vectors will be used without any additional modulation (the output modulation will be a product of the sliding mode control). Independently from the input sinusoidal modulation there is a free choice among the following vectors (multiplied by maximum input phase voltage; 254 V in our case):

3. INDUCTION MACHINE MODEL

In this article, builds on a Gamma frame model. It is defined by the following equation set:

$$\dot{\underline{\Psi}}_\mu(t) - e_s(t) + R_s \underline{i}_s(t) + \omega_B \mathrm{j}\, \underline{\Psi}_\mu(t) = 0, \quad -\dot{\underline{\Psi}}_r(t) + R_r \underline{i}_r(t) + \mathrm{j}\, \underline{\Psi}_r(t)(\omega - \omega_B) = 0 \tag{5}$$

The induction machine is a system with four state variables. Any combination of current and/or flux vectors can be used. Let us to use the variation with stator variables — that means the stator current and flux:

$$\begin{pmatrix} \frac{d\psi_{\mu k}}{dt} \\ \frac{d\psi_{\mu l}}{dt} \\ \frac{di_{sk}}{dt} \\ \frac{di_{sl}}{dt} \end{pmatrix} = \begin{pmatrix} 0 & \omega_B & -R_s & 0 \\ -\omega_B & 0 & 0 & -R_s \\ \sigma_2 & \frac{\omega\sigma_3}{L_\mu L_\sigma} & \sigma_1 & \omega_B - \omega \\ -\frac{\omega\sigma_3}{L_\mu L_\sigma} & \sigma_2 & \omega - \omega_B & -\sigma_1 \end{pmatrix} \cdot \begin{pmatrix} \psi_{\mu k} \\ \psi_{\mu l} \\ i_{sk} \\ i_{sl} \end{pmatrix} + \begin{pmatrix} 1 & 0 \\ 0 & 1 \\ \frac{L_\mu + L_\sigma}{L_\mu L_\sigma} & 0 \\ 0 & \frac{L_\mu + L_\sigma}{L_\mu L_\sigma} \end{pmatrix} \cdot \begin{pmatrix} u_k \\ u_l \end{pmatrix},$$

$$\sigma_1 = -\frac{R_r L_\mu + R_s L_\mu + R_s L_\sigma}{L_\mu L_\sigma}, \quad \sigma_2 = \frac{R_r}{L_\mu L_\sigma}, \quad \sigma_3 = L_\mu + L_\sigma \tag{6}$$

By a proper selection of the coordinate system one of the state variables can be kept at zero value permanently. From the control point of view the system can be in this way regarded as almost a 3rd order system. In this article the system connected with the flux alpha component is chosen.

$$\begin{pmatrix} \frac{d\psi_{\mu k}}{dt} \\ \frac{di_{sk}}{dt} \\ \frac{di_{sl}}{dt} \end{pmatrix} = \begin{pmatrix} 0 & -R_s & 0 \\ \sigma_2 & \sigma_1 & \omega_B - \omega \\ -\frac{\omega\sigma_3}{L_\mu L_\sigma} & \omega - \omega_B & -\sigma_1 \end{pmatrix} \cdot \begin{pmatrix} \psi_{\mu k} \\ i_{sk} \\ i_{sl} \end{pmatrix} + \begin{pmatrix} 1 & 0 \\ \frac{L_\mu + L_\sigma}{L_\mu L_\sigma} & 0 \\ 0 & \frac{L_\mu + L_\sigma}{L_\mu L_\sigma} \end{pmatrix} \cdot \begin{pmatrix} u_k \\ u_l \end{pmatrix} \tag{7}$$
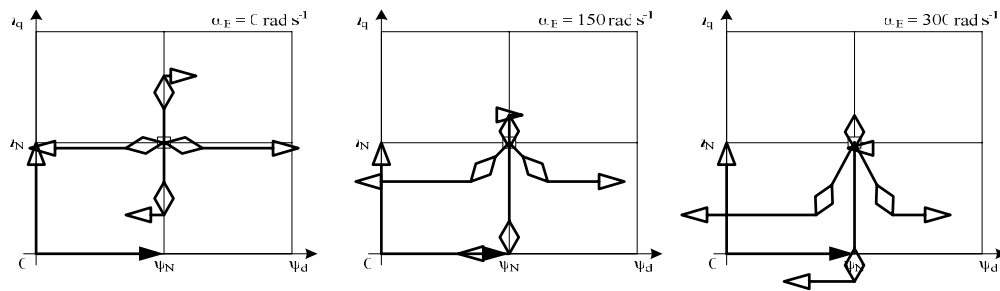
Figure 1: Reaction of the machine on the different voltage vectors.

Table 2: Nominal values of the controlled machine.

Motor Properties		Nominal working point	
Parameter	Value	Parameter	Value
R_S [Ω]	$25.9 \cdot 10^{-3}$	P_N [W]	$87.0 \cdot 10^3$
R_R [Ω]	$18.0 \cdot 10^{-3}$	ω_N [rad $\cdot$ s^{-1}]	150
L_μ [H]	$27.6 \cdot 10^{-3}$	ψ_N [Wb]	0.84
L_σ [H]	$1.3 \cdot 10^{-3}$	Derived nominal values	
p [-]	2	ω_E [rad $\cdot$ s^{-1}]	300.00
Derived nominal values		ω_B [rad $\cdot$ s^{-1}]	305.80
u_d [V]	3.28	i_d [A]	126.78
u_q [V]	262.83	$\underline{i}_q$ [A]	230.16
$u_{a\,\text{max}}$ [V]	262.85	$\underline{i}_{a\,\text{max}}$ [A]	262.77

Table 3: Machine values — Different working conditions.

Nominal working point — zero speed		Nominal working point — half speed	
Parameter	Value	Parameter	Value
P [W]	0	P [W]	$45.5 \cdot 10^3$
ω [rad $\cdot$ s^{-1}]	0	ω [rad $\cdot$ s^{-1}]	75
ψ [Wb]	0.84	ψ [Wb]	0.84
Derived values		Derived values	
ω_E [rad $\cdot$ s^{-1}]	000.00	ω_E [rad $\cdot$ s^{-1}]	150.00
ω_B [rad $\cdot$ s^{-1}]	5.80	ω_B [rad $\cdot$ s^{-1}]	155.80
i_d [A]	126.78	i_d [A]	126.78
$\underline{i}_q$ [A]	230.16	$\underline{i}_q$ [A]	230.16
$\underline{i}_{a\,\text{max}}$ [A]	262.77	$\underline{i}_{a\,\text{max}}$ [A]	262.77
u_d [V]	3.28	u_d [V]	3.28
u_q [V]	10.83	u_q [V]	136.83
u_{aMAX} [V]	11.31	$u_{a\,\text{max}}$ [V]	136.87

4. REACTION TO AN ACTION VOLTAGE VECTOR

First of all, let us to define system states to be investigated. The very first reference point is the nominal working point of the reference 87 kW machine [1].

The reaction of the induction machine to the change of the supply voltage vector is summarized in the Table 4 and also depicted in Fig. 1. It is obvious, that for the different states (speed) of the motor each vector has different influence on the machine. According to this fact and based on the (7) the control algorithm was created.

Let us to investigate two more working point; the same torque and flux, but the half of nominal a zero speed.

Table 4: Time derivatives of state variables — different working conditions.

ω_E [rad · s^{-1}]		000.00		150.00		300.00	
$u_{dq} = 254$ V	u_{dq}	d	q	d	q	d	q
ψ/dt [Wb · s^{-1}]	$\rightarrow$	242	0	242	0	242	0
	$\uparrow$	-3	0	-3	0	-3	0
	$\leftarrow$	-248	0	-248	0	-248	0
	$\downarrow$	-3	0	-3	0	-3	0
di/dt [A · s^{-1}]	$\rightarrow$	192.10^3	-7.10^3	157.10^3	-90.10^3	122.10^3	-172.10^3
	$\uparrow$	62.10^3	153.10^3	27.10^3	70.10^3	-7.10^3	-11.10^3
	$\leftarrow$	-203.10^3	-7.10^3	-237.10^3	-90.10^3	-272.10^3	-172.10^3
	$\downarrow$	-73.10^3	-17.10^3	-107.10^3	-250.10^3	-142.10^3	-332.10^3

(a)   (b)
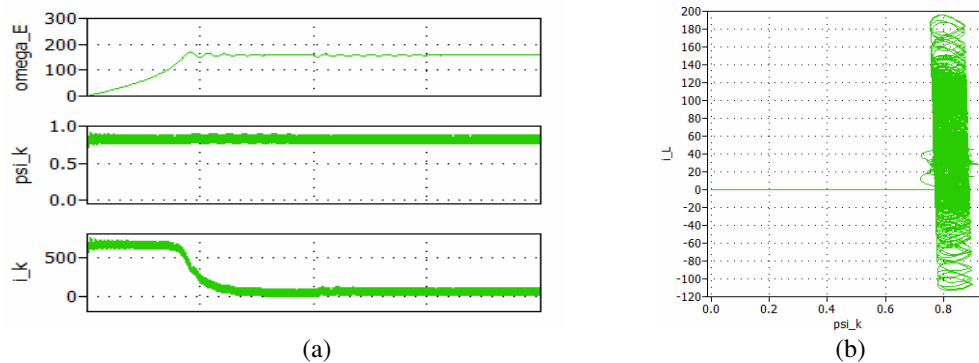
Figure 2: Simulation results of the proposed control algorithm.
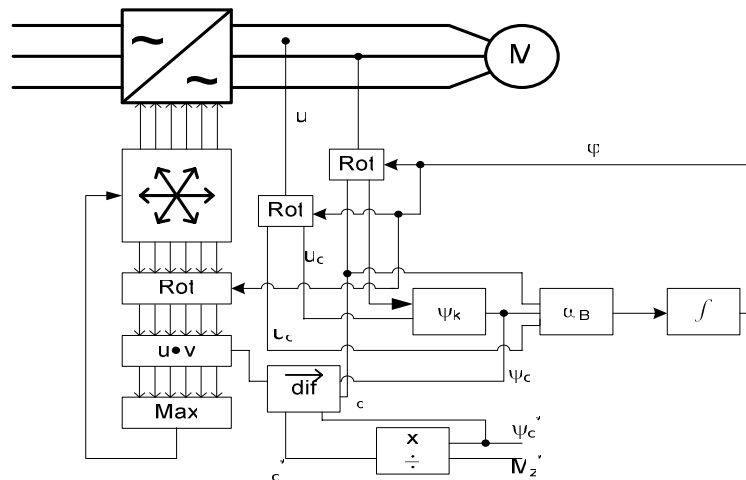
Figure 3: Proposed control algorithm block schema.

5. CONTROL OF THE MATRIX CONVERTER INDUCTION MOTOR DRIVE

The simplified block schema of the controller implemented in Matlab/Simulink is depicted in Fig. 3. From measured voltages and currents values are recalculated, that can not be measured directly — the motor flux. Ψ and the angle of the flux phasor φ. Based on the knowledge of these two variables current values of the. Ψ_k and i_l are calculated. They are then compared to the desired ones and according to their difference the proper voltage vector leading the drive to the desired state is selected. Simulation results of this control are depicted in Fig. 2. Fig. 2(a) shows the results of the drive start up simulation with the proposed control strategy for desired values of $\Psi_k = 0.84$ Wb and desired current $i_L = 160$. In Fig. 2(b) the trajectory of the controlled variables in polar coordinate system is shown. It can be seen, that the flux of the machine firstly reaches

its desired value and then starts chattering around the desired flux line and the orthogonal current component is adjusted according the needed mechanical torque.

6. CONCLUSION

The control strategy of the matrix converter based on the virtual DC/link concept and a generalized sliding mode modulation of the virtual inverter part was presented. The simulation results look very promising and show that the sliding mode control of the virtual inverter part can operate simultaneously with the independent input sinusoidal modulation. However the real impact of the modulation can be evaluated first after the realization of the algorithm on the real converter prototype. Nevertheless, it is a solid base for further investigation and improvement of the suggested control concept for a matrix converter induction motor drive system.

ACKNOWLEDGMENT

REFERENCES

1. Ryvkin, S., R. Schmidt-Obermoeller, and A. Steimel, "Sliding-mode-based control for a three-level inverter drive," *IEEE Transaction on Industrial Electronics*, Vol. 55, No. 11, 3828–3835, 2008.
2. Simanek, J., J. Novak, and O. Cerny, " FOC and flux weakening for traction drive with permanent magnet synchronous motor," *IEEE International Symposium on Industrial Electronics*, Vols. 1–5, 2008.
3. Lettl, J., "Matrix converter induction motor drive," *Proceedings of EPE-PEMC 2006*, Vol. 1–4, 1119–1124, Portoroz, 2006.
4. Lettl, J. and S. Fligl, "PWM strategy applied to realized matrix converter system," *PIERS Proceedings*, 122–125, Prague, Czech Repulic, August 27–30, 2007.
5. Lascu, C., I. Boldea, and F. Blaabjerg, "Variable-structure direct torque control, a class of fast and robust controllers for induction machine drive," *IEEE Trans. Ind. Electron.*, Vol. 51, No. 4, 785–792, 2004.
6. Ryvkin, S., "Sliding mode technique for ac drive," *Proc. 10th Int. Power Electron. & Motion Control Conf.*, EPE — PEMC, Dubrovnik & Cavtat, Croatia, 2005.
7. Utkin, V. I., J. Gldner, and J. Shi, *Sliding Mode Control in Electromechanical System*, Taylor & Francis, London, Philadelphia, 1999.

Voltage Converters with Switched-capacitor

V. Sladecek, **P. Palacky**, **P. Vaculik**, **and J. Oplustil**

Faculty of Electrical Engineering and Computer Science
Department of Electronics, VŠB — Technical University of Ostrava,
17, Listopadu 15, Ostrava-Poruba 70833, Czech Republic

Abstract— In recent years, all industries put emphasis on efficient energy management. This is also true in electronics, where the tendency to achieve maximum efficiency of electronic devices is one of the key criteria for the design of new generation appliances. This, of course, requires a new approach when applying solutions to the already established technologies. As far as power converters are concerned, switched-capacitor converters slowly take the lead as they promise greater efficiency than DC-DC converters used until now, and which use inductance to accumulate energy.

1. INTRODUCTION

Switched-capacitor converters are an alternative to the DC-DC converters with accumulation inductance. Using the switched-capacitor converters leads to a substantial increase in efficiency switching power supply. Switched-capacitor power converters are often used to provide simple power-conversion functions at low power levels. These functions include doubling, halving and inverting the input voltage, and can be combined to achieve other conversion ratios. Typical applications include RS232 level converters and FLASH memory programming voltage generators. These standard converters are often unregulated or supplemented with a linear regulator for voltage regulation.

Switched-capacitor converters are slowly taking the lead also in the field of power converters, which promise greater efficiency than DC-DC converters used until now, and which use inductance to accumulate energy. To get the output voltage (U_{OUT}), which corresponds to the n — multiple of the input voltage, is the basic function of the increasing converter. This n — multiple (for switched-capacitor converters) usually occurs via parallel charging of the internal n — capacitors of the converter. These capacitors are then connected in series to the load. The actual topology of the converter is then determined by the combination of these connections. An important feature of the converter is its internal resistance R_i. This represents the sum of all losses due to parasitic properties of the used components. Efforts to eliminate the internal resistance (impedance) lead to the use of capacitors with low series resistance (low ESR) and to the use of switching elements with uni-polar characteristics with low impedance in the "switched on" (closed) state. The report shows practical results obtained during the design of the DC-DC converter with medium output (about 50 W).

2. CAPACITOR CONVERTERS — DESIGN OPTIONS

Based on the function of switched-capacitor converters we see that to achieve efficiency and performance, we need two basic phases or stages, namely the charging stage (1), when the energy is gathered by capacitors and the discharge stage (2), when the stored energy (power) is transferred to the load. Based on these requirements, we may divide the design of converters according to several switching technologies.

These are for example:

- Ladder topology (Fig. 1)
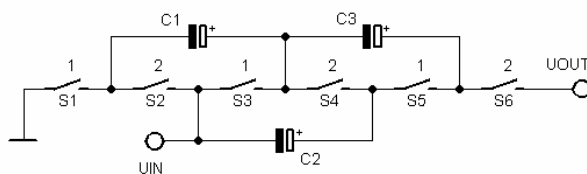
Figure 1: Ladder topology.
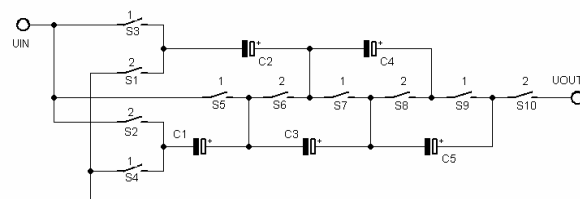
Figure 2: Dickson charge pump.

- Dickson charge pump (Fig. 2)
- Fibonacci Topology (Fig. 3)
- Serial-Parallel Topology (Fig. 4) [1]

3. CONVERTER WITH LADDER TOPOLOGY

The main purpose of this paper is to provide a functional description of a sample switched-capacitor converter with the following parameters:

Input voltage: 12 V
Converter multiplication ratio n: 6
Current consumption: 1 A

The actual converter is controlled by a microcomputer, which generates control pulses for the power switches. The switched-capacitor converter may be divided into several functional blocks (see Fig. 5). The main part of the convertor is the power stage, where the components must be properly designed and rated in order to minimize power losses. In this block, the input voltage is multiplied within the desired ratio. Proper function of the power stage is ensured by the induction stage, which adjusts the control voltage so the power elements of the converter may be reliably switched on and off. Control circuits must generate switching pulses according to the algorithm, in order to avoid unnecessary losses caused by switch commutation in the power section (dead time). The power supply circuits are designed to adapt the input voltage according to the needs of the control circuitry.

The ladder topology was selected for the actual implementation of the converter (see Fig. 1), which is characterized by the same voltage on all circuits of the capacitor. Based on the used topology it is clear that the implementation of the power stage for $n = 6$ will require 9 capacitors. Maximum current will flow through the capacitor $C1$. Because the required output current of the converter is set to 1 A, a current equal to 5 times the required current will flow through the
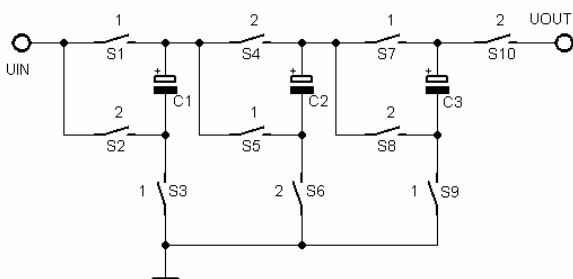
Figure 3: Fibonacci topology.
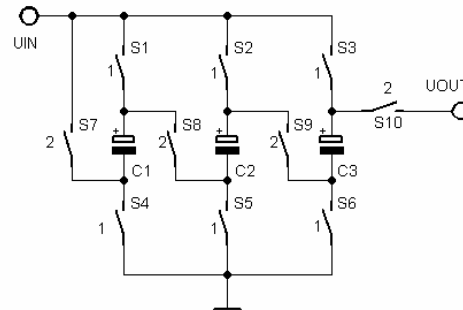
Figure 4: Serial-parallel topology.
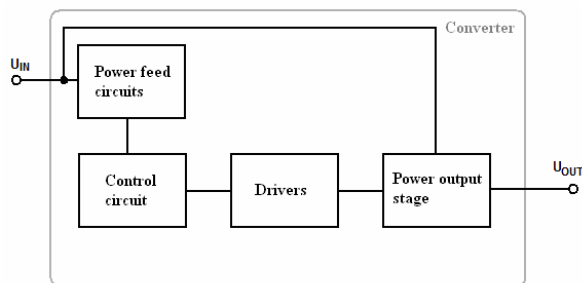
Figure 5: Converter diagram.
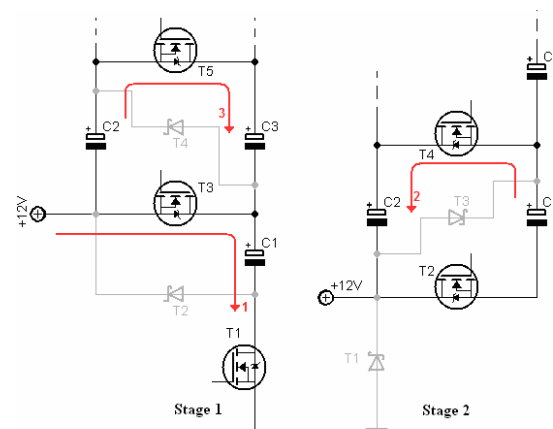
Figure 6: Implementation of switches into the relevant topology.

capacitor — that is 5 A. With regard to the operation and use of the converter it is necessary to select capacitors with low series parasitic impedances, which are designed for pulse modes (low ESR). The basic parameter/requirement for the design of these capacitors is the so-called maximum ripple current, which determines the current value at which the capacitor is able to work. This value is influenced by the operating frequency of the capacitor and by the surrounding temperature. It is evident from the catalogue that a capacitor which is required to work with a current of 5 A must be assembled from multiple elements arranged in parallel. To realize the converter, capacitors $C = 470\,\text{u}/16\,\text{V}$ were selected, which are capable to work with currents up to 675 mA at a maximum operating temperature of 105°C and at an operating frequency of 1 kHz. Given the 20% tolerance of components, the number of capacitors arranged in parallel was established at 2 pcs/A, so the $C1$ will have the capacity equal to:

$$C1 = 10C, \ C2 \text{ and } C3 = 8C, \ \ldots \ C8 \text{ and } C9 = 2C$$

4. SWITCHING ELEMENT DESIGN

Great deal of attention during the design process was paid to the efficiency of the converter. To achieve high efficiency, we must select switching elements with minimal power loss — that is with high conductivity in the conducting ("on or closed") state. These requirements are met by uni-polar MOSFET transistors, which unlike other types of switching elements, offer relatively low resistance of the conductive channel in the closed state (in units of tens of mΩ). The disadvantage, however, may be the way they are controlled — as already demonstrated in practice, in order to achieve good closure ("switched on" state), they need to have a negative voltage at the control electrode. As an ideal component for the construction of the converter, we selected transistor IRLR2908, which offers the maximum R_{DS} (ON) value of 28 mΩ, maximum switching current $I_D = 39\,\text{A}$, U_{DS} voltage $= 80\,\text{V}$, and control voltage $U_{GS} = +/-16\,\text{V}$.

When arranging the switches into the topology we also need to pay attention to the connection of inner reverse diodes, which may (if connected incorrectly) shortcut the already charged capacitors in the converter. We recommend sketching the polarity of the switches and their reversing diodes down to individual stages of the converter topology, whereas in the first stage we shall draw reverse diodes from stage two and vice versa (see Fig. 6).

If all switches in the circuitry are properly polarized, their reverse diodes have a positive effect on converter start-up, when capacities on higher stages are discharged. During the first step as seen on Fig. 6, the capacitor $C1$ is charged through the reverse diode of the transistor $T3$ and through the open transistor $T1$. Transistor $T3$ cannot be opened yet as there is no voltage on the control electrode — the voltage is provided by the higher stage. Transistor $T1$ in stage 1 is switched on (closed) thanks to the input voltage ($+12\,\text{V}$).

During the second stage, the capacitor $C1$ is already charged and therefore the transistor $T2$ may be switched. If the transistor $T2$ is closed, the charge of $C1$ is transferred over to $C2$ through the reverse diode of $T4$. After startup the charge will run through the entire converter in similar way. When the voltage is gradually "copied" over to higher capacities, all transistors in the topology will be gradually switched. This method eliminates power loss in reverse diodes, and therefore only losses caused by the conductivity during the switch on state (closed state) will apply.
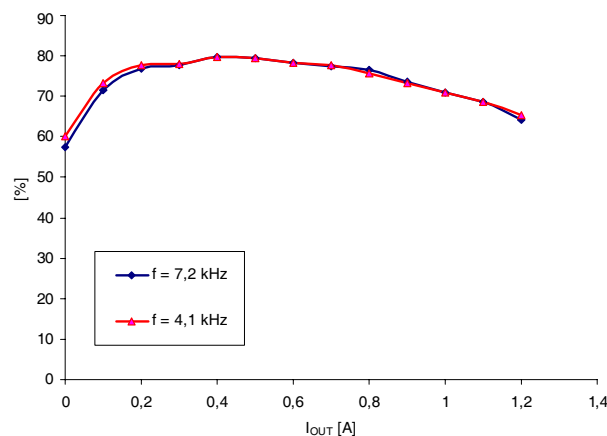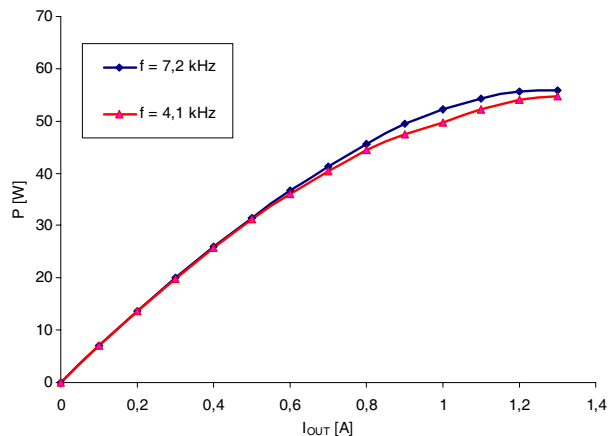

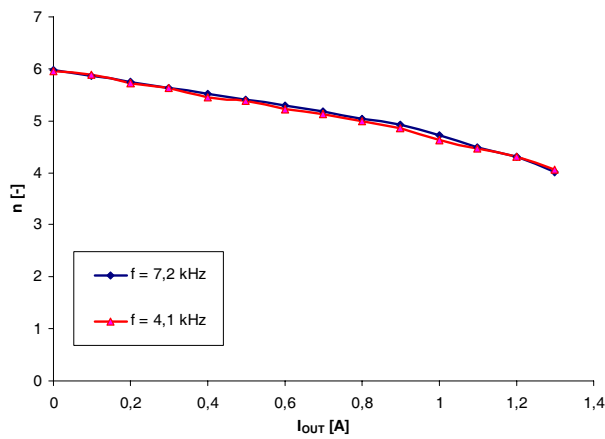Figure 7: Converter efficiency.

Figure 8: Converter power output.

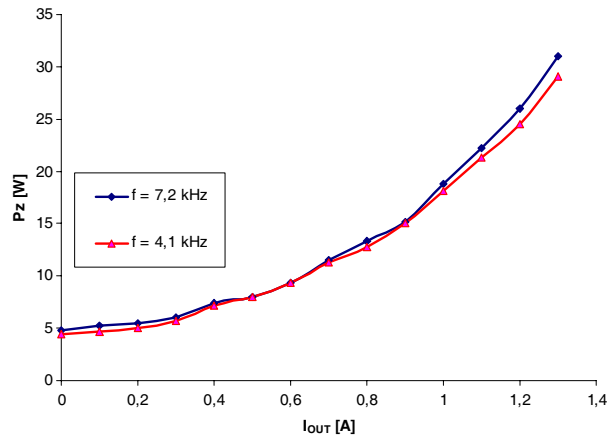Figure 9: Converter load characteristics.

Figure 10: Converter power loss.

5. EXPERIMENTAL RESULTS

The following diagrams show curves obtained by laboratory measurements using a sample converter with the above specified parameters. Curves demonstrate two switching frequencies 7.2 kHz and 4.1 kHz.

From these curves you may see that the switching frequency contributes to the efficiency of the converter. At higher switching frequencies the efficiency increased for higher current consumption. However, if small currents are drawn, losses of the switches dominate the circuit.

Based on this result, it would be ideal to change the switching frequency of the converter during the operation according to the drawn current, so that we may always use the full potential of the converter.

ACKNOWLEDGMENT

REFERENCES

1. Seeman, M. D., "Analytical and practical analysis of switched-capacitor DC-DC converters," Technical Report No. UCB/EECS-2006-111, http://www.eecs.berkeley.edu/Pubs/TechRpts/2006/EECS-2006-111.html.
2. Brandstetter, P., P. Chlebis, and P. Simonik, "Active power filter with soft switching," *International Review of Electrical Engineering — IREE*, Vol. 5, No. 6, 2516–2526, 2010.
3. Brandstetter, P., P. Chlebis, and P. Palacky, "Direct torque control of induction motor with direct calculation of voltage vector," *Advances in Electrical and Computer Engineering*, Vol. 10, No. 4, 17–22, 2010.
4. Brandstetter, P., P. Chlebis, P. Palacky, et al., "Application of RBF network in rotor time constant adaptation," *Elektronika ir Elektrotechnika*, Vol. 113, No. 7, 21–26, 2011.
5. Brandstetter, P., M. Kuchar, and I. Neborak, "Selected applications of artificial neural networks in the control of AC induction motor drives," *International Review on Modelling and Simulations (IREMOS)*, Vol. 4, No. 3, 1084–1093, 2011.
6. Frydrysek, K., P. Kostial, K. Barabaszova, et al., "New ways for designing external fixators applied in treatment of open and unstable fractures," *World Academy of Science, Engineering and Technology,* Vol. 7, 639–644, 2011.

Modern Control Strategies for Power Active Filter

P. Simonik, **D. Slivka**, **P. Hudecek**, and **L. Odlevak**

VSB-Technical University of Ostrava, FEI, 17. listopadu 15, Czech Republic

Abstract— This paper deals with the possibilities of current regulation methods of parallel active power filters and also with applicable techniques for acquisition of the current reference. In our case it was necessary to evaluate the performance of a new hysteresis current control. The hysteresis control strategy is based on current errors and their derivatives calculation each time the zero voltage vector is set on the AC side of the inverter. The results, analyzed by real sample testing, are also presented here.

1. INTRODUCTION

To restrict the undesirable impacts of modern appliances, passive and active power filters are applied. Passive filters have a number of disadvantages. They can be overloaded or detuned under the impact of filter component ageing, they do not enable quick adaptation to other than design conditions, though nowadays in a number of cases it is impossible to determine the frequency of interference signals in advance. The fact that the passive filter creates — together with network impedance — a resonant circuit with precisely tuned resonances is very important as well. The disadvantages indicated above can be eliminated by applying an active power filter. There are three basic modifications of active power filters: a series active power filter intended for compensation of voltage harmonics of the supply network, a parallel filter intended for compensation of current harmonics of the power network and the so-called combined active power filter, compensating both the voltage and the current harmonics.

2. PARALLEL ACTIVE FILTER CONTROL ALGORITHMS

The capabilities of parallel-connected active filter can be summarized in general as follows:

- filtering of the current harmonics of the supply network,
- compensation of the reactive power,
- compensation of unbalanced load of the supply network.

2.1. Determination of Current References

There are a number of possibilities nowadays (verified by practical applications) to determine the current references, including already known methods and the latest progressive methods, e.g., utilization of neural networks. Let us mention, at least briefly, some of the possible methods.

2.2. Calculation of the Reference Current Using the First Harmonic of the Load Current

The method of calculation using the first harmonic of the load current is one of the ways to calculate the reference current of parallel active filters. Calculation of the required value of the phase line current by Equation (1) is the basic definition to solve this method.

$$i_{a\_žad} = I_{1m} \cdot \sin(\omega t) \quad i_{b\_žad} = I_{1m} \cdot \sin(\omega t - 120°) \quad i_{c\_žad} = I_{1m} \cdot \sin(\omega t + 120°) \tag{1}$$

The I_{1m} element is defined as the amplitude of the required phase line current, while ωt represents the instantaneous phase that can be acquired from the course of the network voltage by utilization of the phase locked loop. The reference current of the active filter can be defined, based on Equation (1), as a complement to the overall load current; this fact is reflected by Equation (2). We cannot neglect the fact that if we determine the reference current according to Equation (2), the higher harmonics will be filtered together with the reactive power of the first harmonics.

$$i_{a\_ref} = i_{a\_zátěž} - I_{1m} \cdot \sin(\omega t) \quad i_{b\_ref} = i_{b\_zátěž} - I_{1m} \cdot \sin(\omega t - 120°)$$
$$i_{c\_ref} = i_{c\_zátěž} - I_{1m} \cdot \sin(\omega t + 120°) \tag{2}$$

However, if we also include φ_1 in the calculation of the first harmonic, see Equation (3) below, the resultant reference current will cover the elimination of harmonics only.

$$i_{a\_ref} = i_{a\_zátěž} - I_{1m} \cdot \sin(\omega t) \quad i_{b\_ref} = i_{b\_zátěž} - I_{1m} \cdot \sin(\omega t - 120° - \varphi_1)$$
$$i_{c\_ref} = i_{c\_zátěž} - I_{1m} \cdot \sin(\omega t + 120° - \varphi_1) \tag{3}$$

It is essential to select a suitable method to calculate the first harmonic of the load current. Let us briefly present at least some of the available methods:

- determination of the first harmonic of the load current by applying the Fourier analysis,
- determination of the first harmonic of the load current by applying the mean value p of the instantaneous power component.

2.3. Calculation of the Reference Current Using the full Clarke-Park Current Transformation (i_d, i_q Method)

Calculation of the reference current, based on the Clarke-Park transformation of the current into the $d, q, 0$ rotation orthogonal system, is another method to calculate the reference current, also known as the "i_d, i_q method". This method is applicable for parallel active filter compensation, besides the current harmonic, even the zero equalizing current. The resultant transformed non-harmonic current will contain the $d, q, 0$ components and a traditional three-phase system will be converted into a rotation orthogonal system. However, the same three-phase system has to be converted into the stationary orthogonal system α, β, 0 in advance. The transformation equations can be defined as follows:

$$[C_{\alpha\beta0}] = \sqrt{\frac{2}{3}} \cdot \begin{bmatrix} 1 & 0 & \frac{1}{\sqrt{2}} \\ -\frac{1}{2} & \frac{\sqrt{3}}{2} & \frac{1}{\sqrt{2}} \\ -\frac{1}{2} & -\frac{\sqrt{3}}{2} & \frac{1}{\sqrt{2}} \end{bmatrix} \tag{4}$$

$$[u_{\alpha\beta0}] = [C_{\alpha\beta0}]^T \cdot [u_{abc}] \tag{5}$$

$$[i_{\alpha\beta0}] = [C_{\alpha\beta0}]^T \cdot [i_{abc}] \tag{6}$$

The phase voltages and currents are represented by the u_{abc} and i_{abc} elements. In this way the transformed system can be converted into the $d, q, 0$ rotation orthogonal system, using the full Park transformation:

$$\begin{bmatrix} i_d \\ i_q \\ i_0 \end{bmatrix} = \begin{bmatrix} \cos\theta & \sin\theta & 0 \\ -\sin\theta & \cos\theta & 0 \\ 0 & 0 & 1 \end{bmatrix} \cdot \begin{bmatrix} i_a \\ i_b \\ i_0 \end{bmatrix} \tag{7}$$

The transformation angle θ can be defined as $\theta = \tan^{-1}(u_\beta/u_\alpha)$. The topology of the distribution of the voltage and current space vectors in the stationary orthogonal system α, β, 0 and in the rotation orthogonal system can be seen in Fig. 1 below. The transformation angle is not constant
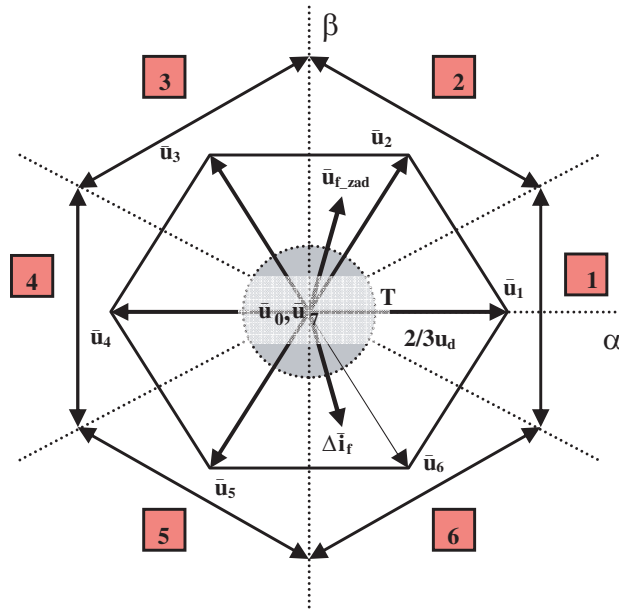
Figure 1: Diagram of the principle of vector hysteresis control.

in time due to the sensitivity of this angle to the voltage harmonics, asymmetry and zero voltage component u_0. The following is applicable to the transformed system with respect to the geometric relations:

$$
\begin{bmatrix} i_d \\ i_q \\ i_0 \end{bmatrix} = \frac{1}{\sqrt{u_\alpha^2 + u_\beta^2}} \cdot \begin{bmatrix} u_\alpha & u_\beta & 0 \\ -u_\beta & u_\alpha & 0 \\ 0 & 0 & \sqrt{u_\alpha^2 + u_\beta^2} \end{bmatrix} \cdot \begin{bmatrix} i_a \\ i_b \\ i_0 \end{bmatrix}
\tag{8}
$$

The instantaneous real and imaginary current components id and iq contain the DC and AC components. The first harmonic of the load current will be transformed into the DC current components i_d and i_q. The active component of the first harmonic will be transformed into the DC component i_d and the reactive component of the first harmonic into the DC component i_q. The reference current of the parallel active filter can then be determined from the alternating components. The alternating component i_d itself is sufficient to filter the harmonics as well as the reactive component of the first harmonic. The mean value can be separated by the high-pass filter or by direct numeric calculation for one period. The following equations is introduced for the final reference current form:

$$
\begin{bmatrix} i_{a\_ref} \\ i_{b\_ref} \\ i_{c\_ref} \end{bmatrix} = \frac{1}{\sqrt{u_\alpha^2 + u_\beta^2}} \cdot \begin{bmatrix} u_\alpha & -u_\beta & 0 \\ u_\beta & u_\alpha & 0 \\ 0 & 0 & \sqrt{u_\alpha^2 + u_\beta^2} \end{bmatrix} \cdot \begin{bmatrix} -\tilde{i}_d + i_{loss} \\ -\tilde{i}_q \\ -i_0 \end{bmatrix}
\tag{9}
$$

$$
[i_{abc\_ref}] = [C_{\alpha\beta 0}] \cdot [i_{\alpha\beta 0\_ref}]
\tag{10}
$$

The $\tilde{i}_d$ and $\tilde{i}_q$ components represent the alternating components of currents i_d and i_q. The i_{loss} component is understood as the current connected with losses in the power part of the parallel active filter converter. If filtering of harmonics is required, i.e., without compensation of the reactive component of the first harmonic, the following equations will be valid for the resultant reference current:

$$
\begin{bmatrix} i_{a\_ref} \\ i_{b\_ref} \\ i_{c\_ref} \end{bmatrix} = \frac{1}{\sqrt{u_\alpha^2 + u_\beta^2}} \cdot \begin{bmatrix} u_\alpha & -u_\beta & 0 \\ u_\beta & u_\alpha & 0 \\ 0 & 0 & \sqrt{u_\alpha^2 + u_\beta^2} \end{bmatrix} \cdot \begin{bmatrix} -\tilde{i}_d + i_{loss} \\ -i_q \\ -i_0 \end{bmatrix}
\tag{11}
$$

$$
[i_{abc\_ref}] = [C_{\alpha\beta 0}] \cdot [i_{\alpha\beta 0\_ref}]
\tag{12}
$$

The non-sinusoidal voltage of the distribution system (supply network) has a negative impact on the correctness of results of the compensation if the method as above is applied.

3. METHODS OF CONTROLLING FILTER CURRENT

This chapter will analyze methods of controlling the parallel active filter current.

3.1. Method of Controlling Double-band Hysteresis

The application of double-band hysteresis controllers in the control circuits of semiconductor inverters represents one of the possibilities of controlling the output current. The simplicity and high current control rate in the preset tolerance zone are undisputable advantages of these controllers. The hysteresis comparators compare the reference (i_{fa,b,c_ref}) and the real (i_{fa,b,c_sk}) current values with the Δi hysteresis. The output comparator signals determine which of the pair of power switches of the branch in question will be switched. A separate comparator is used for each filter phase The double-band hysteresis controller can be of digital or analogue design. If the double-band hysteresis controller is of digital design, then the comparison is performed using the sampling frequency f_{VZ}. Therefore, the peak-to-peak value of the controlled current is higher. To eliminate any undesirable escalation, the double-level controller can be designed as a controller where hysteresis cannot be selected. The hysteresis is then determined by the maximum sampling frequency and by the rate of current rise (in the case of an active filter with soft switching, the hysteresis is determined by the resonance inverter frequency and by the rate of resonance pulse rise). The following relation can be defined for the maximum frequency of switching:

$$
f_{\mathrm{Smax}} = \frac{f_{VZ}}{2}
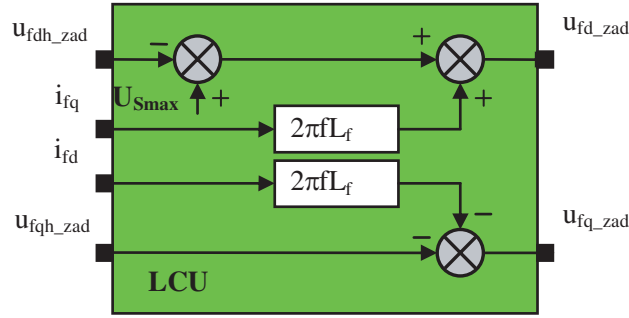\tag{13}
$$

Figure 2: Details of the Link Cancellation Unit (LCU).

3.2. Method of Vector Control with Tolerance Band

The tolerance band controller is functional within the coordinates α, β. First the controller calculates the instantaneous value of the current control deviations in both axes α and β. This can recorded as relations (14) and (15). The defined deviations of instantaneous current values are represented in the vector space by the vector $\Delta \bar{i}_f$. A diagram of the vector space can be seen in Fig. 1 below. If the absolute value of the $\Delta \bar{i}_f$ vector exceeds the tolerance zone T, such suitable voltage vector $\bar{u}_f$ must be selected so that the vector $\Delta \bar{i}_f$ may re-enter the tolerance zone as soon as possible. This is ensured by switching a suitable combination of power switches of the filter inverter.

$$\Delta i_{f\alpha} = i_{f\alpha} - i_{f\alpha\_žad}, \tag{14}$$
$$\Delta i_{f\beta} = i_{f\beta} - i_{f\beta\_žad} \tag{15}$$

It is generally valid that the vector "$\bar{u}_X$" is selected if the deviation vector lies in the corresponding sector "X" (in the diagram above, individual sectors are designated 1–6). The figure above shows the state when the vector $\bar{u}_6$ has been selected. If the deviation vector $\Delta \bar{i}_f$ lies inside the tolerance zone T, the zero vectors $\bar{u}_0$ or $\bar{u}_7$ are selected.

3.3. Method of Controlling PWM Current

This controller includes the PI controllers serving for filter current control in the d, q coordinate system. The required voltage values $u_{fdh\_žad}$ and $u_{fqh\_žad}$ are the output values of the controllers. The current in the axis d and/or q is affected not only by the voltage in the same axis, but even by the voltage in the other axis. There is a mutual (undesirable for us) link between the axes d and q that will be eliminated in the Link Cancellation Unit (Fig. 2). The output voltage signals of this Unit $u_{fd\_žad}$ and $u_{fq\_žad}$ are further transformed into the components in the coordinates α, β. When transformed, these components enter the PWM modulator (e.g., the sinusoidal PWM modulator, vector PWM modulator). Let us define the relations describing the method of link cancellation by the mathematical method.

$$u_{fd\_žad} = U_{Smax} - u_{fdh\_žad} + 2\pi \cdot f \cdot L_f \cdot i_{fq} \tag{16}$$
$$u_{fq\_žad} = -u_{fqh\_žad} - 2\pi \cdot f \cdot L_f \cdot i_{fd} \tag{17}$$

where U_{Smax} is the maximum effective value of the line voltage and L_f is the inductance of the output filter coil. Voltage losses $2\pi f \cdot L_f \cdot i_{fd}$ and $2\pi f \cdot L_f \cdot i_{fq}$ at the output inductance are caused by the active and reactive current. Let us display details of the Link Cancellation Unit described by relations (16) and (17) above.

4. CONCLUSION

The principle behind the activity of parallel active filters is based on the technology of semiconductor switching components which is reflected — compared with other traditionally used compensation devices (compensators of the power factor of the first harmonic, passive filters of higher harmonics) — by very good filtering features at very high dynamics of compensation. The ability to compensate the current asymmetry of the power supply system as well as the deformation and reactive power by the same device is an undisputable advantage of active filters when compared with traditional compensation devices The preceding chapters dealt with the methods of current control of active

power filters. Each of these methods has its own pluses and minuses. Hysteresis controllers are very simple and provide a quick response. However, the frequency current spectrum contains uniformly distributed harmonics within the whole band, because the power switches fail to switch with the constant period. When using a PWM-based controller, the current spectrum will be created only by the harmonics, caused by the constant switching frequency, though with a greater amplitude. On the other hand, this fact concerns only the requirements for the output filter chokes and the requirements for EMC.

ACKNOWLEDGMENT

Accurate Measurement Standards and Calibration Techniques for S-parameter Measurements in Coaxial Line System at Millimeter Wave Frequency

M. Horibe and R. Kishikawa

National Metrology Institute of Japan

National Institute of Advanced Industrial Science and Technology, Japan

Abstract— S-parameter measurements are usually established by the vector network analyzers (VNAs) and reference standards. An air dielectric coaxial line is usually used as a reference standard in the VNA measurements. High accurate and precise mechanical tolerance is required in the reference standard air line. The tolerance must be comparable or smaller than wave length at measuring frequency. This means tolerance should be getting smaller at the millimeter wave frequency. The causes of tolerance are coming from manufacturing tolerance and dimensional measurement accuracy. We improve both manufacturing tolerance and dimensional measurement accuracy for air line as the reference standard at millimeter wave frequency. As a result of this, uncertainty of an S-parameter standard is becoming a half of uncertainty of previous standards in National Metrology Institute of Japan (NMIJ).

1. INTRODUCTION

To use an unsupported precision air dielectric coaxial transmission lines (i.e., air lines) as a reference standard, it is necessary to know the scattering parameters (S-parameters) of the line. For example, values and uncertainties of S-parameter are required in residual error evaluations in vector value [1] and in calibration schemes that use a Vector Network Analyzer (VNA) (i.e., offset load calibration [2]). The scattering parameters (S-parameters) of dielectric coaxial air lines as standards are established by dimensional measurements of diameters [3, 4], and lengths, and electrical conductivity of conductors [5]. This implies the precise determination of the dimensional and material properties of the air line's conductors. The dimensions (i.e., diameters and line length) of the conductors are measured with air-gauging [3] and laser-gauging [4] instruments such that both center and outer conductors can be measured separately for unsupported air lines. The reported our dimensional measurement system [6] was insufficient to accurately calibrate the air line S-parameter at millimeter-wave frequencies where large measurement uncertainties severely impeded accurate calibrations.

This paper describes first, NMIJ's primary air line standards and dimensional evaluation techniques. Next the improvement of the dimensional tolerance and uniformity for air lines in 1.0 mm size is discussed. Finally NMIJ's measurement capability by newly developed standard coaxial air lines is summarized.

2. PRECISION AIR LINES

Standard air lines do not contain the dielectric support beads that position the center conductor inside the outer conductor. The center conductor is held only by connectors of the devices and/or test ports of the measuring instrument to which it is connected. The absence of support beads means the characteristics of air lines more closely approach the ideal characteristics.

The specifications of air line in 1.0 mm line size are described below:

- Insertable (i.e., with a male connector at one end and a female connector at the other end).

- Unsupported (i.e., containing no dielectric support beads to hold the center conductor in place).

- Nominal characteristic impedance of 50 ohms.

- 1.0 mm line size, with nominal outer conductor internal diameter of 1.000 mm and nominal center conductor diameter of 0.434 mm [7, 8].

• Fitted with 1.0 mm precision coaxial connectors [7, 8].

3. DIMENSIONAL CALIBRATION FOR AIR LINE

The outer diameter of the center conductor, (a) and the inner diameter of the outer conductor, (b) were measured using the air-gauging measurement system (AGMS) (Fig. 1(a)) and a laser gauging measurement system (LGMS) (Fig. 1(b)) [8, 9]. The both center and outer conductors were set up vertically to prevent the air probes and center conductors from sagging under their own weight. The lengthwise position of the laser sensors and probes were achieved by means of a programmable stepping motor. With this AGMS we are able to measure an 80 mm long air line for a 1.0 mm connector.

The length, l, of the outer conductor of insertable air lines was also measured using the 3-dimensional coordinate measuring machine (3DCMM) [6]. First, the reference position of the 3DCMM was defined by the termination connecting to the adapter. Then, the desired length of the air line was obtained when air line was inserted between the adapter and termination. In the line length measurements, this measurement scheme should be adopted due to the length of air line was shortened when the line was connected to measurement instruments or devices. These dimensional measurement results are traceable to Japanese national length standards via ring, pin, and block gauge reference standards. An expanded uncertainty of approximately 1.0 µm has been estimated for the diameter measurements. Typical calibration results of commercial air line are shown in Fig. 2 and listed in Table 1.

The effective resistivity, ρ, of the air lines was evaluated by means of an insertion loss measurement using a power ratio technique [5] at microwave and millimeter-wave frequencies. The system can measure small insertion losses (less than 0.1 dB, up to 50 GHz).

Other key sources of accuracy for air line S-parameters are center conductor interface (i.e., center conductor gaps and eccentricities in the connectors). The gaps arise around mated surfaces due to varying pin-recession when the adapters are connected to the air line [6]. The eccentricity and pin-depth of test port adapters used in our calibration system were evaluated using an optical displacement meter [6] and digital linear gauges, respectively.

(a)   (b)   (c)

Figure 1: Measurement system for (a) outer diameter of center conductor, (b) inner diameter of outer conductor, and (c) insertion loss at microwave frequency.

Table 1: Typical results of diameters of air line in the 1.0 mm line size for consumer use.

Parameter	Values (mm)	
S	Avg.	$U\,(k=2)$
a	0.4340	0.0040
b	1.0007	0.0026
l	12.1335	0.0017

4. PRECISION AIR LINE STANDARD DEVELOPMENT

Figure 3 shows the photograph of newly developed insertable air lines and flush short terminations. This standard air lines, especially for outer conductor, have good diameter uniformity result along with line length for lines. The tolerance of inner diameter was within $\pm 0.5\,\mu$m. However, uncertainty of measurement system was much large compared with dimensional uniformity (approximately $1\,\mu$m).Then, uniformity of diameter is 1 digit better than that of commercial air line. The average value of b for the outer conductor of commercial air line (Fig. 2(b)) exhibited poor longitudinal diameter uniformity (difference between the two extreme values was approximately $15.0\,\mu$m).

The dimensionally-derived S-parameters, as a function of frequency, have been calculated on the
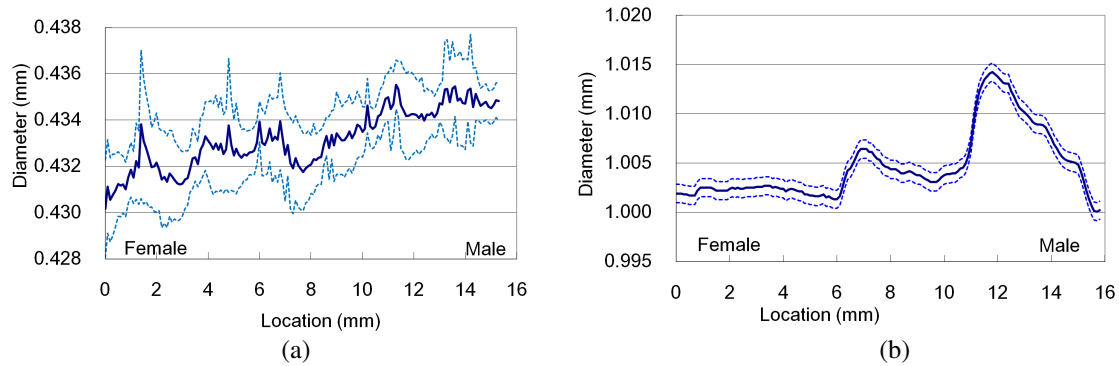
Figure 2: Measurement results for (a) diameter a, and (b) diameter b of $12\,$mm long commercial air lines in $1.0\,$mm line size. Solid lines indicate the calibrated values and broken lines indicate expanded uncertainties.
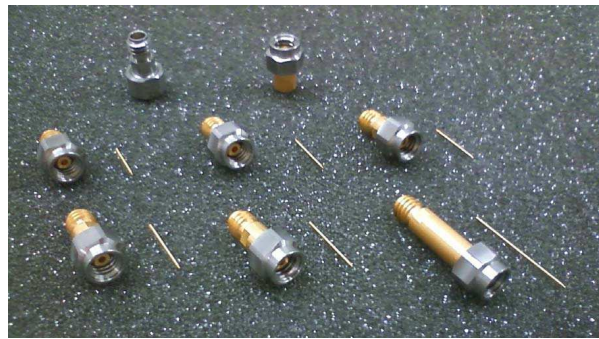
Figure 3: Developed new air lines and flush short terminations in the $1.0\,$mm line size.
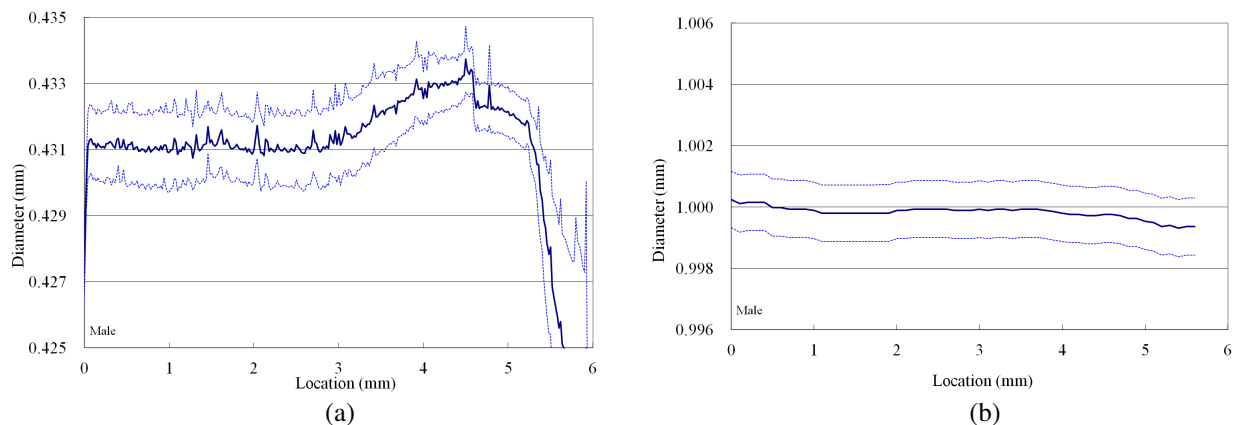
Figure 4: Measurement results for (a) diameter a, and (b) diameter b of $6\,$mm long new air lines in $1.0\,$mm line size. Solid lines indicate the calibrated values and broken lines indicate expanded uncertainties.
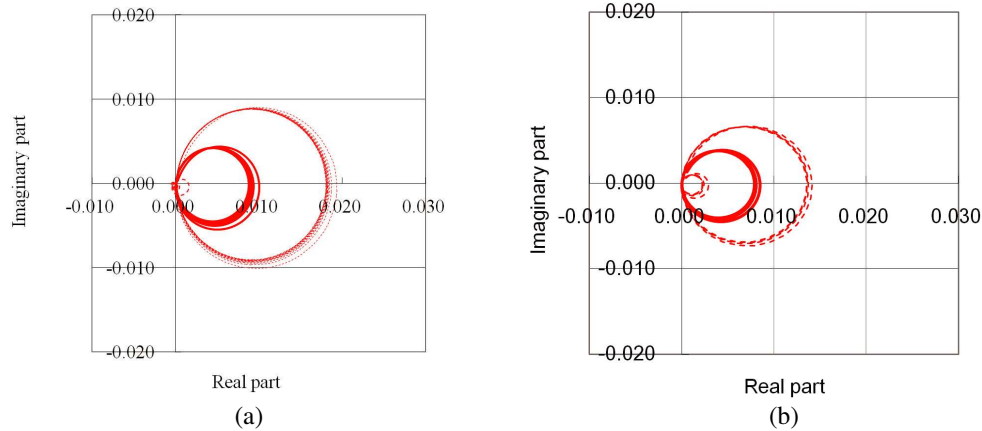
Figure 5: Calculation results of S_{11} for (a) consumer air line, and (b) newly developed air line. Solid lines indicate the calibrated values and broken lines indicate expanded uncertainties.

basis of the method reported in Refs. [5, 6]. In this case, the resistivity of the conductor was defined as $9.0\,\mu\Omega$cm. Figure 5 shows the complex value of S_{11} for (a) the commercial air line and (b) newly developed air line as determined from dimensional measurements. The variation in values of S_{11} of both air lines is attributed to the non-uniformity of diameters a and b along the lines. However, no effects of reflections at the connector ends can be seen in this analysis.

5. CONCLUSIONS

The tolerance of air line was comparable to wave length at measuring frequency (i.e., millimeter wave frequency) due to improvement of the manufacturing tolerance. As a result of this, uncertainty of an S-parameter standard (i.e., approximately 0.005 at 110 GHz) was becoming a half of uncertainty of previous standards (i.e., 0.012 at 110 GHz).

ACKNOWLEDGMENT

REFERENCES

1. Kudo, K., M. Shida, and M. Horibe, NMIJ unpublished report.
2. Horibe, M., N. M. Ridler, M. J. Salter, and C. P. Eio, "Characterization and verification of coaxial open-circuit primary standards for millimeter-wave vector network analyzer calibration," *76th ARFTG Microwave Measurement Conference Digest*, 89–100, Marriott Suites on Sand Key, Clearwater Beach, FL, USA, December 2–3, 2010.
3. Ide, J. P., "Traceability for radio frequency coaxial line standards," *NPL Report DES 114*, National Physical Laboratory, July 1992.
4. Maury, Jr., M. A. and G. R. Simpson, "Two-port verification standards in 3.5 mm and 7 mm for vector automatic network analyzers," *Microwave Journal*, Vol. 27, No. 6, 101–110, June 1984.
5. Horibe, M., M. Shida, and K. Komiyama, "S-parameters of standard airlines whose connector is tightened with specified torque," *IEEE Trans. on Instrum. Meas.*, Vol. 56, No. 2, 401–405, April 2007.
6. Horibe, M., M. Shida, and K. Komiyama, "Development of evaluation techniques for air lines in 3.5 mm and 1.0 mm line sizes," *IEEE Trans. on Instrum. Meas.*, Vol. 58, No. 4, 1078–1083, March 2009.
7. "IEEE Standard for Precision Coaxial Connectors (DC to 110 GHz)," *IEEE 287-2007*, September 2007.
8. "Radio-frequency connectors — Part 31: RF coaxial connectors with inner diameter of outer conductor 1.0 mm (0.039 in) with screw coupling — Characteristic impedance 50 ohms (type 1.0)," *IEC 61169-31*, September 1999.

Establishment of S-parameter Standards of Rectangular Waveguide at Millimeter-wave and THz Frequencies

R. Kishikawa and M. Horibe

National Metrology Institute of Japan

National Institute of Advanced Industrial Science and Technology, Japan

Abstract— Precise S-parameter measurements in the vector network analyzers (VNAs) are established by reference standards with small uncertainty. A standard line section is usually used as a VNA's reference standard. High precise mechanical tolerance of waveguide aperture is required in the reference standard in waveguide system. The tolerance must be smaller than wave length at measuring frequency. This means tolerance (i.e., a few micro meters) should be achieved at the sub-millimeter wave and THz frequencies. The causes of tolerance are coming from manufacturing tolerance and dimensional measurement accuracy. We have already developed the evaluation scheme of dimensions of WR-3 (WM-864) waveguide apertures by three dimensional coordinate measuring machine (3DCMM). However, it is impossible that 3DCMM measures the aperture of THz waveguide (WR-1, WM-250). We developed new dimensional measurement system for small size aperture. As a result of this, an S-parameter standard is established in the frequency range from 110 GHz to 1 THz.

1. INTRODUCTION

In recent years millimeter and THz signals have been used not only in radio astronomy but also in such industrial applications as mobile communications. There the use of millimeter-wave instruments has accelerated in recent years, and operation frequency range of commercial vector network analyzers reaches 1 THz and beyond [1]. Some systems and standards have been available for ensuring the quality of measurements made at frequencies above 110 GHz [2] and inter-laboratory comparisons have been reported [3]. We have thus lunched a research program to develop national measurement standard techniques providing a high level of accuracy in VNA measurements with traceability to primary national standards.

Fabrication tolerances of waveguide are comparable with the precision limits of machining techniques. The problem of flange misalignment is no longer insignificant compared to the aperture sizes of waveguides. In order to establishing accurate measurements in the waveguide measurement system at millimeter and sub-millimeter wave frequencies, accurate evaluation techniques for S-parameter measurement standards have become an important. In the commercial waveguide calibration kits used at millimeter wave frequencies there are common dimensional irregularities that occur in the manufacturing of rectangular waveguides.

This paper describes the evaluation techniques for national standard use in VNA waveguide system that has provided S-parameter measurements in the frequency range above 110 GHz (up to 1 THz).

2. DIMENSIONAL MEASUREMENTS

For metrology purposes the principal measurements for rectangular waveguide have been the aperture dimensions (width and height). At millimeter and sub-millimeter wave frequencies, accurate and reliable measurement standards based on dimensional measurements alone pose a significant challenge.

Measurement traceability to international standards (SI) system was ensured for the VNA's S-parameter measurements via dimensional measurements of a standard quarter wavelength shim. Measurements of the width and height of the waveguide apertures were made using a three dimensional coordinate measuring machine (3DCMM) fitted with a 0.300 mm diameter ball-tip microstylus (Fig. 1(a)) at standard conditions (23°C) of the electrical calibration laboratory. The width dimension was measured at 25 locations and the height dimension was measured at 50 locations. This 2-dimensional grid of measurements was repeated at 64 different locations along the shim thickness inside the aperture. The systematic uncertainty of the 3DCMM measurements was approximately 0.93 μm. Then, the uncertainty of the reproducibility was 0.46 μm ($k = 2$) for the width dimension and 0.38 μm ($k = 2$) for the height dimension. Furthermore dimensional variation of the aperture along the shim thickness was major contribution to the total measurement uncertainty in
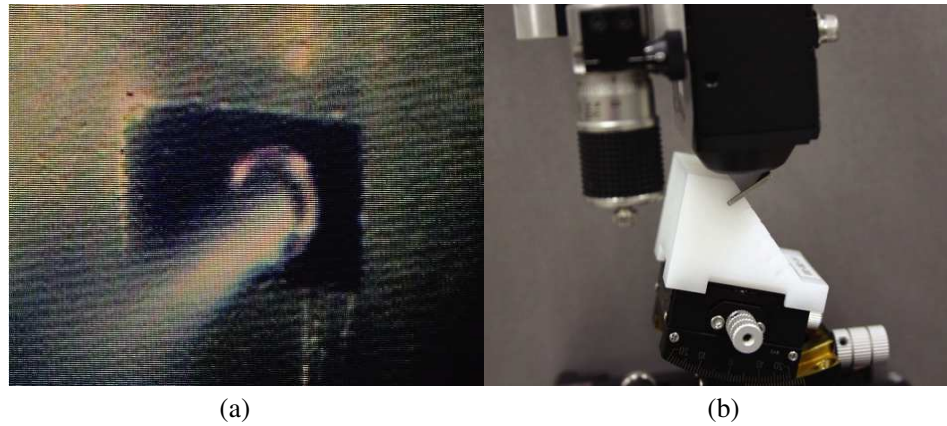
<center>(a)   (b)</center>

Figure 1: Photograph of (a) the 3DCMM measurement and (b) the laser displacement measurement for waveguide aperture of quarter wavelength shim.

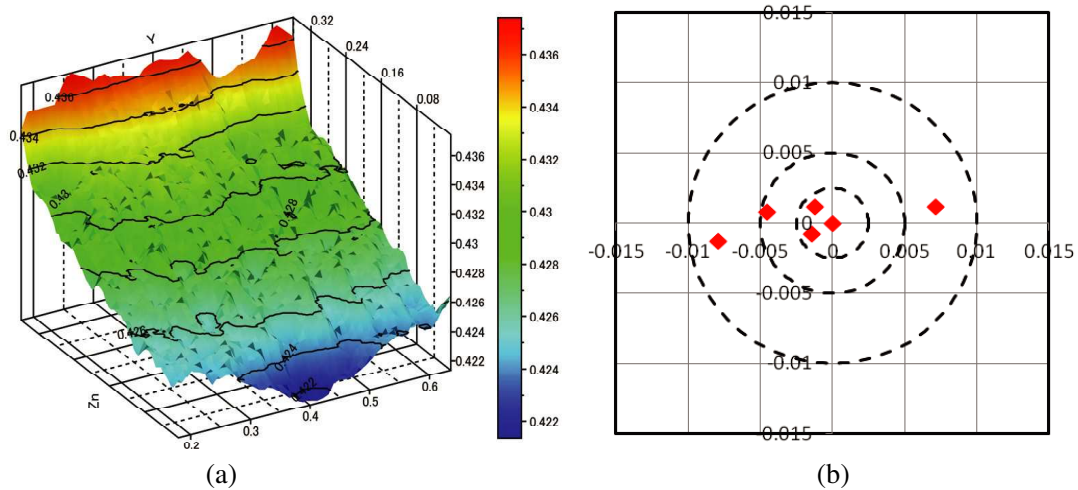<center>(a)   (b)</center>

Figure 2: Measurement results of (a) height dimensions of aperture for WM-864 waveguide shim, and connection repeatability of conventional UG-387 flange.

commercial products [1]. Measurements of the aperture corner radii of a WR-3 (WM-0864) shim using the dimensional measurement apparatus were made by a laser displacement meter with a specialized stage that can adjust the incident angle of the laser beam (Fig. 1(b)).

However, it is impossible to measure width and height inside the waveguide aperture for smaller size waveguide by 3DCMM. The WR-1 (WM-250) aperture dimensions (width of 0.250 mm and height of 125 mm) are smaller than diameter ball-tip micro-stylus of 3DCMM. For dimensional measurement of smaller size aperture, laser displacement meter (Fig. 1(b)) can be used.

3. PRESIZE MEASUREMENT STANDARDS IN WAVEGUIDE SYSTEM

Dimensional variation of the aperture was not uniform along the shim thickness in commercial products [1, 3]. For establishing accurate measurement and precise standards, we specially designed and made a new type flange and precision waveguide standard shim lines (Fig. 3(a)).

The measurements of the width dimensions at varying positions along the height direction and at varying location along the shim thickness are shown in Fig. 2(b). From Fig. 2(b), the 3σ deviation of the broad-wall dimension reaches $0.96\,\mu$m from its mid value of 0.8570 mm. For the height dimensional deviation from the mid value of 0.424 mm was approximately $1.26\,\mu$m. For commercial shim standard the total uncertainty was almost wholly determined by the uniformity of aperture size along shim thickness. However, with new standard reduction of total uncertainty of waveguide shim standard were established.

The shape inside the aperture dimension was evaluated using a laser displacement measurement instrument (LDMS) with a stage adjustment for the incident angle of laser beam for small size

(a)   (b)
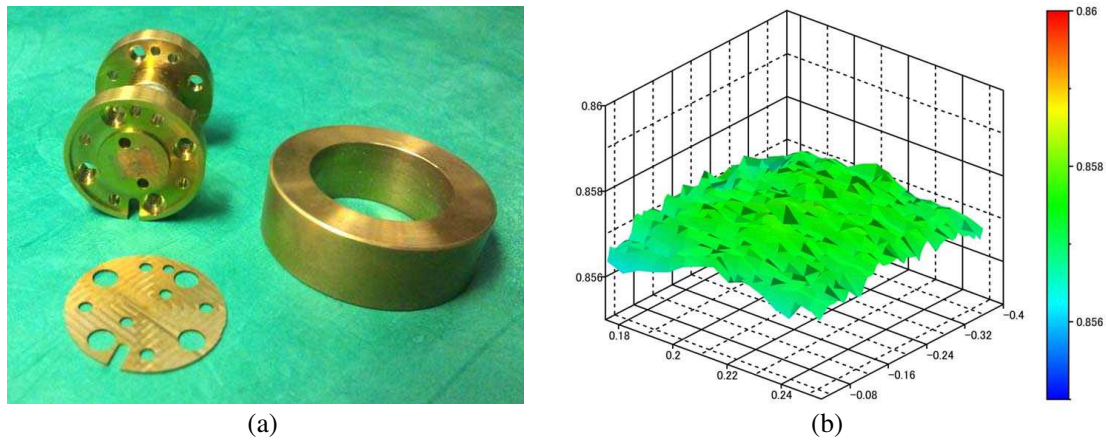
Figure 3: (a) New design of waveguide flange and calibration standard shim (WM-250), and (b) measurement results of broad wall dimension for WM-0864 waveguide aperture of quarter wavelength shim.
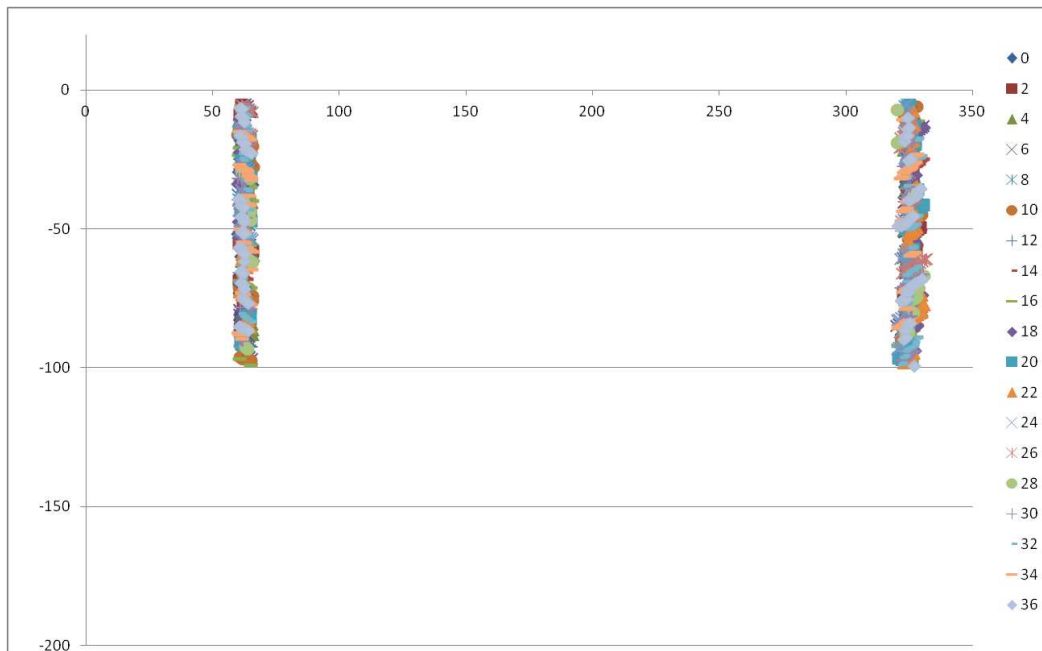
Figure 4: Measurement result of aperture width of calibration standard shim (WM-250) with shim thickness of 0.300 mm. Nominal size is approximately 0.125 mm [2].

waveguide (i.e., WM-250). The laser beam entered the shim aperture at 30 degrees. One of results is shown in Fig. 4. In this measurement, waveguide aperture size was decided along with shim thickness.

4. CONNECTION REPEATABILITY

Repeatability evaluations were made using a PNA Vector Network Analyzer from Agilent Technologies and a WR-3 frequency extension module from Oleson Microwave Inc. (OML), and WR-1 frequency extension module from Virginia Diode Inc. (VDI).

The voltage complex reflection coefficients (complex-VRC) around the flange interface of new design flanges were plotted on the polar charts at representative frequencies in the WM-864 band and WM-250 band in Figs. 5(a) and (b). Then, Fig. 6 show the complex-VRC around the shims. Plots are normalized by averaged value of ten measurands. The ten points correspond to the ten disconnection/reconnection cycles. The repeatability data indicate that the new design flanges have good repeatability (less than −50 dB at 300 GHz, and approximately −40 dB at 1 THz).
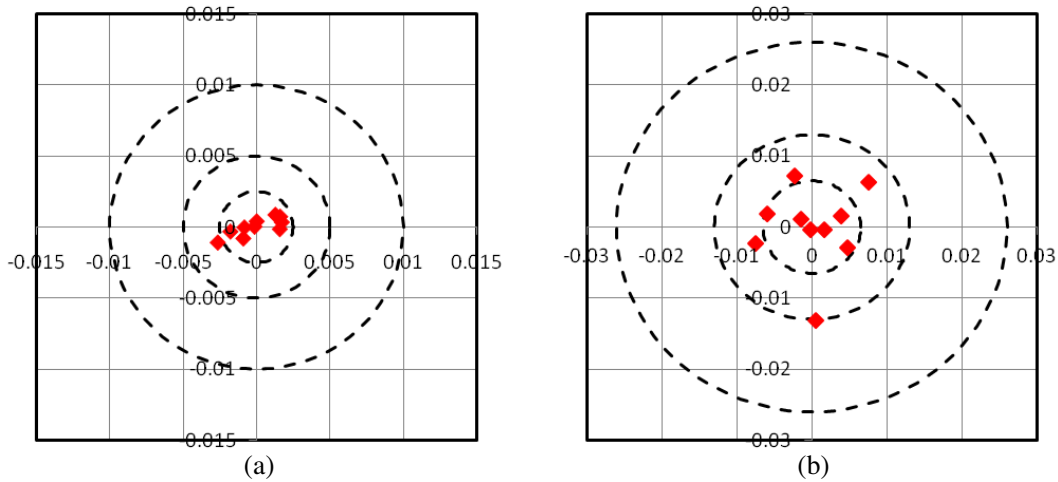
Figure 5: Results of reflection coefficient repeatability for a series of 10 repeat reconnection/disconnection measurements for a pair of new design flanges. (a) S_{11} of WM-864 interface at 330 GHz, and (b) S_{11} of WM-250 at 1 THz.
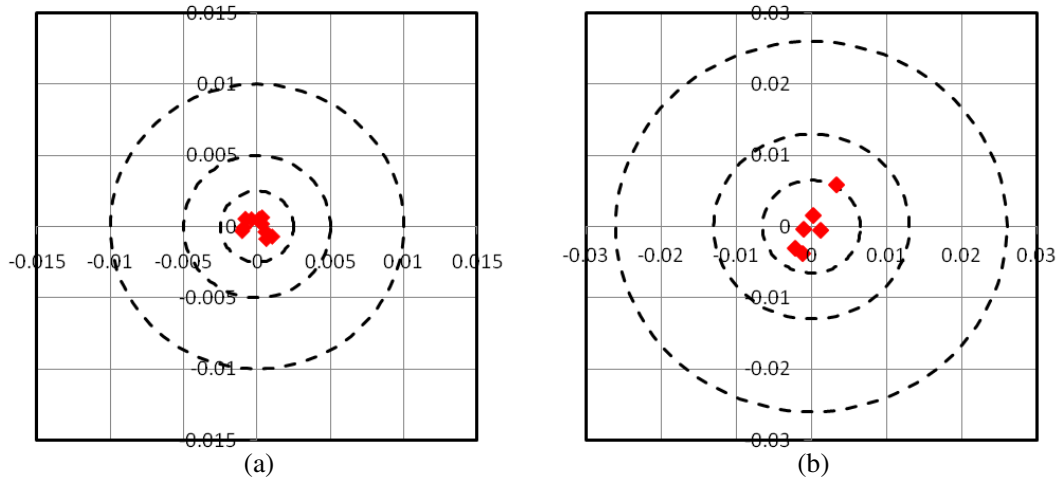
Figure 6: Results of reflection coefficient repeatability for a series of 10 repeat reconnection/disconnection measurements for a shim fitted with new design flanges. (a) S_{11} of WM-864 interface at 330 GHz, and (b) S_{11} of WM-250 at 1 THz.

5. CONCLUSIONS

Precise measurement standard for the vector network analyzers (VNAs) are established by accurate dimensional calibration technique and new type waveguide. A standard line section is made with small dimensional tolerance and good uniformity of aperture dimensions. We have developed the evaluation technique of dimensions of WR-1 (WM-250) waveguide apertures by laser displacement meter. In addition, we developed new type waveguide flange for small size aperture. As a result of this, an S-parameter measurement accuracy is improved in the frequency range from 110 GHz to 1 THz.

REFERENCES

1. Horibe, M., R. Kishikawa, and M. Shida, "Complete characterization of rectangular waveguide measurement standards for vector network analyzer in the range of millimeter and submillimeter wave frequencies," *76th ARFTG Microwave Measurement Conference Digest*, 15–29, Clearwater Beach, FL, USA, Dec. 2010.

2. "IEEE Standard for Rectangular Metallic Waveguides and Their Interfaces for Frequencies of 110 GHz and Above," IEEE P1785, http://grouper.ieee.org/groups/1785.

3. Horibe, M., R. Kishikawa, and M. Shida, "Modification of waveguide flange design for millimeter and submillimeter-wave measurements," *77th ARFTG Microwave Measurement Conference Digest*, Baltimore, ML, USA, Jun. 2011.

Estimation of Terrestrial Rain Attenuation at Microwave and Millimeter Wave Signals in South Africa Using the ITU-R Model

P. A. Owolawi[1], **S. J. Malinga**[1], **and T. J. O. Afullo**[2]

[1]Department of Electrical Engineering, Mangosuthu University of Technology
Umlazi, KwaZulu-Natal 0002, South Africa
[2]Department of Electrical, Electronic, and Computer Engineering, University of KwaZulu-Natal
Durban 4000, South Africa

Abstract— This paper presents the rain rate experimental measurement with the application of the International Telecommunication Union's Recommendations (ITU-R) on rain attenuation model in South Africa. The nineteen chosen sites, at least one from each province in South Africa, are considered for this study. The parameters presented in this paper are specific attenuation and total path attenuation due to rain at horizontal, circular, and vertical polarizations at frequency ranges from 1–400 GHz. The implications of rain attenuation to the system designers are evaluated by finding link distance chart, and design link-budget at the chosen frequency range. The results of this work can be used in planning links for both microwave and millimeter broadband wireless networks in South Africa such as Local-Multipoint-Distributed-Services (LMDs).

1. INTRODUCTION

The interest of many telecommunication companies to provide high speed wireless internet access, broadcast multimedia information, multimedia file transfer, remote access to a local network, interactive video conference and Voice-Over-IP has forced migration from lower frequency bands which are already congested to higher frequency bands such as microwave and millimeter bands. The choice of these bands became the key solution to today's request because of large bandwidth availability, small device size and wide range of spectrum availability. Although with all the inherent advantages, rain is the major offender to optimum performance and usage of these bands. Rain attenuation results in outages that compromise the quality of signal and link availability making it a prime factor to be considered in designing both terrestrial and satellite links. This means that the design of any communication device in this spectrum range requires knowledge of rain fade in order to provide optimum link availability and robust and reliable link to any telecommunication systems that offer aforementioned benefits [1].

The performance metric considered mostly in link analysis is the system availability. That is, the time percentage the link is providing service either at or below the specified given bit error rate. It was confirmed that at frequencies just above 5 GHz, the rain fade depth becomes noticeable and severe at a frequency above 10 GHz [2]. Rain rate measurement is one of the active components needed to estimate the amount of rain fade, which is frequency and location dependent. The extensive work carried out on the rainfall characteristics at different locations in South Africa has confirmed a dynamic distribution of rain rate in the region [3].

This paper presents the application of results found in a rain rate characteristics study in South Africa as documented in [3] and their application to terrestrial links. It provides an analysis on rain fade in the light of the link distance chart and how it relates to the link budget. The outcomes are incorporated into the link budget to determine the maximum link distance and other performance parameters.

2. MATHEMATICS OF RAIN FADE MODEL

Most communication systems at microwave and millimeter bands may experience a loss due to rain attenuation which temporarily makes the link unavailable for use at a given time. Rain attenuation depends on rain rate characteristics, rain shape, rain drop size, and volume density. In instances where the rain attenuation measurements are not available, the rain rate becomes an important parameter for estimating the level of fade due to the rain. An empirical relationship between the rain rate R (mm/hr) and the specific attenuation (dB/km) is given as:

$$\gamma = aR^b \text{ (dB/km)} \tag{1}$$

where a and b are regression coefficients which depend on the drop shape of the falling rain, the raindrop density, the polarization and the frequency. The regression coefficients in Equation (1) are computed by using ITU-R P.838-3 [4]:

$$a = \left[a_H + a_V + (a_H - a_V)cos^2\theta \cos 2\tau \right] /2 \tag{2}$$

$$b = \left[a_H b_H + a_V b_V + (a_H b_H - a_V b_V) \cos^2 \theta \cos 2\tau \right] /2a \tag{3}$$

where τ is the polarization tilt angle relative to the horizontal and θ is the path elevation angle. In the case of linear vertical or horizontal polarization used for radio link transmission, the polarization tilt angle $\tau = 90°$ for vertical polarization and $\tau = 0°$ for horizontal polarization and $\tau = 45°$ for circular polarisation. The path elevation angle $\theta = 0°$ as it is assumed that the angles of arrival and launch make an angle of $0°$ with the ground [5].

The total path attenuation is given as the product of specific attenuation γ (dB/km) and effective path length L_{eff} (km) between the transmitter and the receiver:

$$Att_{(0.01)} = aR^b L_{eff} \, (\text{dB}) \tag{4}$$

where:

$$L_{eff} = \frac{d}{1 + d/d_0} \, (\text{km}) \quad \text{and} \quad d_0 = 35e^{-0.015R_{0.01}} \tag{5}$$

where d is the path length and $R_{0.01}$ is the rain rate exceeded in 0.01% of the time. The fade depth is given at any desired availability for latitudes greater than 30 degrees, North or South as:

$$Att/Att_{0.01} = 0.12p - (0.546 + 0.043 \log (p)) \tag{6}$$

while for latitudes below 30 degrees, North or South it is given as:

$$Att/Att_{0.01} = 0.07p - (0.855 + 0.139 \log (p)) \tag{7}$$

where p is the desired probability (100 — availability) often expressed as a percentage.

3. CUMULATIVE DISTRIBUTION OF RAIN RATE

Rain attenuation prediction depends on the 1-minute rain rate distribution at a defined percentage of exceedence. The cumulative rain rate distribution for different locations in South Africa is
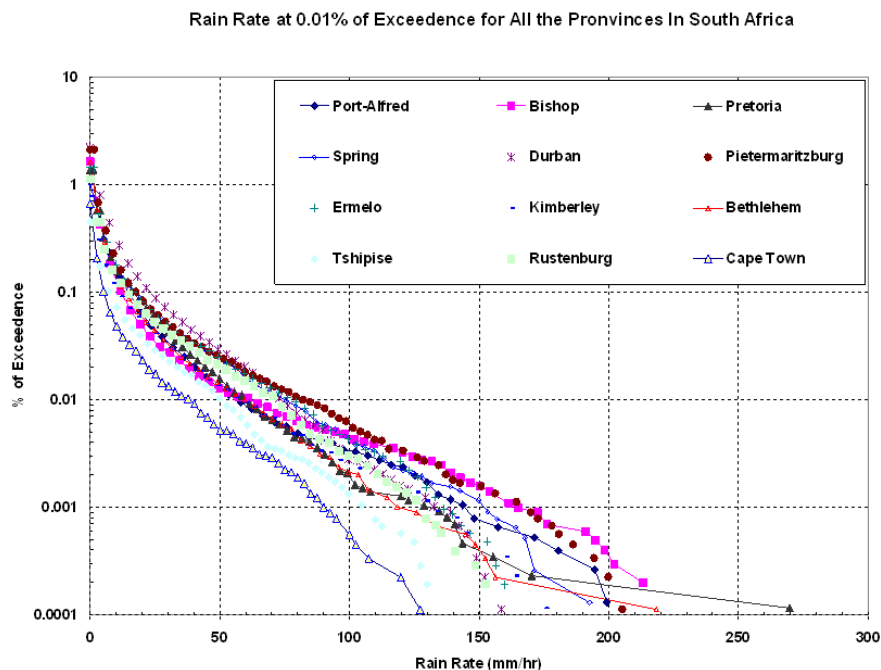
Figure 1: Average cumulative time distribution of the rain rate in all provinces in South Africa.

presented in Figure 1. The method used in converting available rain data from 5-minute integration to 1-minute equivalent is presented in [6].

Table 1 shows a summary of rain rate value at 0.01% of exceedence which is acceptable signal availability threshold for radio systems to perform well.

The minimum rain rate at 0.01% is recorded in the Western Cape Province with an average value of 27.0 mm/hr and the highest rain rate recorded in both Mpumalanga and KwaZulu-Natal provinces with an average record of 78.0 mm/hr and 76.0 mm/hr respectively.

As reported in [6], the conventional designations from both ITU-R and Crane were interpolated with available rain data to determine newly proposed designations for South Africa. It was observed that the ITU-R P.835-5 under-estimates the rain rate values and Crane confirms likewise. Also in [6] the rain rate contour map is presented using Crane and ITU-R designations with their respective values at 0.01% of exceedences. In the mapping, a simple inverse distance weighting (IDW) is employed because of its inherent advantage to consistently select grid points.

Table 1: Rain rate at 0.01% for all the provinces in South Africa.

South Africa Province/Site	Rain Rate at 0.01%mm/hr
Eastern Cape	
• Fort Beaufort	53.0
• Bhisho	57.0
• Umthatha	70.0
• Port-Alfred	58.0
Gauteng	
• Pretoria	61.0
• Spring	75.0
KwaZulu-Natal	
• Durban	73.0
• Ladysmith	75.0
• Pietermaritzburg	79.0
Mpumalanga	
• Ermelo	76.0
• Belfast	79.0
• Nelspruit	78.0
Northern Cape	
• Kimberley	59.0
Free-State	
• Bethlehem	60.0
• Bloemfontein	67.0
Limpopo	
• Tshipise	50.0
North West	
• Klerksdorp	67.0
• Rustenburg	70.0
North West	
• Klerksdorp	67.0
• Rustenburg	70.0
Western Cape	
• Cape Point	20.0
• Cape Town	25.0
• Beaufort	37.0

Table 2: The specific attenuation parameters given by ITU-R.

Frequency GHz	a_H	a_V	b_H	b_V
1	0.000387	0.00000352	0.912	0.880
2	0.00154	0.000138	0.963	0.923
4	0.000650	0.000591	1.121	1.075
6	0.00175	0.0155	1.308	1.265
7	0.00301	0.00265	1.332	1.312
8	0.00454	0.00395	1.327	1.310
10	0.0101	0.00887	1.276	1.264
12	0.0188	0.0168	1.217	1.200
15	0.0367	0.0335	1.154	1.128
20	0.0751	0.0691	1.099	1.065
25	0.124	0.113	1.061	1.030
30	0.187	0.167	1.021	1.000
35	0.263	0.233	0.979	0.963
40	0.350	0.310	0.939	0.929
45	0.442	0.393	0.903	0.897
50	0.536	0.479	0.873	0.868
60	0.707	0.642	0.826	0.824
70	0.851	0.784	0.793	0.793
80	0.975	0.906	0.769	0.769
90	1.06	0.999	0.753	0.754
100	1.12	1.06	0.743	0.744
120	1.18	1.13	0.731	0.732
150	1.31	1.27	0.710	0.711
200	1.45	1.42	0.689	0.690
300	1.36	1.35	0.688	0.689
400	1.32	1.31	0.683	0.684

4. ASSESSMENT OF SPECIFIC ATTENUATIONS

Systems operating at frequencies in the GHz range suffer from attenuation due to rain which makes radio links temporarily unavailable. In order to estimate rain attenuation, two parameters are needed: specific rain attenuation and effective path length which depend on rain rate as given in the expressions (1) to (5). Specific rain attenuation depends on rain drop size, its orientation, and falling velocity while both the specific attenuation and effective path length depend on rain rate.

Using ITU-R P.838, a table can be tabulated for different frequency ranges from 1 GHz to 400 GHz and their specific rain attenuation can then be estimated. The frequency dependent coefficients presented in Table 2 for both horizontal and vertical polarization over frequencies of 1–400 GHz is employed coupled with the details in Section 2 of this paper to compute the values for a and b.

The computations are done for the three major types of polarizations, i.e., horizontal, vertical and circular polarizations. The characteristic behaviours of these phenomena are presented in Figures 2–4.

5. SPECIFIC ATTENUATION DISTRIBUTION FOR ALL THE PROVINCES IN SOUTH AFRICA

The distributions of specific rain attenuation of all the provinces in South Africa are shown in Figures 2 to 4 for horizontal, vertical and circular polarizations respectively. The results on the graphs are calculated using Table 2 coupled with the respective individual province rain rate at 0.01% of exceedences.

The highest specific rain attenuations are recorded in Mpumalanga (Ermelo) and KwaZulu-Natal (Durban) provinces while the lowest is observed in the Western Cape (Cape Town).

At horizontal polarization, the peak specific rain attenuation is observed at 200 GHz with the value of 28.65 dB/km and the lowest is 13.32 dB/km at the same frequency. The majority of the provinces have their specific rain attenuation from 23.00 to 24.00 dB/km at the same frequency of 200 GHz. Using Figures 2 to 4, at the same frequency, it is observed that horizontal, circular and vertical polarization specific rain attenuation values decrease respectively, though by small values.

In addition, the Figures confirm that there is an increase in specific attenuation as rain rate increases. It seems constant above 100 GHz for the individual province rain rate. The reason may be due to degree of impulse of raindrop shape to fast moving poles of electromagnetic wave at such high frequencies may not synchronise with each other.
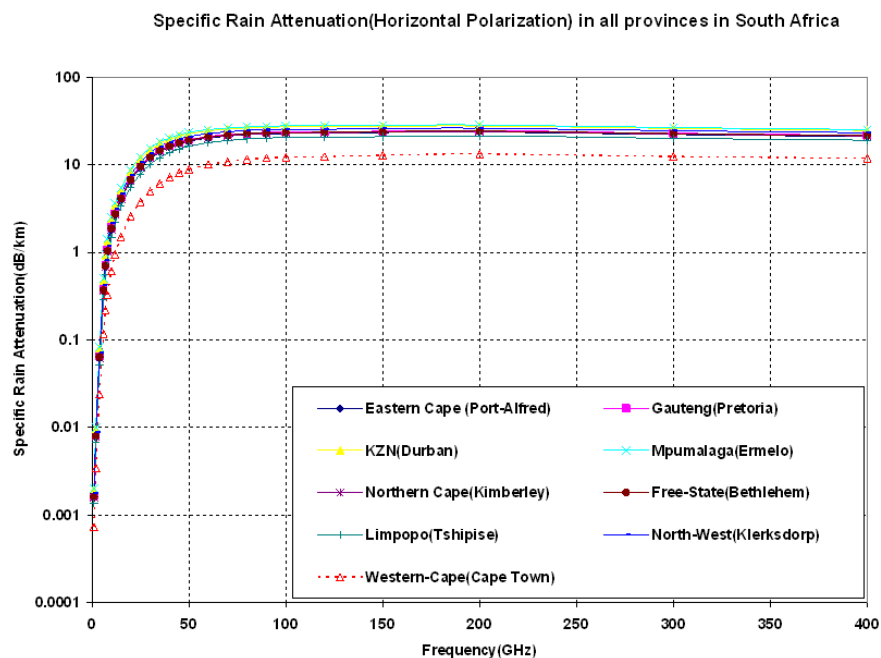
Figure 2: Specific rain attenuation (horizontal polarization) for the provinces in South Africa.
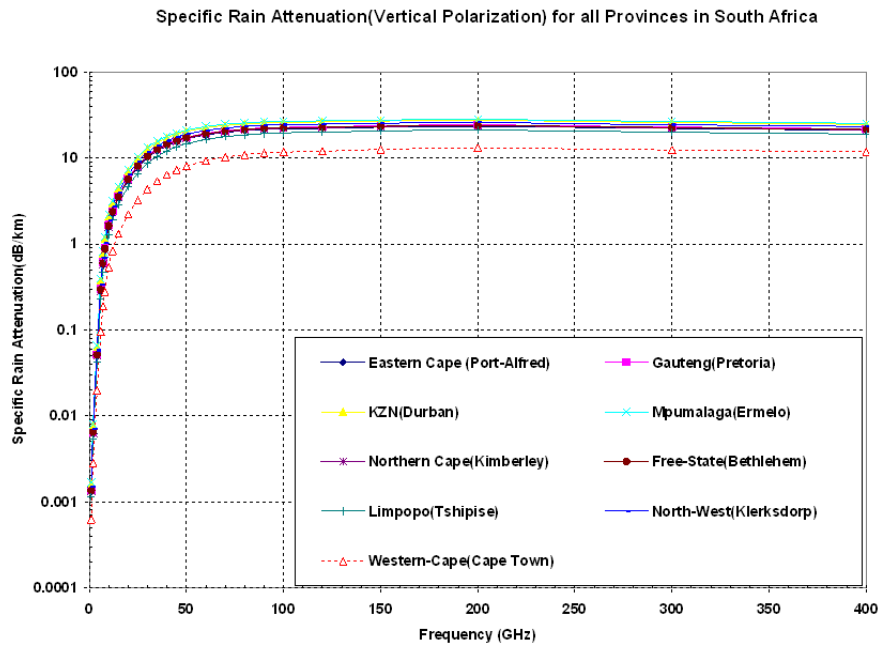
Figure 3: Specific rain attenuation (vertical polarization) for the provinces in South Africa.
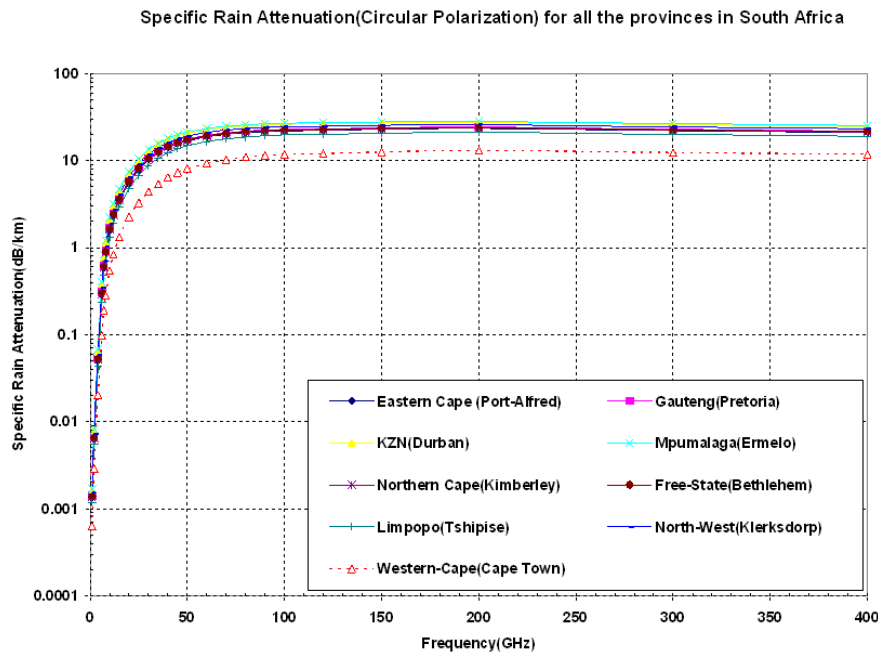
Figure 4: Specific rain attenuation (circular polarization) for the provinces in South Africa.

6. ATTENUATION ESTIMATION FOR SOUTH AFRICA PROVINCES

The expected fade depth is calculated using Equation (4) with an effective path length. The characteristics of the fade depth at different polarization orientations in Durban with respect to propagation frequencies are shown in Figures 5(a) to 5(c). The fade depth is observed at different distance ranges from 1 km to 60 km which is the ITU-R valid distance for the model. The steps to estimate rain attenuation using ITU-R can be summarized as follows:

1. Determine the rain rate at 0.01% of exceedence. This is done by measurement at 1-minute integration time as specified by the ITU-R or by using ITU-R P.837. In this work the former is considered to estimate the rain attenuation.

2. Compute specific rain attenuation at given polarizations, and rain rate of interest as given in

the equations 1, 2 and 3 of this paper.

3. Compute the effective path length by as given in Equation (4), which will lead to the estimated path attenuation at 0.01% of exceedence in dB.

4. For a radio link located at latitude $\geq 30°$, either North or South, the attenuation exceeded for other percentages can be estimated with Equation (6) while for less than $30°$, either North or South, Equation (7) will be appropriate.

In this work, the ratio of attenuation at any given percentage to attenuation at 0.01% of exceedence is given as 0.07 for p equal to 1.0, and for p equal to 0.1, 0.01, 0.001, the ratios are 0.36, 1.0 and 1.44 respectively. Here the fade margins are estimated for availability at 99.99 and at any availability that meets the needs of the operator.

Figures 5(a)–5(c) show that estimated fade depths increase with propagation frequencies up to 40 GHz as recommended by the ITU-R and this can be valid up to 60 km in distance. From 40 GHz to 100 GHz, the attenuation slightly increases in frequency with dependency on the value of rain rate. The extrapolation seems to flatten out at 100 GHz and above. These characteristics are visible in the three major polarization orientations of propagating signals at frequencies above 10 GHz.

South Africa falls under two important latitudes of ITU-R classifications as expressed in Equations (6) and (7). The majority of the provinces lie under the latitude that is less than 30 degrees and the Eastern Cape is the only province that falls under the second counter, i.e., a latitude greater than 30 degrees.

Figures 5(a)–5(c) represent KwaZulu-Natal province with the data from Durban and the Eastern Cape Province with the data from Port-Alfred. These both sites are considered for this study.

(a)

(b)

(c)
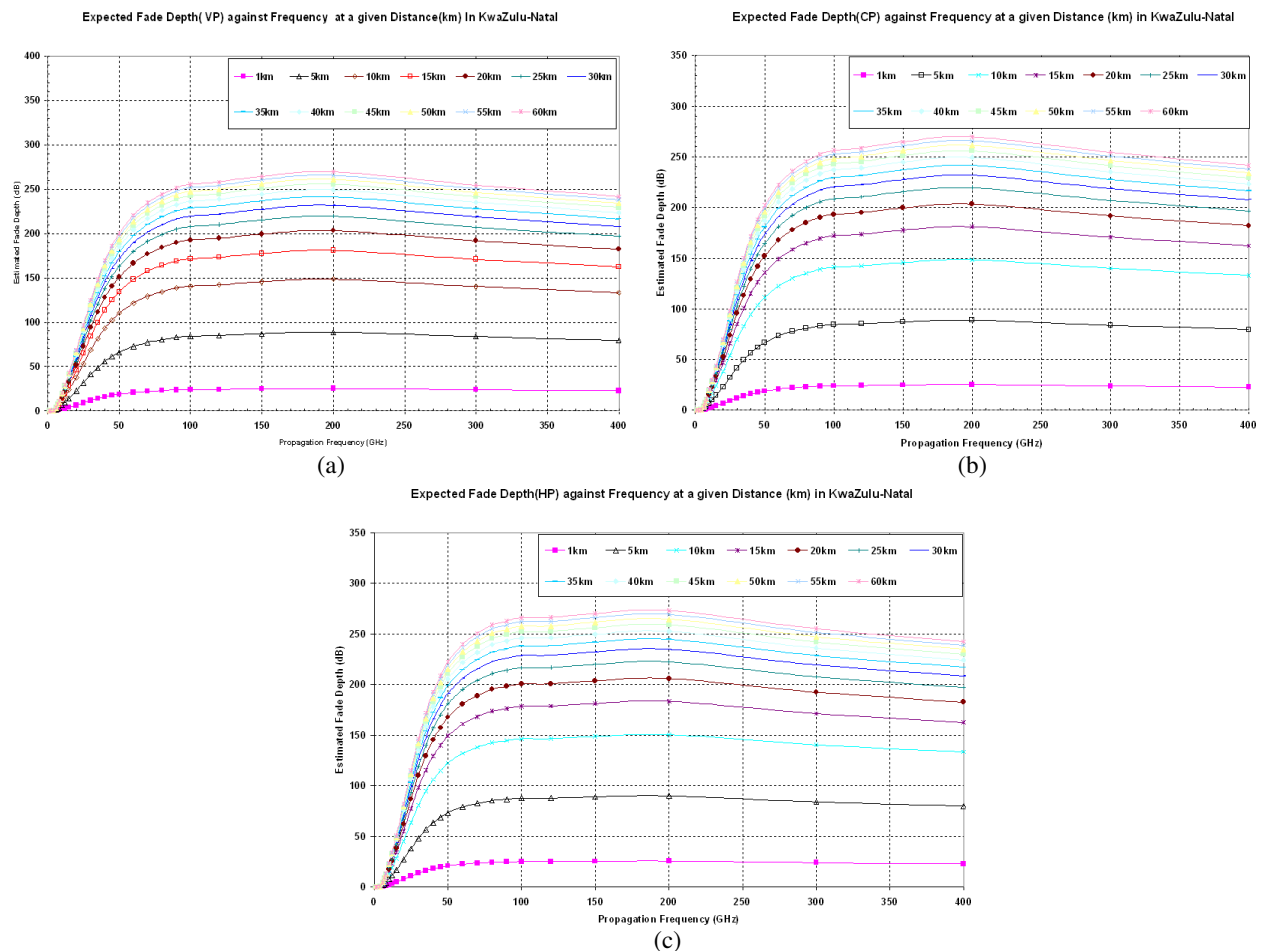
Figure 5: (a) Expected fade depth (VP) at various frequencies at GHz. (b) Expected fade depth (CP) at various frequencies at GHz. (c) Expected fade depth (HP) at various Frequencies at GHz.
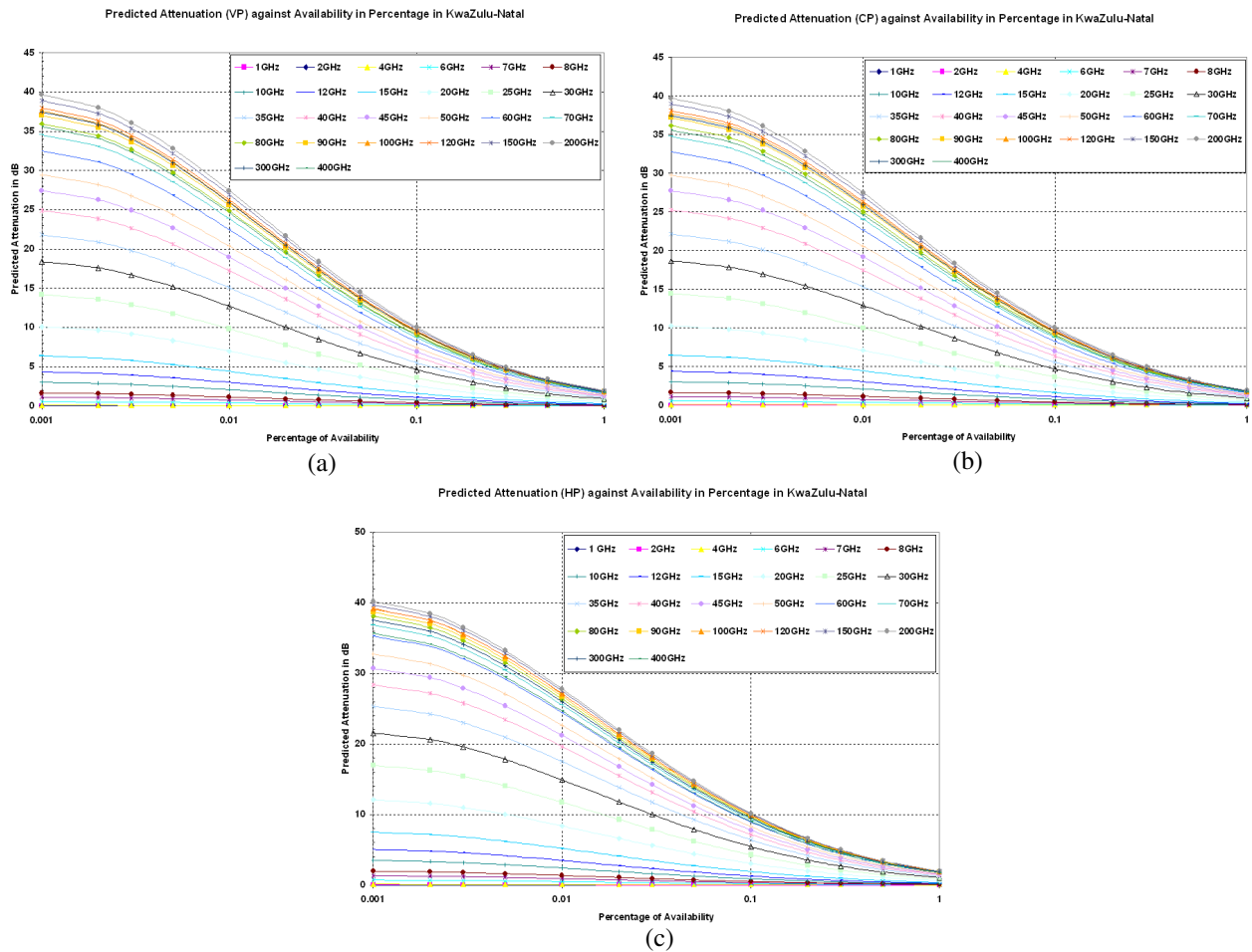
Figure 6: (a) Predicted attenuation (VP) against availability. (b) Predicted attenuation (CP) against availability. (c) Predicted attenuation (HP) against availability.

In general, it is observed that the fade depth progressively increases starting from the vertical polarization, circular polarization and the highest fade depth is observed in horizontal polarization.

In the case of Durban, at 50 GHz, the fade depth is recorded as 18.81 dB for 1 km path length in vertical polarization, while it is 19.0 dB and 20.90 dB for circular and horizontal polarization respectively. In another scenario in Durban, at 50 GHz, the fade depth is recorded as 255.4 dB for 60 km path length in vertical polarization, while it is 202.12 dB and 222.30 dB for circular and horizontal polarization respectively.

At 1 km path length, it is observed that Durban fade depth is more than what is recorded at Port-Alfred (that lies at latitude greater than 30 degrees) by average 14.78%.

In Figures 6(a)–6(c), the attenuation values at defined availability percentage with given frequency are presented. These were done for three different polarization states. This is done specifically for the Durban site which lies in the KwaZulu-Natal Province and similar curves are processed for the Eastern Cape Province. The availability performances can be accessed from Figures 6(a)–6(c). The obtained performance availability at 99.999% for 20 GHz are 10.09 dB, 10.27 dB and 12.09 dB for vertical, circular and horizontal polarization respectively for Durban. In the case of the Eastern Cape (Port-Alfred) the performance availability at 99.999% for 20 GHz are 11.69 dB, 11.90 dB and 13.92 dB for vertical, circular and horizontal polarization respectively.

At the 30 GHz, the obtained performance availability at 99.999% are 18.37 dB, 18.66 dB and 21.54 dB for vertical, circular and horizontal polarization respectively for Durban. For the Eastern Cape (Port-Alfred) the performance availability at 99.999% are 21.62 dB, 21.95 dB and 25.26 dB for vertical, circular and horizontal polarization respectively.

It can be seen that attenuation values decrease as the degree of availability decreases. For example in the case of Durban, the performance availability is 10.09 dB at 99.999% and 2.55 dB at 99.9%. In addition, it is observed that attenuation values at latitudes less than 30 degree are less

when compared with values at latitudes greater than 30 degrees as reflected in the Figure at equal performance availability.

The percentage differences between KwaZulu-Natal (Durban) and Eastern Cape (Port-Alfred) at performance availability of 99.999% falls within 15.86% and for the 99.9% the least percentage difference is 25.75%.

For easy application of Figure 5 and Figure 6, any link design engineer can use frequency scaling to find the estimated value for the undetermined frequency in this reading as given in ITU-R P.530. Based on ITU-R link outages performance yard stick, 99.99% is approximately 53-minute outages per year while 99.999% is approximately 5-minute outages allowance per year.

7. APPLICATION OF EXPERIMENTAL SETUP FOR LOS MICROWAVE LINKS

The signal attenuation measurement was carried out in 2004 at the University of KwaZulu-Natal as reported in [7–9]. The link is set-up between Howard-College (Transmitter) campus and Westville campus (Receiver). In this paper, other campuses will be included as receiver hob stations. The details of Transmitter and Receiver parameters are shown in Table 3.

Agilent 83018A microwave amplifiers are used at receiver and transmitter couple with Valuline.

WR42/R220 parabolic antennas, each with 0.6 meter diameter. The Agilent E8251A signal source is used as a transmitter. The receiver output signal is fed into FS1Q40 spectrum analyser in order to study characteristics behaviour of the signal both in clear air and non-clear air.

The additional links are introduced taking the Howard College campus as the transmitting station and the other four campuses as receiving stations. Figure 7 gives the details of the link topology for the five campuses under the University of KwaZulu-Natal.

Let us consider the microwave communication systems shown in Figure 7. A transmitter output signal of power P_t and fed into a transmitting antenna with a gain of G_t. At the receiver end, the receiving antenna gain is given as G_r and the power received is P_r at distance D. The received power can be calculated considering all the system losses as:

$$P_r = P_t G_t G_r \left(\frac{\lambda_0}{4\pi D} \right)^2 \frac{1}{L_{sys}} \tag{8}$$

Equation (6) is termed the link equation. System loss L_{sys} includes various losses due to components, setting and environmental losses from the transmitter to the receiver systems and $(\frac{\lambda_0}{4\pi D})^2$ is the free space loss (FSL) at any given frequency.

Equation (8) can be converted to decibels by find the logarithm of both sides:

$$10 \log P_r = 10 \log P_t + 10 \log G_t + 10 \log G_r - 20 \log \left(\frac{\lambda_0}{4\pi D} \right) - 10 \log L_{sys} \, \text{dB} \tag{9}$$

The receiver output signal-to-noise ratio (SNR) is determined from the noise factor (F) as: $F = \frac{S_i/N_i}{S_0/N_0}$.

Thus,

$$S_0/N_0 = \frac{S_i}{N_i} \frac{1}{F} = \frac{S_i}{kTBF} = \frac{P_r}{kTBF} \tag{10}$$

Substituting Equation (8) into Equation (10), the resulting equation is given as:

$$S_0/N_0 = \frac{P_r G_t G_r}{kTBFL_{sys}} \left(\frac{\lambda_0}{4\pi R} \right)^2 \tag{11}$$

8. LINK RESOURCES ANALYSIS

Consider the horizontal polarization link as stated in Table 3 above, the calculated free space loss which defined the expected attenuation as the signal travels away from the transmitter. It can be noted as the area covered increases, the power density decreases. This consequently is the effective weakening of the radio signal. The estimated free space loss is 135 dB at the path length of 7 km.

The Receiver Sensitivity Level (RSL) in this design is considered to be -80.5 dB with a sensitivity of 80.2 dB and Net margin of 0.3 dB. In this work, the minimum radio signal power that is required at the input of a receiver is considered at Bit Error Rate (BER 10^{-6}). The Effective Isotropic

Table 3: Link budget parameters for the LOS in the University Of KwaZulu-Natal, South Africa.

Parameter	Value	Remark
Transmitting Power	20 dBm	Carrier Frequency = 19.5 GHz Horizontal Polarization Transmitter altitude = 178 m Height of transmitting antenna above the ground = 24 m
Transmitting antenna gain	38.6 dBi	
Randome loss	−2 dB	
Transmitter loss	−1.5 dB	
EIRP	**55.1 dBm**	
Space loss	−135 dB	Height of receiver antenna above the ground = 20 m Altitude of receiver station = 145 m Transmitter/receiver antenna beamwidth = 1.9 degree Free space loss = 135 dBm Total path loss (H-W) = 171.64 dB Noise Figure = 9.5 dB
Antenna alignment error	−2 dB	
Multipath	−2 dB	
Atmospheric Loss	−0.13 dB	
Rain fade H-W Rain fade H-M Rain fade H-P Rain fade H-E	−31.51 dB −13.24 dB −70.94 dB −71.59 dB	
Loss due to Interference	−1 dB	
Total path losses	**−140.13 -(Rain fade)**	
Radome loss	−2 dB	**Calculated Link gain between Howard and Westville campus = 93.7 Calculated adjusted link between Howard and Westville campus = 88.6**
Receiver antenna gain	38.6 dBi	
Receiver Loss	−1 dB	
Total Receiver gain	**33.6 dB**	
Receiver sensitivity Level (RSL)	**-80.5**	**Expected receive antenna gain = −44.3 dBm**
Sensitivity	**-80.2**	
Net margin	**0.3 dB**	

Radiated Power (EIRP) is estimated to be 55.1 dBm which is equal to the output power radiated from the antenna.

In the work done by Odedina and Afullo [9], the received power for clear air is estimated to −41 dBm, i.e., in the absence of rain. This work confirms the contribution of rain attenuation at the 19.5 GHz which makes the received power to be −80.94 dBm. The net margin here is 0.3 dB, although a large net margin will assist the system to experience little outages while in case the net margin is zero, the system will be susceptible to periodic outages due to path fading phenomena.

In summary, the link feasibility study shows that the link is visible even though with little net margin. The receiver output signal to noise ratio (SNR) as given in the expression (11) is estimated to 29.2 dB. The other two links, the link between Howard College and Pietermariztburg and Edgewood campuses are not visible unless some frequency planning and optimization techniques are employed.

In addition to performance estimation, the link distance chart can be used to estimate the rain fade and its margin as presented in Figure 8. This tool can be used by radio link planners to estimate the hop distance and position to locate transmitter, repeater and receiver. The chart consists of all available fade margins against link distance. The chart is drawn for all the provinces in South Africa and specifically for the application in KwaZulu-Natal where experimental links are setup at the University Of KwaZulu-Natal.

On the rain fade margin against hop-distance, a superimposed plot of differences in system gain and the free space is plotted against the hop-distance. It should be noted that Figure 8 presents the distance chart for a 19.5 GHz, horizontally polarized and at system gain of 120 dB.

On the chart, the point where the system gain intersects the rain fade margin is the maximum distance hop that chosen 99.99% of availability can be optimally useful. The majority of provinces in South Africa at system gain of 120 dB will be comfortable with hop distance ranges between 11 to 16.5 km at this given specifications tabled in Table 3. In the case of the Edgewood campus, the maximum hop distance is 11 km, and the Medical School can still tolerate up to 16 km at the system gain of 120 dB. Cape Town record the maximum hop distance of 32.5 km at the same specifications presented in Table 3.
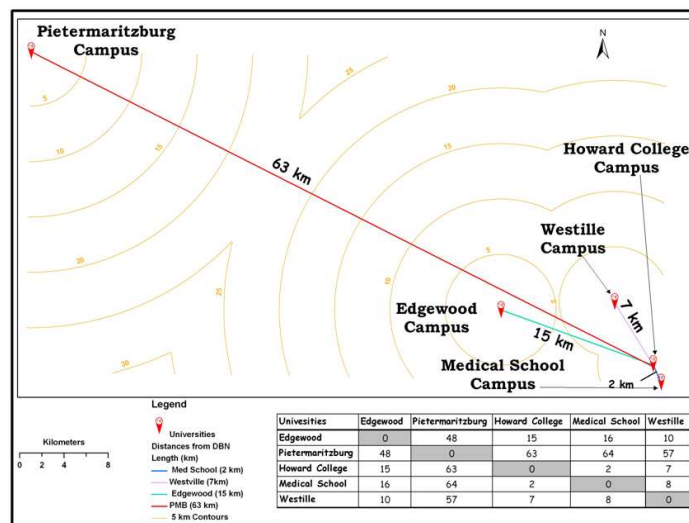
Figure 7: Link topology for microwave LOS in University of KwaZulu-Natal campuses.
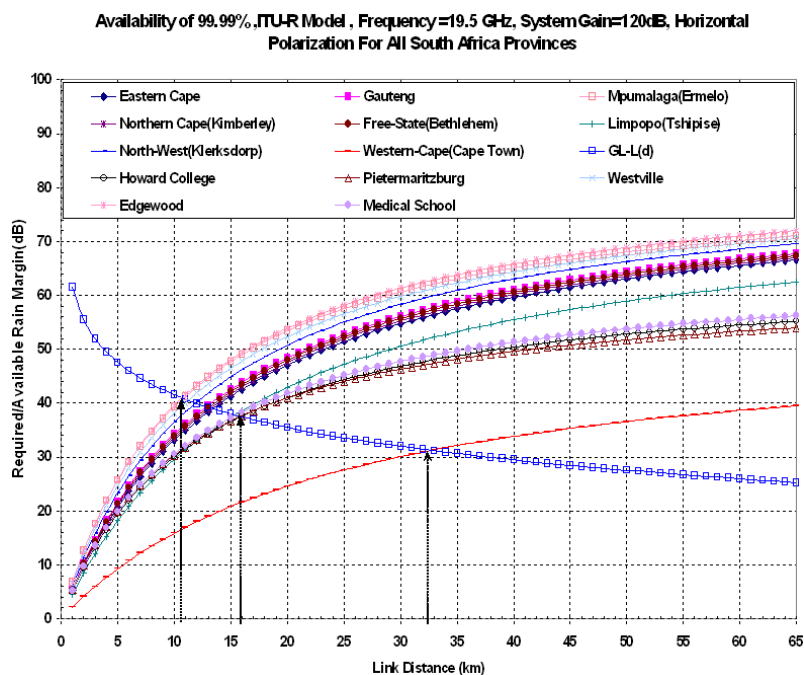
Figure 8: Link distance chart using ITU-R model and measured data.

9. RESULTS AND CONCLUSION

This paper presents rain attenuation estimation using both ITU-R model and measured regional rain rate data collected over 10 years. In addition, the results of 1-year rain attenuation measurement are used to design link budget for the University of KwaZulu-Natal microwave links. Also, the hop distance chart is used to estimate the maximum hop distance a defined link can have under a pre-defined rain fade margin and system gain.

The results in Section 3 to Section 7 can be used by radio network planners in South Africa to estimate link availability, link performance, link budget and finally to manage the link at any frequency ranges from 1 GHz to 400 GHz.

REFERENCES

1. ITU-R P.618-8, "Propagation data and prediction methods required for the design of Earth-space telecommunication systems," ITU, Geneva, Switzerland, 2003.
2. Moupfouma, F., "Improvement of a rain attenuation prediction method for terrestrial microwave links," *IEEE Transactions on Ant. and Prop.*, Vol. 32, No. 12, 1368–1372, 1984.
3. Owolawi, P. A., "Characteristics of rain at microwave and millimetric bands for terrestrial and satellite links attenuation in south africa and surrounding islands," Ph.D. Dissertation, School of Electrical, Electronics and Computer Engineering, University of KwaZulu Natal, Durban, South Africa, July 2010.
4. ITU-R P.838-3-8, "Specific attenuation model for rain for use in prediction methods," ITU, Geneva, Switzerland, 2008.
5. Vasseur, H., "Degradation of availability performance in dual-polarized satellite communications systems," *IEEE Trans. on Communication*, No. 3, Vol. 48, 465–472, March 2000.
6. Owolawi, P. A., "Rainfall rate probability density evaluation and mapping for the estimation of rain attenuation in South Africa and surrounding islands," *Progress In Electromagnetics Research*, Vol. 112, 155–181, 2011.
7. Naicker, K. and S. H. Mneney, "Propagation measurements and modelling for terrestrial line-of-sight links at 19.5 GHz," *IEEE Africon, Gaborone, Botswana*, Vol. 1, 95–100, September 15–17, 2004, ISBN: 0-7803-8605-1.
8. Fashuyi, M. O. and T. J. Afullo, "Rain attenuation prediction and modelling for LOS terrestrial links in South Africa," *Radio Science*, Vol. 42, RS 5006, October 20, 2007, doi:10.1029/2007RS003618.
9. Odedina, P. K. and T. J. Afullo, *Clear-air Signal Level Measurement for Microwave Line-of-sight Link Application in South Africa*, SAIEE, Vol. 101, No. 4, 132–139, December 2010.

Computational Design and Performance Evaluation of Green Painting Absorbing Material

Hasnain Abdullah[1], **Mohd Nasir Taib**[1], **Ida Rahayu Mohamed Noordin**[1],
Norhidayah Saad[1], **Wan Khairuddin Wan Ali**[2], **Rusnani Ariffin**[1],
Ahmad Takiyuddin Abdullah[3], **and Siti Zura A. Jalil**[1]

[1]Faculty of Electrical Engineering, Universiti Teknologi MARA, Malaysia
[2]Faculty of Mechanical Engineering, Universiti Teknologi Malaysia, Malaysia
[3]Industrial Automation Section, UniKL MFI, Malaysia

Abstract— Microwave absorbing materials have received great attention in recent years for both civil and military fields due to various applications in communications, radar, satellite systems, and anechoic chambers. Wireless communication is currently the fastest growth of telecommunication technology. Many studies have indicated that there are harmful radiations produced by transmitting telecommunications structures. Effects on human exposure include dizziness, nausea, vomiting and loss of breath. A way to reduce strong microwave radiations for human is by applying a microwave absorbing paint coating to the wall of the built spaces. The green painting mixed with ingredients from coconut shells is the main material that is analyzed in this research. The findings show that material applied with the green painting can readily absorb the microwave radiations. The wave-absorbing materials are designed by using Computer Simulation Technology (CST) Microwave Studio simulation software. The goal of this simulation is to find the best performing absorber. From dielectric constant value, the modeling and simulation stage of microwave absorber are executed to obtain the reflectivity or S_{11} result using CST Microwave Studio software. Analysis of the S_{11} results and measurement of absorber performance are evaluated to define the microwave absorber performance. A free space measurement setup operating in the frequency of Ku Band is employed to measure absorption. The results show that the green painting with coconut based carbon can be used as coating absorbing material. Each material applied with the green painting shows excellent absorption at 3 to 6 dB range. The most excellent result is shown by double layer coating absorption up to 17 dB.

1. INTRODUCTION

Microwave absorbing materials (MAM) have received great attention from recent years is due to various applications in communications, radar, satellite systems, and anechoic chambers [1–4]. In the anechoic chamber, the electromagnetic wave absorber (EM) is used to absorb the reflected waves that occur in the chamber wall.

Interest in the study of absorbing materials has increased as broadband applications for the system to move towards the high frequency domain. In some cases, for example in modern airborne applications, the transmission network may be required to send certain commands only while pressing the EM wave in one direction to the other direction. Therefore, a suitable absorbent material with absorption characteristics that maintained over the entire operating frequency to be necessary for this system [5, 6].

In the use of absorption, MAM is divided into two types, i.e., coating and structure. The type of coating principle is that the high loss materials coating on the surface of the target can absorb the incident wave and reduce the return loss. Meanwhile, the type of structure is to reduce the reflection by matching the impedance and absorbing materials [7]. This paper emphasizes the type of coating of MAM.

During working with a short impulse signals in a wide frequency range, it is necessary to use effective ingredients that work in various wavelengths. In most instances, the construction of the absorber, ferrite is used to coat the absorber. However, at present, a number of alternatives design have been applied such as carbon fillers and metallized geometrical [2].

Microwave has the ability to cause biological damage through heating effects. Researchers have found that symptoms may effects on human exposure such as headache, nausea, fatigue, brain activity and loss of concentration [8]. In order to avoid the circumstances, a research on the use of paint to absorb wave radiation is performed. The mixture of paint and ingredients from coconut shells are the main materials that are studied in this research.

2. ABSORBER MATERIAL

The purpose of this study is to investigate the application of based carbon coconut shell as absorption of microwave radiation coating material. Considering a normal incident on the surface of absorbing material coated on perfect conductor. The absorption or reflectivity in dB unit is defined as:

$$R = 20 \log |\Gamma| \tag{1}$$

where, the reflection coefficient, Γ

$$\Gamma = \frac{Z_i - 1}{Z_i + 1} \tag{2}$$

where, the characteristic input impedance, Z_i

$$Z_i = \sqrt{\frac{\mu_r}{\varepsilon_r}} \tanh(-jk_0 d\sqrt{\mu_r \varepsilon_r}) \tag{3}$$

where, d is the thickness of absorbing material and k_0 is the wave numbers in free space [9].

The green paint absorbers based on carbon powder coconut shell are fabricated and coated with three difference materials which are elephant board (0.5 mm thickness), plywood (3 mm and 18 mm thickness) and cement block (35 mm thickness). The complex permittivity and permeability of the absorbing material are the basic parameters which reflect the interaction between the electromagnetic wave and material. The simulation of coated absorber is executed to get the S_{11} result using Computer Simulation Technology Microwave Studio (CST MWS) software. The free space reflectivity measurements using arch method is applied to define the absorption performance. Figure 1 shows the setup of absorption measurement.

The similar methodology is repeated for the design of double layer absorbing material which is based on carbon powder and carbon granular of coconut shell. In the measurement of double layer absorbing material, only the elephant board coated is performed.

3. RESULTS AND DISCUSSION

The absorbing material is designed using CST Microwave Studio simulation software. Performance of the absorbent material can be predicted using CST software with the added value of the epsilon or dielectric constant. Figure 2 shows simulation results of predicted performance of absorbing material with varying the epsilon value. The lower the value of epsilon indicates the better the absorption performance.

The measurement of absorber is conducted to determine the performance of four different absorbent materials. Figure 3 shows the absoption of elephant board coated material. The evarage absorption is −3.5 dB and the maximum absoption is 5.1 dB at 11.4 GHz.

Figure 4 shows the absoption of plywood coated material (3 mm thickness). The average absoption is −2.8 dB and maximum absorption is −3.3 dB at 10.86 GHz.

Figure 5 shows the absoption for plywood coated material (18 mm thickness). The average absoption is −3.5 dB and maximum absorption is −6 dB at 9.16 GHz.

Figure 6 shows the absoption of cement block coated material (35 mm thickness). The average absoption is −3.2 dB and maximum absorption is −6 dB at 9.06 GHz.

From Figures 3, 4, 5 and 6, the absorption is about 3 dB in average. This shows that the four different absorbent materials have performed the similar absorption performance.
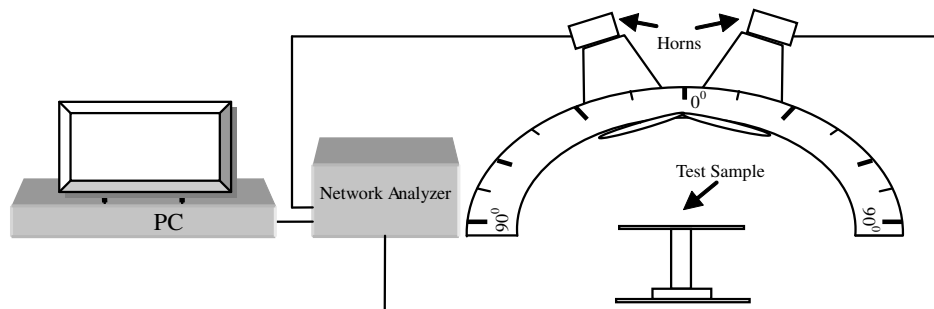
Figure 1: The setup of absorption measurement.
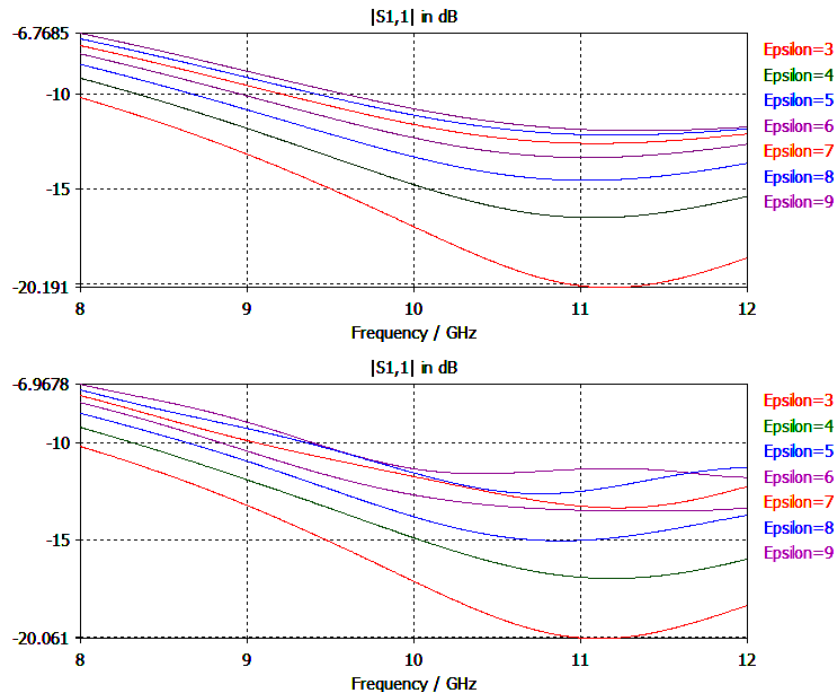
Figure 2: S_{11} simulation results of absorbing materials for epsilon 3 to 9 (a) 1 mm to 3 mm, (b) 18 mm to 35 mm.
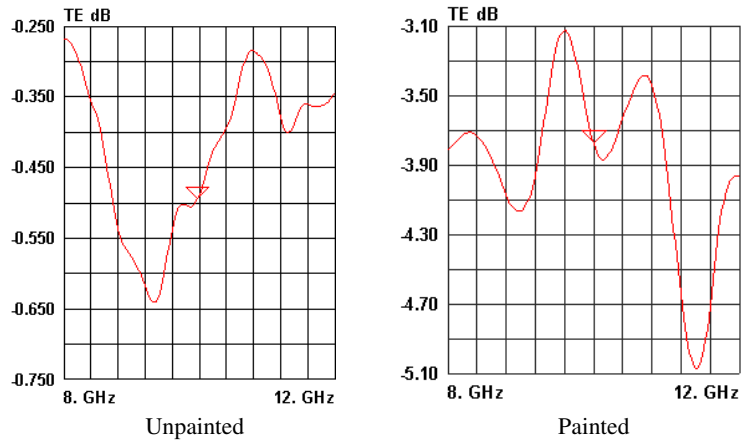
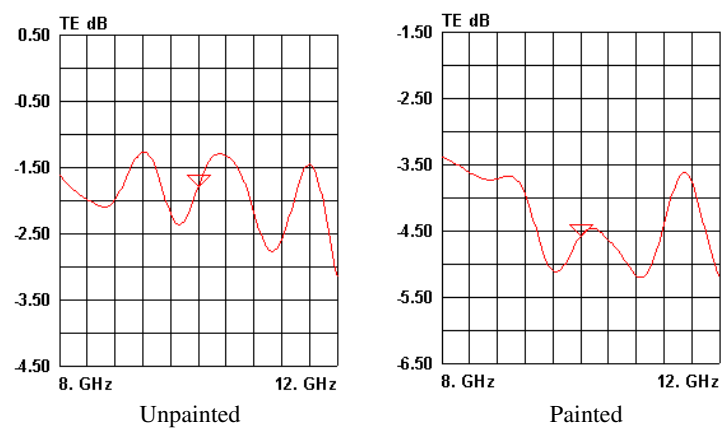Figure 3: Measurement results of elephant board coated material.

Figure 4: Measurement results of plywood coated material (3 mm thickness).
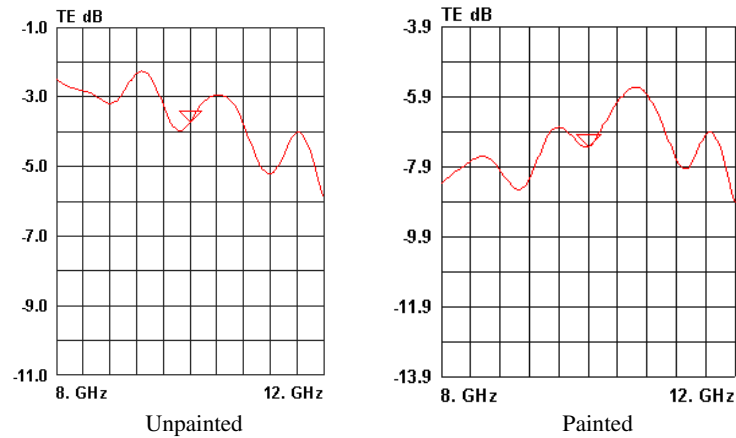
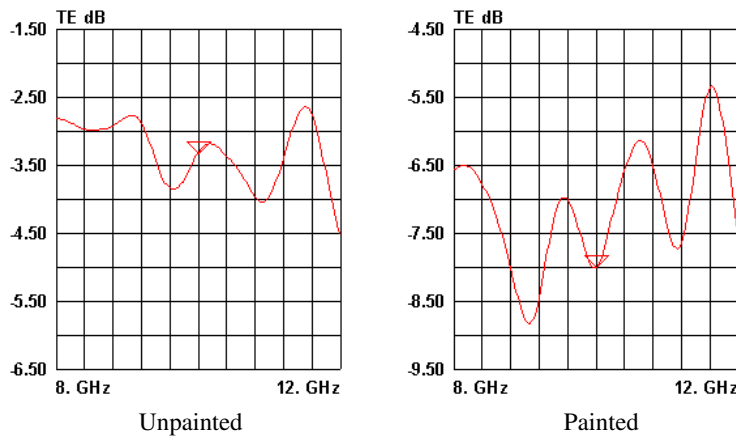Figure 5: Measurement results of plywood coated material (18 mm thickness).

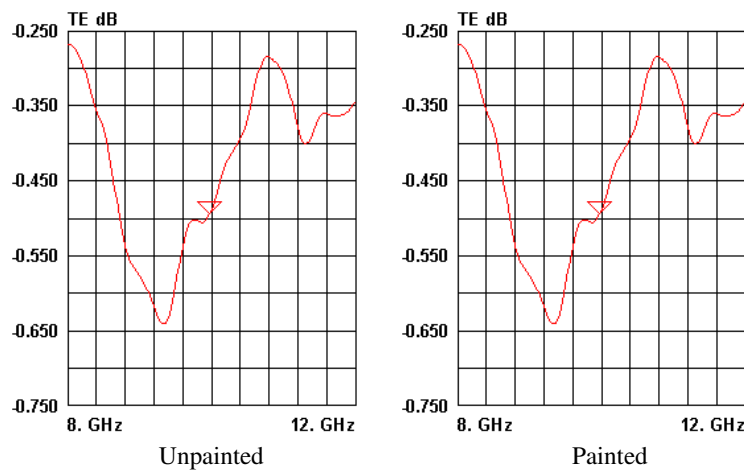Figure 6: Measurement results of cement block coated material.

Figure 7: Measurement results of double layer absorbent material.

Figure 7 shows the absorption of double layer absorbent material. The average absoption is 12 dB and maximum absorption at is 17 dB at 10.02 GHz. This shows that the double layer absorbent material has resulted better absorption performance.

4. CONCLUSIONS

A new green paint absorbing material based on coconut shell is analyzed in this paper. The results show that material applied as coating material can absorb the signal. The average absorption for single layer is about 3 dB. It also shows that any material used contribute the same absorption

performance when applying green paint absorbing material. The double layer absorbent material shows better absorption with 12 dB in average and maximum absorption is 17 dB at 10.02 GHz. For future improvement, further experimental works have to be carried out in determining significant contributing factors to improve the absorption performance.

ACKNOWLEDGMENT

REFERENCES

1. Holloway, C. L., R. R. Delyzer, R. F. German, P. McKenna, and M. Kanda, "Comparison of electromagnetic absorber used in anechoic and semi-anechoic chambers for emissions and immunity testing of digital devices," *IEEE Trans. Electromagn. Compat.*, Vol. 39, 33–46, Feb. 1997.
2. Perini, J. and L. S. Cohen, "Design of broad-band radar absorbing material for large angle of incidence," *IEEE Trans. Electromagn. Compat.*, Vol. 35, 223–230, May 1993.
3. Komori, H. and Y. Konishi, "Wide band electromagnetic wave absorber with thin magnetic layers," *IEEE Trans. Broadcast.*, Vol. 40, 219–222, Apr. 1994.
4. Janaswamy, R., "Oblique scattering from lossy periodic surfaces with application to anechoic chamber absorbers," *IEEE Trans. Antennas Propagat.*, Vol. 40, 162–169, Feb. 1992.
5. Rahman, N., A. Sharma, M. N. Afsar, S. Palreddy, and R. Cheung, "Dielectric characterization and optimization of wide-band, cavity backed spiral antennas," *Applied Computational Electromagnetics Society Conference*, 2010, accepted.
6. Sharma, A. and M. N. Afsar, "Accurate permittivity and permeability measurement of c omposite broadband absorbers at microwave frequencies," *IEEE Instrumentation and Measurement Technology Conference (I2MTC)*, 1–6, 2011.
7. Li, K., X. Zhang, X. Hou, and P. Zhang, "Analysis and design of multilayer Jaumann absorbers," *IEEE International Conference on Microwave Technology & Computational Electromagnetics (ICMTCE)*, 81–84, 2011.
8. Regel, S. J. and P. Achermann, "Cognitive performance measures in bioelectromagnetic research — Critical evaluation and recommendations," *Environmental Health Journal 2011*, 2011, Issn:1476069X.
9. Yu, X., G. Lin, D. Zhang, and H. He, "An optimizing method for design of microwave absorbing materials," *Materials & Design*, Vol. 27, No. 8, 700–705, Elsevier, 2006.

Design of High Performance Low Pass Filter Using Neural Network and Simulated Annealing

Bhabani Sankar Nayak[1], **Subhendu Behera**[1], **Pradyumna Ku Patra**[1], **and R. K. Mishra**[2]

[1]Department of ECE, NIST, Berhampur, Orissa, India
[2]Berhampur University, India

Abstract— A low pass filter using defected ground with multiple numbers of scaled down complementary split ring resonators (CSSR) structures of a micro strip line is designed. The introduction of CSSR unit results in interesting filtering characteristics, like very high attenuation rate, couple of the dimension dependent finite attenuation poles and a very low-pass band ripple level. The scaling of CSSR unit cells is made in a systematic way optimizing the LPF performance. The frequency responses in terms of pass band as well as the stop band are investigated with the simultaneous change of length and gap as variable and the effect on insertion loss is studied. A neural network model is applied for the modeling of frequency response of filter with SSR and CSSR defects. Simulated annealing method is also used for the modeling of frequency response to further minimize the error. The obtained results are compared. The size of split ring resonator is optimized in order to obtain the minimum error in the frequency response. Incremental back propagation learning approach is followed in the training of neural network.

1. INTRODUCTION

A microwave filter is a two- port network device used to control the frequency response at a certain point in a microwave system by providing transmission at frequencies within the pass band of the filter and attenuation in the stop band of the filter. The wide areas of application lay in the microwave communication, satellite communication, radar measurement systems etc [1]. The frequency range below the cut off frequency is known as the pass band and above the cut off frequency is called stop band. A perfect low pass filter should have zero insertion loss in the pass band and infinite attenuation in the stop band. Although it has a simple methodology for designing a LPF [1], but it generally suffers with low attenuation rate as well narrow stop band. In order to avoid these drawbacks, Defected Ground Structures (DGS) came in to feature [2–5]. Compact size, high performance and low cost are presently the most desired requirements of modern microwave communication systems. Recent development in wireless communication system has presented new challenges to design and produce high-quality miniature components. So, in microwave circuit design DGS opens the door to a wide range of applications. DGS has a simple equivalent circuit model [4, 6] and yields a low-pass property with a wide stop-band. DGS periodic structures have attractive properties, including their cutoff and band gap characteristics. They not only make the circuit compact but also makes the stop band wide and deeper with low insertion loss. The DGS section can serve as replacements for a parallel LC resonator circuit in many applications. The various DGS reported in [1–6] are of different geometrical shapes like elliptical, dumbbell, Arrow head, semi circular arc etc. The first DGS was found to be dumbbell shaped and reported in [8]. High-performance LPFs must exhibit high suppression of ripples in the pass band, a high attenuation rate in the transition between the passband and the stopband, and a wide stopband with at least 20 dB of attenuation. The obtained results through the conventional DGS have improved the response of LPF but it is still needed to be further improved. In order to design a high performance LPF, the complementary square split ring resonators DGS based LPF are designed [9]. To avoid the relatively poor attenuation rate DGS with elliptical response should be used [9], so a square split ring resonators (SSR) [9] with 3rd order elliptic function is proposed [10]. Using the negative image concept the complementary square split ring resonators (CSSR) are designed in order to increase the performance of LPF. The design methodology is given briefly in [9]. After we design the LPF with SRR and CSSR defects, we studied the frequency response of the filter by changing the the dimensions of SRR as well as CSSR unit. We model the frequency response of LPF using computational algorithm like Artificial Neural network (Back propagated Neural Network-BPNN) and simulated Annealing (SA) and the results are compared in terms of accuracy. As there exist no formulation for determining the frequency response of LPF for the exact values of dimension of DGS (here l, g), BPNN and SA are used to solve the problem statement. The size of split ring resonator is optimized in order to obtain the minimum error in

the frequency response. Incremental back propagation learning approach is followed in the training of neural network.

2. DESIGN OF LPF WITH SSR AND CSSR DGS AND STUDY OF FREQUENCY RESPONSE

The design procedure is followed from the [9] and carried out in CST microwave studio. The dimensions of the simulated CSSRR unit are $L = 8\,\text{mm}$ and $g = 0.5\,\text{mm}$ as given in [9]. Teflon Duroid with a dielectric constant of 10.20 and thickness of 0.635 mm is used for the design. The width d of the 50 ohm microstrip line is 0.58 mm. The frequency behavior for both the cases are investigated.

Figure 2 shows the simulation results of SRR and CSSR loaded DGS LPF, which clearly demonstrate the superiority of the CSSRR unit over the SSR slot unit in filtering performance. The attenuation rate is more in case of CSSR in comparison to SSR unit. The insertion loss behavior of the CSSRR unit has two attenuation poles at different frequencies, f_{01} and f_{02}. The two poles are located at 1.86 and 4.94 GHz. They produce two band gaps that have 0.1 and 0.3 GHz 10 dB-bandwidth, respectively. The SSR unit exhibited an insertion loss having only one attenuation pole. It is also verified that f_c, f_{01}, f_{02} are directly proportional to g and varies inversely with respect to L.
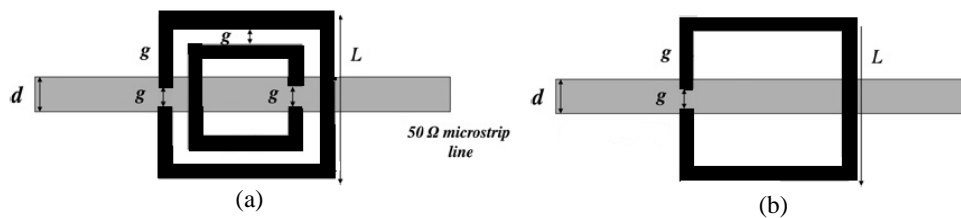
Figure 1: Design of LPF with (a) CSSR and (b) SSR Unit Cell.
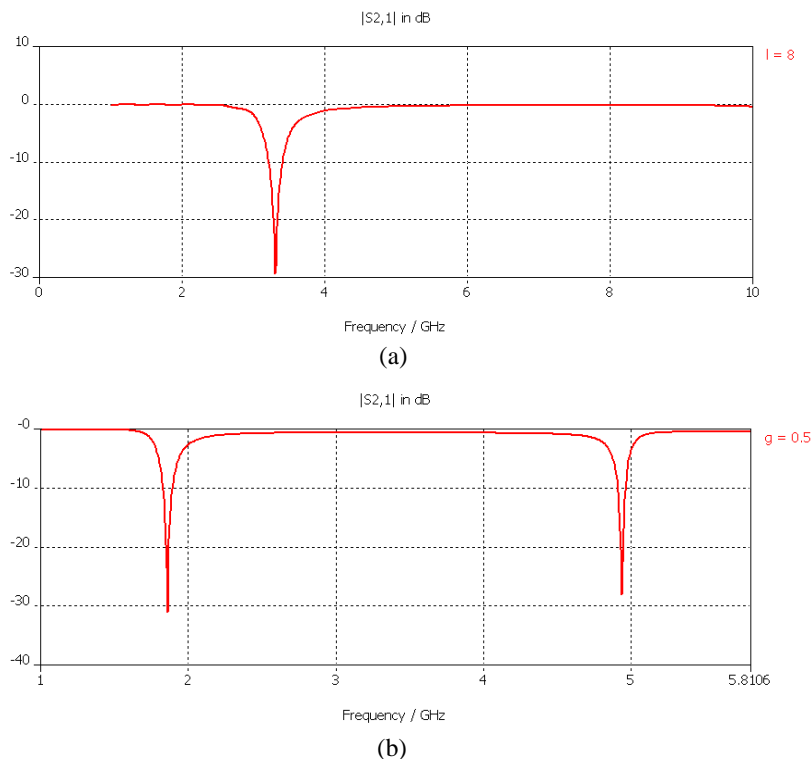
Figure 2: Frequency response of LPF with (a) SSR and (b) CSSR unit cell.

A new Cascaded CSSR DGS based LPF is also designed, where the Unit cell 1 with length L, and gap g has been scaled to half of its dimension with a distance of $g(0.5)$ and repeated with 7

unit cells of DGS and the response is obtained which is giving sharp insertion loss, high attenuation rate, and wider stop band. The net performance obtained from the filter is the linear sum due to all individuals.

3. OPTIMIZATION THROUGH NEURAL NETWORK AND SIMULATED ANNEALING

As there is no certain mathematical formulation available for determining the exact frequency response of an CSSR loaded LPF, This problem is solved by using the Artificial neural network using the back propagation online incremental learning approach [11–13]. The LPF is designed and the input parameters are L, g which are varied and the frequency response is observed for the each case. The lower and upper cutoff frequency are taken as output parameters. Back Propagation algorithm comprises of two phases. First, a training input pattern is presented to the network input layer which is propagated forwarded to the output layer through hidden layers to generate the output [12]. If this output differs from the target output presented then an error is calculated (Here Mean Square Error). This error is back-propagated through the network from the output layer to the input layer and weights are updated. As we are not satisfied with a normal back propagation, we investigated the results with learning rate starting from 0.1 to *1.0* with momentum constant equal to *0.9* to speed up the learning process. The epoch size for each learning rate is *100*.
Algorithm:

Step 1: Set Learning Rate $\lambda = 0.1$, Momentum Constant $\alpha = 0.9$. Initialize No. of Tuples according to dataset.

Step 2: Initialize weights randomly. Set MSEtotal $= 0$ and $i = 0$. The log sigmoid function in Eq. (1) is used as the transfer function associated with the neurons in hidden and output layer

$$F(x) = 1/1 + \exp(-x). \tag{1}$$

Step 3: Present ith input vector $X_{i0}, X_{i1}, \ldots, X_{iN-1}$ and specify the desired output d_{i0}. Calculate actual output Y_{i0} and MSEi.

Step 4: Modify the weights starting from output layer to input layer using delta rule given below.

$$Wjk(t+1) = Wjk(t) + \lambda \delta kxj' + \alpha(Wjk(t) - Wjk(t-1)) \tag{2}$$

where $Wjk(t)$ is the weight from node I to node j at time t; α is momentum constant; xj' is either the output of node j or is input j; λ is learning rate; and δk, is an error term for node k. If node k is an output node, then $\delta k = yk(1 - yk)(dk - yk)$ [3]. Where dk is the desired output of node k and yk is the actual output. If node k is an internal hidden node, then $\delta k = xj'(1 - xj')\Sigma l \delta l W kl$ [4]. Where l is over all nodes in the layer above node k.

Step 5: MSEtotal $=$ MSEtotal $+$ MSEi.

Step 6: Repeat by going to Step 3 if $I <$ No. of Tuples.

Step 7: MSEtotal $=$ MSEtotal/No. of Tuples. Store MSEtotal.

Step 8: Repeat Steps 2–6 No. of epoch size.

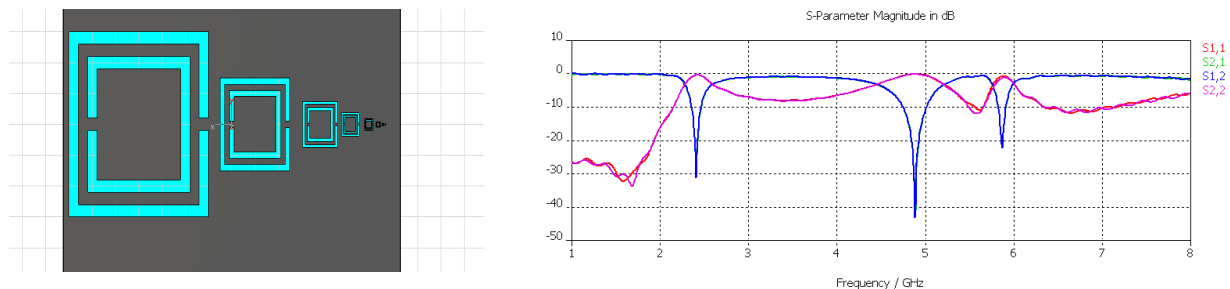
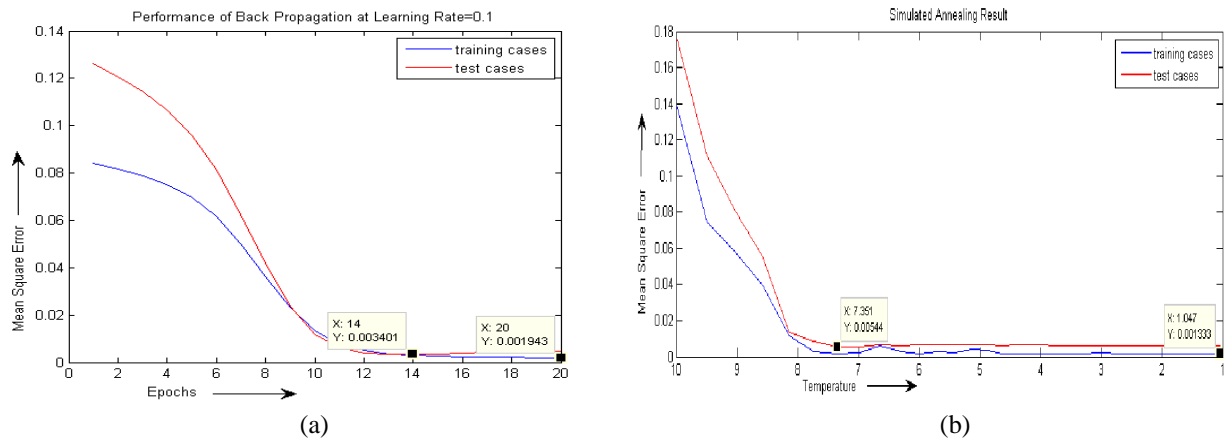Figure 3: Design of LPF with multiple CSSR unit cells as DGS and its frequency response.

Figure 4: Output of (a) BPNN and (b) simulated annealing.

Step 9: $\lambda = \lambda + 1$. Repeat by going to Step 2 if $\lambda <= 1.0$.

The neural network with 3 neurons in 1 hidden layer and best learning rate reduces the error to 0.0019 in 20 epochs only while training the neural network and while testing it comes down to 0.0034 in 14 epochs Fig. 4(a). The obtained results from ANN were checked by designing in CST and the frequency response were matched mostly with respect to the result obtained in ANN. The same case is studied through the simulated annealing with the algorithm used in [14, 15]. Temperature T is a very important parameter of this technique which is the analog of the temperature in physical systems. Starting at a high temperature the algorithm reaches the lowest temperature with gradual decrement with attaining of a "thermal equilibrium" state at each temperature [14]. At each temperature, we randomize the weights. We accept the new set of weights as the newly optimized set of weights if the error with this set is lower than with the old set of weights or with a probability that the current set of weights will lead to the global minima [14, 15]. The results are obtained (Fig. 4(b)) are better in comparision to BPNN, but the time taken for the simulation of SA is more in comparision to BPNN. The results obtained are shown below.

4. CONCLUSIONS

The CSSR and SSR loaded LPF are designed in this paper. The Dimension of CSSR are varied and the frequency response is studied. The Artificial Neural Network (here BPNN) and Simulated Annealing Methods are used to model the frequency response with respect to the dimensions of the CSSR unit cell. The dimensions are further optimized in order to get the minimum error in the frequency response of CSSR unit cell. The following two methods are found to be very useful to determine the frequency response due to the dimension CSSR DGS Unit cell with negligible error.

REFERENCES

1. Bhat, B. and S. K. Koul, *Stripline-like Transmission Lines for Microwave Integrated Circuits*, New Age International (p) Ltd, Publishers, 2007.
2. Ahn, D., J.-S. Park, C.-S. Kim, J. Kim, Y. Qian, and T. Itoh, "A design of the low pass filter using the novel micro strip defected ground structure," *IEEE Trans. Microw. Theory Tech.*, Vol. 49, No 1, 86–93, January 2001.
3. Rahman, A. B., A. K. Verma, et al., "Improved circuit model for DGS based low pass filter," *IEEE APS*, 998–1001, 2004.
4. Park, J.-S., "An equivalent circuit and modeling method for defected ground structure and its application to designs of microwave circuits," *Microwave Journal*, November 2003.
5. Zhong, X.-M. and G.-H. Li, "Design of low pass filter based on a novel defected ground structure," *Journal of Shanghai University (English Edition)*, Vol. 11, No. 4, 396–399, 2007.
6. Qian, Y. and T. Itoh, "Planar periodic structures for microwave and millimeter wave circuit applications," *IEEE MTT-s Dig.*, No. 6, 1533–1536, 1999.
7. Matthaei, G. L., L. Young, and E. M. T. Jones, *Microwave Filters, Impedance Matching Networks and Coupling Structures*, 217–228, Artech House, Norwood, MA, 1980.
8. Kim, C. S., J. S. Park, D. Ahn, and J. B. Lim, "A novel 1-D periodic defectedground structure for planar circuits," *IEEE Microw. Wirel. Compon. Lett.*, Vol. 10, No. 4, 131–133, 2000.

9. Taher, H., "High-performance low-pass filter using complementary square split ring resonators defected ground structure," *IET Microwave Antennas Propagation*, Vol. 5, No. 7, 771–775, 2011.

10. Parui, S. K. and S. Das, "Modeling of split-ring type defected ground structure and its filtering applications," *J. Microw. Opt. Electron. Appl.*, Vol. 8, No. 1, 6–12, 2009.

11. Patnaik, A., R. K. Mishra, G. K. Patra, and S. K. Dash, "An artificial neural network model for effective dielectric constant of microstrip line," *IEEE Transactions on Antennas and Propagation*, Vol. 45, No. 11, 1697, November 1997.

12. Mishra, R. K. and Patnaik, "Designing rectangular patch antenna using the neurospectral method," *IEEE Transactions on Antennas and Propagation*, Vol. 51, No. 8, 1914–1921, August 2003.

13. Pattnaik, S. S., D. C. Panda, and S. Devi, "A novel method of using artificial neural networks to calculate input impedance of circular microstrip antenna," *IJMOT Jul.*, 2006.

14. Kaczmarski, K. and D. Antos, "Use of simulated annealing for optimization of chromatographic separations," *ACTA Chromatographica*, No. 17, 2006.

15. Goldman, F. E. and L. W. Mays, "Water distribution system operation: Application of simulated annealing," *Water Resources Systems Management Tools*, Mays LW (ed.), Chapter 5, McGraw-Hill, New York, 2005.

Numerical Design of Matching Structures for Characteristic Improvement of Finite Periodic Structures

H. Sanada[1] **and J. Ren**[2]

[1]Hokkaido Institute of Technology, Japan
[2]Hokkaido University, Japan

Abstract— This paper describes how to design matching structures for improving the characteristics of one-dimensional finite periodic structures. In particular, it deals with one-dimensional periodic semiconductor superlattice structures. A downhill simplex method is used to determine some of the structural parameters of the matching structure. Numerical examples show that this method is effective in improving the transmission probability of finite periodic structures.

1. INTRODUCTION

Several studies have been carried out in regard to band pass electron filters [1–6]. Thanks to continued advances in computers, a numerical design has a wide range of applications and can handle various situations.

This paper studies how to design matching structures for improving the characteristics of finite periodic structures based on a numerical optimization. The paper deals with one-dimensional semiconductor superlattices. It is known that infinite-length superlattice structures have energy bands. We can control the position and bandwidth of an energy band by adjusting the structural parameters. These characteristics can be used for realizing various semiconductor devices. However, we need to use finite periodic structures instead of infinite periodic structures in real situations. Finite periodic structures have different transmission characteristics from those of infinite periodic structures. For example, finite-length superlattice structures have many sharp transmission peaks instead of energy bands. As a result, the performance of actual devices rarely matches our expectations. In this study, we propose to place matching structures on both sides of a finite periodic structure and to improve transmission characteristics by adjusting some of the parameters of the matching structures on the basis of numerical optimization. The numerical optimization we choose is the downhill simplex method [7]. Judging from results of numerical experiments, we concluded that our methodology improves the transmission characteristics of finite periodic structures.

2. SUPERLATTICE STRUCTURE AND ITS EQUIVALENT CIRCUIT MODEL

The behaviour of the electron wave is described by the Schrödinger equation in the single-band envelope function approximation. Here, we use the equivalent circuit representation for the Schrödinger equation proposed in Ref. [3–5]. By using the equivalent circuit model, we can take adavantage of a variety of cirucit functions and circuit matrices.

Accroding to Ref. [4], a superlattice structure can be expressed as cascade connections of transmission lines with different characteristic impedances for each region, as shown in Figure 1(a). The cascade matrix of a region of length d_i is given by

$$F_i = \begin{pmatrix} \cosh(\gamma_i d_i) & Z_i \sinh(\gamma_i d_i) \\ \frac{1}{Z_i} \sinh(\gamma_i d_i) & \cosh(\gamma_i d_i) \end{pmatrix} \tag{1}$$

The characteristic impedance Z_i and the propagation constant γ_i are given by Eq. (2) if the electron energy E is higher than the potential barrier height U_i of a region i, and by Eq. (3) if U_i is higher than E.

$$Z_i = \sqrt{\frac{X_i}{Y_i}}, \qquad \gamma_i = j\sqrt{X_i Y_i}, \tag{2}$$

$$Z_i = j\sqrt{\frac{X_i}{Y_i}}, \qquad \gamma_i = \sqrt{|X_i Y_i|} = \alpha_i. \tag{3}$$

X_i and Y_i are given as follows:

$$X_i = \frac{m_{ei}}{\hbar}, \qquad Y_i = -2\left(\frac{U_i}{\hbar} - \frac{E}{\hbar}\right), \tag{4}$$
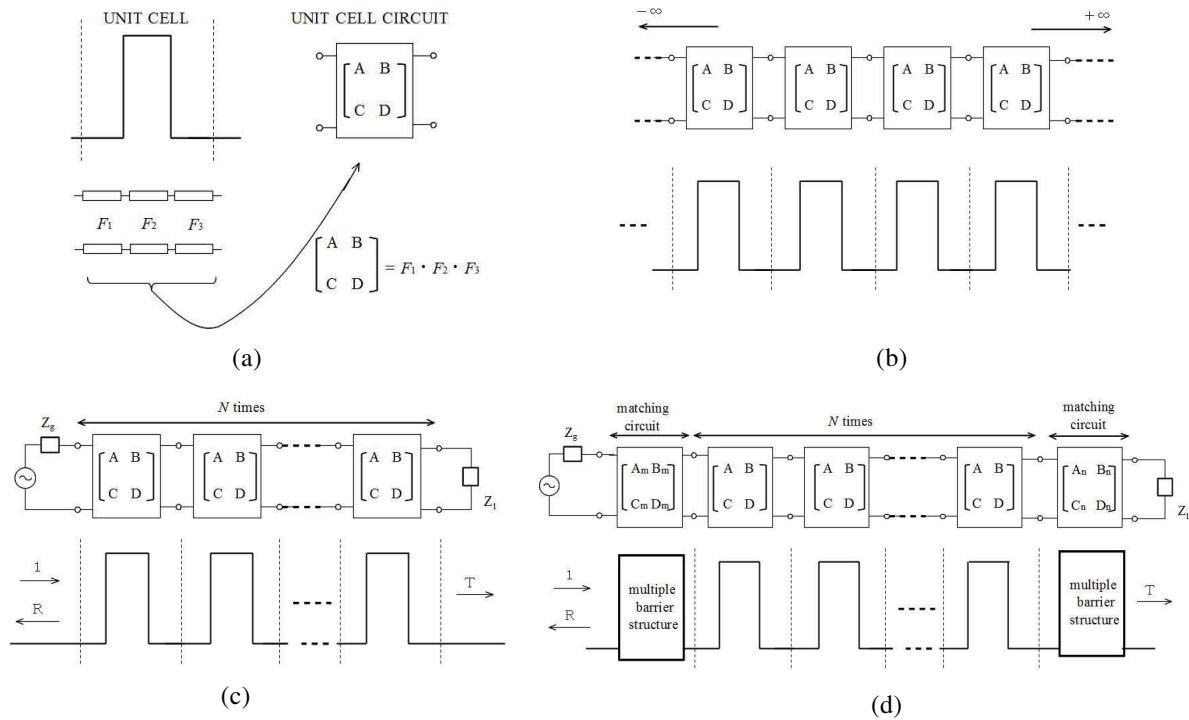
Figure 1: (a) An unit cell and its equivalent circuit. (b) A typical superlattice structure and its equivalent circuit. (c) A finite-length superlattice and its equivalent circuit. (d) A finite-length superlattice with matching structures and its equivalent circuit.

where m_{ei} is the effective mass of a region i and $\hbar$ is Planck's constant.

Figure 1(b) shows a typical superlattice structure and its equivalent circuit representation. The periodic structure is expressed as cascade connections of an unit cell circuit with an $ABCD$ matrix. We can analyze frequency characteristics of periodic structures using the iterative parameter theory [3]. The iterative impedance and the iterative transfer factor are defined by

$$Z_{ri} = \frac{A - D \pm \sqrt{(A - D)^2 - 4}}{2C} \tag{5}$$

and

$$\gamma_{ri} = \alpha + j\beta = \log\left(\frac{A + D}{2} \pm \sqrt{\left(\frac{A + D}{2}\right)^2 - 1}\right), \tag{6}$$

respectively.

If the iterative attenuation factor α in Eq. (6) is a pure imaginary numbers in a partiular frequency range, then that frequency range is a passband. On the other hand, if α is not pure imaginary numbers in a particular frequency range, then that frequency range is a stopband. We can control the position and the bandwidth of these bands to some extent by adjusting the circuit parameters.

The concept of infinite periodic structures is used in various engineering fields [6, 8]. Semiconductor superlattices are a typical example.However, we need to utilize finite periodic structures instead of infinite periodic structures in real situations (See Figures 1(b) and 1(c)). As a result, we cannot obtain complete band structures.

In this paper, we propose to place matching circuits at both sides of an infinite periodic structure as way to improve frequency characteristics (See Figure 1(d)). To design the matching circuit, we must determine the number of parameters. In order to determine those parameters, we adopt Nelder'sdownhill simplex method [7]. Specific design examples are described in the following sections.

3. IMPROVEMENT OF FREQUENCY CHARACTERISTICS WITH MATCHING STRUCTURES

Figure 2 shows the energy bands of an infinite-length superlattie and transmission curves of a finite-length superlattice. The barrier layer width is 20Å and the well layer width is 50Å. The finite-length superlattice consists of four barriers and three wells. The barrier heights U_i and the effective mass m_{ei} are given by

$$U_i = \begin{cases} 0.75x & x \leq 0.45 \\ 0.75x + 0.69(x - 0.45)^2 & x > 0.45 \end{cases}, \tag{7}$$

and

$$m_{ei} = (0.067 + 0.083x)m_o. \tag{8}$$

respectively. We use $x = 0.45$ in Figure 2. As shown in Figure 2, finite length superlattices do not have complete energy bands. Instead, they have sharp transmission peaks within an energy band of the correnponding infinite-length superlattice.

To improve the transmission characteristics of the infinite superlattice, we propose to place the matching structures at both sides of the finite-length superlattice, as shown in Figure 3. The matching structures consist of multiple barriers and wells with various heights and widths. We adopted Nelder's downhill simplex method [7] to adjust the parameters of multiple barriers and wells. To minimize the error defined by Eq. (9), the barrier heights and the layer widths are determined by the downhill simplex method as

$$err = \max\left\{|R(E)|^2\right\}, \quad E_l \leq E \leq E_h \tag{9}$$

where R is the reflection coefficient, and E is the incident electron energy. E_l and E_h are the lower and upper edges of an energy band.
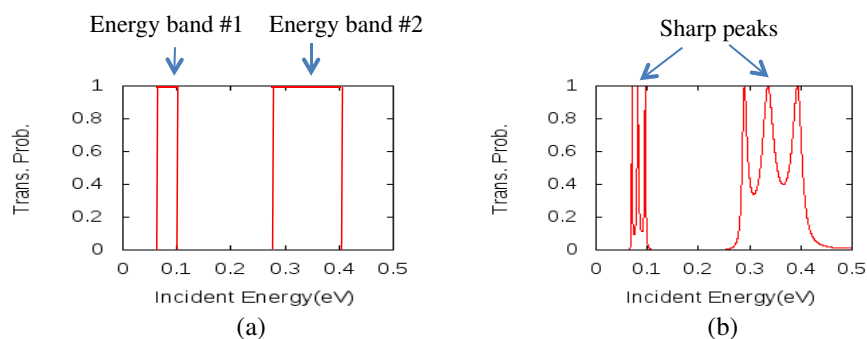
Figure 2: Transmission probability vs. electron energy. (a) Energy band (infinite-length superlattice). (b) Transmission probability (finite-length superlattice).
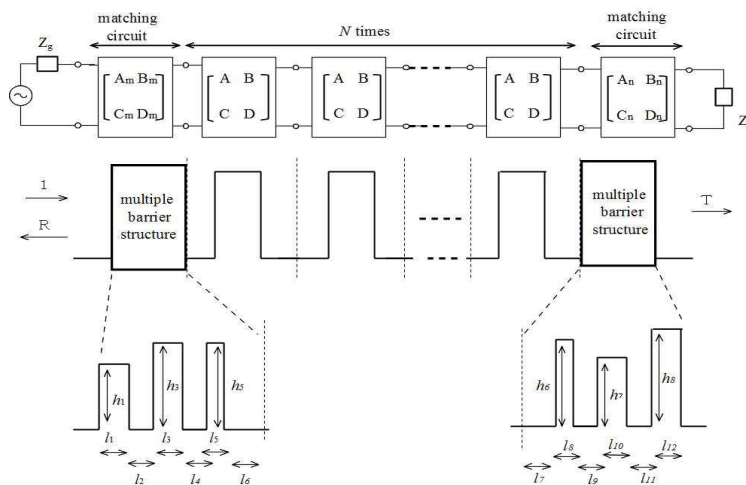
Figure 3: Infinite-length superlattice with matching structures.
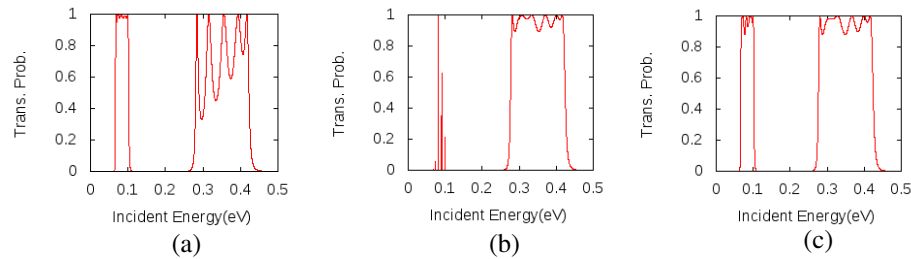
Figure 4: Transmission probability vs. electron energy of infinite-length superlattces with matching structures. (a) Imporvement of the energy band #1 $(l_1, l_2, l_3, l_4, l_5, l_6, l_7, l_8, l_9, l_{10}, l_{11}, l_{12}, h_1, h_2, h_3) = (21.9, 11.2, 22.0, 18.8, 15.3, 23.9, 0.10, 0.05, 0.32)$, unit of l: $\overset{\circ}{A}$, unit of h: eV. (b) Improvement of the energy band #2 $(18.7, 9, 28.7, 9.5, 15.5, 26.0, 0.17, 0.20, 0.37)$. (c) Simultaneous improvement the energy bands #1 and #2 $(8.9, 23.1, 6.4, 23.0, 16.1, 24.7, 0.285, 0.06, 0.32)$.

Figure 4 shows three examples of transmission characteristics that were improved by using the proposed method. In these examples, $N = 4$ and triple barrier structures are used as the matching structure. It is clear that the transmission characteristics are significantly better than those without matching structures. We can improve two energy bands simultaneously.

4. CONCLUSION

We have shown that it is possible to improve the transmission characteristics of finite-length super-lattices by using matching structures. We proposed to use multiple barrier structures as matching structures and a numerical optimization method for adjusting contractual parameters. The next step would be to apply our method to other periodic structures, for example, left-handed materials [8].

REFERENCES

1. Gomez, I., F. Dominguez-Adame, E. Diez, and V. Bellani, "Electron transport across a Gaussian superlattice," *J. Appl. Phys.*, Vol. 85, No. 7, 3916–3921, 1999.
2. Morozov, G. V., D. W. L. Sprung, and J. Martorell, "Design of electron band-pass filters for semiconductor superlattices," *Journal of Physics D: Applied Physics*, Vol. 35, No. 23, 3052, 2002.
3. Sanada, H., K. Asakura, M. Suzuki, and N. nagai, "A circuit theoretical method to synthesize bandpass electron energy filters," *Electonics and Communications in Japan*, Vol. 85, No. 7, 11–21, 2002.
4. Sanada, H. and K. Watanabe, "A study on electron-wave filters using barrier height modulated multiple barrier structures," *Electonics and Communications in Japan*, Vol. 86, No. 9, 11–19, 2003.
5. Asakura, K., H. Sanada, O. Ogurisu, and M. Suzuki, "Practical band estimation for periodic superlattices by using semi-infinite periodic model," *IEEE Int. Symposium on CIT*, 932–935, 2007.
6. Jelev-Vlaev, S., A. Enciso-Muñoz, and D. A. Contreras-Solorio, "Electronic properties of quantum wells structures with gaussian potential profiles," *PIERS Online*, Vol. 5 No. 2, 141–144, 2009.
7. Press, W. H., B. P. Flannery, S. A. Teukolosky, and W. T. Vetterling, *Numerical Recipes in C*, Cambridge University Press, 1992.
8. Caloz, C. and T. Itoh, *Electromagnetic Metamatericals*, Wiley-Interscience, 2006.

Investigation of Spectrally Efficient Transmission in Mixed WDM Systems

V. Bobrovs, A. Udalcovs, and I. Trifonovs

Institute of Telecommunications, Riga Technical University, Latvia

Abstract— The authors have investigated the minimal allowed channel spacing for developed mixed wavelength division multiplexing (WDM) systems in order to obtain the maximum spectral efficiency for system's channels. These fiber optic transmission systems can be considered under the concept of next generation optical networks and is offered as a model for the future design of backbone optical networks.

1. INTRODUCTION

Within the last few years strongly arises demand of transmission systems' channels information throughput. This trend is observed mainly due to rising number of worldwide internet user and data volume itself that is requested per user [1–3]. New information services including data, online and broadband services, such as online video conferences and video on demand, and their rapid advance only contributes to this trend of increase of demand for information capacity [4]. The existing transmission systems will be unable to secure appropriate quality of service (QoS) level and fulfill service level agreements (SLA) if internet traffic keeps doubling every year as it is now [4, 5]. Currently to ensure the requested transmission system's carrying capacity and data throughput of each individual channel required bandwidth of backbone fiber optic transmission system (FOTS) networks is being doubled within a two year period [6, 7].

Currently one of the most intensively studied system's total transmission capacity increment solutions is the increasing of system's channel spectral efficiency. Actually it is more efficient utilization of available bandwidth. It means that more informative bits are transmitted using one hertz from available frequency band. Channel's spectral efficiency can be increased in three different ways. The first one, the reduction of used system's channel spacing. The second one, the increase of per channel bit rate maintaining previously used channel spacing values for separation of transmission channels. And finally the third one is the combination of pervious two ways [8]. Obviously that it is easier to achieve a larger channel's spectral efficiency if for optical signal modulation and coding some of novel modulation formats are used. This novel (or advanced) modulation formats provide narrower optical signals spectrum or multilevel encoding schemes that ensure more bits per one symbol than it is in traditional modulation formats [9, 10]. In a case of different telecom operators' optical networks convergence a necessity to transmit differently modulated optical signals over a single optical fiber even with different per channel bitrates may occur in the soon future. That is why our study object of this paper is the spectral efficiency of the developedmixed WDM system which model is offered for the future design of backbone optical networks and can be considered under the concept of next generation optical network (NGON) [2, 11, 12].

This paper is organized as follows: Section 2 describes the developed model of mixed data rates WDM systems; in the Section 3 authors reveal the accuracy of the obtained results; in Section 4 the results are discussed; Section 5 contains the main conclusions.

2. SIMULATION MODEL

In this paper, as mixed FOTS is offered 9-channel WDM system, where three different modulation formats are used for carrier signal modulation. The first one is the NRZ-OOK, which traditionally used modulation format for FOTS. The second one is the orthogonal binary polarization shift keying (2-POLSK) and the third one is the differential phase shift keying with non-return to zero encoding (NRZ-DPSK). System's channels are divided into three groups with identical configuration of transmitter and receiver as well as modulation formats distribution among channels but with only with different channels' central wavelengths. It was specially done to take into account linear and nonlinear crosstalk influences to optical signal transmission that are experience central's group channels (from the first to the third system channel) from channels of adjacent groups (4th–6th and 7th–9th. For system's performance further analysis we will use channels number 1–3, but 4–6 and 7–9 are used only as a sources of interchannel crosstalk (see Fig. 1).

Then NRZ-OOK, 2-POLSK and NRZ-DPSK modulated optical signals from transmitters are mixed, optically preamplified and send over 50 km of standard single mode optical fiber (SSMF according to ITU-T Recommendation G.652 D). Fiber span length was chosen equal to 50 km in order to avoid in a prohibitive growth of ASE noise which occurs if used EDFA gain is greater than 10 dB [2]. The optimal EDFA fixed output power level and the optimal power level radiated by distributed feedback (DFB) lasers in continuous wavelength (CW) regime, that are used in channels, where NRZ-DPSK modulated optical signals are transmitted, previously were obtained in [13] and is equal to 4 dBm and 3.5 dBm, respectively. For chromatic dispersion (CD) compensation in case of 40 Gbit/s per channel bitrates dispersion post compensation module (DCM) is placed on the other fiber end before optical power splitter. This module compensates CD level that is being accumulated by signal during transmission over whole optical fiber length. Then optical signals are filtered with Super Gaussian optical filters, converted to electrical signals, then filtered with Bessel electrical filters and then detected.

3. SIMULATION ACCURACY

This research is based on powerful and accepted mathematical simulation software OptSim 5.2. It solves complex differential nonlinear Schrödinger equation (NLSE) using split-step Fourier method (SSFM). For the evaluation of system performance will be used such parameter as BER value. The maximum permissible BER value for the signals transmitted at 10 Gbit/s and 40 Gbit/s per channel bitrate is 10^{-12} and 10^{-16}, respectively. The BER confidence interval depends on the total number of simulated bits [14]. In our simulation we have simulated more than 1.024 bits and for such number of bits Q-factor uncertainty is less than 0.77 dB [14]. Using this value the 95% confidence intervals for 1024 simulated bits and nominals of 10^{-12} and 10^{-16} (assuming the Gaussian distribution) are:

$$\lg\{\text{BER}_{\text{for}10^{-12}}\} \in [-12.97; -11.04], \tag{1}$$

$$\lg\{\text{BER}_{\text{for}10^{-16}}\} \in [-17.26; -14.64]. \tag{2}$$

As is seen from Eqs. (1) and (2), the confidence interval for 1024 simulated bits and the nominal of BER $= 10^{-12}$ is less than ± 1 order, while for the nominal of BER $= 10^{-16}$ it is less than ± 2 orders. This evidences that OptSim software allows obtaining sufficiently accurate preliminary results.

4. RESULTS AND DISCUSSIONS

According to the above mentioned configuration of mixed WDM system [1st channel: NRZ-OOK (10, 40 Gbit/s)]-[2nd channel: 2-POLSK (10, 40 Gbit/s), 193.100 THz]-[3rd channel: NRZ-DPSK (10, 40 Gbit/s)], frequency plan of the channels' central wavelength allotment was studied for mixed per channel bitrates of the systems. In this research the investigation of maximum systems channels' spectral efficiency will be performed in order to achieve better utilization of the available frequency band. The channel spacing values were chosen based on the establishment principle of ITU-T Recommendation G.694.1.

Using the previously described configuration of developed mixed WDM system, six different systems with mixed data rates can be formed. All six studied WDM systems for convenience sake were divided into two groups. The first one contains combined WDM systems where only in one channel the optical signals are transmitted at 40 Gbit/s, while in the remaining two channels the per channel bitrate is 10 Gbit/s. The second group comprises the systems where in two channels the optical signals are transmitted at 40 Gbit/s, and only in one channel — with 10 Gbit/s.

It was found that the first system's configuration: [1st: NRZ-OOK (10 Gbit/s)]-[2nd: 2-POLSK (10 Gbit/s)]-[3rd: NRZ – DPSK (40 Gbit/s)] ensures the detected signal BER values that are the highest in a system's channels as compared with the second and the third configurations: [1st: NRZ-OOK (10 Gbit/s)]-[2nd: 2-POLSK (40 Gbit/s)]-[3rd: NRZ-DPSK (10 Gbit/s)] and [1st: NRZ-OOK (40 Gbit/s)]-[2nd: 2-POLSK (10 Gbit/s)]-[3rd: NRZ-DPSK (10 Gbit/s)], respectively. For these two configurations the detected signal BER values do not exceed 10^{-40} for all system channels if 75 GHz channel spacing is used. The first system's worst channel is the first one, where the 10 Gbit/s NRZ-OOK modulated signals are transmitted. At 75 GHz interval it's BER $= 6 \cdot 10^{-29}$ (see the 1st eye in Fig. 2(a)). If we reduce channel spacing to 50 GHz, the BER values for the system's first and second channels still fit maximum acceptable threshold of BER $= 10^{-12}$ (see the 4th and 5th eye in Fig. 2(a)) which was previously defined for 10 Gbit/s. The highest BER value
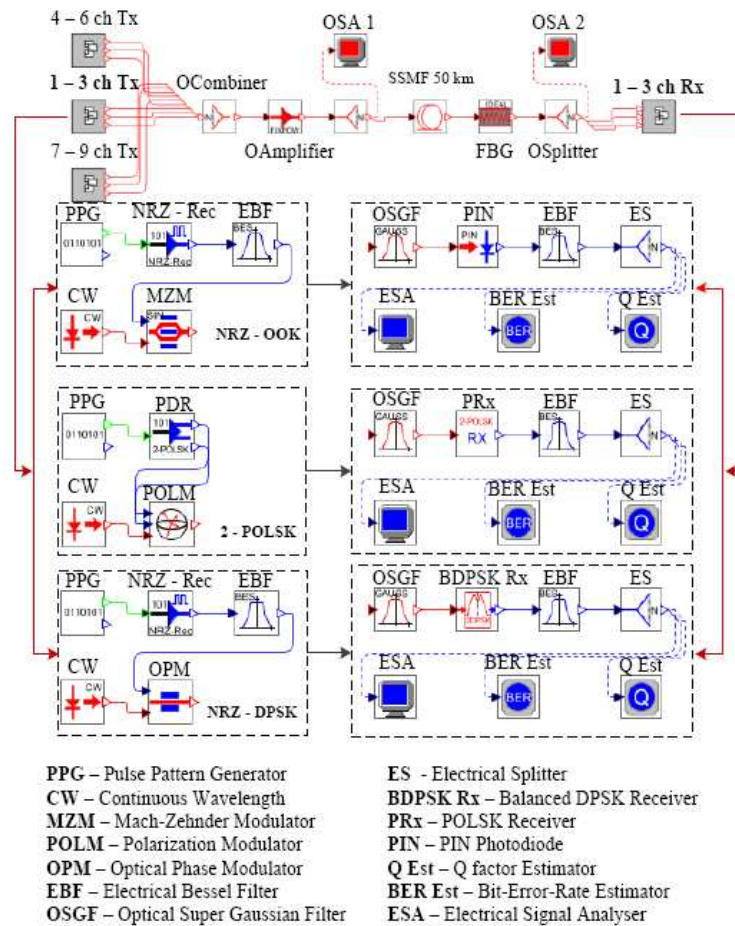
Figure 1: Developed 9-channel mixed WDM system simulation scheme and channels' transmitting and receiving parts block scheme for NRZ-OOK, 2-POLSK and NRZ-DPSK optical signals modulations formats.

for these two channels is for the first one and it is equal to $8 \cdot 10^{-13}$. As for the worst system's channel at 50 GHz spacing, it is the third one. Its BER value far exceeds the maximum acceptable error probability of 10^{-16} and is equal to $3 \cdot 10^{-5}$.

The worst configuration of a combined WDM system where optical signals are transmitted with 40 Gbit/s in two channels is the fourth one — [1st: NRZ-OOK (10 Gbit/s)]-[2nd: 2-POLSK (40 Gbit/s)]-[3rd: NRZ-DPSK (40 Gbit/s)]. It provides the highest average BER value for the detected signals as compared with the fifth and the sixth configurations: [1st: NRZ-OOK (40 Gbit/s)]-[2nd: 2-POLSK (10 Gbit/s)]-[3rd: NRZ-DPSK (40 Gbit/s)] and [1st: NRZ-OOK (40 Gbit/s)]-[2nd: 2-POLSK (40 Gbit/s)]-[3rd: NRZ-DPSK (10 Gbit/s)].

If for the channel separation in the 4th configuration of mixed WDM system the 75 GHz frequency intervals are used, the worst system's channel is the first one and its BER value is sufficiently higher than 10^{-40} and is equal to $1 \cdot 10^{-23}$. As for the rest of the system's channels, their BER values are not higher than 10^{-40}. As could be seen from the system's output optical spectrum, the channels are located maximally close to each other, so further compaction would lead to the signal spectrum overlapping as it is shown for 50 GHz spacing (see Fig. 2(b)). In this case 2-POLSK and NRZ-DPSK channels are overlapping. As a result, the BER value for the signals detected in these channels is considerably higher than 10^{-16} and is equal to $4 \cdot 10^{-4}$ and $8 \cdot 10^{-5}$ (see the 5th and 6th eye in Fig. 2(b)), respectively. Whereas NRZ-OOK channel's BER is $2 \cdot 10^{-12}$ at 50 GHz interval but it still is above the maximum tolerated error probability threshold of 10^{-12}.

Assuming that we operate with discrete noiseless channels and all the sent information is received unchanged at the other end (i.e., BER $\rightarrow 0$), the system's average spectral efficiency (SE, [bit/s/Hz]) has been calculated for the each studied mixed WDM systems and is equal to: 0.40 bit/s/Hz for the 1st, 2nd and 3rd system's configurations, and 0.27 bit/s/Hz for the 4th, 5th and 6th ones.
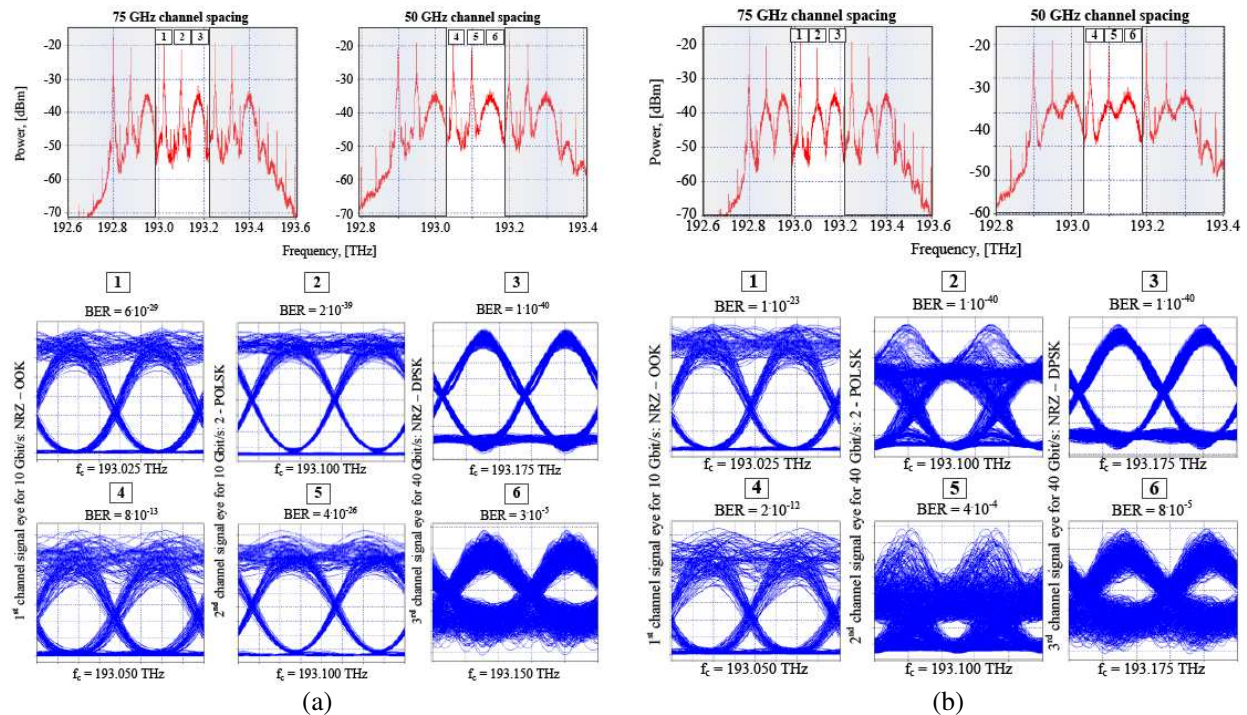
Figure 2: Optical spectrum and the eye diagrams of detected signals for the [1st: NRZ-OOK (10 Gbit/s)]-[2nd: 2-POLSK (40 Gbit/s)]-[3rd: NRZ-DPSK (40 Gbit/s)] 9-channel combined WDM systems at 75 and 50 GHz equal channel spacing: (a) [1st: NRZ-OOK (10 Gbit/s)]-[2nd: 2-POLSK (10 Gbit/s)]-[3rd: NRZ-DPSK (40 Gbit/s)]; (b) [1st: NRZ-OOK (10 Gbit/s)]-[2nd: 2-POLSK (40 Gbit/s)]-[3rd: NRZ-DPSK (40 Gbit/s)].

5. CONCLUSION

The authors have investigated the spectral efficiency of purposed mixed WDM system. This system's model is offered for the future design of the transport optical networks and complies with the following configuration: [1st channel: NRZ-OOK (10 or 40 Gbit/s)]-[2nd channel: 2-POLSK (10 or 40 Gbit/s)]-[3rd channel: NRZ-DPSK (10 or 40 Gbit/s)]. According to this configuration the minimum allowable and equal frequency intervals values between two adjacent channels have been obtained and analyzed for six different WDM systems with mixed per channel bitrates and signals' formats. It is found out that the minimum channel spacing to such WDM systems is not from ITU-T G.694.1. grid and is equal to 75 GHz if optical signals are transmitted with 10 and 40 Gbit/s per channel bitrates. As well as, such system's average spectral efficiency depends on the particular configuration of mixed system. SE is equal to: 0.27 bit/s/Hz if only in one of the three channels of the system $B = 40$ Gbit/s; 0.40 bit/s/Hz if in all system's channels optical signals are transmitted with equal per channel bitrate (10 or 40 Gbit/s) or at least in two of the three channels that form the central group of a system's channels $B = 40$ Gbit/s.

REFERENCES

1. Peucheret, C., "Fibre and component induced limitations in high capacity optical networks," Doctoral Thesis, 1–8, 2004.

2. Udalcovs, A., V. Bobrovs, and G. Ivanovs, "Investigation of allowed channel spacing for differently modulated optical signals in combined HDWDM systems," *Lithuanian Journal of Electronics and Electrical Engineering*, Vol. 6, No. 112, 19–24, 2011.

3. Wietfeld, A. C., "Modeling, simulation and analysis of optical time division multiplexing transmission systems," *Doctoral Thesis*, 9–18, 2004.

4. Bobrovs, V., S. Spolitis, A. Udalcovs, and G. Ivanovs, "Investigation of chromatic dispersion compensation methods for combined HDWDM systems," *Latvian Journal of Physics and Technical Sciences*, No. 5, 13–27, 2011.

5. Gosselin, S. and M. Joindot, "Key drivers and technologies for future optical networks," *European Conf. Optical Commun. (ECOC'06)*, Tutorial We2.2.1, 2006.

6. Dutta, A. K., N. K. Dutta, and M. Fujiwara, "WDM technologies: Optical networks," Elsevier Inc., USA, 2004.

7. Cisco Systems, "Cisco visual networking index — Forecast and methodology 2009–2014," *White Paper*, No. 1, 1–17, 2010.

8. Miyamoto, Y., "Ultra-high capacity transmission for optical transport network," *OFC/NFOEC*, 2011.

9. Sano, A., H. Masuda, T. Kobayashi, M. Fujiwara, K. Horikoshi, E. Yoshida, Y. Miyamoto, M. Matsui, M. Mizoguchi, H. Yamazaki, Y. Sakamaki, and H. Ishii, "Ultra-high capacity WDM transmission using spectrally-efficient PDM 16-QAM modulation and C- and extended L-band wideband optical amplification," *Journal of Lightwave Technology*, Vol. 29, No. 4, 578–586, 2011.

10. Takahashi, H., A. Al Amin, A. Jansen, S. L. Morita, and I. Tanaka, "Highly spectrally efficient DWDM transmission at 7.0 b/s/Hz using 8x65.1-Gb/s coherent PDM-OFDM," *Journal of Lightwave Technology*, Vol. 28, 406–414, 2010.

11. Kikuchi, K., "Coherent transmission systems," *34th European Conference on Optical Communication*, 1–39, 2008.

12. Bottacchi, S., A. Beling, A. Matiss, M. L. Nielsen, A. G. Steffan, and G. Unterborsch, "Advanced photoreceivers for high-speed optical fiber transmission systems," *IEEE Journal of Selected Topics in Quantum Electronics*, Vol. 16, No. 5, 1099–1112, 2010.

13. Udalcovs, A., V. Bobrovs, and G. Ivanovs, "Investigation of differently modulated optical signals transmission in HDWDM systems," *Journal of Computer Technology and Application*, Vol. 2, No. 10, 801–812, 2011.

14. RSoft Design Group, Inc. OptSim User Guide, 157–172, NY, USA, 2008.

Investigation of External Electromagnetic Disturbance in HDWDM System

J. Porins, **G. Ivanovs**, **V. Bobrovs**, **and A. Supe**

Institute of Telecommunications, Riga Technical University
12 Azenes Street, Riga LV-1010, Latvia

Abstract— In the work, variations in the optical signal parameters in high-density wavelength division multiplexing (HDWDM) optical fiber communication system under strong external electro-magnetic (EM) field are analyzed for different modulation formats and transmission speeds. It is established that a 8-channel HDWDM system with NRZ modulation is more sensitive to the polarization state changes on exposure to external EM field as compared with a system in which the polarization state modulation (POLSK) modulation format is used. The BER analysis shows that the EM effect is one of the factors limiting the minimum for the allowed inter-channel interval. If this allowed minimum is chosen to be 0.3 nm for data transmission speed 10 Gbps, in view of the EM influence it should be raised to 0.4 nm in order to ensure the necessary BER level an HDWDM system.

1. INTRODUCTION

The increasing need to access information generates progress of wide development in the field of fiber optics communication systems by WDM. Transmission of high bitrate optical signals and dense optical channel spacing is used for increasing the capacity of the optical long-haul communication systems [1]. The influence of the external electro-magnetic field on its optical properties is rather weak, which, in turn does not cause changes of optical signals in optical fibers. At the same time, this is not so unambiguous for the WDM communication systems with closely spaced channels (HDWDM) as the data transmission speeds are increasing and the channel intervals are decreasing (down to 0.4 or even 0.2 nm). The same refers to the optical fiber cables with metal wires or metallic line armouring, especially to the optical cable lines enclosed in high-voltage ground wires and in the case when the NRZ or POLSK modulation format is used. This format is offered as an alternative to traditionally employed intensity manipulation (IM), and is the newest from the signal modulation formats to be applied just to the optical fiber transmission systems, imparting to them a very valuable property — better resistance to the self phase modulation (SPM) [2].

2. BACKGROUND

External electric, magnetic and electromagnetic (EM) fields can affect light transmission in optical fibers through Kerr effect, Faraday effect and Pockels effect. The point is that changes of state of polarization (SOP) in WDM transmission systems occur not only due to the polarization mode dispersion (PMD) but also due to non-linear effects (NOE). Therefore, the refractivity depends not only on the frequency but also on the intensity of electric field that is propagating through a dielectric medium (fiber) or interacts with it. As the number of channels increases in the core of a single-mode optical fiber, a rather high concentration of electric field is built up, this gives rise to refractivity changes and to such non-linear effects as self-phase modulation (SPM), cross-phase modulation (XPM) and four wave mixing (FWM). The Kerr effect has been found to occur not only under the internal electric field (that of optical signal) but also as being induced by external field. The external electro-magnetic field changes the SOP of the optical signal in the fiber, which, in turn, leads to changes in the process of propagation and reception of such a signal. Apart from changes in the optical signal polarization in fibers also double refraction properties can arise. The rotating angle φ of an optical signal's polarization under the electric field is expressed as [3]:

$$\varphi = 2\pi K E^2 l \tag{1}$$

where K — Kerr coefficient ($K = f(n, T)/\lambda$; E — electric field intensity; l — length; λ — wavelength.

Kerr effect is proportional to the outer square of the field and depends on the refractive index n and temperature T. Difference in the refractive indices in the optical medium due to electro-optic Kerr effect can be calculated using equation [3]:

$$\Delta n = \lambda K(\lambda) E^2, \tag{2}$$

where Δn — refractive index difference between two orthogonal optical waves in the optical medium.

The Kerr coefficient is dependent on the wavelength and assuming that the solids approximation anisotropic molecules turning in a similar way as a liquid or gaseous substance that is obtained [3]:

$$K = \frac{1}{30} \frac{(n^2 - 1) \cdot (n^2 + 2)}{n} \cdot \frac{m\varepsilon_o}{\lambda kT\rho}, \tag{3}$$

where ε_0 — electric constant, m — particle mass of mater, λ — wavelength, k — Boltzmann's constant, T — absolute temperature (Kelvin's).

Faraday effect or Faraday rotation is a magneto-optical phenomenon. It gets as an interaction between light and a magnetic field in a medium. The Faraday effect causes a rotation of the plane of optical radiation polarization. Angle β by which this rotation occurs is linearly proportional to the component of the magnetic field that is oriented to the direction of light propagation. Following equation shows relation between turn angle of polarization state and magnetic field [3]:

$$\beta = \vartheta Bd, \tag{4}$$

where ϑ — Verdet constant, B — magnetic flux density, d — the length of the path where the light and magnetic field interact.

Research of author [3, 4] shows that turning the plane of polarization can occur even up to 45° to 90° if optical fiber affects strong lighting. Change in the polarization state can produce errors in data transmission especially for modulation formats where coherent detection is used. Changes of plane of polarization can cause double refraction and two mutually orthogonally wave components occurrence in optical fibers [5].

3. SIMULATION SCHEME AND PARAMETERS

This research is based on WDM system performance analysis using simulation software Opt-Sim5.2. The method of calculation implemented in this software is based on solving the non-linear Schrödinger equation [6]. The Split Step method to solve the non-linear Schrödinger equation to perform the calculation of the optical wave propagation through the OF is used.

To evaluate EM field influence to FOTS we propose to use a 8 channel WDM transmission systems working in the C band (conventional band from 1530 to 1565 nm wavelength). Whole system can be divided into three main parts: transmitter, transmission line and a receiver part (Fig. 1).

Transmitter part consists of 8 multiplexed optical channels each located at different wavelength. All the channels are located with even spacing. Interval between adjacent channels is chosen according to data transmission speed in channels. For 10 Gbps data transmission speed the adjacent channel interval is set to 0.3 nm [7]. For 12.5 and 40.0 Gbps data transmission speed this interval is set to 0.4 and 1.2 nm accordingly.

Each transmitter consists of random data generator (PPG), code driver (NRZ_driver), laser source (CW_laser) and electro-optical modulator (MZ_modulator). The laser is always switched
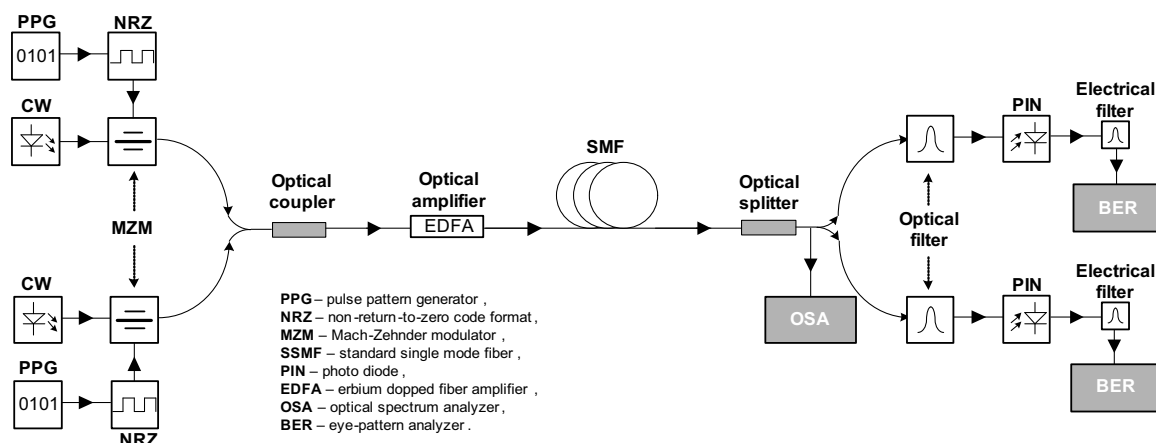
Figure 1: The setup used for investigation of HDWDM transmission system.

on and its lightwaves are modulated via external electro-optic Mach-Zender (MZ) modulator by random data pulse sequence output of a pulse pattern generator (PPG). Data signal from PPG are coded using non-return-to-zero (NRZ) pulse shapes.

Each transmitter MZ modulator output is connected to an optical coupler. Further multiplexed optical signal is sent to a standard single mode fiber (SSMF) ITU-T G.652D, where optical pulses propagates via 40 km length. In the receiver each channel is optically filtered by Bessel filter) to separate channels. Filter bandwidth is set accordingly to the transmission data rate. Optical filter output is connected to polarizer. That simulates polarization dependent losses at the receiver part. After polarizer optical signal is converted to electrical signal using photodiode (PIN) whose sensitivity is -15 dBm. To evaluate the data transmission performance eye diagram measurements of electrical signal have been taken at the output of each channel. Eye diagram gives determination of signal quality factor Q and correspondingly bit error rate (BER). System overall performance will be determined by the worst channel BER.

To determine electric and magnetic field influence we will artificially introduce changes in the proposed WDM system. Electric field influence due to electro-optic Kerr effect can be evaluated by increase in optical fiber PMD and changes of SOP. Whereas magnetic field influence due to Faraday effect will be simulated by inserting optical signal polarization rotator at the output of fiber. EM field influence to the overall WDM system performance will be evaluated by the received data signal worst BER value. For crystals the Kerr constant typically ranges from 10^{-18} to 10^{-14} m^2/V^2 [8]. Optical fiber is an optical radiation waveguide that is created from optical materials based on SiO$_2$. If we assume typical electric field intensity $E = 3.2$ kV/m at ground level from 220 kV power transmission overhead line we get negligible change in refractive indices $\Delta n = 8.41 \cdot 10^{-18}$ [9]. To get more notable interaction it is worth to assume much higher electric field intensity. Faraday effect occurs when magnetic field direction match with optical radiation propagation direction. As an EM field source we chose a case of lightning induced electric flux density that can shift optical radiation polarization plane up to 90°.

4. RESULTS AND DISCUSSION

The experiment was run in two stages in order to simplify analysis of the results. In the first stage, a system was simulated with no electro-magnetic influence and with only tabulated parameters of the elements so that its efficiency is determined in the absence of such influence. In the second stage, under simulation was a system which in the middle of line is affected from outside by a strong electro-magnetic field. Simulations were performed using previously described HDWDM system. Data transmission speed for each channel is set to 10.52, 12.5 and 40 Gbps and two different modulation formats — IM and POLSK. Following two tables show the eye diagrams for 40 Gbps channel data rate as it showed the highest performance decrease determined by BER.

From the results we can see that for higher data transmission speed this influence gives greater increase in BER. So influence of external EM disturbance in optical fibers can become more common especially in long-span high density WDM (HDWDM) systems with high data transmission speed and modulation formats with coherent detection.

If we compare electrical and magnetic field influence then it shows similar results. But magnetic

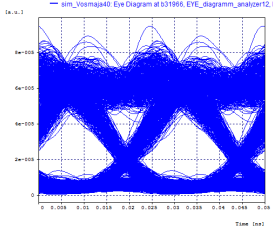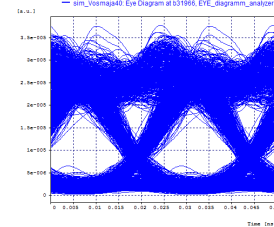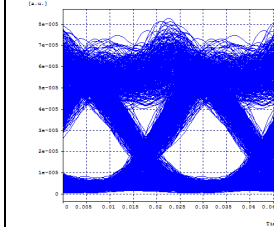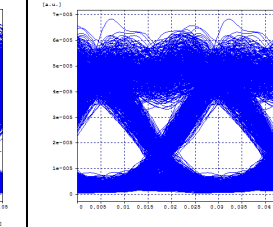Table 1: Achieved eye diagrams and BER values for 40 Gbps WDM system.
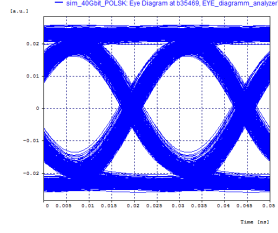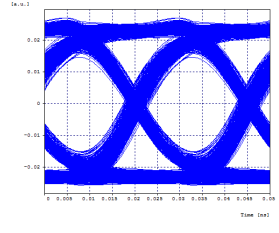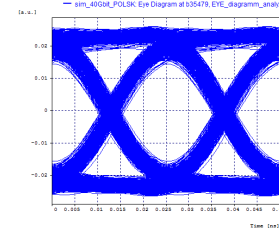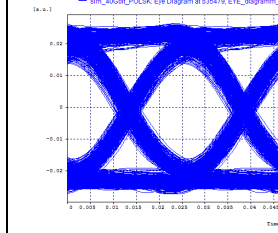
Amplitude modulation (NRZ code)			
Electro-optic Kerr effect		Faraday effect	
without EM field	with EM field	without EM field	with EM field
BER=2.13·10^{-14}	BER=6.66·10^{-12}	BER=1.81·10^{-16}	BER=1.16·10^{-14}

Table 2: Achieved eye diagrams and BER values for 40 Gbps WDM system.

POLSK modulation			
Electro-optic Kerr effect		Faraday effect	
without EM field	with EM field	without EM field	with EM field
BER=7.58·10⁻²⁸	BER=1.64·10⁻²⁴	BER=3.70·10⁻²⁷	BER=7.46·10⁻²⁴

field influence is less likely to have serious problems to FOTS, because it is most effective when magnetic field direction coincide with optical radiation propagation direction. In the case of power transmission lines this condition fulfills only in the case of optical fiber and power line being located mutually orthogonally.

5. CONCLUSION

Simulation results show that BER value increase at EM field interaction in our HDWDM system with POLSK modulation is smaller compared to IM. The obtained eye diagrams show changes pointing to those in the system's quality indices under the EM influence. For the analysis we have used the 1st, 5th, and 8th channels. This choice is explained by a comparatively wide band (1546.8–1552.8 nm) in which the WDM system's channels are arranged, whereas it is known that fiber parameters (attenuation, chromatic dispersion and PMD) are specified for 1550 nm. Therefore, it was of important to give consideration just to side channels (the 1st and 8th, respectively) where the deviations of parameters from designed values are the greatest. When analyzing the eye diagrams degraded after the EM action, it is seen that the eye narrowing occurred owing to the PMD influence, since we observed increased phase jitter and frequency chirps caused by NOE (SPM, XPM). The degradation of eye diagrams corresponds to changes in the signal BER values from $5.43 \cdot 10^{-16}$ to $6.66 \cdot 10^{-12}$. The differences could be interpreted, e.g., as consequences of NOE, since these effects are dependent also on dispersion and attenuation. A great concern as to the really placed optical lines is the influence of high-voltage transmission lines that can arise in the cases of line faults. Obviously, in practice the consequences of external EM influence (considered in the simulation) would not be significant, since the voltage that can arise due to such a fault is much lower (110 kV in the ground wire) — i.e., by 50 kV; however, since the fibers are inserted enclosed in the cables of high-voltage lines, such influence takes place all along the fiber length, which could cause definite changes.

ACKNOWLEDGMENT

REFERENCES

1. Agrawal, G. P., *Fiber-optic Communication Systems*, 2nd Edition, John Wiley & Sons, New York, 1997.
2. Bobrovs, V. and G. Ivanovs, "Investigation of minimal channel spacing in HDWDM systems," *Electronics and Electrical Engineering*, Vol. 4, No. 92, 53–56, 2009.
3. Sokolov, S. A., "Features of polarization mode dispersion in optical cable with a wave seal from lightning," *Proceedings of the 1st Russian Conference on Lightning Protection*, 111–114, Novosibirsk, Russia, Nov. 2007 (in Russian).
4. Sokolov, S. A., "The emergence of polarization mode dispersion under the influence of lightning," *Electrosvyaz*, No. 11, 100–103, 2004 (in Russian).
5. Agrawal, G. P., *Nonlinear Fiber Optics*, 3rd Edition, Academic Press, San Diego, 2001.

6. Zakharov, V. E. and S. V. Manakov, "On the complete integrability of a nonlinear Schrödinger equation," *Journal of Theoretical and Mathematical Physics*, Vol. 19, No. 3, 551–559, 1974.

7. Ivanovs, G., V. Bobrovs, O. Ozolins, and J. Porins, "Realization of HDWDM transmission system," *International Journal of the Physical Sciences*, Vol. 5, No. 5, 452–458, 2010.

8. Saleh, B. E. A. and M. C. Teich, *Fundamentals of Photonics*, 1st Edition, John Wiley & Sons, 1991.

9. Strange, P., *Electric and Magnetic Field Strengths*, Transpower EMF Fact Sheet, New Zealand, 2009.

The Design of HEV Drive Unit with an Axial Flux Rotary Converter

P. Chlebis, **A. Havel**, and **P. Vaculik**

Department of Electronic, VSB — TU Ostrava, 17, 15 Listopadu, Ostrava 70800, Czech Republic

Abstract— This paper describes an efficient axial flux arrangement of the four quadrant rotary converter for hybrid electric vehicles. The main task of here presented solution is to keep an internal combustion engine working in the area of its maximal efficiency during all possible driving conditions to satisfy minimal fuel consumption. In other words, this unit has to convert the optimal torque-speed operation point of the ICE on the input shaft to the required variable torque and speed on the output shaft. The possibility of the axial flux rotary converter (AFRC) arrangement based on the assembly of axial flux permanent magnet and axial flux induction motor with rotors clamped to the belt pulley is discussed in the concluding part of this paper along with the 3D FEM simulations of magnetic flux density in the stator pack.

1. INTRODUCTION

The maximal efficiency of the internal combustion engine (ICE) used in conventional vehicles is due to Carnot's cycle approximately bounded above to 40%. Such efficiency can only be reached in a very small torque-speed area, which leads to the idea of full torque and speed control in hybrid electric vehicle (HEV) conceptions aimed at considerable power savings. Many of today's used HEV conceptions are based on the series-parallel hybrid arrangement, combining the advantages of both essential arrangements together [1].

The AFRC is supplied by the three phase voltage inverter from the DC power source, which can be realized as a combination of two autonomous power sources — LiFePO4 battery pack delivering nominal current and ultracapacitor pack for peak power supplying. Whole system is controlled by the DSP TMS320F28335 with implemented direct torque control algorithm to satisfy sufficient computing power and dynamics of the four quadrant rotary converter (4QRC) drive system [2–4] — see Figure 1.

The proposed solution combines two known principles of electric rotating machines together in one unit, which is composed from synchronous and asynchronous machine having two rotors affixed to the input and output shaft, one wound stator and two axial air gaps $\delta 1$ and $\delta 2$. Due to selected double rotor arrangement it is possible to vary both the speed and the torque between the input and output shaft, hence the transferred power. The input and output power difference is possible to supply or consume by the stator winding, so only a part of the total vehicle drive energy is transferred across the electromagnetic coupling.

The unneeded part of mechanical energy produced by the ICE or the vehicle braking energy can be transferred through the electromagnetic coupling between the outer rotor and stator and then stored into the rechargeable batteries or ultracapacitor pack. On the other hand, during the fluent change of the input and output shaft speed ratio it is possible to simultaneously compensate the peak power consumption needed for dynamic states during speed variation or vehicle loading.

Another advantage of axial flux conception is in the possibility of air gap width adjustment, which allows the optimization of magnetic field depth penetration into the squirrel cage inner rotor.
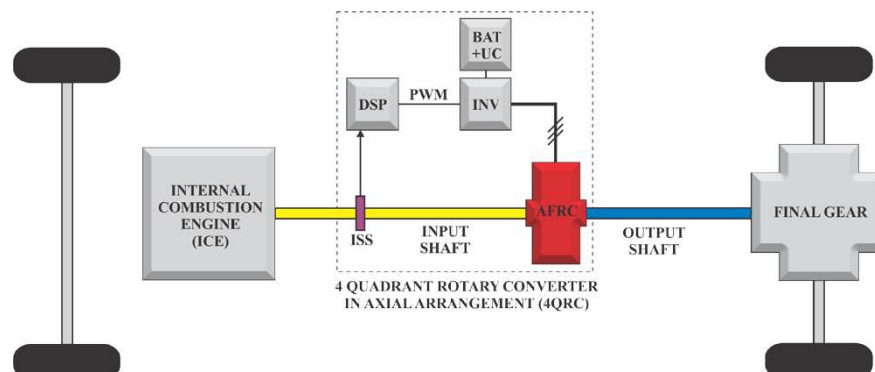

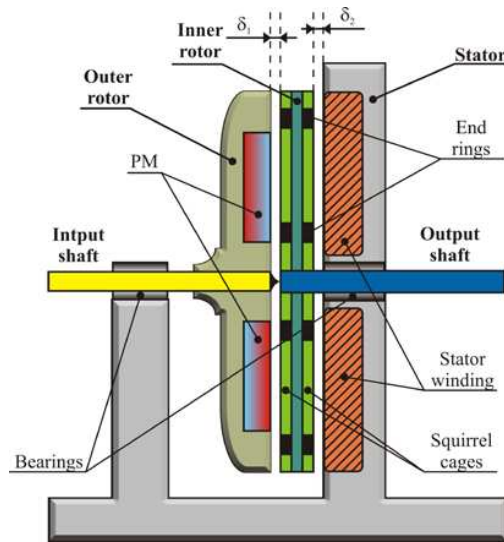Figure 1: Integration of the axial flux rotary converter into the HEV drive unit.

Figure 2: The axial flux rotary converter machine in axial cross section.
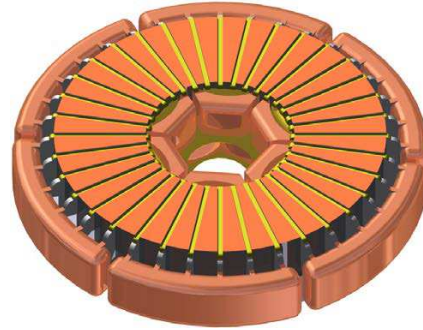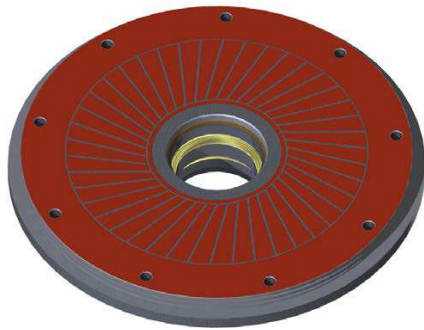

Figure 3: The 3D model of axial flux squirrel cage rotor.

Figure 4: The 3D model of axial flux wound stator.

It also comes through that the AFRC can be run in pure mechanical or electrical mode when only the ICE or batteries are producing the driving power.

Constructional simplicity of presented axial flux rotary converter is ensured by the disc conception with two axial air gaps and double squirrel cage inner rotor. The inner rotor can simultaneously interact with electromagnetic fields from permanent magnet outer rotor and wound stator to create two different asynchronous machines with them — see Figure 2.

2. THE DESIGN POSSIBILITIES, ARRANGEMENTS AND 3D FEM SIMULATIONS OF THE AFRC

The design of the axial flux stator and rotor was based on the design of standard worldwide used cylindrical conception of induction and synchronous motor. The resulting parameters were then recounted to the axial conception, more precisely, to the inner and outer diameters and thicknesses of the axial stator and rotor utilizing the method of constant magnetic circuit cubature. The stator and rotor volume Equations (1) and (2), which were used for the dimensions conversion, are presented below.

$$\frac{\pi l_i}{4} \left[D_e^2 - D^2 \right] = \frac{\pi h_S}{4} \left[D_{OUT}^2 - D_{IN}^2 \right] \tag{1}$$

$$\frac{\pi l_i}{4} \left[D_2^2 - D_i^2 \right] = \frac{\pi h_R}{4} \left[D_{OUT}^2 - D_{IN}^2 \right] \tag{2}$$

where: D_e and D are the outer and inner diameters of cylindrical stator; D_2 and D_i are the outer and inner diameters of cylindrical rotor; l_i is the ideal air gap length D_{IN} and D_{OUT} are the inner and outer disc diameters; h_S and h_R are the axial stator and rotor thicknesses.
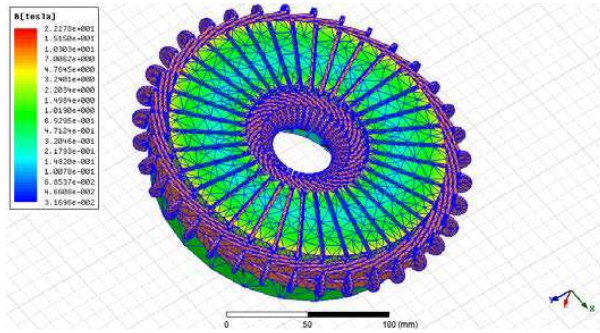
Figure 5: The distribution of magnetic flux density in stator disc.
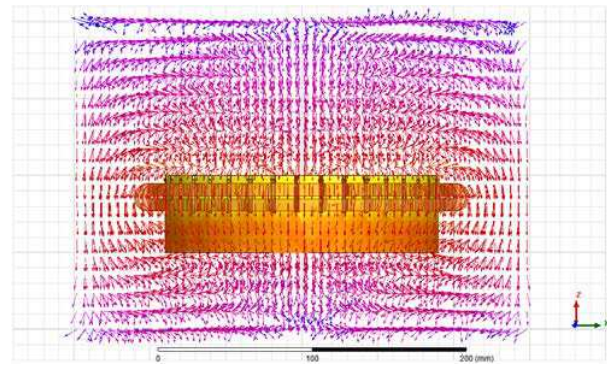
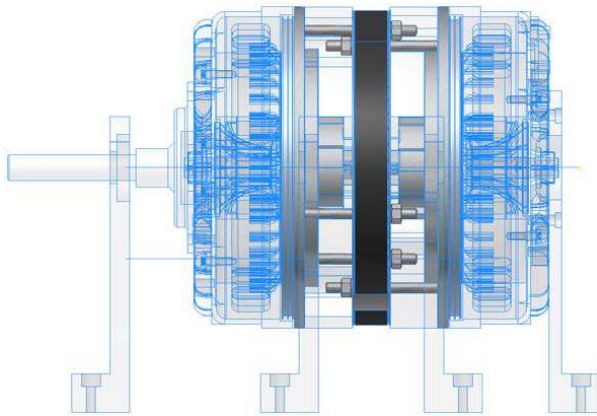Figure 6: The vector map of magnetic flux density around stator.

Figure 7: The front view of both rotors clamping to the belt pulley.
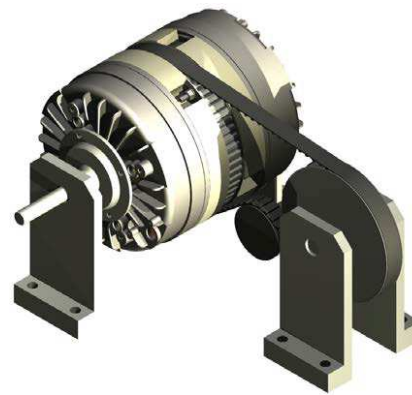

Figure 8: The prototype model of AFRC with belt gearing.

By the comparison of Equations (1) and (2) is possible to express the stator/rotor disc thicknesses ratio (3) and the outer disc diameter dependency (4), which finally leads to all main dimensions of stator and rotor discs.

$$\frac{h_S}{h_R} = \frac{D_e^2 - D^2}{D_2^2 - D_i^2} \tag{3}$$

$$D_{OUT} = \sqrt{\frac{l_i(D_e^2 - D^2)}{h_S} + D_{IN}^2} \tag{4}$$

The right choice of the air gap thicknesses δ_1 and δ_2 has crucial influence on the energetic parameters of the AFRC drive unit. If the size of the air gap is reduced, also the magnetizing current decreases, which leads to better power factor and lower stator losses. However, making the air gap too thin may cause increasing of the amplitude of magnetic flux density pulses in the air gap, hence increasing the surface and pulse losses [5, 7]. Therefore the optimal air gap thickness has to be evaluated as a result of the 3D finite element method simulations.

The 3D models of axial flux wound stator and squirrel cage rotor were created in the 3D CAD application Autodesk Inventor Professional — see Figures 3 and 4.

The CAD geometry was transported to the 3D FEM environments and solvers like Maxwell or RMxprt, towards running the electromagnetic simulations. The output data may become fundamental for further design and optimization of the drive units utilizing the axial flux motors as a main or auxiliary drive.

Due to hardly mechanically viable torque transportation from the inner double squirrel cage rotor to the output shaft (see the Figure 2 again), the laboratory prototype model of AFRC was designed with utilization of the belt gearing comprising two belt pulleys and one stretching pulley — see Figures 7 and 8. This solution is mechanically easier to build, because there is a possibility

of direct employment of fabricated axial flux motors of approximately same output power. The spacer rings are used to adjust the positions of both rotors to satisfy uniform distribution of the torque and minimize vibrations.

3. CONCLUSION

Axial air gap motors may one day become a key candidate for propulsion systems of hybrid or pure electric vehicles. To utilize this technology in practical applications, the 3D finite element analysis is needed for better understanding of electromagnetic conditions such as flux and field behaviors in drive structures involving the axial flux based machines.

ACKNOWLEDGMENT

REFERENCES

1. Larminie, J. and J. Lowry, *Electric Vehicle Technology Explained*, John Wiley & Sons, Ltd., England, 2003, ISBN 0-470-85163-5.
2. Chlebis, P. and J. Dudek, "Comparison of power losses and quality of output voltage from different types of inverters," *35th Annual IEEE Power Electronics Specialists Conference*, Vols. 1–6, 3120–3126, Aachen, Germany, 2004, ISBN 0-7803-8399-0.
3. Brandstetter, P., P. Chlebis, and P. Palacky, "Direct torque control of induction motor with direct calculation of voltage vector," *Advances in Electrical and Computer Engineering*, Vol. 10, No. 4, 17–22, 2010, ISSN 1582-7445.
4. Chlebis, P., A. Havel, P. Vaculik, and Z. Pfof, "Modern instruments for increasing the efficiency of the energy transfer in electric vehicles," *14th EPE-PEMC 2010 International Power Electronics and Motion Control Conference*, Vol. 14, 89–93, Ohrid, Republic of Macedonia, Sep. 6–8, 2010, ISBN 978-1-4244-7854-5.
5. Kopylov, I. P. and Collective, *Construction of Electric Machines*, First Release, 688 Praha, SNTL, 1988.
6. Gieras, J., R. Wang, and M. Kamper, *Axial Flux Permanent Magnet Brushless Machines*, Kluwer Academic Publisher, 2004, ISBN 1-4020-2661-7.
7. Chlebis, P., A. Havel, P. Vaculik, and L. Odlevak, "The design and simulation of the axial air gap induction motor," *12th Electric Power Engineering*, Kouty nad Desnou, Czech Republic, May 17–19, 2011, ISBN 978-80-248-2393-5.

Characterization of the Cerenkov Radiations Generated in Optical Fibers Irradiated by Co-60 Isotope

K. W. Jang[1], W. J. Yoo[1], J. Moon[1], K. T. Han[1], D. Y. Jun[1], S. H. Shin[1], J.-Y. Park[1], B. G. Park[2], S. Kim[3], Y.-H. Cho[4], and B. Lee[1]

[1]School of Biomedical Engineering, Research Institute of Biomedical Engineering
Konkuk University, Korea
[2]Department of Energy & Environmental Engineering, Soonchunhyang University, Korea
[3]Department of Nuclear & Energy Engineering, Applied Radiological Science Research Institute
Cheju National University, Korea
[4]Department of Radiological Science, Catholic University, Korea

Abstract— To develop the fiber-optic Cerenkov radiation sensor, in this study, we characterized the Cerenkov radiations generated in optical fibers irradiated by a Co-60 isotope. We measured and analyzed the intensities of Cerenkov radiations as functions of numerical apertures, OH contents, irradiated lengths and diameters of the optical fibers.

1. INTRODUCTION

Optical fibers have been widely used as sensing elements or a means of relaying signals. General method for measuring physical fluctuations with fiber-optic sensors is to measure light intensities or wavelength shifts of incident lights. Here, the optical fibers can transmit light signals, which are related to physical fluctuations, to light measuring devices without experiencing external influences such as pressure, temperature and humidity [1]. In hazardous radioactive environments, especially, the radiation sensors using optical fibers have a number of advantages such as high spatial resolution, availability in narrow spaces, and real-time measurement [2–4]. The fiber-optic Cerenkov radiation sensor, which is one of the fiber-optic radiation sensors, is composed with optical fibers and a light measuring device without any sensor tip such as a scintillating material. Therefore, this sensor has some advantages, which are caused by the absence of a scintillator such as simple manufacturing process low cost and non-quenching effect.

Generally, a charged particle cannot travel with a velocity greater than that of the light in a vacuum. However, in some transparent medium such as water, silica or PMMA (polymethyl methacrylate), the high energy particle can pass through the medium with a greater velocity than that of the light. Here, the Cerenkov radiation or light can be produced by a charged particle traveling through a medium at a velocity greater than that of light in the same medium [5]. This Cerenkov radiation could be observed easily in boiling-water reactors (BWRs) pressurized-water reactors (PWRs) and spent fuel storage fits.

In cases of the spent fuel storage fits, Compton electrons are produced by gamma rays whose kinetic energies are greater than 423 keV from the spent fuels. Therefore, the Cerenkov radiation depends on the amount and kinetic energies of gamma rays from fission products in a spent fuel assembly. These gamma rays are produced according to the burnup of fuel assembly and the half-life of fission products. Consequently, the intensity of Cerenkov radiation depends on the burnup of fuel assembly in the spent fuel storage pool [6].

In this paper, we characterized the Cerenkov radiations generated in optical fibers irradiated by a Co-60 isotope to develop the fiber-optic Cerenkov radiation sensor. We measured the intensities of Cerenkov radiations as functions of numerical apertures (NAs), OH contents, irradiated lengths and diameters of the optical fibers.

2. MATERIALS AND METHODS

Step-index multimode silica optical fibers (BFLH37, APCH1000, BFL48, BFH48, Thorlabs Inc.) are used to generate the Cerenkov radiation Core and cladding materials of these fibers are pure silica and hard-polymer, respectively. Further properties of the silica optical fibers are listed in Table 1.

Commercial grade plastic multimode optical fibers (SH2001, Mitsubishi Ltd.) are used to guide Cerenkov radiation from the silica optical fibers to the light measuring device. The outer diameter

Table 1: Properties of the silica optical fibers.

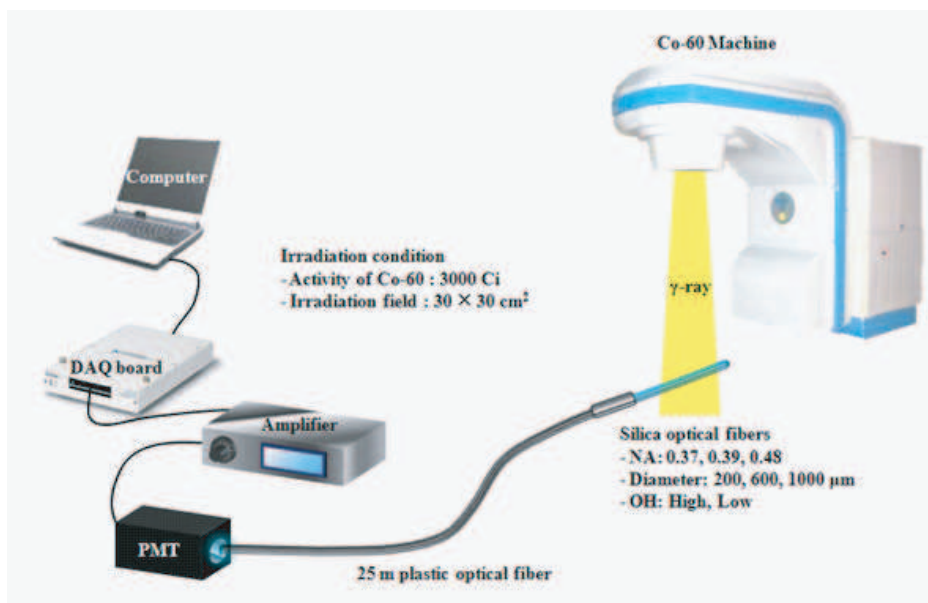| Optical fiber	NA	OH contents	Core diameter
BFL37	0.37	Low	1000 μm
APCH1000	0.39	Low	1000 μm
BFL48	0.48	Low	1000 μm
BFH48	0.48	High	200, 600, 1000 μm

Figure 1: Experimental setup.

of this fiber is 1500 μm and the cladding thickness is 30 μm. The refractive indices of the core and the cladding are 1.492 and 1.402, respectively, and the NA is 0.510.

A PMT (H9305-03, Hamamatsu Photonics Inc.) is used as a light-measuring device. The measurable wavelength range of the PMT is from 185 nm to 900 nm, and the peak wavelength is about 450 nm. Typical and maximum dark currents of this PMT are about 2.0 nA and 10.0 nA, respectively when the control voltage is +1.0 V.

Figure 1 shows the experimental setup for measuring Cerenkov radiation using the silica optical fibers irradiated by γ-rays from a Co-60 machine. A Co-60 isotope with a half-life of 5.271 years is used for γ-ray irradiation and the energies of the γ-rays are 1.173 and 1.332 MeV. The activity of Co-60 isotope used for this study is about 3000 Ci. The γ-ray field size is 30×30 cm^2 and the source to surface distance (SSD), which means the distance between the Co-60 isotope and the surface of the target, is 80 cm. In this study, when γ-rays are irradiated on silica optical fibers, the Cerenkov radiation generated from the silica optical fiber is transmitted to the PMT by a 25 m length of plastic optical fiber. The amplified electric signals of the PMT are measured using a DAQ board.

3. EXPERIMENTAL RESULTS

Figure 2 shows the measured intensities of Cerenkov radiation according to NAs (0.37, 0.39, 0.48) of silica optical fibers. Generally, the NA denotes the light-gathering power and more light can be guided by an optical fiber with a higher NA. As shown in Fig. 2, the silica optical fiber with the NA of 0.48 is most efficient for gathering the Cerenkov radiation generated in the silica optical fiber. Throughout this study, therefore, we used the silica optical fiber whose NA is 0.48.

Generally, attenuations of the optical fibers are different according to the OH content in the core material. It is known that silica optical fibers with low OH content have very low attenuation throughout the near infrared wavelength range (700 $\sim$ 1800 nm). In the case of high OH content optical fibers, there are some absorption peaks at 726 nm, 880 nm, 950 nm, 1136 nm and longer. In the visible light range, the low OH optical fibers are more efficient than high OH optical fibers due to their lower attenuations in the visible range. In this experiment, we measured intensities of
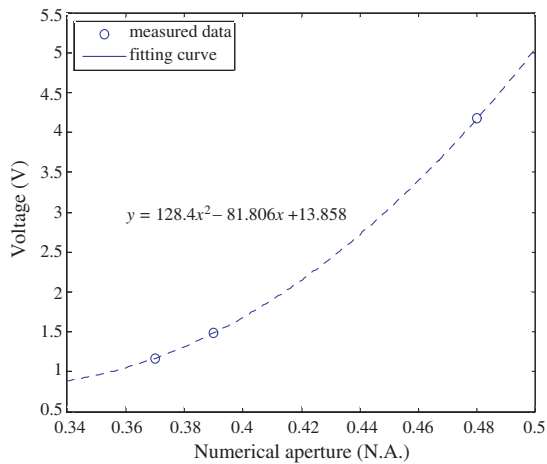
Figure 2: Measured intensities of Cerenkov radiation according to NAs (0.37, 0.39, 0.48) of silica optical fibers.
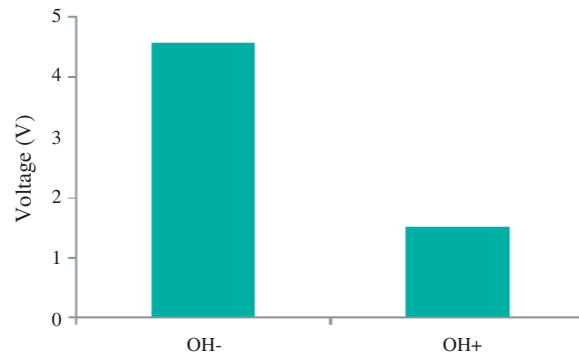

Figure 3: Measured intensities of Cerenkov radiation generated in silica optical fibers according to OH contents.
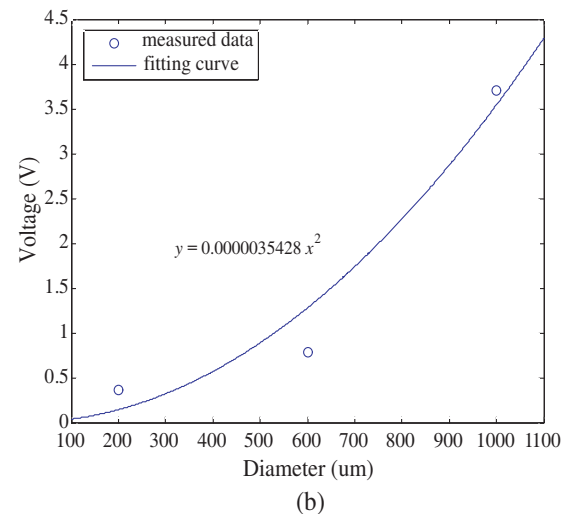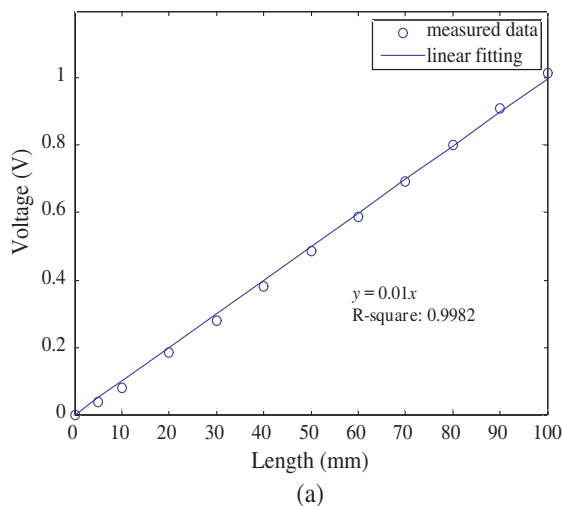

Figure 4: Measured intensities of Cerenkov radiation according to lengths and diameters of silica optical fibers (a) irradiated length, (b) diameter.

Cerenkov radiation generated in silica optical fibers according to OH contents. Although general wavelength range of the Cerenkov radiation is very broad, most of their peak wavelengths generated in the optical fiber are in the visible light region. Therefore, we can find that intensity of the Cerenkov radiation from the low OH content optical fiber is nearly 4 times higher than that of the high OH fiber as shown in Fig. 3.

The measured intensities of Cerenkov radiation according to diameters and lengths of silica optical fibers could be found in Fig. 4. The Cerenkov radiation is produced directly by the interaction between a charged particle and a medium. Therefore, the intensity of Cerenkov radiation depends on the geometry of irradiated medium. The intensity of Cerenkov radiation increased linearly as increasing the irradiated length of optical fiber as shown in Fig. 4(a). For the diameters of optical fiber, the intensity of Cerenkov radiation increased proportional to the square of diameter because irradiated cross section of the optical fiber is proportional to the square of its radius.

4. CONCLUSIONS

In hazardous nuclear reactor environments, the radiation sensors using optical fibers have a number of advantages such as high spatial resolution, availability in narrow spaces, and real-time measurement. The fiber-optic Cerenkov radiation sensor to measure burnup of fuel assembly in the spent fuel storage pool is composed with optical fibers and a light measuring device without any scintillating material. Therefore, this sensor has some strengths such as simple manufacturing process,

low cost and non-quenching effect.

In this study, we characterized the Cerenkov radiations generated in optical fibers irradiated by a Co-60 isotope to develop the fiber-optic Cerenkov radiation sensor. We measured the intensities of Cerenkov radiations as functions of NAs, OH contents, irradiated lengths and diameters of the optical fibers. As the results, the silica optical fiber with the NA of 0.48 and the low OH content was most efficient for gathering the Cerenkov radiation generated in the silica optical fiber. And the measured intensities of Cerenkov radiation for the geometry of optical fiber were proportional to the irradiated length and the square of diameter.

Further studies will be carried out to fabricate a fiber-optic Cerenkov radiation sensor with various kinds of optical fibers and light-measuring devices. It is expected that the fiber-optic Cerenkov radiation sensor can be an effective, accurate and convenient tool for measuring the burnup of fuel assembly in the spent fuel storage pool.

ACKNOWLEDGMENT

REFERENCES

1. Lee, B., W. Y. Choi, and J. K. Walker, "Polymer-polymer miscibility study for plastic gradient index optical fiber," *Polymer Eng. and Sci.*, Vol. 40, 1996–1999, 2000.
2. Bartesaghi, G., V. Conti, M. Prest, V. Mascagna, S. Scazzi, P. Cappelletti, M. Frigerio, S. Gelosa, A. Monti, A. Ostinelli, A. Mozzanica, R. Bevilacqua, G. Giannini, P. Totaro, and E. Vallazza, "A scintillating fiber dosimeter for radiotherapy," *Nucl. Instr. and Meth. Phys. Res. A*, Vol. 572, 228–231, 2007.
3. Frelin, A.-M., J.-M. Fontbonne, G. Ban, J. Colin, and M. Labalme, "Spectral discrimination of Cerenkov radiation in scintillating dosimeters," *Med. Phys.*, Vol. 32, 3000–3006, 2005.
4. Becks, K. H., J. Drees, K. Goldmann, I. M. Gregor, and M. Heintz, "A multichannel dosimeter based on scintillating fibers for medical applications," *Nucl. Instr. and Meth. Phys. Res. A*, Vol. 454, 147–151, 2000.
5. De Boer, S. F., A. S. Beddar, and J. A. Rawlinson, "Optical filtering and spectral measurements of radiation induced light in plastic scintillation dosimetry," *Phys. Med. Biol.*, Vol. 38, 945–958, 1993.
6. Kuribara, M., "Spent fuel burnup estimation by Cerenkov glow intensity measurement," *IEEE Trans. Nucl. Sci.*, Vol. 41, 1736–1739, 1994.

Active Charging Stations for Electric Vehicles Charging

P. Simonik, **A. Havel**, **M. Hromjak**, and **P. Chlebis**

VSB — TU Ostrava, Katedra Elektroniky, 17, 15 Listopadu, Ostrava 70800, Czech Republic

Abstract— This paper deals with the issues of active charging stations for electric vehicles. In the introduction are proposed general presumptions for the electric vehicle's diffusion in the environment of the Czech Republic. Paper also deals with conceptual issues of the charging stations' structure and analyses some requirements on its function. In conclusion is proposed the solution of conceptual design of the resonant ZVS converter with resonant DC circuit. In the paper are shown simulation results and results acquired on physical laboratory model of the converter.

1. INTRODUCTION

Currently is the electromobility one of the most discussed issues in the automobile technology field. The intent of electric vehicles' diffusion assumes that electromobiles will relive extreme ecological situation in cities and especially in their centres and also enables occasional connection between distant locations as well.

Possibilities and the interest in electric vehicles' diffusion in business environment, both as an adequate transport vehicle and the part of so-called green marketing strategy, had been investigated by the marketing research held in 2010 [2]. The results of this research confirmed, among other things, that most then half of companies (56%) use the vehicles above all in interurban traffic, which occasionally require to overcome longer distances (up to approximately 300 km). Most large firms (only 3.6% of respondents) use vehicles in the cities, which meets the expected concentration of charging stations in cities. Another important finding is that 81% of respondents is not able to define where and how to recharge these vehicles at their current purchase. These and other problems resulting from lack of awareness and negative attitude of potential users toward the infrastructure, prevent further spread of the technology. If accessible network of charging stations providing an operation in vehicles' operational areas and also occasional travelling to medium distances (about 300 km) was not be built, entrepreners do not have the interest in electric cars. This assumes deployment of charging stations along major roads within a maximum 50 km.

The Czech Republic is in this branch still distinctive, because electromobilism is rather activity of amateur enthusiasts and the corresponding number of operating electric vehicles is still low. The low number of electric vehicles corresponds to the low density of charging network, which is run mostly by amateurs.

Therefore, the expansion of electric cars goes along the claim to build an adequate network of charging stations and the group of users will create a significant market segment for suppliers of electricity.

2. CONCEPT OF ACTIVE CHARGING STATION

The concept of active charging station has to ensure, that the energy needed for electric vehicles charging will be available regardless network options, e.g., at the time of vehicle shut down period and its charging also at the time of maximum power consumption. Therefore, the station has to be equipped by own accumulation source, which is able to cover the reductions of network supply by accumulated energy and also use energy from various types of renewable sources attainable in given location.

The characteristic feature is usage of more types of energy sources, which significantly decreases primarily the peak load of distribution network. Quite typical is the usage of unconventional and renewable sources, whose timing of energy supply to network together with the accumulation of energy in the charging station creates a stabilizing element.

The involvement of one or more charging stations, in addition to their stabilizing function, has to perform many other functions. These include:

- minimizing reactive energy consumption, EMC, and high frequency disturbance
- maximizing the energy conversion efficiency for all types of converters
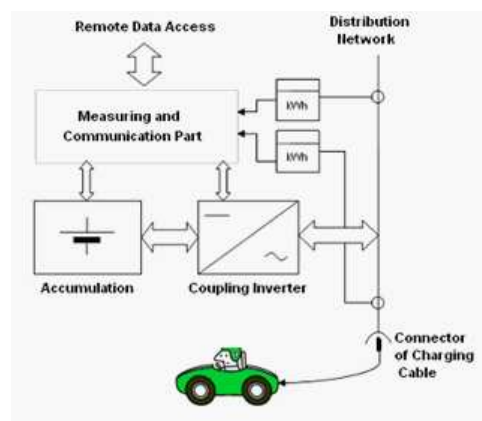
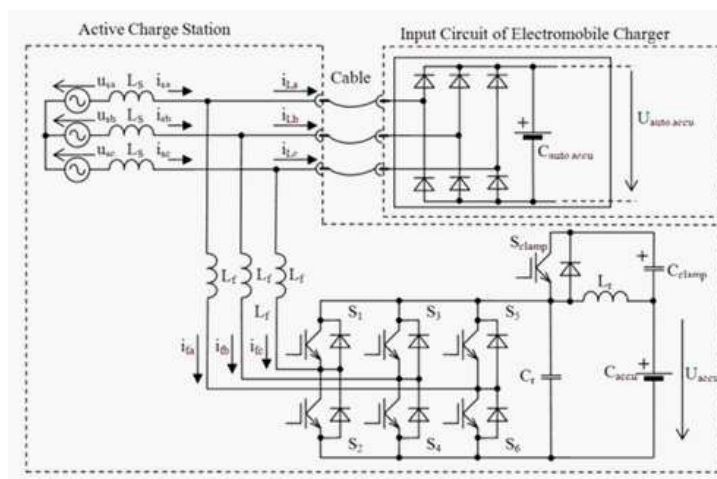Figure 1: Structure of the charging station for the electric vehicles charging.

Figure 2: Scheme of the higher efficiency active charging station connection.

- optional remote control of charging modes from the dispatching centre, e.g., discontinue charging the vehicle from the network and switch for charging from the accumulator of the charging station
- ensuring communication for billing the electricity in terms of electric car user, a charging station owners, and suppliers (distributors) of electrical energy

If all mentioned conditions were met, the active charging stations represent high sophisticated technical device.

2.1. Structure of Active Charging Stations

It is necessary to distinguish whether the electric vehicle will be charged by conventional way, i.e., the long-term charging of the accumulator by low current, or by fast charging. For the conventional charging vehicle usually uses own charging device connected directly to the AC distribution network. Input power usually does not exceed 10–15 kW. But this simple charging method generally brings problems with increased outputs for 3th and 5th harmonics, which is given by the conception of a switching power supply in the charging device. By the mass operation of electric vehicles and their charging from the current distribution network without earlier remedies, could this kind of charging lead to significant problems with electricity quality, especially in regions with a higher number of operated electric vehicles. Concerning common power current protection, this conception does not enable fast charging.

In this paper, we will further discuss the concept of active charging stations with AC output. The block diagram of this concept is shown in the Figure 1 below.

Proposed conception of charging station uses parallel connection of accumulation part to distribution network output. Power blocks create reversible inverter, which allows bidirectional flow of energy between the network and the accumulator. This arrangement allows separate charge of the vehicle only from the distribution network, common charging partly from the accumulator of the charging station and partly from the network, and charging of the accumulator from the network when an electric vehicle is not connected to an electric outlet. The special function of the module could be filtration of line harmonics and reactive power from the car charging device to the network.

The system is controlled by measuring and control unit, which ensures control and setting of above mentioned operation modes, collects and processes data of output energy on unit's output and input for billing the energy, and ensures communication with the superior dispatching and billing system. The advantage of that connection is significant variability in operating conditions, thus ensuring high operational reliability.

2.2. Circuit Conception of Active Charging Station

As is apparent from the foregoing analysis, the power part of the active charging station must meet the following requirements:

- high dynamic control of operating conditions
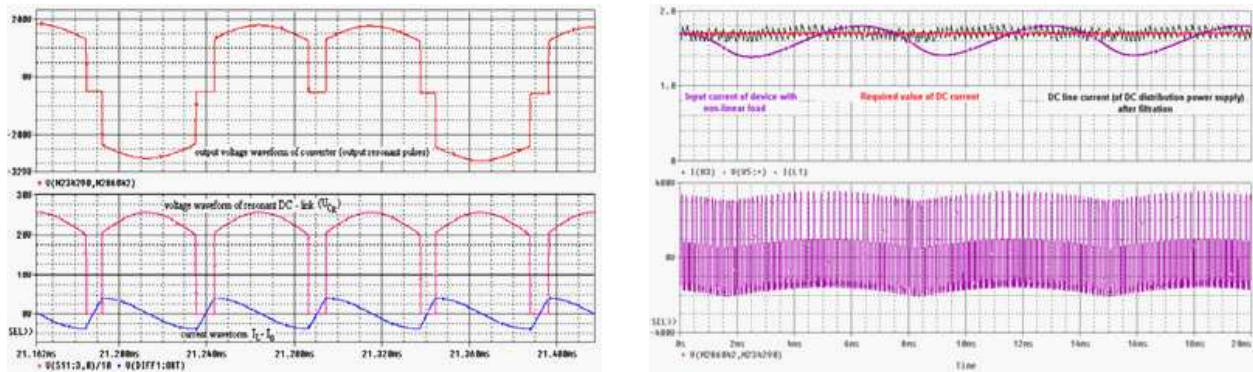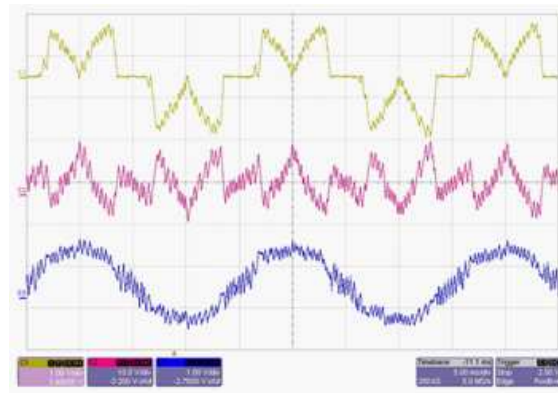- four-quadrant operation due to network

Figure 3: Waveforms in resonant DC circuit of active charging station.

Figure 4: Detail of active station current waveforms. Above — current in electric vehicle charging device ($C = 2200\,\mu\text{F}$). Middle — compensation current of active part. Below — current from AC line.

- wide range of charging and compensation current
- active filtration of line harmonics and reactive power
- high efficiency conversion of electric energy

To achieve these requirements, particularly with regard to the increased efficiency of energy conversion processes in the inverter of the charging station, the following chart was created. In the Figure 2 is the main charging connection presented by the network sources u_{sa}, u_{sb}, u_{sc} and network reactances L_s. By the standard configuration of the electric vehicle is charger of the vehicle connected to the power network (distribution network) through a cable with connector. As the majority of electric vehicles use accumulators with low nominal voltage up to $400\,\text{V}$, the conception with input diode rectifier, filtering capacitor and step-down converter has to be used. The input circuit of this conception is shown also in Figure 2.

Problematic feature of this otherwise very simple concept is the output/consumption of the 5th and 7th line harmonics from the network, which, except increased current consumption in peak time, present also additional deformation power load. Proposed solution enables not only to cover the consumption by drawing power from the auxiliary/additional accumulator of the active charging station, when the network has lack of energy, but also minimize the reactive effects of vehicle's charging device on the charging/power network. The advantage of this solution is also that in the lack of energy in the auxiliary/additional accumulator, the station can only operate as a parallel active filter with the structure as shown below. In the case of inaction of the active parallel part, recharging of the electric vehicle continues, but with all the above-mentioned deficiencies.

To increase efficiency of the active part of charging station, is in the Figure 2 used conception with resonant DC circuit consisting of resonant capacitor C_r and resonant coil L_r. Resonant DC circuit is switched between output of the accumulator and input of the bridge inverter. For a limitation, resp. definition of maximum voltage of resonant pulses is used Clamp circuit consisted of switch S_{clamp} and capacitor C_{clamp}. The energy source C_{accu} on the picture simply represents the involvement of additional accumulator of the active station.

As shown in Figure 3, by the resonant circuit activity occur controlled oscillations (see lower waveform), which ensures switching of switching combinations in inverter by zero voltage value. This eliminates much of switching power losses of the inverter. The form of modulated pulses on the inverter output is in this case created by the sequence of resonant pulses with required polarity (see upper waveform) and by switching the switch combination by the zero voltage (Zero Voltage Switching — ZVS).

In order to active charging station could principally contribute to the network, the actual voltage value of resonant pulse has to be in every moment greater than the actual AC voltage value in compensated line phase of the charging network. The whole system of converter has to be able to work in the inverter mode to supply energy to the network, and in the pulse rectifier mode to recharge the station accumulator. Results of the numeric model by the energy supply in the conditions of DC resonant circuit are shown in Figure 3.

2.3. Laboratory Measurement Results

According to positive results of computer simulations, with some courses mentioned in previous chapter, was realized laboratory model of low power converter with the control unit based on the signal processor TMS320F2812. The control unit ensures correct function and stability of converter processing and further correct function of parallel filter as a whole. The basic task of the control unit is to:

- realize correct control to keep resonant oscillation
- realize correct control of the Clamp circuit of resonant voltage impulses
- realize correct sampling of inverter IGBT switches in resonant circuits by zero voltage
- compute referent current curve using Fast Fourier Transformation (FFT)
- control output currents by appropriate modulating method, e.g., hysteresis modulation
- on the basis of voltage sensing on the DC side of the converter regulate this voltage in case of emergency conditions
- ensure quick switching off the active part of the charging station

Examples of results obtained on laboratory model are shown in Figure 4 below.

3. CONCLUSION

In the paper was given the possibility to use soft switching converters in active charging stations for electric vehicles, which could significantly increase efficiency of electric vehicles operation considering the charging network. In real conditions the benefits of soft switching could occur by the decrease of high frequency disturbance, because by the application of this method are reduced dV/dt by the switching of active parts. For further application of the principally proved method is necessary to optimize the design of parts in resonant DC circuit and minimize losses in resonant coil.

ACKNOWLEDGMENT

REFERENCES

1. Brandstetter, P., P. Chlebis, and P. Simonik, "Active power filter with soft switching," *International Review of Electrical Engineering — IREE*, Vol. 5, No. 6, 2516–2526, 2010, ISSN 1827-6660.
2. Chlebisova, E., J. Kyzekova, and H. Svobodova, "Marketing study of the electric vehicles' diffusion," *11th International Scientific Conference on Electric Power Engineering 2010*, Brno, Czech Republic, 807–811, 2010, ISBN 978-80-214-4094-4.
3. Brandstetter, P., P. Chlebis, and P. Palacky, "Direct torque control of induction motor with direct calculation of voltage vector," *Advances in Electrical and Computer Engineering*, Vol. 10, No. 4, 17–22, 2010, ISSN 1582-7445.
4. Šimoník, P. and P. Chlebiš, "Suppression of line current harmonics by active power filter having converter with resonant DC — Link," *POSTER 2004*, Praha, Čská Republika, 2004.
5. Brandstetter, P., P. Chlebis, P. Simonik, and P. Palacky, "Unconventional soft switched parallel active power filter," *10th International Scientific Conference Electric Power Engineering*, 347–351, Kouty nad Desnou, Czech Republic, 2009, ISBN 978-80-248-1947-1.

Estimation of Induction Machine Electrical Parameters Based on the Genetic Algorithms

P. Simonik, **P. Hudecek**, **P. Palacky**, **and Slivka David**

Department of Electronics, Faculty of Electrical Engineering and Computer Science
VSB Technical University of Ostrava, 17.listopadu 15, Ostrava 708 00, Poruba, Czech Republic

Abstract— This article shows one of many ways how identify parameters of the IM in real time. For identification is used theory of genetic algorithms. The Genetic Algorithms is a search technique used in many fields, like in computer science, to find accurate solutions to large optimization and search problems. The advantage of GAs is flexible and intuitive approach to optimization and demonstrates a higher probability of not converging to local optima solutions compared to traditional gradient based methods. More recently, methods which have appeared in the scientific literature about general GAs become popular and can be successfully ported to power electronics and drives. This article deals with the possibilities to improve dynamics and other properties of the drive with using online parameters estimation integrated in main control algorithm. In this paper at the first there is presented an analysis of the current state of the investigated problem and there is also explained why the problem is discussed. Following chapters show induction machine dynamic model principles and ways of implementation the IM parameters identification. Used genetic algorithm theory and experimental results are demonstrated in the end of this article. The conclusion describes the potential use of this method and discusses further development in the real time estimation of induction machines parameters.

1. INTRODUCTION

The Induction Motors (IM) thanks to its well known advantages of simple construction, reliability, ruggedness and low cost, has found very wide industrial applications. The IMs are often supplied by frequency converters for better performance. Frequency converters commonly use complex control strategies like FOC (Field Oriented Control) or DTC (Direct Torque Control). Both of these control techniques are highly dependent on correct magnetic linkage estimation. It's particularly well known that FOC is very sensitive to variation of rotor time constant T_R while DTC is likewise sensitive to variation of stator resistance R_S during the estimation of IM flux linkage. However in both of these control strategies any inaccuracy in evaluation of one parameter caused a wrong value of magnetic flux (both in amplitude and in angle) and of electromagnetic torque and it is not therefore possible to achieve a correct field orientation [1].

The Genetic Algorithms (GA) is a search technique used in many fields, like computer science, to find accurate solutions to large optimization and search problems. The basic concept of GAs is to emulate evolution processes in natural system following the principles which was first described by Charles Darwin. The advantage of GAs is that it is a very flexible and intuitive approach to optimization and presents a higher probability of not converging to local optima solutions compared to traditional gradient based methods. More recently, research works have appeared in the scientific literature about the use of GAs for control design in power Electronics, drives and general structure identification. This paper describes an automatic real-time estimation procedure of IM parameters based on the genetic algorithms.

2. IMPLEMENTATION PRINCIPLE OF IM PARAMETERS IDENTIFICATION

For the purpose of the present investigation the IM is assumed to be described in the stator reference frame by [2].

$$\frac{d\omega_m}{dt} = \frac{3}{2} \cdot \frac{p \cdot L_h}{J_C \cdot L_R} \cdot (i_{S\beta} \cdot \psi_{R\alpha} - i_{S\alpha} \cdot \psi_{R\beta}) - \frac{M}{J_C} \tag{1}$$

$$\psi_{R\alpha} = \int \left(\frac{M}{T_R} \cdot i_{S\alpha} - \frac{\psi_{R\alpha}}{T_R} - p \cdot \omega_m \cdot \psi_{Rb} \right) dt \tag{2}$$

$$\psi_{R\beta} = \int \left(\frac{M}{T_R} \cdot i_{S\beta} - \frac{\psi_{R\beta}}{T_R} + p \cdot \omega \cdot \psi_{R\alpha} \right) dt \tag{3}$$

$$\frac{di_{S\alpha}}{dt} = \frac{1}{\sigma \cdot L_S} \cdot u_{s\alpha} - \gamma \cdot i_{S\alpha} + \frac{\beta}{T_R} \cdot \psi_{R\alpha} + p \cdot \beta \cdot \omega_m \cdot \psi_{R\beta} \tag{4}$$

$$\frac{di_{S\beta}}{dt} = \frac{1}{\sigma \cdot L_S} \cdot u_{s\beta} - \gamma \cdot i_{S\beta} + \frac{\beta}{T_R} \cdot \psi_{R\beta} - p \cdot \beta \cdot \omega_m \cdot \psi_{R\alpha} \tag{5}$$

$$\beta = \frac{M}{\sigma \cdot L_S \cdot L_R} \tag{6}$$

$$\gamma = \frac{R_S}{\sigma \cdot L_S} + \frac{M^2 \cdot R_R}{\sigma \cdot L_S \cdot L_R^2} \tag{7}$$

$\psi_{R\alpha}$, $u_{S\alpha}$, $i_{S\alpha}$ — are alpha components of rotor flux, stator voltage and current;

$\psi_{R\beta}$, $u_{S\beta}$, $i_{S\beta}$ — are beta components of rotor flux, stator voltage and current;

L_S, L_R, L_h — is stator, rotor and main inductance;

ω_m, σ, p — is mechanical angular speed, leakage factor and number of pole pairs;

J_C, T_R, M — total moment of inertia, the mechanical time constant, moment of IM;

R_S, R_R — is stator and rotor resistance (rotor resistance is oriented to stator).

The method of IM parameter estimation in real time presented here is a method when comes from modification of previous Equations (1) to (7) we get the new relations:

$$K_1 i_{S\alpha} + K_2 u_{S\alpha} + K_3 p\omega_m i_{S\beta} + K_4 \left(\frac{du_{S\alpha}}{dt} + p\omega_m u_{S\beta} \right) + K_5 \frac{di_{S\alpha}}{dt} = \frac{d^2 i_{S\alpha}}{dt^2} + p\omega_m \frac{di_{S\beta}}{dt} \tag{8}$$

$$K_1 = -\frac{R_S}{\sigma L_S T_R}, \quad K_2 = \frac{1}{\sigma L_S T_R}, \quad K_3 = -\frac{R_S}{\sigma L_S}, \quad K_4 = \frac{1}{\sigma L_S}, \quad K_5 = -\frac{R_S L_R + R_R L_S}{\sigma \cdot L_S \cdot L_R} \tag{9}$$

Wanted IM parameters are then:

$$R_S = -\frac{K_3}{K_4}, \quad R_R = \frac{K_3 - K_5}{K_4}, \quad L_S = \frac{K_3 - K_5}{K_2}, \quad L_h = L_S \cdot \sqrt{1 - \frac{1}{K_4} \cdot L_S} \tag{10}$$

Required values of $u_{S\alpha}$, $u_{S\beta}$, $i_{S\alpha}, i_{S\beta}$ we can obtain in SW part from a vector control structure, which is shown on Fig. 1.

On Fig. 1, the Indirect frequency converter supplies an induction motor (M). Phase currents are measured by current sensors. Position of the rotor is measured at the Incremental encoder (IE). True value of mechanical speed ω_m and the rotor angle ε are than evaluated in the Position and speed estimator block. The values in the three-phase stator coordinate system $[a, b, c]$ are transformed into two-axis stator coordinate system $[\alpha, \beta]$ in the T3/2 block. In the block α, β to x, y, vector components are transformed to the oriented two-axis rotating coordinate system $[x, y]$. For vector rotation of components of stator current $i_{s\alpha}, i_{s\beta}$ to the oriented coordinate system $[x, y]$ is used the variables γ, which is calculated in the Magnetizing current estimator block. The components i_{sx}, i_{sy} serve as feedback variables for the current PI controllers R_{isx}, R_{isy}. Control of magnetizing current (or magnetic flux) is realized by a PI controller R_{im}. The block processes a deviation between the desired magnetizing current i_{m*} and value i_m calculated in the magnetizing current estimator block. Angular speed control provides PI regulator R_ω, which handles difference between a speed command ω_{m*} and speed ω_m, which is evaluated as derivation of rotor angle epsilon. The control voltages u_{sa}, u_{sb}, u_{sc} for PWM generator block are obtained from the components u_{sx*}, u_{sy*} by means of the x, y to α, β block and subsequent transformation block T2/3. The PWM modulation generates pulses for IGBT power transistors in the indirect frequency converter.

3. FUNCTIONAL DESCRIPTION OF GA

To describe how the GA actually works is used the relation (8). Consider the following simplistic rule. We know that IM parameters vary only in a certain range of values such as:

$$1\,\Omega \le R_S \le 10\,\Omega, \quad 1\,\Omega \le R_R \le 10\,\Omega, \quad 0.1\,H \le L_S \le 1\,H, \quad 0.1\,H \le L_h \le 1\,H \ldots$$

These ranges can also expand or use other parameters, if needed. Substituting the upper and lower limits from IM parameters range into relations (9) we find K boundaries. Between these boundaries the K unknown could fluctuate. The next procedure can be summarized in four points.
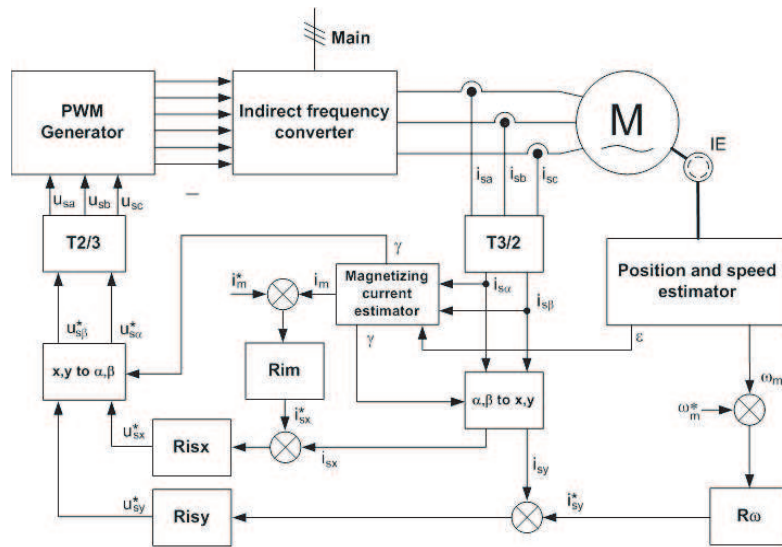
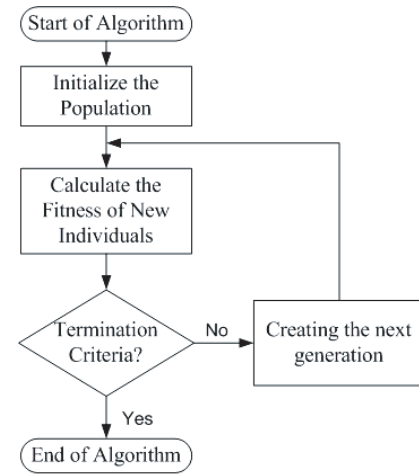Figure 1: Block diagram of the vector control used.

Figure 2: Flowchart of the genetic algorithm used.

Initialize the population — Creates a zero population which is composed from randomly generated individuals. Specifically, an individual is composed of five unknowns K_1 to K_5 randomly generated within the range specified above.

Calculate the Fitness of New Individuals — Is calculated the fitness of new individuals. Than is selected a few individuals with high fitness from a population. In this case, the best marked individual is the individual whose unknowns K have the difference between right and left side of the Equation (8) as much as possible close to zero.

Termination Criteria — If the stop condition isn't fulfilled, continue from point 4 again. Stopping condition may be a number of passes through the loop. This condition affects the speed and accuracy of determination unknown K. Individual with highest fitness is the main algorithm output and represents the best founded solution.

Creating the Next Generation — To create the next generation are used two basic genetic operators. The mutation and the crossing. In some cases it may be useful to keep copies of the parents for the next generation unchanged. Specifically new population we generates as follows:

- *Crossing* — swap parts (unknown K) of a few individuals among them. It is necessary to ensure that unknown through the swapping must have the same index (not for example K_1 with K_5).
- *Mutation* — is a random change of parts of a few individuals or individual. Again, it is necessary to ensure that mutations for example in the K_1 individual were in appropriate range.
- *Reproduction* — the remaining individuals are copied unchanged.

4. EXPERIMENTAL RESULTS

In all simulations was used model of real three-phase IM type CANTONI Sg100L-4A which has the value of stator resistance $R_S = 2.78\,\Omega$ and value of rotor resistance $R_R = 2.84\,\Omega$. The IM was supplied by a model of indirect frequency converter in connection consisting of a DC source voltage at the input and the voltage inverter with IGBT transistors on the output. DC-link voltage was set to $U_d = 300\,\text{V}$. Control of output voltage was made by comparing PWM. The frequency and amplitude of the saw tooth signal was $f_p = 5\,\text{kHz}$, $U_{p\,\text{max}} = \pm 1\,\text{V}$. The incremental encoder model is based on the real encoder type ERN 420/TTL with 2048 pulses/rev. The total moment of inertia was set at $J_C = 0.043\,\text{kgm}^2$.

From Fig. 3, is evident that the value of R_S and R_R has the true values. Identification is not accurate in area of excitation of IM (time 0 to 0.2 s) and during the start of IM (time 0.2 to 0.8 s). This behavior is caused by neglecting of $d\omega/dt$ member during the modification of Equations (1) to (7). This phenomenon can be reduced. The solution can be found in the literature [3].
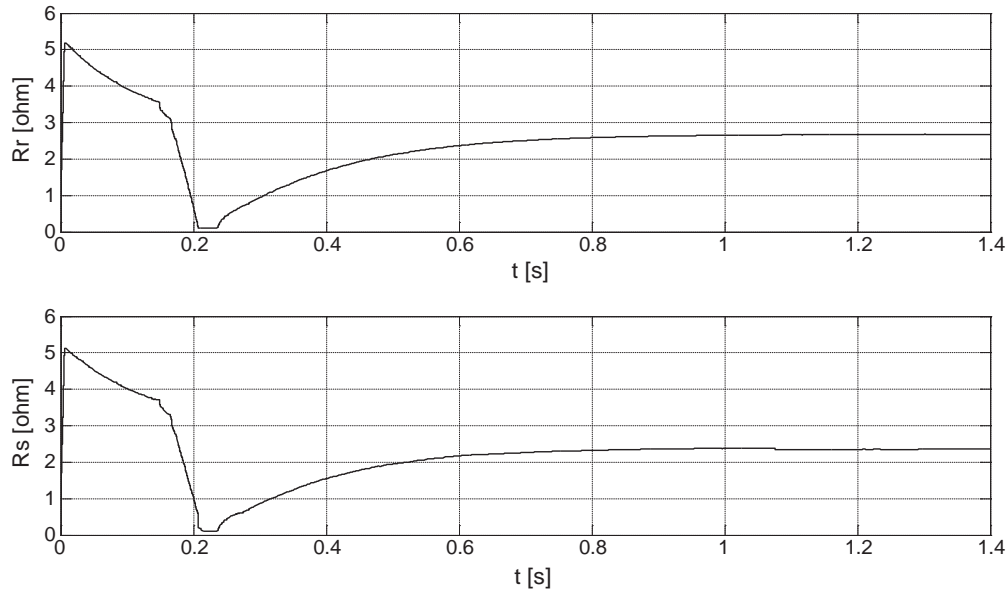
Figure 3: Transients of RS and RR estimation using genetic algorithms.

5. CONCLUSION

Method described here can be used in modern high performance electric drives. Reasons why it is necessary to estimate IM parameters in real time are described in the introduction. Next to IM parameters identification by GA, it is possible to detect the parameters with other methods such is least squares methods (Total Least Squares, Ordinary Least Squares and Recursive Least Squares) or by using theory of neural networks (see literature [2, 3]).

ACKNOWLEDGMENT

REFERENCES

1. Leonhard, W., *Control of Electrical Drives*, Springer, Verlag, Berlin, Germany, 2001, ISBN 3-540-41820-2.
2. Cincirone, M., M. Pucci, G. Cincirone, and G. A. Capolino, "A new experimental application of least-squares techniques for the estimation of the parameter of the induction motor," *IEEE Trans. on Ind. Applications*, Vol. 39, No. 5, 1247–1255, Sep. 2003.
3. Chiasson, J., *Modeling and High-performance Control of Electric Machines*, IEEE Press, USA, 2005, ISBN 0-471-68449-X.
4. Ferková, Ž. and L. Zboray, *Contribution to Parameter Identification of an Induction Motor by Genetic Algorithms*, Acta Electrotechnica et Informatica, Vol. 5, No. 2, 1–5, Košice, 2005, ISSN 1335-8243.
5. Brandstetter, P., *Střídavé Regulační Pohony — Moderní Způoby Řízení*, VŠB-TUO, Ostrava, Czech Republic, 1999, ISBN 80-7078-668-X.

Equivalent Parallel Capacitance Cancellation Utilizing Coupling between Integrated EMI Filter Components

Hui-Fen Huang, **Mao Ye**, **and Liang-Yong Deng**
School of Electronic and Information Engineering
South China University of Technology, Guangzhou 510641, China

Abstract— This paper introduces a technique for improving the high-frequency (HF) performance of integrated common mode (CM) filter by effectively cancelling parasitic winding capacitance. Moreover, the added conductor layer used for cancellation is also served for CM capacitor, which results in reduced fabrication time and cost. To achieve cancellation, the winding structure needs to be newly designed so that the coupling between inductor winding and capacitor can be utilized. A bi-direction winding structure is finally developed with further increased attenuation as compared to the uni-direction case in the frequency range beyond several MHz. Simulation results confirm the effectiveness of proposed cancellation technology.

1. INTRODUCTION

The EMI filter is a necessary interface between the power line and power supplies to attenuate both common mode (CM) and differential mode (DM) switching noises. In order to reduce size and fabrication time, the integrated EMI filter structure has been proposed and implemented based on advanced integration and packaging technologies [1]. However, when planar core replaces toroidal core to achieve low-profile structure, the equivalent parallel capacitance (EPC) of CM inductor can become even larger. Several approaches have been proposed to reduce or cancel the EPC of filter inductors [2–7]. Typically, for integrated CM filter, in [2], a staggered and interleaving winding structure effectively reduce the parasitic winding capacitance, but at the price of greatly increased winding complexity and increased thickness. In [7], only an embedded conductive layer is inserted into the CM winding and grounded to cancel the EPC of CM inductor, which is a very simple solution.

As fundamental element of integrated EMI filter, the LC hybrid winding consists of a dielectric substrate with conductor windings directly deposited on both sides, thus resulting in a structure having both sufficient inductance and capacitance. Define the conductor layer which is connected to ground as CM capacitor layer. In this paper, the added conductor layer used for cancellation in [7] is moved outside and served as CM capacitor layer at the same time. To maintain the cancellation effect, negative coupling between inductor winding and CM capacitor is utilized initially. A simplified equivalent circuit is derived and main influence factors in implementation are investigated. Then the improved method using bi-direction winding structure is developed with somewhat further increased HF attenuation as compared to the uni-direction case. Although no extra component is added, simulation results show performance of the newly proposed filter could be as good as the former improved integrated CM filter [7].

2. EPC CANCELLATION USING NEGATIVE COUPLING BETWEEN FILTER COMPONENTS

Considering an inductor L with the equivalent parallel winding capacitance EPC and neglecting the losses, if another resonance is introduced and the equation $L' \cdot C' = L \cdot \text{EPC}$ is satisfied, the impedance can be that of an ideal inductor.

2.1. The Idea of Using No Additional Components to Achieve Cancellation

In the proposed technique, CM capacitor layer is utilized for EPC cancellation with appropriate designed geometry. To realize this idea, an initial strategy is to make the direction of inductor winding and capacitor layer winding opposite, thus negative mutual inductance between capacitor and CM inductor can be used to generate the required inductance. Together with CM capacitance, the general cancellation condition mentioned above will be satisfied. In this case, EPC cancellation can be achieved without introducing any additional components.

In practical, since the CM capacitance is mainly determined by the conductor area of ground plane after dielectric layer is chosen. Meanwhile, inductance of CM capacitor layer is mainly determined by turns number of conductor winding. Those provide the possibility to separately
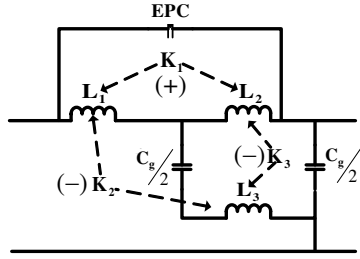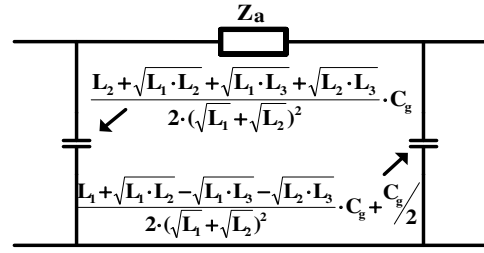
Figure 1: Equivalent circuits of proposed method.

Figure 2: π-equivalent circuit.

adjust CM capacitance and inductance of capacitor layer, the two critical parameters for proposed cancel method.

The integrated L-C structure is a distributed parameter structure. Neglecting loss, the simplified equivalent circuit of proposed cancellation method is shown in Fig. 1. Where L_2 represents inductance of winding part which is parallel with the capacitor winding, L_1 has a relationship with L_2 as $(\sqrt{L_1} + \sqrt{L_2})^2 = L$ (L is the designed CM inductance), L_3 is the equivalent winding inductance of capacitor layer, and C_g represents the capacitance used for cancellation. Coupling polarities are also shown in Fig. 1 and all couplings are assumed to be ideal. With decoupling analysis and Y-Δ transformation, the π-equivalent circuit can be seen in Fig. 2. Forward shunt-capacitance provided by the cancellation winding can further improve HF attenuation.

The series impedance of π-equivalent circuit is given by:

$$Z_a = \frac{(\sqrt{L_1} + \sqrt{L_2})^2}{1 - \omega^2 \cdot \left[(\sqrt{L_1} + \sqrt{L_2})^2 \cdot \text{EPC} - (\sqrt{L_1 \cdot L_2} + \sqrt{L_1 \cdot L_3} - \sqrt{L_2 \cdot L_3} - L_3) \cdot C_g/2 \right]} \quad (1)$$

Therefore the cancellation condition can be expressed as follows:

$$C_g = \frac{2 \cdot (\sqrt{L_1} + \sqrt{L_2})^2 \cdot \text{EPC}}{\sqrt{L_1 \cdot L_2} + \sqrt{L_1 \cdot L_3} - \sqrt{L_2 \cdot L_3} - L_3} \quad (2)$$

For safety reasons, the CM filter capacitance is normally limited to few thousand picofarads (pF). Hence, the total capacitance to ground cannot be a free variable. Suitable turns number of CM capacitor layer should be chosen to ensure the capacitance for cancellation, that is CM capacitance, at a safe level.

2.2. Main Influence Factors in Implementation

In the above analysis, perfect conductance and ideal couplings are considered. In the real application, the effectiveness of EPC cancellation will be influenced by these factors. Firstly, proper conductor resistance is an effective way to suppress resonance. In general, a thin CM capacitor conductor layer whose thickness equals 0.1 mm is preferred to be used.

Then, when considering non-ideal coupling, it is known that the effectiveness of capacitance cancellation is very sensitive to the coupling coefficient. Obviously, closer to ideal coupling will be more likely to achieve the desired performance. The magnetostatic solution shows that magnetic field is not contained within the core as some field leaves the core. As expected, the magnetic field stronger closer to the core, where it decreases with the distance from the core. Objects close to the coil will be more affected by the leakage flux. At the same time, when cancellation conductor moves towards magnetic core, the required capacitance will decrease accordingly.

3. APPLIED TO INTEGRATED CM FILTER WITH AN IMPROVED CANCEL METHOD

While the proposed cancellation technique does improve filter performance, the results are not so good as expected at frequencies beyond several MHz. To overcome the limitation, a bi-direction winding structure is then developed with somewhat increased HF attenuation as compared to the uni-direction case. The basic idea is to make the direction of the CM capacitor layer winding a mix one, which means, part of the winding is positive coupling with the CM inductor, and the other part is negative coupling with the CM inductor.

In implementation of the proposed integrated CM filter, two coupled winding parts with a common end are employed to produce the equivalent negative inductance that can be used to cancel

the inductor parasitic capacitance. The ground line is tapped at a point to maximize capacitance cancellation in the system. The innermost several turns of capacitor winding is abandoned, for the reason that it contributes minimum to CM capacitance while has maximum influence on HF performance. In addition, we can also optimize some parameters like the distance between two adjacent turns and wire dimensions. During the optimization, take into consideration that the processing limitation of the minimum distance between traces is 0.5 mm and the minimum trace width is 0.8 mm. Dimensions of CM inductor winding conductor are 1.2 mm × 0.3 mm with 0.5 mm distance. Also, to save the optimization time, only windings located at one side of leakage layer are used in the simulation.

The cross-section view and final layout of CM capacitor layer whose winding has 3-4 turns are illustrated in Fig. 3, where width of positive coupling winding part $W1$ is 0.8 mm, width of negative coupling winding part $W2$ is 1.8 mm, distance between two adjacent turns Dis is kept constant to 0.5 mm, and another tuning variable L is determined to be 3.6 mm. Fig. 4 shows the simulated Vector_Jsurf at 1 MHz using an Ansoft HFSS solver. It can be clearly observed that the designed winding parts with reversed coupling polarities have opposite current directions. Simulated results show that the new cancellation method improves the attenuation by 20 dB in the frequency range beyond several MHz as will be seen in Fig. 6.

The approach here is particularly applicable thanks to the fact that the required capacitance is only proportional to value of EPC and winding turns ratio, which means, the cancellation effect depends primarily on geometry. Even the properties of magnetic materials vary greatly, the cancellation method can still achieve repeatability and insensitivity. Table 1 lists the properties of materials used in simulation.

As must be pointed out that the modification on CM capacitor layer does not change DM components, hence the DM performance can hold in this design.
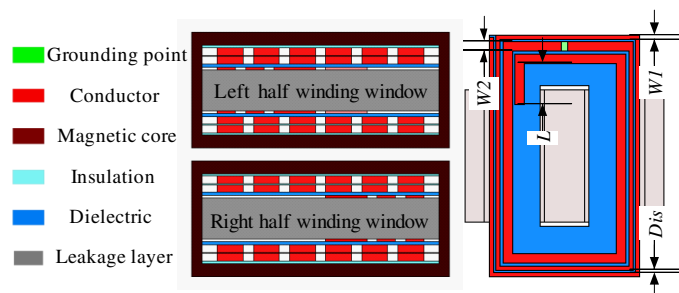

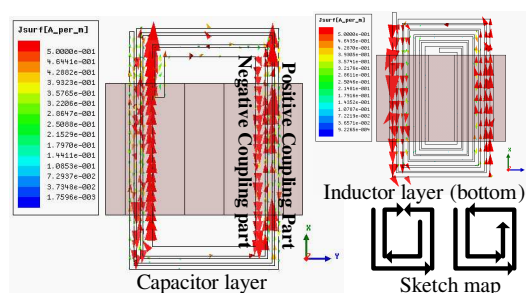Figure 3: The final structure of integrated EMI filter.

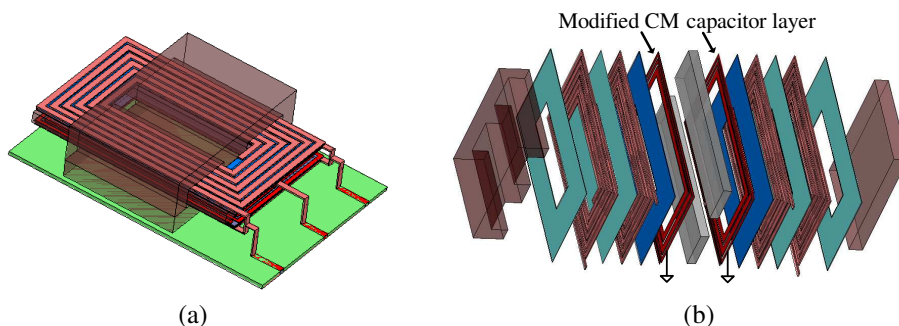Figure 4: The current distribution at 1 MHz.

Figure 5: Simulation model (a) overview, and (b) explored view.

Table 1: Properties of materials used in simulation.

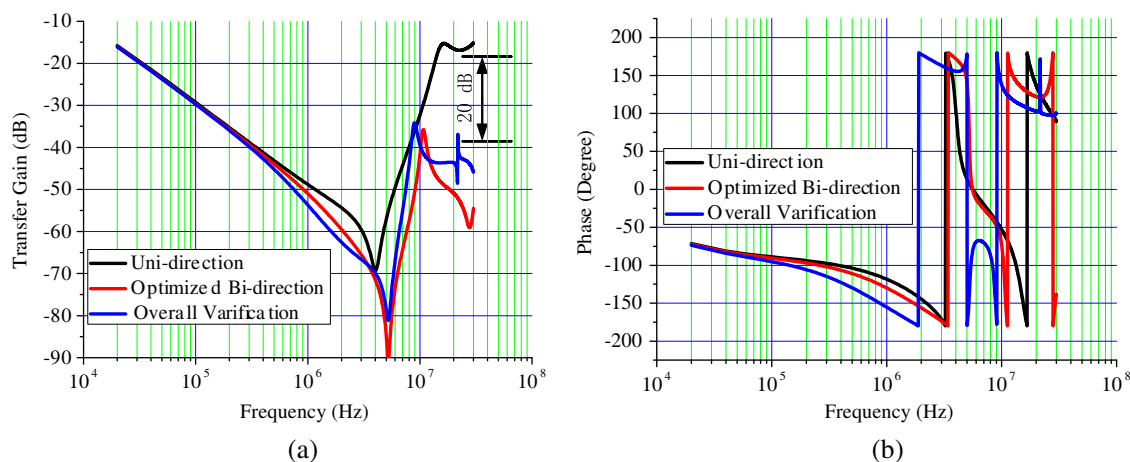| Materials	3E5 (Magnetic core)	Kapton (Insulator)	Ceramic (Dielectric)	Copper (Conductor)
Permittivity	12	3.6	84	1
Thickness	Planar E38 + PLT38	0.05 mm	0.15 mm	0.3/0.1 mm

Figure 6: CM performance comparison, (a) transfer gain comparison, and (b) phase comparison.

Table 2: Design results of the integrated CM filter.

L_{CM}(mH)	C_{CM}(nF)	EPC (pF)	Profile (cm)	Volume (cm³)
4.5	4.23	220.4	1.2	20

4. SIMULATION RESULTS

To validate the optimization result, the performance of overall integrated CM filter with optimized bi-direction winding is evaluated using FEM. The whole structure is directly mounted on print circuit boards. Its overview and explored view are shown in Figs. 5(a) and (b), respectively.

From the simulated results shown in Fig. 6, it is found that the EPC of CM inductor is effectively cancelled, giving improved CM response at high frequencies.

Design results of the integrated CM filter are given in Table 2. This section proves the previous analysis of the proposed cancellation method.

5. CONCLUSIONS

This paper introduces a technique for improving the HF performance of integrated CM filter by cancelling winding parasitic capacitance of planar CM choke. The technique only uses CM capacitance with the help of the mutual inductance between inductor winding and CM capacitor, therefore no extra component is needed. To achieve the best cancellation effect, a bi-direction winding structure is finally developed with further improved HF attenuation as compared to the initial uni-direction case. Simulation results verify the proposed cancel technique.

REFERENCES

1. Lee, F. C., J. D. van Wyk, Z. X. Liang, R. Chen, S. Wang, and B. Lu, "An integrated power electronics modular approach: concept and implementation," *Power Electronics and Motion Control Conference*, 1–13, Xi'an, China, Aug. 2004.

2. Chen, R., J. D. van Wyk, S. Wang, and W. G. Odendaal, "Planar electromagnetic integration technologies for integrated EMI filters," *Proc. of IEEE Industry Application Conference*, 1582–1588, Salt Lake City, Utah, Oct. 2003.

3. Neugebauer, T. C. and D. J. Perreault, "Parasitic capacitance cancellation in filter inductors," *Proc. of the IEEE Power Electronics Specialists Conference*, 3102–3107, Aachen, Germany, Jun. 2004.

4. Neugebauer, T. C. and D. J. Perreault, "Filters with inductance cancellation using printed circuit board transformers," *IEEE Trans. Power Electronics*, Vol. 19, No. 3, 591–602, 2004.

5. Wang, S., F. C. Lee, and J. D. van Wyk, "Inductor winding capacitance cancellation using mutual capacitance concept for noise reduction application," *IEEE Trans. Electromagnetic Compatibility*, Vol. 48, No. 2, 311–318, 2006.

6. Jiang, Y., S. Wang, F. C. Lee, and J. D. van Wyk, "Equivalent parallel capacitance cancellation for noise reduction application," *Applied Power Electronics Conference and Exposition*, 745–750, Austin, Texas, Feb. 2008.

7. Chen, R., J. D. van Wyk, S. Wang, and W. G. Odendaal, "Improving the characteristics of integrated EMI filters by embedded conductive layers," *IEEE Trans. Power Electronics*, Vol. 20, No. 3, 611–619, 2005.

A Novel Integrated EMI Filter Based on Interleaved Planar PCB Windings and Flexible Foils

Huifen Huang and Liangyong Deng
School of Electronic and Information Engineering
South China University of Technology, Guangzhou, China

Abstract— A novel integrated EMI filter structure is proposed based on the planar and flexible PCB integrated L-C winding. Overlapped and interleaved planar PCB windings with proper coupling distance are introduced which greatly reduces equivalent parallel capacitance (EPC) of CM choke and the total thickness. Using the Finite Element Analysis (FEA) software, the calculated EPC of the integrated EMI filter is less than 10pF. In addition, flexible foils are rolled around E core side legs to enhance DM inductance. Compared with the previous Integrated EMI filters, it can reduce total profile by 40%. And the parameter n (turn numbers of Flexible foils) makes the design of DM inductance more flexible. The effectiveness of these technologies has been evaluated by FEA simulation results.

1. INTRODUCTION

More and more power conversion systems use the switching mode power supply (SMPS) for high efficiency and high power density. The switching operation of these systems becomes the potentially large source of the electromagnetic interference (EMI). EMI filters are necessary to insure the electromagnetic compatibility. The conventional discrete EMI filter occupied a large room of the whole converter, and its high frequency performances are discounted by parasitic of components and layout. For the sake of the size, profile and the high frequency performance of the EMI filter, several integration techniques and modeling approaches have been developed in the past few years. Prof. Van. Wyk, J. D. proposed an electromagnetically integrated EMI filter with planar PCB, which integrates inductance and capacitance in a single module [1–3]. However, on one hand, its differential mode (DM) inductor depends on the leakage of the common mode (CM) choke, which is difficult to control. Inserting I core can enhance the leakage but increase the profile, weight and cost of the EMI filter. On the other hand, because of the unavoidable structural parasitic parameters of the distributed components, such as the EPC of CM choke windings and equivalent series inductance (ESL) of capacitors, the high frequency attenuation is affected. Although EPC of the integrated EMI filter is greatly reduced by using a staggered and interleaved winding structure [3], it complicates the manufacturing processes and increases the total thickness. Xiaofeng Wu proposed a novel integrated EMI filter based on the flexible PCB integrated L-C winding, which decreases loss and space [4, 5], but its profile is much higher.

In this paper, a novel integrated EMI filter structure is presented based on planar and flexible PCB integrated L-C windings. To reduce the EPC caused by the coupling of the two CM cascaded windings, overlapped and interleaved planar PCB winding structure is proposed as the CM choke windings. In order to increase the DM inductance of EMI filter, flexible PCB windings are introduced as the DM inductor And the turn numbers of the flexible winding is one more parameter, which makes the design of the DM inductance more flexible.

2. CANCELING OF EPC WITH INTERLEAVED PLANAR PCB WINDING

Because of the unavoidable structural parasitic parameters such as the equivalent parallel capacitance of the CM choke windings and equivalent series inductance of the equivalent capacitors, the high frequency attenuation of the EMI filter is greatly reduced. The typical schematic of EMI filter is shown in Fig. 1, including EPC of filter inductors and ESL of filter capacitors.

As shown in the well-know parallel plate capacitance calculation equation $C = \varepsilon_0 \varepsilon_r S/d$, Capacitance can be reduced by varying the three parameters: reducing plate area S; increasing distance between plates d and reducing relative permittivity ε_r of the dielectric material. Based on above principles a new overlapped and interleaved planar PCB winding structure is proposed as the CM choke windings in this paper. The cross-section view of half winding window of the proposed CM choke winding is shown in Fig. 2(a). The up winding layer is a LC hybrid winding, composed of two thick copper layers and a high permittivity ceramic layer. The down winding layer consists of two thick copper layers, two thin copper layers as ground layers, a high permittivity ceramic layer
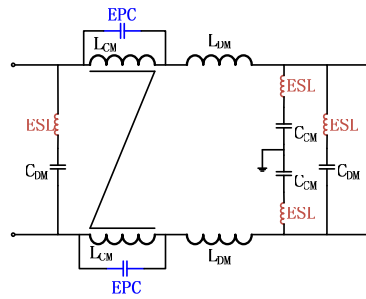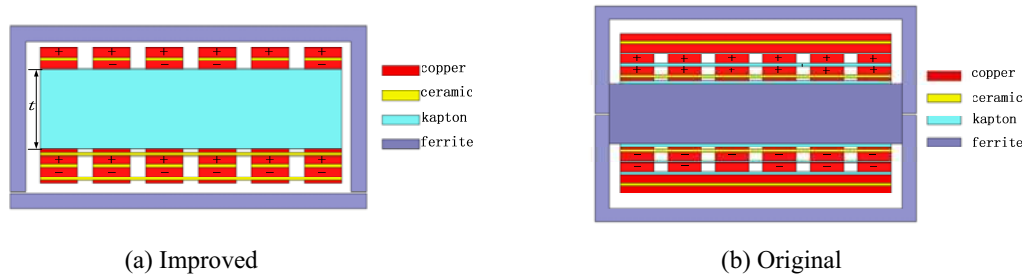
Figure 1: Schematic of EMI filter.

(a) Improved

(b) Original

Figure 2: Cross-section view of half winding window of CM choke winding (Plus, minus signs indicate the DM current direction).
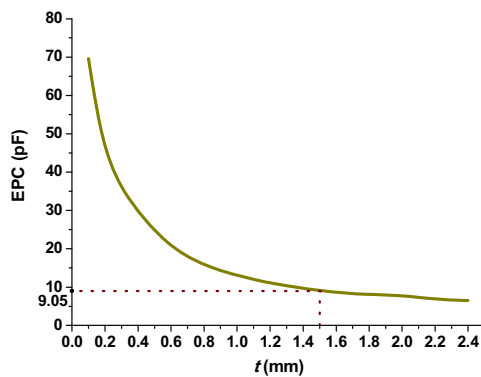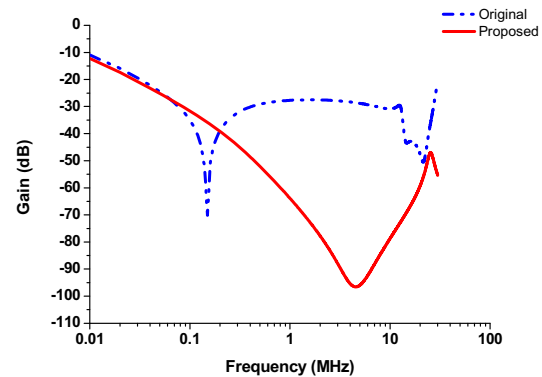

Figure 3: Calculated EPC versus t.

Figure 4: Simulated CM transfer gain of integrated EMI filter.

and a low permittivity ceramic layer. The insulation kapton is inserted between the two winding layers, and its thickness is t. We can properly increase the thickness t of the insulation kapton to greatly reduce the EPC of the CM windings.

Using the FEA software, the calculated EPC versus insulator thickness t of the proposed integrated EMI filter is shown in Fig. 3. It is found that, when t is less than 1 mm, the EPC of the integrated EMI filter decrease sharply, and when t exceeds 1 mm, the EPC changes a little as t increases.

Considering the requirement of the high frequency performance and the thickness of the filter, in this paper the thickness of the insulation kapton gets 1.5 mm. In Fig. 3, we can see that the EPC of the proposed interleaved winding structure is about 9.05 pF, nearly 8 times smaller as compared to the original structure Fig. 2(b) (about 70 pF). The simulated CM transfer gains are shown in Fig. 4. It is evident that with the proposed interleaved winding structure, the structural winding capacitance of the inductor is greatly reduced. However, at the same time, the leakage inductance under DM current excitation greatly reduces. To integrate adequate DM inductor in this structure, flexible foils are introduced to enhance DM inductance covered in next section.
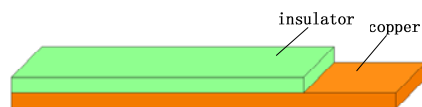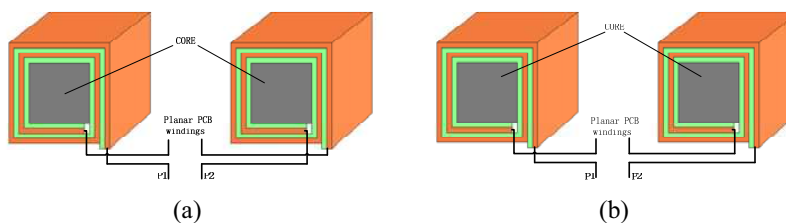
Figure 5: Flexible foil.

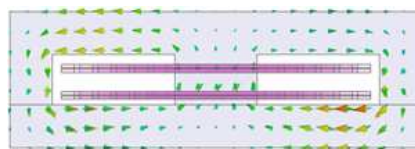Figure 6: Two connection modes of the flexible foils rolled on E core side legs.

Figure 7: Magnetic flux inside filter magnetic core of planar PCB windings under CM excitation.

Figure 8: Magnetic flux inside filter magnetic core of FML foils (a) CM excitation (b) DM excitation.

3. ENHANCEMENT OF DM INDUCTANCE WITH FLEXIBLE FOILS

Overlapped and interleaved planar PCB winding is used as the CM choke resulting in the DM inductance greatly decreased. In order to increase the DM inductance, in case of previous planar integrated EMI filter, the bulky choke should be used for the larger leakage inductor by inserting I core [1–3], However, it is very difficult to control the DM inductance and increases the thickness, cost and size of the filter. In order to solve these problems, flexible foils surrounding on the E core side legs are introduced to enhance the DM inductance in this paper. The flexible foils can be simply described in Fig. 5. It consists of an insulator layer and a copper layer. When rolling it around magnetic core, we can get sufficient. inductance.

Two connection modes of the flexible foils rolled on E core side legs are shown in Fig. 6. Magnetic flux inside filter magnetic core of planar PCB windings under CM excitation is shown in Fig. 7. In order to increase the CM inductance/capacitance ratio [2], the connection mode as shown in Fig. 6(b) is used in the design. When excited by CM currents, as shown in Fig. 8(a), the direction of the magnetic flux produced by the flexible foil windings is the same as planar PCB windings, which can enhance the CM inductance. When excited by DM currents, Fig. 8(b) shows the magnetic flux produced by the flexible foil windings, which implement the DM inductance.

4. INTEGRATED EMI FILTER

Figure 9(a) shows the cross-section view of half winding window of the novel integrated EMI filter structure. It mainly includes three parts: an EI magnetic core, planar PCB winding structure and flexible foil winding structure. The overlapped and interleaved planar PCB windings are connected as transmission line type, and the flexible foils on the side legs are connected as low-pass filter type. As a result, the CM inductors, CM capacitors and DM capacitors are integrated in the planar PCB windings. And the DM inductors are almost integrated in the flexible foil windings. Its simplified lumped parameter equivalent circuit is shown in Fig. 9(b), and L_{leak} is the leakage inductance of the CM choke windings.

The way that windings connect to each other and combine with the magnetic core is shown in Fig. 10. The two overlapped and interleaved planar PCB windings at the center leg get the same
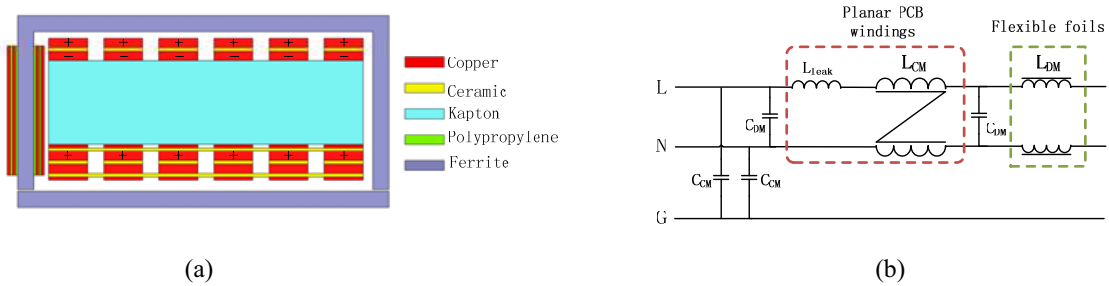

Figure 9: (a) Cross-section view of half winding window of integrated EMI filter structure (b) simplified circuit.
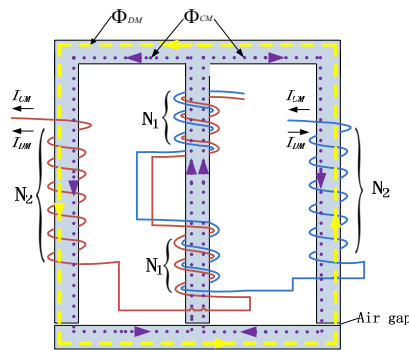

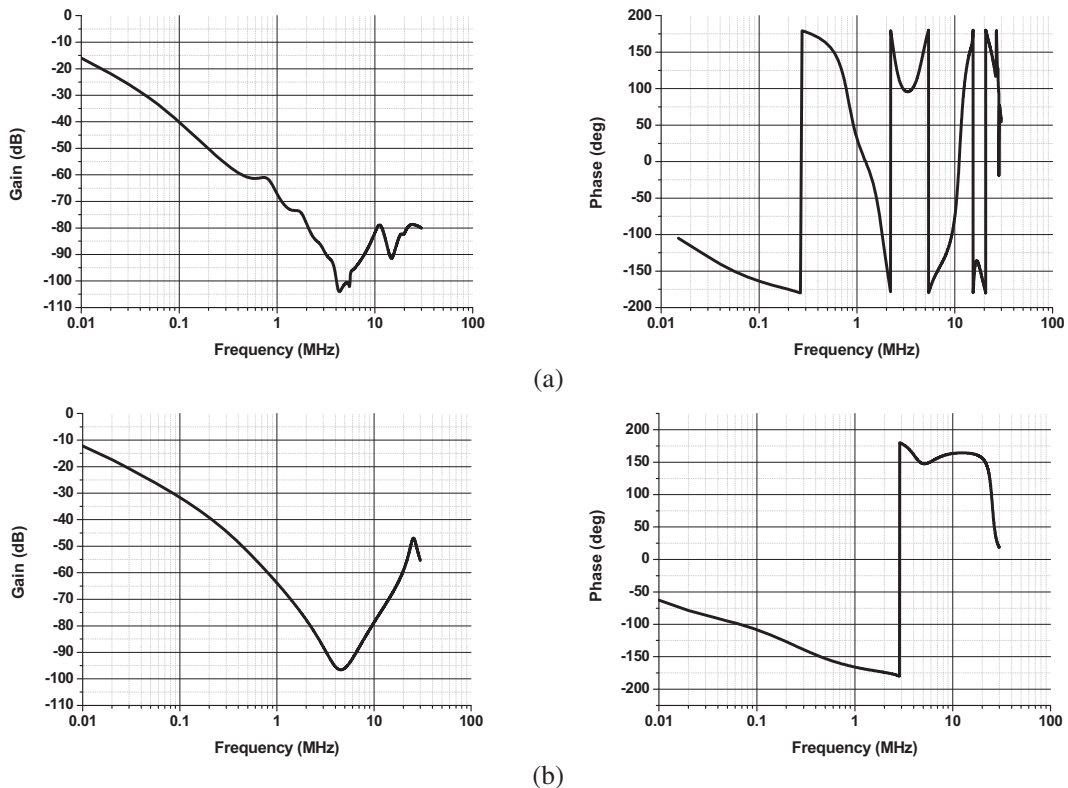Figure 10: Winding structure with magnetic core.

Figure 11: Transfer gain of integrated EMI filter (a) DM transfer gain and phase (b) CM transfer gain and phase.

turns number N1, while the two basic flexible foil windings at the side legs get the same turns number N2. Since the EI core can't eliminate the air gap, there is a designed air gap between E-I cores.

When activated by CM currents, the direction of currents that flow through the windings would follow the way like I_{CM} as shown in Fig. 10. As the currents in the planar windings of center leg and the flexible foil windings of side legs are also in the same direction, the magnetic flux produced by them would strengthen each other.

When activated by DM currents, the direction of currents that flow through the windings would follow the way like I_{CM} as shown in Fig. 10. As the currents in the planar windings of center leg are in opposite directions, the magnetic flux produced by them would cancel each other. While the currents in the flexible foil windings of side legs are in same directions, the magnetic flux produced by them would strengthen each other.

Using the FEA software, the simulated results are showed in Fig. 11. Figs. 11(a) and (b) show the DM and CM transfer gains and phases, respectively. It is noticed that the proposed integrated EMI filter has a good performance, especially in the high frequency.

5. CONCLUSION

A novel integrated EMI filter that is designed with planar PCB windings and flexible foils is presented. The filter EPC is greatly reduced with overlapped and interleaved planar winding structure, and the flexible foils are introduced to increase DM inductor. The total volume can be reduced by 40% compared with it in [1] but with better high frequency performance.

ACKNOWLEDGMENT

REFERENCES

1. Chen, R., J. D. van Wyk, S. Wang, and W. G. Odendaal, "Technology and characteristics of integrated EMI filters for switch mode power supplies," *Proc. of IEEE PESC'2004*, 4873–4880, 2004.
2. Chen, R., J. D. van Wyk, S. Wang, and W. G. Odendaal, "Integration of EMI filter for distributed power system (DPS) front-end converter," *Proc. of IEEE PESC'2003*, Vol. 3, 296–300, 2003.
3. Chen, R., J. D. van Wyk, S. Wang, and W. G. Odendaal, "Planar electromagnetic integration technologies for integrated EMI filters," *Proc. of IEEE IAS'03*, Vol. 3, 1582–1588, 2003.
4. Wu, X., D. Xu, Z. Wen, Y. Okuma, and K. Mino, "Design, modeling and improvement of integrated EMI filter with flexible multi-layer (FML) foils," *IEEE Trans. Power Electron.*, Vol. 26, No. 5, May 2011.
5. Wu, X., D. Xu, Z. Wen, Y. Okuma, and K. Mino, "Integrated EMI filter design with flexible PCB structure," *Proc. of IEEE PESC'2008*, 1613–1617, 2008.